MULTI-SCALE BEHAVIOR AT GEOMATERIAL INTERFACES

VOLUME I

By

Gregory L. Hebeler

MULTI-SCALE BEHAVIOR AT GEOMATERIAL INTERFACES

A Dissertation
Presented to
The Academic Faculty

by

Gregory L. Hebeler

In Partial Fulfillment
of the Requirements for the Degree
Doctor of Philosophy
in the School of
Civil and Environmental Engineering

Georgia Institute of Technology

August, 2005

MULTI-SCALE BEHAVIOR
AT GEOMATERIAL INTERFACES

Approved by:

Dr. J. David Frost, Chairman
School of Civil & Environmental Engineering
Georgia Institute of Technology

Dr. Susan E. Burns
School of Civil & Environmental Engineering
Georgia Institute of Technology

Dr. Paul W. Mayne
School of Civil & Environmental Engineering
Georgia Institute of Technology

Dr. Glenn J. Rix
School of Civil & Environmental Engineering
Georgia Institute of Technology

Dr. Carolyn D. Ruppel
School of Earth & Atmospheric Sciences
Georgia Institute of Technology

Date Approved: 14 June 2005

ACKNOWLEDGEMENTS

A large number of people have aided me in completing this work and their support, knowledge, and insight is greatly appreciated. I would especially like to thank my advisor, Dr. J. David Frost, for providing me the opportunity to pursue this work and for introducing me to the topic of geotechnical interfaces that has proven to provide continued intellectual stimulation and numerous technical challenges. Dr. Frost's knowledge and insight into geotechnical engineering in both practical and academic pursuits are only exceeded by his work ethic and kind hearted treatment of his colleagues, students, and co-workers. It has been a pleasure to work under his guidance, and I truly appreciate all that he has done to help me in my academic pursuits.

I would also like to thank my other committee members: my Master's advisor, Dr. Glenn J. Rix; Dr. Paul W. Mayne; Dr. Carolyn D. Ruppel, and Dr. Susan E. Burns, for their thoughtful insight and constructive comments regarding this thesis and during the long road to its completion. Additionally, to Dr. J. Carlos Santamarina, who unfortunately could not participate in the final committee, whose countless insights and questions into the fundamental behaviors of the world around us have had a tremendous influence on the content of this work. The dedication and enthusiasm for the field of geotechnical engineering, and the inherent kindness shared by all the faculty within the geosystems group at Georgia Tech have provided me with limitless motivation and have helped to make my time here extremely stimulating and enjoyable.

I am also indebted to the Department of Defense which through the National Defense Science and Engineering Graduate Fellowship program supported me over the majority of my PhD studies. Additionally, the combined support of the US National

Science Foundation and the Australian Academy of Science that provided me the exceptional opportunity to pursue research at The University of Western Australia over the summer of 2004 is gratefully acknowledged.

Sincere thanks are expressed to Dr. Jason DeJong, who passed on the original multi friction attachment and on whose earlier excellent research I relied heavily. Dr. Frost, Jason, and Matt Evans are thanked for taking time away from their own pursuits to help in the Vermont field testing across several trips from 2001 to 2004. Their good spirits and hard work made the trips productive, memorable and enjoyable. Alec McGillivray and Billy Camp are thanked for their assistance during the Mount Pleasant, SC testing. The donation of their time, insight, humor, and push equipment; without which the testing would not have been possible, is greatly appreciated. Additionally, I would like to thank Tamara Zettler of Geosyntec Consultants, Atlanta and Ethan Cargill and Billy Camp of S&ME, Charleston who allowed me to conduct MFA investigations in combination with their CPTU tests at a loose sand test site in South Carolina. My sincere gratitude is expressed to Ken Thomas, "the glue that holds the geotech group together," his limitless knowledge, experience, and insight into the best way to get things done is an immeasurable asset.

I would like to acknowledge the hard work and dedication of Andrew Myers, an undergraduate researcher from Johns Hopkins University, who I had the pleasure to work with during the summer of 2002 while he was at Georgia Tech with the NSF SURF program. Andy was instrumental in conducting and setting up the tests presented in Chapter 4 regarding the hook and loop interactions of geomembrane-geotextile systems, and his dedication and interest in the project allowed the research to be a success.

Additionally, the work of Gretchen Davidson, an undergraduate research assistant from Georgia Tech, is appreciated in helping to supplement the data set initiated in Andy's work.

I have also received countless assistance from individuals outside of Georgia Tech. Most specifically Professor Barry Lehane and James Schneider from the University of Western Australia, who welcomed me for the summer of 2004 and provided the opportunity to conduct a large portion of the field studies discussed in this thesis and to learn from their tremendous experiences regarding in situ testing and pile foundations. To James and Marc Senders who graciously opened up their house for my eight week stay in Perth. To the entire faculty, staff, students, and other visitors at UWA and COFS that welcomed me with open arms and provided me with a taste of Australian life, even though most of them were foreigners themselves. I am severely indebted to the support staff at COFS whose dedication and expertise helped make my short stay incredibly productive. To Shane and Don who were able to repeatedly fix any electrical problems that arose throughout the field tests, to Alex Duff for his countless efforts out in the rain and muck of Burswood, and to the rest of the staff that more than earned the case of "Crownies" offered as compensation for their hard work. To Dr. Fiona Chow for freely offering cutting samples from Burswood to conduct the ring shear investigations. To ProbeDrill in Western Australia for their willingness to modify their cone truck to allow the pushing of my oversized device and for their endless patience during the long hours and non-standard procedures that we requested. I also wish to thank the National Science Foundation and the Australian Academy of Science for providing the funding for my trip as part of the East Asia and Pacific Summer Institute program. Special thanks are given

to Nancy and Anise from the AAS who were more than gracious hosts during our introduction to Australia and our stay in Canberra.

I wish to thank the entire student geotechnical group here at Georgia Tech who welcomed me openly and have all become treasured friends over the past 6 years. You have all added to the colorful fabric of daily life here at Georgia Tech and your friendship and support are appreciated. To Alec, Julio, and Matt for the countless lunchtime conversations covering topics from all parts of engineering and life which have made these past six years much more fulfilling and enjoyable than they would have been otherwise. To Matt for putting up with me as an officemate for the past four years, I'll greatly miss having your vast geotechnical, computer, and culinary knowledge at my disposal everyday. Most of all to Tammy for her friendship, motivation, caring, and unending support for which I will always be grateful. I can't wait to start our life together, you make all of the hard work worthwhile.

Finally, none of this would have been possible without the love and support of my family. I would like to thank Tammy's parents Mike and Elaine Zettler for providing support and accepting me into their family. To my brother and sisters for their support and for putting up with my ramblings on engineering over the years. No words can describe the gratitude I feel towards my parents, who have always given me the freedom to pursue my goals, and their full support to allow me to achieve them. I hope to repay all that they've done for me, but if nothing else I hope to have earned their respect. I would especially like to thank my father for the opportunities he has provided me within the field of civil engineering, not just through his generosity but more importantly through the respect he has earned from others.

TABLE OF CONTENTS

VOLUME I

CHAPTER VI. IN SITU INVESTIGATIONS OF GEOTECHNICAL INTERFACE BEHAVIOR

VOLUME II

CHAPTER VII. NON STANDARD PENETRATION INVESTIGATIONS

LIST OF TABLES

LIST OF FIGURES

Chapter I
Introduction

1.1 The Role of Interfaces in Geotechnical Engineering

Interfaces exist in many forms within geotechnical engineering, including: the contact surfaces between soil and man made continua (piles, tunnels, roads, retaining walls); the interaction of adjacent geomaterials (geotextiles, geomembranes, concrete, steel; timber); the boundary between adjacent soil and rock layers, and internal shear surfaces formed within individual soil masses. Additionally, many laboratory and in situ geotechnical testing techniques are influenced by interface behavior or are specifically designed to characterize interface response. As such, interface behavior plays a primary role across the range of encountered geotechnical problems, yet the treatment of interfaces within geotechnical engineering has typically received markedly less attention than the independent assessments of internal soil behavior and geomaterial response. The relative importance of interfaces across a range of geotechnical applications and test methods is presented in Table 1-1 after DeJong (2001).

Typical geotechnical interface design methods utilized in practice are not based on a strong theoretical basis. In many cases, the behavior at an interface is simply estimated by applying a series of adjustment factors to the global macroscopic soil properties, even though interface behavior is typically controlled by characteristics of the soil and counterface on a micromechanical level. In other cases, interface design parameters are determined in the laboratory for general conditions, and then adjusted to account for site specific conditions. Both of these approaches commonly used in geotechnical practice are empirical, with little regard to the fundamental interface

mechanisms controlling site specific interface behaviors. As interfaces are prevalent throughout geotechnical engineering and are oftentimes a critical component of performance, improvement in the ability to quantify interface behavior and available methods to robustly apply those acquired interface characteristics would result in improvements towards the optimization of geotechnical designs.

1.2 Previous Research

Early research into geotechnical interfaces was able to qualitatively assess the importance of specific soil properties on the behavior of interfaces involving common construction materials (Potyondy, 1961; Butterfield and Andrawes, 1972; Brummund and Leonards, 1973). Continued research led to the quantification of the effects that continuum material properties have on geotechnical interface system response (Yoshimi and Kishida, 1981a; 1981b). The development of a framework for normalizing interface behavior by the relative size of surface properties in comparison to the contacting soil particles led to a unified approach to assess interface behavior over a range of soil and continuum material properties (Uesugi and Kishida, 1986a; 1986b). Subsequent research has focused on increasing the fundamental understanding of the mechanisms controlling interface behavior and the ability to accurately and cost effectively measure and implement interface characteristics into the design of geotechnical structures. A more detailed summary of the state of knowledge and practice regarding geotechnical interface behavior is presented in Chapter 2.

1.3 Summary and Motivation for the Current Work

As manufacturing and material processing have progressed in recent years, many new materials and construction methods have been introduced into geotechnical practice. Several examples include the continuous evolution of geosynthetic materials for use in waste containment, subgrade reinforcement, and retaining structure stability; the introduction of fiber reinforced polymers and geofoams as lightweight substitutes for conventional construction materials; and the ability to access and build structures in environments previously too harsh for earlier states of technology, such as deep underground, in deep water offshore, and on suspect ground conditions. Many of these new materials and construction methods have introduced unique interface, stress, and boundary conditions not previously encountered in geotechnical engineering.

With the continuous introduction of new interface conditions, and the often inadequate treatment of interfaces in common geotechnical practice, there exists a need for the continued assessment of fundamental interface behaviors and for robust laboratory and in situ test methods and devices to accurately characterize interface responses. The current work is focused on these needs, specifically investigating: the micromechanics of particulate - continuum shearing; the hook and loop interaction between filaments and textured continua (specifically geotextile - textured geomembrane interfaces); the laboratory and in situ measurement of interface properties; the development and utilization of test devices for the in situ characterization of geotechnical interface behavior across the full range of typically encountered materials; and the improvement of analysis and design methodologies to better incorporate interface behavior into everyday geotechnical practice.

1.4 Outline of the Dissertation

This thesis presents results and discussion generally focused on the topic of geotechnical interface behavior. The scope of the document can be grouped into four sections: (1) an introduction to previous research and the resultant state of knowledge concerning geotechnical interface behavior; (2) laboratory investigations regarding fundamental interface mechanisms focused at the micromechanical level; (3) the design and development of a new testing device to allow for the in situ characterization of geotechnical interface properties in situ within the context of an effective stress framework; and (4) results and discussion regarding the implementation of the newly developed in situ device. The thesis is organized into eight chapters following this introduction, with the content of each chapter summarized below:

Chapter 2: presents a summary of fundamental geotechnical interface behaviors, reviewing the relevant work of previous researchers regarding this topic. Fundamental concepts regarding interface behavior are then summarized, with behaviors grouped into three general categories based on the contacting particulate: coarse particulate-continuum interface behavior, fine particulate-continuum interface behavior, and filament-continuum interface behavior.

Chapter 3: begins with a summary of the importance and dependence of internal and interfacial granular behavior on micromechanical interactions. A brief discussion regarding the response of the conventional in situ interface test, the friction sleeve of the Cone Penetration Test (CPT), in contact with

granular media is presented. The remainder of the chapter focuses on presenting and discussing the results of a detailed laboratory investigation into the shear zone evolution of granular soils in contact with conventional and textured friction sleeves.

Chapter 4: presents a brief overview of the manufacture and use of geosynthetics in geotechnical engineering. This review provides the framework for the presentation of results from a laboratory study conducted to quantify the hook and loop interactions in textured geomembrane - geotextile systems, focused on two commonly used geomembrane texturing processes.

Chapter 5: provides a brief history of cone penetration use in geotechnics. A critical assessment of the current CPT device is presented, specifically focused on the friction sleeve (f_s) measurement. The recently developed device to allow for the simultaneous characterization of interface properties as a function of surface characteristics, the Multi Friction Attachment (MFA) developed by DeJong and Frost (Frost and DeJong, 2001; DeJong and Frost, 2002; Frost and DeJong, 2005), is introduced. A short summary of typical MFA responses is presented to provide a framework to discuss the motivation for developing a new in situ testing device allowing for the effective stress characterization of interface behavior in situ. The design and development of the Multi Piezo Friction Attachment (MPFA) is then presented in detail.

Chapter 6: summarizes the in situ investigations into interface behavior conducted with the MFA and MPFA during the current work. Tests were conducted across a range of geologic conditions, including: a clean sand site in Vermont, USA; a very loose sand site in South Carolina, USA; a structured calcareous clay geology common to the coast of South Carolina, USA; a silica sand site in Perth, Western Australia; a calcareous sand site along the coast of the Indian Ocean 100 km north of Perth, Western Australia; and a soft marine clay in Perth; Western Australia. The results of the in situ interface tests are compared to typical behaviors observed in the laboratory and for geotechnical structures placed in similar geologic conditions. The results of textured shearing from the MFA and MPFA devices are applied to the estimation of destructured values of conventional CPT tip and sleeve measurements in order to assess the level of cementation and structure within virgin in situ conditions. Lastly, a new normalized parameter is introduced based on fundamental interface shearing concepts and the observed trends within the measured in situ interface results. This parameter is applied to the current results across the range of tested materials, and compared to conventional CPT soil classification schemes.

Chapter 7: presents the results of MFA and MPFA investigations using non-standard test procedures. The non-standard procedures incorporated into the current investigations include assessments of: variable penetration rate response, penetrometer response to angled (non-vertical) penetration, small and large

amplitude in situ cycling, the use of the MFA and MPFA devices for model pile investigations; and the utilization of and benefits to monitoring extraction response.

Chapter 8: presents the results of the piezo sensor responses from the MPFA investigations conducted over the course of the current study. Responses are discussed and analyzed based on the measurement condition, including: during conventional (steady-state) penetration; during equalization of the excess pore pressures generated during insertion, monotonic, or cyclic loading; and for loading after or during equalization. These groupings of response were chosen to parallel the life cycle of pile foundations, and responses are compared to previous measurements and analysis methods where available.

Chapter 9: provides a brief summary of the main conclusions and advancements made during the current study. Additionally, recommendations for future work are provided.

Supplementary information is provided in the Appendix:

Appendix A: presents plots of all MFA and MPFA soundings conducted during the current work.

Table 1-1. The Importance of Interfaces in Geotechnical Engineering (DeJong, 2001).

Applications	Significance	Tests	Significance
Canal Liners	High	*In-Situ Tests*	
Foundations		CPT (f_s, q_c)	High / Low
Deep	High	DMT	Low
Shallow	Low	PMT	Low
Landfills	High	SPT	High
Leach Ponds	High	Thin-Walled Sampler	High
Micro-Tunneling	High	*Laboratory Tests*	
Pavements	Low	Casagrande Dish	Medium
Retaining Structures		Consolidometer	Medium
Anchored	High	Interface Shear	High
Gravity	Low	Resonant Column	High
Reinforced	High	Compaction	Low
Soil Nailing	High	Torsional Shear	High
Slope Stability	High	Triaxial	Medium

Chapter II
Review of Geotechnical Interface Behavior

2.1 Introduction

The geotechnical community has realized for many years the crucial role that interfaces play in the response of geotechnical systems. With interface shearing constituting a primary or secondary component in most geotechnical applications and testing methods, it is imperative to possess a strong fundamental understanding of interface shearing mechanisms. Along these lines, a number of researchers have made significant contributions to the understanding of geotechnical interface behavior. Published engineering literature considering the treatment of interfaces in geotechnical design dates back to Coulomb (1773) and his formal mathematical treatment of friction as a function of normal stress, known as Coulombian friction. The beginnings of modern geotechnical interface research were mainly focused on pile foundation applications. The first laboratory investigations, such as those by Potyondy (1961), Butterfield and Andrawes (1972), and Brumund and Leonards (1973) demonstrated the importance of soil properties such as moisture content, particle angularity, particle size, mineralogy, and normal load on interface strength. Continued research, pioneered by Japanese researchers Kishida, Uesugi, and Yoshimi (Yoshimi and Kishida, 1981a; 1981b; Uesugi and Kishida, 1986a; 1986b; Kishida and Uesugi, 1987; Uesugi et al., 1988; Uesugi et al., 1989; Uesugi et al., 1990) began to quantify the importance of continuum material properties, such as surface roughness, on geotechnical interface behavior.

The two main geomaterial types that come into contact with structural elements in common geotechnical applications can be categorized as fine particles and coarse

particles, with filaments being an additional interfacial unit common in some geotechnical areas. Fine particles consist mainly of clays, silts, and organic materials. Coarse particles consist mainly of sands, gravels, and synthetic particulates (e.g. tire chips). Filaments are typically synthetic or metal fabrics and fibers, with typical examples consisting of geotextiles, geonets, and wire meshing. In subsequent discussions in this thesis the term particulate will be used to generally describe all three of the above material categories. A geotechnical or structural member in contact with any of these materials will be denoted as the counterface, and common examples of counterface materials include concrete, steel, fiber reinforced polymer (FRP), geosynthetics, reinforcing strips and fibers, timber, asphalt, and clay pipes to list some of the more common. Fundamental geotechnical interface concepts can also be used to describe the behavior of shear zones within homogeneous soil masses or along lithological boundaries, as discussed by Evans (2005). Compilations of the factors affecting typical geotechnical interface behavior for coarse-grained, fine-grained, and filament materials are shown in Table 2-1 respectively.

As a result of the large role interfaces play in geotechnical systems, the reliable prediction of geotechnical interface behavior is essential for sound and cost effective geotechnical design. While tremendous amounts of geotechnical research has been undertaken to study the behavior of soil masses under a variety of stress-strain conditions, geotechnical interfaces have received markedly less attention. In many cases, the behavior at the interface is simply estimated by applying a series of adjustment factors to the global soil properties. In other cases, an interface strength is determined in the laboratory, and then adjusted to account for site specific conditions. Both of these

approaches are empirical with little theoretical underpinning and depend highly on appropriate engineering judgment regarding numerous key issues including subsurface variability, state of stress, and counterface surface properties, among others. Clearly, improvement in the ability to accurately predict the behavior of geotechnical interfaces is necessary before geotechnical structures can be optimally designed.

2.2 Fundamental Interface Shearing Mechanisms

The properties of a particulate assembly and counterface may become altered as a result of shearing. The contacting particulate assembly can deform partially or completely in one of two mechanisms: sliding and shearing. Pure sliding is characterized by translation with respect to the counterface with no internal particle rearrangement. Pure sliding of a particulate assembly along a counterface can occur under the following conditions: (1) the surface is smooth relative to the contacting particle size, (2) the normal stress remains below the critical stress level, thereby preventing particles from embedding in the surface or fracturing, and (3) the surface is sufficiently hard so that abrasive wear is negligible during shear. In the case of pure sliding, interface friction is generated solely due to sliding at the particle-counterface contacts and therefore volume change in the adjacent particulate structure is negligible.

Shearing of the particulate structure occurs to varying degrees when one of the conditions for pure sliding is not met. A change in the continuum surface roughness, the confining stress, the continuum hardness, or particulate shape can result in sliding at the particle-counterface contacts no longer being the shearing mechanism with the lowest friction coefficient (i.e. requiring the minimum energy). When internal shearing within the particulate medium provides less resistance to shear than sliding at the interface at

least partial shear will occur. For example, for shear against smooth surfaces at low normal stress, sliding at the counterface contacts provides the least resistance, as sliding can occur with essentially no particle rearrangement and therefore no volume dilation or contraction. However, if the surface roughness is increased, sliding at the interface results in higher frictional resistance as particles must displace into the contacting particulate structure to overcome surface asperities. This translational movement requires the contacting particulate structure to deform to allow the particle(s) to pass over the asperity. In conditions where both sliding and shearing occur simultaneously, the internal shear deformation of the particulate structure permits sliding at the interface contacts. The case of pure interface shearing is analogous to shearing within a global particulate mass, and occurs when the interface resistance is higher than the internal resistance over the entire contact area, essentially clogging the interface.

2.3 Review of Coarse Grained Interface (CGI) Behavior

Of the three material categories noted above, interfaces involving coarse grained particles have received by far the most research and practical attention. The focus on coarse grained interface behavior is warranted as interfaces of this type are highly dependant on the properties of both the counterface and particulate material, and can vary greatly from the global response of the particulate assembly typically used as a basis for empirical interface strength estimates.

2.3.1 Effect of Counterface Properties on CGI Behavior

Of the properties shown to have an effect on CGI behavior (Table 2-1), counterface surface roughness is considered to be one of the most important, as variations

in counterface roughness have the potential to alter interface strength by 100% or more. Early adjustment factors to account for varying levels of counterface roughness were limited to qualitative assessments due to a lack of available methods to quantitatively characterize counterface surface properties. The introduction and use of modern surface characterization techniques, including surface profiling and optical image analysis have provided a means to accurately relate interface behavior to changes in surface properties. The most commonly accepted parameters for characterizing surface roughness in the geotechnical community are R_{max} and R_a, with a complete list of roughness parameters shown in Table 2-2. R_{max} is the absolute vertical distance between the highest peak and lowest valley along a surface profile, and is often sampled over length intervals on the order of the mean particle diameter. Average roughness, R_a is defined as,

$$R_a = \frac{1}{L}\int_0^L |z| dx \qquad \text{(Eq. 1-1)}$$

where L is the sample length and z is the absolute height of the profile from the mean line. A thorough discussion of measurement techniques and international standards for surface roughness characterization can be found in Ward (1999), with a detailed discussion focused on geotechnical applications available in DeJong et al. (2002).

Quantifying the role of surface roughness for particulate-continuum interfaces was pioneered by Yoshimi and Kishida (1981a, 1981b) and continued by Uesugi and Kishida (1986a, 1986b), in their laboratory work on sand-steel interfaces. The behavior qualitatively noted by earlier researchers was quantified by a series of interface tests shearing sand against steel plates of varying texture. The results were shown to be

applicable over a range of particle sizes by the introduction of a normalized roughness parameter R_n,

$$R_n = \frac{R_{\max}\left(L = D_{50}\right)}{D_{50}} \qquad \text{(Eq. 2-2)}$$

Using R_n to characterize the surface roughness of the tested counterfaces, the surface roughness-interface shear relationship was found to be bilinear and unique for given particulate-counterface pairings over a large range of coarse particle sizes (Figure 2-1). The interface strength was shown to increase linearly, proportional to the increase in normalized roughness below a certain "critical" roughness value. Above the critical roughness, shearing was observed to transfer away from the interface into the adjacent soil mass with a measured interface strength bounded by the internal shear resistance of the contacting soil.

The bilinear interface shear relationship observed by Uesugi and Kishida (1986b) has been shown to exist for a number of other geomaterial surfaces, including geomembranes, concrete, timber, and fiber reinforced polymers (Uesugi et al., 1988, Dove et al., 1996; Frost and Han, 1999; DeJong et al., 2000). Furthermore, the bilinear relationship has been shown to exist for a number of other surface roughness parameters (Lee, 1998). The existence of this fundamental particulate-continuum interface relationship, regardless of roughness parameter and geomaterial surface type, provides the opportunity to determine the full interface behavior of a soil deposit in situ without prior knowledge of the soil particle characteristics (DeJong and Frost, 2002).

In addition to surface roughness, counterface hardness can also have a significant effect on interface strength and behavior. The ratio of particulate to counterface hardness, in combination with other factors, has been identified to determine the type of contact deformation (e.g. elastic versus plastic), the type of surficial wear (e.g. abrasive versus adhesive), and the size of particulate-continuum contacts, among others. O'Rourke et al. (1990) demonstrated the effect of hardness through interface shear tests with sand and a series of smooth HDPE and PVC geomembranes and pipes. Interface strength was shown to decrease with increasing material hardness, with particle sliding being the primary mechanism during shear against relatively hard materials and particle rolling and plowing mechanisms dominating during shearing against softer materials. Surface changes were observed through the analysis of Scanning Electron Microscope (SEM) images before and after shearing.

Dove and Frost (1999) demonstrated the coupled relationship between normal stress and material hardness for granular materials sheared against relatively smooth surfaces, as shown in Figure 2-2. They showed that for a given hardness, the interface strength at low stress levels will initially decrease as (global) normal stress increases. In this region, the number and area of particles contacting the surface increases with the increasing normal force, causing a decrease in the contact stresses and resulting in lower interface friction. At a critical applied normal stress, the number and area of contacts along the surface reaches a maximum value, causing any additional increase in global normal stress to be directly transmitted to the particle-surface contacts.

Plowing occurs when a local contact stress at the interface exceeds the level required to damage the surface, forcing particles to penetrate the surface and remove or

displace material from the surface during translation. When plowing occurs in addition to sliding, the force required to shear the granular medium relative to the surface increases, resulting in increased interface friction. This observed increase in interface friction is especially evident for softer geomaterials, such as geomembranes, and less significant for harder geomaterials such as steel. Dove and Frost (1999) also found that the dependence of interface behavior on surface hardness appears to be decreased for textured surfaces, as texture seems to disrupt the mechanisms by which particles plow into the surface.

Frost et al. (2002) extended the above experimental studies that showed both continuum surface roughness and hardness to have marked effects on the magnitude of interface friction, through numerical simulations of the interaction of counterface roughness and hardness on interface behavior. They used a discrete element model (DEM) to investigate changes in interface behavior over a wide range of surface properties. The results of their numerical modeling showed a distinct coupled dependence of surface roughness and hardness, represented by the surface shown in Figure 2-3. The above research has shown primary mechanisms dependent on the counterface properties include: the location of failure localization (either at the interface or within the adjacent soil body), the mode of particle movement (rolling or sliding), and the degree of particle embedment and/or plowing (extent of surface damage). A detailed look at the microlevel deformation of particulate assemblies during interface shear is discussed at length in Chapter 4, with additional accounts of particulate-continuum interface behavior found in DeJong (2000).

2.3.2 Effect of Particulate Properties on CGI Behavior

A general list of the primary particulate properties that can effect CGI behavior was shown in Table 2-1. Zettler et al. (2000) extended the above work on counterface

properties by investigating the effects of varying the particulate material properties. They conducted interface shear experiments with various sands and glass beads sheared against a smooth HDPE geomembrane. Results confirmed that the critical stress is dependent on the particulate angularity and showed it to increase with decreasing angularity. Figure 2-2, showed the analogous increase in interface strength that can be attributed to increased particle angularity as also seen in the shear behavior of particulate assemblies. The work of Zettler et al. (2000) additionally showed variations in particle size (within the range of coarse particulates) to have minimal effect on both the critical stress and interface behavior of smooth interfaces. Figure 2-1, previously showed the dependence of interface behavior on the particle size as compared to the size of surface texture, for rough surfaces. This relationship indicates a decrease in interface friction with increased particle size for rough interfaces.

With respect to the progression of particulate densities along an interface as a result of shearing presented in 2.3.1, it is seen that the initial density of the particulate, both globally and locally at the interface, can have an effect on the initial interface behavior. As such, denser initial particle assemblies will demonstrate higher interface strengths at shear levels lower than the residual state. Any means that serve to strengthen the initial structure of the particle assembly, most typically cementation, will increase the interface strength as both particle rotation and rearrangement are restrained. As global cementation breaks down, it results in increased shear resistance against rough surfaces as individual bonds between particles partially remain forming particle clumps that frustrate particle rearrangement and encourage dilation during shear in a similar mechanism to increased particle angularity.

The mineral (or chemical in the case of synthetic particulates) composition of the particulate material can also affect CGI behavior. Al Douri and Poulos (1992) showed results from static and cyclic interface shear tests on calcareous and silica sands. Their results showed that as a result of the softer mineral composition of calcareous materials, that both contact area and density increase more readily than for comparable silica sands. As such, since the stiffness of the individual particulates is directly related to the both the transfer of global stress locally to the contacts and the propensity for dilation, softer particles tend to exhibit lower interface strengths, holding other parameters constant. The effect of varying particulate (and surface) properties on particulate deformation at continuum interfaces is discussed in detail in Chapter 4.

2.3.3 Effect of Boundary Conditions on CGI Behavior

2.3.3.1 Introduction

Boundary conditions, such as the global and local stress state, rate and direction of shear, and interface orientation (or test method in the case of experimental or in situ interface testing) can all have a profound effect on CGI behavior.

2.3.3.2 Normal Stress

Normal stress has a large influence on the strength of CGIs, however, as with other frictional materials, the interface strength can be directly related to the normal stress in most cases through a fundamental Mohr-Coulomb type frictional relationship. This mechanism is complicated for interfaces as the global stress may differ from the local contact stresses present at the interface. As presented in Section 2.3.1, the relationship between normal stress and interface shear resistance, known as the interface friction

angle δ, can vary as a function of global normal stress due to changes in the interface contact stresses or through changes to the surface or particulate properties through plowing or particle breakage mechanisms. However, for most common geotechnical interface material combinations and stress conditions, the interface friction angle is linearly related to normal stress, and fundamental frictional concepts and mechanisms are applicable.

2.3.3.3 Shear Condition

A number of interface shearing conditions occur in laboratory experiments and in situ geotechnical applications. Table 2-3 (after Paikowsky et al., 1995) illustrates the main laboratory interface shear configurations, with typical in situ configurations consisting of pile foundations, retaining walls and systems, landfill liner systems, and roadway reinforcement systems. Each laboratory configuration has advantages and disadvantages, and the correct choice of testing equipment depends on the specific goals of the laboratory study and the in situ application for which the data will be used. The annular stress apparatus is considered the least robust configuration, as the normal stress at the interface is unknown and stress concentrations often exist near the boundary. The unknown interface normal stress is also a primary unknown in pile design, and as such axisymmetric configurations that simulate known installation and boundary conditions can be useful indicators of pile interface response. The direct shear configuration is the most common and easiest to operate proficiently. However, the deformation components (sliding and shearing) can not be separated into comprising components, and results have shown variability with the placement of the continuum surface above or below the particulate as a result of particle leakage. The simple shear configuration allows for the

separation of displacement components, while yielding comparable results to the more common direct shear configuration (Uesugi and Kishida, 1986b). The ring shear configuration, while more common for fine grained material and interface testing and more complex to operate, is the preferred configuration for CGI testing to large displacements (Kishida and Uesugi, 1987b).

In situ interface friction response sometimes differs from conventional laboratory direct shear results due to changes in the local stress at the interface caused by localized volume change (contraction or dilation) at the interface (Boulon, 1989). For most in situ conditions with local volume change at the interface, the surrounding soil can be considered as an elastic confinement media, and the volume change is termed "confined dilatancy" (Porcino et al., 2003). Confined dilatancy can be simulated in the laboratory by modifying the global stress controls to provide a constant normal stiffness (CNS) condition instead of the traditional constant normal load (CNL) condition (Boulon and Foray, 1986; Ooi and Carter, 1987). A unique relationship between CNS and CNL test results does not exist; rather CNS tests tend to highlight the volume change tendency of the given particulate – counterface combination (increased τ_{ult} if dilative, decreased τ_{ult} if contractive) and more accurately simulate the stress conditions typically found in situ for piling and anchor interfaces (Porcino et al., 2003).

2.3.3.4 Strain Rate / Drainage Condition

Consistent with the internal behavior of coarse particulate assemblies, CGI behavior is not significantly affected by changes in strain rate or drainage condition. However, in a study on the response of CGIs to dynamic loading, Brumund and Leonards (1973) found divergence between the monotonic and dynamic friction coefficients.

Brumund and Leonards used an axisymmetric rod shear device, and found an approximately 20% increase in the "dynamic" or impulse load resistance of most CGIs. They did note that interfaces with very low initial interface resistance, e.g. Teflon and graphite counterfaces, showed an even higher increase in dynamic δ as compared to monotonic tests. Increased dynamic CGI stiffness is also noted in the context of dynamic pile loading and testing. A thorough discussion of pile shaft response under dynamic loading as compared to static loading is provided by Randolph (2000).

2.3.3.5 Cycling

Cyclic load considerations can be significant to a number of CGI applications, especially in areas of high seismicity and offshore. As such, a number of laboratory and field studies have investigated the effect of cycling, on interface behavior. Desai et al. (1985) used a direct interface shear device to measure the two-way cyclic response of sand versus various structural and rock counterfaces. They found that the normal stress, initial relative soil density, and amplitude and number of load cycles all had an influence on CGI response. Interface stiffness was shown to increase with increasing normal stress, and also with increased number of cycles, with the rate of increase of initially loose samples exceeding initially dense samples and all samples converging to a unique interface friction response after repeated cycling on the order of 100 cycles.

All of the laboratory tests in the study by Desai et al. (1985) consisted of two-way cycling with shear amplitudes lower than the shear displacement at peak during monotonic loading. As discussed above, minimal sliding occurs before peak shear response for CGIs as shown by Uesugi and Kishida (1986a). To investigate the cyclic response of CGIs when sliding does occur, Uesugi et al., (1989) conducted a series of

simple shear interface tests under both one and two-way loading conditions with strain amplitudes greater than the strain at peak under monotonic conditions. Under one-way cyclic loading Uesugi et al. (1989) found that the monotonic and one-way cyclic friction responses were similar, with the monotonic response providing an upper envelope for the one-way cyclic response. Sliding and shear displacement components were measured separately, and negligible interface sliding was observed during unloading and reloading. For tests under two-way cyclic loading, interface sliding was a low percentage of the total displacement for early cycles, with sliding constituting a majority of the displacement after several two-way load cycles. Under two-way cycling, interface sliding was substantial during reloading stages, and was attributed to the inelastic deformation of the shear zone during stress reversal. Once sliding was observed to occur for sand-steel interfaces, δ reduced from the δ_{max} observed in the initial sliding, and converged to a value close to the residual shear stress ratio upon repeated cycling. The residual cyclic friction coefficient was observed to become constant irrespective of the normalized roughness, except for the smoothest surface ($R_n = 3 \times 10^{-3}$) where residual δ_{cyc} was lower for sands that showed minimal crushing. This behavior is divergent from monotonic CGI behavior which shows a bilinear relationship between δ and R_n as shown in Figure 2-1. Particle crushing along the interface was observed to varying degrees for the three sands tested and was found to have an effect on the cyclic CGI behavior, with increased crushing increasing the residual δ_{cyc}.

One of the primary applications of cyclic CGI behavior involves the response of pile shaft friction under cycling. Al-Douri and Poulos (1991) related CGI experiments to pile behavior and proposed that in the same manner observed for monotonic pile response,

the volume and stress changes at the interface are primary factors controlling shaft friction response. They summarize that soils of all densities will tend to contract under cyclic loading, leading to gradual reductions in skin friction. In a comparison of calcareous to silica sands, they found that soils that experience large volume reductions during shear due to crushing or other mechanisms (e.g. calcareous soils) will experience larger shaft friction reductions than stiffer matrix materials (e.g. silica sands). The manual for the computer program RATZ (Load Transfer Analysis of Axially Loaded Piles), Randolph (2003), describes the treatment of pile shaft friction under cyclic loading in great detail.

2.4 Review of Fine Grained Interface (FGI) Behavior

Whereas, both internal and interfacial coarse grained particulate behavior is governed predominantly by mechanical forces, fine grained particulates are additionally influenced by chemical, electrical, and hydraulic forces. Furthermore, as the counterface materials used in contact with coarse and fine grained particulates are typically similar, the large change in relative scale between the size of individual particulates and counterface surface topography also plays a significant role in governing FGI behavior. Average surface textures of common geomaterials are compared to the range of soil particle sizes in Figure 2-4.

2.4.1 Effect of Counterface Properties on FGI Behavior

As compared to coarse particulates, interfaces with fine particulates as the contacting media are less dependent on the properties of the counterface material. As stated above this is mainly due to the difference in the size, hardness, and controlling

mechanisms of fine grained materials, rather than changes in the types of counterface materials used in common FGI geosystems. Many of the fundamental mechanisms presented in Section 2.3.1 regarding CGI behavior can also be applied to fine grained interfaces. However, the concept of normalizing roughness using only the representative particle size (R_n) is less valid, and more difficult for fine grained materials, as factors such as mineralogy, water content, plasticity, stress and strain history, and particle size distribution all have significant impacts on behavior. Laboratory tests on fine grained materials have shown that R_n is often not a good indicator of interface behavior, as D_{50} becomes an inappropriate parameter to define the "dominant" grain size when a material is composed of a large range of particle sizes (Lemos and Vaughn, 2000). Additionally, since macro roughness is much less significant in FGI behavior, R_a is often the preferred surface roughness parameter for counterfaces in contact with fine grained materials as it better represents the amount of micro roughness on a surface.

As with CGIs, rougher interfaces encourage failure within the contacting fine grained media and mobilize a greater portion of the internal shear resistance (ϕ'). The bilinear relationship between interface friction and counterface roughness, shown in Figure 2-1 for CGIs, has been validated for FGIs in a number of experimental studies (Tsubakihara and Kishida, 1993; Tsubakihara et al., 1993; Sun et al., 2003). With the critical roughness required to mobilize the full internal friction of fine grained materials found to be on the order of 10 μm (R_{max}). Roughnesses above the critical level for a particular material combination are shown to exhibit limited sliding at the interface, with a failure zone existing within the soil mass. For counterfaces with roughnesses lower than the critical value, some amount of sliding at the interface will be present, with the

limiting case of pure sliding occurring for some surfaces of very low roughness. Tsubakihara and Kishida (1993) quantified the proportions of sliding and shearing in FGIs for a range of roughness values using a simple shear interface apparatus. These experiments were able to show that the large sliding deformations always occurred post-peak and that the stress-strain behavior of FGIs both above and below the critical roughness value behaved similarly at strain levels lower than the peak resistance.

Interface shear strengths for FGIs can be less than half the internal shear resistance of the fine grained material. This is especially true for very smooth interfaces, such as painted steel piles, as shown in the significantly reduced capacity of painted vs. exposed steel piles and caissons installed at the Girasol site off the coast of Angola (Colliat and Dendani, 2002). It should be noted that the above concepts and mechanisms hold true for counterfaces with relatively homogenous roughness distributions. For surfaces with highly variable levels of roughness across a surface section (such as smooth surfaces with intermittent large surface asperities or gouges), the interface behavior may be heterogeneous across the surface with the global behavior exhibiting a combined response equaling the superposition of the represented mechanisms. Other surface properties, including surface hardness, have been shown to have little effect on FGI behavior (Stark et al., 1996).

2.4.2 Effect of Particulate Properties on FGI Behavior

2.4.2.1 Clay – Continuum Interfaces

FGI shearing is primarily effected by the same mechanisms governing the internal shear of fine grained soils. As such, changes in fine grained soil properties will affect

interface behavior similarly to internal shear, with both peak and residual conditions having significant influence on design considerations. Unless otherwise specified, the term FGI, refers to the case of fine grained material (specifically clay) without significant coarse particle inclusions. Mixed and intermediate (silt) particulate interface behavior is discussed separately following the presentation of FGI behavior.

Clay mineralogy is probably the most important particulate property controlling FGI behavior as mineralogy defines several other important clay properties such as specific surface, plasticity, and particle shape, among others. As an example of the strong influence of mineralogy, note that for similar steel interfaces pure rock flour (a major constituent of Bothkennar clay) exhibits a residual interface friction angle of $\delta_{res} \approx 33°$ while montmorillonite clay (constituted of platy particles) exhibits a $\delta_{res} \approx 7°$ (Gourvenec et al., 2004). Plasticity is also associated with mineralogy as shown in Casagrande's classical plasticity chart, and increased plasticity has been shown to relate to a reduction in both the internal (Lupini et al., 1981) and interface (Koerner et al., 1986; Lemos and Vaughn, 2000) friction angles. However, it has been noted by the above researchers that plasticity–friction relationships should be used with caution as the results will only be globally consistent if the relationship follows from more fundamental underlying mechanisms.

Other soil properties also have an affect on FGI behavior as shown in Table 2-2. Increasing the water content within the shear zone has been shown to decrease the shear strength holding other parameters constant (Seed and Boulanger, 1991), and can result in large variations in the measured ultimate residual resistance if free water is available to samples that experience volume change during shear. Samples that are partially saturated have shown large increases in interface strength as a result of the increased interparticle

capillary forces (Fishman and Pal, 1994). Cementation, diagenesis, and other fabric stabilizations of clay soils can also significantly increase the peak resistance of FGIs. However, these increases are subject to large, brittle post peak degradations upon large displacement due to the breakdown of the stabilized structure.

The stress and strain history of a clay in contact with a continuum interface has been shown to affect FGI behavior. Tsubakihara and Kishida (1993) found that the FGI shear stress for normally consolidated (NC) clays normalized by the consolidation pressure, τ/p_c, was independent of consolidation pressure for all levels of steel roughness, as is well known for internal shear behavior. Additionally, as is the case for internal clay shearing, FGI shear strength increases with increasing over consolidation ratio (OCR). In general, the concepts of critical state (CS) theory apply to FGI behavior as residual interface shearing mechanisms are very similar to those for internal fine grained shearing, and the interface serves to mobilize a portion or all of the internal soil resistance.

The most common mechanism for the long established post-peak drop in drained shear strength, or brittleness, observed in fine grained soils and FGIs is the orientation of platy clay particulates parallel to the direction of shear (Skempton, 1964; Tika, 1991). The displacement necessary to reach the residual condition for FGIs is much less than for internal shearing and tends to decrease with decreasing surface roughness (Lemos and Vaughn, 2000). The planar geometry (especially of very smooth surfaces) and relative hardness of typical counterfaces promote particle alignment and provide maximum reactive force, respectively, to provide an ideal condition for particle orientation. Clay minerals with more rod and rounded shaped particles have been shown to have significantly lower sensitivity (τ_{peak}/τ_{res}) (Lupini et al., 1981).

2.4.2.2 Intermediate Soil – Continuum Interfaces

While clay fraction is often considered a significant indicator of FGI behavior, the inclusion of intermediate (silt) and coarse (sand) particles within a clay soil can greatly affect interface behavior and are presented as a separate class of interfaces. For pure clay interfaces, Tsubakihara and Kishida (1993) found only two shear conditions. When the counterface was smoother than the critical roughness, pure interface sliding occurred following the peak strength, whereas pure internal shearing of the clay occurred for roughnesses equal to and greater than the critical value. During experiments with sand-clay mixtures, a third transitional shearing mode often occurred, comprised of simultaneous mixed sliding and shearing. This concept is analogous to the mixed shearing mechanism created by a smooth base substrate having intermittent large asperities or gouges, as described in Section 2.4.1. Dependent on the clay fraction (% of clay as a function of mass) the residual behavior of a mixed soil sample will typically exhibit the behavior of either the fine or coarse grained material, with a critical range of clay fractions existing for which both mechanisms will occur simultaneously and global behavior represented by the superposition of the local responses. Peak behavior is more likely to be represented by mixed mode shearing as a minimum displacement is often needed for one mechanism to dominate. This is typically the result of a minimum strain required to allow for the necessary formation of a zone of segregated soil type within the particulate assembly or adjacent to the interface.

As interface and internal friction are typically larger for coarse particles, the residual interface friction of mixed particulates typically increases with decreasing clay fraction (Tsubakihara et al., 1993; Tika and Hutchinson, 1999; Lemos and Vaughn, 2000;

Sun et al., 2003). Lupini et al. (1981) reported that the clay fraction is the primary parameter that defines the residual internal interface strength of clay soils containing silt or sand. However, Tsubakihara et al. (1993) found very little difference in the peak interface strength of sand-clay mixtures down to clay fractions of 14%. They did note a decrease in volumetric strain within a soil mass during interface shearing when the clay fraction was reduced to the point where silt and sand particles could form a solid skeleton. As expected decreasing the clay fraction also serves to increase the critical roughness below which interface sliding occurs. Tsubakihara et al. (1993) also found that post peak brittleness was reduced as clay fraction decreased, and that at a mixture of 14% Kawasaki clay, 19% silt, and 67% Toyoura sand showed no difference between the peak and residual friction angles. This corresponds with Skempton's (1985) finding that there was no appreciable drop in strength from peak to residual for NC soils with clay fractions less than 25%.

Tests on the internal shear strength of Keuper marl, a soil in which clay minerals are aggregated in stable, silt-sized particles, showed an increase in clay fraction within the residual shear zone, indicating a progressive break down of the particle aggregations, and the formation of a weak clay seam (Chandler 1966, 1969). Ramiah, Dayalu, and Purushothamaraj (1970) report that changing the pore water chemistry, from flocculating to dispersive, of a silty clay with clay fraction of only 8% caused a 15% reduction in the internal residual friction angle. As the interface and internal shear behaviors of soils with fine grained materials have been shown to be highly analogous, these mechanisms are believed to be valid for interface shearing as well.

2.4.3 Effect of Boundary Conditions on FGI Behavior

2.4.3.1 Introduction

Boundary conditions can have a large impact on FGI behavior, especially in the interpretation of laboratory data derived from testing apparatuses of varying configurations.

2.4.3.2 Normal Stress

Unlike coarse particulate assemblies, where local interface contact stresses can be significantly different than the applied global stress, fine grained soils do not show large variations in local stress state for homogeneous samples. However, large excess pore pressures can build up locally within the shear zone creating a heterogeneous effective stress distribution within a sample, and often resulting in progressive failure mechanisms. Several studies into the influence of normal stress on NC FGI behavior have found no dependence on changes in normal stress (Tsubakihara et al., 1993; Lemos and Vaughn, 2000; Sun et al., 2003). As such, FGI behavior follows the traditional frictional relationship with no dependence on normal stress, however, as with internal shearing of clays, OCR does have an effect on FGI strength.

2.4.3.3 Shear Condition

Three main laboratory test configurations are used to test FGIs: ring shear, direct shear, and simple shear. Ring shear configurations offer the advantage that shearing can be extended to almost infinite displacements without having to alter the shear direction or other boundary conditions and requiring a very small test sample. Ring shear testing does prohibit the measurement of undisturbed peak behavior as all samples are remolded

during initial sample preparation. A number of researchers have successfully used ring shear tests to study residual FGI behavior (Tika, 1991; Tika et al., 1996; Tika and Hutchinson, 1999; Lemos and Vaughn, 2000)

Tsubakihara and Kishida (1993) conducted a comparison of direct and simple shear devices, on tests of Kawasaki clay. They found that the measured interface friction was always slightly lower than the upper limit of internal shear for the shear box configuration, and related this underestimation to ancillary internal deformation of the sample within the shear box. FGI tests using the simple shear configuration were found to match the internal shear resistance of the clay for rough counterfaces, and allowed for the separate quantification of interface sliding and shearing. The ability to separately measure the proportions of interface sliding and shearing allowed the fundamental mechanisms of FGI shear to be more fundamentally understood, and Tsubakihara and Kishida (1993) recommended the simple shear device over the direct shear configuration.

2.4.3.4 Shearing Rate / Drainage Condition

As with all fine grained behaviors, the shearing rate and drainage condition have a large effect on the response of FGIs. Through a series of interface ring shear tests of London clay on stainless steel, Tika (1991) found that a change in shearing mechanism occurred at shearing rates faster than 110 mm/min. At these fast shearing rates, the failure mechanism changed from pure particle sliding to sliding with some rotation of platy particles. The rotation of the platy particles during rapid shearing prohibited the formation of a weak shear zone comprised of platy particles oriented in the direction of shear. The rotation of platy particles during rapid shear was shown to occur not only during virgin shear, but also following the formation of an oriented shear zone. This

concept correlates well the behavior observed in field studies of pile shaft response showing variability due to the rate of installation (Kraft et al., 1981; Jardine and Bond, 1989).

Lemos and Vaughn (2000) also investigated the effect of shear rate on FGI behavior. They report an increase in peak and residual interface strength with increased strain rate, but also note that a loss of shearing resistance can often occur during fast shear if free water is available to the shear zone. Tsubakihara and Kishida (1993) found that peak interface resistance increased with increasing shear rate (from 0.1 to 10 mm/min), but did not have an appreciable affect on the residual interface strength. They also reported that the influence of shear rate was greater for rougher surfaces, and that the maximum increase in peak interface strength of 19% was consistent with the 22% increase found during internal shear tests on the same material. They also tested samples under both constant volume and pressure, and found no relation between the effective FGI behavior and drainage condition.

2.4.3.5 Cycling

Cyclic loading of FGIs is an especially important consideration, especially in the performance of pile foundations. Upon studying the effects of cycling on the skin friction of piles in clay, Poulos (1981) found that losses in skin friction were a function of both the cyclic displacement prior to failure and the number of cycles. He also noted the common mechanism of particle orientation parallel to the surface was the dominant strength loss mechanism over the development of excess pore pressures due to cycling. Tika (1993) employed a series of cyclic sequences in laboratory interface ring shear tests to simulate various pile installation and driving conditions. These tests showed that

during a series of successive rapid one-way shearing stages (pulses simulating pile installation) or fast stages performed after the slow residual interface state had been established (simulating pile redriving after a loading stage) the coefficient of interface friction was significantly dependent on the rate of penetration, showing a further dependence on cycle rate. Two-way cyclic interface ring shear tests were performed by Lemos and Vaughn (2000) to investigate the effect of strain reversals on residual interface behavior. Their results showed interesting behavior upon strain reversal. Samples appeared to reach a maximum δ after minimal displacement and maintain that value for shear displacements of 1 to 2 mm. After further displacement the samples achieved a secondary peak strength increase followed by a post peak reduction in interface strength approximately equaling the previous residual shear strength. This delayed peak response is believed to be due to the disruption of platy particle orientation parallel to the surface that is then reestablished in the opposite direction upon a large displacement shear reversal.

2.5 Review of Filament-Continuum Interface (FCI) Behavior

2.5.1 Introduction

Filament-continuum interfaces (FCIs) are much less common than fine grained and coarse grained interfaces, and although they are typically treated as a different class of interface, they are governed by many of the same mechanisms as CGIs and FGIs. Throughout this section, needle punched non woven (NPNW) geotextiles will be used as an example of a representative material when considering a common geotechnical filament material. Additionally, while geotextiles and other filaments are placed in

contact with a wide range of materials, this discussion (as did the previous sections of CGIs and FGIs) will concentrate on interfaces involving continuum counterface materials.

In order to relate the particulate (both coarse and fine) interface behaviors to FCIs it is helpful to think of filaments as 1D particles. Where a 1D particle is essentially a line element of variable length and orientation with a common cross-sectional dimension much smaller than the length. The primary differences in the behavior of filaments over particles is the effect that filament length has on interaction with both the counterface and other filaments. The length of most filaments increases the bond between individual filaments and the filament matrix, in a similar mechanism to cementation affecting a particulate media. Additionally, due to the increased length of filaments over particulates, moving laterally around a surface asperity is not a viable mechanism. As such, strain interaction mechanisms are limited to movement over the asperity, densification of the filament matrix, breakage of the filament bond to the matrix, or wear of the surface texture to allow for sliding.

2.5.2 Effect of Counterface Properties on FCI Behavior

As with all particulate-continuum interfaces, surface roughness plays a large role in the behavior of FCIs. Stark et al. (1996) report increases of up to 300% in peak and 200% in residual shear stress for NPNW geotextiles sheared against textured as compared to smooth geomembranes. Unlike the behavior of CGIs and FGIs that were only slightly affected by the type of counterface surface texture, FCI behavior is heavily dependent on the shape and relative orientation of surface texture with respect to the contacting filaments. Due to the large geometric eccentricity, or one dimensionality of filament units, interface interactions are limited to surface texture that contacts perpendicular to the

length of the fiber during shearing. The relative orientation of filaments and surface texture can strongly affect behavior, and as such FCIs are typically anisotropic with regard to shear direction. Textured geomembranes, the most common counterface material in geotechnical FCIs, have inherent anisotropy based on the manufacturing process, and are typically placed such that the machine direction is parallel with the direction of shear to maximize interface interaction.

Frost and Lee (1998) also report results from NPNW geotextile samples sheared against a series of geomembranes, including: "smooth", slightly textured, moderately textured, and heavily textured. They found that the common bilinear relationship between counterface roughness and interface strength is also valid for FCIs, with the critical surface roughness required to fully engage FCIs being typically greater than the critical roughness levels found in coarse and fine grained interfaces. The sensitivity (τ_{peak}/τ_{res}) of FCIs was also determined to be dependent on the level of surface texture, with increasing roughness causing increased sensitivity. Jones and Dixon (1998) report twice the sensitivity in direct and ring shear tests for FCIs using textured as compared to smooth counterfaces. They also report an increase in the strain to peak with increasing counterface texture, as also reported by Hebeler et al. (2005).

Filament contact with surface texture during shearing can result in the common interface mechanism known as hook and loop interaction. The conditions necessary for hook and loop interaction require that the surface texture engage the central portion of a filament that is bonded to the matrix at each end creating a loop element. However, the surface texture does not have to necessarily take on the form of a macro loop as microtexture has been shown to effectively engage filament loops as discussed in Chapter

3. Since hook and loop interactions can account for a large portion of FCI strength, especially peak strength, the percentage of texture that can effectively engage loop elements becomes a major factor in determining the amount of interaction between a continuum counterface and a filament matrix. Additionally the relative levels of micro, meso, and macro texture all affect different portions of FCI stress-strain behavior (Hebeler et al., 2005).

Surface hardness can play a large role in the residual behavior of FCIs as filaments can wear surface asperities by rounding off jagged macro elements or by removing surface texture by completely shearing asperities off of the counterface surface. As such, the bond strength between counterface textural asperities and the base substrate can control the amount of texture that is removed during shear. Stark et al. (1996) report that the polishing of geomembrane surface texture during shearing against NPNW geotextiles is increased for higher normal stresses and softer counterface materials. Jones and Dixon (1998) also note that increased counterface wear is encountered with stiffer filaments, such as geonets used in conjunction with NPNW geotextiles. Wear of smooth counterfaces is typically limited in FCIs due to the circular cross section and moderate hardness of most filaments.

2.5.3 Effect of Filament Properties on FCI Behavior

The most important filament property related to FCI interface behavior is the structure of the filament matrix. Matrix structure is comprised of properties such as: filament orientation (aligned or random), packing density, inter filament bonding (calendaring, stapling, welding, etc.), and cross sectional thickness. The strong inter filament interlocking and bonding that is present in most filament matrices suppresses

many of the particle rearrangement mechanisms that tend to dominate 2D particulate - continuum interface behavior. The only rearrangement of filament matrices typically occurs through a change in packing density or by the oriented alignment of filaments after pullout or tearing (Stark et al., 1996). As such, interface mechanisms similar to those found in cemented CGIs are common in FCIs. With residual behavior often controlled by a breakdown of the inter filament bonds, resulting in a thin zone of loose filaments between the counterface and remaining filament matrix. Stark et al. (1996) also note increased interface peak strength and no effect on residual behavior with increasing fiber length and decreasing matrix thickness. Whereas, Frost and Lee (1998) report an opposing result of increased strength with increased matrix thickness, and Jones and Dixon (1998) note negligible effect of matrix thickness on interface strength.

The composition of filament units can also affect the behavior of FCIs. With typical results indicating increased interface strength with harder fibers and those more resistant to filament wear and tear. Jones and Dixon (1998) studied the effect of filament composition on the interface strength of NPNW – textured geomembrane interfaces. They report similar peak behaviors for PP and HDPE filament geotextiles, but greatly reduced residual strength in the case of the HDPE geotextile FCI due to lower inter-filament friction that allowed for significant stretching of the filament matrix. The minimum energy failure concept still applies for FCIs, and it has been noted that sliding failure occurs for smooth interfaces with internal filament matrix shearing for textured counterfaces (Frost and Lee, 1998). A number of researchers have noted the large post-peak strength drop for typical FCIs, and residual strengths for a common FCI (textured geomembrane - NPNW geotextile) are typically on the order of 50% lower than peak

resistances. However, due to the controlling filament wear mechanisms of filament pullout and tearing, ultimate residual strengths are not achieved until after very large shear displacements as shown in torsional ring shear data.

2.*5.4 Effect of Boundary Conditions on FCI Behavior*

As with all geotechnical interfaces, FCIs are affected by a number of boundary conditions. Since most filament matrices consist of open and loose configurations, changes in normal stress significantly change the density of typical filament assemblies and can affect the controlling mechanisms for FCIs. Similar to the mechanism described for CGIs in Figure 2-2, the density of filaments close to the counterface increases with increasing normal stress at low normal stresses. As such, Wasti and Özdüzgün (2001) report a reduction in interface friction for both smooth and textured FCIs with increasing normal stress for low stresses. This behavior is exaggerated for textured interfaces, as increased normal stress has been shown to encourage greater texture filament interaction in heavily textured counterfaces (Hebeler et al., 2005).

As reported by Stark et al. (1996) very large displacements are typically required to reach the ultimate residual of many FCIs, and as such, ring shear provides better ultimate residual estimates than other shear loading conditions. Jones and Dixon (1998) compared ring and direct shear interface behavior for FCIs. They report that the ultimate residual interface strength found in ring shear tests should be considered a lower bound, and may be an extreme case that does not accurately model field conditions even under large displacement. Wasti and Özdüzgün (2001) compared the behavior of FCIs at low normal stresses with both a direct shear and inclined board apparatus and found minimal difference in residual behavior, but noted a significant difference in the apparent cohesion

of peak behavior. As a result they recommend that direct shear results at low normal stresses may be unconservative. Nonetheless, the peak strength of FCIs is not typically affected by the shear loading condition provided that the orientation of the interface materials is consistent over each test type. Stark et al. (1996) studied FCIs under a series of shear rates ranging from 0.029 – 36.7 mm/min, and found no effect on both peak and residual behavior. Jones and Dixon (1998) conducted a series of experiments on FCIs varying the material used to confine the filament matrix on the external boundary (i.e. non interface surface). They found that cover soil particle shape and grading can both influence FCI shear strength. They noted increased interface strength with increasing particle angularity when particulate assemblies were used as the confining media. If a solid block is used for confinement, it typically results in increased residual strength estimates for smooth counterfaces and conservative estimates for textured counterfaces.

Table 2-1. A Summary of Prominent Factors Influencing Geotechnical Interface Behavior

Factors and Properties Affecting Particulate - Continuum Interface Behavior

Type	Factor	CGI Significance		FGI Significance		FCI Significance		Remarks
		Peak	Residual	Peak	Residual	Peak	Residual	
Particulate	Macro Shape	H	H	H	H	L	M	Angularity / Length / Eccentricity
	Micro Shape	L	L	L	L	L	L	e.g. Particle Roughness
	Cementation / Diagenesis / Calendering	M	L	M	L	L	M	Any strengthening of inter particulate bonds
	Density \ Void Ratio	M	L	M	L	M	L	
	Initial structure	L	L	M	L	L	L	Homogeniety of particulate structure (Floc / Disp)
	Mean particle size (D_{50})	H	H	M	M	H	M	Specific surface for Fine Grained material…
	Mineral / Chemical composition	H	H	H	H	L	M	
	Uniformity coefficient (Cu)	L	M	L	L	---	---	*At this time all geotechnical fabrics have Cu = 1
	Stress History	M/L	M/L	H	H	M	L	OCR, etc.
	Strain History	M/L	M/L	H	M	H	M	
	Plasticity	---	---	H	H	---	---	
	Individual particle strength	H	H	L	L	M	H	Effect of particle crushing / tearing
	Water content / Degree of Saturation	L	L	H	H	L	L	
Continuum	Surface hardness	H	H	L	L	M	H	
	Micro surface roughness	H	H	H	H	H	H	On the order of Rmax < 30 mm
	Macro surface roughness	H	H	M	M	H	H	On the order of Rmax > 100 mm
	Texture Geometry / Manufacturing Process	M	M	L	L	H	H	Directionality and Shape of Textural Asperities
Boundary Conditions	Normal stress	H	H	H	H	H	H	Influence on behavior and τ not just δ
	Current State of Stress	M	M	M	M	M	M	
	Strain Rate	L	L	M	M	L	L	Velocity of Shear
	Drainage	L	L	M	M	L	L	
	Test Geometry	M	M	M	M	M	M	Direct, Simple, Ring, Axisymmetric modes
	Confinement Condition / Media	M	H	M	H	M	M	Physical boundary condition, e.g. CNS vs. CNL
	1-way cycling	H	M	H	M	M	L	Cycling without crossing zero stress
	2-way cycling	H	H	H	M	H	M	Cycling crossing the stress axis

* All catergories are described for ideal properties (e.g. Particulate mixtures of coarse and fine grained materials are not considered)
* CGI - Coarse Grained Interface; FGI - Fine Grained Interface; FCI - Filament Continuum Interface
* FCI - An interface consisting of a needle punched nonwoven geotextile is representative of a geotechnical filament material.

L - Likely to have limited effect on interface behavior
M - Likely to have some effect on interface behavior
H - Likely to have a dominant effect on interface behavior

Table 2-2. Summary of Conventional Roughness Parameters (DeJong, 2001)

Symbol	Name	Definition	Horizontal Distribution	Vertical Distribution	Relative Aspect
R_a	Average Roughness [1]	$R_a = \frac{1}{L} \cdot \int_0^L \lvert Z(x) \rvert dx$ where Z(x) is a profile height function and L is the evaluation length		X	
R_q	Root Mean Square (RMS) Roughness [1]	$R_q = \left(\frac{1}{L} \cdot \int_0^L Z(x)^2 dx \right)^{\frac{1}{2}}$		X	
R_{sk}	Skewness [1]	$R_{sk} = \frac{1}{R_q^3} \cdot \frac{1}{L} \cdot \int_0^L (Z(x))^3 dx$		X	
R_{ku}	Kurtosis [1]	$R_{ku} = \frac{1}{R_q^4} \cdot \frac{1}{L} \cdot \int_0^L (Z(x))^4 dx$		X	
Δ_a	Average Slope [1]	$\Delta_a = \frac{1}{L} \cdot \int_0^L \left\lvert \frac{dZ}{dx} \right\rvert dx$	X	X	
Δ_q	Root Mean Square (RMS) Slope [1]	$\Delta_q = \left[\frac{1}{L} \cdot \int_0^L \left(\frac{dZ}{dx} \right)^2 dx \right]^{\frac{1}{2}}$	X	X	
λ_a	Average Wavelength [1]	$\lambda_a = 2 \cdot \pi \cdot \frac{R_a}{\tan(\Delta_a)}$	X	X	
λ_q	Root Meen Square (RMS) Wavelength [2]	$\lambda_q = 2 \cdot \pi \cdot \frac{R_q}{\tan(\Delta_q)}$	X	X	
R_{max}	Maximum Peak to Valley Roughness [1]	Largest Single Peak to Valley Height		X	
R_p	Maximum Peak to Mean Line Roughness [1]	Largest Single Peak to Mean Line Height		X	
R_t	Mean Line to Lowest Valley Roughness [1]	Largest Mean Line to Valley Height		X	
R_n	Normalized Roughness Parameter [3]	$R_n = \frac{R_{max}(L = D_{50})}{D_{50}}$		X	X
R_L	Profile Roughness Parameter [4]	$R_L = \frac{\text{Actual Profile Length } (L_0)}{\text{Projected Profile Length } (L)}$	X	X	
R_S	3-D Surface Roughness Parameter [4]	$R_s = \frac{\text{Actual Surface Area}}{\text{Projected Surface Area}}$	X	X	
S_m	Average Feature Spacing [1]	$S_m = \left(\frac{1}{n} \right) \cdot \sum_{i=1}^{n} S_{mi}$ where S_{mi} is the mean spacing between profile irregularities	X		

[1] ASME B46.1, 1995

[2] Thomas, 1999

[3] Uesugi and Kishida, 1986b

[4] Gokhale and Underwood, 1990

Table 2-3. Review of Particulate-Continuum Interfacial Friction Testing Apparatuses (Modified from Paikowsky et al. 1995).

Testing Apparatus	Advantages	Disadvantages
Direct Shear 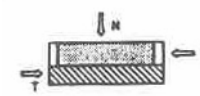 	• Commonly available device • Simple sample preparation and operation • Solid surface can either be above or below soil sample • Constant interface area	• Stress concentration at the ends • Displacement components (soil deformation and relative motion along interface) cannot be independently identified
Axisymmetric Loading  	• Geometric configuration resembles skin friction of piles • Common triaxial device can be modified and employed • Constant surface area	• Stress concentration at the ends • Normal stress on interface unknown • Method and direction of soil placement around the bar may markedly affect the soil/solid interaction • Displacement components cannot be independently identified
Ring Torsion 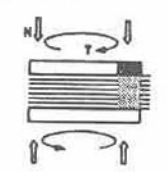 	• No end effects, "endless" constant interface area • Large displacements feasible	• Complicated experimental system, sample preparation, and procedure • Displacement gradient across the interface, and as a result shear strain variation in the sample • Displacement component cannot be independently identified with external measurement (X-ray was used by Yoshimi and Kishida) • Only appropriate for isotropic surfaces
Simple Shear 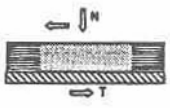 	• Simple sample preparation and operation • Displacement components can be measured independently • Constant interface area	• Stress concentration at the ends • Sample/solid contact different when solid is above sample
Dual Interface 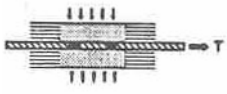 	• Simple or direct shear • No boundary effect within central segment • Single (up or down) or dual interface for same bar • Constant interface area • Displacement components can be measured independently under simple shear conditions	• Requires instrumentation to enable load measurement along the interface • Interface needs to be long enough to enable measurement at locations away from the stress concentrations at the ends • Sample/solid contact different when solid is above sample

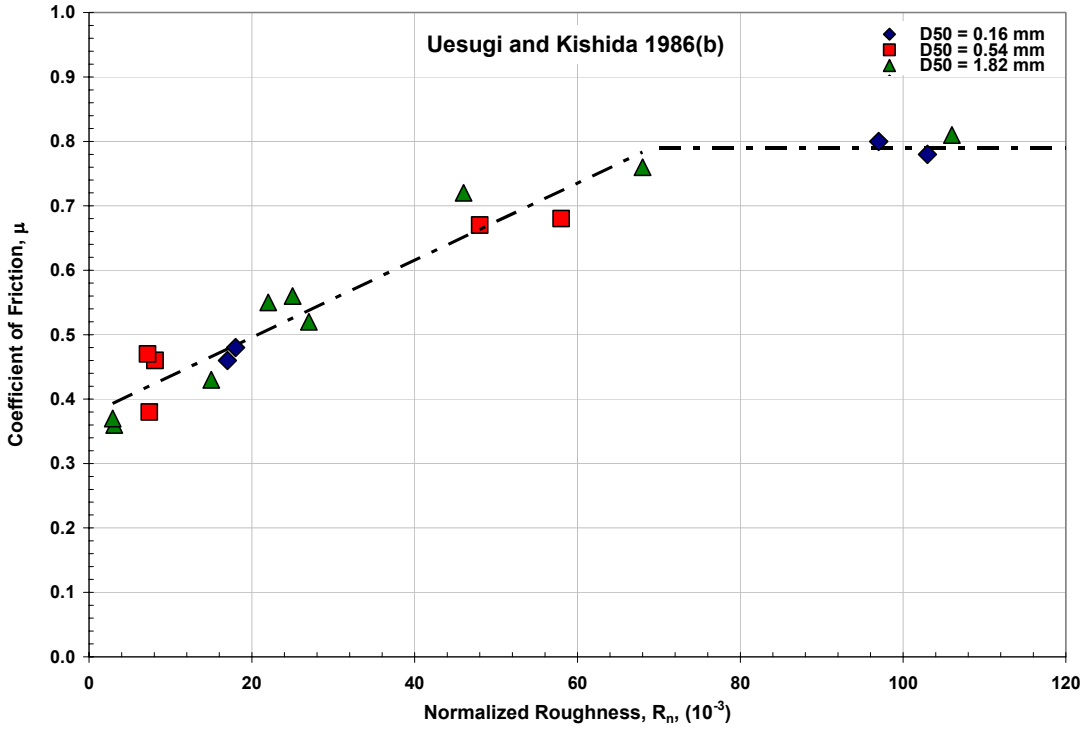

Figure 2-1. Normalized Surface Roughness Versus Coefficient of Friction for Sand-Steel Interfaces (after Uesugi and Kishida, 1986b).

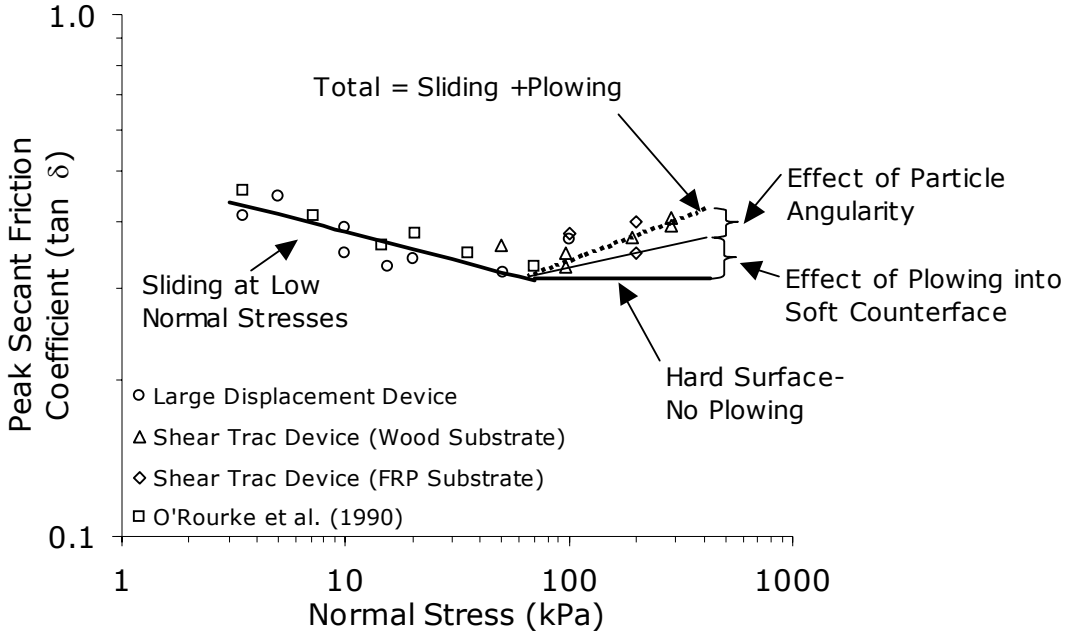

Figure 2-2. The Effect of Normal Stress on Peak Secant Friction Angle for Smooth Counterfaces (after Dove and Frost, 1996).

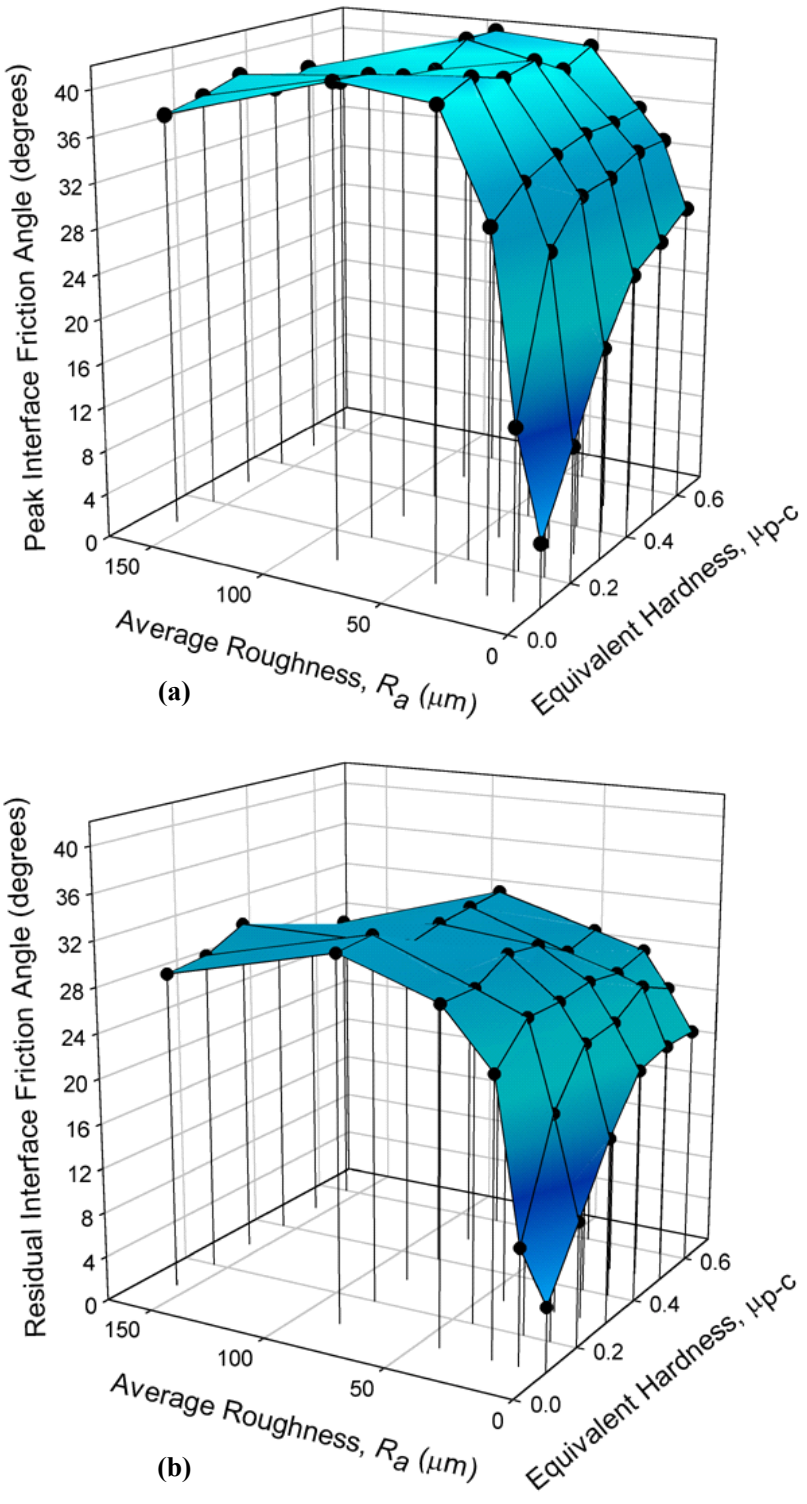

Figure 2-3. Relationship Between Surface Roughness, Hardness, and Interface Friction for DEM Modeling with Uniform Grain Size (a) Peak Interface Friction Angle (b) Residual Interface Friction Angle (Frost et al., 2002).

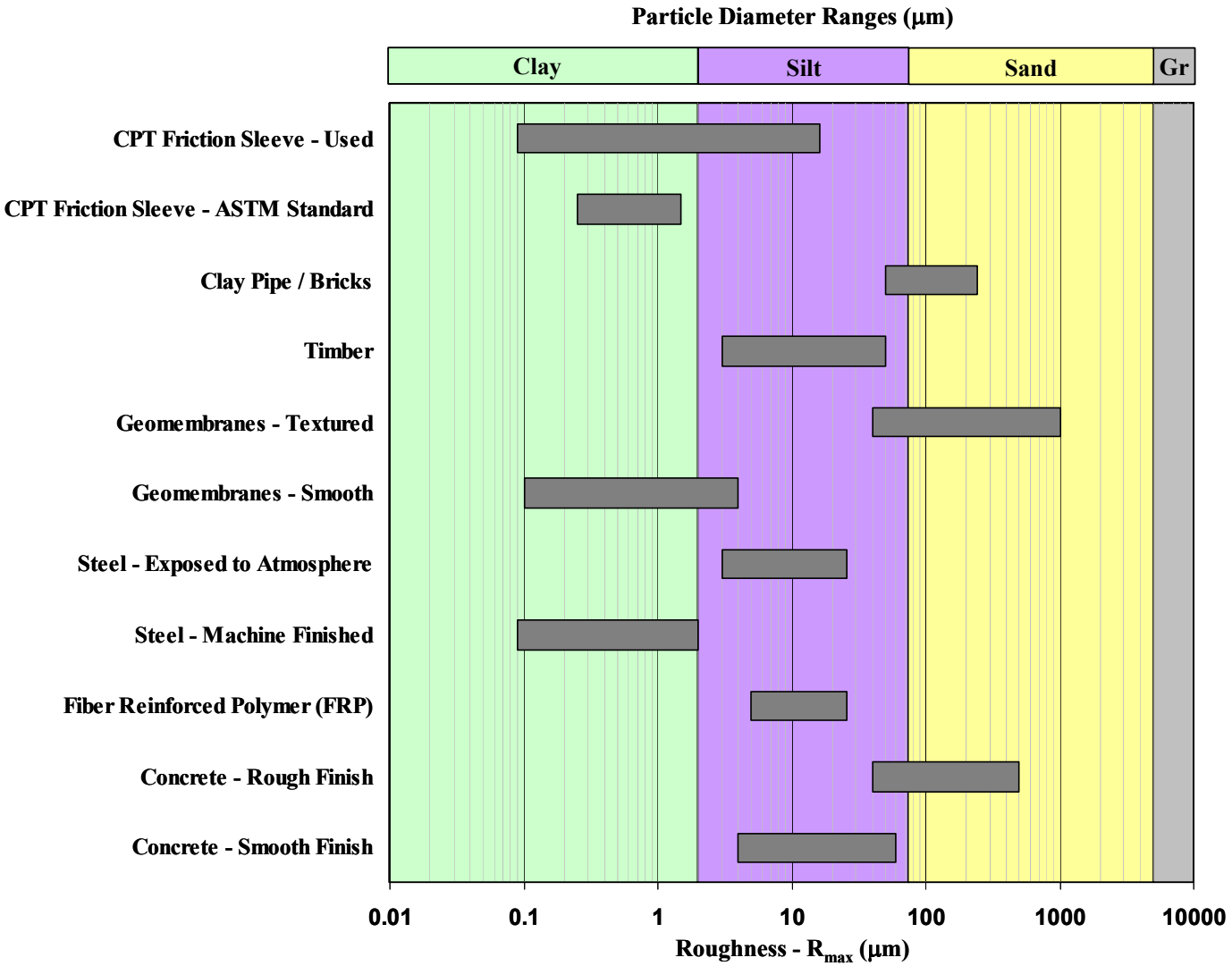

Figure 2-4. Typical Range of Roughness (R_{max}) for Common Construction Counterfaces Overlain on the Distribution of Soil Size Ranges.

Chapter III
Shear Zone Evolution of Granular Soils in Contact with Conventional and Textured Friction Sleeves

3.1 Introduction

As noted in Chapter 2, interface behavior is a primary concern in geotechnical engineering. Common geotechnical applications such as pile design, slope stability, micro tunneling, earth retaining structures, are dependent on the strength of soil-geomaterial interfaces. Additionally, a fundamentally intrinsic aspect of geotechnical design is the joint dependence of macroscopic and micromechanical behaviors. In the closing lecture of the 18th IUTAM Congress, Professor G.I. Barenblatt (1992) described this interdependence aptly: "Micromechanics is the branch of mechanics studying the phenomena for which variations of microstructure are of governing influence for the macroscopic behavior of bodies". As such, a large concern in the design of many geotechnical structures, laboratory equipment, and in-situ testing devices is the zone of influence surrounding the included interfaces. The intrinsic length scales of the problem must be accounted for, to not only understand the extent of behavior but to also ensure that an investigative study is not adversely affected by boundary and other restricting test conditions.

Many commercial geomaterials are selected to either minimize or maximize local particle interactions at the contact interface. As an example, the field of geosynthetics, and particularly textured geomembranes, is constantly evolving, with continual product developments aimed at better engaging various forms of particulate materials (clays, sands, gravels, and filaments). Because interfaces, and the shearing of soil against them,

play such an important role across all aspects of geotechnical engineering, it is imperative to understand the physics and mechanisms of interface processes. This chapter summarizes previous work regarding the micromechanical understanding of interface shear zone formation and progression and presents a thorough parametric laboratory study aimed specifically at the evolution of shear zones adjacent to conventional and textured friction sleeves.

The most common in situ interface shear test conducted in current geotechnical practice is the friction sleeve measurement (f_s) of the cone penetration test (CPT). However, due to a number of factors including device design, variability in measured values, and the resultant poor correlation performance, friction sleeve measurements are used with less frequency than the other CPT measurements of tip stress (q_c) and pore pressure (u). Some of the shortcomings of the f_s measurement are due to the design of the conventional CPT device including: the sleeve location, the sleeve roughness (or lack thereof), and sensor resolution in "subtraction type" load cell configurations. In response to these design shortcomings a Multi Friction Attachment (MFA) for the cone penetrometer was developed to study the effects of sleeve position and sleeve roughness through the use of four independent additional friction sleeves positioned behind a traditional 15 cm^2 CPTU device, as discussed in detail in DeJong and Frost (2002) and Chapter 5. An extension of this multi sensor concept in the form of Multi Piezo Friction Attachment (MPFA) was developed as part of this study, the development and details

In the development of the MFA a number of design considerations that were not considered in the development of the original and subsequent versions of the CPT friction sleeve were introduced. Of the improvements made, the one most pertinent to the context

of the current discussion is the addition of variable levels of sleeve texture to friction sleeves. More information about the development of the friction sleeve texturing and results of its implementation in-situ can be found in: Chapters 5 to 8, Cargill (1999), DeJong et al. (2000), DeJong et al. (2001), DeJong (2001), Frost and DeJong (2001), DeJong and Frost (2002a), Hebeler et al. (2004), and Frost and DeJong (2005). With the development of a new texturing scheme, it was imperative to conduct both in-situ and laboratory proof of concept tests to validate the proposed texture configuration. Initial proof of concept tests are presented by DeJong (2001), DeJong and Frost (2002a), and Frost and DeJong (2005). The current study includes a full parametric laboratory study of the interface shearing mechanisms mobilized by traditional and textured friction sleeves in contact with granular materials. While the testing sequence was focused on friction sleeve interfaces, the fundamental mechanisms and concepts realized through the study are applicable to a much larger range of geotechnical materials and problems.

3.2 Granular Shear Zones

Numerous researchers have studied the evolution of granular (and other particulate) assemblies during shear, and have commented on the complexity of the problem. Granular media are extremely complex materials and differ greatly from many other materials encountered in science and engineering by the nature of their pressure sensitivity, which can be attributed to the existence of internal (or Coulombian) friction. The static fabric of a granular assembly consists of force chains acting through intergranular grain contacts that can change continuously during deformation and loading. As such, naturally observed granular phenomena are not easily reproduced through numerical modeling efforts or easily represented by analytical relationships. While,

current work is closing the gap between engineering and nature with complex two and three dimensional Discrete Element Models (DEM) that individually model the Newtonian interactions of individual particles, and analytical representations using Cosserat continuum (mechanics accounting for rotational interactions) and high gradient approaches, there is still no unified representation that allows for complete prediction of all observed natural granular phenomena.

One of the complicating factors involved in a complete representation of granular behavior is the propensity to form localized zones of progressive failure within the assembly known as shear zones or bands. Desrues et al. (1996) define a shear band as a shear localization that includes intense intergranular slip and dilatancy of the material within the localized zone, attributed to grain rearrangement, slip, and rotation. Problems in modeling and predicting granular behavior stem from the apparent non-uniqueness and instability of localization determination and the introduction of a governing length scale (shear band thickness) over which ultimate failure is controlled. The problem is further complicated by the fact that not all granular assemblies experience localized failure. Strain hardening materials tend to support the development of homogeneous deformation fields, whereas strain softening materials tend to exhibit progressive or localized failures. In their review of localization in particulate materials, Cho and Santamarina (2001) note that a broad range of loading conditions and particle shapes can lead to localizations, including: dilative soil subjected to drained shear (standard case), contractive specimens subjected to undrained shear, dilative specimens that experience cavitation, assemblies of platy (or otherwise highly eccentric) particles, cemented assemblies, partially saturated assemblies, heterogeneity, and combinations of these conditions (when applicable).

As noted by several previous researchers, shear zones form in many geotechnical conditions, including: interface shearing between two continuum surfaces (continuum-continuum), interface shearing of particulates against a continuum counterface (discontinua-continuum), and internal particulate shearing (discontinua-discontinua). The condition of continuum-continuum interfaces is prevalent in the field of rock mechanics and is discussed at length in other texts. Internal and interface shear zones are common in geotechnical applications, and the formation of shear zones within granular assemblies both internally and adjacent to continuum inclusions are controlled by the same underlying fundamental mechanisms (DeJong and Frost, 2002b; Baylac et al., 2003, Frost et al., 2004). More explicitly, interface shear zones have been considered analogous to half shear bands found internally within particulate assemblies. Counterfaces considered smooth in relation to the contacting particle size tend to support homogeneous deformation in the form of pure sliding, and rougher surfaces tend to induce localized failure zones at or near the interface depending on the magnitude of the relative roughness and shear displacement as discussed in Chapter 2.

Previous studies have attempted to document the spatial evolution of shear zones during shear. Tejchman (2000) summarizes the range of experimentally observed shear zone thicknesses normalized by the mean particle diameter (D_{50}) for internal (5 to 20 times D_{50}) and interface (1 to 40 times D_{50}) shear zones. A summary of previous methods used to capture interface shear zone evolution and size include: stereo photographemetry (Andrawes and Butterfield, 1973), x-ray observation with and without the use of lead sphere inclusions (Roscoe et al., 1963; Yoshimi and Kishida, 1981a; Vardoulakis and Graf, 1985; Phillips, 1991), monitoring of the individual contributions of sliding and

shear from the simple shear apparatus (Uesugi and Kishida, 1986a; Uesugi et al., 1988), individual particle tracking through an opaque side wall (Uesugi et al., 1988; Irsyam and Hryciw, 1991), the extension of optical observation through the use of computer based target tracking (Taylor et al., 1998; Paikowsky and Xi, 2000) and Particle Image Velocimetry - PIV (White et al., 2001, DeJong et al., 2003), and soil structure preservation and subsequent dissection (Irsyam and Hryciw, 1991; Frost et al., 1999; DeJong and Frost, 2001; Lee and Frost 2002).

The current study uses an axisymmetric interface shear device developed by DeJong (2001) to investigate the spatial movement of granular particle assemblies with varying mean particle size and characteristic angularity during interface shearing. Changes from the initially prepared sand structure were captured by preparing samples with alternating layers of dyed and naturally colored sands oriented orthogonal to the counterface surface. The post shearing structure of each sample was preserved by heat activating a powder phenolic resin, creating lightly cemented samples that were subsequently dissected and carefully investigated through optical analyses.

3.3 Conventional and Textured CPT Friction Sleeves

Within the scope of this thesis a conventional CPT friction sleeve will be taken as a sleeve located directly behind the tip or u_2 element conforming to ASTM D-5778 (1995) and ISSMFE (1989) standards, which specify a friction sleeve roughness, R_a (average roughness), equal to 0.50 $\pm$ 0.25 μm. The surface roughness of conventional friction sleeves is much lower than that of typical geomaterials used in foundation and construction practice. Figure 2-4 detailed the roughness characteristics of some common construction materials in comparison with both conventional and textured friction sleeves.

The difference in surface roughness between typical construction materials and conventional friction sleeves may be partially responsible for the shortcomings of empirical correlations using f_s to predict practical interface friction response. This concept can be demonstrated using the bilinear relationship between surface roughness and interface friction as introduced in Figure 2-1, and applied to friction sleeves of various roughness in Figure 3-1.

Design considerations used in developing a feasible texturing pattern for use on CPT friction sleeves required that the textured sleeves induce internal shearing of the soil rather than only sliding along the surface, and that the texturing pattern should be easily machinable. Further, a texturing pattern that was not conducive to clogging was required. The resultant texturing pattern consists of an offset diamond shaped texture with variations in the height of the diamonds used to modify the magnitude of surface roughness. The geometric configurations of the textured sleeves used in the current study are presented in Table 3-1 and Figure 3-2. The design of the textured sleeves uses offset rows of diamond shaped features parallel to the sleeve axis. The standard textured friction sleeve design consists of 110 total diamond shaped textural asperities, oriented in 5 pairs of offset circumferential rows and 22 vertical columns oriented parallel to the penetration axis. The diamond shaped texturing is surrounded by sleeve areas with no textural features having surface characteristics equal to a conventional smooth CPT friction sleeve. The sections of smooth surface result in flow paths around or between each of the diamond asperities. This type of pattern was used to induce shearing within the soil by forcing particles to flow between, around, or over the diamonds, and to prevent clogging of the textural features. For more information regarding the full progression of sleeve

texture designs refer to Cargill (1999), DeJong et al. (2001), and DeJong and Frost (2002). To simplify further discussions, the circumferential rings of textured diamonds will be grouped into pairs as every other ring of diamond shaped asperities is offset laterally around the circumference. This offset results in any given particle only being influenced by every other ring of diamonds due to the inherent lateral offset. As such, individual particles are influenced by a maximum of five diamond features during full sleeve penetration, or three diamond features (63.5 mm displacement) in the current tests, as seen in the cross sectional view of Figure 3-3. Over the full shear displacement individual dyed sand layers were exposed to varying percentages of textured and smooth shearing, with the % of textured shearing equal to the length of shearing in contact with the textured sleeve as a function of the full 63.5 mm of displacement.

3.4 Axisymmetric Interface Shear Experimental Procedures

The current study is part of a larger effort at the Georgia Institute of Technology to develop and utilize multi-friction sleeve penetrometer attachments, as detailed in Chapter 5. As such, while the broader scope of the current study is to gain a better understanding of continuum - particulate interface shearing, the design of the current experiments were focused on facets pertaining to interface shearing along CPT, MFSA, and MPFA friction sleeves. Axisymmetric interface shear tests were performed to observe the evolution of the interface shear zone at the particulate level in sand specimens by preserving the post-shear structure through the activation of a powder phenolic resin. The experiments provide quantitative insight into the development, evolution, and spatial extent of the induced shear zones in addition to determining the controlling shear mechanisms for both smooth and textured friction sleeves.

The experimental equipment used in the current testing consisted of an axisymmetric interface shear apparatus developed by DeJong (2001). This apparatus, shown in Figure 3-4, allows for 43.7 mm diameter (standard diameter of a 15 cm^2 CPT) friction sleeves of any length to be mounted in the center of smooth end sections (diameter = 43.7 mm) with standard average surface roughness equal to that of a conventional CPT friction sleeves, R_a = 0.50 μm. The assembled test section is positioned along the center axis of a tri-part steel testing chamber 150 mm in diameter and 375 mm in height. The inside of the chamber is lined with one layer of needle punched nonwoven geotextile (542 g/m^2 and 7 mm thick) and then a latex membrane of 0.64 mm in thickness. The use of the geotextile allows for constant lateral stress conditions during testing resulting in calibration chamber BC1 boundary conditions. The upper and lower boundaries consist of metal end platens with rubber seals at the center through which the test rod penetrates the cell. The chamber boundary conditions compare favorably with confined interface shearing, consistent with in-situ CPT penetration at moderate depths. A displacement system controlled by a worm gear motor with a maximum stroke of 150 mm was used at an average displacement rate of 5 mm/min. All samples were sheared a total of 63.5 mm, equaling 6 individual or 3 paired rows of offset diamond texture, and tested at a constant lateral confining stress of 50 kPa.

The upper rod section includes two pass through holes that allow for the placement of heating elements in the center of the tested sleeve. The remainder of the internal void space around the heating elements is filled with sand to allow for improved heat transfer from the elements into the surrounding sample after shearing. Constant

lateral confinement is applied through air pressure at three external intakes, located at the center point of each tri-part mold section.

The soils used in the current testing consisted of Ottawa 20/30 (0.6 – 0.85 mm) and 50/70 (0.2 – 0.3 mm) graded quartz sand, as well as a local 20/30 (0.6 – 0.85 mm) blasting sand from Atlanta Blasting and Supply Co. The properties of the tested sands are shown in Table 3-2, with photographs of characteristic grains shown in Figure 3-5. The blasting 20/30 sand (A) can be considered the control material in the current experiments, with the Ottawa 20/30 (B) and 50/70 (C) sands used to study the effects of angularity and particle size, respectively. Counterfaces tested in the current study consisted of a conventional smooth friction sleeve R_a = 0.50 μm and four textured friction sleeves varying in surface roughness from R_a = 70 to 230 μm (R_{max} = 250 to 2000 μm). The detailed specifications of the counterfaces used in the current study were listed in Table 3-1. All of the sands were mixed with powder phenolic resin at a concentration of 1% by weight. The phenolic resin was used to preserve the post-shear structure of the sample, by heating the entire specimen above the melting point of the resin (150° to 175° C) and then letting the sample cool, creating light cementation at the contacts through the resolidification of the melted resin. Table 3-3 details the properties of the powder phenolic resin used in the current study.

A portion of the sand to be used in preparing each sample was dyed green by mixing it with a highly concentrated solution of food coloring to a moisture content approximately equaling a saturated surface dry (SSD) condition. The SSD sand was then dried in a soil oven (T ≈ 105° C) to preserve the coloring. This dying process was repeated several times until the sand achieved a dark enough color to easily differentiate

it from the natural color of the quartz sands (light tan to beige). Differentiating the particles in this way did not significantly alter any of the physical properties of the sand, ensuring homogeneous samples. Samples were prepared dry, in thin lifts of 1 cm height using constant fall height air pluviation and light tamping, resulting in uniform specimens of medium density. Natural and dyed layers were alternated in the portion of the sample subjected to shearing against the sleeve. The current technique of investigating the post shear deformations of the soil does not allow for individual particle tracking during shearing. Rather, by alternating the layers of colored and natural sand, the total deformations after shearing are tracked by measuring the relative deformations of each layer. Colored sand layers are aligned such that the bottom of each colored soil layer is positioned along the bottom edge of each alternate row of diamond texture, corresponding to a spacing of 2.2 cm between both the dyed layers and pairs of texture rows.

After cooling, the specimen chamber is lifted from the testing device and two of the three faces of the tri-part chamber are removed to allow access to the sample. The specimens are supported by the remaining tri-part chamber section and placed horizontally on a lab table for investigation. Each specimen is dissected in longitudinal slices along the displacement direction, such that a vertical face of the soil sample perpendicular to the rod axis is exposed for analysis. The radial symmetry of the axisymmetric experimental configuration allows for multiple measures of the shear zone to be made for each sample. As such, multiple dissections were made with the rod and sleeve in place for each sample in addition to supplemental measurements taken of the remaining soil sample after removing the test rod. Examples of a sample dissection with

and without the rod in place are shown in Figures 3-6 and 3-7, respectively. Investigation of the shear zones after the removal of the test rod provides a two-dimensional view of the lateral translation of the deformed shear zones, however, these results are only used for qualitative assessments, as the first layer of contacting particles was often disturbed during the removal of the rod section. For samples with textured sleeves, investigation planes, or slices, were centered either along the top of diamond texture columns or within the passthrough space between the texture features as shown in Figures 3-8 and 3-9 respectively. At a minimum, four total longitudinal slices were taken of each sample, two each centered along the top of the texture features and in the passthrough space between the diamond texture features.

Two main deformation measurements were taken of each dyed layer. The measurements are illustrated in Figure 3-10 and consist of the thickness away from the base sleeve surface to which lateral particle movement was observed, and the length along the contact surface each layer of particles was laterally displaced with respect to the unaffected portion of each layer. Displacements were independently measured at both the leading and trailing edges of each colored layer and averaged to determine the average deformation of each layer. Photographs were taken with magnifying lenses to achieve high-resolution images of the shear zones. Particle displacements were inventoried through measurement of the scaled digital images in AutoCAD®, allowing for high precision and a physical record of all measurements.

The primary results of the axisymmetric interface shear tests are the measurements of shear zone deformation taken from layers continuously sheared against either a smooth or textured surface. Each sample contained two layers continuously

sheared against the textured friction sleeve, each layer experiencing shearing against three rows of diamonds in any longitudinal slice oriented along the penetration axis. However, the nature of the experimental setup provided additional information regarding the initiation and progression of shear zone development through the investigation of layers that experienced other combinations of shearing against smooth and textured surfaces. Reported measurements of both continuous and partial textured shearing are reported as average values of all measurements taken for a specific layer in each specimen. Additionally, the uniformity of the induced shear zones of each sample were investigated by comparing the particle deformations of slices taken along the tops of diamond columns to those taken between the columns of diamond texture. In addition to the quantitative measurements taken from the longitudinal slices, additional qualitative information regarding lateral shear zone uniformity was gained through investigation of each sample after removing the test rod.

3.5 Experimental Results

3.5.1 Introduction

A series of interface shear tests was conducted using an axisymmetric apparatus, Figure 3-4, to monitor the shear zone evolution of three different granular media against steel friction sleeves with textures varying from conventional smooth (R_a = 0.50 μm, R_{max} = 6.4 μm) to heavily textured (R_a = 230 μm, R_{max} = 2000 μm). Three different granular media were chosen to parametrically investigate the effects of both particle size and angularity on the behavior and size of the induced shear zones. The properties of the three granular materials and the tested counterfaces (friction sleeves) were given in Tables 3-1

and 3-2. All tests were conducted over a shearing length of 63.5 mm at a constant lateral stress confining condition of 50 kPa. The shearing distance was chosen to correspond exactly with 6 of the 10 total rings of offset diamond texture or 3 of the 5 pairs of offset diamond texture present on the textured sleeves. A summary of the test details for all investigations performed in this study is provided as Table 3-4.

3.5.2 Results of Conventional Smooth Sleeve Shearing

Analysis of interface shearing with conventional smooth friction sleeves was conducted using two techniques. For the test with Ottawa 20/30 (Sand B), a complete interface shear test was performed with a smooth friction sleeve mounted between the top and bottom smooth rod sections. For the other granular materials (Blasting 20/30 [Sand A] and Ottawa 50/70 [Sand C]) the results presented for shearing against a smooth surface were taken within the framework of tests against textured sleeves. The reported smooth surface (R_a = 0.50 μm) deformations were taken from dyed layers continuously sheared against the top or bottom rod sections during the textured sleeve tests. The results of the axisymmetric interface shear tests for the tested granular materials against counterfaces with roughness properties equivalent to conventional friction sleeves are shown in Table 3-5.

As noted by DeJong (2001) in an initial study of shear zone size, interface shearing of sub-rounded coarse sand (B) against conventional friction sleeves results in a pure sliding failure along the interface with no particle displacements noted after 63.5 mm of displacement. The preserved post shear structure of this test is shown in Figure 3-11. Additionally, tests of smooth interface shearing in contact with a sub-angular sand of similar size (Sand A) showed only minor deformation within the granular media on the

order of 1 particle diameter near the interface. The tests with the smaller size sub-angular sand (Sand C) showed small out of plane and lateral deformation during shearing against conventional smooth friction sleeves, as shown in Table 3-5. These results indicate that fine sands do experience limited induced deformation during shearing against conventional friction sleeves. For Sand C the deformations resulted in a deformed shear zone on the order of 3 to 4 equivalent mean particle diameters orthogonally into the granular media and lateral displacements along the smooth interface equivalent to approximately 2% of the total displacement.

3.5.3 Results of Textured Sleeve Shearing

3.5.3.1 Introduction

In addition to the tests performed in contact with conventional smooth CPT friction sleeves, all three granular materials were tested in combination with 4 textured friction sleeves having the roughness characteristics listed in Table 3-1. The four textured friction sleeves vary only in the out of plane height of the diamond features, with the base diamond dimensions and spacings being the same for all four sleeve designs. The four textures used in the current study consisted of diamond heights of 0.25, 0.50, 1.00, and 2.00 mm. For each test using a textured sleeve, conditions were such that different layers within the sample experienced different levels of textured and smooth shearing. Layers were positioned such that two layers were kept in continuous contact with the textured sleeve. The remainder of the colored layers were positioned throughout the sample to experience either continuous smooth shearing or a combination of textured and smooth

shearing over the entire displacement range. The position of the layers and the amount of textured shearing as a percentage of total displacement was portrayed in Figure 3-3.

The induced shear deformations for all tested surface and soil properties took on the form of a simple shear failure condition as shown in Figures 3-6 to 3-8, showing the post-shear structure of a test with Sand C sheared against the 0.50 mm diamond height textured sleeve. All layers experienced relatively homogeneous shearing across the measured planar layer widths, and as such, shear zone deformation results are presented as average layer deformations. The average layer deformations were calculated by averaging the individual measurements of layer width and height at both the leading and trailing edges of each layer. Additionally, a minimum of four distinct dissection planes were investigated for each specimen, allowing for multiple independent measures of the shear zone deformation of each layer. Unless otherwise noted, as in the discussion of shear zone uniformity, the presented results represent the average shear zone deformation for each layer, and are reported as the average of all measurements taken for that layer within each specimen. The reported values do not include measurements taken after the removal of the test rod section, as the removal of the rod often caused disturbance to the nearest contacting layer of particles. As such, any measurements of the soil specimens after removal of the test rod are used only for qualitative assessments of shear zone deformation and uniformity.

The primary results from the interface shear tests consist of measured shear zone deformations from particles sheared continuously against textured sleeve surfaces. For each specimen, there were two colored layers that experienced continuous shearing against each textured surface. Continuous shearing of all three granular materials was

conducted against four textured surfaces and the previously presented smooth surface. Both the displacement length (63.5 mm) and normal confining stress (50 kPa) were kept constant for all tests. As such, the presented results allow the induced shear zone behavior to be parametrically observed over variations in three distinct properties: the counterface surface roughness (R_a and/or R_{max}), the mean particle diameter (D_{50}) of the granular media, and the representative particle angularity of the granular media. The four tested textured surfaces provided equivalent surface roughnesses ranging from R_a = 70 to 230 μm, R_{max} = 250 to 2000 μm, and R_n = 0.34 to 2.78 and 0.96 to 7.69 for the coarse and fine sands, respectively. Variations in shear zone thickness for the various textured surfaces are presented in units of mm and equivalent multiples of mean particle size (D_{50}) allowing for direct and normalized comparisons. Similarly, variations in the induced length of lateral layer deformations are presented both in terms of the measured deformation (mm) and as a percentage (%) of the total displacement. The results from the tests shearing the granular media against textured friction sleeves are summarized in Table 3-6, and described in detail below.

3.5.3.2 Effect of Sleeve Roughness on Shear Zone Thickness

Surface roughness has been shown by a number of previous researchers to be one of the most important factors affecting the strength of particulate-continuum (soil-geomaterial) interfaces as discussed in Chapter 2. Additionally, the failure mechanism during interface shear is known to be a function of surface roughness. Smooth surfaces typically result in predominantly sliding failures. The percentage of induced shear within the contacting soil mass increases with increased surface roughness up to a critical value, upon which the shear failure becomes governed by the characteristics of the contacting

soil mass. The results of the current study confirm the transition in shearing mechanisms away from the interface and into the soil mass as surface roughness increases. Figures 3-12 and 3-13 show the variations in shear zone thickness as a function of R_{max} and R_n, respectively in terms of both (a) measured thickness (mm) and (b) equivalent mean particle diameter (D_{50}). These results show that shear zone thickness increases with increased surface roughness for all three tested soils. The height of the shear zone increases rapidly from smooth surfaces with the addition of moderate surface texture, with more gradual increases in shear zone thickness observed at values of $R_n \geq 1$, where the asperity height is greater than or equal to the mean particle diameter.

3.5.3.3 Effect of Sleeve Roughness on Shear Zone Length

Uesugi and Kishida (1986a) reported a sharp transition from pure sliding to almost pure shearing for sand – steel interfaces under simple shear loading as a function of increased counterface roughness. They noted that for continuously textured interfaces, surfaces rough enough to induce shearing in the contacting granular soil resulted in predominantly shear failures with very little sliding. As noted earlier, pure shearing failures are undesirable for friction sleeves as this would clog the interface and result in changes in surface properties as a function of depth during penetration. This was taken into account in the design of the textured friction sleeves as noted earlier and the offset diamond texture was designed to be non-clogging. As noted by Uesugi et al. (1988) and discussed in Chapter 2, combined sliding and shearing is typical for heterogeneous surfaces comprised of both slide and shear inducing texture (i.e. both smooth and rough zones). The current measurements of microlevel shear zone deformation allow the relative components of sliding and shearing to be quantified for each friction sleeve-

granular media combination. Figures 3-14 and 3-15 show the variations in shear zone length (i.e. shear component) as a function of R_{max} and R_n, respectively in terms of both measured length (mm) and the percentage of shearing as a function of total displacement. The results show that shear zone length and percentage of shear displacement both increase with increasing surface roughness for all materials. The results from Sand B, the sub-rounded coarse sand, exhibit an upper limit of shear displacement above roughness of R_{max} = 0.5, whereas both of the sub-angular sands (A & C) show a relatively linear increase in shear displacement with increasing roughness. The upper bound of induced shear displacement in the subrounded sand samples is due to the reduced potential for rounded particles to "frustrate" rotation, resulting in particle rotation (not particle sliding) being the controlling failure mechanism at larger surface roughnesses.

3.5.3.4 Uniformity of Induced Interface Shear Zones

The uniformity of induced interface shear zones was investigated by comparing the particle deformations along the tops of the diamonds with those along the passthrough space between columns of diamond texture. As before, the presented results represent an average of all similar measurements taken for each specimen. Table 3-7 shows the results from layers continuously sheared along the tops of the texture, between the texture, and the average of these two measures. Figures 3-16 to 3-18 compare the top and between diamond measurements of the shear zone thickness for each of the granular materials, with Figures 3-19 to 3-21 showing the corollary lateral deformation results. As one can see from the figures and tabulated results, the induced shear zone thickness remains relatively constant circumferentially around the entire shear zone, however the induced lateral displacements are noticeably different for the top and between diamond

measurements. Furthermore, the induced lateral deformations for the coarse granular media (Sands A and B) were fairly homogeneous, with the shear zone length being reduced on the order of 6% (or no more than 1 mean particle diameter) within the passthrough spaces as compared to the deformation directly in line with the diamond asperities. The homogeneity of the lateral deformations in the coarse samples can be clearly seen in the smooth shear zone edges of samples sheared against a 0.5 mm diamond texture as seen in Figures 3-22 and 23. As expected the smaller granular media (Sand C) showed a much larger difference in lateral deformation uniformity, with a reduction on the order of 24% ($\approx 16\ D_{50}$) along the passthrough space as compared to centered over the diamond texture. The heterogeneity of the lateral deformations in the fine granular specimens can be clearly seen in the jagged shear zone of a sample sheared against a 0.5 mm diamond texture, as seen in Figure 3-24. The textured sleeves were designed to induce shear without clogging for all soil types, and as such, some non-homogeneity in the induced shear zone is to be expected for smaller particle sizes.

3.5.3.5 Initiation and Progression of Induced Interface Shear Zones

In addition to the results of continuous textured shearing, sand layers partially sheared against the textured surfaces were used to investigate the initiation and progression of the induced shear zones. Unfortunately, early specimens were not prepared with the full nine layer configuration shown in Figure 3-3 which allows for all possible shearing conditions to be investigated. As such, shear zone progression is presented through comparisons of the shear zones induced from continuous textured shearing with shear zones induced from layers experiencing 67% of their displacement against the textured sleeves, (i.e. shearing against 2 paired rows of texture as compared to

the full 3 paired rows). Figures 3-25 to 3-27 show the progression of shear zone thickness as a function of textured shearing percentage for sands A to C, respectively. Figures 3-28 to 3-29 show corollary comparisons as a function of induced shear zone length. The results show that close to full shear zone thickness is achieved after shearing against two paired rows of diamond texture, with the shear zone heights from the Sand A samples showing the largest difference between partial and full shearing. Measured shear zone length is consistently shorter for the partial textured shearing results as compared to continuous shearing for all soil types measured. This result is to be expected as smooth shearing was shown to induce little to no movement in the contacting granular particles for all materials tested.

3.6 Discussion of Results

3.6.1 Interface Shear Zone Thickness

3.6.1.1 Introduction

The results of granular shearing against smooth CPT friction sleeves resulted in pure sliding for coarse sands, and only minor shear zone deformation in tests with a fine sand. Shear zone thickness was shown to relate to surface roughness in an approximate bilinear trend with increased counterface roughness as seen in Figures 3-12 and 3-13. Unlike the bilinear relationship seen for interface friction, normalizing the roughness by the mean particle size (D_{50}) does not seem to have a unifying effect on shear zone thickness. All three materials did exhibit very similar shear zone thicknesses as a function of R_{max} roughness, and it seems that out of plane asperity height (R_{max}) has a large effect on controlling the thickness of interface shear zones, with an upper limit of interface

shear zone thickness achieved only at texture heights greater than the approximately three times the mean particle diameter for the current intermittent textures.

3.6.1.2 Effect of Particle Angularity

The three testing sands consisted of two sub-angular sands (A and C) of varying mean diameter, and one sub-rounded sand (B) of equivalent grain size distribution to sand A. Previous interface shear studies have shown that while particle angularity can have a large effect on interface strength (Potyondy, 1961; Brumund and Leonards, 1981; others), it has been shown to have a lesser effect on shear zone thickness (Frost et al., 1999). While increases in particle angularity do not increase the thickness of induced shear zones, the void ratio of shear bands comprised of angular particles are often higher, even exceeding global e_{max} locally at the contact surface. The current results confirm previous sentiment that angularity does not largely affect shear zone thickness, as sands A and B show equivalent thicknesses over all tested surface roughnesses. Only minor variations in shear zone thickness were noted between sands A and B, on the order of one particle diameter, with the less angular sand (B) exhibiting slightly thicker shear zones on average.

3.6.1.3 Effect of Mean Particle Size (D_{50})

Figures 3-12 and 3-13 showed the induced shear zone thickness as a function of surface roughness, both directly (mm) and normalized (D_{50} equivalents), respectively. These results contradict the classical notion that an induced interface shear zone within a granular assembly can be represented by a unique (or narrow range) multiple of particle diameter. The results clearly show that the fully developed interface shear zone for all

three sands comprise a zone of almost equivalent thickness. The larger sized sands (A and B) showed an upper limit interface shear zone thickness on the order of 6 to 7 D_{50}, whereas, the smaller sized sand (C) exhibited an upper shear zone thickness of 14 to 16 D_{50}. Normalizing the surface roughness with the particle size (R_n) did not prove to create a unifying trend within the data for the current intermittent textures.

3.6.1.4 Shear Zone Uniformity

The current texturing scheme uses offset asperities of varying out of plane height to create friction sleeves of varying surface texture. While a non-continuous, non-uniform texturing scheme allows the surface texture to be non-clogging, there is the possibility of creating a non-uniform shear zone at different positions around the circumference of the textured sleeve. The uniformity of the induced shear zone thickness was investigated by comparing the measured thicknesses taken along the centerline of diamond asperities with measurements taken along the centerline of the passthrough space between asperities, as shown in Figures 3-19 to 3-21. The results for the two coarse test sands (Sands A and B) showed only slight variations in measured shear zone thickness, with all variations less than one particle diameter. Test sand C, consisting of finer sand particles, showed slightly higher variation in the shear zone thickness, especially at R_{max} = 1 mm. Figures 3-22 to 3-24 show photographs taken after the removal of the textured sleeve, showing the uniformity of the induced shear zones within the coarse sand samples, and the slight heterogeneity of the induced shear zone within the fine sand samples. However, the shear zones at all other R_{max} values showed only minor variations in shear zone thickness across the shear zone, and it seems reasonable to conclude that the current texturing scheme induces shear zones of relatively uniform thickness across the range of

tested parameters. Soils of smaller diameter, or fine grained soils (silts and clays), may behave slightly less uniformly, and future experiments hope to investigate these effects across a larger range of soils.

3.6.1.5 Initiation and Progression of the Shear Zone

Each specimen contained layers exposed to both continuous and partial textured shearing. The initiation and progression of the shear zones induced by the current sleeve texturing pattern was investigated by analyzing the shear zone thicknesses induced by varying percentages and magnitudes of textured shearing. Figures 3-25 to 3-27 showed the progression of shear zone thickness for increasing surface roughness. For Sands B & C, the induced shear zones became fully formed for all levels of surface roughness that created detectable shear zones after shearing against only 2 rows (~ 40 mm) of diamond texture. With a fully formed shear zone taken as any zone for which a constant deformed thickness was maintained for textured shearing of any length over the critical minimum length. Sand A did not show a stabilization of shear zone thickness for textured shear displacements less than 63.5 mm. It is believed that the increased rotational frustration and particle interlocking provided by sub-angular particles results in the delayed formation of the full shear zone thickness of Sand A seen in Figures 3-25 as compared to the sub-rounded shear zone formation seen in Figure 3-26. However, it is supposed that the shear zone thickness formed after 63.5 mm of textured shearing represents a fully formed shear zone, as the thickness converged towards a stable thickness for all roughnesses above R_{max} = 0.5 mm. The current results lead to the possible future application of shortened friction sleeves for in-situ characterization, as constant shear zones were formed after only partial length shearing across a wide range of surface

textures. For the current sleeve texturing pattern, the minimum length required to induce fully formed shear zones appears to be equal to three rows of offset texture. This corresponds to a requisite critical textured shearing length of approximately 65 mm, as compared to the conventional CPT friction sleeve length of 157 mm. For surfaces comprised of continuous homogeneous texture, as opposed to the current offset asperities, the critical minimum length to induce a fully formed shear zone would be further reduced. However, in the case of continuous penetrating measurement devices, such as the CPT, the use of continuous homogeneous texturing is not practically feasible due to clogging considerations.

3.6.2 Shear Zone Deformation Along the Interface

3.6.2.1 Introduction

The addition of texture to the surface of smooth friction sleeves proved to greatly affect the level of lateral deformation seen in the tested sands. As seen in Figures 3-14 and 3-15, the percentage of granular deformation at the contact surface generally increased with increasing surface roughness for all three sands. The maximum observed shearing percentages for the three sands were 23.0, 14.3, and 26.9% observed at the maximum surface roughness value of R_{max} = 2 mm for sands A, B, and C, respectively. The use of offset out-of plane asperities successfully created a non-clogging failure consisting of combined particle sliding and shearing at the interface. As found in previous studies of interface behavior, the counterface surface roughness seems to be a primary controlling component of not only interface strength behavior but also of shear zone extent, uniformity, and initiation.

3.6.2.2 Effect of Particle Angularity

While particle angularity does not appear to have a large influence on shear zone thickness, it does have a defining effect on the lateral shear zone deformation. Figures 3-14 and 3-15 highlighted the divergence in the trends of lateral deformation for the sub-angular and sub-rounded sands. This divergence was marked by an almost linearly increasing lateral deformation for the more angular granular assemblies (Sands A & C), whereas, the tests with the sub-rounded sand (B) showed an upper bound for shear zone deformation at roughness levels of approximately $R_{max} \geq 0.5$ mm. It has long been noted in numerical (Boulon, 1989) and experimental (Oda et al., 1982; Kishida and Uesugi, 1987) models that particle rotation becomes a large component of shear failure for rounded particles. While the current procedures provide no basis for tracking particle movements during shear, and thus no way to track particle rotations, it is hypothesized that the divergence in lateral shear zone deformation for rounded and angular particles is predominantly due to the greater resistance to rotation (or rotational frustration) provided by angular particles, resulting in sliding remaining the lowest energy failure mechanism across a wider range of counterface roughnesses.

3.6.2.3 Effect of Mean Particle Size (D_{50})

Figures 3-14 and 3-15 showed the lateral shear zone deformation as a function of surface roughness, both directly (mm) and normalized (D_{50} equivalents), respectively. As discussed above, the fine sand (C) exhibited minor shear zone deflection for all sleeve textures including the smooth sleeve, whereas the two coarser sands (A & B) only experienced lateral deformation for textured sleeve shearing. The representative shear zone deformations of sands A and C maintained a relatively constant differential across

the range of tested sleeve textures, and as such the mean particle diameter seems to have only a minor influence on the shear zone deformation after the onset of shearing for sub-angular particles. The effect of particle size on the interface shear deformation of sub-rounded sands and other particle types will be investigated in future continuing efforts to better understand the micromechanical deformations of geotechnical interfaces.

3.6.2.4 Shear Zone Uniformity

The current texturing scheme uses offset asperities of varying out of plane height to create friction sleeves of varying surface texture. While a non-continuous, non-uniform texturing scheme allows the surface texture to be non-clogging, there is the possibility of creating a non-uniform shear zone at different positions around the circumference of the textured sleeve. The uniformity of the induced shear zone length was investigated by comparing the measured deformations taken along the centerline of diamond asperities with measurements taken along the centerline of the passthrough space between asperities. The results for the two coarse test sands (A & B) showed only slight variations in measured shear zone length, with all variations less than one particle diameter as seen in Figures 3-19 and 3-20. Test sand C, consisting of finer sand particles, showed considerable variation in the lateral deformation of the shear zone, with the variation increasing with increasing R_{max} roughness as seen in Figure 3-21. As the representative contacting particle diameter decreases, the passthrough space becomes larger with respect to the particle size. As a result, interaction between the particles within the passthrough space and along the line of texture decreases and the shear zone displacement subsequently becomes less uniform. This phenomena will be increased for soils of

smaller diameter than those tested herein (e.g. silts and clays), and future experiments hope to quantify this effect.

3.6.2.5 Initiation and Progression of the Shear Zone

Each specimen contained layers exposed to both continuous and partial textured shearing. The initiation and progression of the shear zone lengths induced by the current sleeve texturing patterns were investigated by analyzing the shear zone deformations induced by varying percentages and magnitudes of textured shearing. Figures 3-28 to 3-30 showed the progression of shear zone lateral deformation as a function of increasing surface roughness. All three of the tested sands exhibit increased shear zone deformation as a result of increased textured shearing. Sands A and C exhibit moderate variations in shear zone length for partial (67%) and full (100%) textured shearing at low textures, with increased lengthening of the shear zones for higher percentages of textured shear exposure as surface roughness increases. Whereas, Sand B displays an approximately constant rate of shear zone deformation as a function of textured shear percentage for all tested surface roughnesses of R_{max} = 0.5 mm and greater. The noted differences in shear zone progression between the tested sands is attributed to the difference in particle angularity and the subsequent increase in particle rotation present in rounded particle assemblies during interface shear. This conclusion is supported by the similarity in behavior of the two sub-angular sands of varying size, highlighting the greater dependence of lateral shear zone deformation on particle angularity.

3.6.3 Comparison with Homogeneously Textured Interfaces

As discussed in Section 3.3, the textured friction sleeves used with the MFSA and MPFA devices utilize an intermittent texturing pattern. Intermittent spacing of raised textural asperities along a smooth base substrate have been shown to discourage clogging of the interface with soil particles during shear against a large range of soil types. This serves to suppress clogging as textured sleeves pass through various soil horizons during penetration. In order to achieve a non-clogging surface texture, the textured friction sleeves must induce at least partial sliding failure for all encountered soil types over the full range of texture levels.

The relative contributions of sliding and shearing as a function of counterface surface roughness were discussed in Chapter 2, with the percentage of sliding reducing with increased counterface roughness for traditional continuously textured interfaces. As seen in the experimental results of Uesugi et al. (1988) and DeJong et al. (2003), shearing becomes the dominant failure mechanism for surfaces of sufficient texture to induce the full internal shear strength of the contacting particulate. As with internal particulate shearing, some sliding does still occur during interface shearing against surfaces above the critical roughness, with 10% sliding reported using PIV for a fully induced *"$\delta = \phi$"* condition by DeJong et al. (2003) for a subrounded coarse sand. As such, it can be seen that the existence of partial sliding does not preclude the full induction of internal soil strength during interface shear. The fundamental question then becomes: *"How does particulate interface shear against continuous texturing compare with shear against intermittently textured surfaces?"*. Figure 3-31, shows a schematic comparing continuous and intermittent texturing.

It is currently proposed that the thickness of the shear zones formed against surfaces of varying types (e.g. continuous vs. intermittent texture) micromechanically governs the behavior of the problem. In other words, the thickness of the active particulate region governs the interface behavior, and surfaces inducing shear zones of comparable size for equivalent particulate structures produce approximately equal interface behaviors holding all other parameters constant. This concept is based on the knowledge that internal shear zone thickness of particulates is known to be unique for a given particulate under specific boundary conditions, and that micromechanical length scale governs the global behavior during localization. The interface shear zone thickness is known to be a dominant factor controlling the transfer of forces between the particulate and continuum materials (e.g. retaining walls, silo walls, piles, etc.), and vice-versa (Tejchman, 2000). Correspondingly, there is also a unique interface shear zone thickness that corresponds to the full induction of internal strength during interface shear. This concept bearing the exception that very rough surfaces may induce more than half particulate shear zones up to the limiting condition of a full internal shear zone forming adjacent to the interface as often reported for fine grained materials (Lehane, 1992; Lehane and Jardine, 1994; Burns and Mayne, 1998) and for granular materials (Tejchman and Wu, 2000). In summary, the proposed hypothesis states that the thickness of induced interface shear zone is the governing parameter of interface behavior irrespective of the surface texturing responsible for the particulate disturbance, or the relative percentage of interface sliding.

To corroborate the current hypothesis, the current results are compared to previous experimental studies of homogenously textured surfaces. Frost and Lee (2002)

investigated the void ratio evolution of Sand B away from geomembranes of varying levels of texture. They reported that fully formed shear zones induced an area on the order of 5 to 6 D_{50} (~ 4 mm) away from the shear zone. DeJong et al. (2003) report interface shear zone thickness ranging from 4.6 to 5.6 mm (~ 6 to 8 D_{50}) for uncemented IMDEX 16-30 subrounded sand. The current texturing scheme induced shear zones of comparable size for textures on the order of R_{max} = 0.5 mm and higher, as seen in Figure 3-12. The intermittent spacing of the current texturing scheme changes the critical roughness required to induce the full internal strength from the typical order of $R_n \approx 0.1$ for continuously textured surfaces to an order of $R_n \approx 1$, based on the induction of similar thickness shear zones. Previous experimental studies using sand similar to Sand C (Yoshimi and Kishida, 1981a; Oda and Kazama, 1998) report full interface shear zones of 1.4 – 2.2 mm (~ 5 to 8 D_{50}) and 1.6 mm (8 D_{50}), respectively. The current texturing scheme induced shear zones similar to the continuously textured surfaces at increased roughness values similar in magnitude to those found for the coarse sands, $R_n \approx 1$. Additionally, Sand C exhibited an upper limit of interface zone thickness on the order of the full internal shear zone typically found for fine subangular sands, on the order of 15 D_{50} equivalents (Mühlhaus and Vardoulakis 1987; Oda and Iwashita, 2000). Future studies furthering this hypothesis are underway, and hopefully coincident measures of shear zone thickness and interface resistance for both continuously and intermittently textured surfaces can be performed parametrically under similar boundary conditions.

3.6.4 Comparison with In-Soil Shear Zones (Bands)

Previous researchers have theorized that interface shear zones are analogous to half in-soil shear bands (Frost and DeJong 2002b; Baylac et al., 2003; Frost et al., 2004).

Internal soil shear zones typically form centered around an internal line of symmetry that can be thought of as a virtual surface within the particulate assembly, as represented in Figure 3-32. Internal shear zone thickness has been shown to vary as a function of mean grain diameter (Vardoulakis, 1980; Yoshida et al., 1994), initial particulate density (Tejchman, 1989; Hassan, 1995), state of stress (Desrues and Hammad, 1989; Tatsuoka et al., 1991, Hassan, 1995), and shear rate and direction (Löffelmann, 1989). With several previous researchers noting that shear zone thickness is unique for specific granular property - boundary condition combinations. The uniqueness of internal shear zone size stems from the dependence of virtual surface roughness on the properties of the particulate media. Whereas, the thickness of interface shear zones is further dependent on the roughness and other characteristics of the counterface surface, and thus non-unique for consistent particulate and boundary conditions. Additionally, some shearing conditions do not form internal shear localizations just as smooth interface shearing typically results in homogeneous non-localizing shear at the interface.

As a result, while the controlling mechanisms of interface and internal shear zones are fundamentally similar, the thickness of interface and half internal shear zones should only be uniquely coincident for interfaces of equivalent roughness to the characteristic roughness of the granular shear surface, denoted herein as virtual roughness. The virtual failure surfaces of internal shear bands can be considered to have relatively continuous and homogenous roughness across the shear zone for homogeneous particulate structures. As a result, the analogy between internal and interface shear zones is only deemed valid for counterfaces consisting of relatively homogeneous texture. Additionally, it is currently theorized that the virtual surface of in-soil shear zones

approximately equals a unique continuum surface roughness equal to the critical roughness required to induce the full internal shear resistance and thus induce a shear zone of equivalent half thickness. A more detailed account of virtual roughness quantification and comparisons to interface behaviors can be found in Evans (2005).

3.7 Conclusions

The current study was aimed at performing a detailed proof of concept test series to investigate the micromechanical response of a variety of granular materials to the current texturing pattern used to roughen friction sleeves employed on the MFS and MPF attachments. The following observations regarding the response of granular materials sheared against traditional and textured friction sleeves have been made:

- Interface shearing of coarse granular media against conventional smooth friction sleeves was shown to not induce a shear zone, and resulted in a pure sliding failure under the current test conditions.
- Interface shearing of a fine sand against conventional smooth friction sleeves was shown to induce only a minimal shear zone, and resulted in a combined failure mechanism consisting mostly of sliding deformation on the order of 98% under the current test conditions.
- The current offset diamond texturing pattern used to add varying levels of surface roughness to friction sleeves, Table 3-1 and Figure 3-2, has been experimentally verified to induce non-clogging shear across the range of sleeve roughnesses and granular soils tested.

- The current results corroborate previous accounts of the independence of interface shear zone thickness and granular particle angularity.
- Interface R_{max} roughness has been shown to have a dominant effect on induced interface shear zone thickness as compared to the contacting particulate size and angularity. This is divergent from the behavior of internal shear zones, and results from the uniqueness of internal "virtual roughness" as compared to the non-uniqueness of interface roughness with respect to the contacting particulate properties.
- The employed offset texturing scheme served to produce shear zones of approximately uniform thickness for all soils tested.
- The percentage of lateral shear deformation was shown to be largely dependent on particle angularity for roughness values above a critical value. Rounded particles exhibited an upper limit of shear displacement with increased interface roughness, while more angular particles exhibited an approximately linear trend between shear deformation and interface roughness over the range of roughnesses tested.
- The lateral deformation induced in the tested coarse sands was approximately uniform, whereas the fine sand exhibited non-uniform lateral deformation as a result of the offset texturing pattern. It is believed, and has been noted in-situ, that the non-uniformity of the induced shear displacement will increase with decreasing particle size, but will remain non-clogging over the range of typically encountered soils.
- The current texturing scheme has been experimentally shown to induce interface shear zones equivalent to those reported for fully formed zones induced by

continuous texture. The critical roughness required to induce full shear zones for the current intermittent texturing scheme ($R_n \approx 1$) is increased by an order of magnitude over that typically required for continuous texturing ($R_n \approx 0.1$). The amount of R_n roughness necessary to fully engage the internal resistance of the contacting particulate (*"$\delta = \phi$"* condition) is believed to be dependent on the spacing and other characteristics of the texture.

- Induced shearing by intermittent textures constitutes a lower percentage of the failure mechanism as compared to failure against continuous textures. It is hypothesized that this disparity in lateral deformation does not preclude the full engagement of particulate resistance for intermittently textured surfaces producing shear zones of equivalent thickness.

The results of the current parametric study have served to validate the ability of the current sleeve texturing scheme to induce shearing within various contacting particulate media across a range of surface roughnesses. The induced shear was shown to be non-clogging across the range of typically encountered granular materials, and is believed to represent an optimal balance between induced shearing and sliding across the range of soils typically encountered in-situ. Sleeve textures of high R_{max} roughness have been shown to induce shear zones of equivalent and greater thickness than interface shear zones known to engage the full internal resistance of contacting particulates during tests with more conventional continuous textures. As such, it is believed that sleeves using the current offset texturing scheme can investigate the complete range of typically encountered interface strengths, ranging from smooth surface sliding up to the full

engagement of internal soil strength. This study has served to not only validate the effectiveness of the current textured sleeves at investigating interface behavior in-situ, but has also further advanced the fundamental understanding of the micromechanical interface interactions necessary to fully understand the behavior of continuum surfaces placed in contact with particulate geomaterials.

Table 3-1. Summary of Smooth and Textured Sleeve Dimensions and Surface Roughness Values.

Sleeve ID#	Height (H)	Pen. Angle (β)	Diagonal Spacing (S)	Percent Pass-through	Width (W)	Angle (α)	R_{max} [1]	R_p [2]	R_t [3]	R_a [4]	Δ_a [5]	R_s [6]
	(mm)	(deg)	(mm)	(%)	(mm)	(deg)	(mm)	(mm)	(mm)	(mm)	(deg)	
SM[7]	N/A	N/A	N/A	100	N/A	N/A	0.0064	0.0021	0.0043	0.0005	7.766	N/A
30H.25S3	0.25	60	6.3	15.7	5.3	45	0.25	0.210	0.040	0.066	0.991	1.015
30H.5S3	0.50	60	6.3	15.7	5.3	45	0.50	0.429	0.071	0.117	1.912	1.030
30H1S3	1.00	60	6.3	15.7	5.3	45	1.00	0.880	0.112	0.185	3.541	1.055
30H2S3	2.00	60	6.3	15.7	5.3	45	2.00	1.864	0.136	0.226	5.950	1.093

Note: All roughness parameters defined in Table 2-2. [1] R_{max}: Maximum peak to valley height; [2] R_p: Maximum peak to mean line height; [3] R_t: Mean line to lowest valley height; [4] R_a: Average roughness; [5] Δ_a: Average slope roughness; [6] R_s: 3-D areal roughness; [7] Actual Measurements of a New CPT Sleeve and therefore high average slope values due to micro texture from machining process. Only R_a = 0.50 μm defined by ASTM Standards.

Table 3-2. Properties of Granular Test Materials.

	Sand A Blasting 20-30	Sand B Ottawa 20-30	Sand C Ottawa 50-70
Predominant Mineral	Quartz	Quartz	Quartz
Grain Shape / Angularity	Sub-angular	Sub-rounded	Sub-angular
G_s	2.65	2.65	2.65
D_{50} (mm)	0.72	0.72	0.26
C_u	1.25	1.25	1.20

Table 3-3. Properties of Powder Phenolic Resin.

Manufacturer	Rutgers-Plenco LLC
Product	Phenolic Compound #10510
Curing Temperature	150-175º C
Curing Time	>10 minutes
% Retained on #200 Sieve	0.70%
Specific Gravity	1.2-1.3
Mixture Percentage By Weight w/ Sand	1%
Solubility in Water	Slight
Appearance	Finely Ground Cream-Tan Powder
Odor	Slight Phenol Odor

Table 3-4. Summary of Microscale Axisymmetric Interface Shear Tests

Sand Type	Test #	Sleeve ID	R_{max} (mm)	R_a (mm)	R_n	Displacement (mm)	D_r	# of Layers
A	10	H0.25	0.25	0.07	0.3	63.5	Med	8
A	11	H0.50	0.50	0.12	0.7	63.5	Med	7
A	9	H1.00	1.00	0.19	1.4	63.5	Med	7
A	8	H2.00	2.00	0.23	2.8	63.5	Med	7
B	1	SM	0.00	0.0064	0.0	63.5	Med	5
B	4	H0.25	0.25	0.07	0.3	63.5	Med	5
B	12	H0.50	0.50	0.12	0.7	63.5	Med	9
B	2	H1.00	1.00	0.19	1.4	63.5	Med	5
B	3	H2.00	2.00	0.23	2.8	63.5	Med	6
C	7	H0.25	0.25	0.07	1.0	63.5	Med	7
C	13	H0.50	0.50	0.12	1.9	63.5	Med	9
C	6	H1.00	1.00	0.19	3.8	63.5	Med	7
C	5	H2.00	2.00	0.23	7.7	63.5	Med	5

Table 3-5. Shear Zone Deformation Measurement for Conventional Friction Sleeves

Sand Type	R_{max} (mm)	R_a (mm)	R_n	Zone Height	Height in D_{50}	Zone Length	% of Disp
A	0.0064	0.0005	0.009	0.0	0.0	0.0	0.0
B	0.0064	0.0005	0.009	0.0	0.0	0.0	0.0
C	0.0064	0.0005	0.025	1.1	4.2	1.4	2.2

Table 3-6. Shear Zone Deformation Measurement for Textured Friction Sleeves

Sand Type	R_{max} (mm)	R_a (mm)	R_n	Zone Height	Height in D_{50}	Zone Length	% of Disp
A	0.25	0.07	0.347	2.2	3.0	1.9	3.0
	0.50	0.12	0.694	3.7	5.0	4.6	7.2
	1.00	0.19	1.389	3.8	5.3	7.3	11.4
	2.00	0.23	2.778	4.5	6.2	14.6	23.0
B	0.25	0.07	0.347	2.6	3.6	2.5	3.9
	0.50	0.12	0.694	3.8	5.3	7.9	12.4
	1.00	0.19	1.389	4.5	6.2	8.3	13.1
	2.00	0.23	2.778	5.0	6.9	9.1	14.3
C	0.25	0.07	0.962	2.5	9.6	3.6	5.6
	0.50	0.12	1.923	3.1	11.8	6.0	9.5
	1.00	0.19	3.846	3.8	14.8	12.8	20.1
	2.00	0.23	7.692	3.9	15.0	17.1	26.9

Table 3-7. Shear Zone Deformation Measurements Detailing the Uniformity of the Induced Shear Zones

				Average Values				Top of Diamonds				Between Diamonds			
Sand Type	**R_{max} (mm)**	**R_a (mm)**	**R_n**	**Zone Height**	**Height in D_{50}**	**Zone Length**	**% Disp**	**Zone Height**	**Height in D_{50}**	**Zone Length**	**% Disp**	**Zone Height**	**Height in D_{50}**	**Zone Length**	**% Disp**
A	0.0064	0.0005	0.01	0.0	0.0	0.0	0.0	0.0	0.0	0.0	0.0	0.0	0.0	0.0	0.0
	0.25	0.07	0.35	2.2	3.0	1.9	3.0	2.3	3.2	2.0	3.1	2.0	2.7	1.9	3.0
	0.50	0.12	0.69	3.7	5.0	4.6	7.2	3.7	5.1	4.8	7.5	3.6	5.0	4.3	6.7
	1.00	0.19	1.39	3.8	5.3	7.3	11.4	3.9	5.4	7.5	11.8	3.8	5.3	7.0	11.1
	2.00	0.23	2.78	4.5	6.2	14.6	23.0	4.6	6.4	14.6	23.0	4.3	6.0	14.6	23.0
B	0.0064	0.0005	0.01	0.0	0.0	0.0	0.0	0.0	0.0	0.0	0.0	0.0	0.0	0.0	0.0
	0.25	0.07	0.35	2.6	3.6	2.5	3.9	2.7	3.8	2.6	4.2	2.5	3.4	2.3	3.7
	0.50	0.12	0.69	3.8	5.3	7.9	12.4	3.9	5.4	8.0	12.6	3.8	5.3	7.7	12.2
	1.00	0.19	1.39	4.5	6.2	8.3	13.1	4.7	6.5	8.5	13.4	4.3	5.9	8.1	12.8
	2.00	0.23	2.78	5.0	6.9	9.1	14.3	5.0	7.0	9.6	15.1	4.9	6.9	8.8	13.9
C	0.0064	0.0005	0.02	1.1	4.2	1.4	2.2	1.1	4.2	1.4	2.2	1.1	4.2	1.4	2.2
	0.25	0.07	0.96	2.5	9.6	3.6	5.6	2.6	9.8	4.1	6.5	2.5	9.4	3.0	4.8
	0.50	0.12	1.92	3.1	11.8	6.0	9.5	3.2	12.1	6.9	10.9	3.0	11.4	5.1	8.1
	1.00	0.19	3.85	3.8	14.8	12.8	20.1	4.1	15.8	14.0	22.1	3.6	13.8	11.5	18.2
	2.00	0.23	7.69	3.9	15.0	17.1	26.9	4.0	15.2	19.5	30.7	3.8	14.8	14.7	23.1

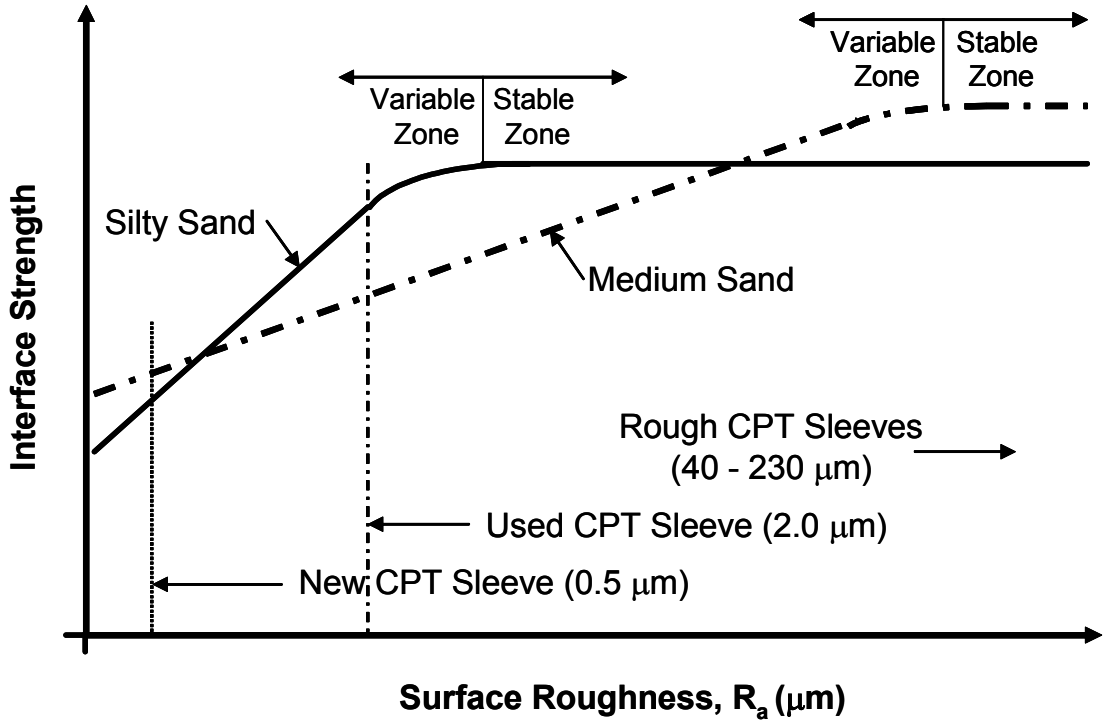

Figure 3-1. Schematic of Bilinear Surface Roughness – Interface Strength Relationship for Two Soils to Demonstrate the Potential Effect of Changes in CPT Friction Sleeve Roughness on f_s Measurements (after DeJong, 2001).

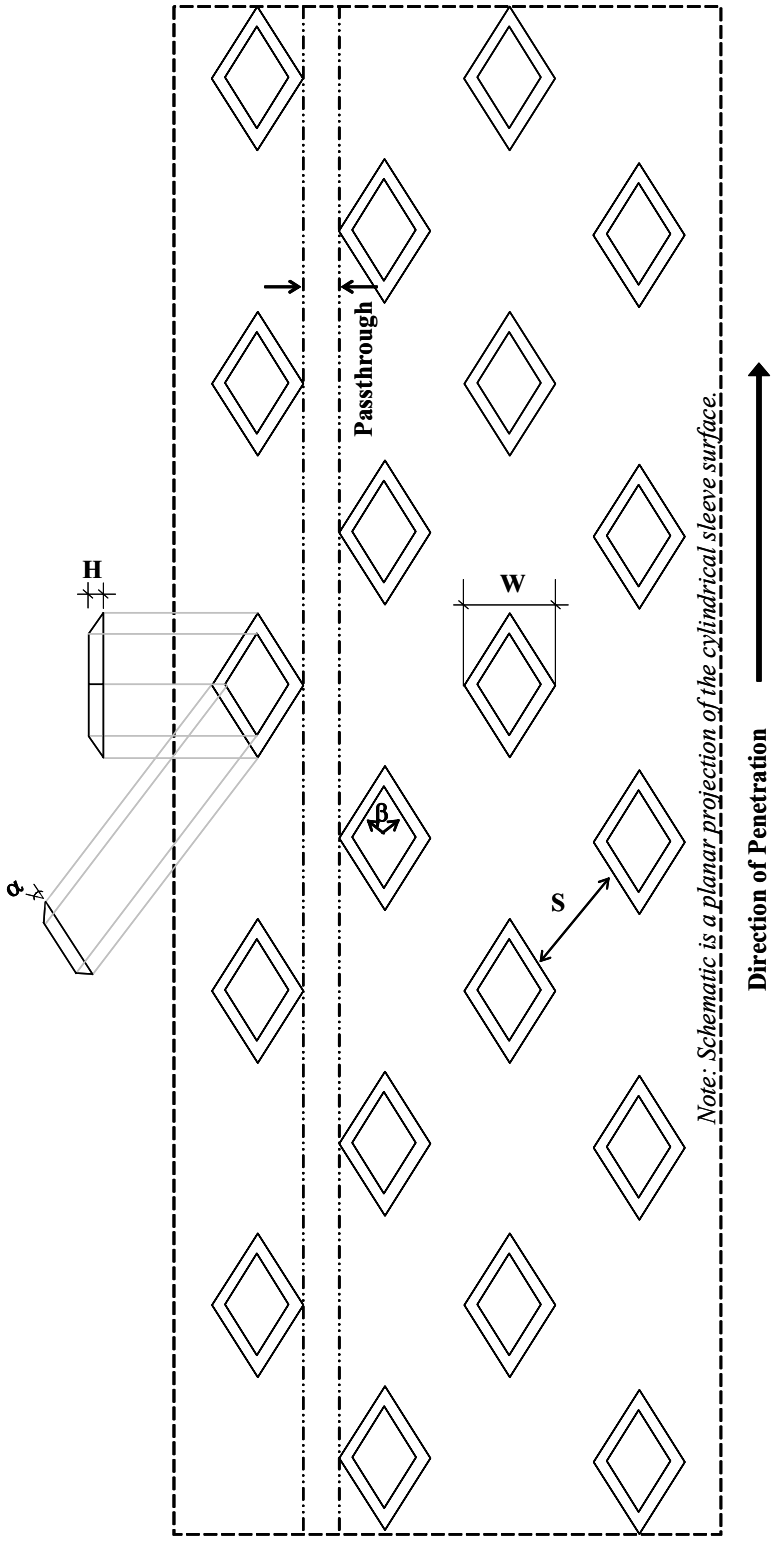

Figure 3-2. Schematic of Diamond Texturing Pattern Used to Create Varying Levels of Surface Texture on Textured Friction Sleeves.

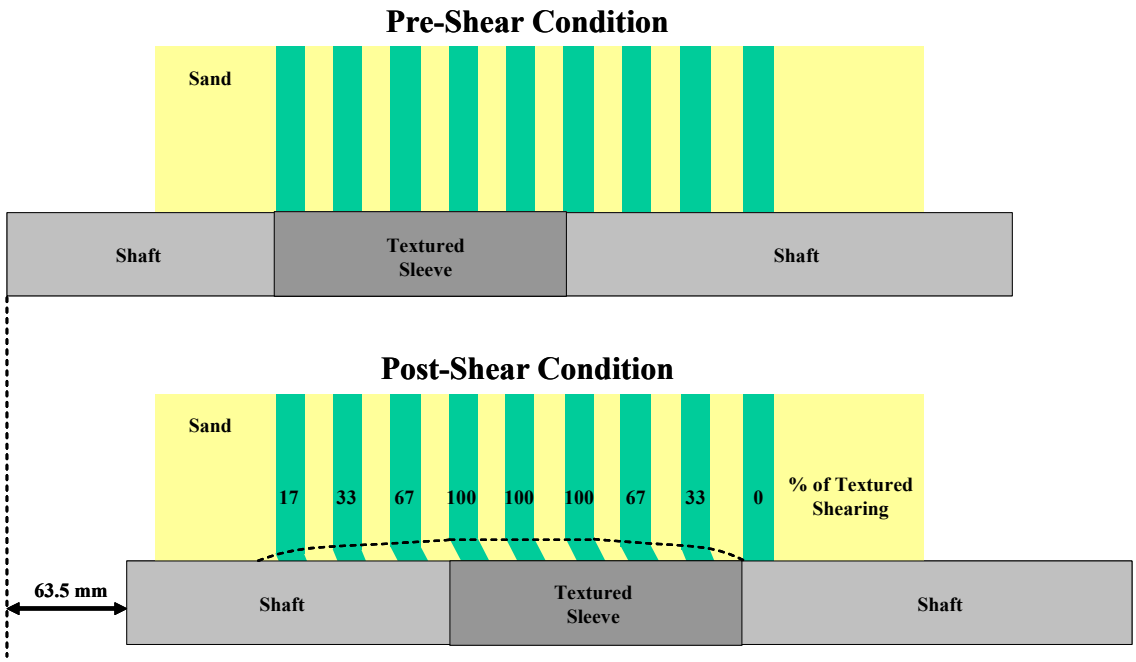

Figure 3-3. Schematic Showing the Configuration of Colored Layers Within Each Axisymmetric Test Sample Both Pre and Post Shear (Total Displacement Equal to 63.5 mm).

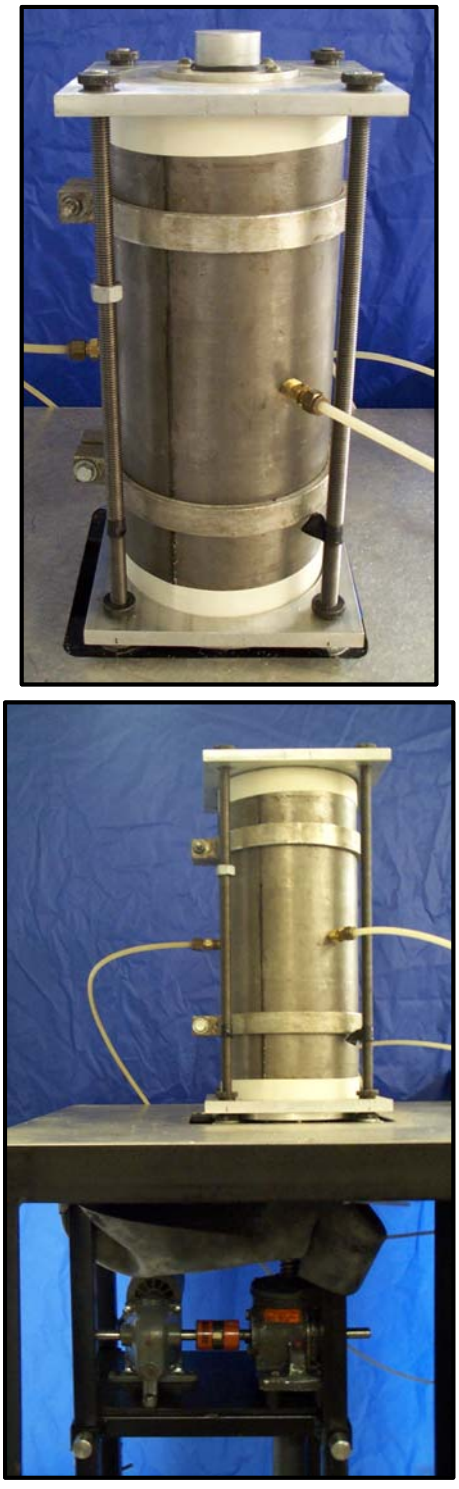

(a)

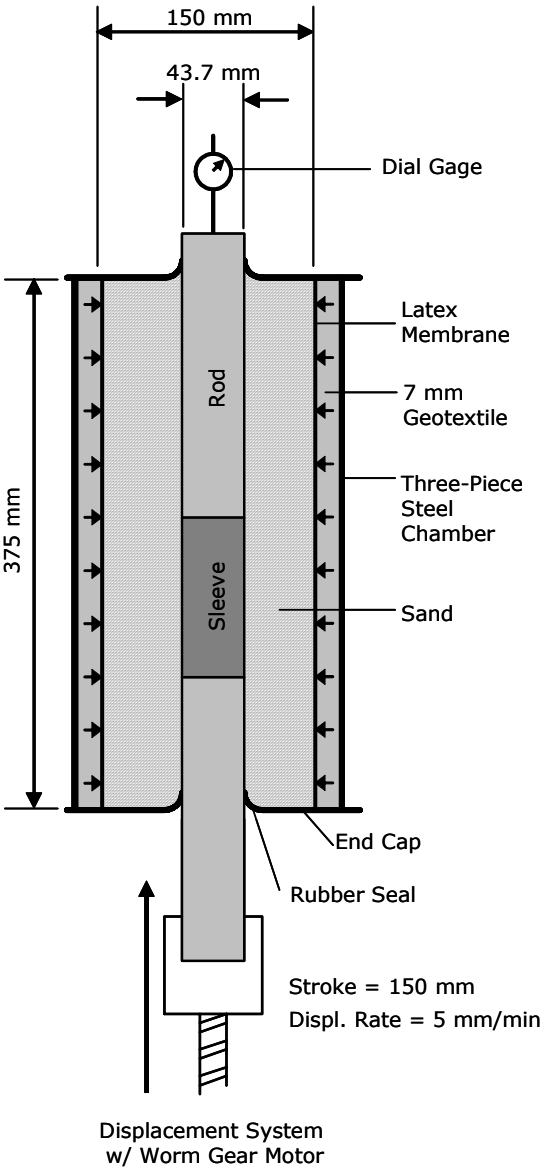

(b)

Figure 3-4. Axisymmetric Shear Apparatus (a) Photographs (b) Schematic. (after DeJong, 2001)

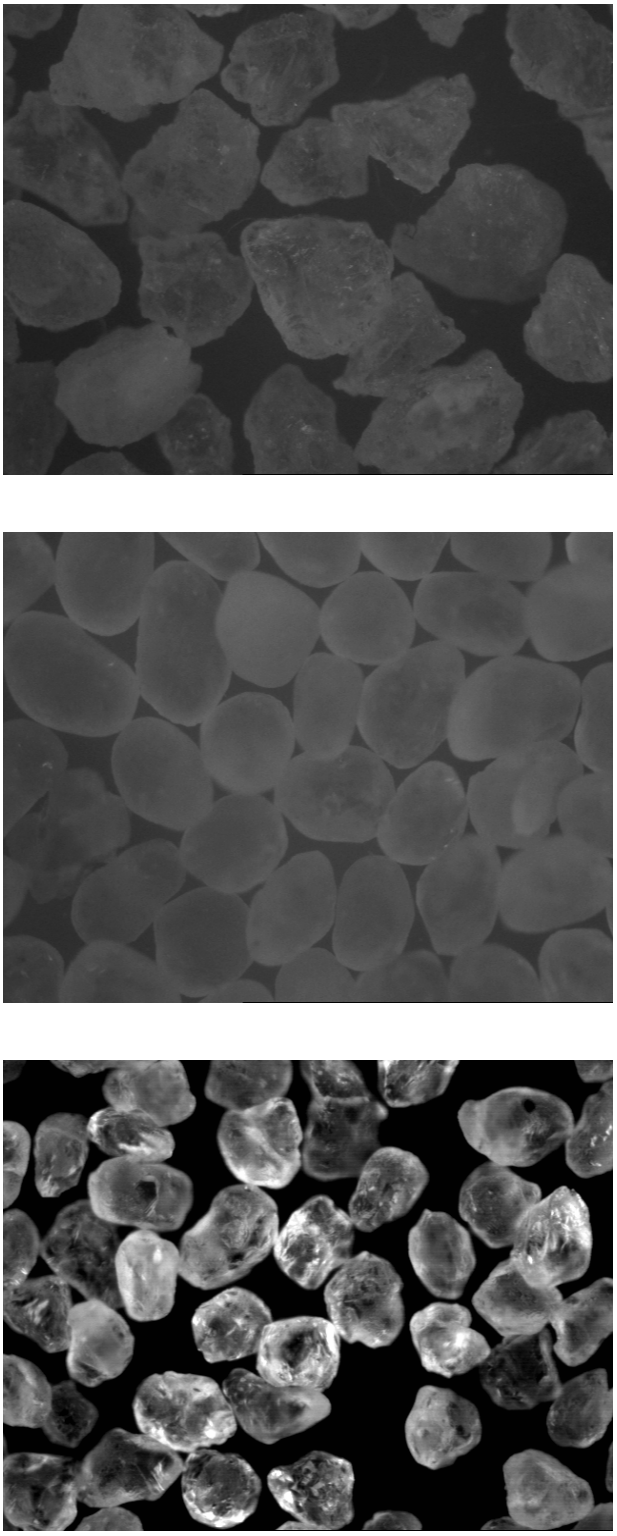

Figure 3-5. Photographs of Test Sands (a) Blasting 20-30, (b) Ottawa 20-30, and (c) Ottawa 50-70.

Figure 3-6. Picture of Axisymmetric Interface Shear Sample with Textured Sleeve and Test Rod Still in Place, Showing a Preserved Post Shear Investigation Plane Ready for Analysis in a Sample of 50-70 Sub-Angular Sand Sheared Against a Sleeve with Surface Texture of R_{max} = 0.5 mm Over a Total Displacement of 63.5 mm.

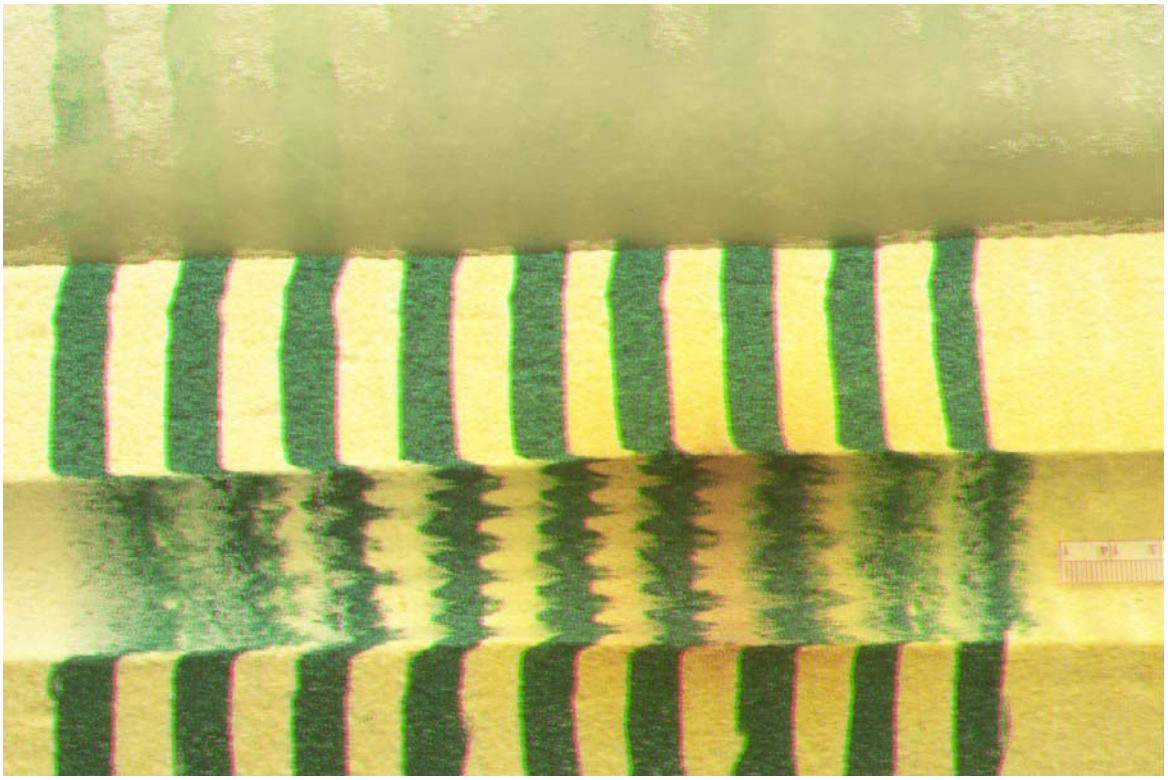

Figure 3-7. Picture of Axisymmetric Interface Shear Sample with Textured Sleeve and Test Rod Removed, Showing Shear Zones Preserved in a Sample of 50-70 Sub-Angular Sand Resultant from Shearing Against a Sleeve with Surface Texture of R_{max} = 0.5 mm Over a Total Displacement of 63.5 mm.

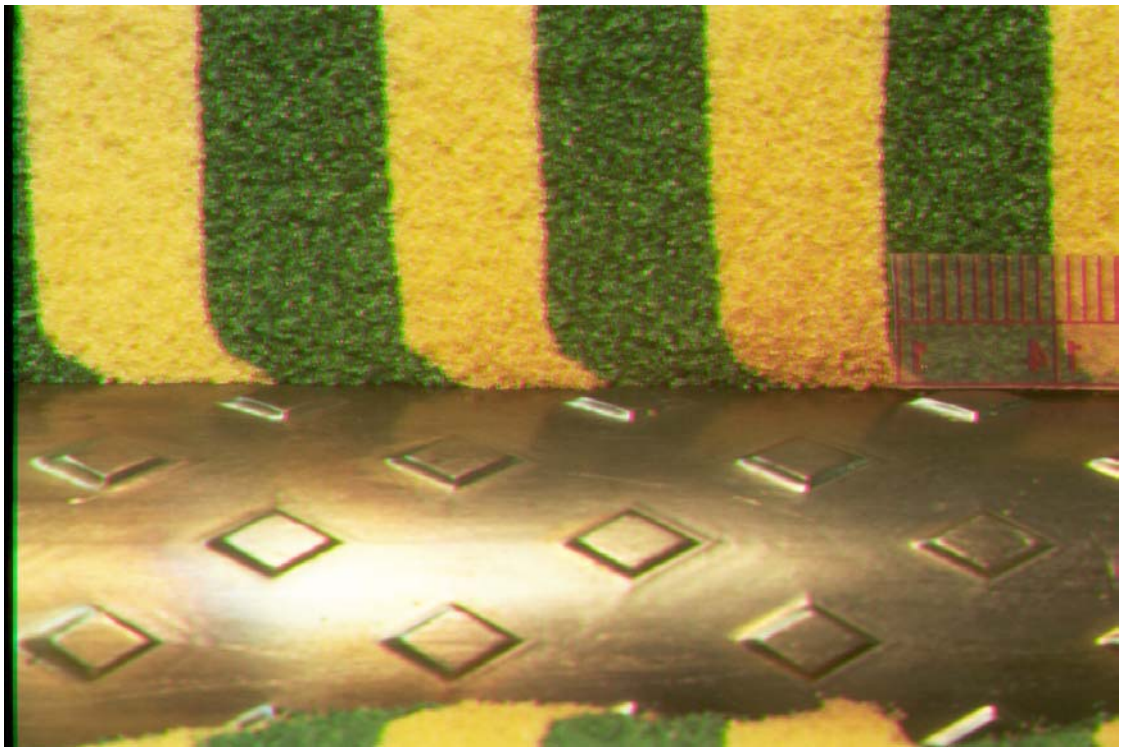

Figure 3-8. Picture Displaying an Investigation Plane Located Along the Centerline of the Passthrough Space Between Diamond Texture Asperities, Post Shear (63.5 mm Total Displacement).

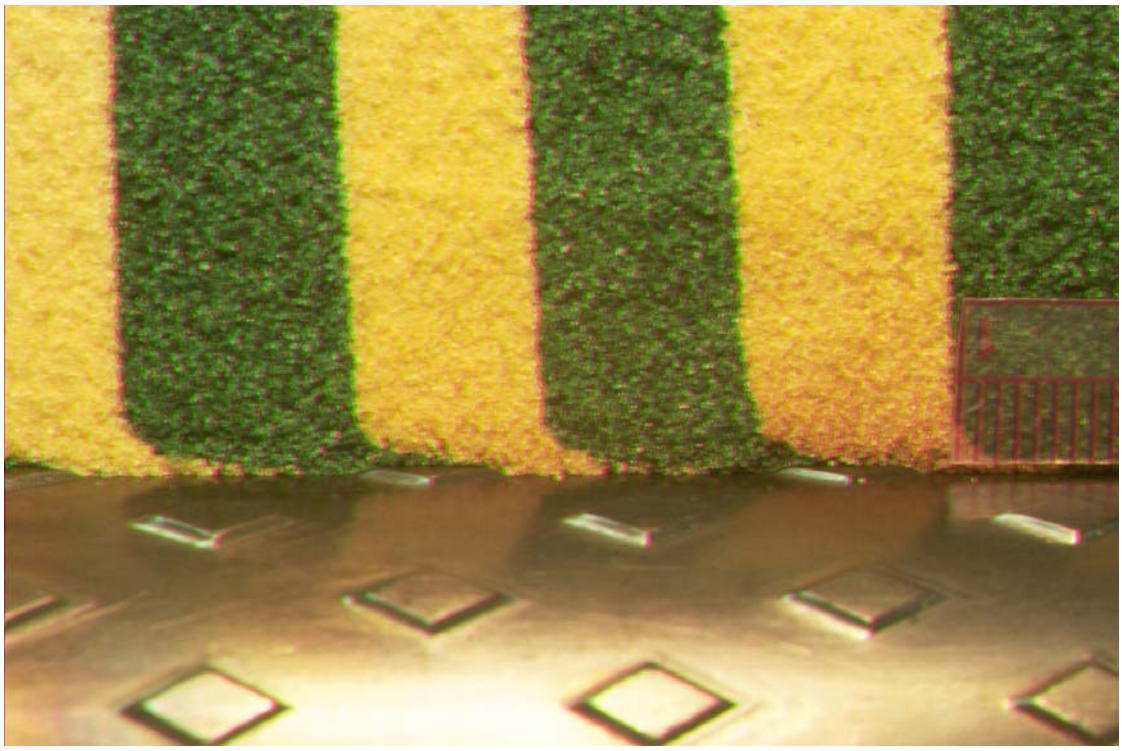

Figure 3-9. Picture Displaying an Investigation Plane Located Along the Centerline of Diamond Texture Asperities, Post Shear (63.5 mm Total Displacement).

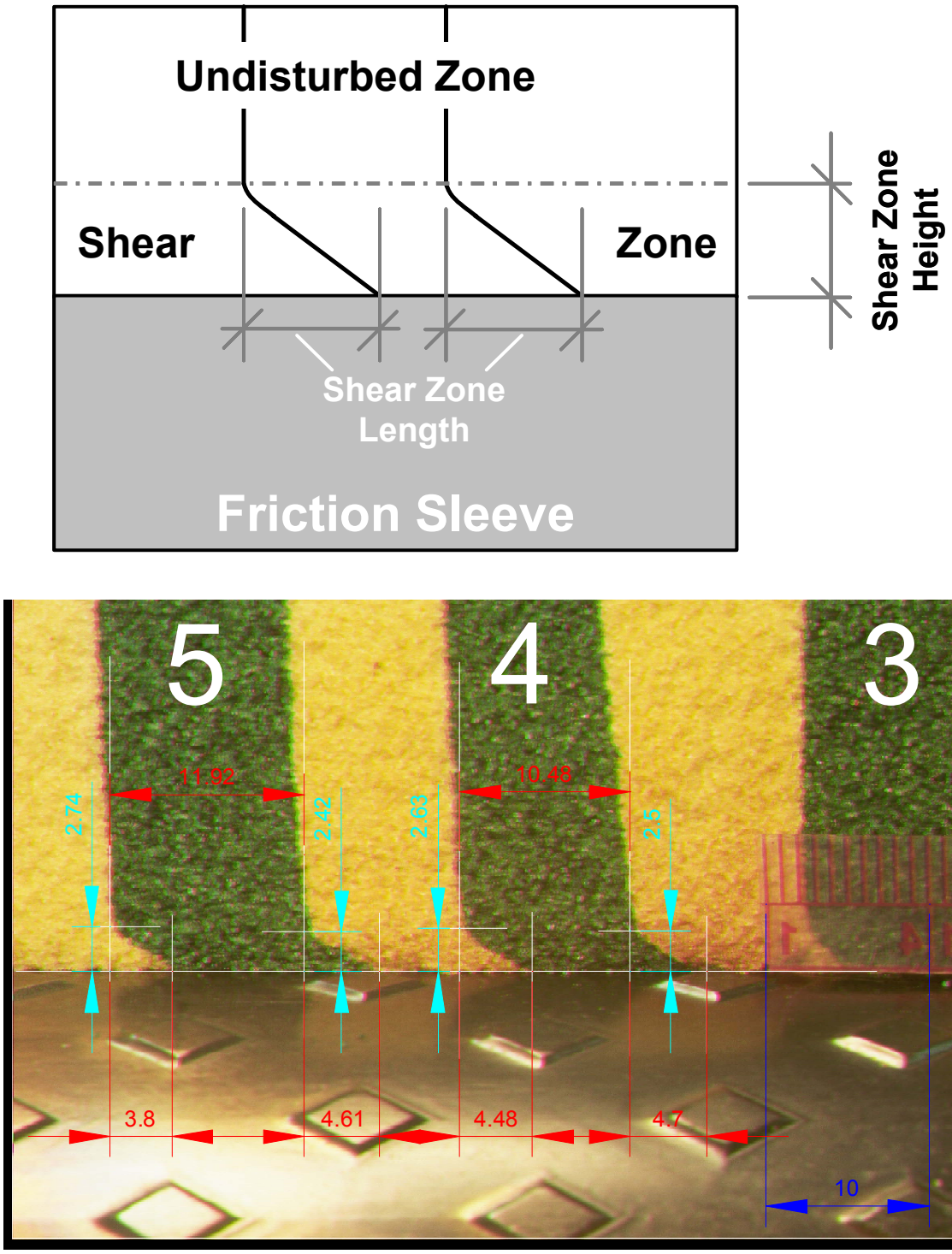

Figure 3-10. (a) Schematic and (b) Picture Demonstrating the Measurements Made to Quantify the Shear Zone Deformation of Each Deformed Layer Within an Investigation Plane.

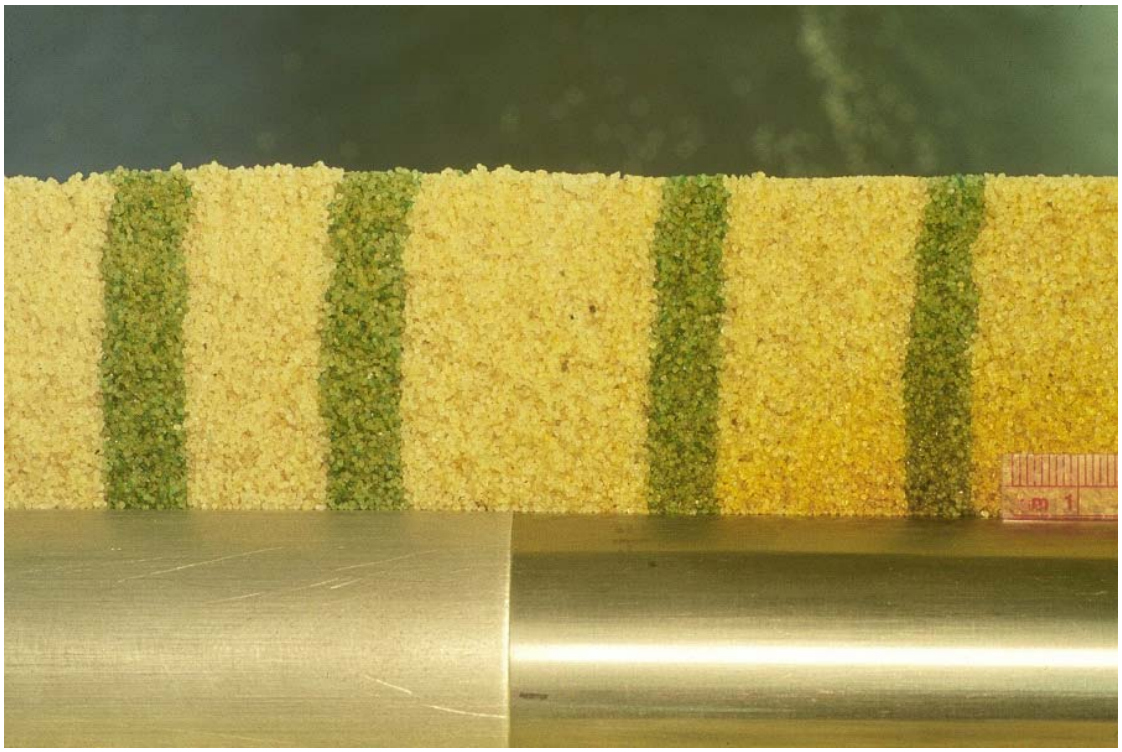

Figure 3-11. Picture Showing the Preserved Post Shear Structure of an Axisymmetric Test of Conventional Friction Sleeve Shearing Against a 20-30 Sub-Rounded (Sand B) Granular Material. Note the Total Shear Displacement is Equal to 63.5 mm with No Measurable Shear Zone Formed.

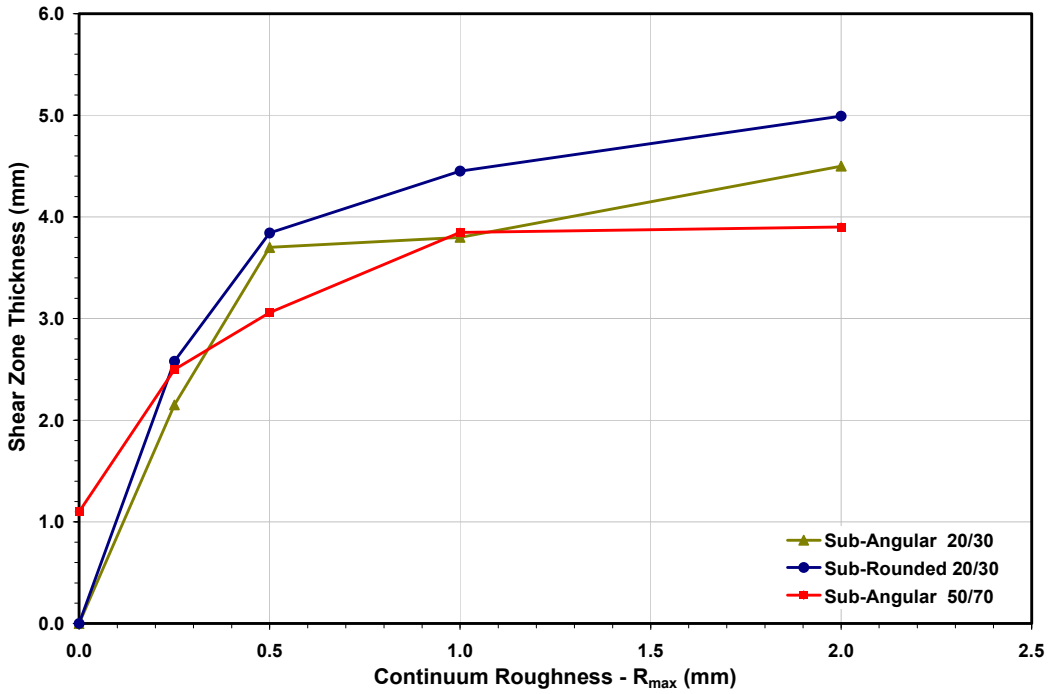

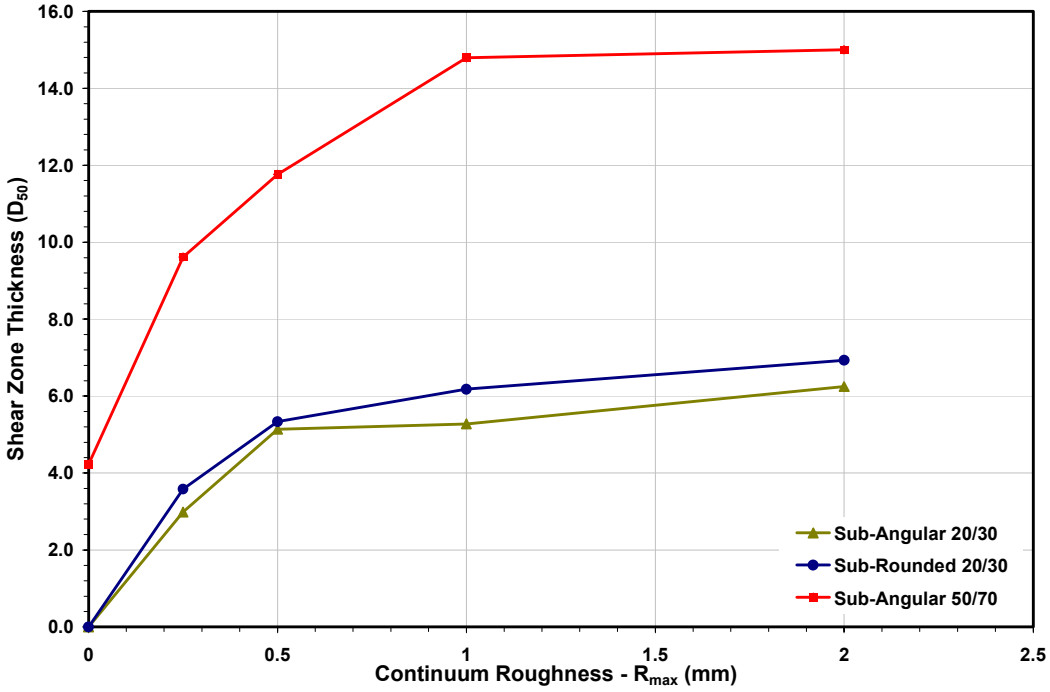

Figure 3-12. Plots of the Variation in Shear Zone Thickness as a Function of R_{max} Surface Roughness for the Three Tested Granular Materials in Terms of (a) Measured Thickness (mm) and (b) Equivalent Mean Particle Diameters (D_{50}).

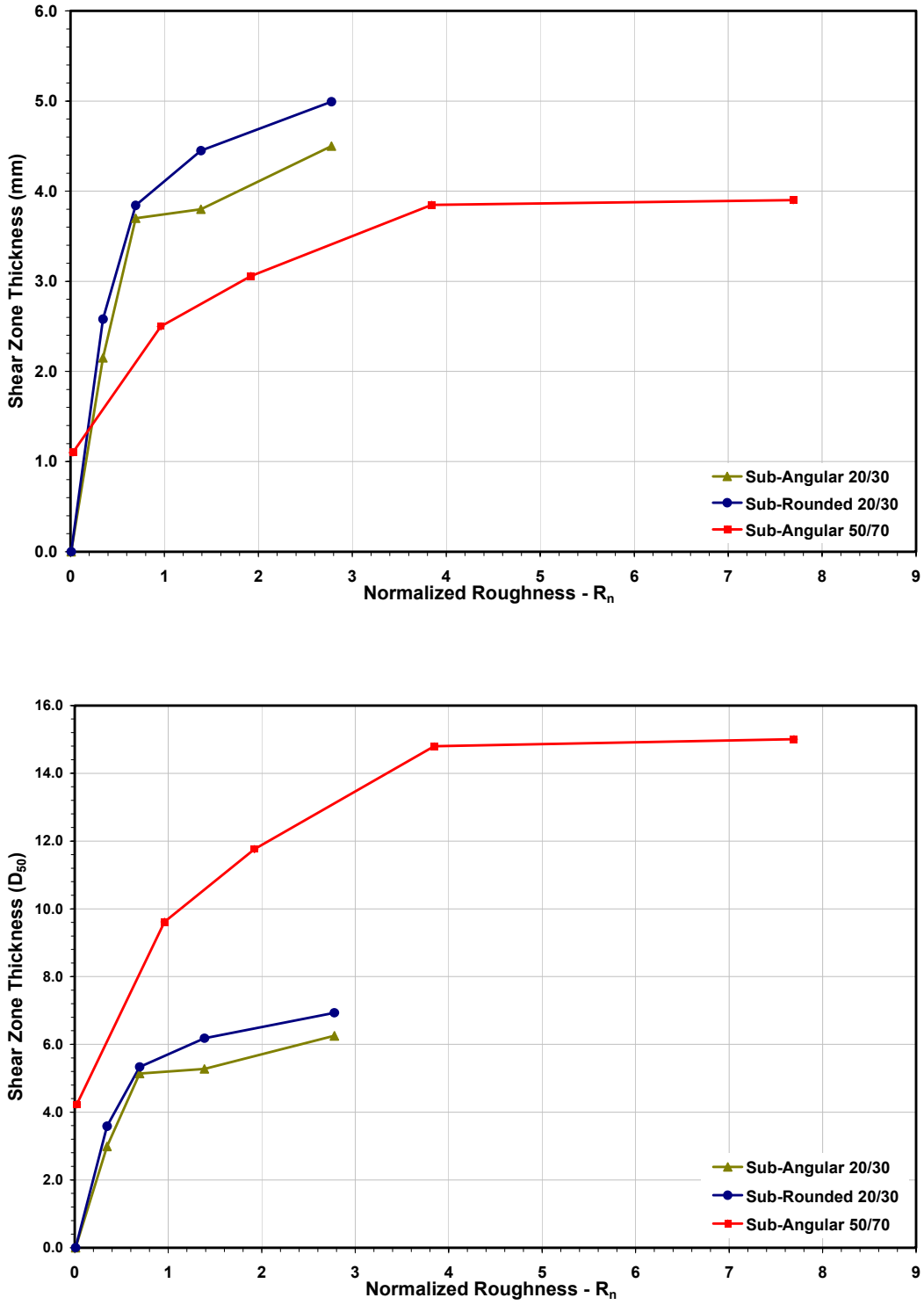

Figure 3-13. Plots of the Variation in Shear Zone Thickness as a Function of Normalized Surface Roughness R_n for the Three Tested Granular Materials in Terms of (a) Measured Thickness (mm) and (b) Equivalent Mean Particle Diameters (D_{50}).

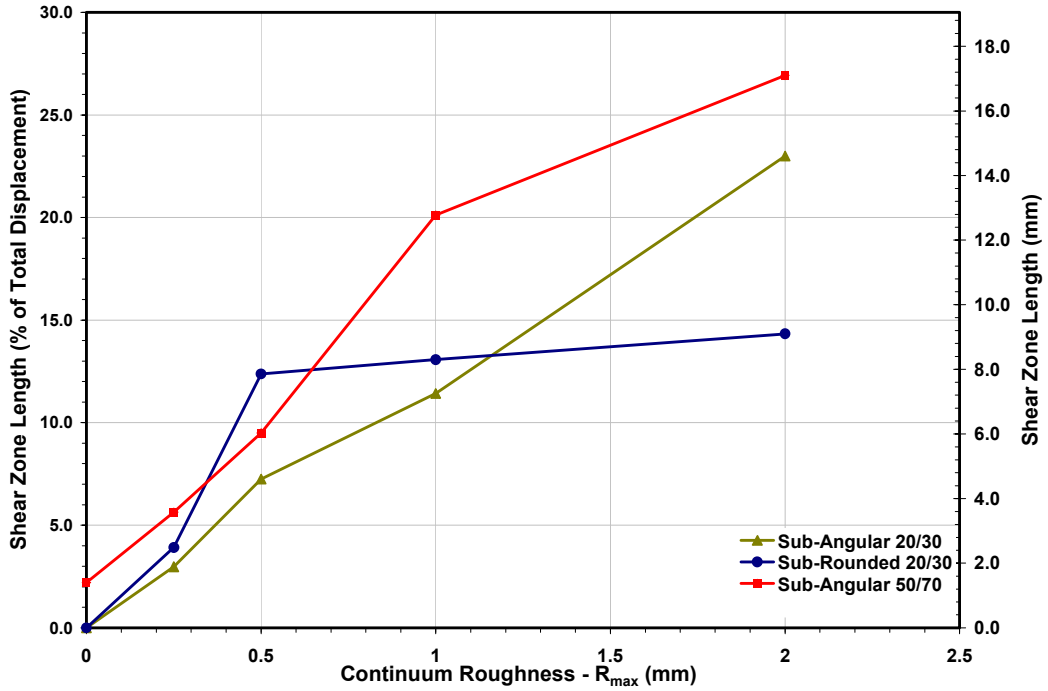

Figure 3-14. Plots of the Variation in Shear Zone Length as a Function of R_{max} Surface Roughness for the Three Tested Granular Materials in Terms of Measured Length (mm) and the Percentage of Total Displacement (%).

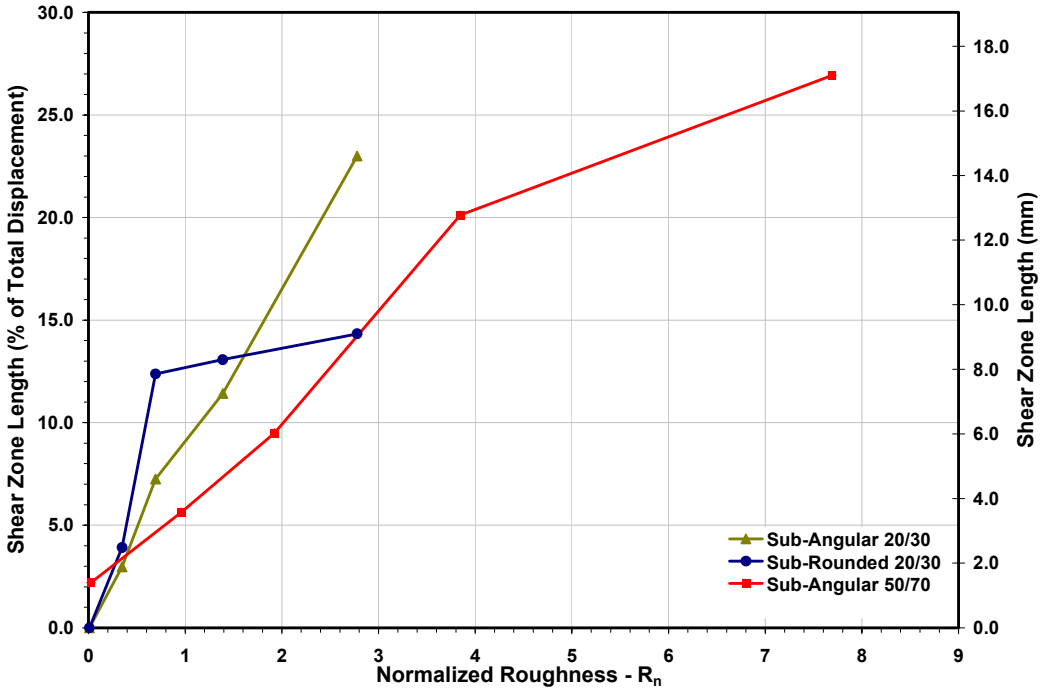

Figure 3-15. Plots of the Variation in Shear Zone Length as a Function of Normalized Surface Roughness R_n for the Three Tested Granular Materials in Terms of Measured Length (mm) and the Percentage of Total Displacement (%).

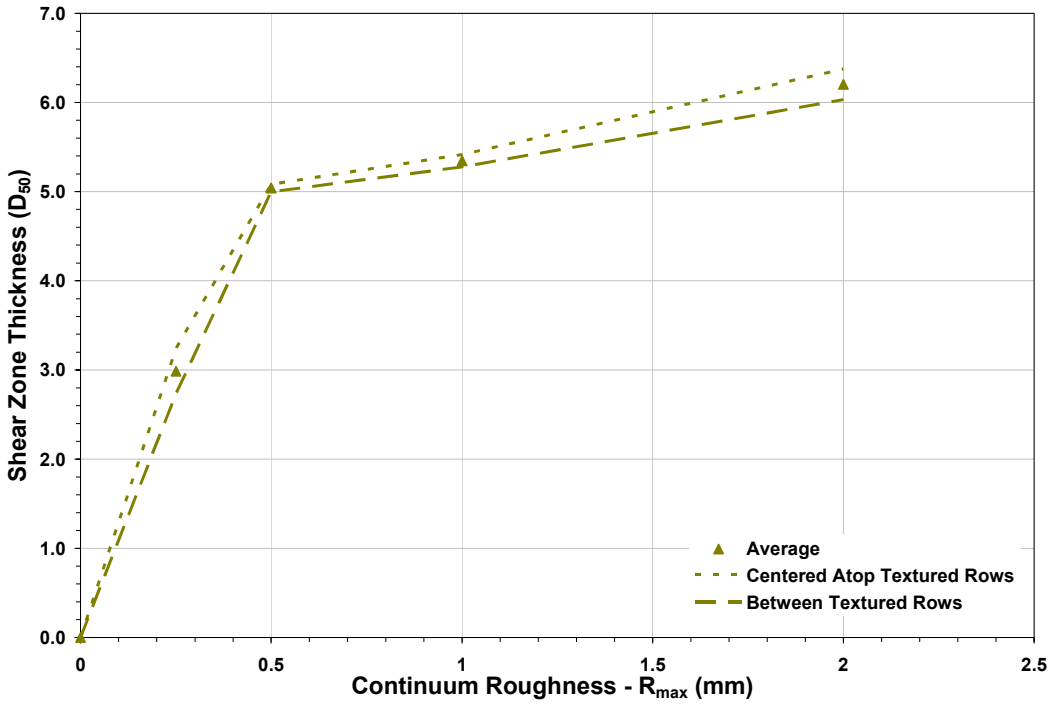

Figure 3-16. Plot Detailing the Uniformity of Induced Shear Zone Thickness for Sand A (Sub-Angular 20-30) as a Function of R_{max} Continuum Roughness.

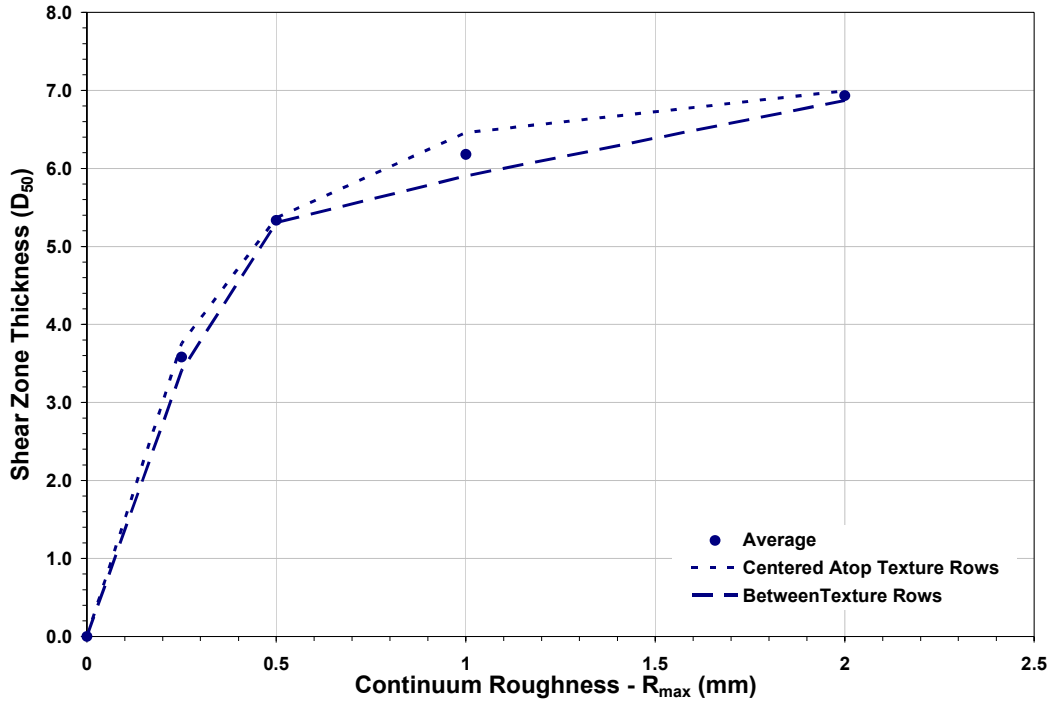

Figure 3-17. Plot Detailing the Uniformity of Induced Shear Zone Thickness for Sand B (Sub-Rounded 20-30) as a Function of R_{max} Continuum Roughness.

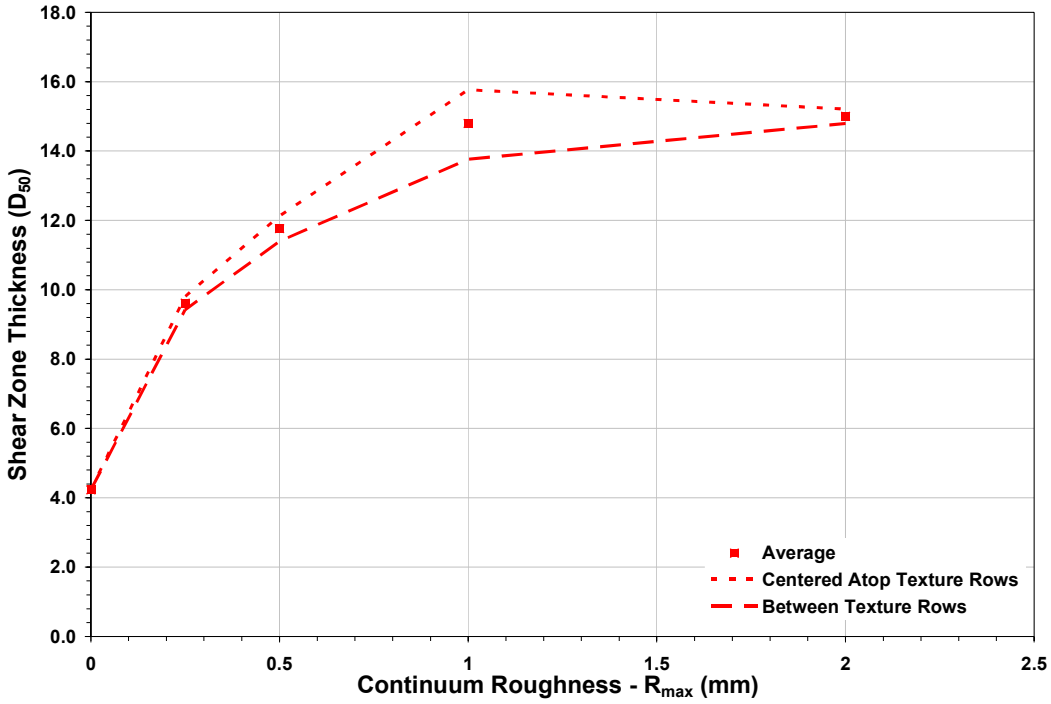

Figure 3-18. Plot Detailing the Uniformity of Induced Shear Zone Thickness for Sand C (Sub-Angular 50-70) as a Function of R_{max} Continuum Roughness.

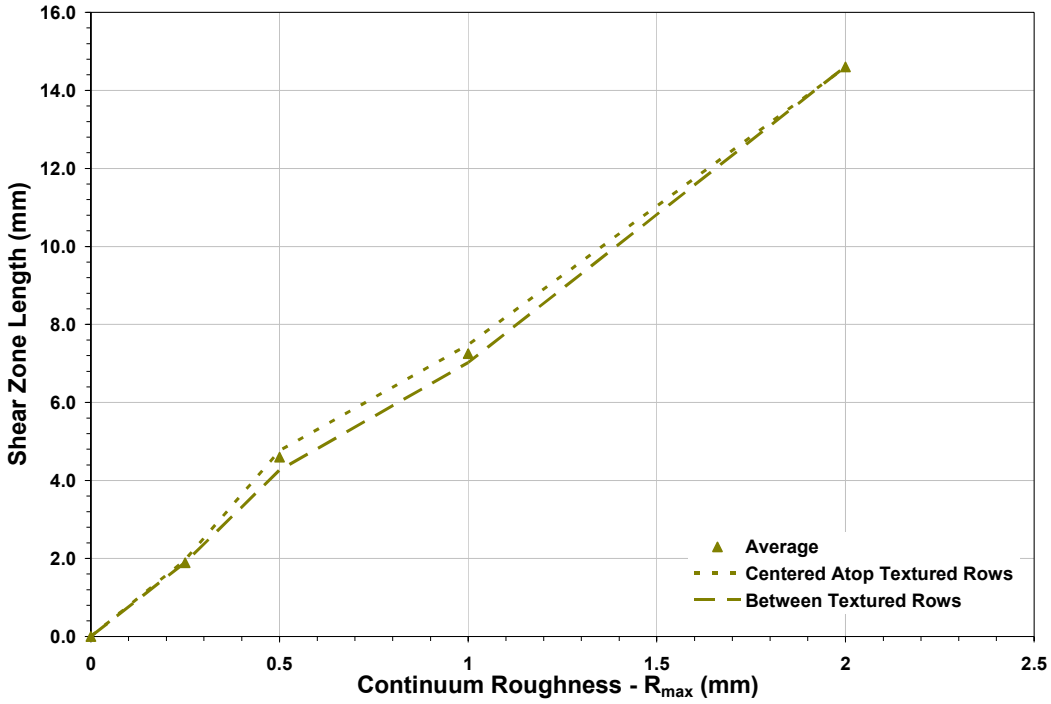

Figure 3-19. Plot Detailing the Uniformity of Induced Lateral Shear Zone Deformation for Sand A (Sub-Angular 20-30) as a Function of R_{max} Continuum Roughness.

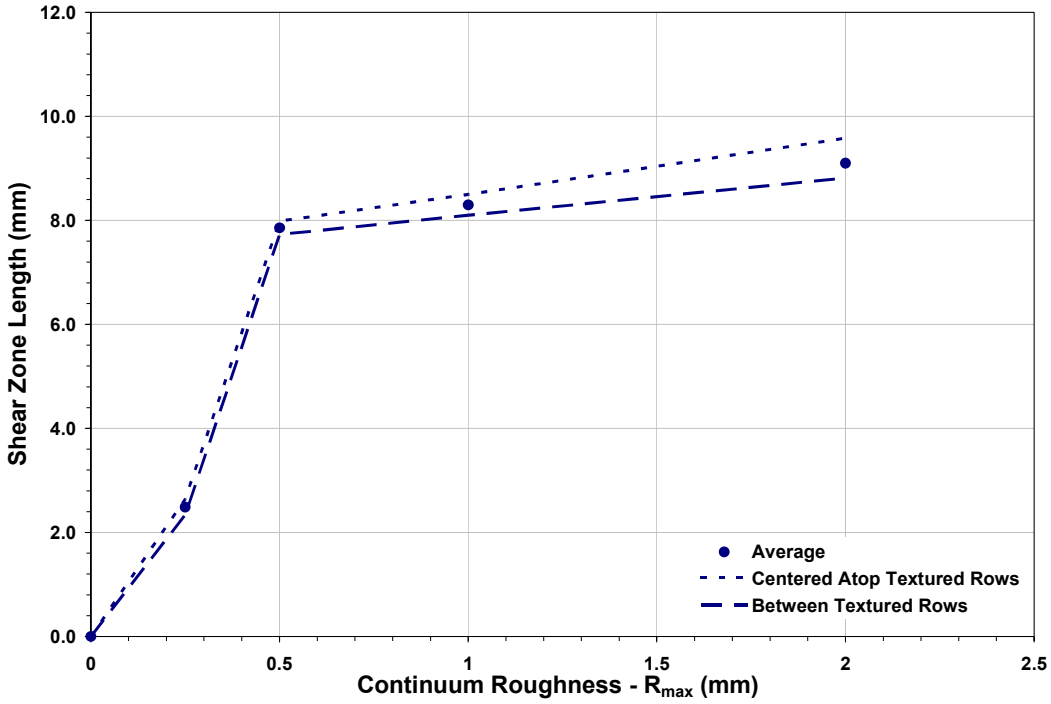

Figure 3-20. Plot Detailing the Uniformity of Induced Lateral Shear Zone Deformation for Sand B (Sub-Rounded 20-30) as a Function of R_{max} Continuum Roughness.

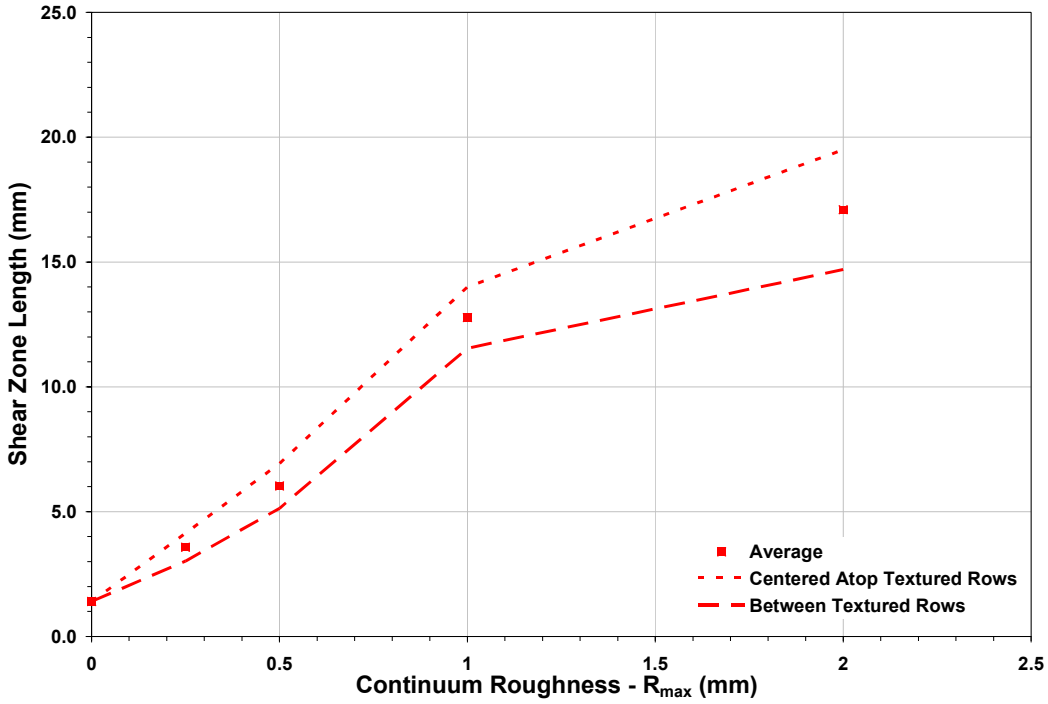

Figure 3-21. Plot Detailing the Uniformity of Induced Lateral Shear Zone Deformation for Sand C (Sub-Angular 50-70) as a Function of R_{max} Continuum Roughness.

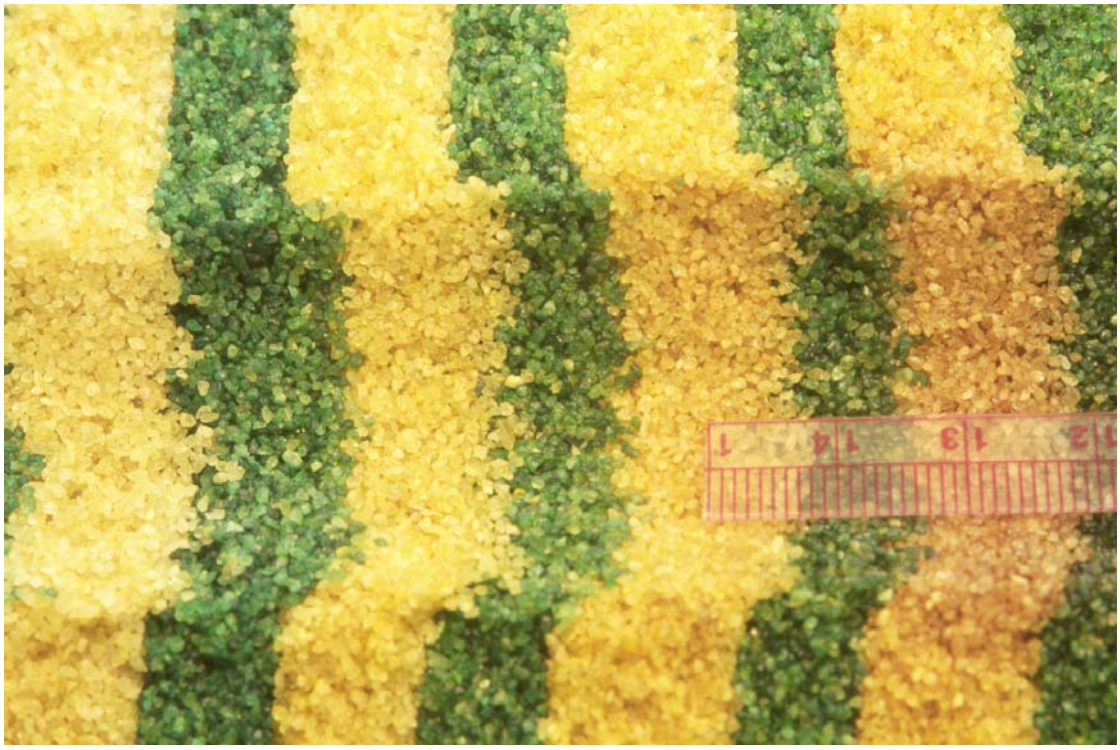

Figure 3-22. Picture of the Induced Lateral Deformation in Sand A (Sub-Angular 20-30) After a Shear Displacement of 63.5 mm Against a Textured Friction Sleeve of R_{max} = 0.5 mm Roughness

Figure 3-23. Picture of the Induced Lateral Deformation in Sand B (Sub-Rounded 20-30) After a Shear Displacement of 63.5 mm Against a Textured Friction Sleeve of R_{max} = 0.5 mm Roughness

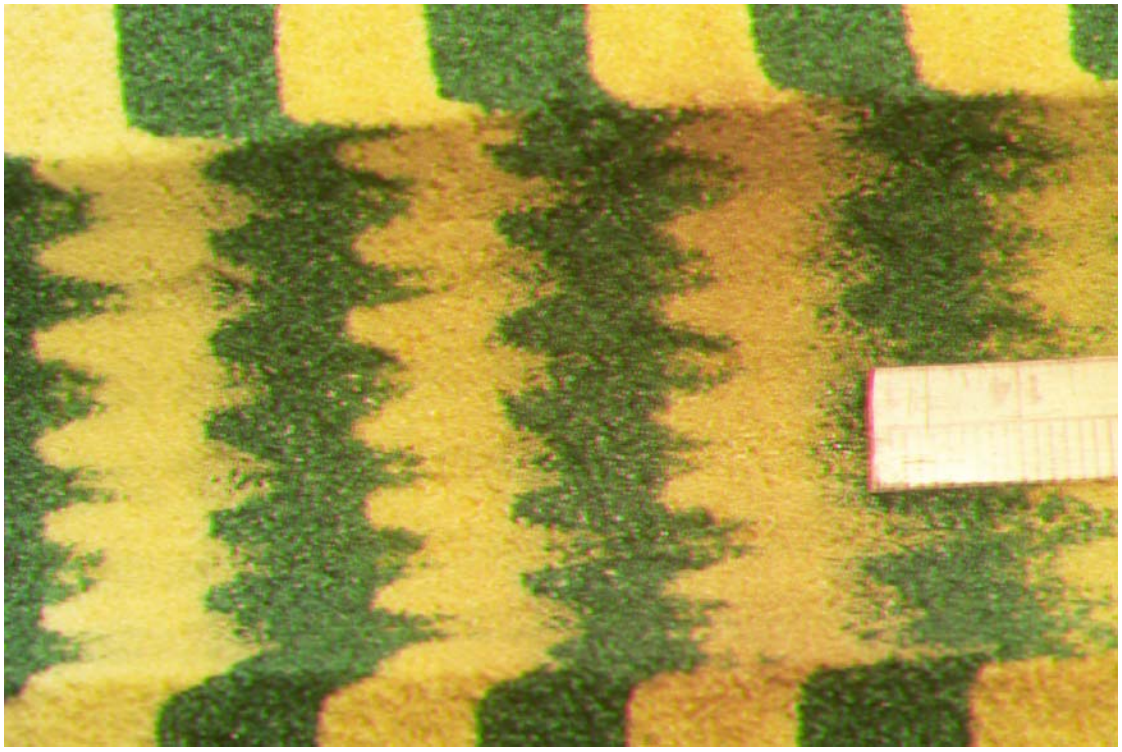

Figure 3-24. Picture of the Induced Lateral Deformation in Sand C (Sub-Angular 50-70) After a Shear Displacement of 63.5 mm Against a Textured Friction Sleeve of R_{max} = 0.5 mm Roughness.

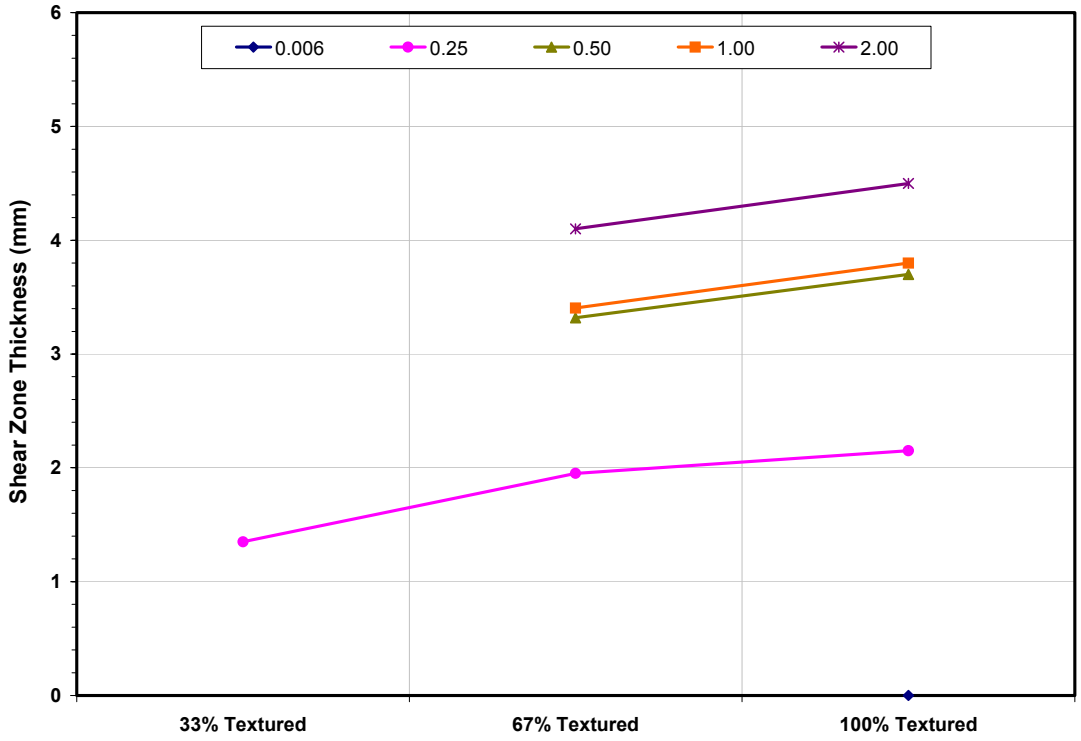

Figure 3-25. Plot Detailing the Initiation and Progression of Induced Shear Zone Thickness for Sand A (Sub-Angular 20-30) as a Function of Percentage of Textured Shearing.

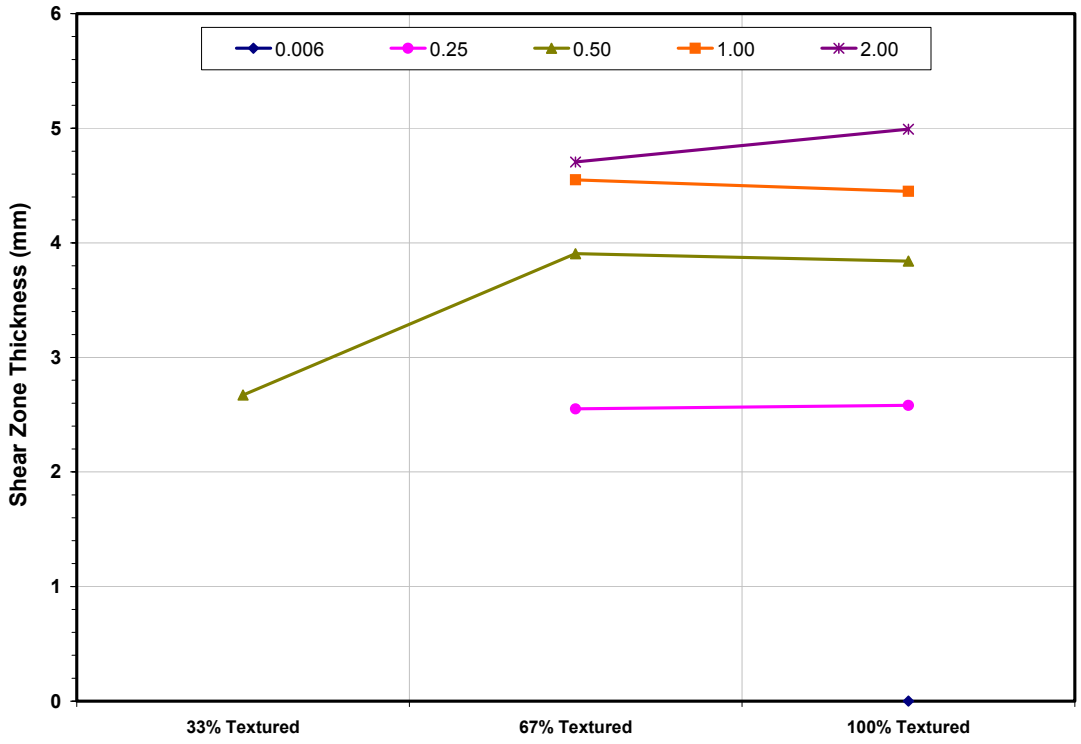

Figure 3-26. Plot Detailing the Initiation and Progression of Induced Shear Zone Thickness for Sand B (Sub-Rounded 20-30) as a Function of Percentage of Textured Shearing.

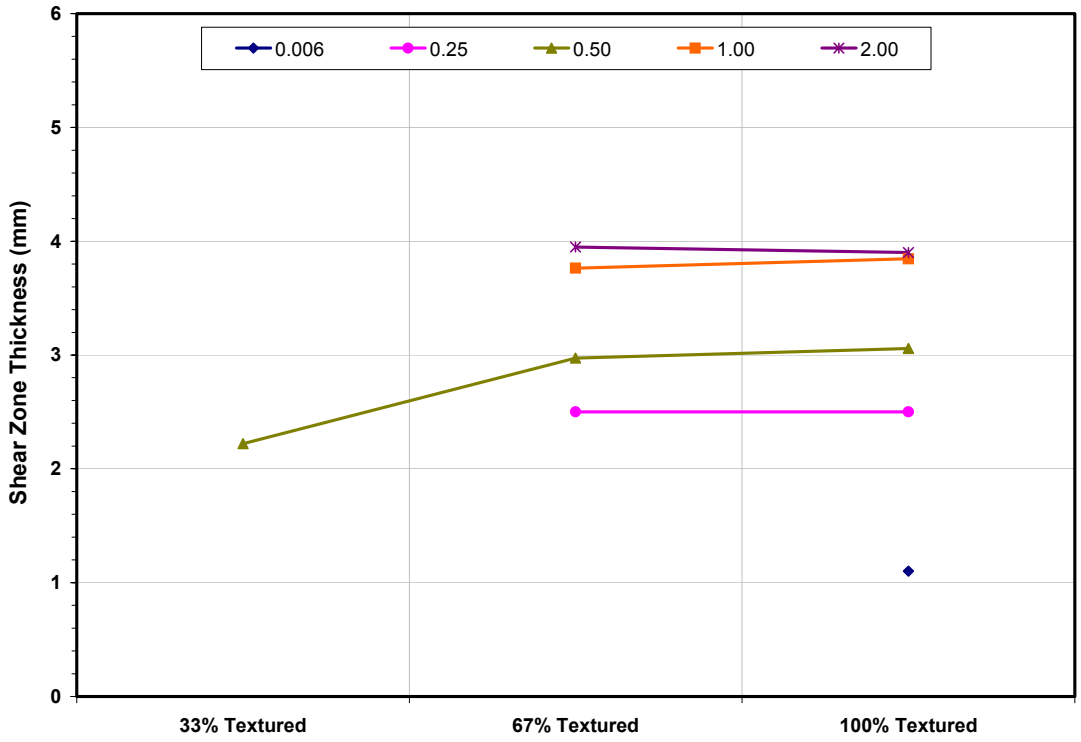

Figure 3-27. Plot Detailing the Initiation and Progression of Induced Shear Zone Thickness for Sand C (Sub-Angular 50-70) as a Function of Percentage of Textured Shearing.

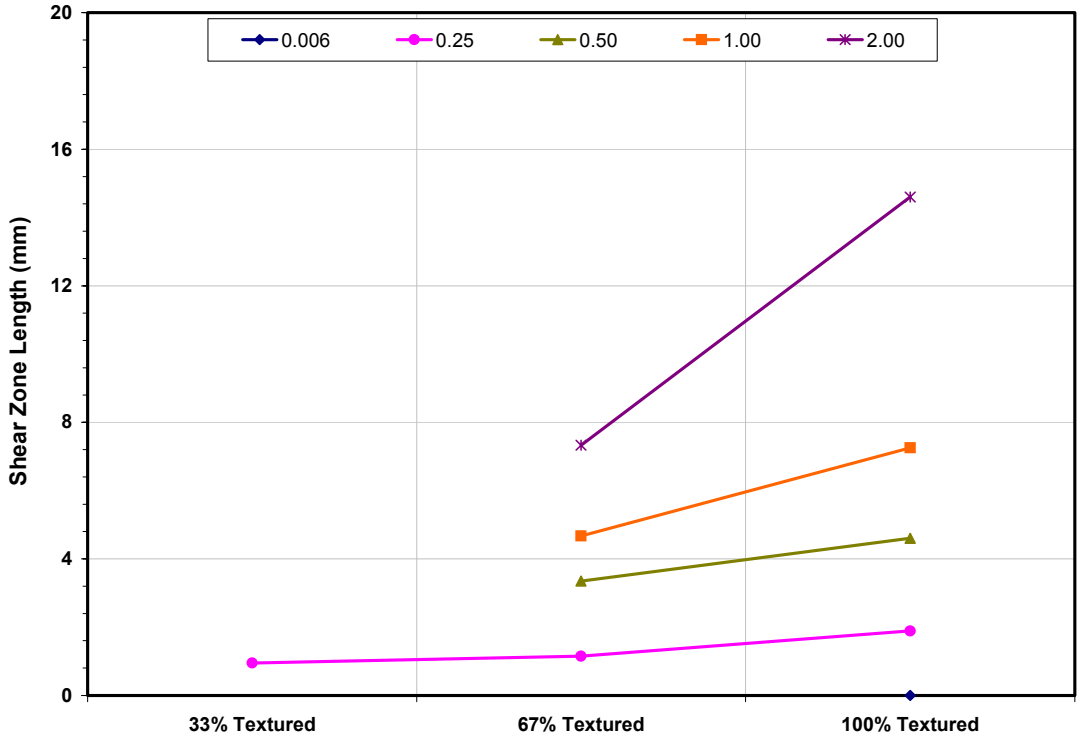

Figure 3-28. Plot Detailing the Initiation and Progression of Induced Lateral Shear Zone Deformation for Sand A (Sub-Angular 20-30) as a Function of Percentage of Textured Shearing.

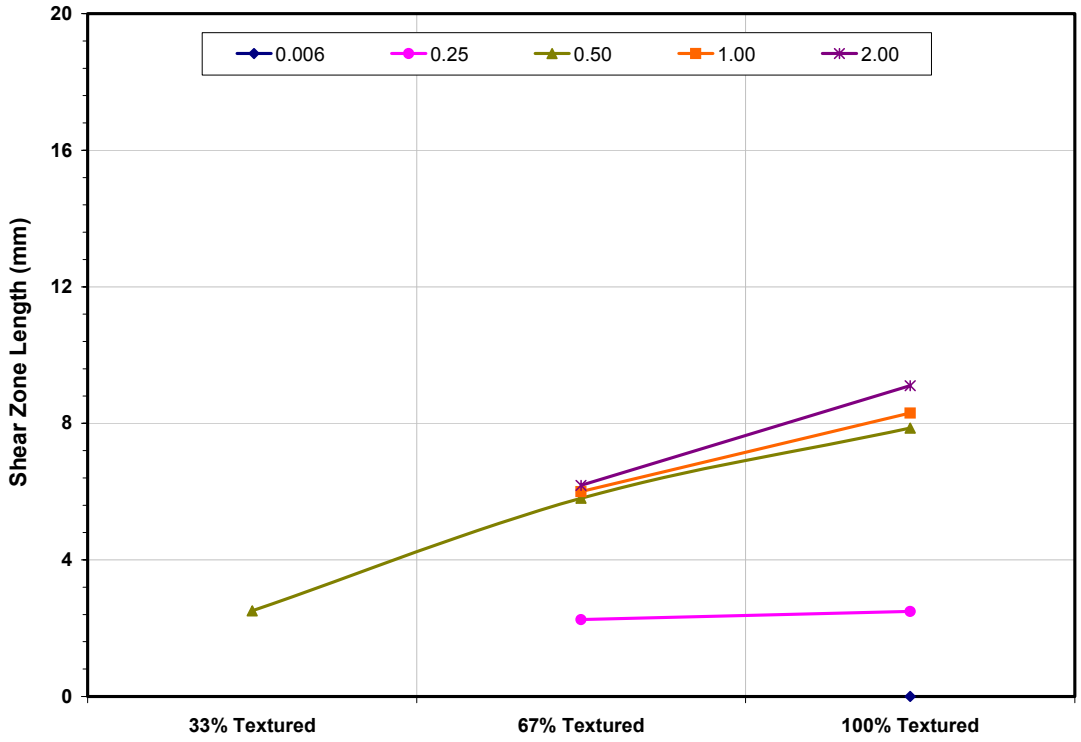

Figure 3-29. Plot Detailing the Initiation and Progression of Induced Lateral Shear Zone Deformation for Sand A (Sub-Rounded 20-30) as a Function of Percentage of Textured Shearing.

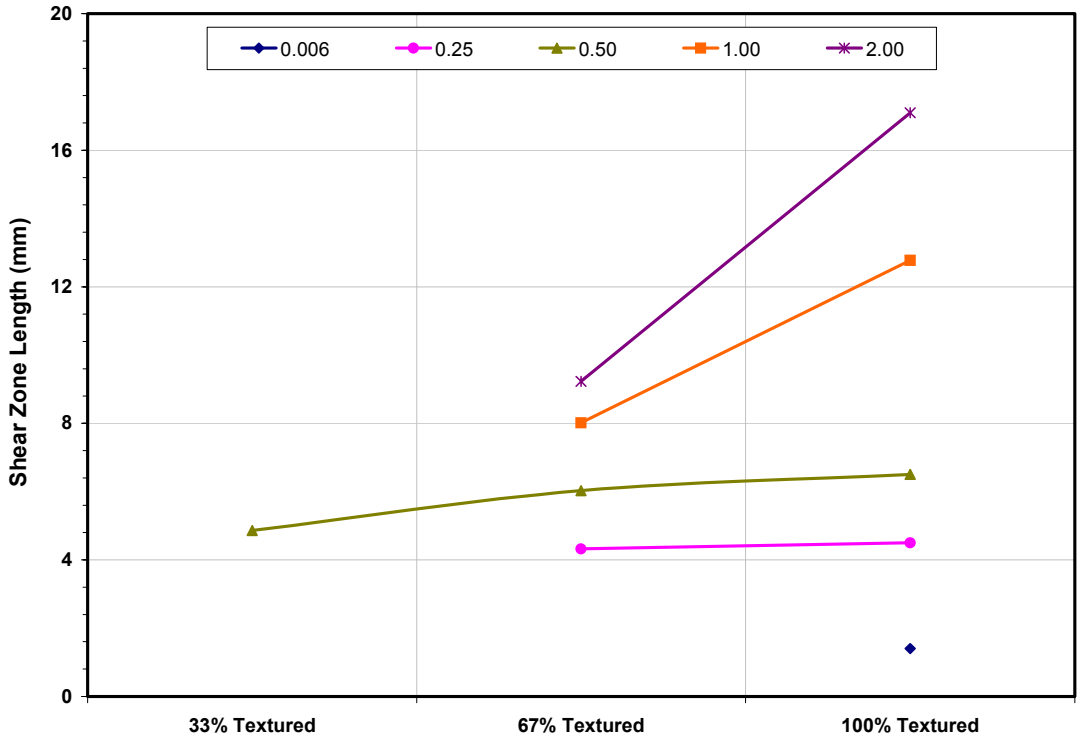

Figure 3-30. Plot Detailing the Initiation and Progression of Lateral Shear Zone Deformation for Sand C (Sub-Angular 50-70) as a Function of Percentage of Textured Shearing.

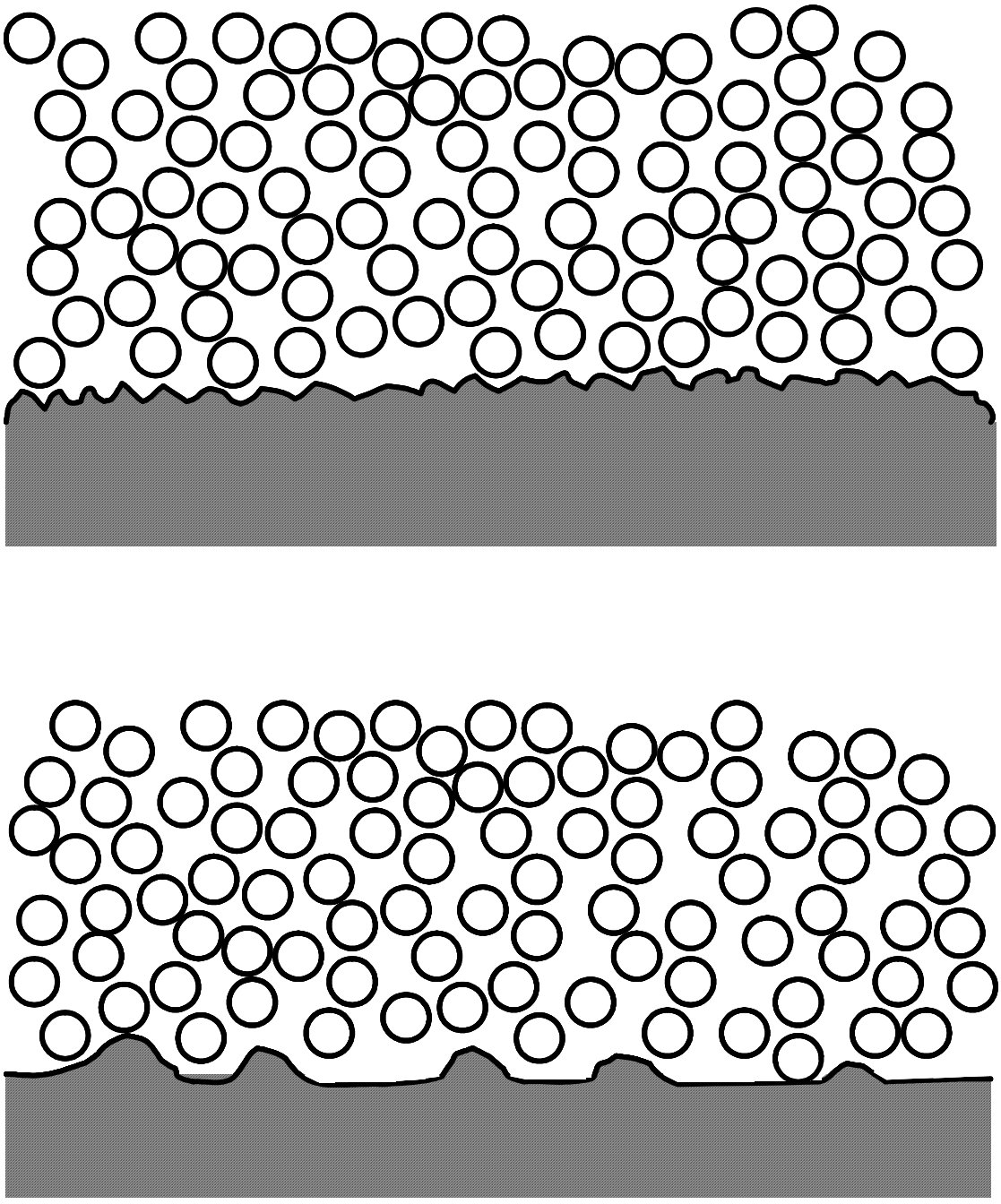

Figure 3-31. Schematics Showing the Difference Between (a) Continuous and (b) Intermittent Continuum Surface Texturing.

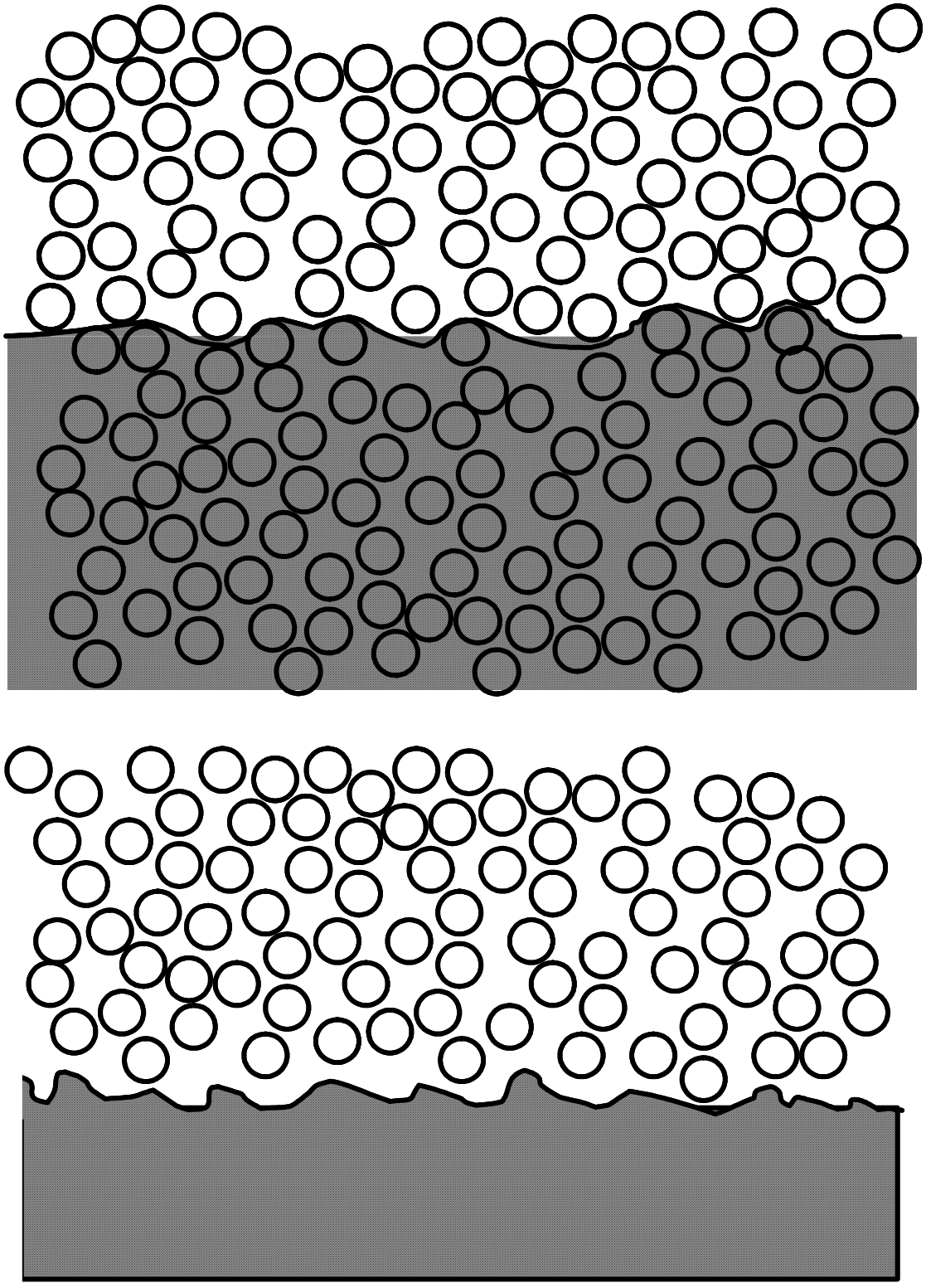

Figure 3-32. Schematics Showing the Concept of a (a) Virtual Surface in Relation to a (b) Conventional Continuum Surface.

Chapter IV
Quantifying Hook and Loop Interaction in Textured Geomembrane–Geotextile Systems

4.1 Introduction

As introduced in Chapter 2, filament – continuum interfaces (FCIs) make up an important subset of the interfaces commonly encountered in geotechnical engineering. This study specifically examines the role of hook and loop interactions on geomembrane-geotextile interface performance. The effects of hook and loop interaction on geosynthetic interface performance are quantified through laboratory interface shear testing, ASTM hook and loop interaction tests, and optical microscopy. The results aid in quantifying behavioral differences observed between geomembranes textured using different manufacturing processes, and provide microscale insight into textured geomembrane-geotextile interaction mechanisms over a range of stress levels.

It is often advantageous in geotechnical design to combine several materials to create hybrid geosystems. The combination of two or more geosynthetics has been used in practice for decades over a wide range of applications. These applications are well documented in Koerner (1998), amongst others. Practical applications of geotextile-geomembrane systems include landfill liners, highway subgrades, leachate and gas collection systems, and retaining structures. Specific geomembrane-geotextile uses include: drainage, resistance to puncture, and controlling tear propagation. Geomembranes used in combination with geotextiles are often textured to allow for better compliance and interaction between the synthetic materials. Hook and loop interaction, which is commonly but incorrectly referred to by the trade name Velcro®, has become a

recent topic of discussion in the geosynthetic community. However, no quantitative studies have been conducted to measure the effect of hook and loop interaction on geosynthetic system performance.

Hook and loop interaction within the geosynthetic field is mainly relevant to systems with textured geomembranes in contact with open structured geotextiles, such as the needle-punched-nonwoven (NPNW) type. As a result, this study is focused on investigating the hook and loop interaction between textured geomembranes and NPNW geotextiles. The primary texturing processes currently used in North American geosynthetic practice are coextrusion and structuring, with impingement widely used as a texturing process outside of North America. The coextrusion process generates random textures over a broad size range of features. Structuring typically produces a more uniform texture consisting of smoother macroscopic patterns, with micro and mesotexture existing on the base substrate only. Practical experiences with these textured geomembranes have shown differences in low normal stress behavior, most notably during installation. Some practitioners note the benefit of additional interaction between a geotextile and textured geomembrane during installation as the system requires minimal or no supplemental restraints or temporary connections during placement and joining of the seams. Other practitioners note the disadvantage of large interaction between the components of a geosynthetic composite system during installation as it greatly restricts realignment and minor adjustments of the geosynthetics after their initial placement. Anecdotal evidence has linked many of the behavioral differences observed during installation to varying levels of hook and loop interaction between the geomembrane texture and NPNW fabric. This study uses a number of laboratory techniques across a

range of normal stress conditions in order to provide quantitative insight into the mechanics and magnitude of hook and loop interaction in textured geomembrane-geotextile systems.

4.2 Geomembrane Manufacturing and Texturing Techniques

To provide a framework for the results presented herein, a brief review of geomembrane manufacturing and texturing techniques is presented, and follows that of Frost et al. (2002).

4.2.1 Manufacturing Techniques

Geomembranes are manufactured from a variety of polymer resins, with the most common types being polyvinyl chloride (PVC), cholorsulfonated polyethylene (CSPE), and polyethylene (PE). The most common variety used in combination with geotextiles, are PE membranes, and these are the focus of the current study. PE membranes are manufactured as either smooth or textured sheets using a screw extrusion process and classified by resin density as high density polyethylene (HDPE), linear low density polyethylene (LLDPE), or very low density polyethylene (VLDPE) (Koerner, 1998). The most common density used in geosynthetic systems is currently HDPE, and is the focus of the current study. The manufacturing process consists of solid resin pellets, and other additives such as antioxidants and process stabilizers being blended in a hopper attached to a barrel system. An Archimedean screw-type feeder system carries the pellets to the die section, while a series of heaters contained along the screw length melt the resin pellets. The melted formulation is forced through one of two common die types: flat dies (cast sheeting) which force the polymer mixture through two horizontal die lips,

or circular dies (blown film) which force the polymer mixture between two vertically oriented concentric die lips (Koerner, 1998).

4.2.2 Texturing Techniques

While the constituents used in the production of HDPE geomembranes are relatively similar for all manufacturers; the texturing techniques, processes, and finished textures can vary widely. Manufacturing methods used to texture geomembranes include: coextrusion, impingement, lamination, and structuring. The lamination texturing process has lost favor in recent years due to a combination of performance issues and the recent merger of several large geosynthetic manufacturers. Impingement is extensively used as a texturing process outside of North America, but is no longer widely used in North America. A brief summary of the two most commonly used texturing methods (coextrusion and structuring) in North America is presented below after Donaldson (1995).

- The coextrusion method uses one or two secondary extruders on the preferred or both sides of a main extruder to deliver a molten resin with an added blowing agent, typically nitrogen. As the mix nears the end of the extrusion system, the reduced pressure and cooler air expands the blowing agent. The texture is formed by the shearing action of the extruder breaking the bubbles formed by the cooling of the blowing agent. The bond strength between the extruded layers (base, top textured surfaces, and bottom textured surface) is controlled by the rate of extrusion. Problems with improper rates include: debonding or limited layer cohesion at fast extrusion rates, and imbedded bubbles of blowing agent in the

core of the geomembrane at slow extrusion rates. Properly executed, coextrusion texturing produces high bond strengths between the geomembrane core and the textured surfaces consisting of variably sized macrotexture with significant microtexturing due to the rapid expansion of the blowing agent. Plan and cross-sectional views of the tested coextruded geomembrane are shown in Figure 4-1. Hooked features of different sizes can be readily seen in the cross-section.

- The structuring process forces a hot flat die extruded geomembrane through two counter-rotating rollers with patterned surfaces. The texture of the embossing rollers is sometimes a box and point pattern, but can be of almost any geometry. An advantage of structuring is the ability to create vastly different textures on the upper and lower geomembrane surfaces. Improper cooling can result in residual stresses under the macrotextural features making the membrane more susceptible to stress cracking in the presence of active surface agents. Structured texture is highly repeatable and consists of uniform macrotexture, with micro and mesotexture present on the base material between macro features. Plan and cross-sectional views of the tested structured geomembrane are shown in Figure 4-2. No distinct macro level hooked features can be seen.

In this study, three distinct size ranges will be used to aid in the discussion of textural features. Macrotexture will refer to base structure, asperities, and or attached features > 0.125 mm in out-of-plane dimension. Microtexture will refer to roughness present on the base sheet or macrotextural features of < 0.05 mm. Texture or roughness

intermediate to those ranges will be described as mesotexture. Texturing technique has been shown to directly influence the strength and durability of both the microtexture, and to a greater extent, the macrotexture created during the texturing process (Frost et al., 2002). This study focuses on investigating properties of various textured geomembranes in which all texture in the current study consists of the same material as the base HDPE geomembrane.

4.3. Experimental Program

4.3.1 Introduction

The experimental program consisted of a series of laboratory investigations designed to quantify the hook and loop interaction of geomembrane-geotextile systems. Testing included: direct interface shear tests, and ASTM standard tests for shear strength (ASTM D5169 - 98) of hook and loop fasteners. The direct interface shear testing was conducted according to ASTM D5321-02 at normal stresses ranging from 0.4 – 312 kPa, over a horizontal displacement of 80 mm, at a displacement rate of 5 mm/min, and deviated from the standard procedure in that tests were only conducted parallel to the machine (roll) direction of the geosynthetics. The ASTM hook and loop interaction tests were conducted on the investigated geosynthetic materials, commercial hook and loop specimens, and hybrid combinations of all materials. Tests with commercial hook and loop materials were conducted to provide a reference for the magnitude of strength of these engineered systems. Optical microscopy provided qualitative insight into the mechanisms present during interface shearing.

4.3.2 Materials Tested

This study focused on the most common geosynthetic materials used in current North American practice when placing geotextiles in combination with geomembranes. As such, two textured HDPE geomembranes (Figures 4-1 and 4-2), one textured using a coextruded process and one textured using a structuring process were tested in combination with a single staple type NPNW geotextile. Additionally, a commercial hook and loop fastener (Figure 4-3), was used to provide a meaningful backdrop for the discussion of hook and loop interaction. Relevant information regarding the tested materials is listed in Table 4-1.

4.3.3 Optical Microscopy

Surface characteristics were evaluated using an integrated digital camera-optical microscope system. Procedures similar to those described by Dove and Frost (1996) were used to prepare the geomembrane coupons for analysis. The procedure involves casting coupons of the geomembranes vertically in a solution of Plaster of Paris™ thereby creating a strong optical contrast between the black geomembrane and the white Plaster of Paris™. A petri dish was used to secure the coupons during curing, and peeled away after the coupons had hardened leaving a circular disk of material with a relatively smooth working surface. The coupons were then additionally prepared through sequential grinding and polishing of the surface to expose cross-sections of the geomembranes using a Beuhler polishing system. Figure 4-4 provides a schematic diagram of a completed coupon ready for imaging. The coupons, from which the images in Figures 4-1c and 4-2c were captured, were prepared in this manner. Images of the other materials were obtained directly from coupons of the materials without surface preparation. All images excluding

4-1a and 4-2a were captured using an integrated camera and microscope system. The large scale images of Figures 4-1a and 4-2a were captured using a standard digital camera. Further information regarding image analysis and microscopy procedures can be found in Frost and Kuo, 1996; Dove and Frost, 1996; and Frost and Lee, 1998.

4.3.4 Direct Interface Shear Testing

A large displacement direct interface shear testing apparatus (Dove and Frost, 1996; Zettler et al., 2000) was used to measure the shear strength of the geomembrane-geotextile interfaces. The device, shown in Figures 4-5 and 4-6, permits large displacements (up to 80 mm) such that pseudo-residual interface strength values can also be obtained. Pseudo-residual shear strengths of the interface systems are the shear strength measured at displacements sufficient to achieve an asymptotic approach of the shear stress to a constant value representative of the true residual strength. The true residual value has been found to exist for textured geomembrane-geotextile systems typically after shearing to very large displacements on the order of 0.5 m or greater, as discussed in the ring shear studies of Stark et al. (1996). In the current study, pseudo-residual values were taken as the average of the shear strength over the last 5 mm of shearing. Normal stress was applied through a free traveling metal cross head connected to an air pressure bellofram for high normal stress tests and to a dead weight load plate for tests below 25 kPa normal stress. Load cells and LVDT's were used to monitor loads and displacements in the normal and shear directions, with data acquired using a LabView® system.

The direct interface testing consisted of shearing NPNW geotextile samples against geomembrane samples. The geomembrane samples consisted of flat sheets, 152

mm wide by 254 mm long, oriented with the manufacturing machine direction aligned parallel with the shear direction. The geomembranes were secured to the testing platform using a screw fastening system consisting of three 25.4 mm wide metal brackets along the side and rear edges of the geomembrane specimen. The geotextile samples were attached to the underside of a 6.4 mm thick 102 mm square aluminum plate using spray adhesive and allowed to cure for 1 hour under 10 kPa normal stress. The geotextile samples were trimmed to the dimensions of the aluminum plate leaving an extended flap along the leading edge. The extended flap was then wrapped completely around the beveled leading edge of the plate and glued to the upper surface. This configuration provided a smooth leading edge, which better approximates large-scale in-situ shearing conditions by allowing the geotextile to be sheared against the geomembrane without peeling. An upper aluminum section 102 mm square was used to secure the extended flap between the aluminum sections. The upper aluminum block also served to transfer the load from the metal crosshead to the geosynthetics being tested.

The direct interface shear tests were conducted according to ASTM D5321-02, except as noted earlier, under a large range of normal stresses from (0.4 – 312 kPa) to a displacement of 80 mm per test at a displacement rate of 5 mm/min. As a verification of the test setup, multiple tests were conducted for both geosynthetic combinations at 100 kPa normal stress, and showed excellent repeatability. Virgin geomembrane and geotextile specimens were used in each test of the primary testing sequence.

An additional wear test sequence was conducted on both geomembrane types at a normal stress of about 100 kPa to allow for the quantification of large displacement geomembrane wear and interface strength behavior. The wear test sequence consisted of

a virgin and three repeat tests resulting in a cumulative shear displacement of 320 mm. Virgin geotextile specimens were used in each of the repeat tests to isolate the effects of geomembrane wear without having to consider large scale geotextile wear factors such as filament pullout and breakage (Gilbert et al., 1995).

4.3.5 ASTM Hook and Loop Testing

Standard ASTM hook and loop shear strength tests (ASTM D 5169 – 98) were conducted using the materials from the direct interface shear tests. Additionally, strips of an industrial strength hook and loop system were tested autonomously and in combination with geotextile or geomembrane specimens. Tests were conducted using an uniaxial tension/compression testing frame. The test configuration provided load resolution of 0.4 N, a large displacement range in excess of 0.5 m, and vertical displacement resolution of 0.1 mm. A total of 6 material combinations were tests as follows:

- Coextruded HDPE geomembrane - NPNW geotextile
- Coextruded HDPE geomembrane - commercial loops
- Structured HDPE geomembrane - NPNW geotextile
- Structured HDPE geomembrane - commercial loops
- Commercial hooks - NPNW geotextile
- Commercial hooks - commercial loops

ASTM test method D 5169 – 98 requires material specimens to be 25.4 mm by 101.6 mm in plan area, with the central 50.8 mm of material overlapped as shown in

Figure 4-7. The materials were oriented with the machine direction of the geosynthetics aligned along the tension direction. The commercial hook and loop materials are manufactured to be bi-directional. As specified by ASTM D5169, the mating of the various "hook" and "loop" materials was achieved by applying a dead weight for 2 seconds and then pushing a weighted roller over the length of the joined strips for 5 successive cycles. The ASTM specified mating process corresponds well with typical construction loads encountered by geosynthetics during installation, and thus adequately models the in-place interaction of the tested materials under zero normal stress conditions. The upper and lower extended portions of each material were then placed into tensile testing grips, and the specimen was pulled at a constant rate of 305 mm/min.

4.4. Test Results

4.4.1 Optical Microscopy Results

As previously noted, cross-sections of the two tested geomembranes, taken along the machine direction, where encased in coupons of Plaster of Paris™ and polished to create a strong optical contrast between the geomembranes and the housing material as depicted in Figure 4-4. Digital images of the coupons were captured with a charge-coupled device (CCD) camera integrated into an optical microscopy system. The captured images were then digitally analyzed to quantify the surface roughness characteristics of the tested geomembranes. A quantitative measure of surface roughness used in the geomaterials community is the profile roughness parameter R_L.

$$R_L = \frac{actual\ profile\ length}{projected\ profile\ length} \qquad \text{(Eq. 4-1)}$$

While the texturing processes of the two tested materials differs greatly, the profile roughness values of the tested materials obtained from the optical microscopy analysis are comparable with R_L values of 1.28 +/- 0.21 and 1.23 +/- 0.05 for the coextruded and structured geomembranes, respectively. Accordingly, it is considered reasonable to directly compare the response of interfaces involving geotextiles and these two geomembranes. The optical microscopy images were further used to provide qualitative insight into the mechanisms controlling geotextile-geomembrane and hook and loop response.

4.4.2 Direct Interface Shear Results

As previously noted, all interface shear tests consisted of an upper NPNW geotextile of 203 g/m^2 sheared against a lower textured geomembrane over a displacement range of 80 mm per test. Direct interface shear tests were conducted on virgin material samples at eleven normal stress levels ranging from (0.4 – 312 kPa). Peak and pseudo-residual (@ 80 mm displacement) interface shear stresses were determined for both material combinations at all normal stress levels. Additionally, a series of four interface shear tests (virgin, 1st retest, 2nd retest, and 3rd retest) were conducted on specimens of both texturing types at a normal stress level of 102 kPa, with a new geotextile specimen used in each retest. A summary of the interface shear testing results is presented in Table 4-2. Shear stress versus displacement plots for all virgin tests on the coextruded and structured geomembranes are summarized in Figures 4-8 and 4-9, respectively. The differences in the scale of parts a and b of these figures is noted. The results for the coextruded geomembrane system shows a post peak softening trend throughout the tested normal stress range. In comparison, the results of the structured

geomembrane system exhibit higher stiffness, lower strength, and limited strain softening at low (< 50 kPa) normal stresses, with post peak softening and mobilized strengths becoming comparable to the coextruded system as normal stress increases.

4.4.3 ASTM D 5169-98 Hook and Loop Shear Strength Results

As noted above, ASTM D 5169-98 hook and loop shear strength tests were conducted on the geosynthetic systems, the industrial strength fastener systems, as well as hybrid combinations of the geosynthetics and commercial hook and loop components as outlined in Table 4-3. All material combinations were tested four successive times to characterize the effect of wear on the interface behavior. Tests using the commercial hook and loop system allowed for a baseline value of engineered hook and loop shear strength to be obtained. The hybrid geosynthetic – commercial hook and loop testing combinations isolated the individual contributions of each geosynthetic material towards the hook and loop shear strength, and allowed for more detailed quantification of hook and loop interaction. Tests performed according to the ASTM standard method result in continuous changes in the sheared area, and as such, the peak load becomes the best indicator of hook and loop shear strength. The results of all tested material combinations are summarized in Table 4-3. The general trend in the results follows an initial portion of increasing strength attributed to the engagement of the "loop" structure by the "hook" material. Following the seating response upon initial displacement, the typical behavior consists of a linear strength increase culminating at a peak resistance, followed by rapid decrease in strength as the contact area decreases to zero. Typical results from the ASTM standard hook and loop strength test for the tested materials exhibiting large hook and loop interaction and those exhibiting minimal but measurable hook and loop interaction

are shown in Figures 4-10a and 4-10b, respectively. The significant difference in scale between these two figures is noted.

4.5. Discussion

4.5.1 Summary of Results

To facilitate discussions herein, two normal stress regions are defined as typically encountered in municipal solid waste landfill practice: liner construction and final cap closure stresses (< 50 kPa), and operational liner stresses (50 kPa to > 1000 kPa). The focus of this study is on liner construction and low to intermediate operational normal stress interaction mechanisms. The direct interface shear results are summarized in Figures 4-11 and 4-12 showing the peak and psuedo-residual interface strength values, respectively, plotted versus applied normal stress. The structured geomembrane system clearly shows a linear peak strength behavior over the entire range of normal stresses tested, as shown in Figure 4-11. In contrast, the coextruded geomembrane system exhibits nonlinear peak response at low normal stresses, transitioning to a linearly increasing peak strength response over the remainder of the tested normal stresses range (15 to 302 kPa.) The trends of the peak interface shear stress results show that the structured system provides slightly higher interface friction than the coextruded system within the operational normal stress range tested, as represented in the conventional Mohr-Coulomb form shown in Equation 4-2:

$$\tau_{s(peak)} = c_a + \tan(\delta'_{peak}) \qquad \text{(Eq. 4-2)}$$

coextruded: $\tau_{s(peak)}$ = 9.5 kPa + tan(30.4°) (Eq. 4-3)

structured: $\tau_{s(peak)}$ = 0 kPa + tan(35.1°) (Eq. 4-4)

where c_a = apparent cohesion and δ'_{peak} = the peak interface friction angle. The pseudo-residual interface behavior presented in Figure 4-12, is based on shear stress values @ 80 mm displacement. The figure shows similar results for tests on specimens of both textures, with the coextruded system again showing slightly stronger response in the low construction stress range (< 25 kPa), and the structured system showing marginally stronger residual response at operational stresses.

4.5.2 Behavior at Construction Level Normal Stresses

Differences in direct interface shear behavior over the low normal stress range for the coextruded and structured geomembranes are illustrated in Figures 4-8b and 4-9b, respectively. The initial stiffness of the low (< 50 kPa) normal stress tests on structured specimens (Figure 4-9b) show predominantly frictional behavior with little to no degradation in small strain stiffness with increasing normal load. In contrast, the tests on coextruded specimens (Figure 4-8b) show much higher peak and residual strengths at low normal stresses, all exhibiting a bilinear pre-peak stiffness behavior consisting of an initial frictional response, followed by a secondary strength increase at lower stiffness representative of supplemental hook and loop interaction. The peak stress is followed by significant post-peak softening for the coextruded samples. The reduction in displacement to peak stress with increasing normal stress seen in Figure 4-8b (13 mm at 0.4 kPa to 8 mm at 26.9 kPa) represents a transition in dominant mechanism, from surficial hook and loop interactions to a more frictional response at higher normal

stresses. While the structured system exhibits linear peak behavior within the low normal stress range as seen in Figure 4-11, a detailed examination of the full shear stress – displacement behavior of the individual low normal stress tests (Figure 4-9b) shows an increase in displacement to peak stress with increasing normal stress (0.1 mm at 0.4 kPa to 4.3 mm at 26.9 kPa) indicative of greater geotextile filament engagement as normal stress increases. In summary, frictional interactions occur at much higher stiffness than hook and loop interactions, and the relative contributions of frictional and hook and loop resistance leads to the observed trends and differences in displacement to peak strength.

To better understand the hook and loop interactions at low normal stresses, the results of the ASTM standard hook and loop shear strength tests presented in Table 4-3 and Figure 4-10 were examined. As discussed earlier, the ASTM hook and loop test occurs at essentially zero applied normal stress, thereby isolating the contributions of hook and loop interaction from frictional mechanisms. The peak strength of the commercial hook and loop system was determined to be 294 N for virgin samples sheared at 305 mm/min over a 1290 mm^2 area. The tests including one or more of the geosynthetic materials showed much lower strengths than the engineered hook and loop system. The structured geomembrane showed no apparent hook and loop strength when paired with either the NPNW geotextile or the commercial loops, further illustrating the absence of hook and loop interaction at low normal stresses for this texturing technique. The coextruded geomembrane showed some limited hook and loop strength, with the peak load of the virgin samples equaling 0.6 N and 3.1 N when paired with the NPNW geotextile and the commercial loops, respectively. The combination of the NPNW geotextile and the commercial hooks provided a significant hook and loop interaction, on

the order of 54 N of peak strength. This hybrid test clearly shows that the fabric structure of NPNW geotextiles can provide considerable hook and loop strength when paired with an ideal hooking material. A comparative review of the images in Figures 4-1c, 4-2c, and 4-3 support these interpretations.

The current low normal stress results provide quantitative insight into mechanisms affecting non-frictional interaction in geotextile-geomembrane systems and complement the findings of Giroud (2004). Giroud investigated the effects of adhesion on the performance of geosynthetic systems at construction level normal stresses and provides guidance in the design of geosynthetic systems under construction conditions accounting for adhesion in any form.

4.5.3 Texture – Filament Interactions

Plots of the responses from three selected normal stresses (14.4, 102, and 262 kPa) are shown in Figure 4-13 for both texture types. These results demonstrate the typical evolution of stiffness and strength behavior over the tested normal stress range for geotextile-geomembrane systems of comparable global geomembrane surface roughness values but formed using different texturing methods. The geomembranes show distinctly different behavior in the low (14.4 kPa) normal stress region where the sharp overlapping texture of the coextruded geomembrane results in a significant hook and loop contribution to the overall interface response. The stiff rounded macrotexture of the structured geomembrane provides a more frictional response of lower strength and higher stiffness. The behavior of the two materials transitions towards a convergent response in the operational stress range where macro and base geomembrane texture begin to control the system behavior.

The divergence in the characteristic behaviors of the coextruded and structured responses for low normal stresses is clearly displayed in the trend of normalized shear response (τ/σ_n), Figure 4-14. The coextruded response, Figure 4-14a, exhibits a reduction in both normalized peak and residual shear stress with increasing normal stress indicative of a reduction in the percentage of total response resultant from hook and loop interactions. The normalized structured shear response, Figure 4-14b, maintains a relatively constant peak shear behavior on the order of 50% of the applied normal stress, with the residual response reducing from 50% at 14.4 kPa to 30% for normal stresses above 200 kPa. A transition in the mechanism controlling hook and loop interaction within the geosynthetic occurs with increased normal stress as the surficial hook and loop interaction dominant at lower normal stresses is exceeded by the effect of the geotextile matrix compression between the macrotextural features of the geomembranes, resulting in matrix level interactions controlling the shear behavior at higher normal stresses.

A schematic showing the transition of textured geomembrane - NPNW geotextile system interactions from the low normal stress range to the operational stress range is shown in Figure 4-15. At low normal stresses, the interaction between the NPNW geotextile and the textured geomembranes consists mostly of individual filaments being engaged by the outward region of the geomembrane texture, as seen in Figure 4-14a. The texture of coextruded geomembranes, consisting of jagged macrotexture containing significant microtexture, results in a greater engagement of individual geotextile filaments than the structured textures rounded macro features containing minimal microtexture. As the applied normal stress increases, the geotextile becomes compressed and increasingly interbedded between the macrotextural features of the contacting

geomembrane resulting in matrix level frictional and hook and loop interactions as seen in Figure 4-15b. As the geotextile becomes interbedded between the macrotexture of the geomembrane the micro and mesotexture of the base substrate become involved in supplemental hook and loop interactions.

As was seen in Figures 4-1b and 4-2b, both the coextruded and the structured geomembranes contain micro and mesotexture across the base substrate providing for the significant hook and loop interactions observed at operational normal stresses. It is proposed that the micro and mesotexture present on the base of the tested geomembranes result in a counterface that provides for the supplemental peak strength gains seen in the virgin direct interface shearing results (Figures 4-8a and 4-9a). The wear results presented in sections 4.5.4 and 4.5.5 further support this statement. The comparable global surface roughness measures of R_L = 1.23 and 1.28 for the structured and coextruded geomembranes respectively, are reflected in the similar stress-displacement behaviors observed in the operational normal stress range. The above results support the hypothesis that as normal stress increases from the construction to the operational stress range, the controlling behavioral mechanisms transfer from surficial to interbedded interactions.

4.5.4 Sensitivity (τ_{peak} / $\tau_{residual}$)

A useful measure to highlight differences in the peak and psuedo-residual responses of the tested geotextile-geomembrane systems is the sensitivity (τ_{peak} / $\tau_{residual}$) of the direct interface shear results, as shown in Figure 4-16 as a function of normal stress. It can be seen that both systems exhibit an initial decrease in sensitivity with increasing normal stresses resulting from the transition in engagement mechanisms depicted in

Figure 4-15. After the initial decrease in sensitivity at low normal stresses the structured geomembrane-geotextile system shows an approximately linear increase in sensitivity from a minimum value of 1.0 at a normal stress of 14.4 kPa to a maximum observed sensitivity of 2.3 at the maximum normal stress level tested (312 kPa). The coextruded geomembrane-geotextile system exhibits higher sensitivity values at low normal stresses exhibiting a measured maximum at the lowest normal stress tested (τ_P/τ_R = 2.2 @ 0.4 kPa). The large sensitivities at low normal stresses stem from the higher peak strengths observed at those normal stresses due to the significant hook and loop contribution. The coextruded system sensitivity shows a decreasing trend with increased normal stress up to 50 kPa at which time the sensitivity increases linearly, but at a slower rate than the structured system. The global interaction mechanisms of the two systems show similar behaviors as a result of the similarities in macro geomembrane surface texture, and the increasing contributions of matrix level geotextile – geomembrane texture interactions. The divergence of the sensitivity trends stems from the differences seen in the peak behavior (Figure 4-11), as the residual behaviors are similar due to their dependence on the consistent geotextile and macro roughness properties. It follows logically that the increase in sensitivity seen at operational normal stresses for the coextruded system would lag that of the structured system as highlighted previously by the peak strength behaviors.

4.5.5 Stiffness considerations

Examination of the interface stress displacement behavior for the various normal stress ranges also reveals some important stiffness considerations. In the low (14.4 kPa) normal stress plots of Figure 4-13, the displacement to peak of the two systems shows

significant divergence, 1.5 and 9.0 mm for the structured and coextruded geomembranes, respectively. Figure 4-17 presents the trend in the displacements at peak as a function of applied normal stress. The displacement to peak for the coextruded response is observed to decrease with increasing normal stress until converging to a constant value on the order of 7 mm for all normal stresses above 25 kPa. The opposite trend is observed in the structured results at low normal stresses, with the behavior approximating the observed coextruded response for normal stresses above 150 kPa. As such, depending on the allowable construction displacement specifications, the added benefits of hook and loop interactions seen for the coextruded texture at low (< 50 kPa) normal stresses may not be achieved throughout the system. The initial interface stiffnesses of the two geomembrane systems are comparable, but are divergent after the structured geomembrane system reaches peak strength, indicating that both textures provide comparable initial frictional stiffness. It follows that the added strength gained through hook and loop interaction is achieved at a much lower stiffness, due to the lower stiffness of individual NPNW filaments that are discretely involved in low normal stress hook and loop response mechanisms. As normal stress increases and similar interaction mechanisms control the behavior of both geomembrane types, the stiffness characteristics of the two geotextile-geomembrane systems are essentially equivalent. The large displacements needed to mobilize the peak strength of both geotextile-geomembrane systems at operational normal stress levels should be noted when specifying the in-place strengths of these types of geosynthetic systems.

4.5.6 Geomembrane Wear Mechanisms

The effect of wear on the textured geomembranes was investigated through repeated direct interface shear tests conducted at 102 kPa normal stress. The geomembrane specimens were tested against four virgin geotextile specimens in succession, for a total cumulative displacement of 320 mm (80 mm per test). The use of virgin geotextile specimens in each retest isolated the role of geomembrane texture degradation on the residual strength of the interfaces. Figure 4-18 presents the results of this test series for the coextruded (Figure 4-18a) and structured (Figure 4-18b) systems, respectively. Both systems show significant loss of peak strength upon retesting, indicating that wear of the geomembrane texture can occur in the operational stress range. The loss of peak strength and the lack of significant degradation to macrotexture upon reshearing at this normal stress level (102 kPa) support the conclusion that micro and mesotexture found on both the base substrate and the macrotextural features not only provide supplemental strength by way of hook and loop interactions, but also become damaged upon shearing past the virgin peak. Figure 4-18b additionally supports the above hypothesis that at higher normal stresses, the mesotexture present on the base of the structured geomembrane provides contact points for filament engagement and strength gains provided by the subsequent matrix level hook and loop interactions. While both geomembrane types show the loss of the hook and loop contribution after the virgin shearing, it can be seen that the coextruded geomembrane shows a much larger peak to residual strength decrease, consistent with the higher level of initial microtexture. This is clearly illustrated in the plot of sensitivity versus cumulative displacement for these test series as seen in Figure 4-19. After significant cumulative shearing both geosynthetic

systems converge to a sensitivity of $\tau_{peak} / \tau_{residual}$ of about 1.2. The relative stability of the measured residual strengths upon reshearing supports the supposition that post-peak interface behavior in these types of systems is predominantly controlled by the normal stress; the mechanical properties and behavior of the geotextile filaments and matrix; and the size, not the shape or associated microtexture of the geomembrane macrotexture.

The same properties that make the coextruded texture conducive to higher hook and loop interaction at lower normal stresses, namely: significant microtexture, overlapping pockets, and sharp extensions results in a macrotexture that was found to be more compressible and fragile through pre and post-shear visual inspection, accounting for the slightly lower peak interface strengths seen at operational normal stress levels. While the difference in the strengths of the two textured interfaces is significant within the low normal stress range, it is only moderately significant within the tested range of operational normal stresses. However, increased degradation and compression of the texture on coextruded geomembranes may become significant at higher applied normal stresses.

4.5.7 Geotextile wear mechanisms

The pseudo-residual interface behavior of the tested materials was presented in Figure 4-12. The plots show similar results for tests on specimens of both textures, with the large displacement strength of the interfaces primarily governed by the properties of the geotextile and the macrotexture of the geomembranes. The average filament length of the staple NPNW geotextile tested is approximately 75-100 mm (3-4 in). At a maximum, only half of the filament length can be engaged before phenomena such as filament pullout and other geotextile wear mechanisms degrade individual filament strength. The

loose filaments pulled and/or torn from the matrix through virgin shearing subsequently detract from the post-peak system strength as they limit continued interactions at the contact surface. As such, geotextile wear mechanisms appear to control the large displacement strength of this type of geosynthetic interface provided the combination of surface texture and normal stress are sufficient to create interactions similar to Figure 4-14b. The combination of sufficient roughness to engage the geotextile fabric globally instead of at individual filaments, and sufficient normal stress to allow the geotextile fabric to fully penetrate into the geomembrane texture allows the full global strength of the NPNW geotextile to be realized for a particular normal stress level (Frost et al., 2002). Figure 4-16, showing sensitivity as a function of cumulative shear displacement against virgin geotextiles at intervals of 80 mm, shows a convergence to a value of $\tau_{peak} / \tau_{residual}$ = 1.2 for both texture types. The convergence of the sensitivity value for both geomembrane types after repeated shearing against virgin geotextile samples represents an isolation of the geotextile wear as the majority of the geomembrane wear occurs within the initial tests of the wear sequence. This residual sensitivity value represents the geotextile strength losses that result from large displacement matrix level interface shearing regardless of the presence of significant hook and loop interaction.

Geotextile wear was also investigated through residual ASTM hook and loop shear strength testing. Residual values were obtained by conducting 3 repeat tests on the same materials and taking the peak load of the 4th test (3rd retest) as the residual value, as listed in Table 4-3. The coextruded geomembrane – NPNW geotextile combination demonstrated an increased residual hook and loop response as compared to the virgin tests due to the loosening of the geotextile fabric upon repeat testing. The loosening of

the fabric allowed the coextruded texture to more easily engage the surficial filaments of the NPNW geotextile, providing a 350% increase in peak strength. The higher observed hook and loop interaction at zero normal stress resulted from more filaments being able to engage the texture between the macrotextural features due to the loosening of the geotextile matrix. This mechanism parallels the increased hook and loop interactions seen in the direct interface shear tests as a result of increasing the applied normal stress. The NPNW geotextile showed a dramatic (92.5%) decrease in strength for the 3rd retest when paired with the commercial hooks, indicating that repeated shearing causes the surficial filaments to be dislodged from their anchorage in the main fabric matrix. The shearing of the filaments from the matrix was not seen after three retests with the coextruded texture because of the reduced level of engagement; however, similar strength reduction was observed after significant retesting (> 10 retests).

4.6. Conclusions

Through a combination of multiple laboratory tests and optical observations, the interface behavior of two textured geomembrane types (coextruded and structured) in contact with NPNW geotextiles was investigated. The direct interface shear and ASTM hook and loop results show distinctive differences in the behavior of the tested interfaces. All geomembrane material properties and dimensions, excluding the texturing processes, were similar. As such, it can be concluded that the observed behavioral differences can be attributed to the differences in the surface texture of the tested geomembranes. A summary of the conclusions from the current study are presented below:

- The texture of the coextruded geomembranes was characterized through optical microscopy as consisting of jagged macrotexture with high levels of micro and mesotexture present along the base substrate and bonded to the macrotextural features.
- The texture of the structured geomembranes was characterized through optical microscopy as consisting of "smooth" rounded macrotexture with no bonded micro or mesotexture but significant micro and mesotexture present along the base substrate.
- Hook and loop interactions in textured geomembrane-geotextile systems were found to be strongly dependent on the level of micro and mesotexture bonded to the surface of the macrotextural features at low normal stresses and on the level bonded to the macrotexture and along the base substrate at higher normal stresses.
- The frictional contributions to the shear response of the two systems were found to be controlled by discrete surficial interactions between surface filaments and textural features at low normal stresses, and dominated by the compression and interbedding of the geotextile between the macrotexture, resulting in more global continuum interactions at higher normal stresses.
- The geomembranes tested contained macrotexture of similar out of plane dimension and spacing, as well as comparable levels of base texture resulting in similar frictional and hook and loop contributions to the peak response within the range of operational stresses tested (50 – 312 kPa). The direct interface shear results within this normal stress range correspond to conventional Mohr-Coulomb

relationships of $\tau_{s(peak)}$ = 9.5 kPa + tan(30.4°) and $\tau_{s(peak)}$ = tan(35.1°) for the coextruded and structured systems, respectively.

- The peak response of the coextruded system was consistently stronger than the structured system within the low normal stress range (< 50 kPa). The structured texture exhibited an almost purely frictional peak response supplemented by insignificant hook and loop interactions at low stresses due to the absence of microtexture away from the base substrate. In contrast, the jagged nature and significant microtexture present on the macrotexture of the coextruded geomembrane provided a counterface conducive to large strength contributions from hook and loop interaction in addition to the comparable frictional response resulting in a highly non-linear peak shear response at low normal stresses.
- ASTM standard hook and loop shear strength tests were used to isolate the low normal stress hook and loop interaction mechanisms. The hook and loop tests confirmed the low normal stress behavior seen in the direct interface shear testing and allowed the individual contributions to the hook and loop interaction to be quantified. The fabric of NPNW geotextiles was found to be well suited to hook and loop interaction when paired with the engineered hook structure of a commercial hook and loop product. The coextruded geomembrane showed limited response during ASTM hook and loop testing when paired with both the NPNW geotextile and commercial loops, while the structured geomembranes provided no measurable response in combination with all tested loop materials.
- The pseudo-residual shear behaviors of the tested geomembranes were similar, and primarily dependent on frictional interactions between the NPNW geotextile

and the macrotextural features of both geomembranes. Additionally, the pseudo-residual shear strengths were found to be strongly dependant on the properties and wear mechanisms of the NPNW geotextile.

- Microtexture, and to a lesser extent mesotexture, on both geomembrane types were found to be susceptible to wear of varying degrees as a result of interface shear at all tested normal stress levels and was therefore not a significant factor in post-peak interaction mechanisms.
- Through visual inspection of the geomembranes pre- and post-shear, the macrotextural features of the coextruded geomembrane were found to be more susceptible to wear and degradation processes from interface shear, as compared to the macrotexture of the structured geomembrane, resulting in slightly lower peak and residual strengths at the operational normal stresses tested.

The current results suggest that hook and loop interaction plays a significant role in the interface shear behavior of NPNW geotextile – textured geomembrane systems across a wide range of normal stress levels. The results and discussions presented herein regarding hook and loop interaction within textured geomembrane-geotextile systems as a result of different geomembrane texturing techniques should allow contractors and design engineers to make more informed decisions regarding the selection and specification of textured geomembranes in practice.

Table 4-1. Summary of Material Properties

Material	Production Process	Thickness or Weight	Polymer Type
HDPE Textured Geomembrane	Blown Coextrusion	1.5 mm	HDPE
HDPE Textured Geomembrane	Hot Embossing	1.5 mm	HDPE
Staple NPNW Geotextile	Needle-Punching	203 g / m^2	PP
Industrial Strength Velcro® Loops	Propreitary	~200 g / m^2 [(1)]	Nylon
Industrial Strength Velcro® Hooks	Propreitary	1.5 mm	Nylon

[(1)] *Does not include mass of adhesive backing material*

Table 4-2. Results of Interface Shear Testing

Test No.	σ_n (kPa)	τ_{peak} (kPa)	d_{peak} (mm)	τ_{resid} (kPa)	Remarks
CE - 1	0.4	3.91	12.88	1.77	NPNW geotextile - coextruded geomembrane
CE - 2	3.6	8.67	13.11	4.05	NPNW geotextile - coextruded geomembrane
CE - 3	5.5	11.33	12.19	5.29	NPNW geotextile - coextruded geomembrane
CE - 4	14.4	18.33	11.02	10.23	NPNW geotextile - coextruded geomembrane
CE - 5	26.9	24.43	7.82	13.55	NPNW geotextile - coextruded geomembrane
CE - 6	51.9	35.16	7.57	21.74	NPNW geotextile - coextruded geomembrane
CE - 7	101.9	65.49	6.63	37.15	NPNW geotextile - coextruded geomembrane
CE - 8	151.9	90.25	7.19	47.64	NPNW geotextile - coextruded geomembrane
CE - 9	201.9	113.73	7.04	59.35	NPNW geotextile - coextruded geomembrane
CE - 10	261.9	146.87	6.71	74.15	NPNW geotextile - coextruded geomembrane
CE - 11	301.9	173.03	7.26	79.28	NPNW geotextile - coextruded geomembrane
ST - 1	0.4	0.65	0.46	0.50	NPNW geotextile - structured geomembrane
ST - 2	2.5	2.14	1.09	1.51	NPNW geotextile - structured geomembrane
ST - 3	4.7	2.89	1.65	2.19	NPNW geotextile - structured geomembrane
ST - 4	14.4	7.05	1.85	7.05	NPNW geotextile - structured geomembrane
ST - 5	26.9	13.55	4.45	11.87	NPNW geotextile - structured geomembrane
ST - 6	51.9	31.24	4.27	23.81	NPNW geotextile - structured geomembrane
ST - 7	101.9	59.07	4.60	40.05	NPNW geotextile - structured geomembrane
ST - 8	151.9	91.83	7.80	55.18	NPNW geotextile - structured geomembrane
ST - 9	211.9	131.63	6.99	63.58	NPNW geotextile - structured geomembrane
ST - 10	261.9	158.77	7.14	75.38	NPNW geotextile - structured geomembrane
ST - 11	311.9	193.15	8.84	84.24	NPNW geotextile - structured geomembrane
CE_R1	101.9	45.80	4.90	34.77	1st Retest of Test CE - 7
CE_R2	101.9	41.08	4.67	31.49	2nd Retest of Test CE - 7
CE_R3	101.9	39.89	4.32	31.94	3rd Retest of Test CE - 7
ST_R1	101.9	45.94	5.02	37.72	1st Retest of Test ST - 7
ST_R2	101.9	45.56	3.99	37.38	2nd Retest of Test ST - 7
ST_R3	101.9	43.43	4.70	35.56	3rd Retest of Test ST - 7

Table 4-3. Summary of ASTM (D5169) Hook and Loop Shear Testing

Hook Material	Loop Material	Virgin Peak Load (N)	Disp at Virgin Peak (mm)	Residual [1] Peak Load (N)	Disp at Residual[1] Peak (mm)
Velcro Hooks	Velcro Loops	294.0	11.6	216.6	7.2
Velcro Hooks	NPNW Geotextile	53.6	20.5	4.0	8.3
Coextruded Geomembrane	NPNW Geotextile	0.6	7.5	2.1	11.2
Coextruded Geomembrane	Velcro Loops	3.1	1.3	1.7	2.7
Structured Geomembrane	NPNW Geotextile	0.0	N/A	0.0	N/A
Structured Geomembrane	Velcro Loops	0.0	N/A	0.0	N/A

[1] *Residual values taken from 3rd retest*

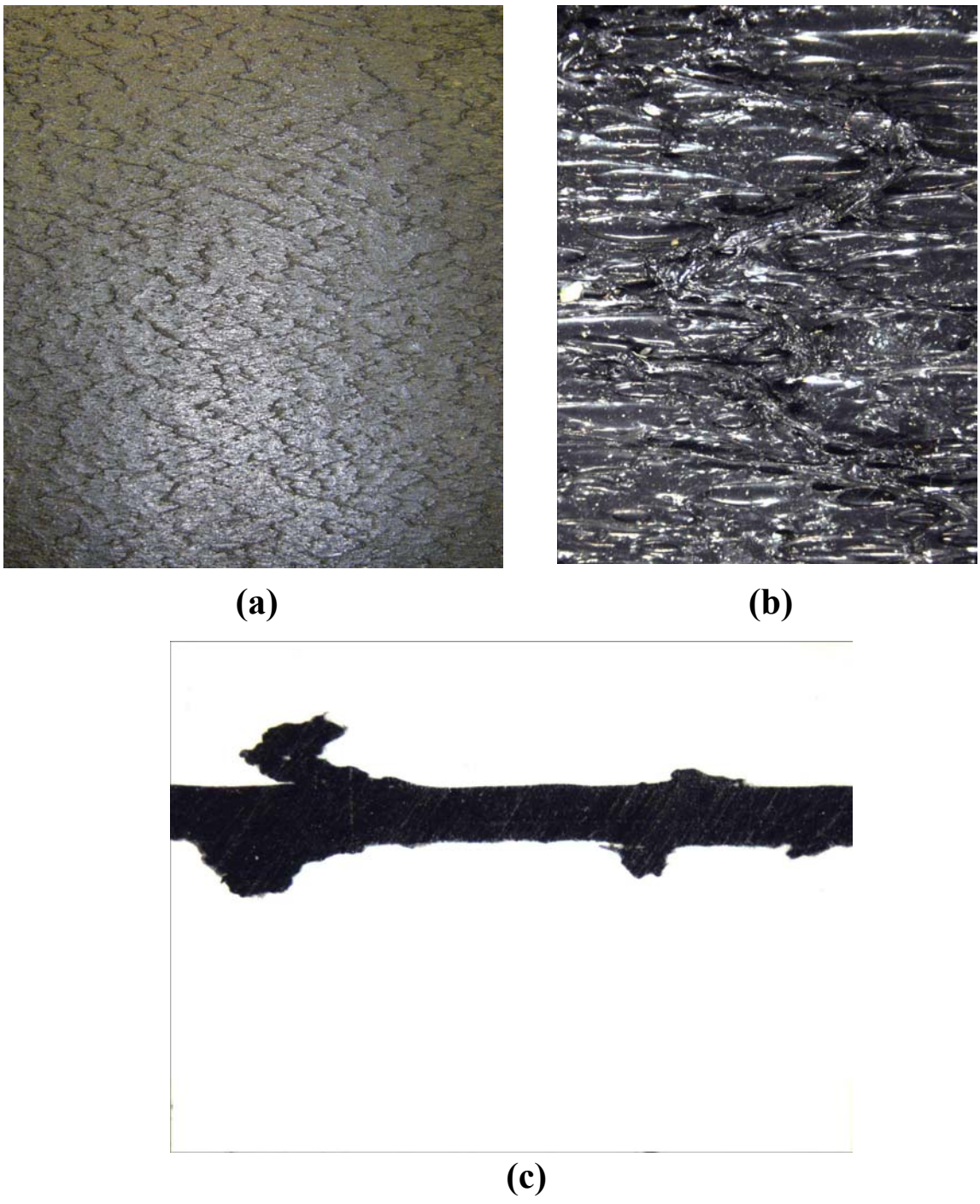

Figure 4-1. Images of Coextruded Geomembrane Used in the Test Program: (a) Plan View - 115 mm x 150 mm, (b) Magnified Plan View - 9 mm x 13 mm, and (c) Machine Direction Cross-Sectional View - 7.5 mm x 10 mm.

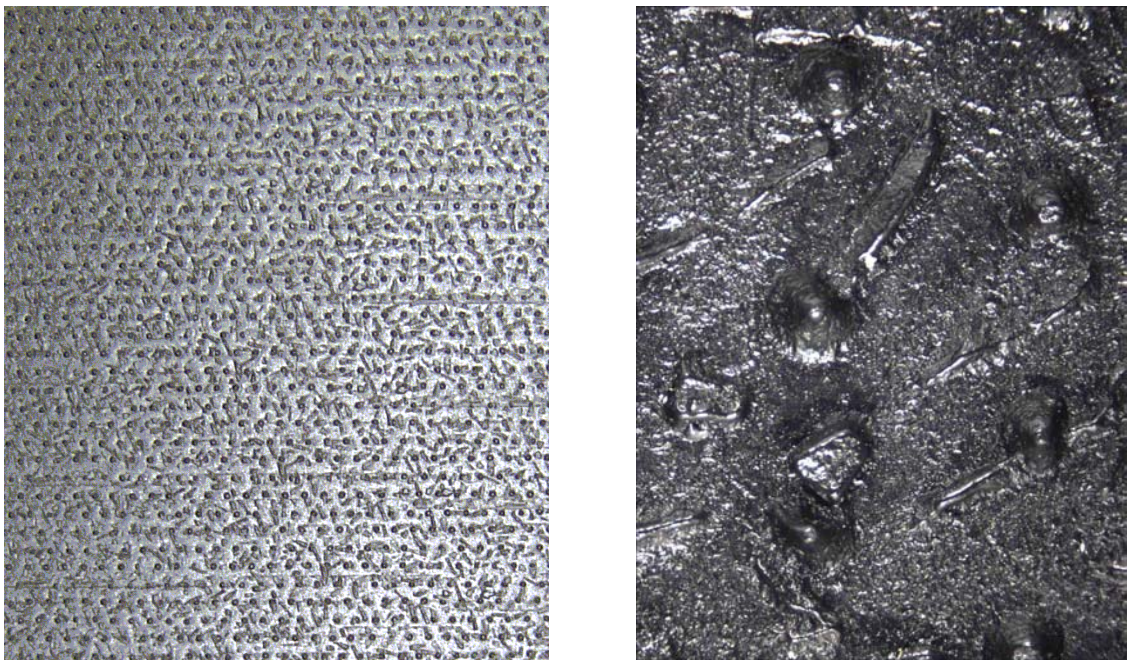

(a) **(b)**

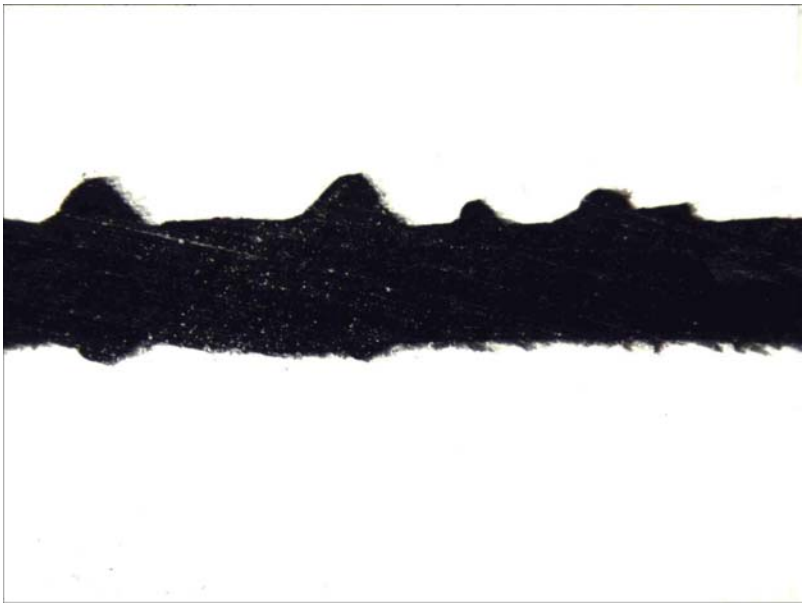

(c)

Figure 4-2. Images of Structured Geomembrane Used in the Test Program: (a) Plan View - 115 mm x 150 mm, (b) Magnified Plan View - 9 mm x 13 mm, and (c) Machine Direction Cross-Sectional View - 7.5 mm x 10 mm.

(a)

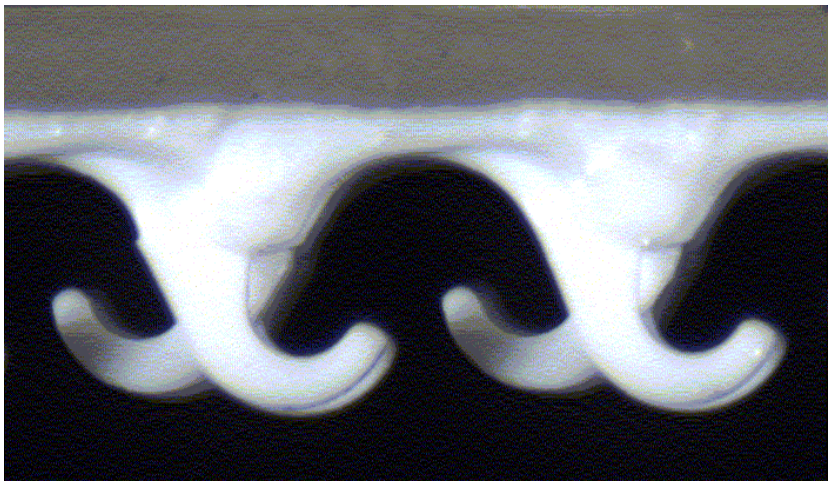

(b)

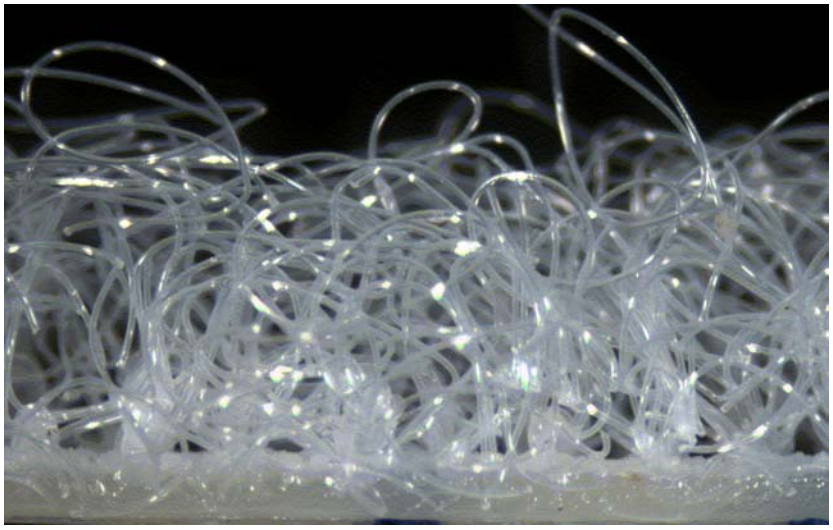

Figure 4-3. Cross-Sectional Images of Velcro® (a) Hooks and (b) Loops. Images are 3 mm Wide.

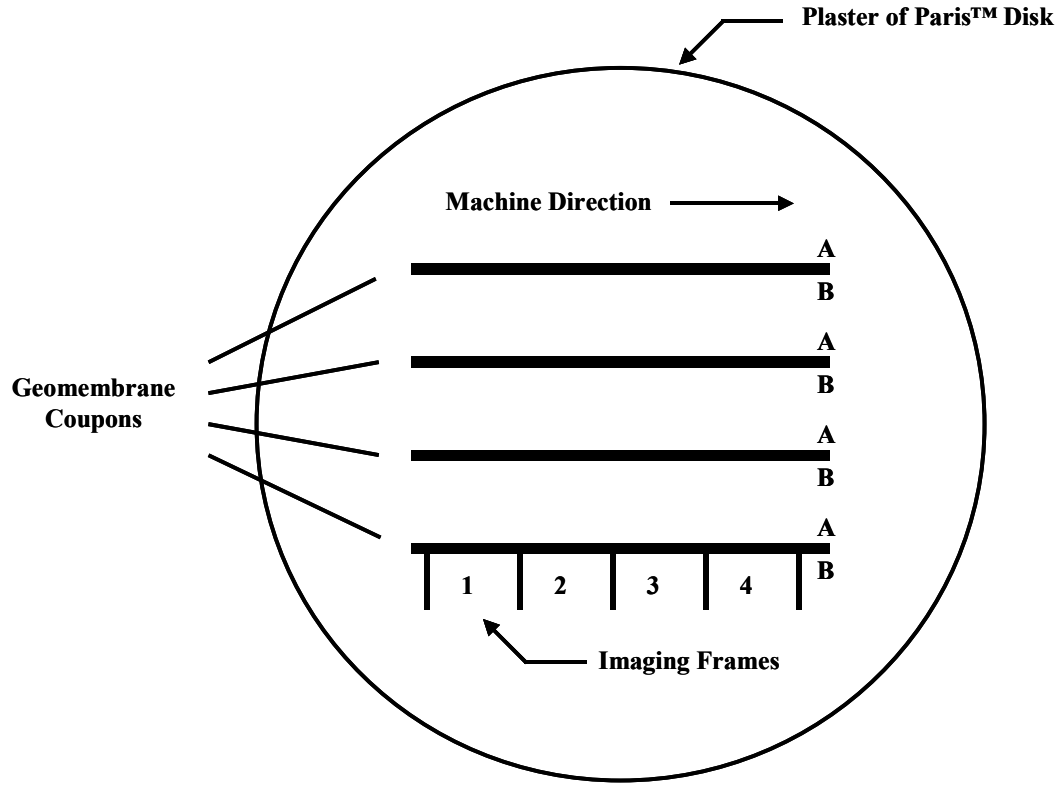

Figure 4-4. Schematic of Optical Microscopy Geomembrane Cross-Sectional Coupons, Adapted from Dove and Frost (1997).

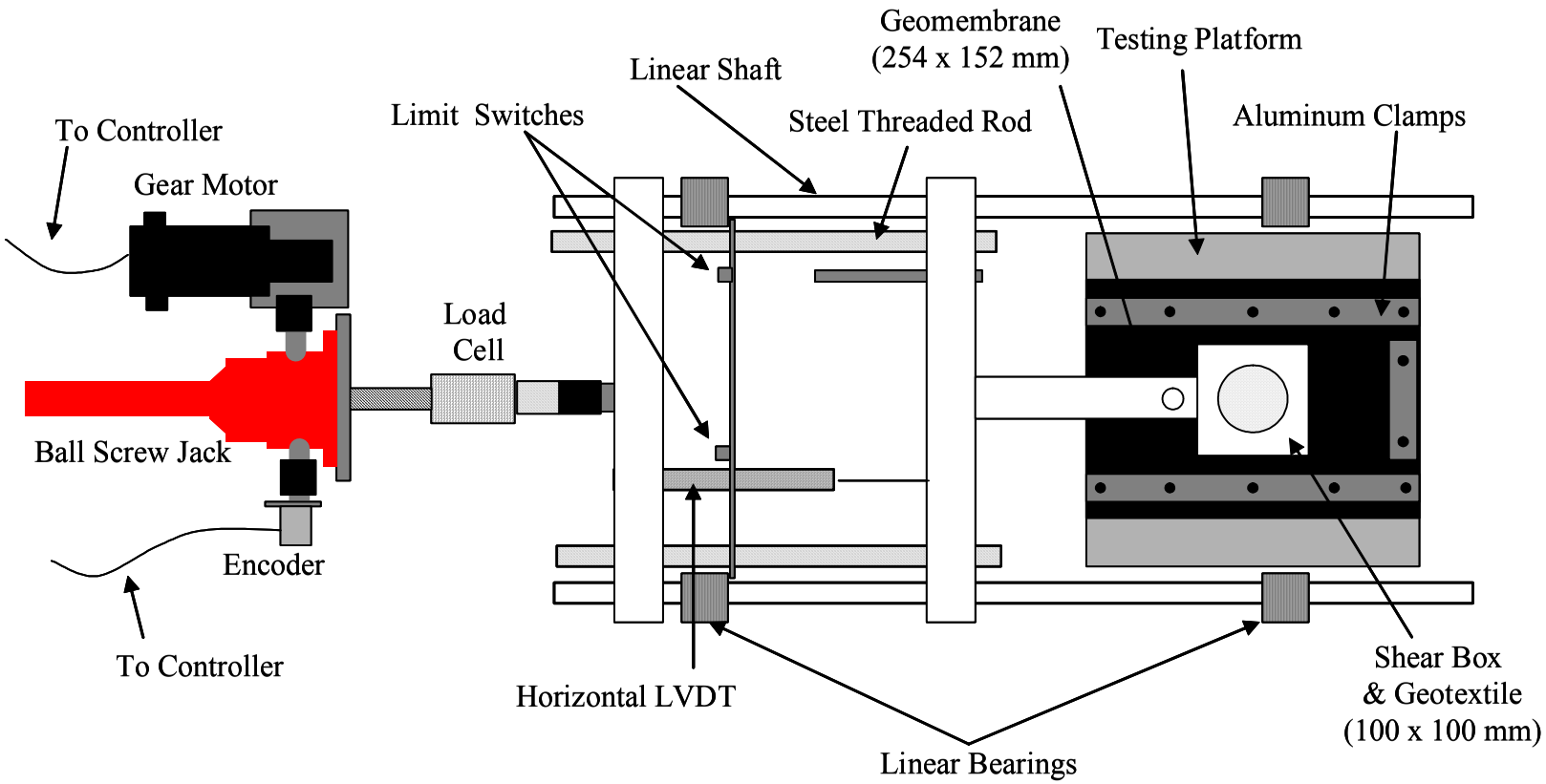

Figure 4-5. Plan View of Interface Shear Device (Vertical LVDTs Not Shown for Clarity), after Zettler (1999)

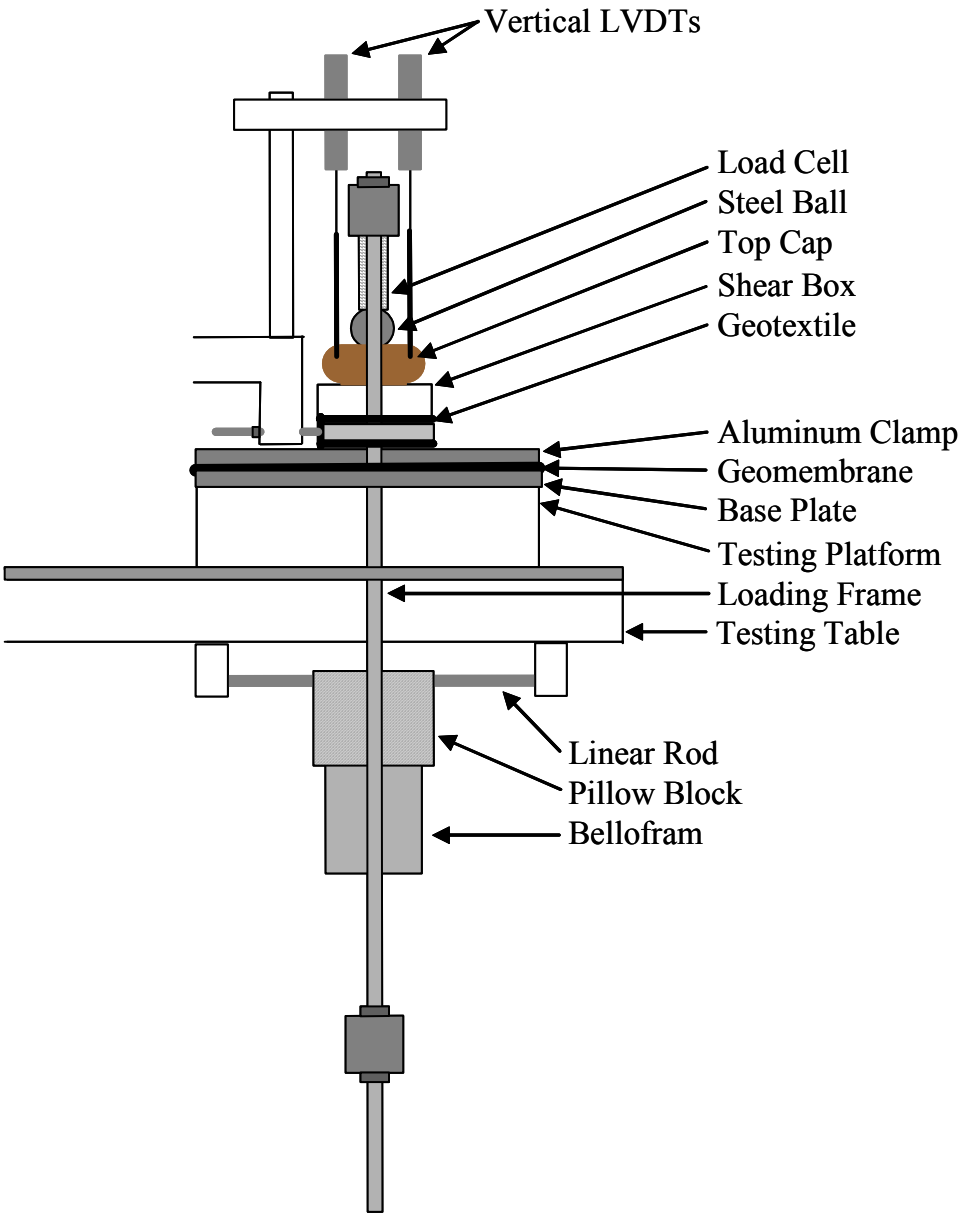

Figure 4-6. Side View of Interface Shear Device , after Zettler (1999)

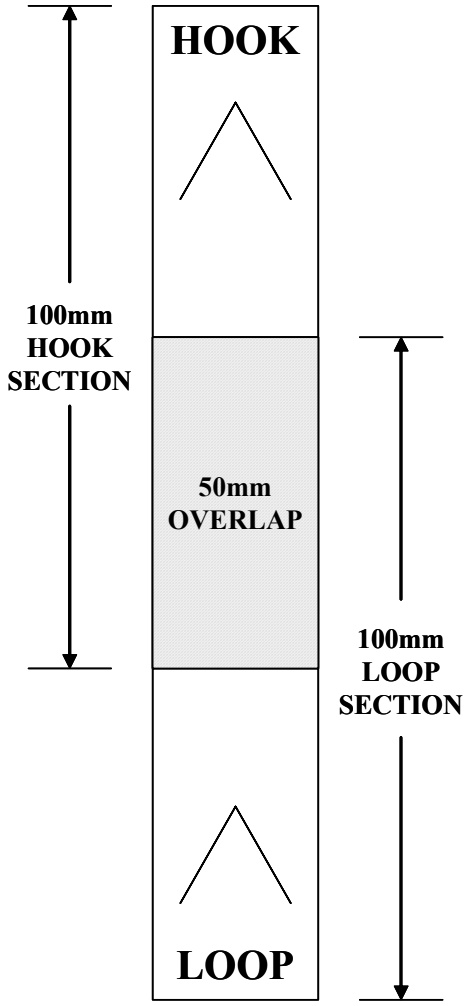

Figure 4-7. Test Configuration for ASTM D 5169-98, Shear Strength of Hook and Loop Fasteners.

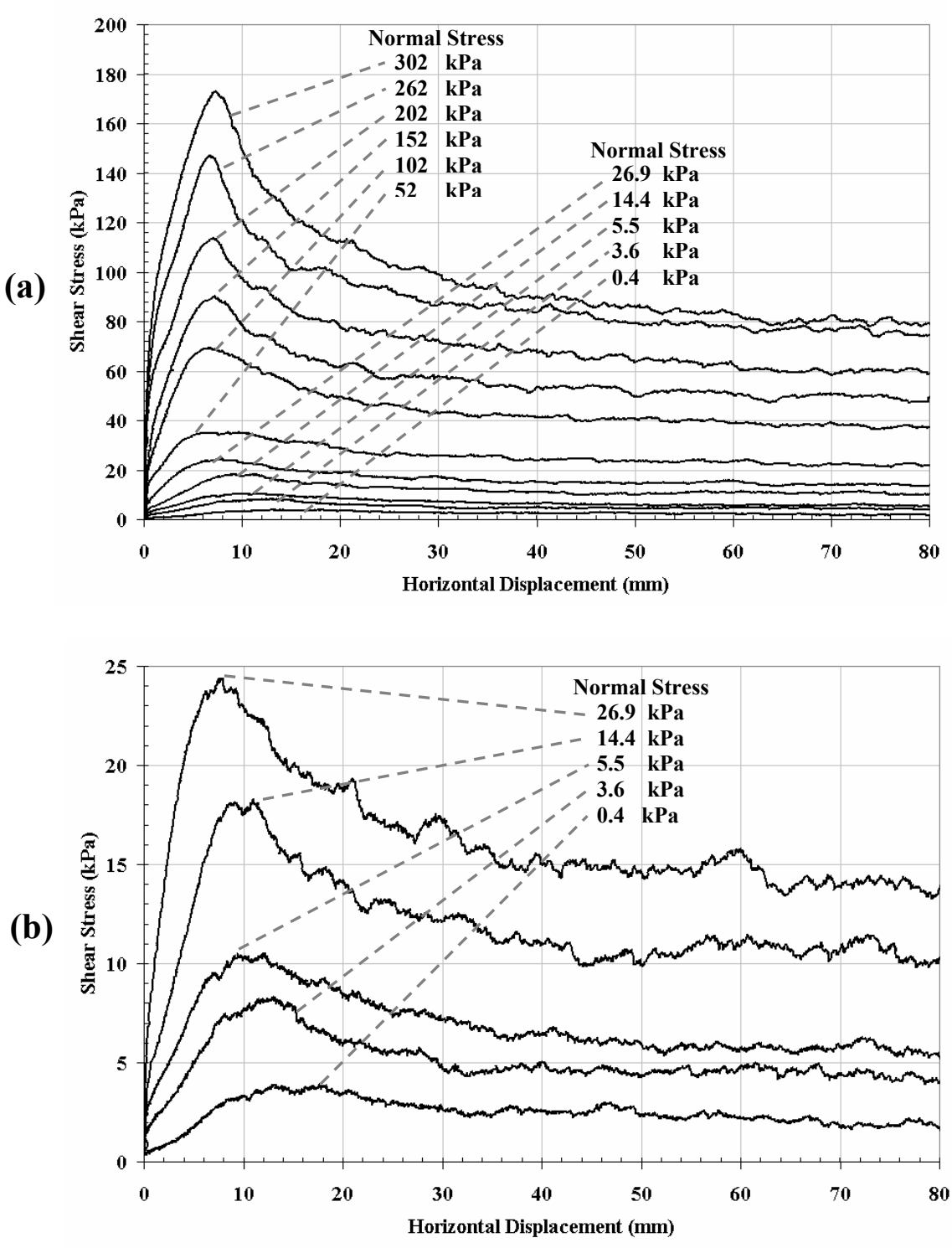

Figure 4-8. Direct Interface Shear Results of a Coextruded HDPE Geomembrane with a Thickness of 1.5 mm Sheared Against Needle-Punched Nonwoven Geotextile Specimens Having a Mass Per Unit Area of 203 g/m^2: (a) All Tests (Normal Stresses from 0.4 – 302 kPa), (b) Exploded View of Low Normal Stress Tests (0.4 – 26.9 kPa).

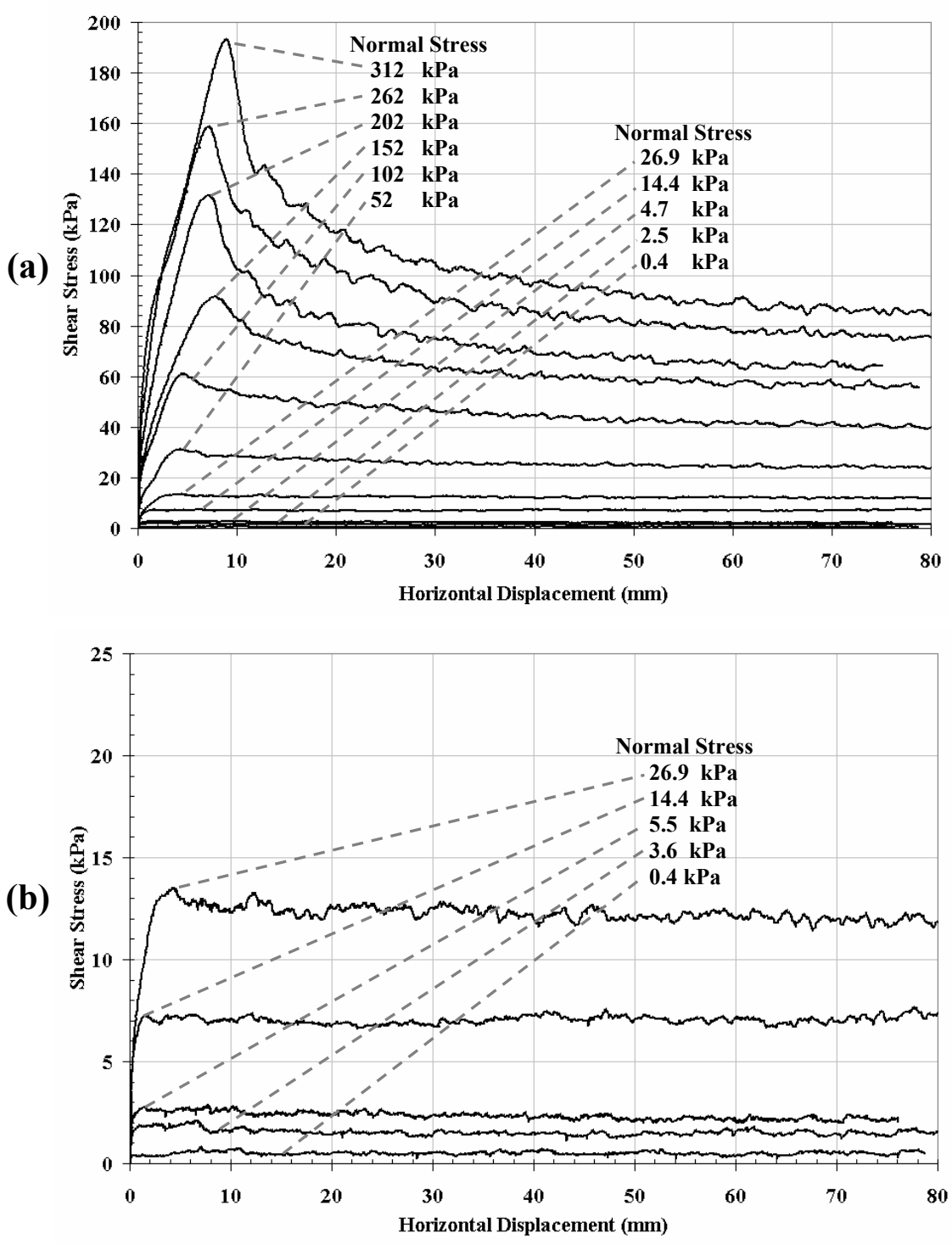

Figure 4-9. Direct Interface Shear Results of a Structured HDPE Geomembrane with a Thickness of 1.5 mm Sheared Against Needle-Punched Nonwoven Geotextile Specimens Having a Mass Per Unit Area of 203 g/m^2: (a) All Tests (Normal Stresses from 0.4 – 312 kPa), (b) Exploded View of Low Normal Stress Tests (0.4 – 26.9 kPa).

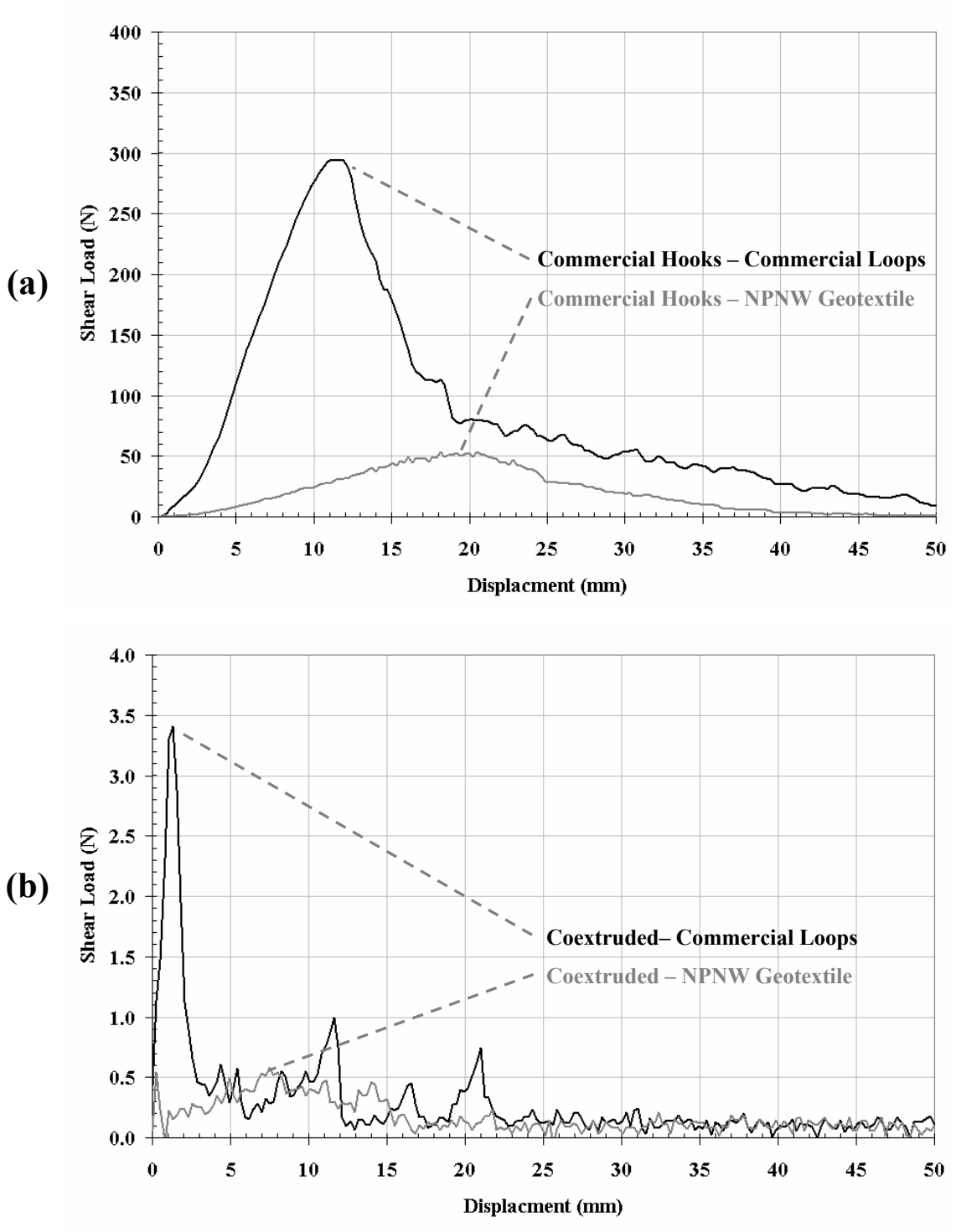

Figure 4-10. Typical Virgin ASTM Standard Hook and Loop Shear Strength Test Results: (a) Combinations Exhibiting Large Hook and Loop Interaction, (b) Combinations Exhibiting Minimal but Measurable Hook and Loop Interaction.

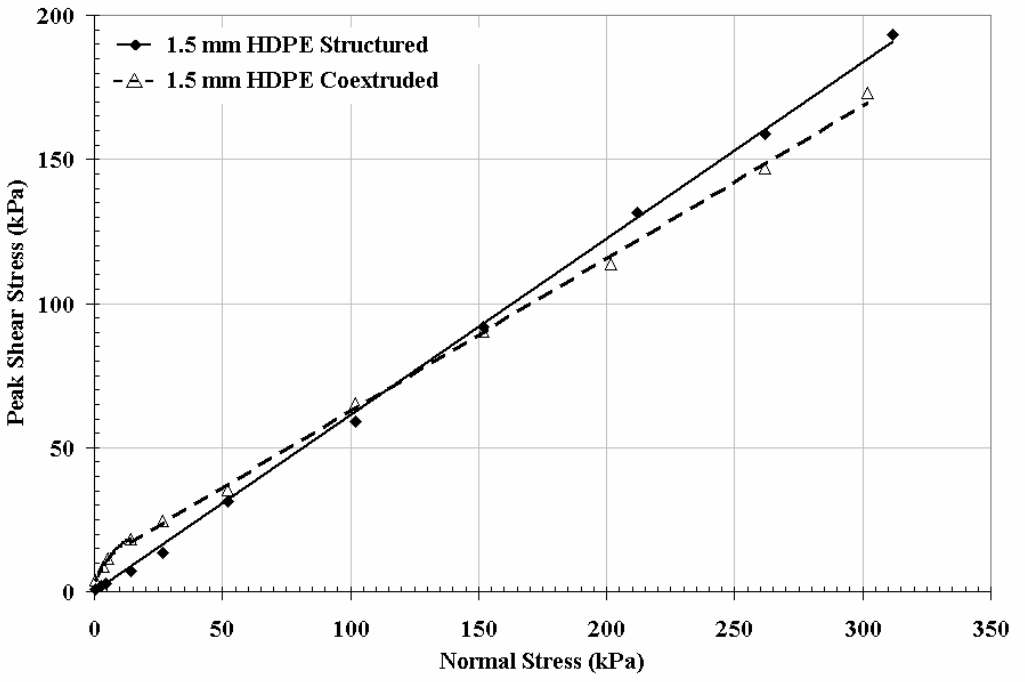

Figure 4-11. Values of Peak Interface Stress as a Function of Normal Stress for the Tested Coextruded and Structured Geomembranes with a Thickness of 1.5 mm in Contact with a Needle-Punched Nonwoven Geotextile Having a Mass Per Unit Area of 203 g/m^2.

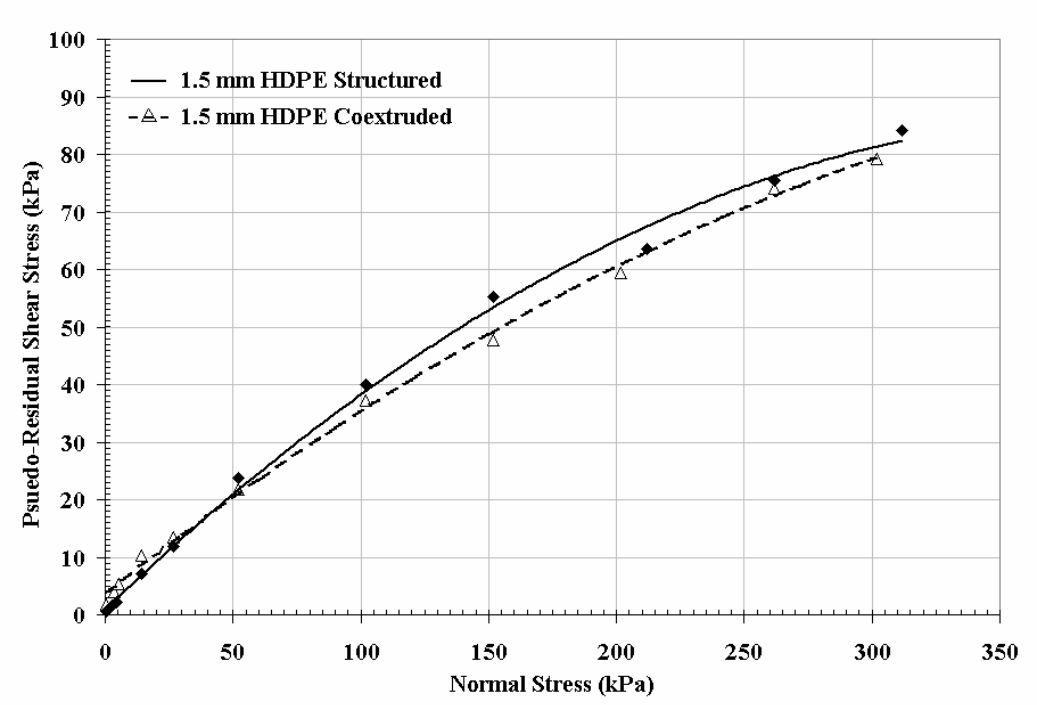

Figure 4-12. Values of Pseudo-Residual Interface Stress, Taken at 80 mm of Displacement, as a Function of Normal Stress for the Tested Coextruded and Structured Geomembranes with a Thickness of 1.5 mm in Contact with a Needle-Punched Nonwoven Geotextile Having a Mass Per Unit Area of 203 g/m^2.

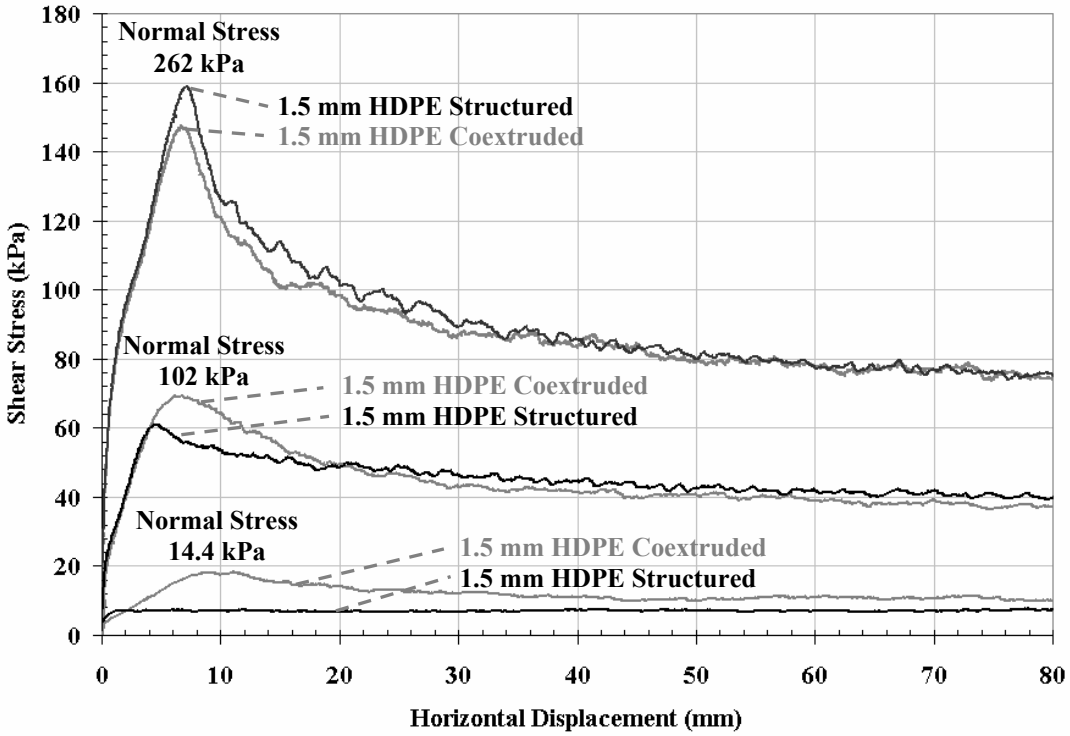

Figure 4-13. Progression of interface shear behavior with increasing normal stress for the tested coextruded and structured geomembranes with a Thickness of 1.5 mm in Contact with a Needle-Punched Nonwoven Geotextile Having a Mass Per Unit Area of 203 g/m^2.

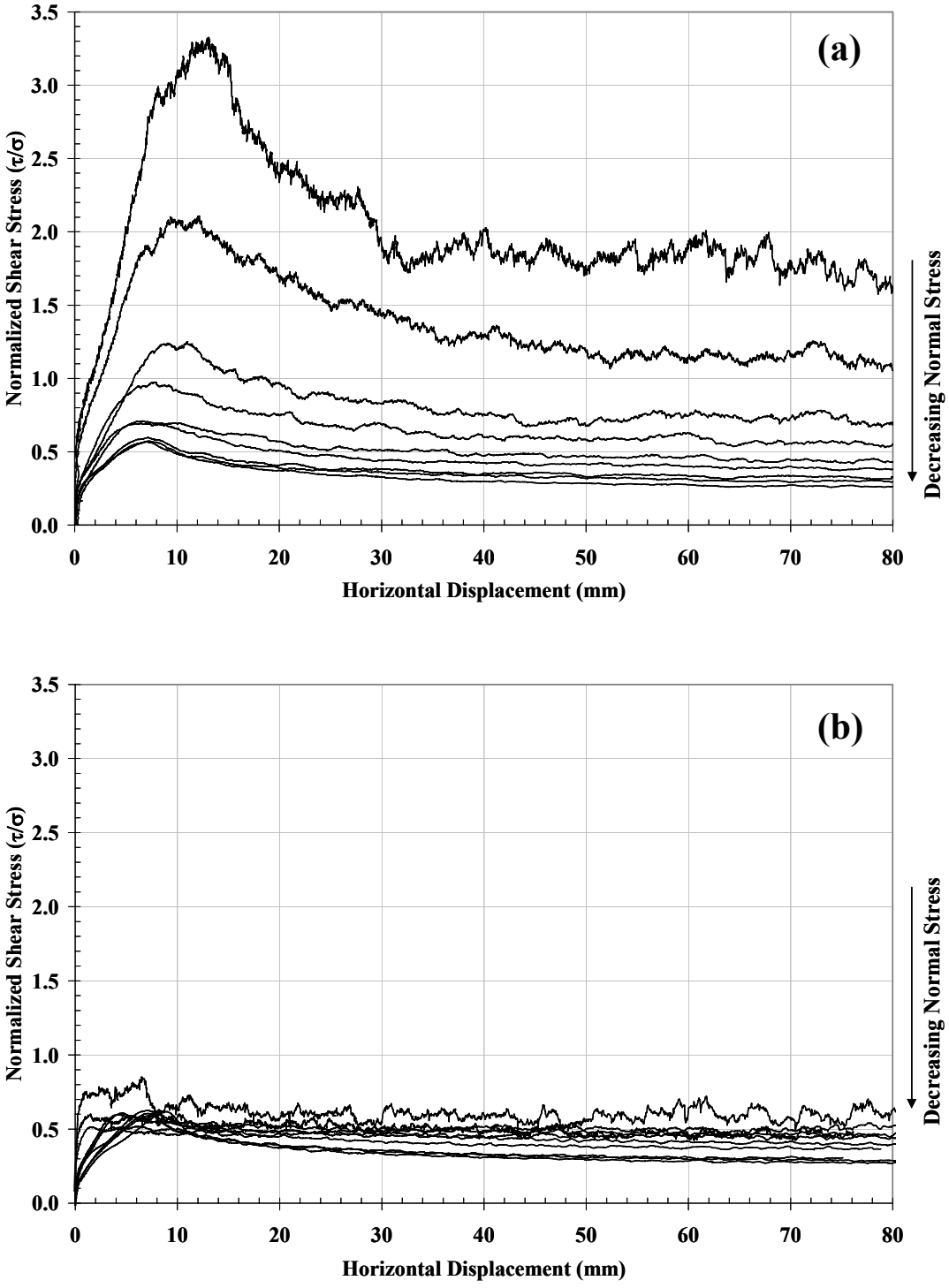

Figure 4-14. Normalized Shear Behavior (τ/σ) Versus Horizontal Displacement, Excluding the Behavior at σ_n = 0.4 kPa, of an HDPE Geomembrane, (a) Coextruded and (b) Structured, with a Thickness of 1.5 mm in Contact with a Needle-Punched Nonwoven Geotextile Having a Mass Per Unit Area of 203 g/m^2.

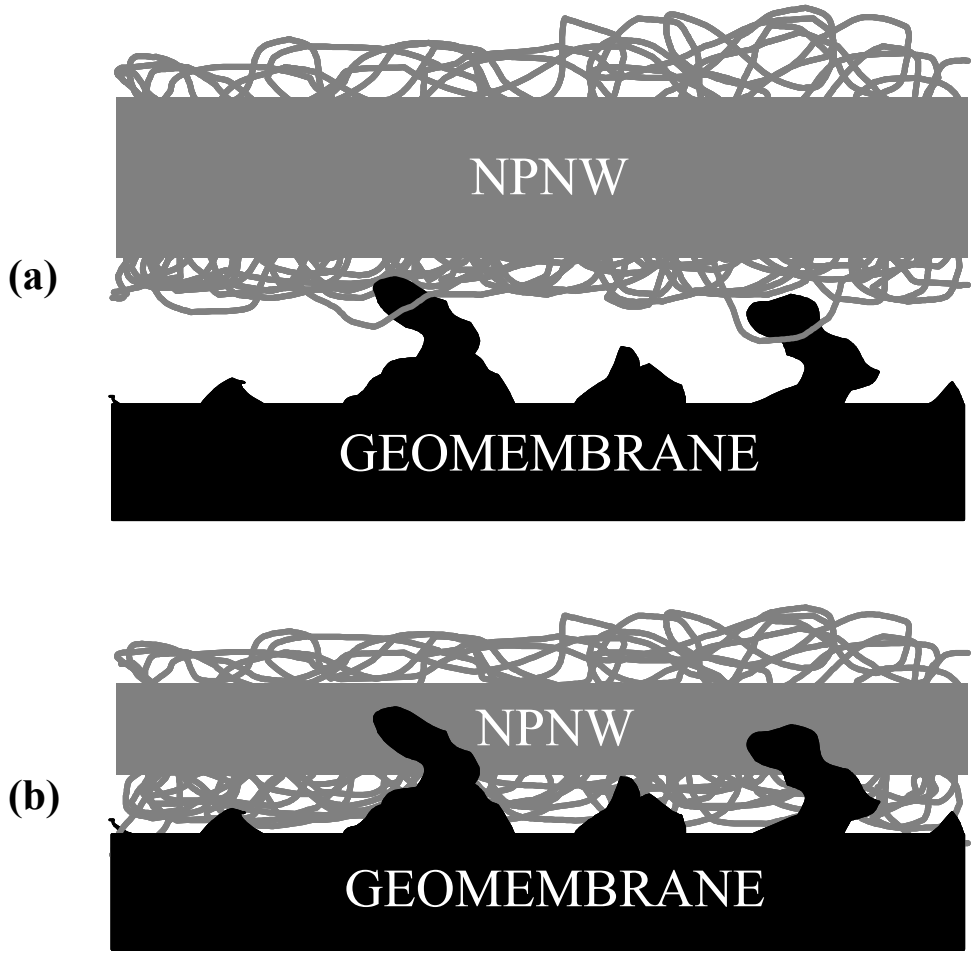

Figure 4-15. Sketch of Interaction Mechanisms Between NPNW Geotextiles and Textured Geomembranes at Different Normal Stresses: (a) Low Normal Stress and (b) High Normal Stress.

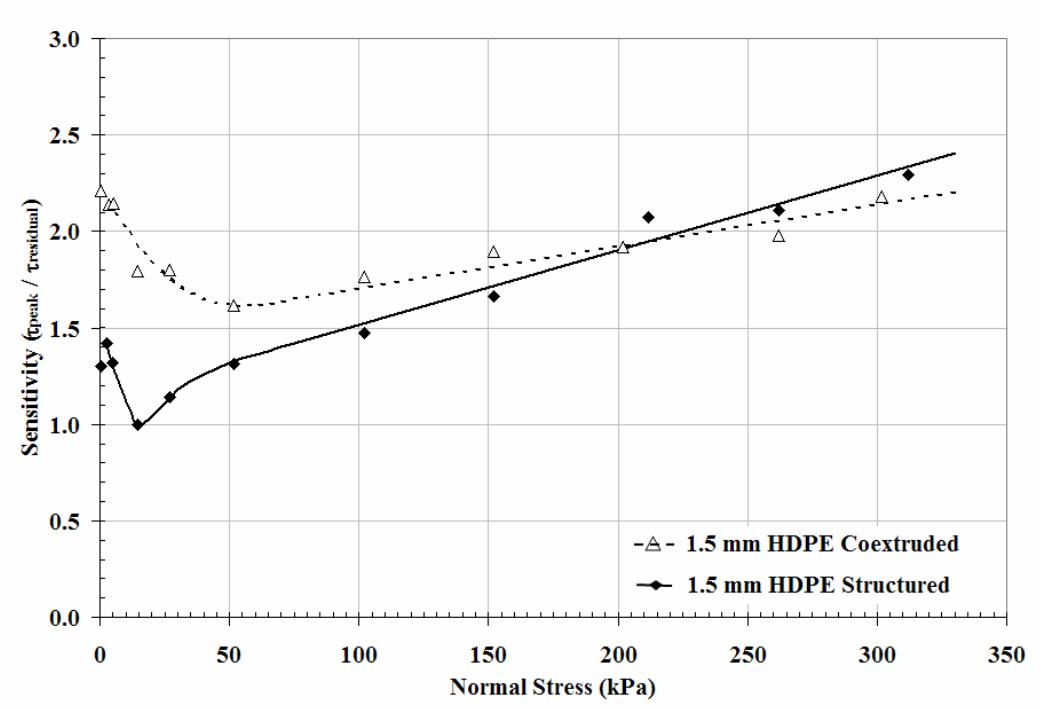

Figure 4-16. Sensitivity (τ_{peak} / $\tau_{residual}$) Versus Normal Stress for the Tested Coextruded and Structured Geomembranes with a Thickness of 1.5 mm in Contact with a Needle-Punched Nonwoven Geotextile Having a Mass Per Unit Area of 203 g/m^2.

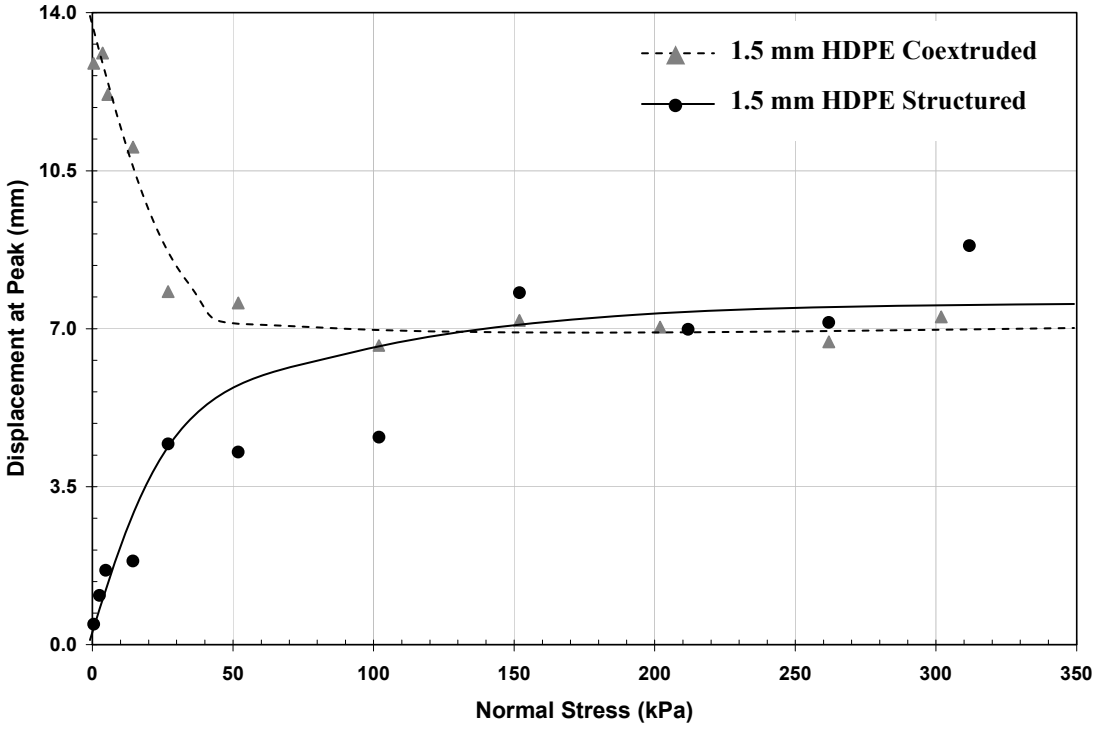

Figure 4-17. Values of Shear Displacement at Peak Across the Range of Applied Normal Stresses for the Tested Coextruded and Structured Geomembranes with a Thickness of 1.5 mm in Contact with a Needle-Punched Nonwoven Geotextile Having a Mass Per Unit Area of 203 g/m^2.

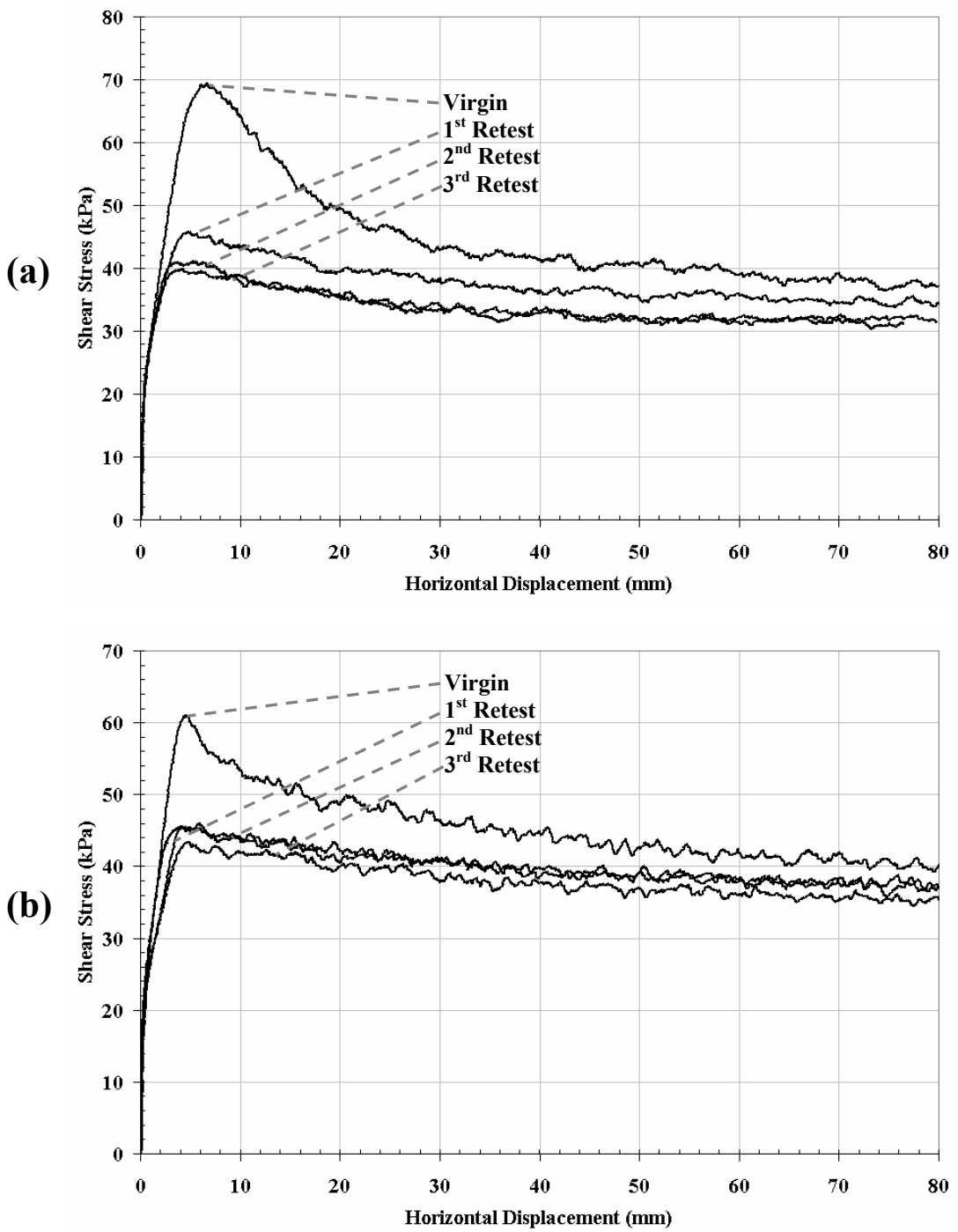

Figure 4-18. Direct Interface Shear Repeat Test Results of an HDPE geomembrane, (a) Coextruded and (b) Structured, with a Thickness of 1.5 mm Sheared Against Virgin Needle-Punched Nonwoven Geotextile Specimens Having a Mass Per Unit Area of 203 g/m^2 at a Normal Stress Level of 102 kPa.

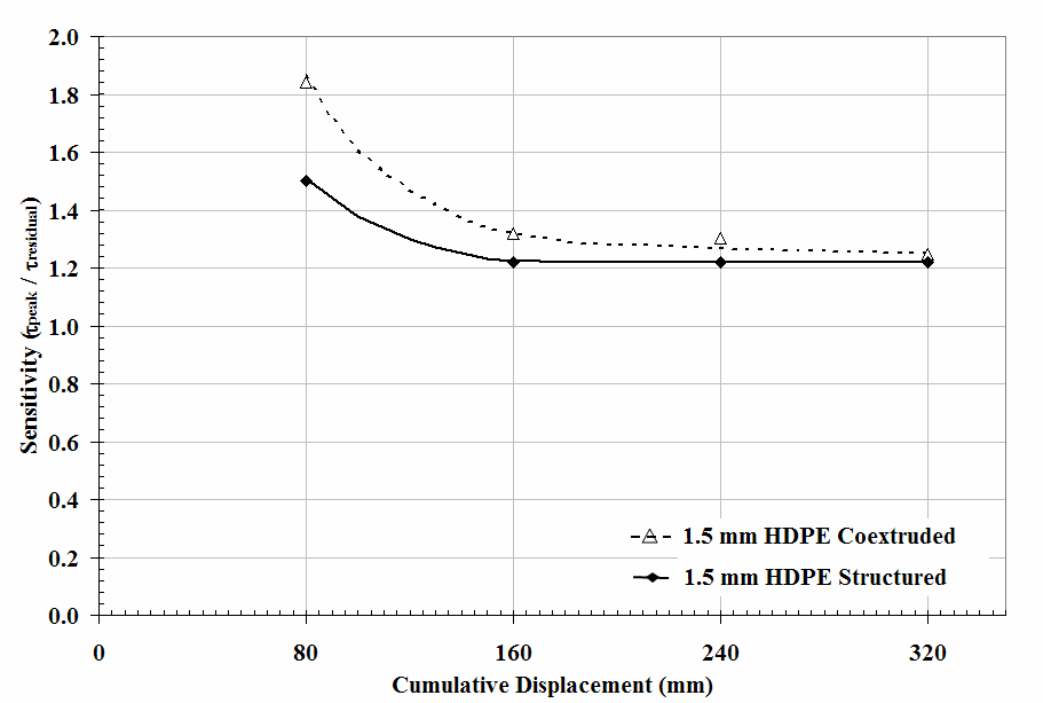

Figure 4-19. Sensitivity (τ_{peak} / $\tau_{residual}$) Versus Cumulative Displacement at 102 kPa Normal Stress for the Tested Coextruded and Structured Geomembranes with a Thickness of 1.5 mm in Contact with a Needle-Punched Nonwoven Geotextile Having a Mass Per Unit Area of 203 g/m^2.

Chapter V
Development of a Multi Piezo Friction Attachment for the Cone Penetrometer

5.1 Introduction

Chapters 2 through 4 have detailed aspects of the importance of interface response on the behavior of geotechnical structures and test devices. A number of the underlying fundamental concepts controlling geotechnical interface behavior were detailed. While the state of knowledge concerning the behavior of interfaces has evolved steadily in the past decades, the application of these underlying principles to improve typical design procedures and testing configurations has been limited. Traditional design principles based on applying empirical adjustment factors to soil properties to estimate interface behavior have been slow to change. A predominant factor in this hesitancy may be the high cost involved in obtaining samples for laboratory interface testing, coupled with the relative lack of confidence in the predominant in situ measure of interface friction, the friction sleeve measurement (f_s) of the cone penetration test (CPT). As a result of the shortage of direct means to infer interface strength for geotechnical problems, a group at the Georgia Institute of Technology has sought to develop a series of new devices to test interface strength in situ over a range of counterface properties. This chapter further details the motivation towards developing these devices and summarizes the design considerations and performance of the new and previously developed (DeJong, 2001), in situ test devices.

5.2 Assessment of the Conventional CPT Device and Sensors

5.2.1. A Brief History of Cone Penetrometers in Geotechnics

5.2.1.1 Introduction

As with any subsurface geotechnical investigation the main objective is to determine the following (after Lunne et al., 1997):

- Nature and sequence of the subsurface strata (geologic regime)
- Groundwater conditions (hydrogeologic regime)
- Physical and mechanical properties of the subsurface strata
- Distribution, composition, and level of contaminants (*if applicable)

Throughout the development of the cone penetration test (CPT) there have been many changes and modifications made to the initial device aimed at better achieving the above objectives. The very first cone devices were completely mechanical and differ greatly from modern penetrometers commonly used in geotechnical engineering.

5.2.1.2 Early Mechanical Penetrometers

The first modern cone penetrometer, known as the Dutch cone penetrometer, was used by P. Barensten, an engineer at the Rijkwaterstaat (Department of Public Works) in Holland in 1932. The first cone consisted of an outer pipe fit over an inner rod with a tip (Sanglerat, 1972), and had a maximum investigation depth on the order of 10 m. Investigations were performed manually and proceeded by pushing both the inner and outer rod together, followed by pushing the inner rod to its full extension, pushing the

outer casing to rejoin the inner cone at its present depth, and then repeating the process to the desired depth or to refusal. Vermeiden (1948) and Plantema (1948) improved the original Dutch cone design by modifying the inner rod to a conical shape to prevent soil from entering the gap between the casing and rods. A more significant advancement was introduced by Begemann (1953, 1969), who added an "adhesion jacket" behind the cone tip. This was the first device to independently measure the skin friction, and Begemann (1965) was the first to introduce the concept of using the friction ratio (sleeve friction / tip resistance) to classify soil type. Several other mechanical cones of similar type were developed in other countries including: Belgium, France, Germany, Russia, and Sweden as outlined by Sanglerat (1972) and Broms and Flodin (1988).

5.2.1.3 The Electronic Cone Penetrometer

The next major advance in cone penetrometers was the development of the electronic cone penetrometer. The main improvements provided by the electronic cone were summarized by Muhs (1978):

- The elimination of erroneous interpretation as a result of unknown internal friction between the inner rods and outer tubes.
- The ability to conduct continuous soundings with constant rates of penetration.
- The electrical cone was more reliable and simpler to operate and record data.

Electric cones were first developed in Holland by a municipal engineer named Bakker, and further developed at the Delft Soil Mechanics Laboratory (DSML) were the first cone with the capability to independently measure the side friction was developed in

1957 (Vlasblom, 1985). In 1965, Fugro developed an electric cone in co-operation with the Dutch State Research Institute (de Ruiter, 1971). The Fugro cone introduced the inclusion of electrical inclinometers to monitor the verticality of the probe during penetration and served as the basis for the first cone standardization provided in the International Reference Test Procedure (ISSMFE, 1977, 1989).

5.2.1.4 Piezocones

The next advancement in penetrometer technology was the ability to continuously monitor pore fluid pressures during penetration. The first published accounts of piezo probes were given at the first European Conference on Penetration Testing (ESOPT-1) by Janbu and Senneset (1974) of the Norwegian Geotechnical Institute (NGI) and Schmertmann (1974) who pushed conventional electrical piezometers in the ground to survey pore pressure response. Both Torstensson (1975) in Sweden and Wissa et al. (1975) in the US developed electronic piezo probes with the specific purpose of monitoring pore water pressures during penetration. The first instance of simultaneous pore fluid pressure and cone resistance was presented by Roy et al. (1980), with a number of other researchers presenting probes capable of measuring pore pressure in combination with both cone tip resistance and sleeve friction at the special session concerning Cone Penetration Testing and Experience at the ASCE national convention held in St. Louis, MO in 1981 (de Ruiter, 1981; Muromachi, 1981; Baligh et al., 1981; Jones et al., 1981; Tumay et al., 1981; Campanella and Robertson, 1981).

These early piezocones included pore pressure sensors in a number of locations. Current commercial penetrometers use piezo elements that are typically designated with a numerical progression of subscripts, and are designated as follows: elements directly on

or protruding from the cone tip (u_t), tip midface (u_1), elements located directly behind the tip (u_2) or (u_{bt}) "shoulder" elements, and elements located directly behind the friction sleeve are designated (u_3) elements. The u_2 element position is the typical element location due to the need for pore water correction to the cone tip resistance $q_c \rightarrow q_t$. Typical piezocones only have a single pore pressure sensor, however, multi element sensors are sometimes used in research applications and offshore (Sills et al., 1988; Bayne and Tjelta, 1987). A tri-element piezocone with elements at all three conventional positions is shown in Figure 5-1, with measured pore pressures typically following a $u_1 > u_2 > u_3$ relationship. A large number of additional sensors and capabilities have been added to conventional penetrometers in the past decades, including the ability to measure shear wave velocity, monitor contaminant levels, electrical resistivity, lateral stress, heat flow, and many other soil properties. A thorough detailing of these sensors and devices is given by Lunne et al., (1997).

5.2.2 Factors Affecting CPT Tip Response

The tip resistance measured in a cone penetration test is the most common and frequently used measurement obtained during CPT soundings. This measurement can be affected by a number of factors, most notably the unequal area effect which influences the total measured stress of all tip geometries. The unequal area effect results from pressure imparted on the inner geometry of the tip by the ambient pore water pressure. The unequal area is quantified by the cone area ratio, a, which is represented by the ratio of the cross-sectional area of the load cell shaft divided by the cross-sectional area of the projected cone area. All CPT tip resistances should be corrected to account for this affect, and can be corrected using the following relationship:

$$q_t = q_c + u_2(1 - a) \quad \text{(Eq. 5-1)}$$

where q_t is the corrected cone tip resistance, q_c is the measured cone tip resistance, u_2 is the pore pressure acting directly behind the cone tip, and a is the cone area ratio. The area correction is especially important in soft soils having high pore pressures during penetration, e.g. soft clays. Enlarged tip geometries (e.g. Ball, T-bar, and Plate shown in Figure 5-2) have recently been introduced for testing in soft soils (typically offshore) to provide better load cell resolution. These large tip geometries, known as full flow probes, have a secondary benefit of not being significantly affected by the net area correction as the correction is further multiplied by the ratio of the shaft area to the projected sensor area, usually on the order of 0.1 to 0.2 (Chung and Randolph, 2004).

Other factors shown to affect the measured tip resistance, include: tip wear, cone apex angle, and rate of penetration, amongst others. Lunne et al. (1997) report that significant tip wear can result in measurement errors on the order of 5%. Conventional CPT tips are standardized at an apex angle of 60°. Durgunoglu and Mitchell (1975) showed that variations in the cone apex angle cause significant changes in measured tip resistance. Penetration rate has also been thoroughly investigated, and its effect on tip resistance has been recently summarized by Randolph and Hope (2004). They note that in low permeability soils, as the rate of cone penetration is reduced, the cone penetration resistance first decreases due to reduced viscous effects, and then increases as partial consolidation occurs ahead of the advancing cone. The transition point is theoretically linked to the non-dimensional penetration rate, vd/c_v, where v is velocity, d the cone diameter, and c_v a measure of the consolidation coefficient for the soil. The effect of penetration rate on tip stress has been shown to be of limited significance for higher

permeability soils such as sands, with Lunne et al. (1997) providing a detailed review of studies investigating the effects of varying the penetration rate on cone penetration response.

5.2.3 Factors Affecting CPT Pore Pressure Response

The pore pressure sensor(s) of cone penetrometers has received by far the most attention of the three main sensor types in both the research and practicing communities. The primary issue with all piezo elements at any location is the rigidity of the pore pressure measuring system and the saturation of that system. All piezo elements need to be fully saturated throughout testing so that the sensors respond rapidly to changes in pore pressure conditions, with Lunne et al. (1997) providing a detailed discussion regarding the importance of saturation and the various saturation procedures used in practice. The rigidity of the pore pressure filter and overall system control the available resolution and response of the measurement to changes in pore pressure conditions. Bruzzi and Battaglio (1987) have observed the level of axial load applied on the tip to cause deformation in certain pore pressure measurement systems. The resultant deformation can subsequently influence the measured pore pressure response as a function of piezo filter element and overall system stiffness.

As briefly indicated earlier, a number of reports have indicated a change in pore pressure response as a function of soil type and element location (Robertson et al., 1986). As a general rule the highest pore pressures are located in the zone directly beneath the cone tip where compressive stresses are maximum. The cylindrical shoulder and shaft along the rods is typically an area of normal stress relief, where the shear stresses induced in the soil dominate the behavior. As a result, an increase in normal stress typically

results in positive pore pressures, whereas an increase in shear stress can result in either positive or negative changes in pore pressure depending on the dilatancy of the soil layer. As such, u_t and u_1 pore pressures are always positive as their response is dominated by the large positive normal stresses present near the tip. The u_2 and other shaft elements are influenced by both the normal and shear stress regime, and have been reported to measure low or even negative pore pressure response in highly dilative soils such as dense silts and sands, and heavily overconsolidated clays. An example of the difference in pore pressure response as a function of element position is noted from the results of a multi element sounding in the heavily over consolidated Gault clay, Figure 5-3 (Lunne et al., 1997).

The u_2 position is seen as the preferred filter location, with the advantages of the u_2 position summarized by Lunne et al. (1997) as follows:

- Measured u_2 pore pressures can be used to directly correct the measured tip resistance.
- Filters at the shoulder position and further up the shaft are much less prone to damage and wear.
- u_2 pore pressure measurements are less influenced by element compressibility as compared to tip and face elements.
- Dissipation results from u_2 sensors are less influenced by procedures (i.e. locking rods or releasing load.)

If only one piezo element is used on a CPT device, the u_2 position is recommended for most applications. However, tip and face elements typically provide more detailed layer profiling capabilities, while u_3 elements are needed to adequately correct the friction sleeve measurement for net area effects, and multiple elements if available can provide additional information, including advantages in determining the groundwater conditions, *OCR*, and K_0.

5.2.4 Factors Affecting Friction Sleeve Response

5.2.4.1 Introduction

As highlighted in earlier discussions, the conventional friction sleeve measurement of the CPT device (f_s) has been shown to be less consistent and repeatable as compared to tip resistance and pore pressure responses (Lunne et al., 1986; Tanaka, 1995). Tanaka conducted a series of soundings in close lateral proximity at a uniform clay site with eight different conventional CPT device configurations. The sensor responses of the q_t, u_2, and f_s sensors from these eight soundings are shown in Figure 5-4, and clearly highlight the increased variability of the f_s measurement as a function of friction sleeve design and condition. Due to the long standing notion that the f_s measurement is more variable than the other CPT measures, a number of research studies have been undertaken to investigate the factors affecting f_s response.

5.2.4.2 Load Cell Configuration

A long standing debate in the CPT community centers around the use of a subtraction type load cell design in which the f_s measurement is calculated from the difference between the tip and combined tip and sleeve resistance, versus the use of

isolated load cells to measure each sensor independently. Subtraction type load cells were the original configuration of most CPT systems and are still popular due to the ease of design and manufacturing. However, advances in technology have enabled newer penetrometer designs to easily implement independent load cells for each sensor. A main disadvantage of the subtraction configuration is the requirement to size the load cells based on the maximum combined response which increases the full scale capacity, and subsequently decreases the resolution of the individual sensors. Tanaka (1995) found the f_s measurement at a soft clay site to range from 1/50 to 1/330 of the full scale capacity of a variety of subtraction type CPT systems. Additionally, ASTM D5778 (1995) reports that the standard deviation of f_s measurements for individual load cell designs is only 5% as compared to 15% for subtraction type designs.

5.2.4.3 Wear

Predominant factors in the response of CPT friction sleeves are the wear and subsequent changes in diameter and surface roughness that occur due to wear. Zuidberg et al. (1982) monitored both the sleeve and tip wear of a CPT unit over 1500 m of penetration. They found that sleeve diameter did not wear uniformly along the length of the sleeve, as shown in Figure 5-5. A subsequent study by Jekel (1988) continued the investigation of wear on f_s measurements, and observed the f_s measurement to decrease by up to 50% as a function of wear. Jekel additionally noted that CPT friction sleeves located in the conventional location directly behind the tip experienced uneven wear concentrated towards the trailing edge of the sleeve, as shown in Figure 5-6. DeJong (2001) noted the pronounced affect that variations in friction sleeve diameter compared to the other component CPT parts can have on the f_s measurement. This effect is most

prominent if the diameter of the friction sleeve is greater than that of the lower cross sections, e.g. in the case where a new friction sleeve is used in combination with a slightly worn tip. Jekel (1988) noted that surface roughness changed continuously as a function of wear and only reached a constant value for continuous penetration at the same uniform site. As most CPT equipment is only used at each site for a short time, the exposure to varying types of subsurface stratigraphy can result in constant variations in friction sleeve surface roughness. A number of practitioners and manufacturers have effectively applied hardening processes or hard surface coatings to diminish the wear of various CPT components.

5.2.4.4 Counterface Roughness

As discussed previously in Chapters 1 through 4, surface roughness plays a dominant role in controlling the response of soil-continuum interfaces. National (ASTM D5778, 1995) and international (ISSMFE, 1999) CPT standards specify friction sleeves to have roughness values equal to R_a = 0.50 μm $\pm$ 0.25 μm. A study by DeJong et al. (2001) reported that many new sleeves, as provided direct from manufacturers, already fall outside the standardized roughness specifications with a range of tested R_a values from 0.28 to 2.08 μm. Additionally in a study documenting the roughness of used friction sleeves, DeJong et al. (2001) found sleeve roughness to range over R_a values of 0.18 to 6.85 μm. While some of this wide range may be attributed to improper monitoring of sleeve wear, it is noted that sleeve wear occurs actively during penetration and the roughness can be considered to be changing continuously with depth, causing the test conditions to change and possibly become outside of the specification standard during penetration within a given sounding. As shown in Figure 3-1, changes in surface

roughness on the order of the variations observed by DeJong et al. (2001), can significantly affect friction sleeve response, as interface response is very sensitive to counterface roughness.

5.2.4.5 Sleeve Position

As discussed during the presentation of factors affecting the pore pressure response of CPT measurements, the sensor location has also been shown to have an effect on friction sleeve response. Huntsman et al. (1986) hypothesized that variations in f_s as a function of position were primarily due to variations in the local horizontal stress acting along the CPT shaft, which can be separated into two components: the initial "baseline" in situ lateral stress, and the change in lateral stress caused by CPT penetration. As shown by a number of researchers using various analytical and laboratory methods, there exists a zone directly surrounding and behind the tip that displays a complex and varied stress state. A number of researchers have directly monitored the variation in friction sleeve response as a function of sleeve position (Campanella and Robertson, 1981; Konrad, 1987; Parez, 1987; DeJong, 2001).

Campanella and Robertson (1981) found that friction sleeve measurements increased as a function of distance behind the tip for medium to dense sands, reaching a maximum for sleeve positions centered approximately 20 cm behind the tip. For sleeve positions farther up the shaft, sleeve friction was shown to reduce until approximately 35 cm behind the tip at which point f_s remained stable with increased distance from the tip. Campanella and Robertson (1981) also found that the effect of sleeve position on f_s values increased with increasing soil density. A detailed study investigating the effect of sleeve position on friction sleeve response was conducted by DeJong (2001), with the

variation in friction sleeve response as a function of sleeve position found to be less pronounced than the results of Campanella and Robertson (1981). The results of DeJong still demonstrate a variable influence zone around the tip, however, the measured zone was restricted to sensors centered at offsets less than 15 cm behind the tip, with f_s approximately stable for increased tip offsets in the loose to medium sand deposit tested. The current study included supplement investigations into the effect of sleeve position on smooth and textured sleeve response, with the results presented in detail in Section 6.3. Although the variability of the stress conditions directly behind the tip has been noted by many researchers, most CPT systems are still configured with the friction sleeve directly behind the tip sensor as per national standards (ASTM D5778, 1995). A notable exception to this is the Laval piezocone (Virely et al., 1995), which is configured with the friction sleeve sensor 5 diameters behind the tip.

5.2.4.6 Sleeve Length

The conventional friction sleeve length was originally designed to result in approximate load equality between the tip and sleeve sensors such that the use of a subtraction type load cell configuration could be optimized. After the introduction of independent load cells, the traditional friction sleeve area was maintained at 15,000 mm^2 and results in conventional friction sleeve lengths of 133.7 and 109.3 mm for 10 and 15 cm^2 penetrometer geometries respectively. In practice other length penetrometer sleeves are used, typically ranging from 94.6 to 189.2 mm, with areas between 20,000 and 30,000 mm^2 typical for 15 cm^2 devices (Lunne et al., 1997). The f_s measurement is comprised of the average response over the full sleeve length. With the conventional location of CPT friction sleeves within a zone of highly variable stress state, and variations in soil

properties existing at scales smaller than the typical sleeve length, it follows that sleeve length will have a direct impact on f_s response. Further, the high sleeve length to measurement increment ratio results in filtering and smoothing of friction data, thereby causing the variability in measured interface friction to be underestimated (Saussus et al., 2005; Frost et al., 2005). They conducted analytical investigations regarding the effect of sleeve length on soil classification and interface detection, as shown in Figures 5-7 and 5-8. With advances in electronics and sensor technology, friction sleeves are no longer confined to conventional lengths and future designs may incorporate friction sleeves of shorter length.

5.2.4.7 Secondary Factors

In addition to the above prominent factors affecting friction sleeve measurements there are a number of other secondary factors that can affect f_s measurements. Most prominent among these is the CPT module stiffness, as reported by Voung et al. (1988) based on a series of calibration chamber tests. It was found that bending of the probe during penetration could impart artificial stresses onto the friction sleeve measurement and cause a change in the expected reading. As a result, CPT designs of higher stiffness are desirable to not only limit the effects of bending on the sensor measurements, but also to prevent damage to the CPT unit during penetration. In addition to bending, variations in temperature, inclination, calibration accuracy, and other common sensor considerations are important to achieve robust sensor and composite CPT design. Most of these secondary factors can be accounted for through the use of self compensating full bridge strain gauge configurations and through diligent equipment upkeep.

5.3 Review of the Multi Friction Sleeve Attachment (MFA)

5.3.1 Motivation for Development

The local response at interfaces often controls the global behavior of many geotechnical structures, including: deep foundations, tunnels, underground conduits, retaining structures, and landfill liners. The range of responses includes surfaces meant to fully engagement the internal strength of the contacting soil to surfaces designed and lubricated to minimize soil-structure interaction such as the outer surfaces of jacked pipes and tunnels. Additionally, numerous material types are used across the range of construction requirements and often change based on design and locally available materials. As such, it is known that any tool aimed at directly measuring in situ interface interaction has to be flexible enough to accommodate the wide range of counterface properties typically used in geotechnical construction. Additionally, as the geotechnical and other engineering communities are often slow in adapting new technologies, it is often desirable to incorporate new measurement systems into a device already accepted and used in common engineering practice, e.g. the addition of shear wave velocity (V_S) measurements to the CPT and Flat Plate Dilatometer (DMT). To this end, a family of devices have been developed to provide tools capable of directly measuring interface response over a range of counterface properties, and are compatible for simultaneous use behind a conventional 15 cm^2 CPT unit. The piggy-backing of devices allows for the continued implementation of the large range of design and classification methods currently based on CPT measurements, while additionally providing the ability to directly measure in situ interface strength.

5.3.2 Overview of MFA Specifications

The multi friction sleeve attachment, developed by Frost and DeJong (Frost and DeJong, 2001; Frost and DeJong, 2005; DeJong and Frost 2002), was designed to allow for the direct in situ assessment of soil-continuum interface behavior over a range of surface characteristics simultaneously within a single sounding. The direct measurement of interface behavior in situ is achieved through the use of four independent friction sleeves, connected in series along a cylindrical housing equal in diameter to the conventional 15 cm^2 CPT device. Each of the factors discussed in Section 5.2.4 concerning the response of CPT friction sleeves were considered in the design and development of the MFA unit. The MFA was designed to be compliant for use directly behind a conventional 15 cm^2 CPTU module, allowing for the collection of conventional CPTU measurements (q_t, f_s, and u_2) during MFA soundings. The use of a 15 cm^2 geometry, as opposed to the more conventional 10 cm^2 geometry, was chosen to provide addition internal passthrough space to accommodate the large amount of wiring required in the MFA device. Lunne et al. (1997) report that the response of corrected parameters from cone penetrometers ranging from 5 to 15 cm^2 all provide nearly equivalent response. An overview of the MFA is provided in Figure 5-9, with a detailed schematic and photograph of the independent friction sleeve mandrels used in the MFA shown in Figure 5-10. Figure 5-11 displays the data acquisition (DA) architecture used in the combined CPT – MFA configuration. Additionally, the MFA unit can also be utilized with a series of uninstrumented "dummy" tips that allow the unit to investigate the effects of sleeve location with respect to the tip on interface behavior, Figure 5-12. The MFA device is manufactured by the Vertek Division of Applied Research Associates. More detailed

descriptions of the original MFA are provided by DeJong (2001) and DeJong and Frost (2002).

5.4 Friction Sleeve Texturing

As discussed previously conventional CPT friction sleeves conforming to ASTM D-5578 (1995) and ISSMFE (1989) standards, have specified surface properties of R_a equal to 0.50 ± 0.25 μm. The hardness of conventional friction sleeves is not specified by the governing standards, however most friction sleeves are designed to minimize wear through hardening processes or the application of hard surface coatings. The surface roughness of conventional friction sleeves is much lower than that of typical geomaterials used in foundation and construction practice. Figure 2-4 detailed the roughness characteristics of some common construction materials in comparison with both conventional and textured friction sleeves.

A primary consideration in the design of the MFA was the development of a feasible texturing scheme that could be incorporated onto friction sleeves. Sleeve texturing schemes were developed by considering the concepts of soil – continuum interaction garnered from previous fundamental laboratory studies, and analytical interaction models such as the centroid trace method (DeJong, 2001). Design considerations required that the textured sleeves induce internal shearing of the soil rather than only sliding along the surface, and that the texturing pattern should be easily machinable. Additionally, friction sleeve texture needs to be non-clogging so that the counterface properties do not change with depth as soil particles become interbedded into the surface texturing. As a result of the above considerations, sleeve texture consisting of peak features above a smooth base substrate equivalent to that of a conventional friction

sleeve were deemed ideal. After a progression of sleeve texturing schemes were tested in the lab and in situ (Cargill, 1999; DeJong, 2001) a standardized texturing scheme was developed. The resultant texturing scheme consists of offset diamond shaped textural asperities with variations in the height of the diamonds used to modify the magnitude of surface roughness. The final geometric configurations of the textured sleeves were developed after a detailed parametric assessment of diamond spacing, size, and shape was undertaken by DeJong (2001), with assistance from the author.

The developed texturing geometry is presented in Table 5-1 and Figures 5-13 and 5-14, showing the textured sleeve specifications, a sleeve schematic, and photographs capturing a range of sleeve textures, respectively. The design of the textured sleeves uses offset rows of diamond shaped features parallel to the sleeve axis. The optimum texture pattern determined through the parametric evaluation was found to consist of diamonds with a penetration angle of 60°, a diamond width of 5.3 mm, a diagonal spacing of 6.3 mm resulting in a passthrough of 15.7%, and a texture slope of 45° (DeJong, 2001). The standard textured friction sleeve design consists of 110 total diamond shaped textural asperities, oriented in 10 offset circumferential rows and 22 vertical columns oriented parallel to the penetration axis. The diamond shaped texturing is surrounded by sleeve areas with no textural features and surface characteristics equal to a conventional smooth CPT friction sleeve. The sections of smooth surface result in flow paths around or between each of the diamond asperities. This type of pattern was chosen to induce shearing within the soil by forcing particles to flow between, around, or over the diamond shaped asperities, and to prevent clogging of the textural features. As discussed in Chapter 3, the use of intermittent texturing provides non clogging surfaces that allow for

continuous in situ testing, but subsequently necessitate increased magnitudes of R_{max} roughness in order to engage equivalent levels of shearing achieved with continuously textured surfaces (e.g. those found in conventional laboratory testing and practical interface applications). For more information regarding the full progression of sleeve texture designs refer to Cargill (1999), DeJong et al. (2001), and DeJong and Frost (2002).

5.5 Typical Results from MFA Soundings

5.5.1 Introduction

After the initial development of the Multi Friction Attachment (MFA), it was used to conduct an initial set of in situ proof tests to evaluate the device performance. This series of proof tests consisted of 39 soundings at a relatively uniform glacial outwash site in central Vermont comprised mostly of loose to medium sand, (DeJong and Frost, 2002; Frost and DeJong, 2005). This initial test series was aimed at:

- Evaluating the overall MFA device operation and performance
- Determining the effect of attachment assembly / disassembly on performance
- Investigating the response of each sensor over a range of sleeve roughness configurations.
- Conducting a full parametric evaluation of the chosen textured geometry, varying the diamond height, spacing, attack angle, and width.
- Determining the effect of sleeve position behind the tip on the response of the friction sleeves, through the use of varying the tip configuration (CPT, short dummy, long dummy) as diagramed in Figure 5-12.

The findings of this work are summarized in detail by DeJong (2001) and Frost and DeJong (2005). The author participated in conducting the fieldwork and the data analysis for all soundings presented in the above works other than those conducted in July of 2000 , S1-S9. To provide the reader with a framework for discussing typical MFA results and the subsequent development of the Multi Piezo Friction Attachment (MPFA), this section presents the results from a selection of insightful MFA configurations. The results of the presented configurations are taken from a combination of the previous work by DeJong (2001) and soundings conducted for the current study. To allow for efficient discussion of various sleeve configurations, the following conventions will be followed: SM = smooth (equivalent surface properties to traditional CPT f_s), Hx.xx = a textured sleeve with an out of plane diamond height equal to x.xx mm, e.g. H0.25, H1.00, H2.00 represent diamond heights of 0.25, 1.00, and 2.00 mm, respectively. A detailed listing of all MFA and MPFA soundings conducted as part of the current study are included in Chapter 6 as Tables 6-1 and 6-2, with a detailed description of each test site provided in Table 6-3.

5.5.2 Results of Common Device Configurations

5.5.2.1 MFA Results for Configurations with All Smooth Sleeves

The most basic MFA configuration is one in which the four attachment mandrels are configured with smooth sleeves. Figure 5-15 shows the results of a CPTU-MFA sounding in which the MFA was configured with all smooth sleeves, denoted as: (SM - SM - SM - SM) corresponding to MFA mandrels (f_{a1} - f_{a2} - f_{a3} - f_{a4}), respectively. It can be clearly seen from Figure 5-15 that the response of smooth friction sleeves is very

stable within the zone tested by the MFA, i.e. 0.6 to 1.2 m behind a 15 cm^2 CPTU tip. The response of the four MFA smooth sleeves is slightly reduced as compared to the CPT f_s measurement, as seen in the overlay of the sensor traces, and in comparing the average sensor response over depths of 1 to 10 m, f_s = 92 kPa as compared to $f_{a(avg)}$ = 77 kPa, a 16% reduction. Figures 5-16 and 5-17 show results of MFA soundings conducted with the short and long uninstrumented dummy tips, respectively. The sensor positions for the short and long dummy encompass sensor locations 205 to 655 mm and 1105 to 1555 mm behind the tip, respectively. The sensor traces all show very repeatable trends over the sounding with the average values not varying in excess of 5%, denoting a relatively constant response over those sensor positions.

5.5.2.2 MFA Results for Configurations Combining Smooth and Textured Sleeves

The two bounding configurations consisting of both smooth and textured sleeves consist of one textured sleeve configured in either the first (f_{a1}) or last (f_{a4}) position on the MFA, with all other positions configured with smooth sleeves. Figures 5-18 and 5-19 show CPT – MFA soundings with a H2.00 sleeve located in position f_{a1} and f_{a4}, respectively. Similar to the mechanisms controlling the reduction in pushrod friction through the use of friction reducers (larger diameter rings welded intermittently onto CPT push rods), the increase in annular volume created by the textured sleeves creates a similar "backshadow" effect lowering the contact stresses on subsequent areas of lower, albeit standard, diameter further up the shaft. This concept can be clearly seen in the sensor traces of Figure 5-18, where the smooth sleeves located in positions f_{a2}, f_{a3}, and f_{a4} show a consistent but substantially lower trend as compared to other smooth traces taken without a preceding textured sleeve, a reduction on the order of 67% for the largest

roughness sleeve (H2.00). The reduction in sleeve stress due to backshadowing has been shown to be constant for smooth sleeves located at any MFA position behind a textured sleeve, Figure 5-20.

In addition to a "backshadow" effect, textured shearing also results in increased normal stresses forward of the textured sleeve position as a result of the forces generated by the local punching shear failure created at the leading edge of each textured sleeve of increased diameter. The additional normal stress imparted on a limited region forward of a textured sleeve is termed the "foreshadow" effect. The extent of the foreshadow effect can be clearly seen in the variation of the smooth sensor traces located in forward positions to the H2.00 textured sleeve in Figure 5-19. The magnitude of fore and backshadow for a range of texture levels was measured by DeJong (2001) through a series of soundings with configurations of a single textured sleeve located in position f_{a3}, and is reproduced herein as Figure 5-21. The fore and backshadow effects are further quantified in Figure 5-22, showing the percentage increase in measured adjacent smooth sleeve stresses across a range of textures. The foreshadow effect is seen to be restricted to MFA positions directly adjacent to the textured sleeve, as seen in the constant response of the f_{a1} sensors in Figure 5-21. The interference between adjacent sleeves due to fore and backshadow effects were considered in detail in the development of the successor to the MFA, the MPFA, as discussed in detail in Section 5.6.

5.5.2.3 MFA Results for Configurations of Constant Texture

Figure 5-23 shows the results of a CPTU-MFA sounding in which the MFA was configured with four sleeves of the same texture (H1.00 - H1.00 - H1.00 - H1.00). The divergence of the individual H1.00 sensor traces indicates that textured sleeves placed in

series engage a different set of mechanisms than four concurrent smooth sleeves, Figure 5-15. The transition from smooth shearing, against smooth sleeves and mandrel housings, to textured shearing requires the contacting particles to rearrange in order to accommodate the increased annular volume of the textural asperities, resulting in a local punching shear at the leading edge of the sleeve texture. The local punching shear failure results in the application of an Annular Penetration Force (APF) imparted onto any protrusion with a diameter greater than the previously encountered device elements. The increased response exhibited by the first textured attachment sleeve in the sounding configured with all H1.00 sleeves, Figure 5-23, results from the supplementary force applied due to the APF in addition to the forces generated due to interface shearing. The decrease in sleeve stress registered by additional sleeves placed in series is typically minimal, and is controlled by mechanisms similar to the degradation of interface strength at large shear displacements observed in laboratory results.

To further investigate the effect and variability of APF forces on the measured textured sleeve responses, a full investigation across the range of textures was completed using a combination of results from the preliminary soundings of DeJong (2001) and MFA soundings conducted for the current work. The APF was investigated by conducting soundings that varied the number of rows of texture placed in series. The results of each sounding were averaged over a common depth range of 1-10 m, resulting in a single representative value for each sounding. To investigate texture lengths less than a full sleeve, a series of textured sleeves were produced with partial texturing equal to 20, 40, and 70% of the full texture, as shown in Figure 5-24. Figure 5-25 shows the averaged sleeve force plotted against the number of consecutive diamond rings for a range of

textures, with the intercepts at zero rings denoting the APF for a given diamond height. The linear increase of sleeve stress with increasing exposure length to textured shear confirms that the effect of APF is isolated to the first 2 rows of offset texture for the current texturing geometry. The relationship between textured sleeve stress can then be represented as in Equation 5-2,

$$F_a = F_r * N_r + APF \qquad \text{(Eq. 5-2)}$$

where F_a = average attachment sleeve force, F_r = average force per ring of texture (slope), N_r = # of consecutive rings of texture, and APF = annular penetration force (intercept). The concept of an APF mechanism is further supported by the trend of successive smooth sleeve forces resulting in an observed intercept, or APF, of zero. As the H1.00 sleeve was used as the reference sleeve throughout the initial MFA investigations, there exist many more data of H1.00 response in Figure 5-26, with the slight variability observed for similar textured shearing lengths are believed to be the result of lateral variability at the site.

As observed in the results, the response of textured sleeves are controlled by a combination of two primary mechanisms: interface shearing and sliding along the sleeve length (the isolated interface or shear response), and a punching shear or bearing capacity type failure located at the onset of sleeve texturing (the annular penetration component), Equation 5-3.

$$f_{total} = f_{shear} + f_{annular\ penetration} \qquad \text{(Eq. 5-3)}$$

The isolated interface component of measured textured sleeve response, is representative of conditions experienced in situ and in the laboratory for continuously textured surfaces, and as such is the quantity applicable to interface design. Results from DeJong (2001) and the current study have shown that the magnitude of APF at every discrete measurement depth can be calculated by directly scaling the corresponding CPTU q_t response to the appropriate annular area of sleeve texture, Equations 5-4 and 5-5. Subtracting the discrete values of the APF component from the total measured response allows the isolated interface response to be determined at each measurement depth, Equation 5-6:

$$APF(R) = q_t \cdot A_{texture\ annulus} \qquad \text{(Eq. 5-4)}$$

$$f_{annular\ penetration} = \frac{APF(R)}{A_{sleeve}} \qquad \text{(Eq. 5-5)}$$

$$f_{shear} = f_{total} - q_T \cdot \frac{A_{texture\ annulus}}{A_{sleeve}} \qquad \text{(Eq. 5-6)}$$

where $A_{texture\ annulus}$ = the annular area of textural asperities, A_{sleeve} = friction sleeve surface area, and $APF(R)$ = the annular penetration force for a specific texture height, R. The ability to isolate the components of textured shearing from the total measured values allows the isolated interface behavior over a wide range of roughnesses to be quantified in situ.

5.5.2.4 MFA Results for Configurations of Increasing Texture

As a result of the influence of backshadow effects on sleeve stress measurements, it was suggested by DeJong (2001), DeJong and Frost (2002), and Frost and DeJong (2005) to place sensors in configurations of increasing texture. Figures 5-26 and 5-27 show CPT – MFA soundings in which the MFA unit was configured with sleeves of increasing texture: (SM - H.125 - H.25 - H.50) and (H.25 - H.50 - H1.00 - H2.00), respectively. A number of interesting behaviors can be noted in Figures 5-26 and 5-27, most notably the marked increase in measured sleeve resistance as a function of increased texture height. While the magnitude of sleeve stress increases with increasing surface texture, it is important to note that each sensor trace follows the same stratigraphic changes with depth, irrespective of roughness indicating that a series of interface tests can be successfully conducted within the same sounding. The magnitudes of each sleeve texture tested in the above multi textured configurations were compared to soundings where each sleeve was tested individually by DeJong and Frost (2002). They reported that the variation in average sleeve stress between independent and combined soundings were never more than 10% and were mainly due to lateral site variations, as determined by comparing the CPTU sensor responses. The simultaneous measurement of interface strength across a range of interface properties was the primary goal of the MFA development, and these figures show that the MFA is a feasible tool to conduct such tests in situ. This claim is further supported through Figure 5-28 showing that the common bilinear relationship between interface strength and surface roughness can be reproduced in situ using the MFA, as shown by Frost and DeJong (2005).

5.6 Development of the Multi Piezo Friction Attachment (MPFA)

5.6.1 Motivation

As shown in the previous sections, the MFA provides a clear means to obtain four simultaneous measures of interface friction over a range of surface textures simultaneously in combination with conventional CPTU measurements. However, there existed a couple of areas in which the original MFA design could be improved. The two main deficiencies of the MFA unit are (1) the inability to monitor the pore fluid conditions at the multi friction sleeve locations, and (2) the close spacing of the MFA sleeve sensors allowing for the sleeve texture of one sleeve to interfere with the sensor response of adjacent friction sleeves. The remainder of the MFA design components met or exceeded initial expectations during the initial laboratory and field proof testing stages. As a result, it was determined that while the MFA device provides an extremely useful addition to the geotechnical engineering community, that a second device with increased capabilities could be created that diminished the shortcomings of the original MFA device. As with the MFA device, the design of the MPFA was led by Georgia Tech personnel with assistance and input from the CPT manufacturer, Vertek. The subsequent device created as a result of this redesign is the multi piezo friction attachment, and its detailed design and development are discussed herein.

5.6.2 Addition of Piezo Sensors

5.6.2.1. Motivation

Similar to the addition of piezo elements to conventional cone penetrometers resulting in the advanced tool known as the CPTU device, it was considered

advantageous to consider adding piezo elements to the multi friction attachment concept. The addition of piezo elements to the MFA concept would allow for a number of device advantages:

- The ability to distinguish between drained, undrained, and partially drained conditions at the various MPFA sensor locations.
- The ability to consider the measured friction sleeve data within the robust framework of effective stress analysis.
- The ability to evaluate flow and consolidation characteristics along the length of the MPFA unit both laterally and vertically through the use of multiple piezo sensors placed in series.
- The ability to better assess hydrostatic ground water conditions due to the placement of the sensors within the stable shear zone along the penetrometer shaft.
- The ability to provide additional data towards improved stratigraphic profiling.
- The ability to further understand and directly measure the pore pressure distribution surrounding penetrometers in a range of in situ conditions.
- The ability to determine the magnitude of induced pore pressures due to the introduction of textured friction sleeves of various roughness.

It is believed that with the addition of multiple piezo elements along the shaft placed in series that the MPFA unit would have increased abilities to not only determine in situ interface behavior, but to also obtain a more complete assessment of soil and groundwater conditions with or without the use of the multi friction sensors. There have

been several previous devices that have included multiple piezo sensors as shown by Campanella and Robertson (1988) and reproduced here as Figure 5-29. In addition to the configurations shown in Figure 5-29, several other researchers have developed additional multi piezo CPT configurations: Bayne and Tjelta, 1987; Sully et al., 1988; Sills et al., 1988; Campanella et al., 1990; etc. These devices are all described in detail by Lunne et al. (1997) in their comprehensive book concerning CPT use in geotechnical practice.

5.6.2.2. Piezo Sensor Design Considerations

As discussed by Campanella and Robertson (1998) and Lunne et al. (1997), there are several factors that influence the reliability and accuracy of pore pressure sensors used in penetrometers. The main factors typically considered in piezo element design are the choice of element filter material, the accuracy and range of the pressure transducer, the properties of the saturation fluid, the location of the sensor along the probe, the geometry and size of the piezo element, and the mechanical design and specifically rigidity of the pore pressure measuring system. The first consideration addressed in the design of the piezo sensors for the MPFA unit was the element geometry and size. The two main element types used in penetrometers consist of the common ring elements typically used in the u_1, u_2, and u_3 sensor positions, and circular elements known as "button' type elements that are sometimes used when piezo sensors are placed along the penetrometer shaft. Ring type elements require that the device be able to screw apart at the sensor location to facilitate the saturation of the pore pressure reservoir, whereas button type elements are saturated from the outside of the device without the need to disassemble the unit. Due to the internal wiring configuration of the MFA unit that limits the available internal space to place large reservoirs and the necessity to disassemble the

unit from the back towards the tip, it was decided that button type elements would provide a better solution within the confines of the original MFA design framework. The current multi piezo sensors consist of a small fluid reservoir equivalent in diameter and depth to the size of the element filters (12.5 mm in diameter, and 3.3 mm in thickness) connected to the sensor pressure diaphragm by a short angled cylindrical tube machined directly into the penetrometer housing. As with the u_2 element used in the CPT devices manufactured by Vertek, the current filter elements are made of polypropylene and the saturation fluid is a viscous silicon oil.

5.6.2.3. Piezo Sensor Locations

During the initial design phase of the MPFA development it was determined that an optimum configuration of piezo elements would include an element located adjacent to each multi friction sleeve and an additional fifth attachment piezo element located nearer to the tip than the other sensors to serve as a baseline piezo sensor. In order to accurately monitor the pore pressures acting across the majority of the attachment sleeves, the location of the four other piezo sensors was chosen to adjoin the uphole end of each sleeve. The sensors were subsequently centered 1.5 cm behind the trailing edge of each friction sleeve, resulting in a solid mandrel section of 7.5 mm between the edges of each friction sleeve and paired piezo sensor in order to maintain adequate structural stiffness and durability. The baseline piezo element location was determined by balancing the required distance from the first attachment sleeve to ensure isolated response and efforts to minimize the total length of the penetrometer. As such, the baseline piezo sensor was positioned on an independent module 100 mm in length with the piezo element placed at the front edge in an identical configuration to the other attachment piezo elements. The

detailed dimensions and specifications of the attachment piezo sensors are detailed in Section 5.6.4.

5.6.3 Spacing of Attachment Friction Sleeves

As discussed in Section 5.5, the original spacing of the attachment friction sleeves on the MFA device created variable levels of fore and backshadow interference as a function of sleeve texture. Figure 5-21 presented the interference experienced by smooth sleeves placed in the adjoining fore and aft positions to textured sleeves of varying roughness. The backshadow effect of a textured sleeve was shown to be constant with increasing distance over the range of measured distances up to 0.5 m behind a textured sleeve as shown in Figure 5-22. As such, it was subsequently determined that the backshadow effect could not be eliminated by increasing the spacing between the attachment friction sleeves. Consequently, multi friction configurations utilizing textured friction sleeves require configurations that consist of constant or increasing texture that have been shown to not be affected by backshadowing, as seen in Figures 5-26 and 5-27. While backshadow effects are not limited to small distances behind an increase in diameter along a penetrometer as seen above and through the effective use of friction reducers, foreshadowing has been shown to have only a limited range of influence. Figure 5-21 showed that across the range of textured sleeves currently used that all textures of 0.25 mm and greater height caused foreshadowing on sleeves located in the adjacent forward sleeve position (40 mm in front) with no effect for even the largest texture (2.00 mm) on sleeves located two MFA positions forward of a textured sleeve (190 mm in front).

In order to optimize the spacing of the friction sensors on the MPFA unit to eliminate foreshadow effects for the range of textures used, a detailed study was undertaken to determine the extent of foreshadowing for each level of texture. To allow for additional sleeve spacings to be tested without altering other device components, two mandrel spacers of 50 and 100 mm were manufactured, as shown in Figure 5-30. Due to the design of the MFA unit, it was required that the total attachment length remain constant, and as such the two spacers were used in place of one of the three forward modular friction mandrels, allowing sleeve spacings of 40, 90, 140, 190, and 340 mm to be investigated. Figure 5-31 shows the sleeve spacing variations provided with the MFA configured with the spacers and from the original four sleeve MFA configuration, consisting of spacings equal to 40, 190, and 340 mm. A series of soundings were performed, as detailed in Table 6-2b, to determine the extent of foreshadowing across the range of developed sleeve textures. Figure 5-32 details the magnitude of the foreshadow effect as a function of inter sleeve spacing. Previously, as shown in Figure 5-21, it was determined that the foreshadow effect extended farther than 40 mm in front of the leading edge of sleeves for all texture heights $\geq$ 0.25 mm and less than 190 mm for all texture magnitudes. The data in Figure 5-32 corroborate the earlier findings concerning the bounding limits of the foreshadow influence and provide additional data in between those limits. Through analysis of the 91 soundings performed with the MFA to that stage and the results of the sleeve spacing investigation it was concluded that a friction sleeve spacing of 150 mm between attachment sensors would eliminate the foreshadow interference of textured sleeves on adjacent sensors.

5.7 Summary of Multi Piezo Friction Attachment Design

The primary goals of the MPFA development consisted of maintaining the effective elements of the original MFA device while adding additional features in the form of pore pressure sensors and improved sensor spacing. A detailed investigation into available sensor technologies and proper sensor placement was undertaken as described in Sections 5.6.2 and 5.6.3. The resulting device, termed the Multi Piezo Friction Attachment, is summarized in Figure 5-33 and Table 5-2. As with the MFA, the developed device is configured to work behind a conventional 15 cm^2 CPTU unit, or as a stand alone device behind an uninstrumented dummy tip. The MPFA unit has an assembled length of 1.88 m, that extends to 2.49 m when configured with a digital Vertek 15 cm^2 CPTU unit (0.61 m in length). The MPFA device consists of four piezo friction mandrels 260 mm in length, accepting friction sleeves of 110 mm in length at the front of the mandrel, followed by a solid housing 150 mm in length and 43.7 mm in diameter containing a 12.5 mm diameter button type piezo element centered 15 mm behind the trail edge of the friction sleeve, as shown in Figure 5-34. In addition to the four piezo mandrels, the MPFA is also equipped with a baseline piezo mandrel 100 mm in length containing a 12.5 mm diameter button type piezo element centered 15 mm behind the front edge of the mandrel, as shown in Figure 5-35. The MPFA configuration from the downhole side consists of the baseline piezo mandrel, followed by four identical piezo friction mandrels, a short connecting mandrel with no sensors, and the attachment digital housing containing two digital circuit board assemblies. The MPFA system allows for the simultaneous measurement of four friction measurements (f_{a1}, f_{a2}, f_{a3}, and f_{a4}) and five pore pressure measurements (u_{a0}, u_{a1}, u_{a2}, u_{a3}, and u_{a4}) for a total of nine independent

measurements. When configured with the CPTU unit equipped to measure tip stress (q_c), pore pressure (u_2), sleeve friction (f_s), and dual axis inclination (i_x and i_y) the total number of independent measurements is fourteen. The uphole data acquisition (DAQ) system hardware used by the MPFA system is a Vertek DataPack 2000, the same as that used with the MFA device. The DAQ architecture of the MPFA device is presented in Figure 5-36. Penetration depth is monitored with an uphole wireline potentiometer. Results of MPFA soundings from various sites and geologies, and over a range of test conditions are presented in the subsequent chapters.

5.8 Verification of MPFA Operation

After the completion of manufacturing, the MPFA was tested in the parking lot of the Vertek shop, on the 4th of May 2003, to ensure proper operation of the MPFA sensors. The geology of the subsurface at the Vertek shop consists of a glacial till and outwash comprised of sand, silty sand, with some gravel and interspersed cobbles. The results of these two preliminary CPTU-MPFA soundings are shown in Figures 5-37 and 5-38, respectively. In the first sounding, denoted Z04Y0402C, the MPFA was configured with four smooth attachment friction sleeves, and all sensors showed proper response. For the second sounding the MPFA friction sleeve configuration was changed to consist of a H0.25 - H2.00 - SM - SM configuration as highlighted by the increased response of f_{a1} and f_{a2} in Figure 5-38.

As with the MFA device, it is necessary to disassemble the MPFA unit from the rear forward to change out the friction sleeves and to prevent twisting of the internal wiring. The internal wiring consists of a main umbilical wire that runs through the center of the MPFA device. This umbilical wire bundle connects to the output of the CPTU

Analog to Digital (A/D) circuit board at the downhole end, and runs internally through the MPFA device with takeoff locations for the individual MPFA mandrels to connect to the main device excitation and acquisition wiring. As a result of the increased number of sensors in the MPFA device as compared to the MFA device the internal wiring is more congested within the device cavity and is more prone to damage during assembly and disassembly. During the sleeve changeover between the two soundings described above some of the internal wiring became damaged resulting in the loss of sensors u_{a2}, u_{a3}, f_{a4}, and u_{a4} during the second sounding. In response to the constraints provided by the limited internal passthrough space, the internal wiring was subsequently reworked in an effort to limit damage opportunities during sleeve changeover. MPFA response across a range of test and site conditions and subsequent marked observations and analysis of the observed in situ interface behavior are presented in detail in Chapters 6 to 8.

Table 5-1. Summary of Smooth and Textured MFSA Friction Sleeve Properties

Sleeve ID#	Diamond Dimensions							Surface Roughness Values					
	Height (H)	Pen. Angle (β)	Diagonal Spacing (S)	Percent Pass-through	Width (W)	Angle (α)	# Diamond Rings	R_{max} [1]	R_p [2]	R_t [3]	R_a [4]	Δ_a [5]	R_s [6]
	(mm)	(deg)	(mm)	(%)	(mm)	(deg)	(#)	(mm)	(mm)	(mm)	(mm)	(deg)	
Conventional Smooth Sleeve [7]													
SM	N/A	N/A	N/A	100.0	N/A	N/A	N/A	0.0064	0.0021	0.0043	0.0005	7.766	N/A
Variations in Texture Height													
H0.125	0.125	60	6.3	15.7	5.3	45	10	0.125	0.10	0.02	0.04	0.51	1.01
H0.25	0.250	60	6.3	15.7	5.3	45	10	0.250	0.21	0.04	0.07	0.99	1.02
H0.50	0.500	60	6.3	15.7	5.3	45	10	0.500	0.43	0.07	0.12	1.91	1.03
H0.75	0.750	60	6.3	15.7	5.3	45	10	0.750	0.66	0.10	0.16	2.76	1.04
H1.00	1.000	60	6.3	15.7	5.3	45	10	1.000	0.88	0.11	0.19	3.54	1.06
H1.50	1.500	60	6.3	15.7	5.3	45	10	1.500	1.37	0.13	0.22	4.89	1.08
H2.00	2.000	60	6.3	15.7	5.3	45	10	2.000	1.86	0.14	0.23	5.95	1.09

Note: All roughness parameters defined in Table 2-2. [1] R_{max}: Maximum peak to valley height; [2] R_p: Maximum peak to mean line height; [3] R_t: Mean line to lowest valley height; [4] R_a: Average roughness; [5] D_a: Average slope roughness; [6] R_s: 3-D areal roughness; [7] Actual measurements of a new CPT sleeve and therefore high average slope values due to micro texture from machining process. Only R_a = 0.50 μm is defined by ASTM Standards.

Table 5-2. Summary of CPTU, MFSA, and MPFA Specifications.

	15 cm^2 CPTU Module	**Multi Friction Sleeve Attachment**	**Multi Piezo Friction Attachment**
Total Length	0.61 m	1.09 m	1.88 m
Baseline Diameter	43.7 mm	43.7 mm	43.7 mm
Tip Resistance			
Capacity	225 kN	N/A	N/A
Overload Capacity	150%		
Accuracy	0.2%		
Pore Pressure			
Capacity	3.5 MPa	N/A	3.5 MPa
Overload Capacity	150%		200%
Accuracy	0.1%		0.1%
Hysteresis	1.8 kPa		1.8 kPa
Sensor Geometry	Ring		Button
Element Size	6.4 mm Thickness		12.5 mm Diameter
Sleeve Friction			
Capacity	45 kN	45 kN	45 kN
Overload Capacity	150%	150%	150%
Precision	44-89 N	44-89 N	44-89 N
Hysteresis	22 N	22 N	22 N
Length	163.9 mm	110.0 mm	110.0 mm
Surface Area	225 cm^2	150 cm^2	150 cm^2
Surface Roughness (R_a)	0.50 μm	0.50 - 250 μm	0.50 – 250 μm
Inclination			
Range	20°	N/A	N/A
Accuracy	10%		

Figure 5-1. A Triple Element Piezocone with u_1, u_2, and u_3 Pore Pressures Sensors (Photograph Courtesy of Prof. Paul Mayne).

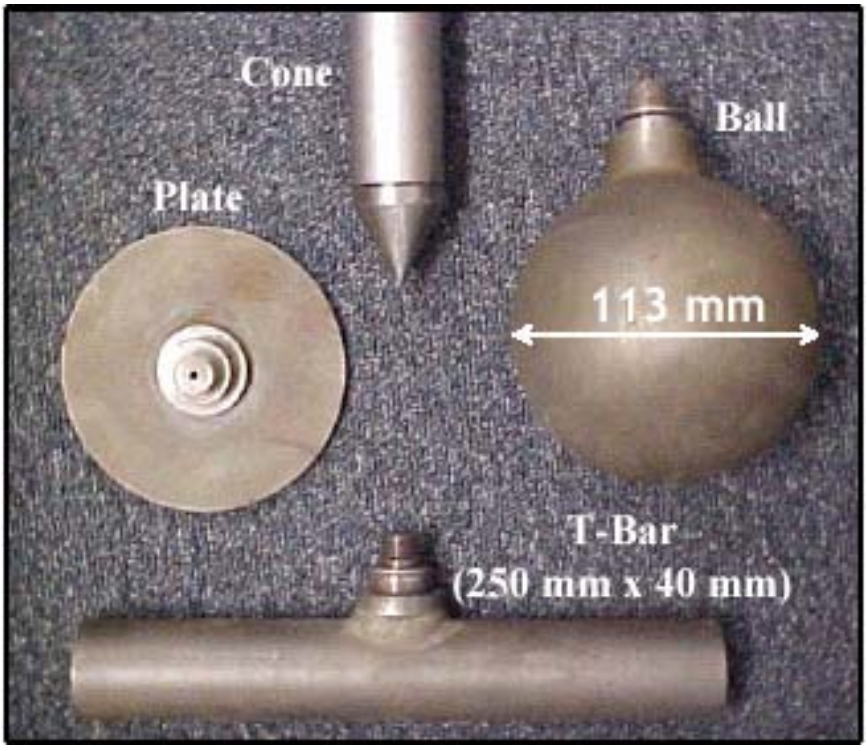

Figure 5-2. Conventional Cone Penetrometer Shown with Alternative Tip Geometries (Randolph, 2004).

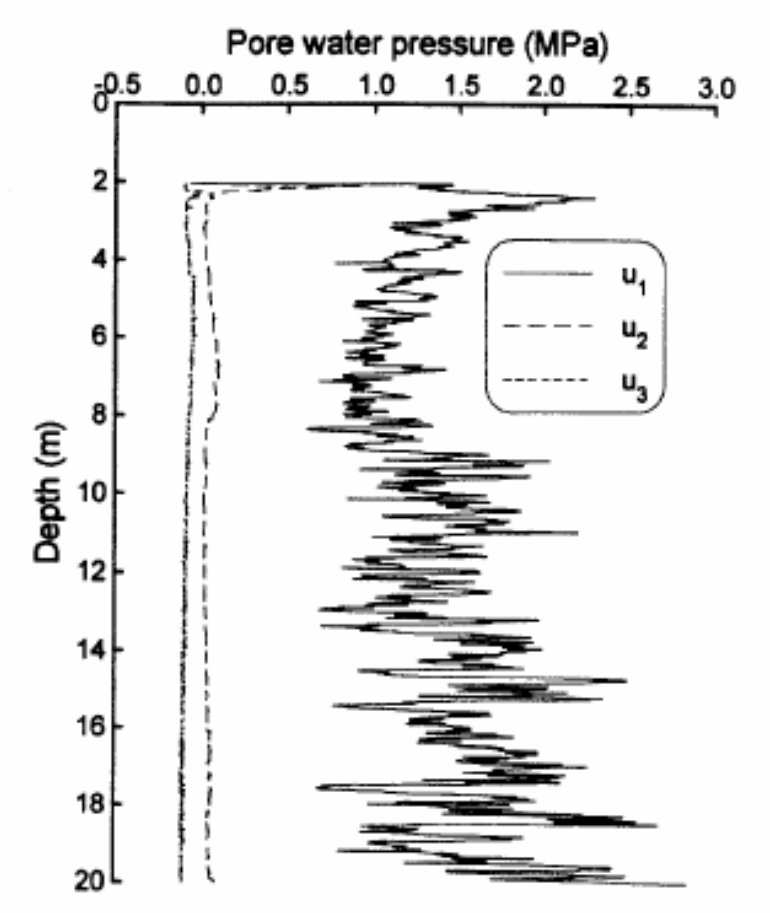

Figure 5-3. Variations in Pore Pressure Response as a Function of Sensor Location for a Sounding Taken in the Heavily Overconsolidated Gault Clay (Lunne et al., 1997).

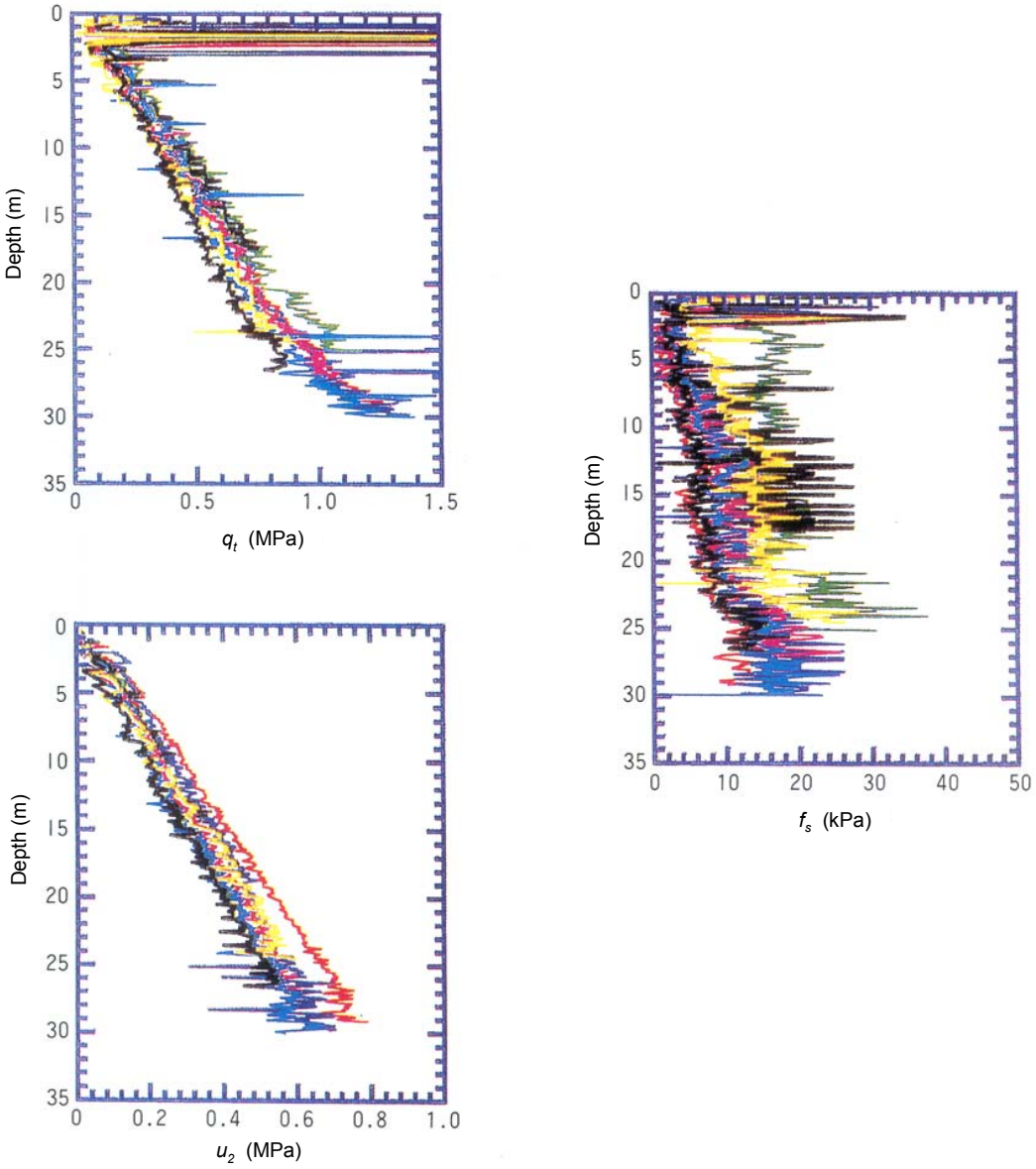

Figure 5-4. Results of Soundings Performed with Eight Different CPT Modules at a Uniform Clay Site (Tanaka 1995).

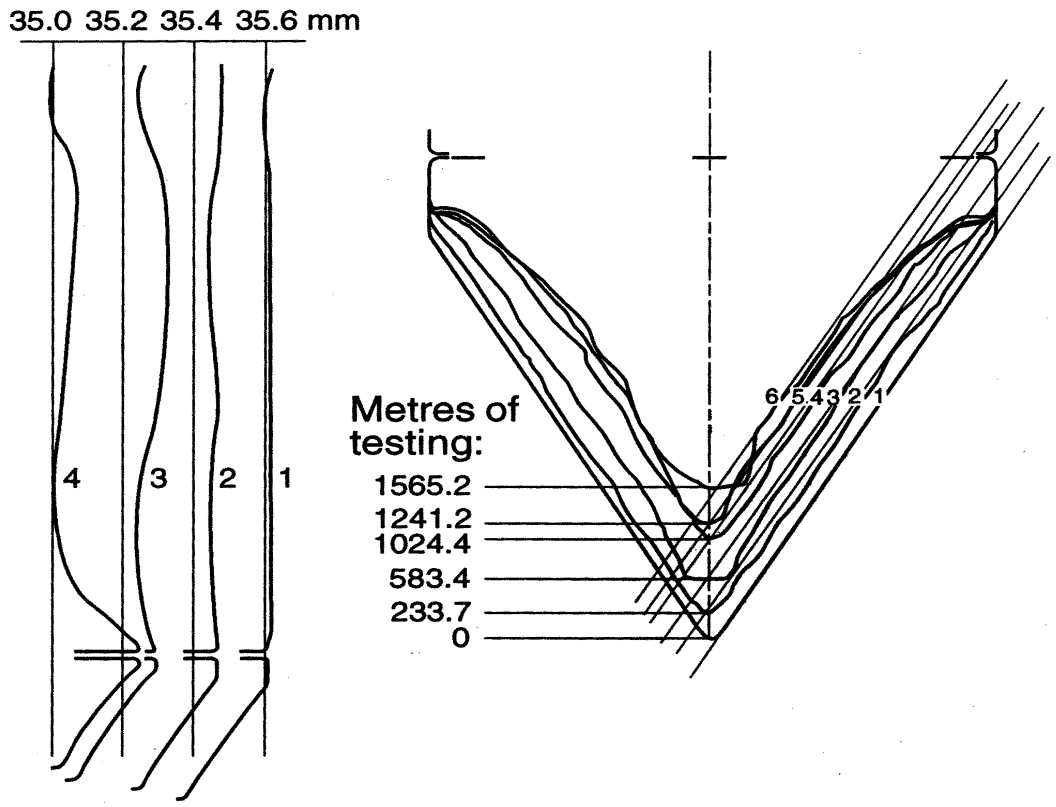

Figure 5-5. Measurements of CPT Tip and Sleeve Wear (Zuidberg et al., 1982).

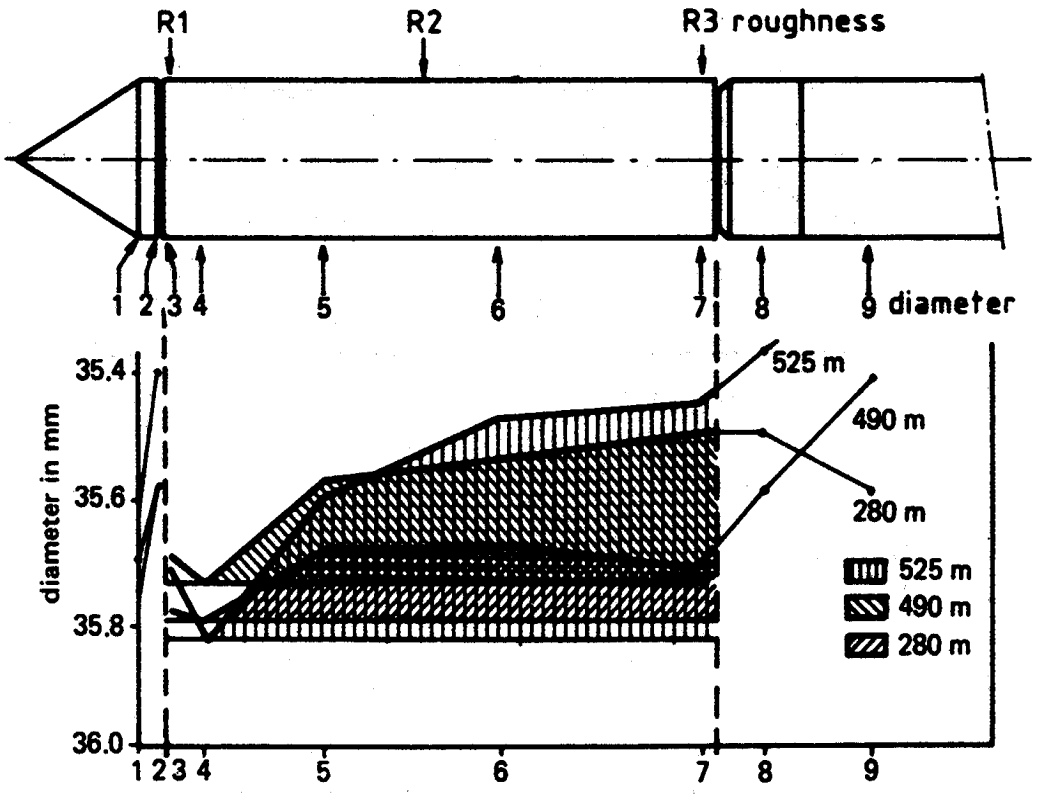

Figure 5-6. Measurements of CPT Tip and Sleeve Wear (Jekel, 1988).

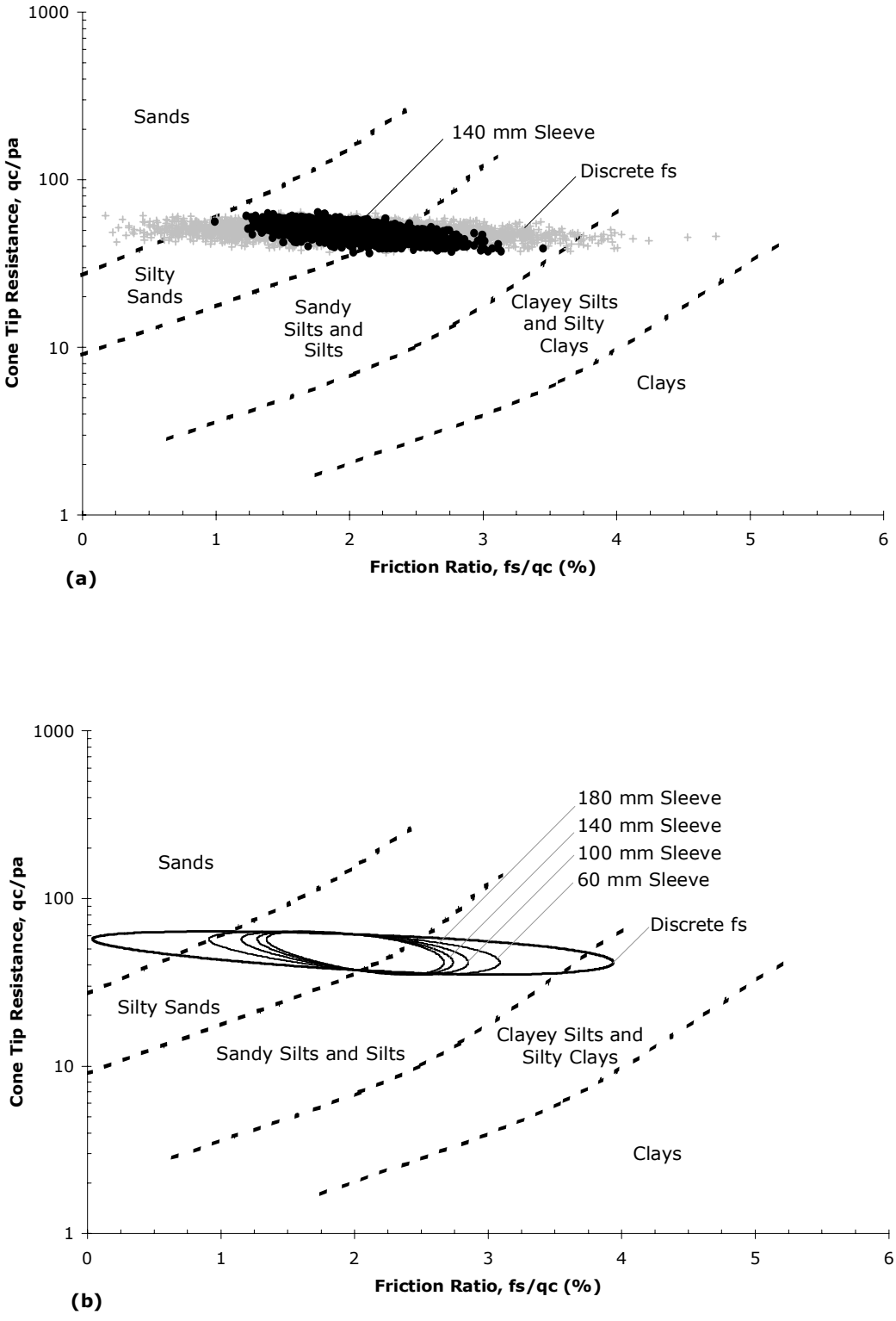

Figure 5-7. Simulations Demonstrating the Effect of Friction Sleeve Length on Soil Classification: (a) Conventional Sleeve Length Versus a Discrete Measurement, (b) Varying Sleeve Lengths (Saussus et al., 2005).

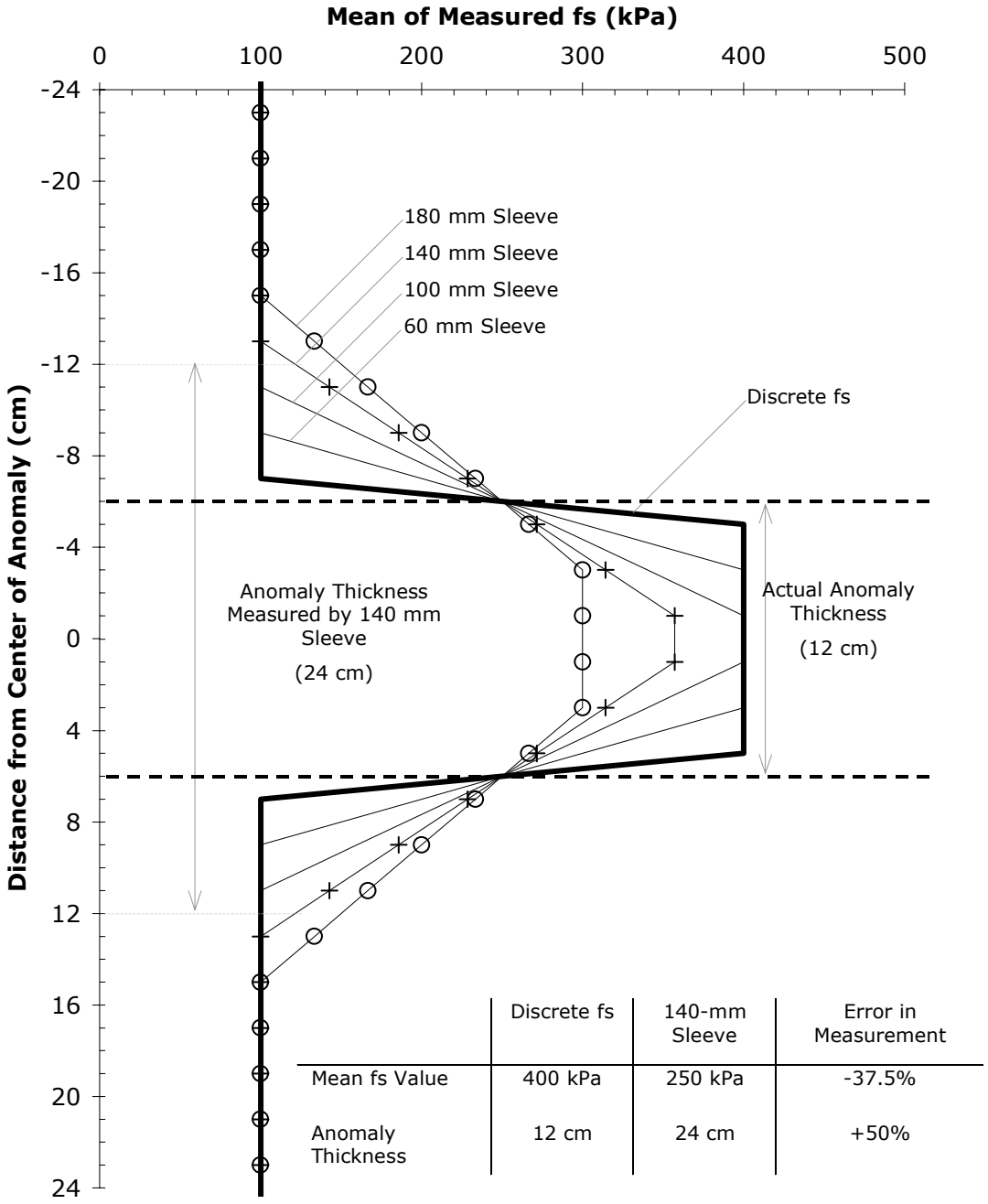

Figure 5-8. Effect of Sleeve Length on Mean of Measured *fs* Across Anomaly and on Anomaly Thickness (Frost et al., 2005).

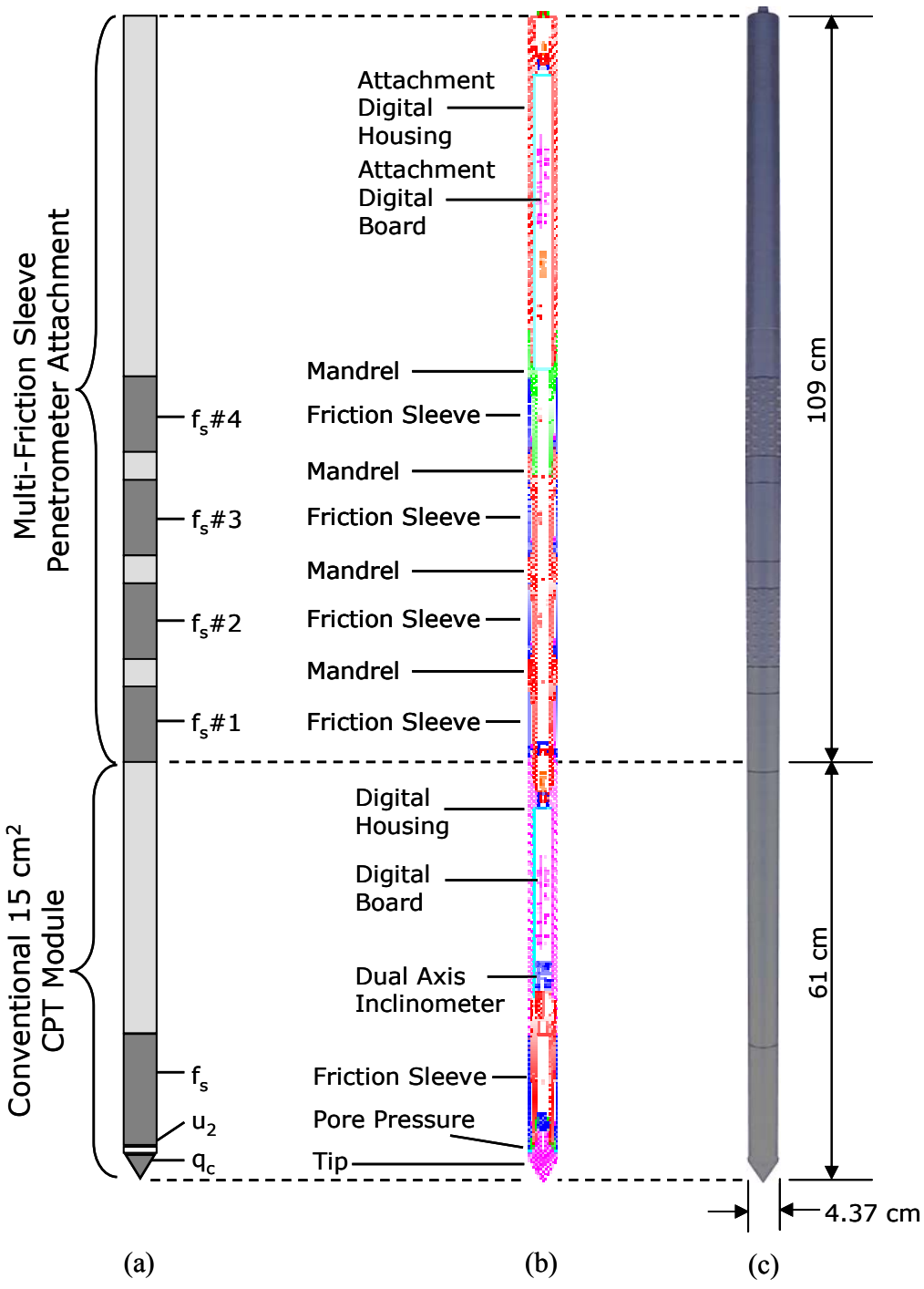

Figure 5-9. Multi Friction Sleeve Attachment Configured with Conventional CPT Module (a) Schematic (b) Design Detail (c) Photograph (after DeJong, 2001).

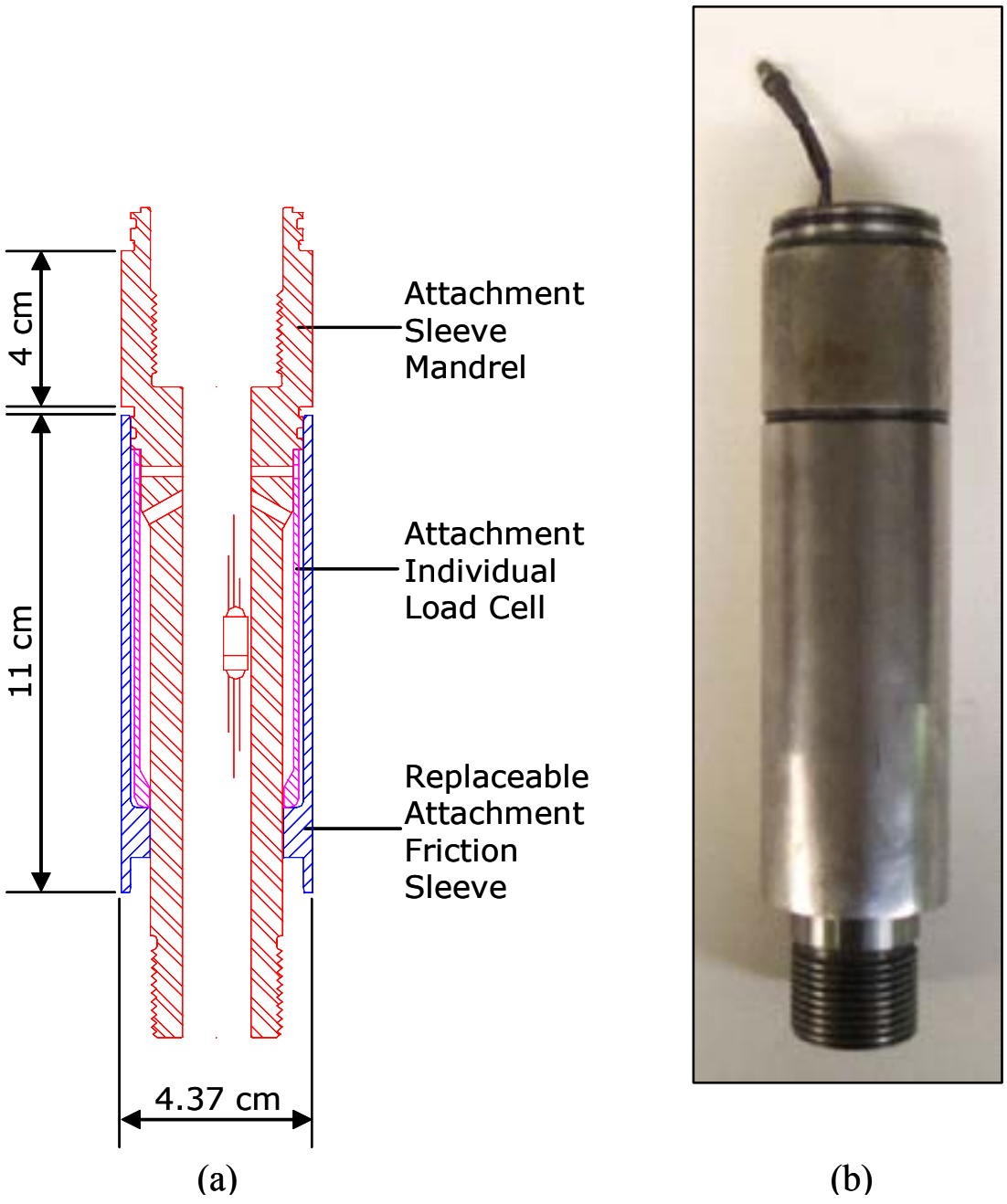

Figure 5-10. Friction Sleeve Mandrels for the MFA device: (a) Schematic, (b) Photograph (after DeJong, 2001).

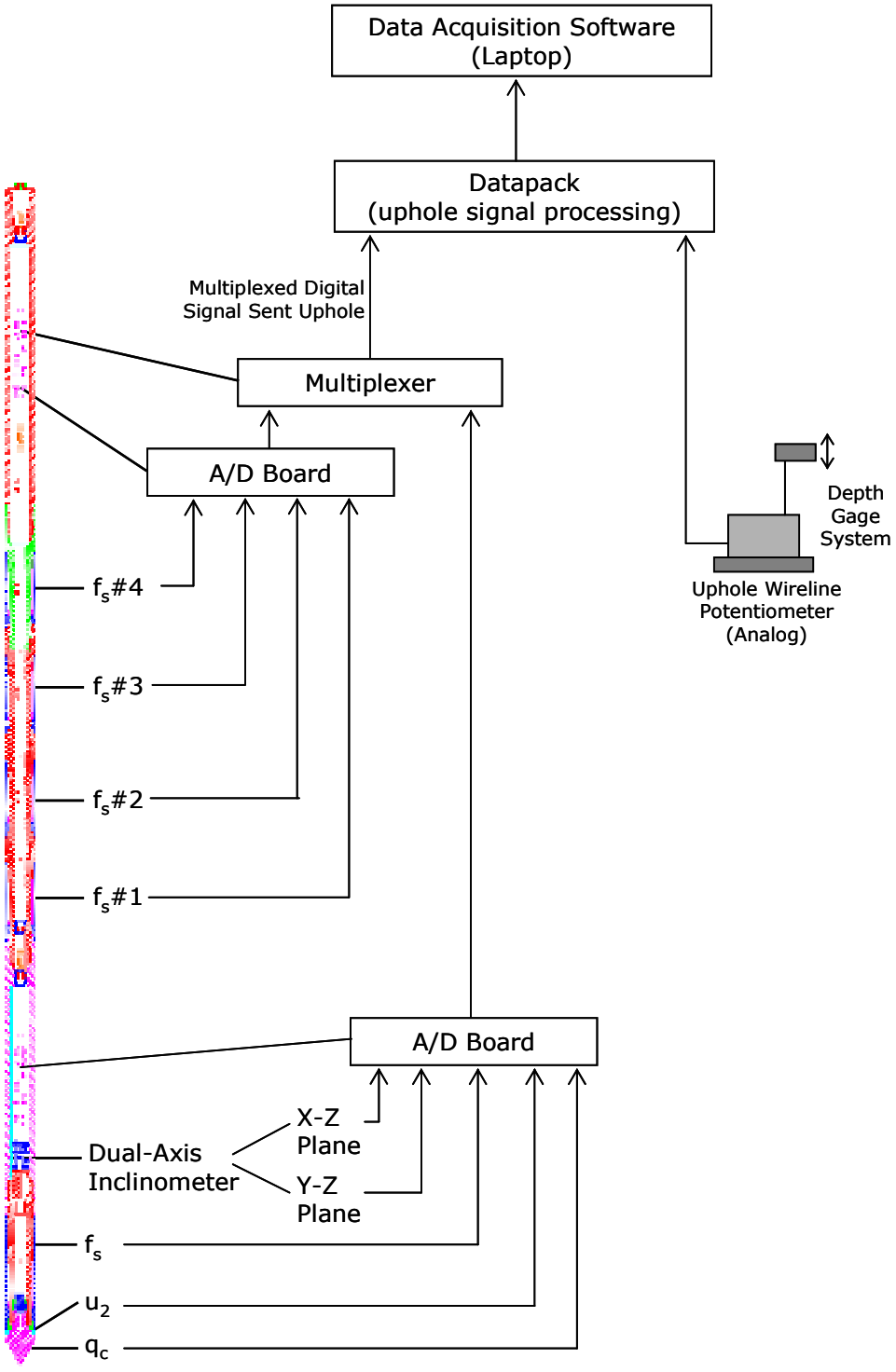

Figure 5-11. Schematic of the MFA Data Acquisition Architecture (after DeJong, 2001).

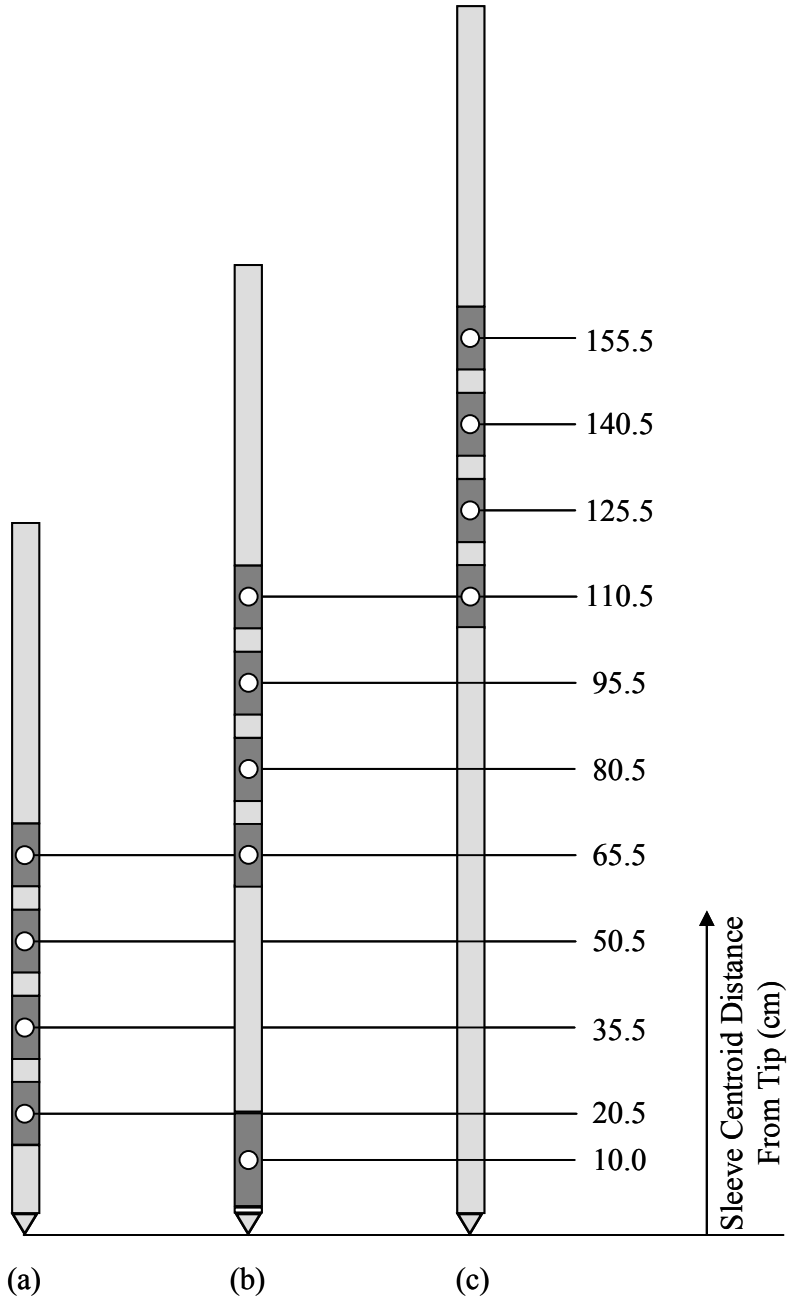

Figure 5-12. Schematic of Sleeve Centroid Positions Relative to the Tip for the MFA Configured with (a) Short Uninstrumented Tip (163 mm) (b) Conventional CPTU Module (601 mm), (c) Long Uninstrumented Tip (1062 mm) (after DeJong, 2001).

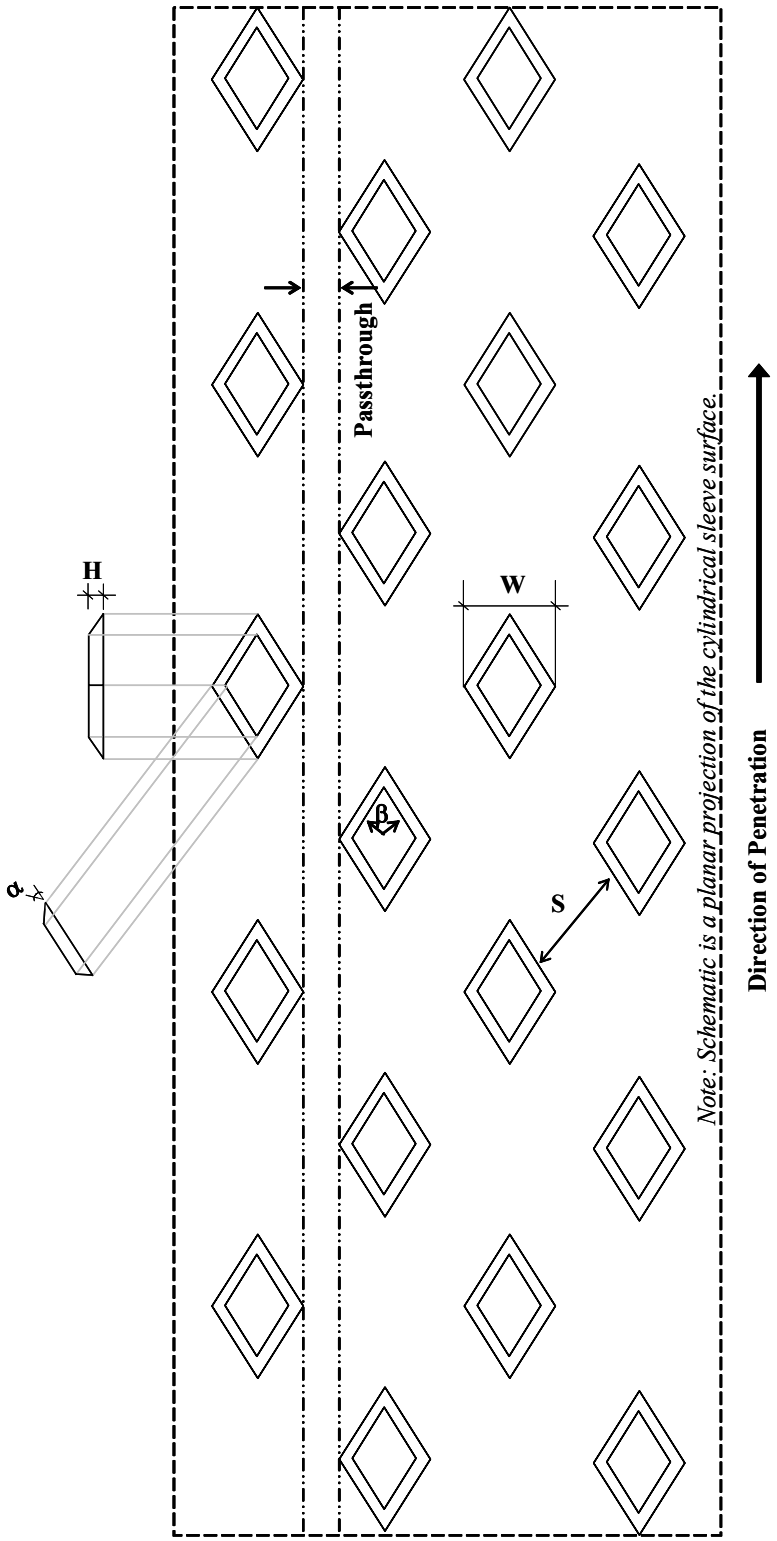

Figure 5-13. Schematic of Diamond Texturing Pattern Used to Create Varying Levels of Surface Texture on Textured Friction Sleeves (after DeJong, 2001).

Figure 5-14. Photographs of Selected Textured Sleeves: (a) a Collection of Sleeves Highlighting the Variations in Texture Geometry Tested to Optimize the Sleeve Texture Geometry, (b) Sleeves of Varying Texture Height for the Optimum Texture Geometry (after DeJong 2001).

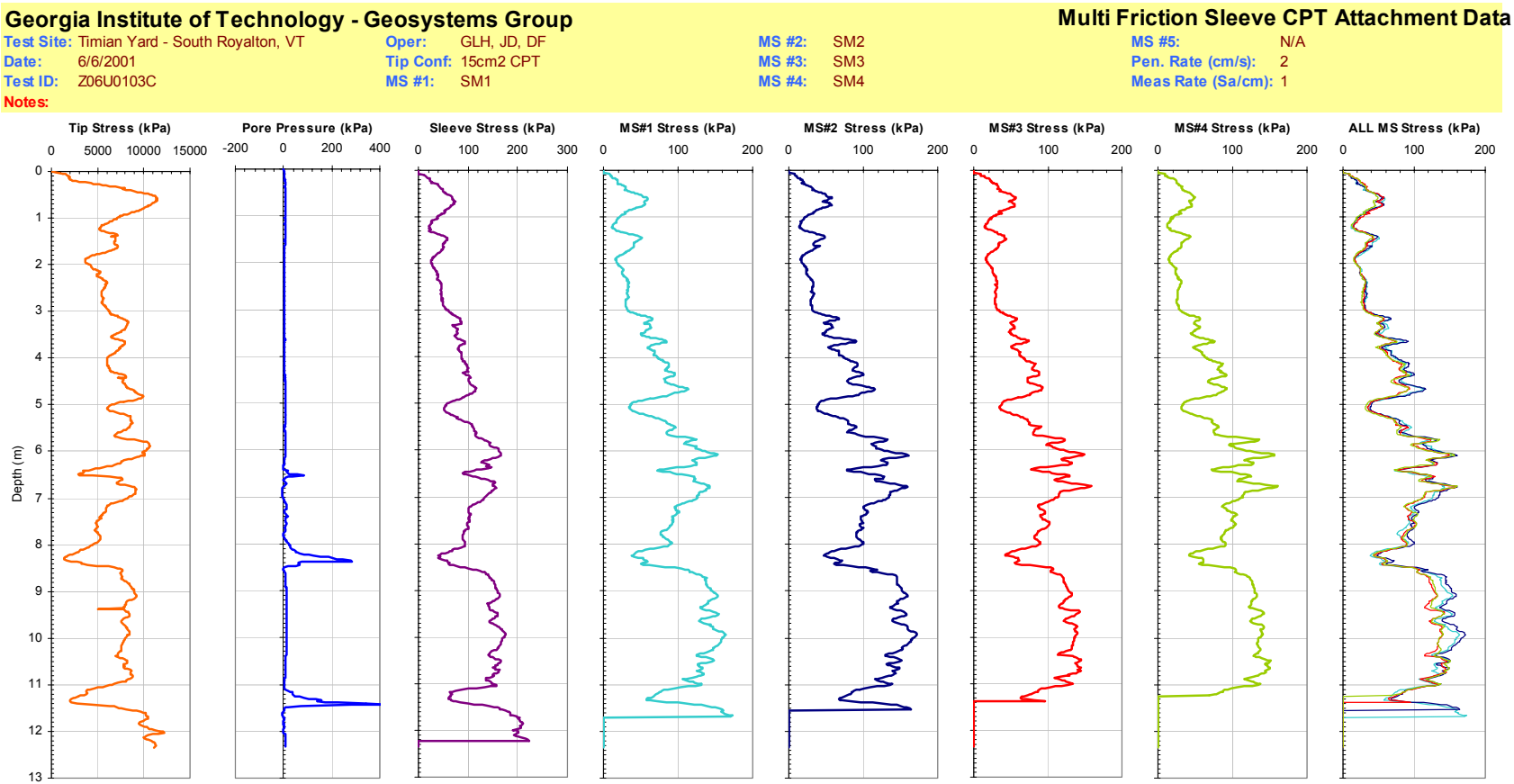

Figure 5-15. Results of a CPTU – MFSA (SM – SM – SM – SM) Sounding at the South Royalton, Vermont Sand Test Site Highlighting the Response of Four Smooth Sleeves Tested in Series.

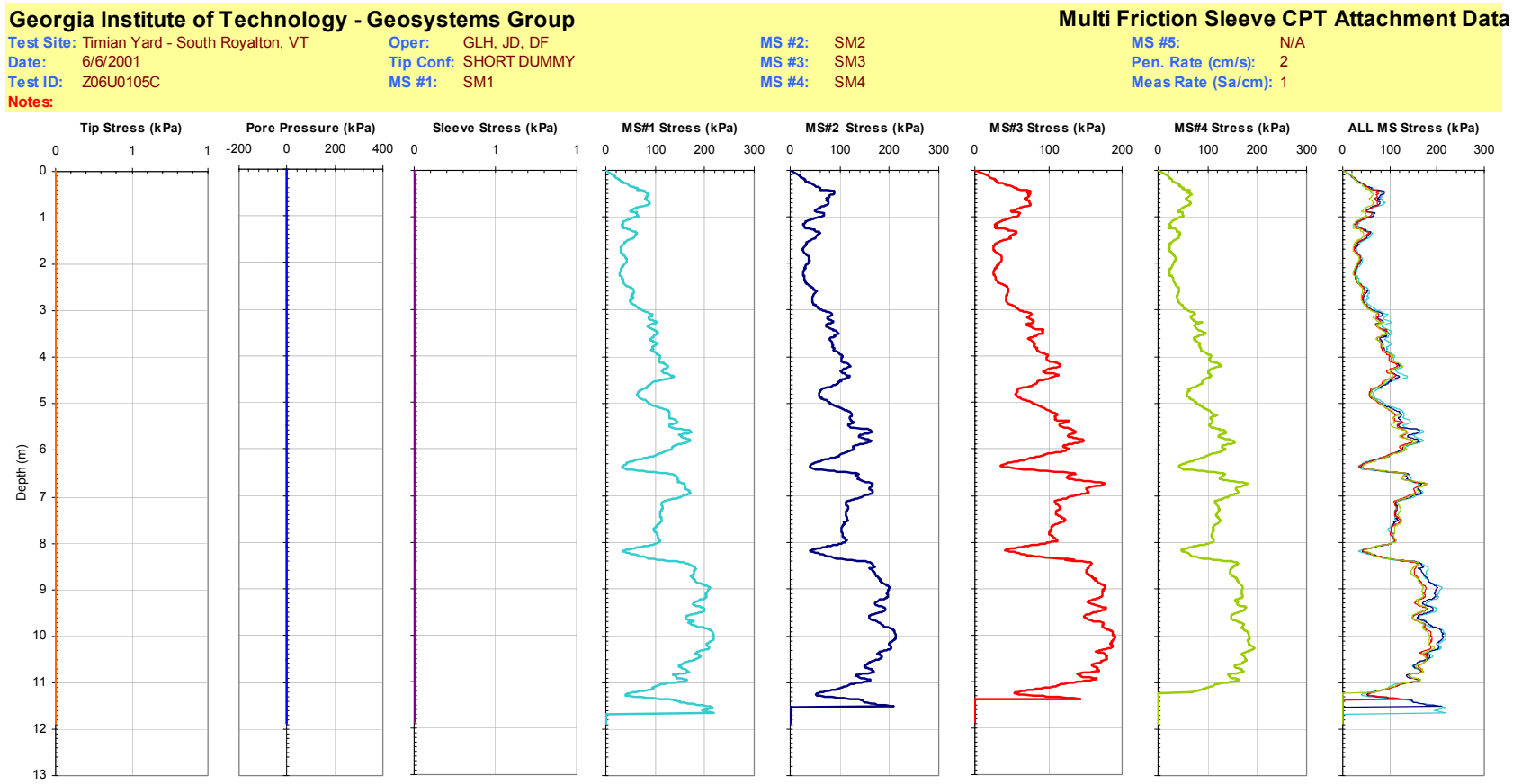

Figure 5-16. Results of an MFSA (SM – SM – SM – SM) Sounding with the Short Uninstrumented Tip (163 mm) at the South Royalton, Vermont Sand Test Site Highlighting the Response of Four Smooth Sleeves Tested in Series When Located Within Close Proximity to the Tip.

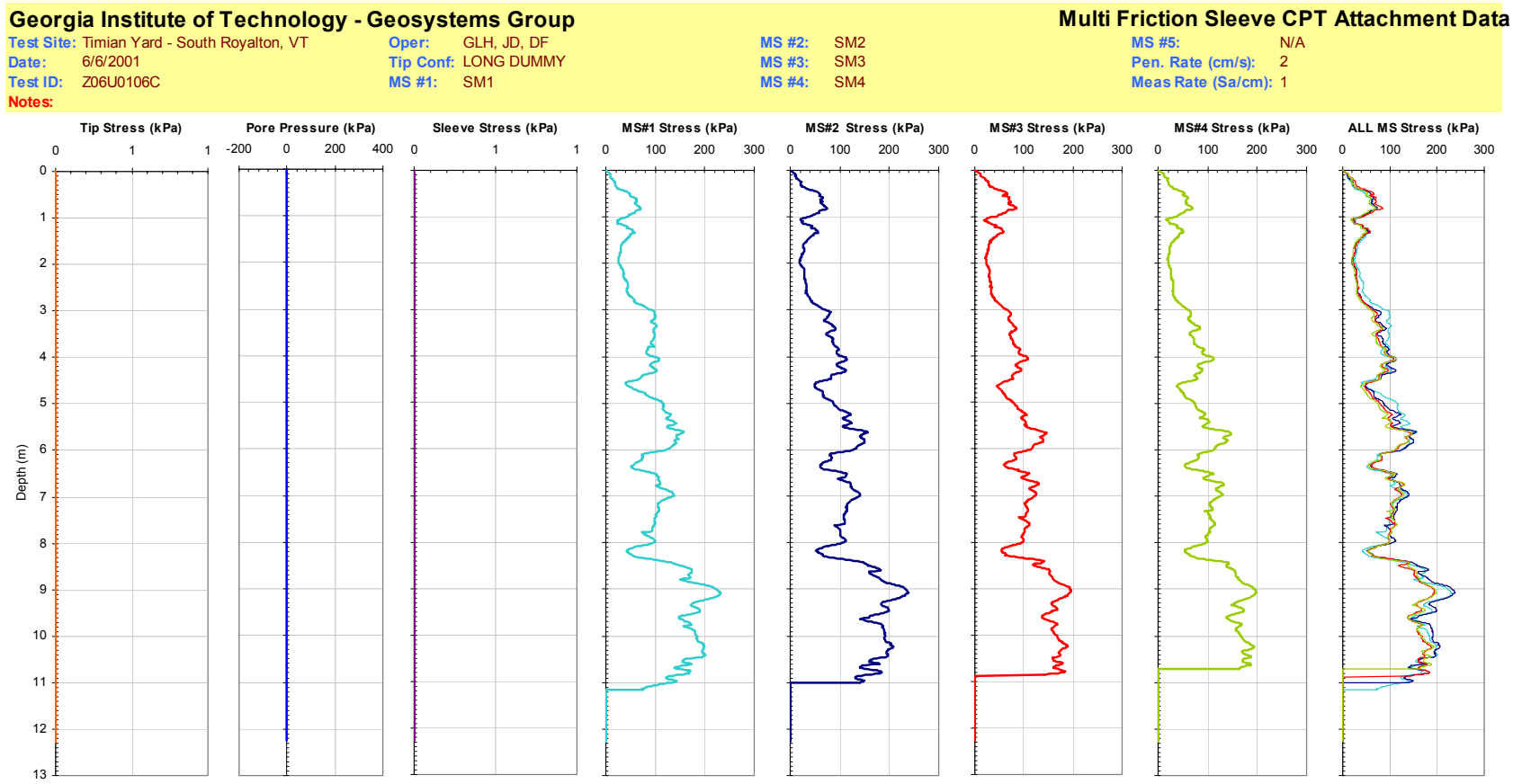

Figure 5-17. Results of an MFSA (SM – SM – SM – SM) Sounding with the Long Uninstrumented Tip (1062 mm) at the South Royalton, Vermont Sand Test Site Highlighting the Response of Four Smooth Sleeves Tested in Series When Located Within Close Proximity to the Tip.

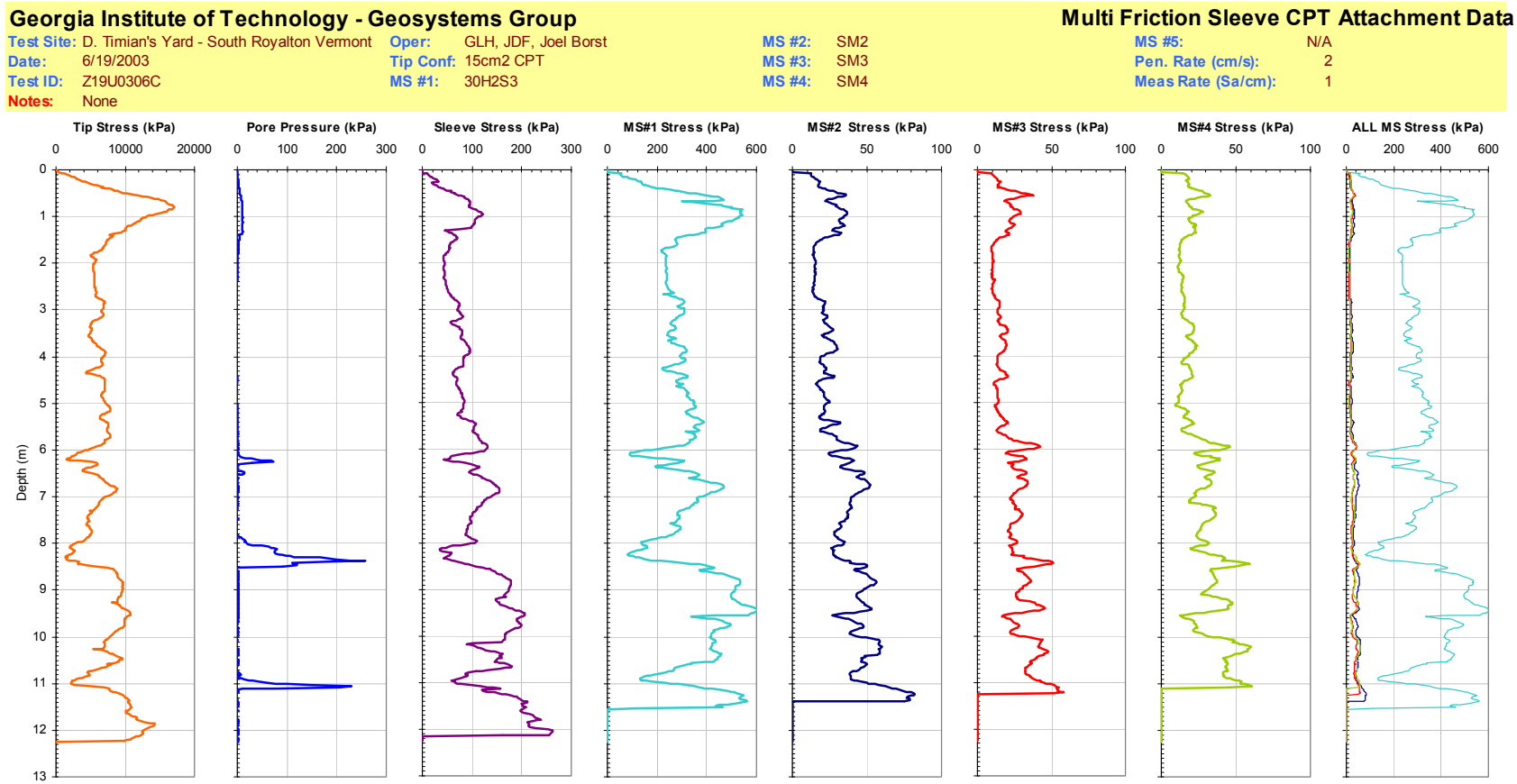

Figure 5-18 Results of a CPTU - MFSA (H2.00 – SM – SM – SM) Sounding at the South Royalton, Vermont Sand Test Site Highlighting the Backshadow Effect for the Highest Sleeve Texture (H2.00).

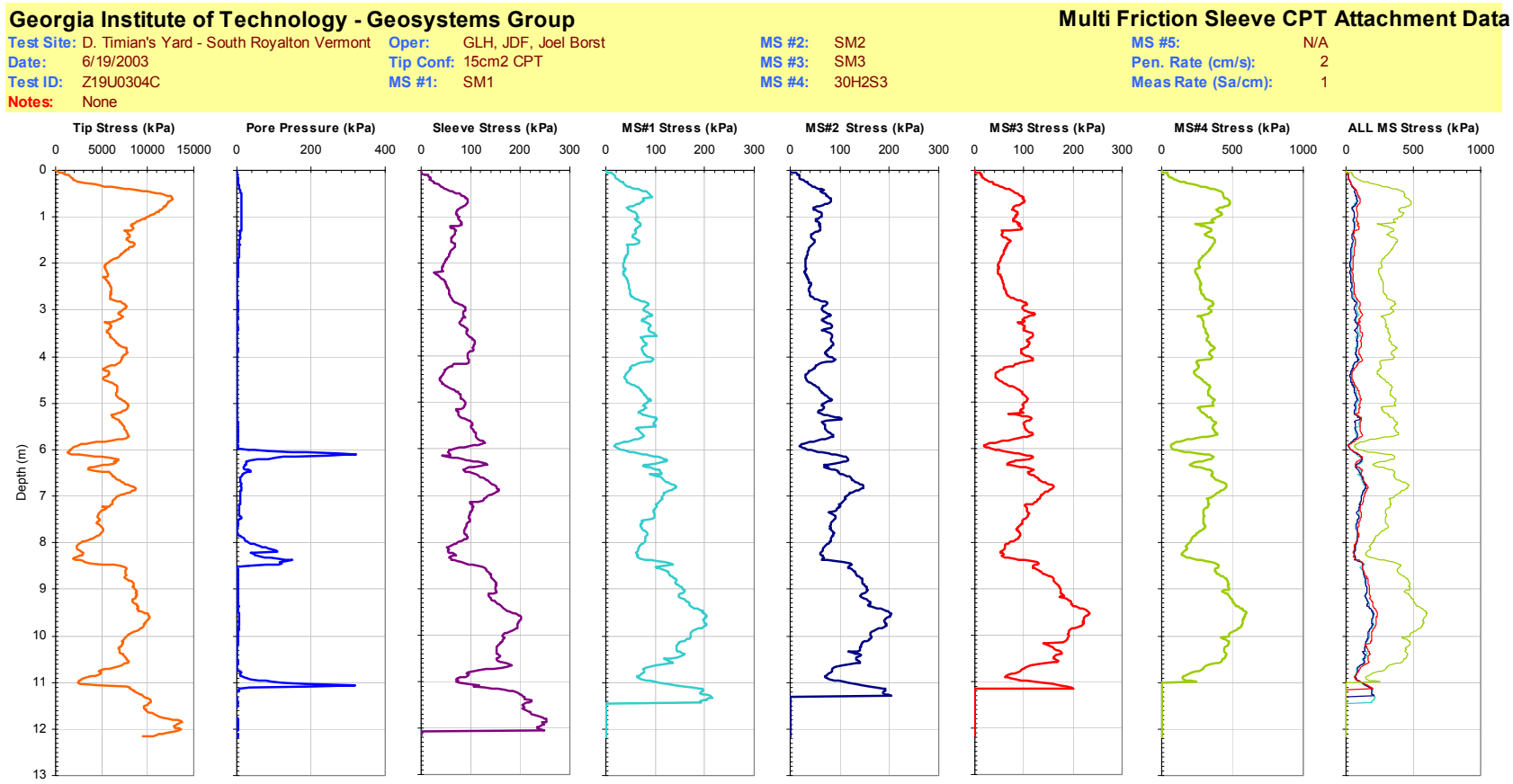

Figure 5-19 Results of a CPTU - MFSA (SM – SM – SM – H2.00) Sounding at the South Royalton, Vermont Sand Test Site Highlighting the Foreshadow Effect for the Highest Sleeve Texture (H2.00).

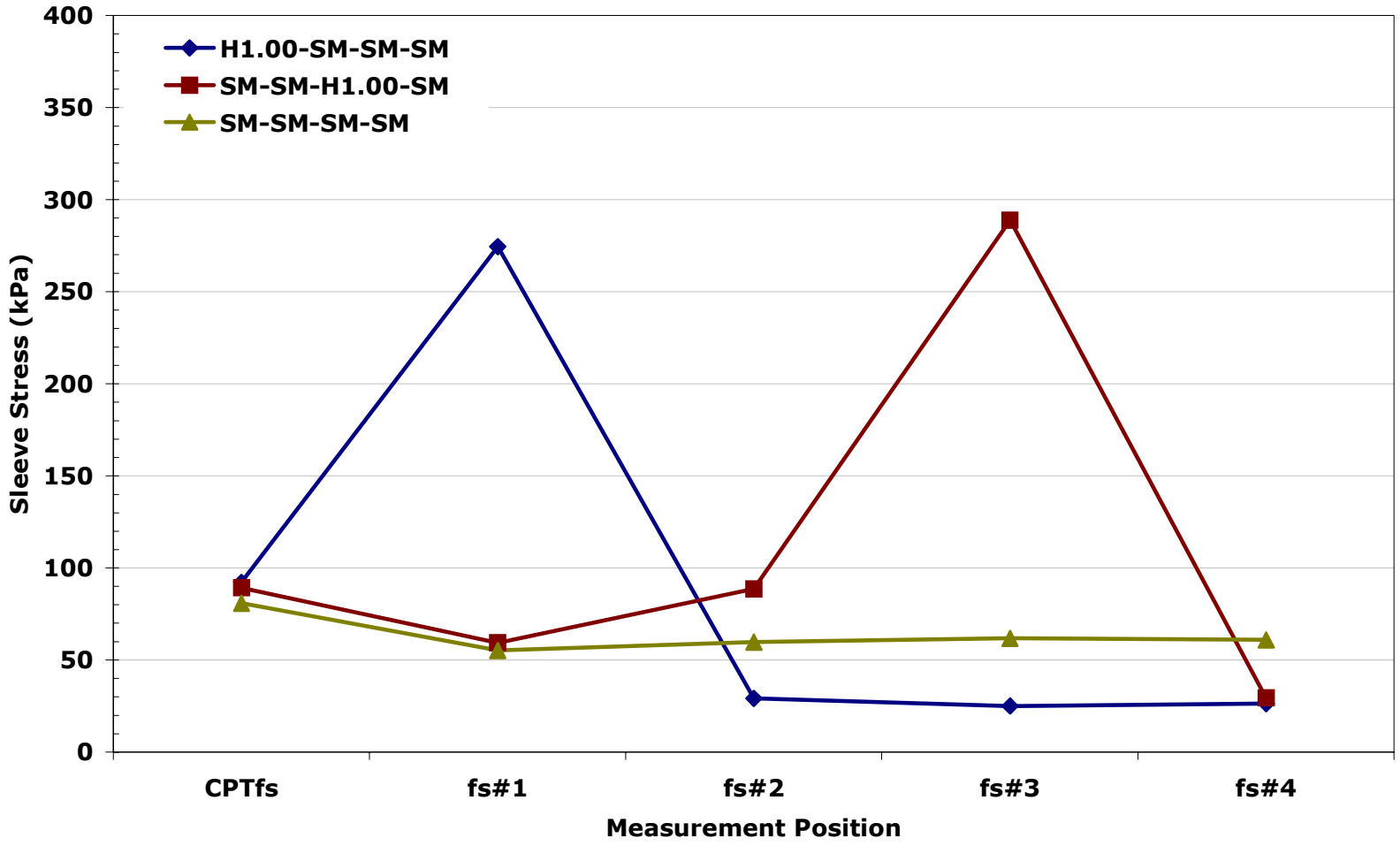

Figure 5-20 Plot Showing the Constant Magnitude of Backshadow Influence For Smooth Sleeves Positioned in Any MFA Position Behind a Textured Sleeve for the Average Sleeve Response at the South Royalton, Vermont Test Sand Test Site.

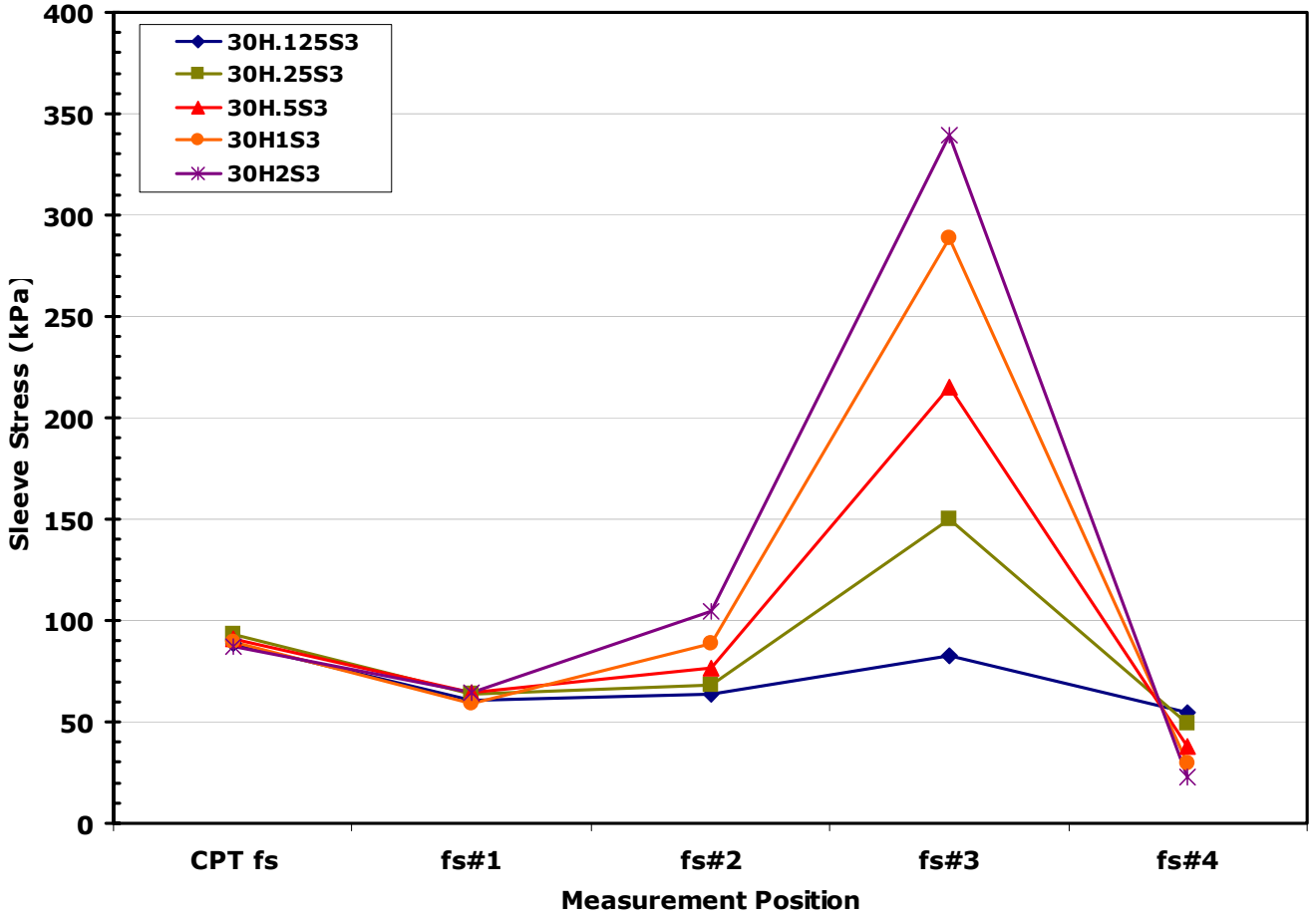

Figure 5-21 Plot Showing the Average Sleeve Stress Measured for MFSA Soundings at the South Royalton, Vermont Sand Test Site for Configurations with Three Smooth and One Textured Sleeve Placed in Position f_{a3} Highlighting the Fore and Backshadow Influence of Various Textures (after DeJong, 2001).

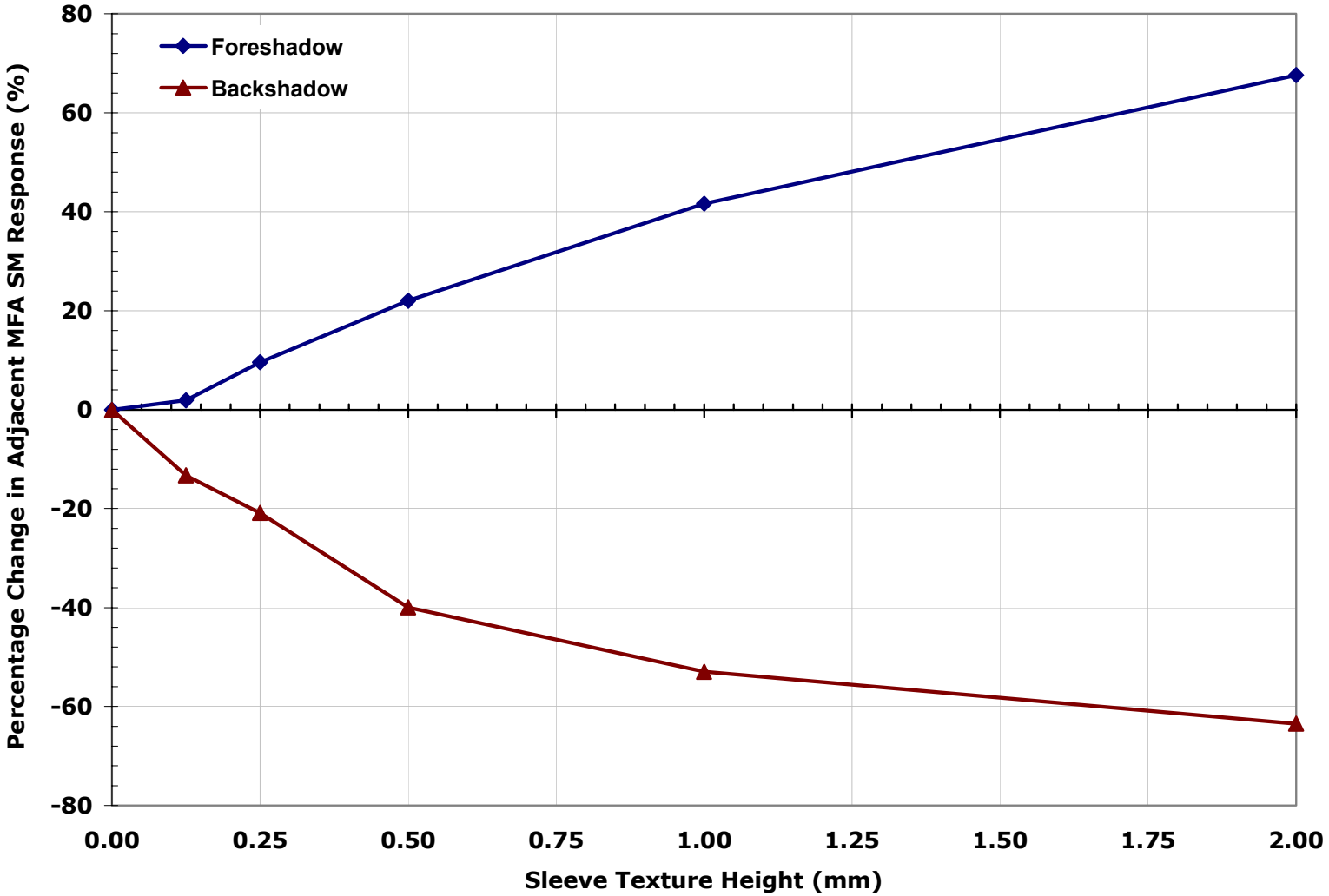

Figure 5-22 Plot Showing the Average Percentage of Fore and Backshadow Effects on Smooth Sleeves Positioned Adjacent to Textured Sleeves in the MFA Device Across a Range of Sleeve Textures. All Results are From the South Royalton, Vermont Sand Test Site For Configurations with Three Smooth and One Textured Sleeve Placed In Position f_{a3}.

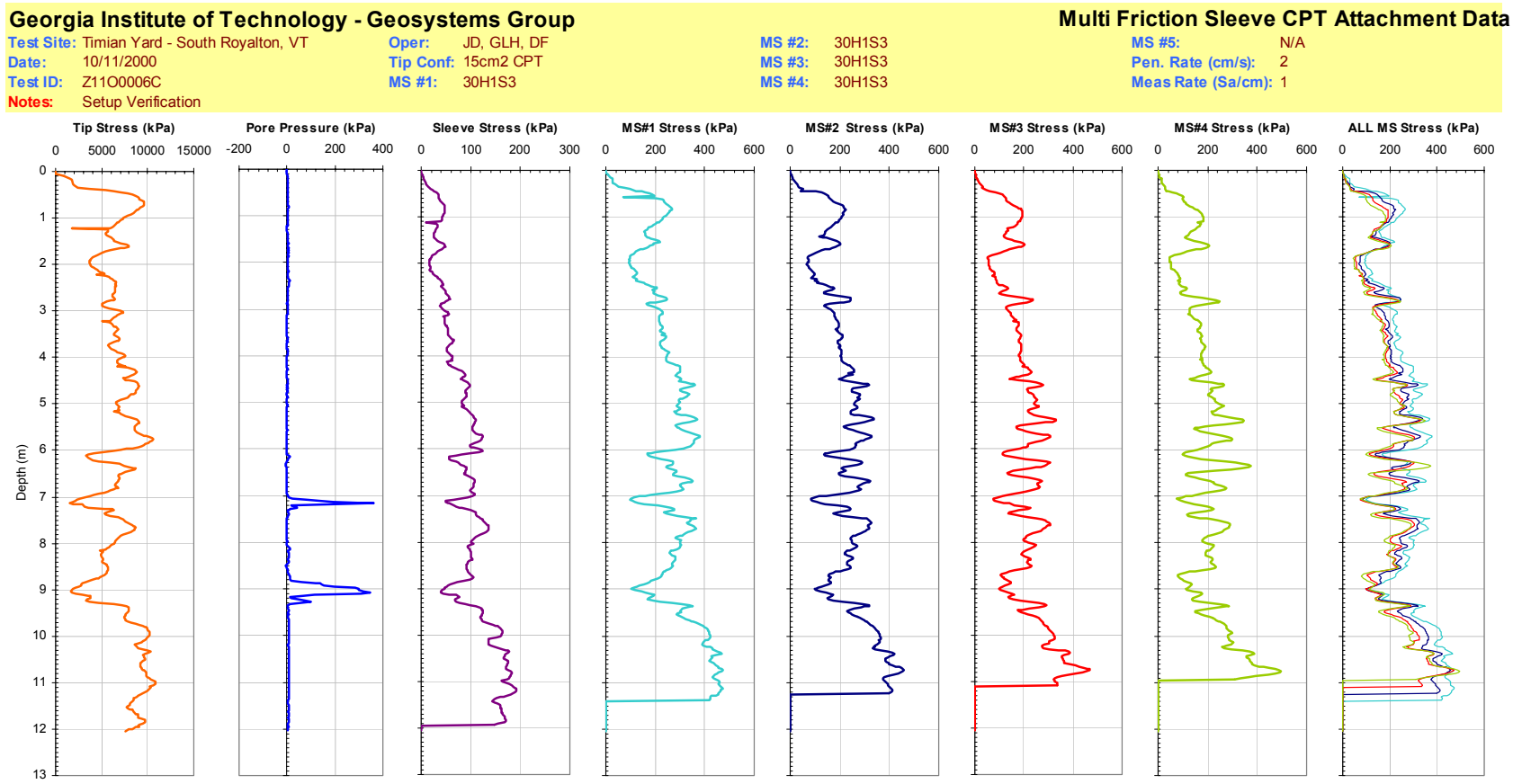

Figure 5-23. Results of a CPTU – MFSA (H1.00 – H1.00 – H1.00 – H1.00) Sounding at the South Royalton, Vermont Sand Test Site Highlighting the Response of Four Equal Textured Sleeve Tested in Series (after DeJong, 2001).

Figure 5-24. Photographs of Textured Sleeves Showing Variations in Textured Length.

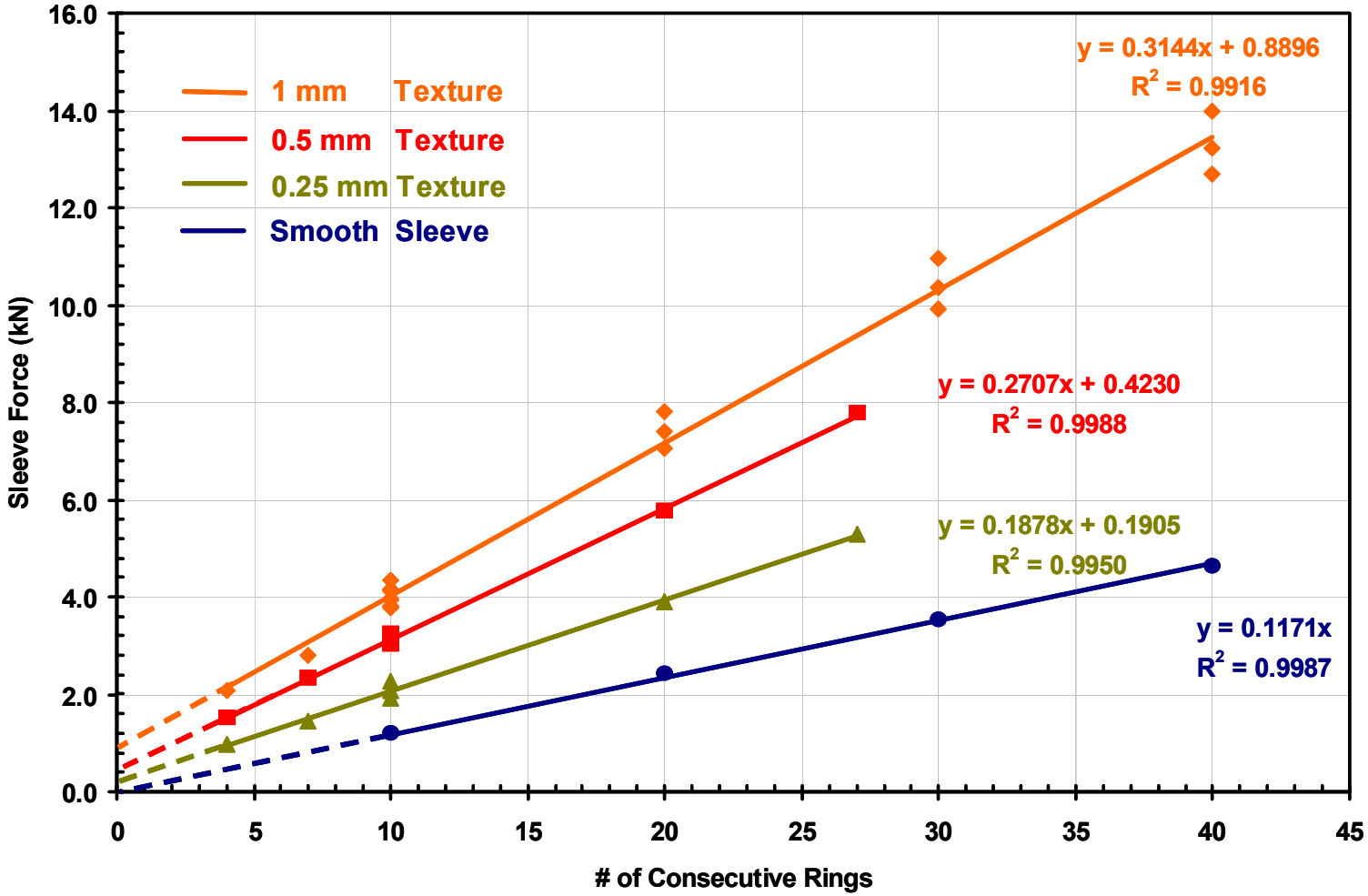

Figure 5-25. Plot Showing the Sleeve Force Measured on Sleeves of Varying Roughness as a Function of Textured Length (10 Rings of Texture = 110 mm, or a Full MFSA Friction Sleeve). The y-Intercept is Equivalent to the Annular Penetration Force (APF) Registered at the South Royalton, Vermont Test Site.

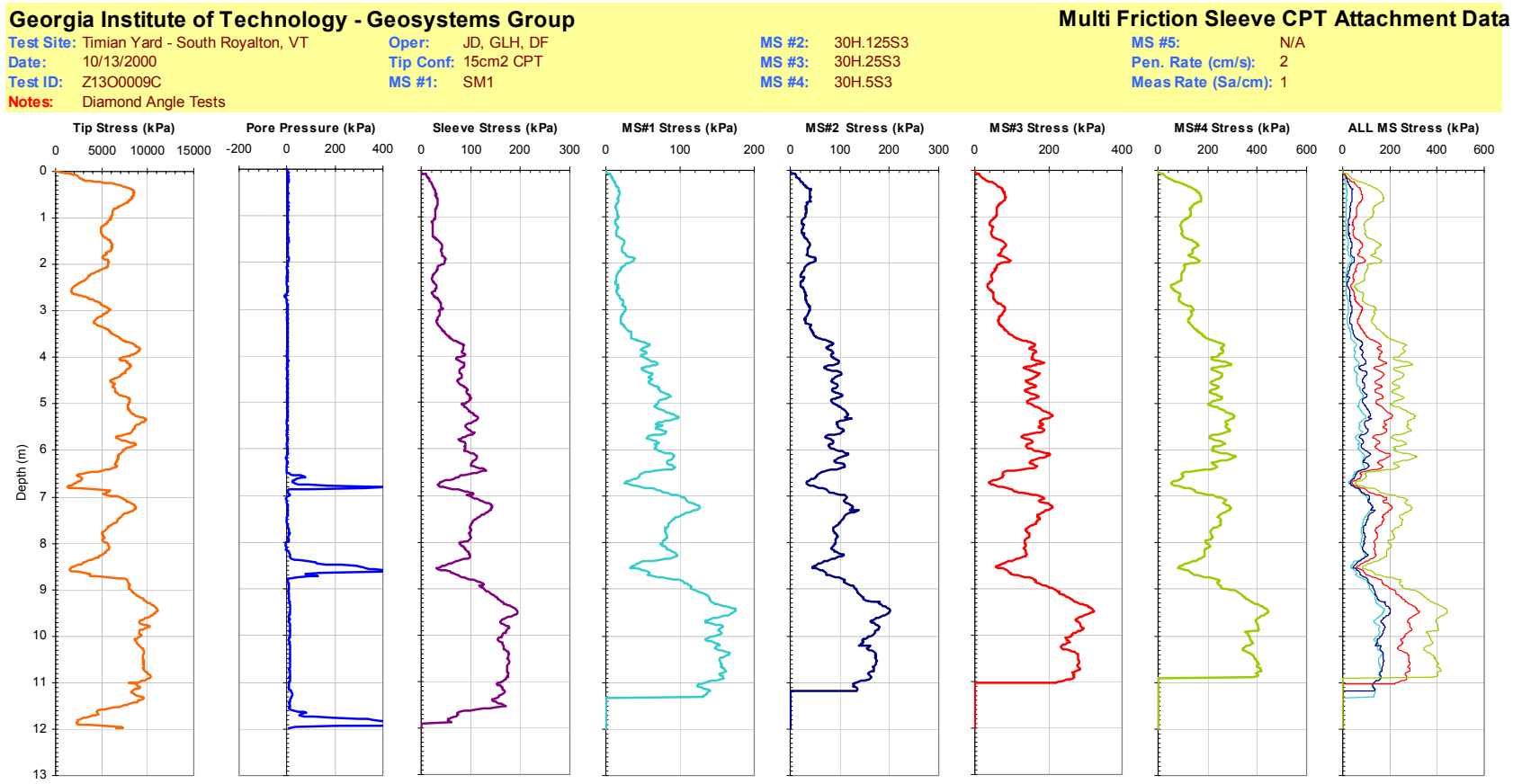

Figure 5-26 Results of a CPTU - MFSA (SM – H0.125 – H0.25 – H0.50) Sounding at the South Royalton, Vermont Sand Test Site Highlighting the Response of Sensors Sequenced in Order of Increasing Texture. (after DeJong, 2001).

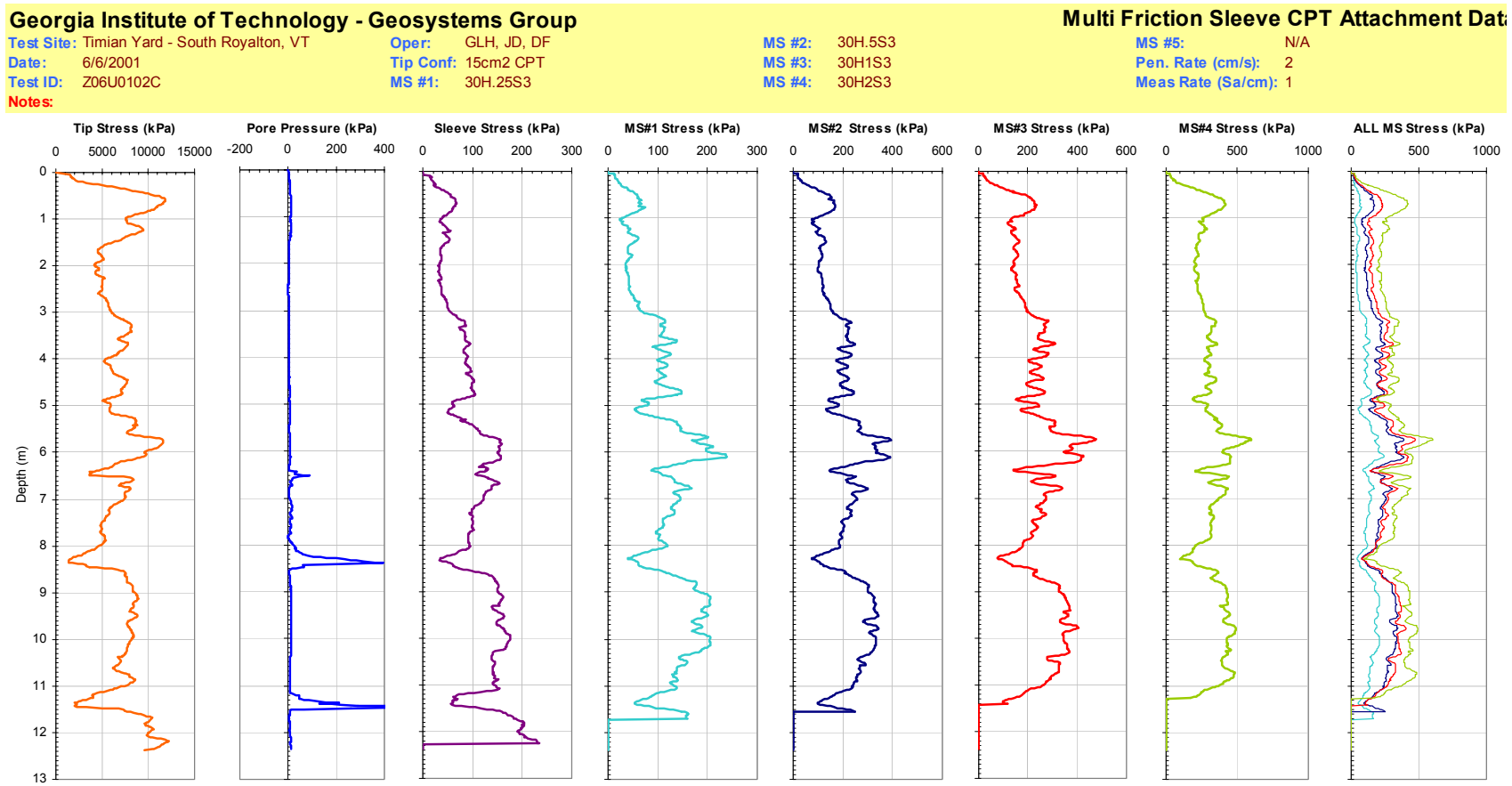

Figure 5-27 Results of a CPTU - MFSA (H0.25 – H0.50 – H1.00 – H2.00) Sounding at the South Royalton, Vermont Sand Test Site Highlighting the Response of Sensors Sequenced in Order of Increasing Texture.

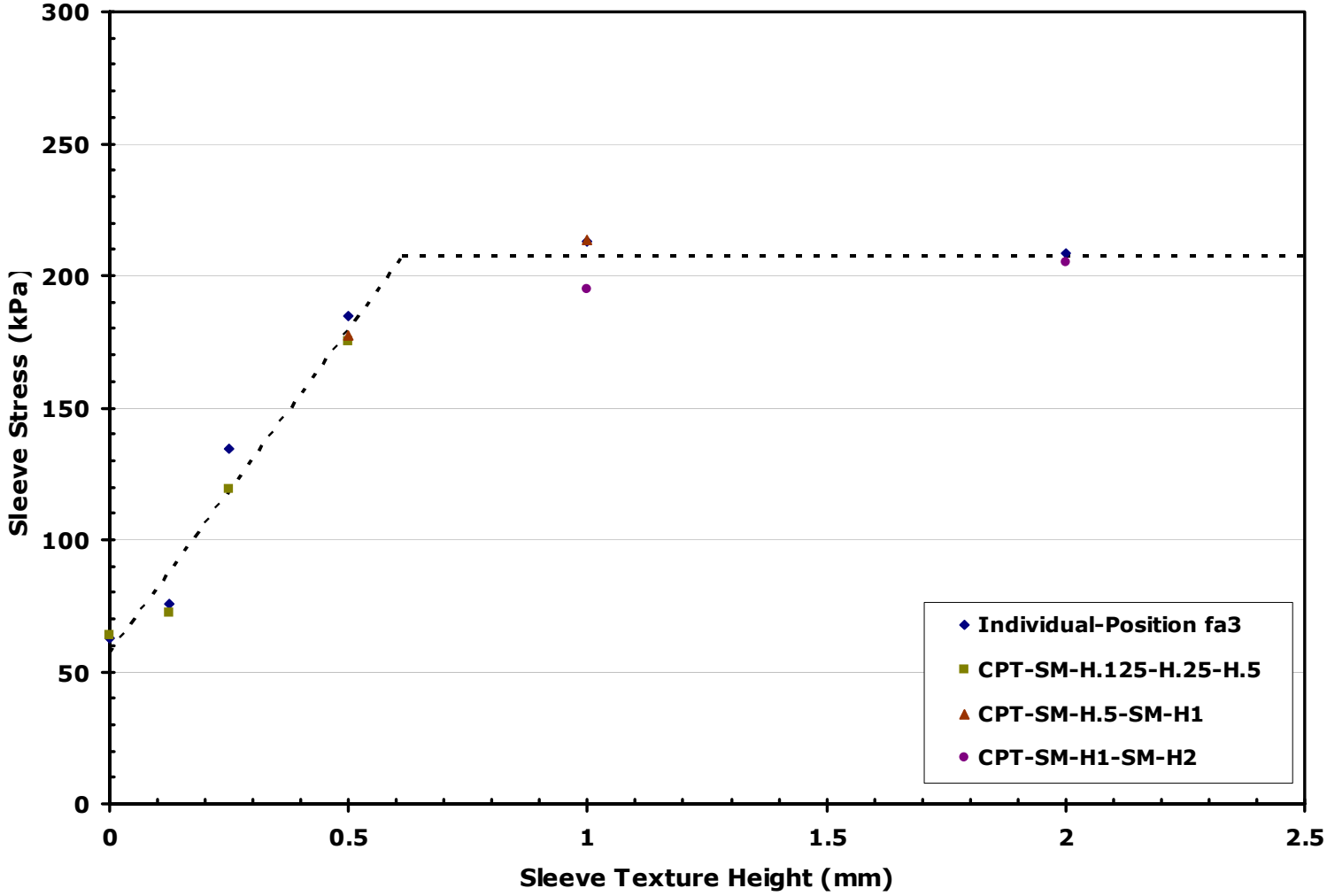

Figure 5-28 Bilinear Interface Strength – Surface Texture Relationship Plotted for MFSA In Situ Data (after DeJong and Frost, 2005).

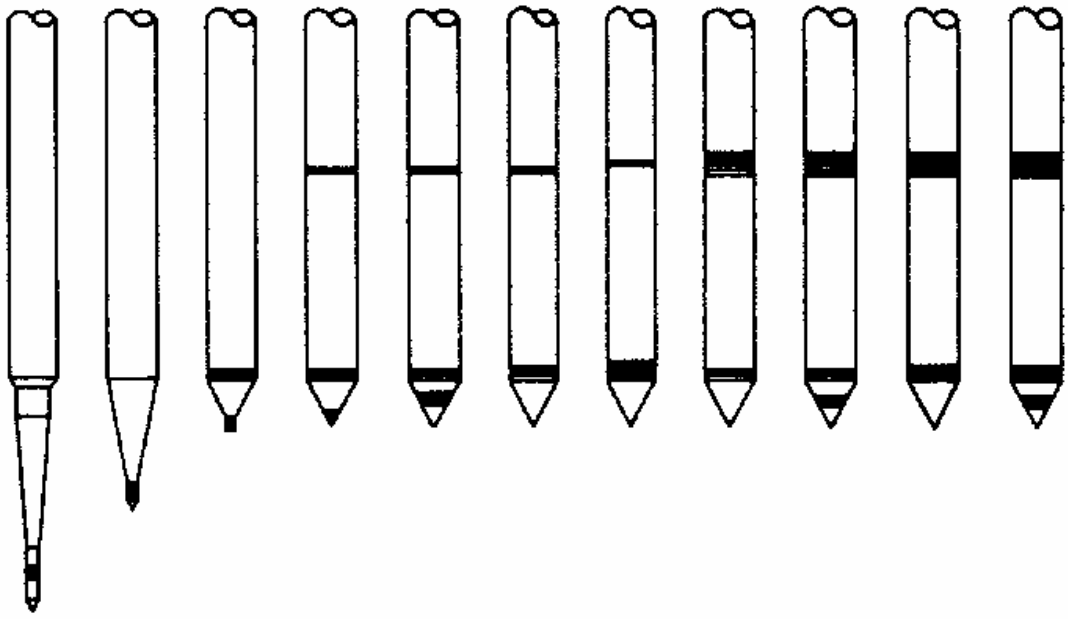

Figure 5-29. Examples of Penetrometers with Varying Pore Pressure Sensor Locations as of 1988 (Campanella and Robertson, 1988).

Figure 5-30. Photograph of 50 and 100 mm Spacers Designed to Allow for the Testing of Intermediate Sleeve Spacings with the MFSA Device to Determine the Influence Range of Foreshadow Effects.

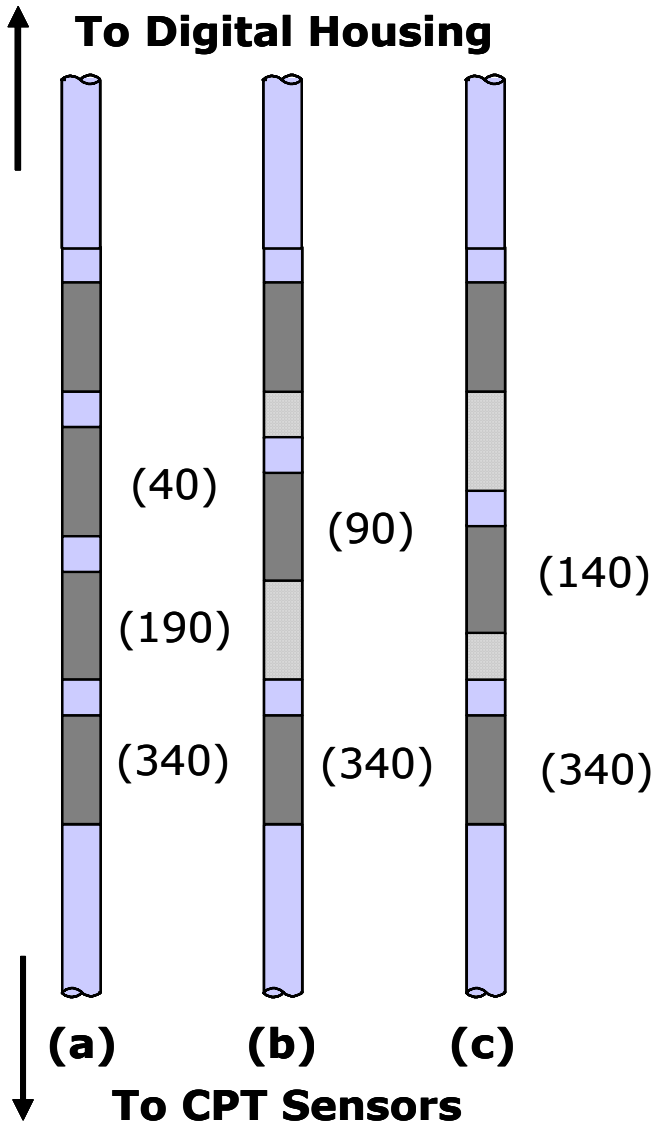

Figure 5-31. Schematic Detailing the Distance Between Sleeve f_{a4} and the Other Sleeves for (a) Conventional MFSA Setup, (b) 5 mm Spacer Positioned Adjacent to f_{a4}, (c) 10 mm Spacer Positioned Adjacent to f_{a4}, Bracketed Numbers Indicate Sleeve Spacing in mm.

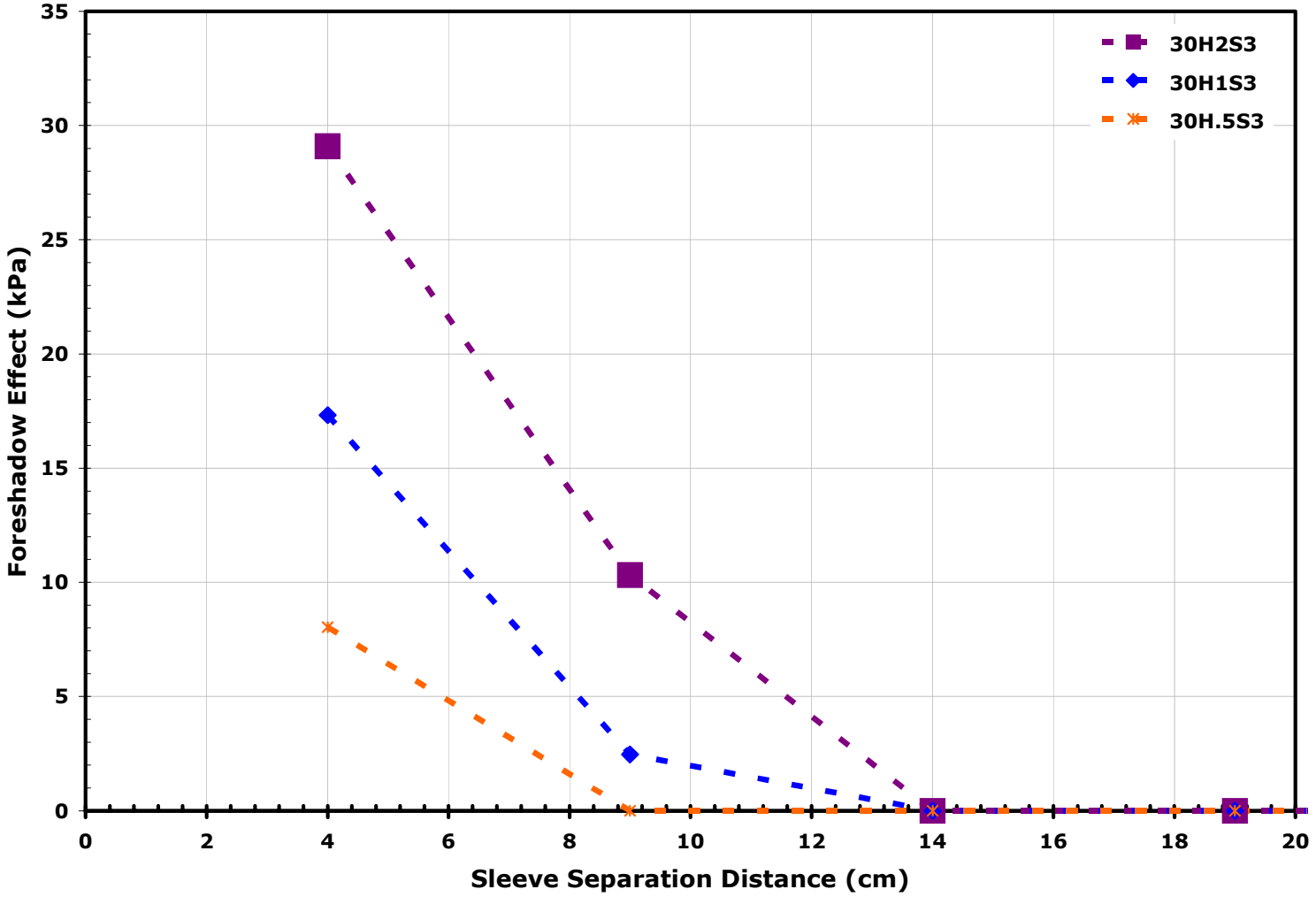

Figure 5-32 Plot of the Foreshadow Influence Caused by Textured Sleeves of Varying Texture Height at the South Royalton, Vermont Sand Test Site as a Function of Sleeve Separation Distance.

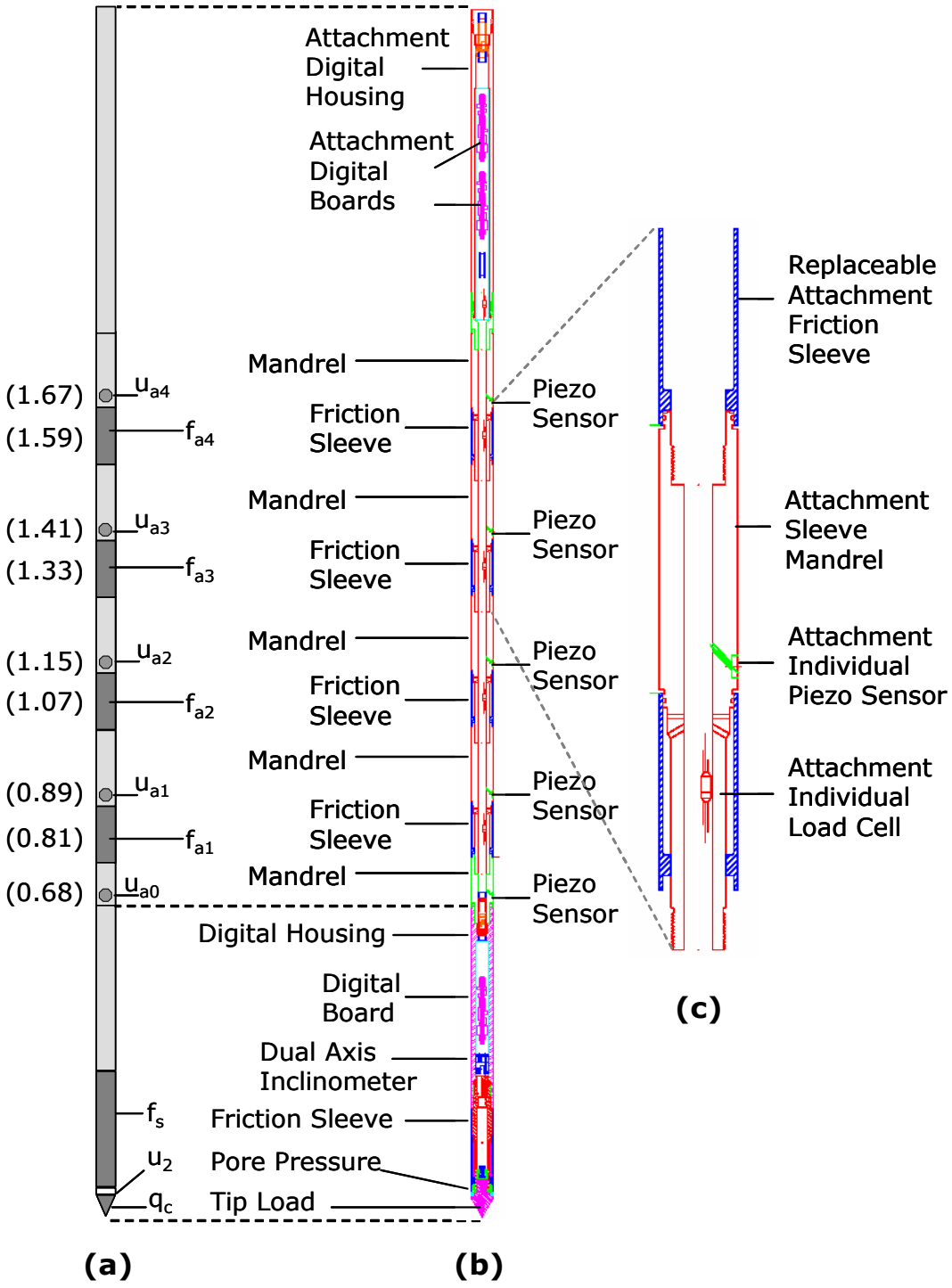

Figure 5-33. Multisleeve Piezo Friction Attachment Configured with Conventional CPTU Module. (a) Schematic - Brackets Indicate Sensor Offset From Tip in Meters, (b) Design Detail, and (c) Piezo Friction Sleeve Mandrel Design Detail.

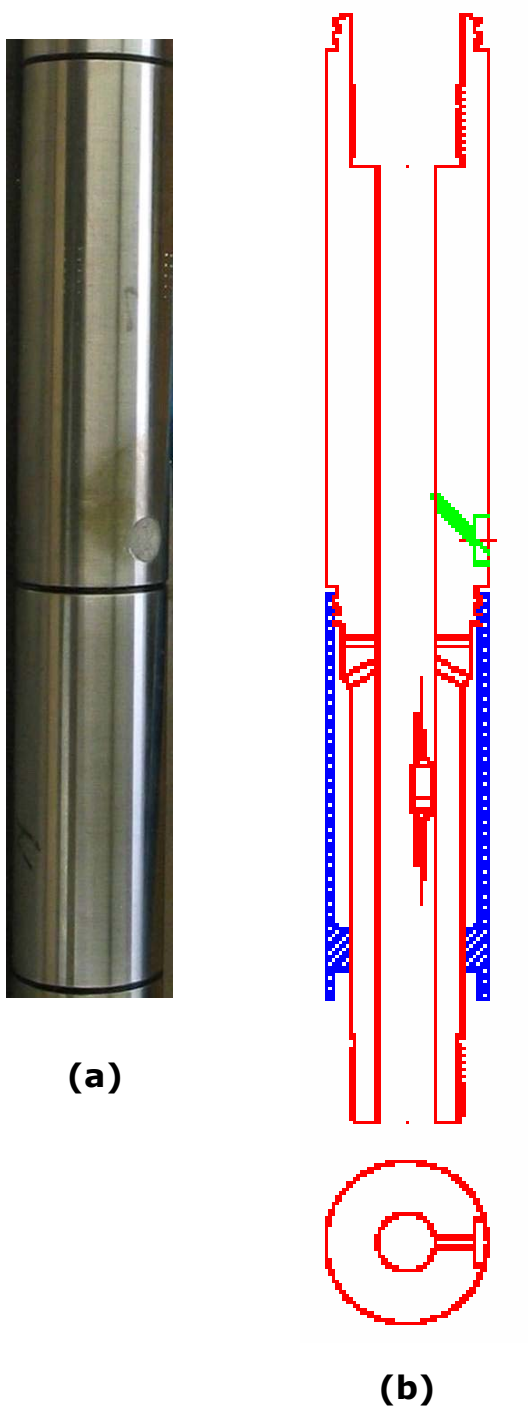

Figure 5-34. MPFA Piezo Friction Mandrel (a) Photograph, (b) Design Detail.

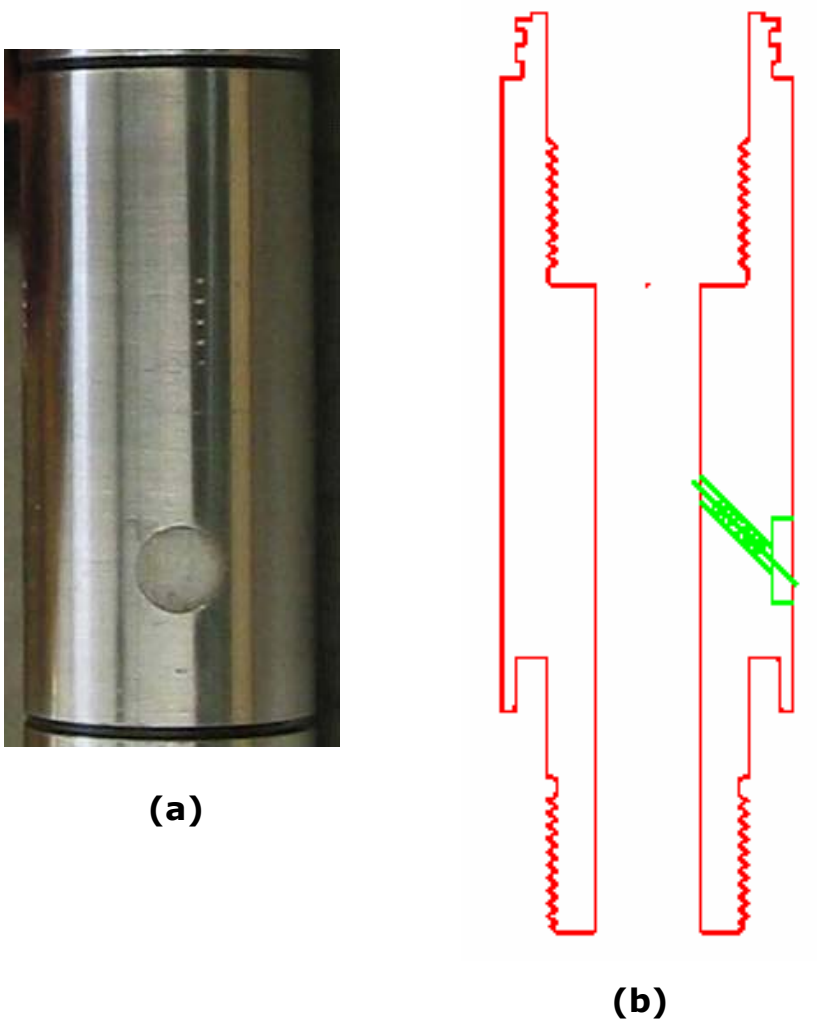

Figure 5-35. MPFA Baseline Piezo Mandrel (a) Photograph, (b) Design Detail.

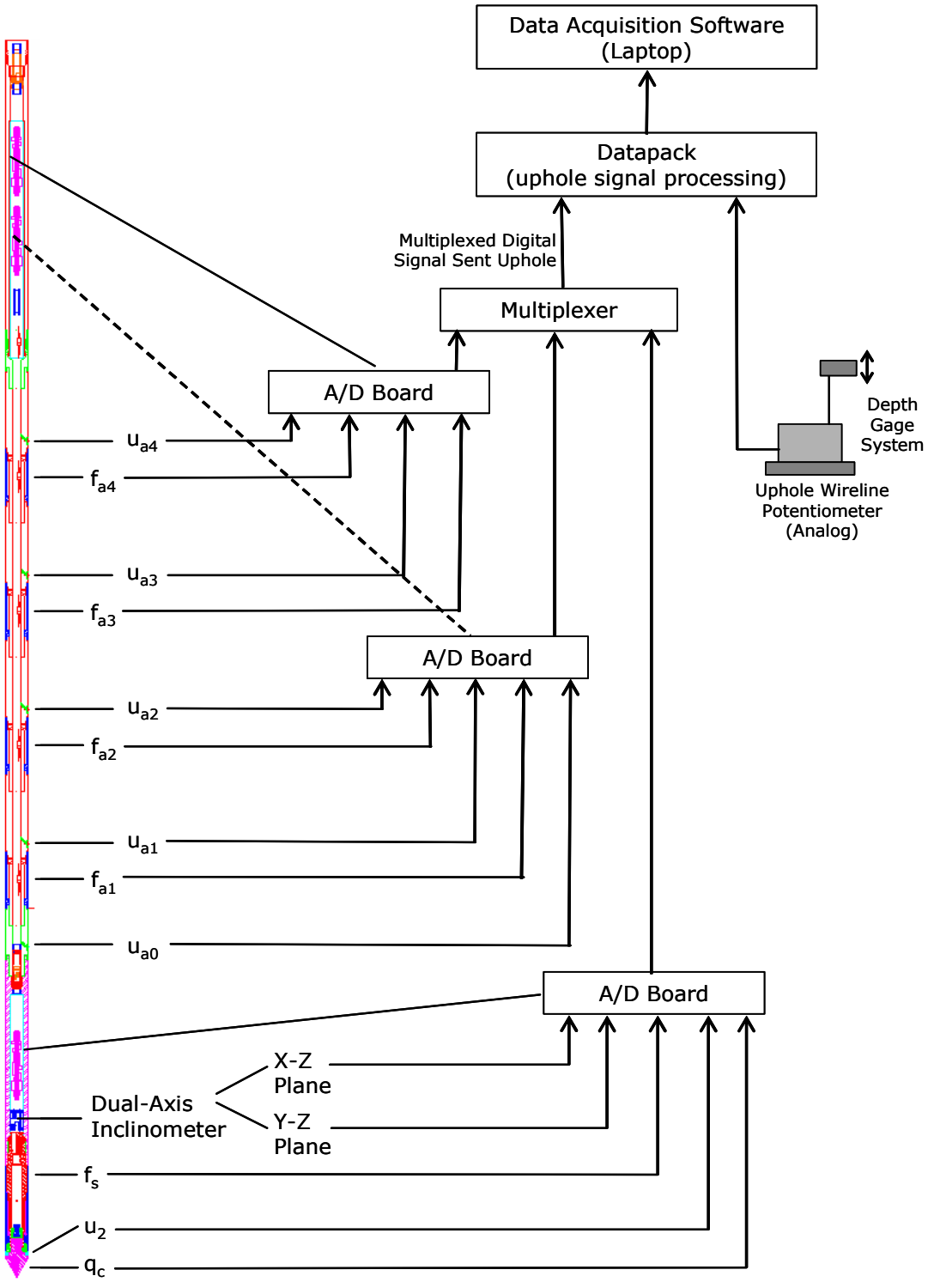

Figure 5-36. Schematic of the CPTU - MPFA Data Acquisition Architecture.

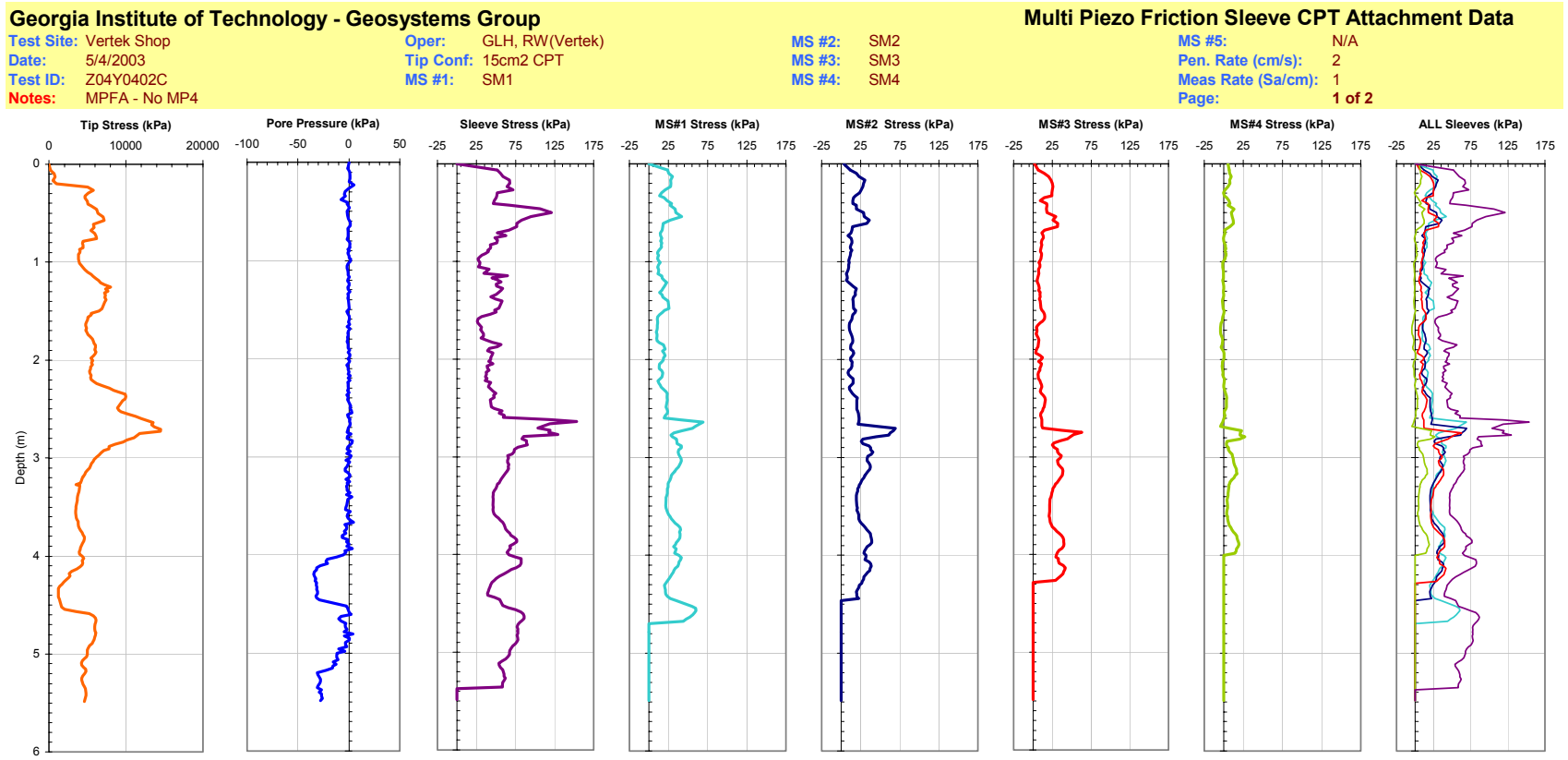

Figure 5-37a. Plots of All CPTU and the MPFA Friction Sensors from Sounding MPFA_1 at the SRVT Site. Verification of MPFA Device Operation, Test 1 of 2.

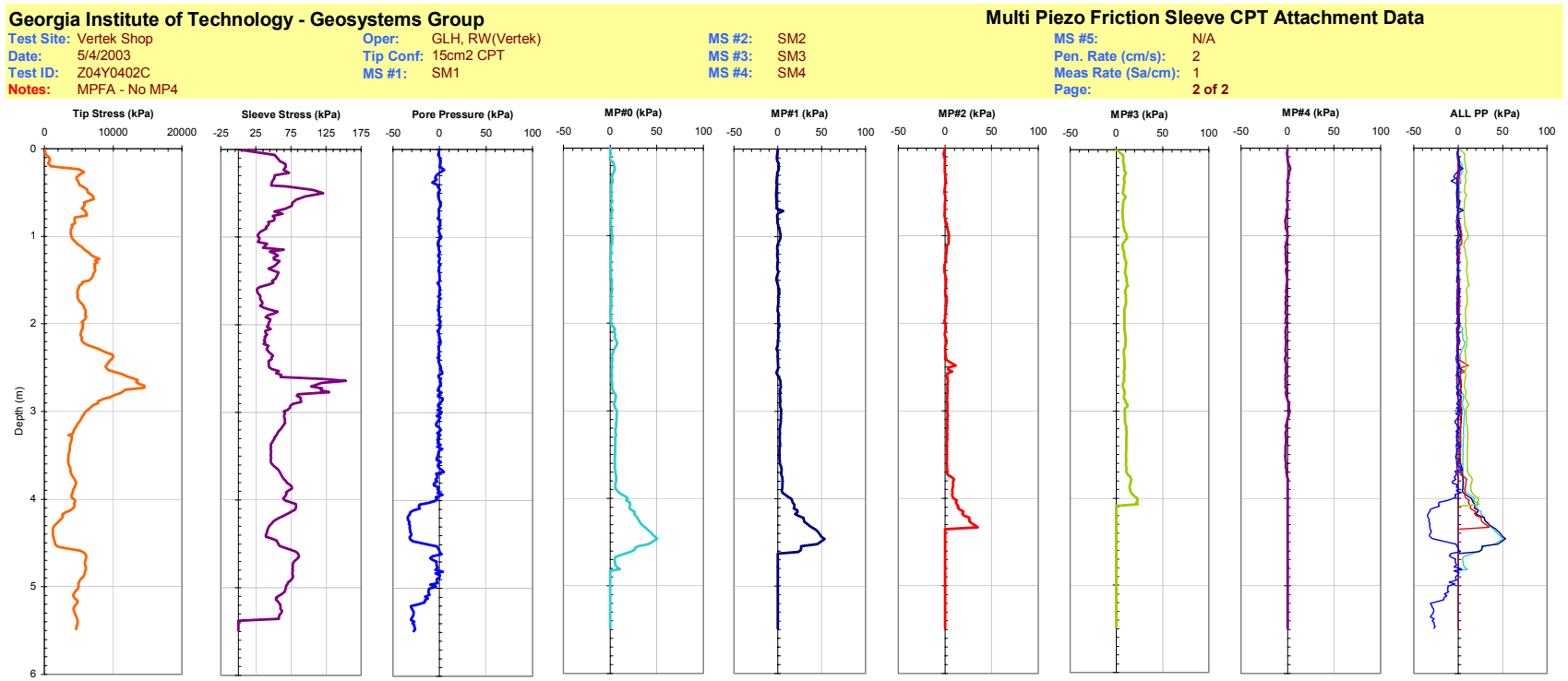

Figure 5-37b. Plots of All CPTU and the MPFA Piezo Sensors from Sounding MPFA_1 at the SRVT Site. Verification of MPFA Device Operation, Test 1 of 2.

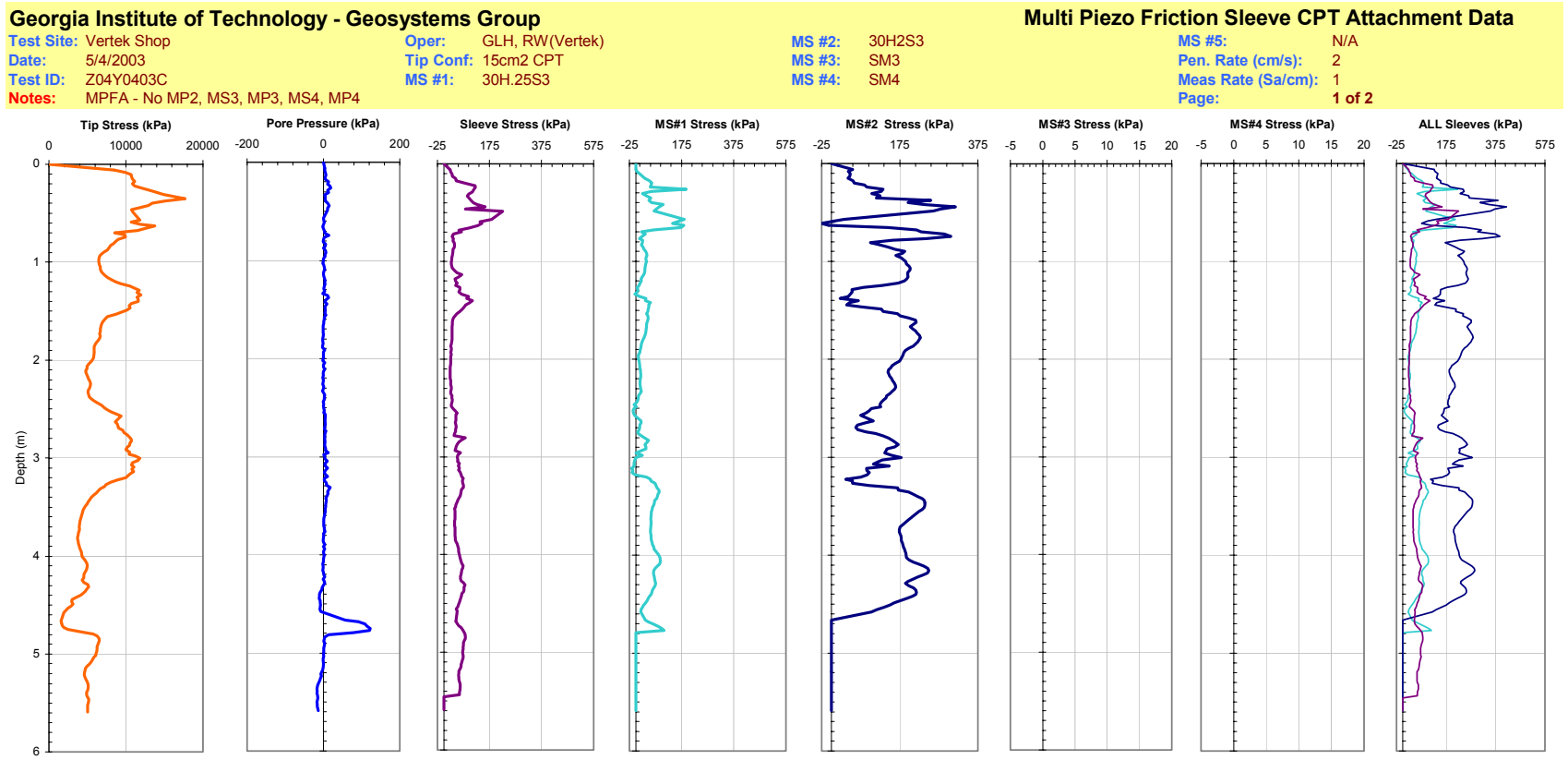

Figure 5-38a. Plots of All CPTU and the MPFA Friction Sensors from Sounding MPFA_2 at the SRVT Site. Verification of MPFA Device Operation, Test 2 of 2.

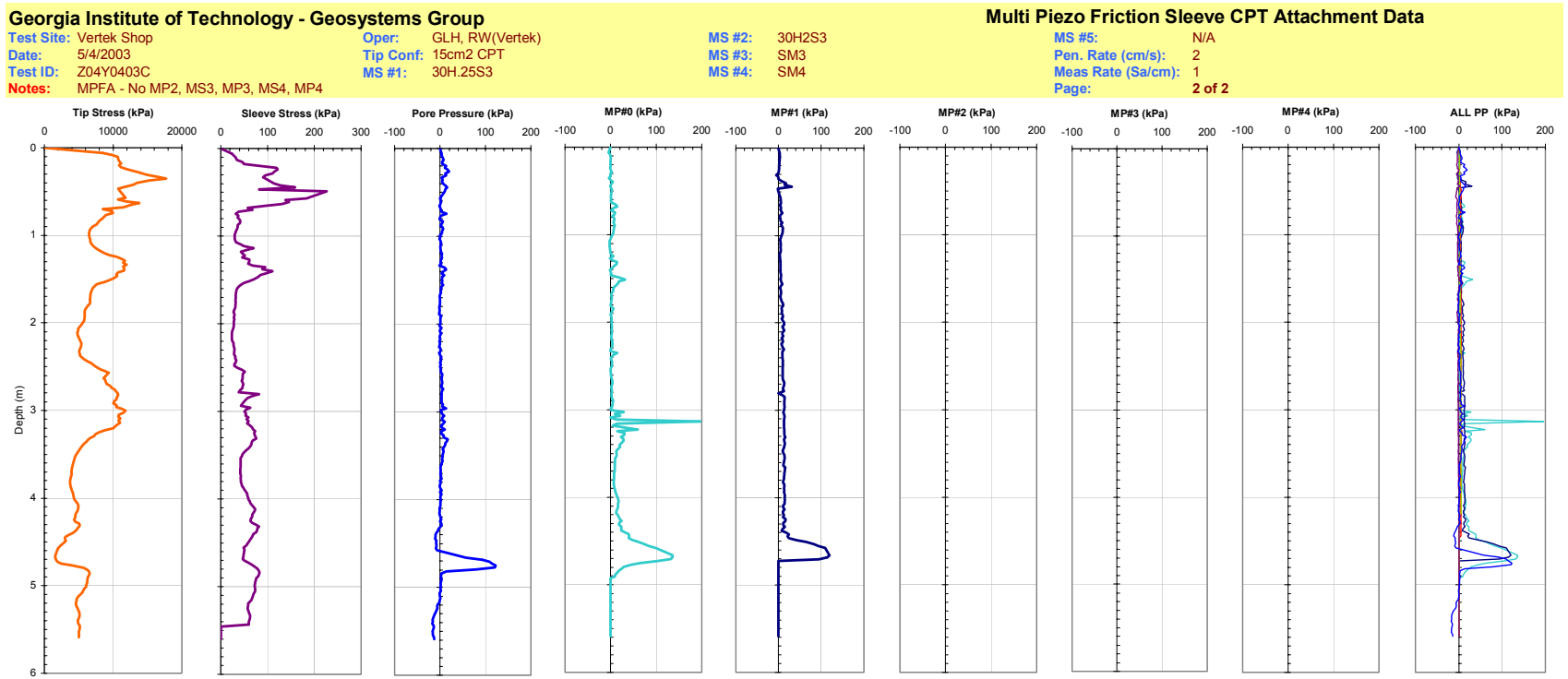

Figure 5-38b. Plots of All CPTU and the MPFA Piezo Sensors from Sounding MPFA_2 at the SRVT Site. Verification of MPFA Device Operation, Test 2 of 2.

Chapter VI
In Situ Investigations of Geotechnical Interface Behavior

6.1 Introduction

Throughout the course of the current work, a number of investigations into in situ interface behavior were conducted with both the multi friction attachment (MFA) and the multi piezo friction attachment (MPFA). This chapter presents investigations undertaken with the MFA and MPFA devices to investigate the behavior of smooth and textured sleeves across a range of soil properties, surface roughness conditions, and sensor locations. All presented investigations were conducted at one of seven sites that are described herein.

6.2 Overview of MFA and MPFA Testing

6.2.1 Summary of MFA and MPFA Testing

A total of 159 penetrometer soundings have been performed as part of the research and development effort at Georgia Tech into the use of advanced penetrometer technologies to assess the in situ interface behavior of soils. Table 6-1 summarizes all soundings conducted to date with the MFA device, with Table 6-2 summarizing the MPFA soundings. The first 9 soundings listed were conducted without the assistance of the author, and are summarized in DeJong (2001) and DeJong and Frost (2002). The author assisted in performing MFA soundings 10 to 39, which are summarized in detail by DeJong (2001) and Frost and DeJong (2005). The remaining soundings were specifically conducted by the author for the current study. Some of these sounding were

used in Chapter 5 to demonstrate generic MFA and MPFA response for varied sleeve friction roughnesses and penetrometer tip configurations. A detailed overview of the site conditions and geology at each site utilized for MFA and MPFA investigations to date is described in Section 6.2.2, with plots from the current study included in Appendix A.

6.2.2 Overview of Test Sites from the Current Study

A total of seven test sites have been investigated to date with the MFA and MPFA devices. These sites are located across the United States and Australia, with relevant site details described herein, and summarized in Table 6-3.

6.2.1.1 South Royalton, Vermont (SRVT) Test Site

As briefly described in Chapter 5, the South Royalton, Vermont (SRVT) test site was used in the majority of the initial investigations with the MFA unit, with a total of 94 soundings conducted at this site. The SRVT test site is comprised of glacial outwash material consisting mainly of uniform fine sand of loose to medium density. The typical profile consists of clean sand to a depth of approximately 6.5 m, followed by silty sand and sand interspersed with silt and clay seams to the extent of the current investigations, at a maximum depth of 30 m. Thin silt seams on the order of 0.3 m thickness at approximately 6.5 and 8.5 m depth can be seen in all profiles at the SRVT site. The site was found to be relatively laterally homogenous with minor variations in subsurface layer thickness and depth. The lateral variability of the site was observed by monitoring the CPTU measurements for applicable soundings. Several discrete samples were collected and basic index properties are summarized in Figure 6-1 after DeJong (2001). Figure 6-2

details the layout of the soundings conducted at the SRVT site over the course of all Georgia Tech investigations (DeJong, 2001).

6.2.2.2 Loose Sand (LS) Test Site

As part of a site investigation conducted by a geotechnical firm, the author was able to conduct 21 CPTU-MFA soundings at a sand site with a layer of very loose sand possibly susceptible to liquefaction. The upper sand layer (surface to 8.5 m depth) consists of fine clean sand of medium density, with the loose layer (between 9 to 11 m depth on average) consisting of fine sand with included black non plastic fines on the order of 3% of the total mass. The sand layers are underlain by a calcareous silt material known locally as the Cooper Marl, and described in detail in Section 6.2.4. Detailed properties of the upper and lower sand layers at the LS test site are presented in Table 6-4.

6.2.2.3 Vertek Shop Parking Lot (VSPL) Test Site

In the initial verification tests of the MPFA device, two CPTU-MPFA soundings were conducted in the Parking Lot of the Vertek shop. The tests were conducted to a shallow depth. The general geology of the site consists of a glacial till consisting primarily sand, silty sand, and gravely sand with included cobbles. The general site profile can be discerned from the CPTU data obtained during the MPFA soundings presented in Section 6.3.

6.2.2.4 Mount Pleasant, South Carolina (MPSC) Test Site

Two MPFA soundings were conducted at a site near Charleston, South Carolina to assess the response of MPFA sensors in a sandy clay to sandy silt formation known locally as the Cooper Marl. The Cooper Marl is predominantly calcareous in composition,

and comprised of the skeletal remains of microscopic sea organisms, quartz sand, phosphate, and clay minerals. The Cooper Marl has a typical standard penetration test N-value ranging from 10 to 20, is stiff to very stiff in consistency, olive in color, open in structure, and high in moisture content (40 to 60 percent). Typical properties of the Cooper Marl include an undrained shear strength ranging from 100 to 200 kPa, OCR ranging from 4 to 6, and a peak friction angle on the order of $\phi'_p = 44°$ (Camp, 2004). Disturbance and collapse of the open structure of the Cooper Marl is known to produce very large excess pore pressures during cone penetration and pile driving operations, and typically shows a large reduction in pile shaft resistance with increased disturbance and stress reversals (Camp, 2004). The Cooper Marl is located between depths of approximately 13 and 20 m at the MPSC test site overlain by layers of sand and sandy silt and overlying a cemented strata. More information regarding the Cooper Marl geology can be found in Camp (2004).

6.2.2.5 Shenton Park Western Australia (SPWA) Test Site

The Shenton Park site is located in the suburbs of Perth, Western Australia on an educational reserve operated by the University of Western Australia (UWA). The site geology consists of surficial aeolian silicaceous sand of loose to medium density overlying variably cemented limestone, with intermittent limestone spires at varied spacing and depth. The sand is part of the Spearwood Dune system, and consists of well graded fine to medium quartz grains with traces of feldspar, with a critical state friction angle $\phi'_{cs} = 34°$ obtained from direct shear tests of the surficial soils (Byrne and Randolph, 2003). The sand grains range from sub-rounded to sub-angular in shape and the in situ bulk density is relatively uniform with depth on the order of 1670 ± 25 kg/m^3

(Lehane et al., 2004). Fundamental soil index properties for the Shenton Park sand are provided in Figure 6-3, with the ground water table located at approximately 6 m depth during the current investigations. Figure 6-4 details the relative locations of the soundings conducted at the SPWA site during the current investigation.

6.2.2.6 Ledge Point Western Australia (LPWA) Test Site

Ledge Point is a small coastal community located approximately 100 km north of Perth, Western Australia along the coast of the Indian Ocean. The current testing was conducted on the beach, to depths on the order of 12 m, or until encountering the underlying limestone. The Ledge Point soil is a coastal aeolian calcareous soil, and is part of the Quindalup dune system, a narrow strip of calcareous sand dunes that formed along the shoreline of the Perth coastal plane in the past 10,000 years (Sharma, 2004). A typical grading curve of the LPWA soil is shown in Figure 6-5. The soil consists of calcareous uniform fine sand (SP). The D_{50} grain size is 0.24 mm, the sand has less than 5 percent fines, and the maximum void ratio ranges from approximately 1.2 to 1.4. Typical microscopic images of LPWA soil obtained from Ismail (2000), presented in Figure 6-6, suggest that the majority of the LPWA soil is comprised of bioclastic grains with discernible marine organisms. The soil consists of a variety of particle shapes, with the predominant shapes being angular to subangular. The critical state friction angle was found to be ϕ'_{cs} = 39.3° from triaxial tests completed by Sharma (2004). Figure 6-7 details the relative locations of the soundings conducted at the LPWA site during the current investigation.

6.2.2.7 Burswood Western Australia (BWDWA) Test Site

The Burswood site is located along the Swan River, two kilometers upstream from the centre of Perth, Western Australia. The water table was located between the ground surface and 0.5 m below ground surface over the course of the current investigations. Previous fluctuations in water table have created a lightly overconsolidated region in the upper few meters. The main geologic formation consists of soft, high plasticity clay (LL=60 to 80, PI=40 to 50) with shell fragments and silt lenses. The base depth of the clay deposit in the areas tested varies from approximately 14 to 19 m. Above a depth of approximately 12 m, the soil contains shell fragments and silt lenses. The typical stratigraphy at the site consists of a 3 m thick overconsolidated crust interlayered with thin sand layers, underlain by the soft clay layer consisting of a gradually increasing shear strength profile from a minimum of about 16 kPa at 4 m depth to 35 kPa at 17 m depth, with an apparent OCR due to ageing of 1.5 to 2. The sensitivity based on field vane data shows values between 4 and 9 above 7 m, and between 2 and 4 below 7 m (Chung and Randolph, 2002). The saturated unit weight of the clay is between 14 and 14.5 kN/m^3 at depths above 6 m, increasing to 16 kN/m^3 at 13 to 14 m depth before reverting to around 14.5 kN/m^3 at greater depths. Figure 6-8 shows profiles of Atterberg limits, water contents and unit weights at the BWDWA site from Schneider et al. (2004). Figure 6-9 details the relative locations of the soundings conducted at the BWDWA site during the current investigation.

6.3 Friction Sleeve Response as a Function of Sleeve Position

6.3.1 Introduction

Several previous researchers have studied the effect of position on the response of smooth friction sleeves (Campanella and Robertson, 1981; Konrad, 1987; Parez, 1987; DeJong, 2001) as described in Section 5.2.4.5. The current study included a repeat investigation of the DeJong (2001) study, to further investigate the change in smooth sleeve stress as a function of sleeve position using the MFA unit configured with the short and long uninstrumented tips and a conventional 15 cm^2 CPTU unit as depicted in Figure 6-10. Additionally an investigation was undertaken to compare the response of a textured sleeve as a function of distance behind the tip. The H2.00 sleeve texture was tested in all 10 positions afforded using the three available tip configurations as shown in soundings 80-90 listed in Table 6-1.

6.3.2 Effect of Sleeve Position on Smooth Interface Behavior

The effect of smooth sleeve position was tested in the current study in soundings 55 to 57, as described in Table 6-1 and shown in Figures 6-11 to 6-13. As can be seen, the response of the four MFA smooth sleeves are all very similar within each sounding for the varying tip configurations. DeJong (2001) found sleeve stress to be strongly influenced by the variations in the diameter of the tip and other elements forward of a friction sleeve sensor. This mechanism is simply explained based on the changes in local lateral stress and subsequent sleeve friction due to an increase or drop in diameter along the friction sleeve as compared to the preceding penetrating elements. DeJong (2001), and the author, have noted the existence of a 0.3 mm difference in the shaft diameters of

the CPTU unit as compared to the short and long uninstrumented dummy tips used with the multi friction attachments. This small variation in diameter results in the offset in average sleeve stresses for the three tested configurations in the current and DeJong (2001) studies, as shown in Figure 6-14a. The offset in the smooth MFA responses for the CPTU tip and uninstrumented dummy configurations are similar for both the short and long dummy tips, indicating that the shift in response is due to variations in tip module diameter and not sensor position.

The behavior and average value of each sleeve within the MFA unit (f_{a1} to f_{a4}) all show consistent response, within 6% of the average MFA sleeve stress for each sounding. Due to the overlapping measurements provided by the first and last sensors of the uninstrumented tip configurations with the conventional CPTU-MFA configuration it is possible to adjust the data to correct for the difference in tip module diameter, as shown in Figure 6-14b. This plot shows that friction sleeve response is not largely affected by sensor position for tip offsets greater than 200 mm for the loose to medium dense sand site tested, with both data sets exhibiting similar trends, apart from the seasonal offset present in the friction response magnitudes. Both data sets do show a decrease in the measured MFA smooth sleeve responses, as compared to the conventional CPTU f_s position. The reduction in stress between the f_a and f_s measurements were observed to be on the order of 15 and 25 kPa for the current and DeJong(2001) studies respectively. The results do show that the MFA positions have a slight offset with respect to each other that remains consist for each of the three tip configurations, and these small variations are believed to be due to small variations in friction sleeve diameter. The corrected results

confirm the notion that smooth friction sleeve response is highly dependent on the diameter of the forward penetrometer elements, and should be monitored regularly.

6.3.3 Effect of Sleeve Position on Textured Interface Behavior

The effect of textured sleeve position was tested in the current study using the H2.00 textured sleeve in one of the four MFA positions with the other three positions configured with smooth sleeves. This investigation was conducted over soundings 80 to 90 as described in Table 6-1. Figure 6-15 shows the response of the H2.00 sleeve for each sounding overlain with the other sensor responses for that tip configuration. The sleeve response of the four sensor positions associated with the CPTU-MFA configuration (centered from 655 to 1105 mm behind the tip) all show very similar response over the entire sounding depth. The results of the soundings with the short and long dummy show larger variations between the individual sleeve responses. At the time of the current investigation soundings, the H2.00 sleeve had been used throughout the early testing phases, and the forward diamond textures started to wear during the later stages of the testing sequence. All of the smooth and textured sleeves used on the multi friction attachments are heat treated to increase wear resistance, however, the heat treatment only affects the hardness to a finite depth into the metal and the textured sleeve exhibited rapid degradation after the onset of wear below the depth of hardening exposure. Unfortunately, a duplicate H2.00 sleeve was not available for replacement, and the later soundings in the test series were conducted with the worn H2.00 sleeve. Figure 6-16 shows the sleeve condition after sounding 90 (Table 6-1) where the wear of the diamond asperities, especially the forward texture, can be clearly seen. Future work hopes to perform a similar test series to better explore this behavior.

6.3.4 Design of a Quick Sleeve Profilometer (QSP)Device

As a result of the observed wear of the H2.00 sleeve during this investigation, it was proposed to design and fabricate a device to quickly and accurately check the height of sleeve texture asperities in the field for future investigations. Figures 6-17 shows a photograph of the QSP device, respectively. The QSP device is designed so that textured sleeves can be measured along the centerline of the offset textured patterns, or along any linear length of a smooth friction sleeve. The device not only allows for the appraisal of sleeve textures but also allows macroscopic sleeve wear for conventional friction sleeves to be monitored. Figure 6-18 shows a plot displaying traces of friction sleeve measurements conducted with the QSP device, including: the severely worn H2.00 sleeve, a used H1.00 sleeve, and a well used MFA SM sleeve. This figure clearly shows the wear of the previously discussed H2.00 sleeve in soundings 80 to 90 as well as the uniform wear of smooth MFA and MPFA friction sleeves. Uniform wear of the attachment smooth sleeves is expected due to the stable shearing regime present along penetrating shafts. This is contrary to the uneven wear of sleeves placed in the conventional f_s position directly behind the tip or u_2 pore pressure element, as discussed in Section 5.2.4.3, and highlights another advantage to placing friction sleeves further up the shaft of penetrometers.

6.4 Summary of In Situ Interface Behavior in Different Geologies

6.4.1 Introduction

Testing with the MFA and MPFA units has been conducted at seven sites in the current study. Three of those test sites have a predominant silica sand geology, one

consists of calcareous sand, one includes a layer of cemented calcareous silty clay, another consists of a glacial till geology, and the final site consists of a very soft clay geology. Detailed descriptions of the locations and soil properties of the tests sites were described in Section 6.2. This section serves to summarize the in situ interface behavior of various geologies as tested using the MFA and MPFA devices.

As discussed in Section 5.5 the response of textured sleeves during penetration is controlled by a combination of two main mechanisms: interface shearing and sliding along the sleeve length and a punching shear or bearing capacity type failure located at the onset of sleeve texturing. This second mechanism, was earlier introduced as the Annular Penetration Force (APF), occurring at all increases in radial thickness over the main penetrometer housing diameter. Preliminary results have shown that subtracting out this force by directly scaling the corresponding CPTU tip response (q_t) to the appropriate annular area of sleeve texture, results in the isolation of the sliding and shearing components from the total measured textured sleeve response, Equations 5-2 through 5-4. The isolation of the interface sliding and shearing components of the measured sleeve stress provides a measure equivalent to shearing against a continuous surface, allowing for direct comparison with conventional laboratory interface data or for direct implementation into geotechnical design applications. In order to maintain a wide perspective on the data, both the field measured sleeve stresses and the APF corrected or isolated interface response are presented whenever applicable. The results in this chapter focus on the interface friction measurements obtained with the MFA and MPFA devices, with the measurement and influence of pore pressure presented in Chapter 8.

6.4.2 In Situ Interface Behavior in Silica Sand Geologies

6.4.2.1 Introduction

Three of the test sites consist of predominant silica sand geology: the South Royalton Vermont (SRVT) test site, the Loose Sand (LS) test site, and the Shenton Park Western Australia (SPWA) test site. Conventional geotechnical interface behavior for coarse grained particulates was summarized in Section 2.3, and a number of these concepts apply to the behaviors observed in situ with the MFA and MPFA devices. The SRVT test site was the location of 94 MFA soundings, and as such there is a large data base of in situ interface data at this site. The LS site was only tested with two fully textured sleeves and so the subsequent analysis of in situ interface behavior as a function of surface roughness is limited at that site. However, the LS site does provide for the comparison of silica sand interface behavior over two distinctly different in situ densities: medium (from 3 to 5 m) and very loose (from 9 to 11 m). During the summer of 2004, a total of 17 soundings were conducted at the SPWA site with the MFA and MPFA units Tables 6-1 and 6-2. Ten of these tests were part of a collaborative study with the University of Western Australia (UWA) focused on scale and installation effects regarding pile behaviors and will not be presented herein, but can be found in Schneider (in progress). The other seven soundings discussed herein were conducted with the MPFA device and allow for a comparison of MFA and MPFA response in silica sand geologies.

6.4.2.2 Comparison of Measured Total Sleeve Response

Figures 6-19 to 6-21 show the measured total response of the MFA and MPFA friction sensors across a range of sleeve roughness values at the SRVT, LS, and SPWA sites, respectively. Each sleeve response is compared to the response of a conventional CPTU f_s sensor for that sounding where available. The overlay subplot at the far right in each of these figures allows for the response of the various sleeve textures to be compared directly over the full sounding depths. All three sites show the expected trend of increasing total measured sleeve stress with increasing sleeve roughness. It is noted that the sensor traces in the above figures are oftentimes taken from several soundings at each site in order to present the full range of tested sleeve textures, with some minor lateral variability in the subsurface stratigraphies seen across the various sites. It is interesting to note the lower variation in measured sleeve response as a function of roughness within the silt seams at the SRVT test site, located at approximately 6.5 and 8.5 m depth respectively, as shown in Figure 6-19. This trend is expected from the fundamental geotechnical interface concepts presented in Chapter 2, as interface friction is known to be a function of relative and not absolute roughness. The in situ interface response of textured sleeves in intermediate and fine grained soils is presented in detail in Section 6.4.4.

Figure 6-22 and Table 6-5 show the average sleeve response as a function of R_{max} surface roughness from the prominent silica sand strata present at the SRVT, LS, and SPWA test sites. Figure 6-22 clearly shows the increase in total measured average sleeve response with increased sleeve roughness at each of the three sites. The variation in textured sleeve response as a function of virgin in situ soil density is clearly demonstrated

by comparing the textured response from the upper (medium to loose density) and lower (very loose) sand layers at the LS test site. The divergence in the average sleeve stresses between the medium dense and very loose sand layers increases with increasing sleeve texture, from a 32% reduction for the H.125 texture to a 48% reduction at H0.50. The SPWA site showed notable lateral variability, as the average response of the H0.75 and H1.50 textures from sounding MPFA_19 show a significant increase in response over the other SPWA sounding traces. Due to the variability of sounding MPFA_19 as compared to the other SPWA data, the values for that sounding are presented as SPWA silica sand set B. The SPWA site is underlain by limestone bedrock and includes a number of narrow limestone pillars that extend close to the surface at intermittent spacings throughout the test area, as is common in limestone formations. Sounding MPFA_19 may have been located within close proximity to one of these pillars creating an increase in lateral stress and a subsequent increase in measured response.

Effects of variations in lateral stress on the response of friction sleeves can be clearly seen in the average silica sand responses presented in Figure 6-22. The lateral stress along the penetrometer within the LS very loose sand layer (9 to 11 m) is expectantly lower than for the other sand layers, and results in the lower measured sleeve stresses within this layer. The average measured sleeve responses from the deeper sand layer (7 to 8 m) at the SRVT site exhibited response on the same order as at the SPWA-B layer from sounding MPFA_19, both of which were distinctly higher than the other average behaviors. The other prominent sand layers: LS (3 to 5 m), SRVT (1 to 5 m), and SPWA (3 to 7 m) all exhibit very similar response over the range of textures greater than or equal to H0.25. However, the smooth and H0.125 behaviors for these same materials

seem to show some amount of variability, with the SRVT (1 to 5 m) layer exhibiting an increased average response over the LS (3 to 5 m) and SPWA-A (3 to 7 m) layers. It is believed that these results confirm the hypothesis that conventional smooth and slightly textured friction sleeves are more prone to variability, as discussed in Chapter 5. Additionally, the silica sand results from all three sites show variable levels of reduction in measured attachment smooth sleeve stress as compared to the conventional CPTU f_s measurement, as seen in Table 6-5. This data serves to further corroborate the concept of a highly stressed shear zone surrounding the tip, resulting in increased lateral stresses being placed on the f_s sensor as compared to the f_{a1-4} sensors located further up the penetrometer shaft for the MFA and MPFA devices.

6.4.2.3 Comparison of the Isolated Interface Sleeve Response

In order to analyze the in situ data collected with the MFA and MPFA devices within the framework of conventional geotechnical interface shearing concepts it is necessary to isolate the forces caused by interface sliding and shearing mechanisms from the annular penetration force (APF) imparted onto the textured sleeves. The APF component of each sensor trace was subtracted from the total response for each textured sleeve response presented in Section 6.4.2.2, using the process detailed in Section 5.5. The resultant stresses correspond to the isolated interface responses of each sleeve. Utilizing the isolated interface response allows for a parallel comparison of in situ interface measurements to conventional laboratory test results and behaviors and are thus a direct measure of isolated interface sliding and shearing.

Figures 6-23 to 6-25 show plots of the isolated interface response of the sensor traces from Section 6.4.2.2, Each sleeve response is compared to the response of a

conventional CPTU f_s sensor where available, with each trace overlain for comparison in the far right subplot. The trend of isolated interface response with increasing sleeve roughness at the SRVT site, as presented in Figure 6-23, again increases with increasing roughness for all textures up to H1.00. However, as expected from the concept of an upper bounding critical roughness for soil - continuum interfaces presented in Chapter 2, the H1.00 and H2.00 textures show approximately equivalent response with depth, excepting minor variations believed to be the result of lateral variability. The isolated interface responses from the SPWA site show similar behavior for the heavily textured sensors as shown in Figure 6-23. The heavily textured sensors from sounding MPFA_19 (H0.75 & H1.50) show equivalent isolated interface response with depth , as do the heavily textured traces from MPFA_15 (H1.00 & H2.00), indicating that the critical roughness value for the SPWA sand is lower than R_{max} = 0.75 mm for the current texturing pattern.

As a result of the fewer sleeve textures used at the LS site, and the greater lateral variability present at the SPWA site, the isolated interface responses from those sites are more clearly displayed by comparing the average behaviors. Figure 6-26 and Table 6-6 present the average isolated interface response from the prominent silica sand strata at the SRVT, LS, and SPWA test sites. The data from the current silica sand testing again can be grouped into three categories of response: very loose silica sand - (LS 9-11 m layer), loose to medium (LS 3-5 m, SRVT 1-5m, and SPWA-A 3-7m), and medium to dense (SRVT 7-8m and SPWA-B 3-7m). Using the known bilinear relationship between surface roughness and interface response as a framework it is possible to define the in situ interface response of these three groupings as shown in Figure 6-27. Due to the limited

data from the very loose silica layer, the interface response for this grouping can only be extended through the range of roughnesses from R_{max} = 0.0064 to 0.50 mm. The other two groupings consist of a full range of surface roughnesses and allow for full interface relationships to be determined. The critical roughness values for the loose to medium and medium to dense groupings were calculated as 0.65 and 0.66 mm, respectively. It is important to note that these values correspond to the specific intermittent texturing pattern of the textured sleeves and may vary for continuously or differentially textured surfaces. It follows that the critical roughnesses from this data set converge to a unique value, as the sand layers all consist of fine silica sand with similar D_{50} values as listed in Section 6.2.

The isolated interface response from the various silica sand layers can be further analyzed by utilizing the knowledge that the interface friction angle (δ) is approximately equivalent to the internal soil friction angle (ϕ') at roughness values greater than the critical roughness. While empirical equations exist to determine the friction angle of sands from conventional CPT data, those equations only provide an estimate of the peak friction angle, and shearing along the friction sleeves of the MFA and MPFA devices is better modeled using the critical state friction angle (ϕ_{cs}') due to the large displacements involved. The critical state friction angle of the SPWA sand was determined to be 34° through laboratory testing as reported by Byrne and Randolph (2003). Using the critical state friction angle and the measured isolated interface response at roughnesses greater than the critical roughness one can determine the approximate lateral stress applied to the attachment friction sleeves during the soundings. The lateral stress along the attachment can be estimated using Equation 6-1:

$$\sigma_n = \frac{\tau}{\tan(\delta)} \qquad \text{(Eq. 6-1)}$$

where τ is the shear stress, σ_n is the normal stress, and δ is the interface friction angle taken equal to ϕ_{cs}' for surface roughnesses greater than the critical roughness. The calculated normal stresses for the loose to medium and medium to dense silica sand groupings are calculated as 270 and 400 kPa, respectively. Assuming a typical soil unit weight of 1800 kg/m^3 the average stress ratio ($K = \sigma_h / \sigma_v$) at the attachment sensor locations can be approximated as K =3.0, 3.0, 4.4, and 5.0 for the SRVT (7-8m), SPWA-A (3-7m), SPWA-B (3-7m), and SRVT (1-5m) layers, respectively. These values are expected to be much higher than the virgin K_0 stress state (typically on the order of 0.4 for sands) due to the disturbances resulting from the CPTU and textured sleeve penetrations, and are on the order of measurements observed for model pile installations in sand (Lehane, 1992; Chow, 1996).

6.4.3 In Situ Interface Behavior in Calcareous Sand Geologies

6.4.3.1 Introduction

The Ledge Point Western Australia (LPWA) test site is comprised of a calcareous sand geology. Carbonate soils are typically found in warm marine environments and originate from the sedimentation of marine skeletal debris, and often contain some level of structure typically in the form of precipitated calcite cementation (Sharma, 2004). Carbonate soils are prone to particle crushing and typically exist at larger in situ void ratios than other sand geologies due to the open and angular structure of the constituent grains. Two layers are taken from the LPWA test site and used as the focus for the current study: the soil from 1-2 m consists of a lightly cemented calcareous sand, and the

soil from 4-5, 6-7 m consists of a relatively uniform uncemented or only very slightly cemented calcareous sand. The layer from 1 to 2 m is believed to have prominent cementation due to the repetitive wet and dry cycles experienced through tidal action resulting in a buildup of cementing agents precipitated from the saline ocean water. Over the course of two days in the summer of 2004 ten total soundings were conducted at the LPWA test site. Five of those soundings were CPTU-MPFA soundings, with one being a very short sounding of only 2.5 m and not used for analysis. The other five soundings were CPTU-MFA soundings with two of those included in the current analysis, with the other three a part of the study by Schneider described earlier, and not included herein.

6.4.3.2 Comparison of Measured Total Sleeve Response

Figure 6-28 shows the measured total response of the MFA and MPFA friction sensors across a range of sleeve roughness values at the LPWA test site. Each sleeve response is compared to the response of a conventional CPTU f_s sensor, with each trace overlain for comparison in the far right subplot. Variations in the horizontal scale of the plots in Figure 6-28 are used to highlight the response of the sleeves with lower texture, and should be noted. The range of attachment sleeves tested at the LPWA site includes: SM, H0.125, H0.25, H0.75, H1.00, H1.50, and H2.00, and the overlay plot at the far right of the figure allows for the response of these textures to be compared directly over the full sounding depth. The stiffer response from 1 to 2 m depth is clearly visible in each of the sensor traces, with some lateral site variability apparent within the data. The in situ response of the attachment friction sleeves again show an increasing response with increased texture, with the separation of sensor traces more pronounced within the lightly cemented region. The average sensor response over the two regions highlighted earlier

(1-2 m and 4-5, 6-7 m) is presented for each sleeve type in Figure 6-29 and Table 6-7. The increased response of all sleeves within the lightly cemented layer (1-2 m) is clearly evident from the figure, with the percentage increase in measured sleeve stress varying from 77% for a SM sleeve to 313% for the H2.00 texture. The response of the uncemented calcareous region exhibits low friction response typical of that found in calcareous soils; whereas, the high response measured within the cemented calcareous layer shows the large influence particulate structure and bonding can have on interface response. Similar increases in monotonic shear strength have been reported for both artificially and naturally cementation to sands, irrespective of sand type as summarized by Sharma (2004).

6.4.3.3 Comparison of Isolated Interface Response

Figure 6-30 shows the isolated interface response of the sleeve traces presented in Figure 6-28. Each sleeve response is compared to the response of a conventional CPTU f_s sensor, with each trace overlain for comparison in the far right subplot. The isolated interface behaviors of the tested textured sleeves at the LPWA site exhibit similar trends to the silica sand behavior noted earlier except in two layers: within the near surface cemented region and at approximately 2.7m. Within the cemented region near the surface their exists some lateral variability between soundings as shown by the H0.75 and H1.00 textures showing greater response than the H2.00 sleeve. Additionally, the isolated interface response never converges to a limiting value for the heavily textured sleeves within the cemented zone. The considerable effects cementation can induce on shear behavior were discussed in Chapter 2 and in Section 6.4.3.2 and are believed to result in the continued increase in measured interface response across the full range of tested

surface roughnesses. The second phenomena within the calcareous behavior that diverges from the silica sand behavior is the calculation of negative isolated interface values over a limited depth centered around 2.7 m for the heavily textured sleeves, as seen in Figure 6-30. This result indicates that either the soil or stress state within this depth range undergoes a significant change between the initial tip penetration and the exposure to the textured sleeve. Due to the nature of calcareous soils it is believed that particle crushing may have occurred within this region during initial tip penetration causing the stresses registered on the textured friction sleeves as a result of the APF phenomena to be significantly lower than the corresponding tip stresses. The behavior of the remainder of the sounding generally follows conventional interface shearing concepts and highlights the low in situ shear resistance typically found in calcareous sand geologies.

Figure 6-31 and Table 6-8 present the isolated interface response from the array of sleeve textures tested at the LPWA calcareous sand test site. The isolated interface response of the highlighted uncemented calcareous region (4-5, 6-7 m) exhibits the traditional bilinear interface shear - surface roughness relationship, with a critical roughness on the order of the H1.00 texture for the given texturing pattern. The lightly cemented layer (1-2 m), however, never induces a stable interface response over the range of textures tested, as seen in Figure 6-30. One possible explanation is that the additional stiffness provided by the cementation in the layer restricts the transfer of the failure mechanism away from the interface and results in the continued increased in isolated interface response.

Coop and Airey (2003) report that a typical critical state friction angle for most calcareous sands can be taken as $\phi_{cs}' = 40°$. As before, the normal stress acting on the

heavily textured sleeves during penetration can be estimated using the critical state friction angle and the measured isolated interface shear stress from the uncemented calcareous layer, τ = 74.83 kPa, and gives σ_n = 89.2 kPa. As is typical for in situ investigations and pile foundations placed in calcareous materials, the sleeve response (or pile shaft resistance) is much lower for the calcareous sand than for the silica sands presented in Section 6.4.2. The lateral stress induced by the penetration into the calcareous sand is much lower the values induced in the silica sands described above, and results in a lateral stress ratio along the textured sleeves of K = 1.0, again using γ_t = 1800 kg/m^3. Since the specific cementation characteristics of the cemented calcareous layer are not known, and natural cementation in calcareous sands is known to vary widely, the induced lateral stress and stress ratio of this region are not calculated herein.

6.4.4 In Situ Interface Behavior of Silt and Clay Geologies

6.4.4.1 Introduction

Throughout the course of the MFA and MPFA soundings completed, several silt and clay strata have been investigated with an array of friction sleeves of varying roughness. Up to this point all presented responses have been characteristic of drained conditions, whereas the fine grained responses presented herein correspond to either partial drainage or fully undrained conditions. Fine grained soil strata tested to date include: two silt seams at the SRVT test site, the Cooper Marl geology from the MPSC test site, and the soft clay from the BWDWA test site. The silt seams at the SRVT test site are nominally located at 6.8 and 8.6 m depth and have an average thickness of 0.3m. The Cooper Marl geology, comprised of highly structured calcareous sandy clay to sandy

silt, was present at the MPSC test site between nominal depths of 14 to 20 m for the two soundings performed. At the BWDWA test site, the upper one meter was prebored with a hand auger for all soundings to allow for the use of the long MPFA probe with the available testing equipment. As such the top meter of soil was not tested in any of the BWDWA soundings. The surficial soils consisted of approximately 3 m of desiccated clay crust and sand layers. Underlying these surface layers is a deposit of very soft uniform clay with included shell fragments and silt lenses, extending to depths on the order of 14 m below ground surface. The current investigations at the BWDWA site were typically limited to tip depths on the order of 10 to 12 m below ground surface, and as such the analysis of the soft clay layer is focused on data between depths of 4 to 8 m.

6.4.4.2 Comparison of Measured Total Sleeve Response

Figures 6-20 and 6-32 to 6-33 show the measured total response of the MFA and MPFA friction sensors across a range of sleeve roughness values for the SRVT, MPSC, and BWDWA test sites, respectively. Each sleeve response is compared to the response of a conventional CPTU f_s sensor, with each trace overlain for comparison in the far right subplot. The prominent fine grained layers encountered were outlined above and consist of two silt seams, a highly structured calcareous silty clay, and a very soft clay. As briefly discussed in Section 6.4.2.2, the in situ response of the textured sleeves within the two silt seams at the SRVT test site exhibited a smaller divergence of response across the range of tested surface roughnesses in comparison to the response within the sand and silty sand layers.

The response within the Cooper Marl stratigraphy yielded approximately equivalent response for the f_s, H0.25, and H0.50 sleeves with the SM response being only

slightly lower. The response of the H1.00 texture, however, is significantly higher than the other tested sleeves, as depicted in Figure 6-32. It is theorized that the tested sleeve roughnesses below the H1.00 texture all act within a thin radial zone of fully destructured soil resultant from the initial CPTU tip penetration, and that this zone is restricted to a radial distance between 0.5 and 1.0 mm around the penetrometer. As such, the H1.00 heavily textured sleeve is believed to extend radially outward to a distance greater than the originally disturbed zone, into a zone of soil exhibiting characteristics closer to the virgin structure of the Cooper Marl geology. A similar, albeit smaller, divergence in textured sleeve responses was observed in the cemented calcareous strata from the LPWA site, with penetration in structured geologies possibly resulting in a reduction in the zone of disturbance surrounding a penetrometer. Unfortunately no other heavily textured measurements within the Cooper Marl have been made to date to confirm this supposition. However, future work is planned to revisit this geology to conduct supplemental testing.

The measured sleeve responses at the BWDWA soft clay site all exhibit very low response, as is expected in a soft clay geology. A number of the soundings conducted at the BWDWA site included one or more holding dissipation tests on the order of two hours in length, and large scale cycling, 10 $\pm$ 1 m cycles, in order to investigate the hydrogeologic and cyclic soil behaviors as shown in Table 6-1 detailing the test procedures for each sounding. The supplemental cyclic and dissipation test procedures and results are discussed at length in Chapters 7 and 8 respectively, but their influence on the measured sleeve responses can be seen in the data of Figure 6-33. In analyzing the effect of various dissipation and cyclic tests, it is important to recall that each of the

textured sleeves in Figure 6-33 was tested in position f_{a2}, which is centered 1.07 m behind the CPTU tip sensor for the MPFA device configuration. An example of the influence of a dissipation test on the sleeve response can be seen in the H0.50 trace between the depths of 5.7 and 6.7 m where the two hour delay after initial penetration reduced the pore pressures acting on the sleeve through this region, subsequently increasing the lateral effective stress and the subsequent H0.50 sleeve response. The trace of the H1.50 sleeve shows a reduction in response due to the large scale cycling of the tip occurring from 5.7 to 6.7 m as seen in the one meter of response offset from the consistent trend of sleeve response within the soft clay stratigraphy seen at other depths.

The average sensor response over the primary fine grained layers of interest identified above are presented in Figure 6-34 and Table 6-9. The general trends described above are clearly displayed in Figure 6-34 and highlight the fundamental interface concept of reduced influence of surface roughness as a function of decreasing particle size. The two silt seams show some amount of lateral variability as a function of the relatively thin layer thickness, especially prominent in the average response of the H1.00 sleeve within Silt Seam A. The average sleeve responses from the Cooper Marl stratigraphy clearly show the unusual trend noted previously, with the average H1.00 showing a significant increase in response over the other fine grained layers. Again this behavior is believed to indicate that the H1.00 sleeve response was at least partially influenced by a region of Cooper Marl that retained the highly structured virgin characteristics of this material. Future testing with both the MFA and MPFA sensors will hopefully provide additional measurements across a wider range of fine grained

geologies allowing for more definitive conclusions regarding in situ interface response as a function of surface roughness and soil characteristics to be formulated.

6.4.4.3 Comparison of Isolated Interface Response

Figures 6-23, 6-35, and 6-36 show the isolated interface response of the sleeve traces from the SRVT, MPSC, and BWDWA test sites. Each sleeve response is again compared to the response of a conventional CPTU f_s sensor, with all traces overlain for comparison in the far right subplot. The response of textured sleeves is less affected by APF in fine grained geologies as the resistance to penetration by both the CPT tip and annular texture are greatly reduced as compared to coarse grained soils. As such, the trends seen in the traces of isolated interface response are very similar to the total measured sleeve responses presented in Section 6.4.4.2. Unfortunately, due to the necessity of having a CPT tip measurement at the same depth and occurring under the same conditions as the sleeve response in order to isolate the interface response from the total measured sleeve stress, the isolated interface response as a function of cycling for the BWDWA data can not be computed. As such the isolated interface BWDWA data is shown as continuous traces depicting the response of each sensor during its virgin penetration at each depth.

The average isolated interface responses from the tested fine grained stratigraphies are presented in Figure 6-37 and Table 6-10. The BWDWA results show only a minor reduction from the total measured results due to the very low tip stresses generated within the soft clay strata. The responses from the very soft clay stratigraphy show only minor variation as a function of varying the surface texture of friction sleeves, and indicate that the critical roughness for this material at standard CPT penetration rates

is lower than the standard roughness of smooth penetrometer friction sleeves R_{max} = 6.4 μm. The isolated interface responses from both the Cooper Marl and SRVT silt seams show moderate reductions from the total measured responses. The average interface behavior from Silt Seam B indicates that the critical roughness for this layer is on the order of the H0.25 texture for the given intermittent texturing pattern. The data from Silt Seam A seems to be highly influenced by lateral variations within the layer and does not show a distinct trend as a function of surface roughness. The isolated interface response of the Cooper Marl stratigraphy continues to exhibit a change in mechanism between the H0.50 and H1.00 textures that will hopefully be more completely understood with the addition of supplemental future data.

6.4.5 Summary of Observed In Situ Interface Behaviors

The full range of observed behaviors across the highlighted stratigraphies can be seen in the plots of average total measured sleeve response and isolated interface response shown in Figures 6-38 and 6-39, respectively. The H1.00 response within the Cooper Marl has been removed from these plots, as additional testing needs to be completed in order to corroborate the unusual behavior observed for that trace. The range of observed interface response within the plots shows that the soft clay of the BWDWA site provides the minimum response. The cemented calcareous sand from the LPWA site exhibits the maximum response at high sleeve roughnesses, with the deeper silica sand layer from the SRVT site exhibiting the largest response for smooth and moderately textured sleeves. The measured in situ isolated interface behaviors exhibited in Figure 6-39 for the most part show excellent agreement with conventional interface concepts. All of the selected layers, except for the cemented calcareous sand, exhibit the tradition

bilinear interface response as a function of sleeve roughness, with the values of critical roughness decreasing with increasing tendency toward characteristic fine grained behavior. The calcareous sand exhibits the largest apparent critical roughness, observed to be equivalent to the H1.00 textured sleeve, with the value for silica sand on the order of H0.66, the silt value on the order of H0.25, and the soft clay showing almost no affect of surface roughness over the measured range. The slope of the linearly increasing portion of bilinear behavior for the tested soils shows a distinct trend to decrease with increasing clay like behavior. This result is parallel to findings from laboratory studies conducted across a similar range of materials as discussed in Chapter 2.

In summary, the observed measurements of in situ interface response showed the following:

- Good agreement with fundamental interface behaviors known to exist for laboratory samples of similar materials.
- The variation in isolated interface response with increasing roughness was observed to decrease for strata exhibiting fine grained behaviors.
- The contribution of isolated interface (i.e. the sliding and shearing components) response to the total measured sleeve stress can be effectively isolated from the annular penetration component inherent to textured sleeve measurements.
- Isolated interface response can be effectively measured in situ across a wide range of surface roughness values and soil conditions.
- The range of sleeve textures currently implemented appears to provide a sufficient coverage across both the range of surface properties utilized in practice and the range of soils typically encountered in situ.

- f_s response was observed to consistently be slightly higher than measured smooth attachment responses across a range of geologic conditions, and is believed to be due to larger lateral stresses present in the vicinity of the penetrating tip.
- The position of MFA and MPFA friction sleeves appear to be within a stable shearing regime across all tested soil types for standard steady-state CPT penetration.
- The interface behaviors of structured materials measured in situ appear to be controlled by additional internal and interface interaction mechanisms, which appear to affect both the magnitude of measured shear resistance and the extent of the influence zone created by the penetrometer.

These results show promise in the ability to measure geotechnical interface response in situ across a range of geologic conditions. Future work will attempt to provide a larger database of MFA and MPFA in situ interface measurements in order to verify and substantiate the observed behaviors.

6.5 Utilizing Textured Friction Sleeves in Problematic Stratigraphies and for Improved Identification of Soil Structure

6.5.1 Introduction

The use of the cone penetrometer, and other invasive in situ testing techniques, has not been feasible in certain stratigraphies due to difficulties with sensor overload, verticality, and large unsupported rod lengths. Conditions that can lead to these penetration difficulties include conglomerates, gravels, highly cemented soils, stiff desiccated crusts, and stiff layers underlying thick soft layers typically found in coastal

and/or alluvial regions (Lunne et al., 1997). The necessity to have cone tip (q_c) load cell resolution on the order of 1 N (~ 1 kPa for a 10 cm^2 CPT) limits the maximum tip load to 200 kN for most conventional CPT systems. As a result, sensor overloading at the tip can be common during testing in areas with natural gravels, desiccated crusts, and cemented layers. In many cases, these stiff layers are thin (on the order of 1-2 m) and occur near the surface, thereby obscuring the underlying soils from CPT classification. Consequently the use of penetrometers has been limited in these conditions, relegating engineers to the use of less robust in-situ techniques such as the standard penetration test (SPT) and visual classification. Sleeve friction (f_s) measurements are typically less subject to sensor overloading due to the much lower forces associated with sleeve penetration and the associated shear loading mechanisms.

In addition to stiff strata constraints, the identification and quantification of cementation and other forms of soil structure is often difficult with common forms of in situ testing. The retrieval of undisturbed field samples of cemented and otherwise structured soils for laboratory testing is especially problematic, making in situ investigations better suited to obtain accurate properties in most structured soil stratigraphies. Wave based techniques are typically excellent tools to identify structured soils, however they are limited to the small strain regime, and as such, are typically paired with other geotechnical measurements to asses the response over the full range of strains applicable to geotechnical problem. In situ tests, such as the CPT, are inherently affected by soil structure, however, conventional interpretation of these test results often is not able to clearly differentiate between highly structured soils and other less sensitive materials exhibiting similar response. The current MFA and MPFA devices provide

multiple measures of several basic in situ measurements and therefore may provide an opportunity to better diagnose and quantify soil structure through the detailed analysis of these multiple measurements. Fundamental concepts of interface shearing have been applied to the in situ results of MFA and MPFA soundings using textured friction sleeves, highlighting exciting new interpretation techniques to overcome the abovementioned limitations of conventional CPT testing.

6.5.2 Utilizing the Mechanics of Textured Sleeve Penetration

As presented in previous sections, the response of textured friction sleeves are controlled by two main mechanisms: a combination of interface sliding and shearing resistance and the resistance created by the punching shear failure at the transition in annular diameter between the attachment housings and the textured sleeve asperities. The previous section provided a review of the differences between measured and isolated geotechnical interface response. As seen in that section, the existence of the APF force can cause some difficulty in the interpretation of in situ results within the framework of conventional interface behavior. However, the inherent presence of an APF in the measurement of textured sleeve stresses can in fact provide significant insight into the behavior of the tested soil when interpreted within the framework of known interface shearing concepts.

In returning to the concept of critical roughness, above which the interface shear strength becomes constant and equal to the internal shear resistance of the soil, any divergence in measured sleeve stresses for textures above the critical roughness can be attributed to varying levels of APF. As such, the mathematical difference between the measured forces of sleeves with texturing above the critical roughness value (e.g. the

H1.00, H1.50, and H2.00 sleeves for most soil types) represents the force resultant from the difference in APF of the two different sized textural asperities. The difference in APF forces can then be converted to a stress by dividing by the affected area, the difference in annular area between the two heavily textured sleeves. This stress provides a measure of disturbed "tip" stress, that can then be compared to the CPT tip stress measurement that is largely controlled by the virgin in situ soil conditions. Comparing the original CPT tip response to a measure of disturbed "tip" response may then provide insight into changes in soil behavior that occurr due to penetration. A similar concept has been previously applied by Bloomquist et al. (1999) using an instrumented annular wedge of A_{proj} = 10 cm^2 placed approximately 1 m behind a conventional 10 cm^2 CPT in order to detect the presence of cementation in tested materials, Figure 6-40.

In a parallel manner to the response of textured sleeves greater than the critical roughness, the isolated interface response of two textured sleeves below the critical roughness provides the ability to calculate a profile of disturbed smooth sleeve values. Because the trend of isolated interface response below the critical roughness is known to be linear, the deviations in the isolated interface stresses for roughnesses along this line can be used to estimate a disturbed "smooth" sleeve response. With either the MFA or MPFA configured with two sleeves above and two sleeves below the critical roughness value in order of increasing roughness, it is possible to calculate disturbed end bearing ("tip") and side friction ("smooth sleeve") profiles from a single sounding.

The calculated disturbed end bearing and side friction values are not to be confused with attempted predictions of the CPT q_c and f_s measurements. The stress and soil conditions controlling the CPT response differ greatly from those affecting the multi

friction attachments. Additionally, the resolution of the textured friction sleeves is much finer than either the CPT tip or friction sleeve due to the vastly different stress conditions and geometric configurations controlling each sensor. The influence zone of the CPT tip has been extensively studied and while not fully understood has been found to be heavily dependent on the probe diameter, in addition to the in situ state of stress and soil conditions (e.g. Vesic, 1972 and Baligh, 1985). As such, the differences in the CPT tip area and the annular area of the textured friction sleeves can be associated with the size of the influence zone around each sensor. The CPT tip diameter is constant at D_{tip} = 43.7 mm, with the maximum annular area of the textured friction sleeves resulting from the R_{max} = 2 mm sleeve, and equaling $D_{annular}$ = 4.00 mm. The MFA and MPFA are outfitted with shorter friction sleeves (110 mm) than the conventional CPT friction sleeve currently used (164 mm), again resulting in a higher vertical resolution. In addition to the differing levels of resolution between the various sensors, in situ stress and soil conditions are distinctly affected by the act of CPT penetration. The resultant soil conditions encountered by the MF attachments are close to the residual state in a vastly different stress field to that experienced by the CPT tip and friction sleeve. Noted differences in resolution and stress level can be inferred by comparing the measured CPT and calculated MF trends, providing additional insight into the tested soil behavior.

6.5.3 Preliminary Results

Four of the test sites contain soundings for which two heavily textured sleeves above the critical interface roughness value were both operational within the same sounding: SRVT, SPWA, LPWA, and BWDWA. Figure 6-41 shows disturbed end bearing and side friction profiles, calculated from an MFA sounding at the SRVT site,

overlain on the measured CPT q_t and f_s values. While a disturbed smooth sleeve profile can be more easily obtained by simply using a smooth sleeve in any of the MFA or MPFA positions, the side friction comparison shown in Figure 6-41 reinforces the validity of the presented framework. The equivalent disturbed "tip" response calculated from the H1.00 and H2.00 measurements shows fairly good agreement with the measured CPTU q_t tip stress. On average the calculated disturbed profile is slightly higher than the measured q_t trace, most likely a result of the increase in lateral stresses created by the CPT penetration, and corresponds with the results of Bloomquist et al. (1999) for uncemented soils. The disturbed tip profile shows the finer vertical resolution expected for the MFA end bearing response, and exhibits a divergence from the average trend for the depth range between 0.5 and 1.5 m. As is typical for most geologies it is believed that this divergence identifies the characteristic surficial crust caused by typical weather related wet/dry cycling.

Figures 6-42 to 6-44 show the calculated disturbed end bearing response and where available the calculated smooth side friction response for the SPWA, LPWA, and BWDWA test sites, respectively. Figure 6-42 shows that for the SPWA test site the calculated disturbed tip stress follows a similar trend to the measured tip stress over the majority of the measured depth range. The general trend of the two responses diverge around 5 m, from 6 to 8 m, and from 9.5 to 10m. The response at 5 m and between 9.5 and 10 m indicate slightly structured material also seen in the larger difference between the two textured sleeve traces shown in the right most subplot. The disturbed response from 6 to 8 m shows a reduction in calculated end bearing response possibly indicating soil crushing or another strength loss phenomena occurring within this depth range.

Figure 6-43 shows promising results of the presented framework for the LPWA test site, with the known cemented layer from 1 to 2 m showing a much higher end bearing response from the MFA calculation as compared to the measured q_t response. The cementation within the layer is believed to result in the continued increases in sleeve response above the value of critical surface roughness. The remainder of the calculated disturbed end bearing response with depth is similar to the measured q_t trace. Unfortunately, two sleeves below the critical roughness of the LPWA site were never operational within the same sounding, as the f_{a1} sensor position was inoperative for the entire test series. Figure 6-44 compares the disturbed end bearing and side friction traces calculated from the multi friction data as compared to the measured q_t and f_s values for the BWDWA site. Due to the extremely low sleeve and tip response within the soft clay at the BWDWA site the calculations expectantly show greater fluctuation, with the calculated disturbed end bearing stress approximating a zero value over a large portion of the measured depths. The calculated disturbed sleeve response is also highly variable but does show similar response to the measured values within most of the soft clay layer again showing a positive indication that the presented framework may be promising.

6.5.4 Summary

The concept of analyzing multiple textured friction sleeve measurements within a single sounding to allow for the calculation of disturbed end bearing and side friction traces has been presented. A summary of the observations regarding this concept are listed below:

- Within most of the soil strata tested, the results of the MF based tip and sleeve calculations produced values on the order of the measured CPT q_t and f_s values.
- The ability to estimate CPT q_t and f_s values could lead to the implementation of the multi friction devices in stratigraphies traditionally problematic to traditional CPT devices.
- A number of the conventional penetration testing limitations associated with traditional CPT measurements: sensor overload, verticality, and wear in abrasive soils are accentuated by the placement of the CPT sensors at the front of the penetration zone, where abrasion and wear on devices is the highest, and the stress state is the most variable. The possibility of using a "dummy" tip with improved structural integrity ahead of devices like the MFA and MPFA may provide a way to test in some intermediate conditions previously too harsh for conventional CPT use.
- The use of non CPT tip configurations ahead of the MFA/MPFA devices could be further extended for use in stratigraphies with included impenetrable layers and for angled or horizontal pushes using modern drilling technologies by trailing a multi friction attachment behind a drill head.
- Within the limited tested strata that showed inherent soil structure, the calculated disturbed end bearing responses showed an increase over the respective q_t measurements within that depth range.

Future testing is planned at additional sites with known structured strata, which will hopefully determine if the presented framework is a viable method for identifying and possibly quantifying the level of structure or sensitivity within tested soils.

6.6 Soil Classification Using MF Interface Data

6.6.1 A Brief Review of CPT Soil Classification Methodologies

A main objective in all geotechnical site investigations is to determine the type, extent, and properties of the geologic materials in as much detail as possible within the constraints of the given site conditions and project budget. Cone penetrometers, specifically piezocones, offer a site investigation tool that can effectively identify the behavioral type and extent of tested stratigraphy, and provide unparalleled profiling ability, with CPTU response times typically sufficiently fast to identify very thin layers (< 5 mm) (Lunne et al., 1997). Accurate geostratification and classification are paramount to successful geotechnical engineering practice, as the soil layering and classification often serve as the basis for all subsequent analyses and calculations. The values of CPT data are functions of a number of fundamental soil characteristics, and as such, the variations in measured response can be used to identify both the layering and properties of tested soils.

There are currently five methods for determining geostratification from CPT data: visual examination of the sensor traces, soil classification charts, probability methods, variograms, and clustering analysis (Liao, 2005). Of these methods, only visual examination and automated processing using classification charts are widely used in current practice. Both the visual and automated classification methods are based on

experience with CPTU data, and are based on the general changes in CPTU sensor response as a function of soil behavior. It is important to note that classification based on cone penetrometer data does not provide accurate determination of particle size and distribution, but rather distinguishes materials based on differences in soil behavior (Douglas and Olson, 1981). All CPT soil classification methods are based on the general trends known to exist for CPT response. The general trends being that: sandy soils tend to produce high q_t (> 3 MPa), low R_f, and very low Δu ($\Delta u = u_m - u_0$); clay soils tend to produce low q_t (< 2 MPa), high R_f, and very high Δu; and organic soils tend to produce very low q_t, very high R_f, and very high Δu. Sensitive soils tend to produce higher q_t, lower R_f, and higher Δu; and soils with high OCR tend to produce higher q_t and R_f but lower or even negative Δu than similar soils at lower OCR (Lunne et al., 1997). While visual examination of CPT records can often lead to accurate identification of the main layers with the tested stratigraphy, subtle differences in sensor response resulting from changes in soil properties (e.g. OCR, PI, ϕ', S_u, etc.) are often more easily determined through the use of objective computer algorithms and classification charts.

The use of soil classification charts is popular in engineering practice, because they allow for the simple evaluation of soil type through the application of computer algorithms. There have been a number of soil classification systems defined in the geotechnical literature, as summarized in Table 6-11 (Liao, 2005). This table groups soil classification systems based on the sensors utilized, and includes the particular normalization scheme employed in each method. The most commonly used cone penetrometer classification charts are those of Robertson (1990, 1991), and are shown as Figures 6-45 and 6-46. The implementation of these classification charts typically follows

a point by point comparison of the normalized CPT data with the defined range of typical values for various soil types. Once each depth is classified as exhibiting a certain behavior type, the soil stratigraphy is generated by grouping the data points into distinct layering. The resolution of the layering is often performed via user discretion and can result in a range of determined classifications ranging from fine to coarse layering. The process of clustering has been presented in the research as a more robust method for choosing layer boundaries based on statistical confidence and variation within the classification data, as seen in Hegazy and Mayne (1998, 2002) and Liao (2005), however, it is typically not used in conventional practice.

6.6.2 In Situ Interface Behavior as a Function of Soil Type

As presented earlier in Chapter 2 and Section 6.4, the interface behavior of soils is known to vary as both a function of soil type and the contacting interface properties. Most notably soil - continuum interface response is known to be primarily affected by the angle of internal friction of the soil and the surface roughness of the counterface material. The multi friction attachment devices have the ability to provide in situ measurements of interface behavior across the full range of typical surface roughness properties encountered in geotechnical engineering (Figure 2-4) and for all soil conditions amenable to penetrometer investigations. This section looks into analyzing the friction data obtained for the various geologic conditions tested to date, to see if the use of MFA/MPFA data can provide an improved means for soil classification.

As presented in Section 6.4.5, the soils from the seven sites tested to date showed a range of interface behaviors based on soil type and other factors such as mineralogy, density, and cementation. The general trend within the range of responses showed that

interface response increased with increasing particle size, in situ density, and level of cementation. Additionally, all of the non structured geologies showed good agreement with conventional concepts of geotechnical interface behavior, showing increased isolated interface response up to a critical roughness after which the behavior remained relatively constant. The critical roughness values observed, ranged from $R_{max} \approx 1.00$ mm for the uncemented LPWA calcareous sand down to $R_{max} \leq 6.4$ μm for the BWDWA soft clay. The critical roughnesses decreased as a function of particle size and were seen to be larger for the current intermittent texturing than traditionally found for continuously textured surfaces. As the interface response of the non-structured materials showed no appreciable change across the range of large textures, it becomes more advantageous to focus comparisons towards lower roughnesses in order to maximize the observed differences in behavior.

In the search for a parameter to define the interface response as a function of soil type, several primary requirements were held paramount: nondimensionality, normalization with depth and/or state of stress, maintaining continuity with current CPT soil classification parameters, and a means to clearly differentiate changes in response as a function of soil type. A number of different parameters were investigated in order to most clearly differentiate the behaviors of the tested soil types as a function of the measured in situ interface behavior. In the end a parameter was chosen that best met the criteria defined above, and is herein called the Multi Friction Classification Parameter (*MFCP*):

$$MFCP = \frac{2.5 * \sigma_{v0}}{\tau_{H0.50} - \tau_{SM}} \qquad \text{(Eq. 6-2)}$$

where σ_{v0} = total vertical stress, $\tau_{H0.50}$ = the isolated interface stress for a H0.50 textured attachment sleeve, and τ_{SM} = the measured sleeve stress for a smooth attachment sleeve.

While CPT and MFA/MPFA measurements are more directly affected by lateral as opposed to vertical stress (Salgado et al., 1997), reliable estimates of in situ lateral stress are still not available with conventional geotechnical methods. As such, as with other normalized classification parameters, the total vertical stress is used to normalize the behavior with changes in stress state. The denominator in the *MFCP*, the mathematical difference of textured and smooth interface response, represents the slope of isolated interface response as a function of surface roughness. Variations in interface response as a function of surface roughness are characterized by the difference between the SM and H0.50 isolated interface response. These sleeves are focused towards the sensitive range of lower surface textures while still providing a significant difference in response across a wide range of soil behaviors. Interface response as a function of surface roughness is known to deviate as a function of fundamental soil characteristics, as discussed for known laboratory behavior in Chapter 2 and shown for in situ results in Figure 6-41. The form of the above expression was chosen so that the response of the *MFCP* was seen to exhibit similar trends in response the conventional normalized CPT friction ratio $F_R = f_s / (q_t - \sigma_{v0})$], i.e. values that generally increase from hard sand to soft clay behaviors. The adjustment factor of 2.5 in the *MFCP* expression was chosen so that the *MFCP* provides approximately equivalent response to F_R for clean silica sand geologies.

6.6.3 Preliminary Results

6.6.3.1 Introduction

A main objective of this preliminary investigation into delineating soil class based on variations in interface response was to calibrate and compare the response of the *MFCP* with other popular CPT classification schemes. As described earlier, the *MFCP* exhibits similar trends in response as a function of soil behavior as the F_R parameter. Similarity in the response of these parameters is expected as they are both fundamentally dependent on interface behavior. Direct comparisons between F_R and *MFCP* with depth are used to highlight prominent variations between the parameters as a function of characteristic soil behavior. Additionally, the widely used CPTU soil classification scheme of Robertson (1990, 1991), as outlined in Figures 6-45 and 6-46, was used to define baseline conventional CPTU soil classifications for the tested soils.

While most of the test sites contain the necessary combination of a SM and H0.50 sleeve within a single sounding to determine the *MFCP*, the LPWA soundings do not include an operational H0.50 sleeve trace, the MPSC and LPWA soundings do not provide a SM and textured attachment trace within a single sounding, and the SPWA soundings do not include an operational *SM* of f_s trace. Unfortunately, the absence of a smooth sleeve measurement excluded the SPWA site from the current analyses. However, in order to include the MPSC and LPWA sites within the context of the current analysis, the f_s measurement is substituted for the *SM* trace for both the LPWA and MFCP sites, with an *H1.00* sensor additionally substituted for the *H0.50* measurement at the LPWA site. These substitutions, although not ideal, are considered acceptable within the context of the current preliminary investigation. The *MFCP* using the *H1.00* in place of *H0.50* is

further modified by using an adjustment constant of 5 instead of 2.5 to account for the doubling of the surface roughness range. This adjustment maintains the denominator of the *MFCP* as linearly related to the slope of interface behavior and is deemed acceptable for the calcareous sand as the critical roughness was determined to be on the order of the H1.00 sleeve for that material.

6.6.3.2 Summary of Overall Response

In order for the reader to develop general familiarity with the new normalized classification parameter, the response from the full range of tested geologies is presented first. Both the conventional (Q_t, F_R, and B_q) and newly introduced (*MFCP*) classification parameters are calculated over the full range of tested depths for all sites excepting the SPWA site. As in Section 6.5, several prominent layers of known soil type and properties are used to highlight the observed trends within the data. Figures 6-47 and 6-48 present the response of all measured data points for each of the prominent layers within the framework of the Robertson (1990, 1991) classification system. These figures show the conventional soil classification of the current soils, and provide a baseline for the current discussions into using multi friction data to conduct soil classification. Table 6-12 lists the average and range of values for the Q_t, F_R, B_q, and *MFC* parameters within the highlighted layers. In order to accentuate trends in the behavior the table is shown in quadricate, sorted by magnitude for each of the four classification parameters listed.

It can be seen that although F_R and *MFCP* show similar trends with regard to the characteristic soil type, the *MFCP* is seen to effectively vary over four orders of magnitude from 10^{-1} to 10^{3}, whereas the F_R parameter only varies over two orders of magnitude from 10^{-1} to 10^{1}. This increase in the range of response of the *MFCP* shows

promise at better delineating between than the traditional F_R parameter. The F_R parameter exhibits minimal variation as a function of sand mineralogy and density across the range of tested soils. Whereas, the *MFCP* parameter shows significant variation as a function of mineralogy, as seen in the divergent response for the silica and calcareous sands. Additionally, the *MFCP* shows only minimal variation across the range of typical sand densities, with the response for the unconventional very loose sand being significantly different.

Figures 6-48 to 6-49 present plots showing *MFCP* response as a function of Q_t and B_q, respectively, with Figure 6-47 and 6-51 showing the comparative F_R - Q_t and F_R - B_q responses. Parallel plots showing only the average values of each layer with the full range of measured values represented by error bars are presented in Figures 6-52 to 6-55, respectively. Figure 6-49 exhibits the expected trend of increasing *MFCP* with increasing clay-like response. The cemented calcareous sand exhibits the lowest *MFCP*, with an average response of *MFCP* = 0.6, with the structured silty clay of the Cooper Marl showing the largest response, with an average value of *MFCP* = 457. The larger range of responses for the *MFCP* does not seem to increase the spread of values observed within each layer. The response for the Cooper Marl shows a fair amount of scatter in *MFCP* across the layer thickness, however, this increased scatter was also seen for the F_R parameter and is believed to result from the inherent heterogeneity of this deposit. Using the conventional Robertson (1990, 1991) classification system, the Cooper Marl is identified as a silty sand by the Q_t - F_R behavior, exhibiting similar response to the very loose silica sand layer, and as a clay by the Q_t - B_q behavior. The *MFCP* more clearly differentiates between the Cooper Marl and very loose silica sand layers, exhibiting the

expected shift towards the clay end of the behavior spectrum for the Cooper Marl response.

6.6.3.3 Summary of Individual Site Response

While the classification style plots provide a useful perspective on the data across a range of characteristic soil types, it is also insightful to observe the continuous behavior of the *MFCP* with depth for the various sites. Figure 6-56 presents data from the SRVT site, showing traces of q_t; u_2; f_s; *SM*; *H0.50*; *H1.00*; Robertson 1990-91 Classification; and an overlay of F_R, *MFCP* in the subplots from left to right. The Robertson (1990, 1991) classification system denotes the stratigraphy at the SRVT test site as sand to sandy silt behavior over the range of tested depths, excepting the thin layers at approximately 6.8 and 8.5 m, corresponding to thin silt seams. The conventional normalized friction ratio (F_R) and the multi friction classification parameter (*MFCP*) both show similar trends in behavior with depth. The friction parameters both show slightly increasing response with depth indicative of a relative increase in soil density with depth, and all show a marked increase in response within the depth range of the two silt seams. From a purely visual identification perspective, one could argue that the *MFCP* more clearly differentiates between the sandy and silty behaviors found at this site as compared to the F_R as a result of the larger changes in response seen within the silt layers.

Figure 6-57 presents data from the LS test site, showing traces of q_t, u_2, f_s, an overlay of *SM and H0.50*, *MFCP*, F_R, Robertson 1990-91 Classification, and an overlay of F_R *and MFCP* in the subplots from left to right. The Robertson (1990) classification system denotes the stratigraphy at the LS test site as clean sand to a depth of 8 m, followed by a thin layer of clay, a silty sand to sandy silt from 8.5 to 11 m, a thin layer of

clayey silt to silty clay, and then clean sand from 12 to 14 m. However, the layer from 8.5 to 11 m is known to be a very loose silica sand layer from sampling at the site. The FR and *MFCP* traces again show similar response within the upper silica sand layer, yet show a large divergence within the lower stratigraphies. The *MFCP* correctly identifies the significant decrease in side friction exhibited within this layer, with the value of *MFCP* being similar to the response of the SRVT silt layers and the uncemented calcareous sand. It should be noted that soil classification based entirely on only two parameters can result in the misclassification of soils exhibiting behaviors near the limits of conventional response for various materials. In the case of the very loose sand layer, additional insight into the soil type can be gained by looking at the pore pressure response. The lack of excess pore generation within the layer indicates that the soil is coarse grained yet has very low frictional resistance due to either a very low density, or as a function of mineralogy as seen for the calcareous sand layers. In this case the normalized tip response can be used to separate the behavior of the calcareous sand, which typically exhibits high tip stresses from the moderate tip stresses observed within the loose sand layer more representative of silica sand geologies.

Figure 6-58 shows data from the LPWA test site, showing traces of q_t, u_2, f_s, an overlay of *f_s and H1.00*, *MFCP*, F_R, Robertson 1990-91 Classification, and an overlay of *F_R and MFCP* in the subplots from left to right. The Robertson (1990, 1991) classification system denotes the stratigraphy at the LPWA test site as gravelly sand to sand from the surface to 3m and then clean sand to silty sand through the extent of the sounding, excepting a thin layer at 5.8 m classified as a silty sand to sandy silt. The response of *MFCP* and F_R are relatively equivalent through the top two meters of soil,

with the *MFCP* showing transitional response from 2 to 4 meters, and then exhibiting significantly increased response as compared to F_R, on the average of *MFCP* = 13, with the fine grained layer noted above at 5.8 m again denoted by the *MFCP* response. While these initial results do not provide viable means for making general conclusions regarding the response of the *MFCP* in all soil conditions, the current results show promise in differentiating between sands of varying mineralogy and level of structure or cementation.

Figure 6-59 shows data from the MPSC test site, showing traces of q_t, u_2, f_s, an overlay of f_s *and H0.50*, *MFCP*, F_R, Robertson 1990-91 Classification, and an overlay of F_R *and MFCP* in the subplots from left to right. The Robertson (1990, 1991) classification shows no clear defined response within the upper 14 m, with response ranging gravelly sand to clay behaviors. Within the Cooper marl stratigraphy the two Robertson (1990, 1991) classification plots show clear but different response, with the Q_t - F_R chart indicating silty sand behavior and the Q_t - B_q chart indicating clay behavior. The *MFCP* also shows a range of responses through the upper soil stratigraphies, and shows a varied but consistently high response through the Cooper Marl material indicative of the known silty clay mineralogy. The calcareous mineralogy and highly structured in situ state of the Cooper Marl is believed to cause some of the variations in the *MFCP*. Additionally, the *MFCP* inherently exhibits greater mathematical sensitivity to changes in measured interface behavior at higher values of *MFCP* (as the denominator approaches zero equating to equivalent smooth and textured response), however, the logarithmic scale typically used for friction parameters in most soil classification schemes maintains the grouping of the data for higher values.

Figure 6-60 shows data from the BWDWA test site, showing traces of q_t, u_2, an overlay of *SM and H0.50*, *MFCP*, F_R, Robertson 1990-91 Classification, and an overlay of F_R *and MFCP* in the subplots from left to right. As noted before the upper 1 m of soil was prebored and was not tested at this site. The remainder of the stratigraphy is classified using Robertson (1990) as two upper layers of sand interbedded with a thin clay layer, followed by a clay material to the extent of the sounding. The current data is slightly affected by a dissipation test performed at a tip depth of approximately 6.8 m as can be seen in the traces of each of the subplots of Figure 6-60, keeping in mind that time domain events are offset with depth for the various sensors. The *MFCP* behavior shows variable response within the upper few meters, followed by relatively constant response within the soft clay until 7 m depth, on the order of *MFCP* = 25 to 50, and increasing with depth from that point downward. The adverse affect of time domain changes in procedure, such as long dissipations and cycling, can be seen in the ill behaved response of the *MFCP* and to a lesser extent F_R parameters at these depths.

6.6.4 Summary and Conclusions Regarding MFA/MPFA Soil Classification

A parameter has been developed using the available MFA and MPFA data in an attempt to aid in the classification and identification of soil type and characteristic behaviors. This formulation and benefits of this parameter, termed the Multi Friction Classification Parameter (*MFCP*), are summarized herein:

- The MFCP is fundamentally based on the concept that the differential magnitude between smooth and moderately textured interface response provides a good indication of soil behavior and type.

- The MFCP is mathematically formulated similar to other classification parameters, in that it is dimensionless and is normalized with the total overburden stress to reduce the affect of measurement depth on the parameter response.
- An adjustment factor is applied within the MFCP formula such that the response within typical silica sand geologies was observed to be equivalent to the conventional normalized friction parameter (F_R).
- The MFCP effectively varies over four orders of magnitude for the wide range of soil types tested to date, while still exhibiting clustering of response within individual soil layers similar to the other normalized CPT parameters.
- The increased variation in the MFCP across four orders of magnitude, as compared to the two orders of magnitude variation representative of the F_R parameter, leads to more clearly defined changes in response for a number of the soil conditions tested.

It is duly noted that the robust formulation of any in situ based soil classification parameter or system requires a large database of data. While the current data does cover a fair range of soil behaviors, the author readily notes the preliminary nature of the presented parameter and all conclusions made with regard to the response of the presented parameter.

Table 6-1a. Summary of MFA Soundings Conducted By DeJong (2001). All Soundings Nominally 12 m in Depth Unless Otherwise Specified.

SND #	Test Site	File Number	Date	Purpose / Comments	Lead Module	Attachment Configuration f_{a1}	f_{a2}	f_{a3}	f_{a4}	Notes
1	SRVT	Z07L0011C	7-Jul-00	July	15cm^2 CPT	SM1	SM2	SM3	SM4	
2		Z07L0012C	7-Jul-00	Testing	15cm^2 CPT	SM1	SM2	SM3	SM4	
3		Z08L0003C	7-Jul-00		Short	SM1	SM2	SM3	SM4	
4		Z07L0001C	7-Jul-00		Long	SM1	SM2	SM3	SM4	
5		Z07L0002C	7-Jul-00		Long	60H1S5	60H1S5	60H1S5	60H1S5	
6		Z07L0003C	7-Jul-00		Short	60H1S5	60H1S5	60H1S5	60H1S5	
7		Z07L0004C	7-Jul-00		15cm^2 CPT	60H1S5	60H1S5	60H1S5	60H1S5	
8		Z07L0005C	7-Jul-00		15cm^2 CPT	60H1S5	60H1S5	60H1S5	60H1S5	
9		Z08L0001C	8-Jul-00		15cm^2 CPT	SM1	60H1S5	SM3	60H1S5	
10	SRVT	Z11O0002C	11-Oct-00	Setup	15cm^2 CPT	SM1	SM3	SM2	SM4	
11		Z11O0003C	11-Oct-00	Verification	15cm^2 CPT	SM1	SM3	SM2	SM4	
12		Z11O0004C	11-Oct-00		15cm^2 CPT	SM1	SM3	SM2	SM4	
13		Z11O0005C	11-Oct-00		15cm^2 CPT	SM1	SM3	SM2	SM4	
14		Z11O0006C	11-Oct-00		15cm^2 CPT	30H1S3	30H1S3	30H1S3	30H1S3	
15		Z11O0007C	11-Oct-00		15cm^2 CPT	30H1S3	30H1S3	30H1S3	30H1S3	
16		Z11O0008C	11-Oct-00		15cm^2 CPT	30H1S3	30H1S3	30H1S3	30H1S3	
17		Z12O0004C	12-Oct-00		15cm^2 CPT	SM1	SM2	SM3	SM4	
18	SRVT	Z12O0005C	12-Oct-00	Diamond	15cm^2 CPT	SM1	SM2	30H.125S3	SM4	
19		Z12O0006C	12-Oct-00	Height	15cm^2 CPT	SM1	SM2	30H.25S3	SM4	
20		Z12O0007C	12-Oct-00		15cm^2 CPT	SM1	SM2	30H.5S3	SM4	
21		Z12O0008C	12-Oct-00		15cm^2 CPT	SM1	SM2	30H1S3	SM4	
22		Z12O0009C	12-Oct-00		15cm^2 CPT	SM1	SM2	30H2S3	SM4	
23	SRVT	Z13O0001C	13-Oct-00	Diamond	15cm^2 CPT	SM1	SM2	30H1S1	SM4	
24		Z13O0002C	13-Oct-00	Spacing	15cm^2 CPT	SM1	SM2	30H1S2	SM4	
25		Z13O0003C	13-Oct-00		15cm^2 CPT	SM1	SM2	30H1S4	SM4	
26	SRVT	Z13O0004C	13-Oct-00	Diamond	15cm^2 CPT	SM1	SM2	15H1S3	SM4	
27		Z13O0005C	13-Oct-00	Angle	15cm^2 CPT	SM1	SM2	22.5H1S3	SM4	
28		Z13O0006C	13-Oct-00		15cm^2 CPT	SM1	SM2	37.5H1S3	SM4	
29		Z13O0007C	13-Oct-00		15cm^2 CPT	SM1	SM2	45H1S3	SM4	
30	SRVT	Z13O0008C	13-Oct-00	Combinations	15cm^2 CPT	30H1S3	SM2	SM3	SM4	
31		Z13O0009C	13-Oct-00		15cm^2 CPT	SM1	30H.125S3	30H.25S3	30H.5S3	
32		Z13O0010C	13-Oct-00		15cm^2 CPT	SM1	30H.5S3	SM3	30H1S3	
33		Z14O0001C	14-Oct-00		15cm^2 CPT	SM1	30H1S3	SM3	30H2S3	
34		Z14O0002C	14-Oct-00		15cm^2 CPT	SM1	30H1S3	SM3	30H1S4	
35		Z14O0003C	14-Oct-00		15cm^2 CPT	SM1	30H1S1	SM3	30H1S3	
36		Z14O0006C	14-Oct-00		Short	SM1	30H.125S3	30H.25S3	30H.5S3	
37		Z14O0007C	14-Oct-00		Long	SM1	30H.125S3	30H.25S3	30H.5S3	
38		Z14O0008C	14-Oct-00		15cm^2 CPT	SM1	SM2	30H1S3-4 Rings	SM4	
39		Z14O0009C	14-Oct-00		15cm^2 CPT	SM1	SM2	30H1S3-7 Rings	SM4	

Table 6-1b. Summary of MFA Soundings Conducted for the Current Study at the SRVT Test Site. All Soundings Nominally 12 m in Depth Unless Otherwise Specified.

SND #	Test Site	File Number	Date	Purpose / Comments	Lead Module	Attachment Configuration f_{a1}	f_{a2}	f_{a3}	f_{a4}	fa5	Notes
40	SRVT	Z04U0100C	4-Jul-01	30H1S3 APF	15cm^2 CPT	SM1	SM2	30H1S3	SM4	N/A	
41		Z04U0101C	4-Jul-01		15cm^2 CPT	SM1	SM2	30H1S3 (2R)	SM4	N/A	
42	SRVT	Z04U0102C	4-Jul-01	30H.5S3 APF	15cm^2 CPT	SM1	SM2	30H.5S3 (4R)	SM4	N/A	
43		Z04U0103C	4-Jul-01		15cm^2 CPT	SM1	SM2	30H.5S3 (7R)	SM4	N/A	
44		Z04U0104C	4-Jul-01		15cm^2 CPT	SM1	SM2	30H.5S3	SM4	N/A	
45		Z04U0105C	4-Jul-01		15cm^2 CPT	SM1	30H.5S3	30H.5S3	30H.5S3 (7R)	N/A	
46	SRVT	Z05U0101C	5-Jul-01	30H.25S3 APF	15cm^2 CPT	SM1	30H.25S3	30H.25S3	30H.25S3 (7R)	N/A	
47		Z05U0102C	5-Jul-01		15cm^2 CPT	SM1	SM2	30H.25S3	SM4	N/A	
48		Z05U0103C	5-Jul-01		15cm^2 CPT	SM1	SM2	30H.25S3 (7R)	SM4	N/A	
49		Z05U0104C	5-Jul-01		15cm^2 CPT	SM1	SM2	30H.25S3 (4R)	SM4	N/A	
50		Z05U0106C	5-Jul-01	Pen Angle	15cm^2 CPT	SM1	SM2	7.5H1S3	SM4	N/A	
51	SRVT	Z05U0107C	5-Jul-01	Spacing	15cm^2 CPT	SM1	SM2	30H1S1	SM4	N/A	
52		Z05U0108C	5-Jul-01		15cm^2 CPT	SM1	SM2	30H1S0	SM4	N/A	
53		Z06U0101C	6-Jul-01	Pen Angle	15cm^2 CPT	SM1	SM2	15H1S3	SM4	N/A	
54		Z06U0102C	6-Jul-01	Combinations	15cm^2 CPT	30H.25S3	30H.5S3	30H1S3	30H2S3	N/A	
55	SRVT	Z06U0103C	6-Jul-01	SM - Position	15cm^2 CPT	SM1	SM2	SM3	SM4	N/A	
56		Z06U0105C	6-Jul-01		SHORT	SM1	SM2	SM3	SM4	N/A	
57		Z06U0106C	6-Jul-01		LONG	SM1	SM2	SM3	SM4	N/A	
58	SRVT	Z06U0107C	6-Jul-01	Angle Set	15cm^2 CPT	SM1	30H.25S3	SM3	30H1S3	N/A	45° Push Ang
59		Z07U0101C	7-Jul-01		15cm^2 CPT	SM1	30H.25S3	SM3	30H1S3	N/A	67.5° Push Ang
60		Z07U0102C	7-Jul-01		15cm^2 CPT	SM1	30H.25S3	SM3	30H1S3	N/A	90° Push Ang
61	SRVT	Z07U0107C	7-Jul-01	SMR Probe	SMR - CPT	No Attachment - ARA Devices					
62		Z07U0108C	7-Jul-01		SMR - CPT	No Attachment - ARA Devices					
63		Z07U0109C	7-Jul-01	Vision	ARA - Dummy	No Attachment - ARA Devices					
64		Z08U0105C	8-Jul-01	Setup Test	15cm^2 CPT	SM1	30H.25S3	SM3	30H1S3	N/A	
65	SRVT	Z08U0107C	8-Jul-01	H1 - Position	15cm^2 CPT	SM1	SM2	SM3	30H1S3	N/A	No fa3
66		Z08U0108C	8-Jul-01		15cm^2 CPT	30H1S3	SM2	SM3	SM4	N/A	No fa2 & fa3
67		Z08U0110C	8-Jul-01		LONG	SM1	SM2	SM3	30H1S3	N/A	No fa3

Table 6-1c. Summary of MFA Soundings Conducted for the Current Study at the SRVT Test Site (cont.). All Soundings Nominally 12 m in Depth Unless Otherwise Specified.

SND #	Site	File Number	Date	Purpose / Comments	Lead Module	Attachment Configuration f_{a1}	f_{a2}	f_{a3}	f_{a4}	f_{a5}	Notes
68	SRVT	Z18U0302C	18-Jun-03	Spacer	15cm^2 CPT	SM1	10 cm Spac	SM3	5 cm Spac	30H1S3	
69		Z18U0304C	18-Jun-03	Tests	15cm^2 CPT	SM1	10 cm Spac	SM3	5 cm Spac	30H2S3	
70		Z18U0306C	18-Jun-03		15cm^2 CPT	SM1	10 cm Spac	SM3	5 cm Spac	30H.5S3	
71		Z18U0307C	18-Jun-03		15cm^2 CPT	SM1	5 cm Spac	SM3	10 cm Spac	30H1S3	
72		Z18U0308C	18-Jun-03		15cm^2 CPT	SM1	5 cm Spac	SM3	10 cm Spac	30H2S3	
73		Z18U0309C	18-Jun-03		15cm^2 CPT	SM1	5 cm Spac	SM3	10 cm Spac	30H.5S3	
74		Z18U0310C	18-Jun-03		15cm^2 CPT	SM1	5 cm Spac	30H1S3	10 cm Spac	30H2S3	
75		Z18U0311C	18-Jun-03		15cm^2 CPT	SM1	5 cm Spac	30H.5S3	10 cm Spac	30H1S3	
76		Z18U0312C	18-Jun-03		15cm^2 CPT	SM1	10 cm Spac	30H.5S3	5 cm Spac	30H1S3	
77		Z18U0313C	18-Jun-03		15cm^2 CPT	SM1	10 cm Spac	30H1S3	5 cm Spac	30H2S3	
78		Z19U0301C	19-Jun-03		15cm^2 CPT	SM1	SM2	30H.5S3	30H1S3	N/A	
79		Z19U0302C	19-Jun-03		15cm^2 CPT	SM1	SM2	30H1S3	30H2S3	N/A	
80	SRVT	Z19U0303C	19-Jun-03	H2 - Position	15cm^2 CPT	SM1	SM2	30H2S3	SM4	N/A	
81		Z19U0304C	19-Jun-03		15cm^2 CPT	SM1	SM2	SM3	30H2S3	N/A	
82		Z19U0305C	19-Jun-03		15cm^2 CPT	SM1	30H2S3	SM3	SM4	N/A	
83		Z19U0306C	19-Jun-03		15cm^2 CPT	30H2S3	SM2	SM3	SM4	N/A	
84		Z19U0310C	19-Jun-03		LONG	30H2S3	SM2	SM3	SM4	N/A	
85		Z19U0311C	19-Jun-03		SHORT	30H2S3	SM2	SM3	SM4	N/A	
86		Z19U0312C	19-Jun-03		SHORT	SM1	30H2S3	SM3	SM4	N/A	
87		Z19U0313C	19-Jun-03		LONG	SM1	30H2S3	SM3	SM4	N/A	
88		Z19U0314C	19-Jun-03		LONG	SM1	SM2	30H2S3	SM4	N/A	
89		Z19U0315C	19-Jun-03		SHORT	SM1	SM2	30H2S3	SM4	N/A	
90		Z19U0316C	19-Jun-03		LONG	SM1	SM2	SM3	30H2S3	N/A	
91	SRVT	Z20U0301C	20-Jun-03	Tip	15cm^2 CPT	SM1	30H0.125S3	SM3	30H0.25S3	N/A	
92		Z20U0303C	20-Jun-03	Prediction	15cm^2 CPT	SM1	30H0.25S3	SM3	30H0.5S3	N/A	
93		Z20U0304C	20-Jun-03	Tests	15cm^2 CPT	SM1	30H1S3	SM3	30H2S3	N/A	To - 101.7 ft
94		Z20U0305C	20-Jun-03		15cm^2 CPT	30H0.25S3	30H0.5S3	30H1S3	30H2S3	N/A	To - 101.8 ft

Table 6-1d. Summary of MFA Soundings Conducted for the Current Study at the LS Test Site. All Soundings Nominally 13 m in Depth Unless Otherwise Specified.

SND #	Site	File Number	Date	Study Comments	Lead Module	Attachment Configuration f_{a1}	f_{a2}	f_{a3}	f_{a4}	Notes
95	LS	Z10N0303C	10-Nov-03	Pre	15cm^2 CPTU	SM1	30H.125S3	SM3	30H.5S3	
96		Z10N0304C	10-Nov-03	Blast	15cm^2 CPTU	SM1	30H.125S3	SM3	30H.5S3	
97		Z10N0305C	10-Nov-03		15cm^2 CPTU	SM1	30H.125S3	SM3	30H.5S3	Slow Penetration in Loose Layer
98		Z10N0306C	10-Nov-03		15cm^2 CPTU	SM1	30H.25S3 (7R)	SM3	30H1S3 (7R)	
99		Z10N0307C	10-Nov-03		15cm^2 CPTU	SM1	30H.25S3 (7R)	SM3	30H1S3 (7R)	
100		Z10N0308C	10-Nov-03		15cm^2 CPTU	SM1	30H.25S3 (7R)	SM3	30H1S3 (7R)	
101		Z10N0309C	10-Nov-03		15cm^2 CPTU	SM1	30H.25S3 (7R)	SM3	30H1S3 (7R)	
102		Z10N0310C	10-Nov-03		15cm^2 CPTU	SM1	30H1S3 (2R)	SM3	30H1S3 (7R)	
103		Z10N0311C	10-Nov-03		15cm^2 CPTU	SM1	30H1S3 (2R)	SM3	30H1S3 (7R)	Slow Penetration in Loose Layer
104		Z10N0312C	10-Nov-03		15cm^2 CPTU	SM1	30H1S3 (2R)	SM3	30H1S3 (7R)	
105		Z10N0313C	10-Nov-03		15cm^2 CPTU	SM1	30H1S3 (2R)	SM3	30H1S3 (7R)	
106	LS	Z11D0301C	11-Dec-03	Post	15cm^2 CPTU	SM1	30H.125S3	SM3	30H.5S3	
107		Z11D0302C	11-Dec-03	Blast	15cm^2 CPTU	SM1	30H.125S3	SM3	30H.5S3	
108		Z11D0303C	11-Dec-03	Seq #1	15cm^2 CPTU	SM1	30H.125S3	SM3	30H.5S3	Slow Penetration in Loose Layer
109	LS	Z28J0402C	28-Jul-04	Post	15cm^2 CPTU	SM1	30H.125S3	SM3	30H.5S3	Slow Penetration in Loose Layer
110		Z28J0403C	28-Jul-04	Blast	15cm^2 CPTU	SM1	30H.125S3	SM3	30H.5S3	
111		Z28J0404C	28-Jul-04	Seq #2	15cm^2 CPTU	SM1	30H.125S3	SM3	30H.5S3	
112		Z28J0406C	28-Jul-04		15cm^2 CPTU	SM1	30H.125S3	SM3	30H.5S3	
113		Z28J0407C	28-Jul-04		15cm^2 CPTU	SM1	30H.125S3	SM3	30H.5S3	
114		Z28J0408C	28-Jul-04		15cm^2 CPTU	SM1	30H.125S3	SM3	30H.5S3	
115		Z28J0409C	28-Jul-04		15cm^2 CPTU	SM1	30H.125S3	SM3	30H.5S3	

Table 6-1e. Summary of MFA Soundings Conducted for the Current Study at the Western Australia Test Sites. All Soundings Nominally 11 m in Depth Unless Otherwise Specified.

SND #	Site	File Number	Date	Study Comments	Lead Module	Attachment Configuration f_{a1}	f_{a2}	f_{a3}	f_{a4}	Notes
116	SPWA	J09G0402C	9-Aug-04	James	SHORT	SM	SM	SM	SM	Load Test #1
117		J09G0404C	9-Aug-04	Schneider	SHORT	SM	SM	SM	SM	Load Test #2
118		J09G0405C	9-Aug-04	Load Tests	SHORT	SM	SM	SM	SM	Load Test Seq #2 *1st Part
119		J09G0408C	9-Aug-04		SHORT	SM	SM	SM	SM	Load Test Seq #2 *2nd Part
120		J09G0402C	9-Aug-04		SHORT	SM	SM	SM	SM	Load Test Seq #3
121		J10G0401C	10-Aug-04		15cm^2 CPT	SM	SM	SM	SM	2 LT Hole1
122		J10G0403C	10-Aug-04		15cm^2 CPT	SM	SM	SM	SM	2 LT Hole2
123		J11G0402C	11-Aug-04		SHORT	SM	SM	SM	SM	Load Test #1 Day 3
124		J11G0404C	11-Aug-04		SHORT	SM	SM	SM	SM	LT #2 - 1 way 28 mm cycles
125		J11G0406C	11-Aug-04		SHORT	SM	SM	SM	SM	LT #3A - 2 way 28 mm cycles
126	LPWA	Z12G0401C	12-Aug-04	Combination	15cm^2 CPTU	30H.125S3	30H.25S3	30H1S3	30H2S3	Push and Pull to 8.5m
127		MF12G0404C	12-Aug-04		15cm^2 CPTU	SM	30H1S3	SM	30H2S3	Push and Pull to 8.5m
128	LPWA	MF13G0401C	13-Aug-04	James	15cm^2 CPTU	SM	SM	SM	SM	Hole1 - straight push to 4m
129		MF13G0402C	13-Aug-04	Schneider	15cm^2 CPTU	SM	SM	SM	SM	Hole2 - 2-way 28mm cyc - LT @ 4m
130		MF13G0403C	13-Aug-04	Load Tests	15cm^2 CPTU	SM	SM	SM	SM	Hole3 - 1 way 28 mm cyc LT @ 4m
131	BWDWA	MF16G0401C	16-Aug-04	Twitch Test	15cm^2 CPTU	30H.25S3	30H.5S3	30H1S3	30H2S3	Twitch test @ 6.8m pre & post cyc

Table 6-2. Summary of MPFA Soundings Conducted for the Current Study. All Soundings Nominally 12 m in Depth Unless Otherwise Specified.

SND #	Site	File Number	Date	Study Comments	Lead Module	Attachment Configuration f_{a1}	f_{a2}	f_{a3}	f_{a4}	Notes
MPFA_1	VTK	Z04Y0402C	4-May-03	MPFA	15 cm^2 CPTU	SM1	SM2	SM3	SM4	No MP4
MPFA_2		Z04Y0403C	4-May-03	Verification	15 cm^2 CPTU	30H.125S3	30H2S3	SM3	SM4	No MP2, MP3, MP4
MPFA_3	MP_SC	Z20Y0407C	20-May-03	Cooper	15 cm^2 CPTU	SM1	SM2	SM3	SM4	No MP3, MP4
MPFA_4		Z20Y0408C	20-May-03	Marl	15 cm^2 CPTU	30H.125S3	30H.25S3	30H.5S3	30H1S3	No MS1, MP1, MP3, MP4
MPFA_5	BWDWA	Z08L0401C	8-Jul-04	Soft Clay	15 cm^2 CPTU	SM1	SM2	SM3	SM4	No fs, MP2
MPFA_6		MP15L0402C	15-Jul-04	Textured	15 cm^2 CPTU	SM1	30H1S3	SM3	SM4	No fs
MPFA_7		MP18L0401C	18-Jul-04	Behavior	15 cm^2 CPTU	SM1	30H.5S3	SM3	SM4	No fs
MPFA_8		MP19L0402C	19-Jul-04		15 cm^2 CPTU	SM1	30H.25S3	SM3	SM4	No fs, MS1, MP1, MS4, MP4, Twitch
MPFA_9		MP21L0401C	21-Jul-04		15 cm^2 CPTU	SM1	30H.125S3	SM3	SM4	No, fs, MS4, MP4 - Cycling at 6.8 m
MPFA_10		MP22L0401C	22-Jul-04		15 cm^2 CPTU	SM1	30H2S3	SM3	SM4	No, fs, MS4, MP4 - Cycling at 6.8 m
MPFA_11		MP27L0401C	27-Jul-04		15 cm^2 CPTU	SM1	30H1.5S3	SM3	SM4	No, fs, MS4, MP4 - Cycling at 6.8 m
MPFA_12		MP29L0402C	29-Jul-04		15 cm^2 CPTU	SM1	30H.75S3	SM3	SM4	No, fs, MS4, MP4 - Cycling at 6.8 m
MPFA_13	SPWA	MP30L0402C	30-Jul-04	Silica	15 cm^2 CPTU	30H.25S3	30H.5S3	30H1S3	30H2S3	No fs - Short Test ~1.5m
MPFA_14		MP30L0406C	30-Jul-04	Textured	15 cm^2 CPTU	30H.25S3	30H.5S3	30H1S3	30H2S3	No fs - Short Test ~5m
MPFA_15		MP30L0409C	30-Jul-04	Behavior	15 cm^2 CPTU	30H.25S3	30H.5S3	30H1S3	30H2S3	No fs
MPFA_16		Z30L0411C	30-Jul-04		SHORT	30H.25S3	30H.5S3	30H1S3	30H2S3	No MP0, MS1, MP1, MS3
MPFA_17		Z30L0412C	30-Jul-04		SHORT	30H.125S3	30H.25S3	30H.75S3	30H1.5S3	No MP0, MS1, MP1, MS3
MPFA_18		Z30L0414C	30-Jul-04		15 cm^2 CPTU	30H.125S3	30H.25S3	30H.75S3	30H1.5S3	No fs, MP0, MS1, MP1, MS2 ~6.5m
MPFA_19		Z30L0415C	30-Jul-04		15 cm^2 CPTU	30H.125S3	30H.25S3	30H.75S3	30H1.5S3	No fs, MS1, MP1, MS2
MPFA_20	LPWA	Z12G0404C	12-Aug-04	Calcareous	15 cm^2 CPTU	SM1	30H.25	30H.75S3	30H1.5S3	No fs, MS1, MP1 - Short Test ~2.5m
MPFA_21		Z12G0401C	12-Aug-04	Textured	15 cm^2 CPTU	SM1	30H.25	30H.75S3	30H1.5S3	No fs, MS1, MP1
MPFA_22		MP12G0403C	12-Aug-04	Behavior	15 cm^2 CPTU	SM1	30H2S3	SM3	SM4	No, fs, MP0, MS1, MP1
MPFA_23		MP12G0404C	12-Aug-04		15 cm^2 CPTU	SM1	30H1S3	30H1S3	30H1S3	No, fs, MP0, MS1, MP1 - Cycles 7-8m
MPFA_24		MP12G0405C	12-Aug-04		15 cm^2 CPTU	SM1	30H.125S3	30H.125S3	30H.125S3	No, fs, MP0, MS1, MP1 - Cycles 7-8m
MPFA_25	BWDWA	MP17G0401C	17-Aug-04	CPTU-MPFA	15 cm^2 CPTU	SM1	SM2	SM3	SM4	No, fs - Load Test Hole #1
MPFA_26		MP17G0402C	17-Aug-04	Load	15 cm^2 CPTU	SM1	SM2	SM3	SM4	No, fs - Load Test Hole #2
MPFA_27		MP18G0401C	18-Aug-04	Tests	15 cm^2 CPTU	SM1	SM2	SM3	SM4	No, fs - Load Test Hole #2 (cont...)
MPFA_28		MP18G0402C	18-Aug-04		15 cm^2 CPTU	SM1	SM2	SM3	SM4	No, fs - Load Test Hole #3

Table 6-3. Summary of Test Sites Used During the Current Study.

Abbreviated Site Name	Site Location	Stratigraphic Description
SRVT	South Royalton Vermont, USA	The South Royalton, Vermont test site consists of glacial outwash material comprised predominantly of medium dense uniform sand with occasional silt lenses. More Data can be found in DeJong (2001) and DeJong and Frost (2002).
LS	(30 km N of Charleston) South Carolina,USA	The South Carolina test site is located within the a coatal plain geology consisting of medium dense sand overlying a 3 m layer of very loose sand
MPSC	Mount Pleasant, South Carolina	The Mount Pleasant, South Carolina test site consists of mixed soil to a depth of 14 m followed by a thick calcaresou silty clay to sandy clay deposit locally known as the Cooper Marl to a depth of 20 m.
VSPL	Vertek Shop Parking Lot	The Vertek Shop Parking Lot test site is located adjacent to the Vertek CPT manufacturing facility in South Royalton, Vermont and consists of a glacial till geology.
SPWA	Shenton Park Perth, W. Australia	The Shenton Park site is located in Perth, Western Australia on an educational reserve operated by the University of Western Australia. The geology consists of surficial aeolian silicaceous sand of loose to medium density overlying variably cemented limestone, with intermittent limestone spires at various spacing and depth.
LPWA	Ledge Point (100 km N or Perth), W. Australia	The Ledge Point site is located approximately 100 km north of Perth, Western Australia, along the coast of the Indian Ocean. Ledge Point consists of an uncemented calcareous uniform fine sand (SP). The D_{50} grain size is 0.24 mm, the sand has less than 5 percent fines, and the maximum void ratio ranges from approximately 1.2 to 1.4.
BWDWA	Burswood Perth, W. Australia	Burswood consists of soft, high plasticity clay (LL=80, PI=40 to 50) with shell fragments and silt lenses. The undrained shear strength profile gradually increases from approximately 16 kPa at 4 m depth to 35 kPa at 17 m depth, with an apparent OCR due to ageing of 1.5 to 2. The sensitivity based on field vane data shows values between 4 and 9 above 7 m, and between 2 and 4 below 7 m. Additional information and test results from the Burswood site are contained in Randolph (2004) and Chung & Randolph (2004).

Table 6-4. Summary of Discrete Samples from the LS Test Site.

Sample Depth Increment (m)	USCS Classification	D_{50} (mm)	C_u	C_c	% Passing #200
3.0 – 5.0	SP	0.19	1.25	1.01	0.71
9.0 - 11.0	SP	0.19	1.75	1.15	3.76

Table 6-5. Summary of the Average Total Measured Sleeve Responses for the Selected Silica Sand Strata.

Layer Description	f_s	SM	H0.125	H0.25	H0.50	H0.75	H1.00	H1.50	H2.00
SRVT - Silica Sand (1-5 m)	56.99	37.14	49.75	118.16	173.69	---	235.06	---	289.08
SRVT - Silica Sand (7-8 m)	123.37	88.84	109.84	179.11	251.18	---	327.05	---	379.68
LS - Silica Sand (3-5 m)	27.32	21.61	28.31		170.70	---	---	---	---
LS - Very Loose Silica Sand (9-11 m)	19.03	18.56	19.36		87.99	---	---	---	---
SPWA - Silica Sand A (3 - 7 m)	40.00	---	---	117.46	171.51	---	---	---	313.18
SPWA - Silica Sand B (3 - 7 m)	---	---	---	---	---	319.99	---	372.35	---

**Note SPWA Average f_s value from Lehane et al. (2004)*

Table 6-6. Summary of the Average Isolated Interface Responses for the Selected Silica Sand Strata.

Layer Description	f_s	SM	H0.125	H0.25	H0.50	H0.75	H1.00	H1.50	H2.00
SRVT - Silica Sand (1-5 m)	56.99	37.14	43.31	103.26	145.39	---	180.89	---	184.91
SRVT - Silica Sand (7-8 m)	123.37	88.84	102.19	164.04	221.79	---	268.12	---	270.69
LS - Silica Sand (3-5 m)	27.32	21.61	17.46	---	27.45	---	---	---	---
LS - Very Loose Silica Sand (9-11 m)	19.03	18.56	12.42	---	74.24	---	---	---	---
SPWA - Silica Sand A (3 - 7 m)	40.00	---	---	97.94	134.44	---	---	---	178.38
SPWA - Silica Sand B (3 - 7 m)	---	---	---	---	---	265.99	---	258.50	---

**Note SPWA Average f_s value from Lehane et al. (2004)*

Table 6-7. Summary of the Average Total Measured Sleeve Responses for the Selected Calcareous Sand Strata.

Layer Description	f_s	SM	H0.125	H0.25	H0.50	H0.75	H1.00	H1.50	H2.00
LPWA - Calcareous Sand (4-5, 6-7 m)	19.54	15.93	15.78	30.97	---	93.40	116.49	---	158.25
LPWA - Cemented Calcareous Sand (1-2 m)	40.74	31.75	50.89	129.38	---	310.30	417.03	---	686.36

Table 6-8. Summary of the Average Total Measured Sleeve Responses for the Selected Calcareous Sand Strata.

Layer Description	f_s	SM	H0.125	H0.25	H0.50	H0.75	H1.00	H1.50	H2.00
LPWA - Calcareous Sand (4-5, 6-7 m)	19.54	15.93	10.38	16.72	---	47.99	61.68	---	55.22
LPWA - Cemented Calcareous Sand (1-2 m)	40.741	31.754	33.085	95.133	---	207.74	292.26	---	433.61

Table 6-9. Summary of the Average Total Measured Sleeve Responses for the Selected Fine Grained Strata.

Layer Description	f_s	SM	H0.125	H0.25	H0.50	H0.75	H1.00	H1.50	H2.00
SRVT - Silt Seam A (6.8 m)	72.51	45.17	35.18	63.55	104.54	---	148.09	---	120.92
SRVT - Silt Seam B (8.6 m)	42.69	41.08	48.77	81.10	89.63	---	110.92	---	121.79
MPSC - Cooper Marl (14-20 m)	35.64	22.21	---	32.43	42.27	---	327.48	---	---
BWDWA - Soft Clay (4-8 m)	6.39	11.16	12.98	14.45	15.39	12.02	14.07	16.79	16.15

Table 6-10. Summary of the Average Total Measured Sleeve Responses for the Selected Fine Grained Strata.

Layer Description	f_s	SM	H0.125	H0.25	H0.50	H0.75	H1.00	H1.50	H2.00
SRVT - Silt Seam A (6.8 m)	72.51	45.17	33.09	59.69	92.89	---	123.95	---	82.05
SRVT - Silt Seam B (8.6 m)	42.69	41.08	46.93	77.49	81.67	---	93.97	---	91.46
MPSC - Cooper Marl (14-20 m)	35.64	22.21	---	23.60	24.77	---	293.50	---	---
BWDWA - Soft Clay (4-8 m)	6.39	11.16	12.67	13.99	14.20	10.12	11.55	13.64	12.18

Table 6-11a. Summary of CPT Based Soil Classification Methods Sorted by Utilized Sensors (a) Based on Tip Resistance and Sleeve Friction (Liao, 2005).

Data Normalization Scheme	Reference
q_c and f_s	Begemann (1965)
q_c and f_s/q_c	Sanglerat et al. (1974)
q_c and f_s	Fugro symposium (1972)
q_c and f_s/q_c	Schmertmann (1978)
q_c and f_s/q_c	Doublas and Olsen (1981)
f_s/q_c	Vos (1982)
q_c and f_s/q_c	Robertson and Campanella (1983)
q_c and f_s/q_c	Erwig (1988)
$q_{c1} = \frac{q_c}{\left(\sigma_{vo}'\right)^n}$ and $FR_1 = \frac{f_s \Big/ \sigma_{vo}'}{q_c \Big/ \left(\sigma_{vo}'\right)^n}$	Olsen and Malone (1988)
q_{c1} and f_s/q_c	Olsen and Mitchell (1995)
Soil index U=f(x, y), and in situ state index V=f(x, y) $x = 0.1539(f_s/q_c) + 0.8870\log(q_c) - 3.35$ $y = -0.2957(f_s/q_c) + 0.4617\log(q_c) - 0.37$	Zhang and Tumay (1996a, b)
$q_E = q_T - u_2$ and f_s	Eslami and Fellenius (1997)

Table 6-11b. Summary of CPT Based Soil Classification Methods Sorted by Utilized Sensors (b) Based on Tip Resistance and Pore Pressure (Liao, 2005).

Data Normalization Scheme	Reference
$(q_c - \sigma_{vo})/\sigma_{vo}$ and $(u_b - u_o)/u_o$	Jones et al. (1981)
$(q_T - \sigma_{vo})$ and $(u_b - u_o)$	Jones and Rust (1982)
q_T and $B_q = \dfrac{u_b - u_o}{q_T - \sigma_{vo}}$	Senneset and Janbu (1985)
q_T and B_q	Parez and Fauriel (1988)
q_T and B_q	Senneset et al. (1989)
$q_T/(\gamma_w h)$ and $B_q = \dfrac{(u_b - u_o)}{q_T - \gamma_w h}$	Chang-hou et al. (1990)
q_T, B_q, and t_{50}	Jian et al. (1992)

Table 6-11c. Summary of CPT Based Soil Classification Methods Sorted by Utilized Sensors (c) Based on Tip Resistance, Sleeve Friction, and Pore Pressure (Liao, 2005).

Data Normalization Scheme	Reference
q_T, f_s /q_T, and B_q	Robertson et al. (1986)
$Q = \frac{q_T - \sigma_{vo}}{\sigma_{vo}'}$, B_q, and $F = \frac{f_s}{q_T - \sigma_{vo}}$	Robertson (1990, 1991)
Method A: $q_{tn} = (q_t - \sigma_{vo})$ and B_q	Larsson and Mulabdic (1991)
Method B: q_{tn} and $\left(1/B_q - f_s/\sigma_{vo}'\right)$	
$Q(1-B_q)$ and F	Jefferies and Davies (1991)

Table 6-12. Summary of the Average Normalized Soil Classification Parameters for the Highlighted Layers Used in the Current Study. Reproduced in Quadricate to Facilitate Observing the Trends Within the Data.

Table of Summary Averages - Sorted by Qt

Site	Soil Type	Depth Range	Qt	FR	Bq	MFCP
LPWA	Cemented Calcareous Sand	1 - 2 m	600.03	0.25	0.00	0.60
SRVT	Silica Sand	1 - 5 m	126.51	0.92	0.00	1.34
LPWA	Calcareous Sand	3 - 5 m	90.74	0.31	0.00	13.07
LS	Silica Sand	3 - 5 m	87.05	0.60	0.00	1.65
SRVT	Silica Sand	7 - 8 m	45.79	1.98	0.00	2.80
LS	Very Loose Silica Sand	9 - 11 m	26.39	0.67	0.01	8.64
MPSC	Calcareous Silty Clay	14 - 20 m	22.02	0.97	0.60	456.62
SRVT	Silt	6.8 m	18.38	3.80	0.00	7.18
SRVT	Silt	8.6 m	9.21	2.79	0.02	8.82
BWDWA	Soft Clay	4 - 8 m	4.55	5.22	0.43	47.00

Table of Summary Averages - Sorted by Bq

Site	Soil Type	Depth Range	Qt	FR	Bq	MFCP
MPSC	Calcareous Silty Clay	14 - 20 m	22.02	0.97	0.60	456.62
BWDWA	Soft Clay	4 - 8 m	4.55	5.22	0.43	47.00
SRVT	Silt	8.6 m	9.21	2.79	0.02	8.82
LS	Very Loose Silica Sand	9 - 11 m	26.39	0.67	0.01	8.64
SRVT	Silt	6.8 m	18.38	3.80	0.00	7.18
SRVT	Silica Sand	7 - 8 m	45.79	1.98	0.00	2.80
SRVT	Silica Sand	1 - 5 m	126.51	0.92	0.00	1.34
LPWA	Calcareous Sand	3 - 5 m	90.74	0.31	0.00	13.07
LPWA	Cemented Calcareous Sand	1 - 2 m	600.03	0.25	0.00	0.60
LS	Silica Sand	3 - 5 m	87.05	0.60	0.00	1.65

Table of Summary Averages - Sorted by Fr

Site	Soil Type	Depth Range	Qt	FR	Bq	MFCP
BWDWA	Soft Clay	4 - 8 m	4.55	5.22	0.43	47.00
SRVT	Silt	6.8 m	18.38	3.80	0.00	7.18
SRVT	Silt	8.6 m	9.21	2.79	0.02	8.82
SRVT	Silica Sand	7 - 8 m	45.79	1.98	0.00	2.80
MPSC	Calcareous Silty Clay	14 - 20 m	22.02	0.97	0.60	456.62
SRVT	Silica Sand	1 - 5 m	126.51	0.92	0.00	1.34
LS	Very Loose Silica Sand	9 - 11 m	26.39	0.67	0.01	8.64
LS	Silica Sand	3 - 5 m	87.05	0.60	0.00	1.65
LPWA	Calcareous Sand	3 - 5 m	90.74	0.31	0.00	13.07
LPWA	Cemented Calcareous Sand	1 - 2 m	600.03	0.25	0.00	0.60

Table of Summary Averages - Sorted by MFCP

Site	Soil Type	Depth Range	Qt	FR	Bq	MFCP
MPSC	Calcareous Silty Clay	14 - 20 m	22.02	0.97	0.60	456.62
BWDWA	Soft Clay	4 - 8 m	4.55	5.22	0.43	47.00
LPWA	Calcareous Sand	3 - 5 m	90.74	0.31	0.00	13.07
SRVT	Silt	8.6 m	9.21	2.79	0.02	8.82
LS	Very Loose Silica Sand	9 - 11 m	26.39	0.67	0.01	8.64
SRVT	Silt	6.8 m	18.38	3.80	0.00	7.18
SRVT	Silica Sand	7 - 8 m	45.79	1.98	0.00	2.80
LS	Silica Sand	3 - 5 m	87.05	0.60	0.00	1.65
SRVT	Silica Sand	1 - 5 m	126.51	0.92	0.00	1.34
LPWA	Cemented Calcareous Sand	1 - 2 m	600.03	0.25	0.00	0.60

Sample Depth Increment (m)	USCS Classification	D_{50} (mm)	C_u	C_c	% Passing #200
3.5 – 4.0	SM	0.23	2.1	1	4
6.2 – 6.7	MH	0.035	4.6	1.2	91

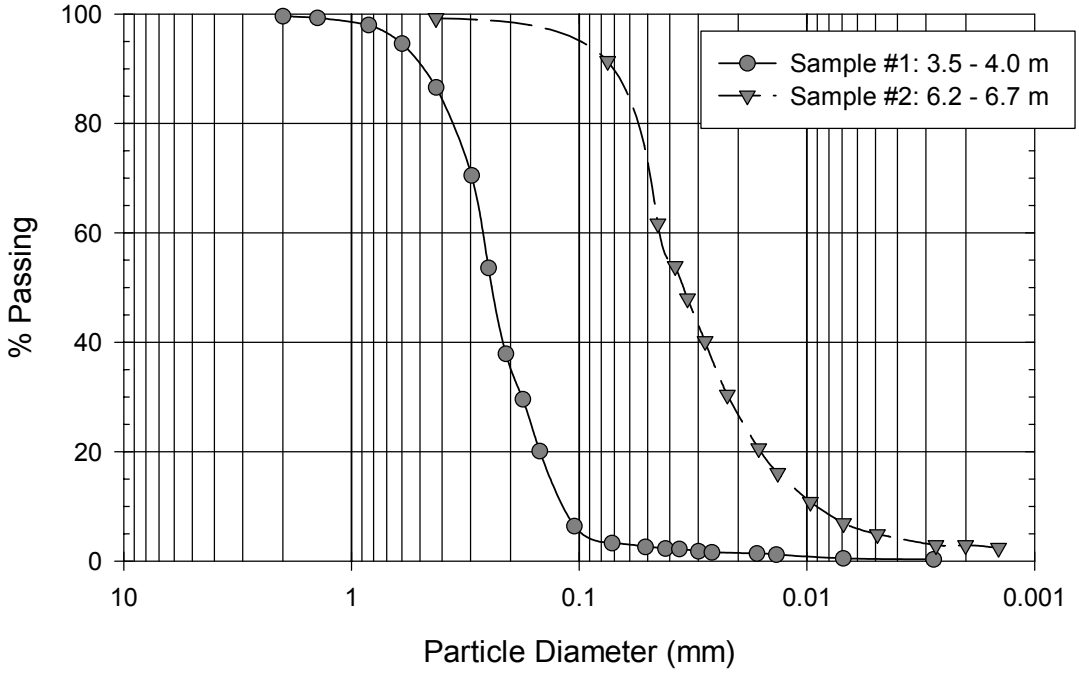

Figure 6-1. Soil Properties and Grain Size Distribution Curves from Discrete Samples Taken from the SRVT Test Site (after DeJong, 2001).

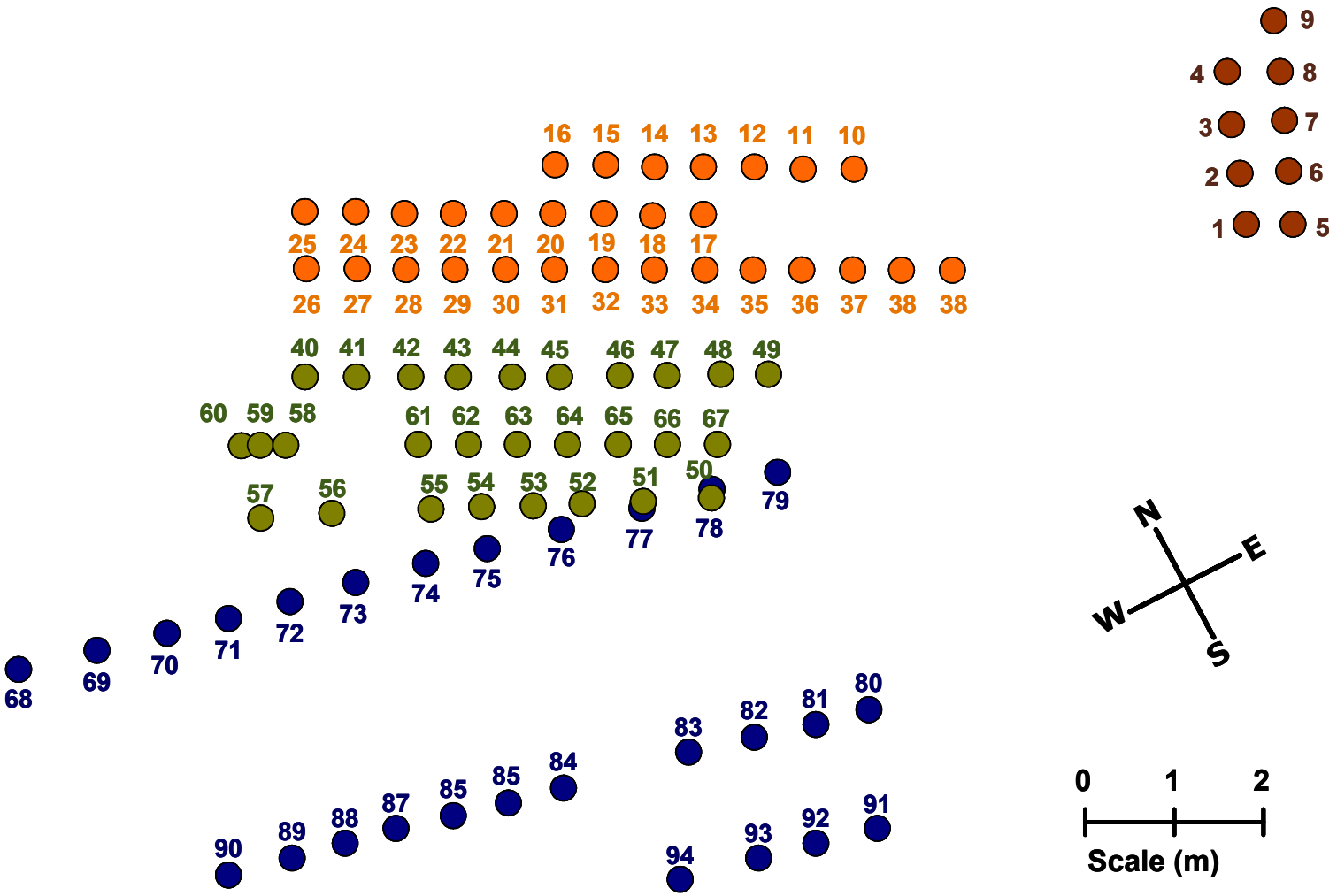

Figure 6-2. Layout of Sounding Locations for the SRVT Test Site. Soundings are Nominally Spaced at 1 Meter Intervals.

Sample Depth Increment (m)	USCS Classification	D_{50} (mm)	C_u	C_c	% Passing #200
0.5 - 1.0	SP	0.36	2.19	1.04	0.73

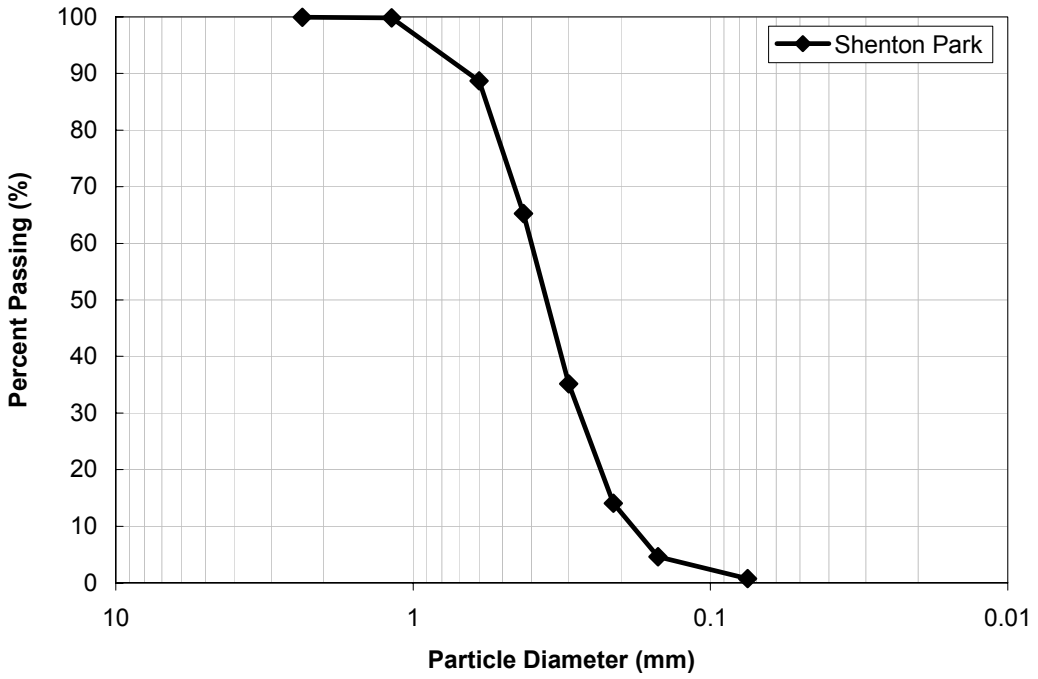

Figure 6-3. Soil Properties and Grain Size Distribution Curve for a Discrete Sample from the SPWA Test Site.

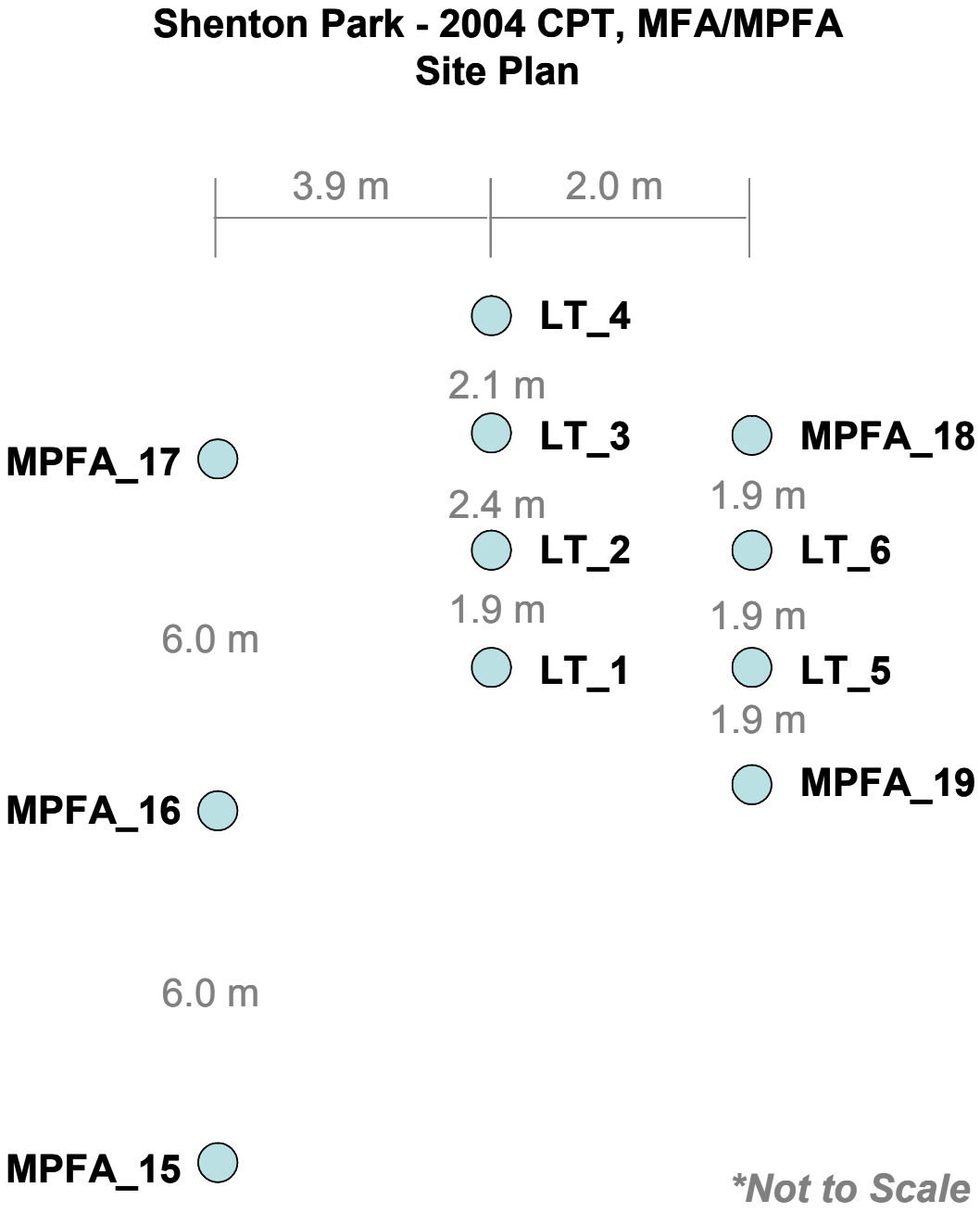

Figure 6-4 Layout of Sounding Locations for the SPWA Test Site.

Sample Depth Increment (m)	USCS Classification	D_{50} (mm)	C_u	C_c	% Passing #200
4.5 - 5.0	SP	0.21	2.55	1.12	4.11

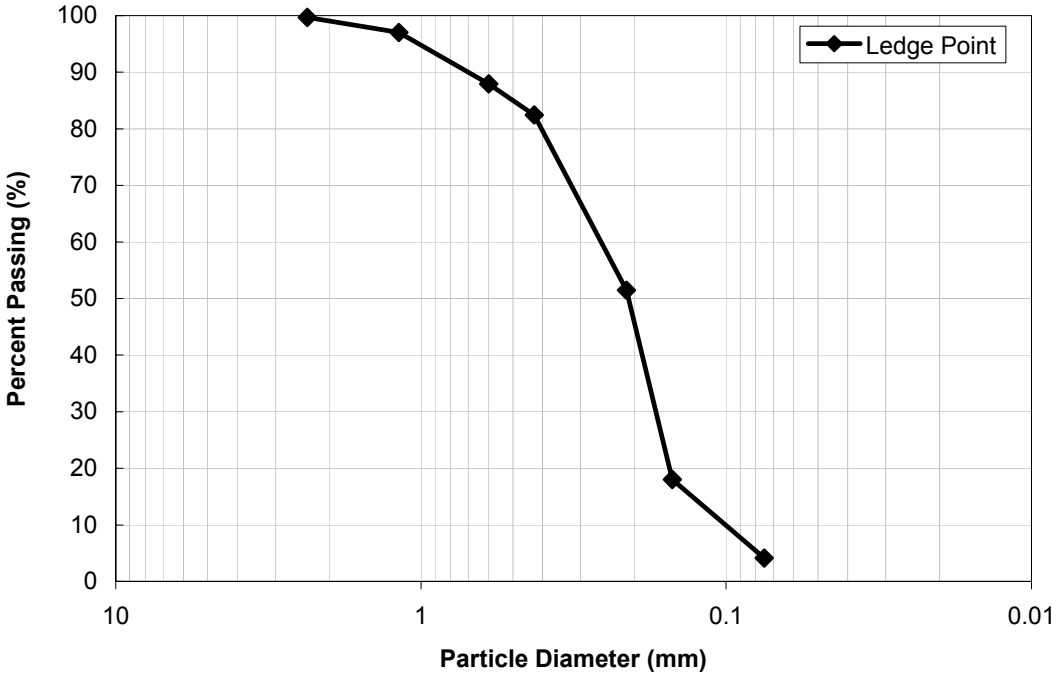

Figure 6-5. Soil Properties and Grain Size Distribution Curve for a Discrete Sample from the LPWA Test Site.

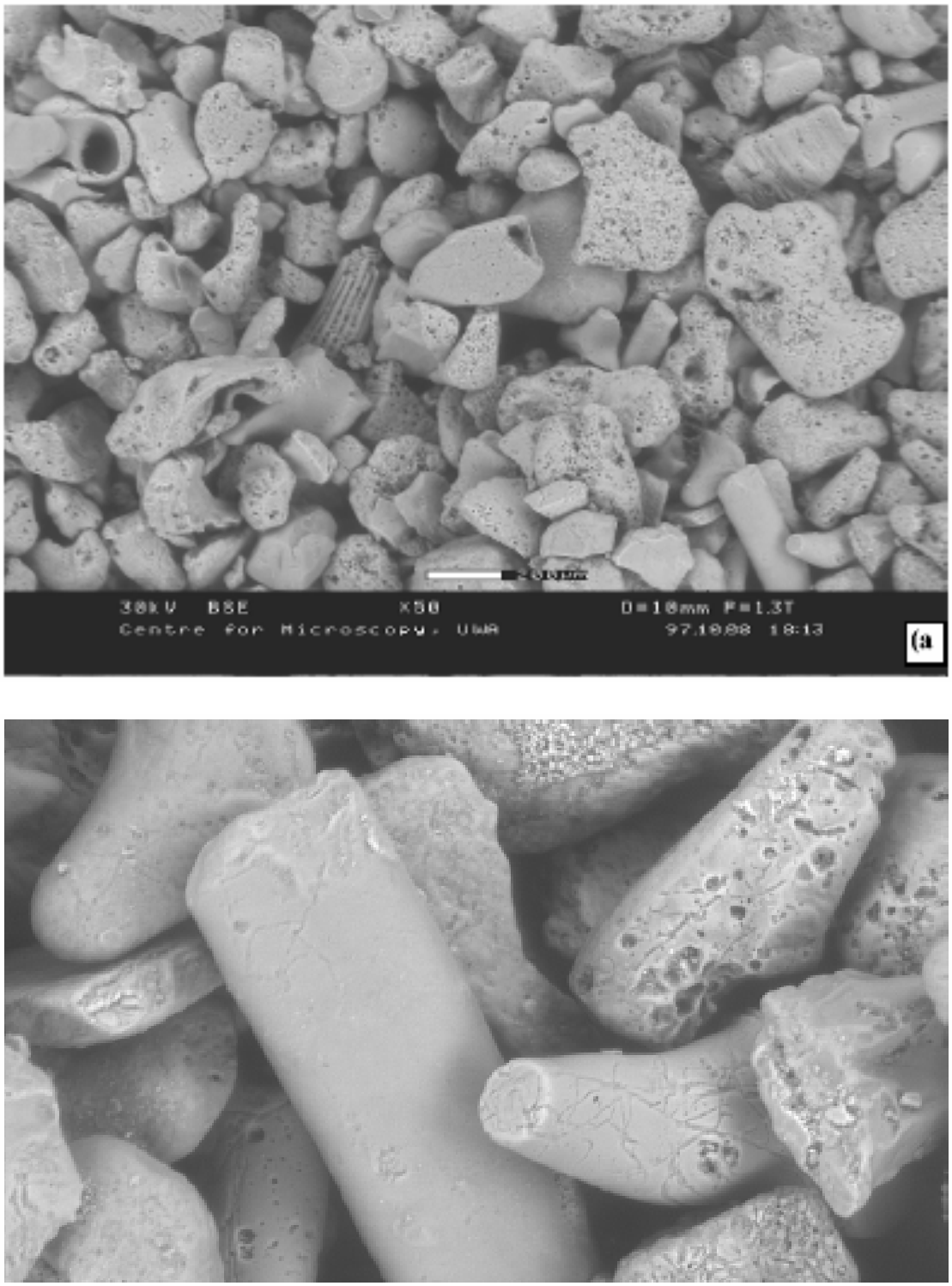

Figure 6-6. ESEM Micrographs for LP Soil: (a) Overview of Various Particle Characteristics, (b) Close up View of Particles (after Ismail, 2000).

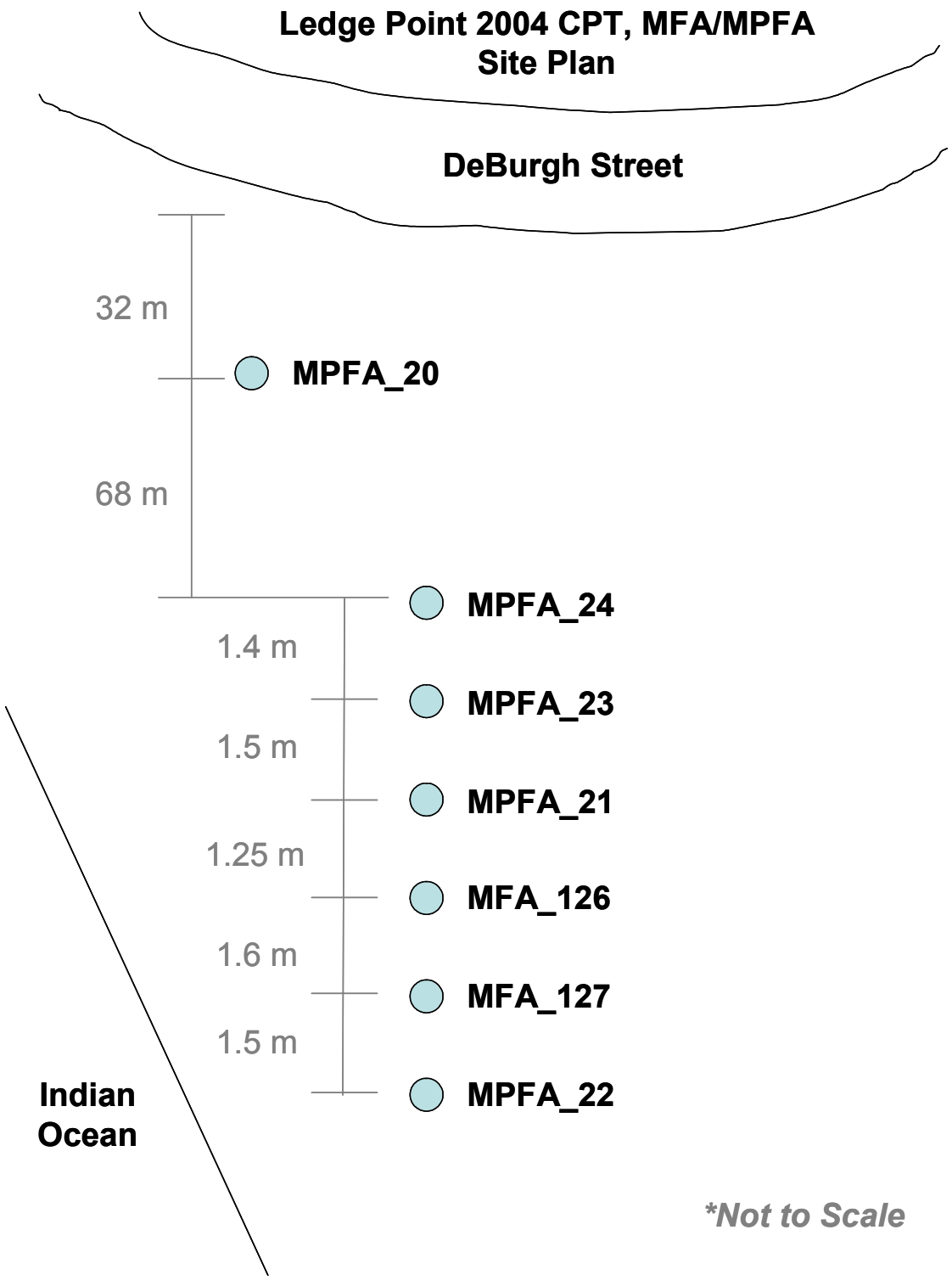

Figure 6-7 Layout of Sounding Locations for the LPWA Test Site.

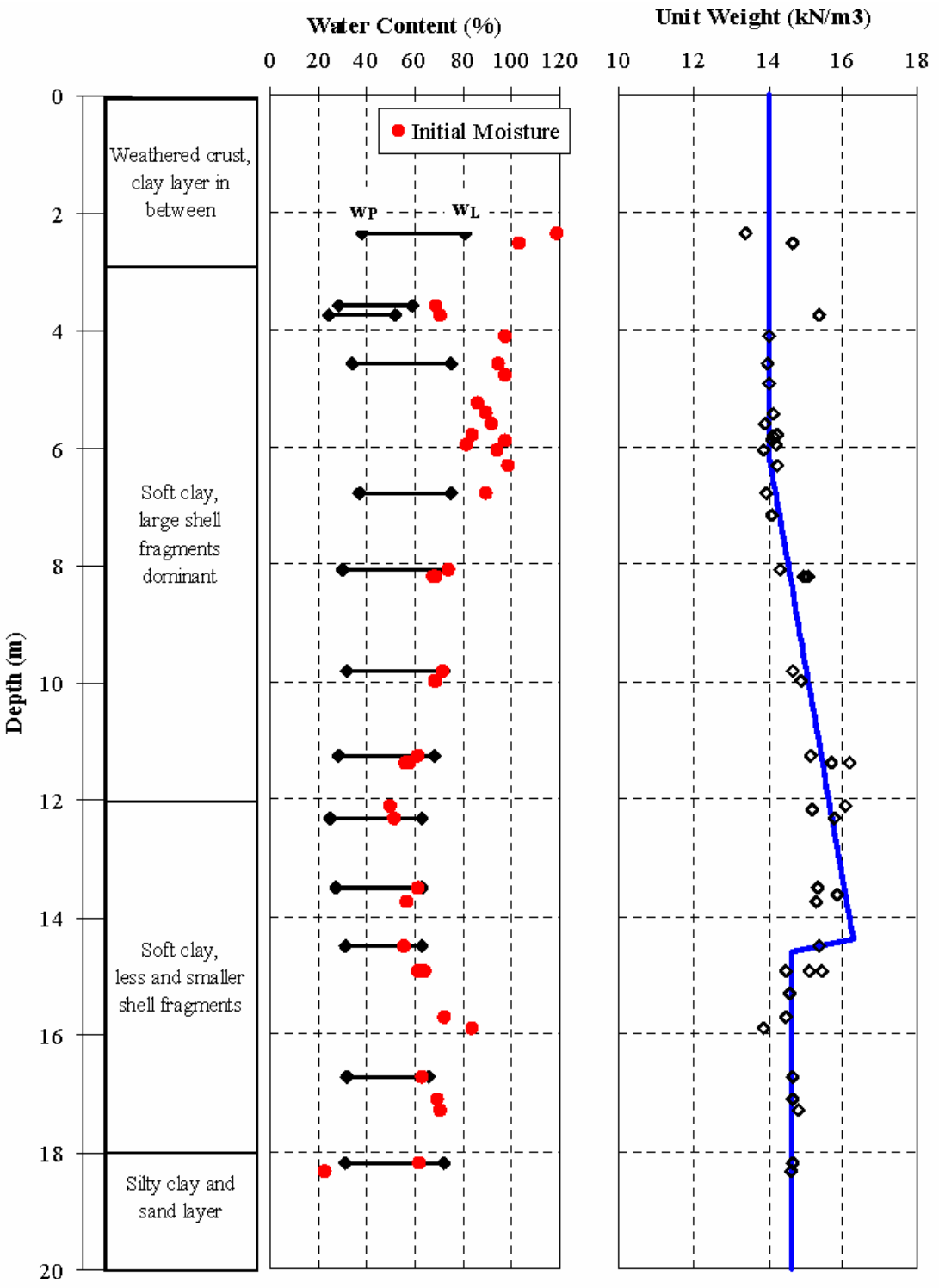

Figure 6-8. Profiles of Natural Water Content, Atterberg Limits, and Unit Weight from the BWDWA Test Site (Schneider et al., 2004).

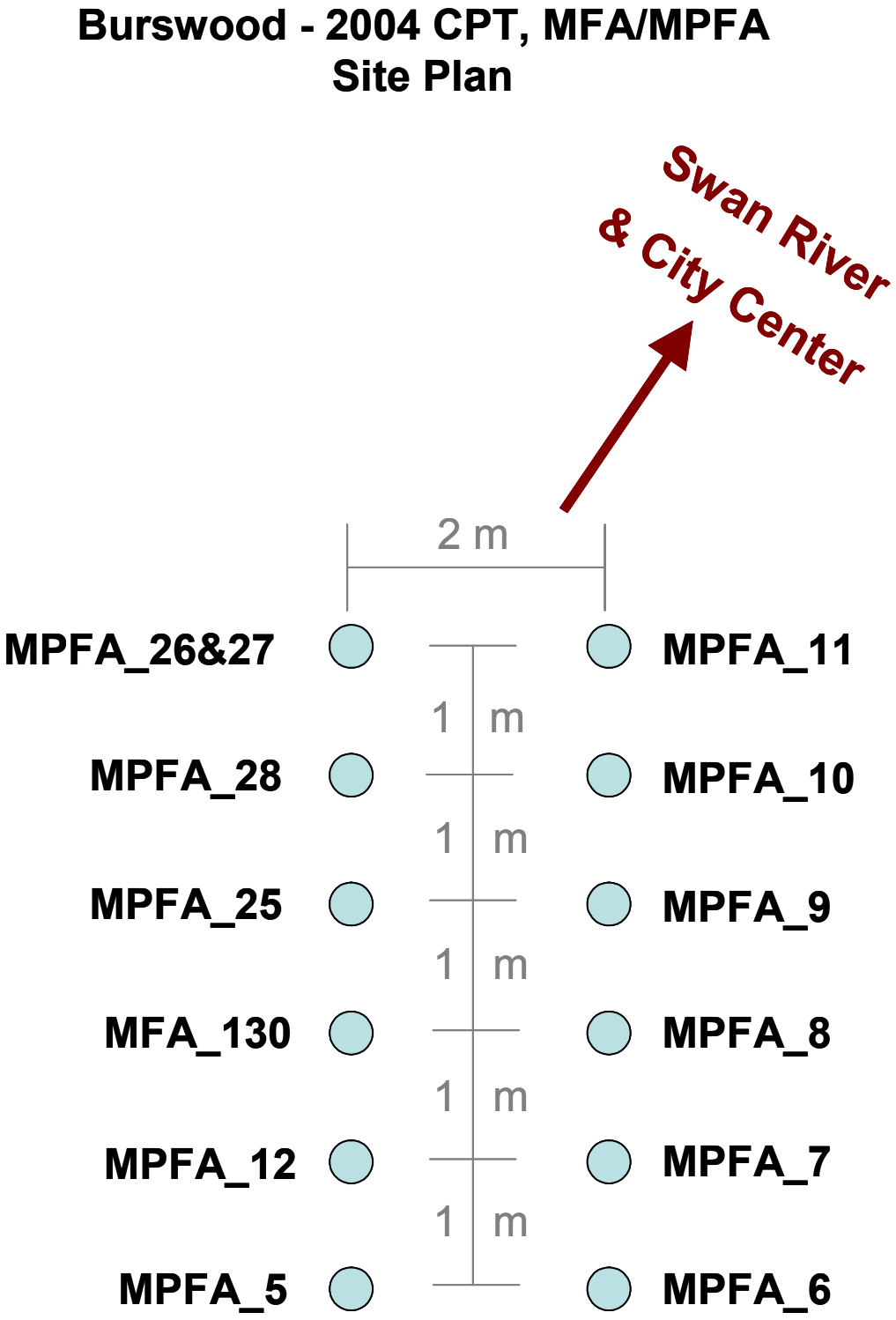

Figure 6-9 Layout of Sounding Locations for the BWDWA Test Site.

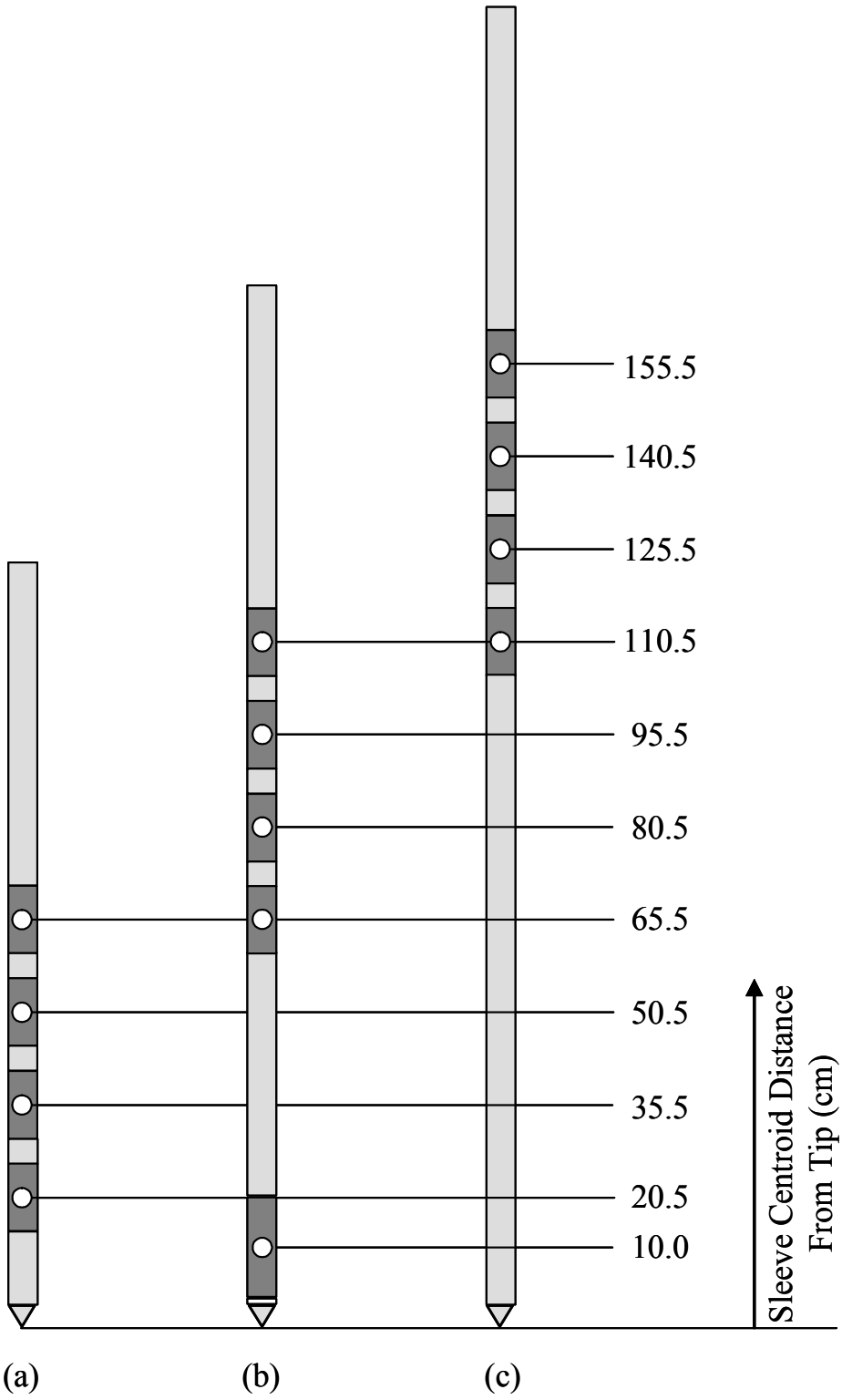

Figure 6-10 MFA Tip Configurations: (a) Short Uninstrumented Tip, (b) 15 cm^2 CPTU, and (c) Long Uninstrumented Tip (after DeJong, 2001).

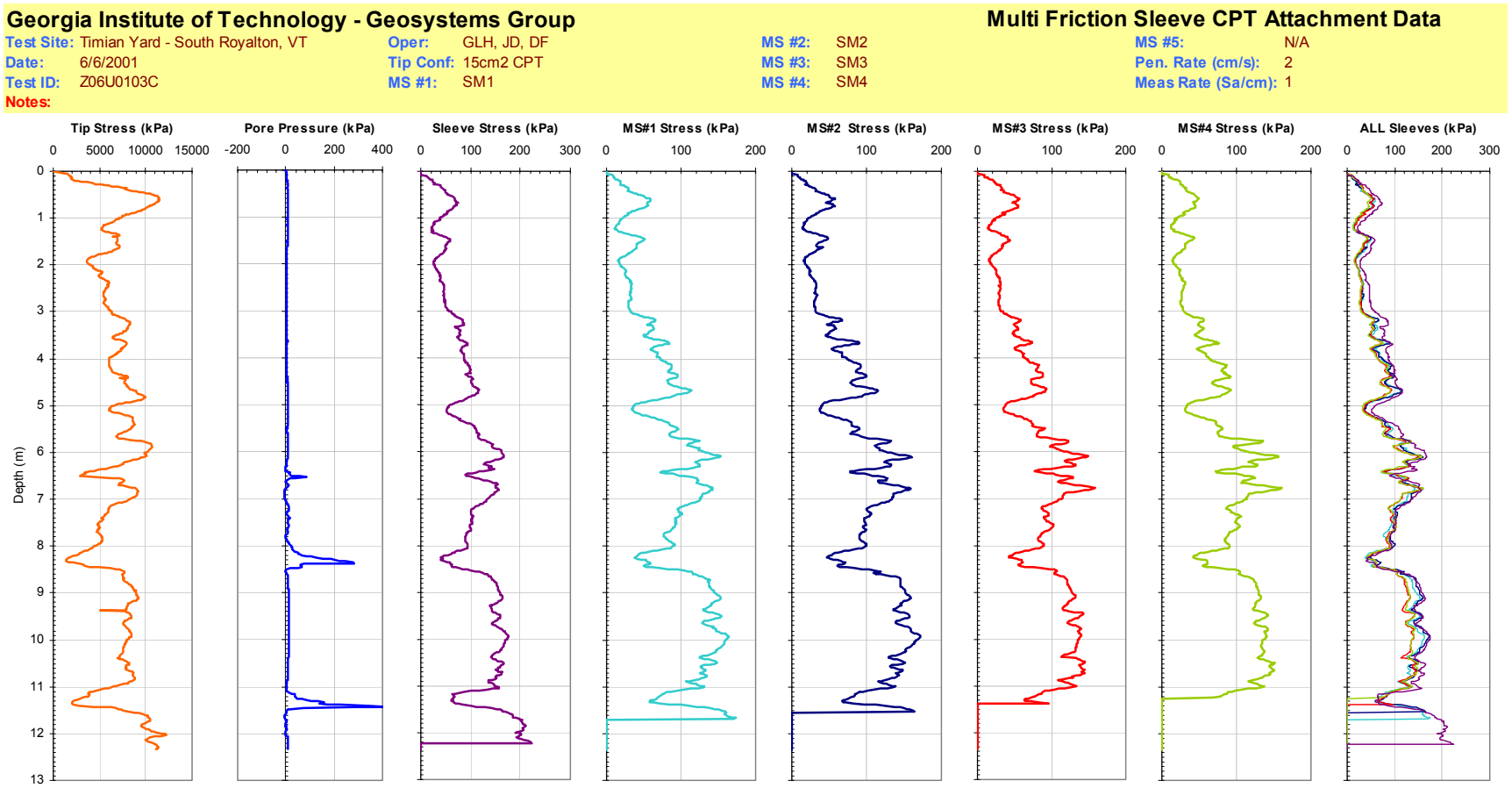

Figure 6-11. Results of an CPTU-MFA Sounding at the SRVT Site to Determine the Influence of Position on Smooth Sleeve Response.

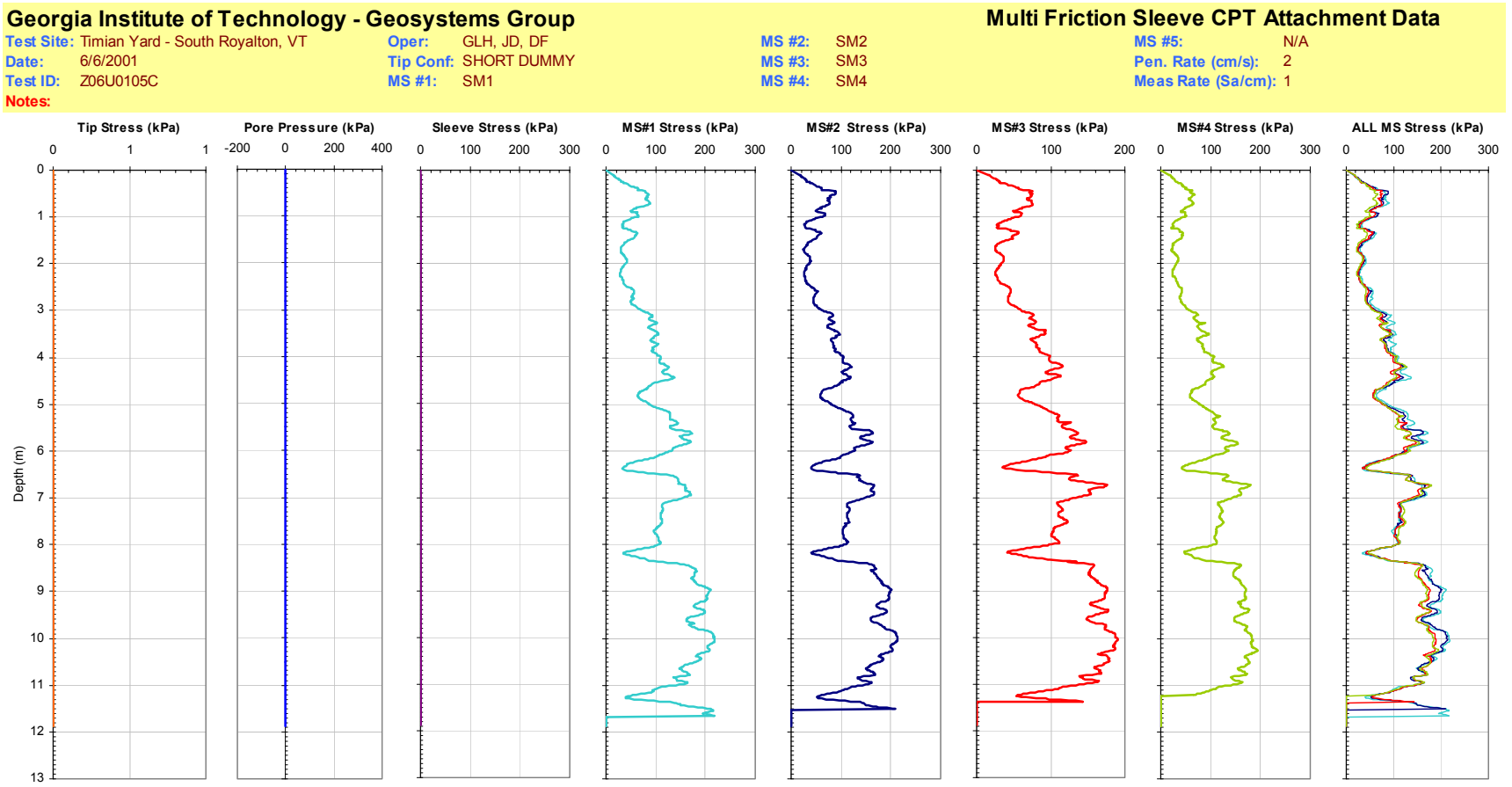

Figure 6-12. Results of an MFA Sounding with the Short Uninstrumented Tip at the SRVT Site to Determine the Influence of Position on Smooth Sleeve Response.

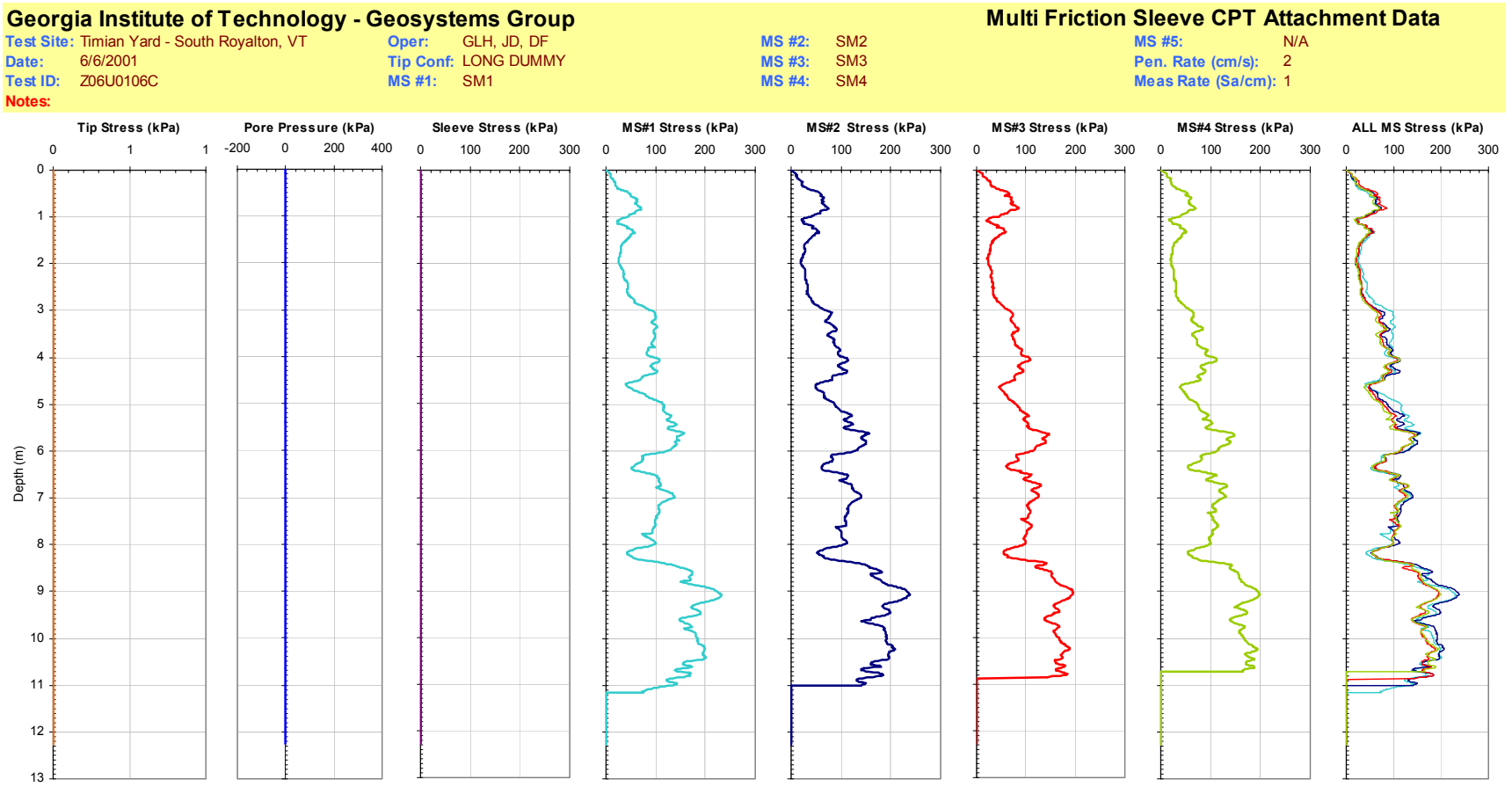

Figure 6-13. Results of an MFA Sounding with the Long Uninstrumented Tip at the SRVT Site to Determine the Influence of Position on Smooth Sleeve Response.

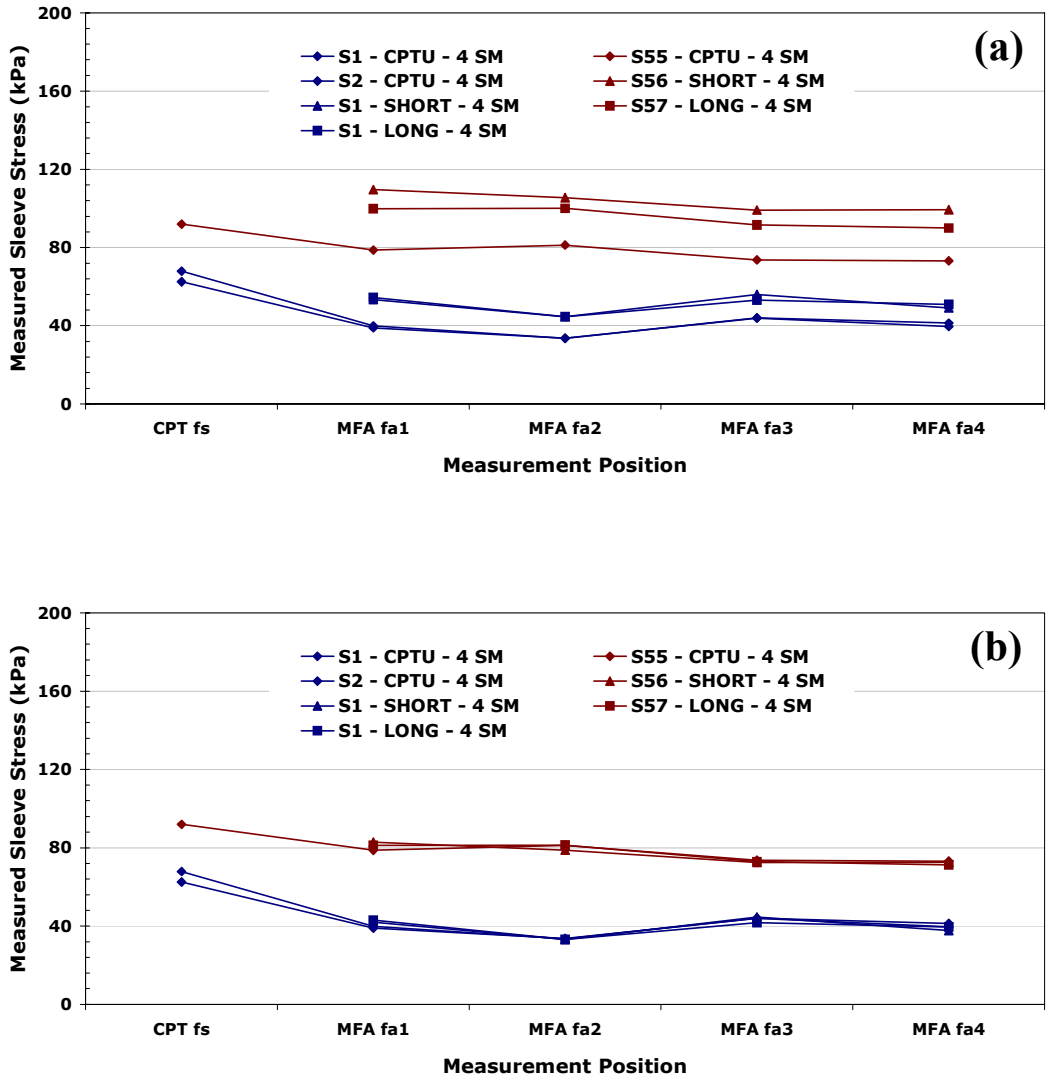

Figure 6-14 Results of Investigation into the Influence of Position Behind a Penetrometer Tip on Smooth Sleeve Response: (a) Measured Stresses, (b) Stresses Adjusted for Tip Module Diameter Variations. Blue Traces Represent DeJong (2001) data, Maroon Traces Represent Data From the Current Study.

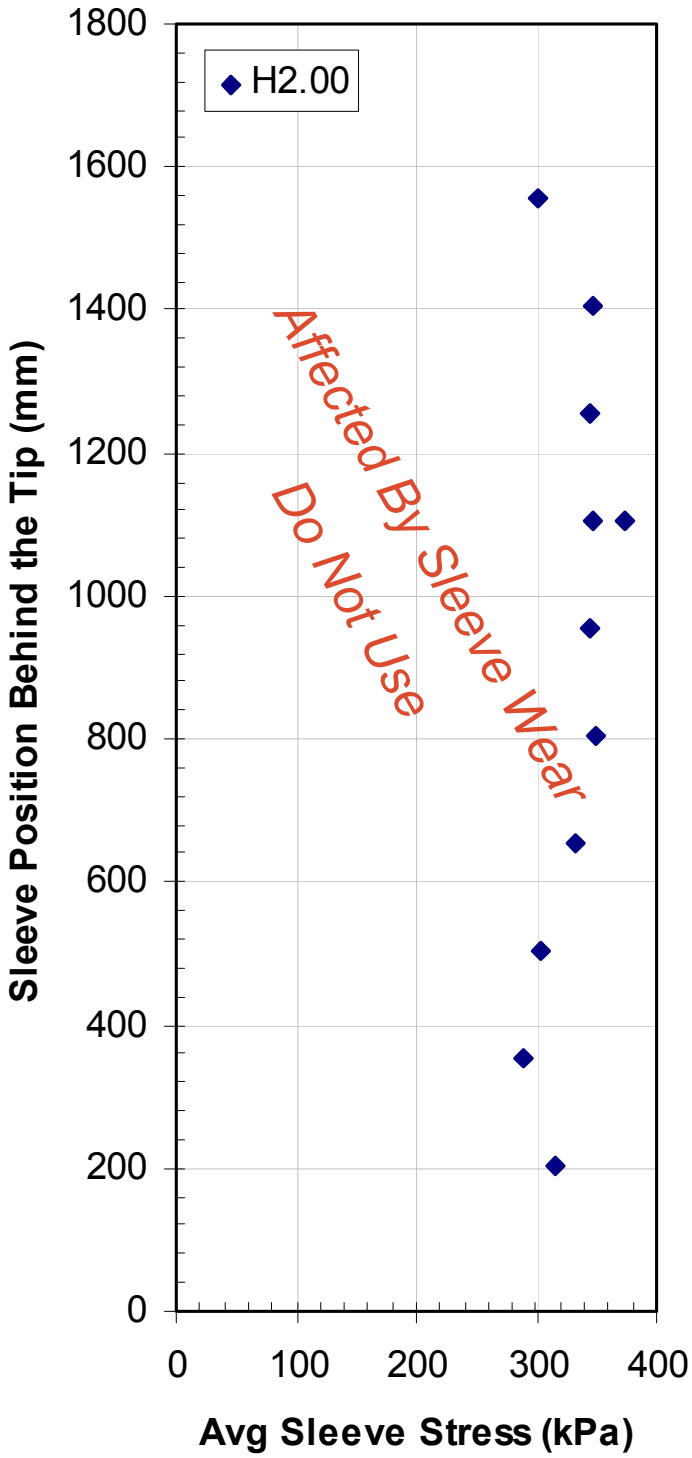

Figure 6-15 Results of an Investigation into the Influence of Position Behind a Penetrometer Tip on Heavily Textured Sleeve Response. *Note: Values are Severely Affected By Sleeve Wear and Should Not Be Used.*

Figure 6-16 Photograph of Severely Worn H2.00 Sleeve After the Completion of Sounding 90 (Table 6-1).

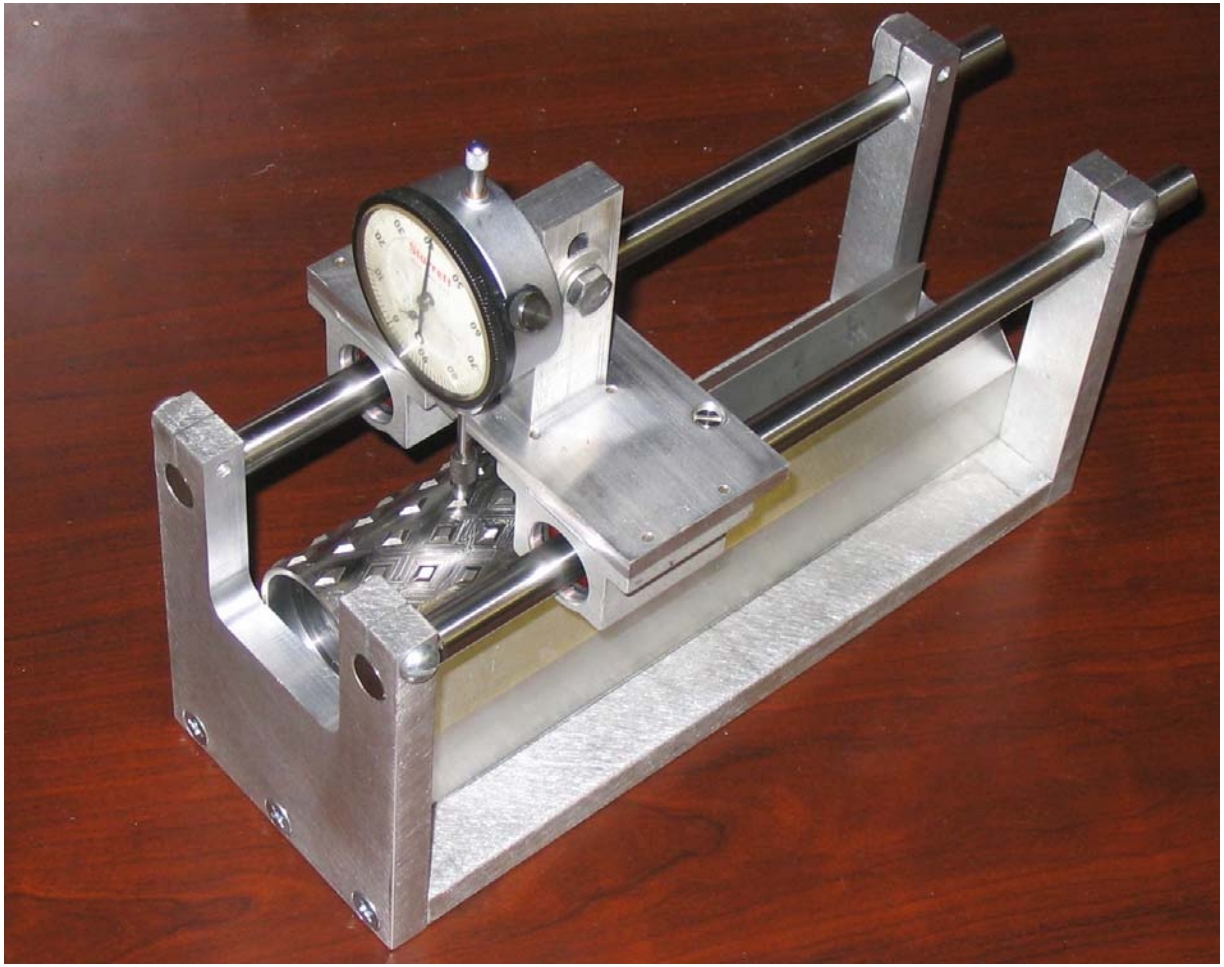

Figure 6-17. Photograph of the Quick Sleeve Profilometer Device Constructed to Monitor Sleeve Wear.

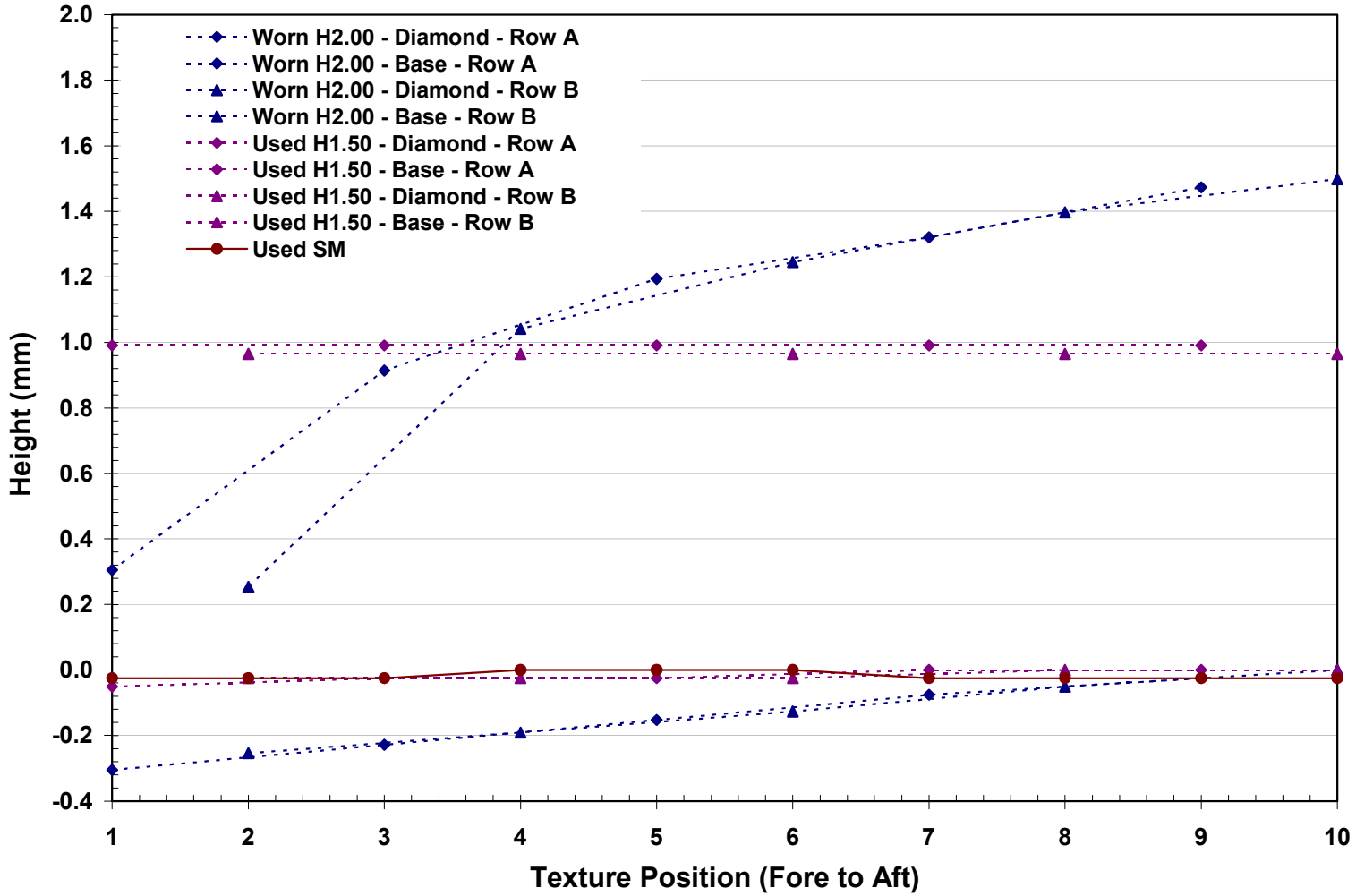

Figure 6-18. Macroscopic Measurements of Sleeve Wear Taken with the Quick Sleeve Profilometer Device. Blue Traces Represent the Condition of the Worn H2.00 Sleeve in Figure 6-16, Purple Traces Represent a Used H1.00 Sleeve, and the Maroon Trace Shows Wear of a Smooth MFA Sleeve.

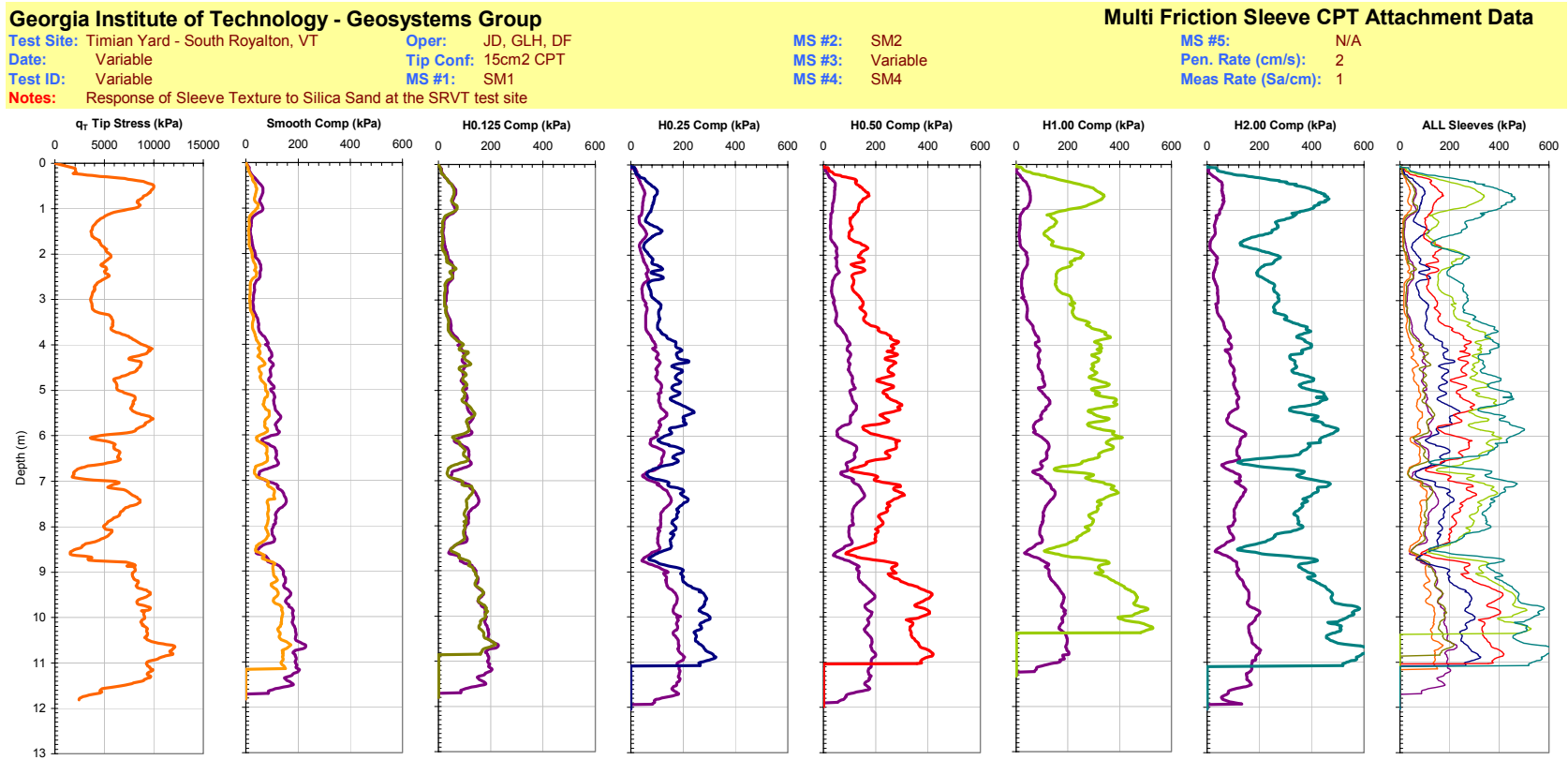

Figure 6-19. Plots Showing the Total Measured Sleeve Traces for the Range of Sleeve Textures Tested at the SRVT Test Site. Individual MFA Sensor Traces are Compared to f_s Response, with the Far Right Subplot Comparing All Sleeve Responses.

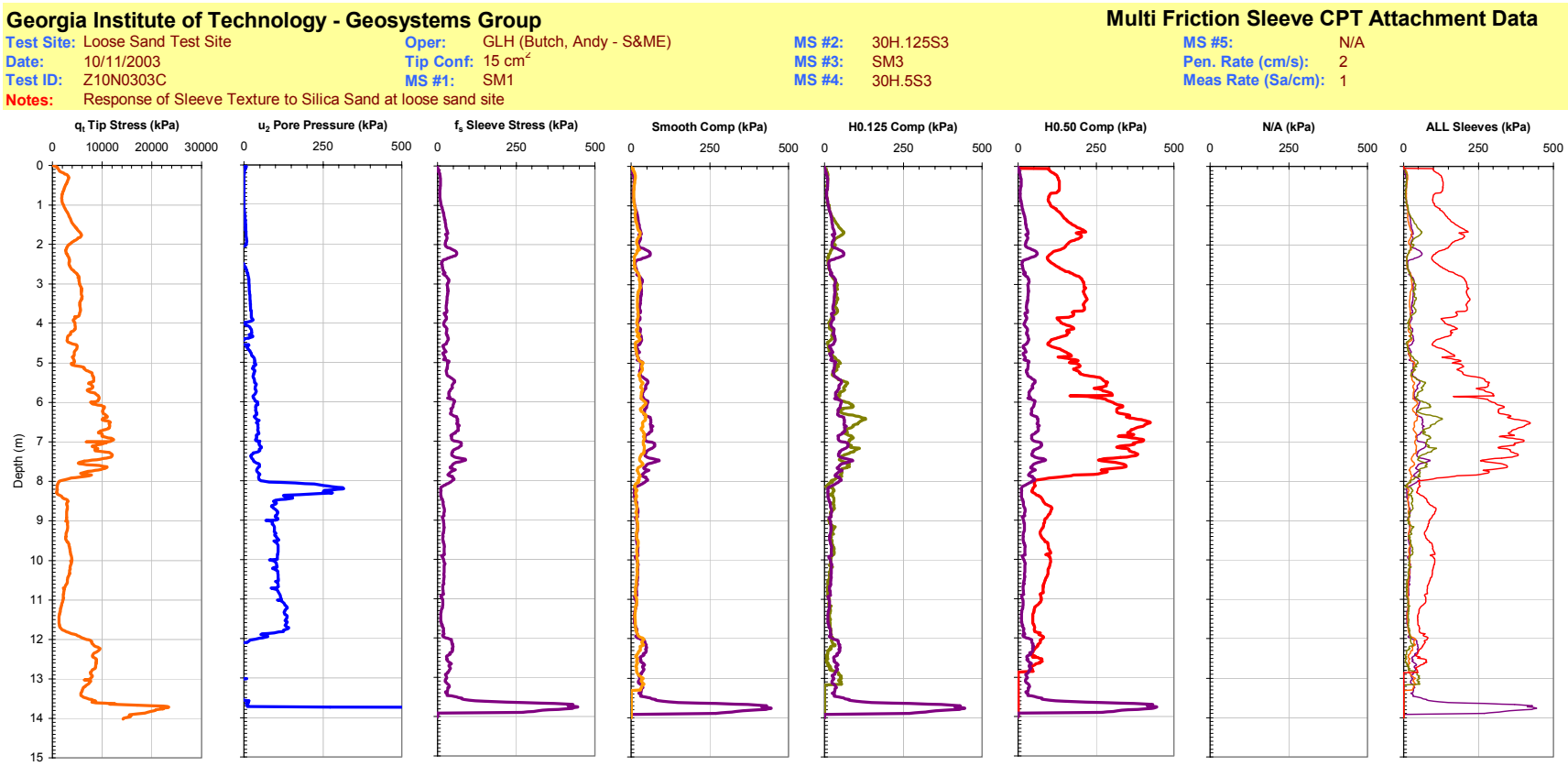

Figure 6-20. Plots Showing Total Measured Sleeve Traces for the Range of Sleeve Textures Tested at the LS Test Site. Individual MFA Sensor Traces are Compared to f_s Response, with the Far Right Subplot Comparing All Sleeve Responses.

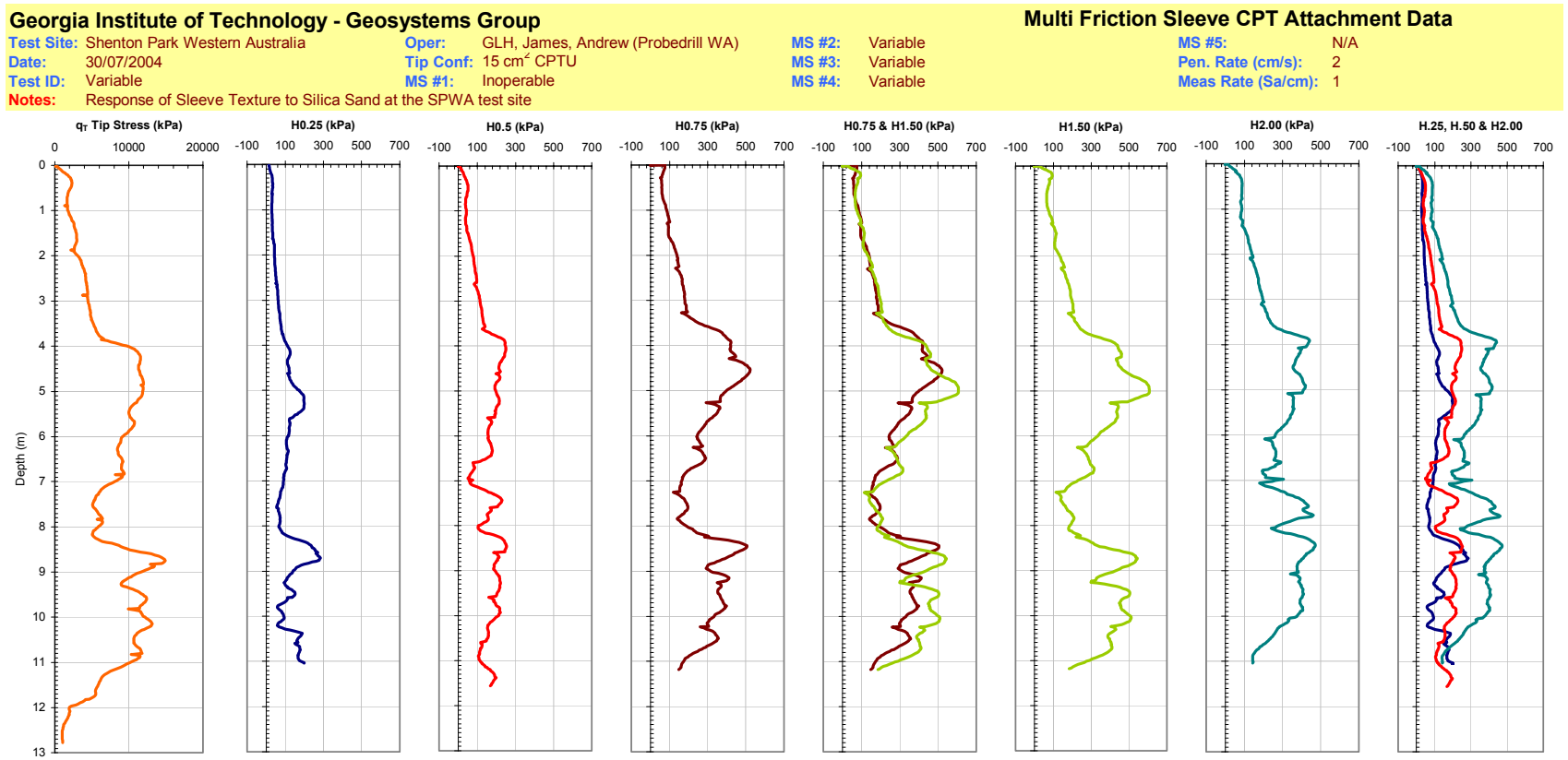

Figure 6-21. Plots Showing the Total Measured Sleeve Traces for the Range of Sleeve Textures Tested at the SPWA Test Site. No f_s trace is Available for Comparison at the SPWA site. The Behaviors are Separated into Two Subsets: (a) H0.25, H0.50, and H2.00; (b) H0.75 and H1.50. The Data from Subset (b) Are Indicative of Increased Lateral Stress Conditions Believed to be Resultant from the Sounding Being Conducted Within Close Proximity to One of the Limestone Pillars Present at the Site.

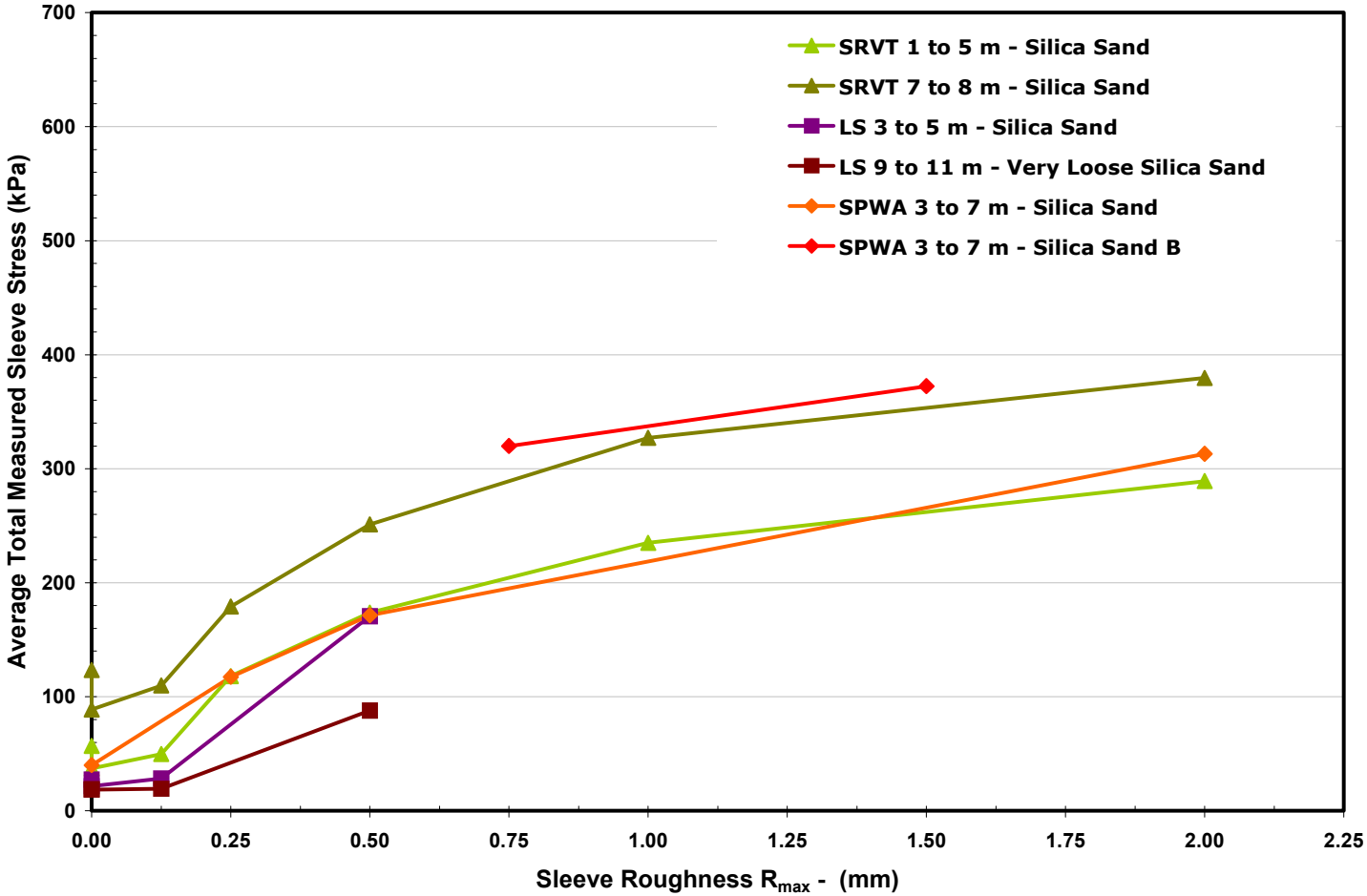

Figure 6-22. Plot Showing the Average Total Measured Sleeve Response as a Function of Sleeve Texture for the Selected Silica Sand Layers from the Current Study.

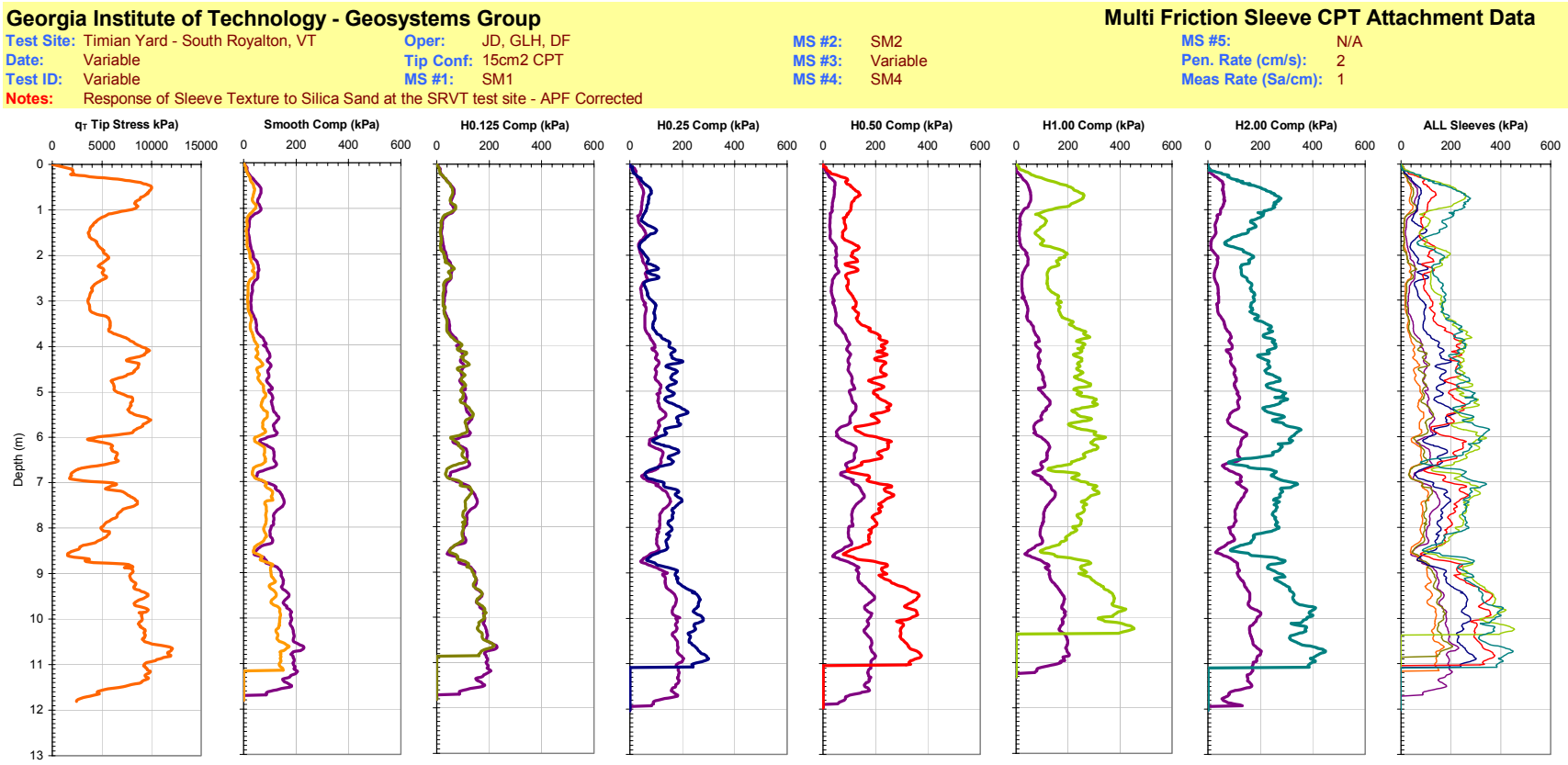

Figure 6-23. Plots Showing the Isolated Interface Sleeve Traces for the Range of Sleeve Textures Tested at the SRVT Test Site. Individual MFA Sensor Traces are Compared to f_s Response, with the Far Right Subplot Comparing All Sleeve Responses.

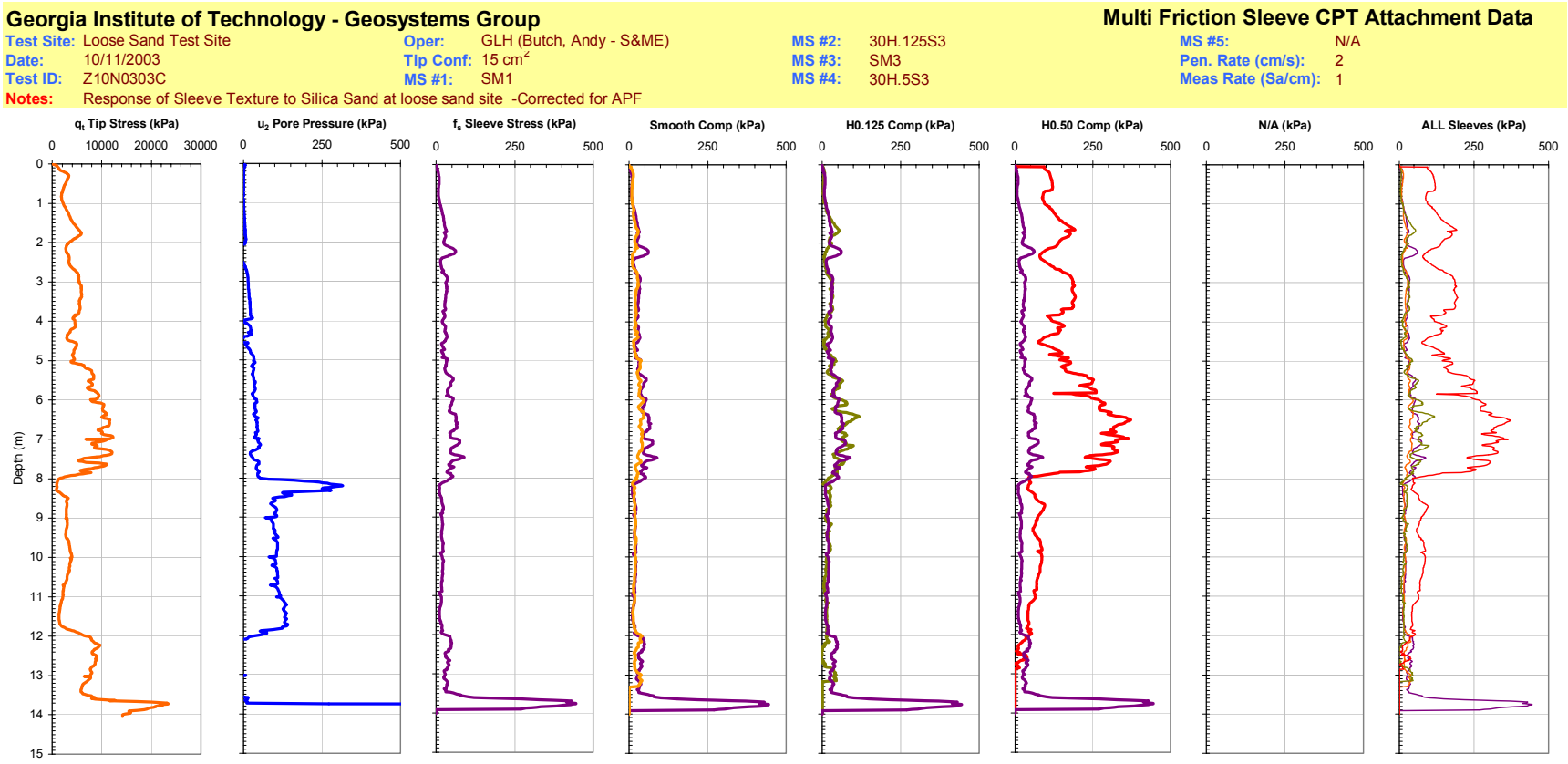

Figure 6-24. Plots Showing the Isolated Interface Sleeve Traces for the Range of Sleeve Textures Tested at the LS Test Site. Individual MFA Sensor Traces are Compared to f_s Response, with the Far Right Subplot Comparing All Sleeve Responses.

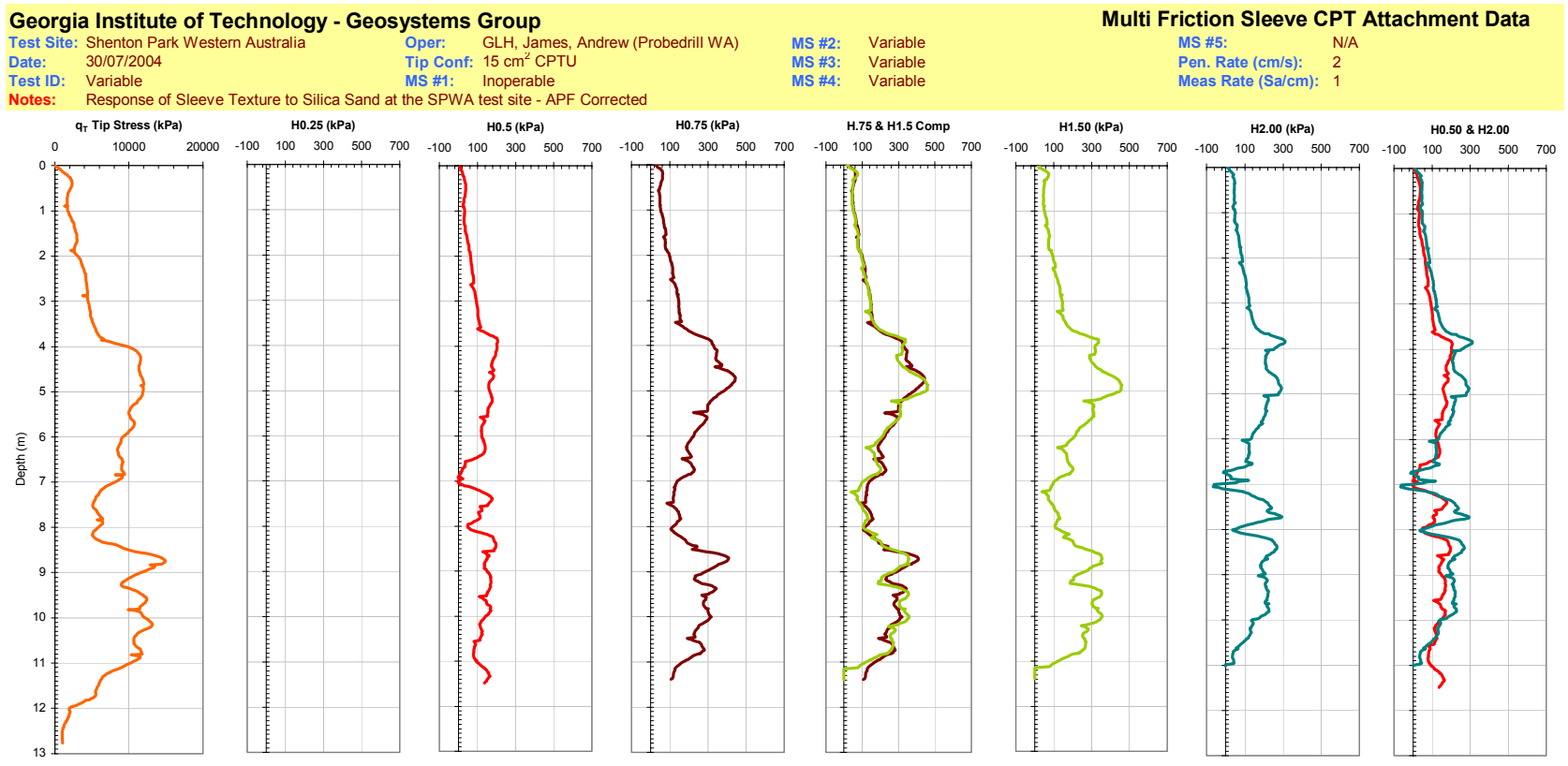

Figure 6-25. Plots Showing the Isolated Interface Sleeve Traces for the Range of Sleeve Textures Tested at the SPWA Test Site. No f_s trace is Available for Comparison at the SPWA site. The Behaviors are Separated into Two Subsets: (a) H0.25, H0.50, and H2.00; (b) H0.75 and H1.50. The Data from Subset (b) Are Indicative of Increased Lateral Stress Conditions Believed to be Resultant from the Sounding Being Conducted Within Close Proximity to One of the Limestone Pillars Present at the Site.

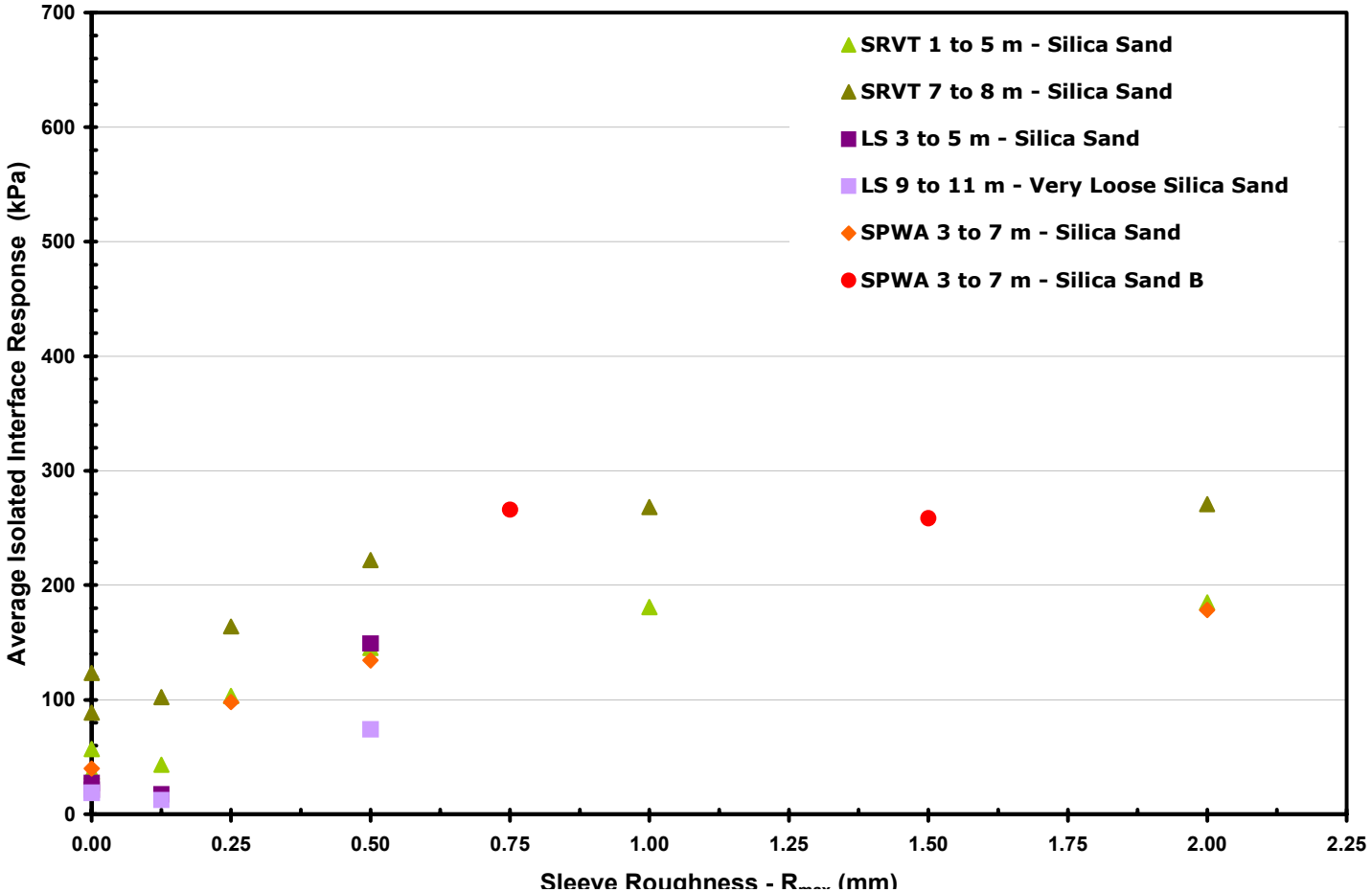

Figure 6-26. Plot Showing the Average Isolated Interface Sleeve Response as a Function of Sleeve Texture for the Selected Silica Sand Layers from the Current Study.

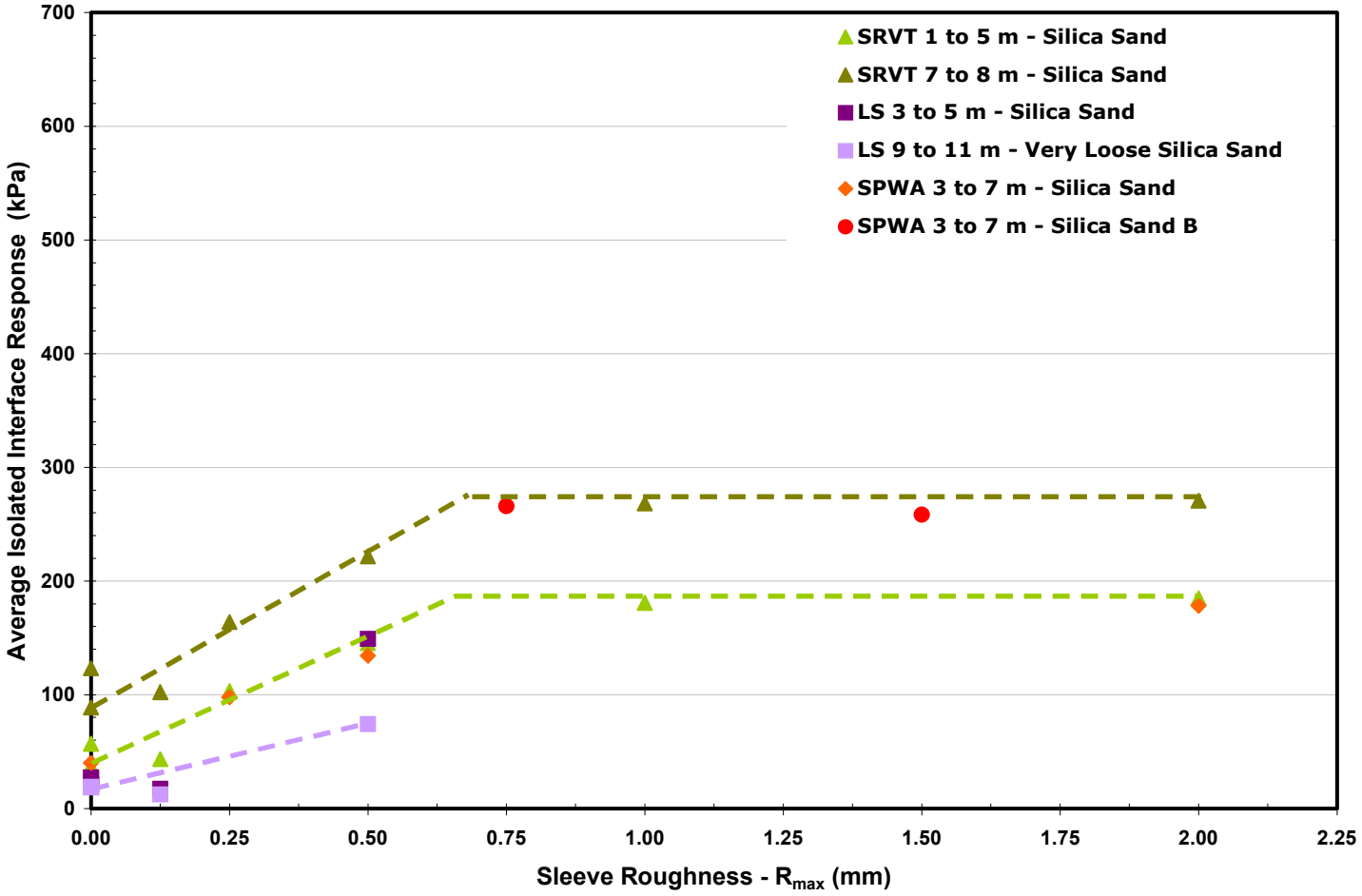

Figure 6-27. Plot Showing the Average Isolated Interface Sleeve Response as a Function of Sleeve Texture for the Highlighted Silica Sand Layers from the Current Study. The Lines Highlight the Conventional Bilinear Interface Response Trends as a Function of Surface Roughness for the Range of Silica Sands Tested.

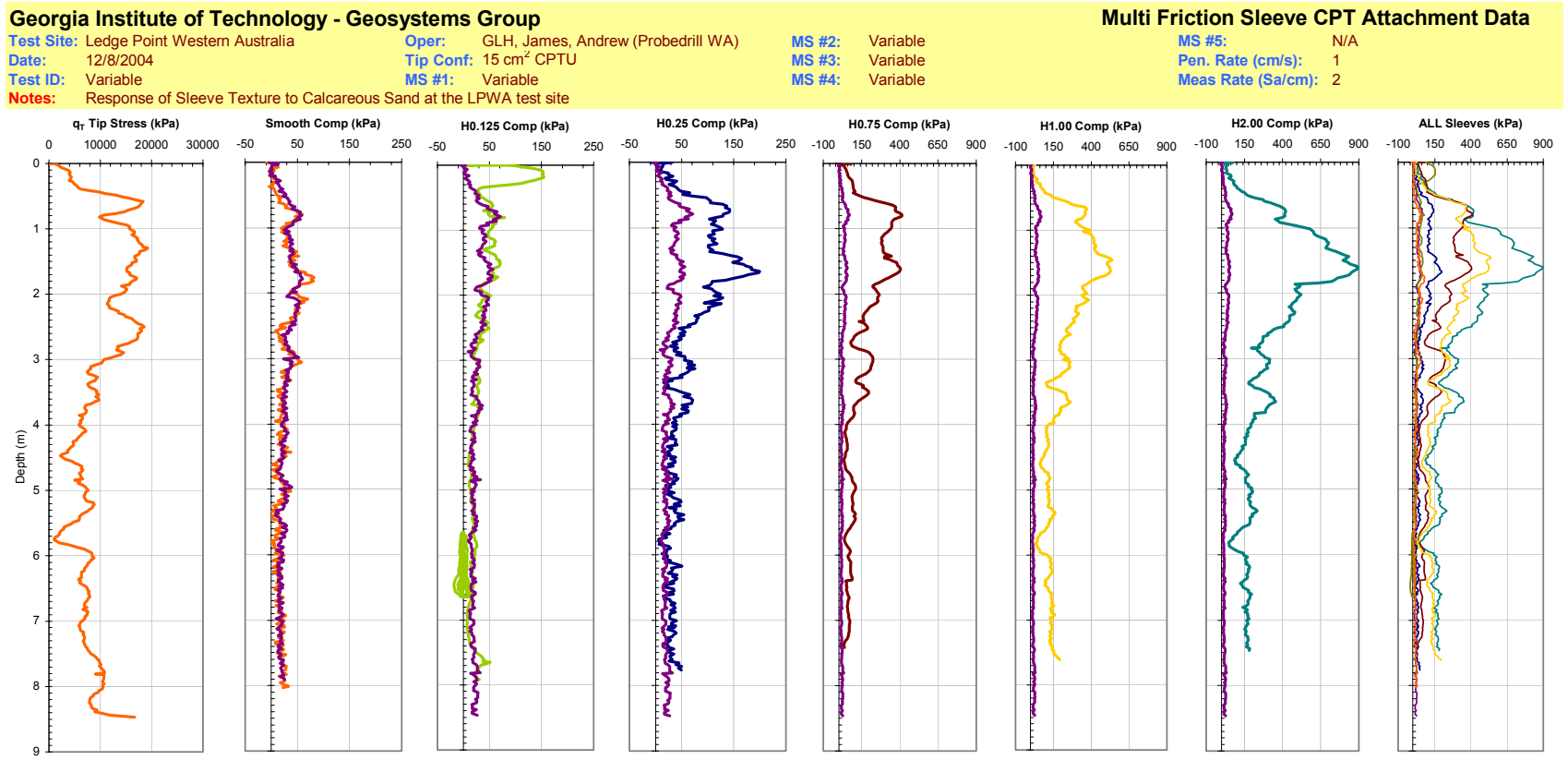

Figure 6-28. Plots Showing the Total Measured Sleeve Traces for the Range of Sleeve Textures Tested at the LPWA Test Site. Individual MFA Sensor Traces are Compared to f_s Response, with the Far Right Subplot Comparing All Sleeve Responses.

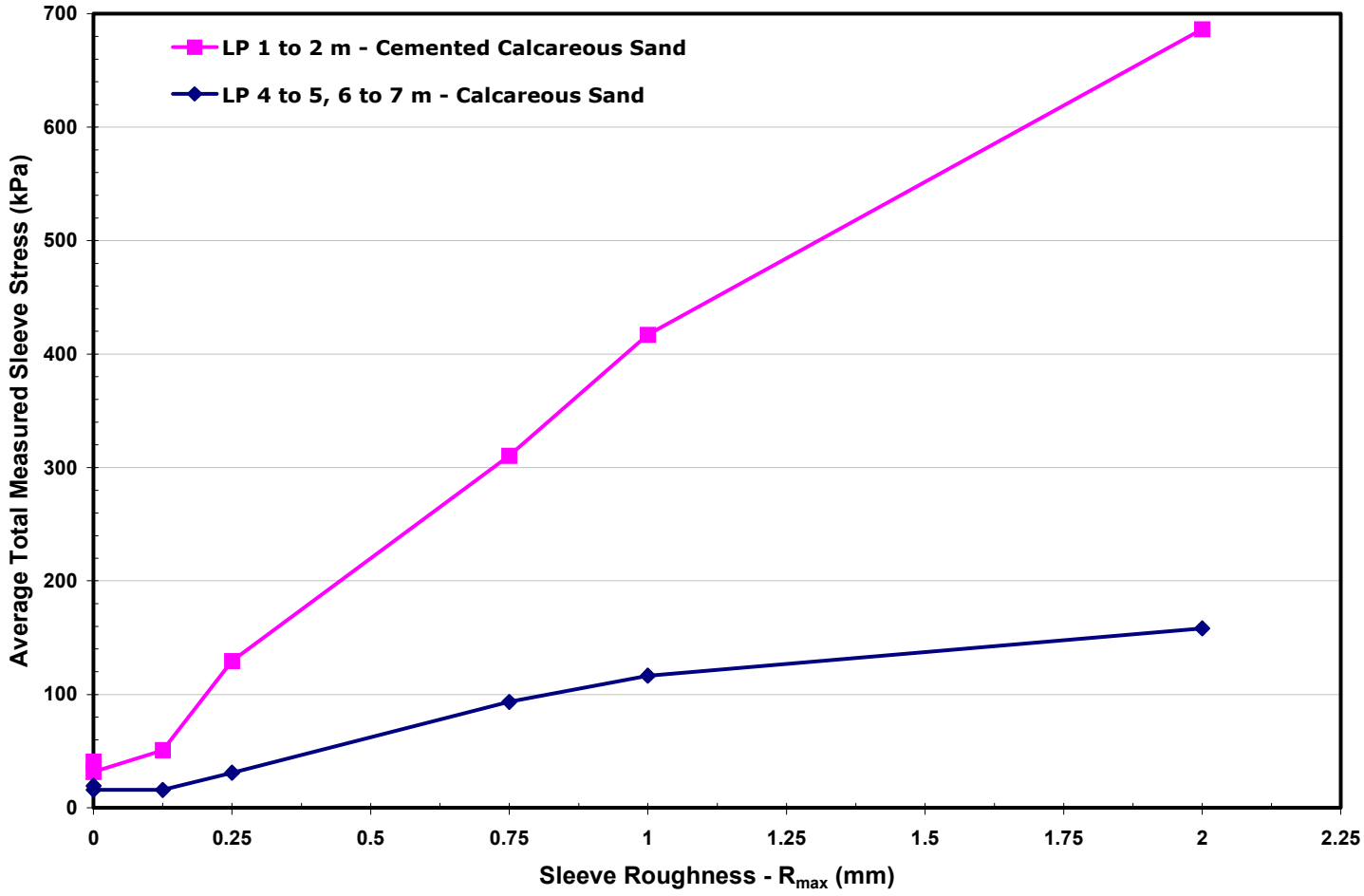

Figure 6-29. Plot Showing the Average Total Measured Sleeve Response as a Function of Sleeve Texture for the Selected Calcareous Sand Layers from the Current Study.

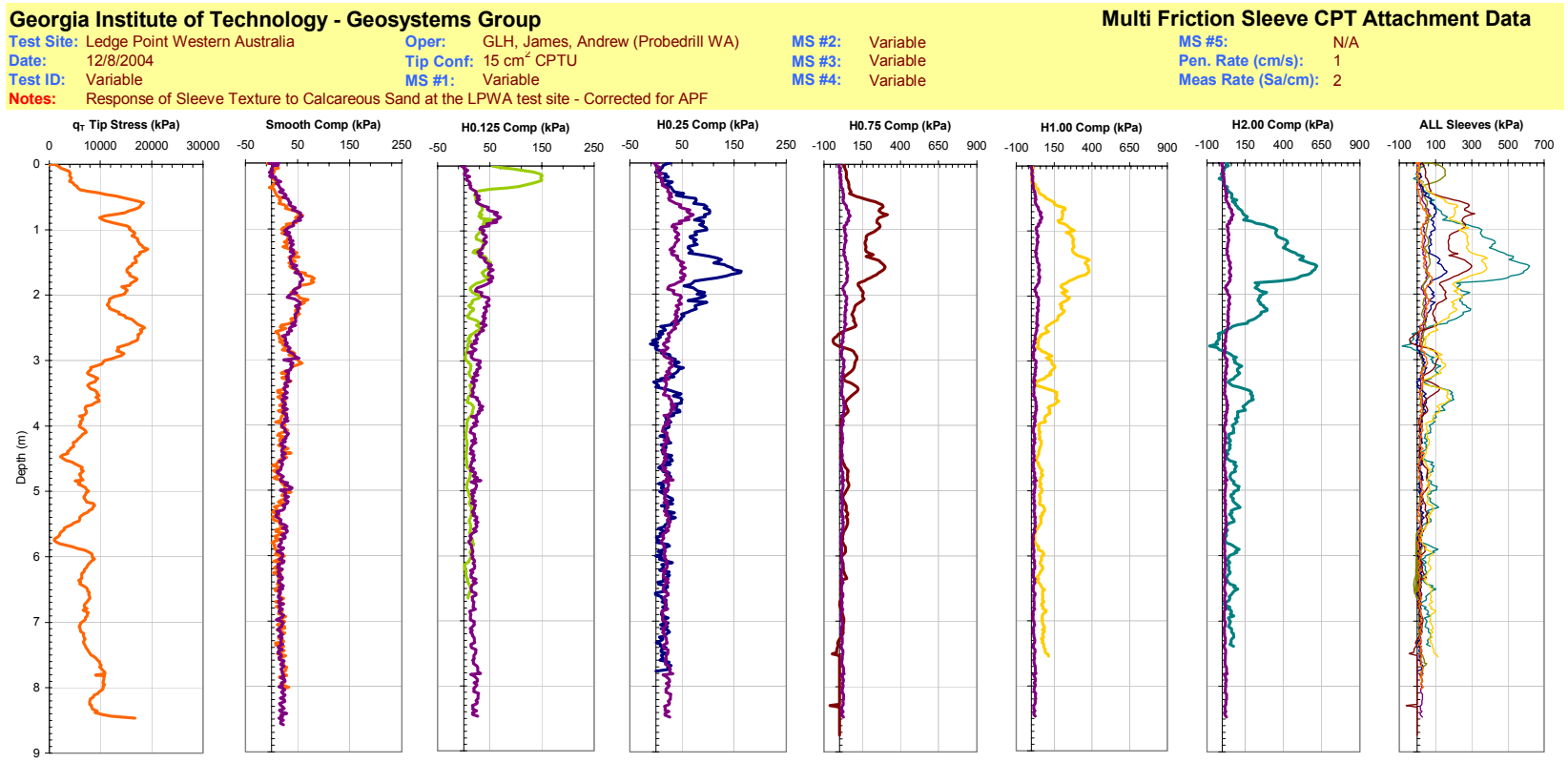

Figure 6-30. Plots Showing the Isolated Interface Sleeve Traces for the Range of Sleeve Textures Tested at the LPWA Test Site. Individual MFA Sensor Traces are Compared to f_s Response, with the Far Right Subplot Comparing All Sleeve Responses.

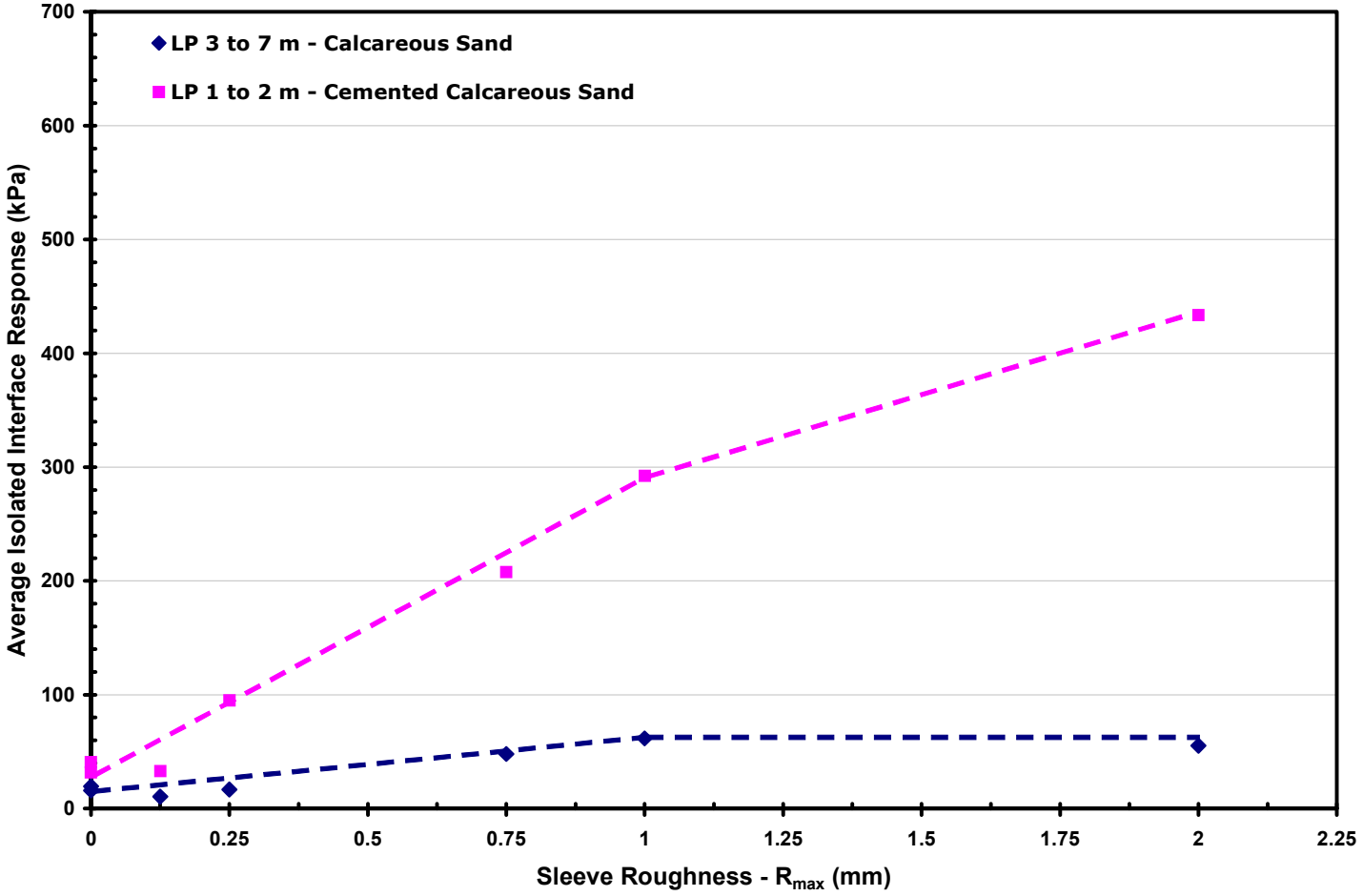

Figure 6-31. Plot Showing the Average Isolated Interface Sleeve Response as a Function of Sleeve Texture for the Selected Calcareous Sand Layers from the Current Study. The Lines Highlight the Conventional Bilinear Interface Response Trends as a Function of Surface Roughness for the Range of Calcreous Sands Tested.

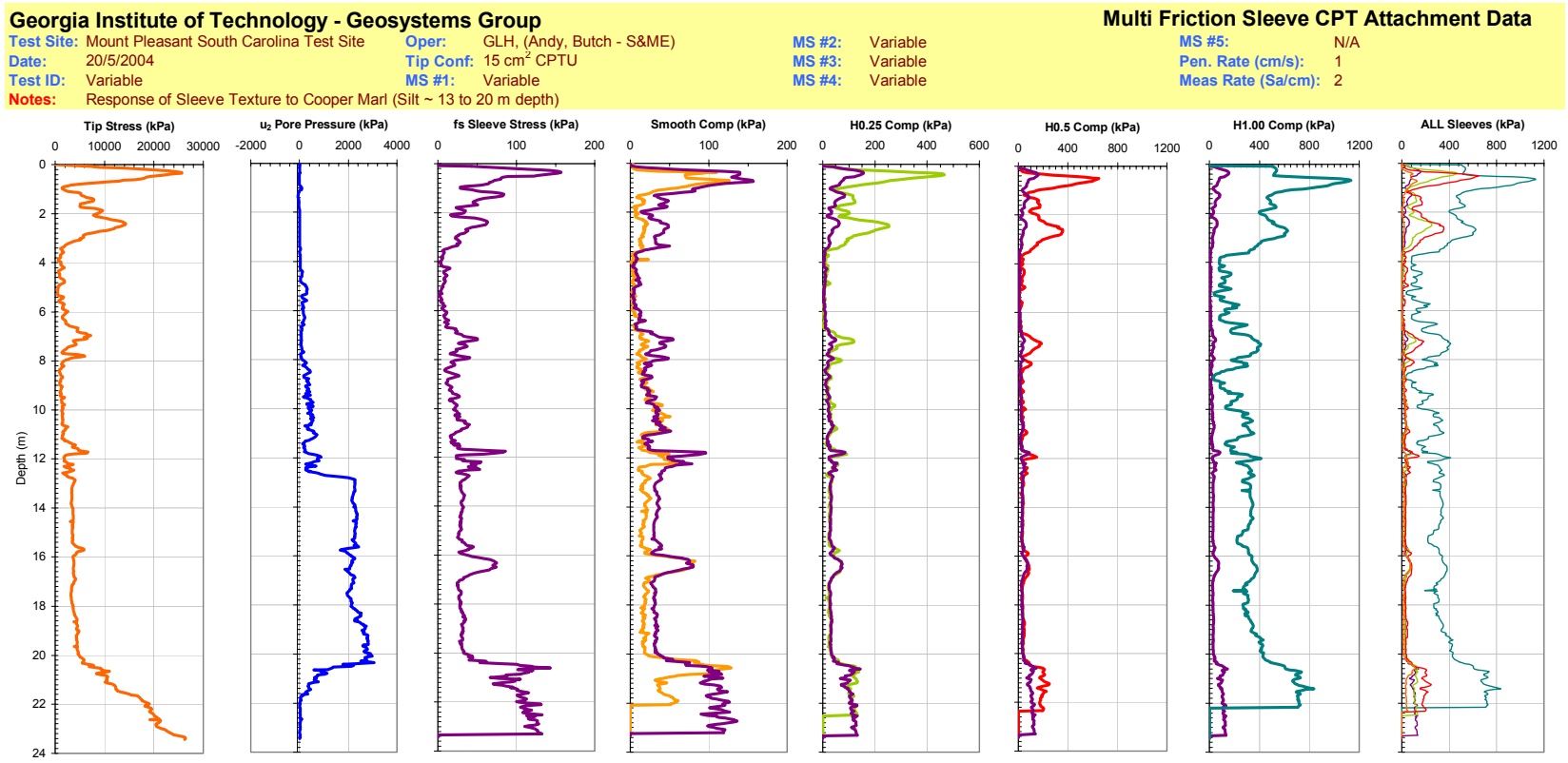

Figure 6-32. Plots Showing the Total Measured Sleeve Traces for the Range of Sleeve Textures Tested at the MPSC Test Site. Individual MFA Sensor Traces are Compared to f_s Response, with the Far Right Subplot Comparing All Sleeve Responses.

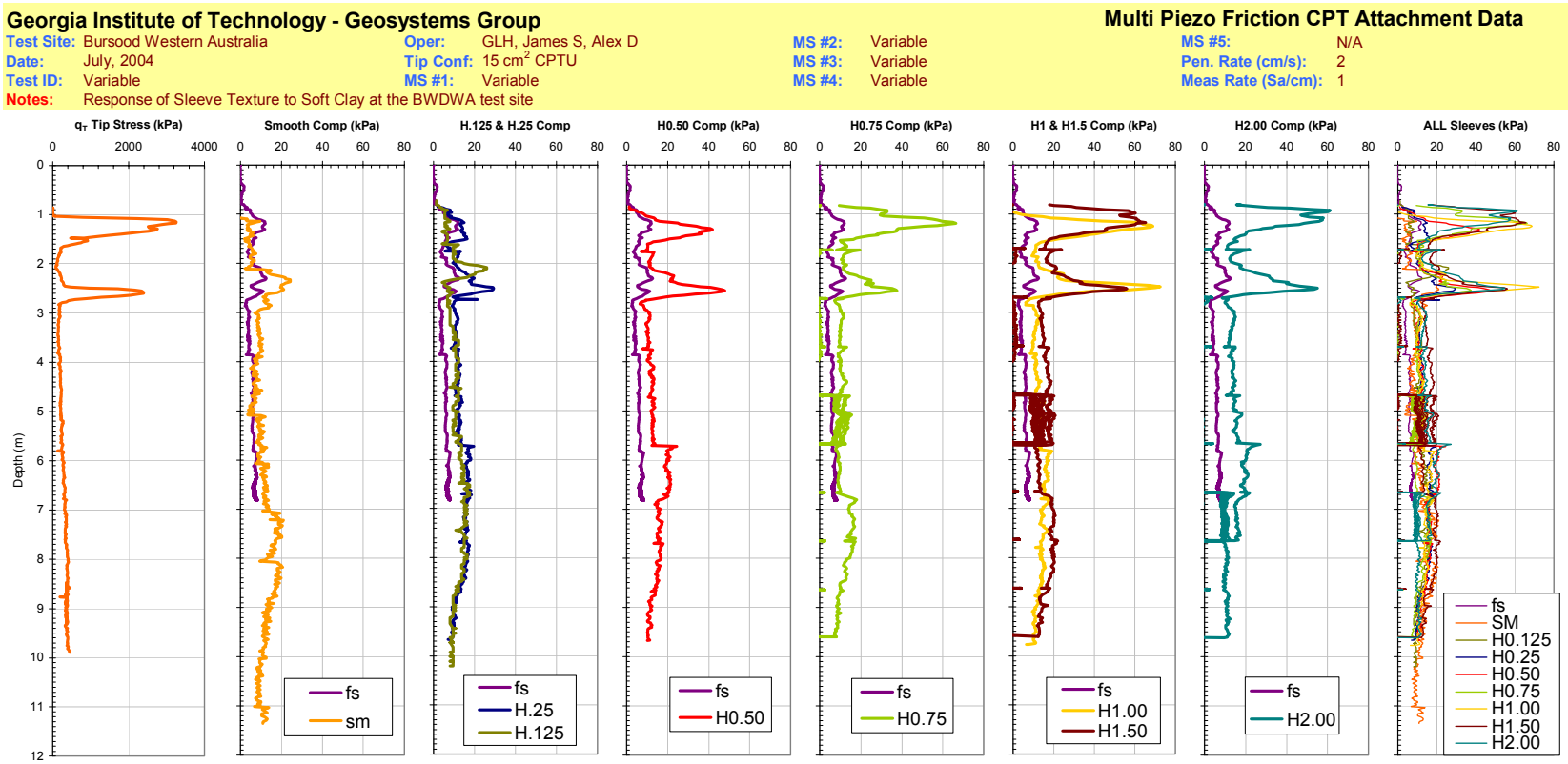

Figure 6-33. Plots Showing the Total Measured Sleeve Traces for the Range of Sleeve Textures Tested at the BWDWA Test Site. Individual MFA Sensor Traces are Compared to f_s Response, with the Far Right Subplot Comparing All Sleeve Responses.

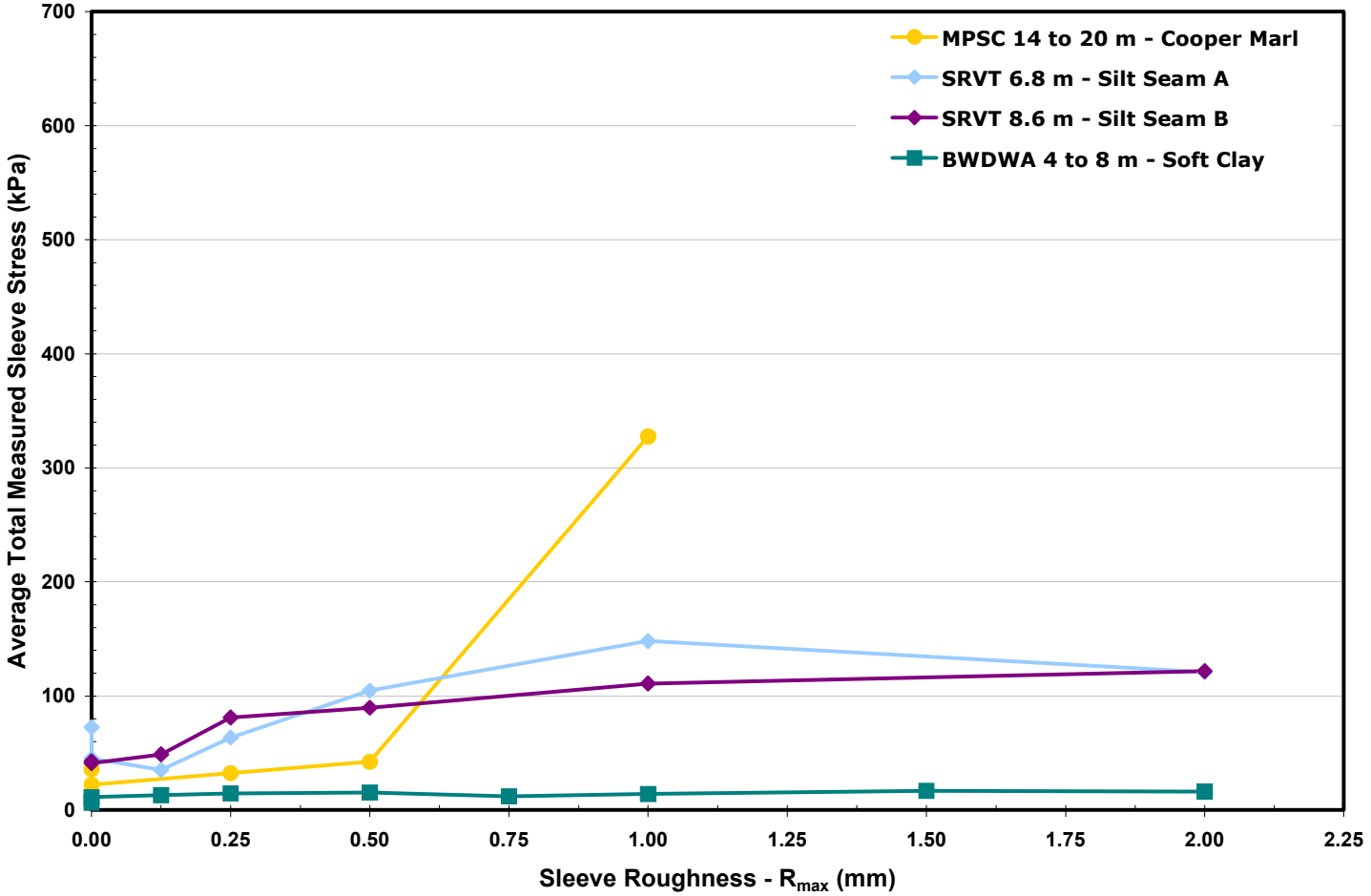

Figure 6-34. Plot Showing the Average Total Measured Sleeve Response as a Function of Sleeve Texture for the Selected Fine Grained Layers from the Current Study.

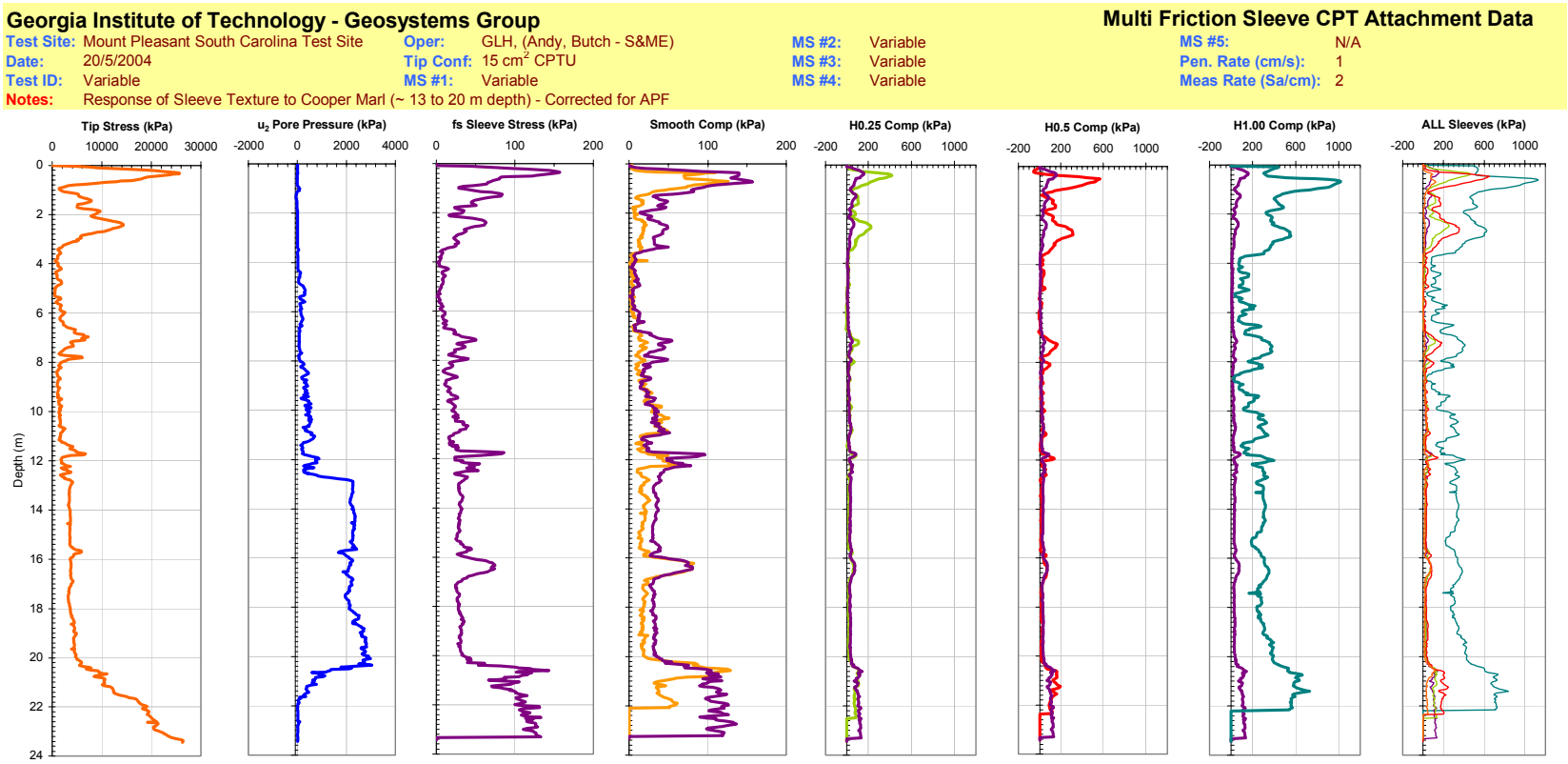

Figure 6-35. Plots Showing the Isolated Interface Sleeve Traces for the Range of Sleeve Textures Tested at the MPSC Test Site. Individual MFA Sensor Traces are Compared to f_s Response, with the Far Right Subplot Comparing All Sleeve Responses.

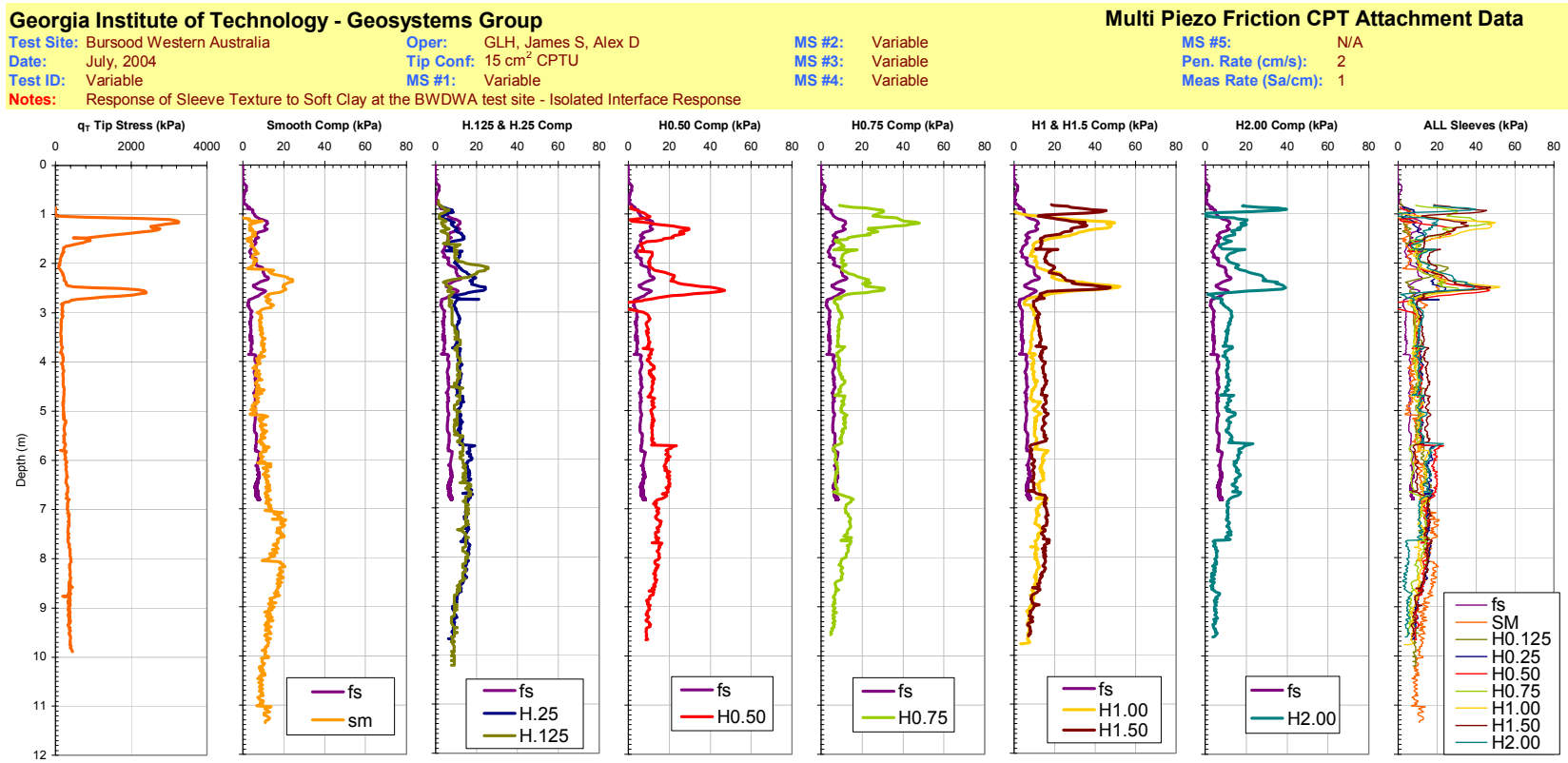

Figure 6-36. Plots Showing the Isolated Interface Sleeve Traces for the Range of Sleeve Textures Tested at the BWDWA Test Site. Individual MFA Sensor Traces are Compared to f_s Response, with the Far Right Subplot Comparing All Sleeve Responses.

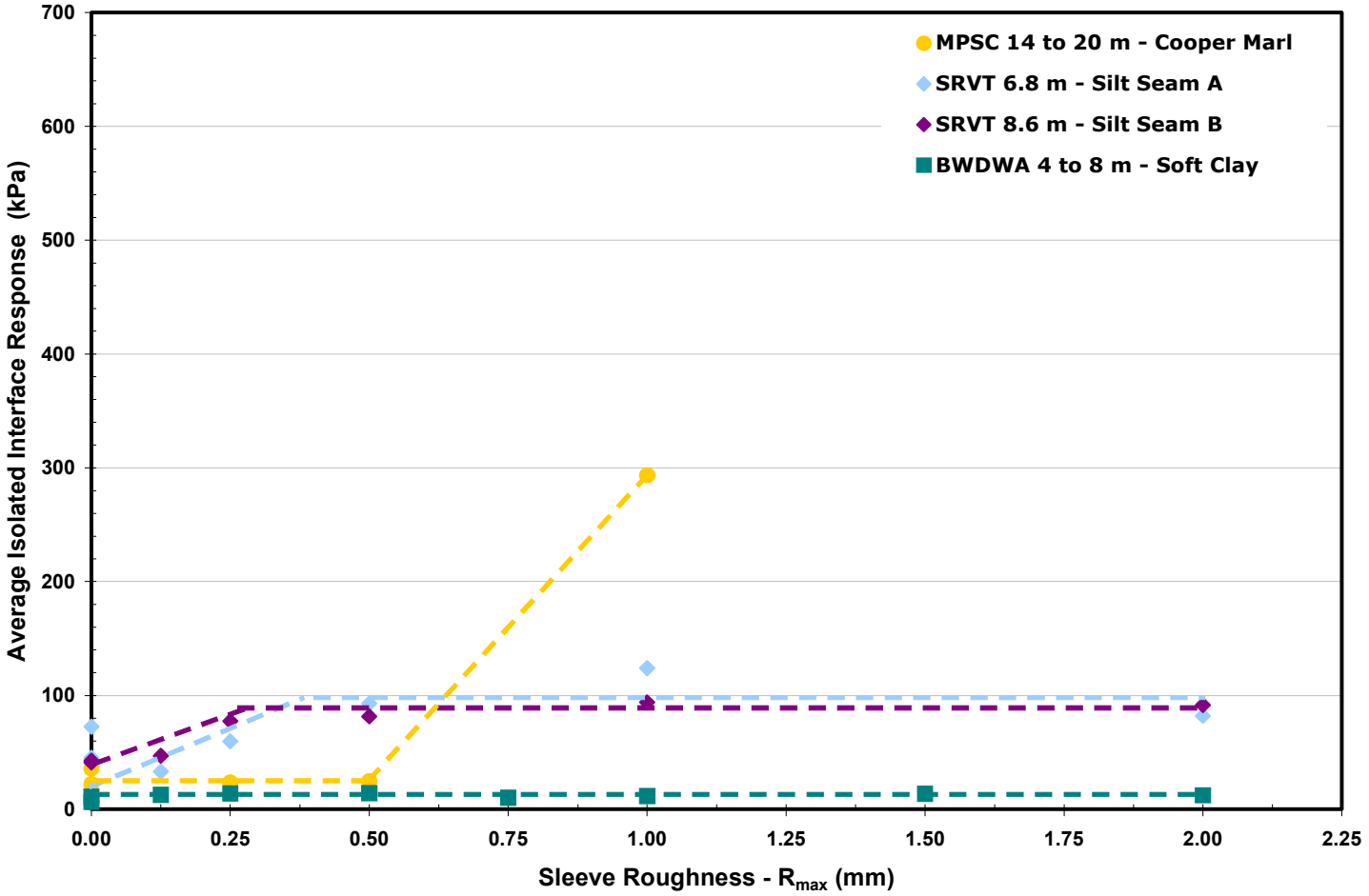

Figure 6-37. Plot Showing the Average Isolated Interface Sleeve Response as a Function of Sleeve Texture for the Selected Fine Grained Layers from the Current Study. The Lines Highlight the Conventional Bilinear Interface Response Trends as a Function of Surface Roughness for the Range of Fine Grained Soils Tested.

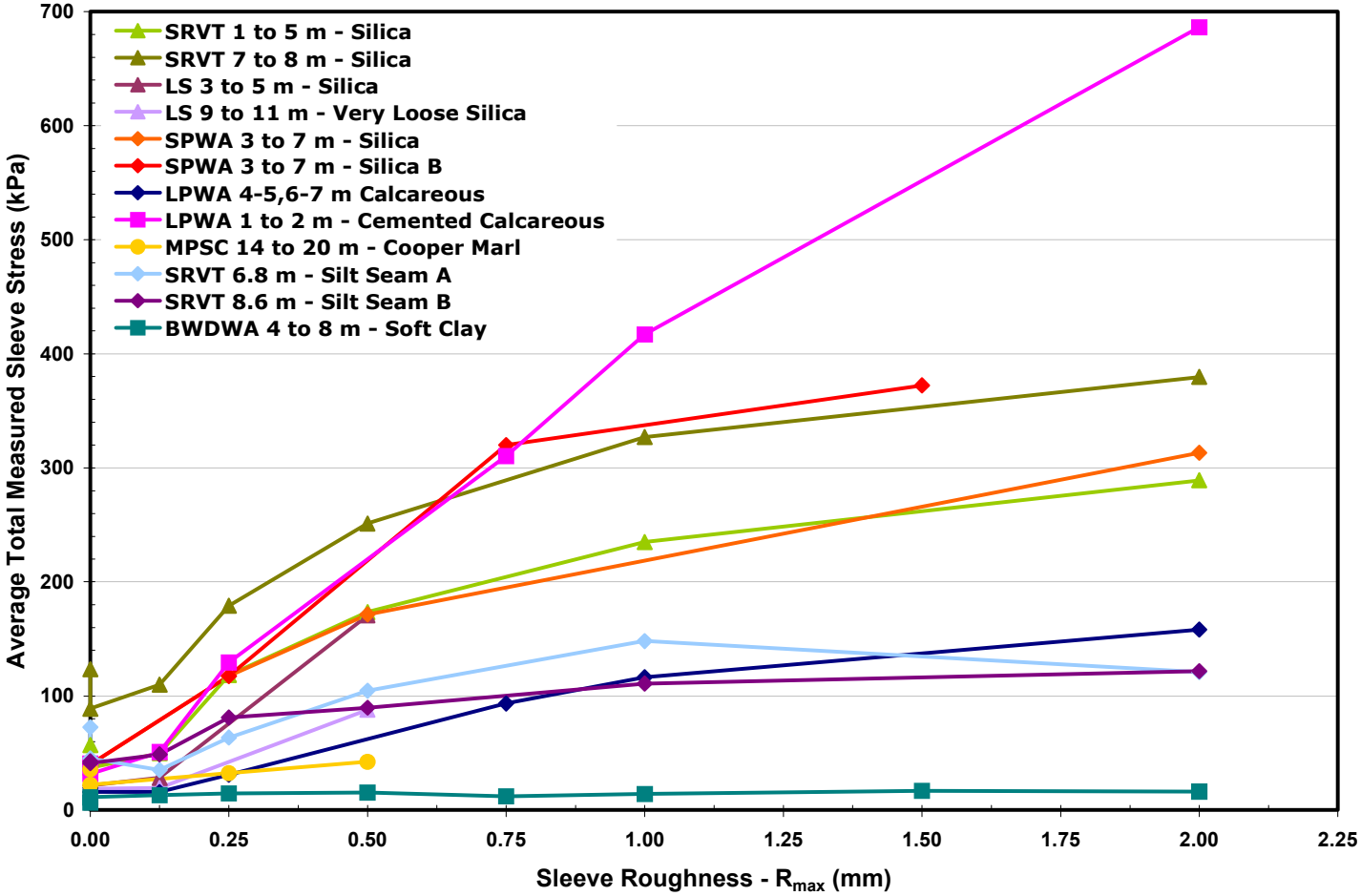

Figure 6-38. Plot Showing the Average Total Measured Sleeve Response as a Function of Sleeve Texture for All of the Selected Layers from the Current Study.

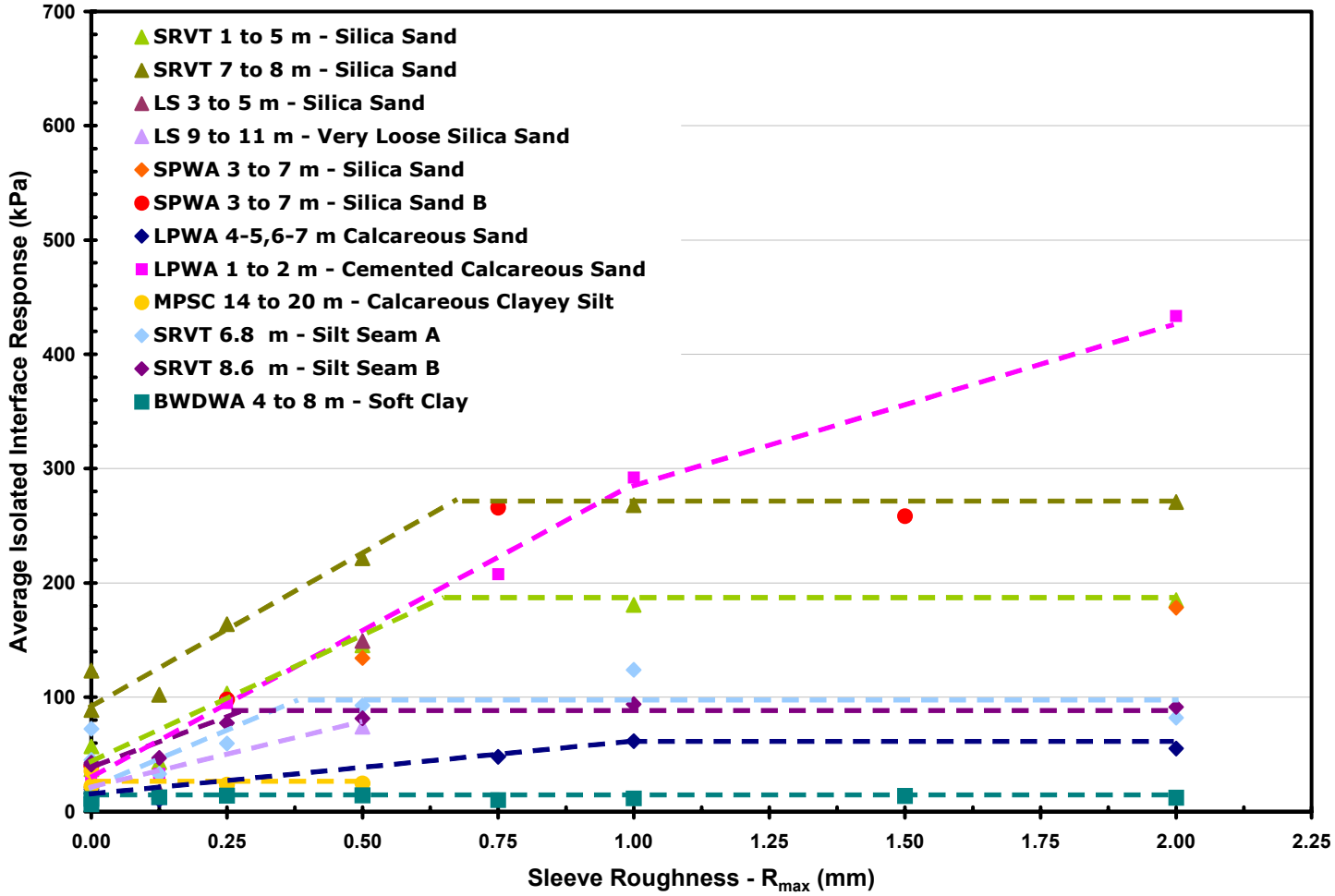

Figure 6-39. Plot Showing the Average Isolated Interface Sleeve Response as a Function of Sleeve Texture for All of the Selected Layers from the Current Study. The Lines Highlight the Conventional Bilinear Interface Response Trends as a Function of Surface Roughness for the Range of Soils Tested

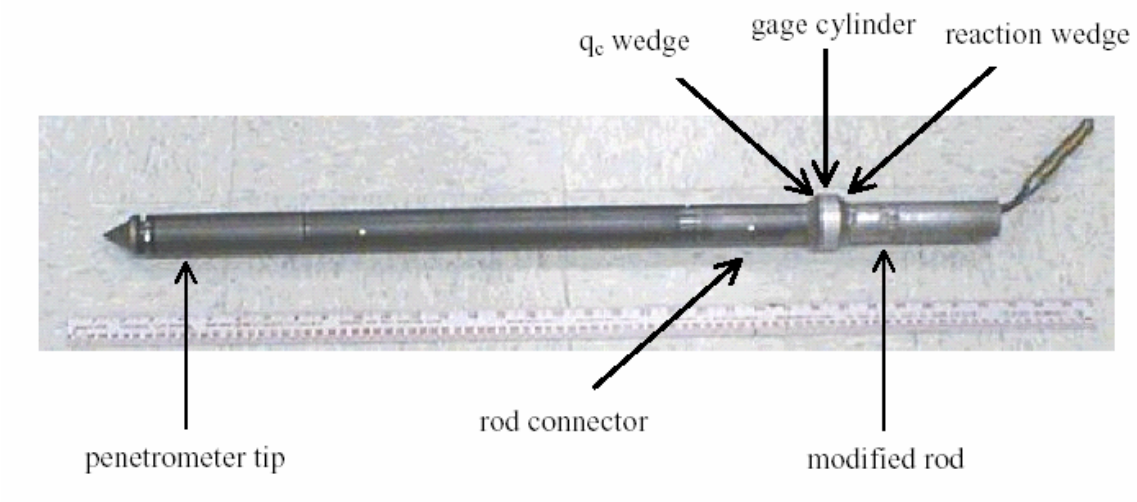

Figure 6-40. Penetrometer Developed at the University of Florida to Quantify Levels of Soil Structure and Cementation (Bloomquist et al., 1999).

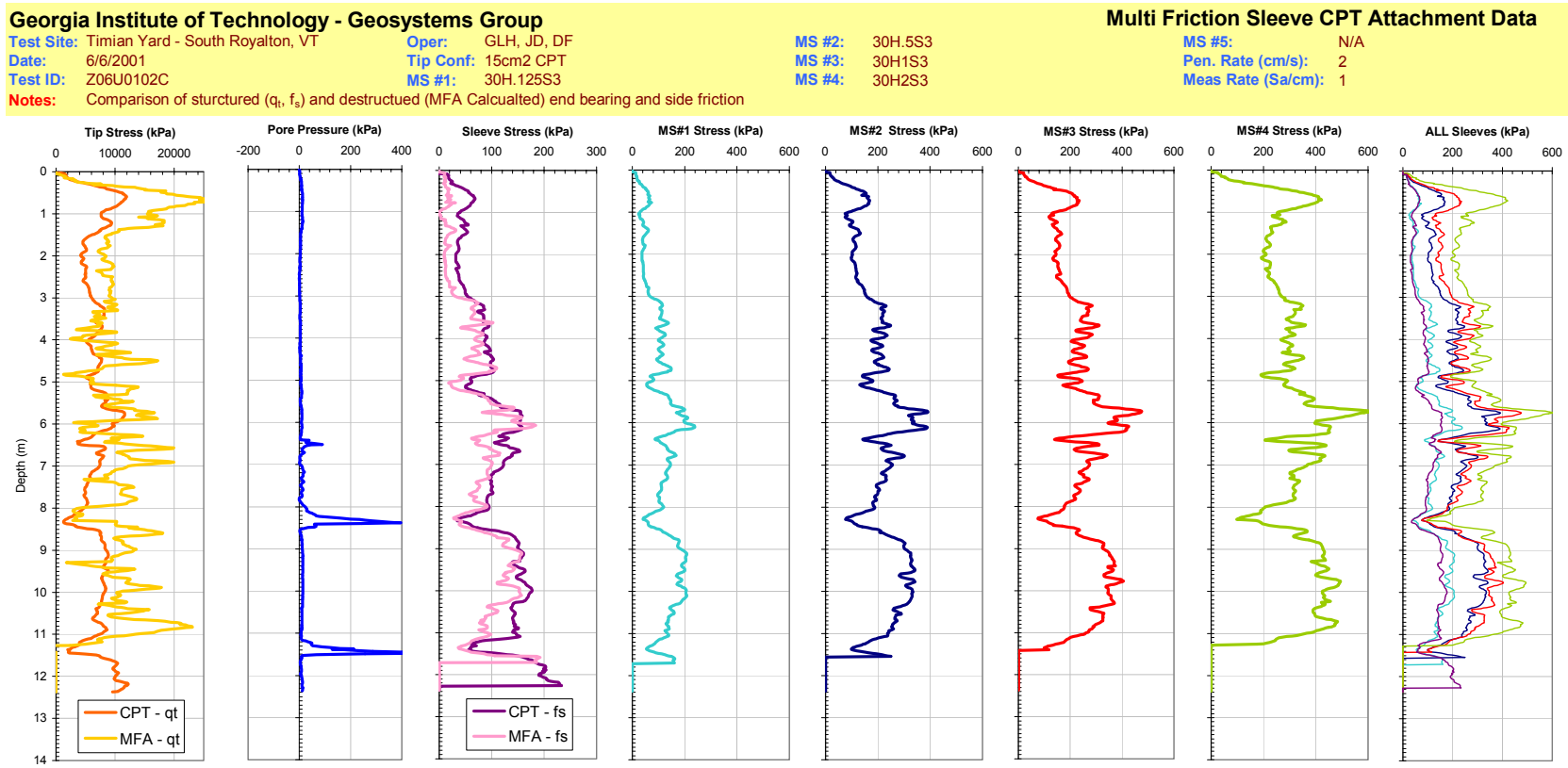

Figure 6-41. Plots Comparing the Measured CPTU-MFA Sensor Traces with Values of Disturbed End Bearing and Side Friction Calculated Using MFA Textured Sleeve Responses for the SRVT Test Site.

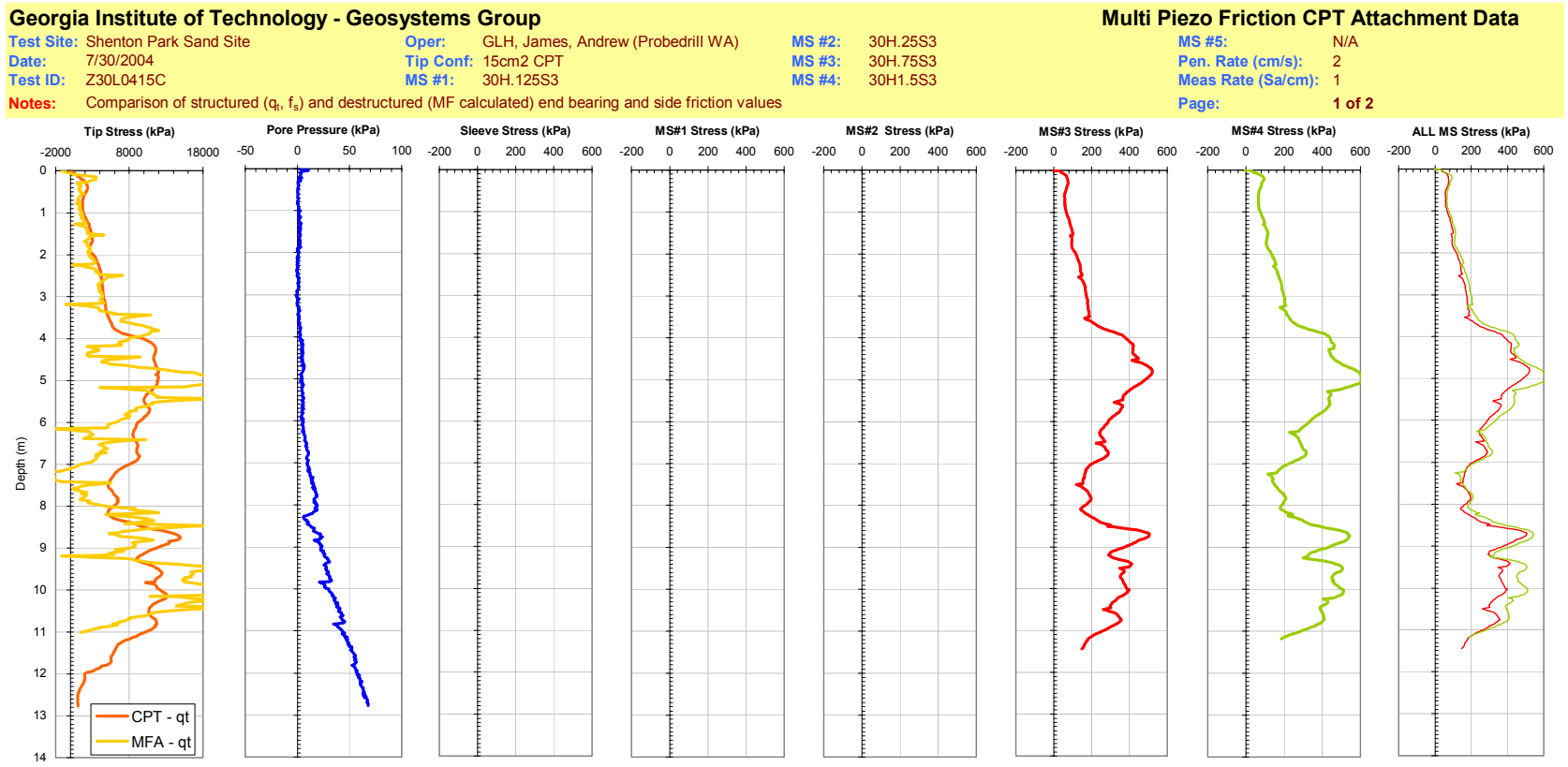

Figure 6-42. Plots Comparing the Measured CPTU-MFA Sensor Traces with Disturbed End Bearing Calculated Using MFA Textured Sleeve Responses for the SPWA Test Site.

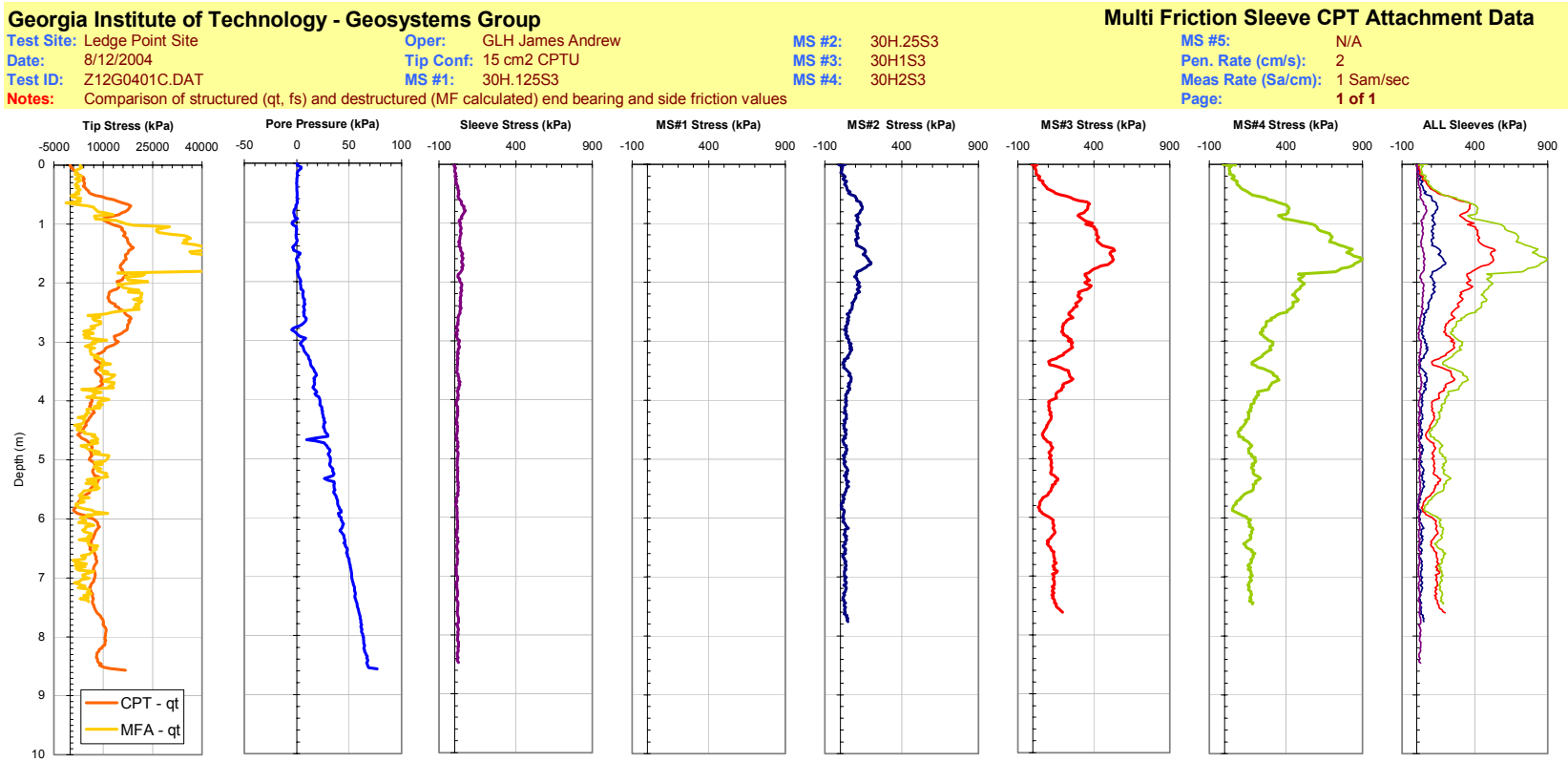

Figure 6-43. Plots Comparing the Measured CPTU-MFA Sensor Traces with Disturbed End Bearing Calculated Using MFA Textured Sleeve Responses for the LPWA Test Site.

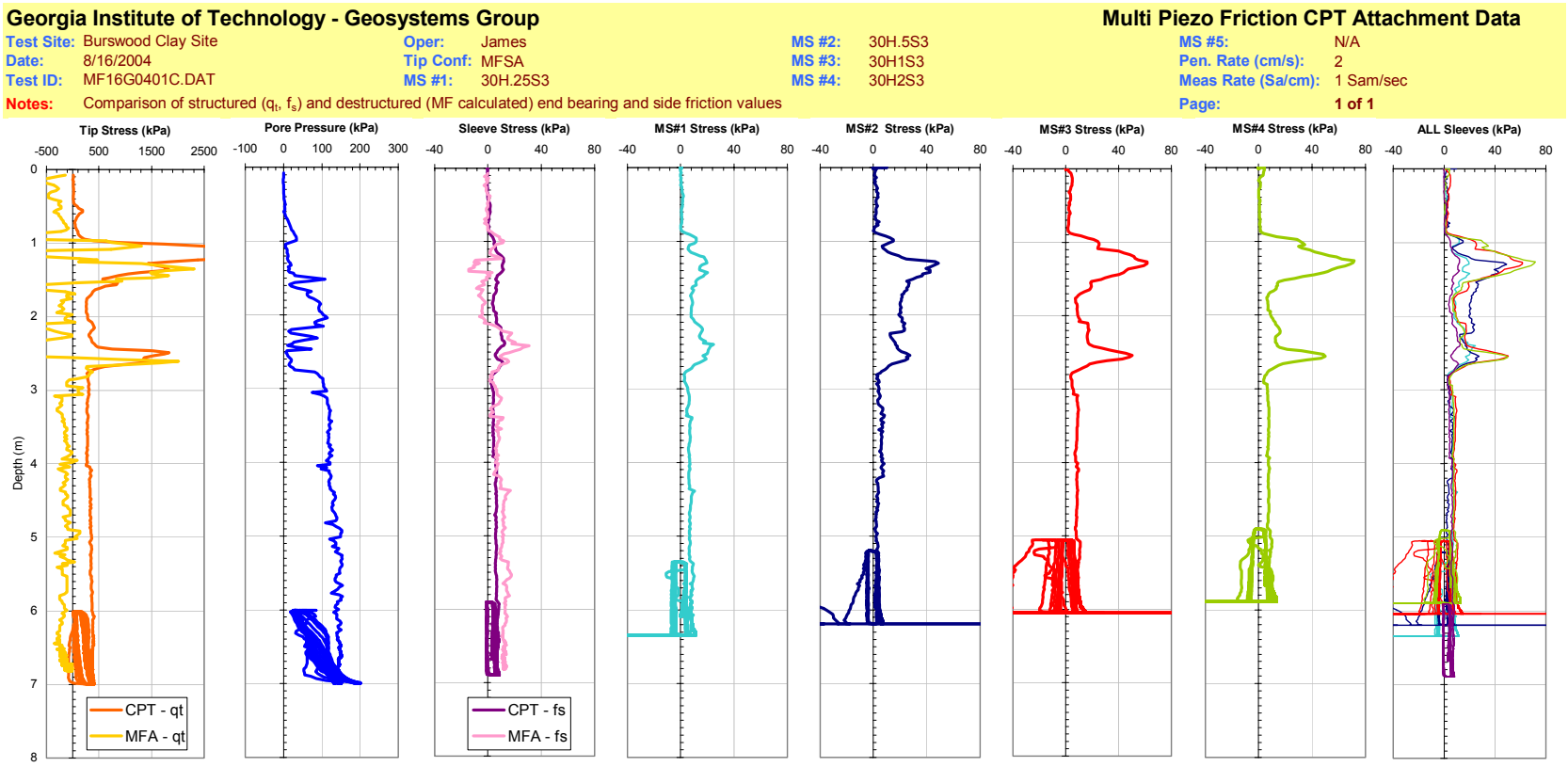

Figure 6-44. Plots Comparing the Measured CPTU-MFA Sensor Traces with Disturbed End Bearing Calculated Using MFA Textured Sleeve Responses for the BWDWA Test Site.

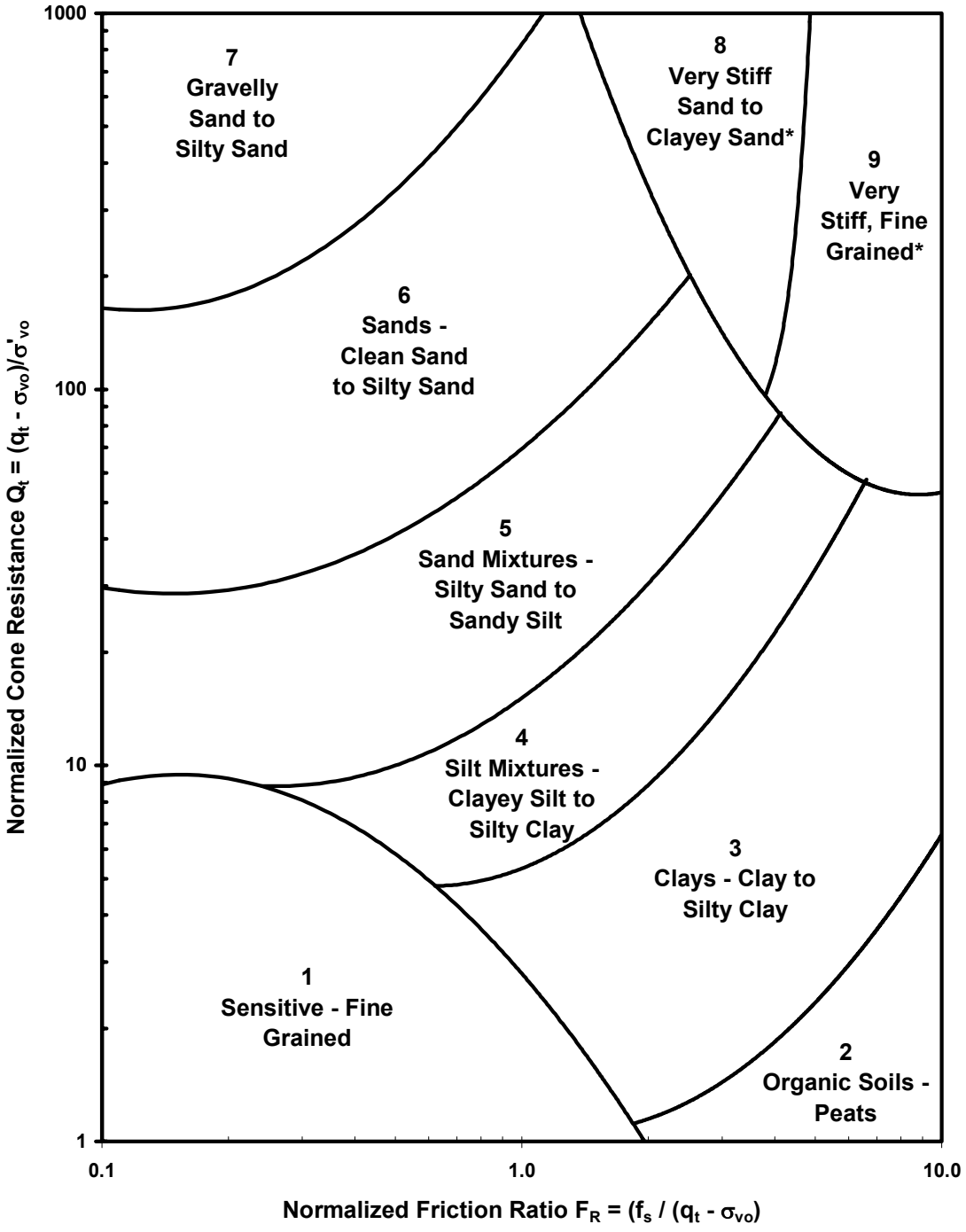

Figure 6-45. Half of the Robertson (1990, 1991) Soil Classification System Based on the Response of Normalized CPTU Parameters. This Chart Compares the Response of Normalized Cone Resistance (Q_t) to Normalized Friction Ratio (F_R).

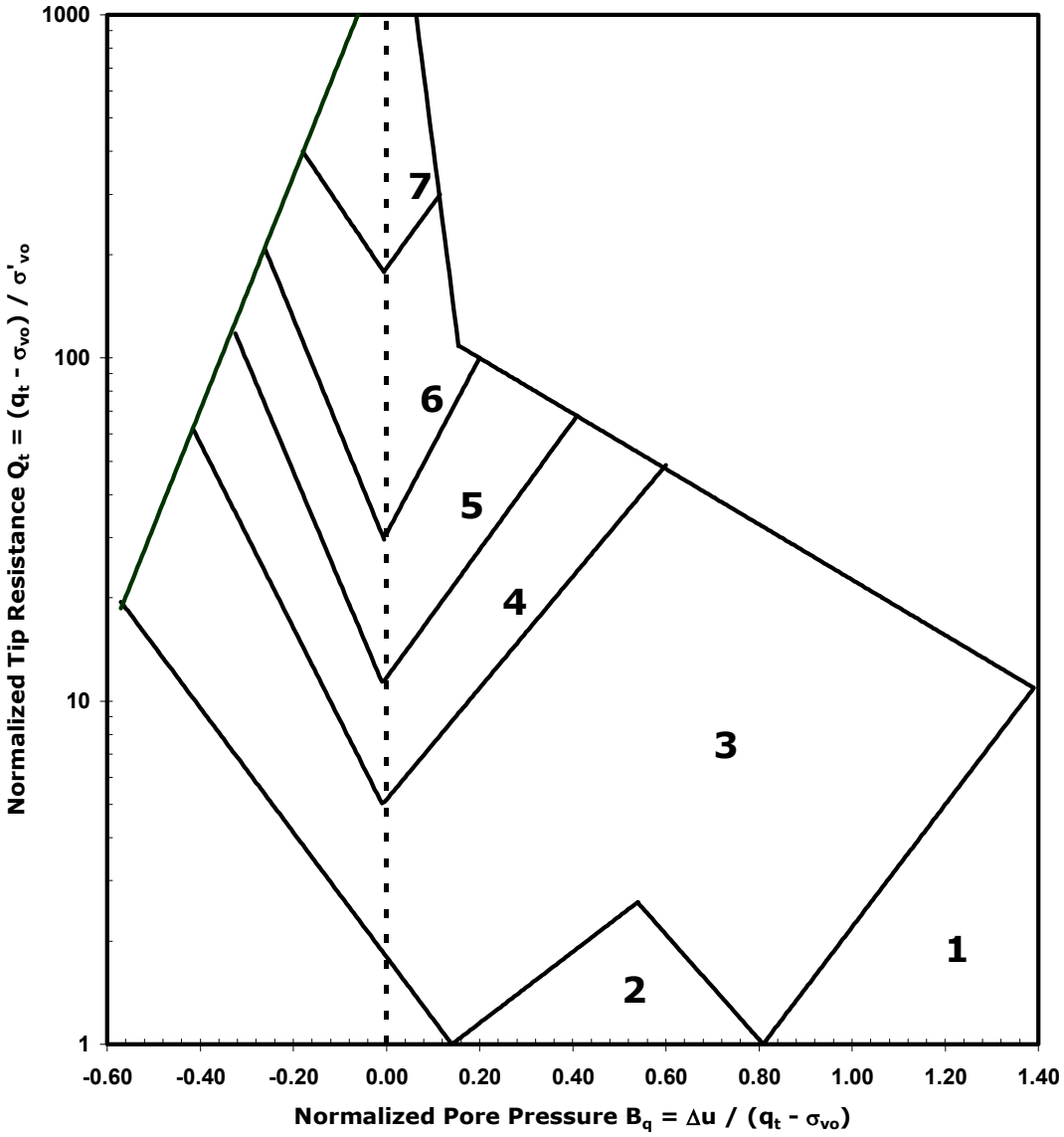

Robertson (1990, updated 1991) Qt - Bq CPTU classification chart. Zones are as follows: 1, sensitive, fine grained; 2, organic soils - peats; 3, clays - clay to silty clay; 4, silty mixtures - clayey silt to silty clay; 5, sand mixtures - silty sand to sandy silt; 6, sands - clean sand to silty sand; 7, gravelly sand to sand.

Figure 6-46. Half of the Robertson (1990, 1991) Soil Classification System Based on the Response of Normalized CPTU Parameters. This Chart Compares the Response of Normalized Cone Resistance (Q_t) to Normalized Pore Pressure(B_q).

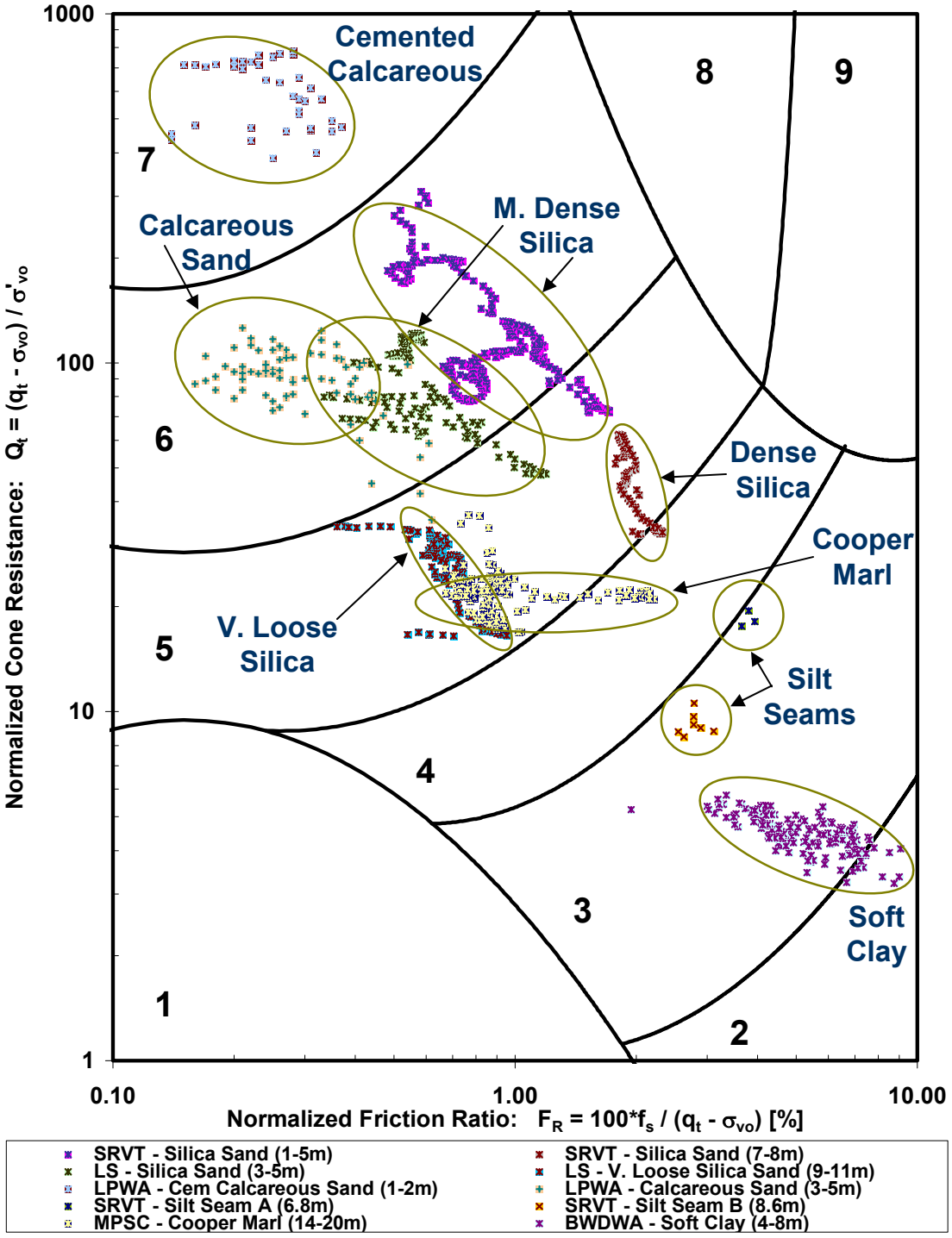

Figure 6-47. Response of the Selected Soil Layers from the Current Study Within the Q_t - F_R Robertson (1990, 1991) Soil Classification Framework.

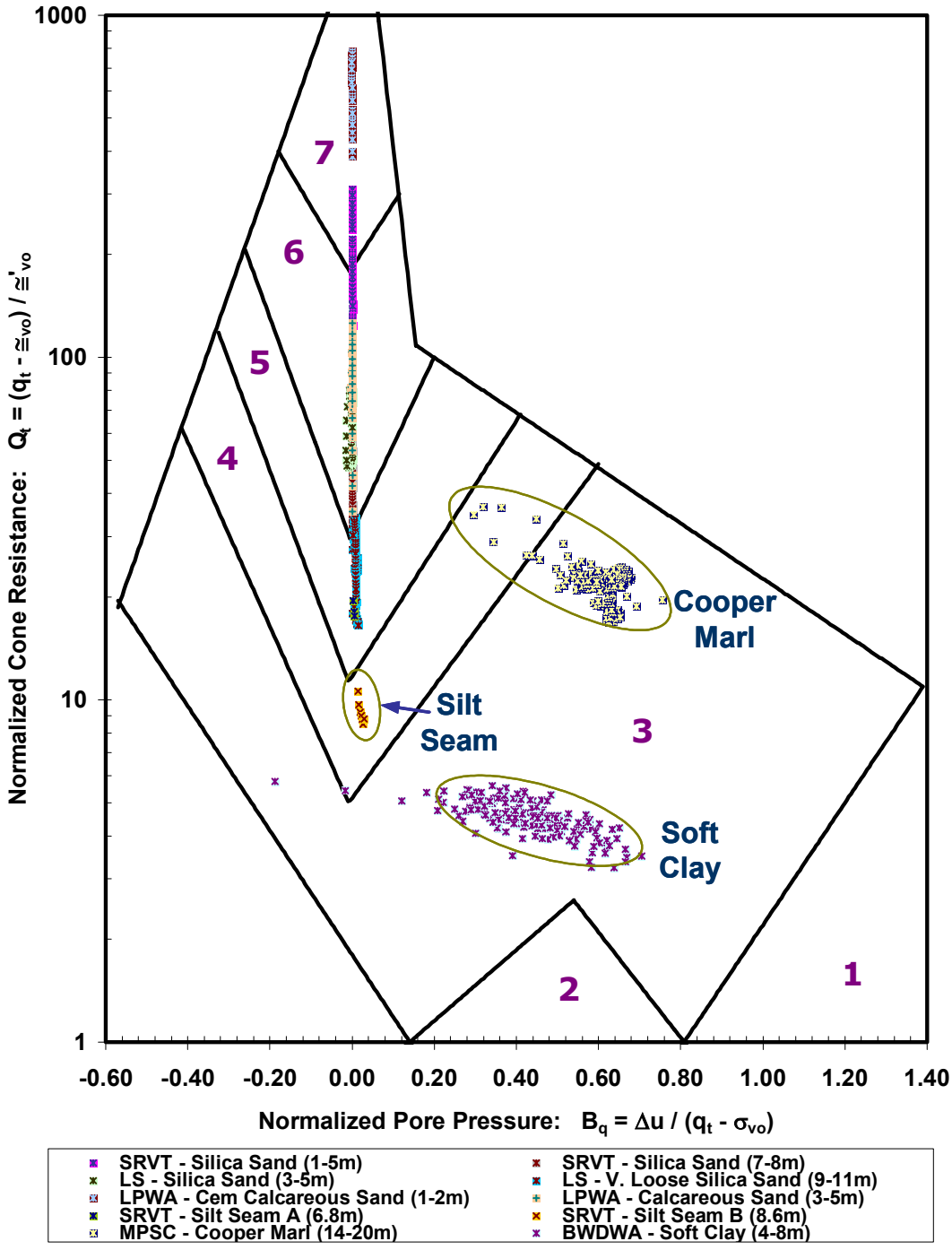

Figure 6-48. Response of the Selected Soil Layers from the Current Study Within the Q_t - B_q Robertson (1990, 1991) Soil Classification Framework.

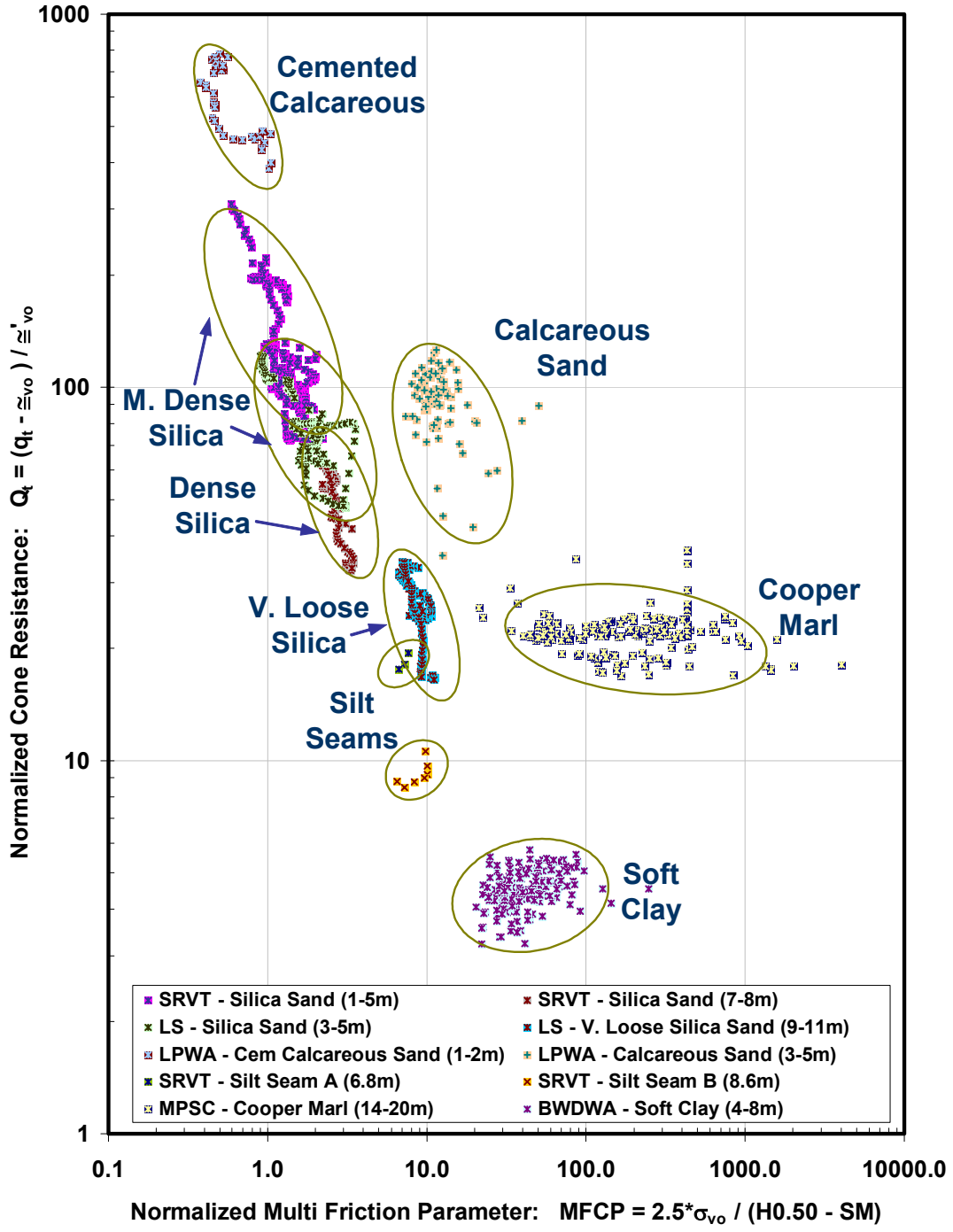

Figure 6-49. Response of the Selected Soil Layers from the Current Study As a Function of Normalized Cone Resistance (Q_t) and the Newly Developed Multi Friction Classification Parameter (*MFCP*).

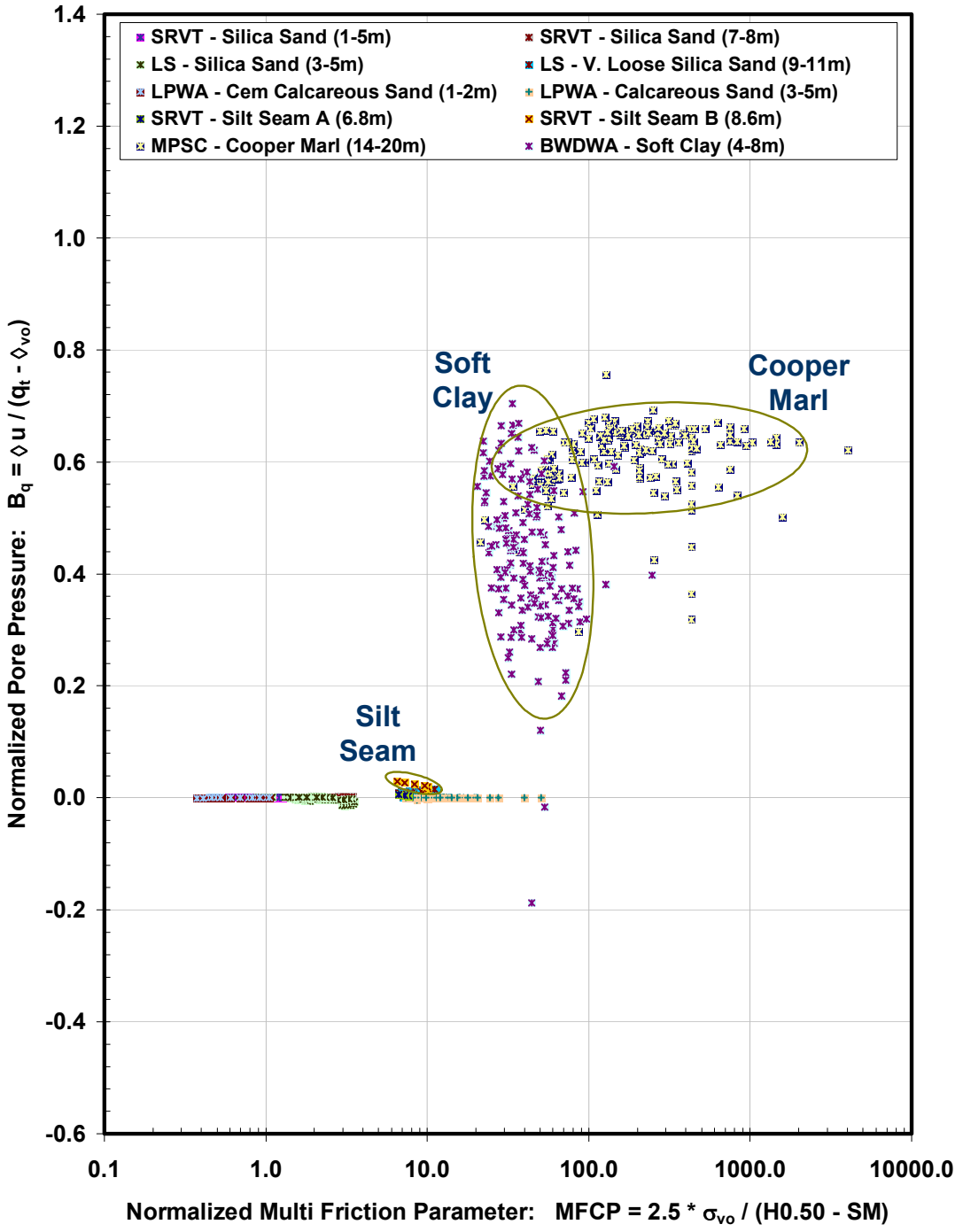

Figure 6-50. Response of the Selected Soil Layers from the Current Study As a Function of Normalized Pore Pressure (B_q) and the Newly Developed Multi Friction Classification Parameter (*MFCP*).

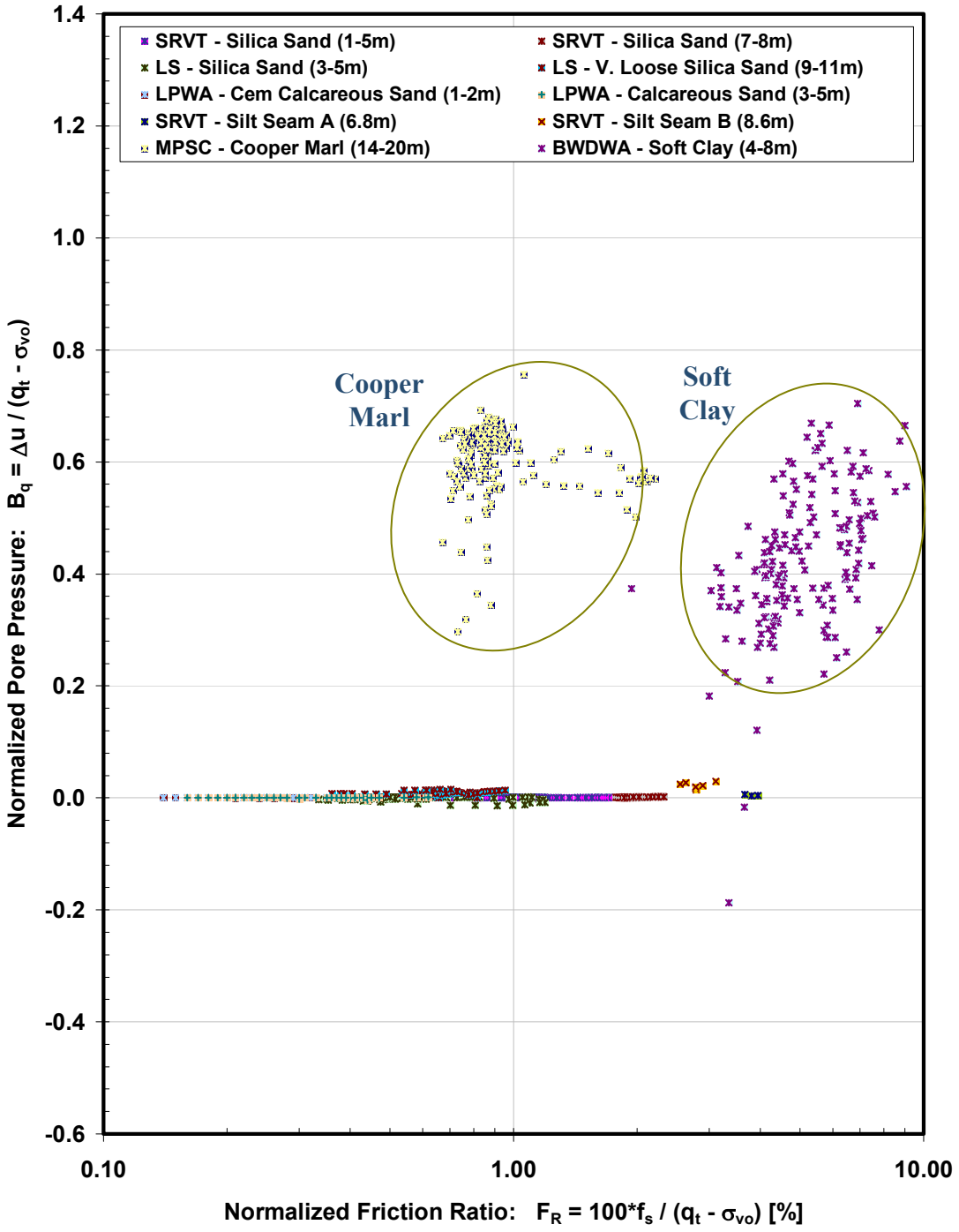

Figure 6-51. Response of the Selected Soil Layers from the Current Study As a Function of Normalized Pore Pressure (B_q) and Normalized Friction Ratio (F_R).

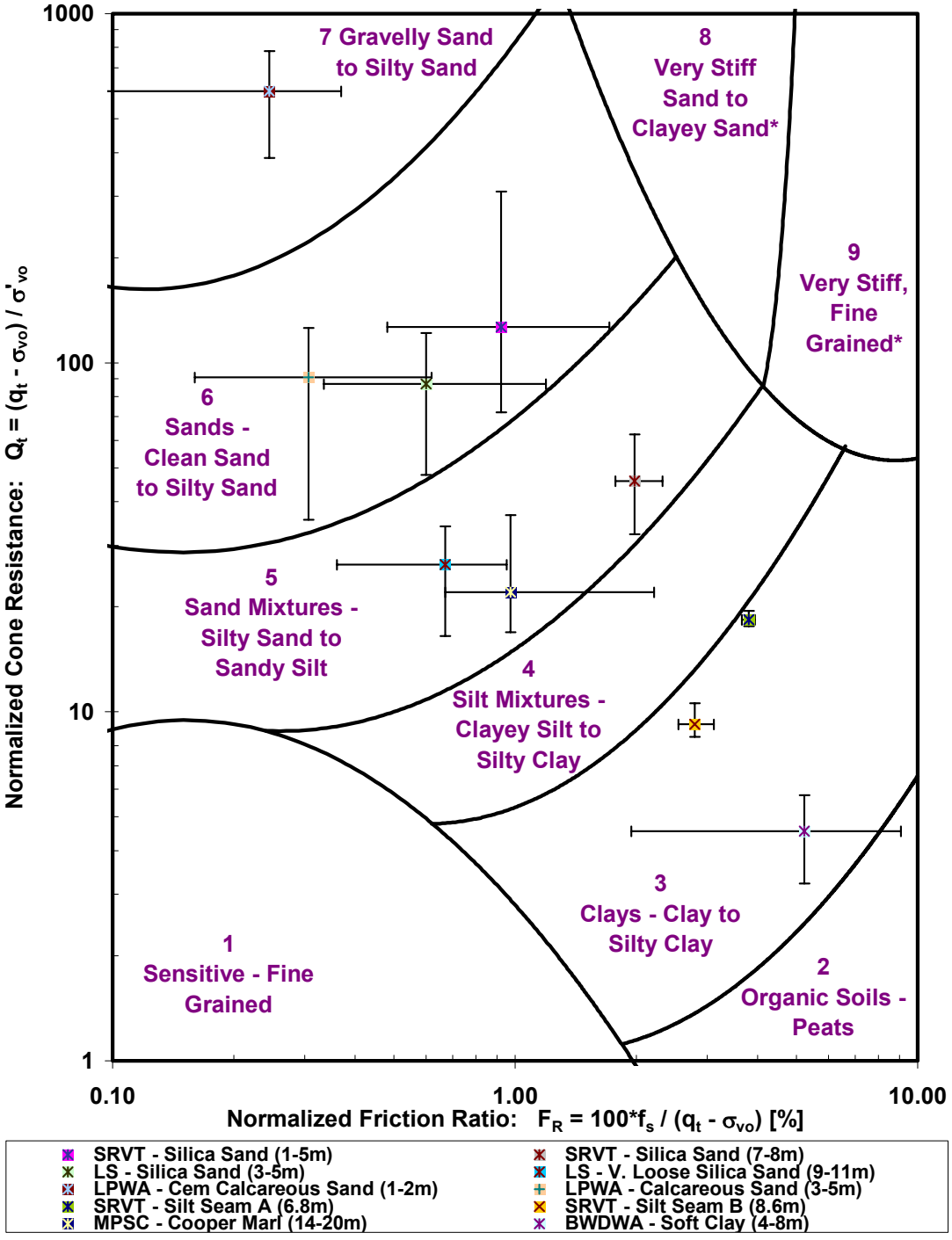

Figure 6-52. Average Response of the Selected Soil Layers from the Current Study Within the Q_t - F_R Robertson (1990, 1991) Soil Classification Framework. Error Bars Denote the Range of Values Measured for Each Selected Layer.

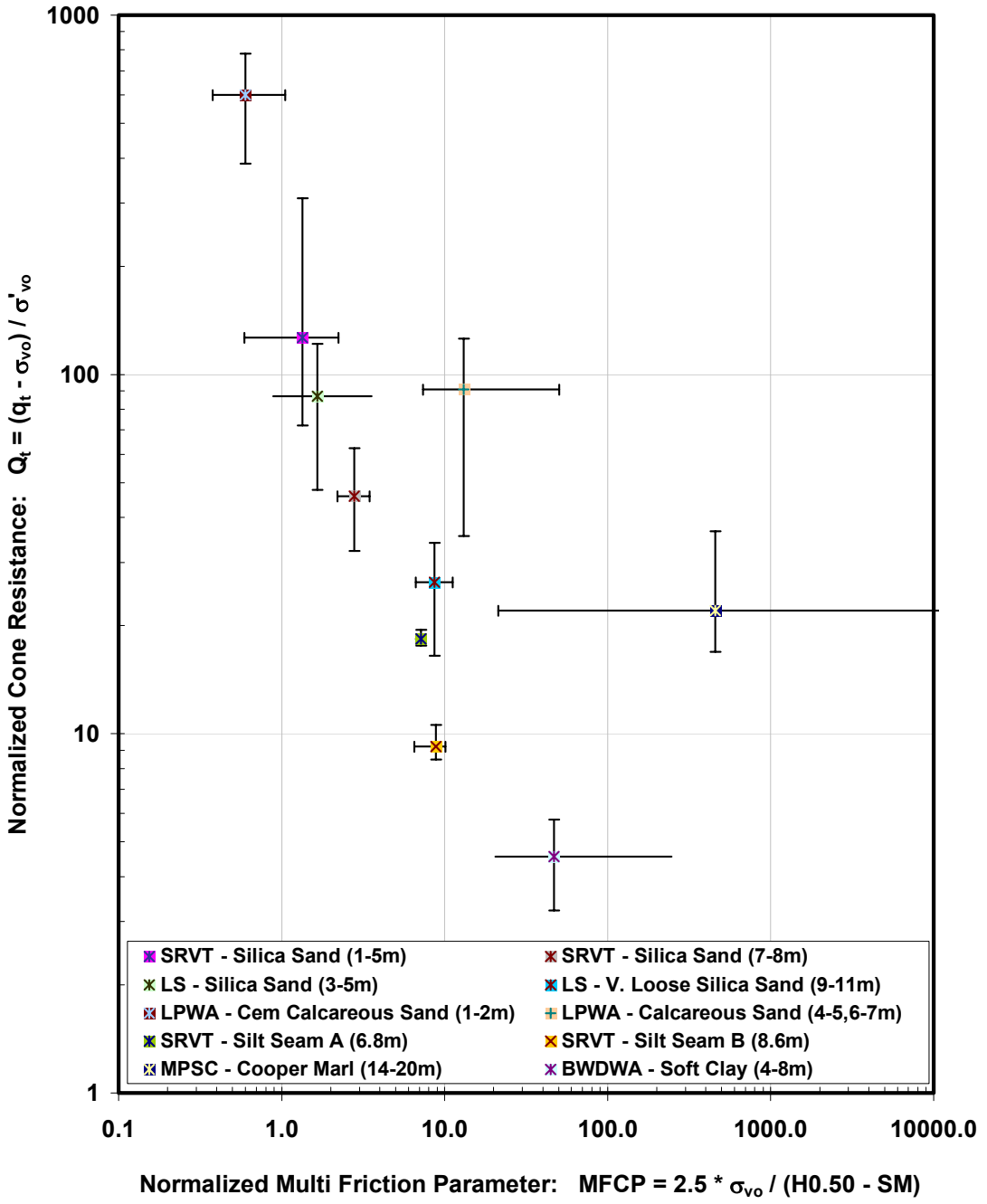

Figure 6-53 Response of the Selected Soil Layers from the Current Study As a Function of Normalized Cone Resistance (Q_t) and the Newly Developed Multi Friction Classification Parameter (*MFCP*). Error Bars Denote the Range of Values Measured for Each Selected Layer.

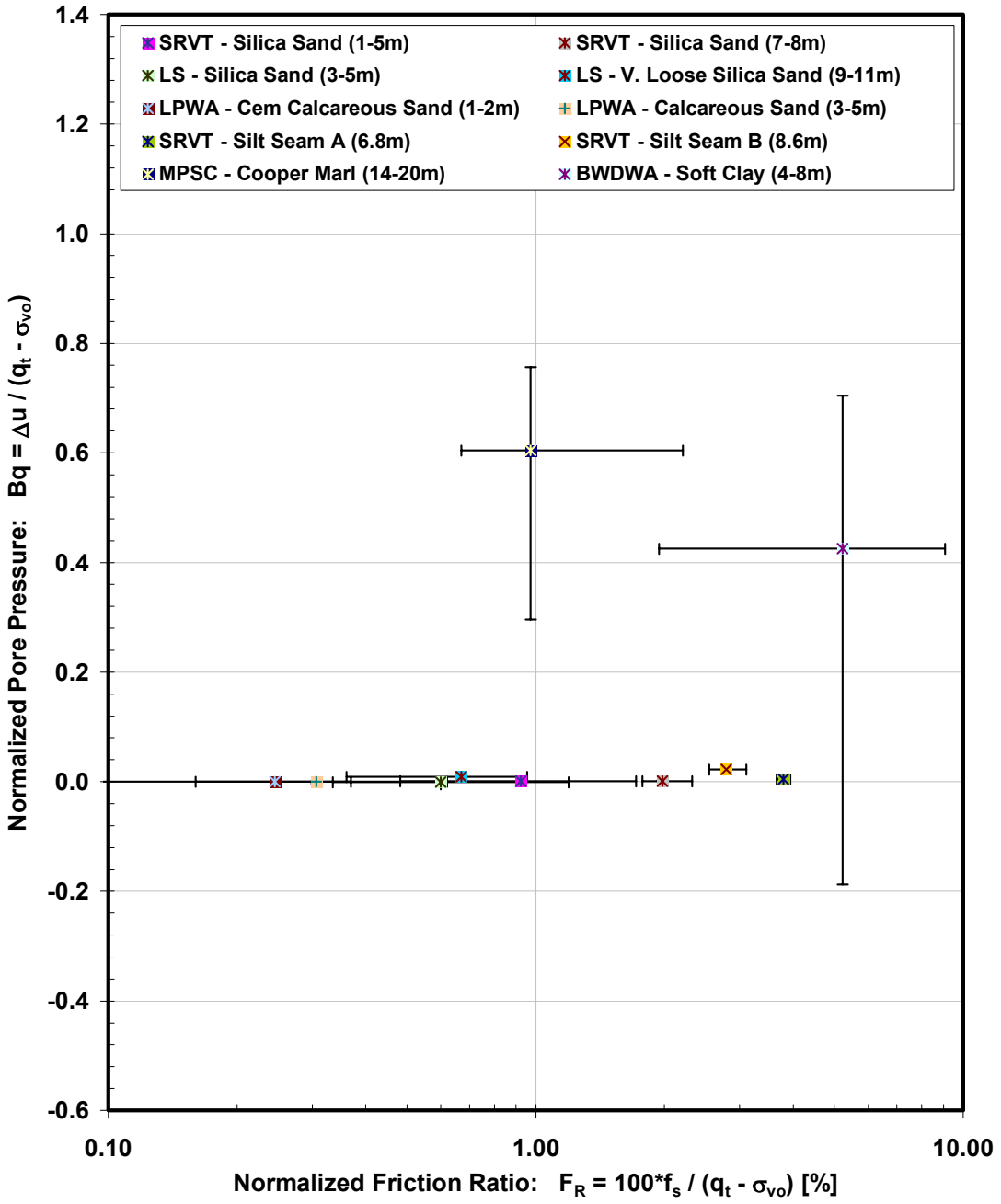

Figure 6-54. Response of the Selected Soil Layers from the Current Study As a Function of Normalized Pore Pressure (B_q) and the Newly Developed Multi Friction Classification Parameter (*MFCP*). Error Bars Denote the Range of Values Measured for Each Selected Layer.

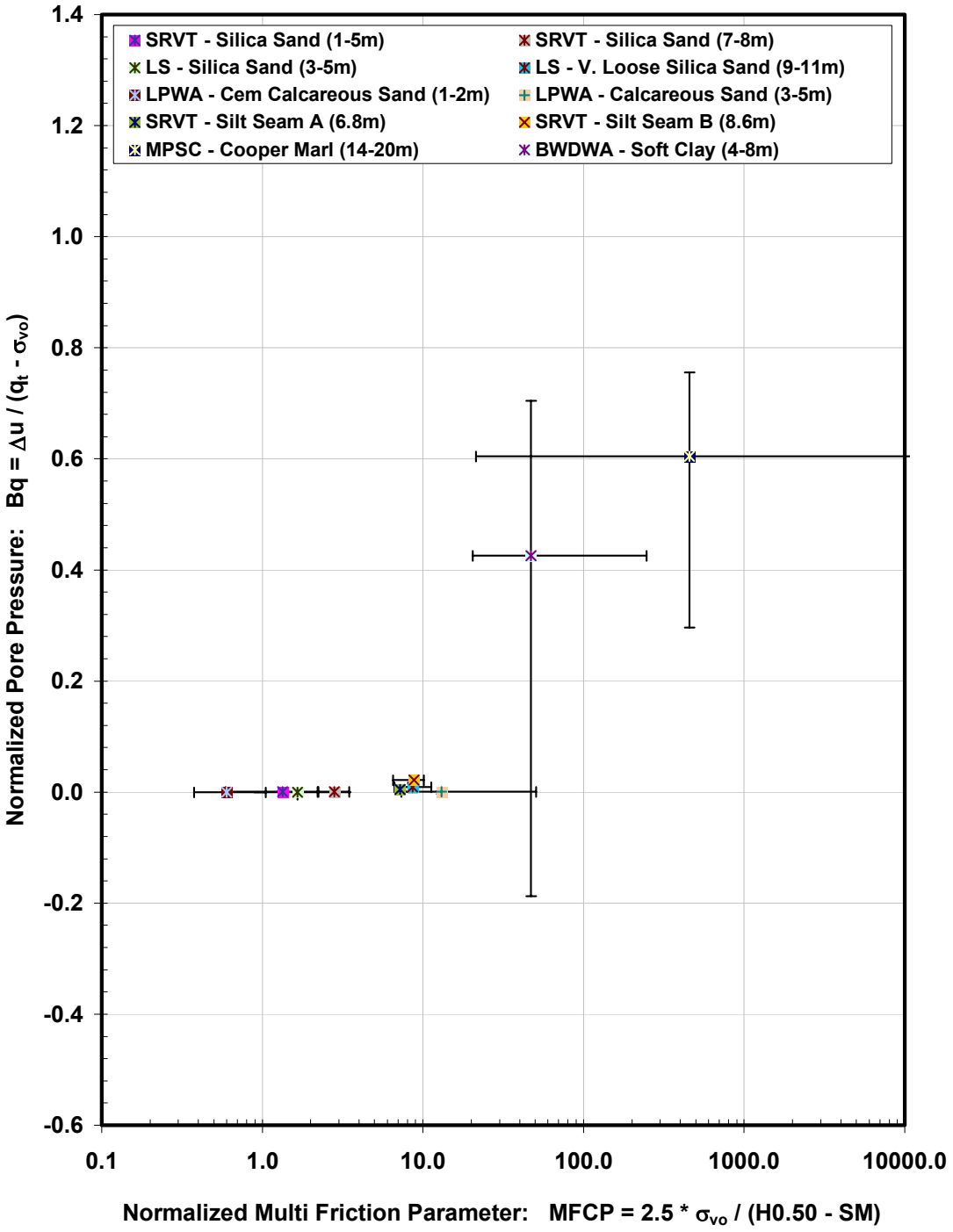

Figure 6-55. Response of the Selected Soil Layers from the Current Study As a Function of Normalized Pore Pressure (B_q) and Normalized Friction Ratio (F_R). Error Bars Denote the Range of Values Measured for Each Selected Layer.

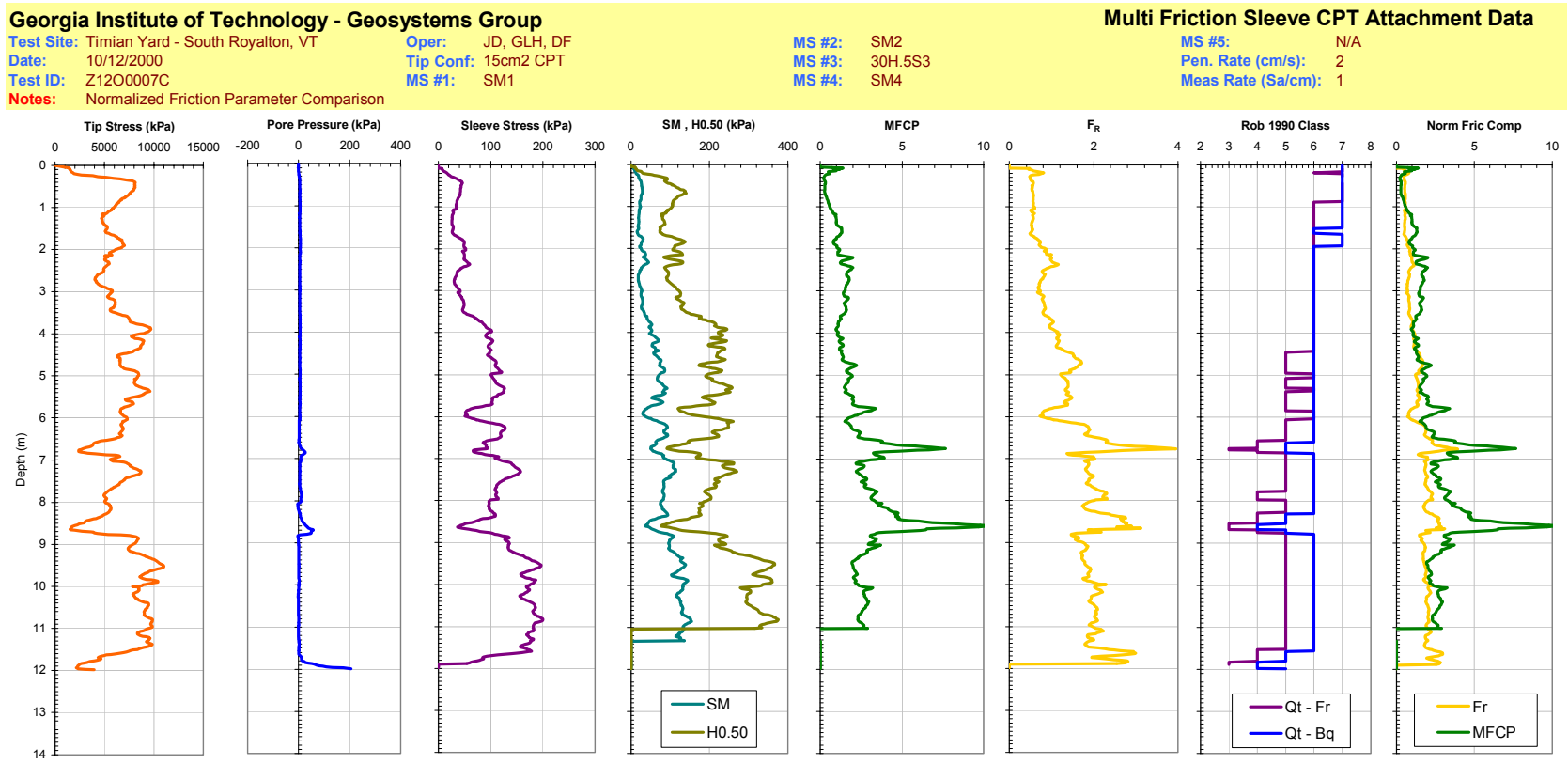

Figure 6-56. Plots Showing the Response of Select CPTU-MFA Sensors, Normalized Friction Ratio (F_R), Robertson (1990, 1991) Soil Classification, and the Newly Developed Multi Friction Classification Parameter (MFCP) for the SRVT Test Site.

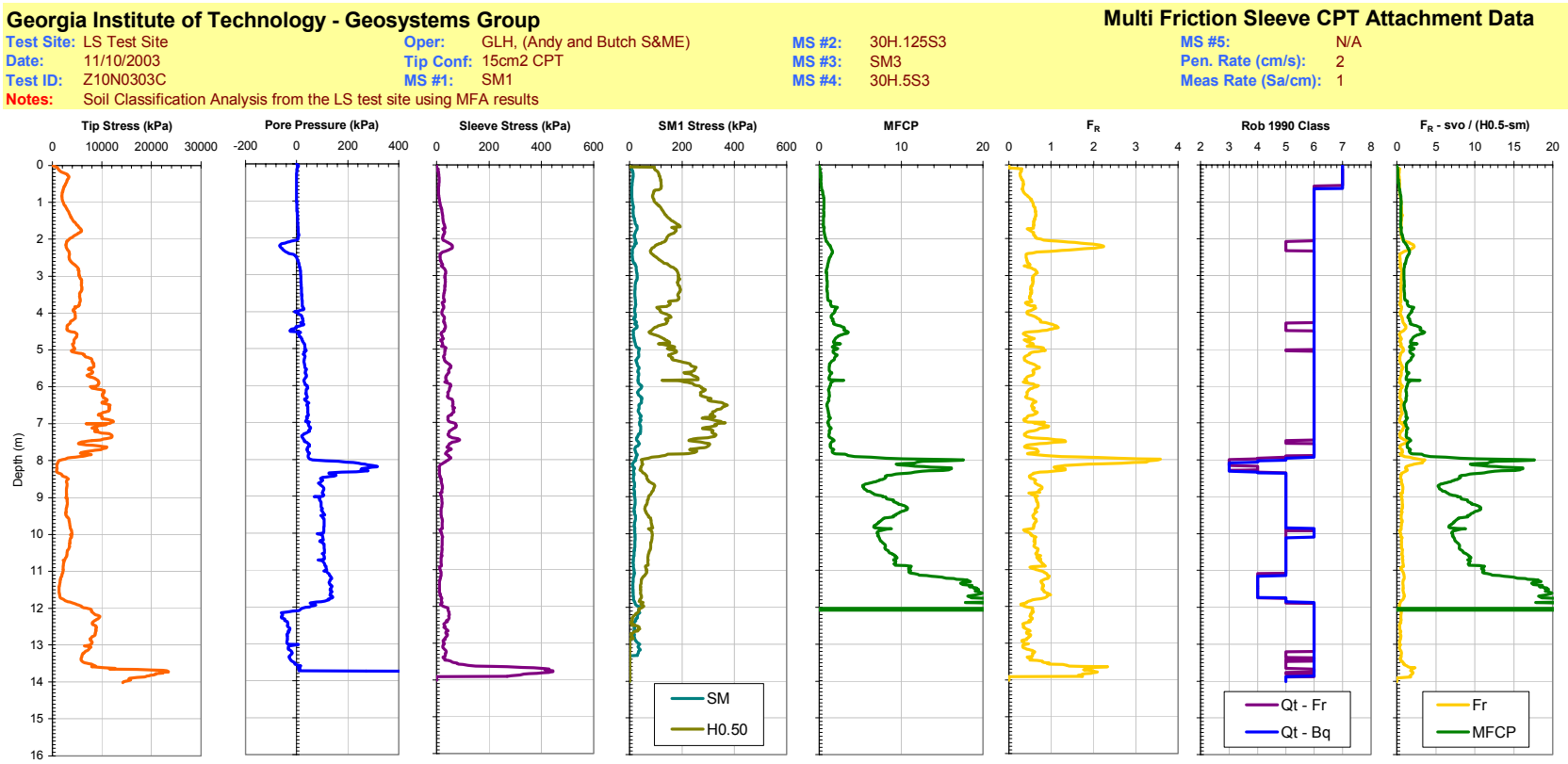

Figure 6-57. Plots Showing the Response of Select CPTU-MFA Sensors, Normalized Friction Ratio (F_R), Robertson (1990, 1991) Soil Classification, and the Newly Developed Multi Friction Classification Parameter (MFCP) for the LS Test Site.

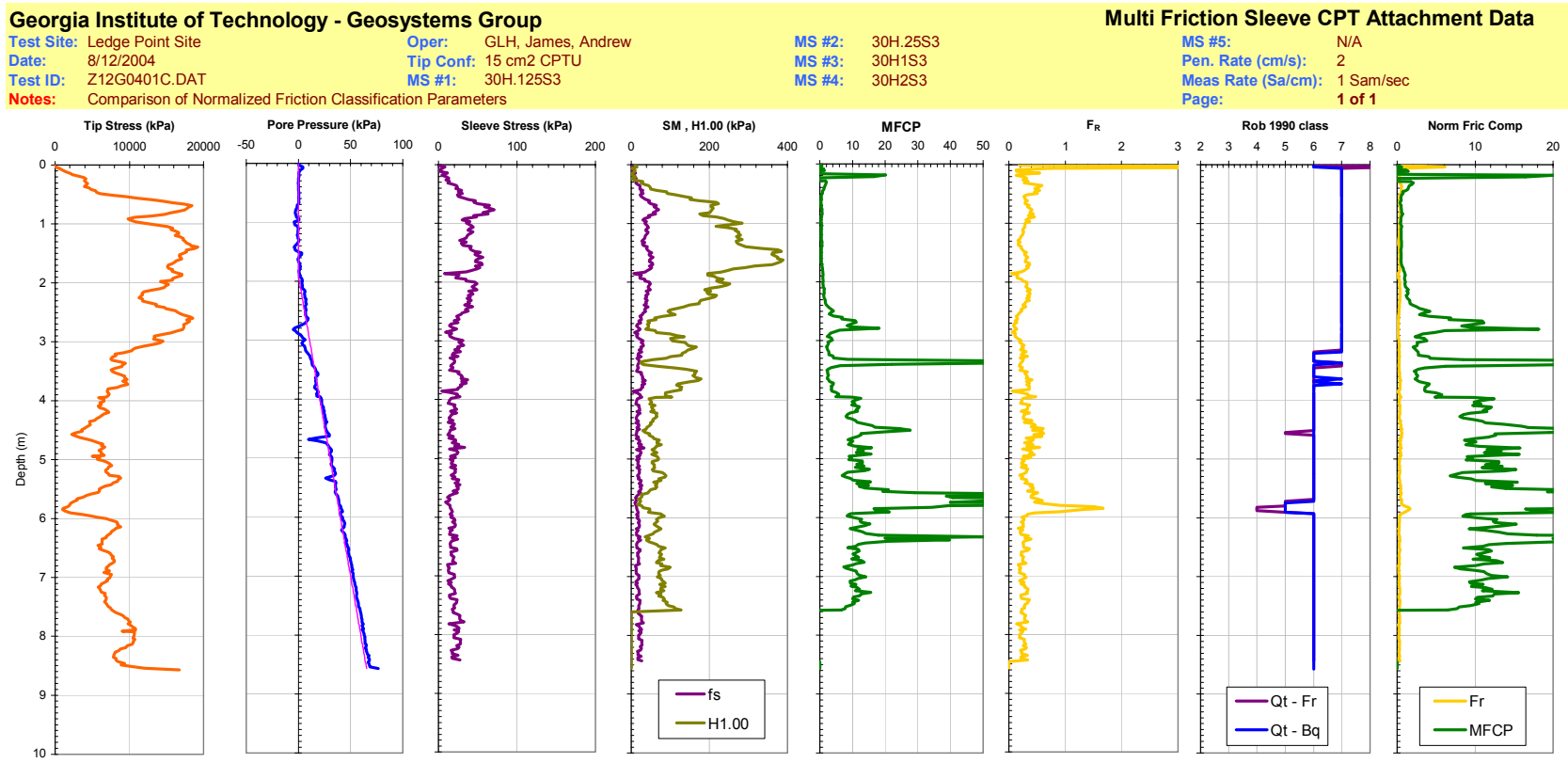

Figure 6-58. Plots Showing the Response of Select CPTU-MFA Sensors, Normalized Friction Ratio (F_R), Robertson (1990, 1991) Soil Classification, and the Newly Developed Multi Friction Classification Parameter (MFCP) for the LPWA Test Site.

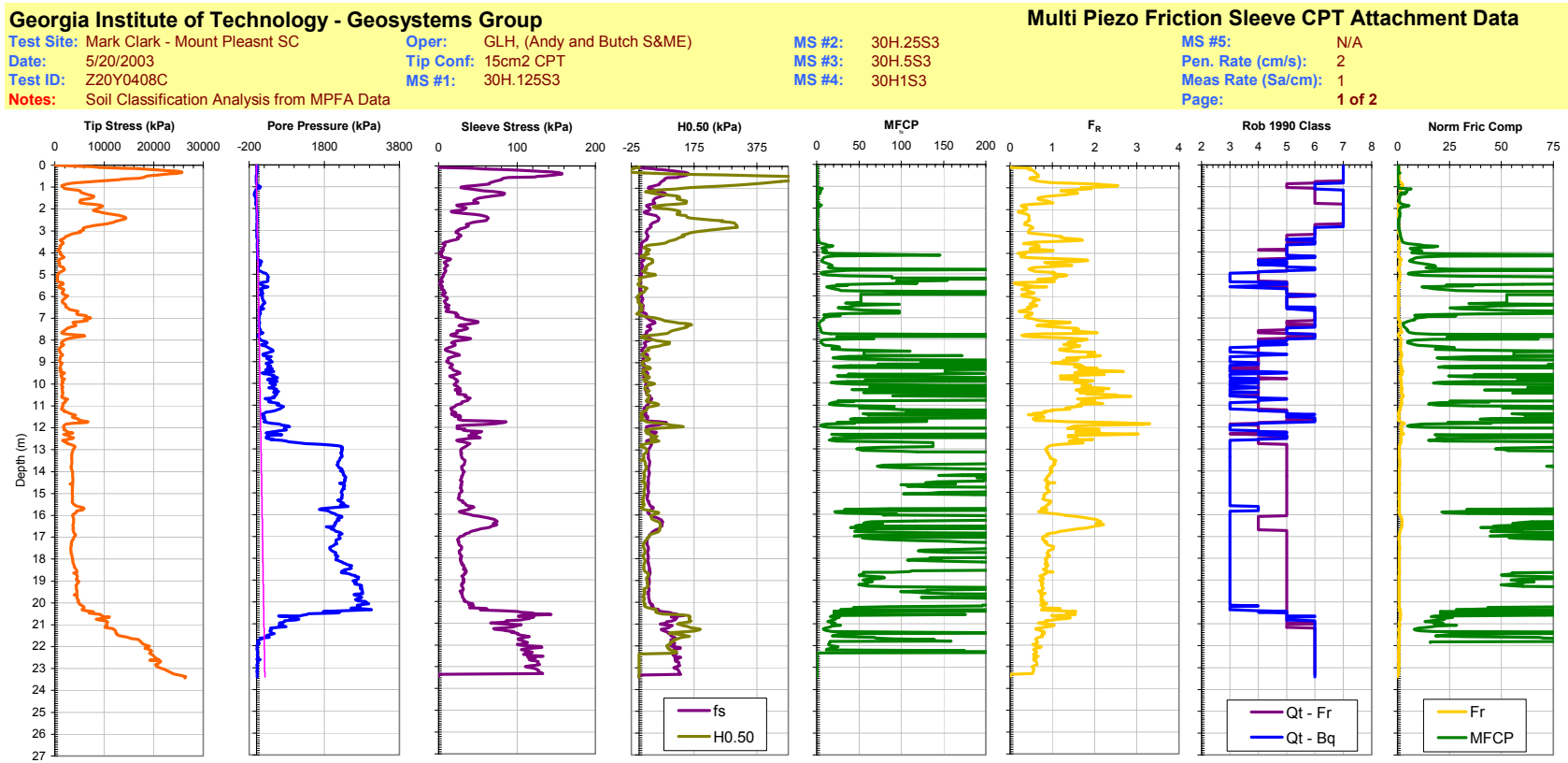

Figure 6-59. Plots Showing the Response of Select CPTU-MFA Sensors, Normalized Friction Ratio (F_R), Robertson (1990, 1991) Soil Classification, and the Newly Developed Multi Friction Classification Parameter (MFCP) for the MPSC Test Site.

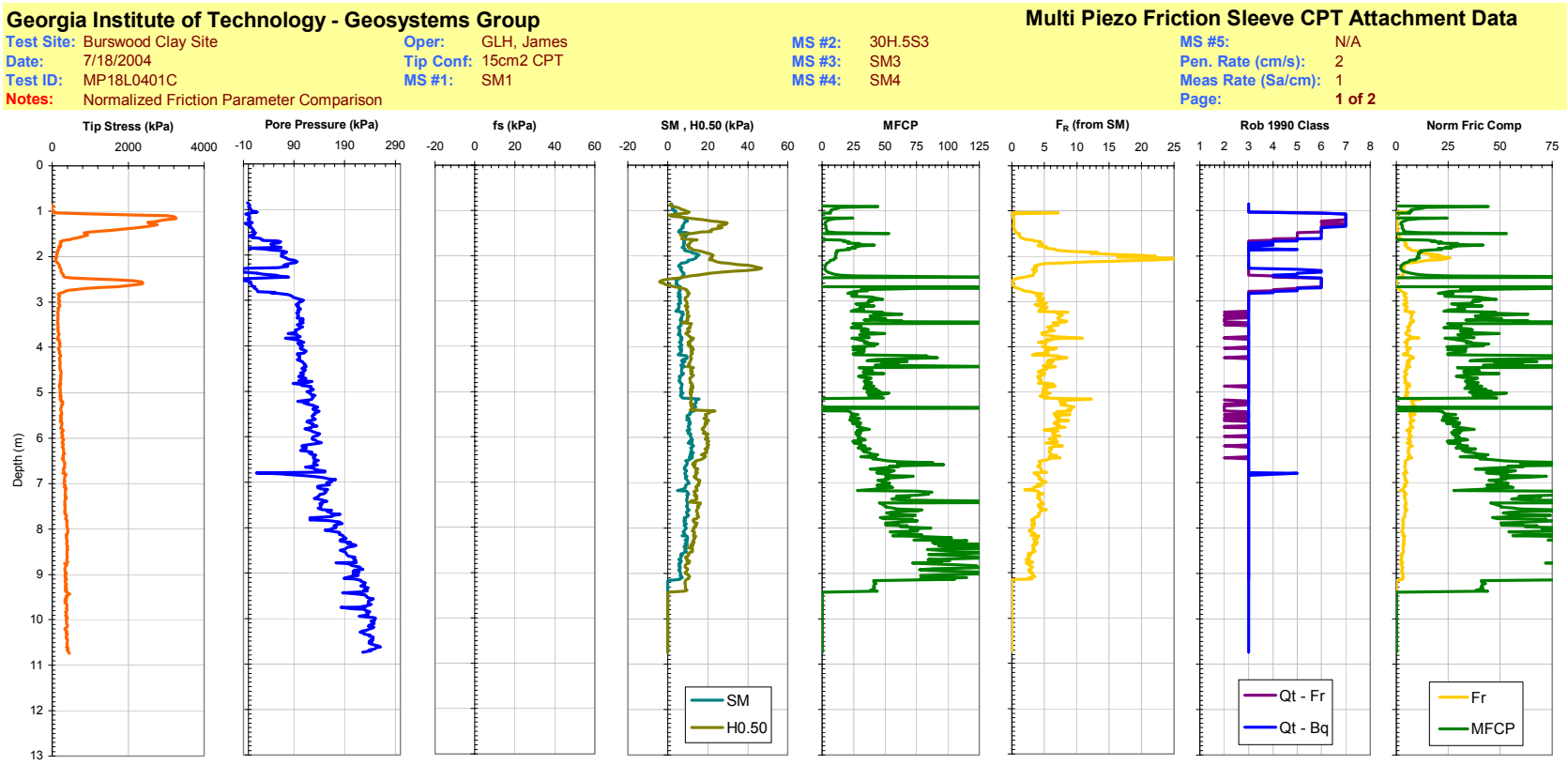

Figure 6-60. Plots Showing the Response of Select CPTU-MFA Sensors, Normalized Friction Ratio (F_R), Robertson (1990, 1991) Soil Classification, and the Newly Developed Multi Friction Classification Parameter (MFCP) for the BWDWA Test Site.

MULTI-SCALE BEHAVIOR AT GEOMATERIAL INTERFACES

VOLUME II

By

Gregory L. Hebeler

Chapter VII
Non Standard Penetration Investigations

7.1 Introduction

The use of robust in situ tests such as the cone penetration test (CPT), flat plate dilatometer test (DMT), pressuremeter test (PMT), vane shear test (VST), and geophysics have become increasing popular in geotechnical practice. While these tests provide the opportunity to determine a vast range of in situ soil characteristics, it is often desirable to obtain supplemental information by adding other sensors or including supplemental test procedures. Examples of these supplemental procedures include the addition of downhole seismic measurements or static pore pressure dissipation procedures to conventional CPT profiling. This chapter presents results using the MFA and MPFA devices for a range of non standard penetration procedures that have been investigated to study the capability of providing additional insight into soil characterization. The non standard procedures investigated in the current study include: non vertical or inclined penetration, cyclic response, variable rate penetrations, model pile load testing, and measuring response during penetrometer extraction. A number of these procedural modifications have been investigated previously in the geotechnical literature for various penetration devices. However, the aim of the current discussion is to investigate whether the unique capabilities of the MFA and MPFA devices can provide additional insight into soil characterization and foundation response through the implementation of these procedures, and whether supplemental test procedures, such as those presented, should become more readily used in conventional geotechnical practice.

7.2 Non Vertical (Angled) CPTU-MFA Penetration

7.2.1 Introduction

Most conventional geotechnical site investigations are primarily concerned with the identification and characterization of the vertical stratigraphy for a site, with the lateral stratigraphy only indirectly defined by comparing the results of laterally spaced vertical investigations. However, certain specific geotechnical conditions warrant the more complete determination of lateral soil property variability as compared to the vertical stratigraphy. Conditions where lateral variations in soil properties are more pertinent to geotechnical design include utility installation, tunneling, and the detection or monitoring of lateral contaminant flow in cases where vertical penetration could introduce problematic changes to the flow paths.

7.2.2 Review of Previous Similar Investigations

A few previous studies have been conducted into the applicability of using horizontal CPT to characterize lateral site conditions (Broere and van Tol; 1998 & 2001; van Deen et al., 1999; and Clementino et al., 1999). The studies by Broere and van Tol (1999 & 2001) compared the response of vertical and horizontal CPT results in coarse grained materials using a calibration chamber by varying the soil density and particle characteristics. Van Deen et al. (1999) used horizontal CPTs to profile the ground conditions ahead of a tunnel boring machine (TBM) during the excavation of a tunnel in the Netherlands. Clementino et al. (1999) modified a horizontal directional drilling (HDD) assembly in order to allow for "CPT like" measurements to be made with their developed Horizontal Directional Pre-Bored Cone Penetration Test (HD-PB-CPT) system.

The current investigation into non vertical penetration was performed at the SRVT Test Site (Table 6-2), and was conducted using a track CPT Rig provided by Vertek with the capability of adjusting the head thrust (or push angle) from 90° (Vertical) through 45°. It was proposed in the current study to infer directional anisotropy within the tested soil properties from observed variations in CPT and MFA sensor response, and also to possibly infer the behavior of horizontal penetration from the comparison of the vertical and angled penetrations. A similar investigation to the current study using a miniature CPT system was conducted by Wei et al., (2005).

The influence of stress state on CPT measurements is well known and documented, with many investigators (Teh and Houlsby, 1991; Salgado et al., 1997; and Yu et al. 2000) reporting that horizontal in situ stresses, as opposed to vertical stress conditions, predominantly control the response of q_t and f_s. In light of the controlling influence of σ_h on tip resistance, it follows that the rotation of penetration angle with regard to the in situ principal stresses would result in a change in sensor response for all conditions other than $K_0 = 1$. The prevailing notion is that for conditions of $K_0 > 1$ that both tip resistance and side friction decrease for angles deviating from vertical, reaching a minimum for horizontal penetrations. The opposite trend would be expected for $K_0 < 1$ conditions, where the vertical penetration response would represent the minimum condition (Wei et al., 2005). The results of Wei et al. (2005) generally coincided with the above theory, with the tip response showing good agreement for the $K_0 > 1$ case and the sleeve response showing good agreement for the $K_0 < 1$ condition. The calibration chamber studies of Broere and van Tol (1998 & 2001) showed that q_c was increased by a factor of 1.2 for horizontal as compared to vertical penetrations in medium dense sands.

They found no effect of sand type on the ratio of horizontal to vertical tip resistance (q_{th} / q_{tv}), but reported that the similar ratio for f_{sh} / f_{sv} decreased significantly with increasing particle size for sands. The HDD study of Clementino et al. (1999) showed promise for their newly introduced probe, with the measured cone resistance and sleeve friction exhibiting lower response than conventional vertical CPT response. The friction ratio calculated from the device showed good agreement with conventional CPT response and the data provided accurate classification when applied to the Robertson (1990) system. The study of van Deen et al. (1999), using horizontal CPT ahead of a TBM to detect changes in soil properties also showed promise, with the measured (q_{th} / q_{tv}) exhibiting consistent response on the order of 1.5 - 2 for peat, clay, and sand soil types. The ratio of the friction sleeve (f_{sh} / f_{sv}) response being close to unity for the soft peat, 0.6 for the clay, and 1.8 for the tested sand. The pore pressure response showed little variation between horizontal and vertical penetrations, as would be expected.

7.2.3 Comparison of Vertical to Inclined CPTU-MFA Response

As shown in Table 6-1, three soundings were conducted to investigate the influence of penetration angle on both CPTU and MFA response at the SRVT Test Site. The three configurations included the MFA sleeve mandrels outfitted with a configuration of (SM-H0.25-SM-H1.00) and a standard 15 cm^2 CPTU unit as the forward module for each sounding. Penetration angles of 90° (vertical), 67.5°, and 45° were tested in the current study, during June of 2001. Unfortunately the test conducted at a penetration angle of 67.5° contained a problem with an internal probe connection creating significant noise within the response. As such, only one successful inclined push was achieved during the current study. Figure 7-1 shows an overlay of the sensor traces from

the 90° and 45° pushes at the SRVT site. Qualitatively the response of the vertical and inclined penetrations show similar response with depth through the various stratigraphy at the site. The tip stresses show slight variations with depth, most notably at 10.5 m depth, but show very similar response on average. The u_2 response was very consistent between the two soundings with only a slight variation in the location of the silt seam nominally located at 8.5 m, as also apparent in the traces of q_t. The 45° traces of f_s, f_{a1} (SM), and f_{a2} (H0.25) all show slightly increased response over the corresponding vertical traces, with the vertical and inclined f_{a3} and f_{a4} traces exhibiting relatively consistent response.

The results of the limited data set indicate that the inclined CPTU and forward MFA sensors showed a slightly increased response over the adjacent vertical sounding as would be expected for the stress state of a shallow uncemented sand site, where typically $K_0 < 1$. As seen from the more equivalent response of the aft MFA sensors, the effect of anisotropy in the initial in situ stress state (K_0) on the variation in response as a function of penetration angle seems to decrease with increasing distance from the penetrating tip. A second vertical CPTU-MFA sounding with the same sensor configuration was performed within close proximity (5.5 m) to the soundings presented in Figure 7-1. A site plan for the area over which the inclined penetration investigations were performed is included as Figure 7-2. Figure 7-3 shows the comparison of the 45° sounding to the second similar vertical sounding, #64 from Table 6-1. Tables 7-1 and 7-2 summarize and compare the average responses of all three soundings for the two silica sand layers used in the analyses of Chapter 6: 1-5 m and 7-8m. Comparisons between the two vertical

soundings indicate the magnitude of variations that can be attributed to lateral variability at the SRVT test site.

The average responses indicate that the tip response was not largely affected by penetration angle within the analyzed layers at the SRVT site, with all variations in angled response on the order of variations observed due to lateral variability. The large variations in u_2 pore pressure response between the three soundings are indicative of small changes in the thickness and location of fine grained lenses within the stratigraphy, with the current study into unsaturated sand not providing a good means to gauge the affect of penetration angle on pore pressure response. The CPTU f_s response shows significant variation between the inclined and vertical penetrations, with the 45° penetrations showing an increase for both sand layers ranging from 13 to 56%. The variations in the smooth attachment sleeve in position f_{a1} shows only slight variation (~10%) in response for the 1-5m layer, with a larger increase (~21-24%) noted for the 7-8m sand layer. The H0.25 textured sleeve in position f_{a2}, exhibited a consistent increase response for the inclined penetration ranging from 21 to 34% over both highlighted layers, as compared to the lateral variability between the vertical soundings showing a maximum deviation of 11%. The response of the sleeves in positions f_{a3} (SM) and f_{a4} (H1.00) exhibit only slight variation between all three soundings indicating that the influence of both sand density and state of stress may diminish with distance from the tip. This finding fits into the framework of critical state soil mechanics, as the large deformations occurring before the soil strata interact with the f_{a3} and f_{a4} sensors should allow for the stabilization of the shear zone and surrounding stress conditions. The findings presented herein are based on limited tests, and future testing is planned to expand the data set and

to hopefully better understand the mechanisms controlling penetrations at push angles ranging from vertical to horizontal.

7.3 Cyclic CPTU-MPFA Investigations

7.3.1 Introduction

Waves, wind, earthquakes, industrial equipment, construction activities, and even large crowds can apply various levels of cyclic loading to foundation elements. This cyclic loading may lead to generation of pore pressures, degradation of strength, and settlement. The significance of cyclic loading effects is a function of amplitude, frequency, number, and other load cycle characteristics. Typically the assessment of cyclic degradation is addressed through laboratory test studies (e.g., Andersen et al., 1980; Jewell & Randolph, 1988; Airey et al., 1992), although, some recent offshore site investigations have included a component of cyclic penetration testing (Hefer & Neubecker, 1999; Randolph, 2004; and Peuchen et al., 2005). Evaluation of cyclic degradation through in situ testing may be more appropriate for soil types that may incur significant disturbance during sampling, such as very soft clays, silts, sands, or structured materials.

The addition of cycling into an in situ testing program adds little cost, and typically requires no design modifications to most common in-situ penetration devices and push equipment. However, the added data obtained relating to large strain cyclic degradation can be effectively used to assess issues such as soil sensitivity and post installation pile shaft friction. Most previous cyclic penetration studies have been conducted for offshore applications and were focused solely on tip resistance, including

cone, ball, and T-bar geometries. The current cyclic soundings were performed using a conventional 15 cm^2 CPTU unit configured with the MPFA. The 4 additional friction and 5 additional pore pressure sensors along the shaft of the MPFA device provide a detailed representation of cyclic shaft response. The current study represents an investigation into the use of such sensors to evaluate the rate and magnitude of cyclic interface friction degradation. Data from two onshore sites in Western Australia, the Burswood soft clay site and the Ledge Point calcareous sand site (Table 6-2), are used to investigate the viability of the testing methods and device performance.

7.3.2 Cyclic CPTU-MPFA Results from the Burswood Soft Clay Site

7.3.2.1 Introduction

Two different magnitude cyclic investigations were performed at the Burswood test site. Three large magnitude cyclic investigations were performed, comprised of ten full length (1 m) 2-way cycles carried out at 20 mm/s in soundings MPFA_10-12 (Table 6-1). The cyclic investigations of sounding MPFA_11 and MPFA_12 were conducted between tip depths of 5.8 and 6.8 m, while the cyclic investigation of sounding MPFA_10 was conducted between depths of 7.7 and 8.7 m. A secondary phase of cyclic investigations was performed during the MPFA load test program. This phase consisted of two small amplitude cyclic tests, each comprised of 200 short (5 mm) 2-way cycles performed between tip depths from 4.995 to 5.000 m and 7.495 to 7.500 m, respectively during load test hole #2, sounding MPFA_26 (Table 6-1). The cumulative strain of the shorter magnitude cycles corresponds with one full length 2-way large displacement cycle, allowing for comparisons of cyclic degradation as a function of cyclic amplitude.

7.3.2.2 Large Amplitude Cyclic Response

For the large amplitude cyclic investigations performed during soundings MPFA_11 and MPFA_12, dissipation tests were performed for approximately 2 hours before and after cycling to investigate the effect of large scale cycling on the flow regime around the MPFA device. The first dissipations were performed after the initial virgin penetration to the bottom depth of each cyclic investigation, before the initial upward half cycle. The second dissipation test was conducted at the same depth (6.8 m) upon completion of cycling. The detailed results and analyses of these dissipation tests are presented in Chapter 8, however, they are noted here as the effective stress changes occurring over the course of the dissipation time lags does affect the observed monotonic and cyclic responses. Figures 7-4 to 7-6 show the full soundings during which large amplitude cyclic investigations were performed. Detailed views of the cyclic responses are shown in the corresponding Figures, 7-7 to 7-9. The q_t and u_2 measurements show hysteresis loops that are affected by the relative position of the sensors within the cycle, as a result of the large influence zone around the tip. However, the multi sleeve and piezo sensors located farther up the shaft (> 0.67 m behind the tip) measure the behavior over a smaller influence zone, with large variations within each cycle representative of variations in the soil stratigraphy with depth, and not due to the cyclic excitation.

To quantify the effect of cycling on the various sensor results, the average value for each full stroke (or half cycle) is shown as a function of cycle number in Figures 7-10 to 7-12 for each of the BWDWA large amplitude cyclic investigations. This framework is comparable to that discussed in Matlock & Foo (1980), but it is noted that the cumulative strain is as important as the number of stress reversals (cycles) when quantifying cyclic

degradation (Poulos, 1981). The large amplitude cycles (1 m in length) are relatively large and create a stable cyclic response, as compared to the smaller amplitude cycles (5 mm) which are not sufficient to create a stable response within each individual cycle. To better quantify the cyclic degradation as a function of cycling, Tables 7-3 to 7-5 present the average values per cycle and also the normalized degradation in response as compared to the virgin penetration response.

Average degradation of q_t with large scale cycling is observed in part (a) of Figures 7-10 to 7-12 for the BWDWA tests. The average large amplitude tip response (q_t) exhibits similar behavior for each of the three soundings, with the results corresponding to MPFA_10 showing the expected increases in response due to the increased depth of the investigation. The q_t resistance for all tests decreases for each successive cycle, with a majority of the decrease in average response due to the large changes present in the initial portions of each downward cycle, which exhibit negligible resistance. The initial extraction resistance is relatively high for the MPFA_11 and MPFA_12 investigations due to the aforementioned dissipation tests, with subsequent cycles showing higher resistance during insertion as compared to extraction. The cyclic degradation of tip stress after ten full 2-way 1-m cycles ranged from 60 to 80% of the virgin response. These values correlate well with the known sensitivity of the Burswood clay which ranges between 3 and 4, as observed in field vane tests (Chung and Randolph, 2004). The negative q_t responses observed for the upward cycles are representative of suction created during extraction, with negative q_t values being physically limited by pore fluid cavitation, effectively limiting negative tip response to values of $p_{atm} + u$, where p_{atm} =

atmospheric pressure and u = the ambient pore pressure. Extraction response is discussed in greater detail for all sensors in Section 7.6.

The cyclic u_2 pore pressure responses, part (b) of Figures 7-10 to 7-12, mirror the observed cyclic cone tip response for downward penetrations, with only minor observed variations in extraction resistance as a function of cycling. It is believed that the downward u_2 penetration resistance mirrors the q_t response, since Δu_2 is more strongly influenced by the reduction in octahedral pore pressures caused by degradations in soil strength than the increase in Δu_2 caused by shear induced pore pressures from soil destructuring, as seen for model pile behavior by Lehane (1992). As observed in the cyclic q_t response, the average u_2 cyclic responses are also heavily influenced by the large reductions in pore pressure observed toward the top of each cycle, where conditions of minimal soil resistance surrounding the probe are present due to extraction. The low hydraulic conductivity of the Burswood clay (~10^{-9} m/s; Levy et al., 2002), and the high strain rate (20 mm/s), create conditions corresponding to undrained response during both penetration and cycling as determined by previous investigations into this material by Chung and Randolph (2004) and Randolph and Hope (2004).

The cyclic degradation of shaft friction and pore pressure can be assessed through the response of the MPFA sensors, in parts (c - L) of Figures 7-10 to 7-12. The reader is reminded that each MPFA sensor investigates a different range of depths during the cyclic investigations, with some of the observed differences in behavior attributed to both vertical soil variability and distance behind the tip. Additionally, all MPFA sensors behind the u_{a1} sensor are located more than 1 m behind the tip (Figure 5-36), and as such investigate steady state cycling of soils continuously in contact with the penetrometer

during the 1-m large amplitude cycles. Of further note, the sleeves in positions f_{a2} during each of the investigations were textured sleeves H2.00, H1.50, and H0.75, respectively for soundings MPFA_10 to MPFA_12. The presence of the dissipation tests after the virgin downward penetration in soundings MPFA_11 and MPFA_12, and the subsequent increases in effective stress state, clearly effect the initial post dissipation responses of shaft friction, as the 2nd downward cycle for these tests shows only a minimal decrease or an increase in response after one cycle. Sounding MPFA_10, with no dissipation time lag, exhibits the expected decreasing sleeve friction response with increased cycling from the onset of cycling.

The trends of cyclic shaft response are similar across the MPFA sleeve positions and test conditions, with the results from sounding MPFA_10 providing the clearest indication of cyclic degradation due to the absence of a pre-cycling dissipation test. The cyclic shaft friction degradation after one full large amplitude cycle was observed to be on the order of 30%, with only minor further reductions in shaft resistance for continued cycling past three full cycles, resulting in total reductions on the order of 50% of the virgin response after ten full cycles. During the test series, the tensile and compressive shaft frictions shows similar levels of degradation with increased cycling, although some variability between the positions within the stratigraphy is observed.

The pore pressure response along the shaft of the penetrometer does not experience significant variations due to cycling. There is an initial drop in pore pressures due to the 2 hour dissipation in soundings MPFA_11&12, and variable rates of dissipation response with continued cycling, and time, as a function of the encountered soil stratigraphies. The multi piezo sensors coupled with smooth friction sleeves

(positions f_{a1}, f_{a3}, and f_{a4}) show very little influence of cycling and no apparent variation between penetration and extraction. However, the multi piezo sensors coupled with the textured sleeves (f_{a2}) show an increase in extraction response as compared to the penetration response, believed to be the result of the influence zone created by the increased annular area of the textural asperities, as the multi piezo sensors are located adjacent to the uphole end of each multi sleeve sensor. This mechanism is further supported by the divergence between insertion and extraction u_{a2} pore pressures increasing with texture height: H2.00 (MPFA_10), H1.50 (MPFA_11), and H0.75 (MPFA_12).

7.3.2.3 Small Amplitude Cyclic Response

Small amplitude (5 mm) 2-way cycles were also performed during CPTU-MPFA investigations at the BWDWA site. These investigations were performed as part of the load test program in sounding MPFA_26 at nominal tip depths of 5.0 and 7.5 m. Unfortunately the sampling rate of the CPTU-MPFA data acquisition system was not able to sample fast enough to synchronize with the small amplitude cycling occurring at a rate at 20 mm/s. As a result, some amount of digital sampling distortion is present in the data, i.e. the data points do not correspond to the same position within each cycle causing the signature burst type response characteristic of under sampled signals. As such, the under sampling results in the data not being correspondent to consistent depths within each small amplitude cycle, and consequently, the data is presented as a function of time. However, the sampling rate was sufficient to quantitatively capture the effects of small amplitude cycling over ranges of cyclic excitation. Figure 7-13 and 7-14 present the

response of the CPTU-MPFA sensors for the two small amplitude cyclic investigations, with the full response of sounding MPFA_26 presented in Figures 7-15.

A summary of the response of the small amplitude cyclic tests are provided in Tables 7-6 and 7-7, respectively for the 5 m and 7.5 m investigations. Due to the aforementioned under sampling of the data, it is not possible to separate out the response of the downward and upward cycles, but rather the data is summarized as the degradation in response for bracketed ranges of cycles. Figures 7-16 and 7-17 present the tensile and contractive cyclic responses over a range of small amplitude cycles for each of the CPTU-MPFA sensors. The small amplitude cyclic q_t response for the two investigations experiences a large drop off from the monotonic penetration response as expected, with slower cyclic degradation continuing with increased cyclic straining. The ratio between the tensile and compression q_t behaviors is similar to the average large amplitude cyclic responses, and is nominally on the order of 50%. The degradation of q_t with small amplitude straining was observed to be on the order of 30% of the initial response after a cumulative strain of +/- 1 m. The large amplitude cyclic responses showed degradation of approximately 35% after an equivalent cumulative strain (i.e. one full 2-way 1 m cycle).

The u_2 pore pressure responses are seen to decrease with small amplitude cycling, on the same order as standard dissipation behavior in the BWDWA soft clay. The pore pressures do not seem to be largely affected by the small amplitude cycling, other than the constant separation of the insertion and extraction responses on the order of 20 kPa in both cases. In future cyclic tests it would be ideal to allow for full pore pressure dissipation to occur before performing a cyclic investigation, as the effects of cycling on both the tip and shaft pore pressures resultant from the cyclic excitation in the current

study are masked by the large changes in pore pressure resultant from the dissipation of excess penetration pore pressures. The shaft friction response does not experience any significant degradation due to cycling, with the insertion and extraction responses showing almost equivalent but opposite signed magnitudes in most cases. The pore pressures along the shaft exhibit similar trends to the u_2 pore pressure response, with the divergence between the insertion and extraction responses decreasing to a unique response with increased distance behind the tip. It will be beneficial in future investigations to observe the variation in cyclic shaft response of the CPTU f_s sensor to see if the cyclic response is dependent on the magnitude of pre-cycling penetration strain, i.e. the relative distance from the tip (h/r). Unfortunately, this was not possible in the current investigation due to the inoperability of the f_s sensor in the current investigations, and the location of all of the MPFA friction sensors at large h/r values (> 25) known to exhibit relatively stable behavior (Lehane, 1992).

7.3.3 Cyclic CPTU-MPFA Results from the Ledge Point Calcareous Sand Site

7.3.3.1 Introduction

Only large amplitude cyclic investigations were performed at the Ledge Point test site. Two cyclic investigations were performed, comprised of ten full length (1 m) 2-way cycles carried out at 20 mm/s in soundings MPFA_23 and MPFA_24 (Table 6-1). It is important to note the use of textured sleeves in these soundings (SM-H1.00- H1.00-H1.00 for MPFA_23 and SM-H.125-H.125-H.125 for MPFA_24), especially for the heavily textured sensor responses may not directly correlate to the shaft response of typical geomaterials such as steel piles. The cyclic investigations were conducted

between tip depths of 6.7 and 7.7 m. The Ledge Point site consists of calcareous beach sand overlying limestone bedrock, with the sand strata ranging in extent from 10 to 14 m in thickness. As the soil is sandy in composition the penetration and cyclic investigations occur under predominantly drained conditions, and no pore pressure dissipation tests were performed in any of the soundings.

7.3.3.2 Large Amplitude Cyclic Response

Figures 7-18 and 7-19 show the full response of the CPTU-MPFA sensors for the soundings containing the large amplitude cyclic investigations at the LPWA calcareous sand test site. Figures 7-20 and 7-21 present detailed views of the large amplitude cyclic response from the LPWA test site. Figures 7-22 and 7-23 and Tables 7-8 and 7-9 present the average cyclic response of each full stroke (half cycle) for each sensor over the ten (1-m) 2-way cycles. Part (a) of Figures 7-22 and 7-23 show the average downward tip response increasing from the 4th cycle onward. This response is not indicative of an increase in soil strength, but rather denotes an increase in soil density caused by collapse of the soil during extraction and the subsequent compression of the infilling soil at the bottom of each cycle stroke. This effect is quantified by the q_t stress at the bottom of penetration increasing from virgin values on the order of 10 MPa to values approximating 23 MPa after 10 full cycles. The tip behavior shows negligible resistance for the upper half of each downward stroke, and shows no resistance during the upward strokes.

The u_2 pore pressure shows a slight divergence between upward and downward cycling, with slightly positive excess pore pressures during downward penetration and slightly negative excess pore pressures during upward penetration. The pore pressures along the shaft parts (h-L) of Figures 7-22 and 7-23, measured by the MPFA sensors also

show minimal change with large scale cycling. Cyclic sleeve friction behavior is shown in parts (c-f) of Figures 7-22 and 7-23. The friction response of both textured sleeve types show large degradation due to cycling. The average reduction in shaft friction after the first full cycle was 60% for the slightly textured H0.125 sleeve and 80% for the heavily textured H1.00 sleeve. Further degradation to only 13% of the initial resistance (or 7.5 times lower) after three 2-way cycles is observed for the lightly textured sleeve. The degradation of the heavily textured sleeve is even larger, with the response after three full cycles only 6% of the virgin resistance, a reduction of more than 16 times the initial response. Continued cycling past three full 1-m amplitude cycles resulted in only minimal additional degradation of shaft friction. As discussed for the tests at Burswood, the MPFA can provide an indication of the ratio of tension to compression (T/C) capacity. The shaft friction (T/C) remains relatively constant for the lightly textured sleeve at approximately 50%. Whereas, the initial (T/C) ratio for the heavily textured sleeves is only approximately 15%, remaining approximately constant for the upper textured sleeve response and increasing to a value approximating 50% for the forward sleeve due to similar densification mechanisms observed for the "artificial" increase in q_t resistance for later cycles.

Low pile shaft friction in calcareous soils is well known, and typically attributed to grain crushing and contraction at the interface during installation and loading. Shaft friction evaluated from model tests and conductor pullout tests at the North Rankin A platform off the Northwest shelf, Australia, reduced from monotonically installed values of approximately 40 kPa to cyclically installed (driven) values of 5 to 20 kPa (Abbs et al., 1988; Poulos et al., 1988). Interface friction at large displacements was seen to reduce by

approximately an additional 50% (Poulos et al., 1988). For conductor load tests offshore South Africa, Ebelhar et al. (1988) show CPT sleeve friction values of 20 to 40 kPa, and conductor pullout resistances of 10 to 20 kPa.

Field results at North Rankin A and offshore South Africa are in general agreement with the MPFA observations at Ledge Point. As such, cyclic data collected during site characterization can provide insight into sands with a high potential for cyclic contraction. However, the rate of degradation for cyclic MPFA tests should be much higher than that of large diameters piles, since the rate of degradation will be influenced by the normal stiffness condition, and thus pile diameter (k_{CNS}=4G/D; see, Boulon & Fouray, 1986; Lehane et al., 1993; White, 2005). Additionally, the minimum achievable shaft friction is probably not solely a function of active earth pressure, but also arching behavior around the pile or penetrometer (Randolph, 2003). These effects, among others, need to be quantified in a theoretical framework before cyclic MPFA results can be applied quantitatively to large diameter pile design.

7.3.4 Summary of Cyclic CPTU-MPFA Results

Results of cyclic piezocone tests with high quality sleeve friction readings using the MPFA have illustrated the significance of cyclic interface degradation at soft clay and calcareous sand sites. The addition of cyclic investigations to conventional penetration testing methods requires little modification to currently available in situ testing equipment, with cyclic testing previously shown to be successful in even the harsh testing environments found offshore (e.g., Peuchen et al., 2005). Cyclic MPFA or MFA measurements show promise as a method for identifying soils with the potential for significant interface contraction and a resulting loss of friction during cyclic loading. The

main design applications are related to pile design, drivability studies, and determining the effects of various installation sequences on soil degradation. Currently the assessment of cyclic MPFA and MFA soundings are predominantly qualitative, but results agree with frameworks for assessing cyclic loading of piles, as outlined by Poulos (1981) and Matlock & Foo (1980).

The large amplitude (1 m) cycles used in the current study seem excessive for friction degradation studies, and increase the potential for gapping, especially for coarse grained soils. However, these large amplitude cycles may provide an opportunity to determine the relative magnitude of degradation expected as a result of pile driving or other large strain installation techniques. The short amplitude cyclic tests also seem to be outside of the ideal cyclic amplitude for cyclic degradation field studies, as the small displacement lengths did not induce shaft friction degradation over the values observed in standard penetration, for the tested soft clay material. Additionally, it would be beneficial to conduct cyclic investigations in fully equalized pore pressure conditions to be able to separate cyclic induced pore pressure response from that of static dissipation. The small amplitude cycles are most likely outside the range of amplitudes that will create a stable cyclic shearing regime as described by Poulos (1981) and Poulos et al. (1988), however they may be well suited to simulate cyclic movements experienced by in-place structures. Cycling over a length of 2 to 3 diameters (approximately 1 friction sleeve length) may provide conditions that result in a relatively constant large displacement range, while decreasing the testing time and gapping concerns. The MPFA device is advantageous for cyclic investigations because it contains sensors along a range of distances behind the tip allowing not only for h/r effects to be investigated, but for a wide range of cyclic

amplitudes from 0 to 1 m to be investigated without the influence of gapping on all sensors. The optimum cyclic investigation procedures to use for various soil conditions and design considerations are not well known to date. At this stage in the implementation of cyclic penetration investigations it is prudent to consider a range of test conditions specific to the goal of each investigation, as differences in cyclic response as a function of test procedures may be observed for various stratigraphies, warranting additional investigations to optimize cyclic penetration procedures and interpretation on a site by site basis.

7.4 Variable Penetration Rate Investigations

7.4.1 Introduction

Rate effects in fine grained soils are well known to affect a wide variety of soil responses as summarized in detail by Leroueil and Hight (2003). The typical rate dependent trend in soil behavior is dependent on two main phenomena related to the fluid phase of soils: viscous effects and consolidation effects. Viscous effects create an increase in soil strength at high strain rates that diminishes with decreasing strain rate down to a critical rate, below which viscous effects no longer significantly influence soil behavior (Craig, 1985). Consolidation effects are well known to affect soil behavior as a function of strain rate, and also increase soil strength and response across a range of properties controlled by soil density and stiffness through reductions in the volumetric fluid phase. The critical rate at which consolidation begins to affect soil response is the transition from undrained to partially drained behavior and effects extend through the transition condition until fully drained conditions are reached.

Specific effects of strain rate on penetration investigations are discussed in detail by House et al. (2001a and 2001b). They note the influence of strain rate on behavior in fine and intermediate soils (clay, silt, and peat), and propose variable rate test procedures in order to both define the point at which consolidation begins to influence measured response, and to quantify the viscous effects for the particular soil being tested. House et al. (2001a) also propose that the coefficient of consolidation (c_v) can be determined by comparing the change in response as a function of penetration rate to a known backbone curve behavior. Finnie and Randolph (1994) demonstrated that the limits for drained and undrained conditions in most soils correspond to non-dimensional velocities ($V = vd/c_v$) of approximately 0.01 and 30 in their analysis on shallow circular foundations, where v = velocity or penetration rate and d = diameter of the foundation or probe.

7.4.2 Results of the Current Variable Rate CPTU-MFA Investigation

One CPTU-MFA sounding was conducted at the BWDWA soft clay site during the current investigation which included a variable rate investigation between tip depths of 6.0 to 7.0 m. The MFA was configured with four textured (H0.25-H0.50-H1.00-H2.00) sleeves in order to investigate rate effects as a function of sleeve texture, in addition to the observation of the conventional q_t, f_s, and u_2 CPTU responses. The procedure of the variable rate investigation is listed in Table 7-10 detailing the penetration rates and depth ranges used in the investigation, ranging from the conventional rate of 20 mm/s to 0.04 mm/s. Figure 7-24 shows the response of the CPTU-MFA sensors over the full sounding, with Figure 7-25 and Table 7-11 detailing the response from the variable rate investigation.

Figures 7-26 presents the absolute variations of CPTU tip and pore pressure response as a function of non-dimensional velocity (V), with Figure 7-27 presenting the parallel sleeve responses. Figure 7-28 presents the normalized response for all CPTU-MFA sensors as a function of non-dimensional velocity. While the conventional CPTU q_t and f_s responses exhibit the typical concave upward behavior as a function of penetration rate, the observed variations in the MFA sleeve sensors seem to only be effected by consolidation and not viscous effects, as the MFA sleeve behaviors are approximately constant from $V \approx 6000$ to 200 and increase only with further reductions in V. The different behavior of the MFA sensors, as opposed to the CPTU sensors, is to be expected as the MFA sensors are controlled by residual soil behavior, and residual soil strength has been shown by a number of researchers to be less influenced by viscous effects (Tika, 1996).

The variable rate penetration investigation took on the order of 66 minutes to complete, and as such it is important to consider the changes in effective stress that occurred for each sensor based on the dissipation of excess pore pressures and the relative positions of the sensors. The dissipation of u_2 pore pressures observed over that time period during static dissipation tests was observed to be on the order of 50 kPa or approximately 50% dissipation, as presented in detail in Chapter 8. The dissipation of the multi piezo sensors of the MPFA device during static dissipation tests were on the order of approximately 50%, but exhibited variability from 30-70% based on the particular stratigraphy. The reduction in u_2 excess pore pressures during the variable rate dissipation test was on the order of 20 kPa, indicating that penetration at slow rates is still inducing positive excess pore pressures during penetration, although of a lower magnitude than

conventional penetration rates. The q_t and q_{cnet} tip responses show approximate linear behavior from $V \approx 6000$ to 1500, decreasing until $V \approx 200$, and then increasing slightly with decreasing V over the range of tested velocities.

The behavior of the MFA and CPTU friction sleeves all exhibit similar behavior over penetration rates ranging from 20 to 1 mm/s. At lower penetration velocities, the f_s response exhibits a similar trend to q_t, and the MFA friction sensors show increased response with decreasing velocity. At this time it is not possible to determine if the separation of the MFA sleeve responses at low velocities is due to the varying surface textures or simply the result of differences in effective stress do to increased dissipation of excess pore pressures further behind the CPTU tip. As the variations in response are on the order of 3 kPa, it seems reasonable that the observed differences in MFA sleeve response at low penetration rates are due to the relative position of the sleeves, as the resultant difference in hydrostatic pressures between the first and last MFA sleeve positions is on the same order (4 kPa). Additionally the location of the f_s sensor located approximately 0.5 m ahead of the forward MFA sleeve also may account for the observed divergence in friction sleeve response, on the order of 5 kPa at the minimum tested velocity. In summary, this initial investigation into the effect of variable penetration rates on the MFA sensors showed that friction along the shaft was not largely influenced by changes in penetration rate from 20 to 0.04 mm/s, with the observed variations being on the order of the changes in effective stress due to pore pressure dissipation during the investigation.

7.5 Model Pile Load Tests with the MPFA Device

7.5.1 Introduction

Model piles are instrumented small scale versions of piles that can be used to investigate pile behavior across a range of soil and test conditions at substantially lower cost than full scale pile load tests. A number of researchers and practitioners have investigated piling behavior using model pile tests, as summarized in Table 7-12, Paikowsky and Hart (2000). The main objectives of most model pile devices are to investigate pile behavior during the three main phases of pile history: installation, equalization, and loading (Lehane and Jardine, 1994). The advantage of model piles is that a series of tests can be conducted for relatively small cost to determine the variability in pile performance as a function of varying the conditions during each of the three stages of pile history. Model piles achieve the above investigation goals through the use of significant instrumentation at both the tip and spaced along the shaft of the model pile. Typical sensors include: load cells, lateral stress cells, pore pressure transducers, friction sleeves, strain gauges, accelerometers, inclinometers, and displacement transducers. The current CPTU-MPFA device provides an excellent model pile setup for jacked installation investigations, as the device contains 14 sensors consisting of 1 tip load cell, 2 inclinometers, 5 shaft friction sensors, and 6 piezo sensors. The CPTU-MPFA device is not rugged enough for driven investigations and does not contain direct measurements of lateral stress, however, it does have the added advantage of providing conventional rate profiling capabilities that are not present in most model pile devices.

7.5.2 Summary of the Current Model Pile Tests

As discussed during the summary of soundings completed during the current investigations (Section 6.2), a series of load tests were carried out using the MFA and MPFA devices in Western Australia. The load test programs conducted at the SPWA and LPWA sand tests sites were part of the PhD work of Schneider (in progress) investigating a number of variables on the the performance of piles in sand. As such, those investigations are not presented herein and will be published at a later date. Additional load testing was conducted with the MPFA device at the BWDWA test site, and the results of those tests are presented herein. The BWDWA MPFA load test program consisted of 8 load tests conducted within 3 soundings. It was decided that due to the low failure loads expected during the CPTU-MPFA load tests due to the small "pile" diameter and soft stratigraphy, that strain controlled loading would allow for the highest quality data to be obtained. As such, a failure criterion was predetermined to constitute displacement to one pile diameter, D = 43.7 mm.

The load test series aimed to investigate the influence of strain rate, equalization time, and cycling on the measured pile load response. Loading rates of 0.24 mm/s and 0.72 mm/s were used throughout the test program, resulting in testing times of approximately 30 and 10 minutes, respectively. Equalization times of 2, 30, 120, and 480 minutes were used to determine the influence of various effective stress conditions on the pile load response. The effects of small amplitude cycling were also investigated, through the application of 200 (+/- 5 mm) 2-way cycles before two of the load tests. Details of the load test sequence and the distribution of testing parameters are listed in Table 7-13. All of the load tests were conducted using the 10kN lightweight UWA CPT rig, equipped

with a computer controlled electronic motor capable of providing stable push rates from 20 to 0.002 mm/s.

7.5.3 CPTU-MPFA Load Test Results

The load tests for the current study were all conducted within conventional CPTU soundings, and the full traces of those soundings are presented in Figures 7-29 to 7-31, with each sounding presented over two figures. When analyzing the load test results it is important to note that the stratigraphy of the BWDWA site changes at approximately 10 m depth from the relatively uniform soft clay, that was the focus of the current investigations, to another material of higher permeability and stiffness. This change in stratigraphy was not known prior to the initiation of the load test program, and unfortunately the q_t and u_2 measurements for the load tests located at 10 m depth exhibit behaviors characteristic of this secondary soil and are not readily comparable to the q_t and u_2 results from the 5 and 7.5 m tests. Fortunately, the MPFA sensors are located far enough behind the tip (> 0.67 m) that they were fully located within the main soft clay layer, allowing for comparison of MPFA sensor response across all eight load test investigations.

Table 7-14 presents the response of each operational CPTU-MPFA sensor at failure, which was taken at either the formation of a stable response or at 43.7 mm (1 diameter) of displacement, whichever was achieved first. The strains to failure are defined as the displacement at which the sensor response becomes approximately stable, where applicable. The table also presents the variation in response of each sensor from the initial to final condition, allowing for the magnitude of residual stresses at the tip and along the shaft and variations in pore pressure response during loading to be quantified.

The two part table is also presented in quadricate, sorted by: (a) chronological test sequence, (b) tip depth, (c) strain rate, and (d) equalization time to better differentiate the effect of changing the test variables on the response. To clearly differentiate the changes in response as a function of the variations in the tested parameters, the load test behavior of the q_t, f_{a1}, f_{a2}, and f_{a4} sensors are shown overlain with each other for each of the eight load tests in Figure 7-32. Additionally, similar plots are presented as Figures 7-33 to 7-35 with the response at each tip elevation presented separately to more clearly discern variations in behavior outside of those dependent on the vertical variations in stratigraphy.

From the q_t responses in Figure 7-32, the difference in stratigraphy previously noted for the tests at 10 m depth is clearly evident by the large increase in tip resistance over the other load tests. Additionally, all of the sensor responses for load test (LT) #1 exhibit effects from the head clamp not being released during equalization, subsequently affecting the stress conditions during equalization and the load test response. The general observed trends within the MPFA sleeve sensors all show a general trend of increasing shaft resistance at failure and increasing strain to failure with increasing depth. This follows logically from the known site conditions of slightly increasing s_u with depth, on the order of 1.5 kPa per m (Schneider et al., 2004). As seen from the data, friction fatigue (or decreases in shaft resistance with increasing distance from the tip, *h/r*) does not seem to significantly affect the response of the MPFA shaft sensors. This finding correlates well with the summary of model pile behavior compiled by Lehane (1992), who found that reductions in lateral stress with increasing *h/r* ratio due to friction fatigue became relatively stable for $h/r > 22$, with the current MPFA sensors located at *h/r* values of 37, 49, 61, and 73 respectively. Unfortunately the CPTU f_s measurement was not operational

for the current study to quantify the effects of friction fatigue within the zone of greatest influence, $h/r < 22$.

Figure 7-33 presented the data from the load tests at 5 m tip depth (LT#3 and LT#6) and showed that the responses of tip and shaft sensors were not largely influenced by the application of small amplitude cycling prior to load testing for the quicker loading rate of 0.72 mm/s. The other pair of load tests used to investigate the effects of small amplitude cycling investigation were tested at the slower loading rate of 0.24 mm/s, and consisted of LT #1 and LT #4. Unfortunately, as noted earlier, LT #1 was affected by the failure to release the head clamp during equalization and the results do not provide definitive conclusions.

The results of varying the equalization time from 2, to 30, 120, and 480 minutes (LT#6, LT#7, LT#8, and LT#5) are not clearly defined for the tip responses, as the tip data is again influenced by the variations in strata at 10 m depth. However, the sleeve responses can be compared as they were all located within the soft clay strata across the variations in equalization time. The absolute measured responses of the shaft sensors do not exhibit any significant variation across the wide range of tested equalization times, however, the variations from initial to final load test response for the MPFA shaft sensors do show a clear trend of increasing response with increased equalization time as detailed in Table 7-14d. This result seems to indicate that the residual stresses along the pile are dissipating with increased equalization time, but the ultimate shaft resistance is not largely affected by equalization time for this soft clay material. From these results it follows that the shearing imposed during CPT penetration was sufficient to induce residual shearing for the Burswood clay.

The effects of varying the strain rate in the current load tests can be observed by comparing load tests #2 and #8, both tested at 10 m, after 120 minutes of equalization, and not including cycling. The tip response of the load test at the slower strain rate of 0.024 mm/s shows a significant decrease in response as compared to the test at 0.072 mm/s (Table 7-14). This response is expected from the viscous effects observed and described in Section 7.4 concerning variable rate penetration investigations. The shaft response exhibits an increased response for the slower strain rate. This result also compares favorably with the findings of Section 7.4 which showed that the MPFA shaft resistances at various strain rates were predominantly controlled by the changes in effective stress regime and not variations in viscosity as a function of rate. The pore pressures observed during LT #2, conducted at the slower strain rate, were on the order of 10 kPa lower than those observed in LT #8.

Table 7-15 compares the measured load test responses at one diameter of displacement (43.7 mm) with the average monotonic response during conventional penetration at 20 mm/s for the soil in the 0.25 m prior to each load test. The q_t responses within the soft clay layer (excluding the 10 m load tests) all show a decrease in tip response for the slower load test conditions ranging in variation from 8 to 33 percent lower than the measured monotonic q_t response. The q_t responses for the 10 m load tests all show a large increase in response during the load tests due to the significant dissipation of pore pressures between the load tests and CPTU penetrations, ranging from Δu = 90 to 150 kPa. The shaft sensor responses show very little change in response for the 5 m and 7.5 m data sets, as seen in the variations in sleeve response listed in Table 7-15d on the order of 1 to 3 kPa. The sleeve response for the 10 m data sets show more

substantial increases in response for the load tests as again the dissipation of excess pore pressures at these locations was quite large between the monotonic and static tests, on the order of 25 to 50 kPa along the shaft. These results indicate the complex influences of installation, equalization, and loading effects on pile response, and highlight some of the reasons that conventional 20 mm/s penetration results should typically be adjusted for these affects before direct implementation into pile design analyses. The MPFA device has been shown to be a practical device for conducting jacked installation model pile investigations, and shows promise for continued investigations across a wider range of materials and load test conditions.

7.6 Measuring the Extraction Response of Penetrometer Devices

Typical CPT procedures consist of only measuring the installation penetration response without recording data during the extraction phase of the test. However, monitoring the sensor response during extraction as well can be beneficial in a number of situations, and does not involve major modifications to most DAQ and penetration systems. The measurement of extraction response can be especially beneficial in soft fine grained sediments (Randolph, 2004). Figure 7-5 demonstrated the response of CPTU-MPFA sensors during both insertion and extraction at the BWDWA test site in sounding MPFA_12. Measuring the extraction response in sediments that constitute undrained conditions at conventional penetration rates (~20 mm/s) is especially beneficial as all sensors, including the tip, can provide an estimate of the ratio of tensile to compression behavior. The ratio of tensile to contractive pile shaft response has long been a point of contention among geotechnical engineers (O'Neil 2001). Penetrometer designs that allow for the measurement of contractive and tensile stresses are ideal, as they allow for the

ratio of insertion to extraction response to be easily quantified through direct measurement as a function of depth. The current MPFA friction sleeve only allow for the measurement of tensile stresses on the order of -20 kPa due to the current friction sleeve design. However, this magnitude was sufficient to monitor the extraction shaft resistance at the BWDWA and LPWA test sites. On average, the ratio of insertion to extraction resistance at BWDWA and LPWA was shown to range from 10 to 100% with most responses around 50%. These results compare favorably with the generic relation proposed by Elhakim and Mayne (2002) which shows the average extraction shaft response to be on the order of 0.7 of the insertion response for piles across a range of materials.

Additionally, for investigations that occur over long time periods, or for which large variations in temperature are present, measuring response through full extraction provides a means to quantify any drift that may have occurred across various sensors from the beginning to end of testing. A number of CPT procedures involve extraction rates that are increased from the installation rate to improve productivity. While quantitatively using the extraction results for higher rates may not be possible, the ability to check sensor drift and to qualitatively observed trends in behavior are still available with no loss to productivity.

7.7 Benefits of Conducting Non Standard Investigations

This chapter has discussed the use of penetrometer devices across a range of non standard investigation procedures. As a large percentage of the costs inherent to most geotechnical site investigations are related to mobilization of resources, it is paramount to maximize the quality, quantity, and range of data collected during each investigation. As

an engineering community, geotechnical engineers should look more closely at optimizing the amount and type of data available with the assortment of in situ and laboratory testing techniques. The MFA and MPFA devices have shown promise in providing additional measures of commonly desired geotechnical data, and have also shown flexibility in application that may provide for the affordable implementation of parametric intermediate scale investigations in place of costly full scale tests that are limited in the range of investigated parameters.

Table 7-1. Comparison of Vertical and Inclined CPTU-MFA Average Responses for the Silica Sand Layer from 1 to 5 m at the SRVT Site.

Average Response of the CPTU-MFA Sensors

Penetration Angle - Test ID	q_t (kPa)	u_2 (kPa)	f_s (kPa)	f_{a1} (kPa)	f_{a2} (kPa)	f_{a3} (kPa)	f_{a4} (kPa)
45º - S58	6167.21	9.86	66.57	49.89	100.07	45.62	211.70
90Aº -S60	6105.47	6.13	58.66	51.07	78.14	46.78	228.75
90Bº - S64	6107.02	4.24	42.76	45.35	75.61	46.57	225.68

Comparison of Vertical and Inclined Penetrations

Penetration Angle - Test ID	q_t (kPa)	u_2 (kPa)	f_s (kPa)	f_{a1} (kPa)	f_{a2} (kPa)	f_{a3} (kPa)	f_{a4} (kPa)
(90Aº - 45º)	-61.75	-3.73	-7.92	1.18	-21.93	1.15	17.05
(90Bº - 45º)	-60.19	-5.62	-23.81	-4.54	-24.46	0.95	13.98
(90Aº - 90Bº)	-1.56	1.89	15.90	5.72	2.53	0.21	3.07

+ Values Indicate a Reduction in Response for the 45º Sounding

Percent Variation in Vertical and Inclined Penetrations

Penetration Angle - Test ID	q_t (%)	u_2 (%)	f_s (%)	f_{a1} (%)	f_{a2} (%)	f_{a3} (%)	f_{a4} (%)
(90Aº - 45º)%	-1.01	-60.82	-13.50	2.32	-28.06	2.46	7.45
(90Bº - 45º)%	-0.99	-132.59	-55.69	-10.01	-32.35	2.03	6.19
(90Aº - 90Bº)%	-0.03	30.85	27.10	11.21	3.24	0.44	1.34

+ Values Indicate a Reduction in Response for the 45º Sounding

Table 7-2. Comparison of Vertical and Inclined CPTU-MFA Average Responses for the Silica Sand Layer from 7 to 8 m at the SRVT Site.

Average Response of the CPTU-MFA Sensors

Penetration Angle - Test ID	q_t (kPa)	u_2 (kPa)	f_s (kPa)	f_{a1} (kPa)	f_{a2} (kPa)	f_{a3} (kPa)	f_{a4} (kPa)
45º - S58	5130.85	30.11	120.43	109.69	161.95	87.23	254.29
90Aº -S60	4998.65	19.03	92.50	90.56	121.12	83.14	257.79
90Bº - S64	5512.69	7.02	89.70	88.15	134.10	88.53	268.04

Comparison of Vertical and Inclined Penetrations

Penetration Angle - Test ID	q_t (kPa)	u_2 (kPa)	f_s (kPa)	f_{a1} (kPa)	f_{a2} (kPa)	f_{a3} (kPa)	f_{a4} (kPa)
(90Aº - 45º)	-132.20	-11.08	-27.93	-19.13	-40.84	-4.09	3.51
(90Bº - 45º)	381.84	-23.09	-30.73	-21.55	-27.85	1.30	13.75
(90Aº - 90Bº)	-514.05	12.02	2.80	2.42	-12.99	-5.39	-10.24

+ Values Indicate a Reduction in Response for the 45º Sounding

Percent Variation in Vertical and Inclined Penetrations

Penetration Angle - Test ID	q_t (%)	u_2 (%)	f_s (%)	f_{a1} (%)	f_{a2} (%)	f_{a3} (%)	f_{a4} (%)
(90Aº - 45º)%	-2.64	-58.20	-30.19	-21.12	-33.72	-4.92	1.36
(90Bº - 45º)%	6.93	-329.06	-34.26	-24.44	-20.77	1.47	5.13
(90Aº - 90Bº)%	-10.28	63.13	3.03	2.67	-10.72	-6.48	-3.97

+ Values Indicate a Reduction in Response for the 45º Sounding

Table 7-3. Summary of the Average Large Amplitude (1-m) Cyclic Response for Each Full Stroke (Half-Cycle) of Sounding MFPA_10 at the BWDWA Site.

Absolute Cycle Averages

Cycle Number	Depth (m)	q_t (kPa)	u_2 (kPa)	f_s (kPa)	f_{a1} (kPa)	f_{a2} (kPa)	f_{a3} (kPa)	f_{a4} (kPa)	u_{a0} (kPa)	u_{a1} (kPa)	u_{a2} (kPa)	u_{a3} (kPa)	u_{a4} (kPa)
1 m before cycling	7.25	286.34	167.07		13.50	20.10	6.09		75.44	96.25	88.08	84.41	
virgin	8.23	361.60	208.78		11.10	16.36	4.99		114.06	134.77	132.58	117.30	
down 2	8.23	233.81	173.84		7.72	11.17	3.31		127.96	131.71	129.96	123.27	
down 3	8.24	204.75	159.80		7.39	10.30	2.89		122.05	132.58	127.49	123.64	
down 4	8.23	193.01	147.84		7.16	9.82	3.11		118.98	129.00	125.77	123.69	
down 5	8.23	183.61	141.89		7.11	9.39	2.92		113.68	125.22	122.98	123.10	
down 6	8.23	173.86	134.17		7.06	9.24	2.67		109.03	121.29	122.68	122.60	
down 7	8.23	167.45	130.14		6.95	9.10	2.54		104.69	117.79	120.89	122.10	
down 8	8.23	164.24	125.51		6.68	8.94	2.53		100.18	115.41	120.65	121.11	
down 9	8.23	161.43	124.75		6.74	8.76	2.47		95.79	113.65	119.19	120.51	
down 10	8.23	156.46	117.77		6.48	8.65	2.34		94.71	111.67	118.08	119.77	
down 11	8.23	149.97	116.41		6.33	8.69	2.18		91.90	109.33	117.24	119.65	
1 m after cycling	9.21	367.36	238.90		6.72	10.27	2.65		152.14	153.52	122.70	105.36	
up 1	8.21	-45.74	90.92		-3.39	-5.55	-6.62		130.39	139.74	172.56	132.90	
up 2	8.20	-24.87	91.68		-2.57	-4.20	-6.44		122.36	133.95	154.76	129.12	
up 3	8.22	-11.40	93.16		-2.41	-3.43	-5.84		117.65	130.60	155.58	129.32	
up 4	8.21	-8.73	89.94		-0.94	-2.81	-5.68		114.54	127.06	154.62	128.57	
up 5	8.20	-4.11	88.91		-1.57	-2.80	-5.66		109.69	123.62	153.40	127.02	
up 6	8.21	-1.84	89.00		-1.66	-2.57	-5.47		105.47	120.06	151.89	126.45	
up 7	8.21	2.12	88.74		-1.57	-2.44	-5.33		101.54	116.92	149.81	126.58	
up 8	8.21	7.69	88.36		-1.44	-2.20	-5.20		99.18	114.83	148.03	126.10	
up 9	8.22	10.37	89.40		-1.41	-2.18	-5.13		96.09	112.67	147.00	125.80	
up 10	8.20	5.57	86.97		-1.40	-2.03	-5.11		93.34	110.90	145.91	124.74	
up after full penetration	8.21	-14.66	65.63		-2.42	-4.18	-5.88		99.61	116.75	142.88	130.25	

Normalized Cycle Averages

Cycle Number	Depth (m)	q_t (kPa)	u_2 (kPa)	f_s (kPa)	f_{a1} (kPa)	f_{a2} (kPa)	f_{a3} (kPa)	f_{a4} (kPa)	u_{a0} (kPa)	u_{a1} (kPa)	u_{a2} (kPa)	u_{a3} (kPa)	u_{a4} (kPa)
1 m before cycling	7.25	0.79	0.80		1.22	1.23	1.22		0.66	0.71	0.66	0.72	
virgin	8.23	1.00	1.00		1.00	1.00	1.00		1.00	1.00	1.00	1.00	
down 2	8.23	0.65	0.83		0.69	0.68	0.66		1.12	0.98	0.98	1.05	
down 3	8.24	0.57	0.77		0.67	0.63	0.58		1.07	0.98	0.96	1.05	
down 4	8.23	0.53	0.71		0.64	0.60	0.62		1.04	0.96	0.95	1.05	
down 5	8.23	0.51	0.68		0.64	0.57	0.59		1.00	0.93	0.93	1.05	
down 6	8.23	0.48	0.64		0.64	0.57	0.54		0.96	0.90	0.93	1.05	
down 7	8.23	0.46	0.62		0.63	0.56	0.51		0.92	0.87	0.91	1.04	
down 8	8.23	0.45	0.60		0.60	0.55	0.51		0.88	0.86	0.91	1.03	
down 9	8.23	0.45	0.60		0.61	0.54	0.49		0.84	0.84	0.90	1.03	
down 10	8.23	0.43	0.56		0.58	0.53	0.47		0.83	0.83	0.89	1.02	
down 11	8.23	0.41	0.56		0.57	0.53	0.44		0.81	0.81	0.88	1.02	
1 m after cycling	9.21	1.02	1.14		0.60	0.63	0.53		1.33	1.14	0.93	0.90	
up 1	8.21	-0.13	0.44		-0.31	-0.34	-1.33		1.14	1.04	1.30	1.13	
up 2	8.20	-0.07	0.44		-0.23	-0.26	-1.29		1.07	0.99	1.17	1.10	
up 3	8.22	-0.03	0.45		-0.22	-0.21	-1.17		1.03	0.97	1.17	1.10	
up 4	8.21	-0.02	0.43		-0.08	-0.17	-1.14		1.00	0.94	1.17	1.10	
up 5	8.20	-0.01	0.43		-0.14	-0.17	-1.14		0.96	0.92	1.16	1.08	
up 6	8.21	-0.01	0.43		-0.15	-0.16	-1.10		0.92	0.89	1.15	1.08	
up 7	8.21	0.01	0.43		-0.14	-0.15	-1.07		0.89	0.87	1.13	1.08	
up 8	8.21	0.02	0.42		-0.13	-0.13	-1.04		0.87	0.85	1.12	1.08	
up 9	8.22	0.03	0.43		-0.13	-0.13	-1.03		0.84	0.84	1.11	1.07	
up 10	8.20	0.02	0.42		-0.13	-0.12	-1.02		0.82	0.82	1.10	1.06	
up after full penetration	8.21	-0.04	0.31		-0.22	-0.26	-1.18		0.87	0.87	1.08	1.11	

Table 7-4. Summary of the Average Large Amplitude (1-m) Cyclic Response for Each Full Stroke (Half-Cycle) of Sounding MFPA_11 at the BWDWA Site.

Absolute Cycle Averages

Cycle Number	Depth (m)	q_t (kPa)	u_2 (kPa)	f_s (kPa)	f_{a1} (kPa)	f_{a2} (kPa)	f_{a3} (kPa)	f_{a4} (kPa)	u_{a0} (kPa)	u_{a1} (kPa)	u_{a2} (kPa)	u_{a3} (kPa)	u_{a4} (kPa)
1 m before cycling	5.27	216.50	120.67		7.43	16.95	6.31		89.80	94.54	85.80	85.31	
virgin	6.25	266.23	126.42		7.59	17.76	7.37		95.65	105.77	106.23	99.89	
down 2	6.24	158.93	102.25		7.90	18.10	8.51		70.11	84.49	81.72	70.48	
down 3	6.23	115.18	103.76		6.75	14.92	6.97		73.37	86.35	86.54	68.46	
down 4	6.23	97.62	102.51		5.58	13.59	6.36		72.06	87.46	88.06	70.60	
down 5	6.25	94.38	99.36		5.29	12.30	5.67		72.01	86.34	87.94	72.37	
down 6	6.24	80.08	97.27		5.29	11.50	5.45		70.45	85.89	89.02	71.00	
down 7	6.23	72.32	88.20		5.00	10.74	5.17		71.17	86.47	88.71	71.87	
down 8	6.24	73.08	86.26		5.18	10.58	5.17		69.37	88.23	86.74	72.03	
down 9	6.23	67.02	83.49		4.93	9.94	5.07		70.67	87.43	86.50	71.02	
down 10	6.23	57.67	75.69		4.72	9.95	4.82		67.02	85.91	86.50	72.41	
down 11	6.23	57.69	71.42		4.85	10.23	4.92		67.58	86.44	87.35	71.67	
down 12	6.24	58.31	71.76		4.39	9.77	4.74		65.86	85.62	87.78	71.15	
1 m after cycling	7.24	308.48	167.27		4.97	12.65	3.94		104.06	104.88	88.62	63.22	
up 1	6.25	-99.68	66.73		-3.01	-6.12	-6.18		85.46	85.93	82.74	68.51	
up 2	6.24	-52.99	68.42		-1.41	-3.16	-4.38		86.38	94.22	89.44	74.26	
up 3	6.22	-56.10	64.28		-1.64	-3.23	-5.11		79.07	88.40	92.69	64.07	
up 4	6.22	-47.20	68.65		-0.97	-2.26	-4.46		75.97	86.70	94.23	69.03	
up 5	6.23	-41.78	68.07		-1.06	-2.08	-4.52		73.08	85.15	96.38	71.48	
up 6	6.23	-34.57	68.61		-0.50	-1.31	-4.31		75.13	85.71	98.12	71.65	
up 7	6.24	-38.97	67.06		-0.47	-1.14	-4.35		72.86	85.82	100.19	72.20	
up 8	6.24	-37.43	67.95		0.05	-0.99	-4.04		72.33	88.06	100.80	72.83	
up 9	6.23	-37.01	66.42		-0.02	-1.05	-4.32		70.23	85.70	101.23	71.39	
up 10	6.23	-32.11	65.07		0.15	-1.12	-4.21		69.87	86.78	102.09	71.08	
up 11	6.23	-40.03	62.98		-0.28	-0.81	-4.38		68.34	86.24	102.17	71.44	
up after full penetration	6.23	-39.73	36.47		-2.94	-5.92	-5.87		64.61	82.14	98.36	85.93	

Normalized Cycle Averages

Cycle Number	Depth (m)	q_t (kPa)	u_2 (kPa)	f_s (kPa)	f_{a1} (kPa)	f_{a2} (kPa)	f_{a3} (kPa)	f_{a4} (kPa)	u_{a0} (kPa)	u_{a1} (kPa)	u_{a2} (kPa)	u_{a3} (kPa)	u_{a4} (kPa)
1 m before cycling	5.27	0.81	0.95		0.98	0.95	0.86		0.94	0.89	0.81	0.85	
virgin	6.25	1.00	1.00		1.00	1.00	1.00		1.00	1.00	1.00	1.00	
down 2	6.24	0.60	0.81		1.04	1.02	1.15		0.73	0.80	0.77	0.71	
down 3	6.23	0.43	0.82		0.89	0.84	0.95		0.77	0.82	0.81	0.69	
down 4	6.23	0.37	0.81		0.74	0.77	0.86		0.75	0.83	0.83	0.71	
down 5	6.25	0.35	0.79		0.70	0.69	0.77		0.75	0.82	0.83	0.72	
down 6	6.24	0.30	0.77		0.70	0.65	0.74		0.74	0.81	0.84	0.71	
down 7	6.23	0.27	0.70		0.66	0.60	0.70		0.74	0.82	0.84	0.72	
down 8	6.24	0.27	0.68		0.68	0.60	0.70		0.73	0.83	0.82	0.72	
down 9	6.23	0.25	0.66		0.65	0.56	0.69		0.74	0.83	0.81	0.71	
down 10	6.23	0.22	0.60		0.62	0.56	0.65		0.70	0.81	0.81	0.72	
down 11	6.23	0.22	0.56		0.64	0.58	0.67		0.71	0.82	0.82	0.72	
down 12	6.24	0.22	0.57		0.58	0.55	0.64		0.69	0.81	0.83	0.71	
1 m after cycling	7.24	1.16	1.32		0.65	0.71	0.53		1.09	0.99	0.83	0.63	
up 1	6.25	-0.37	0.53		-0.40	-0.34	-0.84		0.89	0.81	0.78	0.69	
up 2	6.24	-0.20	0.54		-0.19	-0.18	-0.59		0.90	0.89	0.84	0.74	
up 3	6.22	-0.21	0.51		-0.22	-0.18	-0.69		0.83	0.84	0.87	0.64	
up 4	6.22	-0.18	0.54		-0.13	-0.13	-0.61		0.79	0.82	0.89	0.69	
up 5	6.23	-0.16	0.54		-0.14	-0.12	-0.61		0.76	0.81	0.91	0.72	
up 6	6.23	-0.13	0.54		-0.07	-0.07	-0.58		0.79	0.81	0.92	0.72	
up 7	6.24	-0.15	0.53		-0.06	-0.06	-0.59		0.76	0.81	0.94	0.72	
up 8	6.24	-0.14	0.54		0.01	-0.06	-0.55		0.76	0.83	0.95	0.73	
up 9	6.23	-0.14	0.53		0.00	-0.06	-0.59		0.73	0.81	0.95	0.71	
up 10	6.23	-0.12	0.51		0.02	-0.06	-0.57		0.73	0.82	0.96	0.71	
up 11	6.23	-0.15	0.50		-0.04	-0.05	-0.59		0.71	0.82	0.96	0.72	
up after full penetration	6.23	-0.15	0.29		-0.39	-0.33	-0.80		0.68	0.78	0.93	0.86	

Table 7-5. Summary of the Average Large Amplitude (1-m) Cyclic Response for Each Full Stroke (Half-Cycle) of Sounding MFPA_12 at the BWDWA Site.

Absolute Cycle Averages

Cycle Number	Depth (m)	q_t (kPa)	u_2 (kPa)	f_s (kPa)	f_{a1} (kPa)	f_{a2} (kPa)	f_{a3} (kPa)	f_{a4} (kPa)	u_{a0} (kPa)	u_{a1} (kPa)	u_{a2} (kPa)	u_{a3} (kPa)	u_{a4} (kPa)
1 m before cycling	5.27	217.74	146.12		5.42	10.65	4.59	7.65	84.45	82.60	79.80	81.45	72.75
virgin	6.27	262.92	150.06		6.86	12.48	5.66	8.14	88.42	92.27	102.56	96.88	76.06
down 2	6.27	170.73	119.17		4.50	11.91	6.18	10.93	79.67	70.78	83.50	71.44	45.43
down 3	6.28	138.55	119.65		3.29	9.69	5.02	9.60	89.86	79.98	87.46	73.14	58.31
down 4	6.27	114.84	111.84		2.64	8.85	4.57	9.19	86.05	78.60	88.23	74.27	61.72
down 5	6.27	100.81	109.03		2.68	8.52	4.51	8.97	82.98	80.33	88.45	72.17	64.72
down 6	6.27	89.47	106.51		2.98	8.35	4.38	8.80	79.62	80.27	87.75	71.35	62.76
down 7	6.27	84.86	103.69		2.52	8.17	4.28	8.81	75.63	79.50	86.10	71.96	63.28
down 8	6.27	77.99	96.10		2.34	8.06	4.47	8.84	78.61	79.75	85.45	72.94	62.23
down 9	6.27	71.72	92.40		2.73	8.53	4.41	8.83	72.77	80.82	85.98	71.15	63.58
down 10	6.28	76.23	92.66		2.66	8.37	4.28	8.89	69.70	72.56	85.74	70.13	56.78
down 11	6.26	66.16	88.15		2.84	8.57	4.68	9.02	67.13	72.66	83.64	70.30	59.26
1 m after cycling	7.24	303.01	181.39		4.52	9.22	4.17	10.00	111.55	86.14	72.34	53.46	43.24
up 1	6.27	-152.06	80.80		-6.88	-10.57	-9.89	-10.60	62.90	70.42	80.46	46.26	21.97
up 2	6.26	-90.03	79.34		-4.84	-5.66	-6.96	-8.59	84.40	83.28	91.54	67.69	44.63
up 3	6.27	-60.92	80.10		-3.78	-4.29	-5.96	-7.84	87.77	85.64	96.29	70.89	50.65
up 4	6.27	-54.31	76.39		-3.57	-3.86	-5.72	-7.57	84.67	86.11	96.92	72.61	52.14
up 5	6.26	-51.25	72.59		-3.24	-3.46	-5.73	-7.52	81.88	84.30	95.47	71.65	45.03
up 6	6.27	-43.65	75.44		-3.28	-3.42	-5.62	-7.27	79.41	83.71	97.18	73.33	49.38
up 7	6.27	-39.69	75.41		-3.36	-3.28	-5.58	-7.29	76.46	83.32	95.70	72.43	48.74
up 8	6.27	-38.96	70.41		-3.02	-3.46	-5.64	-7.34	77.05	83.73	92.90	71.61	44.33
up 9	6.26	-43.59	71.16		-3.45	-3.47	-5.68	-7.31	72.30	81.20	94.13	72.32	44.46
up 10	6.27	-42.10	71.65		-3.25	-3.61	-5.74	-7.28	69.58	77.67	95.59	71.69	42.64
up after full penetration	6.26	-67.68	47.21		-4.46	-7.74	-5.88	-4.13	69.62	71.13	95.87	68.99	62.68

Normalized Cycle Averages

Cycle Number	Depth (m)	q_t (kPa)	u_2 (kPa)	f_s (kPa)	f_{a1} (kPa)	f_{a2} (kPa)	f_{a3} (kPa)	f_{a4} (kPa)	u_{a0} (kPa)	u_{a1} (kPa)	u_{a2} (kPa)	u_{a3} (kPa)	u_{a4} (kPa)
1 m before cycling	5.27	0.828	0.974		0.790	0.854	0.811	0.940	0.955	0.895	0.778	0.841	0.957
virgin	6.27	1.000	1.000		1.000	1.000	1.000	1.000	1.000	1.000	1.000	1.000	1.000
down 2	6.27	0.649	0.794		0.656	0.954	1.093	1.343	0.901	0.767	0.814	0.737	0.597
down 3	6.28	0.527	0.797		0.480	0.777	0.888	1.179	1.016	0.867	0.853	0.755	0.767
down 4	6.27	0.437	0.745		0.385	0.709	0.808	1.130	0.973	0.852	0.860	0.767	0.812
down 5	6.27	0.383	0.727		0.391	0.683	0.798	1.103	0.938	0.871	0.862	0.745	0.851
down 6	6.27	0.340	0.710		0.434	0.669	0.775	1.081	0.900	0.870	0.856	0.737	0.825
down 7	6.27	0.323	0.691		0.367	0.655	0.757	1.082	0.855	0.862	0.839	0.743	0.832
down 8	6.27	0.297	0.640		0.341	0.646	0.790	1.086	0.889	0.864	0.833	0.753	0.818
down 9	6.27	0.273	0.616		0.399	0.684	0.779	1.085	0.823	0.876	0.838	0.734	0.836
down 10	6.28	0.290	0.617		0.388	0.671	0.756	1.093	0.788	0.786	0.836	0.724	0.747
down 11	6.26	0.252	0.587		0.414	0.686	0.827	1.108	0.759	0.788	0.816	0.726	0.779
1 m after cycling	7.24	1.152	1.209		0.660	0.739	0.737	1.229	1.262	0.934	0.705	0.552	0.569
up 1	6.27	-0.578	0.538		-1.004	-0.847	-1.748	-1.302	0.711	0.763	0.784	0.478	0.289
up 2	6.26	-0.342	0.529		-0.706	-0.454	-1.230	-1.056	0.954	0.903	0.892	0.699	0.587
up 3	6.27	-0.232	0.534		-0.551	-0.344	-1.054	-0.964	0.993	0.928	0.939	0.732	0.666
up 4	6.27	-0.207	0.509		-0.521	-0.309	-1.011	-0.930	0.958	0.933	0.945	0.749	0.685
up 5	6.26	-0.195	0.484		-0.473	-0.277	-1.014	-0.924	0.926	0.914	0.931	0.740	0.592
up 6	6.27	-0.166	0.503		-0.478	-0.274	-0.994	-0.893	0.898	0.907	0.947	0.757	0.649
up 7	6.27	-0.151	0.503		-0.490	-0.263	-0.987	-0.896	0.865	0.903	0.933	0.748	0.641
up 8	6.27	-0.148	0.469		-0.440	-0.277	-0.998	-0.902	0.871	0.907	0.906	0.739	0.583
up 9	6.26	-0.166	0.474		-0.503	-0.278	-1.004	-0.898	0.818	0.880	0.918	0.747	0.585
up 10	6.27	-0.160	0.477		-0.474	-0.289	-1.014	-0.894	0.787	0.842	0.932	0.740	0.561
up after full penetration	6.26	-0.257	0.315		-0.651	-0.620	-1.040	-0.507	0.787	0.771	0.935	0.712	0.824

Table 7-6. Summary of the Small Amplitude (5-mm) Cyclic Response at 5 m Tip Depth in Sounding MFPA_26 at BWDWA.

Absolute Values - Upper +/- 5 mm cycling from 4.995 - 5.000 m (BWDWA)

Cycles Number	Depth (m)	q_t (kPa)	u_2 (kPa)	f_s (kPa)	f_{a1} (kPa)	f_{a2} (kPa)	f_{a3} (kPa)	f_{a4} (kPa)	u_{a0} (kPa)	u_{a1} (kPa)	u_{a2} (kPa)	u_{a3} (kPa)	u_{a4} (kPa)
0.25 m before cycling	4.87	254.79	120.64		9.32	5.49		11.83	64.75	80.64	86.59	74.15	51.01
Baseline	5.00	170.55	130.84		6.41	2.96		6.01	85.54	87.01	90.94	82.51	64.13
Down 1-10	5.00	179.82	138.91		8.39	3.71		7.49	94.51	94.77	92.98	83.44	73.12
Down 11-50	5.00	158.88	135.44		9.77	3.98		6.94	88.10	92.66	92.48	81.59	72.86
Down 51-100	5.00	147.01	129.18		10.04	4.25		6.67	85.45	90.29	91.41	80.30	71.83
Down 101-150	5.00	134.44	124.22		10.32	4.80		7.49	82.50	87.90	90.12	79.49	71.00
Down 151-190	5.00	132.13	117.62		10.58	4.80		7.76	78.57	86.32	88.59	78.19	69.63
Down 191-200	5.00	131.26	113.33		11.15	5.07		7.76	76.66	82.68	87.52	76.92	68.40
Up 1-10	5.00	72.78	122.90		-11.63	-2.50		-2.55	77.71	84.44	90.84	79.43	65.55
Up 11-50	5.00	60.53	116.40		-12.18	-3.05		-1.74	79.56	86.31	89.55	79.18	68.82
Up 51-100	5.00	46.55	109.78		-13.01	-4.13		-1.74	77.19	83.43	88.51	78.35	70.16
Up 101-150	5.00	45.90	103.85		-13.29	-4.67		-2.83	74.76	81.78	87.16	77.33	68.65
Up 151-190	5.00	34.81	95.74		-14.10	-4.95		-3.10	62.76	71.98	82.64	68.55	59.59
Up 191-200	5.00	35.33	97.35		-13.01	-4.95		-2.82	70.84	79.79	85.52	76.22	66.90
0.25 m after cycling	*Not available due to subsequent load test*												

Normalized Values - Upper +/- 5 mm cycling from 4.995 - 5.000 m (BWDWA)

Cycles Number	Depth (m)	q_t (kPa)	u_2 (kPa)	f_s (kPa)	f_{a1} (kPa)	f_{a2} (kPa)	f_{a3} (kPa)	f_{a4} (kPa)	u_{a0} (kPa)	u_{a1} (kPa)	u_{a2} (kPa)	u_{a3} (kPa)	u_{a4} (kPa)
0.25 m before cycling	4.87	1.42	0.87		1.11	1.48		1.58	0.69	0.85	0.93	0.89	0.70
Baseline	5.00	0.95	0.94		0.76	0.80		0.80	0.91	0.92	0.98	0.99	0.88
Down 1-10	5.00	1.00	1.00		1.00	1.00		1.00	1.00	1.00	1.00	1.00	1.00
Down 11-50	5.00	0.88	0.97		1.16	1.07		0.93	0.93	0.98	0.99	0.98	1.00
Down 51-100	5.00	0.82	0.93		1.20	1.15		0.89	0.90	0.95	0.98	0.96	0.98
Down 101-150	5.00	0.75	0.89		1.23	1.29		1.00	0.87	0.93	0.97	0.95	0.97
Down 151-190	5.00	0.73	0.85		1.26	1.29		1.04	0.83	0.91	0.95	0.94	0.95
Down 191-200	5.00	0.73	0.82		1.33	1.37		1.04	0.81	0.87	0.94	0.92	0.94
Up 1-10	5.00	0.40	0.88		-1.39	-0.67		-0.34	0.82	0.89	0.98	0.95	0.90
Up 11-50	5.00	0.34	0.84		-1.45	-0.82		-0.23	0.84	0.91	0.96	0.95	0.94
Up 51-100	5.00	0.26	0.79		-1.55	-1.11		-0.23	0.82	0.88	0.95	0.94	0.96
Up 101-150	5.00	0.26	0.75		-1.58	-1.26		-0.38	0.79	0.86	0.94	0.93	0.94
Up 151-190	5.00	0.19	0.69		-1.68	-1.33		-0.41	0.66	0.76	0.89	0.82	0.81
Up 191-200	5.00	0.20	0.70		-1.55	-1.33		-0.38	0.75	0.84	0.92	0.91	0.91
0.25 m after cycling	*Not available due to subsequent load test*												

Table 7-7. Summary of the Small Amplitude (5-mm) Cyclic Response at 7.5 m Tip Depth in Sounding MFPA_26 at BWDWA.

Absolute Values - Lower +/- 5 mm cycling from 7.495 - 7.500 m (BWDWA)

Cycles Number	Depth (m)	q_t (kPa)	u_2 (kPa)	f_s (kPa)	f_{a1} (kPa)	f_{a2} (kPa)	f_{a3} (kPa)	f_{a4} (kPa)	u_{a0} (kPa)	u_{a1} (kPa)	u_{a2} (kPa)	u_{a3} (kPa)	u_{a4} (kPa)
0.25 m before cycling	7.37	281.22	176.18		12.16	7.26		9.01	90.31	121.32	121.45	108.25	79.67
Baseline	7.50	190.06	167.61		7.23	3.85		4.64	127.24	129.61	137.61	119.68	99.13
Down 1-10	7.50	209.72	180.33		5.12	2.63		4.23	136.49	131.89	138.38	121.31	104.84
Down 11-50	7.50	178.27	183.59		11.15	3.44		5.32	128.02	133.33	139.63	120.61	106.05
Down 51-100	7.50	166.96	178.84		11.42	4.26		6.13	128.31	134.91	140.03	120.61	106.07
Down 101-150	7.50	176.95	176.53		12.23	4.53		6.67	125.37	132.87	138.81	118.94	104.88
Down 151-190	7.50	176.09	171.18		11.15	5.06		6.67	123.19	130.65	135.78	115.57	102.51
Down 191-200	7.50	164.79	167.30		11.97	4.53		6.13	119.79	130.23	132.89	111.50	99.20
Up 1-10	7.50	103.09	167.11		-10.54	-2.50		-0.39	114.12	126.64	134.64	116.31	99.14
Up 11-50	7.50	101.70	169.74		-13.28	-4.67		-2.02	122.48	128.38	136.45	118.48	102.80
Up 51-100	7.50	91.34	166.14		-13.83	-5.21		-3.10	122.07	131.15	137.85	117.85	104.34
Up 101-150	7.50	90.07	162.21		-14.94	-6.02		-3.39	119.89	129.46	135.52	114.87	102.12
Up 151-190	7.50	89.10	158.86		-14.10	-5.75		-3.38	114.59	128.33	132.81	110.92	98.95
Up 191-200	7.50	110.05	157.82		-13.55	-4.12		-2.01	114.99	126.41	132.13	110.26	98.24
0.25 m after cycling	*Not available due to subsequent load test*												

Normalized Values - Lower +/- 5 mm cycling from 7.495 - 7.500 m (BWDWA)

Cycles Number	Depth (m)	q_t (kPa)	u_2 (kPa)	f_s (kPa)	f_{a1} (kPa)	f_{a2} (kPa)	f_{a3} (kPa)	f_{a4} (kPa)	u_{a0} (kPa)	u_{a1} (kPa)	u_{a2} (kPa)	u_{a3} (kPa)	u_{a4} (kPa)
0.25 m before cycling	7.37	1.34	0.98		2.38	2.76		2.13	0.66	0.92	0.88	0.89	0.76
Baseline	7.50	0.91	0.93		1.41	1.46		1.10	0.93	0.98	0.99	0.99	0.95
Down 1-10	7.50	1.00	1.00		1.00	1.00		1.00	1.00	1.00	1.00	1.00	1.00
Down 11-50	7.50	0.85	1.02		2.18	1.31		1.26	0.94	1.01	1.01	0.99	1.01
Down 51-100	7.50	0.80	0.99		2.23	1.62		1.45	0.94	1.02	1.01	0.99	1.01
Down 101-150	7.50	0.84	0.98		2.39	1.72		1.58	0.92	1.01	1.00	0.98	1.00
Down 151-190	7.50	0.84	0.95		2.18	1.92		1.58	0.90	0.99	0.98	0.95	0.98
Down 191-200	7.50	0.79	0.93		2.34	1.72		1.45	0.88	0.99	0.96	0.92	0.95
Up 1-10	7.50	0.49	0.93		-2.06	-0.95		-0.09	0.84	0.96	0.97	0.96	0.95
Up 11-50	7.50	0.48	0.94		-2.59	-1.77		-0.48	0.90	0.97	0.99	0.98	0.98
Up 51-100	7.50	0.44	0.92		-2.70	-1.98		-0.73	0.89	0.99	1.00	0.97	1.00
Up 101-150	7.50	0.43	0.90		-2.92	-2.29		-0.80	0.88	0.98	0.98	0.95	0.97
Up 151-190	7.50	0.42	0.88		-2.76	-2.18		-0.80	0.84	0.97	0.96	0.91	0.94
Up 191-200	7.50	0.52	0.88		-2.65	-1.57		-0.47	0.84	0.96	0.95	0.91	0.94
0.25 m after cycling	*Not available due to subsequent load test*												

Table 7-8. Summary of the Average Large Amplitude (1-m) Cyclic Response for Each Full Stroke (Half-Cycle) of Sounding MFPA_23 at the LPWA Site.

Absolute Cycle Averages

Cycle Number	Depth (m)	q_t (kPa)	u_2 (kPa)	f_s (kPa)	f_{a1} (kPa)	f_{a2} (kPa)	f_{a3} (kPa)	f_{a4} (kPa)	u_{a0} (kPa)	u_{a1} (kPa)	u_{a2} (kPa)	u_{a3} (kPa)	u_{a4} (kPa)
1 m before cycling	6.20	7607.74	41.72			103.20		92.36			38.14	35.21	26.55
virgin	7.18	8148.82	55.66			161.55		133.63			47.57	45.17	35.47
down 2	7.17	3166.30	57.03			25.70		34.80			48.14	38.13	35.33
down 3	7.18	2343.34	57.58			14.13		25.42			49.28	41.24	37.99
down 4	7.18	2373.17	57.82			9.61		23.62			49.55	42.50	38.51
down 5	7.18	2456.26	57.96			7.41		23.80			49.66	43.35	38.38
down 6	7.17	2382.20	58.30			6.33		23.35			49.46	43.66	38.47
down 7	7.18	2651.06	58.62			6.19		24.48			49.25	44.11	38.82
down 8	7.17	2675.46	58.57			5.82		23.55			49.41	44.12	38.65
down 9	7.17	2635.96	58.86			5.02		22.60			49.32	43.95	38.77
down 10	7.18	3264.29	58.96			6.86		25.73			49.25	44.38	39.06
down 11	7.17	3011.47	59.10			5.35		24.42			49.11	44.24	38.92
1 m after cycling	8.20	10898.18	55.76			103.15		61.14			60.51	58.43	50.06
up 1	7.18	-29.03	48.44			-20.98		-20.99			57.01	26.28	17.29
up 2	7.17	-2.48	47.79			-12.76		-10.29			58.70	46.87	43.33
up 3	7.18	-2.89	49.72			-5.72		-4.69			56.55	44.39	41.99
up 4	7.17	-2.53	50.16			-4.09		-3.15			54.65	44.76	42.34
up 5	7.17	-3.25	50.40			-3.48		-2.71			53.17	44.49	41.68
up 6	7.19	-0.67	51.17			-3.22		-2.22			52.59	44.74	41.72
up 7	7.19	-2.29	50.76			-3.01		-1.80			52.30	45.03	41.58
up 8	7.18	0.13	51.30			-2.54		-1.56			52.01	44.80	41.01
up 9	7.18	0.72	51.07			-2.71		-1.50			52.03	44.83	40.86
up 10	7.17	-4.45	51.30			-2.70		-1.71			51.73	44.71	40.34
up after full penetration	7.18	0.80	49.43			-6.51		-9.26			49.47	43.54	37.14

Normalized Cycle Averages

Cycle Number	Depth (m)	q_t (kPa)	u_2 (kPa)	f_s (kPa)	f_{a1} (kPa)	f_{a2} (kPa)	f_{a3} (kPa)	f_{a4} (kPa)	u_{a0} (kPa)	u_{a1} (kPa)	u_{a2} (kPa)	u_{a3} (kPa)	u_{a4} (kPa)
1 m before cycling	6.20	0.934	0.750			0.639		0.691			0.802	0.780	0.748
virgin	7.18	1.000	1.000			1.000		1.000			1.000	1.000	1.000
down 2	7.17	0.389	1.025			0.159		0.260			1.012	0.844	0.996
down 3	7.18	0.288	1.034			0.087		0.190			1.036	0.913	1.071
down 4	7.18	0.291	1.039			0.060		0.177			1.042	0.941	1.086
down 5	7.18	0.301	1.041			0.046		0.178			1.044	0.960	1.082
down 6	7.17	0.292	1.047			0.039		0.175			1.040	0.967	1.085
down 7	7.18	0.325	1.053			0.038		0.183			1.035	0.976	1.094
down 8	7.17	0.328	1.052			0.036		0.176			1.039	0.977	1.090
down 9	7.17	0.323	1.057			0.031		0.169			1.037	0.973	1.093
down 10	7.18	0.401	1.059			0.042		0.193			1.035	0.983	1.101
down 11	7.17	0.370	1.062			0.033		0.183			1.032	0.979	1.097
1 m after cycling	8.20	1.337	1.002			0.638		0.458			1.272	1.294	1.411
up 1	7.18	-0.004	0.870			-0.130		-0.157			1.198	0.582	0.487
up 2	7.17	0.000	0.859			-0.079		-0.077			1.234	1.038	1.222
up 3	7.18	0.000	0.893			-0.035		-0.035			1.189	0.983	1.184
up 4	7.17	0.000	0.901			-0.025		-0.024			1.149	0.991	1.194
up 5	7.17	0.000	0.905			-0.022		-0.020			1.118	0.985	1.175
up 6	7.19	0.000	0.919			-0.020		-0.017			1.106	0.990	1.176
up 7	7.19	0.000	0.912			-0.019		-0.013			1.099	0.997	1.172
up 8	7.18	0.000	0.922			-0.016		-0.012			1.093	0.992	1.156
up 9	7.18	0.000	0.917			-0.017		-0.011			1.094	0.992	1.152
up 10	7.17	-0.001	0.922			-0.017		-0.013			1.087	0.990	1.137
up after full penetration	7.18	0.000	0.888			-0.040		-0.069			1.040	0.964	1.047

Table 7-9. Summary of the Average Large Amplitude (1-m) Cyclic Response for Each Full Stroke (Half-Cycle) of Sounding MFPA_24 at the LPWA Site.

Cycle Averages

Cycle Number	Depth (m)	q_t (kPa)	u_2 (kPa)	f_s (kPa)	f_{a1} (kPa)	f_{a2} (kPa)	f_{a3} (kPa)	f_{a4} (kPa)	u_{a0} (kPa)	u_{a1} (kPa)	u_{a2} (kPa)	u_{a3} (kPa)	u_{a4} (kPa)
1 m before cycling	6.22	7975.414	40.802			16.449					35.553	32.232	30.716
virgin	7.21	7788.242	54.281			19.068					46.706	42.643	42.253
down 2	7.22	3212.080	54.301			7.132					45.943	40.744	41.325
down 3	7.37	2912.206	54.368			2.579					48.372	43.271	40.601
down 4	7.21	2243.243	54.800			2.999					46.994	40.600	39.777
down 5	7.21	2454.310	55.217			2.770					47.417	41.663	39.568
down 6	7.22	2721.911	55.499			2.717					47.304	42.317	39.141
down 7	7.21	2903.623	55.616			2.500					47.106	42.314	39.527
down 8	7.21	2936.801	56.179			2.506					47.596	41.524	39.624
down 9	7.22	3277.351	56.254			2.500					47.805	42.347	39.663
down 10	7.22	3483.807	56.060			2.698					47.696	42.557	39.559
down 11	7.21	3469.089	55.651			2.602					47.365	42.544	39.557
1 m after cycling	8.21	11136.377	56.310			14.645					56.774	55.318	49.093
up 1	7.21	-43.216	48.604			-9.098					49.237	25.714	33.582
up 2	7.22	8.734	47.236			-3.816					45.408	39.103	37.702
up 3	7.21	15.622	48.872			-2.803					45.082	39.271	37.795
up 4	7.22	23.443	49.341			-2.360					45.806	39.116	37.947
up 5	7.23	20.760	49.364			-2.238					46.678	39.858	37.329
up 6	7.23	27.680	49.221			-1.763					47.815	40.514	37.700
up 7	7.22	41.675	49.662			-1.438					47.321	40.101	37.776
up 8	7.21	42.879	49.822			-1.444					47.295	40.364	37.606
up 9	7.20	49.481	49.998			-1.309					47.442	40.455	37.708
up 10	7.22	51.714	49.719			-1.278					47.379	39.894	37.835
up after full penetration	7.21	27.938	47.779			-0.796					47.201	39.990	37.898

Normalized Cycle Averages

Cycle Number	Depth (m)	q_t (kPa)	u_2 (kPa)	f_s (kPa)	f_{a1} (kPa)	f_{a2} (kPa)	f_{a3} (kPa)	f_{a4} (kPa)	u_{a0} (kPa)	u_{a1} (kPa)	u_{a2} (kPa)	u_{a3} (kPa)	u_{a4} (kPa)
1 m before cycling	6.22	1.024	0.752			0.863					0.761	0.756	0.727
virgin	7.21	1.000	1.000			1.000					1.000	1.000	1.000
down 2	7.22	0.412	1.000			0.374					0.984	0.955	0.978
down 3	7.37	0.374	1.002			0.135					1.036	1.015	0.961
down 4	7.21	0.288	1.010			0.157					1.006	0.952	0.941
down 5	7.21	0.315	1.017			0.145					1.015	0.977	0.936
down 6	7.22	0.349	1.022			0.142					1.013	0.992	0.926
down 7	7.21	0.373	1.025			0.131					1.009	0.992	0.935
down 8	7.21	0.377	1.035			0.131					1.019	0.974	0.938
down 9	7.22	0.421	1.036			0.131					1.024	0.993	0.939
down 10	7.22	0.447	1.033			0.141					1.021	0.998	0.936
down 11	7.21	0.445	1.025			0.136					1.014	0.998	0.936
1 m after cycling	8.21	1.430	1.037			0.768					1.216	1.297	1.162
up 1	7.21	-0.006	0.895			-0.477					1.054	0.603	0.795
up 2	7.22	0.001	0.870			-0.200					0.972	0.917	0.892
up 3	7.21	0.002	0.900			-0.147					0.965	0.921	0.894
up 4	7.22	0.003	0.909			-0.124					0.981	0.917	0.898
up 5	7.23	0.003	0.909			-0.117					0.999	0.935	0.883
up 6	7.23	0.004	0.907			-0.092					1.024	0.950	0.892
up 7	7.22	0.005	0.915			-0.075					1.013	0.940	0.894
up 8	7.21	0.006	0.918			-0.076					1.013	0.947	0.890
up 9	7.20	0.006	0.921			-0.069					1.016	0.949	0.892
up 10	7.22	0.007	0.916			-0.067					1.014	0.936	0.895
up after full penetration	7.21	0.004	0.880			-0.042					1.011	0.938	0.897

Table 7-10. Summary of the Variable Rate CPTU-MFA Investigation Procedures Used in the Current Study.

Test ID	Depth (m)	Rate (mm/s)
1	6.030	20.00
	6.296	20.00
2	6.296	10.00
	6.384	10.00
3	6.384	5.00
	6.472	5.00
4	6.472	2.00
	6.560	2.00
5	6.560	1.00
	6.648	1.00
6	6.648	0.40
	6.736	0.40
7	6.736	0.20
	6.824	0.20
8	6.824	0.10
	6.912	0.10
9	6.912	0.04
	7.000	0.04

Table 7-11. Summary of the CPTU-MFA Responses from the Variable Rate Investigation at the BWDWA Site.

Average Values

Depth (m)	q_t (kPa)	u_2 (kPa)	f_s (kPa)	H0.25 (kPa)	H0.50 (kPa)	H1.00 (kPa)	H2.00 (kPa)	Rate mm/s	Time at Rate (H:M:S)	$V = vd/c_v$ N/A
6.162	386.919	142.935	7.174	7.489	7.418	7.335	7.536	20.00	0:00:13	5826.67
6.337	389.298	140.696	7.281	7.075	7.821	7.755	7.505	10.00	0:00:09	2913.33
6.428	392.527	144.805	7.722	7.760	8.128	7.707	7.371	5.00	0:00:17	1456.67
6.517	377.871	147.654	7.813	7.651	7.983	7.257	7.500	2.00	0:00:42	582.67
6.605	366.253	149.941	7.271	7.577	7.981	7.493	7.953	1.00	0:01:28	291.33
6.693	363.423	144.617	6.609	7.547	8.219	7.847	8.448	0.40	0:03:38	116.53
6.781	366.379	142.327	6.626	8.100	8.741	8.079	9.254	0.20	0:07:30	58.27
6.869	369.045	140.218	6.837	8.826	9.991	9.059	10.967	0.10	0:15:07	29.13
6.955	379.090	133.114	7.416	10.460	11.414	11.383	12.459	0.04	0:36:52	11.65

Normalized Values

Depth (m)	q_t (kPa)	u_2 (kPa)	f_s (kPa)	H0.25 (kPa)	H0.50 (kPa)	H1.00 (kPa)	H2.00 (kPa)	Rate mm/s	Time at Rate (H:M:S)	$V = vd/c_v$ N/A
6.162	1.00	1.00	1.00	1.00	1.00	1.00	1.00	20.00	0:00:13	5826.67
6.337	1.01	0.98	1.01	0.94	1.05	1.06	1.00	10.00	0:00:09	2913.33
6.428	1.01	1.01	1.08	1.04	1.10	1.05	0.98	5.00	0:00:17	1456.67
6.517	0.98	1.03	1.09	1.02	1.08	0.99	1.00	2.00	0:00:42	582.67
6.605	0.95	1.05	1.01	1.01	1.08	1.02	1.06	1.00	0:01:28	291.33
6.693	0.94	1.01	0.92	1.01	1.11	1.07	1.12	0.40	0:03:38	116.53
6.781	0.95	1.00	0.92	1.08	1.18	1.10	1.23	0.20	0:07:30	58.27
6.869	0.95	0.98	0.95	1.18	1.35	1.23	1.46	0.10	0:15:07	29.13
6.955	0.98	0.93	1.03	1.40	1.54	1.55	1.65	0.04	0:36:52	11.65

Deviation from Conventional Response = Response at Each Rate - Response at 20 mm/s

Depth (m)	q_t (kPa)	u_2 (kPa)	f_s (kPa)	H0.25 (kPa)	H0.50 (kPa)	H1.00 (kPa)	H2.00 (kPa)	Rate mm/s	Time at Rate (H:M:S)	$V = vd/c_v$ N/A
6.161868	0.000	0.000	0.000	0.000	0.000	0.000	0.000	20.00	0:00:13	5826.667
6.33676	2.379	-2.240	0.107	-0.413	0.402	0.420	-0.031	10.00	0:00:09	2913.333
6.427606	5.608	1.870	0.549	0.271	0.709	0.372	-0.165	5.00	0:00:17	1456.667
6.51701	-9.048	4.719	0.640	0.163	0.565	-0.077	-0.036	2.00	0:00:42	582.6667
6.605008	-20.667	7.006	0.097	0.088	0.563	0.158	0.417	1.00	0:01:28	291.3333
6.693001	-23.497	1.681	-0.565	0.059	0.800	0.512	0.912	0.40	0:03:38	116.5333
6.780594	-20.541	-0.608	-0.547	0.612	1.322	0.744	1.718	0.20	0:07:30	58.26667
6.868796	-17.874	-2.717	-0.337	1.337	2.572	1.724	3.431	0.10	0:15:07	29.13333
6.954667	-7.830	-9.822	0.242	2.972	3.996	4.048	4.923	0.04	0:36:52	11.65333

Table 7-12. Summary and Details of Previous Model Pile Investigations (after Paikowsky and Hart, 2000).

	Cone Penetrator	PLS	G&R Test Pile	NGI Test Pile	3.0-inch Model Pile	"X"-Probe	IMP	Imperial College	MDMP
Diameter (mm)	35.7	38.4	25.4	152.4	76.2	43.7	80.0	102	76.2
Length (cm)	varies	26.8 + Tip	88.9	500.4	245 + 245 Shoe	143.5	113.5	700	286.5
Load Cells Position	2 Cone/Sleeve	1 Behind Tip	None	1 Top	2 Sleeve	1 Sleeve	3 Sleeve	4 Behind/Tip/Top/Sleeve	3 Tip/Sleeve
Strain Gauges Position	None	None	4 Sleeve	6 Bottom/Sleeve	None	None	4 Sleeve	None	None
Pore Pressure Transducer Position	up to 3 Clone/Sleeve	1 Behind Tip	1 Middle of Sleeve	4 Bottom/Sleeve	1 Middle of Sleeve	1 Sleeve	3 Tip/Sleeve	3 Behind/Tip/Top	1 Middle of Sleeve
Lateral Pressure Transducer Type Position	None	1 Cylindrical Lat Stress cell Behind Tip	None	4 Bottom/Slave	1 Total Pressure Cell Middle of Sleeve	1 1-Middle	4 Total Radial Stress Sleeve	3 Behind/Tip/Sleeve	1 Total Pressure Cell Middle of Sleeve
Displacement Transducer	None	None	None	1 top	LVDT Behind Cut Shoe	1 Behind Tip	None	3 Top	LVDT Behind Cut Shoe
Accelerometer	None	None	None	None	4	None	None	None	3
Temp. Sensor	Special	Behind Tip	None	None	None	None	None	3	None
Slope Sensor	Special	None	None	None	None	None	None	None	None
Pile Type	Probe	Probe	6061 AL Tube	Steel Pipe	Steel Pipe	Probe	Steel Pipe	Steel Pipe	Steel Pipe
Testing Sites	Numerous Locations	Saugus, MA	Sabine, Texas	Oslo, Norway	CA, TX, LA B.C.	CA, TX, LA B.C.	England	Several sites in England	Newbury, MA
References	De Ruiter, 1982 Van Den Berg 1982 ASTM 3441-86 Chen & Mayne, 1994	Wissa et al., 1975 Morrison, 1984 Azzouz, 1985 Azzouz & Lutz, 1986	Grosch & Reese, 1980	Karlsrud and Haugen, 1981, 85a, 85b	Bogard & Matlock, 1985, 1990a, 1990b, 1990c	Bogard & Matlock, 1985, 1990a, 1990b, 1990c	Coop & Wroth, 1989 Lehane, 1992	Bond & Jardine, 1991, 1995 Bond et al., 1991 Jardine et al., 1992 Lehane & Jardine, 1994	Paikowsky and Hart, 2000

PLS - *Piezo-Lateral Stress (Wissa et al., 1975)*
G&R - *Grosch and Reese Model Pile (Grosch and Reese, 1980)*
NGI - *Norwegian Geotechnical Institute Model Pile (Karlsrud and Haugen, 1981)*
3" Model Pile - *Earth Technology Corporation (Bogard et al., 1985)*
X-Probe - *Earth Technology Corporation (Bogard and Matlock, 1985)*
IMP - In Situ Model Pile *(Coop and Wroth, 1989)*
Imperial - *Imperial College Pile (ICP) (Bond et al., 1991)*
MDMP - Multiple Deployment Model Pile *(Paikowsky and Hart, 2000)*

Table 7-13. Summary of the CPTU-MPFA Load Test Investigation Procedures Used in the Current Study.

Load Test #	Sounding ID #	Tip Depth (m)	Equalization Time (min)	Strain Rate (mm/s)	Short Amplitude Cycling (Y/N)
1	MPFA_25	7.5	120	0.024	N
4	MPFA_26	7.5	120	0.024	Y
2	MPFA_25	10.0	120	0.024	N
3	MPFA_26	5.0	2	0.072	Y
6	MPFA_28	5.0	2	0.072	N
7	MPFA_28	7.5	30	0.072	N
8	MPFA_28	10.0	120	0.072	N
5	MPFA_27	10.0	480	0.072	N

Table 7-14a. Summary of CPTU-MFPA Load Test Response, Sorted Chronologically.

Load Test #	Sounding ID #	Test Tip Depth (m)	Equalization Time (min)	Strain Rate (mm/s)	Short Amplitude Cycling (Y/N)	Measured Response at Failure (Disp = 43.7 mm = 1 Diameter)												Strain to Failure				
						q_t (kPa)	u_2 (kPa)	f_s (kPa)	f_{a1} (kPa)	f_{a2} (kPa)	f_{a3} (kPa)	f_{a4} (kPa)	u_{a0} (kPa)	u_{a1} (kPa)	u_{a2} (kPa)	u_{a3} (kPa)	u_{a4} (kPa)	q_t (mm)	f_{a1} (mm)	f_{a2} (mm)	f_{a3} (mm)	f_{a4} (mm)
1	MPFA_25	7.5	120	0.024	N	181.20	117.52	----	21.13	11.28	----	17.18	93.92	95.97	92.93	81.13	77.22	7.0	2.8	2.8	----	4.2
2	MPFA_25	10.0	120	0.024	N	597.17	72.56	----	22.73	10.98	----	17.86	93.37	107.23	105.42	104.47	108.51	>44	6	6	----	3.2
3	MPFA_26	5.0	2	0.072	Y	189.22	103.76	----	8.97	6.00	----	9.12	48.83	68.14	75.96	60.82	52.89	1.60	1.6	1.6	----	1.6
4	MPFA_26	7.5	120	0.024	Y	260.59	132.09	----	12.26	9.07	----	11.66	81.78	100.89	98.83	81.52	68.85	5.5	5.5	5.5	----	5.5
5	MPFA_27	10.0	480	0.072	N	660.66	88.23	----	11.94	10.00	----	11.84	76.28	77.78	90.67	75.78	84.20	>44	7.0	7.0	----	7.0
6	MPFA_28	5.0	2	0.072	N	197.48	105.02	----	11.01	6.48	----	7.85	54.25	72.11	78.00	69.13	60.92	2	2.0	2.0	----	2.0
7	MPFA_28	7.5	30	0.072	N	196.58	138.76	----	12.21	10.78	----	11.29	97.08	101.25	97.47	84.35	81.83	4.50	5.0	5.0	----	5.0
8	MPFA_28	10.0	120	0.072	N	769.98	87.64	----	11.05	6.87	----	9.36	103.03	119.00	138.96	116.11	118.84	>44	4.0	4.0	----	4.0

[*] *Note that for load tests conducted at 10 m the CPTU sensors appear to be in a different strata.*

[+] *Note that load test #2 is a repeat of load test #1 since the head load was not released in test #1*

Load Test #	Sounding ID #	Test Tip Depth (m)	Equalization Time (min)	Strain Rate (mm/s)	Short Amplitude Cycling (Y/N)	Variation from Initial to Failure Response												Strain to Failure				
						q_t (kPa)	u_2 (kPa)	f_s (kPa)	f_{a1} (kPa)	f_{a2} (kPa)	f_{a3} (kPa)	f_{a4} (kPa)	u_{a0} (kPa)	u_{a1} (kPa)	u_{a2} (kPa)	u_{a3} (kPa)	u_{a4} (kPa)	q_t (mm)	f_{a1} (mm)	f_{a2} (mm)	f_{a3} (mm)	f_{a4} (mm)
1	MPFA_25	7.5	120	0.024	N	128.71	13.99	----	6.05	6.15	----	7.69	-0.47	4.51	1.84	2.90	1.01	7.0	2.8	2.8	----	4.2
2	MPFA_25	10.0	120	0.024	N	473.18	-8.36	----	24.37	10.71	----	20.30	-6.06	0.21	-1.00	-3.01	-5.79	>44	6	6	----	3.2
3	MPFA_26	5.0	2	0.072	Y	92.02	9.99	----	5.51	4.45	----	4.35	-12.85	-5.20	-4.83	-7.18	-6.73	1.60	1.6	1.6	----	1.6
4	MPFA_26	7.5	120	0.024	Y	139.73	27.48	----	20.88	10.22	----	9.60	-0.93	2.73	0.34	1.32	2.77	5.5	5.5	5.5	----	5.5
5	MPFA_27	10.0	480	0.072	N	383.42	1.30	----	10.83	13.52	----	14.56	-7.81	-9.58	3.95	-3.34	5.75	>44	7.0	7.0	----	7.0
6	MPFA_28	5.0	2	0.072	N	76.64	-10.15	----	7.16	4.04	----	5.13	-25.46	-12.47	-7.79	-6.76	-10.21	2	2.0	2.0	----	2.0
7	MPFA_28	7.5	30	0.072	N	77.23	30.73	----	9.74	9.16	----	9.12	1.97	4.59	3.55	4.29	4.57	4.50	5.0	5.0	----	5.0
8	MPFA_28	10.0	120	0.072	N	513.56	0.48	----	12.70	6.87	----	7.19	-6.67	-12.83	-3.19	-3.50	-10.22	>44	4.0	4.0	----	4.0

[*] *Note that for load tests conducted at 10 m the CPTU sensors appear to be in a different strata.*

[+] *Note that load test #2 is a repeat of load test #1 since the head load was not released in test #1*

Table 7-14b. Summary of CPTU-MFPA Load Test Response, Sorted by Tip Depth.

Load Test #	Sounding ID #	Test Tip Depth (m)	Equalization Time (min)	Strain Rate (mm/s)	Short Amplitude Cycling (Y/N)	Measured Response at Failure (Disp = 43.7 mm = 1 Diameter)												Strain to Failure				
						q_t (kPa)	u_2 (kPa)	f_s (kPa)	f_{a1} (kPa)	f_{a2} (kPa)	f_{a3} (kPa)	f_{a4} (kPa)	u_{a0} (kPa)	u_{a1} (kPa)	u_{a2} (kPa)	u_{a3} (kPa)	u_{a4} (kPa)	q_t (mm)	f_{a1} (mm)	f_{a2} (mm)	f_{a3} (mm)	f_{a4} (mm)
3	MPFA_26	5.0	2	0.072	Y	189.22	103.76	----	8.97	6.00	----	9.12	48.83	68.14	75.96	60.82	52.89	1.6	1.6	1.6	----	1.6
6	MPFA_28	5.0	2	0.072	N	197.48	105.02	----	11.01	6.48	----	7.85	54.25	72.11	78.00	69.13	60.92	2	2	2	----	2
1	MPFA_25	7.5	120	0.024	N	181.20	117.52	----	21.13	11.28	----	17.18	93.92	95.97	92.93	81.13	77.22	7.00	2.8	2.8	----	4.2
4	MPFA_26	7.5	120	0.024	Y	260.59	132.09	----	12.26	9.07	----	11.66	81.78	100.89	98.83	81.52	68.85	5.5	5.5	5.5	----	5.5
7	MPFA_28	7.5	30	0.072	N	196.58	138.76	----	12.21	10.78	----	11.29	97.08	101.25	97.47	84.35	81.83	4.5	5.0	5.0	----	5.0
2	MPFA_25	10.0	120	0.024	N	597.17	72.56	----	22.73	10.98	----	17.86	93.37	107.23	105.42	104.47	108.51	>44	6.0	6.0	----	3.2
5	MPFA_27	10.0	480	0.072	N	660.66	88.23	----	11.94	10.00	----	11.84	76.28	77.78	90.67	75.78	84.20	>44	7.0	7.0	----	7.0
8	MPFA_28	10.0	120	0.072	N	769.98	87.64	----	11.05	6.87	----	9.36	103.03	119.00	138.96	116.11	118.84	>44	4.0	4.0	----	4.0

[*] *Note that for load tests conducted at 10 m the CPTU sensors appear to be in a different strata.*

[+] *Note that load test #2 is a repeat of load test #1 since the head load was not released in test #1*

Load Test #	Sounding ID #	Test Tip Depth (m)	Equalization Time (min)	Strain Rate (mm/s)	Short Amplitude Cycling (Y/N)	Variation from Initial to Failure Response												Strain to Failure				
						q_t (kPa)	u_2 (kPa)	f_s (kPa)	f_{a1} (kPa)	f_{a2} (kPa)	f_{a3} (kPa)	f_{a4} (kPa)	u_{a0} (kPa)	u_{a1} (kPa)	u_{a2} (kPa)	u_{a3} (kPa)	u_{a4} (kPa)	q_t (mm)	f_{a1} (mm)	f_{a2} (mm)	f_{a3} (mm)	f_{a4} (mm)
3	MPFA_26	5.0	2	0.072	Y	92.02	9.99	----	5.51	4.45	----	4.35	-12.85	-5.20	-4.83	-7.18	-6.73	1.6	1.6	1.6	----	1.6
6	MPFA_28	5.0	2	0.072	N	76.64	-10.15	----	7.16	4.04	----	5.13	-25.46	-12.47	-7.79	-6.76	-10.21	2	2	2	----	2
1	MPFA_25	7.5	120	0.024	N	128.71	13.99	----	6.05	6.15	----	7.69	-0.47	4.51	1.84	2.90	1.01	7.00	2.8	2.8	----	4.2
4	MPFA_26	7.5	120	0.024	Y	139.73	27.48	----	20.88	10.22	----	9.60	-0.93	2.73	0.34	1.32	2.77	5.5	5.5	5.5	----	5.5
7	MPFA_28	7.5	30	0.072	N	77.23	30.73	----	9.74	9.16	----	9.12	1.97	4.59	3.55	4.29	4.57	4.5	5.0	5.0	----	5.0
2	MPFA_25	10.0	120	0.024	N	473.18	-8.36	----	24.37	10.71	----	20.30	-6.06	0.21	-1.00	-3.01	-5.79	>44	6.0	6.0	----	3.2
5	MPFA_27	10.0	480	0.072	N	383.42	1.30	----	10.83	13.52	----	14.56	-7.81	-9.58	3.95	-3.34	5.75	>44	7.0	7.0	----	7.0
8	MPFA_28	10.0	120	0.072	N	513.56	0.48	----	12.70	6.87	----	7.19	-6.67	-12.83	-3.19	-3.50	-10.22	>44	4.0	4.0	----	4.0

[*] *Note that for load tests conducted at 10 m the CPTU sensors appear to be in a different strata.*

[+] *Note that load test #2 is a repeat of load test #1 since the head load was not released in test #1*

Table 7-14c. Summary of CPTU-MFPA Load Test Response, Sorted by Strain Rate.

Load Test #	Sounding ID #	Test Tip Depth (m)	Equalization Time (min)	Strain Rate (mm/s)	Short Amplitude Cycling (Y/N)	Measured Response at Failure (Disp = 43.7 mm = 1 Diameter)												Strain to Failure				
						q_t (kPa)	u_2 (kPa)	f_s (kPa)	f_{a1} (kPa)	f_{a2} (kPa)	f_{a3} (kPa)	f_{a4} (kPa)	u_{a0} (kPa)	u_{a1} (kPa)	u_{a2} (kPa)	u_{a3} (kPa)	u_{a4} (kPa)	q_t (mm)	f_{a1} (mm)	f_{a2} (mm)	f_{a3} (mm)	f_{a4} (mm)
1	MPFA_25	7.5	120	0.024	N	181.20	117.52	----	21.13	11.28	----	17.18	93.92	95.97	92.93	81.13	77.22	7.0	2.8	2.8	----	4.2
4	MPFA_26	7.5	120	0.024	Y	260.59	132.09	----	12.26	9.07	----	11.66	81.78	100.89	98.83	81.52	68.85	5.5	5.5	5.5	----	5.5
2	MPFA_25	10.0	120	0.024	N	597.17	72.56	----	22.73	10.98	----	17.86	93.37	107.23	105.42	104.47	108.51	>44	6.0	6.0	----	3.2
3	MPFA_26	5.0	2	0.072	Y	189.22	103.76	----	8.97	6.00	----	9.12	48.83	68.14	75.96	60.82	52.89	1.6	1.6	1.6	----	1.6
6	MPFA_28	5.0	2	0.072	N	197.48	105.02	----	11.01	6.48	----	7.85	54.25	72.11	78.00	69.13	60.92	2.0	2.0	2.0	----	2.0
7	MPFA_28	7.5	30	0.072	N	196.58	138.76	----	12.21	10.78	----	11.29	97.08	101.25	97.47	84.35	81.83	4.5	5.0	5.0	----	5.0
8	MPFA_28	10.0	120	0.072	N	769.98	87.64	----	11.05	6.87	----	9.36	103.03	119.00	138.96	116.11	118.84	>44	4.0	4.0	----	4.0
5	MPFA_27	10.0	480	0.072	N	660.66	88.23	----	11.94	10.00	----	11.84	76.28	77.78	90.67	75.78	84.20	>44	7.0	7.0	----	7.0

[*] *Note that for load tests conducted at 10 m the CPTU sensors appear to be in a different strata.*

[+] *Note that load test #2 is a repeat of load test #1 since the head load was not released in test #1*

Load Test #	Sounding ID #	Test Tip Depth (m)	Equalization Time (min)	Strain Rate (mm/s)	Short Amplitude Cycling (Y/N)	Variation from Initial to Failure Response												Strain to Failure				
						q_t (kPa)	u_2 (kPa)	f_s (kPa)	f_{a1} (kPa)	f_{a2} (kPa)	f_{a3} (kPa)	f_{a4} (kPa)	u_{a0} (kPa)	u_{a1} (kPa)	u_{a2} (kPa)	u_{a3} (kPa)	u_{a4} (kPa)	q_t (mm)	f_{a1} (mm)	f_{a2} (mm)	f_{a3} (mm)	f_{a4} (mm)
1	MPFA_25	7.5	120	0.024	N	128.71	13.99	----	6.05	6.15	----	7.69	-0.47	4.51	1.84	2.90	1.01	7.0	2.8	2.8	----	4.2
4	MPFA_26	7.5	120	0.024	Y	139.73	27.48	----	20.88	10.22	----	9.60	-0.93	2.73	0.34	1.32	2.77	5.5	5.5	5.5	----	5.5
2	MPFA_25	10.0	120	0.024	N	473.18	-8.36	----	24.37	10.71	----	20.30	-6.06	0.21	-1.00	-3.01	-5.79	>44	6.0	6.0	----	3.2
3	MPFA_26	5.0	2	0.072	Y	92.02	9.99	----	5.51	4.45	----	4.35	-12.85	-5.20	-4.83	-7.18	-6.73	1.6	1.6	1.6	----	1.6
6	MPFA_28	5.0	2	0.072	N	76.64	-10.15	----	7.16	4.04	----	5.13	-25.46	-12.47	-7.79	-6.76	-10.21	2.0	2.0	2.0	----	2.0
7	MPFA_28	7.5	30	0.072	N	77.23	30.73	----	9.74	9.16	----	9.12	1.97	4.59	3.55	4.29	4.57	4.5	5.0	5.0	----	5.0
8	MPFA_28	10.0	120	0.072	N	513.56	0.48	----	12.70	6.87	----	7.19	-6.67	-12.83	-3.19	-3.50	-10.22	>44	4.0	4.0	----	4.0
5	MPFA_27	10.0	480	0.072	N	383.42	1.30	----	10.83	13.52	----	14.56	-7.81	-9.58	3.95	-3.34	5.75	>44	7.0	7.0	----	7.0

[*] *Note that for load tests conducted at 10 m the CPTU sensors appear to be in a different strata.*

[+] *Note that load test #2 is a repeat of load test #1 since the head load was not released in test #1*

Table 7-14d. Summary of CPTU-MFPA Load Test Response, Sorted by Equalization Time.

Load Test #	Sounding ID #	Test Tip Depth (m)	Equalization Time (min)	Strain Rate (mm/s)	Short Amplitude Cycling (Y/N)	Measured Response at Failure (Disp = 43.7 mm = 1 Diameter)												Strain to Failure				
						q_t (kPa)	u_2 (kPa)	f_s (kPa)	f_{a1} (kPa)	f_{a2} (kPa)	f_{a3} (kPa)	f_{a4} (kPa)	u_{a0} (kPa)	u_{a1} (kPa)	u_{a2} (kPa)	u_{a3} (kPa)	u_{a4} (kPa)	q_t (mm)	f_{a1} (mm)	f_{a2} (mm)	f_{a3} (mm)	f_{a4} (mm)
3	MPFA_26	5.0	2	0.072	Y	189.22	103.76	----	8.97	6.00	----	9.12	48.83	68.14	75.96	60.82	52.89	1.6	1.6	1.6	----	1.6
6	MPFA_28	5.0	2	0.072	N	197.48	105.02	----	11.01	6.48	----	7.85	54.25	72.11	78.00	69.13	60.92	2	2	2	----	2
7	MPFA_28	7.5	30	0.072	N	196.58	138.76	----	12.21	10.78	----	11.29	97.08	101.25	97.47	84.35	81.83	4.50	5.0	5.0	----	5.0
1	MPFA_25	7.5	120	0.024	N	181.20	117.52	----	21.13	11.28	----	17.18	93.92	95.97	92.93	81.13	77.22	7	2.8	2.8	----	4.2
2	MPFA_25	10.0	120	0.024	N	597.17	72.56	----	22.73	10.98	----	17.86	93.37	107.23	105.42	104.47	108.51	>44	6.0	6.0	----	3.2
4	MPFA_26	7.5	120	0.024	Y	260.59	132.09	----	12.26	9.07	----	11.66	81.78	100.89	98.83	81.52	68.85	5.5	5.5	5.5	----	5.5
8	MPFA_28	10.0	120	0.072	N	769.98	87.64	----	11.05	6.87	----	9.36	103.03	119.00	138.96	116.11	118.84	>44	4.0	4.0	----	4.0
5	MPFA_27	10.0	480	0.072	N	660.66	88.23	----	11.94	10.00	----	11.84	76.28	77.78	90.67	75.78	84.20	>44	7.0	7.0	----	7.0

[*] *Note that for load tests conducted at 10 m the CPTU sensors appear to be in a different strata.*

[+] *Note that load test #2 is a repeat of load test #1 since the head load was not released in test #1*

Load Test #	Sounding ID #	Test Tip Depth (m)	Equalization Time (min)	Strain Rate (mm/s)	Short Amplitude Cycling (Y/N)	Variation from Initial to Failure Response												Strain to Failure				
						q_t (kPa)	u_2 (kPa)	f_s (kPa)	f_{a1} (kPa)	f_{a2} (kPa)	f_{a3} (kPa)	f_{a4} (kPa)	u_{a0} (kPa)	u_{a1} (kPa)	u_{a2} (kPa)	u_{a3} (kPa)	u_{a4} (kPa)	q_t (mm)	f_{a1} (mm)	f_{a2} (mm)	f_{a3} (mm)	f_{a4} (mm)
3	MPFA_26	5.0	2	0.072	Y	92.02	9.99	----	5.51	4.45	----	4.35	-12.85	-5.20	-4.83	-7.18	-6.73	1.6	1.6	1.6	----	1.6
6	MPFA_28	5.0	2	0.072	N	76.64	-10.15	----	7.16	4.04	----	5.13	-25.46	-12.47	-7.79	-6.76	-10.21	2	2	2	----	2
7	MPFA_28	7.5	30	0.072	N	77.23	30.73	----	9.74	9.16	----	9.12	1.97	4.59	3.55	4.29	4.57	4.50	5.0	5.0	----	5.0
1	MPFA_25	7.5	120	0.024	N	128.71	13.99	----	6.05	6.15	----	7.69	-0.47	4.51	1.84	2.90	1.01	7	2.8	2.8	----	4.2
2	MPFA_25	10.0	120	0.024	N	473.18	-8.36	----	24.37	10.71	----	20.30	-6.06	0.21	-1.00	-3.01	-5.79	>44	6.0	6.0	----	3.2
4	MPFA_26	7.5	120	0.024	Y	139.73	27.48	----	20.88	10.22	----	9.60	-0.93	2.73	0.34	1.32	2.77	5.5	5.5	5.5	----	5.5
8	MPFA_28	10.0	120	0.072	N	513.56	0.48	----	12.70	6.87	----	7.19	-6.67	-12.83	-3.19	-3.50	-10.22	>44	4.0	4.0	----	4.0
5	MPFA_27	10.0	480	0.072	N	383.42	1.30	----	10.83	13.52	----	14.56	-7.81	-9.58	3.95	-3.34	5.75	>44	7.0	7.0	----	7.0

[*] *Note that for load tests conducted at 10 m the CPTU sensors appear to be in a different strata.*

[+] *Note that load test #2 is a repeat of load test #1 since the head load was not released in test #1*

Table 7-15. Comparison of Load Test Response at Failure to Monotonic Penetration Response.

Load Test #	Sounding ID #	Test Tip Depth (m)	Equalization Time (min)	Strain Rate (mm/s)	Short Amplitude Cycling (Y/N)	Monotonic Response 0.25 m Prior to Each Load Test											
						q_t (kPa)	u_2 (kPa)	f_s (kPa)	f_{a1} (kPa)	f_{a2} (kPa)	f_{a3} (kPa)	f_{a4} (kPa)	u_{a0} (kPa)	u_{a1} (kPa)	u_{a2} (kPa)	u_{a3} (kPa)	u_{a4} (kPa)
3	MPFA_26	5.0	2	0.072	Y	238.31	120.46	----	9.27	5.63	----	11.86	63.88	80.28	86.88	74.21	50.41
6	MPFA_28	5.0	2	0.072	N	237.18	123.28	----	9.07	5.66	----	9.06	72.71	79.95	85.05	74.25	45.79
1	MPFA_25	7.5	120	0.024	N	204.4	170.8	----	22.18	9.01	----	14.67	100.80	109.23	102.27	90.73	89.74
4	MPFA_26	7.5	120	0.024	Y	281.74	175.72	----	12.12	7.29	----	9.03	90.61	120.35	119.49	108.16	79.16
7	MPFA_28	7.5	30	0.072	N	295.19	169.06	----	12.32	7.98	----	8.12	109.52	116.23	117.61	94.94	75.74
2	MPFA_25	10.0	120	0.024	N	249.94	232.16	----	16.93	4.92	----	17.01	147.64	145.75	138.20	129.84	131.77
5	MPFA_27	10.0	480	0.072	N	358.90	178.43	----	7.45	2.16	----	9.54	128.42	155.67	141.91	129.75	130.16
8	MPFA_28	10.0	120	0.072	N	378.92	189.40	----	6.69	5.01	----	11.62	149.04	148.50	131.45	122.69	125.40

Load Test #	Sounding ID #	Test Tip Depth (m)	Equalization Time (min)	Strain Rate (mm/s)	Short Amplitude Cycling (Y/N)	Load Test Response at Disp = 43.7 mm = 1 Diameter											
						q_t (kPa)	u_2 (kPa)	f_s (kPa)	f_{a1} (kPa)	f_{a2} (kPa)	f_{a3} (kPa)	f_{a4} (kPa)	u_{a0} (kPa)	u_{a1} (kPa)	u_{a2} (kPa)	u_{a3} (kPa)	u_{a4} (kPa)
3	MPFA_26	5.0	2	0.072	Y	189.22	103.76	----	8.97	6.00	----	9.12	48.83	68.14	75.96	60.82	52.89
6	MPFA_28	5.0	2	0.072	N	197.48	105.02	----	11.01	6.48	----	7.85	54.25	72.11	78.00	69.13	60.92
1	MPFA_25	7.5	120	0.024	N	181.20	117.52	----	21.13	11.28	----	17.18	93.92	95.97	92.93	81.13	77.22
4	MPFA_26	7.5	120	0.024	Y	260.59	132.09	----	12.26	9.07	----	11.66	81.78	100.89	98.83	81.52	68.85
7	MPFA_28	7.5	30	0.072	N	196.58	138.76	----	12.21	10.78	----	11.29	97.08	101.25	97.47	84.35	81.83
2	MPFA_25	10.0	120	0.024	N	597.17	72.56	----	22.73	10.98	----	17.86	93.37	107.23	105.42	104.47	108.51
5	MPFA_27	10.0	480	0.072	N	660.66	88.23	----	11.94	10.00	----	11.84	76.28	77.78	90.67	75.78	84.20
8	MPFA_28	10.0	120	0.072	N	769.98	87.64	----	11.05	6.87	----	9.36	103.03	119.00	138.96	116.11	118.84

Load Test #	Sounding ID #	Test Tip Depth (m)	Equalization Time (min)	Strain Rate (mm/s)	Short Amplitude Cycling (Y/N)	Percent Increase in Final Load Test Response over Monotonic Response											
						q_t (%)	u_2 (%)	f_s (%)	f_{a1} (%)	f_{a2} (%)	f_{a3} (%)	f_{a4} (%)	u_{a0} (%)	u_{a1} (%)	u_{a2} (%)	u_{a3} (%)	u_{a4} (%)
3	MPFA_26	5.0	2	0.072	Y	-20.60	-13.87	----	-3.26	6.55	----	-23.05	-23.56	-15.12	-12.57	-18.04	4.92
6	MPFA_28	5.0	2	0.072	N	-16.74	-14.81	----	21.41	14.57	----	-13.41	-25.39	-9.81	-8.29	-6.90	33.03
1	MPFA_25	7.5	120	0.024	N	-11.36	-31.19	----	-4.74	25.18	----	17.09	-6.83	-12.14	-9.14	-10.57	-13.95
4	MPFA_26	7.5	120	0.024	Y	-7.51	-24.83	----	1.13	24.39	----	29.18	-9.74	-16.17	-17.29	-24.63	-13.02
7	MPFA_28	7.5	30	0.072	N	-33.40	-17.92	----	-0.88	35.12	----	39.13	-11.36	-12.89	-17.13	-11.16	8.04
2	MPFA_25	10.0	120	0.024	N	138.93	-68.75	----	34.25	123.01	----	4.99	-36.76	-26.43	-23.72	-19.54	-17.65
5	MPFA_27	10.0	480	0.072	N	84.08	-50.55	----	60.28	361.99	----	24.15	-40.60	-50.04	-36.11	-41.59	-35.31
8	MPFA_28	10.0	120	0.072	N	103.20	-53.73	----	65.23	37.09	----	-19.44	-30.87	-19.86	5.71	-5.37	-5.23

Load Test #	Sounding ID #	Test Tip Depth (m)	Equalization Time (min)	Strain Rate (mm/s)	Short Amplitude Cycling (Y/N)	Increase in Final Load Test Response over Monotonic Response											
						q_t (kPa)	u_2 (kPa)	f_s (kPa)	f_{a1} (kPa)	f_{a2} (kPa)	f_{a3} (kPa)	f_{a4} (kPa)	u_{a0} (kPa)	u_{a1} (kPa)	u_{a2} (kPa)	u_{a3} (kPa)	u_{a4} (kPa)
3	MPFA_26	5.0	2	0.072	Y	-49.10	-16.71	----	-0.30	0.37	----	-2.73	-15.05	-12.14	-10.92	-13.39	2.48
6	MPFA_28	5.0	2	0.072	N	-39.70	-18.26	----	1.94	0.82	----	-1.22	-18.46	-7.84	-7.06	-5.12	15.13
1	MPFA_25	7.5	120	0.024	N	-23.23	-53.27	----	-1.05	2.27	----	2.51	-6.88	-13.26	-9.34	-9.59	-12.52
4	MPFA_26	7.5	120	0.024	Y	-21.15	-43.63	----	0.14	1.78	----	2.63	-8.83	-19.46	-20.66	-26.64	-10.31
7	MPFA_28	7.5	30	0.072	N	-98.61	-30.30	----	-0.11	2.80	----	3.18	-12.44	-14.98	-20.14	-10.59	6.09
2	MPFA_25	10.0	120	0.024	N	347.24	-159.60	----	5.80	6.06	----	0.85	-54.27	-38.52	-32.78	-25.37	-23.26
5	MPFA_27	10.0	480	0.072	N	301.76	-90.20	----	4.49	7.84	----	2.30	-52.13	-77.89	-51.24	-53.97	-45.96
8	MPFA_28	10.0	120	0.072	N	391.06	-101.76	----	4.36	1.86	----	-2.26	-46.00	-29.50	7.51	-6.58	-6.56

[*] *Note that for load tests conducted at 10 m the CPTU sensors appear to be in a different strata.*

[+] *Note that load test #2 is a repeat of load test #1 since the head load was not released in test #1*

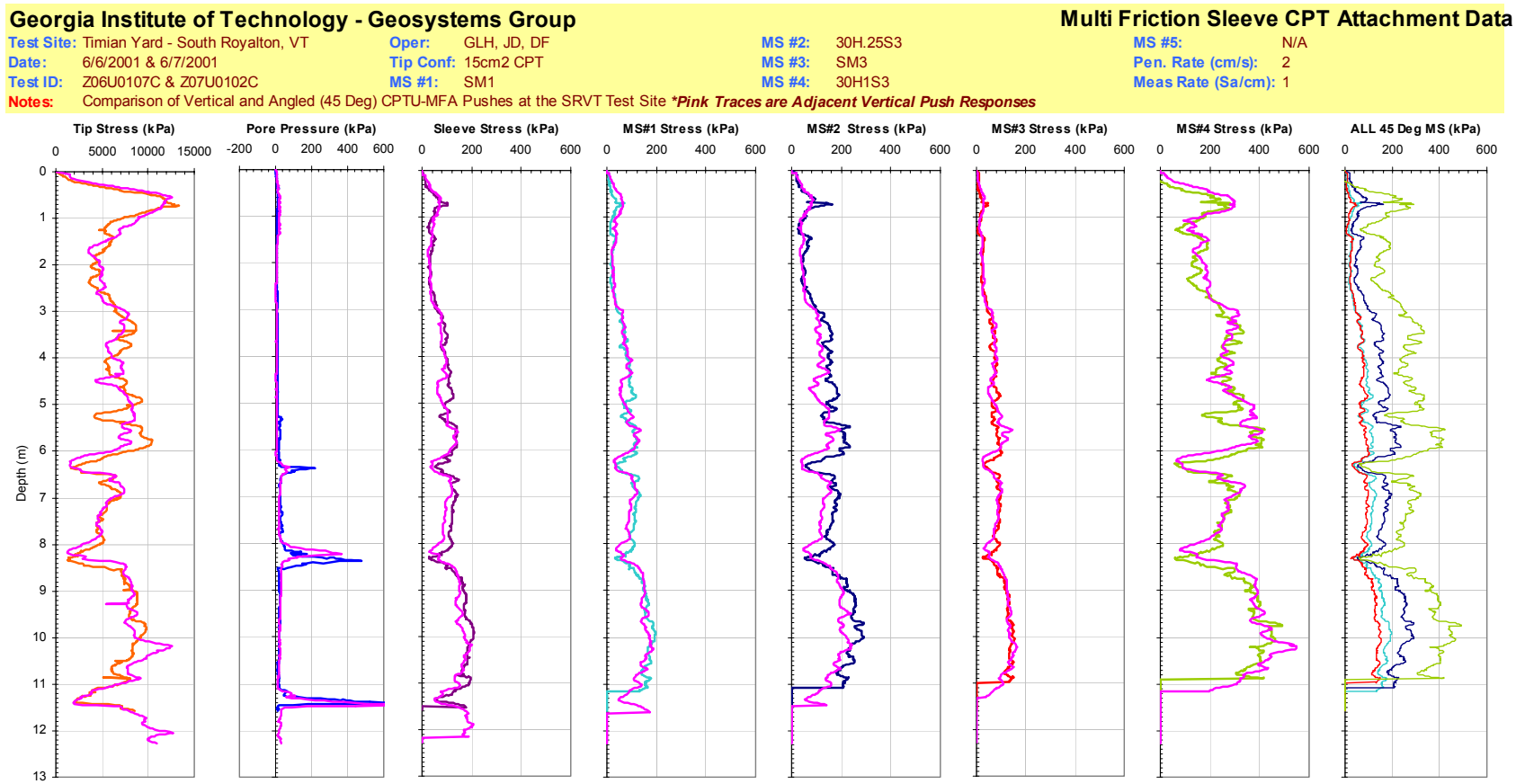

Figure 7-1. Comparison of Adjacent Vertical (Pink Traces) and Angled (45° - Multicolor Traces) CPTU-MFA Soundings from the SRVT Test Site.

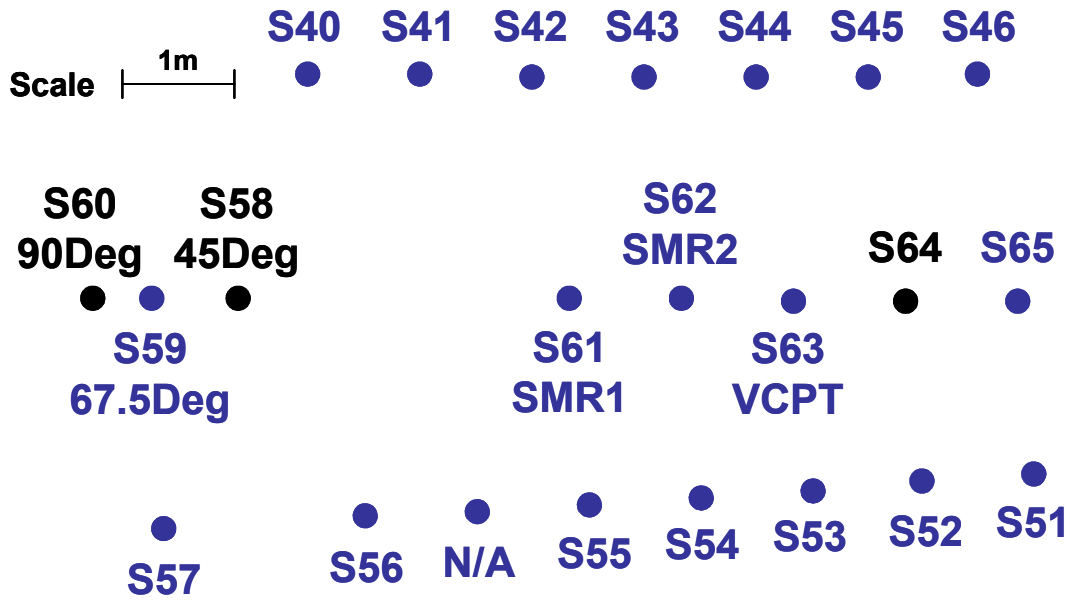

Figure 7-2. Site Plan of the Location of Inclined CPTU-MFA Soundings (S58 and S59) Conducted at the SRVT Test Site.

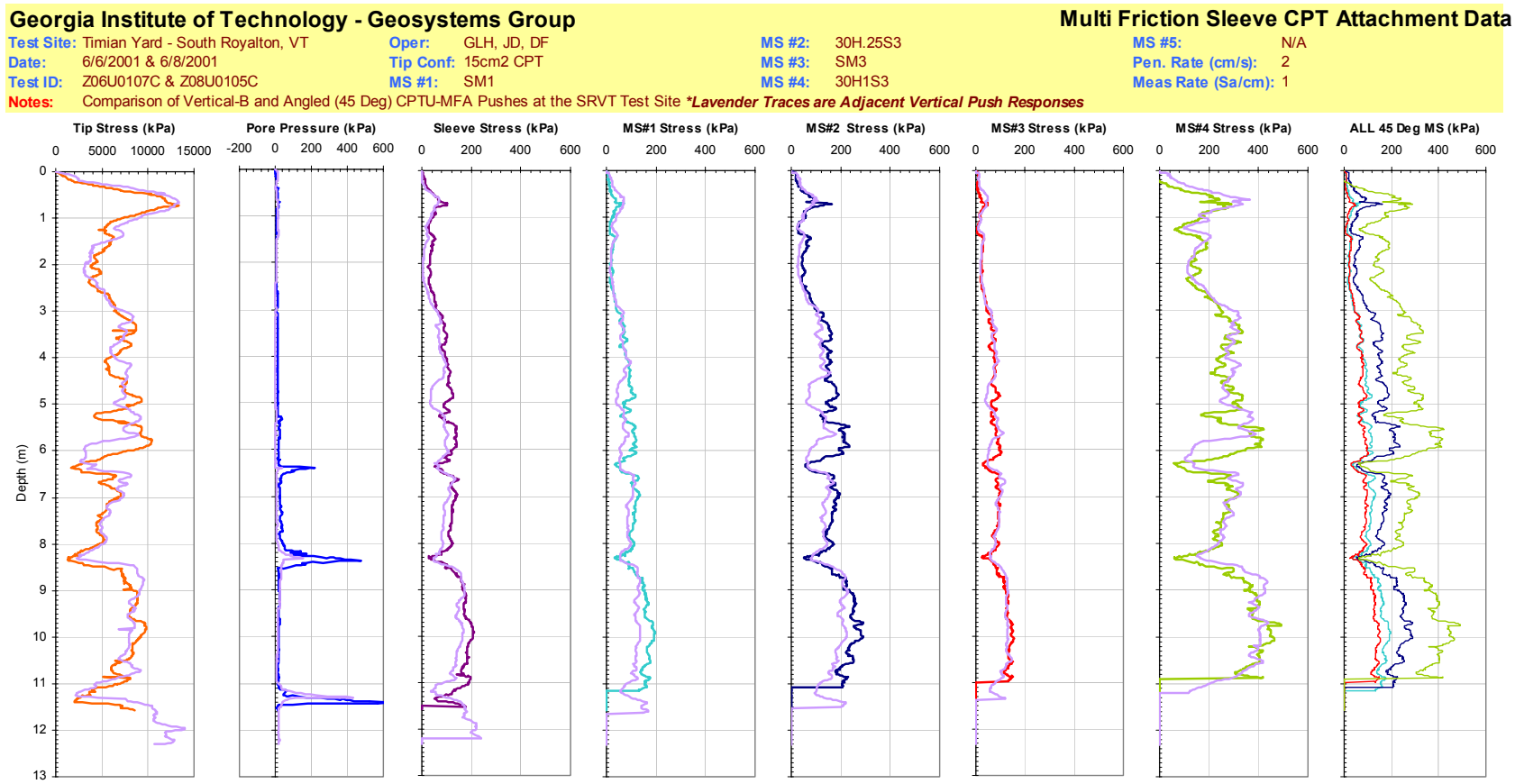

Figure 7-3. Comparison of Nearby Vertical (Lavender Traces) and Angled (45° - Multicolor Traces) CPTU-MFA Soundings from the SRVT Test Site.

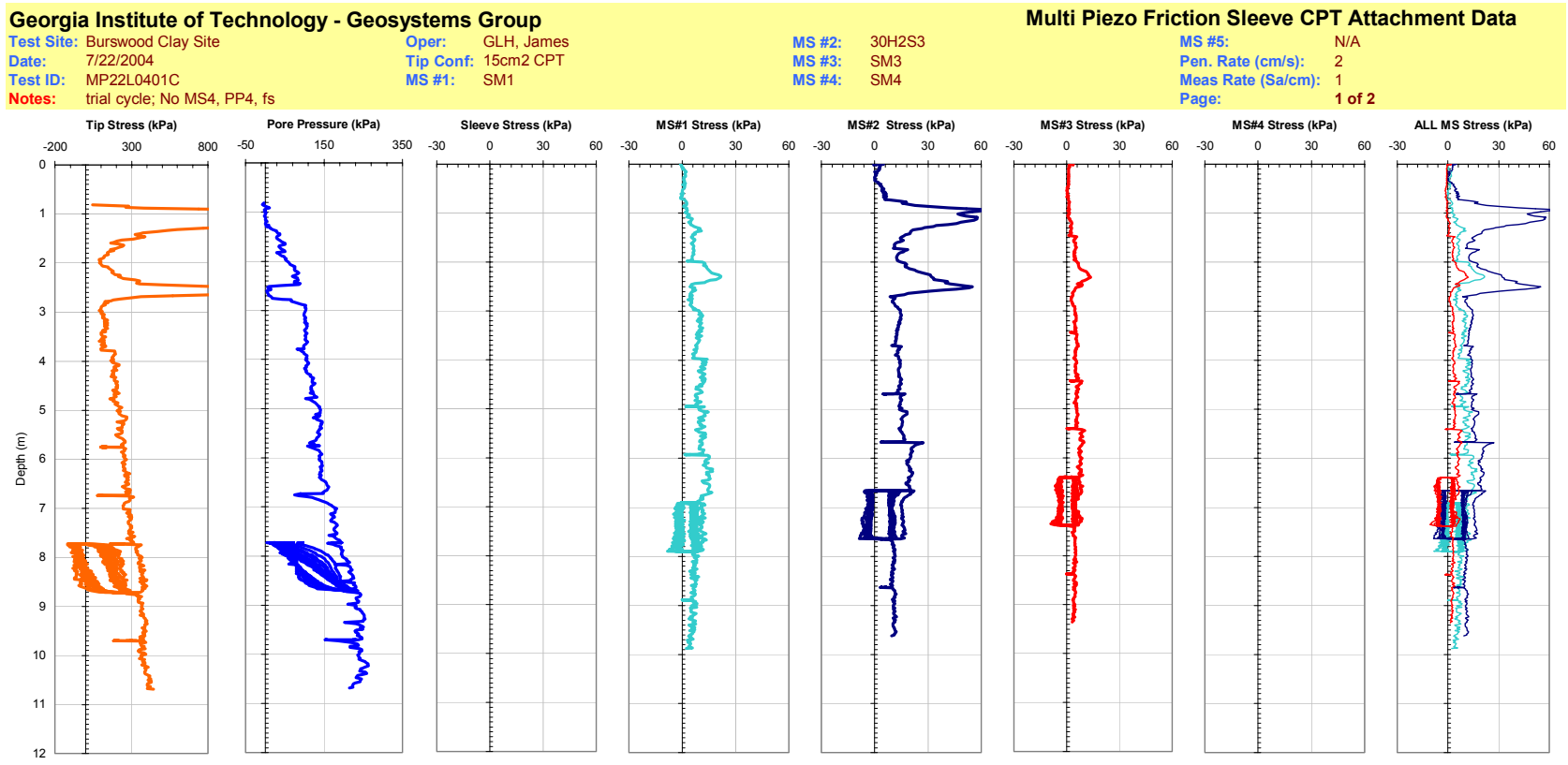

Figure 7-4a. Plots of all CPTU and the MPFA Friction Sensors from Sounding MPFA_10 at the BWDWA Site. Note the Large Amplitude (1 m) Cyclic Investigation from Tip Depths of 7.7 to 8.7 m.

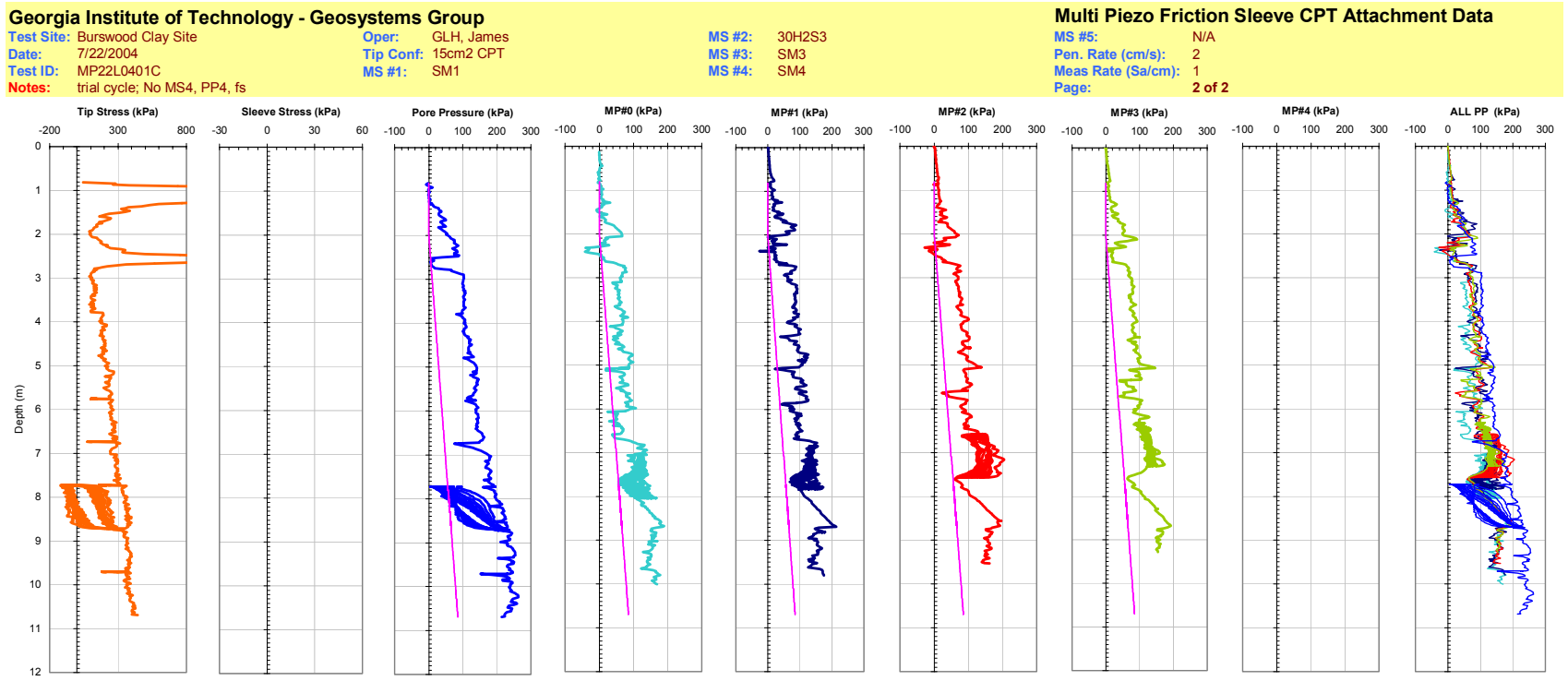

Figure 7-4b. Plots of all CPTU and the MPFA Piezo Sensors from Sounding MPFA_10 at the BWDWA Site. Note the Large Amplitude (1 m) Cyclic Investigation from Tip Depths of 7.7 to 8.7 m.

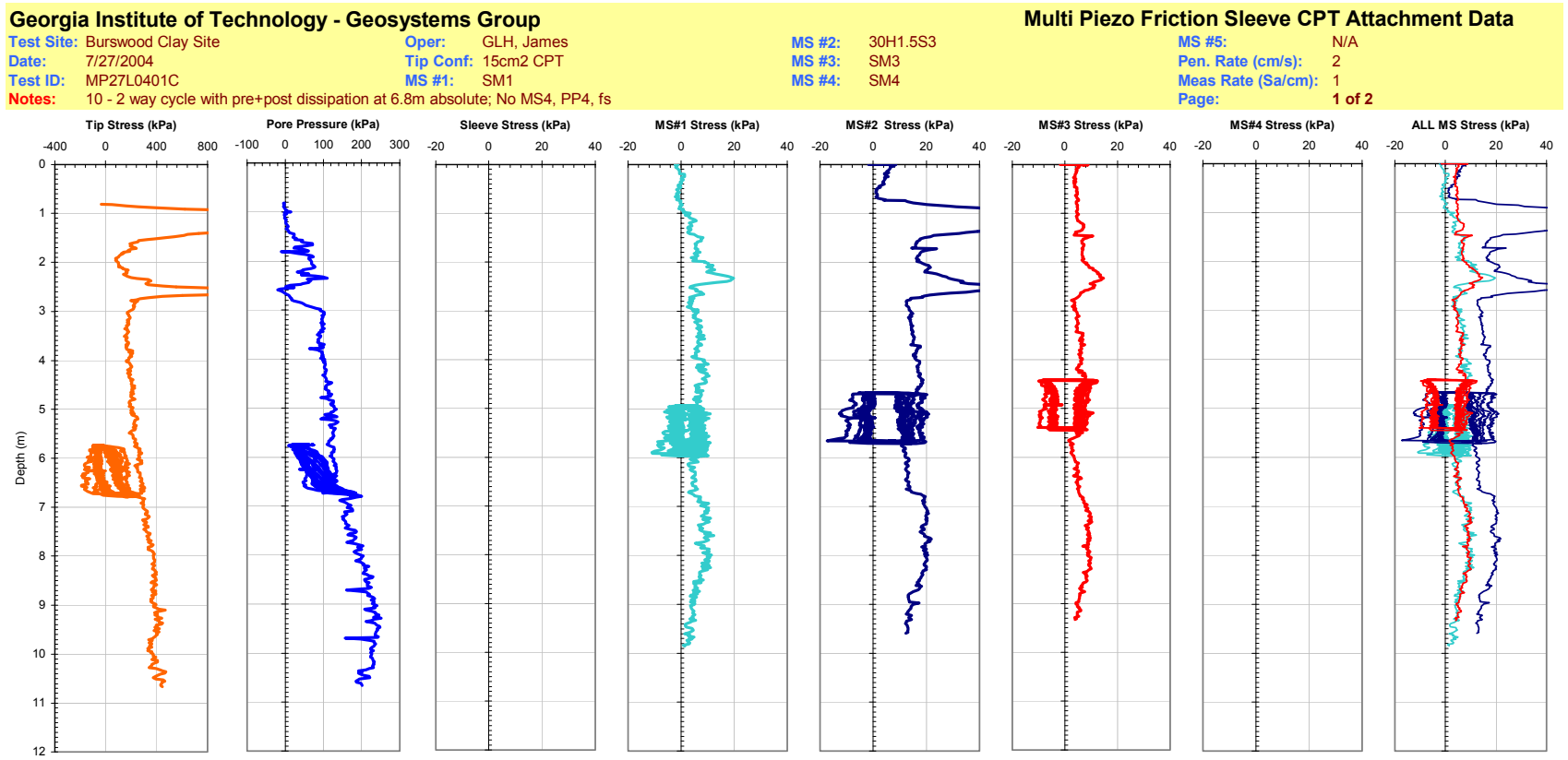

Figure 7-5a. Plots of all CPTU and the MPFA Friction Sensors from Sounding MPFA_11 at the BWDWA Site. Note the Large Amplitude (1 m) Cyclic Investigation from Tip Depths of 6.8 to 7.8 m.

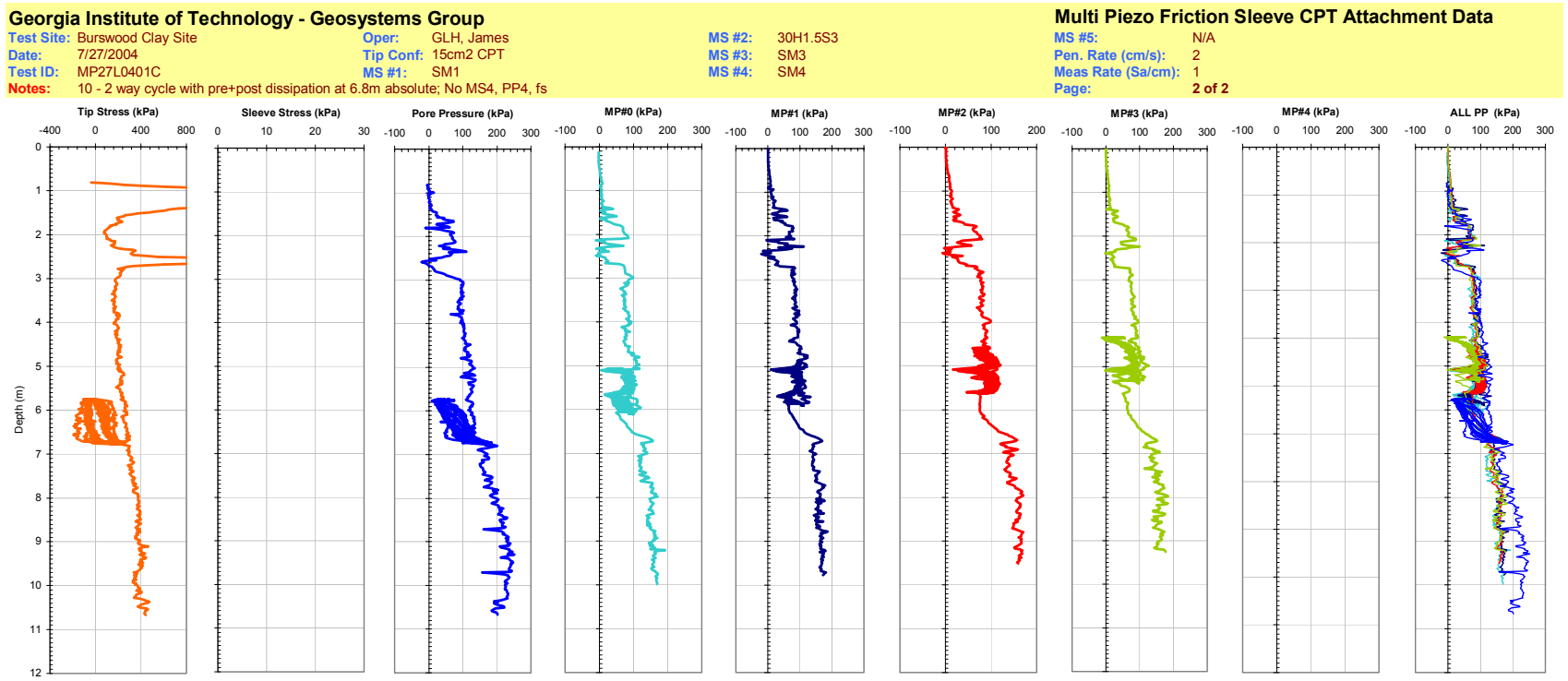

Figure 7-5b. Plots of all CPTU and the MPFA Piezo Sensors from Sounding MPFA_11 at the BWDWA Site. Note the Large Amplitude (1 m) Cyclic Investigation from Tip Depths of 6.8 to 7.8 m.

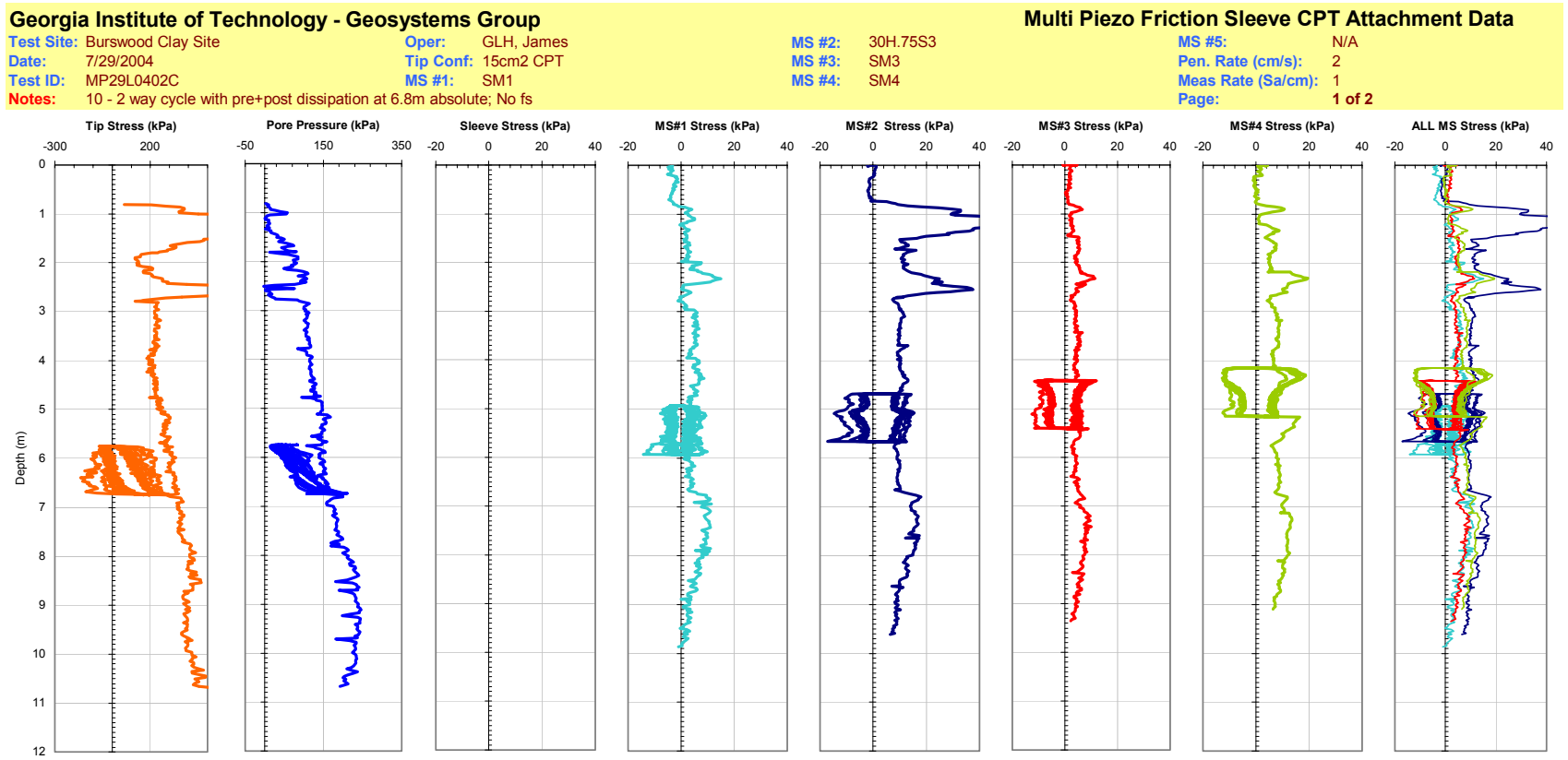

Figure 7-6a. Plots of all CPTU and the MPFA Friction Sensors from Sounding MPFA_12 at the BWDWA Site. Note the Large Amplitude (1 m) Cyclic Investigation from Tip Depths of 6.8 to 7.8 m.

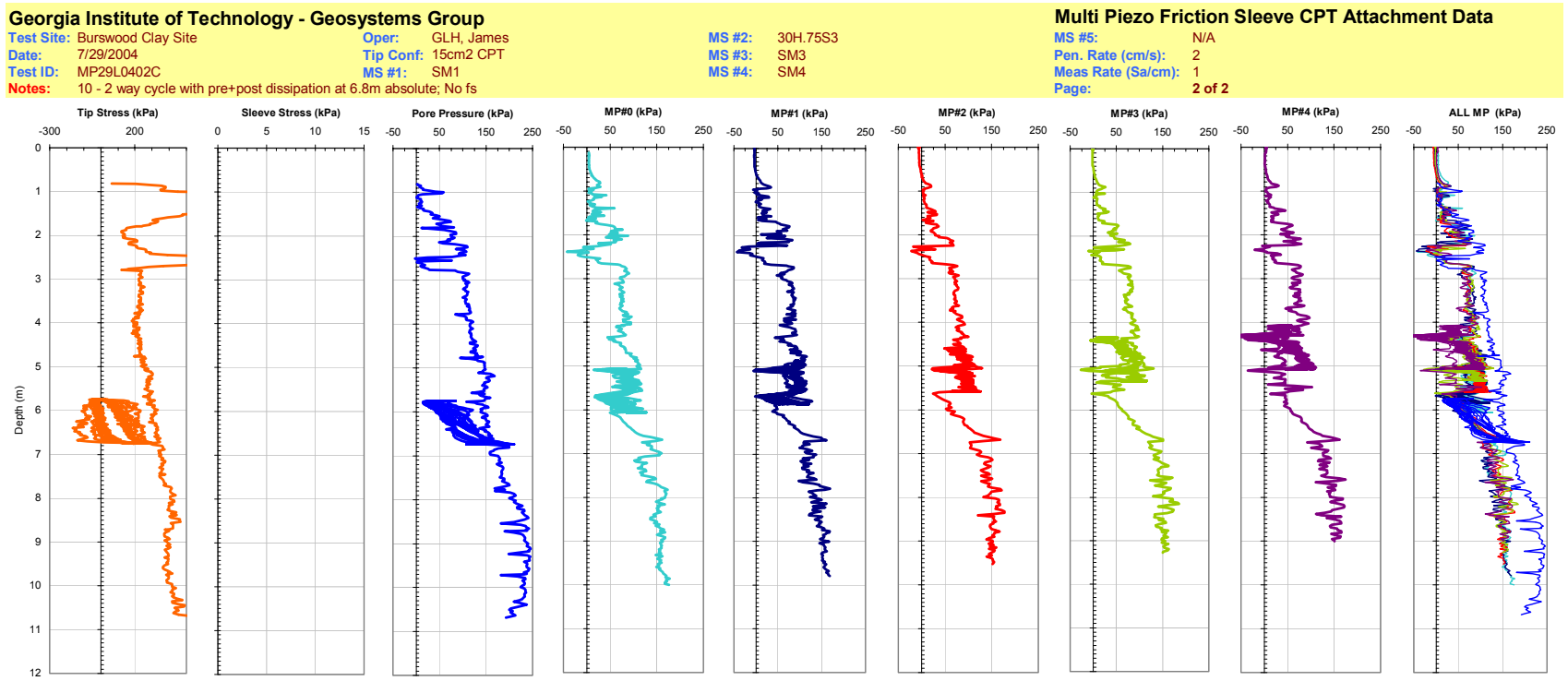

Figure 7-6b. Plots of all CPTU and the MPFA Piezo Sensors from Sounding MPFA_12 at the BWDWA Site. Note the Large Amplitude (1 m) Cyclic Investigation from Tip Depths of 6.8 to 7.8 m.

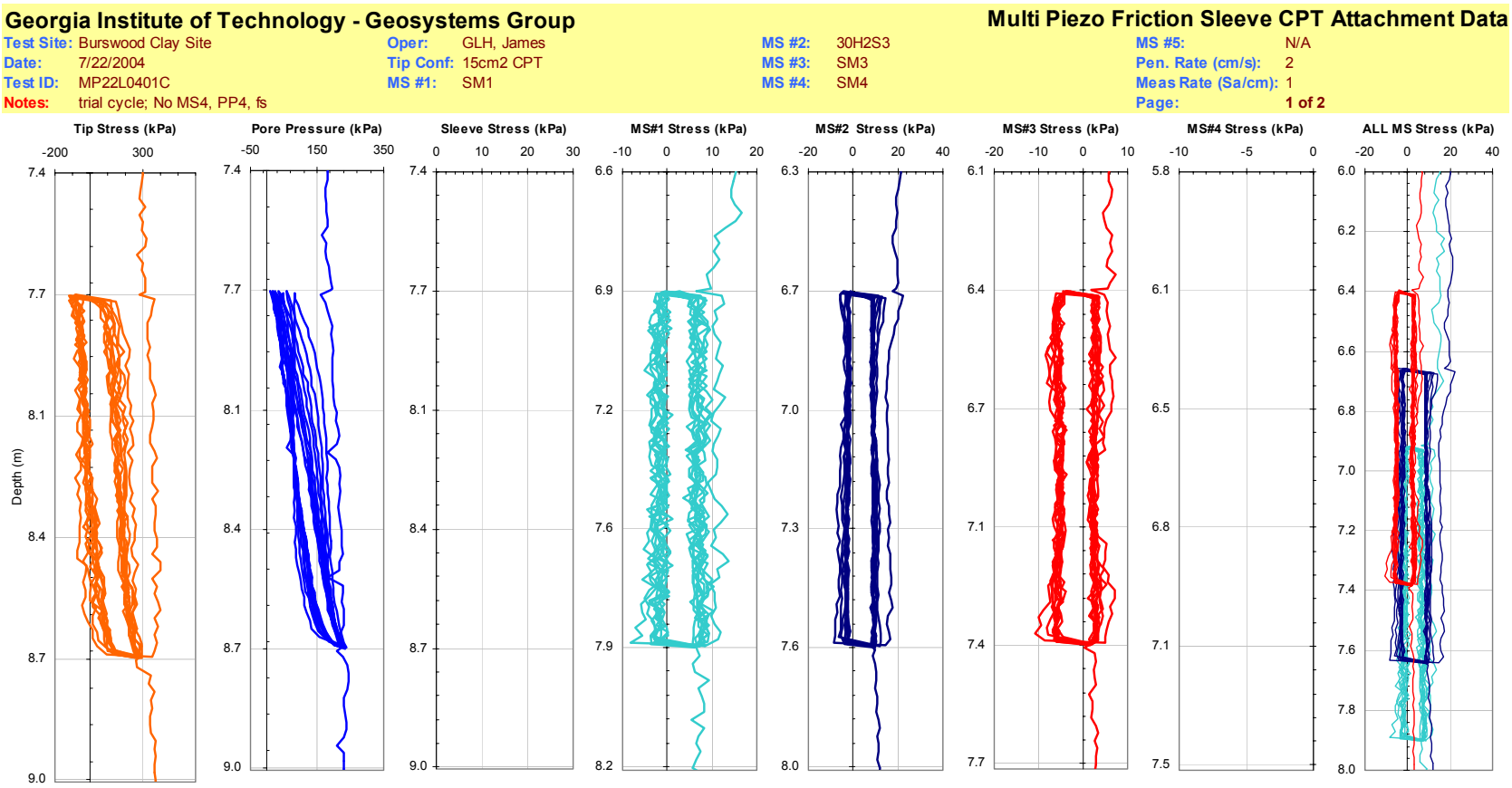

Figure 7-7a. Plots of all CPTU and the MPFA Friction Sensors from Sounding MPFA_10 at the BWDWA Site Highlighting the Large Amplitude (1 m) Cyclic Investigation from Tip Depths of 7.7 to 8.7 m.

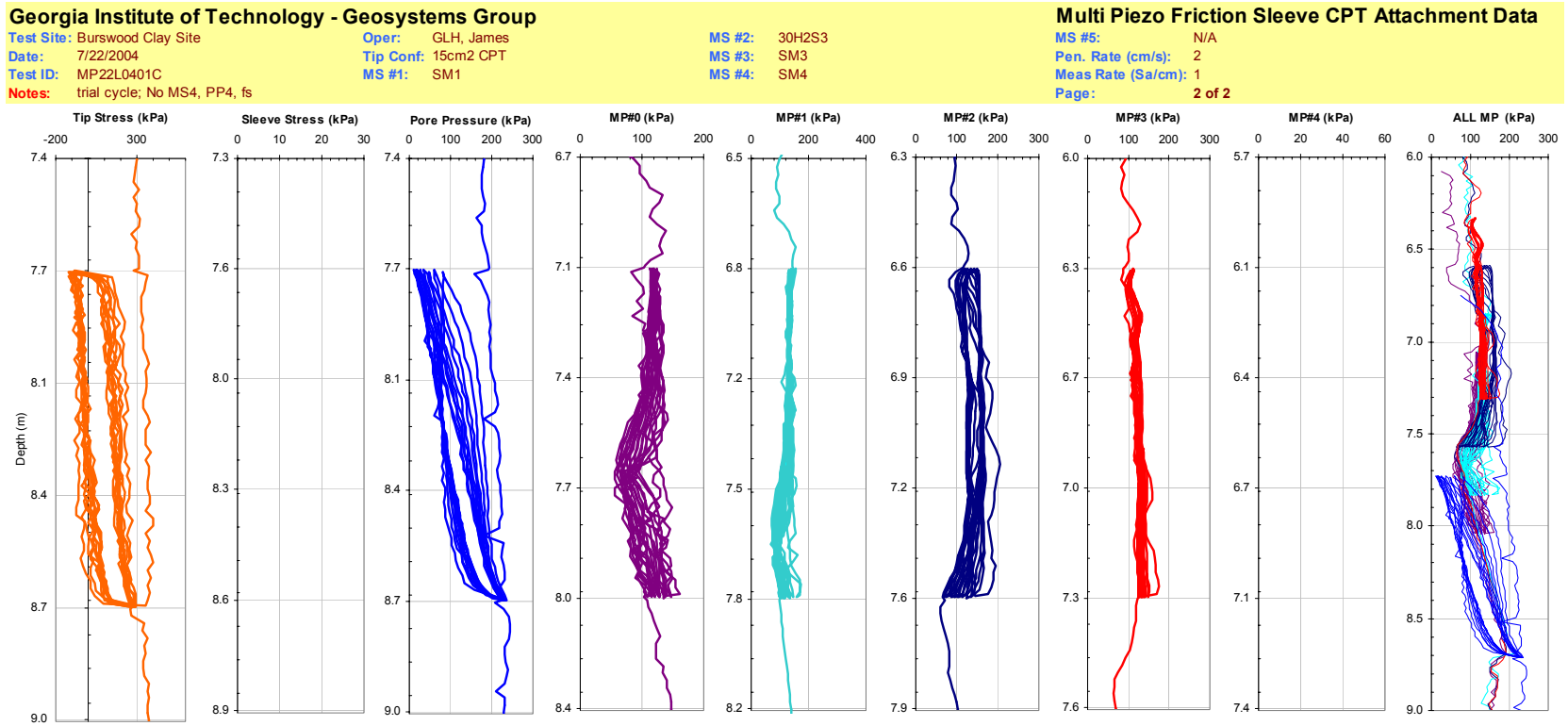

Figure 7-7b. Plots of all CPTU and the MPFA Piezo Sensors from Sounding MPFA_10 at the BWDWA Site Highlighting the Large Amplitude (1 m) Cyclic Investigation from Tip Depths of 7.7 to 8.7 m.

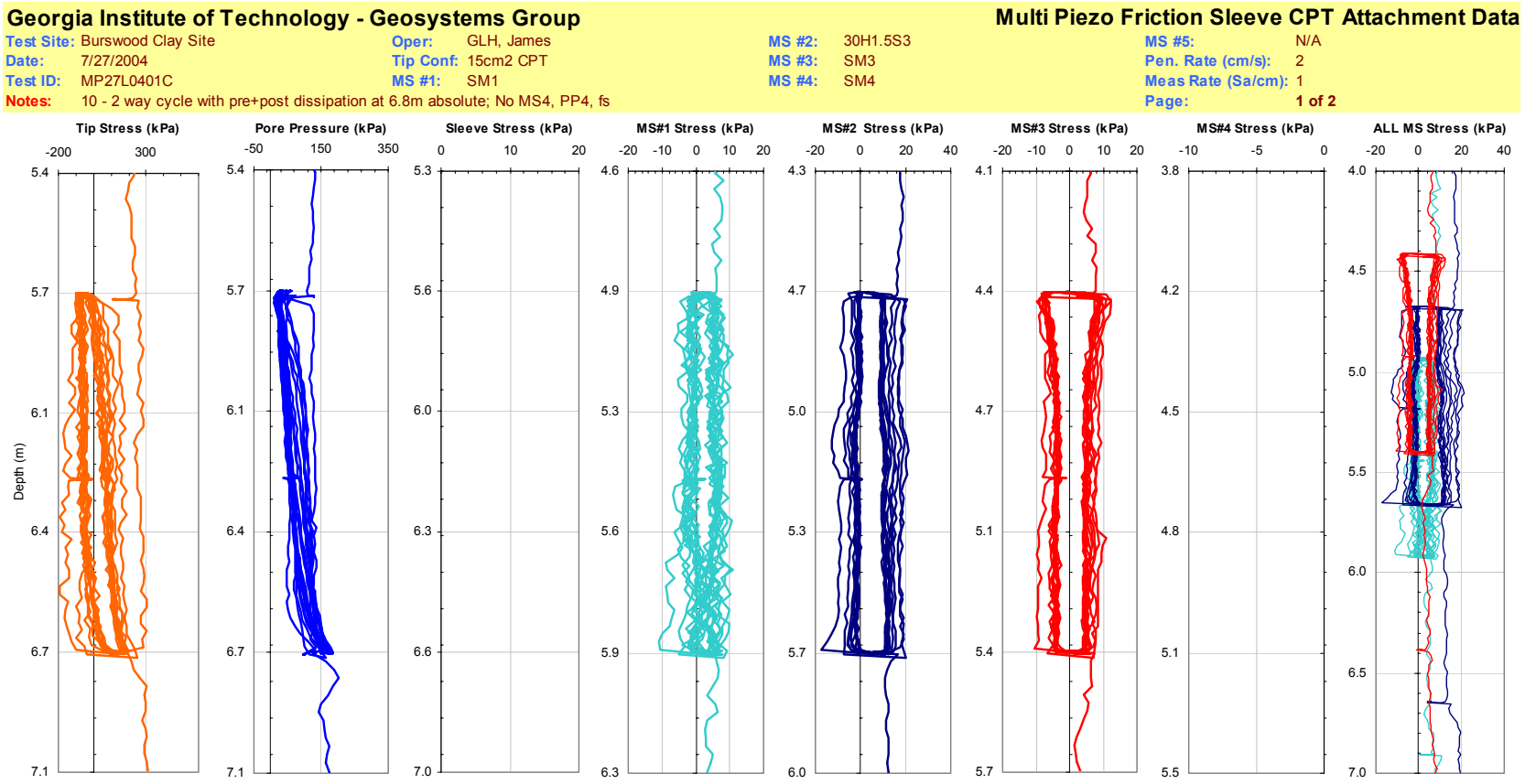

Figure 7-8a. Plots of all CPTU and the MPFA Friction Sensors from Sounding MPFA_11 at the BWDWA Site Highlighting the Large Amplitude (1 m) Cyclic Investigation from Tip Depths of 6.8 to 7.8 m.

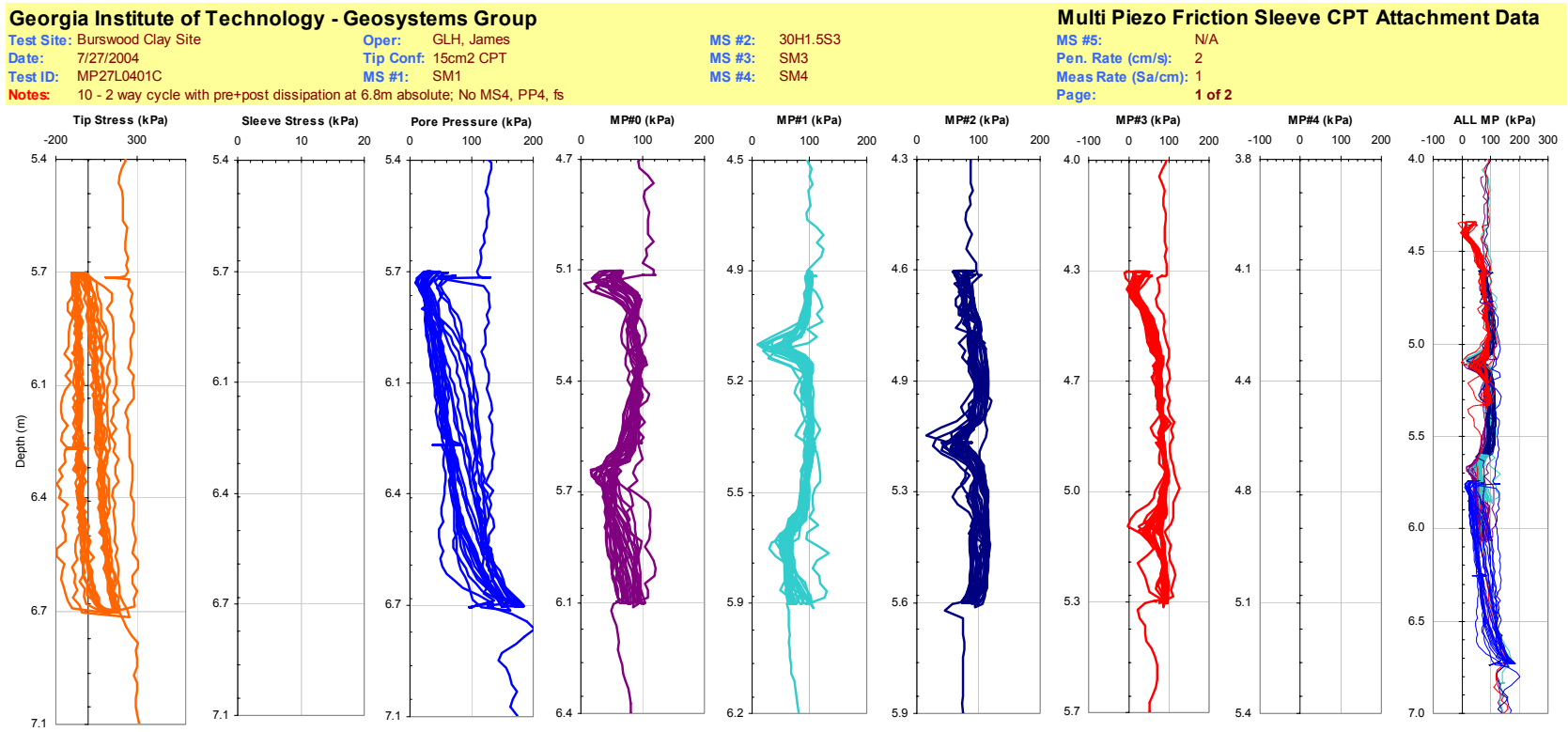

Figure 7-8b. Plots of all CPTU and the MPFA Piezo Sensors from Sounding MPFA_11 at the BWDWA Site Highlighting the Large Amplitude (1 m) Cyclic Investigation from Tip Depths of 6.8 to 7.8 m.

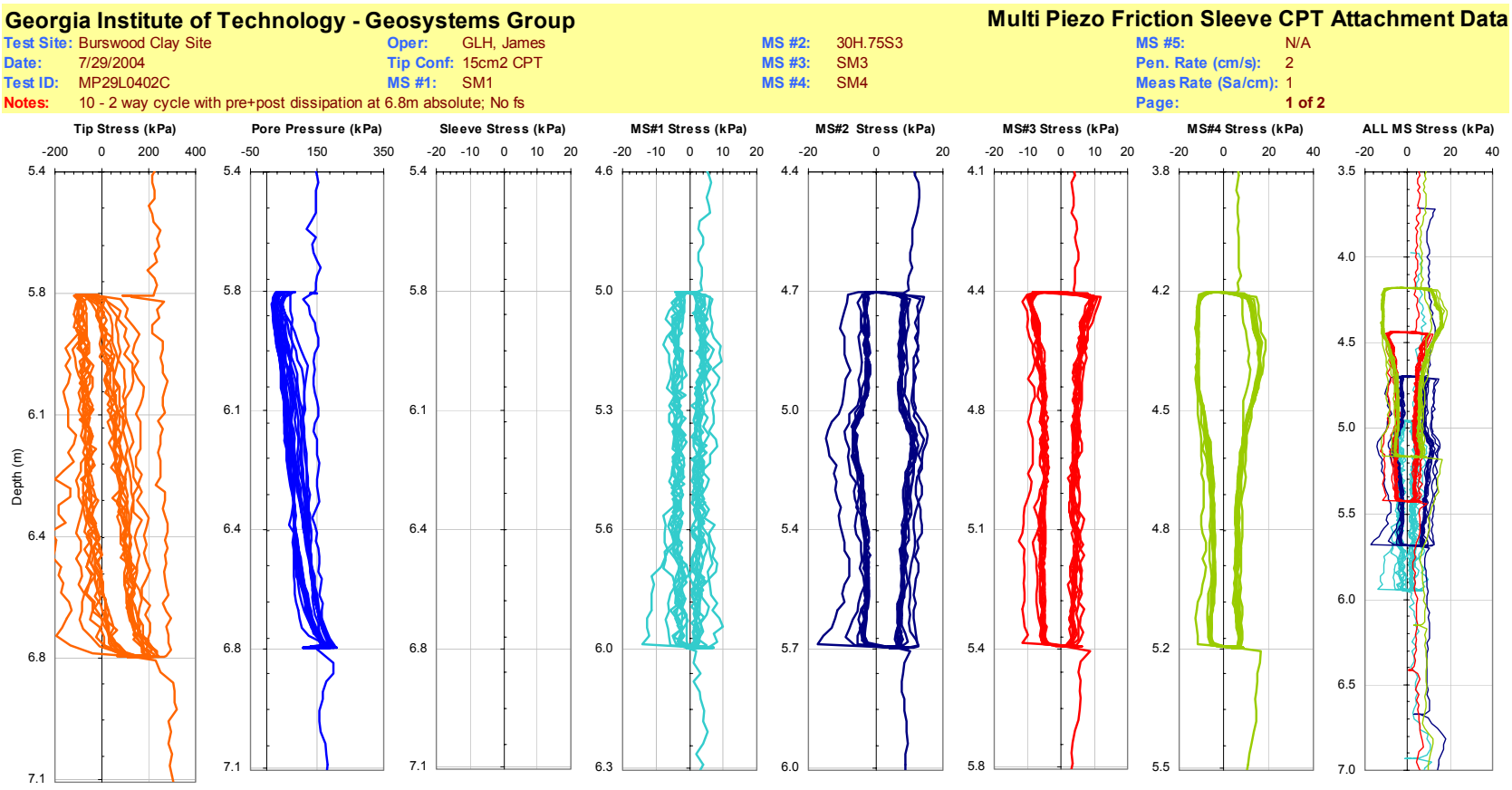

Figure 7-9a. Plots of all CPTU and the MPFA Friction Sensors from Sounding MPFA_12 at the BWDWA Site Highlighting the Large Amplitude (1 m) Cyclic Investigation from Tip Depths of 6.8 to 7.7 m.

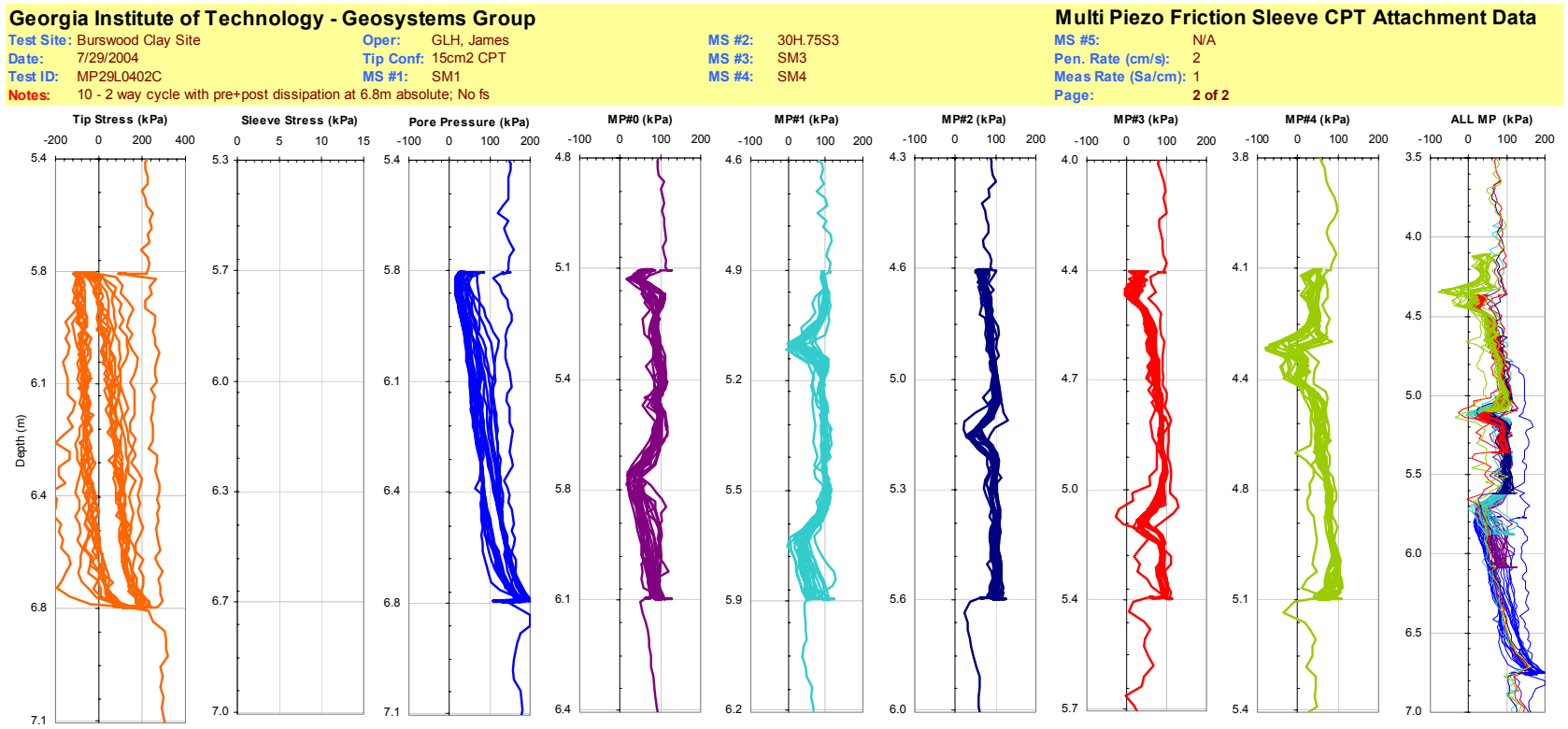

Figure 7-9b. Plots of all CPTU and the MPFA Piezo Sensors from Sounding MPFA_12 at the BWDWA Site Highlighting the Large Amplitude (1 m) Cyclic Investigation from Tip Depths of 6.8 to 7.8 m.

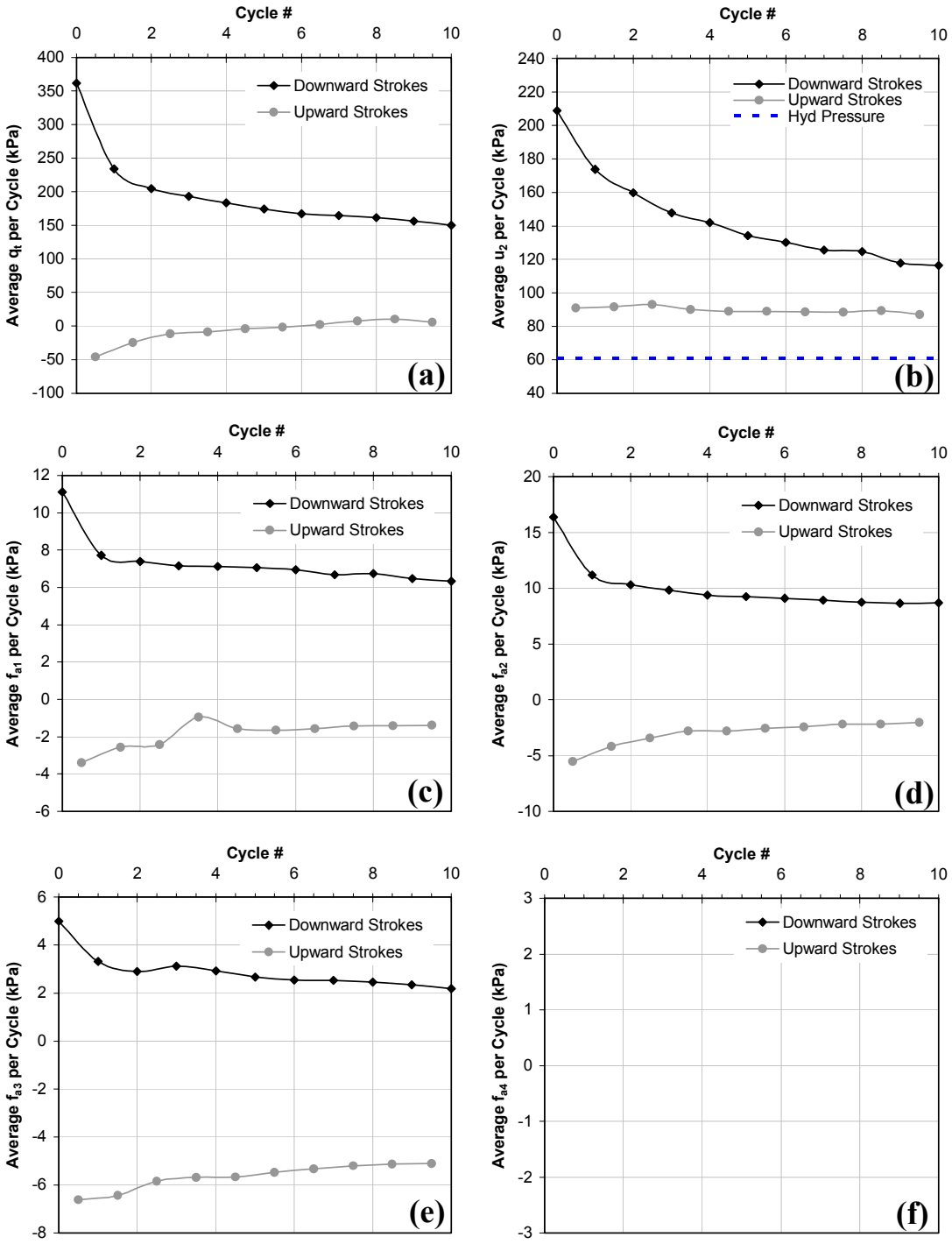

Figure 7-10(a-f). Average Large Amplitude Cyclic Response from Sounding MPFA_10 at the BWDWA Site: (a) q_t, (b) u_2, (c) f_{a1}, (d) f_{a2}, (e) f_{a3}, (f) f_{a4}.

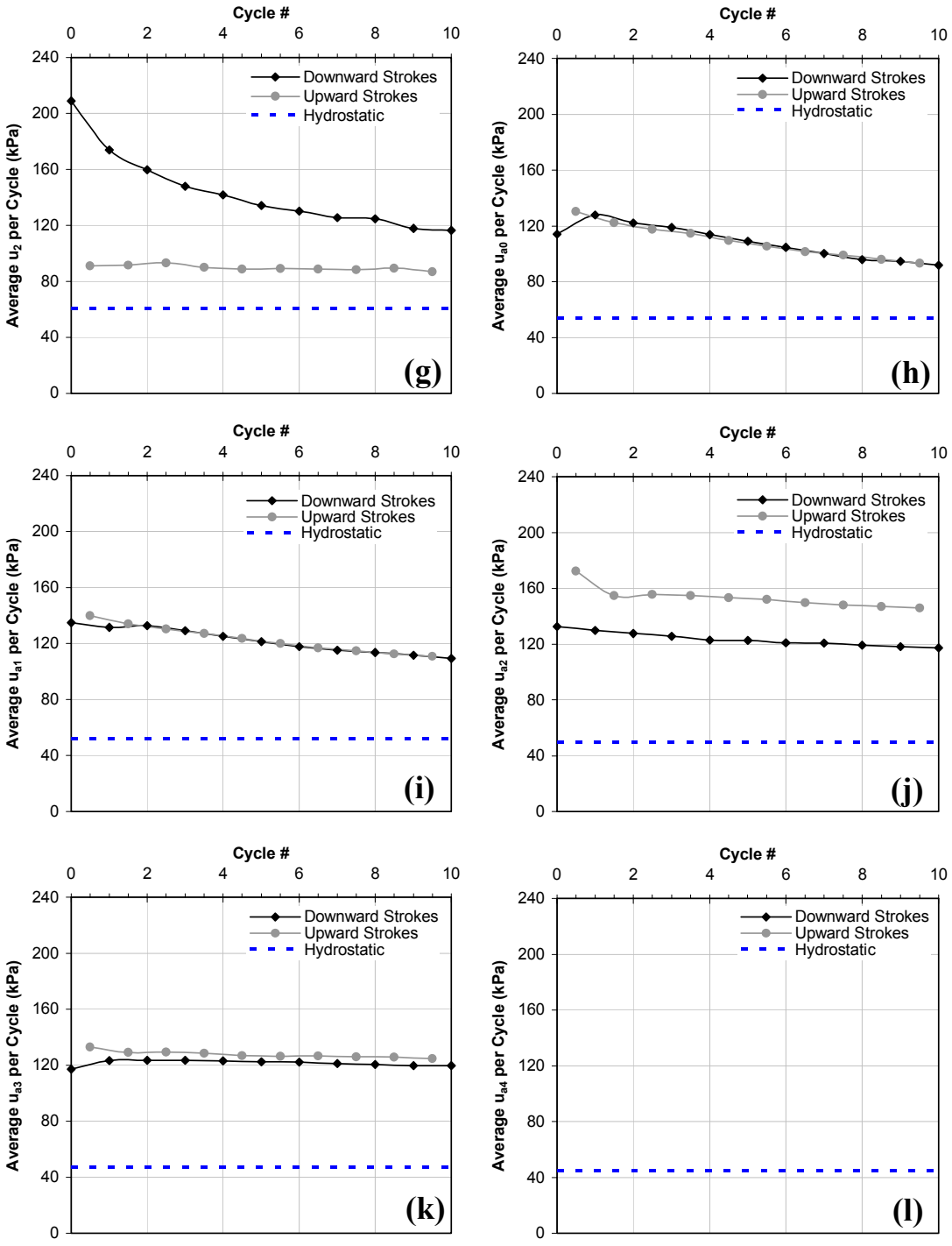

Figure 7-10(g-l). Average Large Amplitude Cyclic Response from Sounding MPFA_10 at the BWDWA Site: (g) u_2, (h) u_{a0}, (i) u_{a1}, (j) u_{a2}, (k) u_{a3}, (l) u_{a4}.

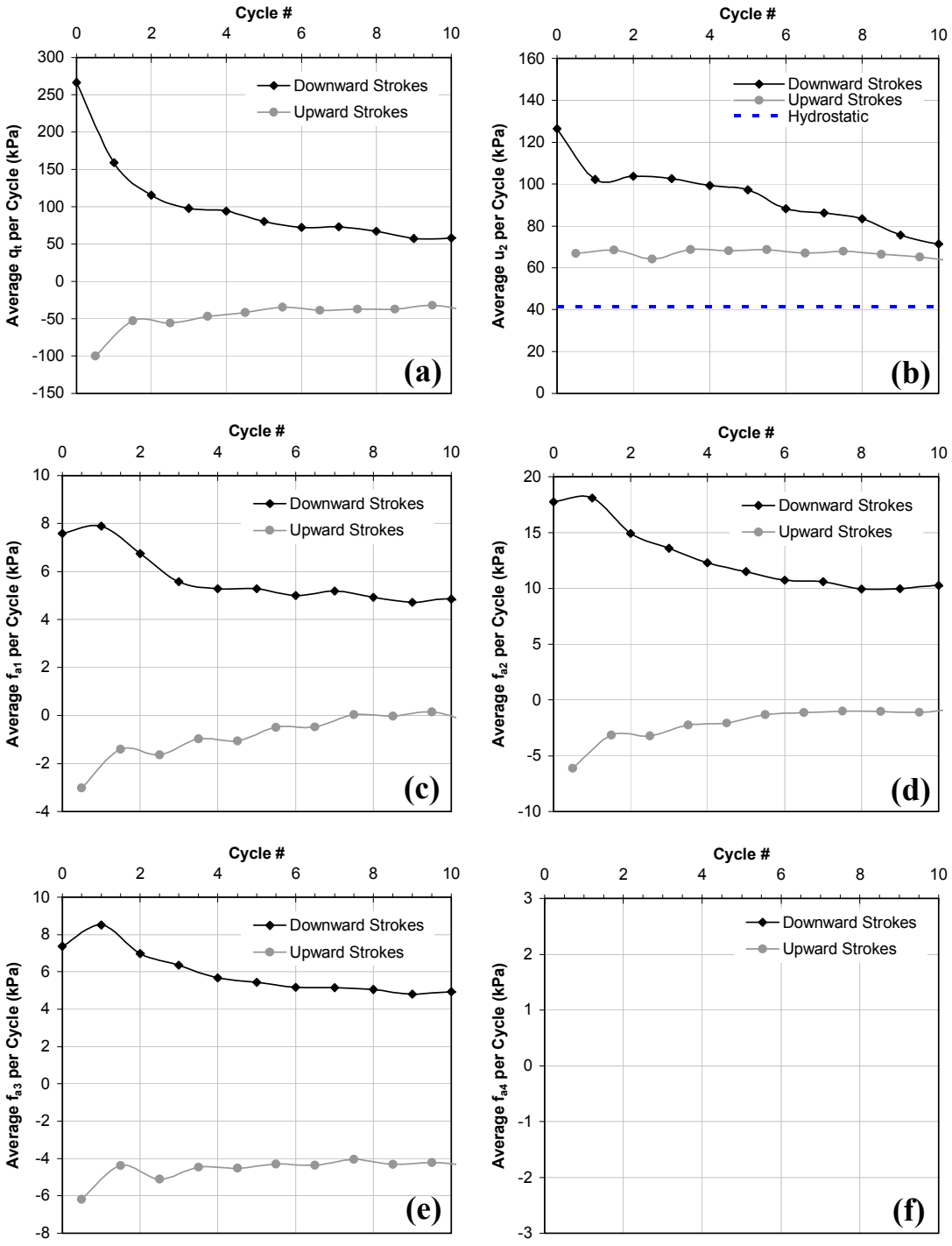

Figure 7-11(a-f). Average Large Amplitude Cyclic Response from Sounding MPFA_11 at the BWDWA Site: (a) q_t, (b) u_2, (c) f_{a1}, (d) f_{a2}, (e) f_{a3}, (f) f_{a4}.

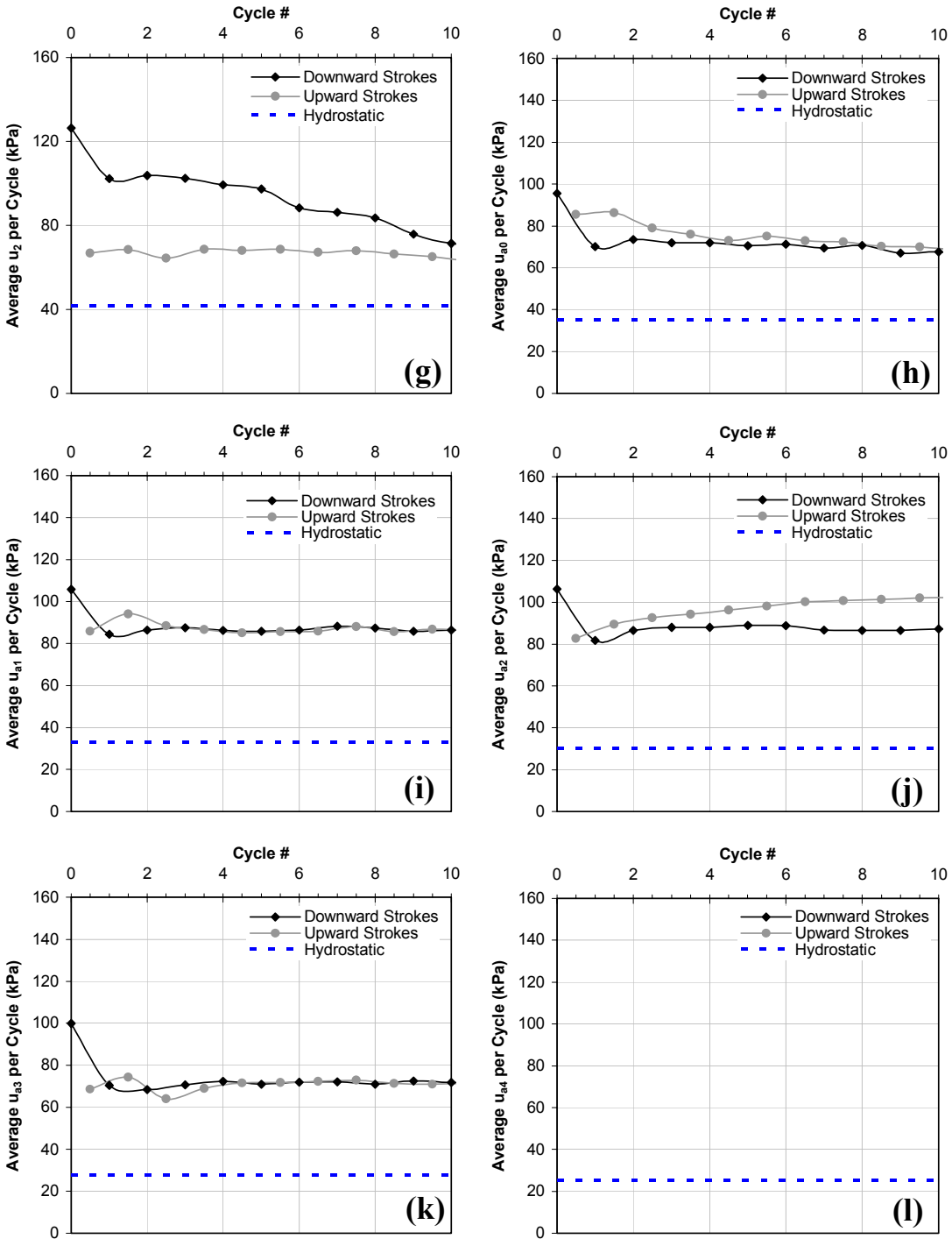

Figure 7-11(g-l). Average Large Amplitude Cyclic Response from Sounding MPFA_11 at the BWDWA Site: (g) u_2, (h) u_{a0}, (i) u_{a1}, (j) u_{a2}, (k) u_{a3}, (l) u_{a4}.

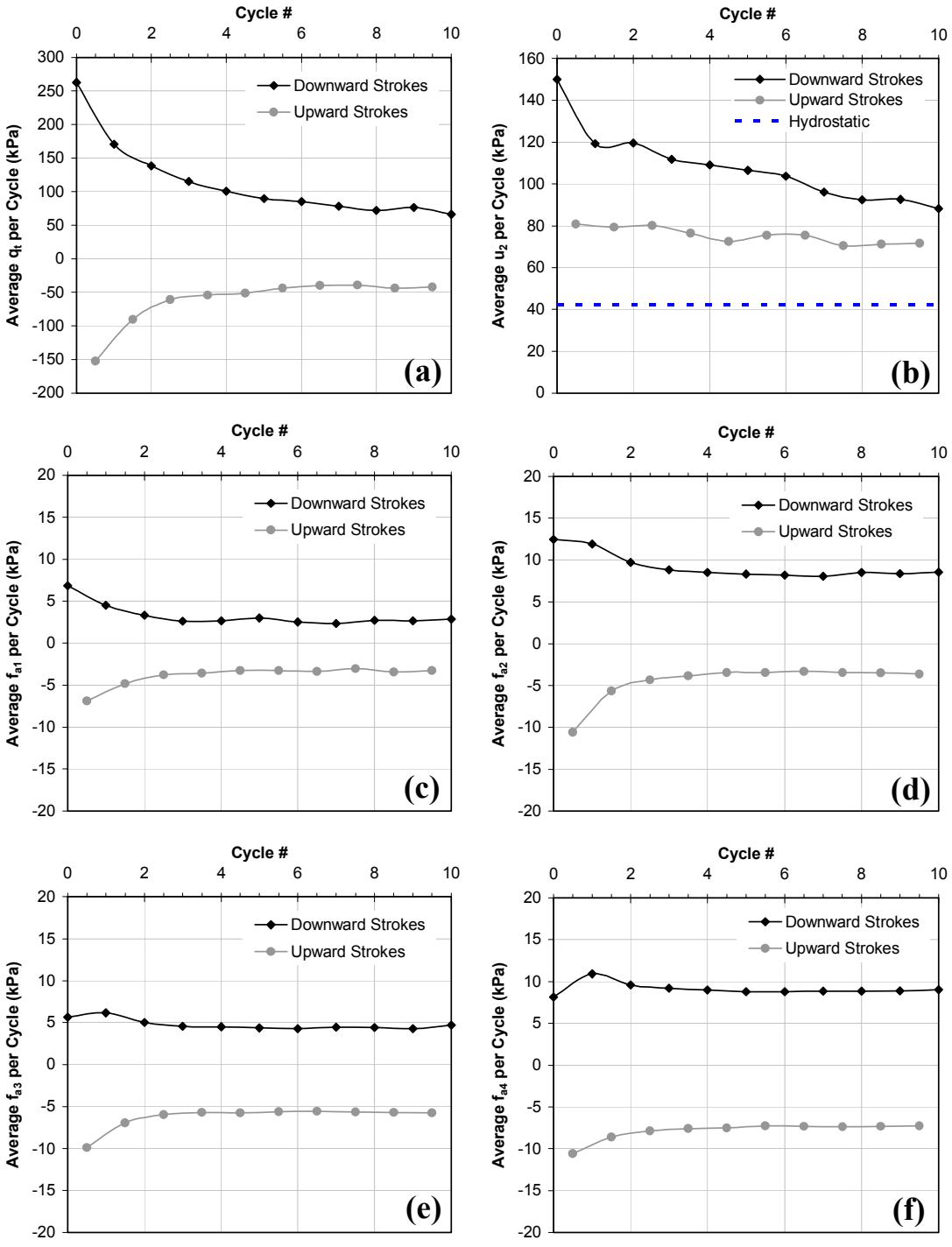

Figure 7-12(a-f). Average Large Amplitude Cyclic Response from Sounding MPFA_12 at the BWDWA Site: (a) q_t, (b) u_2, (c) f_{a1}, (d) f_{a2}, (e) f_{a3}, (f) f_{a4}.

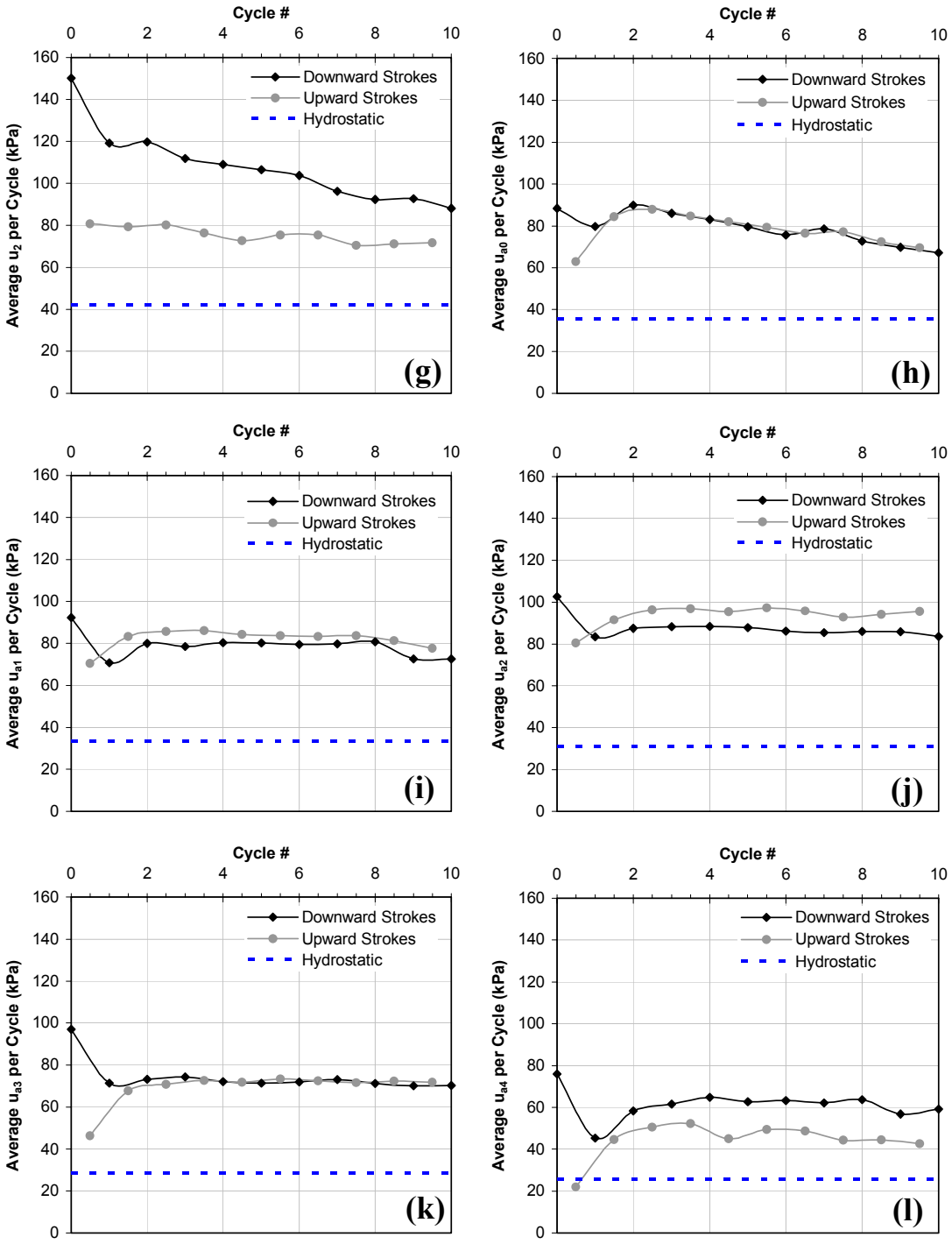

Figure 7-12(g-l). Average Large Amplitude Cyclic Response from Sounding MPFA_12 at the BWDWA Site: (g) u_2, (h) u_{a0}, (i) u_{a1}, (j) u_{a2}, (k) u_{a3}, (l) u_{a4}.

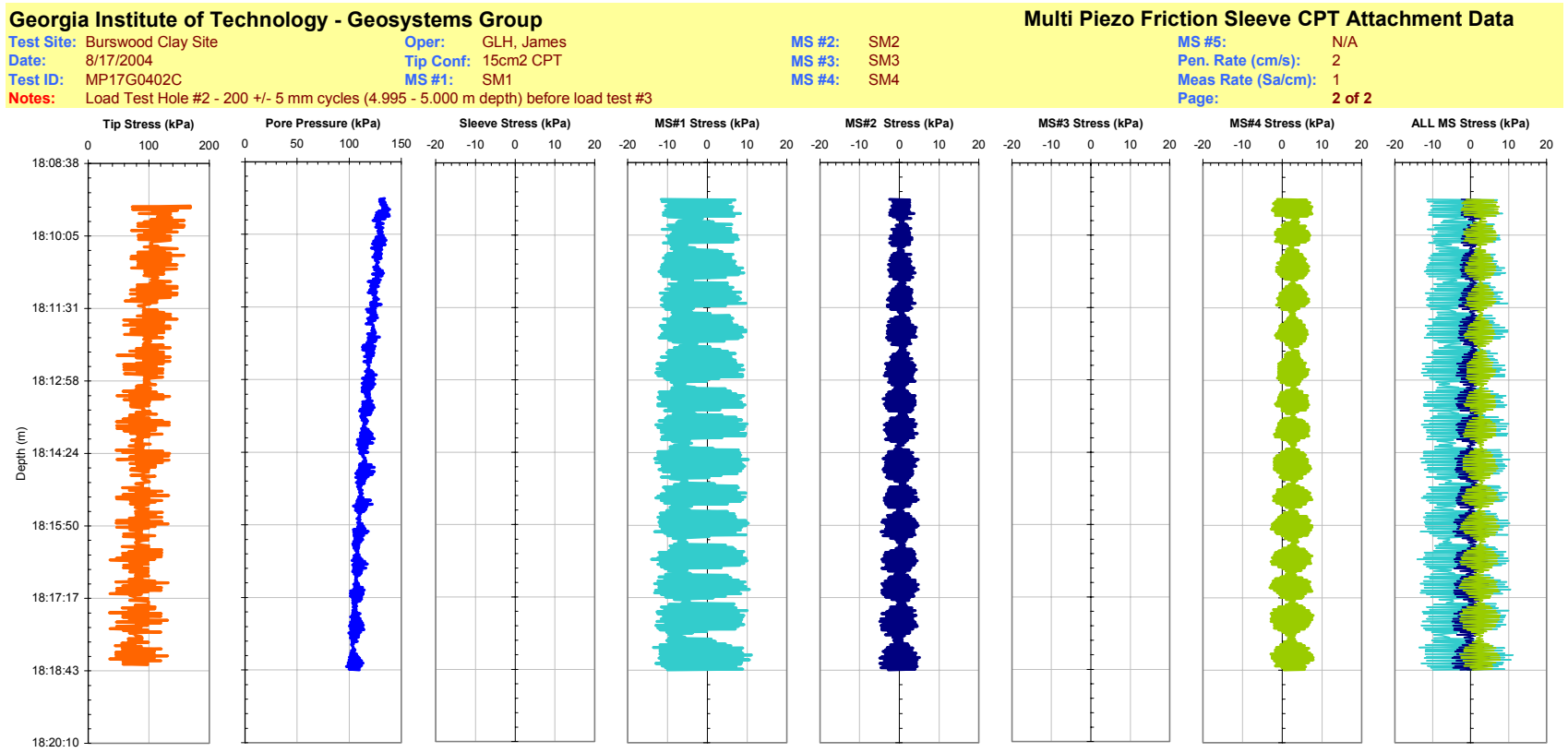

Figure 7-13a. Plots of all CPTU and the MPFA Friction Sensors, as a Function of Time, from Sounding MPFA_26 at the BWDWA Site Highlighting the Small Amplitude (5 mm) Cyclic Investigation from Tip Depths of 4.995 to 5.000 m.

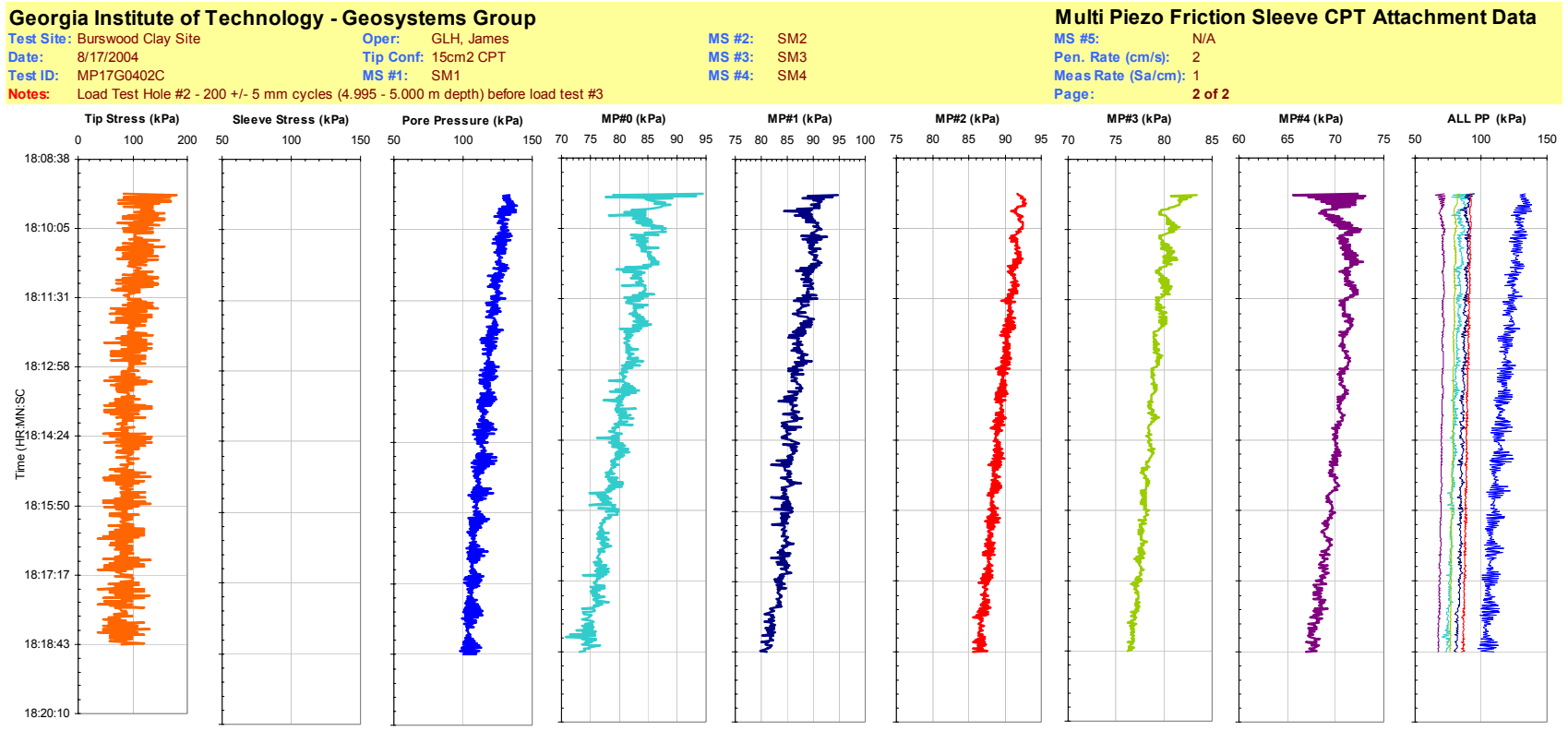

Figure 7-13b. Plots of all CPTU and the MPFA Piezo Sensors, as a Function of Time, from Sounding MPFA_26 at the BWDWA Site Highlighting the Small Amplitude (5 mm) Cyclic Investigation from Tip Depths of 4.995 to 5.000 m.

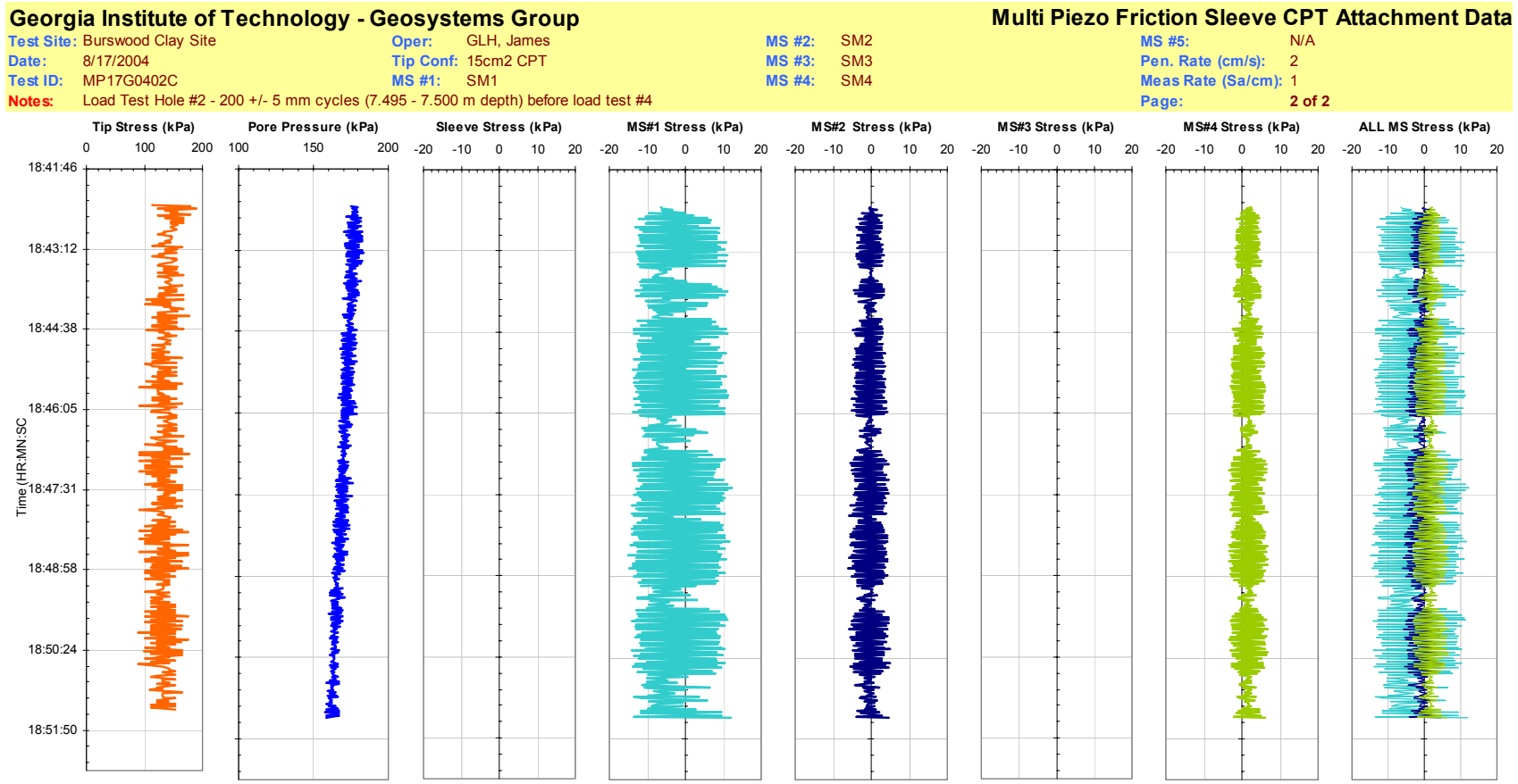

Figure 7-14a. Plots of all CPTU and the MPFA Friction Sensors, as a Function of Time, from Sounding MPFA_26 at the BWDWA Site Highlighting the Small Amplitude (5 mm) Cyclic Investigation from Tip Depths of 7.495 to 7.500 m.

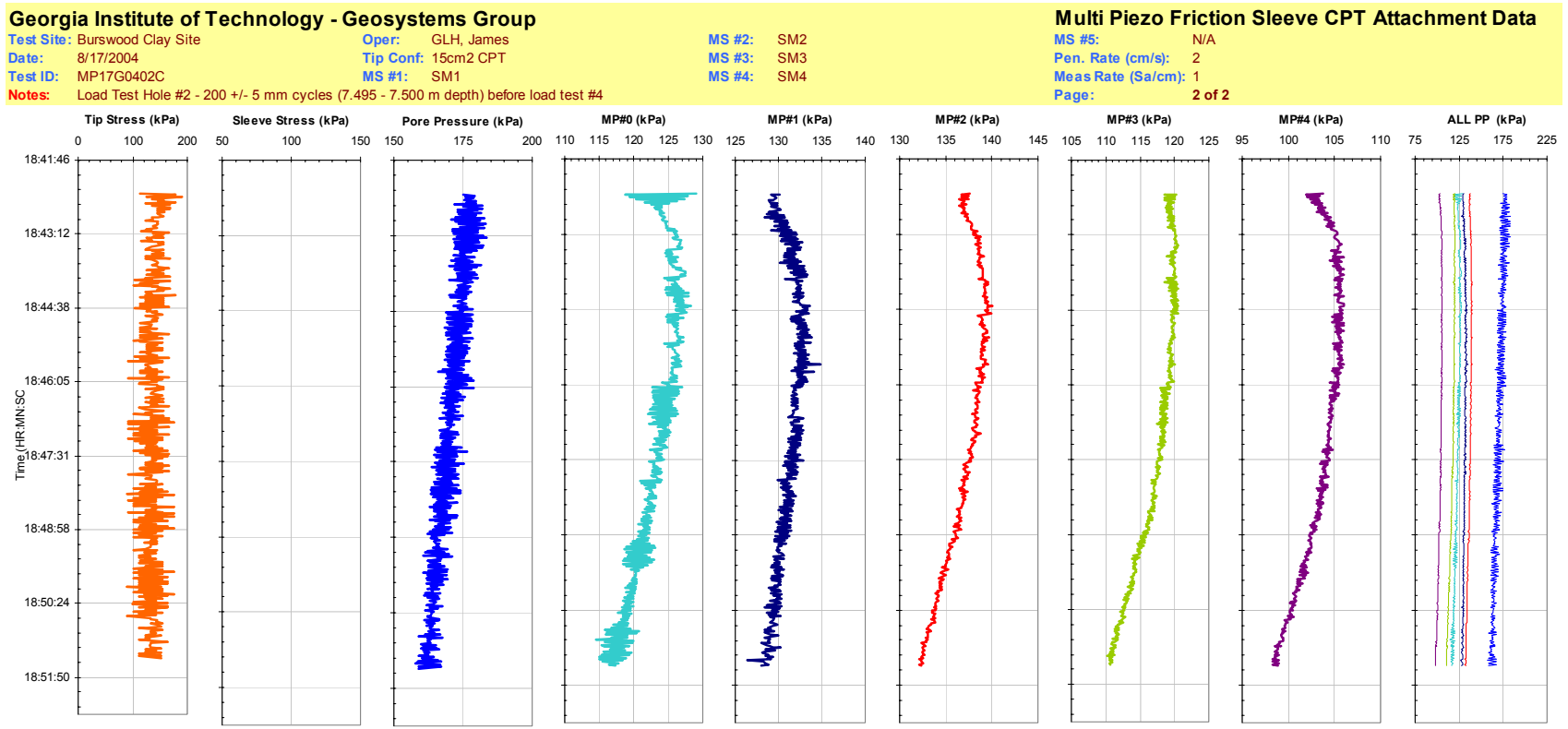

Figure 7-14b. Plots of all CPTU and the MPFA Piezo Sensors, as a Function of Time, from Sounding MPFA_26 at the BWDWA Site Highlighting the Small Amplitude (5 mm) Cyclic Investigation from Tip Depths of 7.495 to 7.500 m.

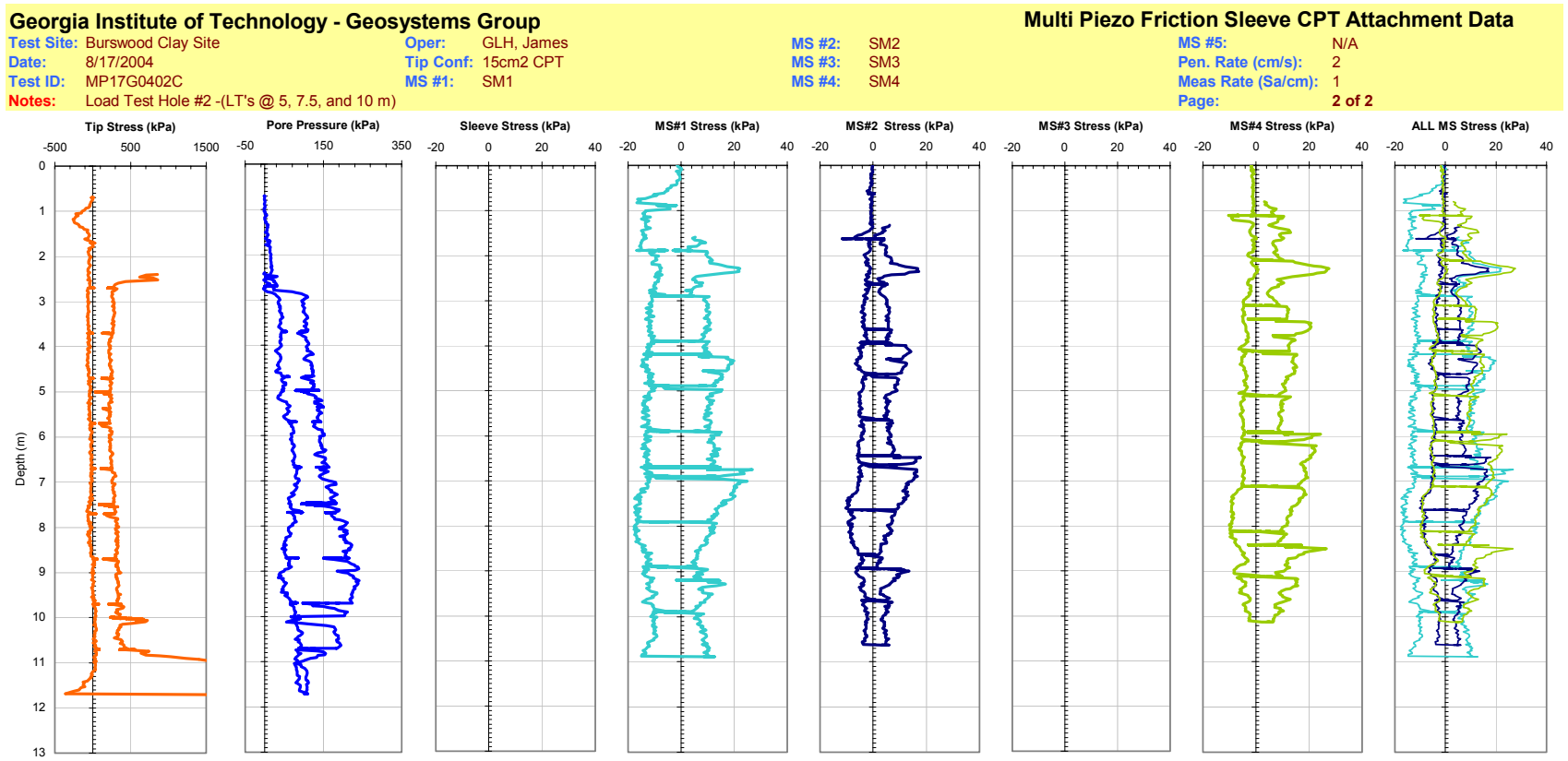

Figure 7-15a. Plots of all CPTU and the MPFA Friction Sensors from Sounding MPFA_26 at the BWDWA Site. Small Amplitude (5 mm) Cyclic Investigations were Conducted at Tip Depths of 5.0 and 7.5 m.

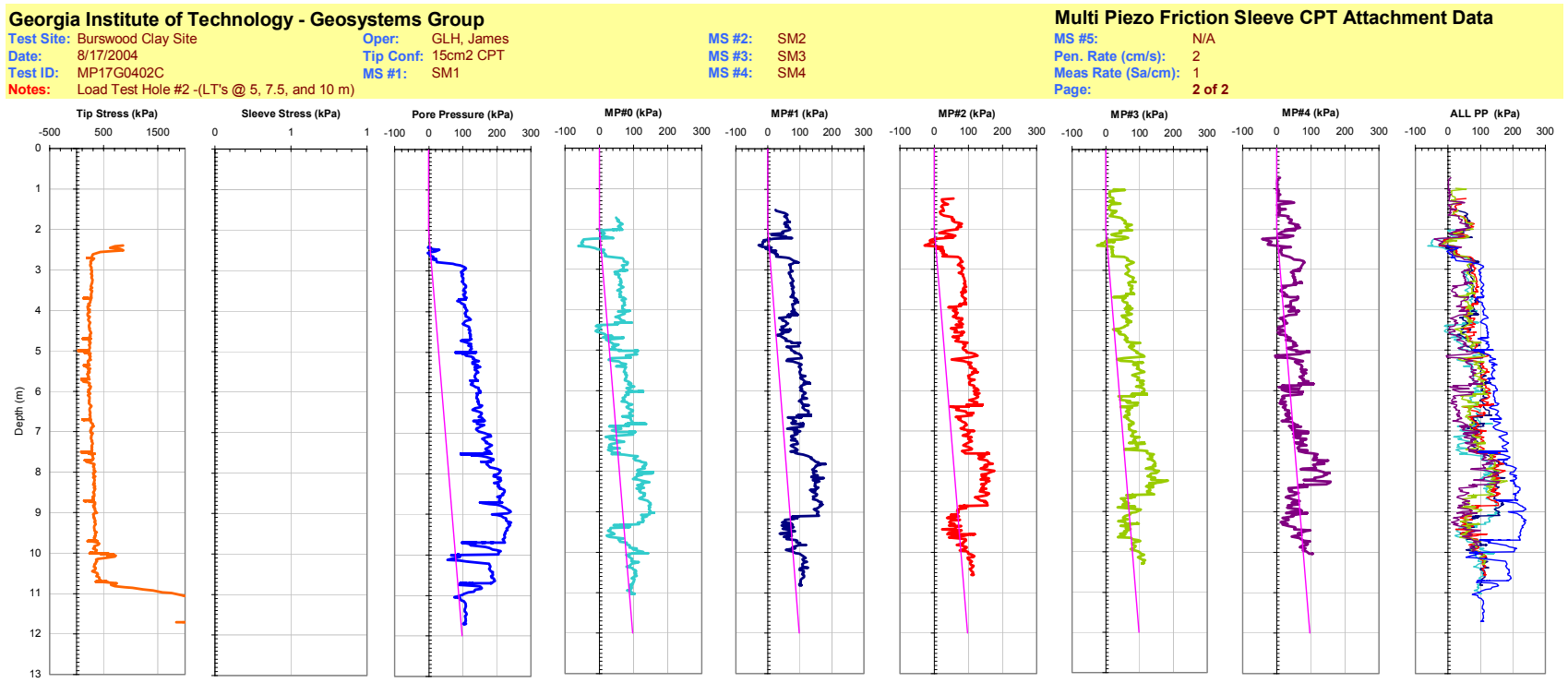

Figure 7-15b. Plots of all CPTU and the MPFA Piezo Sensors from Sounding MPFA_26 at the BWDWA Site. Small Amplitude (5 mm) Cyclic Investigations were Conducted at Tip Depths of 5.0 and 7.5 m.

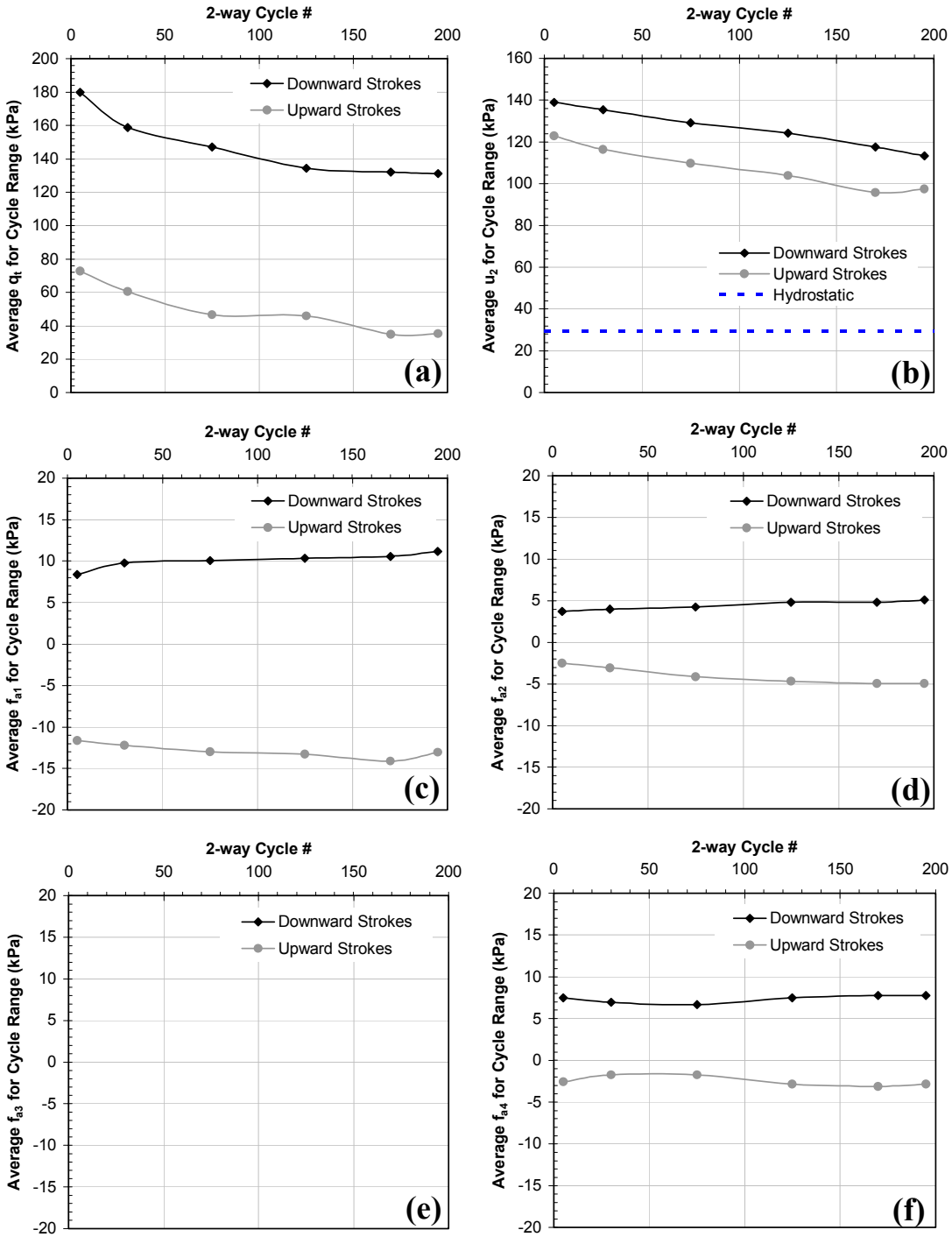

Figure 7-16(a-f). Average Small Amplitude Cyclic Response at 5 m Tip Depth from Sounding MPFA_26 at the BWDWA Site: (a) q_t, (b) u_2, (c) f_{a1}, (d) f_{a2}, (e) f_{a3}, (f) f_{a4}.

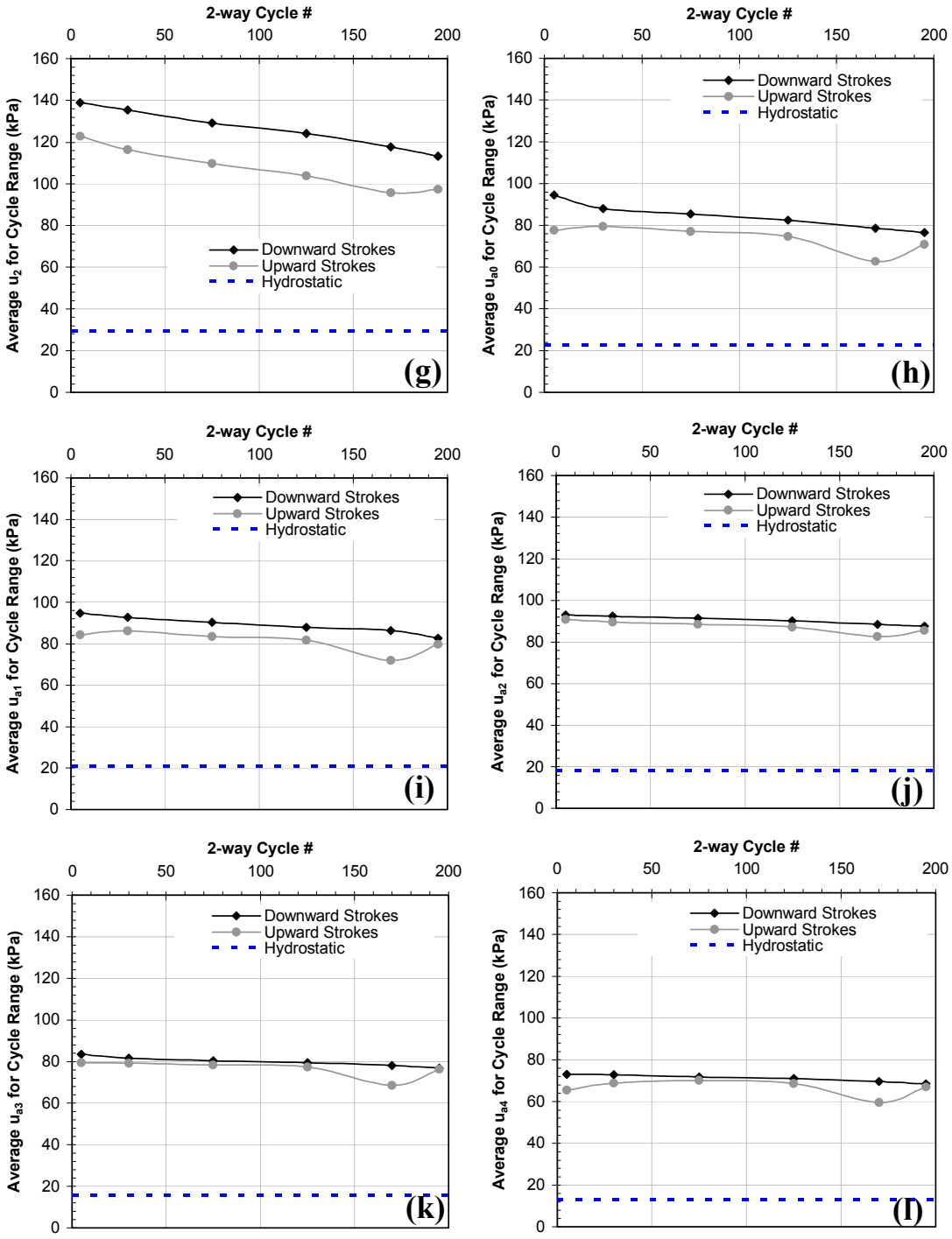

Figure 7-16(g-l). Average Small Amplitude Cyclic Response at 5 m Tip Depth from Sounding MPFA_12 at the BWDWA Site: (g) u_2, (h) u_{a0}, (i) u_{a1}, (j) u_{a2}, (k) u_{a3}, (l) u_{a4}.

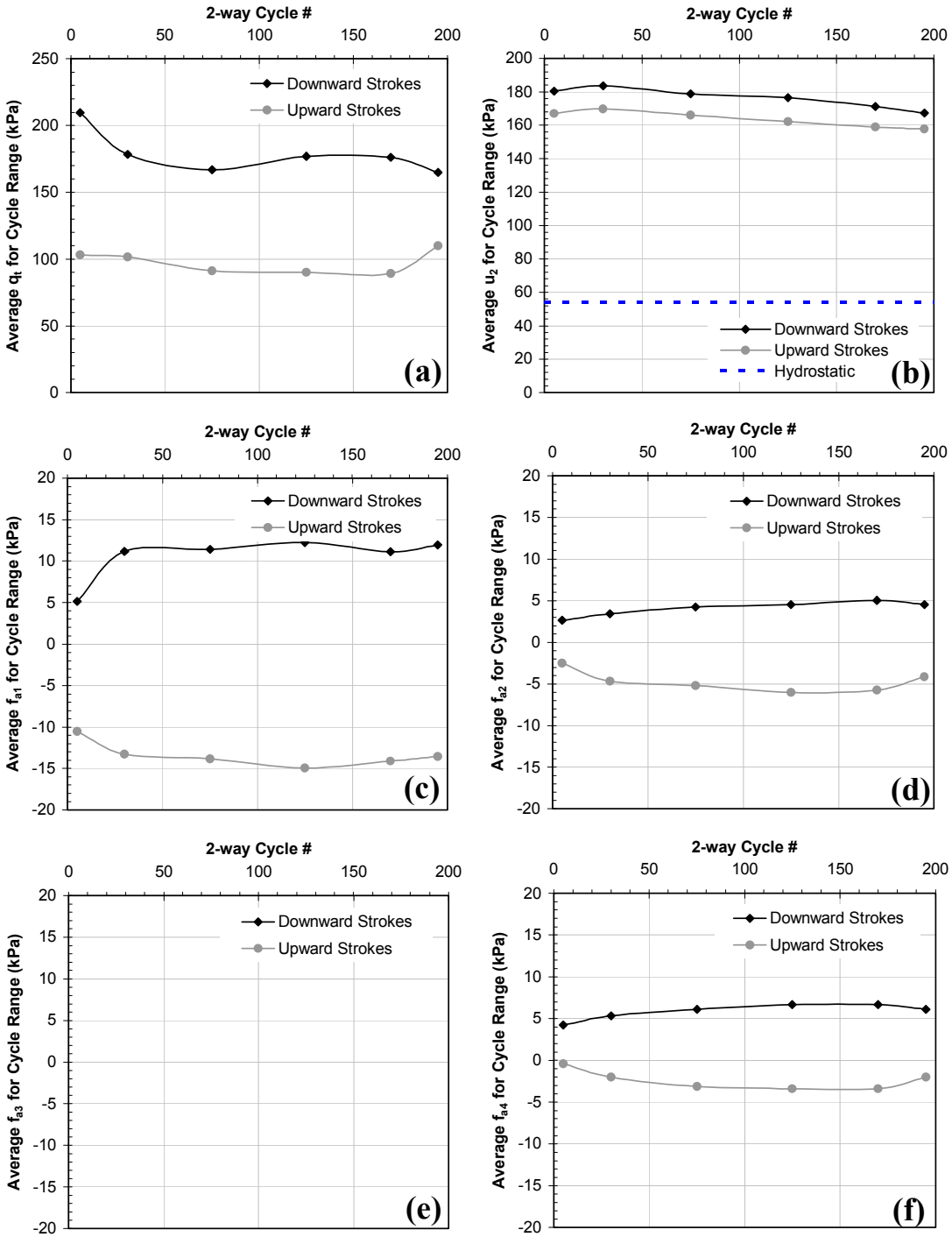

Figure 7-17(a-f). Average Small Amplitude Cyclic Response at 7.5 m Tip Depth from Sounding MPFA_26 at the BWDWA Site: (a) q_t, (b) u_2, (c) f_{a1}, (d) f_{a2}, (e) f_{a3}, (f) f_{a4}.

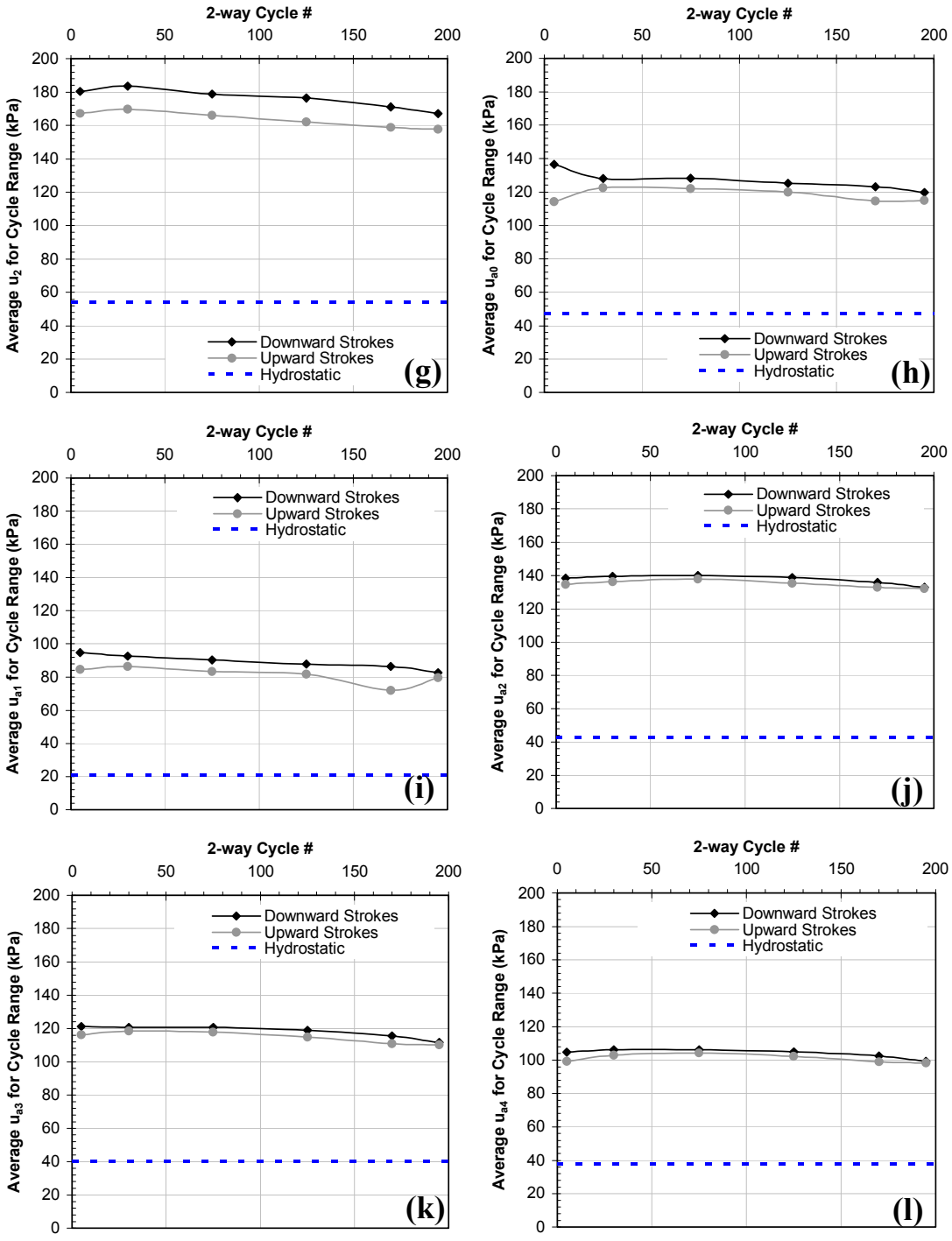

Figure 7-17(g-l). Average Small Amplitude Cyclic Response at 7.5 m Tip Depth from Sounding MPFA_12 at the BWDWA Site: (g) u_2, (h) u_{a0}, (i) u_{a1}, (j) u_{a2}, (k) u_{a3}, (l) u_{a4}.

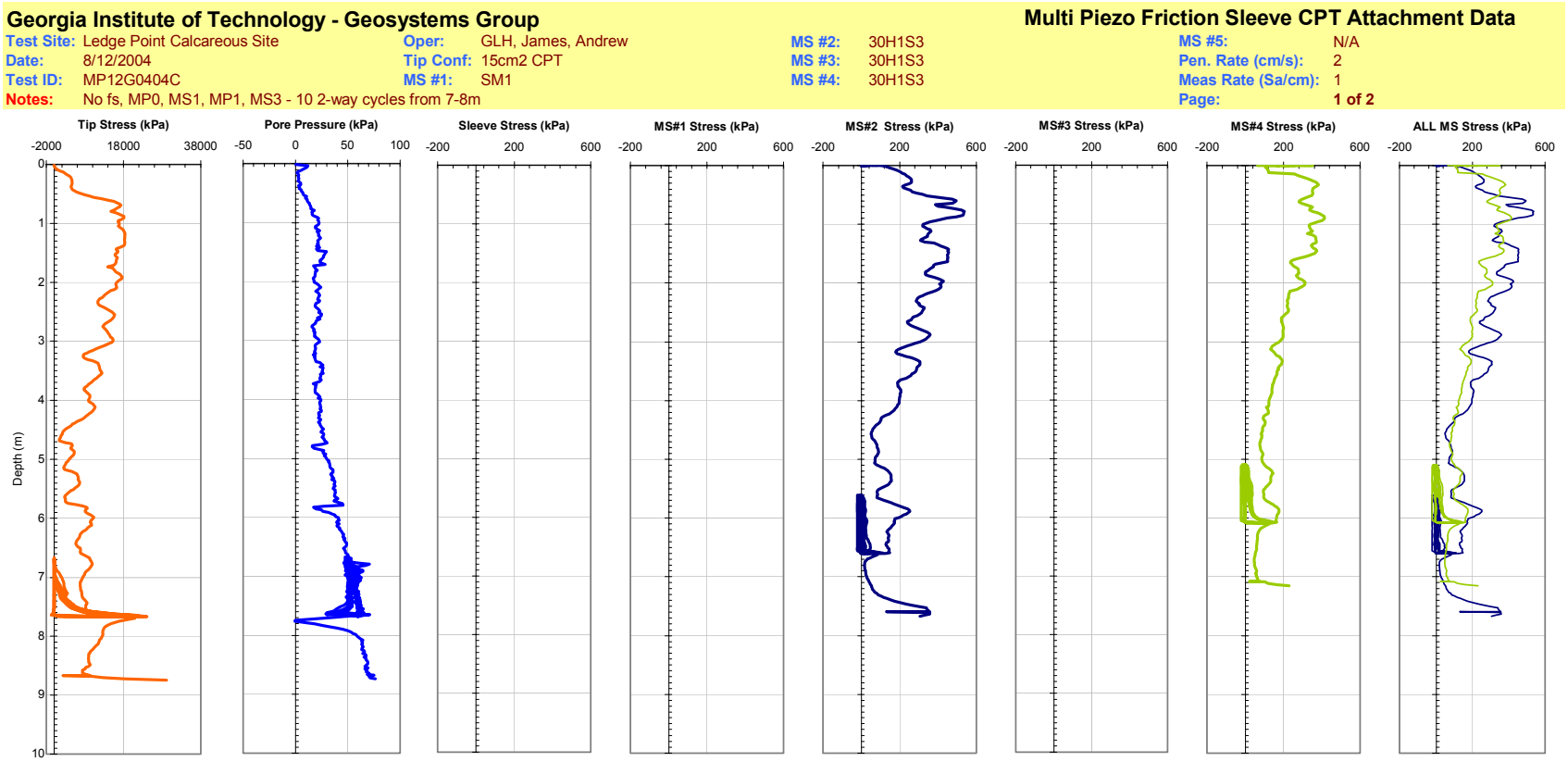

Figure 7-18a. Plots of all CPTU and the MPFA Friction Sensors from Sounding MPFA_23 at the LPWA Site. Note the Large Amplitude (1 m) Cyclic Investigation from Tip Depths of 6.7 to 7.7 m.

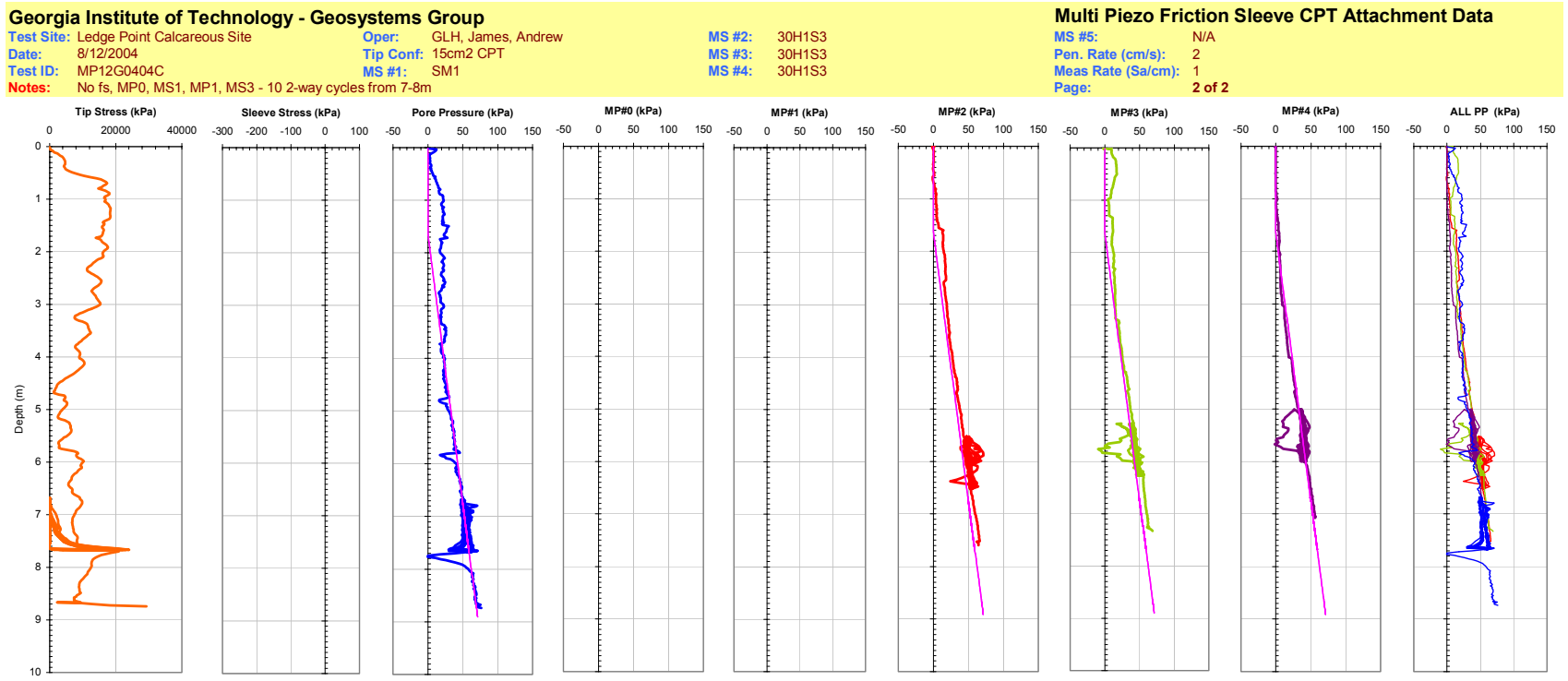

Figure 7-18b. Plots of all CPTU and the MPFA Piezo Sensors from Sounding MPFA_23 at the LPWA Site. Note the Large Amplitude (1 m) Cyclic Investigation from Tip Depths of 6.7 to 7.7 m.

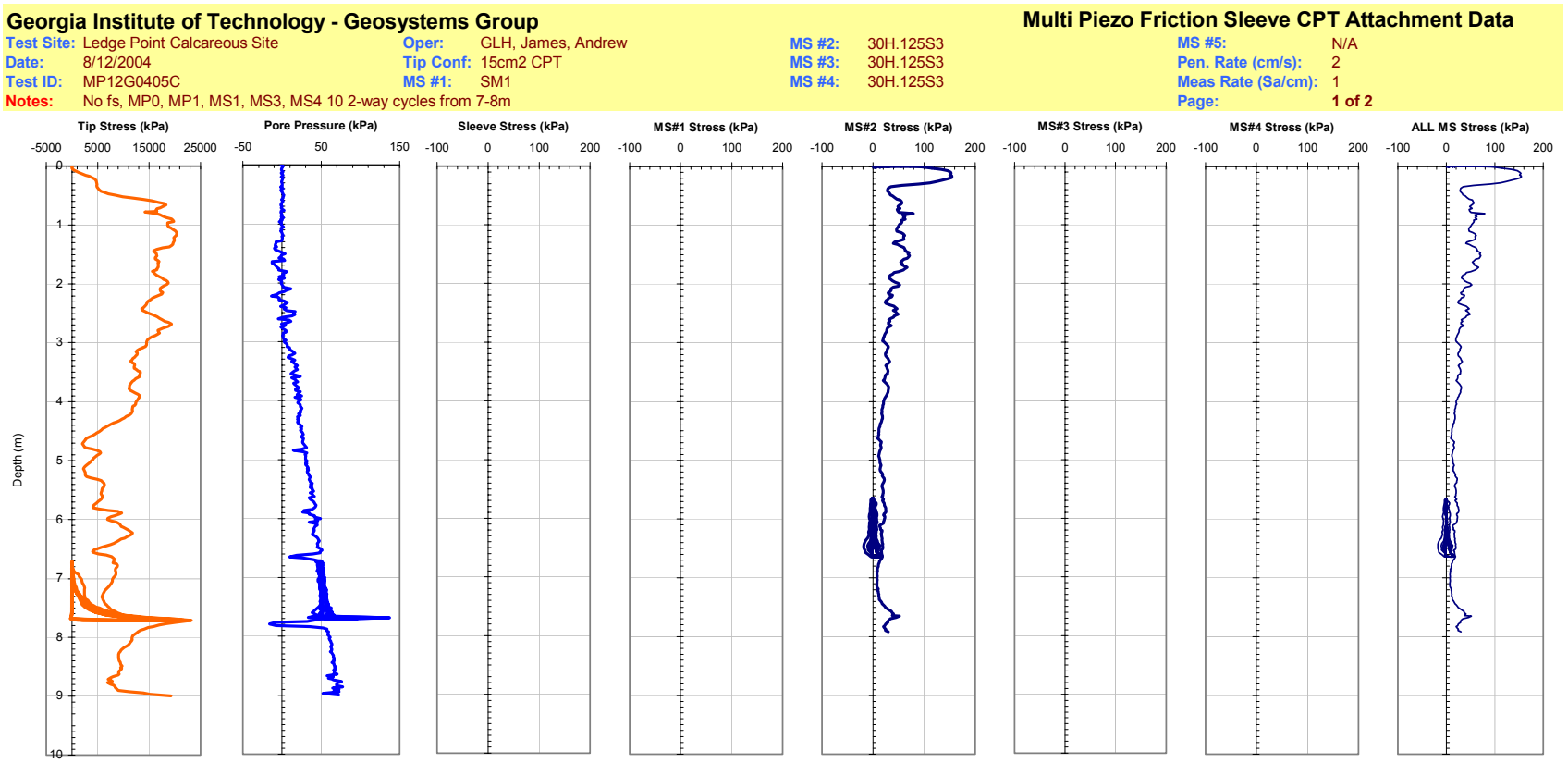

Figure 7-19a. Plots of all CPTU and the MPFA Friction Sensors from Sounding MPFA_24 at the LPWA Site. Note the Large Amplitude (1 m) Cyclic Investigation from Tip Depths of 6.7 to 7.7 m.

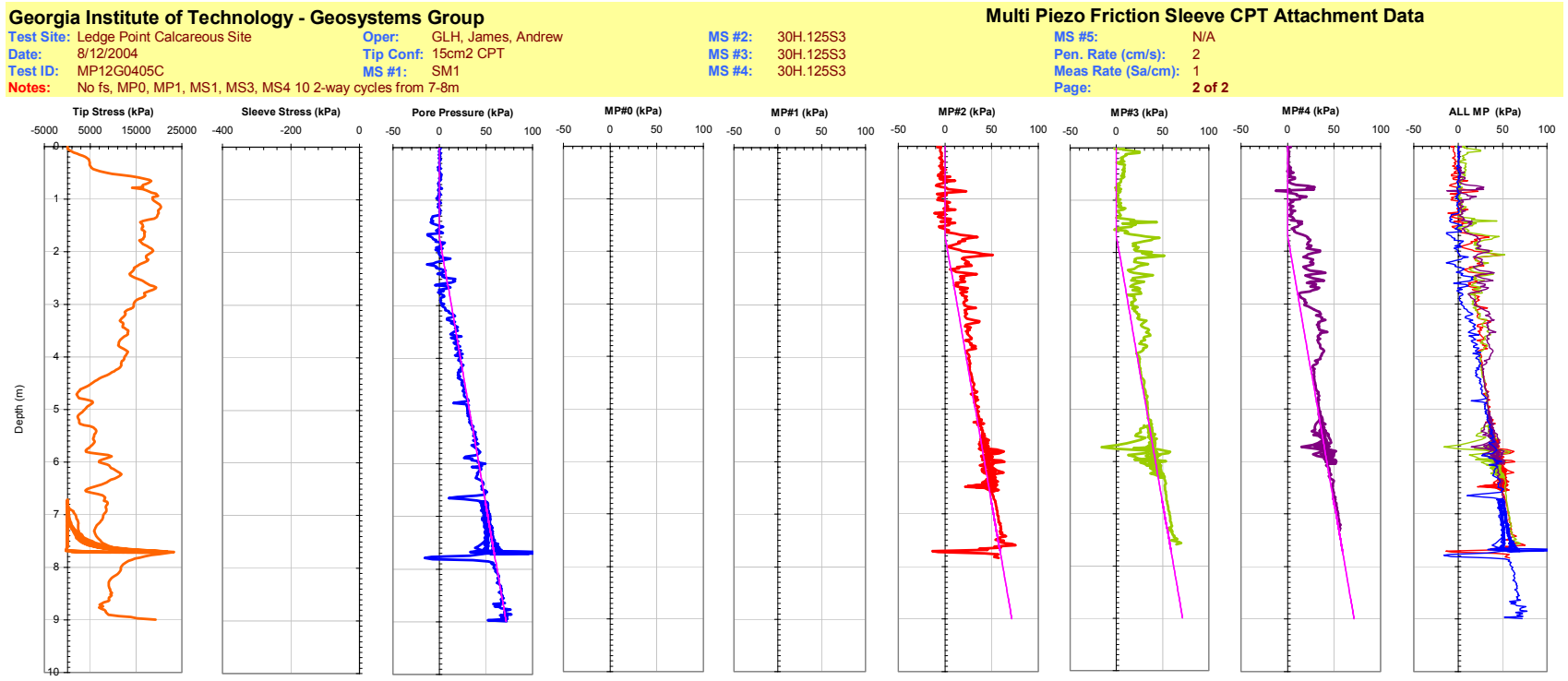

Figure 7-19b. Plots of all CPTU and the MPFA Piezo Sensors from Sounding MPFA_24 at the LPWA Site. Note the Large Amplitude (1 m) Cyclic Investigation from Tip Depths of 6.7 to 7.7 m.

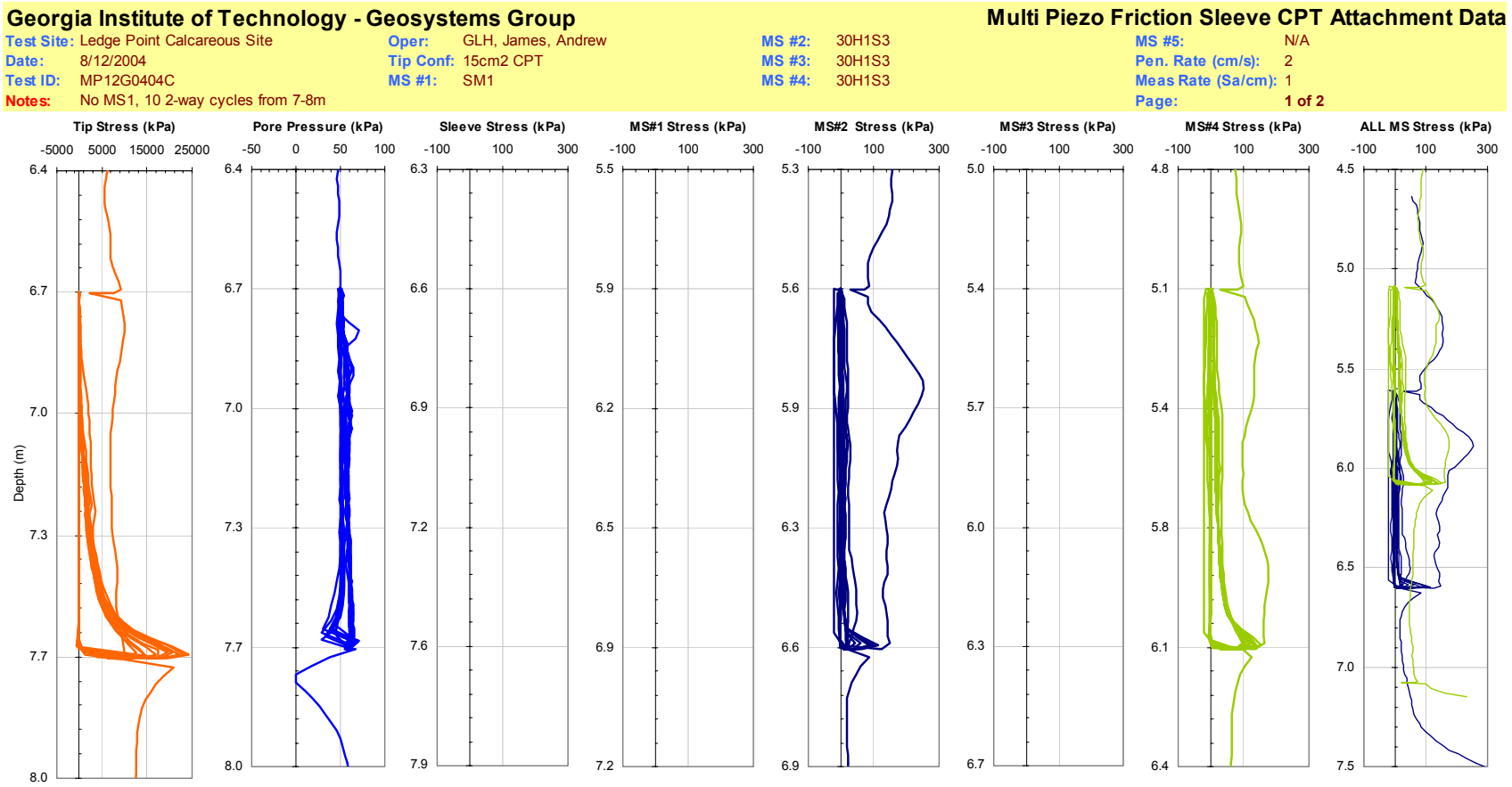

Figure 7-20a. Plots of all CPTU and the MPFA Friction Sensors from Sounding MPFA_23 at the LPWA Site Highlighting the Large Amplitude (1 m) Cyclic Investigation from Tip Depths of 6.7 to 7.7 m.

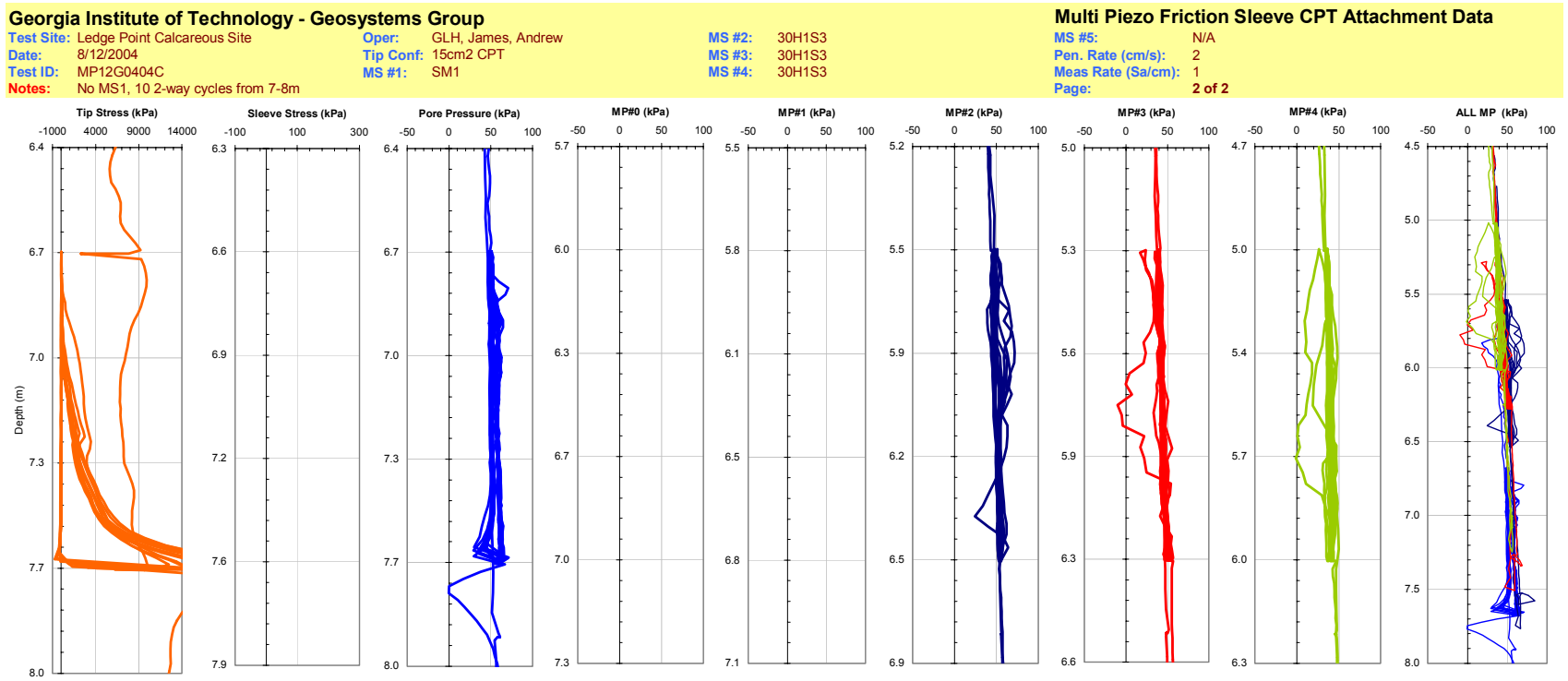

Figure 7-20b. Plots of all CPTU and the MPFA Piezo Sensors from Sounding MPFA_23 at the LPWA Site Highlighting the Large Amplitude (1 m) Cyclic Investigation from Tip Depths of 6.7 to 7.7 m.

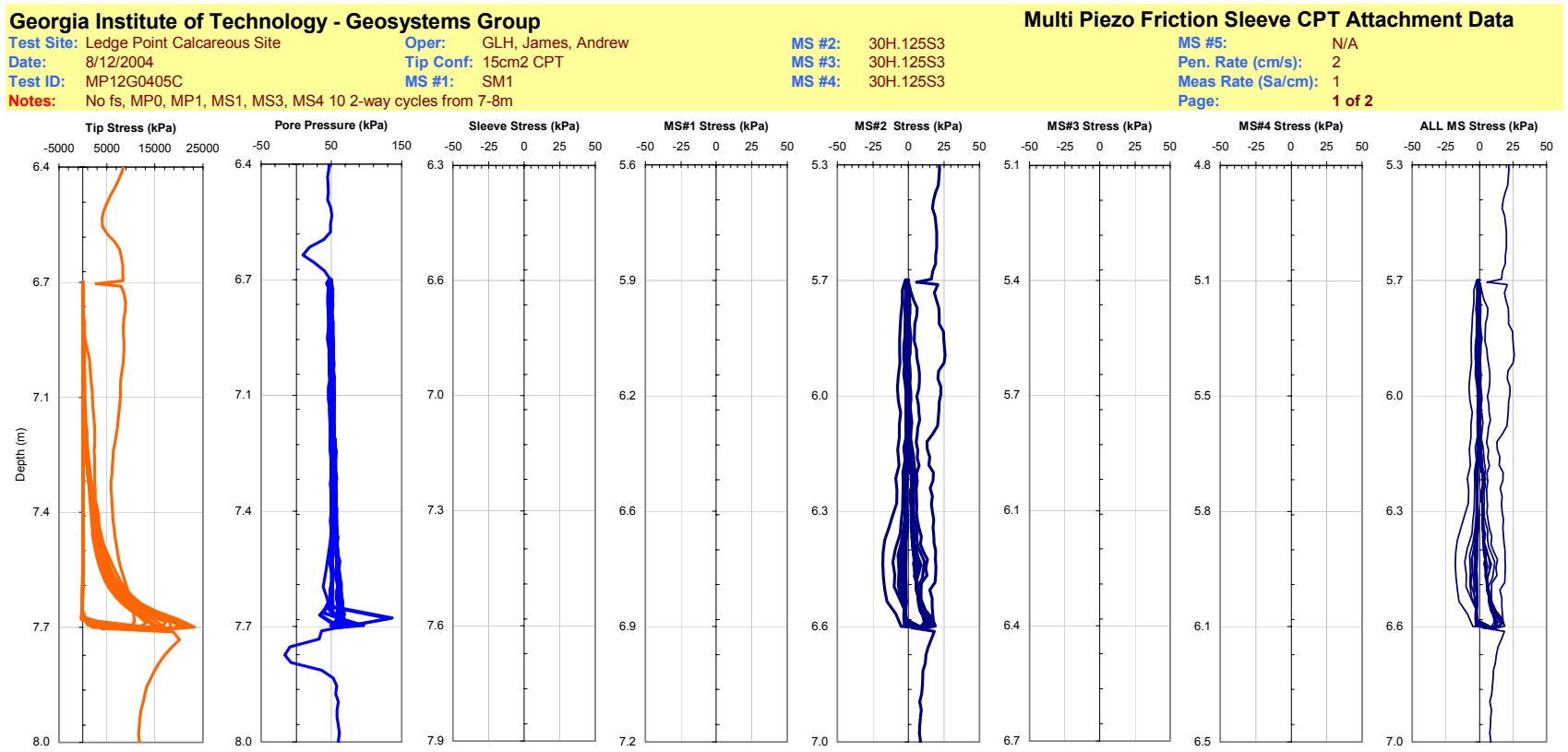

Figure 7-21a. Plots of all CPTU and the MPFA Friction Sensors from Sounding MPFA_24 at the LPWA Site Highlighting the Large Amplitude (1 m) Cyclic Investigation from Tip Depths of 6.7 to 7.7 m.

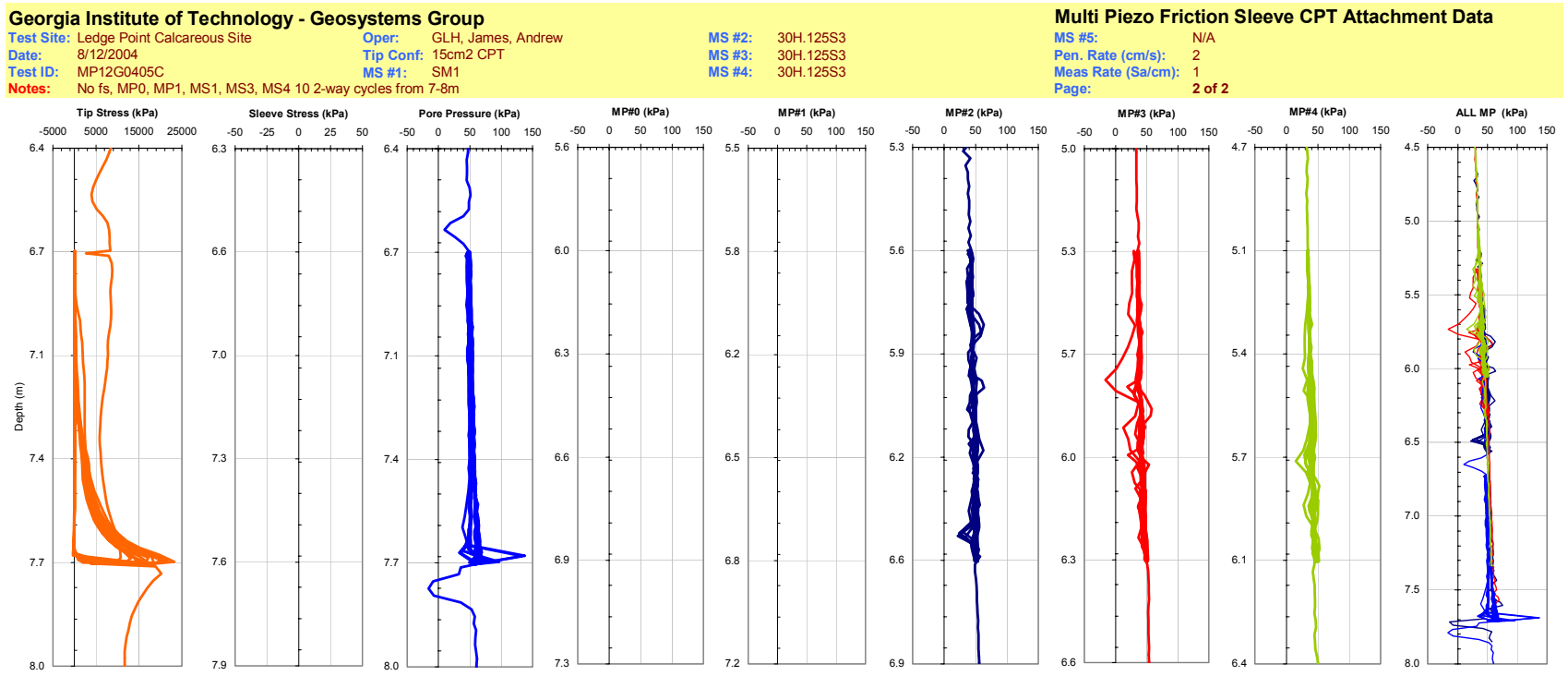

Figure 7-21b. Plots of all CPTU and the MPFA Piezo Sensors from Sounding MPFA_24 at the LPWA Site Highlighting the Large Amplitude (1 m) Cyclic Investigation from Tip Depths of 6.7 to 7.7 m.

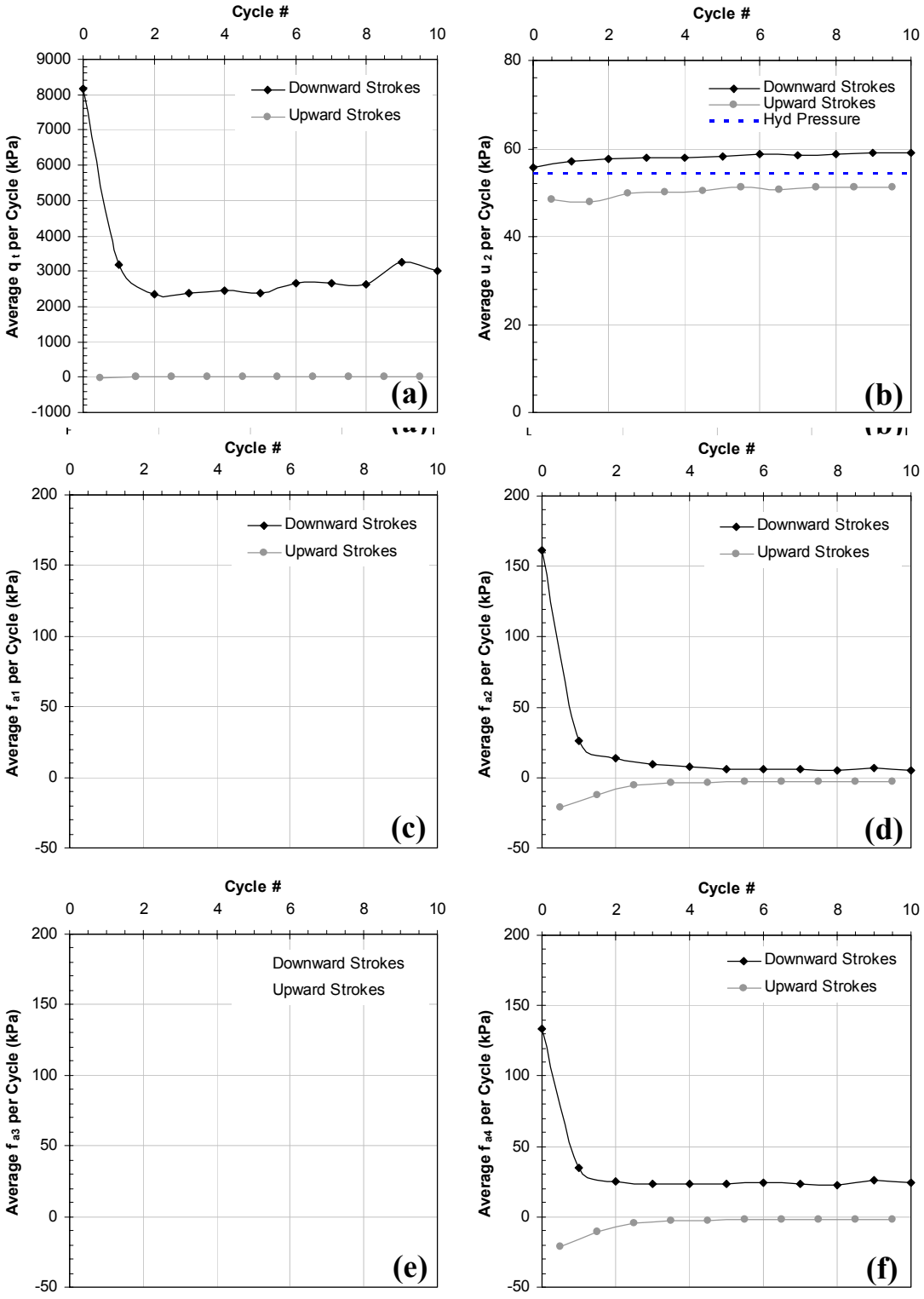

Figure 7-22(a-f). Average Large Amplitude Cyclic Response from Sounding MPFA_23 at the LPWA Site: (a) q_t, (b) u_2, (c) f_{a1}, (d) f_{a2}, (e) f_{a3}, (f) f_{a4}.

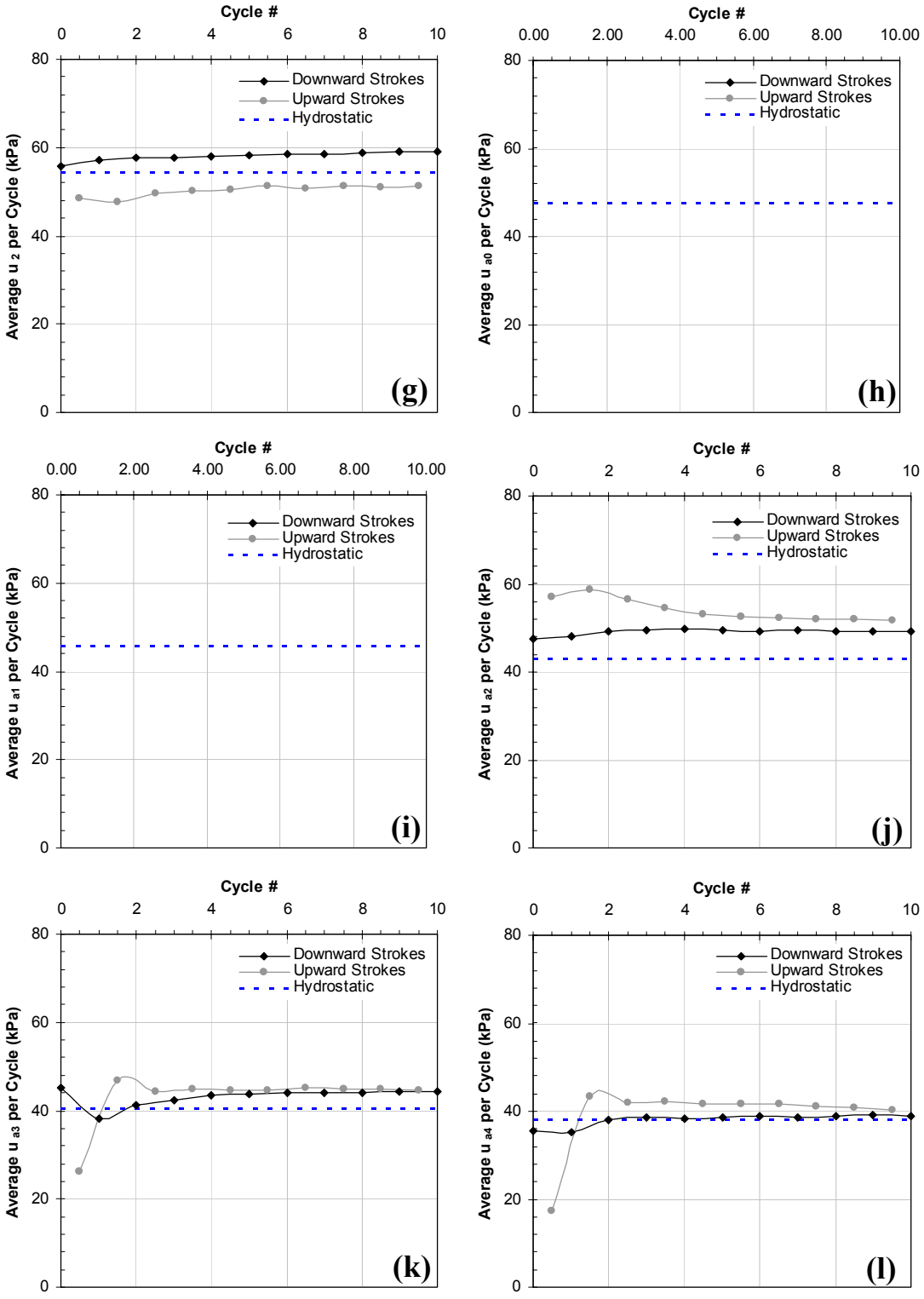

Figure 7-22(g-l). Average Large Amplitude Cyclic Response from Sounding MPFA_23 at the LPWA Site: (g) u_2, (h) u_{a0}, (i) u_{a1}, (j) u_{a2}, (k) u_{a3}, (l) u_{a4}.

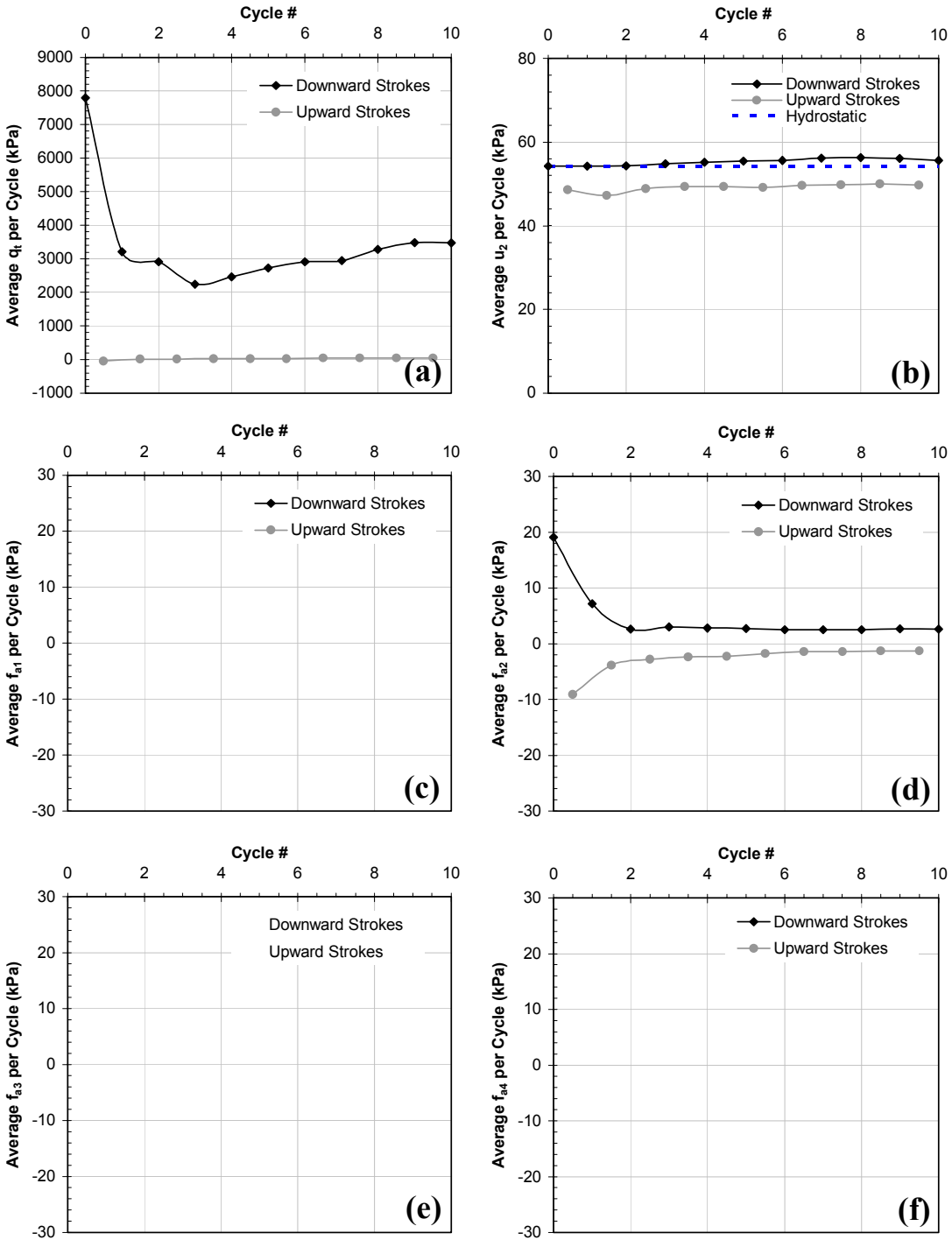

Figure 7-23(a-f). Average Large Amplitude Cyclic Response from Sounding MPFA_24 at the LPWA Site: (a) q_t, (b) u_2, (c) f_{a1}, (d) f_{a2}, (e) f_{a3}, (f) f_{a4}.

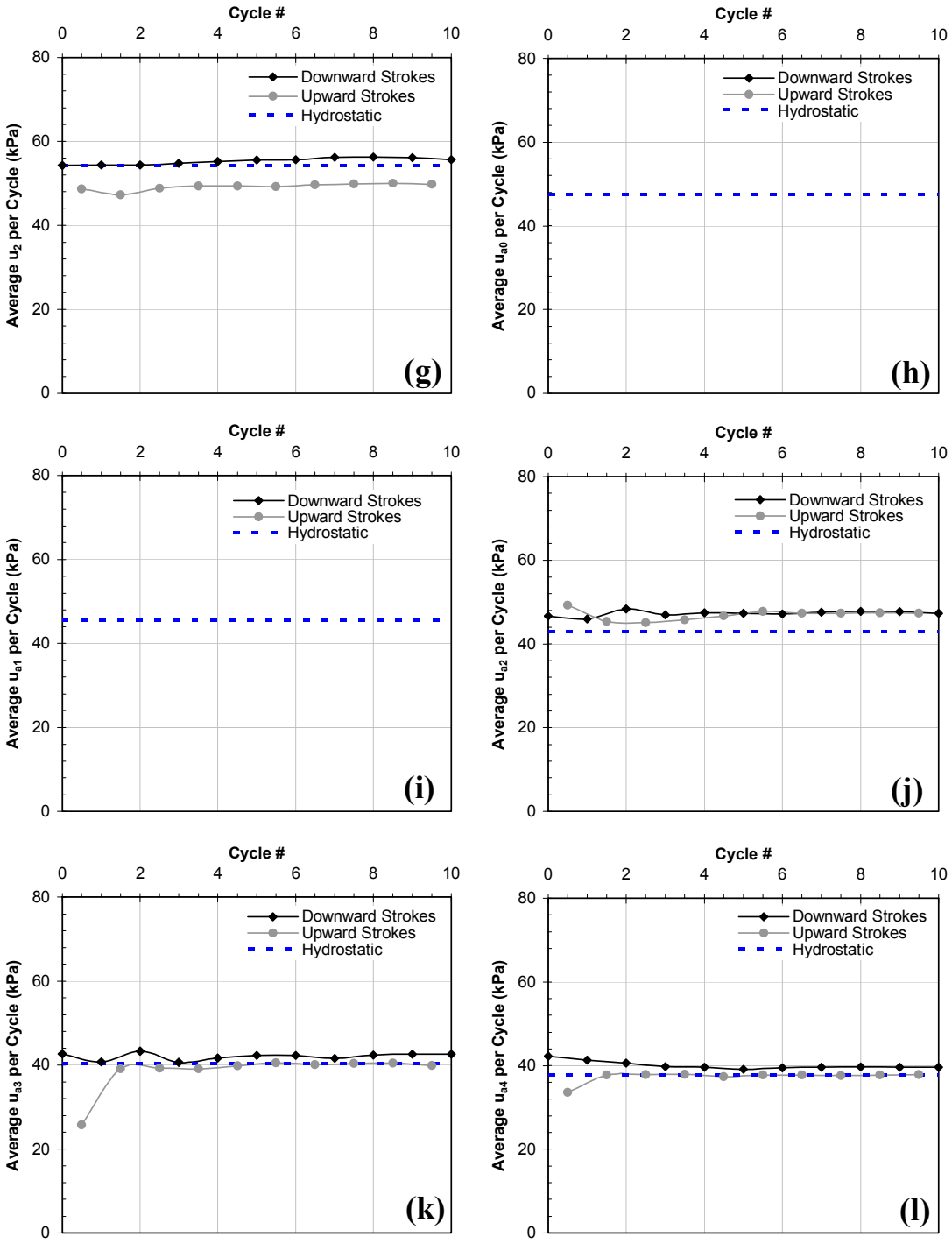

Figure 7-23(g-l). Average Large Amplitude Cyclic Response from Sounding MPFA_24 at the LPWA Site: (g) u_2, (h) u_{a0}, (i) u_{a1}, (j) u_{a2}, (k) u_{a3}, (l) u_{a4}.

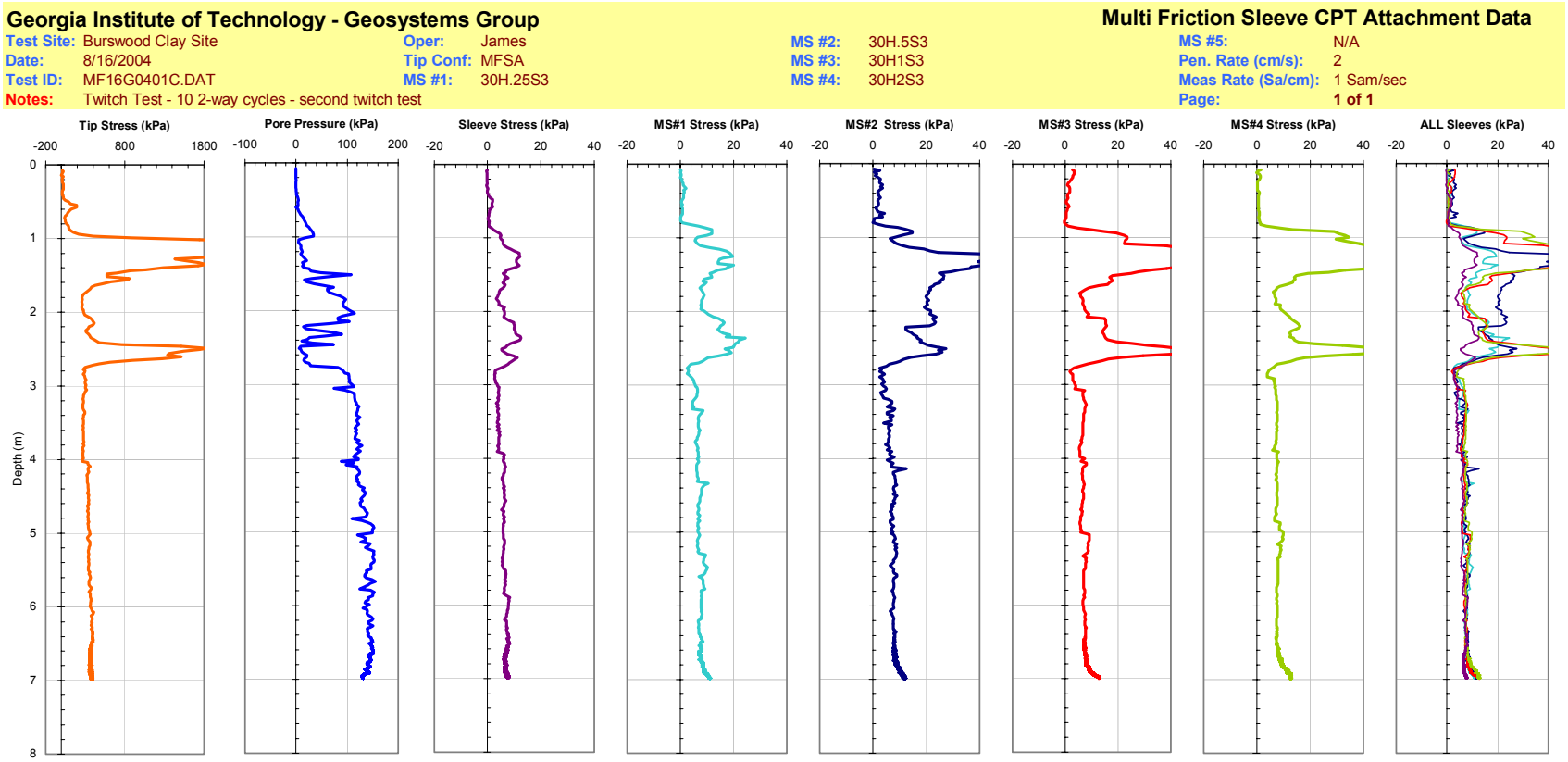

Figure 7-24. Plots of the Full CPTU-MFA Sensors Traces for Sounding #131, Including a Variable Penetration Rate Investigation Between Tip Depths of 6.0 and 7.0 m..

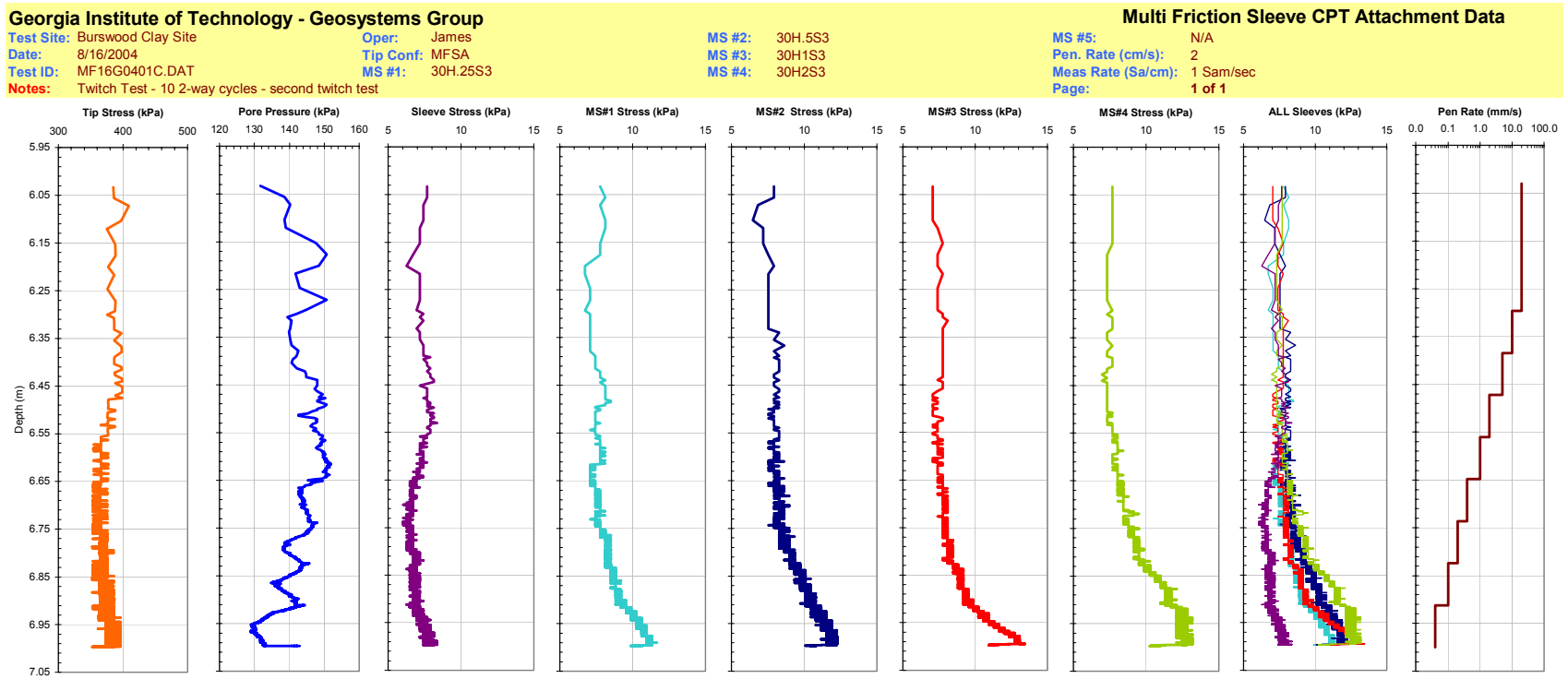

Figure 7-25. Plots of the CPTU-MFA Sensors Traces for Sounding #131 Highlighting the Variable Penetration Rate Investigation Between Tip Depths of 6.0 and 7.0 m..

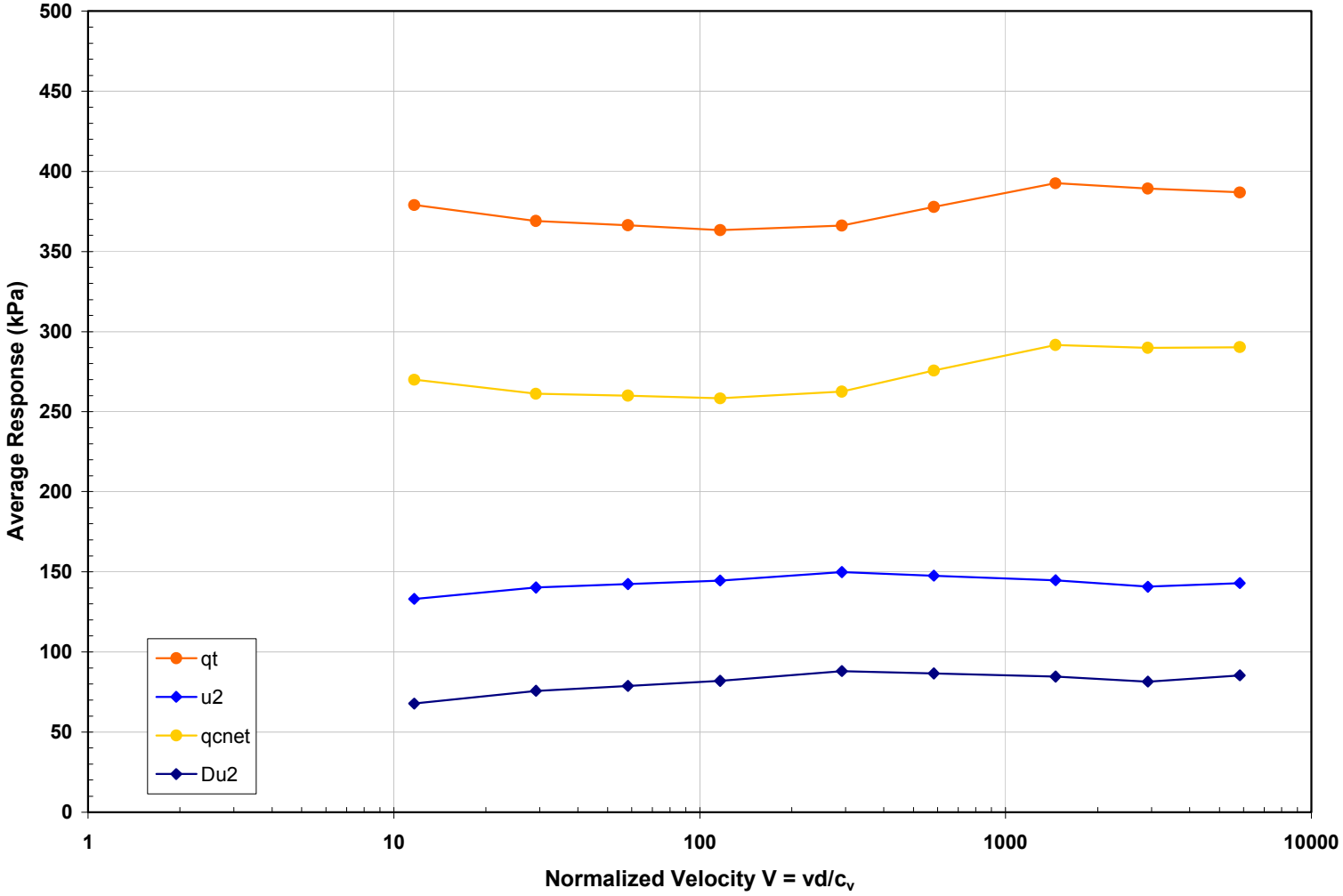

Figure 7-26. Plots of q_t, q_{cnet}, u_2, and Δu_2 Response as a Function of Normalized Penetration Velocity ($V = vd/c_v$) from Sounding #131 at the BWDWA Site.

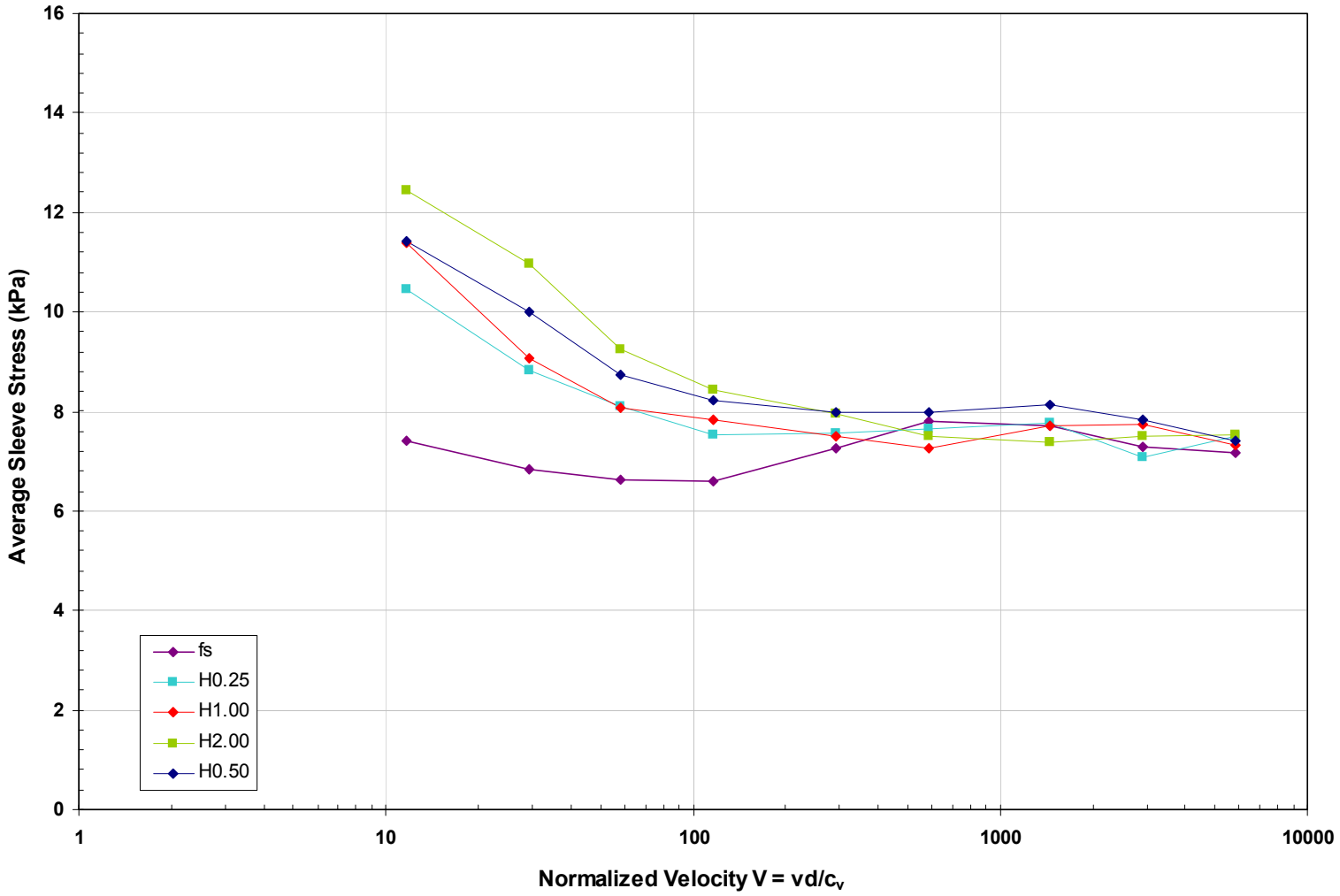

Figure 7-27. Plots of f_s, f_{a1}, f_{a2}, f_{a3}, and f_{a4} Response as a Function of Normalized Penetration Velocity ($V = vd/c_v$) from Sounding #131 at the BWDWA Site.

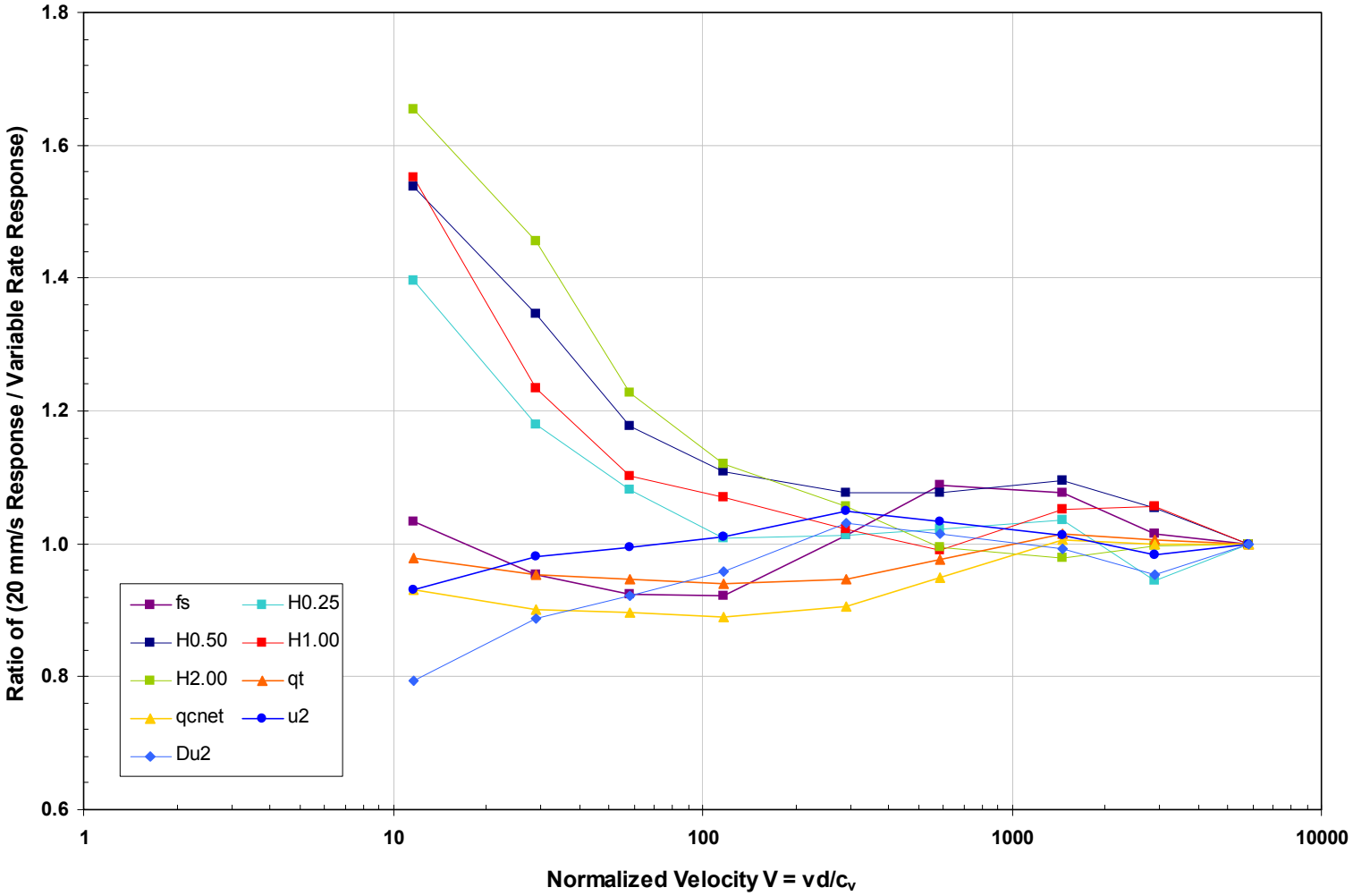

Figure 7-28. Plots of Normalized Response for all CPTU-MFA Sensors as a Function of Normalized Penetration Velocity ($V = vd/c_v$) from Sounding #131 at the BWDWA Site.

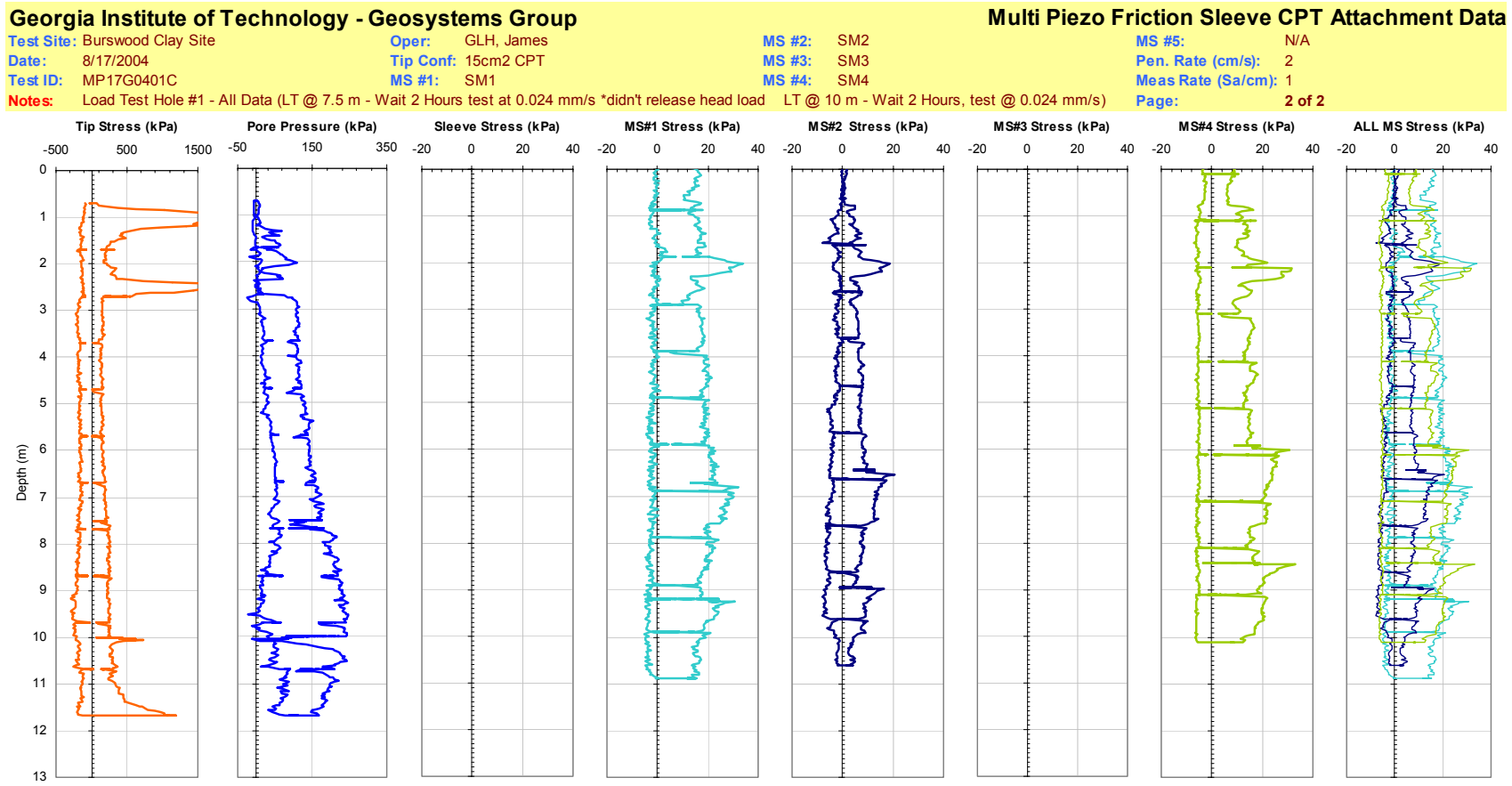

Figure 7-29a. Plots of the Full Response for all CPTU and the MPFA Friction Sensors from Sounding MPFA_25 at the BWDWA Site. Load Tests were Conducted at Tip Depths of 7.5 and 10.0 m.

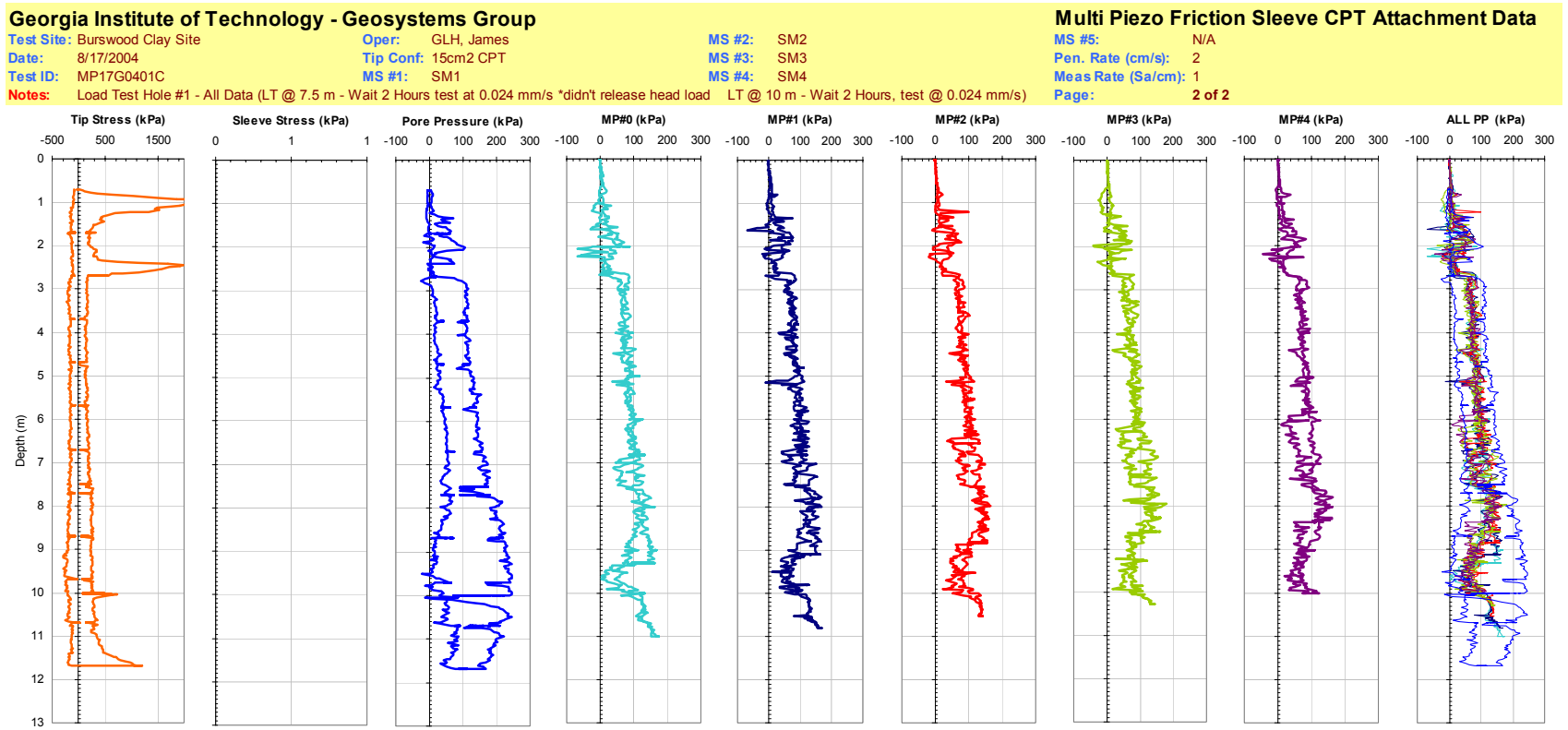

Figure 7-29b. Plots of the Full Response for all CPTU and the MPFA Piezo Sensors from Sounding MPFA_25 at the BWDWA Site. Load Tests were Conducted at Tip Depths of 7.5 and 10.0 m.

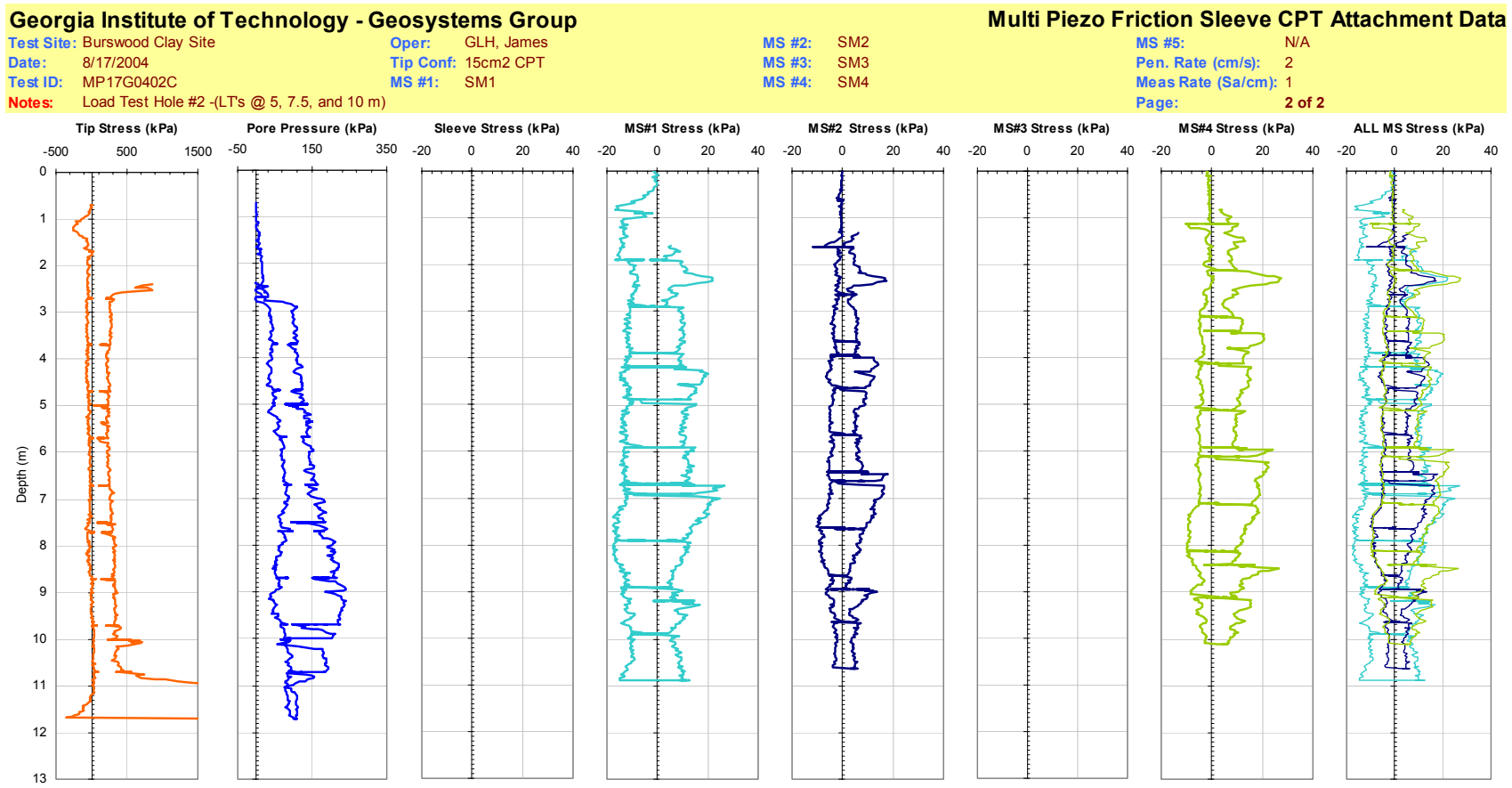

Figure 7-30a. Plots of the Full Response for all CPTU and the MPFA Friction Sensors from Sounding MPFA_26 at the BWDWA Site. Load Tests were Conducted at Tip Depths of 5.0, 7.5, and 10.0 m.

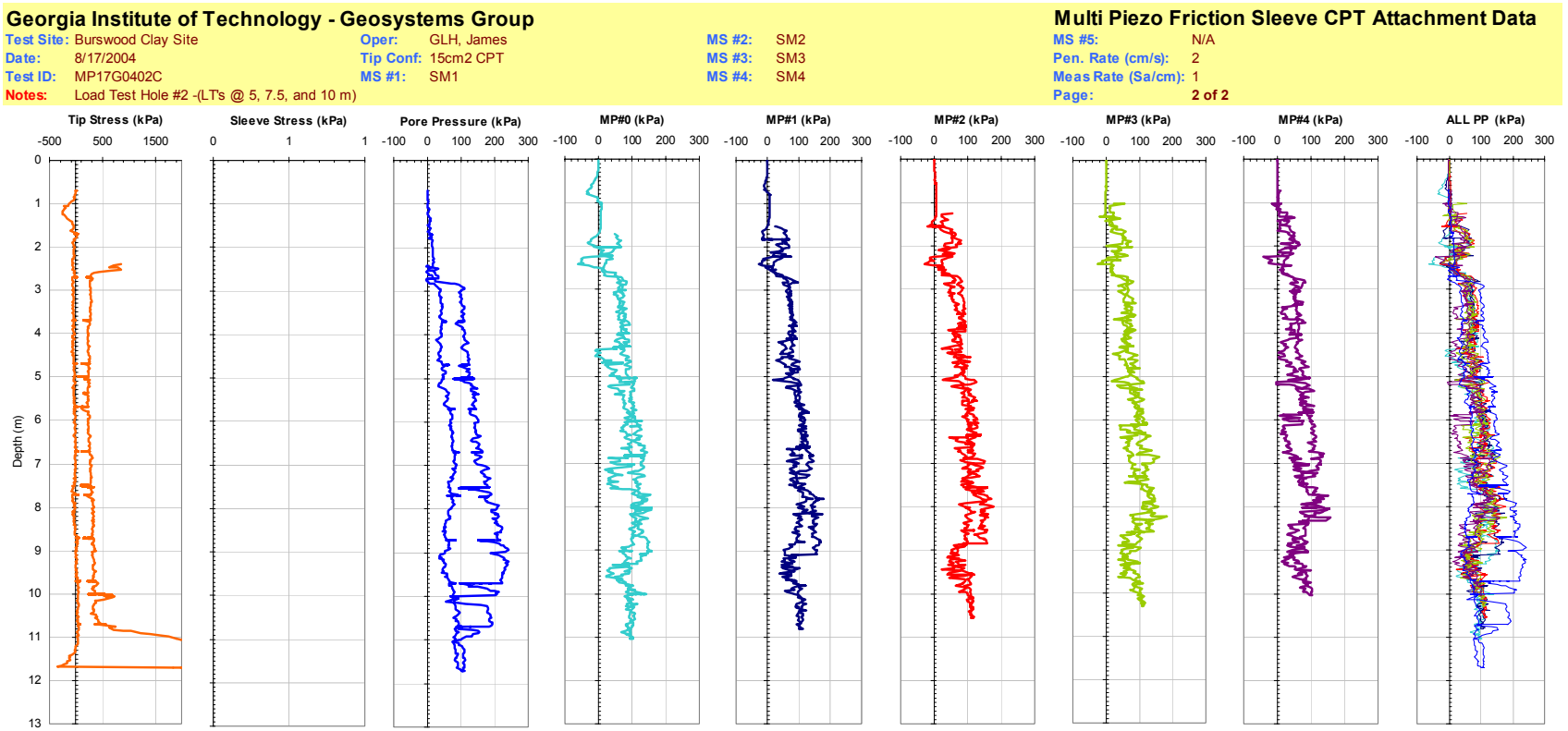

Figure 7-30b. Plots of the Full Response for all CPTU and the MPFA Piezo Sensors from Sounding MPFA_26 at the BWDWA Site. Load Tests were Conducted at Tip Depths of 5.0, 7.5, and 10.0 m.

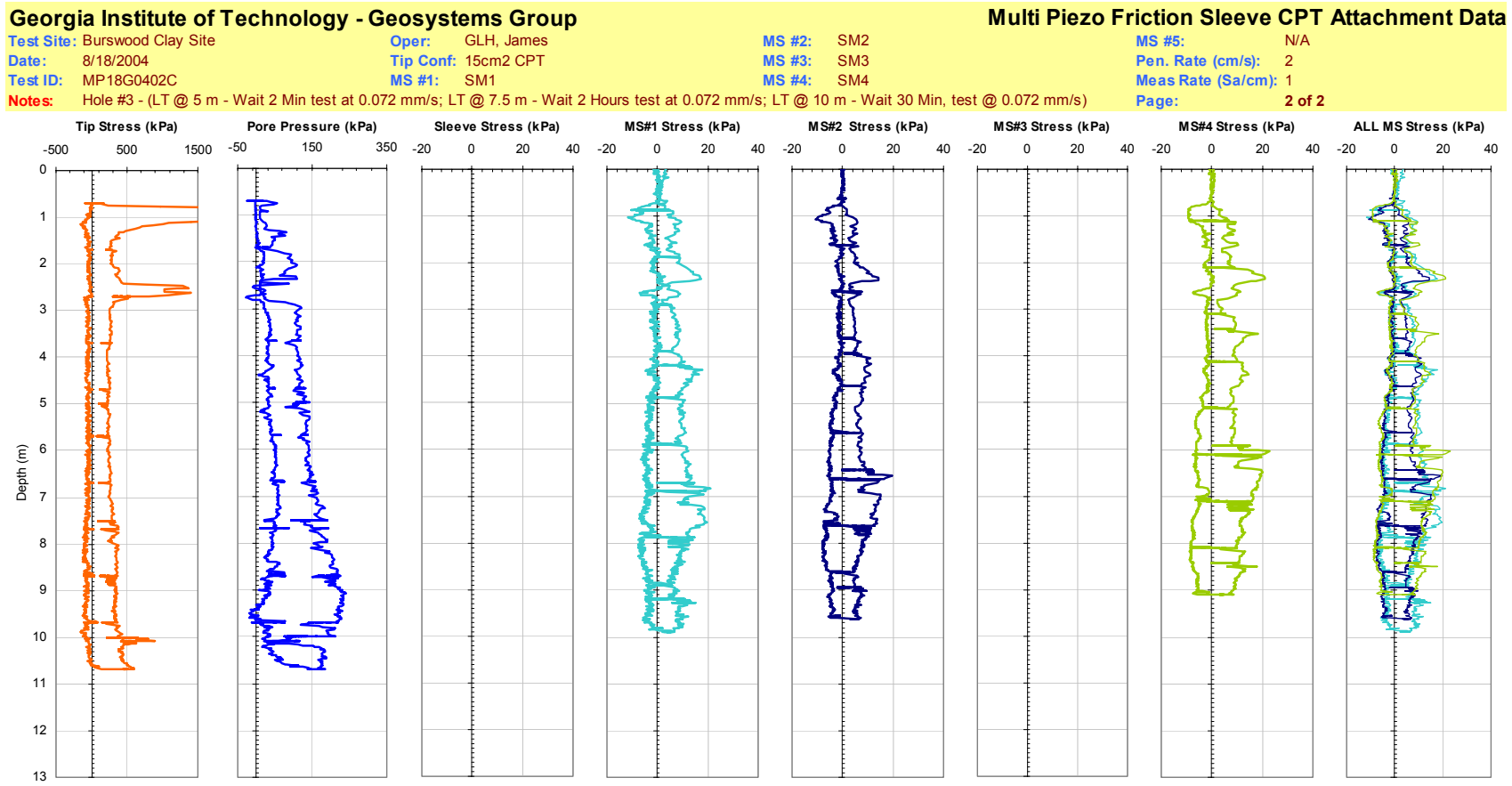

Figure 7-31a. Plots of the Full Response for all CPTU and the MPFA Friction Sensors from Sounding MPFA_28 at the BWDWA Site. Load Tests were Conducted at Tip Depths of 5.0, 7.5, and 10.0 m.

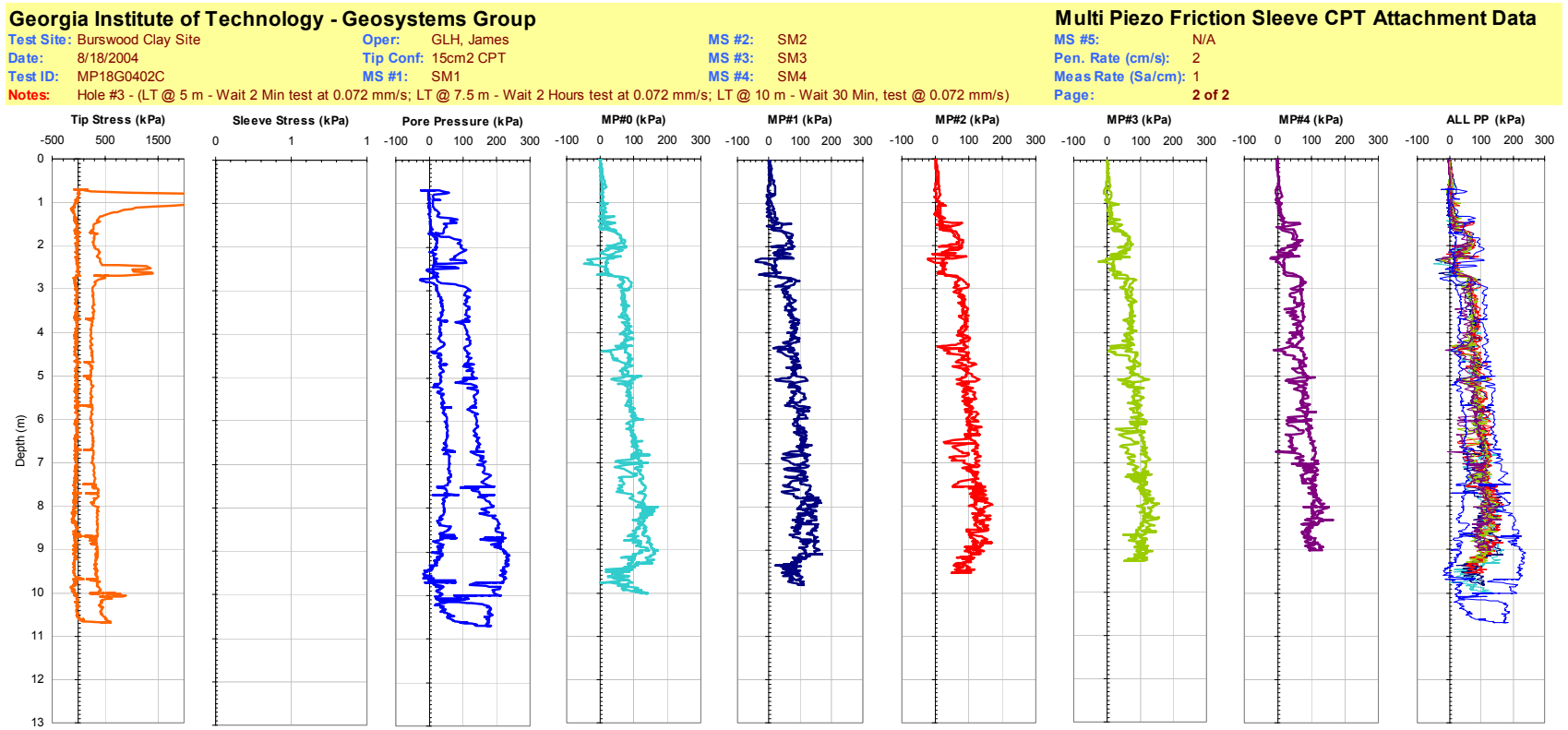

Figure 7-31b. Plots of the Full Response for all CPTU and the MPFA Piezo Sensors from Sounding MPFA_28 at the BWDWA Site. Load Tests were Conducted at Tip Depths of 5.0, 7.5, and 10.0 m.

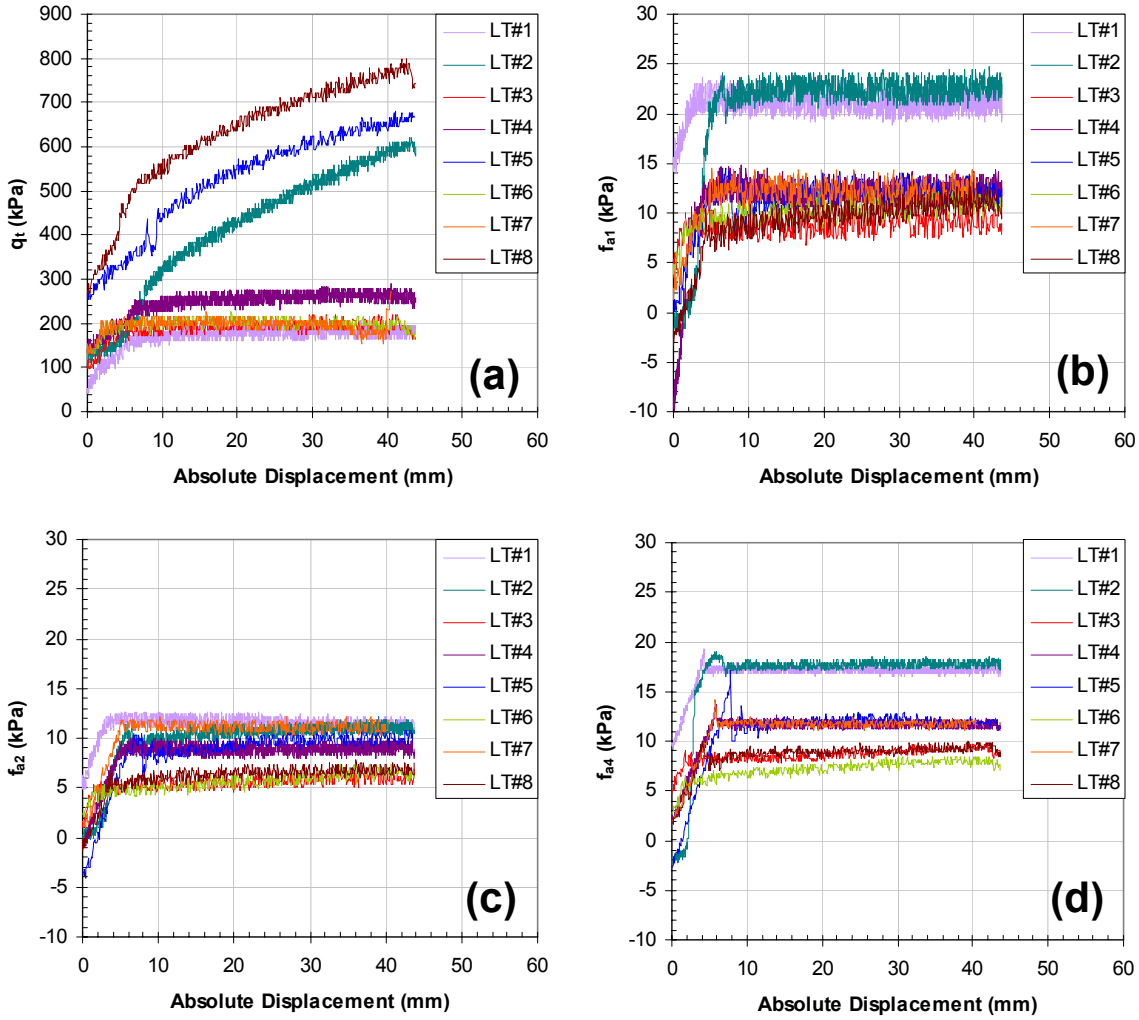

Figure 7-32. Plots of the (a) q_t, (b) f_{a1}, (c) f_{a2}, and (d) f_{a4} Responses from the Load Tests Conducted at the BWDWA Site.

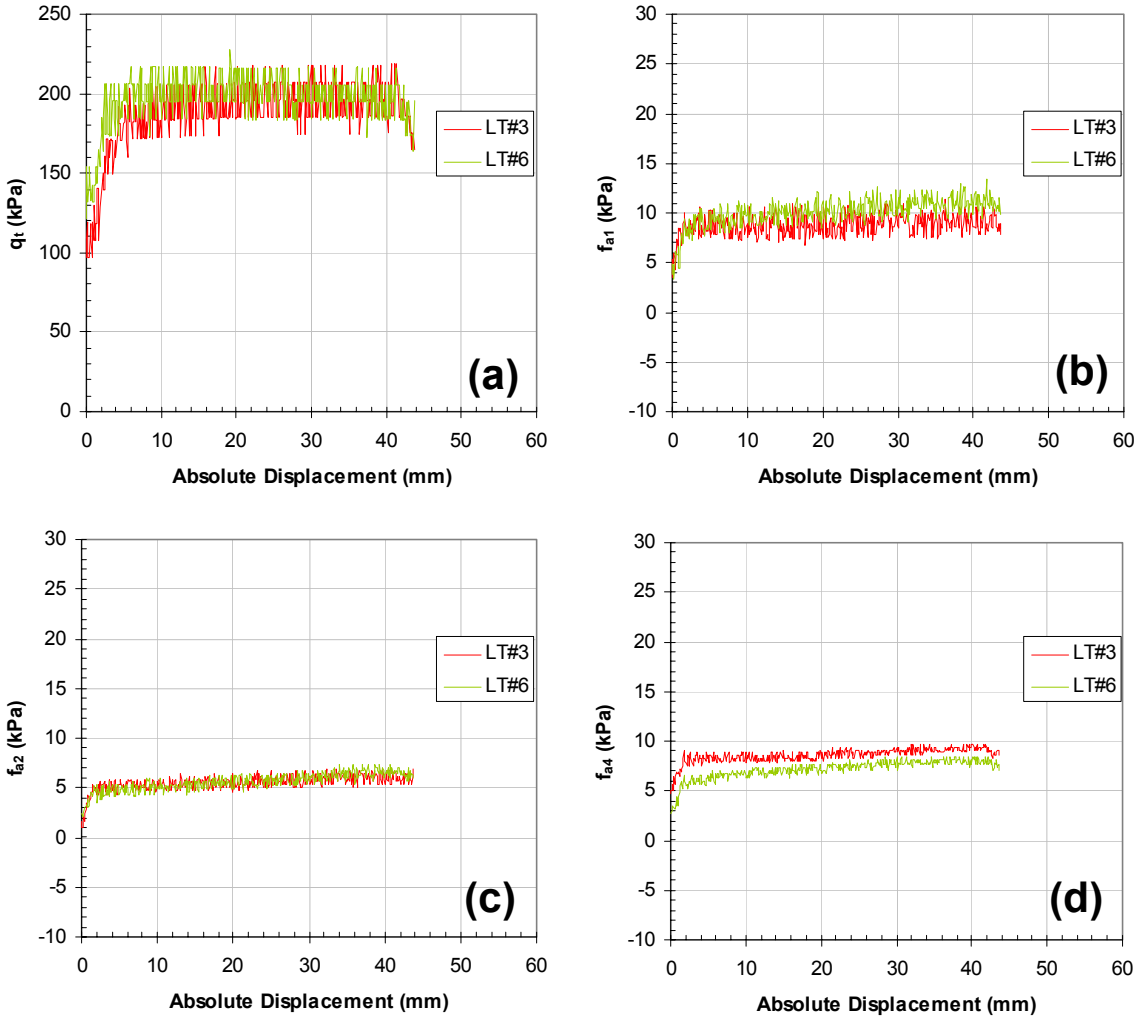

Figure 7-33. Plots of the (a) q_t, (b) f_{a1}, (c) f_{a2}, and (d) f_{a4} Responses from the Load Tests Conducted at 5.0 m Tip Depth at the BWDWA Site.

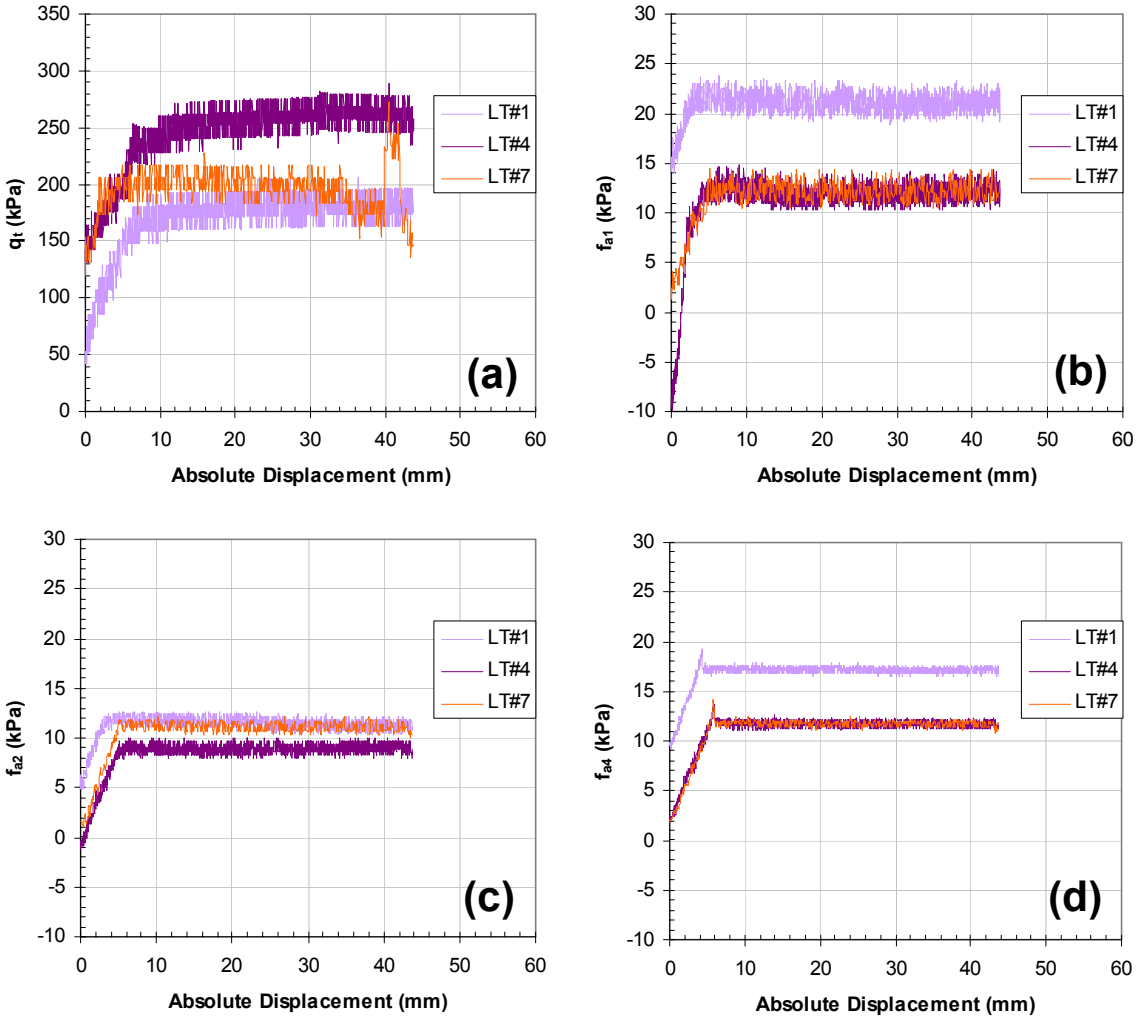

Figure 7-34. Plots of (a) q_t, (b) f_{a1}, (c) f_{a2}, and (d) f_{a4} Responses from the Load Tests Conducted at 7.5 m Tip Depth at the BWDWA Site.

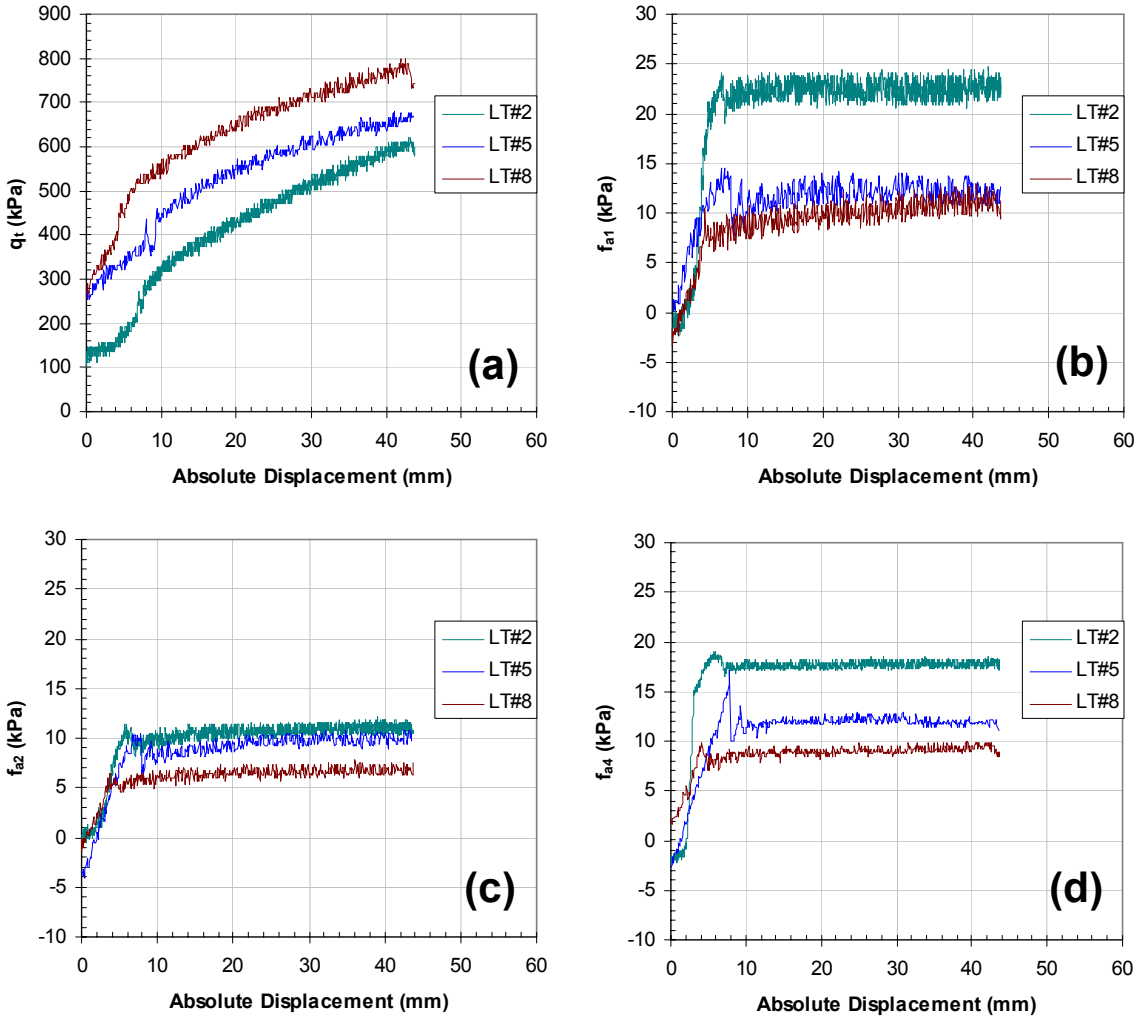

Figure 7-35. Plots of the (a) q_t, (b) f_{a1}, (c) f_{a2}, and (d) f_{a4} Responses from the Load Tests Conducted at 10.0 m Tip Depth at the BWDWA Site.

Chapter VIII
MPFA Pore Pressure Response

8.1 Introduction

8.1.1 An Brief Overview of Conventional Piezocone Response

The first published accounts of in situ piezo probe implementation are from the first European Conference on Penetration Testing (ESOPT-1) by Janbu and Senneset (1974) and Schmertmann (1974); who pushed conventional electrical piezometers in the ground to survey pore pressure response. Both Torstensson (1975) and Wissa et al. (1975) developed electronic piezo probes with the specific purpose of monitoring pore water pressures during penetration. The first instance of simultaneous pore fluid pressure and cone resistance was presented by Roy et al. (1980), with a number of other researchers presenting probes capable of measuring pore pressure in combination with both cone tip resistance and sleeve friction at the special session concerning Cone Penetration Testing and Experience at the ASCE national convention held in St. Louis, MO in 1981 (de Ruiter, 1981; Muromachi, 1981; Baligh et al., 1981; Jones et al., 1981; Tumay et al., 1981; Campanella and Robertson, 1981).

These early piezocones included pore pressure sensors in a number of locations. Current commercial penetrometers use piezo elements that are typically designated with a numerical progression of subscripts, as follows: directly on, or protruding from the cone tip (u_t), tip midface (u_1), located at the shoulder position directly behind the tip (u_2) or (u_{bt}), and located directly behind the friction sleeve (u_3); with measured pore pressures typically following a $u_1 > u_2 > u_3$ relationship (Lunne et al., 1997). The u_2 element

position has become the typical element location in many regions due to the need for pore water correction to the cone tip resistance $q_c \rightarrow q_t$, with u_1 and u_t elements also popular in in certain geographic regions due to their increased profiling ability. Typical piezocones only have a single pore pressure sensor, with multi element sensors sometimes used in research applications and offshore (Sills et al., 1988; Bayne and Tjelta, 1987; current work).

8.1.2 A Review of the MPFA Piezo Sensing Capabilities

The development and configuration of the MPFA device is detailed in Section 5.7, and is briefly summarized herein to remind the reader of the unique features and sensor configuration of the MPFA device. The MPFA device is typically used in conjunction with a digital 15 cm^2 CPTU unit, configured with a u_2 pore pressure sensing element. The MPFA device can be used with any number of instrumented or uninstrumented forward modules, however, the results obtained in the current work are restricted to the above CPTU unit and two uninstrumented dummy tips of lengths 163 and 1062 mm, respectively. The MPFA device, Figure 8-1, is outfitted with five additional piezo sensors, located at distances of 670, 880, 1140, 1400, and 1660 mm behind the CPTU tip, and are denoted as sensors u_{a0}, u_{a1}, u_{a2}, u_{a3}, and u_{a4} respectively. While the CPTU u_2 element is comprised of a ring element, each of the MPFA sensors is comprised of a disk (or button) element 12.5 mm in diameter. The elements are hydraulically connected to pore fluid reservoirs housing the pressure transducers, with high viscosity silicon oil used as the permeant fluid to saturate both the elements and sensor reservoirs in the current device. As shown in Figure 8-1, sensors u_{a1} - u_{a4} are located adjacent to the uphole end of the MPFA friction sleeves, with the u_{a0} sensor providing a baseline measurement of shaft

pore pressure before encountering the MPFA sleeves. All pore pressure transducers included in the CPTU-MPFA have a working capacity of 3.5 MPa, and an accuracy of 0.1% of the working range.

8.1.3 Primary Objectives of Measuring Penetration Pore Pressures

The two primary objectives when measuring penetration pore pressures are to define the basic hydrogeologic conditions of the area, and to use the observed magnitudes of generated excess pore water pressures to characterize the properties of soil. The definition of the hydrogeologic domain typically consists of defining the current ground water table elevation, the qualitative degree of saturation of various strata, the existence of perched or confined water conditions, and the overall flow regime of the system. Masking the identification of the hydrostatic groundwater conditions during penetration is the disturbance of the soil induced during probe penetration, resulting in the possible generation of excess pore water pressures and the creation of previously nonexistent vertical flow paths.

8.1.4 Changes in the Pore Pressure Regime due to Penetration

There exist three major phases over the course of any CPT investigation or piling installation; consisting of: installation, equalization, and subsequent loading after or during equalization. This section details the fundamental concepts that control the changes in the pore pressure regime surrounding a probe or pile over the course of these three phases.

8.1.4.1 Installation Pore Pressures

Excepting penetration in the top few meters, CPT penetration is typically considered a deep penetration problem, as the soil has minimal freedom to deform axially and the deformations are predominantly forced in the lateral direction (Houlsby and Teh, 1988). This constrained deformation induces changes in the pore pressure regime surrounding a penetrometer. Penetration pore pressures measured at any location on a penetration device can be divided into two components: the in situ equilibrium value u_0, controlled by the local ground water regime; and the excess pore pressures, Δu, generated by the penetration procedures(steady-state, extraction, cyclic, etc.). The magnitude of Δu being controlled by the soil behavior and probe geometry. Under drained penetration conditions the generated excess pore pressures are negligible, with CPT penetration at standard rates in sands typically corresponding to a fully drained condition. Standard rate CPT penetration in intermediate soils (e.g. silts, peats) typically occurs at a state of partial drainage, whereas, standard penetration in soils of low hydraulic conductivity (e.g. clays), typically occurs under fully undrained conditions. For the cases of partially drained and undrained penetration, excess pore pressures are generated by both the increase in mean normal stress caused by the displacement of pore fluid during installation and the increase in mean shear stress resultant from the large induced shear strains. The formulation of Henkel (1959) provides a framework to describe the changes in pore pressure as a function of changes to mean normal and shear stress:

$$\Delta u = \beta \cdot \Delta \sigma_{oct} + \alpha \cdot \Delta \tau_{oct} \qquad \text{(Eq. 8-1)}$$

where α and β are Henkel's pore pressure parameters, with β taken equal to 1 for saturated clays, and α dependent on the soil behavior and applied stress path.

CPT penetration, and the parallel procedure of pile installation, have been the focus of a large number of studies reported in the geotechnical literature. A rigorous analysis technique for fully modeling deep cone penetration for realistic soil and installation conditions is not currently available, as detailed in the recent reviews carried out by Yu and Mitchell (1998) and Lunne et al. (1997). Some of the main difficulties in rigorously analyzing deep cone penetration stem from the large deformations; the existence of very large stress and pore pressure gradients; soil anisotropy, viscous effects, nonlinear soil and interface behavior; the presence of water and/or gas requiring multiphase analyses, and installation procedures typically involving disruptions in penetration. As such, a number of approaches have been formulated to study cone penetration and pile installation which involve simplifying assumptions regarding the soil behavior, failure mechanism, boundary conditions, and/or installation procedures. The most common approaches include: cavity expansion theory, bearing capacity theory, steady-state deformation analysis, incremental finite-element analysis, and the strain path method (Yu et al., 2000).

The strain path method is a robust methodology used to study deep steady-state undrained penetration developed by Baligh (1975, 1985). This method relies on observations made by Baligh (1975), that soil deformations and strains are predominantly independent of soil strength for deep penetration problems due to the severe kinematic constraints. The application of this observation relies on the fact that deep penetration problems are strain-controlled, unlike shallow problems, which are stress controlled. As

such, it is possible to estimate the strain field caused by deep penetration using simple soil properties such as isotropy, homogeneity, and incompressibility. If one assumes that inertial effects can be neglected, the problem of deep penetration is reduced to a flow problem with soil particles moving along streamlines around a fixed rigid body. Several researchers have found that using the behavior of an inviscid fluid as an initial estimate of the soil flow field is acceptable for modeling saturated clays (Baligh, 1985; Teh and Houlsby, 1991). After calculating the flow line resultant from the steady state installation of the modeled geometry, the strain level at any location can be calculated by integrating the strain along a flow line from a point outside the influence zone to the point of interest. Subsequent implementation of a constitutive soil model to the calculated initial strain field allows the state of stress and pore pressure regime surrounding a CPT or pile to be defined.

A drawback of the strain path method is that the resulting stresses derived from this approach typically do not satisfy all of the equilibrium conditions (Baligh, 1985, 1986; Houlsby et al., 1985; Teh, 1987; and Teh and Houlsby, 1991). Additionally, the strain path method is not well suited for dilative (i.e. high OCR) clays or frictional soils, as the resultant stress fields after penetration are more heavily coupled to the in situ soil properties. Burns and Mayne (1998) developed an analytical cavity expansion, critical state soil mechanics formulation capable of modeling dilatory dissipation responses (increasing initial dissipation response followed by decreasing response to hydrostatic conditions). Dilatory responses have also been observed in normally consolidated materials, with Lehane (1992) hypothesizing that the initial increase in excess pore pressure is the result of pore pressures migrating from the shear zone to the probe surface,

with the actual shear zone located a short radial distance from the interface. Recent work by Yu et al. (2000) describes the development of a steady state finite element scheme that solves for the initial stress-strain-pore pressure regime after CPT installation without the need for time domain iteration. Their method alleviates some of the above problems associated with the strain path method by satisfying the equilibrium conditions, and is applicable across a wide range of constitutive relations. This technique can theoretically also be applied to the penetration of dilatant and frictional soils, and Yu et al. (2000) indicated that future work is continuing in this direction.

The finite element and strain path approaches both require involved numerical analysis in order to determine the stress-strain and pore pressure regime induced by deep cone penetration and are restricted in applicability across certain soil types and for layered stratigraphy. As such, several authors have indicated that simpler solutions often provide adequate estimates of pore pressure response and are typically applied in practice (Lunne et al., 1997). The most commonly applied approach, is the theory of cavity expansion (Tavenas et al., 1973; Roy et al., 1974; Torstensson, 1975), which was formulated for an ideal elasto-plastic Mohr-Coulomb soil by Vesić (1972). The failure zone near the tip is taken comparable to the expansion of a spherical cavity and the failure zone surrounding the penetrometer shaft is taken comparable to that generated by the expansion of a cylindrical cavity. Assuming the initial stress conditions are isotropic, the pore pressures induced at any point within the plastic zone created by the cavity expansion (either spherical or cylindrical) can by obtained from Equations 8-2 and 8-3 for spherical and cylindrical cavities, respectively (Vesić, 1972; Massarsch, 1976):

$$\frac{\Delta u_{oct}}{s_u} = 4\ln\left[\frac{a}{r}\cdot I_r^{1/3}\right] + 0.94\alpha_f \quad \textit{(Spherical)} \qquad \text{(Eq. 8-2)}$$

$$\frac{\Delta u_{oct}}{s_u} = 2\ln\left[\frac{a}{r}\cdot \sqrt{I_r}\right] + 0.82\alpha_f \quad \textit{(Cylindrical)} \qquad \text{(Eq. 8-3)}$$

where a = radius of the cavity (penetrometer or pile), r = radial variable at which Δu is computed, s_u = undrained shear strength, $I_r = G/s_u$ = rigidity index, and a_f = Henkel's pore pressure coefficient at failure. The above equations apply within the plastic zone created by the cavity expansion, the extent of which is theoretically defined by Equations 8-4 and 8-5:

$$R_P = a\cdot I_r^{1/3} \quad \textit{(Spherical)} \qquad \text{(Eq. 8-4)}$$

$$R_P = a\cdot \sqrt{I_r} \quad \textit{(Cylindrical)} \qquad \text{(Eq. 8-5)}$$

where R_P = the radial extent of the plastic zone created by the expansion of a cavity of radius, a.

The selection of an appropriate rigidity index applicable to the soil conditions during installation is important, with Leroueil et al. (1979) noting reductions of lab calculated I_r and s_u on the order of 50 and 30% respectively for the destructured conditions present along the shaft after installation in natural clays. Fully applying the above reduction factors across the entire plastic zone has shown to under predict observed pore pressures at larger radial distances (Roy et al., 1981). As such, the variation in the level of destructuring with radial distance should be considered when applying reductions to structured soil parameters. In the current study, all of the

measurements are conducted at the pile interface corresponding to the maximum level of destructuring during installation.

Field methods conducted under similar stress-strain conditions typically produce reliable estimates of s_u and other soil properties for use in predicting excess pore pressures generated by installation. As such, an estimate of s_u is typically obtained from the penetration resistance through a bearing capacity formulation, as shown by Lunne et al. (1997):

$$s_u = \frac{q_{tnet}}{N_{kt}} \ , \ q_{tnet} = \left(q_t - \sigma_{vo}\right) \qquad \text{(Eq. 8-6)}$$

where N_{kt} = the empirical cone factor. Unfortunately, the value of N_{kt} has been shown to be highly site specific when compared with laboratory or other in situ s_u determinations, varying over a wide range from 8 to 30; dependent on soil properties (predominantly I_P and G), sample disturbance, and test type. Subsequent research into the wide range of N_{kt} values has somewhat narrowed this range to 8 to 20 for unfissured clays, however, it is still considered prudent to obtain a correlation between the undrained strength values determined from the CPT tip resistance and a standard reference test method (e.g. field vane, laboratory tests) on a site specific basis (Lunne et al., 1997).

Estimates of I_r applicable to cone penetration problems are typically determined by degrading the small strain modulus (G_0) determined from shear wave velocity (V_S) measurements and an estimate of the total mass density (ρ_{tot}), Equation 8-7. The modified hyperbola modulus degradation framework of Fahey and Carter (1993) is typically used and is presented as Equation 8-8:

$$G_0 = \rho_{tot} \cdot V_S^2 \qquad \text{(Eq. 8-7)}$$

$$\frac{G_{\sec}}{G_0} = 1 - f\left(\frac{q}{q_{ult}}\right)^g \qquad \text{(Eq. 8-8)}$$

where q/q_{ult} = strength mobilization ratio, with f and g the fitting parameters of the model. For penetration in most clays, Mayne (2001) recommends that taking f = 1, g = (0.2 to 0.4), and q/q_{ult} = 0.5 typically provides good agreement with measured response. In cases where V_S is not available, Mayne (2001) provides a relationship to calculate I_r from I_P and *OCR* based on the CAUC triaxial data of Keaveny and Mitchell (1986), Equation 8-9; with Mayne and Rix (1995) providing a relationship for V_S based on q_t and e_0, Equation 8-10:

$$I_r = \frac{\exp\left[\dfrac{137 - I_P}{23}\right]}{\left[1 + \ln\left(1 + \dfrac{(OCR-1)^{3.2}}{26}\right)\right]^{0.8}} \qquad \text{(Eq. 8-9)}$$

$$V_S = 14.02 \cdot q_t^{0.364} \cdot e_0^{-0.49} \qquad \text{(Eq. 8-10)}$$

where I_P = plasticity index and OCR = Overconsolidation Ratio. If the I_P of the given material is greater than 60, the value of I_r calculated using Eq. 8-9 should be determined using I_P = 60.

8.1.4.2 The Equalization of Excess Pore Pressures

During interruptions in penetration or after pile installation, any excess pore pressures generated during installation will begin to equalize. The equalization of pore pressures surrounding an installed probe or pile results in consolidation or swelling of the soils within the influence zone dependent on the state of pore pressures with respect to the equilibrium conditions. Fahey and Lee Goh (1995) suggest that typical conditions

during equalization, range from consolidation near the interface to swelling at greater radial distances. As such, they suggest that the appropriate I_r for this condition is best determined using the geometric mean of the small and large strain shear moduli.

The dissipation of excess pore pressures (either positive or negative) is primarily controlled by the initial pore pressure regime, the coefficient of consolidation, and the hydraulic conductivity of the soil. The fundamental relationship between these two soil parameters is presented as Equation 8-11:

$$c = k \cdot \frac{M}{\gamma_w} \qquad \text{(Eq. 8-11)}$$

where c = the coefficient of consolidation, k = the hydraulic conductivity (also termed the geotechnical permeability), M = constrained modulus relevant to the problem being modeled (i.e. unloading, reloading, virgin loading), and γ_w = the unit weight of water. Due to soil and stratigraphic anisotropy both c and k can have different values in the horizontal (c_h, k_h) and vertical (c_v, k_v) directions. Equation 8-12 shows the relationship between the directional values of c and k, with typical ranges of k_h/k_v summarized by Baligh and Levadoux (1980) and reproduced as Table 8-1.

$$c_h = c_v \cdot \frac{k_h}{k_v} \qquad \text{(Eq. 8-12)}$$

The c and k flow parameters vary over many orders of magnitude and are some of the most difficult parameters to accurately determine in geotechnical engineering; with accuracy on the order of one order of magnitude typically considered an acceptable estimate (Lunne et al., 1997).

A typical procedure for determining the coefficient of consolidation using a piezocone is to conduct a dissipation test. A dissipation test consists of stopping cone penetration and monitoring the change in pore pressures as a function of elapsed time, simulating the equalization of pore pressures after full pile installation at the test depth. The changes in pore pressures over time are typically compared in normalized form as shown in Equation 8-13:

$$U = \frac{u_t - u_0}{u_i - u_0} \qquad \text{(Eq. 8-13)}$$

where U = normalized excess pore pressure, u_0 = hydrostatic pore pressure, u_t = measured pore pressure at time t, and u_i = the initial pore pressure. The measured normalized response is then compared to a theoretical solution to determine the coefficient of consolidation, which varies as a function of both pile geometry and sensor location.

Baligh and Levadoux (1886) conducted a comprehensive review of piezocone dissipation studies and found three prominent conclusions. Simple uncoupled solutions provide a reasonable estimate of the dissipation process surrounding penetrometers and piles; the initial distribution of excess pore pressures around the probe has a significant influence on the modeled and in situ dissipation behavior; and consolidation is predominantly occurring in the recompression mode for normalized consolidation levels of $U < 50\%$. The work by Torstensson (1977) and Teh and Houlsby (1991) have shown that the soil stiffness significantly influences both the magnitude of generated excess pore pressures and the subsequent dissipation of those excess pressures during equalization. While the shape of theoretical and actual dissipation responses often differ, Baligh and Levadoux (1986) found that the differences in response are typically minimized at U =

0.5, with comparisons at this value providing the best correlation to other measurements of c.

The typical approach taken to determine the coefficient of consolidation from piezocone dissipation data is to compare the measured response to one of the available theoretical solutions. Dissipation response is a function of cone geometry, measurement location, and soil properties; with theoretical solutions for various common piezo sensor positions available in the literature. A summary of the available theoretical solutions for dissipation response were summarized by Burns and Mayne (1998), and is reproduced as Table 8-2. Most of the theoretical solutions utilize a normalized time variable to generalize the results, with the two most common factors being T and T*, as shown in Equations 8-14 and 8-15 (Teh and Houlsby, 1991):

$$T = \frac{t \cdot c}{a^2} \qquad \text{(Eq. 8-14)}$$

$$T^* = \frac{t \cdot c}{a^2 \sqrt{I_r}} \qquad \text{(Eq. 8-15)}$$

where t = time, c = coefficient of consolidation (methods typically correlate better with either c_v or c_h), a = probe or pile radius, and I_r = the rigidity index. The reader should note that the methods of Burns and Mayne (1998, 2002a, 2002b) use a T^* factor in which the rigidity index is taken to the 0.75 power, instead of to the 0.5 power as introduced by Teh and Houlsby (1991).

The most popular theoretical solutions used in practice are the cavity expansion solutions of Torstensson (1977), the strain path method proposed by Baligh (1985), the combined strain path - large strain finite elements approach of Teh and Houlsby (1991),

and the cavity expansion - critical state soil mechanics solutions of Burns and Mayne (1998). The theoretical spherical and cylindrical cavity expansion solutions of Torstensson (1977) are presented for T* values in Table 8-3. The theoretical log time solutions of Teh and Houlsby (1991) for the 5 sensor locations reported are listed in Table 8-4, with a charted version of this solution for t_{50} data compiled by Robertson et al. (1992) and presented as Figure 8-2. Table 8-5 presents the Teh and Houlsby (1991) theoretical dissipation gradients (M) for interpretation using the square root of time method. The measured gradient (m) can be determined as shown in the inset of Figure 8-2, with the coefficient of consolidation then calculated using Equation 8-16.

$$c_h = \left(\frac{m}{M}\right)^2 \cdot \sqrt{I_r} \cdot a^2 \qquad \text{(Eq. 8-16)}$$

The square root of time method is recommended for short dissipation tests, where dissipation has not progressed to at least a value of t_{50}. Mayne (2001) presents a simplified version of the analytical solution presented in Burns and Mayne (2002a) for the u_2 sensor position. The initial pore pressures predicted with the simplified method are determined using Equations 8-17 to 8-19:

$$\Delta u_i = \left(\Delta u_{oct}\right)_i + \left(\Delta u_{shear}\right)_i \qquad \text{(Eq. 8-17)}$$

$$\left(\Delta u_{oct}\right)_i = \frac{2}{3}\mathrm{M} \cdot \sigma'_{v0}\left(\frac{OCR}{2}\right)^{\Lambda} \ln\left(I_r\right) \qquad \text{(Eq. 8-18)}$$

$$\left(\Delta u_{shear}\right)_i = \sigma'_{v0}\left(1 - \left[\frac{OCR}{2}\right]^{\Lambda}\right) \qquad \text{(Eq. 8-19)}$$

$$\Delta u = \frac{\left(\Delta u_{oct}\right)_i}{1 + 50T^*} + \frac{\left(\Delta u_{shear}\right)_i}{1 + 5000T^*} \qquad \text{(Eq. 8-20)}$$

where $\Lambda = 1 - \kappa/\lambda$ = plastic volumetric strain ratio (κ = CSSM swelling index and λ = CSSM isotropic compression index) and T^* is defined as noted in Equation 8-15 with the exception of $I_r^{0.75}$ as opposed to $I_r^{0.5}$. The dissipation of excess pore pressures as a function of time can then calculated using Equation 8-20, and a table of T^* values calculated based on the known soil properties and an initial estimate of c. The Teh and Houlsby (1991) and Burns and Mayne (2002a) approaches are considered the most rigorous methods that are easily applicable in practice. The Teh and Houlsby (1991) method provides theoretical solutions for a range of conventional piezo sensor positions, and the Burns and Mayne (2002a) method allows for the estimation of dilatory dissipation response. The Teh and Houlsby method typically compares favorably with c_h, and the Burns and Mayne solution typically compares more favorable with c_v.

8.2 Penetration Pore Pressure Responses Measured with the CPTU-MPFA

8.2.1 Introduction

To date, the MPFA device has been tested at five locations, depicted as: VTK, MPSC, BWDWA, SPWA, and LPWA according to the naming convention adopted in Chapter 6. The results from the VTK site are not included in the current results as the conducted soundings were limited in depth and were conducted above the ground water table. Two of the remaining sites consist of predominantly sand geologies (SPWA and LPWA) while the other two sites contain prominent clay stratigraphies (MPSC and BWDWA). Penetration pore pressures were monitored at each site using conventional CPT test procedures consisting of penetration at a constant push rate of 20 mm/sec with breaks at each 1 meter interval to add additional push rods. As discussed in Chapter 7,

several non conventional procedures were also conducted during the current investigations, however, the results presented in this section are only resultant from conventional installation procedures.

8.2.2 Penetration Pore Pressures Observed with the MPFA in Coarse Grained Geologies

As outlined in Table 6-2, a total of eight applicable soundings (soundings for which all MPFA sensors were penetrated below the water table for several meters) were conducted with the MPFA device at the SPWA (MPFA_15-17,19) and LPWA (MPFA_21-24) sites. The MPFA soundings at the SPWA site consisted of two soundings conducted with the 15 cm^2 CPTU as the lead module and two soundings conducted with the short uninstrumented dummy tip (length 163 mm) as the lead module. All of the applicable MPFA soundings conducted at the LPWA test site were conducted using the CPTU as the lead module, with the friction sensors configured with a range of textured sleeves as detailed in Table 6-2. Full traces of the piezo response from each of the eight soundings are presented as Figures 8-3 to 8-10, with the estimated hydrostatic conditions shown for reference. As expected for sandy geologies all of the CPTU and MPFA piezo sensor traces generally follow the hydrostatic pore pressure conditions. The tests at SPWA indicate that the ground water table is located at approximately 5.7 m. The tests conducted at the LPWA site were conducted along the beach, and the variable ground water table elevations inferred from 1 to 3 m are indicative of the ground surface sloping towards the ocean.

The MPFA piezo sensors (u_{a0} to u_{a4}) experience slightly increased pore pressure response over the CPTU u_2 sensor for a few of the sand soundings. This behavior is accentuated by looking at the average pore pressure responses over selected stratigraphies

below the ground water table at the two sites: 7-9 m at the SPWA site and 4-6 m at the LPWA site. The average response of the operational CPTU and MPFA piezo sensors for the eight sand soundings are presented in Figure 8-11, with Figure 8-12 showing the responses normalized to the apparent hydrostatic condition. The variations as a function of sensor position shown in Figures 8-11 and 8-12 are somewhat affected by intermittent spikes present in the responses, however, a slight offset between the u_{ax} and u_2 sensors is still present in several soundings, as most pronounced in the traces of Figures 8-6 and 8-7. The observed offsets are believed to be the result of pressures induced by filter compression, with the large lateral stresses present along the shaft of the probe in sand geologies results in a slight artificial increase in the MPFA pore pressures, with the lateral stresses further increased for configurations including textured sleeves. The maximum level of this increase was observed to be on the order of 10 kPa, with lower values observed for smooth and low textured sleeves. Future work hopes to test the use of stiffer filter elements to help reduce the lateral stress influence observed in the current work. However, the observed trends with the current MPFA filter elements seem to provide an accurate estimate of the ground water conditions in sand geologies; with the magnitude of lateral stress induced sensor errors reduced for fine grained stratigraphies.

8.2.3 Penetration Pore Pressures Observed with the MPFA in Fine Grained Geologies

8.2.3.1 Introduction

As outlined in Table 6-1f, a total of ten MPFA soundings using conventional penetrometer procedures were completed at sites containing prominent fine grained stratigraphies. Two soundings were conducted at the MPSC site (MPFA_3-4), with eight

applicable soundings conducted at the BWDWA test site (MPFA_5-12). Figures 8-13 to 8-14 present the CPTU-MPFA measured pore pressure responses from the two soundings conducted at the MPSC test site, with the subplots from left to right showing the traces of $q_t, f_s, u_2, u_{a0}, u_{a1}, u_{a2}, u_2/u_{ax}$, and Overlain Δu. Figures 8-15 to 8-22 show parallel plots for the soundings conducted at the BWDWA test site, with traces of both measured and excess pore water pressure shown for each piezo sensor. Both cyclic loading and pore pressure dissipation tests were conducted during many of the BWDWA soundings, and as such the penetration pore pressures measured over certain depth ranges are affected by these test procedures, with the affect of these procedures on the measured piezo responses discussed in Section 8.4.4.

8.2.3.2 Response in the Cooper Marl (Calcareous Clay) Stratigraphy

The penetration pore pressures generated within the Cooper Marl formation, a highly structured calcareous clay material located between nominal depths of 14 and 20 m in Figures 8-13 and 8-14, are extremely large, with the average measured excess pore pressure responses on the order of 2300, 1100, 970, and 950 kPa for the u_2, u_{a0}, u_{a1}, and u_{a2} sensors respectively (Table 8-6). The large generated excess pore pressures are typical of this geology (Camp, 2004), and are caused by the combination of displacement due to the penetrometer insertion, collapse of the clay structure during penetration, and sufficiently low hydraulic conductivity to provide undrained loading conditions. Comparing the measured Δu_2 pore pressure response with those predicted using cavity expansion (Equations 8-2 and 8-3) requires values for s_u, I_r, and α_f for the stratigraphy. Camp (2004) provides typical values for the Cooper Marl of $s_u \approx 200$ kPa, and $G_0 \approx 425$ MPa. G_0 can be degraded to the appropriate strain level corresponding to CPT penetration

using Equation 8-8, providing a $G_{pen} \approx 80$ MPa; leading to an $I_r \approx 400$ representative of the conditions during penetration. Using the above values of $s_u = 200$ kPa and $I_r = 400$, and neglecting the α_f term in this instance, provides an estimated $\Delta u_{sph} \approx 1600$ kPa, with the corresponding cylindrical cavity expansion prediction resulting in $\Delta u_{cyl} \approx$ 1200 kPa.

The predicted Δu from spherical cavity expansion underestimates the magnitude of observed excess pore pressures seen at the shoulder location in the Cooper Marl, as the idealized framework of cavity expansion does not account for shear induced pore pressures. Equation 8-19 allows the level of shear induced pore pressures to be estimated for saturated clays based on CSSM, with values of OCR between 1 and 2 resulting in positive shear induced pore pressures and OCRs greater than 2 resulting in negative shear induced pressures; signifying contractive and dilative behaviors, respectively. This framework does not accurately model the behavior of structured clays for which the OCR may be greater than 2, as the collapse of the structure controls behavior and results in contractive behavior. The Cooper Marl is such a material, exhibiting severely contractive behavior in spite of OCR values ranging from 3 to 6 (Camp, 2004). As such, the use of Equation 8-19 in this case predicts $-100 > \Delta u_{shear} > -400$, resulting in an increased deviation between the predicted and observed excess penetration pore pressures.

The predicted Δu from cylindrical cavity expansion corresponds well with the excess penetration pore pressures measured by the MPFA piezo sensors along the shaft. Shaft response is typically indicative of destructured soil behavior (Leroueil et al., 1979), and as such, it follows that the observed excess pore pressures along the shaft would be closer to the estimated Δu_{oct}. The trend in measured Δu_a values is observed to decrease with increasing offset from the tip during penetration, indicating the absence of fully

undrained conditions for shaft positions located more than $h/r \approx 30$ behind the tip for the Cooper Marl stratigraphy. Future testing in this stratigraphy with the short uninstrumented dummy tip could better define the h/r value at which undrained conditions no longer prevail. Figure 8-23 shows the average excess pore pressures as a function of sensor offset (m and h/r) for the operational sensors within the Cooper Marl stratigraphy for the two MPSC soundings. The small sampling of pore pressures measured surrounding textured sleeves shows no apparent affect of the textured sleeves on the observed penetration pore pressures along the shaft, however, the small data set does not lead to any definitive conclusions in this regard.

8.2.3.3 Response in the Burswood Soft Clay Stratigraphy

The Burswood clay formation is a soft marine clay located between nominal depths of 3 and 11 m in Figures 8-15 and 8-22, with a change in the observed pore pressure responses noted at a nominal depth of 7 to 8 m across the soundings. The penetration pore pressures generated within the upper (3-7 m) layer, for an MPFA configuration with all smooth sleeves (MPFA_5), exhibit average measured excess pore pressure responses of 100, 46, 52, N/A, 44, and 37 kPa for Δu_2, Δu_{a0}, Δu_{a1}, Δu_{a2}, Δu_{a3}, and Δu_{a4}, respectively. The parallel Δu_{avg} responses in the lower layer (8-10 m) were observed to be 159, 90, 89, N/A, 74, and 68 kPa corresponding to the Δu_2, Δu_{a0}, Δu_{a1}, Δu_{a2}, Δu_{a3}, and Δu_{a4} responses, respectively. A dissipation test was conducted at a nominal depth of 7.8 m in this sounding, with the affected depths not included in the above averages.

As shown above for the Cooper Marl stratigraphy, the level of induced Δu_{max} along the shaft can be estimated using a combination of cavity expansion and critical

state soil mechanics. Values for s_u and I_r were determined from a large array of field and laboratory tests by the UWA, as presented by Schneider et al. (2004). An average value of N_{kt} = 10.5 was determined to correspond well with uncorrected vane shear data at the Burswood (BWDWA) test site, with s_u values in the clay on the order of 20 kPa and generally increasing slightly with depth. A value of $I_r \approx 70$ was determined applicable for penetration conditions at the BWDWA test site, with the apparent OCR ranging from 1 to 2 (Schneider et al., 2004). Based on the above parameters, the Δu_{oct} values predicted using spherical and cylindrical cavity expansion are calculated as 113 and 85 kPa, respectively; with Δu_{shear} values predicted by CSSM ranging from 32 to 0 kPa for OCR values ranging from 1 to 2. These calculations result in predicted excess pore pressures ranging from 145 to 113 kPa for spherical CE conditions and ranging from 117 to 85 kPa for cylindrical CE conditions.

As discussed previously in Chapter 6, a full range of textured sleeves from SM to H2.00 were tested at the BWDWA site. Figure 8-24 plots the average excess pore pressure responses within the upper BWDWA clay material (3 to 7 m) for each sounding as a function of sensor offset and (h/r). The excess pore pressures observed for sensors u_{a1} to u_{a4} seem to be slightly influenced by the presence of the textured sleeves in position u_{a2}, as observed in Figure 8-24. As with the initial generation of pore pressures due to penetrometer installation, the change in pore pressures due to textured sleeve penetration can be separated into octahedral and shear components. The level of $\Delta u_{max(oct)}$ (i.e. along the shaft) is theoretically only a function of the soil properties and not the cavity radius. As such, it follows that the textured sleeves should only induce additional octahedral pore pressures along the shaft if partial dissipation has occurred before the soil

encounters the textured sleeve. The soil conditions and the time lag between the tip and u_a sensors encountering a soil layer control the level of Δu dissipation, with the u_{a0} and u_{a1} sensors encountering soil depths within the same penetration strokes as the tip (on the order of 35 - 45 seconds after the tip for conventional CPT penetration rates), and the aft u_a sensors (u_{a2} to u_{a4}) encountering the same soil stratigraphy in the subsequent penetration stroke (time lags on the order of 1 to 2 minutes). As the observed Δu_{a1} responses are on the order of, or larger than the aft u_a sensors it follows that the changes in Δu along the shaft at the BWDWA site are only due to changes in Δu_{shear}. In fine grained geologies the soil along the shaft typically exists in a stable residual state with a fully formed shear zone prior to encountering the MPFA sensors, as seen in the friction responses presented in Chapter 6. As such, increases in Δu_{shear} are not caused by increased shearing induced by the textured sleeves but rather are resultant from the forced radial movement of the shear zone away from the shaft to a plane outside of the extent of textured asperities.

8.3 Pore Pressure Dissipation Response Observed with the CPTU-MPFA

8.3.1 Introduction

As outlined in Section 8.4.1.2, excess pore pressures generated during installation begin to equalize during interruptions in penetration or pile installation. Piezocone dissipation tests consist of stopping cone penetration and monitoring the changes in pore pressures as a function of elapsed time. These tests simulate the stress and pore pressure conditions around a fully installed pile foundation and allow for the characterization of the flow and consolidation properties corresponding to that condition to be determined.

Eleven standard dissipation tests were conducted with the CPTU-MPFA configuration at the BWDWA test site during the current study, ranging in test time from 30 to 680 minutes and performed at tip depths of 5, 6.7, 7.5, 7.7, and 10 m as detailed in Table 8-7. Each of these dissipation tests was conducted directly after standard steady-state CPT penetration to the investigation depth, with five of those tests conducted during the load test series described in Section 7.5.

8.3.2 Results of Standard CTU-MPFA Dissipation Tests

Dissipation results were obtained for all operable sensor positions in each of the dissipation tests. Table 8-8 summarizes the dissipation results from the ten standard tests, providing a summary of sensor depth, u_0, Δu_i, Δu_{max}, $\Delta u_{max}/\sigma'_{vo}$, t_{50}, $\Delta u(t_{50})$, and the MPFA sleeve configuration. Figures 8-25 to 8-35 present the normalized dissipation response for the CPTU-MPFA dissipation tests numbered 1 through 10 in Table 8-7. The response of the measured pore pressures were seen to vary significantly within the first few seconds after pausing penetration due to the rapid changes in the induced stress conditions. These variations were often seen as an initial decrease in U before exhibiting the characteristic dilatory increase found in the majority of pore pressure response curves. This delay, prior to the formation of stable dissipation, was observed to be slightly longer for the u_2 sensor as compared to the MPFA piezo sensors. These initial few seconds of measured response not representative of the remainder of the dissipation record were removed from the plots as recommended by previous researchers (Lehane, 1992). The choice of the initial dissipation point should correspond with the observed trend over the initial portion of the dissipation response, and can be very critical to the quantitative use of the response, especially in dilative materials.

The previously noted change in stratigraphy at a nominal depth of 8 m is also clearly seen in the dissipation data. This change in stratigraphy is noticeably evident in the u_2 dissipation response at 10 m depth showing significantly increased dissipation rates, with the forward MPFA piezo sensors also showing increased dissipation for the 10 m tip depth tests. The u_2 dissipation responses exhibit quicker dissipation for all of the tested depths, as expected from the theoretical predictions discussed in Section 8.1.4.2. However, the MPFA piezo sensors do not exhibit a clear trend with increasing offset from the tip (*h/r*), with the observed behaviors predominantly controlled by the localized stratigraphy surrounding each sensor. Significant variations in u_{ax} response are observed for adjacent (max spacing = 0.26m) MPFA piezo sensors within several of the dissipation responses (most notably Figures 8-27 and 8-28). This behavior follows the theoretical solutions, which state that shaft dissipations at large *h/r* positions are predominantly controlled by radial drainage conditions, and lead to the conclusion that the interface along the penetrometer does not provide an artificial drainage path. The BWDWA clay material includes several silt seams and large shell fragments that lead to observed variations in dissipation response.

All of the shaft dissipations, in addition to several of the shoulder (u_2) dissipations, exhibit dilatory dissipation response. Dilatory dissipation response is indicative of the pore pressure at the sensor position along the penetrometer interface being reduced from the pressure conditions at some nearby axial or radial position. This behavior is typically seen in soils prone to dilation upon shearing, for which the negative shear induced pore pressures are increased for the maximum shear condition along the penetrometer interface. However, this behavior has also been observed along the shaft of model piles

installed in normally or only lightly OCR materials (Bond, 1989; Lehane, 1992; Chow, 1996) who propose that the dilatory response is due to the shear zone (and thus the plane of maximum shear) being located a finite radial distance away from the pile interface where the measurements are taken. In the case of the MPFA device, the aft MPFA piezo sensors are located more than 1 m behind the tip, and as such the encountered soil may become partially overconsolidated during pauses in penetration required to add addition push rods. This behavior is common for piles, where installation typically proceeds more intermittently and at slower rates than CPT penetration. The Burswood clay formation exhibits normally consolidated behavior, with apparent values of OCR found to be on the order of 1 to 2 as noted above. As such, the observed dilatory response is likely due to a combination of the shear zone being located at some finite radial distance away from the interface, and the onset of consolidation occurring before the MPFA sensors encounter the tested soil stratigraphy. However, the normalized levels of dilation response during dissipation do not seem to be controlled by the relative position either forward or aft of the rod break point, as seen in Figures 8-27, 8-28, and 8-31 for example, with the observed MPFA responses believed to be representative of the local stratigraphic properties.

Figures 8-36 to 8-41 present the overlain responses across all of the dissipation tests for the individual u_2, u_{a0}, u_{a1}, u_{a2}, u_{a3}, and u_{a4} responses, respectively. The responses are color grouped by the depth of investigation, with blue tinted traces representing tests at tip depths of 10 m, red traces representing tests at tip depths of 7.5 and 7.74 m, and the green traces representing tests at tip depths of 6.74 m. The u_2 responses within the main clay stratigraphy show slight dilation on the order of U = 1.2, reaching a maximum

within the first minute of equalization. The tests at 10 m depth clearly exhibit a different behavior, with 50% dissipations occurring between 1 and 5 minutes. The u_a sensors all show good grouping as a function of test depth, with the rates of dissipation very consistent with slight changes in the level of dilation response resulting in t_{50} times within the main clay layer typically on the order of 1 to 2 hours with a maximum observed response on the order of 1 day.

8.4 Pore Pressure Responses Observed with the CPTU-MPFA as a Result of Monotonic and Cyclic Loading

8.4.1 Introduction

The third phase in the life cycle of pile foundations or installed penetration devices is the response to monotonic/cyclic loads applied during service or testing after full or partial equalization. The current study looked into the response of the CPTU-MPFA device through monotonic strain controlled load test conditions, through the application of large and small amplitude cycling, and steady-state penetration after equalization. The procedures and load cell responses corresponding to the series of load tests conducted at the BWDWA site, was outlined in Section 7.5, with the pore pressure response presented herein. The cyclic investigations conducted at the BWDWA site were also presented earlier, Section 7.3.2, with the pore pressure responses both during and after cycling analyzed in the current discussion.

8.4.2 Measured Tip and Shaft Pore Pressure Responses During the Load Test Investigations

8.4.2.1 Introduction

A total of eight load tests were conducted at the BWDWA site, consisting of two investigations at 5 m tip depth, three investigations at 7.5 m tip depth, and three investigations at 10 m tip depth. All load tests were conducted under strain controlled conditions to final displacements equal to the device diameter (43.7 mm). Strain controlled loading was conducted at two loading rates, 0.024 mm/s and 0.072 mm/s, resulting in load test times of 30 and 10 minutes, respectively. Equalization times of 2, 30, 120, and 480 minutes were utilized across the load test series, with the full installation and equalization procedures outlined in Table 7-13. Figures 8-42 to 8-44 present the pore pressure response for the load tests conducted at tip depths of 5, 7.5, and 10 m respectively.

8.4.2.2 Observed Influence of Filter Caking on Load Test Pore Pressure Measurements

The pore pressure responses of the CPTU-MPFA sensors measured during the monotonic load tests all contain abrupt transitions in response. These abrupt transitions, or "spikes" in behavior, were of varied magnitude and occurred at various displacement levels ranging from 2 to 7 mm. At first it was believed that these spikes in the responses were due to a voltage spike within the DAQ system, or some other electrical interference. However, upon closer inspection of the data, the cause of these spikes in the pore pressure responses are believed to be the result of shearing of the filter cake formed across the interface of the pore pressure filter elements that has become partially consolidated and to various degrees during the equalization process. This conclusion is

based on the following observations: (1) The magnitude of the observed "spike" variations are directly related to the equalization time of the various tests, with increased magnitudes observed for longer equalization times and consequently greater levels of consolidation; (2) None of the spiked variations occur at displacements greater than the size of the filter elements (u_2 = 7.5 mm thick, u_a = 12.5 mm in diameter); (3) The spikes in the individual sensor responses within each sounding occur at comparable but not exactly similar displacements, discounting a possible electrical influence which would act over a constant time interval; and (4) "Filter cakes" of fine material are known to form over the surface of piezo elements during CPT penetration. The spike in the u_2 response of the LT4 data at a displacement of 32 mm is believed to be resultant from the sensor encountering a large shell fragment, which are known to be prevalent throughout the stratigraphy as observed by Levy et al. (2002) from laboratory test samples and as shown in the x-ray image of a tube sample presented in Figure 8-45.

The formation of filter cakes across the surface of pore pressure elements typically results in improved piezo sensor response during conventional CPT procedures, as the filter cake helps to maintain saturation in the elements during penetration through unsaturated soil layers. However, it has become apparent that this phenomenon is detrimental to the quantitative assessment of the pore pressures for slow rate load tests after equalization and future tests may be able to apply different filter elements or other sensing technologies to alleviate this issue. While it is positive that the spikes in response seem to be the result of soil behavior and not electrical or other external influences, these spikes eliminate the ability to quantify changes in the pore pressure response during the load tests, and the results are consequently only described qualitatively.

8.4.2.3 Summary of Load Test Pore Pressure Response

The observed pore pressure responses in the current load testing program are due to a combination of the hydrostatic conditions, the excess pore pressures generated due to the monotonic load tests, and the continued dissipation of the generated excess penetration pore pressures. Figures 8-31 to 8-35 presented the dissipation results for load tests LT1, LT2 , LT5, LT7, and LT8 respectively, with the load tests commencing immediately after the final dissipation levels shown. The dissipation responses from LT3 and LT4, which included the small amplitude cycles, are shown in Figures 8-46 and 8-47, with the short 2 minute equalization time of LT6 not shown.

8.4.2.4 The Effect of Loading Rate on Load Test Pore Pressure Response

Two loading rates were used in the current study, consisting of 0.024 mm/s and 0.072 mm/s. The effects of loading rate on the pore pressure response can be observed in comparisons of LT1 and LT7 both conducted at tip depths of 7.5 m and allowed to equalize for 2 hours without applied cycling. The behaviors of the shaft piezo sensors for both tests are largely similar based on qualitative assessment. Some amount of excess pore pressures are generated along the shaft in both tests, qualitatively on the order required to hinder dissipation during the load test, but not large enough to produce significant increases in absolute pressure along the shaft. The shoulder elements both exhibit increases in absolute measured response over the first 30 mm of displacement. The induced excess pore pressures in LT1, conducted at the slower rate, were observed to cause absolute changes in pore pressure on the order of 0.6 kPa/mm, or 0.85 kPa/min. The observed increase in absolute pressure of u_2 in LT7, conducted at the faster rate, were observed to be on the order of 2.2 kPa/mm, or 9.36 kPa/min. The response of LT1

conducted at the slower rate remains relatively constant throughout the load test, with the u_2 response in LT7 observed to level out after the generation of Δu on the order of 40 kPa.

8.4.2.4 The Effect of Equalization Time on Load Test Pore Pressure Response

The load tests conducted at 10 m tip depth were used to investigate the effects of equalization time on the observed load test response, with equalization times of 30, 120, and 480 minutes used in load tests LT8, LT2, and LT5 respectively. It is noted that LT2 was conducted at 0.024 mm/s, whereas LT5 and LT8 were both conducted at 0.072 mm/s and provide the most direct comparison of behaviors. As noted earlier, the change in stratigraphy at a nominal depth of 8 m at the test site was not observed until after the initiation of the load test program, and as such the tip responses measured at this depth are representative of different soil conditions. The shaft responses observed for LT5 generally exhibit constant response, indicating no excess pore pressure generation at this load rate as the dissipation of the installation Δu_{shaft} pressures were predominantly dissipated before the load test, Figure 8-33. The response of the shaft pressures during LT8 showed response predominantly controlled by continued dissipation of installation pore pressures. The u_2 piezo responses between LT5 and LT8 exhibit similar response, however, this is expected as full dissipation of u_2 installation pressures was observed to occur in under 5 minutes in all tests.

8.4.2.5 The Effect of Small Amplitude Cycling on the Load Test Pore Pressure Response

Two load tests were conducted after only brief equalization (2 minutes) at tip depths of 5 m using the 0.072 mm/s loading rate, with the only procedural difference between these tests being the inclusion of short amplitude cycling in LT3 as compared to

LT6 which did not include cycling. The response of LT6, conducted after only 2 minutes of equalization and without cycling shows only a minor influence of the observed filter cake shearing, with the dissipation of excess pore pressures dominating the observed response for all sensors. The response of LT3, which included small amplitude cycling shows distinctly different response. The qualitative results of LT3 indicate that the small amplitude shearing before monotonic load testing created conditions prone to excess pore pressure generation during the monotonic load test, as the total response of all sensors was observed to increase or remain constant over the course of the load test.

The other comparison of behaviors with and without small amplitude cycling is observed in the behaviors of LT4 and LT1, which were each allowed to equalize for 2 hours and tested at a constant strain rate of 0.024 mm/s. LT4 included small amplitude cyclic loading before the equalization time and; while LT1 did not include cycling. The response of all of the piezo sensors along the shaft and at the shoulder position show very similar behavior in the two load tests (excepting the u_2 response originating from the encountered shell fragment in LT4). The dissipation response of LT4 after cycling is comparable to that of LT1, and the similarity in the load test pore pressure responses indicates that short amplitude cycling does not have a large affect on the induced loading pore pressures after significant equalization has occurred.

8.4.3 The Effect of Large and Small Amplitude Cycling Loading on Equalization

8.4.3.1 Introduction

The effects of both large and small amplitude cycling were investigated in the current test series conducted at the BWDWA test site. Within two of the soundings in

which large amplitude (10 $\pm$ 1 m cycles) cycling investigations were performed, the equalization of the pore pressure regime surrounding the CPTU-MPFA device was monitored both prior to and after the cyclic event. These tests enabled the effects of large amplitude cycling on both the generation and dissipation of excess pore pressures at various locations surrounding the penetrometer to be quantified. The small amplitude (200 $\pm$ 5 mm cycles) cyclic investigations were conducted directly after steady state penetration to the test depths of 5 and 7.5 m, without conducting pre-cycling dissipations. The average behaviors of the tip and friction behaviors of these investigations was detailed in Section 7.3, with only the pore pressure responses detailed herein.

8.4.3.2 Observed Effects of Large Amplitude Cycling

Figures 8-48 and 8-49 presented the continuous absolute pore pressure response for the soundings containing large amplitude cyclic investigations (MPFA_11 and MPFA_12), including: the pre-cycle dissipation, the large amplitude cyclic event, and the post-cycle dissipation behavior. The reader is reminded that the corresponding normalized dissipation responses prior to cycling were previously presented as Figures 8-34 and 8-35, with both pre-cycle dissipations monitored for 80 minutes. The large amplitude cycles serve to generate Δu_2 on the order of 90 kPa from the beginning to end of cycling in each of the large amplitude tests at the BWDWA site. The subsequent rate of u_2 dissipation follows the pre-cycle dissipation rate, only shifted by the Δu generated during cycling as seen in Figures 8-48 and 8-49.

The individual shaft sensor responses show a wide range of post-cyclic behaviors, however, the responses of each shaft sensor (u_{a0} to u_{a3}) exhibit similar responses between the two separate investigations. It follows from this observation that the response of the

various sensors is predominantly controlled by the local stratigraphy. Two of the shaft sensors (u_{a0} and u_{a1}) are located within one meter of the tip, resulting in dissipations resulting from full insertion and extraction cycles. The u_{a0} sensor responses, shown in magenta, exhibit changes in absolute pressure from 80 and 85 kPa before cycling to 65 and 78 kPa directly after cycling for the MPFA_11 and MPFA_12 soundings, respectively. The post cycle behavior for the u_{a0} sensors follow the same rate as those measured prior to the cyclic event. The u_{a1} sensors, shown in yellow, both exhibit a significant decrease in pore pressure from values of 97 and 94 kPa before cycling to values of 60 and 53 kPa after cycling. The u_{a1} sensors exhibit swelling response after cycling, indicating the generation of pronounced negative pore pressures during large amplitude shearing at that depth.

The other three MPFA shaft sensors (u_{a2}, u_{a3}, and u_{a4}) are located more than one meter behind the tip, and as such the sensors are only cycled over regions continuously in contact with the shaft. The u_{a2} responses both exhibit reductions in the post cyclic pressure as compared to the pre-cycle values, with observed reductions from 95 and 91 kPa to 76 and 84 kPa respectively. It is important to note that the u_{a2} sensor is located directly behind the sleeve position for which textured sleeves were used in these investigations. The sleeve texture in the MPFA_11 test was H1.50, whereas the sleeve texture in the MPFA_12 Test was H0.75. The above results seem to indicate that large scale cycling caused an increased reduction in absolute pore pressures for the more heavily textured sleeve, most likely due to an increase in the level of shear induced negative pore pressures. The response of the u_{a3} sensors exhibit almost identical response between the two tests, with pre cycling pore pressures observed to be 77 and 75 kPa and

post cycling pore pressures observed to be 94 and 96 kPa, respectively for soundings MPFA_11 and MPFA_12. The trend in u_{a3} post cyclic dissipation shows a rapid initial decrease in pore pressure, with the absolute values returning to the trend formed before cycling behavior after 30 minutes on average.

8.4.3.3 Observed Effects of Small Amplitude Cycling

Two of the load test installation sequences included small amplitude cyclic investigations directly following steady state insertion. The small amplitude cycling, was conducted at a constant rate of 20 mm/s, with 200 $\pm$ 5 mm cycles performed with the load test depth used as the lower cyclic limit. LT3 was conducted at a tip depth of 5 m two minutes after the small amplitude cycling event, with LT4 conducted 2 hours after the small amplitude cyclic event at a depth of 7.5 m. These small amplitude cyclic investigations were performed to simulate the conditions present during installation and the cyclic loading of foundations offshore, however, they also model laboratory tests such as the cyclic direct simple shear. Figures 8-46 and 8-47 present the continuous normalized excess pore pressure responses for both test sequences from the stop point of steady state installation until the initiation of the monotonic load test.

Figure 8-46 shows the normalized response from LT3, in which the u_2 sensor exhibits cyclic variations in pore pressure centered along the typical dissipation behavior, indicating only a minor change from the equilibrium dissipation response. The u_{a2} and u_{a3} shaft sensors show very little variation during the cyclic excitation, but show a much quicker dissipation rate after cycling indicating the generation of positive pore pressures during cycling. Shaft sensors u_{a0} and u_{a1} show grouped normalized response, exhibiting larger variations during cycling, with an even more pronounced increase in the post

cycling dissipation rate. The soil surrounding sensor u_{a4} is most affected by the short amplitude cycling with large variations in initial response, and the generated average pore pressures maintained until almost the end of cycling, where some reduction in value occurs. The u_{a4} sensor also exhibits a significant increase in the rate of dissipation after the end of cycling, indicating the existence of positive excess pore pressures induced by the cyclic excitation.

The normalized u_2 response from LT4 exhibits an increased dilatory response before cycling indicating a change in characteristic soil properties from those measured at 5 m depth in LT3. As observed for the LT3 response, the average trend in the normalized u_2 behavior of LT4 does not seem to be largely affected by the small scale cycling, with cyclic variations on the order of 5% of the initial pore pressure observed over the course of cycling. The u_{a1} and u_{a2} shaft responses, also seem to be relatively unaffected by the small amplitude cycling, with the trends before and after cycling matching up well with the response during cycling. The u_{a3} and u_{a4} responses initially exhibit moderate cyclic induced excess pore pressures over the first 5 to 10 cycles, with further cycling resulting in a delay of normal dissipation response, but not resulting in further variations in Δu with continued cycling. This behavior seems to indicate that the soil at these positions has reached a condition near the critical state after 5 to 10 small amplitude cycles. The u_{a0} sensor exhibits significant cyclic induced pore pressures over the first 5 to 15 cycles, indicating a more sensitive material than the other tested locations. The response again stabilizes after the initial several cycles with a slight delay to equilibrium dissipation behavior apparent over the remainder of cycling.

8.4.3.4 The Future Use of Cyclic Penetration Investigations

The results observed during the large and small amplitude cyclic investigations show promise in being able to determine the response of various stratigraphic layers to cyclic installation procedures and the susceptibility to induced pore pressures from cyclic loading. Cyclic CPTU-MPFA tests may provide a cost effective alternative to expensive sampling and subsequent laboratory cyclic investigations, especially for conditions particularly prone to cyclic loading, such as those existing offshore. More studies involving the use of small and large amplitude cyclic penetration tests are necessary before specific procedural and analysis methods can be proposed, but the presented results seem to provide a solid basis for future studies.

8.4.4 The Effect of Equalization on Steady State Shaft Response

The equalization of previously penetrated pore pressures creates a change in both the friction and piezo response along the shaft of a pile or penetrometer, as the local soil in contact with the pile typically becomes overconsolidated as compared to the virgin in situ state. This mechanism is known as pile setup, and has been observed since pile foundations were first introduced in fine grained materials. Figure 8-15 presented the response of a CPTU-MPFA sounding for which the MPFA was configured with all smooth sleeves. As shown in Chapter 6, the response of smooth sleeves located at large h/r positions are essentially constant for the BWDWA clay for conventional testing procedures. As clearly evident in Figure 8-15, the equalization of pore pressures over the penetrated regime creates a condition for which the subsequent pore pressures measured during steady state penetration over these depths are significantly reduced. The vertical thickness of the influence zones, apparent in the u_a traces are directly correspondent to

the sensor offset from the tip, with all four sensors exhibiting similar reductions in piezo response over the influenced zones. The reduction in excess pore pressure response seen in Figure 8-3 are representative of 2 hours of equalization and the generation of negative shear induced pore pressures within the overconsolidated influenced zone. The reductions in Δu values were observed to be on the order of -10 to 10 kPa in sounding MPFA_5, indicating the magnitude of negative shear induced pore pressures to be on the order of the remaining excess pore pressure. These results exhibit the ability of the MPFA device to quantify the level of friction setup along the shaft of the penetrometer as a function of equalization time. This relationship could then be used in pile design analysis or to determine the minimum time lag between installation and load testing for a particular material.

Table 8-1. Range of Possible Variations in the Directional Heterogeneity of *k* for Soft Clays (after Jamiolkowski et al., 1985).

Nature of Clay	k_h/k_v
No macrofabric, or only slightly developed macrofabric, essentially homogeneous deposits	1 to 1.5
From fairly well- to well-developed macrofabric, e.g. sedimentary clays with discontinuous lenses and layers of more permeable material	2 to 4
Varved clays and other deposits containing embedded and more or less continuous permeable layers	3 to 15

Table 8-2. Available Solutions to Calculate the Coefficient of Consolidation from Dissipation Response (Burns and Mayne, 1998).

Reference	Cavity Type	Soil Model	Initial Pore Pressure, Δu_i	Consoli-dation	Comments
Soderburg (1962)	Cylindrical, radius R	Elasto-plastic	$\Delta u/\Delta u_i = R/r$	1-D	Consolidation surrounding driven piles; Finite Difference
Torstensson (1975, 1977)	Cylindrical Spherical	Elasto-plastic	$\Delta u_i = 2s_u\ln(r_p/r)$ $\Delta u_i = 4s_u\ln(r_p/r)$	1-D	No shear stresses; Finite Difference
Randolph and Wroth (1979b)	Cylindrical	Elasto-plastic	$\Delta u_i = 2s_u\ln(r_p/r)$	1-D	Consolidation surrounding driven piles; Analytical
Baligh and Levadoux (1980); Levadoux and Baligh (1986)	Piezocone Model	Non-linear	From strain path method; Total stresss soil model	2-D	
Battaglio et al. (1981)	Cylindrical Spherical	Elasto-plastic	$\Delta u_i = 2s_u\ln(r_p/r)$ $\Delta u_i = 4s_u\ln(r_p/r)$	1-D	Shear by empirical method; Finite Difference
Jones and Van Zyl (1981)	n/a	Empirical approach	n/a	n/a	Correlation between measured t_{50} and oedometer measured values of c_h
Kavvadas (1982)	Piezocone Model	Non-linear	From strain-path method; Effective stress-strain model	1-D	
Senneset et al. (1982)	Cylindrical	Elasto-plastic	$\Delta u_i = 2s_u\ln(r_p/r)$	1-D	
Tumay et al. (1982)	Piezocone Model	Linear	From strain path method; Experimental data	1-D	
Gupta and Davidson (1986)	Piezocone Model	Elasto-plastic	Modified cavity expansion; dissipation as cone penetrates	1-D	Isotropic and anisotropic
Soares et al. (1987)	Piezocone Model	Non-linear	Corrected by visual examination and regression analysis	2-D	
Whittle (1987)	Piezocone Model	Non-linear	From strain-path method; Effective stress-strain model	1-D	
Houlsby and Teh (1988); Teh and Houlsby (1991)	Piezocone Model	Non-linear	Predicted by large strain finite element analysis and strain path method	1-D	Finite Difference
Elsworth (1990; 1993)	Point Dislocation Theory	Elasto-plastic	From point dislocation theory	2-D	Not applicable for u_2 measurements
Aubeny (1992)	Piezocone Model	Non-linear	From strain path method; Effective stress-strain model	2-D	Coupled consolidation
Sully and Campanella (1994)	Piezocone Model	Non-linear	Predicted by large strain finite element analysis and strain path method	1-D	Empirical time shift to u_{max} for OC dissipation
Burns and Mayne (1995a)	Spherical	Elasto-plastic	$\Delta u_{oct}=4s_u\ln(r_p/r)$ $\Delta u_{shear}=\sigma_{vo}'[1-(OCR/2)^{0.8}]$	1 D	Incorporates shear stresses; models OC dissipation; Finite Difference
Burns (1997) This Study	Spherical	Elasto-plastic	$\Delta u_{oct}=4s_u\ln(r_p/r)$ $\Delta u_{shear}=\sigma_{vo}'[1-(OCR/2)^{0.8}]$	1 D	Incorporates shear stresses; models OC dissipation; Analytical

*Modified after Lunne et al. (1992) and Jamiolkowski (1995)

Table 8-3. Modified Time Factors, T^*, for Piezocone Dissipation from Spherical and Cylindrical Cavity Expansion Theory (Torstensson, 1977).

Solutions by Torstensson (1977)		
	Cylindrical CE	**Spherical CE**
U (%)	**T***	**T***
90	0.0058	
80	0.026	0.0069
70	0.068	0.015
60	0.13	0.029
50	0.24	0.053
40	0.45	0.090
30	0.77	0.16
20	1.4	0.28
10	2.4	0.54

Table 8-4. Modified Time Factors, T^*, for Piezocone Dissipation from Combined Strain Path - Large Strain Finite Element Analyses (Teh and Houlsby, 1991).

T^* Values from Teh and Houlsby (1991) Solution					
Degree of Consolidation	**u_t**	**u_1**	**u_2**	**5r Above Shoulder**	**10r Above Shoulder**
0.2	0.001	0.014	0.038	0.294	0.378
0.3	0.006	0.032	0.078	0.503	0.662
0.4	0.027	0.063	0.142	0.756	0.995
0.5	0.069	0.118	0.245	1.11	1.46
0.6	0.154	0.226	0.439	1.65	2.14
0.7	0.345	0.463	0.804	2.43	3.24
0.8	0.829	1.04	1.60	4.10	5.24

Table 8-5. Theoretical Values for the Gradient of the Dissipation Curve (M), Root Time Plot (Teh and Houlsby, 1991).

M **Values for Teh and Houlsby (1991) Root Time Solution**			
u_t	u_1	u_2	**5r Above Shoulder**
1.3	1.63	1.15	0.62

Table 8-6. Average Generated Excess Pore Pressures within the Cooper Marl Measured with the CPTU-MPFA Device at the MPSC Site from 13- 20 m Tip Depths.

MPFA_3 - MPSC -SM-SM-SM-SM

u_2 (kPa)	u_{a0} (kPa)	u_{a1} (kPa)	u_{a2} (kPa)
2355.0	1064.8	952.4	920.7

MPFA_4 - MPSC - H0.125-H0.25-H0.50-H1.00

u_2 (kPa)	u_{a0} (kPa)	u_{a1} (kPa)	u_{a2} (kPa)
2265.1	1079.4		937.0

Table 8-7. Summary of the Conventional Dissipation Tests Conducted with the CPTU-MPFA at the BWDWA Site.

Test #	Sounding ID	Dissipation Time (min)	Tip Depth (m)
D1	MPFA_5	267	7.74
D2	MPFA_6	48	6.74
D3	MPFA_7	317	6.75
D4	MPFA_10	93	6.74
D5	MPFA_11	167	6.74
D6	MPFA_12	77	6.75
D7	LT1	120	7.50
D8	LT2	120	10.00
D9	LT5	680	10.00
D10	LT7	120	7.50
D11	LT8	30	10.00

Table 8-8a. Summary of the Conventional Dissipation Responses.

Test ID		u_2	u_{a0}	u_{a1}	u_{a2}	u_{a3}	u_{a4}
MPFA_5	**Depth (m)**	7.74	7.07	6.86	6.60	6.34	6.08
MPFA_5	**u_0 (kPa)**	56.69	50.07	47.99	45.42	42.85	40.28
MPFA_5	**Δu_i (kPa)**	80.93	76.24	68.61		65.57	61.71
MPFA_5	**Δu_{max} (kPa)**	82.10	88.39	85.86		80.26	70.12
MPFA_5	**$\Delta u_{max}/\sigma_{vo}'$**	1.38	1.58	1.57		1.54	1.38
MPFA_5	**t_{50} (s)**	>16000	4000	>16000		>16000	11500
MPFA_5	**Δu @ t_{50} (s)**	68.81	63.15	58.30		54.21	51.00
MPFA_5	**MPFA Sleeves**	-----	-----	SM	SM	SM	SM
MPFA_6	**Depth (m)**	6.74	6.07	5.86	5.60	5.34	5.08
MPFA_6	**u_0 (kPa)**	46.87	40.25	38.17	35.60	33.03	30.47
MPFA_6	**Δu_i (kPa)**	110.30	77.98	91.64	71.64	66.98	
MPFA_6	**Δu_{max} (kPa)**	120.46	91.36	100.92	88.39	80.86	
MPFA_6	**$\Delta u_{max}/\sigma_{vo}'$**	2.22	1.80	2.03	1.82	1.72	
MPFA_6	**t_{50} (s)**	> 2900	> 2900	> 2900	> 2900	> 2900	
MPFA_6	**Δu @ t_{50} (s)**	78.58	59.11	64.90	53.62	50.01	
MPFA_6	**MPFA Sleeves**	-----	-----	SM	H1.00	SM	SM
MPFA_7	**Depth (m)**	6.75	6.08	5.87	5.61	5.35	5.09
MPFA_7	**u_0 (kPa)**	46.89	40.27	38.19	35.63	33.06	30.49
MPFA_7	**Δu_i (kPa)**	103.13	67.05		86.68	73.85	
MPFA_7	**Δu_{max} (kPa)**	115.54	89.21		98.00	88.97	
MPFA_7	**$\Delta u_{max}/\sigma_{vo}'$**	2.13	1.75		2.02	1.89	
MPFA_7	**t_{50} (s)**	4800	4600		20000	9600	
MPFA_7	**Δu @ t_{50} (s)**	75.01	53.66		61.15	53.45	
MPFA_7	**MPFA Sleeves**	-----	-----	SM	H0.50	SM	SM
MPFA_10	**Depth (m)**	6.74	6.07	5.86	5.60	5.34	5.08
MPFA_10	**u_0 (kPa)**	46.87	40.25	38.17	35.60	33.03	30.47
MPFA_10	**Δu_i (kPa)**	109.83	57.22	64.56	75.29	76.21	
MPFA_10	**Δu_{max} (kPa)**	115.69	77.31	83.15	90.99	80.21	
MPFA_10	**$\Delta u_{max}/\sigma_{vo}'$**	2.13	1.52	1.67	1.88	1.70	
MPFA_10	**t_{50} (s)**	1900	5000	> 5600	> 5600	3000	
MPFA_10	**PP @ t_{50} (s)**	78.35	48.73	51.37	55.45	54.62	
MPFA_10	**MPFA Sleeves**	-----	-----	SM	H2.00	SM	SM
MPFA_11	**Depth (m)**	6.74	6.07	5.86	5.60	5.34	5.08
MPFA_11	**u_0 (kPa)**	46.88	40.26	38.18	35.61	33.04	30.47
MPFA_11	**Δu_i (kPa)**	93.58	68.45	86.84	74.62	72.87	
MPFA_11	**Δu_{max} (kPa)**	117.01	82.11	96.40	86.85	79.28	
MPFA_11	**$\Delta u_{max}/\sigma_{vo}'$**	2.16	1.61	1.94	1.79	1.68	
MPFA_11	**t_{50} (s)**	> 10000	> 10000	> 10000	> 10000	> 10000	
MPFA_11	**Δu @ t_{50} (s)**	70.23	54.35	62.51	55.12	52.96	
MPFA_11	**MPFA Sleeves**	-----	-----	SM	H1.50	SM	SM
MPFA_12	**Depth (m)**	6.75	6.08	5.87	5.61	5.35	5.09
MPFA_12	**u_0 (kPa)**	46.93	40.31	38.24	35.67	33.10	30.53
MPFA_12	**Δu_i (kPa)**	112.79	62.26	63.30	89.64	77.57	
MPFA_12	**Δu_{max} (kPa)**	129.52	81.41	86.82	95.15	83.67	
MPFA_12	**$\Delta u_{max}/\sigma_{vo}'$**	2.38	1.60	1.74	1.96	1.77	
MPFA_12	**t_{50} (s)**	> 4600	> 4600	> 4600	> 4600	> 4600	
MPFA_12	**Δu @ t_{50} (s)**	79.86	51.28	50.77	62.65	55.34	
MPFA_12	**MPFA Sleeves**	-----	-----	SM	H0.75	SM	SM

Table 8-8b. Summary of the Conventional Dissipation Responses (cont.).

Test ID		u_2	u_{a0}	u_{a1}	u_{a2}	u_{a3}	u_{a4}
LT1	**Depth (m)**	7.50	6.83	6.62	6.36	6.10	5.84
LT1	**u_0 (kPa)**	54.34	47.72	45.65	43.08	40.51	37.94
LT1	**Δu_i (kPa)**	115.78	55.99	51.88	71.83	55.01	46.92
LT1	**Δu_{max} (kPa)**	120.53	85.96	80.91	86.55	68.40	78.41
LT1	**$\Delta u_{max}/\sigma_{vo}'$**	2.07	1.57	1.51	1.65	1.34	1.58
LT1	**t_{50} (s)**	5600	> 8500	> 8500	> 8500	> 8500	> 8500
LT1	**Δu @ t_{50} (s)**	85.06	51.86	48.77	57.46	47.76	42.43
LT1	**MPFA Sleeves**	-----	-----	SM	SM	SM	SM
LT2	**Depth (m)**	10.00	9.33	9.12	8.86	8.60	8.34
LT2	**u_0 (kPa)**	79.05	72.43	70.35	67.78	65.21	62.64
LT2	**Δu_i (kPa)**	157.73	78.25	68.71	64.90	56.94	61.43
LT2	**Δu_{max} (kPa)**	157.73	89.78	91.54	88.53	95.63	91.16
LT2	**$\Delta u_{max}/\sigma_{vo}'$**	2.22	1.33	1.38	1.36	1.50	1.46
LT2	**t_{50} (s)**	230	4500	> 8600	> 8600	> 8600	> 8600
LT2	**Δu @ t_{50} (s)**	118.39	75.34	69.53	66.34	61.08	62.04
LT2	**MPFA Sleeves**	-----	-----	SM	H1.00	SM	SM
LT5	**Depth (m)**	10.00	9.33	9.12	8.86	8.60	8.34
LT5	**u_0 (kPa)**	79.05	72.43	70.35	67.78	65.21	62.64
LT5	**Δu_i (kPa)**	109.35	46.64	85.54	85.89	60.82	48.36
LT5	**Δu_{max} (kPa)**	109.35	67.03	90.17	98.78	72.94	66.80
LT5	**$\Delta u_{max}/\sigma_{vo}'$**	1.54	0.99	1.36	1.52	1.14	1.07
LT5	**t_{50} (s)**	52	1150	1640	4800	5746	4824
LT5	**PP @ t_{50} (s)**	94.20	59.53	77.95	76.84	63.02	55.50
LT5	**MPFA Sleeves**	-----	-----	SM	H2.00	SM	SM
LT7	**Depth (m)**	7.50	6.83	6.62	6.36	6.10	5.84
LT7	**u_0 (kPa)**	54.34	47.72	45.65	43.08	40.51	37.94
LT7	**Δu_i (kPa)**	123.47	83.55	63.02	70.03	57.97	60.74
LT7	**Δu_{max} (kPa)**	137.63	99.20	80.18	88.26	77.59	74.45
LT7	**$\Delta u_{max}/\sigma_{vo}'$**	2.37	1.81	1.49	1.69	1.52	1.50
LT7	**t_{50} (s)**	5400	>8350	>8350	>8350	>8350	>8350
LT7	**Δu @ t_{50} (s)**	88.90	65.64	54.33	56.55	49.24	49.34
LT7	**MPFA Sleeves**	-----	-----	SM	H1.50	SM	SM
LT8	**Depth (m)**	10.00	9.33	9.12	8.86	8.60	8.34
LT8	**u_0 (kPa)**	79.05	72.43	70.35	67.78	65.21	62.64
LT8	**Δu_i (kPa)**	123.37	70.13	85.56	82.02	70.06	90.43
LT8	**Δu_{max} (kPa)**	124.15	83.57	97.99	99.38	81.59	102.46
LT8	**$\Delta u_{max}/\sigma_{vo}'$**	1.75	1.24	1.47	1.53	1.28	1.64
LT8	**t_{50} (s)**	72	>2000	>2000	>2000	>2000	>2000
LT8	**Δu @ t_{50} (s)**	101.21	71.28	77.95	74.90	67.64	76.54
LT8	**MPFA Sleeves**	-----	-----	SM	H0.75	SM	SM

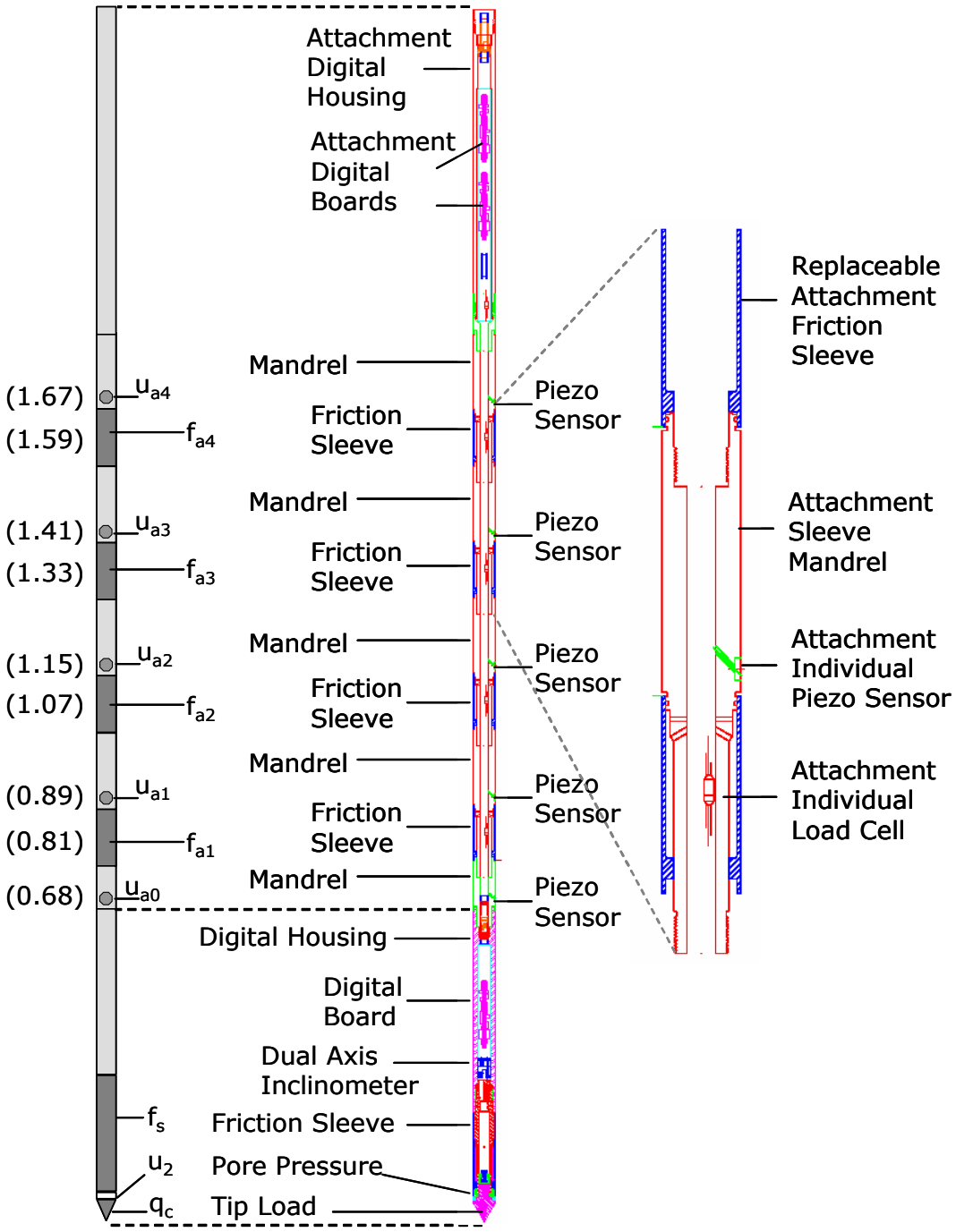

Figure 8-1. Multisleeve Piezo Friction Attachment Configured with Conventional CPTU Module. (a) Schematic - Brackets Indicate Sensor Offset from Tip in Meters, (b) Design Detail, and (c) Piezo Friction Sleeve Mandrel Design Detail.

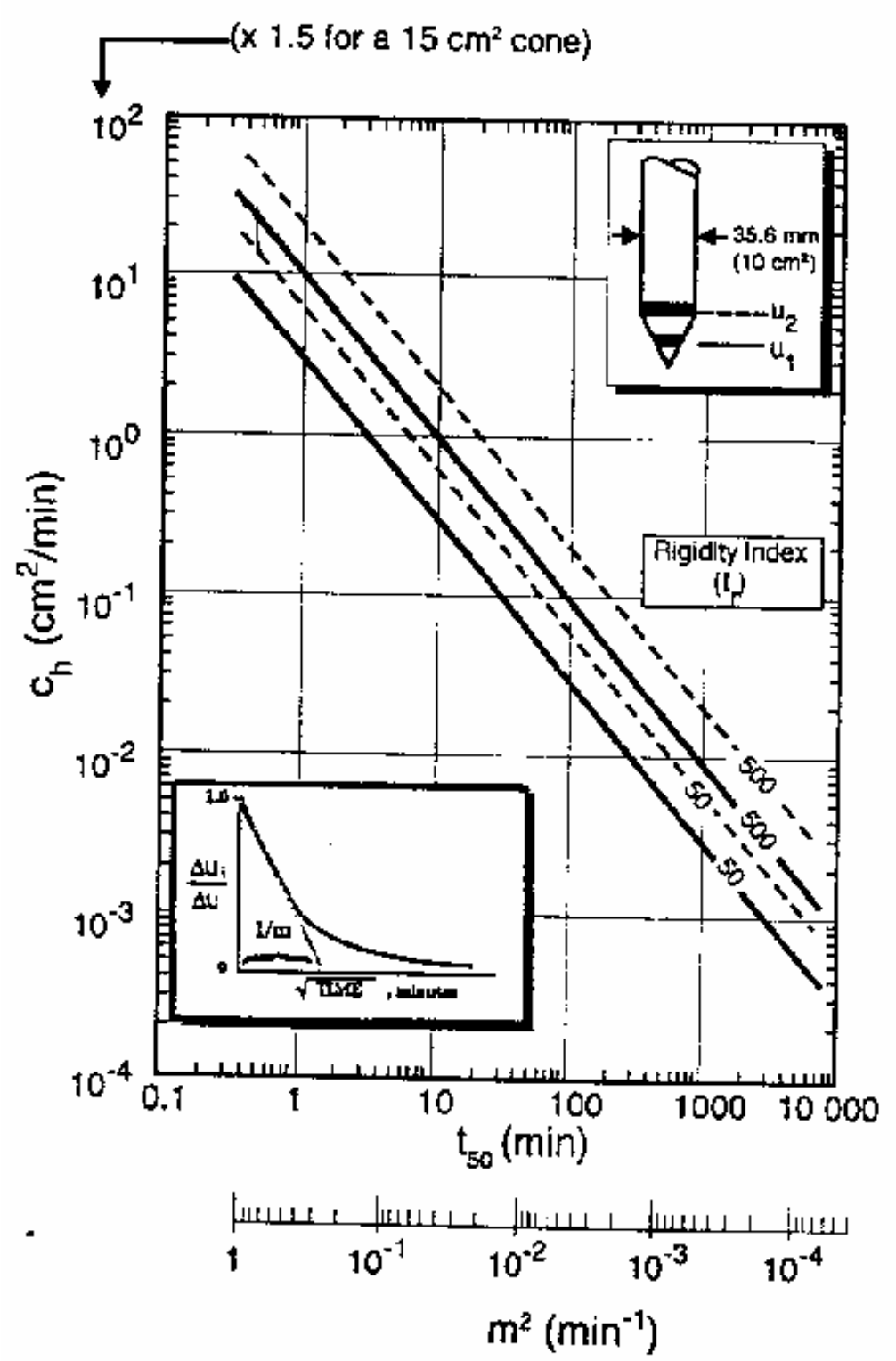

Figure 8-2. Chart for Finding c_h from t_{50}, with the Inset Figure Diagramming the Root Time Approach to c_h Estimation (Lunne et al., 1997 after Robertson et al., 1992).

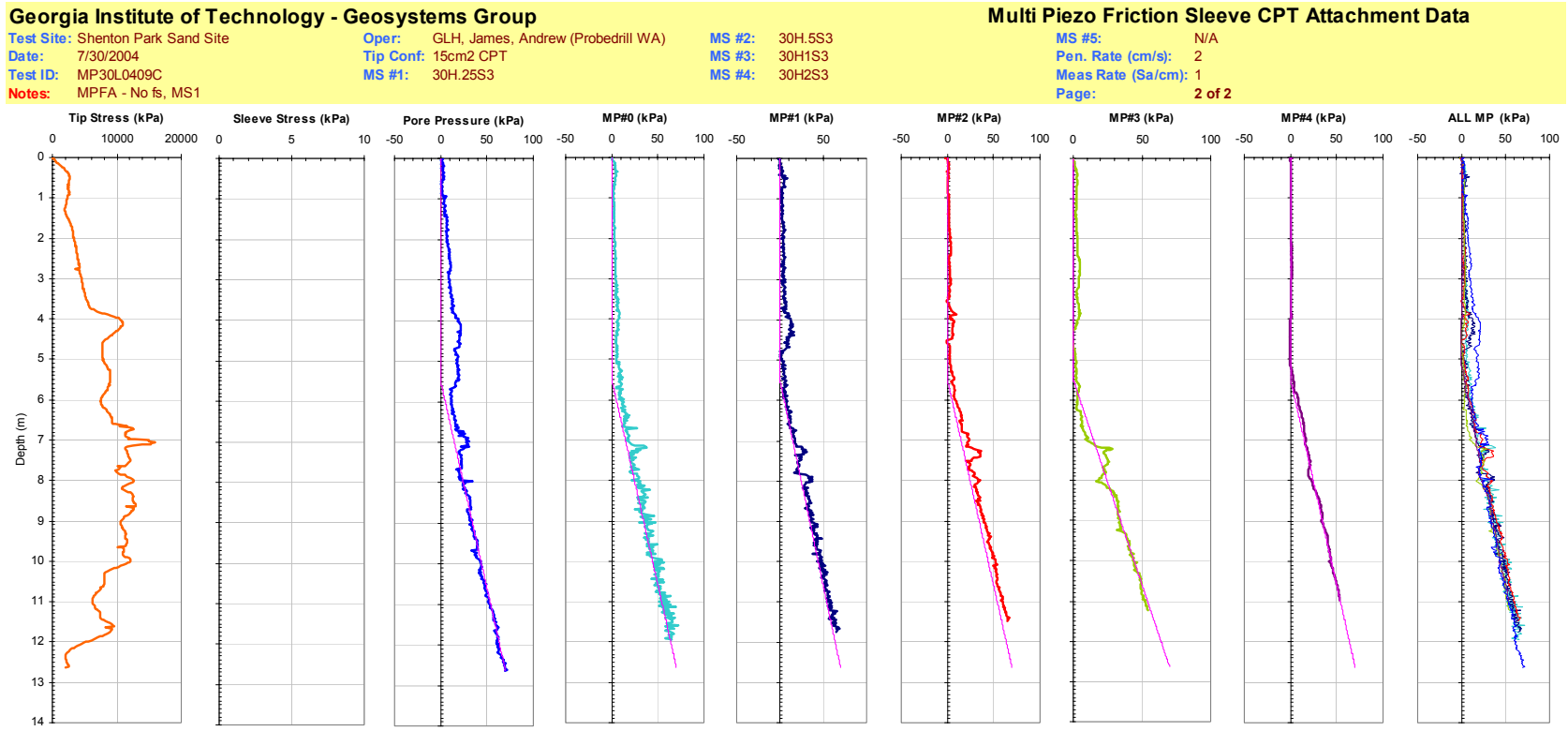

Figure 8-3. Plots of all CPTU and the MPFA Piezo Sensors from Sounding MPFA_15 at the SPWA Site.

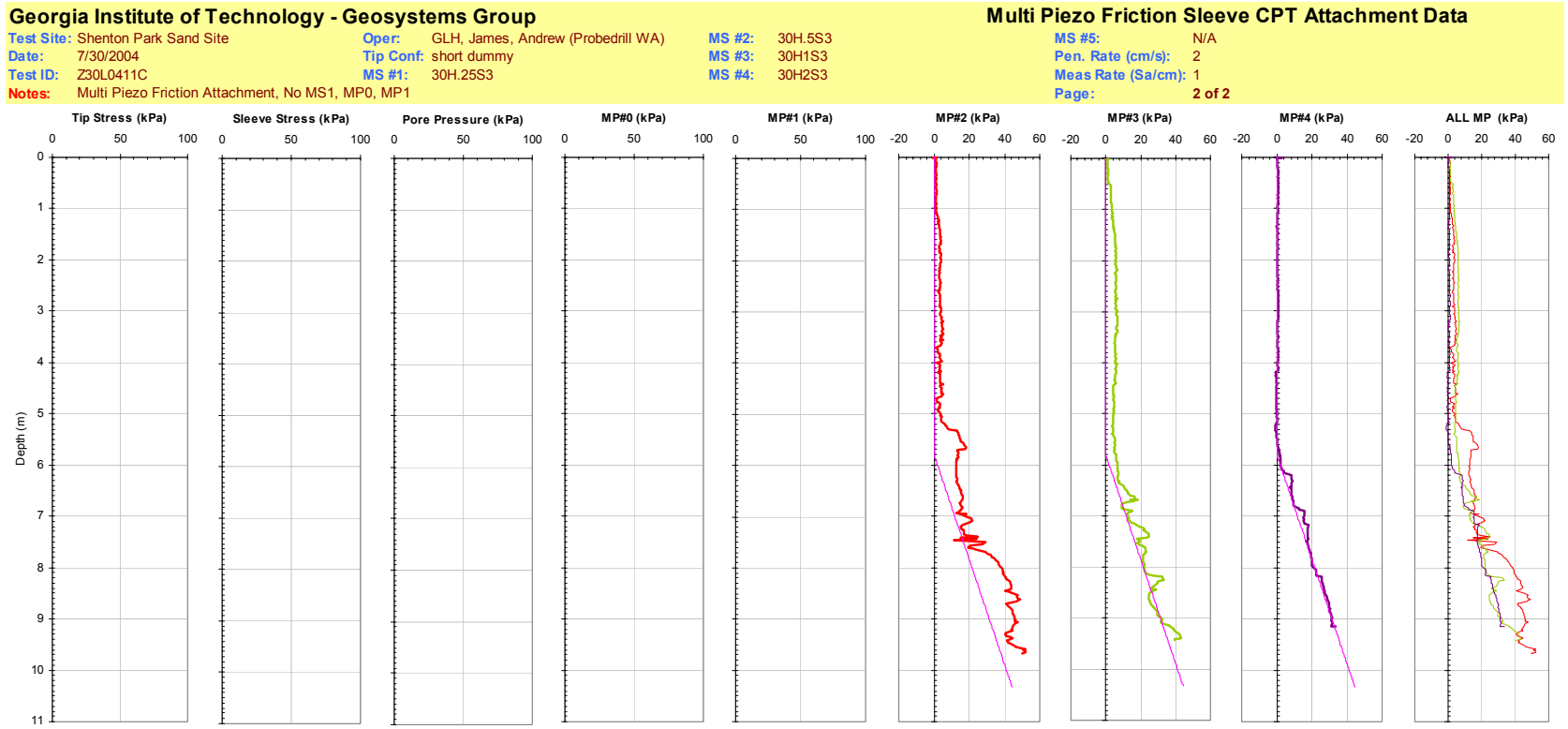

Figure 8-4. Plots of the MPFA Piezo Sensors from MPFA Sounding MPFA_16 at the SPWA Site. The Short Dummy Tip (length 163 mm) was Used as the Lead Module for this Sounding.

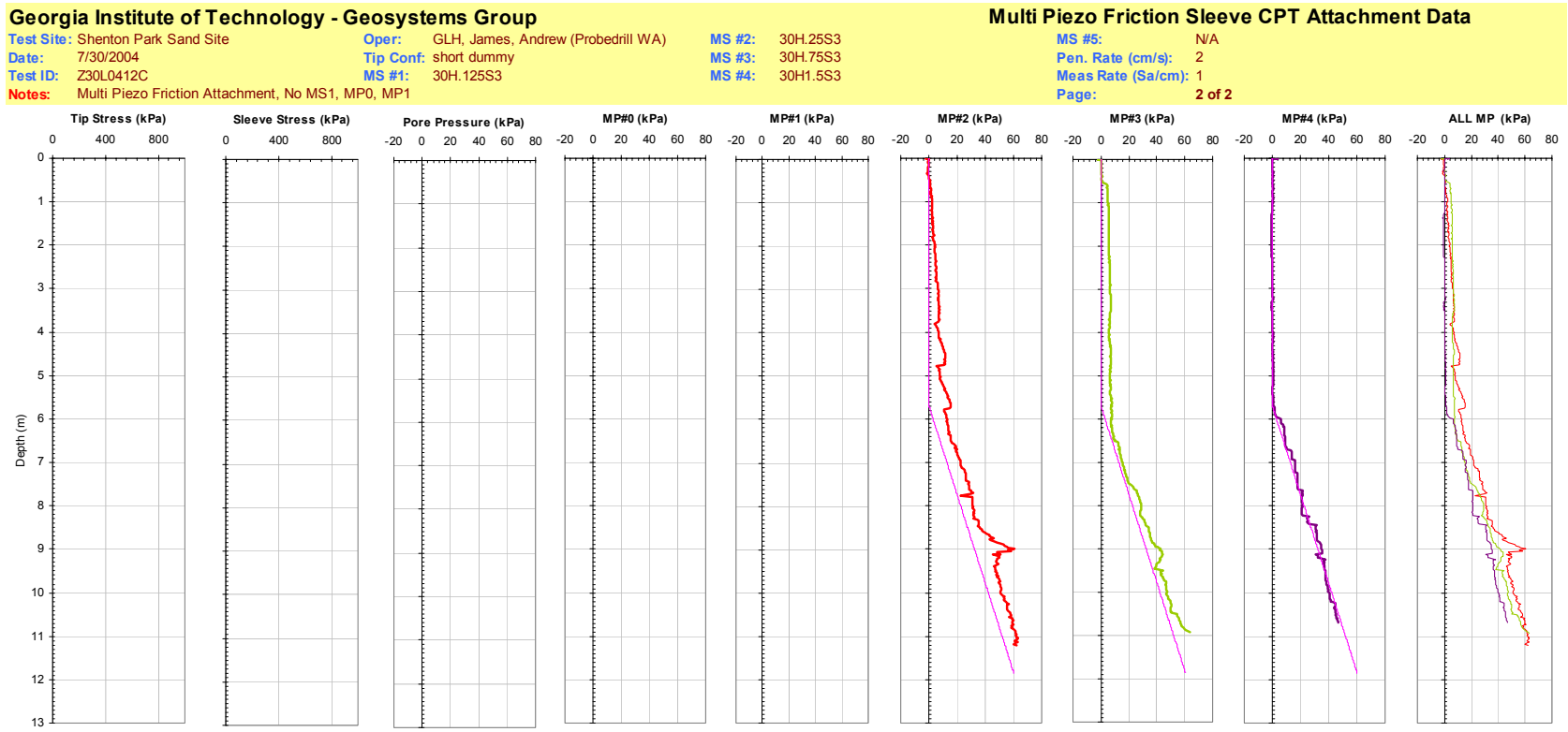

Figure 8-5. Plots of the MPFA Piezo Sensors from MPFA Sounding MPFA_17 at the SPWA Site. The Short Dummy Tip (length 163 mm) was Used as the Lead Module for this Sounding.

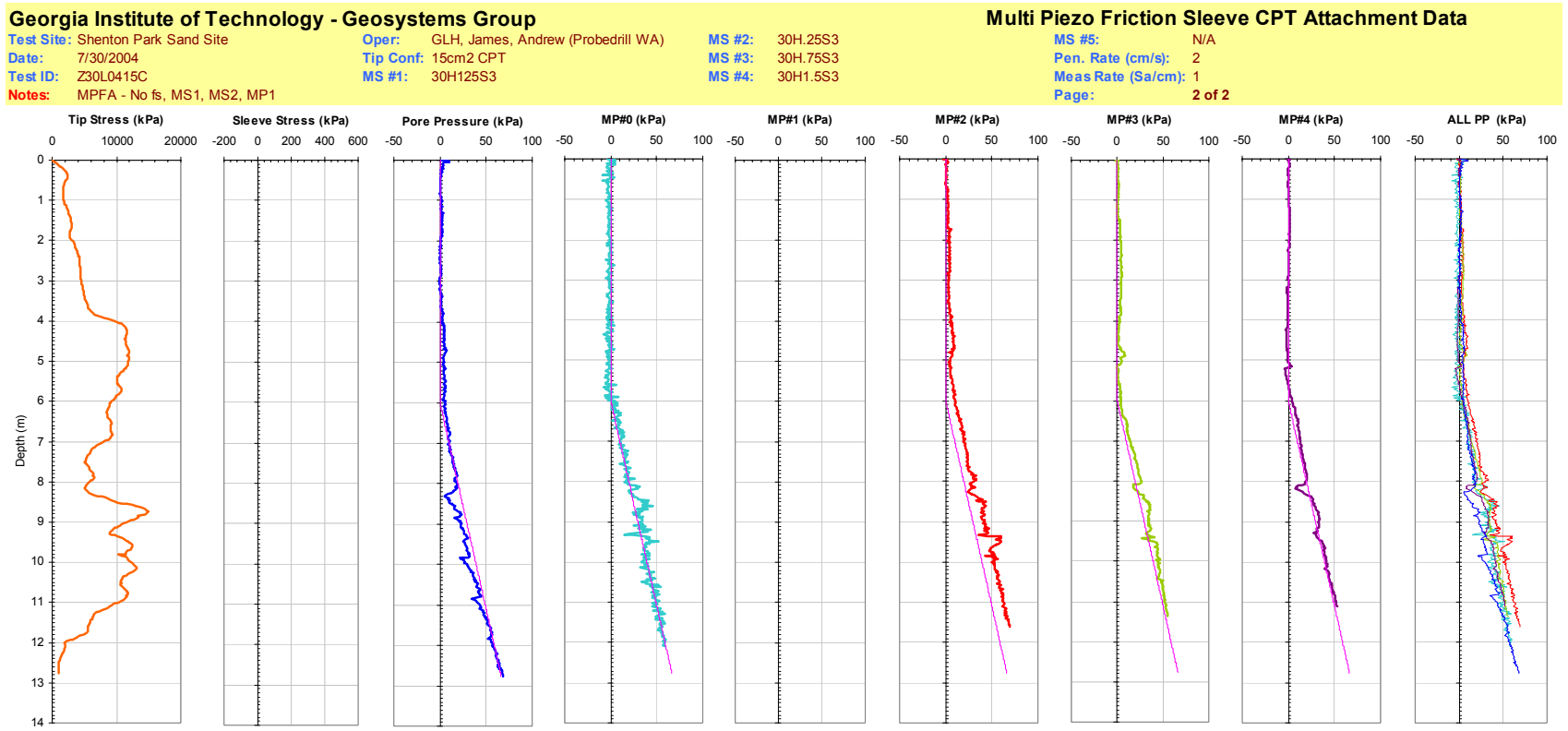

Figure 8-6. Plots of all CPTU and the MPFA Piezo Sensors from Sounding MPFA_19 at the SPWA Site.

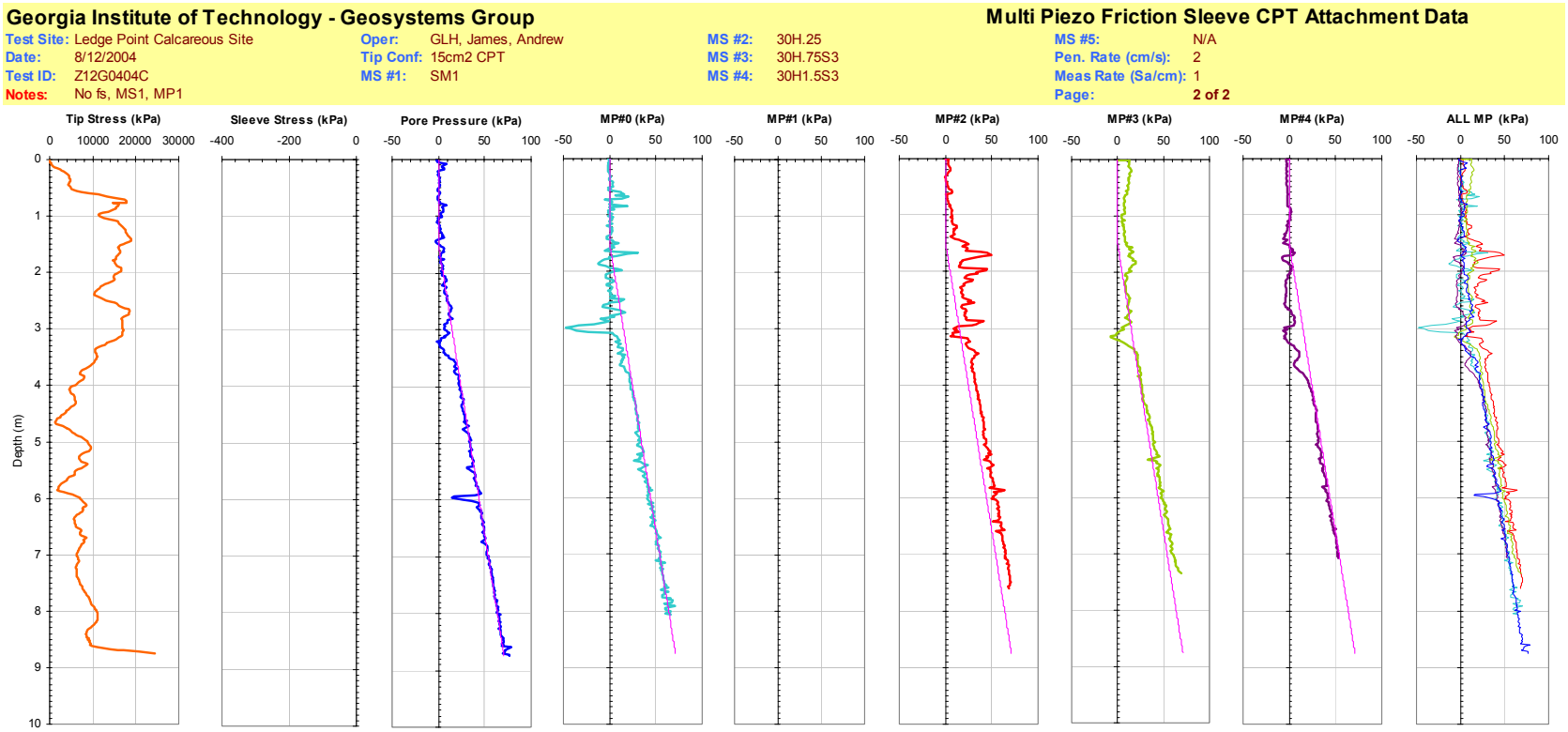

Figure 8-7. Plots of all CPTU and the MPFA Piezo Sensors from Sounding MPFA_21 at the LPWA Site.

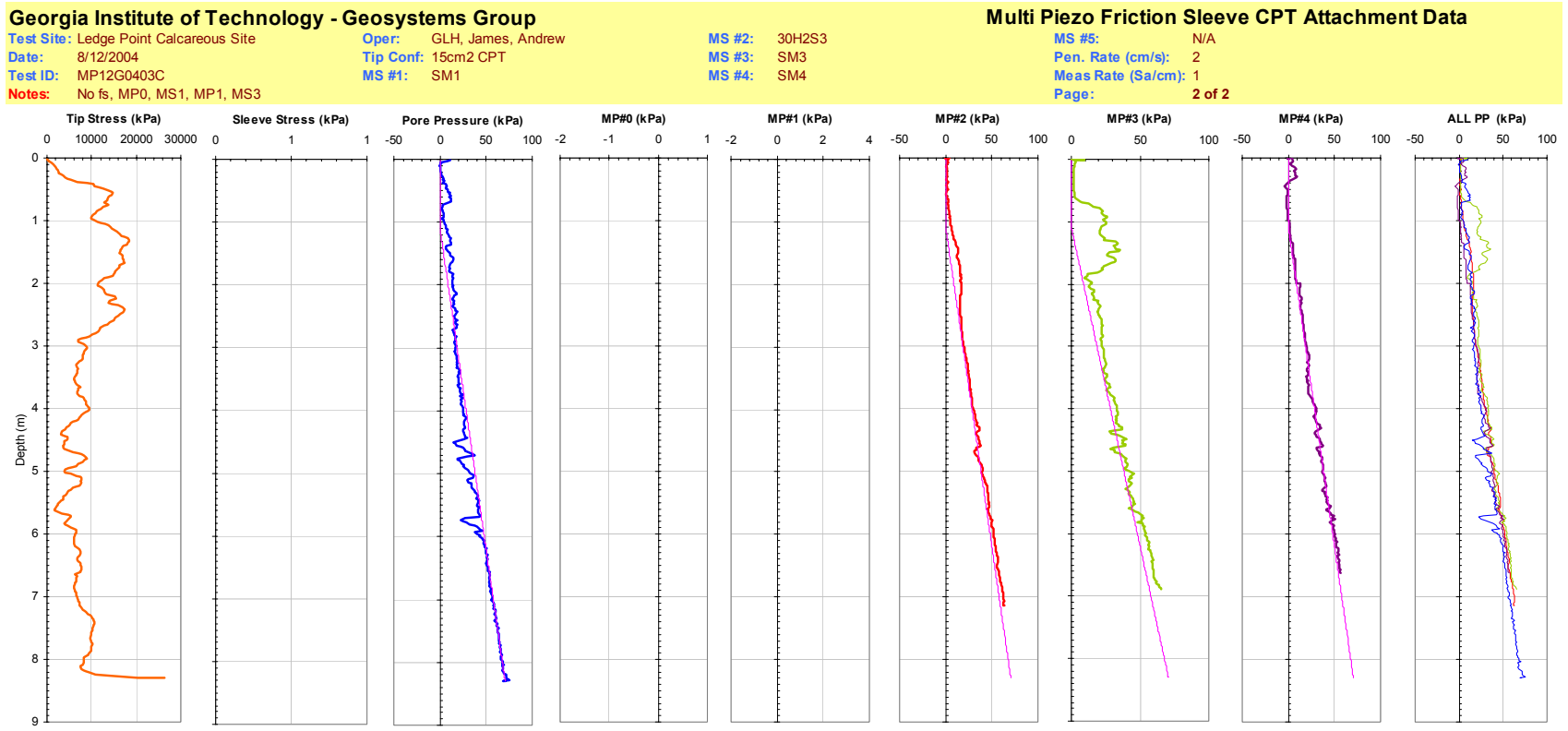

Figure 8-8. Plots of all CPTU and the MPFA Piezo Sensors from Sounding MPFA_22 at the LPWA Site.

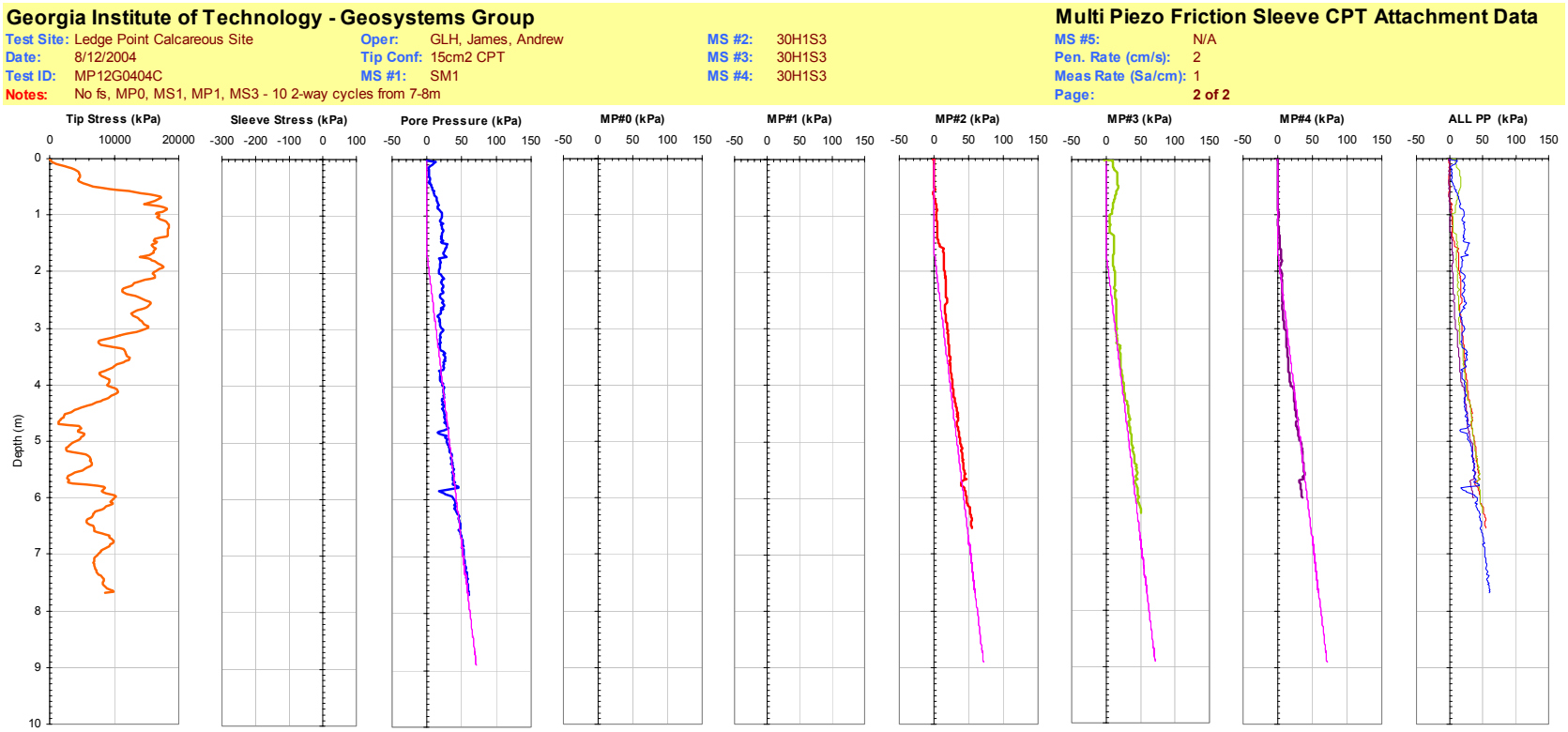

Figure 8-9. Plots of all CPTU and the MPFA Piezo Sensors from Sounding MPFA_23 at the LPWA Site.

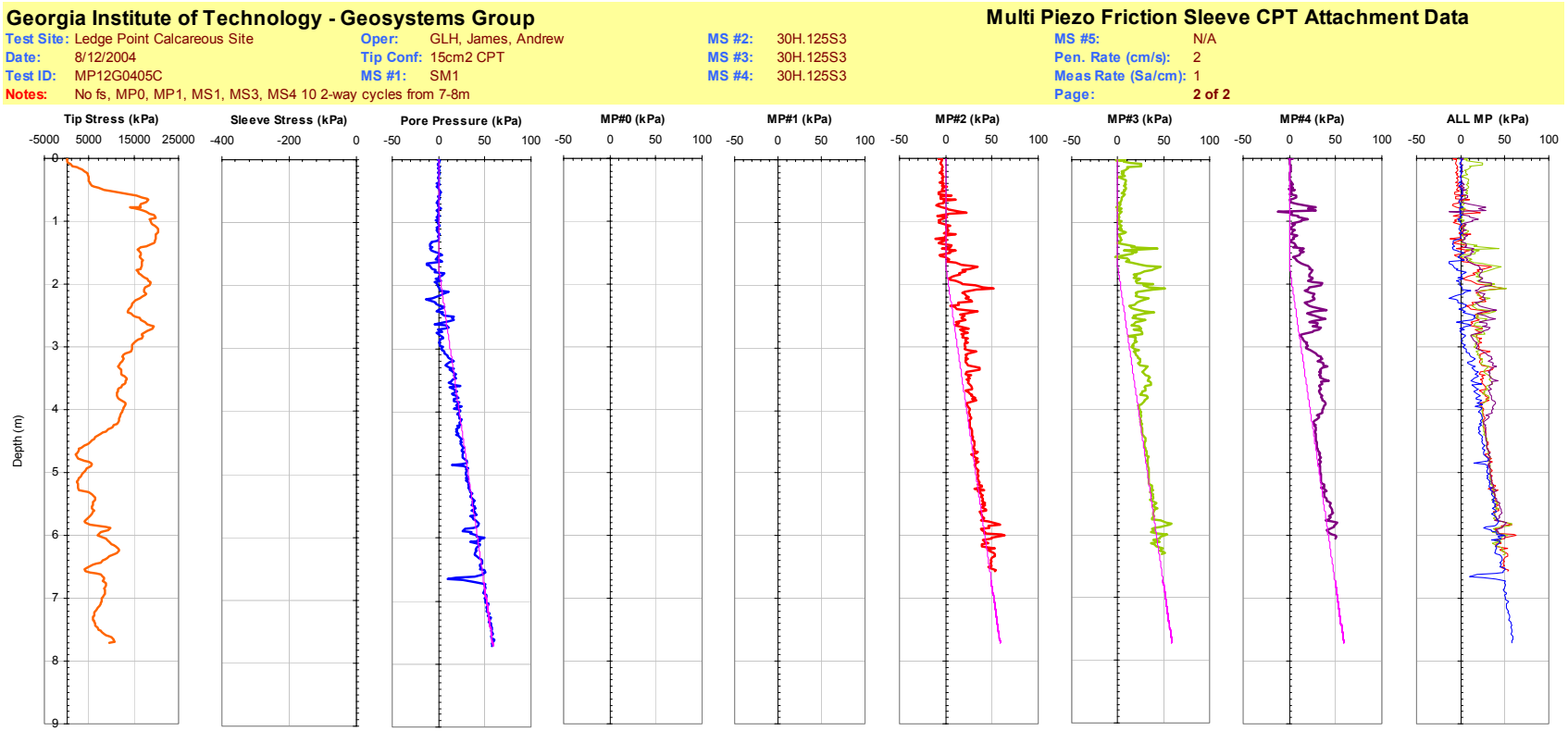

Figure 8-10. Plots of all CPTU and the MPFA Piezo Sensors from Sounding MPFA_24 at the LPWA Site.

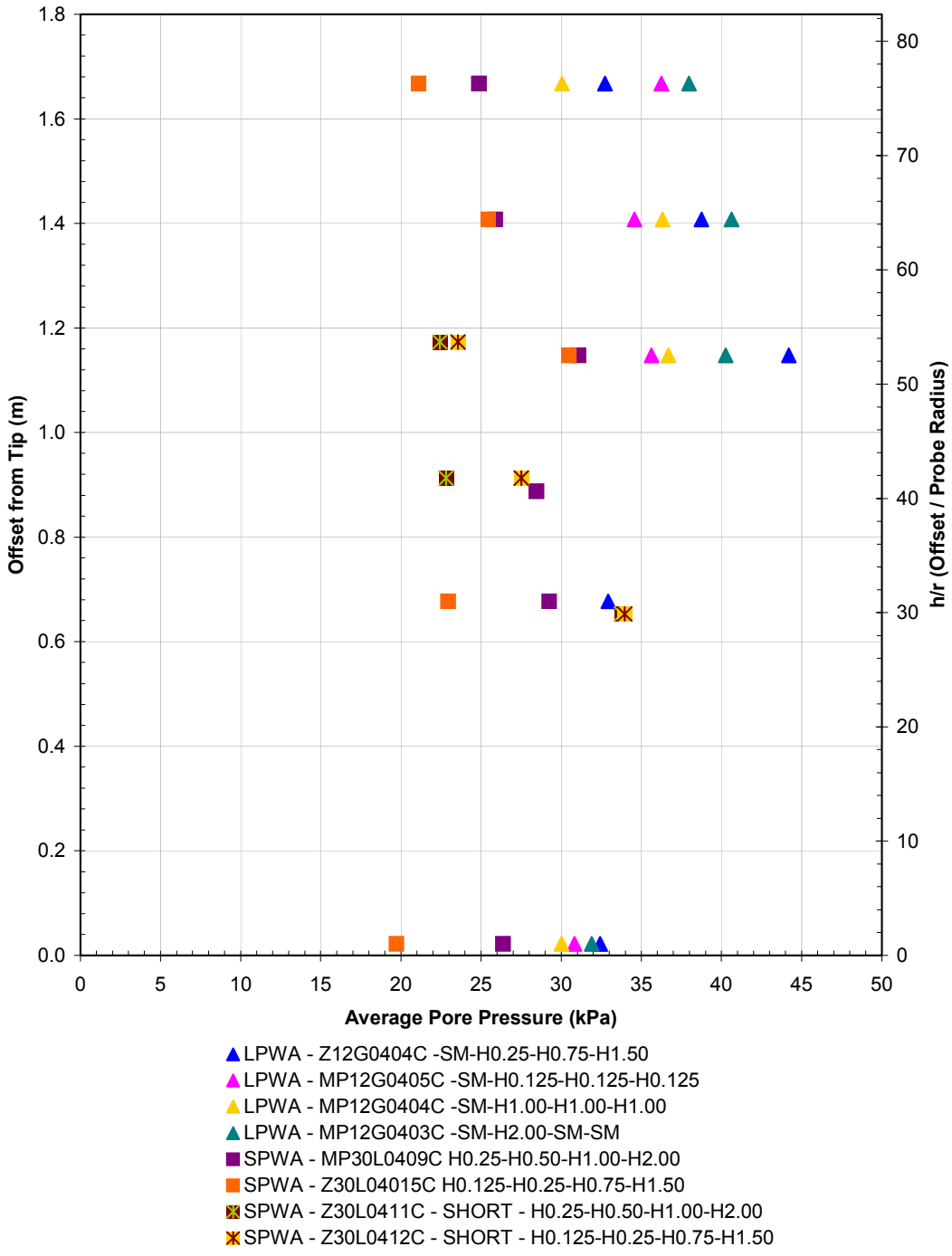

Figure 8-11. Average Absolute CPTU-MPFA Piezo Responses from the Prominent Sand Stratigraphies Encountered in the Current Study. SPWA Averages taken from 7-9m and LPWA Averages taken from 4-6m.

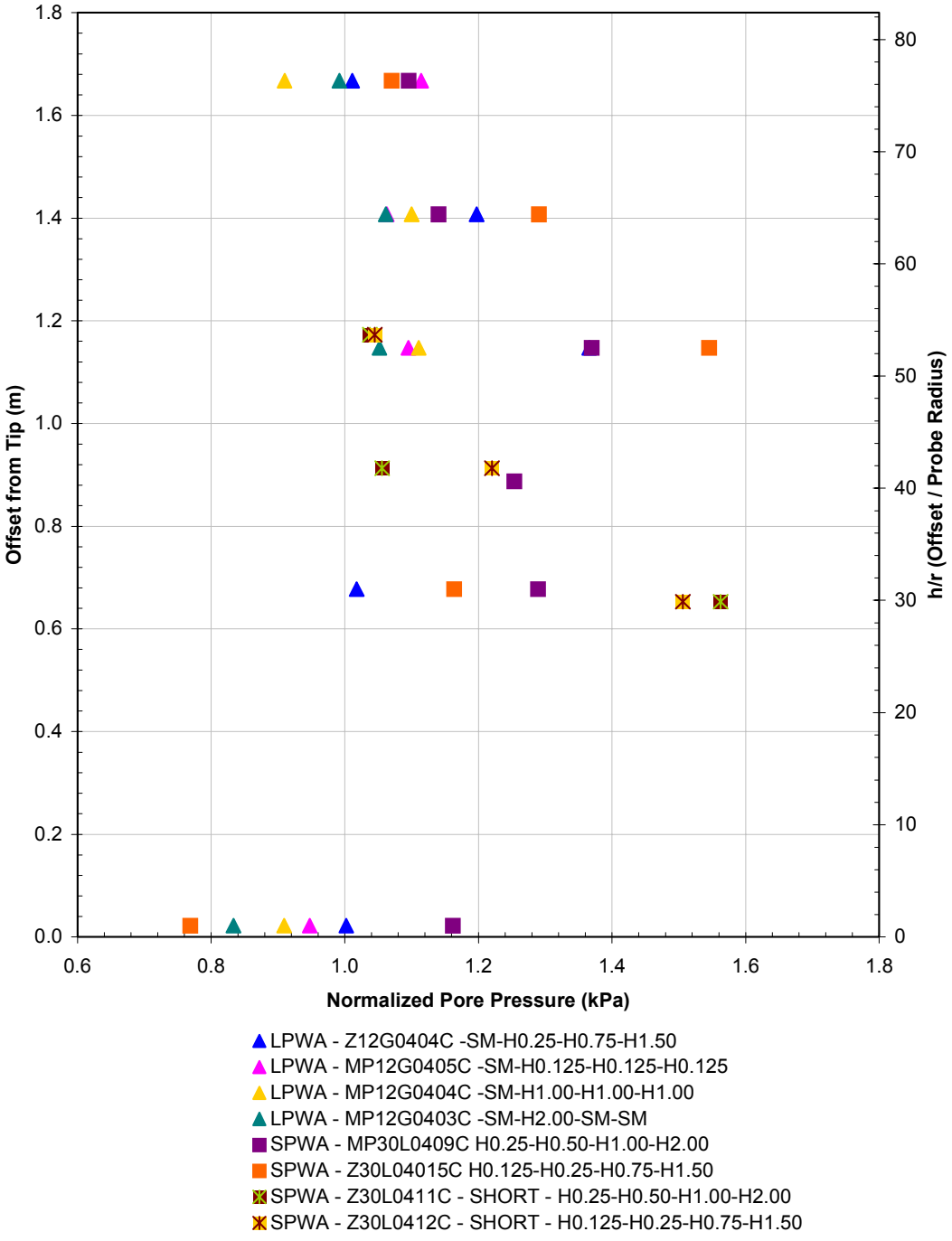

Figure 8-12. Average Normalized CPTU-MPFA Piezo Responses from the Prominent Sand Stratigraphies Encountered in the Current Study. SPWA Averages taken from 7-9m and LPWA Averages taken from 4-6m.

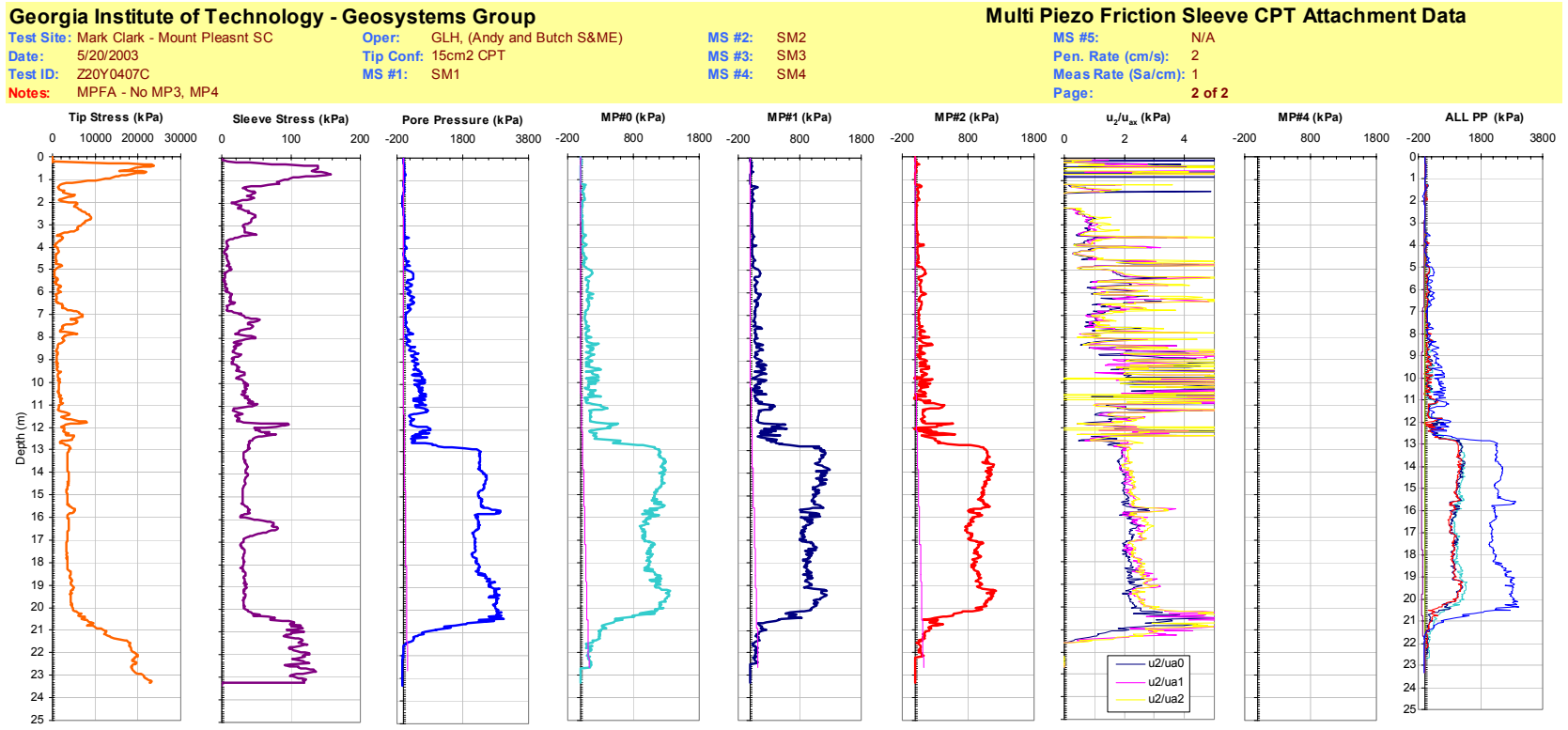

Figure 8-13. Plots of all CPTU and the MPFA Piezo Sensors from Sounding MPFA_3 at the MPSC Site.

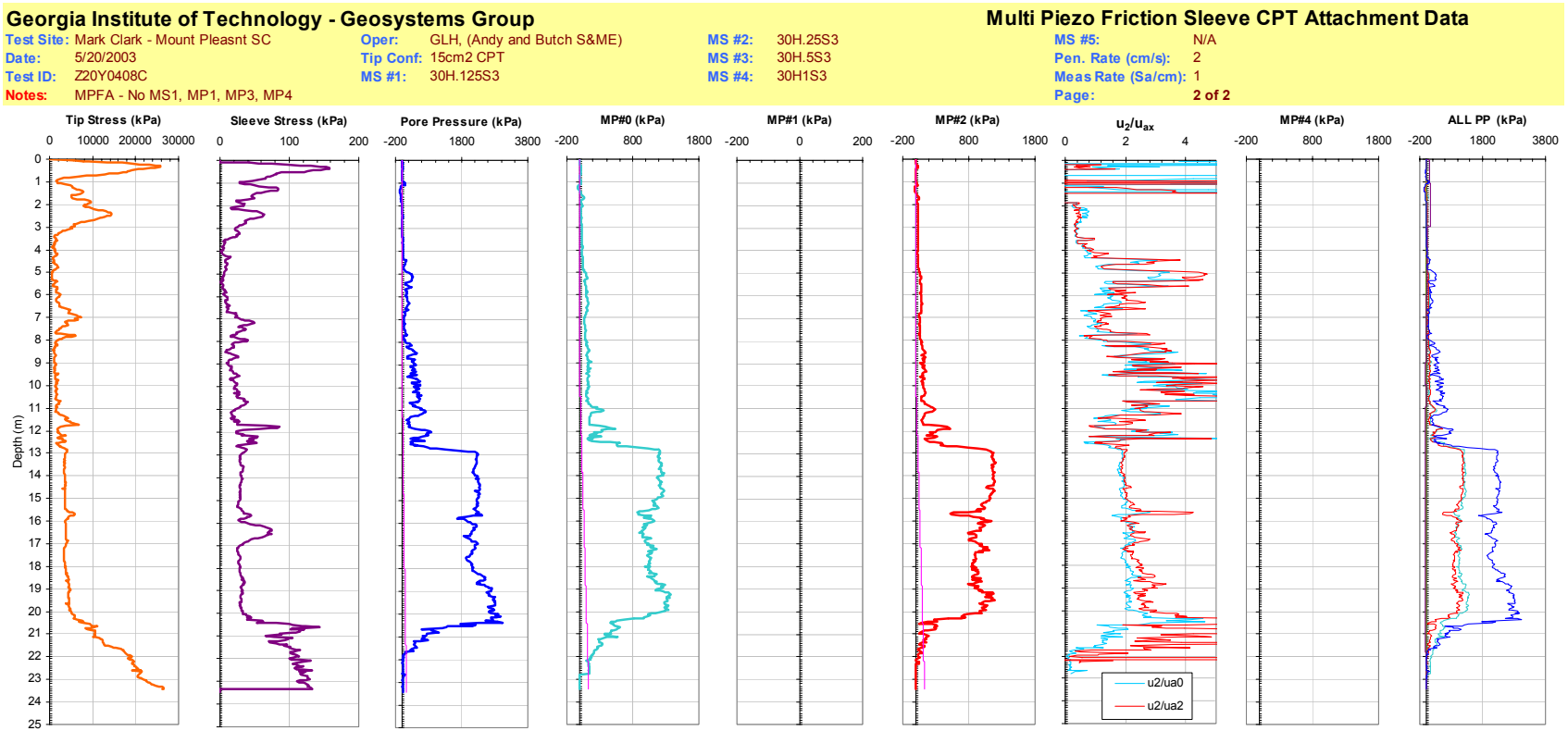

Figure 8-14. Plots of all CPTU and the MPFA Piezo Sensors from Sounding MPFA_4 at the MPSC Site.

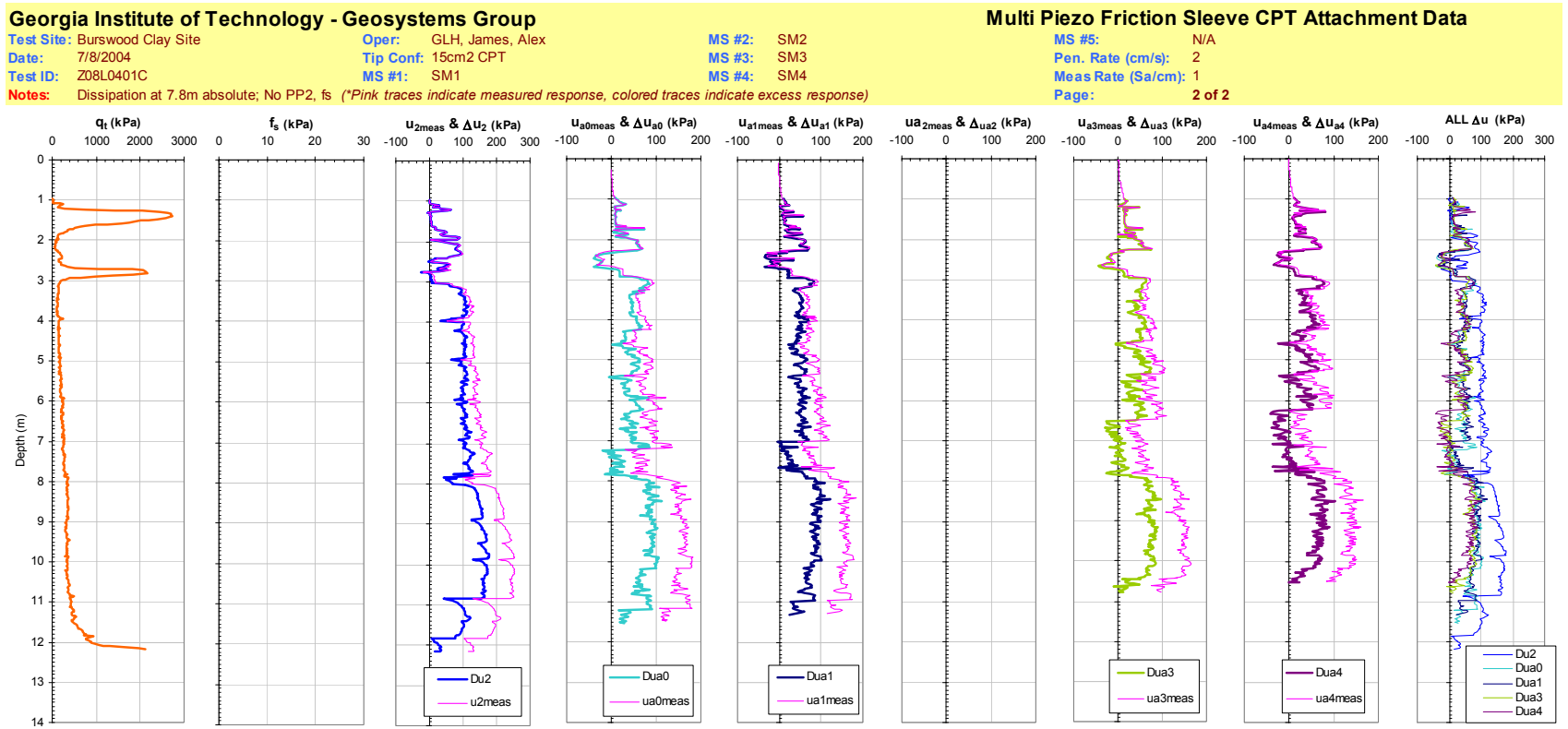

Figure 8-15. Plots of CPTU q_t and Overlain Excess and Absolute Pore Pressures for the CPTU-MPFA Piezo Sensors from Sounding MPFA_5 at the BWDWA Site.

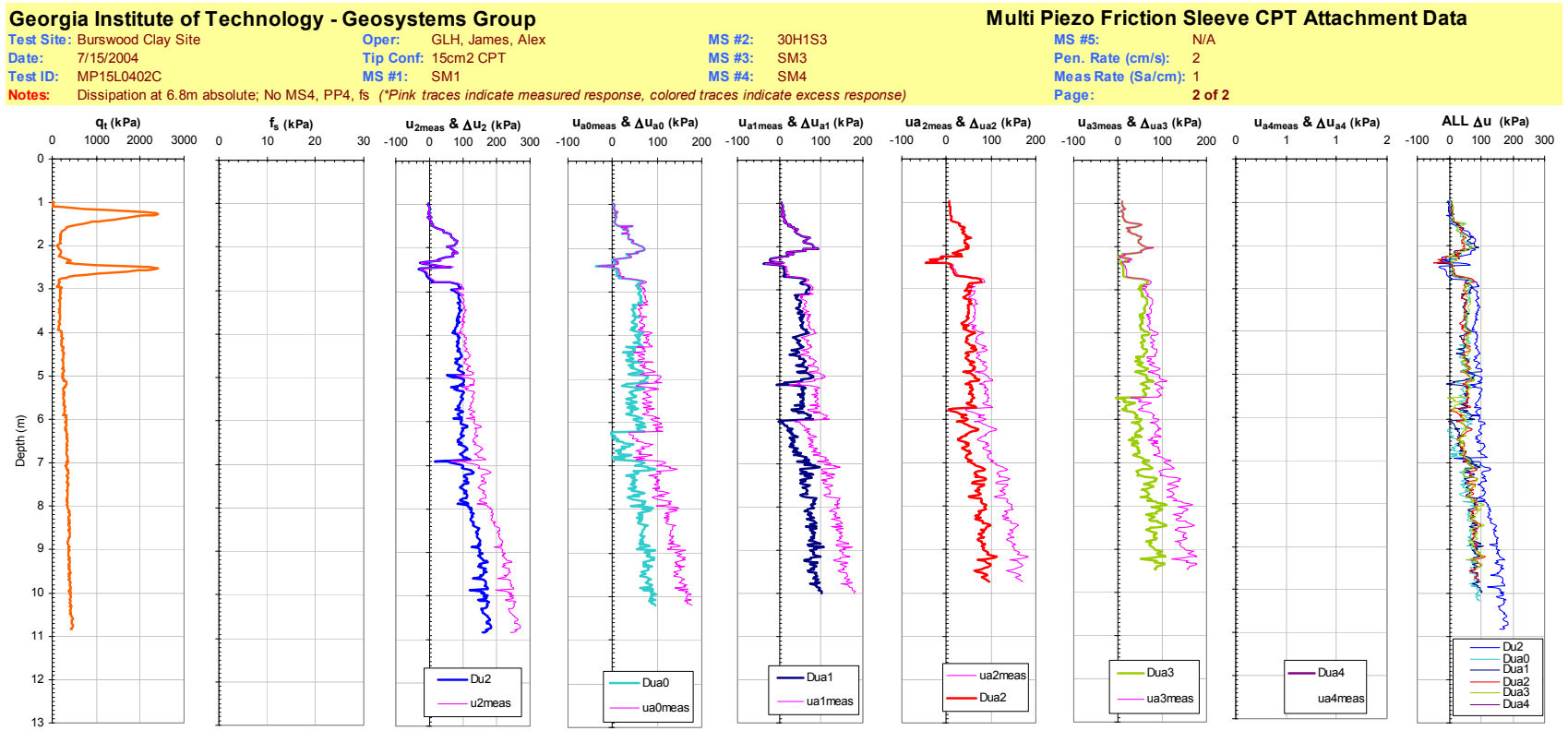

Figure 8-16. Plots of CPTU q_t and Overlain Excess and Absolute Pore Pressures for the CPTU-MPFA Piezo Sensors from Sounding MPFA_6 at the BWDWA Site.

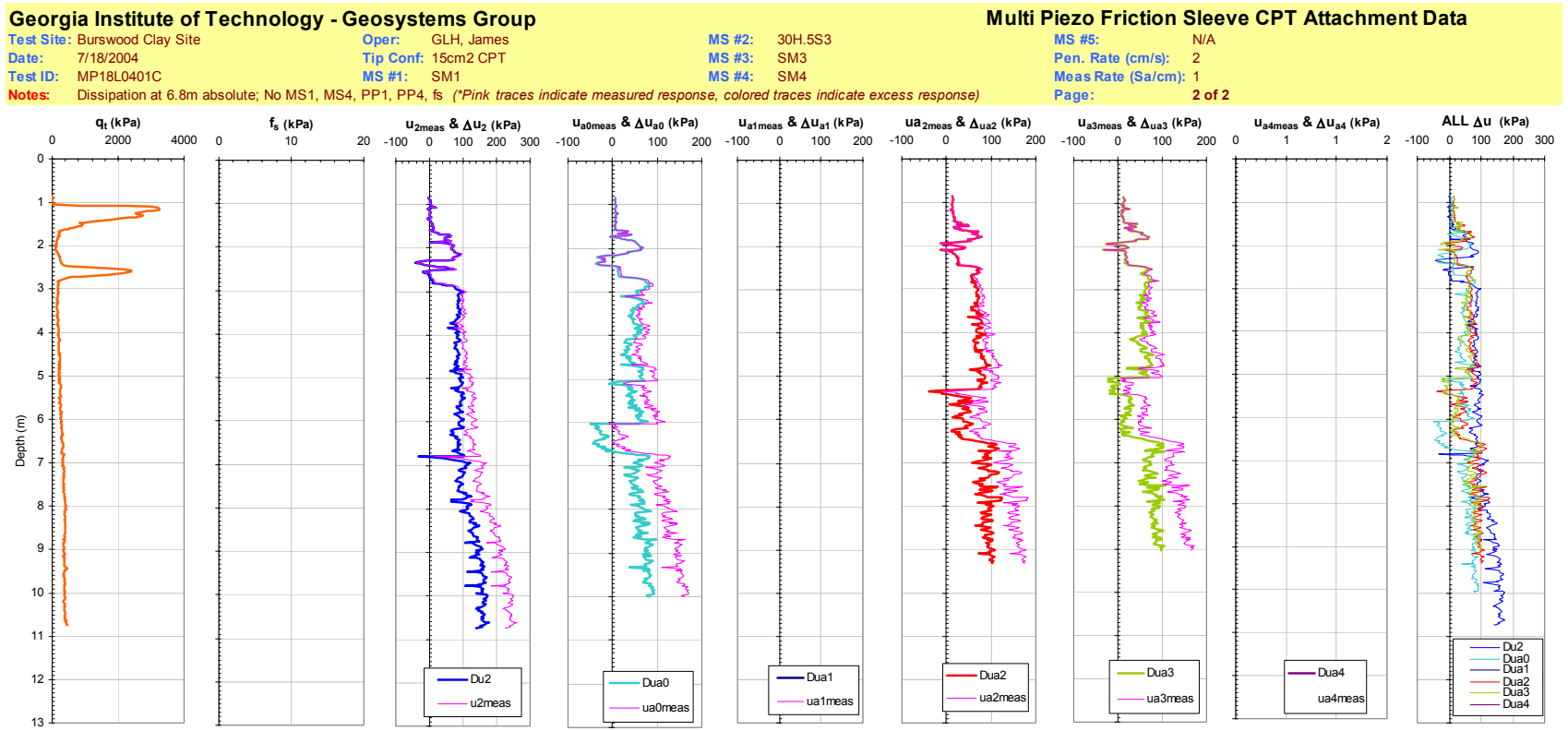

Figure 8-17. Plots of CPTU q_t and Overlain Excess and Absolute Pore Pressures for the CPTU-MPFA Piezo Sensors from Sounding MPFA_7 at the BWDWA Site.

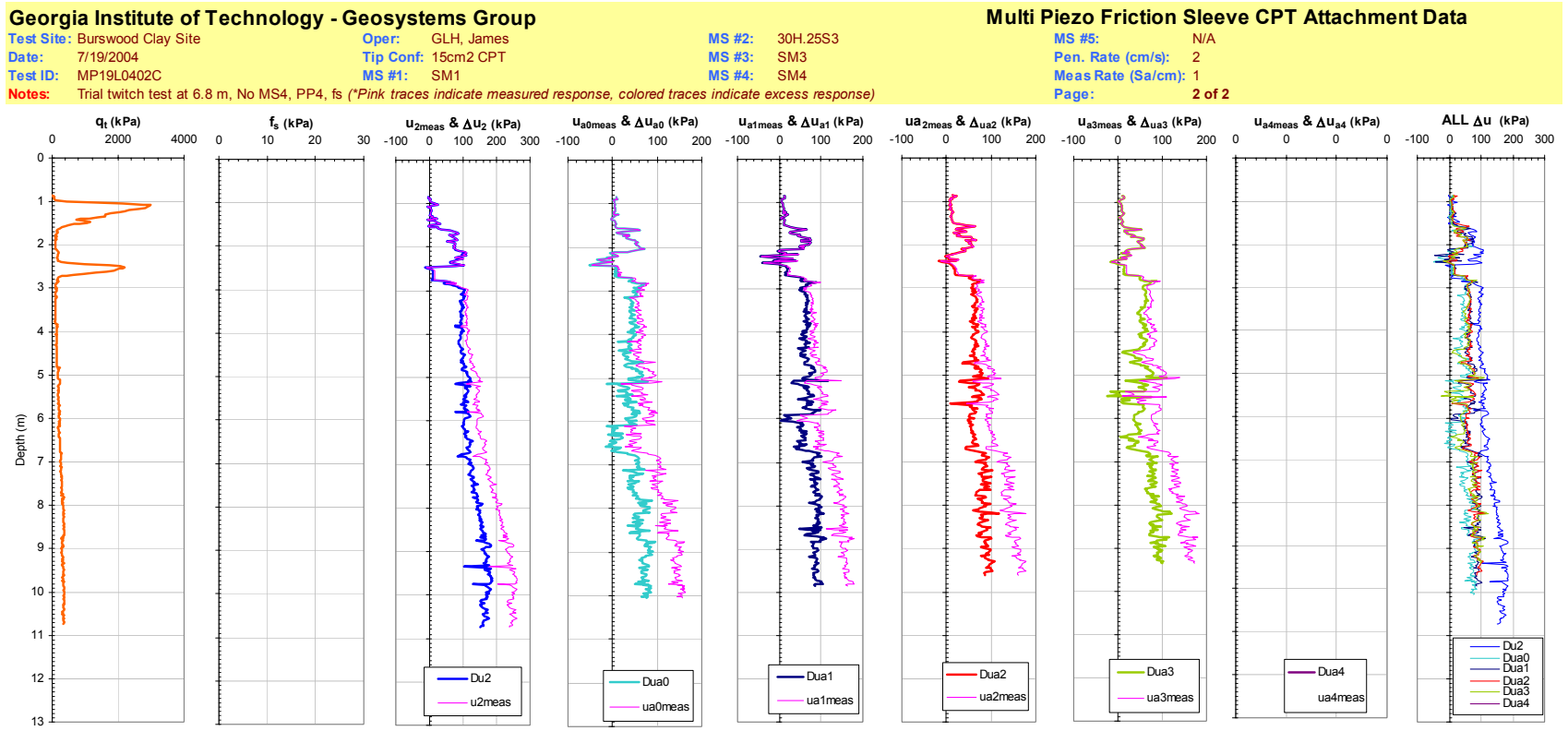

Figure 8-18. Plots of CPTU q_t and Overlain Excess and Absolute Pore Pressures for the CPTU-MPFA Piezo Sensors from Sounding MPFA_8 at the BWDWA Site.

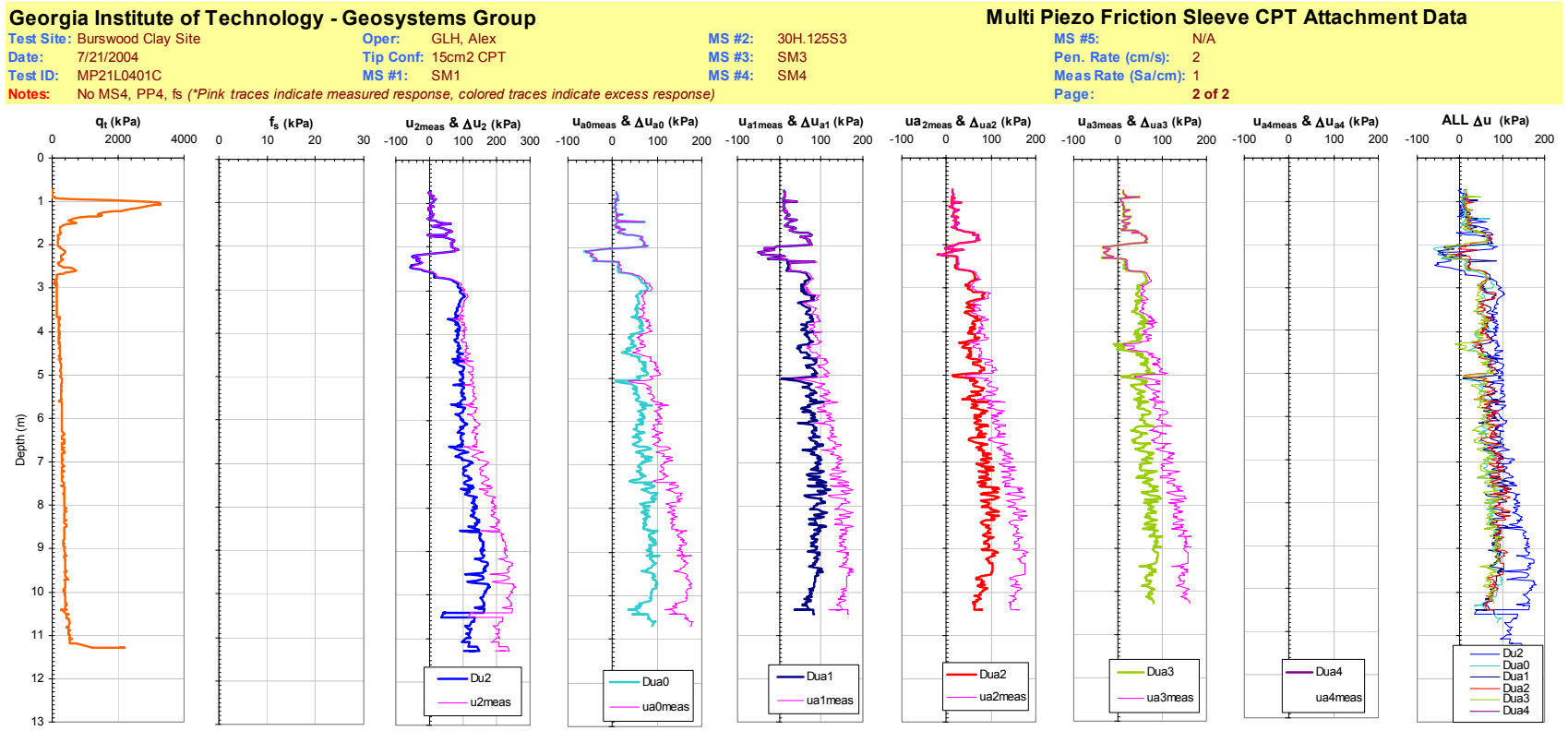

Figure 8-19. Plots of CPTU q_t and Overlain Excess and Absolute Pore Pressures for the CPTU-MPFA Piezo Sensors from Sounding MPFA_9 at the BWDWA Site.

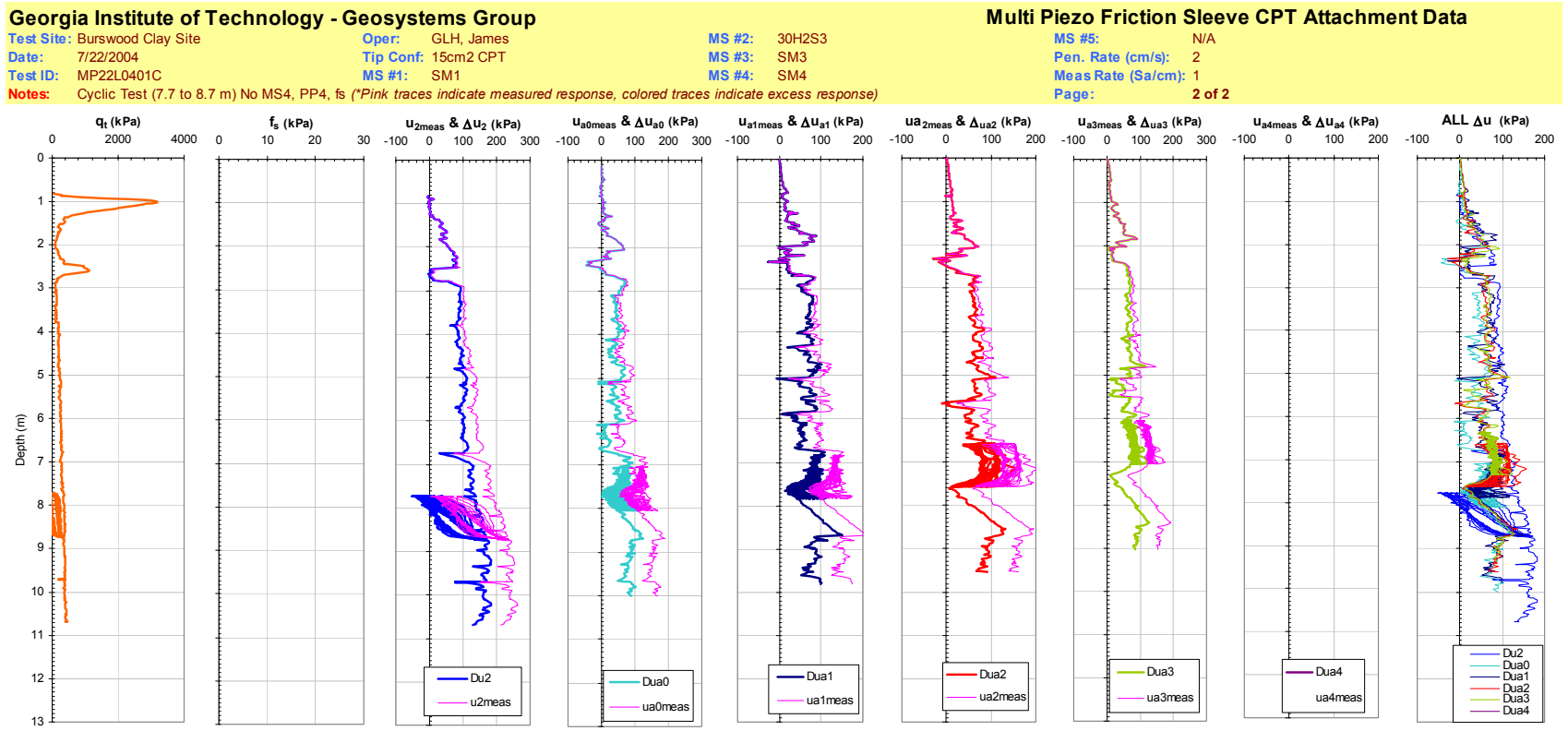

Figure 8-20. Plots of CPTU q_t and Overlain Excess and Absolute Pore Pressures for the CPTU-MPFA Piezo Sensors from Sounding MPFA_20 at the BWDWA Site.

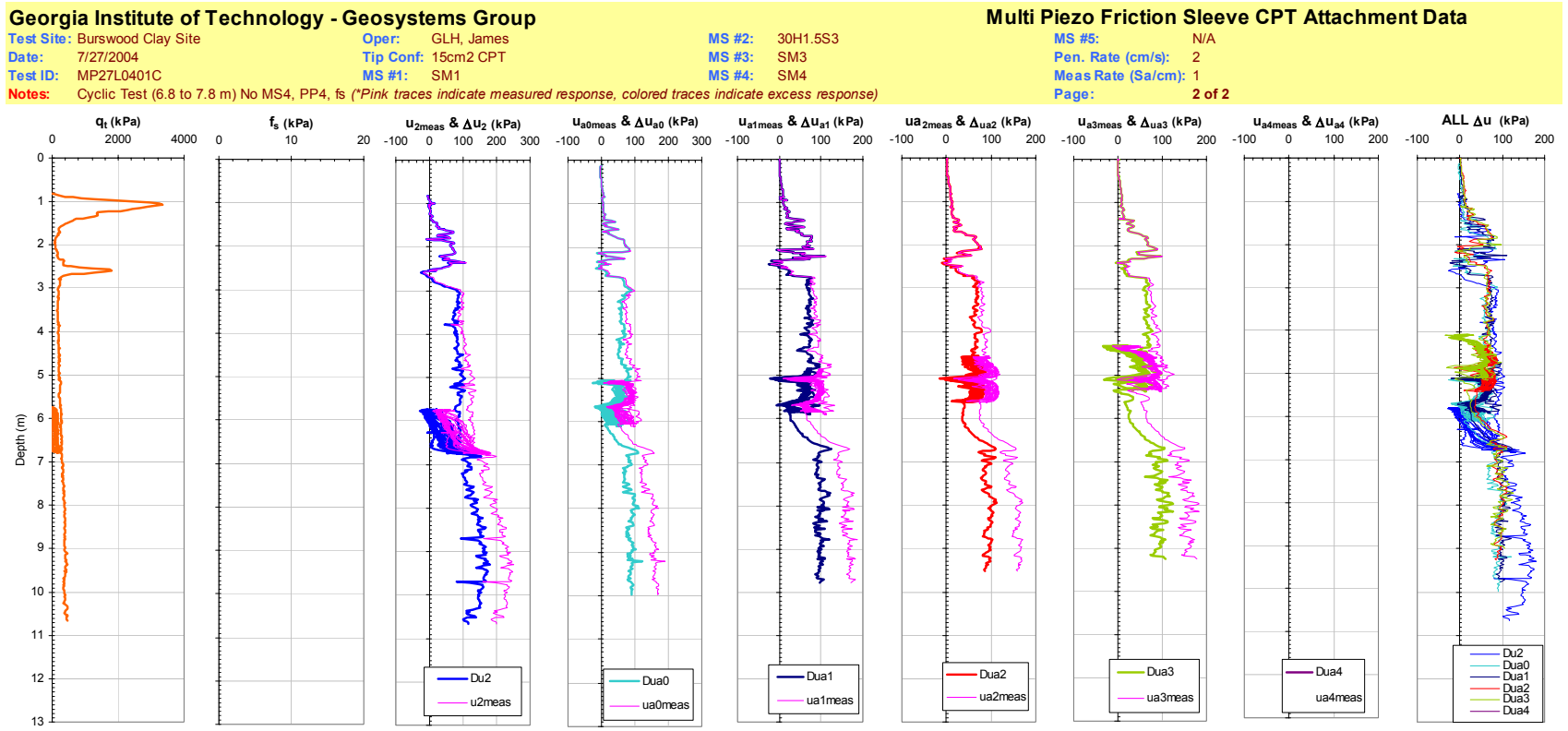

Figure 8-21. Plots of CPTU q_t and Overlain Excess and Absolute Pore Pressures for the CPTU-MPFA Piezo Sensors from Sounding MPFA_21 at the BWDWA Site.

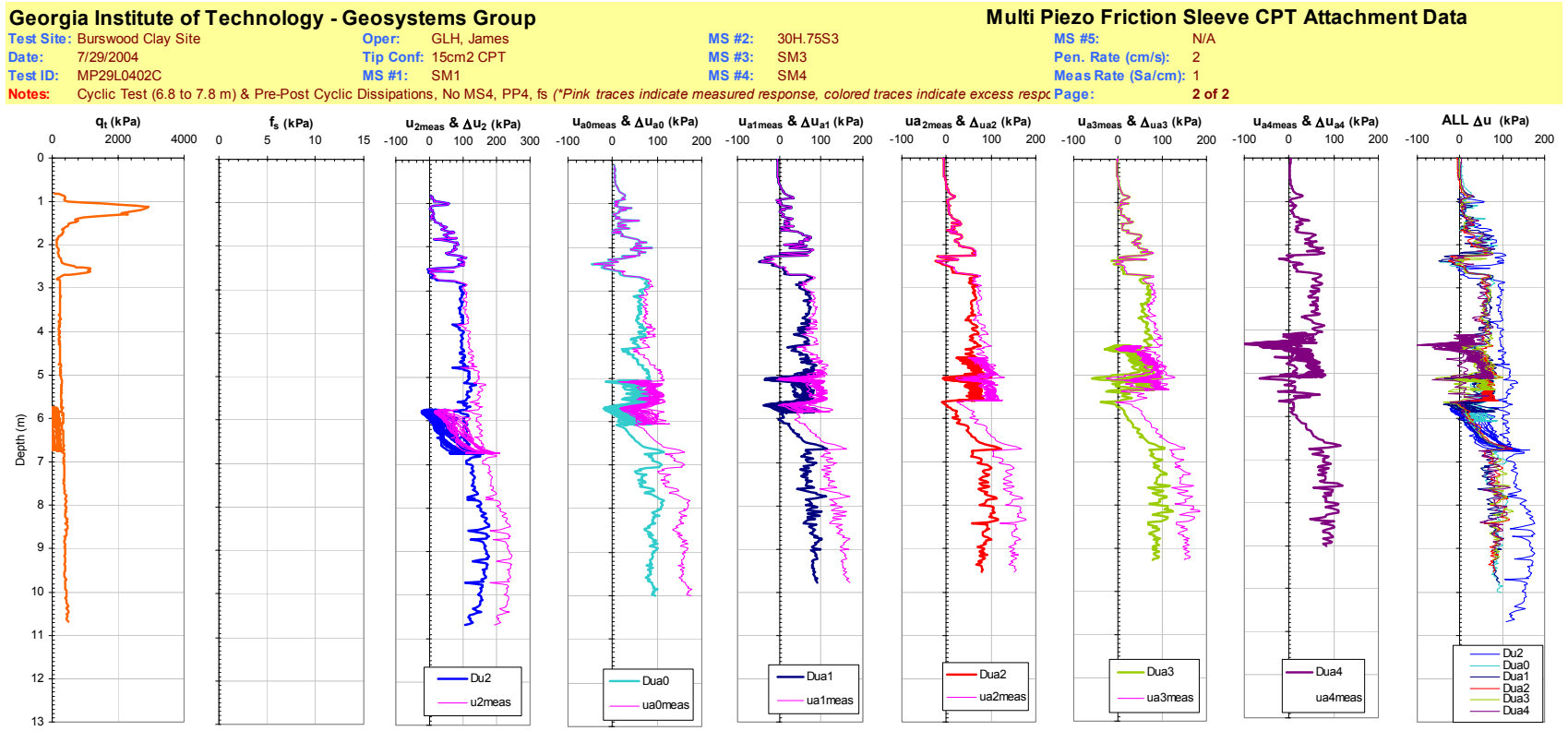

Figure 8-22. Plots of CPTU q_t and Overlain Excess and Absolute Pore Pressures for the CPTU-MPFA Piezo Sensors from Sounding MPFA_22 at the BWDWA Site.

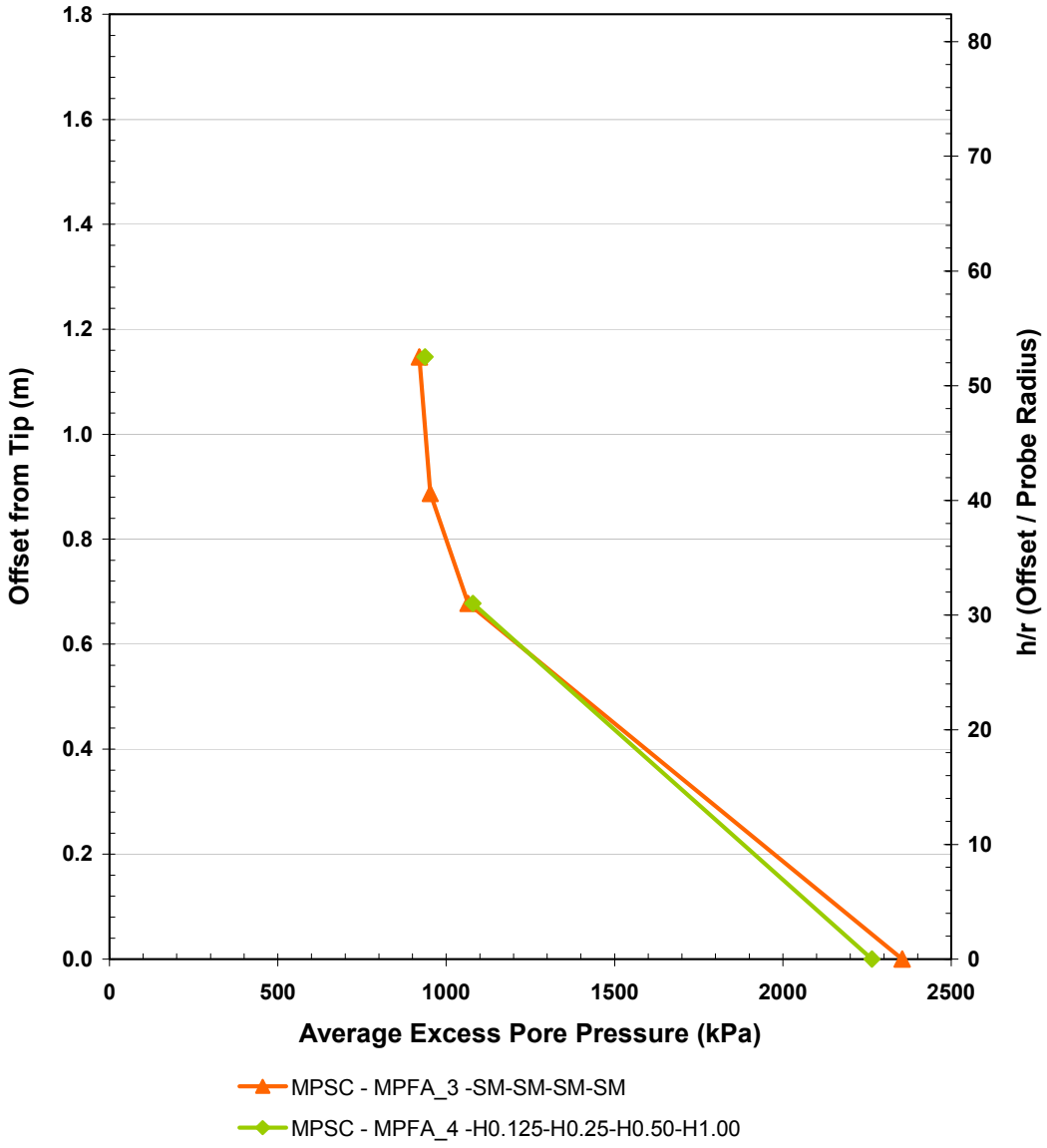

Figure 8-23. Average Excess CPTU-MPFA Piezo Responses from the Cooper Marl Calcareous Clay Stratigraphy between tip depths of 14 and 20 m.

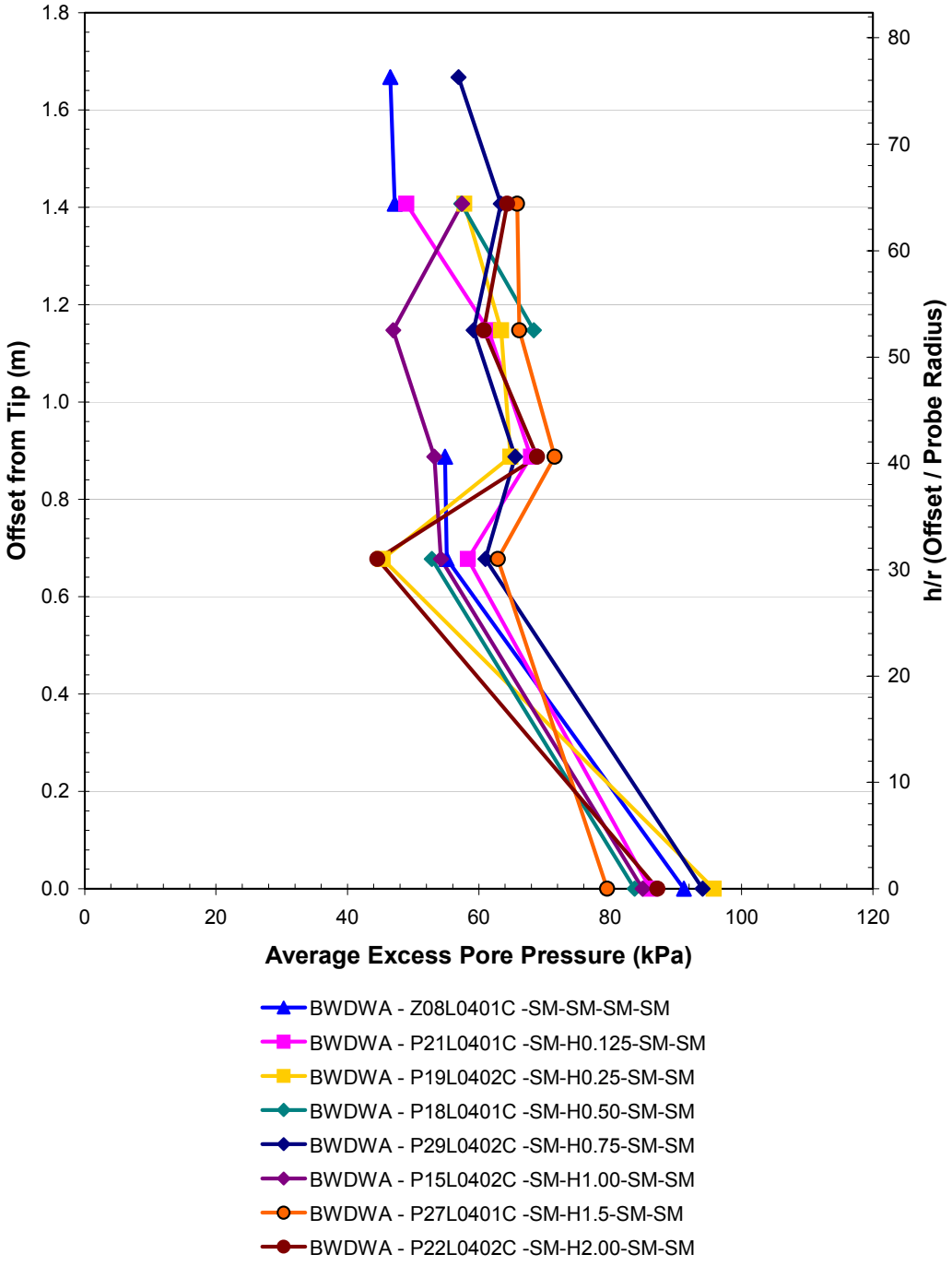

Figure 8-24. Average Excess CPTU-MPFA Piezo Responses from the Burswood Soft Clay Stratigraphy between tip depths of 3 and 7 m.

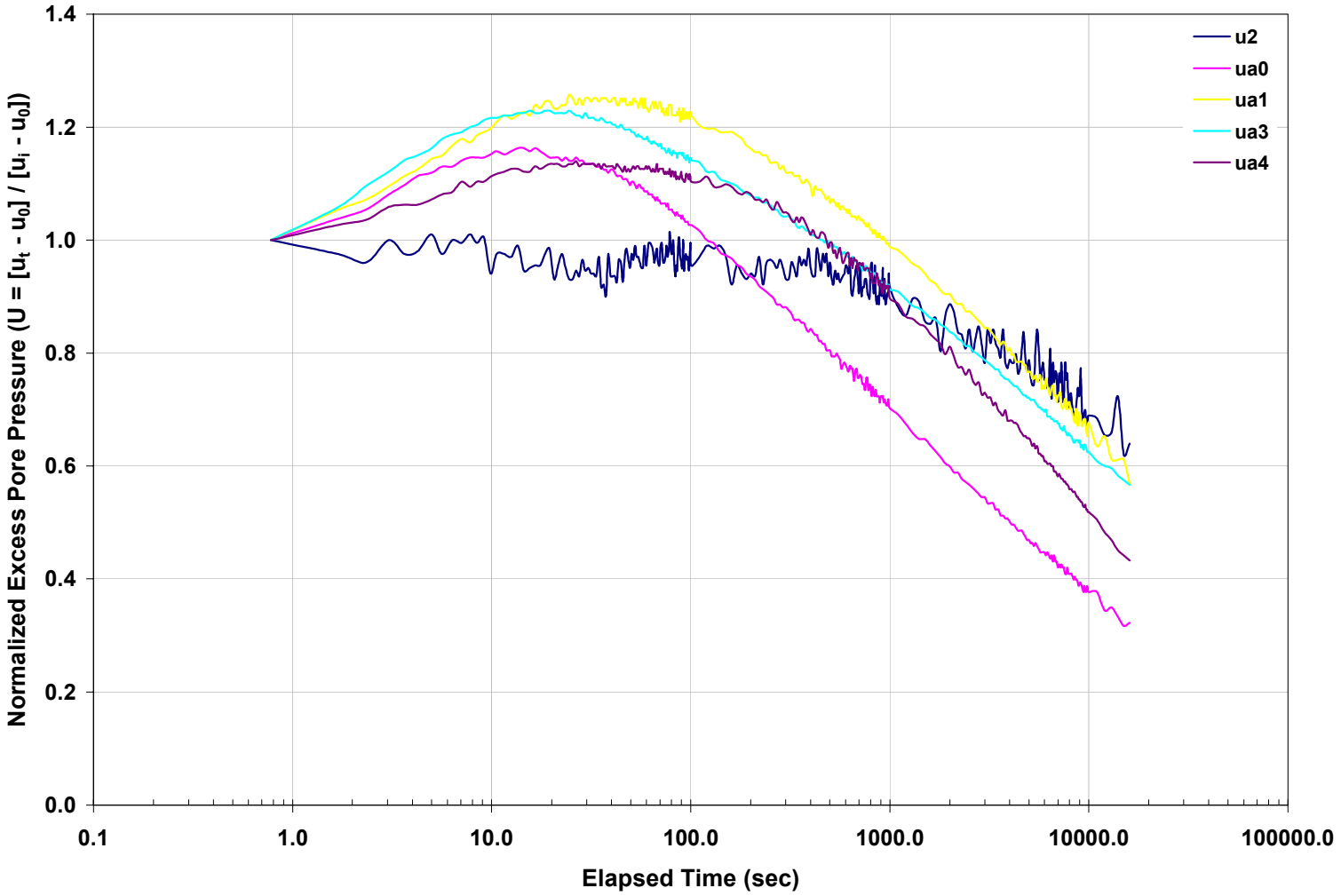

Figure 8-25. Plots of the Normalized Excess Pore Pressure Dissipation Responses for the CPTU-MPFA sensors in Sounding MPFA_5 for a Tip Depth of 7.74 m at the BWDWA Site.

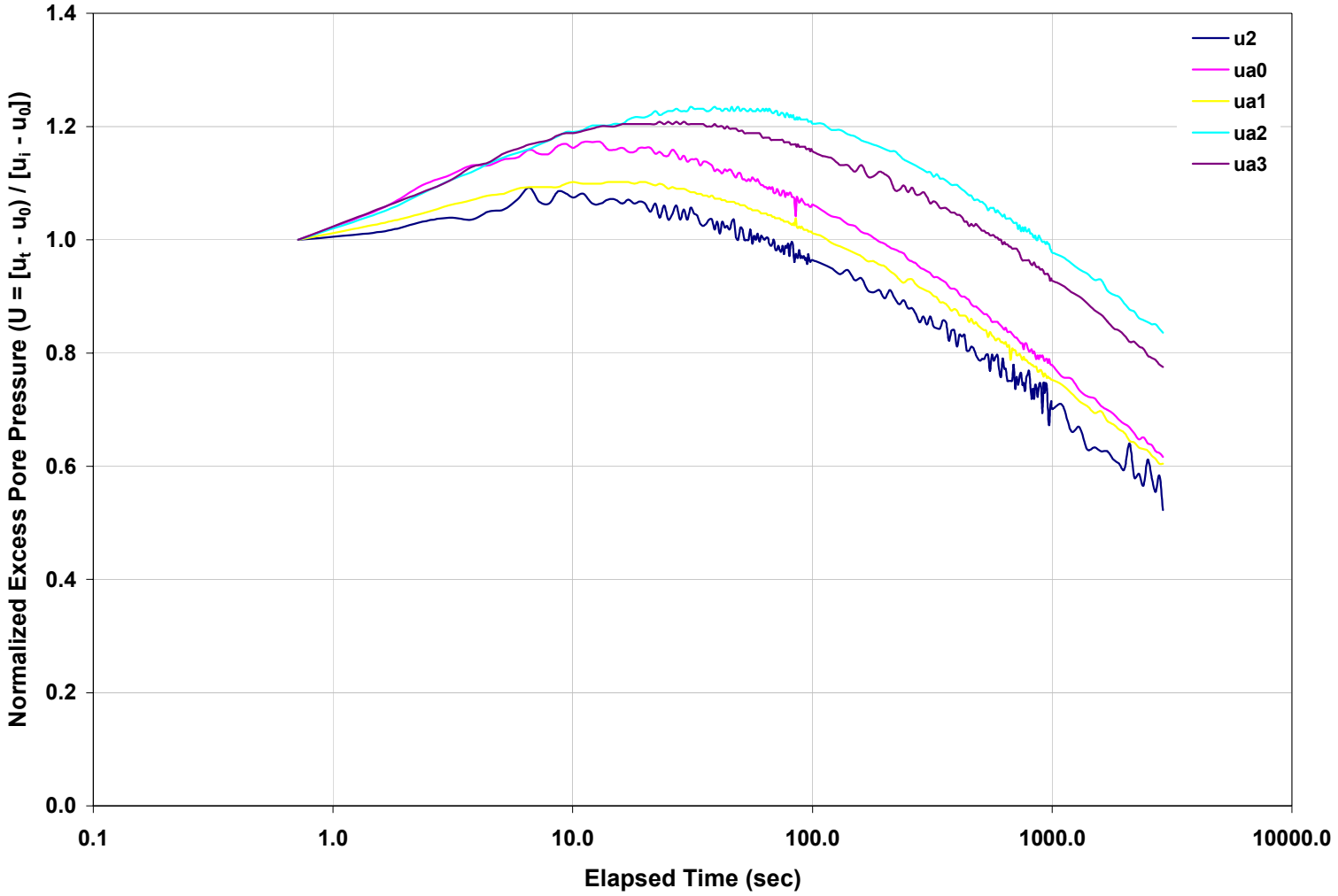

Figure 8-26. Plots of the Normalized Excess Pore Pressure Dissipation Responses for the CPTU-MPFA sensors in Sounding MPFA_6 for a Tip Depth of 6.74 m at the BWDWA Site.

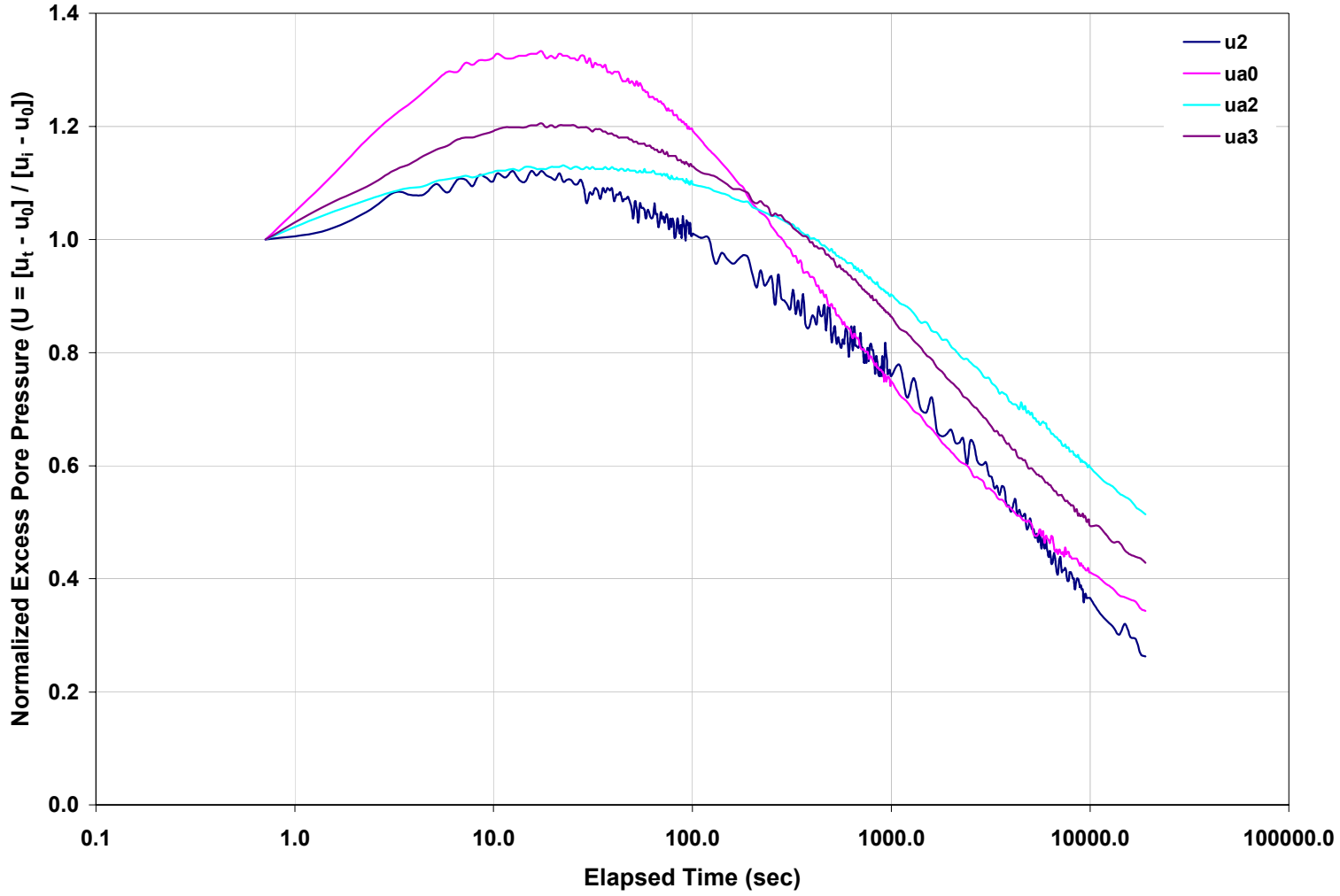

Figure 8-27. Plots of the Normalized Excess Pore Pressure Dissipation Responses for the CPTU-MPFA sensors in Sounding MPFA_7 for a Tip Depth of 6.75 m at the BWDWA Site.

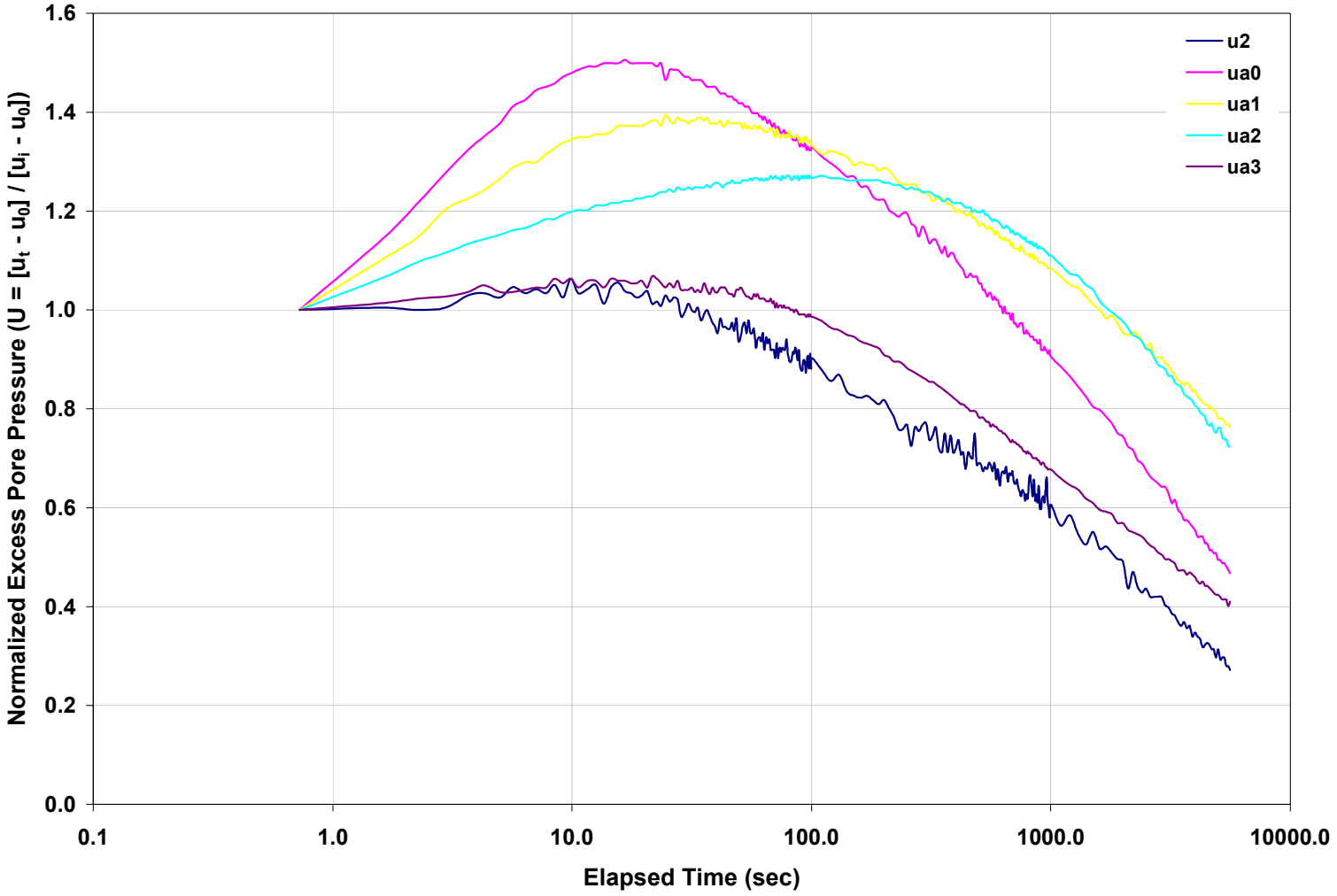

Figure 8-28. Plots of the Normalized Excess Pore Pressure Dissipation Responses for the CPTU-MPFA sensors in Sounding MPFA_10 for a Tip Depth of 6.74 m at the BWDWA Site.

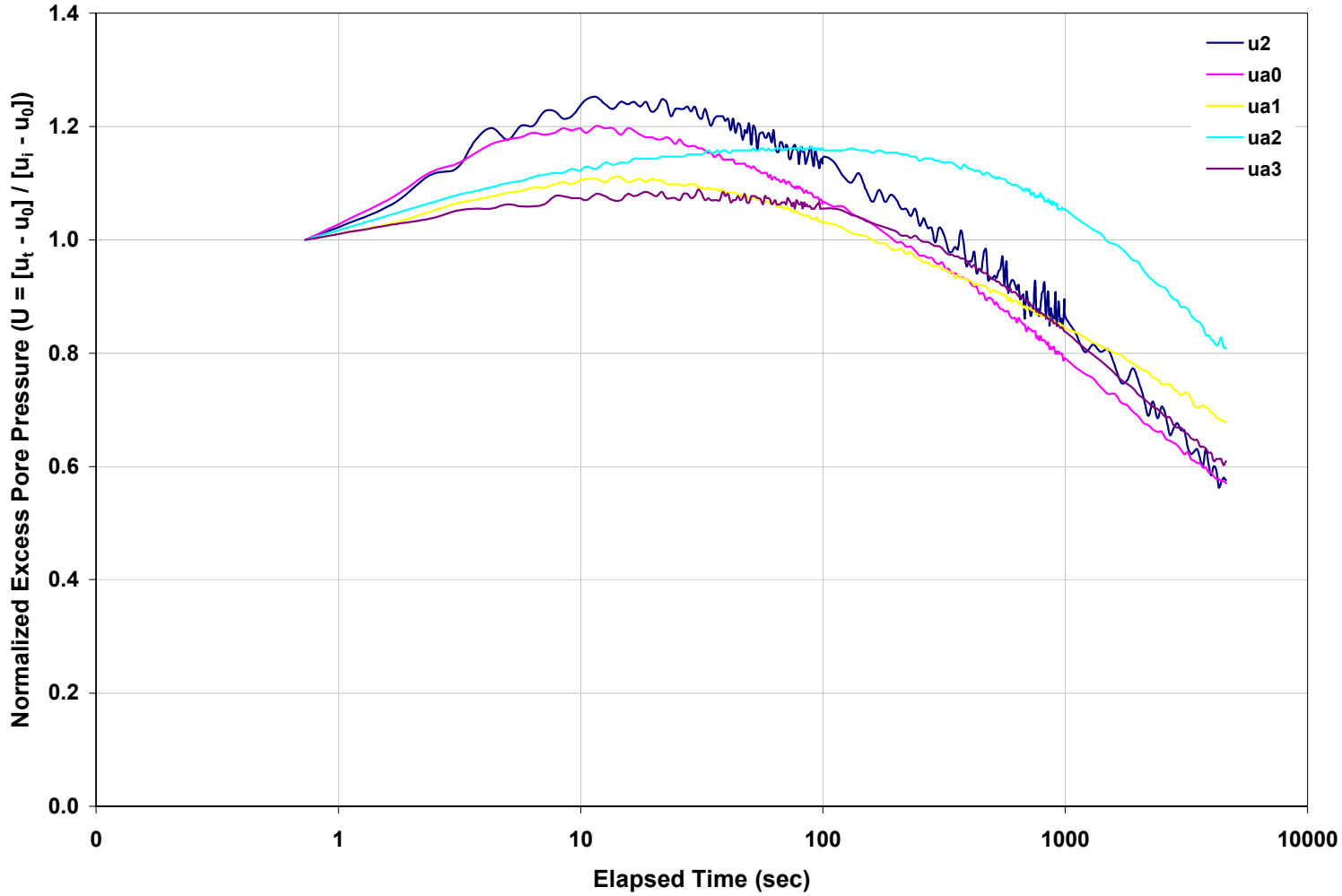

Figure 8-29. Plots of the Normalized Excess Pore Pressure Dissipation Responses for the CPTU-MPFA sensors in Sounding MPFA_11 for a Tip Depth of 6.74 m at the BWDWA Site.

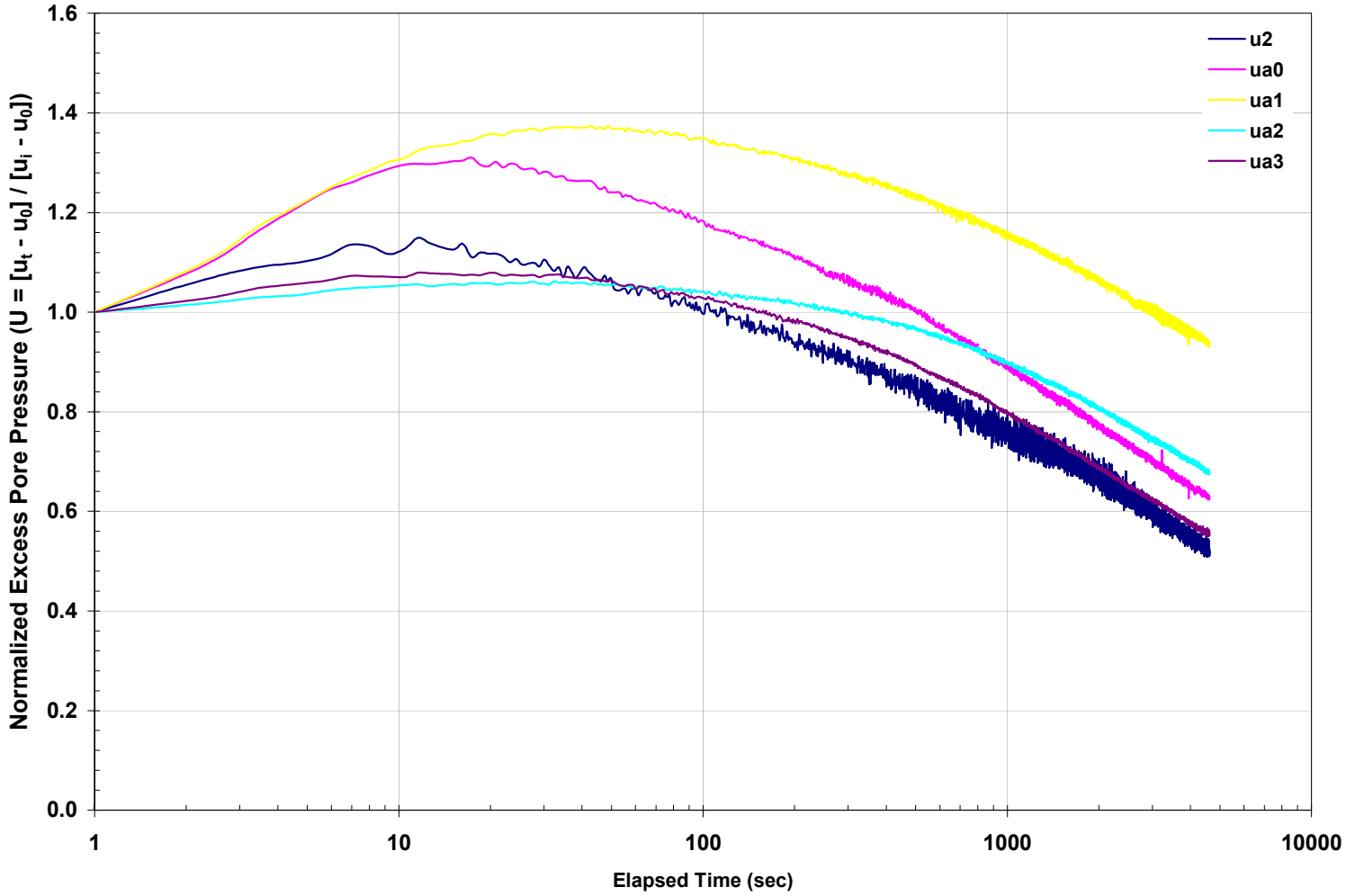

Figure 8-30. Plots of the Normalized Excess Pore Pressure Dissipation Responses for the CPTU-MPFA sensors in Sounding MPFA_12 for a Tip Depth of 6.75 m at the BWDWA Site.

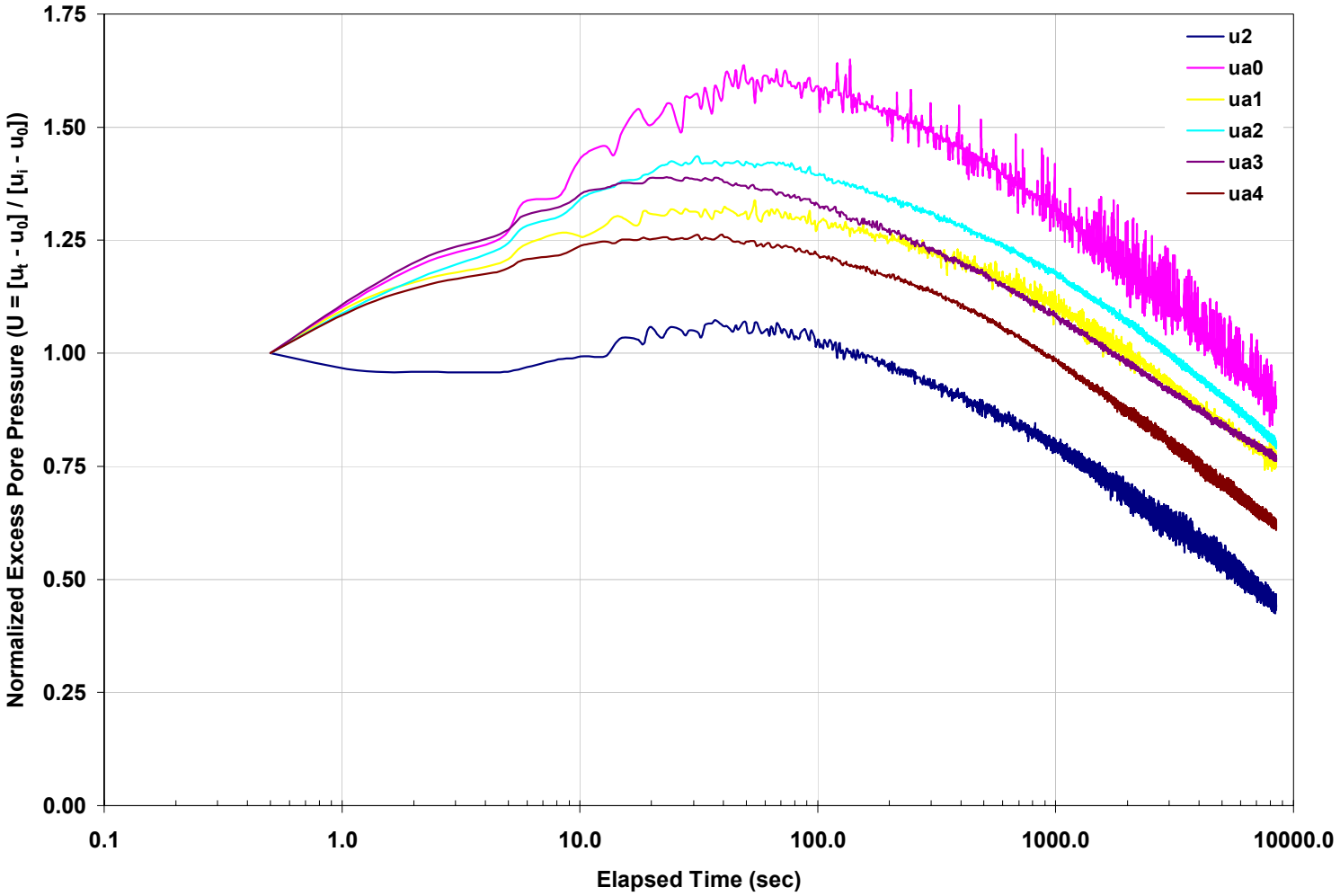

Figure 8-31. Plots of the Normalized Excess Pore Pressure Dissipation Responses for the CPTU-MPFA sensors in LT1 for a Tip Depth of 7.5 m at the BWDWA Site.

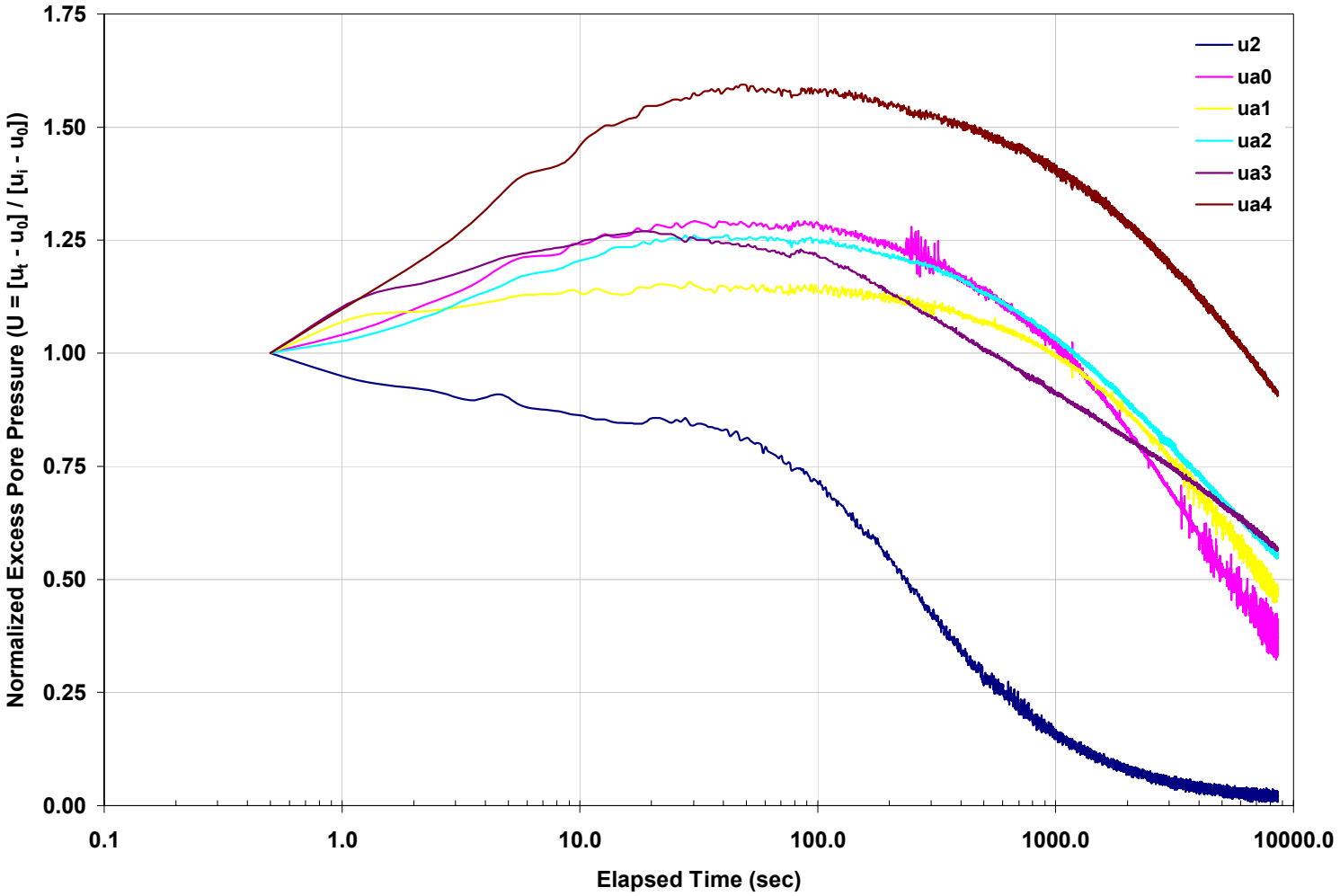

Figure 8-32. Plots of the Normalized Excess Pore Pressure Dissipation Responses for the CPTU-MPFA sensors in LT2 for a Tip Depth of 10.0 m at the BWDWA Site.

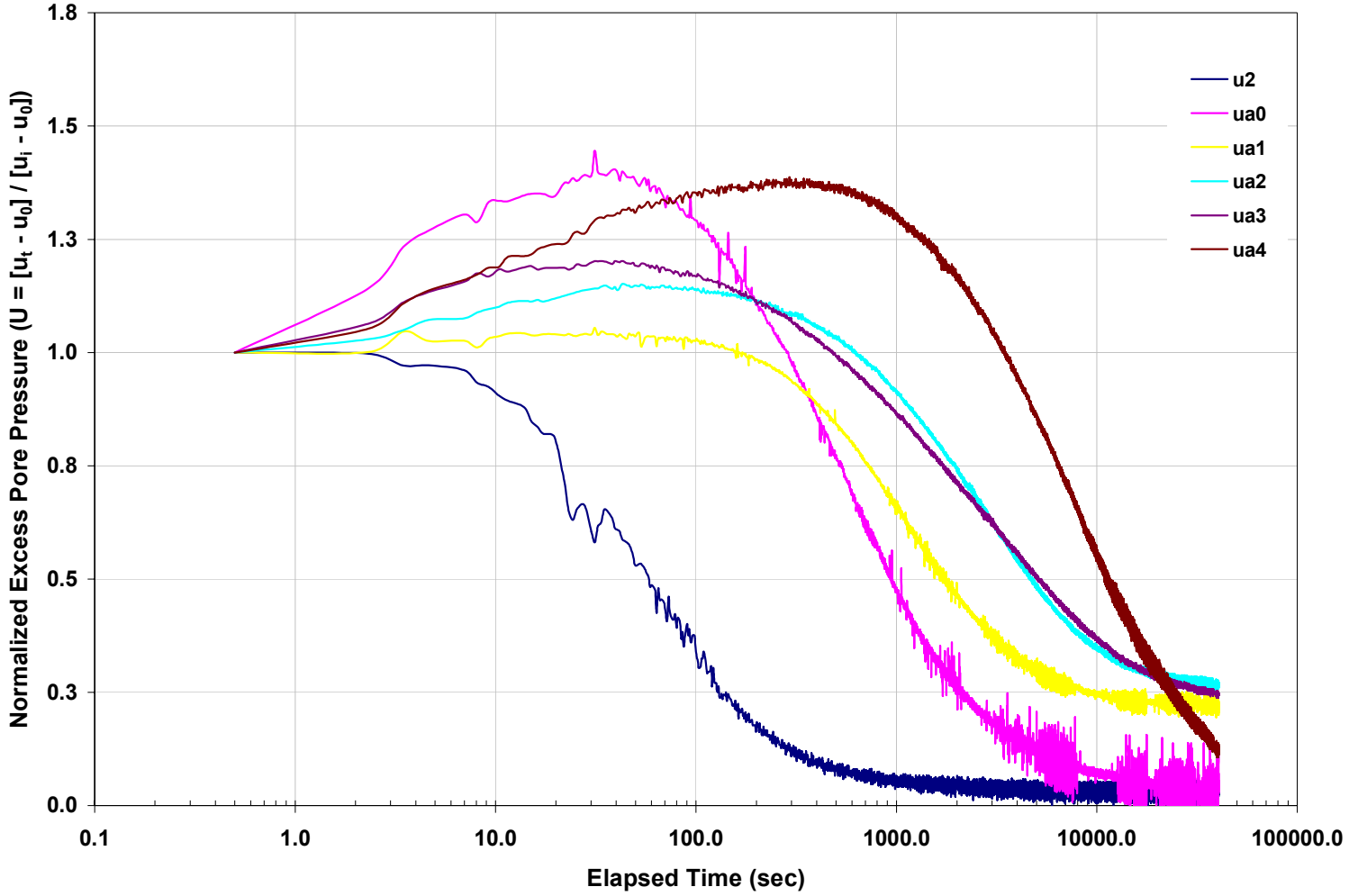

Figure 8-33. Plots of the Normalized Excess Pore Pressure Dissipation Responses for the CPTU-MPFA sensors in LT5 for a Tip Depth of 10.0 m at the BWDWA Site.

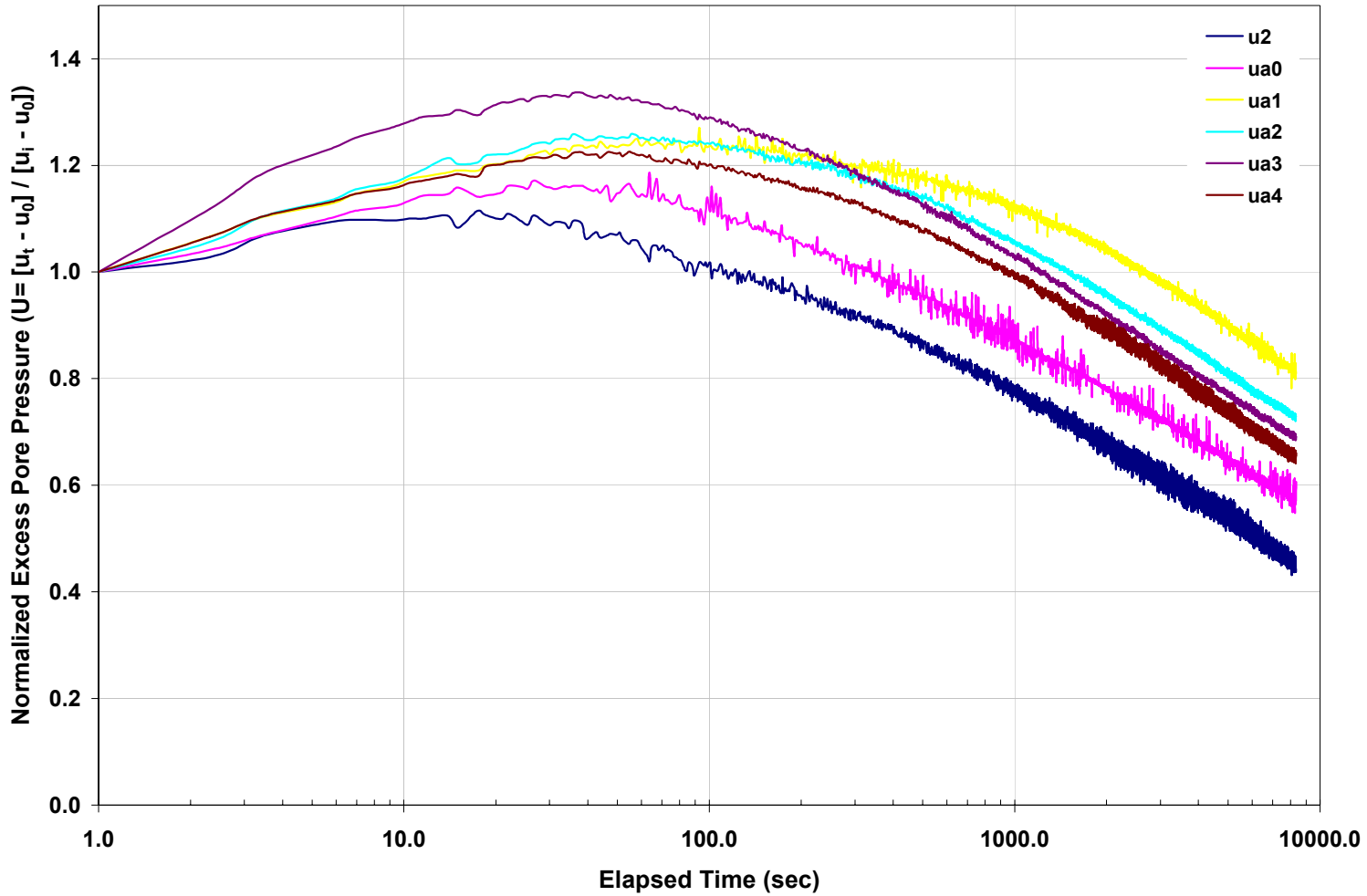

Figure 8-34. Plots of the Normalized Excess Pore Pressure Dissipation Responses for the CPTU-MPFA sensors in LT7 for a Tip Depth of 7.5 m at the BWDWA Site.

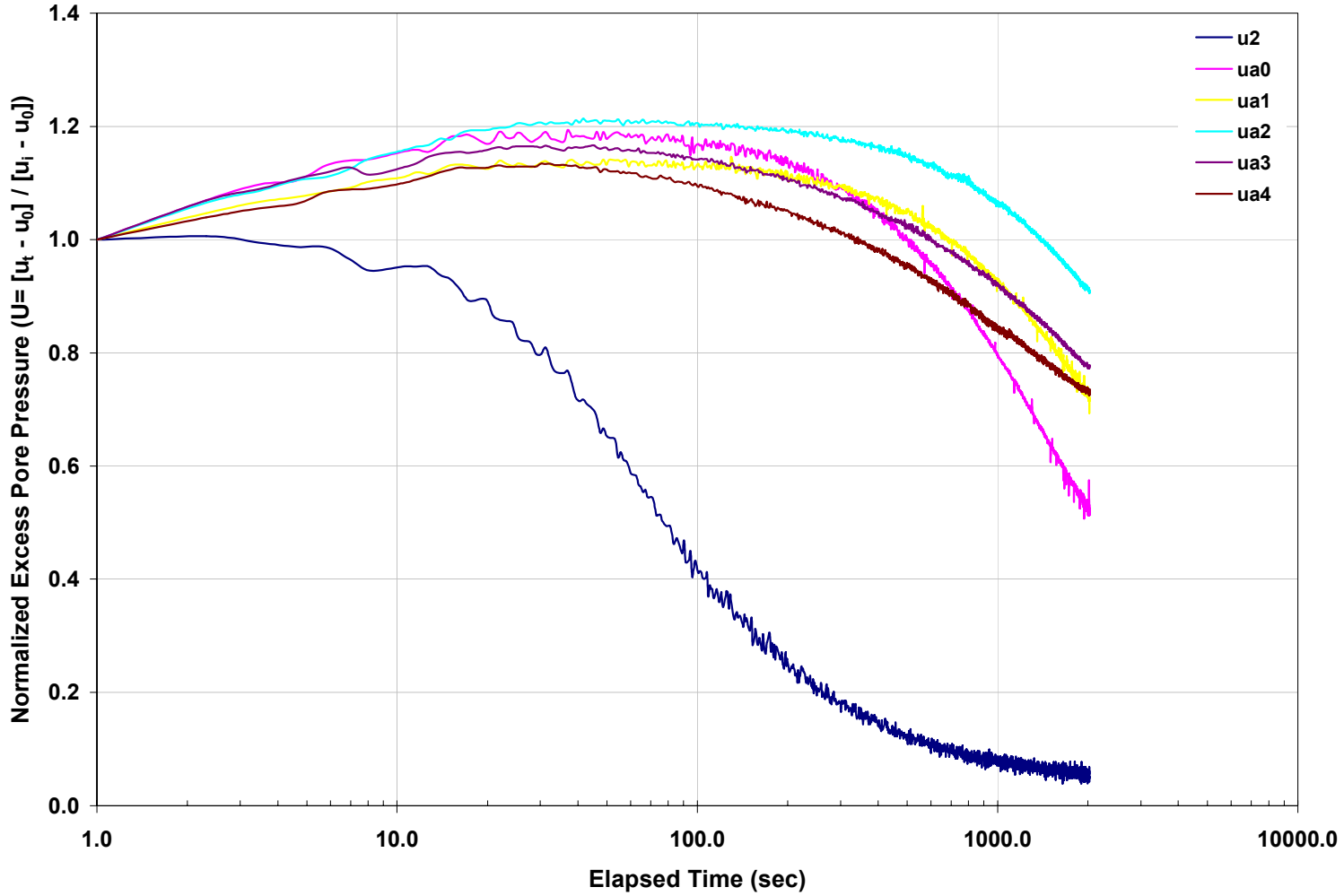

Figure 8-35. Plots of the Normalized Excess Pore Pressure Dissipation Responses for the CPTU-MPFA sensors in LT8 for a Tip Depth of 10.0 m at the BWDWA Site.

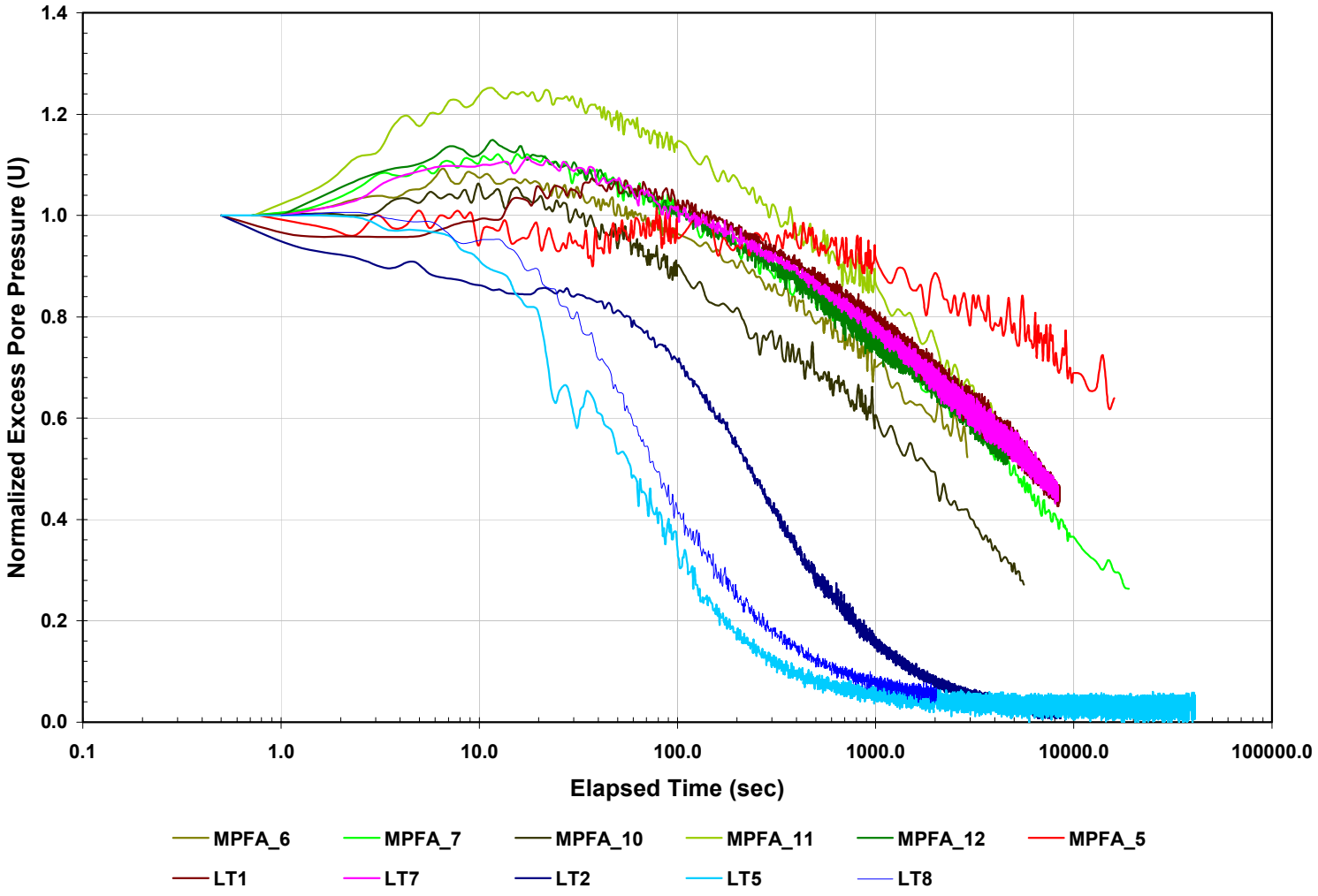

Figure 8-36. Overlay Plot of All u_2 Normalized Excess Pore Pressure Responses for the Conventional Dissipation Tests Conducted at BWDWA. Green, Red, and Blue Tinted Traces are from Tip Depths of 6.74 m, 7.5&7.74 m, and 10.0 m, Respectively.

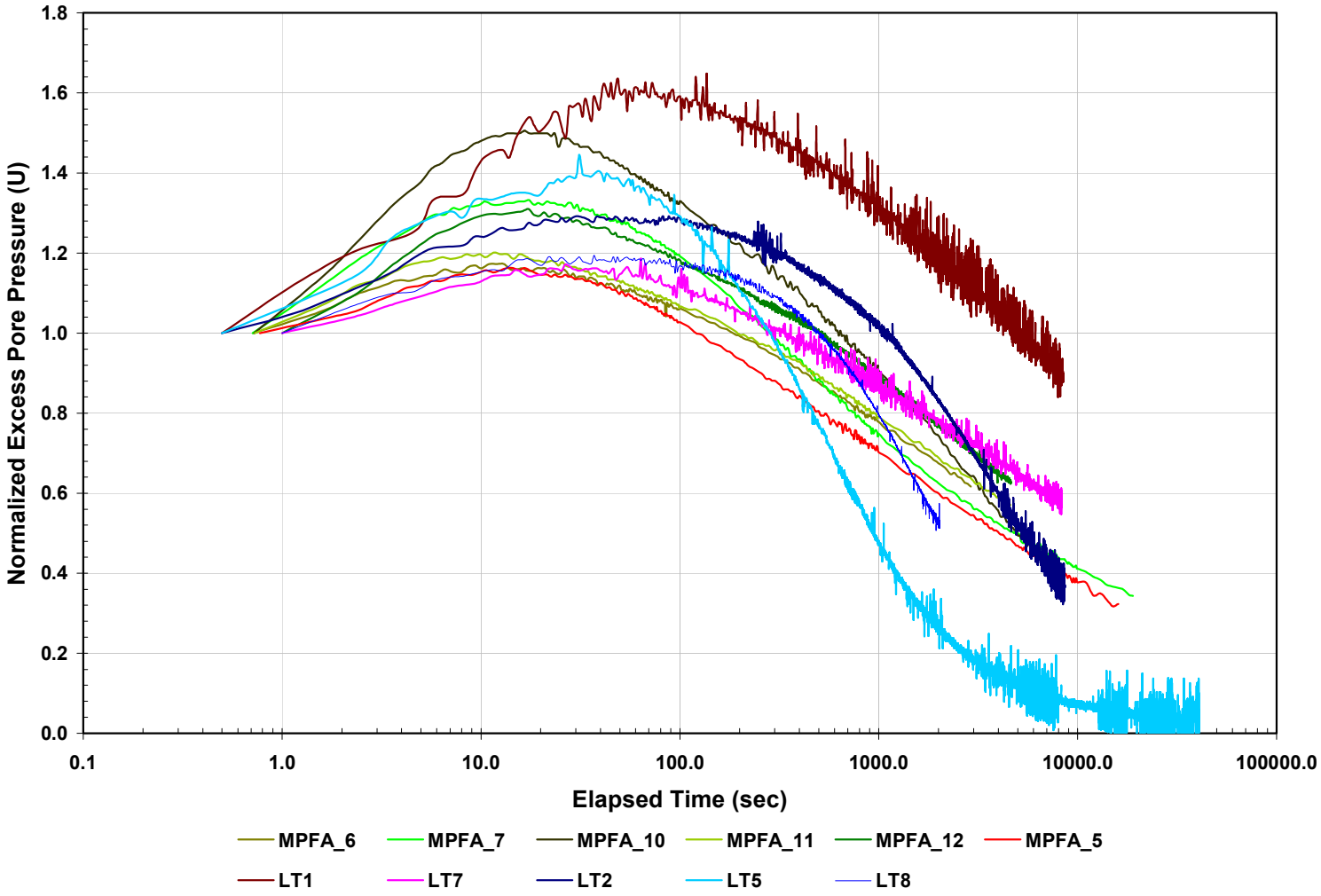

Figure 8-37. Overlay Plot of All u_{a0} Normalized Excess Pore Pressure Responses for the Conventional Dissipation Tests Conducted at BWDWA. Green, Red, and Blue Tinted Traces are from Tip Depths of 6.74 m, 7.5&7.74 m, and 10.0 m, Respectively.

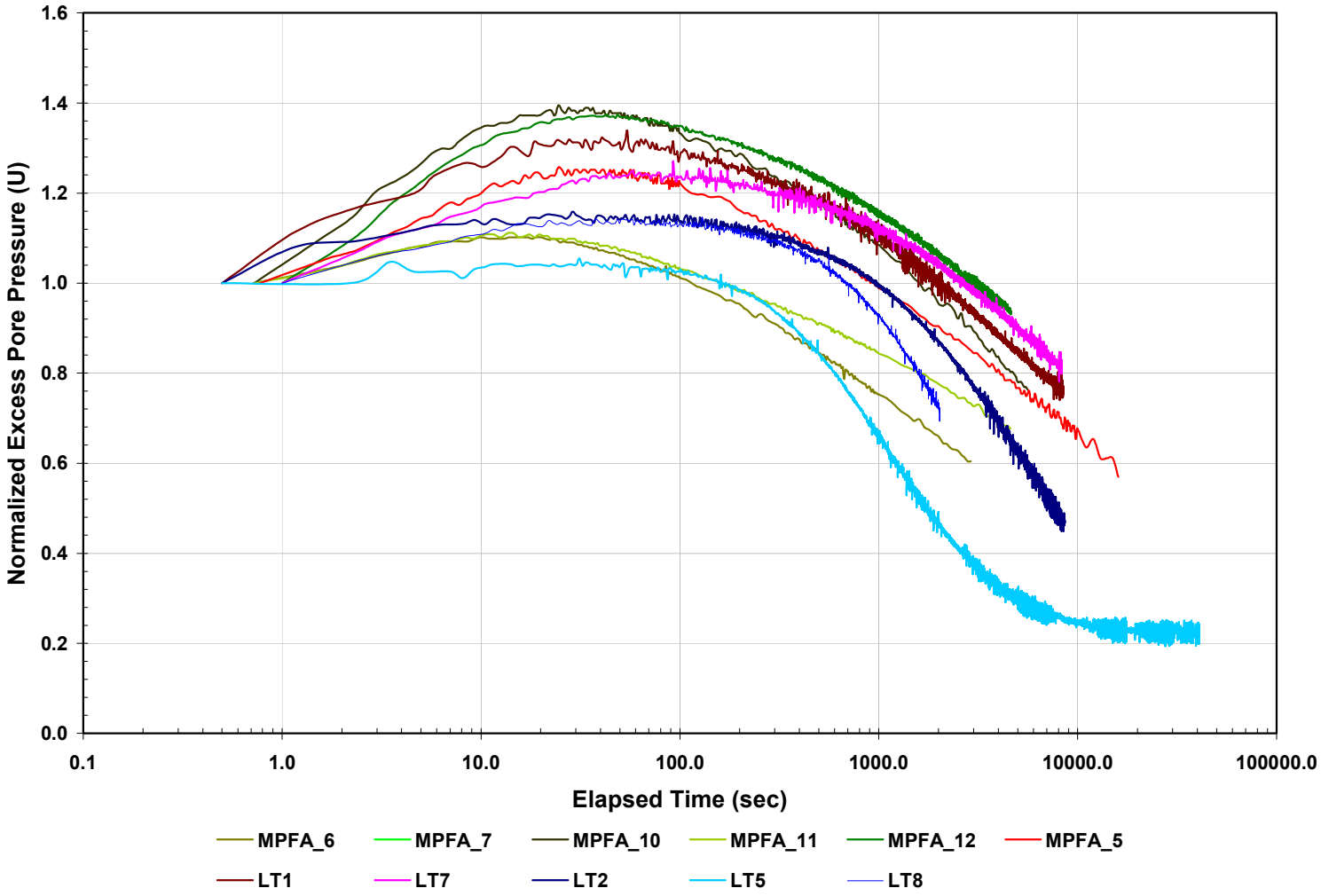

Figure 8-38. Overlay Plot of All u_{a1} Normalized Excess Pore Pressure Responses for the Conventional Dissipation Tests Conducted at BWDWA. Green, Red, and Blue Tinted Traces are from Tip Depths of 6.74 m, 7.5&7.74 m, and 10.0 m, Respectively.

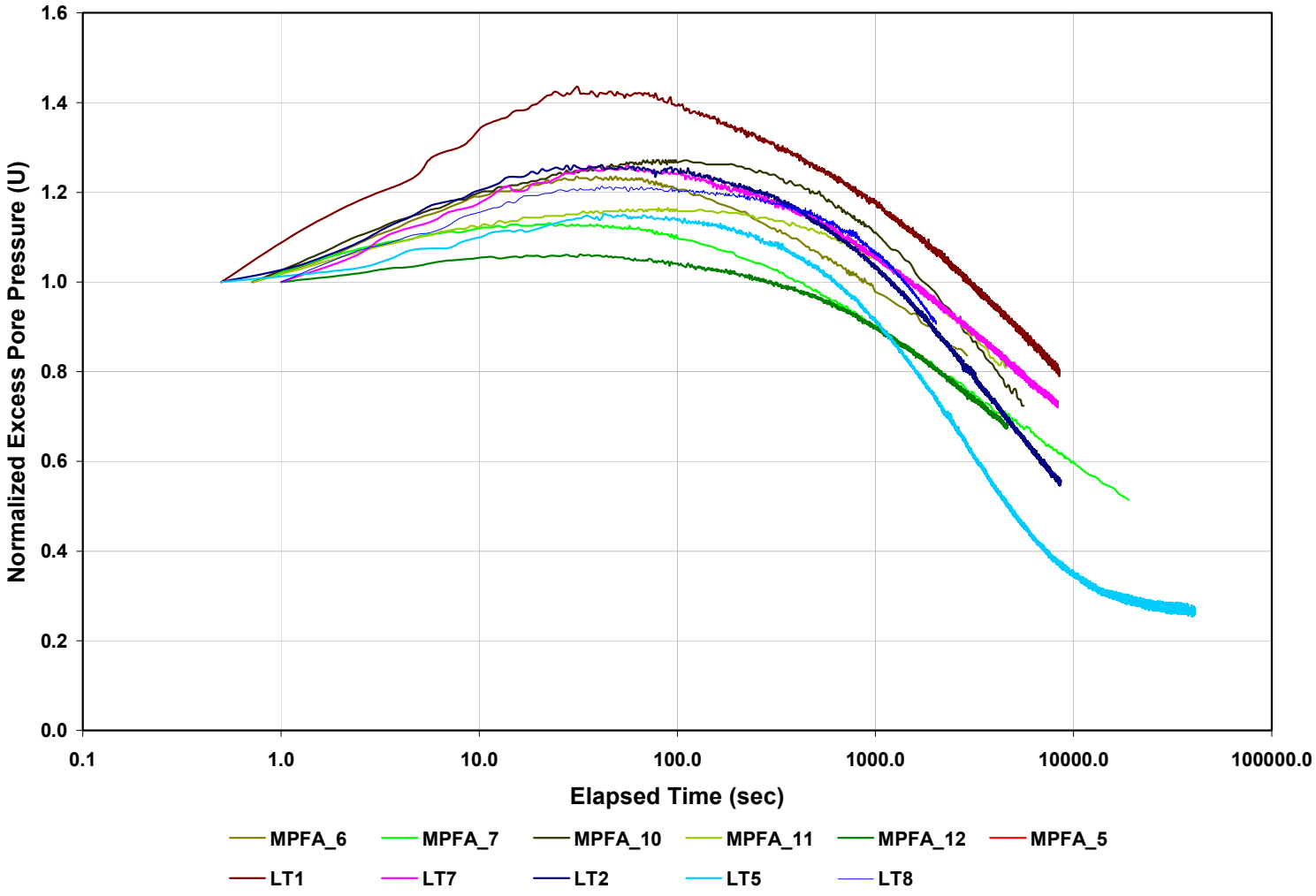

Figure 8-39. Overlay Plot of All u_{a2} Normalized Excess Pore Pressure Responses for the Conventional Dissipation Tests Conducted at BWDWA. Green, Red, and Blue Tinted Traces are from Tip Depths of 6.74 m, 7.5&7.74 m, and 10.0 m, Respectively.

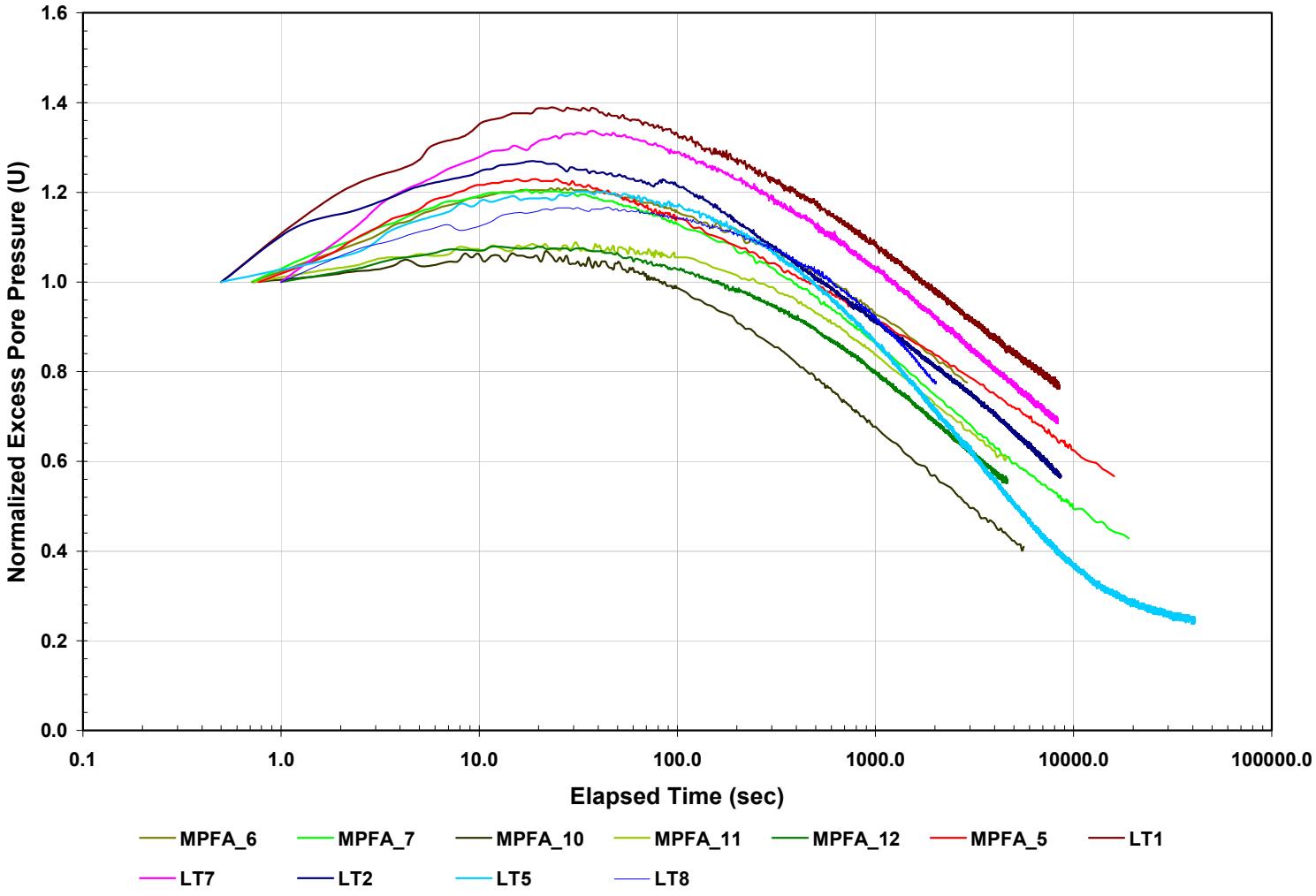

Figure 8-40. Overlay Plot of All u_{a3} Normalized Excess Pore Pressure Responses for the Conventional Dissipation Tests Conducted at BWDWA. Green, Red, and Blue Tinted Traces are from Tip Depths of 6.74 m, 7.5&7.74 m, and 10.0 m, Respectively.

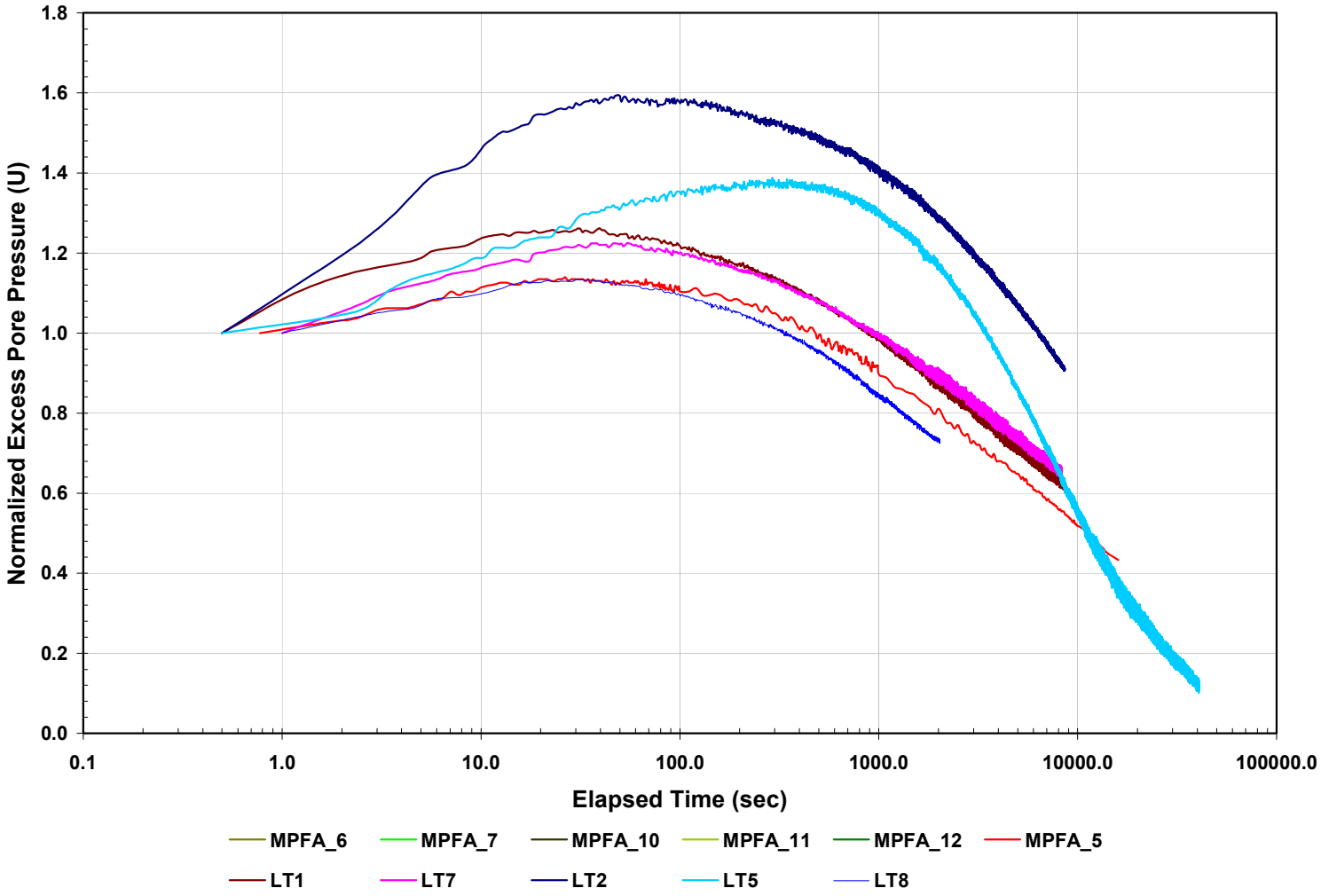

Figure 8-41. Overlay Plot of All u_{a4} Normalized Excess Pore Pressure Responses for the Conventional Dissipation Tests Conducted at BWDWA. Green, Red, and Blue Tinted Traces are from Tip Depths of 6.74 m, 7.5&7.74 m, and 10.0 m, Respectively.

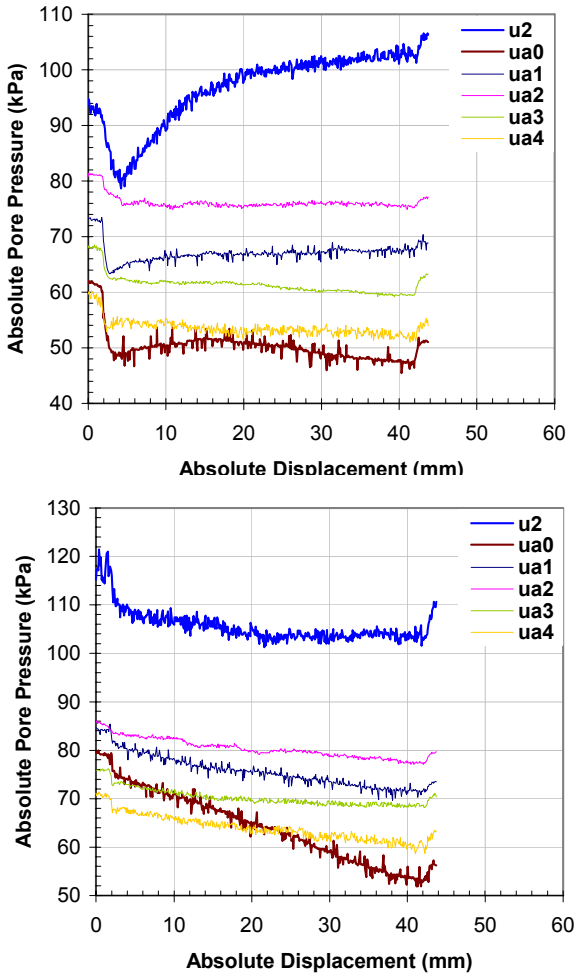

Figure 8-42. Absolute Pore Pressure Response of the CPTU-MPFA Piezo Sensors During the Load Tests Conducted at 5.0 m Tip Depth (LT3 and LT6)

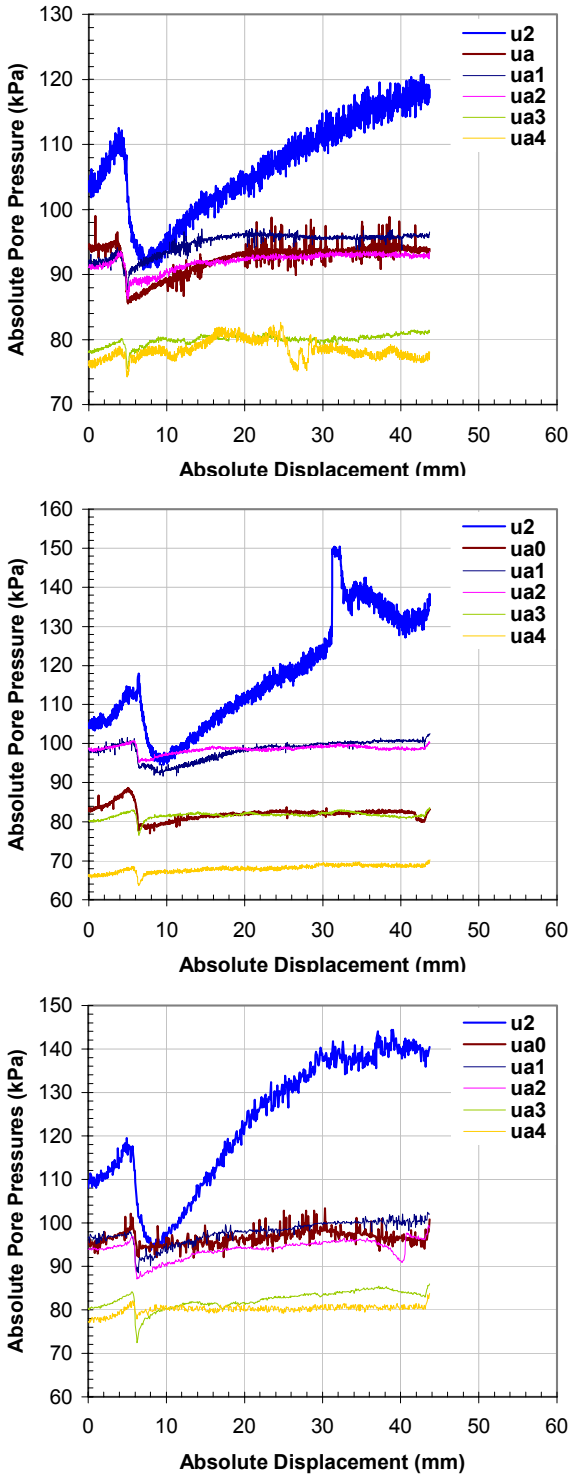

Figure 8-43. Absolute Pore Pressure Response of the CPTU-MPFA Piezo Sensors During the Load Tests Conducted at 7.5 m Tip Depth (LT1, LT4, and LT7)

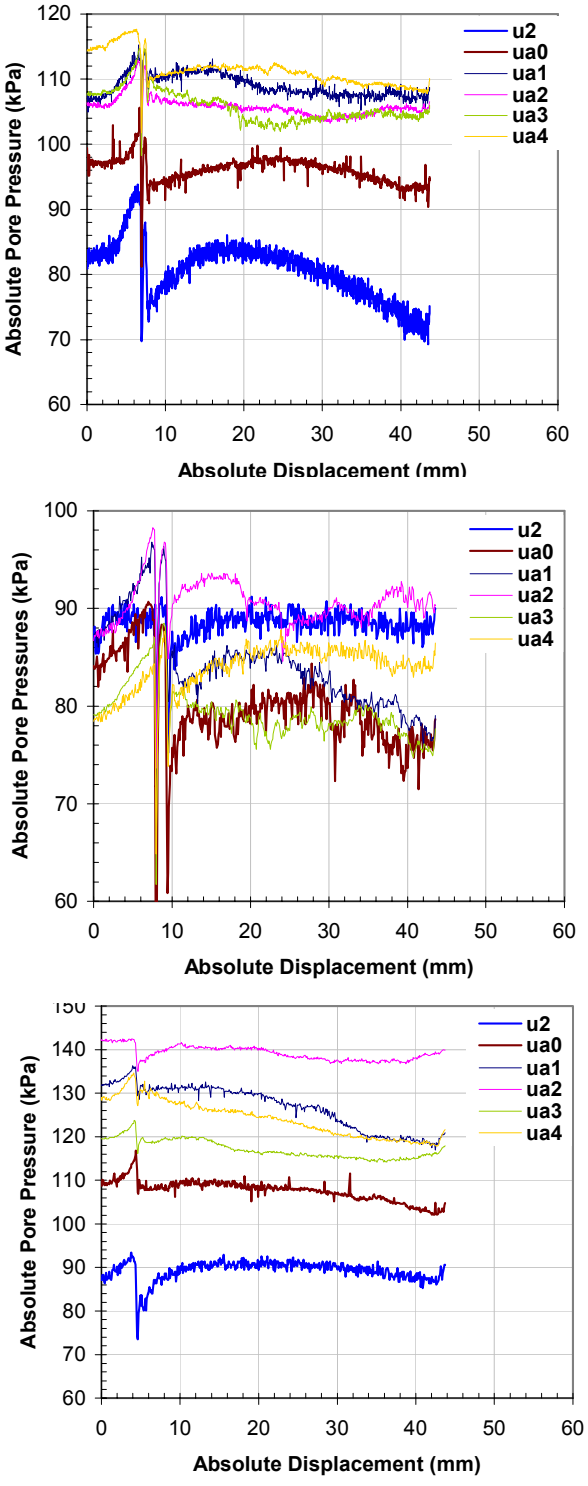

Figure 8-44. Absolute Pore Pressure Response of the CPTU-MPFA Piezo Sensors During the Load Tests Conducted at 10.0 m Tip Depth (LT2 , LT5, and LT8)

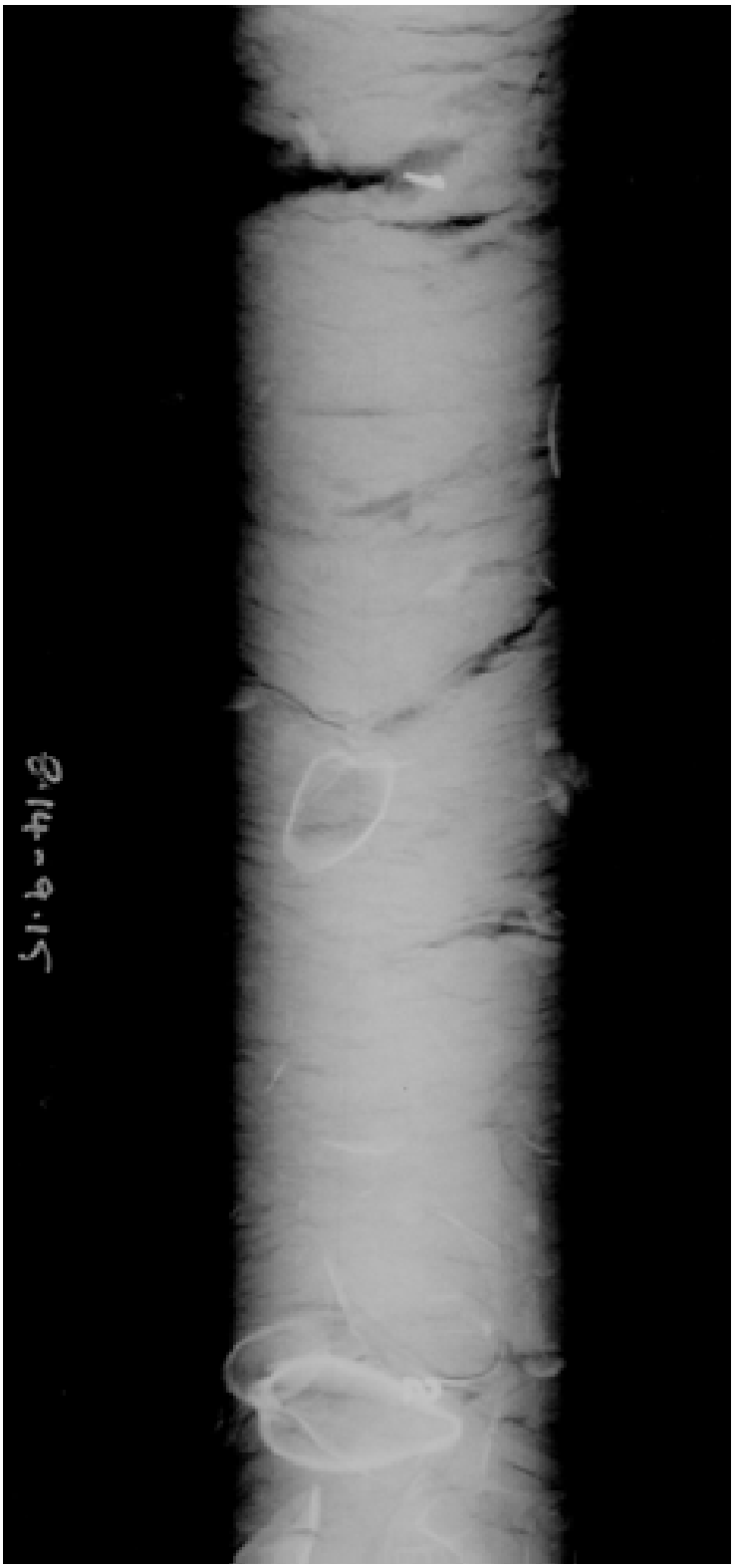

Figure 8-45. An X-ray Image of a 1-m Long Tube Sample from the BWDWA Site Showing the Inclusion of Large Shell Fragments (Levy et al., 2002)

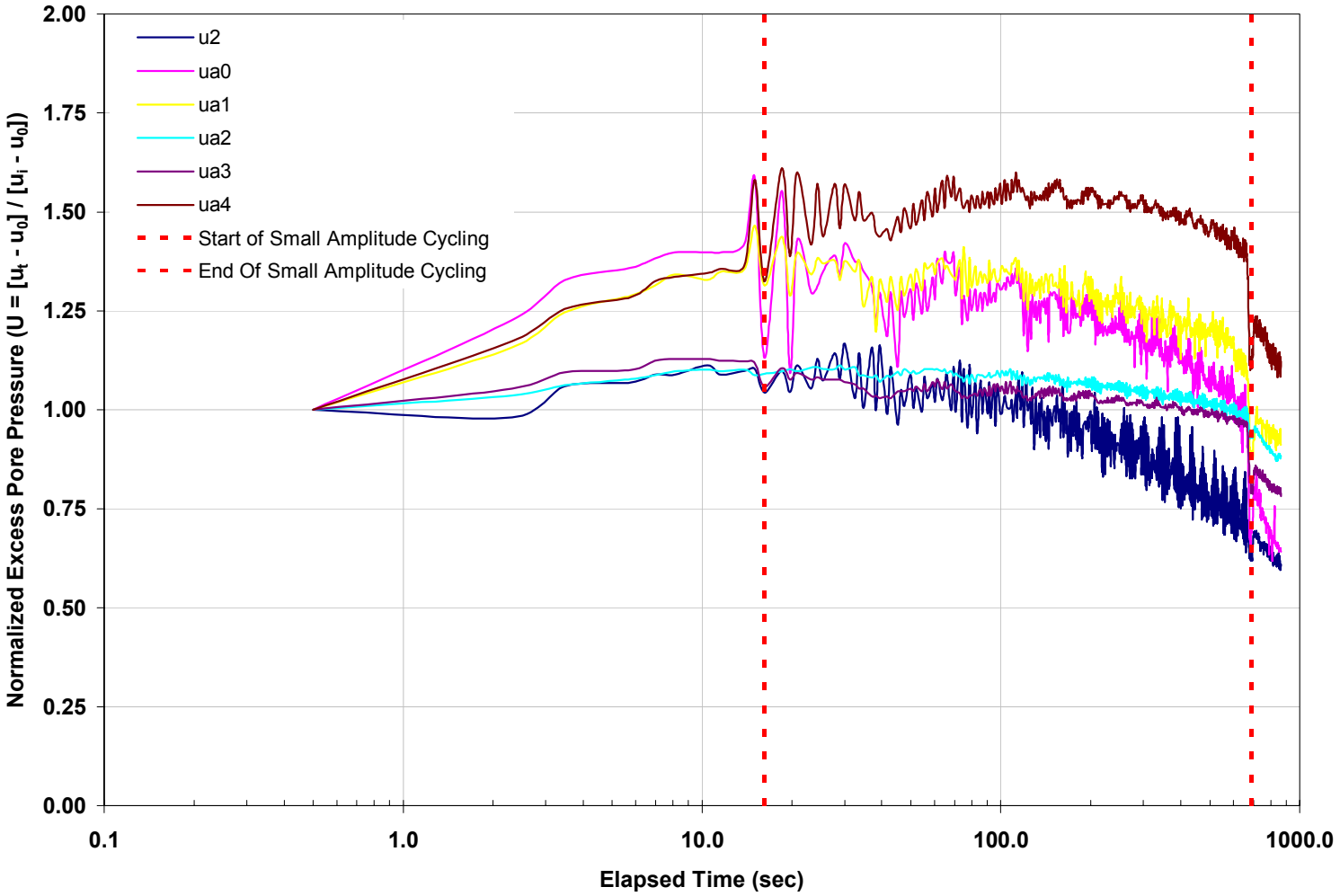

Figure 8-46. Plots of the Normalized Excess Pore Pressure Dissipation Responses for the CPTU-MPFA Sensors Before LT3 at a Tip Depth of 5.0 m at the BWDWA Site. Small Amplitude Cycling (200 $\pm$ 5 mm Cycles) was Performed Directly After Steady-State Penetration and Prior to the Load Test.

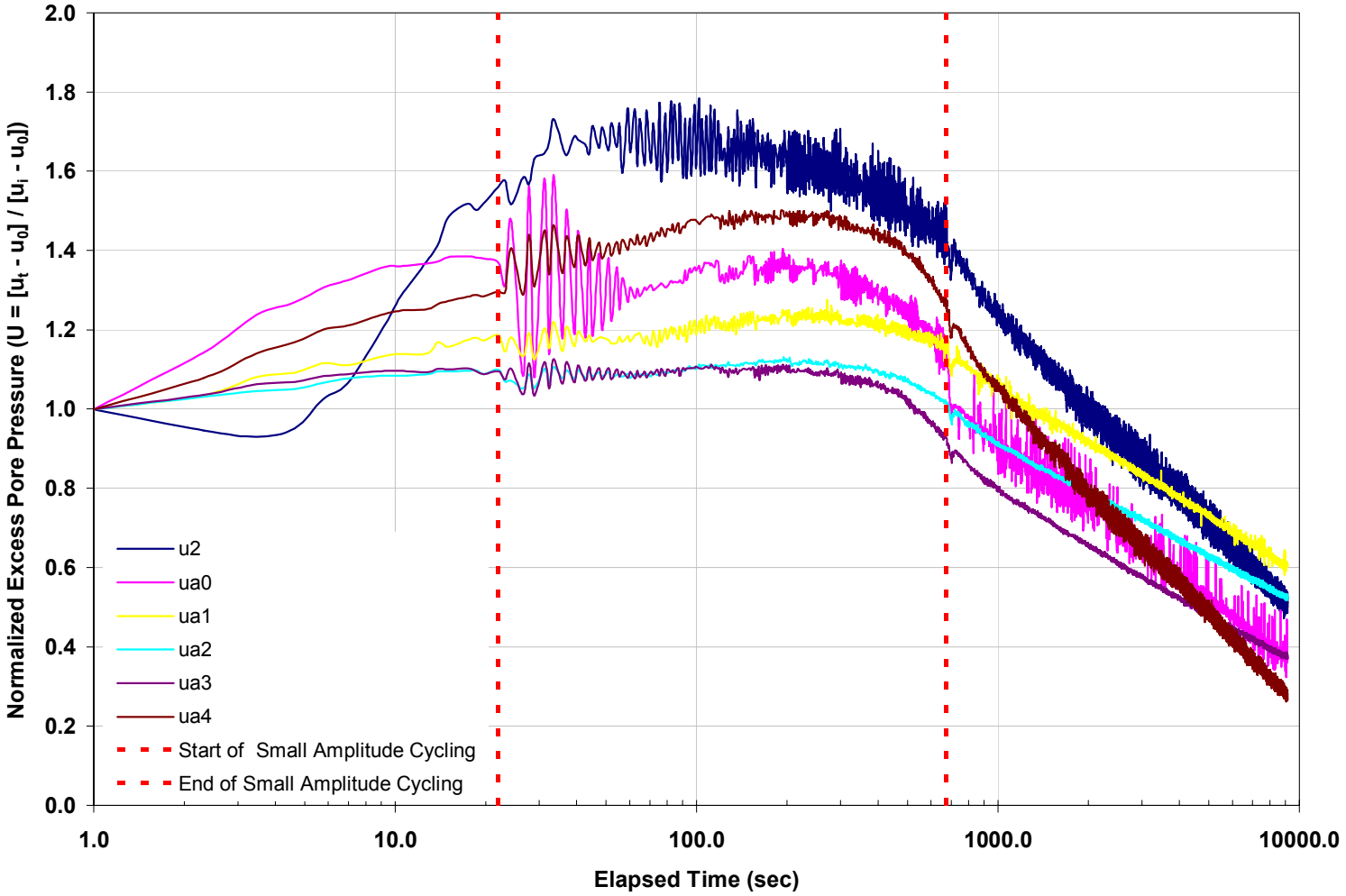

Figure 8-47. Plots of the Normalized Excess Pore Pressure Dissipation Responses for the CPTU-MPFA Sensors Before LT4 at a Tip Depth of 7.5 m at the BWDWA Site. Small Amplitude Cycling (200 $\pm$ 5 mm Cycles) was Performed Directly After Steady-State Penetration and Prior to the Load Test.

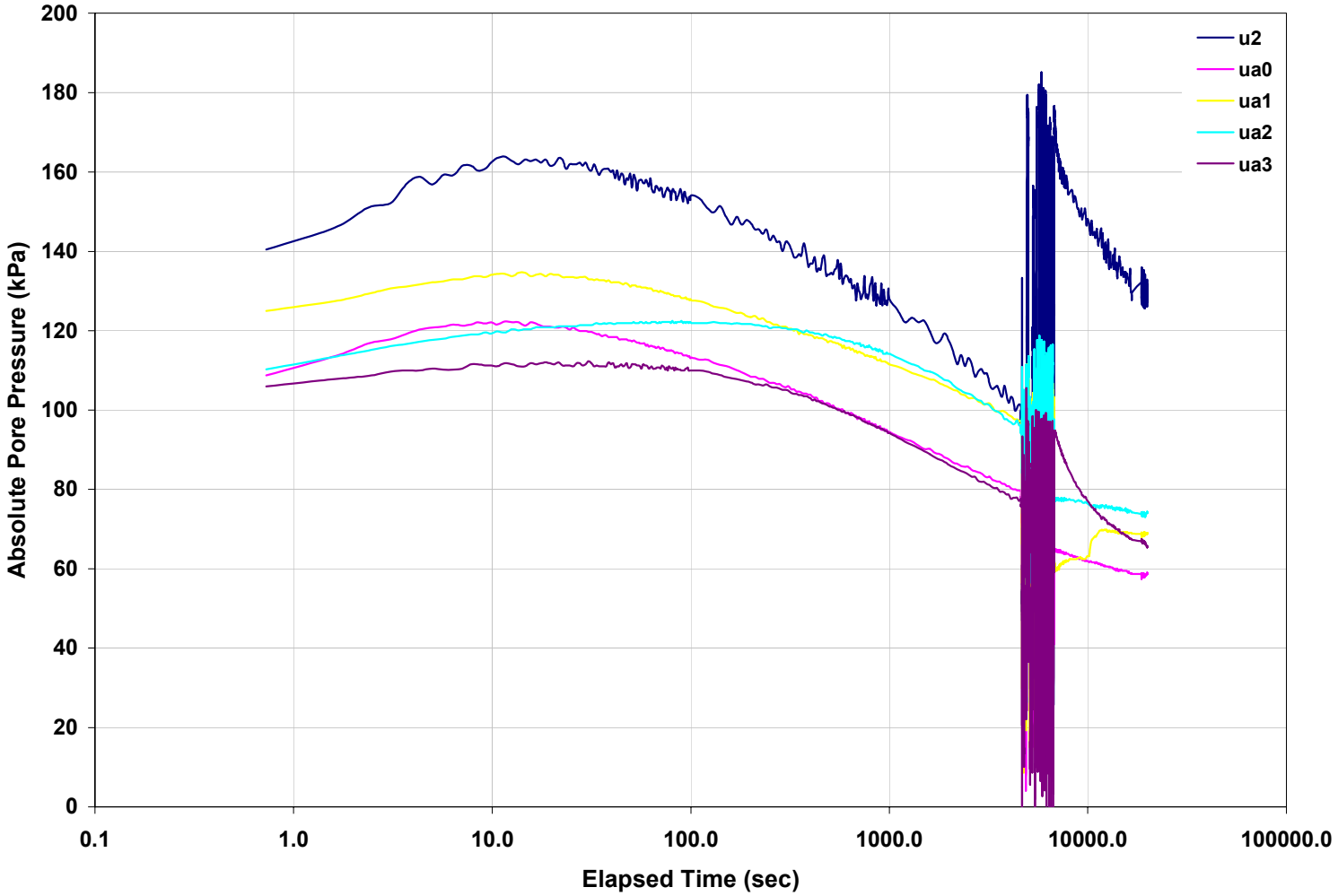

Figure 8-48. Plots of the Normalized Excess Pore Pressure Dissipation Responses for the CPTU-MPFA Sensors Before, During, and After Large Amplitude Cycling in MPFA_11 Conducted at the BWDWA Site.

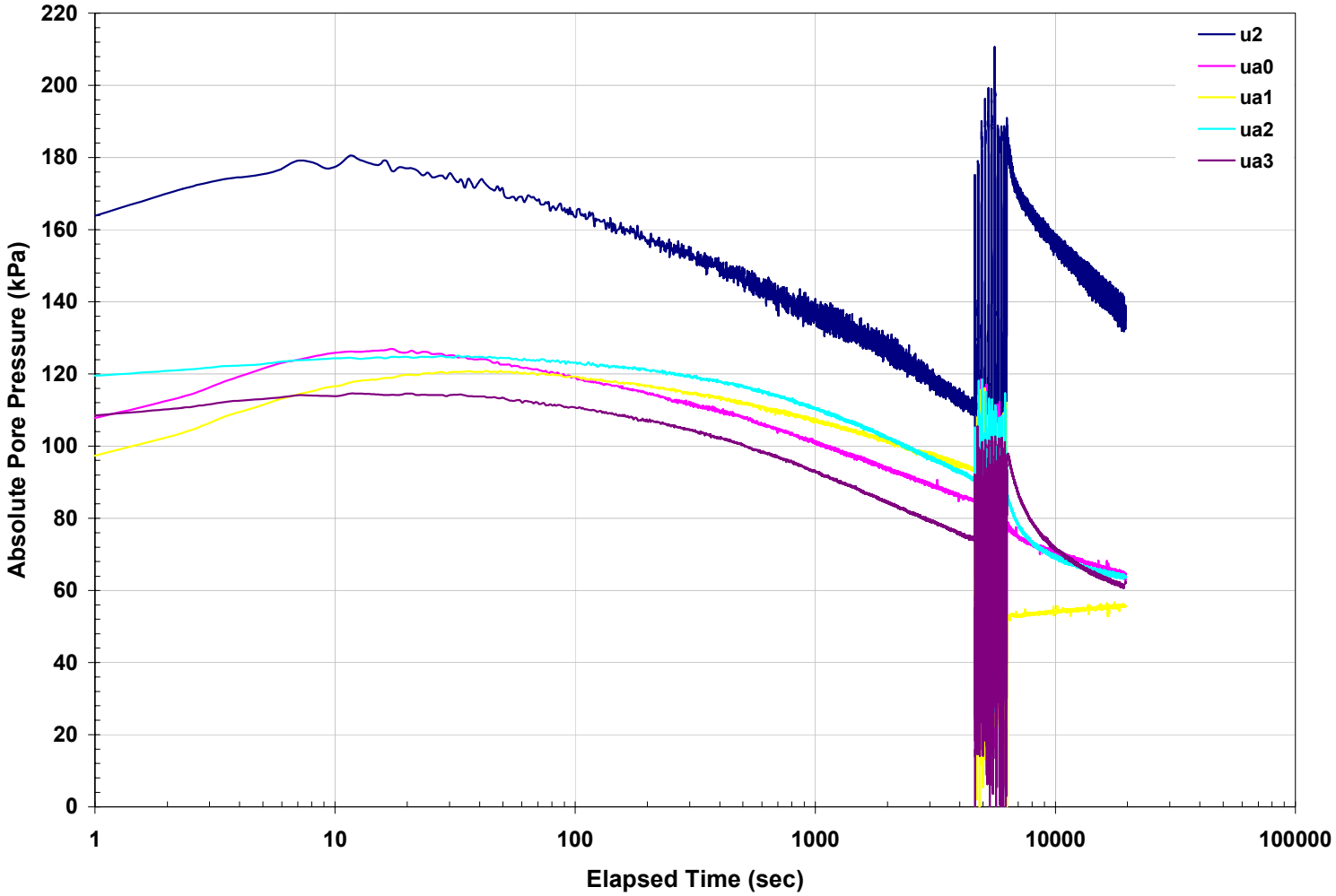

Figure 8-49. Plots of the Normalized Excess Pore Pressure Dissipation Responses for the CPTU-MPFA Sensors Before, During, and After Large Amplitude Cycling in MPFA_12 Conducted at the BWDWA Site.

Chapter IX
Summary of Conclusions

9.1 Introduction

This dissertation has presented results from studies focused on geotechnical interface behavior. The scope of the current studies covered three main topics: (1) laboratory investigations at the micromechanical level regarding fundamental interface mechanisms; (2) the design and development of a new device, the Multi Piezo Friction Attachment (MPFA), to allow for the characterization of geotechnical interface properties in situ within the context of an effective stress framework; and (3) analysis and discussion regarding the implementation of the newly developed MPFA device in situ. The conclusions determined from these investigations, and recommendations for future research, are summarized in this chapter.

9.2 Conclusions From Laboratory Interface Investigations

9.2.1 Shear Zone Evolution of Granular Soils in Contact with Conventional and Textured Friction Sleeves

A detailed proof of concept series of tests were performed to investigate the micromechanical response of a range of granular soils to shearing against conventional and textured friction sleeves. These tests were performed on homogeneous sand specimens containing thin layers of dyed sand in an axisymmetric interface shear apparatus. The post shear deformations of the soil were preserved by activating a powder phenolic resin, with the contrast between the dyed and natural sand layers allowing the quantification of shear zone evolution. Specimens were dissected to produce observation

planes, allowing photographs and subsequent quantitative analysis to be conducted. The following conclusions concerning the evolution and formation of granular shear zones adjacent to smooth and textured friction sleeves were observed:

- Interface shearing of coarse granular media against conventional smooth friction sleeves was shown to not induce a shear zone, and resulted in a pure sliding failure under the current test conditions.
- Interface shearing of a fine sand against conventional smooth friction sleeves was shown to induce only a minimal shear zone, and resulted in a combined failure mechanism consisting mostly of sliding deformation on the order of 98% under the current test conditions.
- The offset diamond texturing pattern currently used to add varying levels of surface roughness to friction sleeves has been experimentally verified to induce non-clogging shear across the range of sleeve roughnesses and granular soils tested.
- The results corroborate previous accounts of the independence of interface shear zone thickness and granular particle angularity.
- Interface R_{max} roughness has been shown to have a dominant effect on induced interface shear zone thickness as compared to the contacting particulate size and angularity. This is divergent from the behavior of internal shear zones, and results from the uniqueness of internal "virtual roughness" as compared to the non-uniqueness of interface roughness with respect to the contacting particulate properties.

- The employed offset texturing scheme served to produce shear zones of approximately uniform thickness for the range of particle sizes and angularities tested.
- The percentage of lateral shear deformation was shown to be largely dependent on particle angularity for roughnesses above a critical value. Rounded particles exhibited an upper limit of shear displacement with increased interface roughness, while more angular particles exhibited an approximately linear trend between shear deformation and interface roughness over the full range of tested roughnesses.
- The lateral deformation induced in the tested coarse sands was approximately uniform between and over top of the textured asperities, whereas the fine sand exhibited non-uniform lateral deformation as a result of the offset texturing pattern. It is believed, and has been noted in-situ, that the non-uniformity of the induced shear displacement will increase with decreasing particle size, but will remain non-clogging over the range of typically encountered soils.
- The induced shear was shown to be non-clogging across the range of typically encountered granular materials, and is believed to represent an optimal balance between induced shearing and sliding across the range of soils typically encountered in-situ.
- Sleeve textures of high R_{max} roughness using the current texturing scheme have been experimentally shown to induce interface shear zones equivalent to those reported for fully formed zones induced by continuous texture. The critical roughness required to induce full shear zones for the current intermittent texturing

scheme ($R_n \approx 1$) is increased by an order of magnitude over that typically required for continuous texturing ($R_n \approx 0.1$). The amount of R_n roughness necessary to fully engage the internal resistance of the contacting particulate ("$\delta = \phi$" condition) is believed to be dependent on the spacing and other characteristics of the texture.

- Induced shearing by intermittent textures constitutes a lower percentage of the failure mechanism as compared to failure against continuous textures. It is hypothesized that this disparity in lateral deformation does not preclude the full engagement of particulate resistance for intermittently textured surfaces producing shear zones of equivalent thickness.
- It is believed that sleeves using the current offset texturing scheme can investigate the complete range of typically encountered interface strengths, ranging from smooth surface sliding up to the full engagement of internal soil strength.

The results of the current parametric study served to validate the ability of the current sleeve texturing scheme to induce shearing within various contacting particulate media across a range of surface roughnesses. This study has served to not only validate the effectiveness of the current textured sleeves at investigating interface behavior in-situ, but has also further advanced the fundamental understanding of the micromechanical interface interactions necessary to fully understand the behavior of continuum surfaces placed in contact with granular soils.

9.2.2 Quantifying Hook and Loop Interaction in Textured Geomembrane-Geotextile Systems

Through a combination of multiple laboratory tests and optical observations, the interface behavior of textured geomembrane - NPNW geotextile systems was investigated. Direct interface shear and ASTM hook and loop testing was used to quantify differences in the behavior of the tested interfaces. All geomembrane material properties and dimensions, excluding the texturing processes, were maintained similar throughout the current study. As such, it can be concluded that the observed behavioral differences are attributed to the differences in the surface texturing of the tested geomembranes. A summary of the conclusions from the current study are presented as follows:

- The texture of coextruded geomembranes was characterized through optical microscopy as consisting of jagged macrotexture with high levels of micro and mesotexture present along the base substrate and bonded to the macrotextural features.
- The texture of structured geomembranes was characterized through optical microscopy as consisting of "smooth" rounded macrotexture with no bonded micro or mesotexture but significant micro and mesotexture present along the base substrate.
- Hook and loop interactions in textured geomembrane-geotextile systems were found to be strongly dependent on the level of micro and mesotexture bonded to the surface of the macrotextural features at all normal stresses, with hook and loop

interactions at higher normal stresses additionally dependent on the level of micro and mesotexture bonded along the base substrate.

- The frictional contributions to the shear response of the two systems were found to be controlled by discrete surficial interactions between surface filaments and textural features at low normal stresses, and dominated by the compression and interbedding of the geotextile between the macrotexture, resulting in more global continuum interactions at higher normal stresses.
- The geomembranes tested contained macrotexture of similar out of plane dimension and spacing, as well as comparable levels of base texture resulting in similar frictional and hook and loop contributions to the peak response within the range of operational stresses tested (50 – 312 kPa). The direct interface shear results within this normal stress range correspond to conventional Mohr-Coulomb relationships of $\tau_{s(peak)}$ = 9.5 kPa + tan(30.4°) and $\tau_{s(peak)}$ = tan(35.1°) for the tested coextruded and structured systems, respectively.
- The peak response of the coextruded system was consistently stronger than the structured system within the low normal stress range (< 50 kPa). The structured texture exhibited an almost purely frictional peak response supplemented by insignificant hook and loop interactions at low stresses due to the absence of microtexture away from the base substrate. In contrast, the jagged nature and significant microtexture present on the macrotexture of the coextruded geomembrane provided a counterface conducive to large strength contributions from hook and loop interaction in addition to the comparable frictional response resulting in a highly non-linear peak shear response at low normal stresses.

- ASTM standard hook and loop shear strength tests were used to isolate the low normal stress hook and loop interaction mechanisms. The hook and loop tests confirmed the low normal stress behavior seen in the direct interface shear testing and allowed the individual contributions to the hook and loop interaction to be quantified. The fabric of NPNW geotextiles was found to be well suited to hook and loop interaction when paired with the engineered hook structure of a commercial hook and loop product. The coextruded geomembrane showed limited response during ASTM hook and loop testing when paired with both the NPNW geotextile and commercial loops, while the structured geomembranes provided no measurable response in combination with all tested loop materials.
- The pseudo-residual shear behaviors of the tested geomembranes were similar, and primarily dependent on frictional interactions between the NPNW geotextile and the macrotextural features of both geomembranes. Additionally, the pseudo-residual shear strengths were found to be strongly dependant on the properties and wear mechanisms of the NPNW geotextile.
- Microtexture, and to a lesser extent mesotexture, on both geomembrane types was found to be susceptible to wear of varying degrees as a result of interface shear at all tested normal stress levels and was therefore not a significant factor in post-peak interaction mechanisms.
- Through visual inspection of the geomembranes pre- and post-shear, the macrotextural features of the coextruded geomembrane were found to be more susceptible to wear and degradation processes from interface shear, as compared

to the macrotexture of the structured geomembrane, resulting in slightly lower peak and residual strengths at the operational normal stresses tested.

The current results suggest that hook and loop interaction plays a significant role in the interface shear behavior of textured geomembrane - NPNW geotextile systems across a wide range of normal stress levels. The results and discussions presented herein regarding hook and loop interaction within textured geomembrane-geotextile systems as a result of different geomembrane texturing techniques should allow contractors and design engineers to make more informed decisions regarding the selection and specification of textured geomembranes in practice.

9.3 The Development of a Multi Piezo Friction Attachment

DeJong and Frost (Frost and DeJong, 2001; DeJong and Frost, 2002; Frost and DeJong, 2005) developed a Multi Friction Attachment (MFA) that provides four independent measures of interface friction (f_{a1}, f_{a2}, f_{a3}, and f_{a4}), in addition to the ability to simultaneously collect conventional CPTU measurements (q_t, f_s, and u_2). The MFA device was developed to provide a means to directly obtain multiple measures of in situ geotechnical interface behavior for a range of continuum surface conditions. The performance of the MFA during the introductory field tests conducted by DeJong (2001) demonstrated that the full relationship between interface strength and surface roughness can be determined in situ within a single MFA sounding. Additionally, during these initial investigations the performance and operation of the MFA device met or exceeded initial expectations.

However, two main deficiencies were determined to exist in the original MFA design: (1) the inability to monitor pore fluid conditions at the multi sleeve locations, and (2) the close spacing of the MFA sleeve sensors resulted in sensor interference for sleeves placed adjacent to textured sleeves in certain configurations. As a result, it was determined that while the MFA device provides an extremely useful addition to the geotechnical engineering community, the development of a second device with increased capabilities could diminish the shortcomings of the original MFA device. The design of the MPFA device allows for a number of device advantages over other available in situ test devices:

- The ability to distinguish between drained, undrained, and partially drained conditions at the various MPFA sensor locations.
- The ability to consider the measured friction sleeve data within the robust framework of effective stress analysis.
- The ability to evaluate flow and consolidation characteristics along the length of the MPFA unit both laterally and vertically through the use of multiple piezo sensors placed in series.
- The ability to better assess hydrostatic ground water conditions due to the placement of the sensors within the stable shear zone along the penetrometer shaft.
- The ability to provide additional data towards improved stratigraphy profiling.
- The ability to further understand and directly measure the pore pressure distribution surrounding penetrometers in a range of in situ conditions.

- The ability to determine the magnitude of induced pore pressures due to the introduction of textured friction sleeves of various roughness.
- The elimination of foreshadowing interference between adjacent friction sensors.

The Multi Piezo Friction Attachment (MPFA) device was developed during the current work through the collaboration of personnel from Georgia Tech and the CPT manufacturer, Vertek. Increasing the spacing between friction sensors and adding multiple piezo elements along the shaft placed in series provide the MPFA unit with increased abilities to not only better determine in situ interface behavior, but to also obtain more complete assessments of soil and groundwater conditions in conjunction with or independently of traditional CPTU measurements.

9.4 In Situ Interface Responses Measured with the MFA and MPFA Devices

To date 171 soundings have been conducted with the MFA and MPFA devices. A portion (39) of those soundings were conducted by DeJong (2001), with another 13 soundings conducted as part of the study by Schneider (in progress). The remainder of the investigations are presented in the current work, and results from the full range of investigations provide a large data set of in situ interface measurements. The interface results from the MFA and MPFA investigations are separated by behavior into the following topics: (1) fundamental observations regarding friction sleeve measurements, including: conventional CPT (f_s), smooth attachment sleeve response (f_a), and textured attachment sleeve response (f_a); (2) characteristic interface behaviors observed across the range of tested geologic conditions and implemented test procedures; (3) and

characteristic pore pressure behaviors observed across the range of geologic conditions and implemented test procedures.

9.4.1 Fundamental Mechanics of Smooth and Textured Friction Sleeve Response

Investigations in the current work have supplemented the initial work of DeJong (2001) regarding the fundamental mechanics of smooth and textured friction sleeve behaviors. The current work consisted of investigations into: the effect of friction sleeve position on sensor response, continued assessment of the extent of changes in local stress state induced by textured sleeve penetration, the fundamental understanding of textured sleeve shear mechanisms, and the use of (f_a) sleeve measurements to provide a quantitative assessment of soil structure. The relevant conclusions formulated during the current work in regard to these topics are:

- Conventional penetration rate friction sleeve response, for sleeves of conventional roughness (R_a = 0.50 μm, nominally smooth), was observed to be independent of sensor position when offset more than 200 mm behind the tip, corresponding to a normalized *h/r* offset of 4.6 for the 15 cm^2 cone used in the current study. This behavior is different than that observed for driven pile foundations, where stress cycling in the form of repeated loadings and relaxations results in a large influence of *h/r* on interface response.
- CPT f_s measurements were consistently observed to be higher than comparable roughness MFA/MPFA f_a measurements in sandy geologies, with the magnitude of the observed differences varying as a function of site conditions. Future work

hopes to quantify the observed increases, with initial speculation relating the observed increase in f_s to the increased lateral stress conditions surrounding the tip.

- The forward zone of influence created from textured sleeve penetration ("foreshadowing") was determined to be limited to sensor offsets smaller than 150 mm for all sleeve textures used in the current study ($\leq$ H2.00).
- The backshadowing influence of textured sleeves on the response of smooth sleeves was observed to be constant for sensors spacings up to 500 mm.
- The backshadowing influence of textured sleeves on sleeves of similar or greater texture was observed to be negligible for both the MFA and MPFA sensor spacing configurations.
- The fore- and backshadowing behaviors observed for textured sleeve shearing have also been observed to affect smooth sleeve response for minor changes in penetrometer diameter present forward or directly aft of penetrometer friction sleeves. As such, it has been shown that small changes in penetrometer module diameter can significantly affect friction sleeve responses and concluded that penetrometer module diameters should be monitored closely for consistency.
- Textured sleeve shearing has been shown to be controlled by a combination of two primary mechanisms: interface sliding and shearing along the sleeve length, and a punching shear or bearing capacity type failure located at the onset of sleeve texturing (termed the annular penetration force or APF herein).
- CPTU-MFA/MFPA results have shown that the magnitude of APF can be estimated at each measurement depth by directly scaling the corresponding CPT (q_t) tip response to the appropriate annular area of sleeve texture.

- It has been shown that isolated interface shearing response can be determined by subtracting the calculated APF component from the total measured textured sleeve response.
- The isolated interface component of measured textured sleeve response is representative of conditions experienced in situ and in the laboratory for continuously textured surfaces, and as such is the quantity applicable to interface design.

9.4.2 Interface Behaviors Observed In Situ with the MFA and MPFA Devices

9.4.2.1 General Conclusions Regarding the Observed In Situ Interface Behaviors

In summary, the observed measurements of in situ interface response showed the following:

- Good agreement with fundamental interface behavior known to exist for laboratory samples of similar materials.
- The critical roughness required to achieve full internal soil shearing was seen to vary as a function of soil type.
- The variation in isolated interface response with increasing roughness was observed to decrease for strata exhibiting fine grained behaviors.
- The characteristic bilinear relationship between interface strength and surface roughness observed in laboratory investigations, has been observed in situ across a range of soil types.

- The contribution of interface (i.e. the sliding and shearing components) response to the total measured sleeve stress can be effectively isolated from the annular penetration component inherent to textured sleeve measurements for all tested geologic conditions.
- Isolated interface response can be effectively measured in situ across a wide range of surface roughness values and soil conditions.
- The range of sleeve textures currently implemented appears to provide a sufficient coverage across both the range of surface properties utilized in practice and the range of soils typically encountered in situ.
- The position of MFA and MPFA friction sleeves appear to be within a stable shearing regime across all tested soil types for standard steady-state CPT penetration.
- Observed interface responses for uncemented calcareous geologies were observed to be lower than interface responses of uncemented silica geologies, in agreement with the typical responses observed in pile foundations.
- The interface behaviors of structured or cemented materials measured in situ appear to be controlled by additional internal and interface interaction mechanisms, which appear to affect both the magnitude of measured shear resistance and the extent of the influence zone created by the penetrometer.

These results show significant promise in the ability of the MFA and MPFA devices to measure geotechnical interface response in situ across a range of geologic conditions.

Future work will attempt to provide a larger database of MFA and MPFA in situ interface measurements in order to verify and substantiate the observed behaviors.

9.4.2.2 The Use of Textured Friction Sleeves to Quantify Soil Structure

The concept of analyzing multiple textured friction sleeve measurements within a single sounding to allow for the calculation of disturbed end bearing and side friction traces has been presented. A summary of the observations regarding this concept are listed below:

- The APF component of textured friction sleeve shearing has been shown to allow for the calculation of q_t and f_s estimates based solely on multi friction measurements.
- Within most of the soil strata tested, the results of the MF based tip and sleeve calculations produced values on the order of the measured CPT q_t and f_s responses.
- The ability to estimate CPT q_t and f_s values could lead to the implementation of the multi friction devices in stratigraphies traditionally problematic to traditional CPT devices.
- A number of the conventional penetration testing limitations associated with traditional CPT measurements: sensor overload, verticality, and wear in abrasive soils are accentuated by the placement of the CPT sensors at the front of the penetration zone, where abrasion and wear on devices is the highest, and the stress state is the most variable. The possibility of using a "dummy" tip with improved structural integrity ahead of devices like the MFA and MPFA may

provide a way to test certain site conditions previously too harsh for conventional CPT use.

- The use of non CPT tip configurations ahead of the MFA/MPFA devices could be further extended for use in stratigraphies with included impenetrable layers and for angled or horizontal pushes using modern drilling technologies by trailing a multi friction attachment behind a drill head.
- Within the limited tested strata that showed inherent soil structure, the MF calculated end bearing responses showed an increase over the respective q_t measurements within that depth range.

Future testing is planned at additional sites with known structured strata, which will hopefully determine if the presented framework is a viable method for identifying and possibly quantifying the level of structure or sensitivity within tested soils.

9.4.2.3 MFA/MPFA Soil Classification

A parameter has been proposed using the available MFA and MPFA data in an attempt to aid in the classification and identification of soil type and characteristic behaviors. The formulation and benefits of this parameter, termed the Multi Friction Classification Parameter (*MFCP*), are summarized herein:

- The MFCP is fundamentally based on the concept that the differential magnitude between smooth and moderately textured interface response provides a good indication of soil behavior and type.

- The MFCP is mathematically formulated similar to other classification parameters, in that it is dimensionless and is normalized with the total overburden stress to reduce the affect of measurement depth on the parameter response.
- An adjustment factor is applied within the MFCP formula such that the response within typical silica sand geologies was observed to be equivalent to the conventional normalized friction parameter (F_R).
- The MFCP effectively varies over four orders of magnitude for the wide range of soil types tested to date, while still exhibiting clustering of response within individual soil layers similar to other normalized CPT parameters.
- The increased variation in the MFCP across four orders of magnitude, as compared to the two orders of magnitude variation representative of the F_R parameter, leads to more clearly defined changes in response for a number of the soil conditions tested.

It is duly noted that the robust formulation of any in situ based soil classification parameter or system requires a large database of data. While the current data does cover a reasonable range of soil behaviors, the author readily notes the preliminary nature of the proposed parameter and all conclusions made with regard to the response of the parameter.

9.4.3 MFA and MPFA Response During Non Standard Investigation Procedures

Over the course of the current study, several procedures supplemental to conventional CPT penetration procedures were investigated to determine the capability of providing additional insight into soil characterization. The non standard procedures

investigated in the current study, included: inclined penetration, small and large amplitude cyclic response, variable rates of penetration, model pile load testing, and the measurement of penetrometer extraction response. A summary of the conclusions gained from these non standard investigations is presented herein.

9.4.3.1 Inclined Penetration

The effect of inclined penetration was investigated in the current study by conducting CPTU-MFA soundings at 45° and 67.5° to the ground surface, with 90° indicating vertical response. Unfortunately, the results of the 67.5° sounding were affected by a disconnect within the internal wiring of the MFA device and did not provide a usable data set for comparison. The results of comparing the 45° (inclined) sounding to two equivalently configured 90° (vertical) CPTU-MFA penetrations at the sand site in South Royalton, Vermont are summarized below:

- The tip response was observed to be minimally affected by penetration angle within the tested loose to medium sand.
- The CPTU f_s response exhibited significant variation between the inclined and vertical penetrations, with the 45° penetrations showing an increase for the upper (1-5m) and lower (7-8m) sand layers ranging from 13 to 56%.
- The variations in the smooth attachment sleeve configured in position f_{a1} showed only slight variation (~10%) in response for the 1-5m sand layer, with a larger increase (~21-24%) noted for the 7-8m sand layer.
- The H0.25 textured sleeve configured in position f_{a2}, exhibited a consistent increase in response for the inclined penetration ranging from 21 to 34% over

both selected sand stratigraphies. For comparison the lateral variability of this response between the vertical soundings showed a maximum deviation of 11%.

- The response of the sleeves in positions f_{a3} (SM) and f_{a4} (H1.00) exhibited only slight variations between the inclined and vertical soundings, indicating that the influence of both sand density and state of stress may diminish with distance from the tip. This finding fits into the framework of critical state soil mechanics, as the large deformations occurring before the soil strata interact with the f_{a3} and f_{a4} sensors should allow for the stabilization of the shear zone and surrounding stress conditions.

Future testing is planned to expand the data set and to hopefully better understand the mechanisms controlling penetrations at push angles ranging from vertical to horizontal.

9.4.3.2 Small and Large Amplitude Cyclic Investigations

Both small (± 5 mm strokes) and large (± 1 m strokes) amplitude cyclic investigations were performed with the CPTU-MPFA during the current study. These investigations were aimed at providing a framework to evaluate the cyclic response of soils and pile foundations to large amplitude cycling (representative of installation conditions), and to small amplitude cycling (representative of wave, wind, earthquake, industrial, or other applicable in service cyclic loading conditions). Both small and large amplitude investigations were performed at the Burswood soft clay test site in Perth, Western Australia; with only large amplitude cyclic investigations performed at the Ledge Point calcareous sand site. The results of these investigations are summarized as follows:

- The results of cyclic piezocone tests performed with the CPTU-MPFA device have illustrated the significance of cyclic interface degradation at soft clay and calcareous sand sites.
- The cyclic degradation of CPTU tip response due to large amplitude cycling was observed to be on the order of 60 to 80% for the soft clay site, and was not quantified at the calcareous sand site due to gapping and collapse behavior.
- The f_a shaft friction response was seen to degrade to 30% in the soft clay after one full cycle, further degrading to 50% of the virgin response after ten full cycles.
- The f_a shaft friction response was seen to degrade to between 60 and 80% of the virgin response after one full cycle at the calcareous sand site, with further degradations to values from only 13 and 6% of the virgin response after ten full cycles across the range of textured sleeves tested.
- The average shaft pore pressure responses due to large scale cycling exhibited similar trends during insertion and extraction for sensors adjacent to smooth sleeves.
- The shaft pore pressure response adjacent to textured sleeves during large amplitude cycling exhibited an offset between insertion and extraction responses due to the generation of positive pore pressures resulting from the punching shear surrounding the textured asperities.
- The ratio between tension and compression q_t behaviors for the large and small amplitude cycles were observed to be consistent, and on the order of 50%.
- The degradation of q_t with small amplitude cycling was observed to be on the order of 30% of the initial response for the tested soft clay after cumulative strain

of $\pm$ 1 m. The equivalent large amplitude cyclic degradation after an equivalent level of cumulative strain was on the same order, at 35% of the initial values.

- The average response of the shaft f_a sensors were seen to be minimally affected by small amplitude cycling, with the discrete values of tensile and compression behavior observed to be on the same absolute order, but of opposite sign.
- The shaft pore pressures were seen to be variably sensitive to small amplitude cycling, with the variations in response believed to represent variations in the sensitivity of the local strata to cyclic excitation. However, the variations in shaft pore pressure response during small amplitude cycling were observed to converge to a stable behavior after 5 to 15 cycles.
- The addition of cyclic loading procedures to conventional penetration soundings requires little modification to currently available in situ testing equipment, with cyclic testing previously shown to be successful in even the harsh testing environments found offshore (e.g., Peuchen et al., 2005).

Cyclic MPFA or MFA measurements show promise as a method for identifying soils with the potential for significant interface contraction and a resulting loss of friction during cyclic loading. The main design applications are related to pile design, drivability studies, and determining the effects of various installation sequences on soil degradation. The MPFA device is advantageous for cyclic investigations because it contains sensors along a range of distances behind the tip allowing not only for h/r effects to be investigated, but for a wide range of cyclic amplitudes from 0 to 1 m to be investigated without the influence of gapping on all sensors. The optimum cyclic investigation

procedures to use for various soil conditions and design considerations are not well known to date. At this stage in the implementation of cyclic penetration investigations, it is prudent to consider a range of test conditions specific to the goal of each investigation, as differences in cyclic response as a function of test procedures may be observed for various stratigraphies, warranting additional investigations to optimize cyclic penetration procedures and interpretation on a site by site basis.

9.4.3.2 Variable Rate Penetrations

A variable rate penetration investigation was performed with the CPTU-MFA device at the Burswood clay site between tip depths of 6.0 and 7.0 m. The results of that investigation are summarized herein:

- The behavior of the MFA and CPTU friction sleeves, for textures ranging from SM to H2.00, all exhibited similar behavior over penetration rates ranging from 20 to 1 mm/s within the Burswood soft clay stratigraphy, indicating the existence of fully undrained conditions at all sensor locations for these penetration rates.
- The q_t and f_s responses exhibit similar responses over the tested penetration rates, with decreasing penetration rate showing initial decreases due to the diminishing influence of viscous effects. The q_t and f_s behaviors began to increase again for penetration rates below 0.4 mm/s due to the influence of partial consolidation.
- The MFA friction sensors exhibited increased response with decreasing velocity for all rates lower than 1 mm/s, with the observed behaviors believed to be primary controlled by the onset of partial consolidation during the slower penetration rates.

- At this time it is not possible to determine if the magnitude of sleeve texture influences shaft friction response at slow penetration rates, as the data seem to indicate no change in response over the tested range of penetration rates.

In summary, this initial investigation into the effect of variable penetration rates on the MFA sensors showed that friction along the shaft was not largely influenced by changes in penetration rate from 20 to 0.04 mm/s, with the observed variations being on the order of the changes in effective stress due to pore pressure dissipation during the investigation.

9.4.3.2 CPTU-MPFA Model Pile Investigations

A series of eight load tests were conducted within three soundings using the CPTU-MPFA device at the Burswood clay site. The installation, equalization, and loading conditions were varied to investigate the influence of these parameters on the measured strain controlled load test responses. A summary of the conclusions from these investigations is provided:

- The MPFA shaft friction responses showed a general trend of increasing resistance to failure and increasing strain to failure with increasing depth. These results follow logically, as s_u is known to increase with depth at an approximate rate of 1.5 kPa/m at this site.
- Friction fatigue was not seen to influence the measured MPFA shaft friction resistances for the sensor positions located at h/r values of 37 and greater. This result follows that observed by Lehane (1992), who observed the influence of h/r to be less significant for h/r > 22.

- The tip and friction stresses did not seem to be influenced by the addition of small amplitude cycling directly before monotonic loading.
- The residual shaft stresses generated during installation were observed to decrease with increasing equalization time, however the absolute values of shaft resistance were observed to be relatively independent of equalization time.
- The values of q_t measured during the model pile load tests were observed to range from 8 to 33% lower than the q_t values observed for conventional CPT test conditions.
- The shaft friction responses were observed to differ from those generated during conventional CPT test conditions only for pile load test conditions where significant equalization consolidation had occurred.

The CPTU-MPFA results indicate the complex influences of installation, equalization, and loading effects on pile response, and highlight some of the reasons that conventional 20 mm/s penetration results should typically be adjusted for these affects before direct implementation into pile design analyses. The MPFA device has been shown to be a practical device for conducting jacked installation model pile investigations, and shows promise for continued investigations across a wider range of materials and load test conditions.

9.4.4 MPFA Piezo Responses

The MPFA device contains five independent pore pressure sensors located along the shaft of the attachment. Four of these sensors are placed adjacent to the uphole end of the MPFA friction sensors, with the fifth sensor located in the foremost position ahead of

all attachment sleeves, providing a baseline measure of pore pressure response along the shaft. The pore pressure response has been observed with the MPFA device in both coarse and fine grained geologies. Additionally, responses can be grouped into those measured during conventional penetration, during pauses in penetration allowing for the equalization of the pore pressure conditions, and during subsequent monotonic or cyclic loading.

9.4.4.1 MPFA Pore Pressure Response During Penetration

The penetration pore pressure responses measured at various tip offsets along the shaft have been monitored with the MPFA device during conventional penetration as summarized herein:

- The shoulder (u_2) and shaft (u_a) piezo sensor responses followed the observed hydrostatic conditions for all penetration investigations in sand.
- The MPFA piezo sensors experienced slight artificial increases in measured pore pressure response over the hydrostatic conditions within a few of the sand soundings. This behavior is believed to be the result of lateral stress induced compression of the filter elements.
- Within the tested fine grained stratigraphies: a soft marine clay and a highly structured calcareous clay geology, the MPFA pore pressures were observed to be consistently on the order of 50% of the u_2 pore pressures during penetration.
- The predicted Δu from cylindrical cavity expansion corresponded well with the excess penetration pore pressures measured by the MPFA piezo sensors along the shaft in the Cooper Marl calcareous clay stratigraphy.

- The trend in measured Δu_a values was observed to decrease with increasing offset from the tip during penetration in the Cooper Marl, indicating the absence of fully undrained conditions for shaft positions located at positions behind the tip of $h/r >$ 30 in this geology.
- The response of the MPFA penetration pore pressures was observed to be slightly influenced by the presence of adjacent textured sleeves. The induction of slight positive excess pore pressures for textured sleeve penetrations are believed to be the result of the forced radial movement of the shear zone away from the shaft to a plane outside the extent of the textural asperities.

9.4.4.2 MPFA Pore Pressure Response During Equalization

A total of eleven standard dissipation tests were conducted with the CPTU-MPFA configuration at the Burswood clay test site during the current study, ranging in test time from 30 to 680 minutes and performed at tip depths of 5, 6.7, 7.5, 7.7, and 10 m. Each of these dissipation tests was conducted directly after standard steady-state CPT penetration to the investigation depth, with five of these tests representative of equalization during the load test series. A summary of the main conclusions observed for CPTU-MPFA dissipations are summarized:

- The u_2 responses within the main clay stratigraphy showed slight dilation on the order of $U = 1.2$, reaching a maximum within the first minute of equalization.
- The tests at tip depths of 10 m depth clearly exhibit different u_2 response indicative of a change in stratigraphy between 8 and 10 m depth, with 50% dissipations occurring between 1 and 5 minutes.

- The MPFA shaft dissipation responses were all observed to exhibit dilatant initial response, even though the Burswood clay is known to be normally consolidated, with the apparent OCR due to ageing ranging from 1.5 to 2. Dilatory dissipation response along the shaft has been previously observed in the model pile tests at Imperial College (Bond, 1989; Lehane, 1992; Chow, 1996) and is believed to result from the shear zone (or plane of maximum shearing) being located a finite distance away from the shaft (i.e. sensor position).
- All five u_a sensor responses show good grouping as a function of test depth, with the rates of dissipation very consistent, and the observed variations in t_{50} dissipation times corresponding to the level of dilation response. The t_{50} times within the main clay were observed to be on the order of 1 to 2 hours with a maximum observed t_{50} response on the order of 1 day for the maximum dilatory response of $U_{max} = 1.6$.
- The rate of MPFA shaft dissipation was observed to increase with increased dilatory response, i.e. response achieving large values of normalized excess pore pressure during initial dissipation.
- The MPFA piezo sensors exhibited response controlled by the localized stratigraphy, with adjacent sensors (spaced at a maximum of 0.26 m) often recording significant differences in dissipation response. These variations in adjacent sensor responses seem to be indicative of the known stratigraphic silt and clay interlayering at the Burswood site, and indicate that dissipation is primarily dependent on local radial dissipation and not vertical flow along the device interface for this clay.

- Future testing across a range of other fine grained stratigraphies will hopefully clarify the fundamental mechanisms involved in observed MPFA dissipation responses.

9.4.4.3 Summary of Piezo Response During Model "Pile" Testing

The CPTU-MPFA configuration was used to conduct eight strain controlled load tests at the Burswood clay site, with variations in the equalization time, loading rate, and inclusion of small amplitude cycling used to assess response. The pore pressure responses observed during the model "pile" testing program are summarized:

- The u_2 and u_a piezo sensor responses were all observed to be affected for initial displacements up to the vertical thickness of the piezo filter elements. This behavior seems to be the result of the filter cake formed across the filter element surfaces during penetration becoming consolidated into the surface of the surficial filter pore spaces during equalization, with the resultant shearing of this material out of the filter element upon displacement often causing spikes in the pore pressure response upon brittle shear failure.
- The magnitude of and displacement at which these spikes in response occurred were directly related to the level of consolidation (i.e. equalization time).
- The spikes in response resultant from this behavior impede the quantitative analysis of pore pressure responses during load testing, with the use of other filter elements and sensors possibly diminishing the effects observed in the current clay.
- The observed pore pressure responses during load testing conducted using the CPTU-MPFA configuration were due to a combination of the hydrostatic

conditions, the excess pore pressures generated due to the monotonic load tests, and the continued dissipation of the excess penetration pore pressures.

- Applied strain rate was observed to affect the magnitude of shear induced u_2 pore pressures for loading after 2 hours of equalization resulting in generated Δu_2 on the order of 0.6 kPa/mm or 0.9 kPa/min for the 0.024 mm/s rate and 2.2 kPa/mm or 9.4 kPa/min for the 0.072 mm/s load rate.
- Small amplitude cyclic excitation applied directly after installation was observed to influence the piezo response of all CPTU-MPFA sensors for load tests conducted 2 minutes after cycling, but not to affect response for load tests conducted 2 hours after cycling. Small amplitude cycling was observed to promote the generation of positive excess pore pressures during subsequent loading in the tested Burswood clay.
- The MPFA piezo sensors along the shaft did not register significant changes in Δu due to other variations in the load testing conditions across the range of those tested, with changes in Δu observed to be on the order of equilibrium dissipation responses seen in the conventional dissipation tests.

9.4.4.3 Summary of Piezo Response Resulting from Cycling

Both small and large amplitude cycling were performed with the CPTU-MPFA unit at the Burswood site. These test procedures were used to assess the response due to various cyclic loading and installation conditions. The results from the large amplitude cycling are summarized as follows:

- Large amplitude cycling ($\pm$ 1 m strokes) was observed to create large variations in installation and extraction pore pressure response for all sensors, with the peak to peak changes in absolute pore pressure on the order of 160 kPa for u_2 and between 80 and 100 kPa for the MPFA u_a shaft sensors at the Burswood site.
- A comparison of the two independent large amplitude cyclic investigations conducted in separate soundings at the same test depth indicated very similar responses between equivalent sensors across the two tests.
- The behaviors of the individual CPTU-MPFA sensors were observed to vary between the tip (u_2) and shaft (u_a) positions as a function of the locally induced stress conditions.
- Variations were also observed between the individual u_a shaft sensors, with the variations observed to be independent of h/r but highly dependent on the local soil conditions at the test depth.
- Large amplitude cycling was observed to create an offset in normalized excess pore pressure (U) at the u_2 position, with pre- and post- cycling dissipations occurring at an equivalent rate but offset by an absolute pore pressure on the order of 90 kPa.
- The effect of large amplitude cycling on the shaft dissipation were observed to create a range of post cyclic dissipation responses, ranging from quick initial dissipation to levels representative of equilibrium dissipation, offset dissipation occurring at the same rate but shifted to higher absolute pore pressures (as seen for u_2), to post cyclic swelling observed at one test depth in both of the independent tests.

- As such, while the responses during large amplitude cycling were observed to be relatively consistent, the post cycle dissipations were observed to be highly dependent on the local soil conditions around the sensor locations.

The pore pressure responses observed due to small amplitude cycling are summarized as follows:

- The u_2 response was observed to experience cyclic peak to peak variations in U on the order of 20% with minimal changes observed as compared to equilibrium pore pressure dissipations.
- The u_a shaft sensor responses were observed to experience cyclic peak to peak variations in U ranging from 5 to 60% within the first 20 cycles believed to be a function of local soil sensitivity to cyclic loading.
- Minimal cyclic pore pressure variations were observed for all u_a sensors for continued cycling from 20 to 200 two way cycles.
- The average u_a responses exhibited two characteristic behaviors: (1) the generation of positive excess pore pressures throughout cycling, followed by initial rapid post-cycle dissipation back to the trend of equilibrium dissipation behavior or (2) minimal divergence from typical dissipation response after the first 5 to 10 small amplitude cycles. These behaviors did not show dependence on *h/r* and are believed to be representative of variations in local soil properties at the various u_a sensor positions.

9.5 Summary of Current Study

The current research has improved the understanding of the fundamental mechanisms governing geotechnical interface response, and has developed a new testing tool for improved characterization of geotechnical interface behavior in situ. The evolution of granular shear zones adjacent to smooth and textured friction sleeves was thoroughly investigated, with the shear zone evolution found to be dependent on the characteristics of the granular soil and continuum counterface. These observations have also allowed for a greater understanding of in situ smooth and textured friction sleeve measurements, aiding in the interpretation of the measured in situ data. An investigation into the role of hook and loop interactions on filament continuum interactions for textured geomembrane - NPNW geotextile systems has provided insight into both the specific interface behavior of this geosynthetic system and the general framework with which geotechnical interfaces are considered.

A new in situ testing device has been developed to provide the unique ability to obtain multiple measures of penetration shaft friction (f_{a1}, f_{a2}, f_{a3}, f_{a4}) and pore pressure (u_{a0}, u_{a1}, u_{a2}, u_{a3}, u_{a4}) response at each depth within a single sounding simultaneous to obtaining conventional CPTU measurements of (q_t, f_s, and u_2). This newly developed device, identified as the Multi Piezo Friction Attachment (MPFA), has been shown to provide excellent response, on the order of or exceeding conventional CPT penetration sensor response over the extensive in situ investigations conducted for the current study. The multi friction modules utilize exchangeable textured sleeves in order to investigate the influence of surface roughness on interface behavior in situ. The MPFA device has shown the ability to measure the full relationship between interface strength and surface

roughness across a range of soil conditions including: silica sands, calcareous sand, calcareous clay, and soft marine clay. The MFA and MPFA devices have also shown the ability to accurately characterize in situ soil conditions across a range of non standard penetration procedures, including: small and large amplitude cycling, inclined penetration, variable rate penetration, for use as a model pile, and for monitoring extraction response.

9.5 Recommendations for Future Work

The current work has focused on laboratory and in situ investigations into geotechnical interface behavior. Several key observations and conclusions regarding geotechnical interface behavior have been made, however, the research has brought to light additional issues where future research could improve the understanding and measurement of geotechnical interface behavior. The prominent topics seen as needing future study, are:

- Quantification of the size and extent of shear zones formed adjacent to friction sleeves and at other interfaces for fine grained soils. These tests will help to corroborate the hypotheses currently used to interpret shaft friction and pore pressure behaviors of penetrometers and pile foundations.
- Continued implementation of the MFA and MPFA devices across a wider range of soil and site conditions to expand the database of measured in situ interface measurements.
- Conducting a feasibility study towards eliminating the internal wiring of the MFA and MPFA modular devices in order to facilitate the exchange of textured sleeves without risk of damaging the internal data acquisition components. It is believed

that the use of wireless technologies could facilitate an improvement in the current design.

- Continued assessment of non vertical penetrations, as the ability to continuously assess both lateral and vertical soil properties would enable the improved understanding and characterization of soil anisotropy.
- Further implementation of non standard investigation procedures with the MFA/MPFA devices and standard geotechnical penetration devices to improve the amount and quality of data gathered through in situ testing.
- Further investigations of MFA/MPFA behavior using both conventional penetration procedures and for model pile investigations in order to facilitate the use of the measured interface data within piling design procedures. It is especially important that future soundings be conducted in conjunction with or at sites containing high quality pile load test data.
- Further investigations in structured and/or cemented stratigraphies to determine the ability of the multi friction devices to quantify soil structure in situ, and to provide the ability to characterize soils for difficult site conditions.
- The development of a robust framework for better incorporating interface response into the design of geotechnical structures, including the use of direct in situ measurements of interface response.
- The development of a model correspondent to the MPFA piezo sensor locations able to estimate both installation and dissipation pore pressure responses across both homogeneous and heterogeneous fine grained soil conditions.

- Numerical modeling of smooth and textured interface shearing as a function of sensor positions coupled with an analysis of the generated and dissipation of pore pressures due to interface shearing.
- The laboratory assessment of filter cake formation on the response of piezo sensors as a function of shearing rate across the filter face and after equalization.

REFERENCES

Abbs, A.F., Waterton, C.A., Bell, R.A., Khorshid, M.S., and Jewell, R.J. (1988) "Evaluation of Pile Friction from Conductor Load Test," *Proceedings of the International Conference on Engineering for Calcareous Sediments,* 2, Perth, 607-616.

Acar, Y.B., Durgunoglu, H.T., and Tumay, M.T. (1982) "Interface Properties of Sand," *Journal of the Geotechnical Division*, 108, No. GT4, 648-654.

Airey, D.W., Al-Douri, R.H., and Poulos, H.G. (1992) "Estimation of Pile Friction Degradation from Shearbox Tests," *ASTM Geotechnical Testing Journal*, 15, No. 4, 388-392.

Al-Douri, R.H. and Poulos, H.G. (1991) "Static and Cyclic Direct Shear Tests on Carbonate Sands," *ASTM Geotechnical Testing Journal*, 15, No. 2, 138-157.

Allersma, H.G.B. (1988) "Optical Analysis of Stress and Strain Around the Tip of a Penetrating Probe," *Proceedings of the International Symposium on Penetration Testing, ISOPT-1*, Orlando, 2, 615-620.

Aloufi, M. and Santamarina, J.C. (1995). "Low and High Strain Mechanical Properties of Grain Masses - The Effect of Particle Eccentricity," *Transactions of the American Society of Agricultural Engineers,* 38, No. 3, 877-887.

Andersen, K.H., Pool, J.H., Brown, S.F., and Rosenbrand, W.F. (1980) "Cyclic and Static Laboratory Tests on Drammen Clay," *Journal of the Geotechnical Engineering Division*, 106, No. GT5, 499-529.

Anderson, W.F. and Hammoud, F. (1988) "Effect of Testing Procedure in Ring Shear Tests," *ASTM Geotechnical Testing Journal*, 11, No. 3, 204-207.

Andrawes, K.Z., and Butterfield, R. (1973) "The Measurement of Planar Displacements of Sand Grains," *Géotechnique*, 23, No. 5, 571-576.

Arthur, J.R.F., Dunstan, T., Al-Ani, Q.A.J., and Assadi, A. (1977) "Plastic Deformation and Failure of Granular Media," *Géotechnique*, 27, No. 1, 53-74.

ASME B46.1 (1995) "Surface Texture (Surface Roughness, Waviness, and Lay)," New York, NY, 112 pp.

ASTM D3441-94 (1994) "Standard Test Method for Deep, Quasi-Static, Cone and Friction-Cone Penetration Tests of Soil," West Conshohocken, PA.

ASTM D5169 (1998) "Standard Test Method for Shear Strength (Dynamic Method) of Hook and Loop Touch Fasteners," West Conshohocken, PA.

ASTM D5170 (1998) "Standard Test Method for Peel Strength ("T" Method) of Hook and Loop Touch Fasteners," West Conshohocken, PA.

ASTM D5321 (2002) "Standard Test Method for Determining the Coefficient of Soil and Geosynthetic or Geosynthetic and Geosynthetic Friction by the Direct Shear Method," West Conshohocken, PA.

ASTM D5778-95 (1995) "Standard Test Method for Performing Electronic Friction Cone and Piezocone Penetration Testing of Soils," West Conshohocken, PA.

Bagster, D.F., Arnold, P.C., Roberts, A.W., and Fitzgerald, T.F. (1974) "The Interpretation of Ring Shear Cell Results," *Powder Technology*, 9, 135-139.

Baligh, M. M. (1975) ''Theory of Deep Site Static Cone Penetration Resistance,'' *Research Report No. R75-56*, Order No. 517, Dept. of Civil Engineering., MIT, Cambridge, Sept, 133 pg.

Baligh, M.M. (1985) "Strain Path Method," *Journal of Geotechnical Engineering*, 111, No. 9, 1108-1109.

Baligh, M.M. (1986a) "Undrained Deep Penetration, I: Shear Stresses," *Géotechnique,* 36, No. 4, 471-485.

Baligh, M.M. (1986b) "Undrained Deep Penetration, II: Pore Pressures," *Géotechnique,* 36, No. 4, 487-501.

Baligh, M.M., Azzouz, A.S., Wissa, A.Z.E., Matyin, R.T., and Morrison, M.H. (1981) "The Piezocone Penetrometer. Cone Penetration Testing and Experience," *Proceedings of the ASCE National Convention: Cone Penetration Testing and Experience*, St. Louis, 247-263.

Baligh, M.M. and Levadoux, J.N. (1986) "Consolidation After Undrained Piezocone Penetration. I: Interpretation," *Journal of Geotechnical Engineering,* 112, No. 7, 727-745.

Baylac, B., Masson, S., Martinez, J., and Hellou, M. (2003) "Multiscale Analysis of the Shear Behaviour of Soil-Inclusion Interfaces," *Proceedings of the 3rd International Symposium on Deformation Characteristics of Geomaterials*, IS Lyon 03 (di Benedetto et al. editors), September, 179-186.

Bayne, J.M., and Tjelta, T.I. (1987) "Advanced Cone Penetrometer Development for In Situ Testing at Gulfaks C," *Offshore Technology Conference, OTC*, Richardson, TX, Paper No. 5420, 531-540.

Begemann, H.K.S.Ph. (1953) "Improved Method of Determining the Resistance to Adhesion by Sounding Through a Loose Sleeve Placed Behind the Cone," *Proceedings of the 3rd International Conference on Soil Mechanics and Foundation Engineering*, Zürich, 1, 213-217.

Begemann, H.K.S.Ph. (1965) "The Friction Jacket Cone as an Aid in Determining the Soil Profile," *Proceedings of the 6th International Conference on Soil Mechanics and Foundation Engineering*, Montreal, 1, 17-20.

Begemann, H.K.S.Ph. (1969) "The Dutch Static Penetration Test with the Adhesion Jacket," *LGM Mededelingen*, 12, No. 4, 69-100.

Bishop, A.W., Green, G.E., Garga, V.K., Andresen, A., and Brown, J.D. (1971) "A New Ring Shear Apparatus and Its Application to the Measurement of Residual Strength," *Géotechnique*, 21, No. 4, 273-328.

Bloomquist, D., Hand, R.S., and Anderson, J.B. (1999) "Development of a Cemented Sand Module for the Electronic Cone Penetrometer," *Transportation Research Record*, *No. 1675,* 10-16.

Bogard, J.D., Matlock, H., Audibert, J.M.E., and Bamford, S.R. (1985) "Three Years' Experience With Model Pile Segment Tool Tests," *Proceedings of the 17th Annual Offshore Technology Conference*, Houston, TX.

Bond, A.J. and Jardine, R.J. (1991) "Effects of Installing Displacement Piles in a High OCR Clay," *Géotechnique,* 41, No. 3, 341-363.

Bond, A.J., Jardine, R.J., and Lehane, B.M. (1993) "Factors Affecting the Shaft Capacity of Displacement Piles in Clay," *Offshore Site Investigation and Foundation Behavior*, 28, 585-606

Boulon, M. (1989) "Basic Features of Soil-Structure Interface Behavior," *Computer and Geotechnics,* 7, 115-131.

Boulon, M., and Foray, P. (1986) "Physical and Numerical Simulation of Lateral Shaft Friction Along Offshore Piles in Sand," *Proceedings of the 3rd International Conference on Numerical Methods in Offshore Piling,* Nantes, 127-147.

Briaud, J.-L. (1988) "Evaluation of Cone Penetration Test Methods Using 98 Pile Load Tests," *Proceedings of the International Symposium on Penetration Testing, ISOPT-1*, Orlando, 2, 687-697.

Broms, B.B., and Flodin, N. (1988) "History of Soil Penetration Testing," *Proceedings of the International Symposium on Penetration Testing, ISOPT-1*, Orlando, 1, 157-220.

Broere, W. and van Tol, A.F. (1998) "Horizontal Cone Penetration Testing," *Proceedings of the International Conference on Geotechnical Site Characterization, ISC 1998*, Atlanta, 989-994.

Broere, W. and Van Tol, A.F. (2001) "Horizontal Cone Penetration Testing in Sand," *Proceedings of the International Conference on In-Situ Measurement of Soil Properties & Case Histories, In-Situ 2001*, Bali, 649-654.

Brumund, W.F. and Leonards, G.A. (1973) “Experimental Study of Static and Dynamic Friction Between Sand and Typical Construction Materials,” *ASTM Journal of Testing and Evaluation*, 1, No.2, 162-165.

Brumund, W.F. and Leonards, G.A. (1987) Discussion to “Influential Factors of Friction Between Steel and Dry Sands,” *Soils and Foundations*, 27, No. 2, 66-68.

Bruzzi, D. and Battaglio, M. (1987) “Pore Pressure Measurements During Cone Penetration Test,” ISMES Research Report No. 229, Milan, Italy, 246 pp.

Burns, S.E., and Mayne, P.W. (1995) “Coefficient of Consolidation (c_h) from Type 2 Piezocone Dissipation in Overconsolidated Clay,” *Proceedings of the International Symposium on Cone Penetration Testing, CPT ’95*, Linköping, Sweden, 2, 137-142.

Burns, S.E. and Mayne, P.W. (1998a) “Monotonic and Dilatory Pore-pressure Decay During Piezocone Tests in Clay,” *Canadian Geotechnical Journal*, 35, No. 6, 1063-1073.

Burns, S.E. and Mayne, P.W. (1998b) “Penetrometers for Soil Permeability and Chemical Detection,” Report No. GIT-CEEGEO-98-1, Georgia Institute of Technology, July, 144 pp.

Burns, S.E., and Mayne, P.W. (1999) “Pore Pressure Dissipation Behavior Surrounding Driven Piles and Cone Penetrometers,” *Transportation Research Record, No. 1675*, 17-23.

Burns, S.E., and Mayne, P.W. (2002a) “Analytical Cavity Expansion-Critical State Model for Piezocone Dissipation in Fine-Grained Soils,” *Soils and Foundations*, 42, No. 2, 131-137.

Burns, S.E., and Mayne, P.W. (2002b) “Interpretation of Seismic Peizocone Results for the Estimation of Hydraulic Conductivity in Clays,” *ASTM Geotechnical Testing Journal*, 25, No. 3, 334-341.

Butterfield, R. and Andrawes, K.Z. (1972) "On the Angles of Friction Between Sand and Plane Surfaces," *Journal of Terramechanics*, 8, No. 4, 15-23.

Camp, W.M. III. (2004) “Drilled and Driven Foundation Behavior in a Calcareous Clay,” Proceedings of Geosupport 2004, Joint ADSC-ASCE GeoInstitute Conference - GSP 124, Orlando, 1-18.

Campanella, R.G. and Robertson, P.K. (1981) “Applied Cone Research,” *Proceedings of the ASCE National Convention: Cone Penetration Testing and Experience*, St. Louis, 343-362.

Campanella, R.G. and Robertson, P.K. (1988) “Current Status of the Piezocone Test,” *Proceedings of the International Symposium on Penetration Testing, ISOPT-1*, Orlando, 1, 93-116.

Campanella, R.G., Sully, J.P., Greig, J.W., and Jolly, G. (1990) "Research and Development of a Lateral Stress Piezocone," *Transportation Research Record, No. 1278*, 215-224.

Cargill, P.E. (1999) "The Influence of Friction Sleeve Roughness on Cone Penetration Measurements," *M.S. Thesis*, School of Civil and Environmental Engineering, Georgia Institute of Technology, Atlanta, 140 pp.

Chandler, R.J. (1966) "The Measurement of Residual Strength in Triaxial Compression," *Géotechnique,* 16, No. 3, 181-186.

Chandler, R.J. (1969) "The Effect of Weathering on the Shear Strength Properties of Kueper Marl," *Géotechnique,* 19, No. 3, 321-324.

Cho, G.C. and Santamarina, J.C. (2001) "Unsaturated Particulate Materials – Particle-Level Studies," *Journal of Geotechnical and Geoenvironmental Engineering*, 127, No. 1, 84-94.

Cho, G.C. and Santamarina, J.C. (2003) "The Omnipresence of Localizations in Particulate Materials," *Proceedings of the 3rd International Symposium on Deformation of Geomaterials IS Lyon 03* (Di Benedetto et al. editors), September, Lyon, France, 465-473.

Chow, F.C. (1996) "Investigations into the Behavior of Displacement Piles for Offshore Foundations," *PhD Dissertation*, University of London (Imperial College), London, December, 766 pp.

Chung, S.F., and Randolph, M.F. (2002) "Characterization of Soft Soils for Deep Water Developments – Report on Field Test at Burswood Site, *Report GEO:01254*, Centre for Offshore Foundation Systems, The University of Western Australia, April (Revised), 57 pp.

Chung, S.F., and Randolph, M.F. (2004a) "Penetration Resistance in Soft Clay for Differed Shaped Penetrometers, *2nd International Conference on Site Characterization, ISC-2*, Porto, 7 pp.

Claquin, C. and Emeriault, F. (2002) "Interface Behavior of Granular Materials: Discrete Numerical Simulation of a Ring Simple Shear Test," *Proceedings of the 15th Engineering Mechanics Conference*, New York, 8 pp.

Clementino, R.V., Robertson, P.K., Biggar, K.W., and Cyre, G. (1999) "A Novel Approach for Horizontal Soil Characterization," *Geotechnical News*, December, 46-52.

Colliat, J.-L. and Dendani, H. (2002) "Girassol: Geotechnical Design Analyses and Installation of the Suction Anchors," *Proceedings of the Offshore Technology Conference*, Houston, OTC 14209, 107-119.

Coop, M.R. and Wroth, C.P. (1989) "Field Studies of an Instrumented Model Pile in Clay," *Géotechnique,* 39, No. 4, 679-696.

Cornforth, D.H. (1964) "Some Experiments on the Influence of Strain Conditions on the Strength of Sand," *Géotechnique*, 36, No. 4, 143-167.

Coulomb, C.A. (1773) "On an application of the rules of maximum and minimum to some statistical problems, relevant to architecture." *Mémoires de Mathématique & de Physique, présentés a l'Académie Royale des Sciences par divers Savans, &lus dans ses Assemblées*, 7, Paris, 343-382.

Craig, W. H. (1980). "Installation Studies for Model Piles," *Proceedings of the Symposium on Application of Centrifuge Modelling to Geotechnical Design*, Manchester, 440- 452.

Craig, W. (1985). "Modelling Pile Installation in Centrifuge Experiments," *Proceedings of the 11th International Conference on Soil Mechanics and Foundation Engineering,* San Francisco, 2, 1101-1104.

Cundall, P.A. (1989) "Numerical Experiments on Localization in Frictional Materials," *Ingenieur-Archiv*, 59, 148-159.

Danziger, F.A.B., Almeida, M.S.S., and Sills, G.G. (1997) "The Significance of the Strain Path Method Analysis in the Interpretation of Piezocone Dissipation Data," *Géotechnique,* 47, No. 5, 901-914.

Day, R.A. and Potts, D.M. (1998) "Short Communication: The Effect of Interface Properties on Retaining Wall Behavior," *International Journal for Numerical and Analytical Methods in Geomechanics*, 22, No. 12, 1021-1033.

de Ruiter, J. (1971) "Electrical Penetrometer for Site Investigations," *Journal of the Soil Mechanics and Foundation Division, ASCE*, 97, SM2, 457-472.

de Ruiter, J. (1981) "Current Penetrometer Practice: Cone Penetration Testing and Experience," *Proceedings of the ASCE National Convention: Cone Penetration Testing and Experience*, St. Louis, 1-48.

de Ruiter, J. (1982) "The Static Cone Penetration Test," State-of-the-Art-Report, *Proceedings of the 2nd European Symposium on Penetration Testing*, ESOPT-II, Amsterdam, 2, 389-405.

DeJong, J.T. (2001) *Investigation of Particulate-Continuum Interface Mechanics and Their Assessment Through a Multi-Friction Sleeve Penetrometer Attachment,* PhD Dissertation, Georgia Institute of Technology, Atlanta, May, 360 p.

DeJong, J.T. and Frost, J.D. (2002a) "A Multi-Friction Sleeve Attachment for the Cone Penetrometer," *ASTM Geotechnical Testing Journal,* 25, No. 2, 111-127.

DeJong, J.T. and Frost, J.D. (2002b) "Physical Evidence of Shear Banding at Granular-Continuum Interfaces," *Proceedings of the 15th Engineering Mechanics Conference*, New York, 8 pp.

DeJong, J.T., Frost, J.D., and Cargill, P.E. (2001) "Effect of Surface Texturing on CPT Friction Sleeve Measurements," *Journal of Geotechnical and Geoenvironmental Engineering*, 127, No. 2, 158-168.

DeJong, J.T., Frost, J.D., and Sacs, M. (2000) "Relating Quantitative Measures of Surface Roughness and Hardness to Geomaterial Interface Strength," *Proceedings of Geo-Eng 2000*, Sydney, AUS, CD-ROM.

DeJong, J.T., Frost, J.D., Saussus, D.R. (2002) "Relative Aspect of Surface Roughness at Particulate-Solid Interfaces," *ASTM Journal of Testing and Evaluation*, 30, No. 1, 8-19.

DeJong, J.T., Randolph, M.F., and White, D.J. (2003) "Interface Load Transfer Degradation During Cyclic Loading: A Microscale Investigation," *Soils and Foundations,* 43, No. 4, 81-93.

DeJong, J.T., White, D.J., and Randolph, M.F. (2003) "Effect of Cementation on Cyclic Soil-Structure Interface Behavior," *Proceedings of the 16th Engineering Mechanics Conference,* 1, Seattle, WA, 4 pp.

Desai, C.S., Drumm, E.C., and Zaman, M.M. (1985) "Cyclic Testing and Modeling of Interfaces," *Journal of Geotechnical Engineering,* 111, No. 6, 793-815.

Desai, C.S. and Rigby, D.B. (1995) "Modelling and Testing of Interfaces," *Mechanics of Geomaterial Interfaces*, Selvadurai, A.P.S. and Boulon M.J. (Eds.), 487-512.

Desrues, J., Chambon R., Mokni, M., and Mazerolle, F. (1996) "Void Ratio Evolution Inside Shear Bands in Triaxial Sand Specimens Studied by Computed Tomography," *Géotechnique,* 46, No. 3, 529-546.

Desrues, J. and Hammand, W. (1989) "Shear Banding Dependency on Mean Pressure Level in Sand," *Proceedings of the International Workshop on Numerical Methods for Localasation and Bifurcation of Granular Bodies*, Gdansk, Poland.

Donaldson, J.J. (1995) "Texturing Techniques," *Proceedings of the Eighth Conference on Geosynthetic Resins, Formulations, and Manufacturing*, Philadelphia, PA 116-125.

Dove, J.E. and Frost, J.D. (1996) "A Method for Measuring Geomembrane Surface Roughness," *Geosynthetics International*, 3, No. 3, 369-392.

Dove, J.E. and Frost, J.D. (1999) "Peak Friction Behavior of Smooth Geomembrane-Particle Interfaces," *Journal of Geotechnical and Geoenvironmental Engineering*, 125, No. 7, 544-555.

Dove, J.E., Frost, J.D., Han J., and Bachus, R.C. (1997) "The Influence of Geomembrane Surface Roughness on Interface Strength," *Proceedings of Geosynthetics '97*, 2, 863-876.

Dove, J.E. and Harpring, J.C. (1999) "Geometric and Spatial Parameters for Analysis of Geomembrane/Soil Interface Behavior," *Proceedings of Geosynthetics '99*, Boston, MA, 1, 575-588.

Durgunoglu, H.T. and Mitchell, J.K. (1975) "Static Penetration Resistance of Soils," I-II. *Proceedings of the ASCE Specialty Conference on In Situ Measurement of Soil Properties*, Raleigh, NC, 1, 151-189.

Dutt, R.N., Doyle, E.H., Collins, J.T., and Ganguly, P. (1995) "A Simple Model to Predict Soil Resistance to Driving for Long Piles in Deepwater Normally Consolidated Clays," *Offshore Technology Conference, OTC*, Houston, TX, Paper No. 7668, 257-269.

Ebelhar, R.J., Young, A.G., and Stieben, G.S. (1988) "Cone Penetration and Conductor Pullout Tests in Carbonate Soils Offshore Africa," *Proceedings of the International Conference on Engineering for Calcareous Sediments,* 1, Perth, 155-163.

Elsworth, D. (1990) "Theory of Partially Drained Piezometer Insertion," *Journal of Geotechnical Engineering*, 116, No. 6, 899-914.

Evans, T.M. (2005). "Microscale Physical and Numerical Investigations of Shear Banding in Granular Soils," *PhD Dissertation*, Georgia Institute of Technology, in progress.

Evgin, E. and Fakharian, K. (1996) "Effect of Stress Paths on the Behaviour of Sand-Steel Interfaces," *Canadian Geotechnical Journal,* 33, No. 6, 853-865.

Fahey, M. and Lee Goh, A. (1995) "A Comparison of Pressuremeter and Piezocone Methods of Determining the Coefficient of Consolidation, *Proceedings of the 4th International Symposium on the Pressuremeter and Its New Avenues*, Quebec, 153-160.

Fakharian, K. and Evgin, E. (1996) "An Automated Apparatus for Three-Dimensional Monotonic and Cyclic Testing of Interfaces," *ASTM Geotechnical Testing Journal*, 19, No. 1, 22-31.

Finno, R.J., Harris, W.W., Mooney, M.A., and Viggiani, G. (1996) "Strain Localization and Undrained Steady State of Sand," *Journal of Geotechnical Engineering,* 122, No. 6, 462-473.

Finno, R.J. and Rechenmacher, A.L. (2003) "Effects of Consolidation History on Critical State of Sand," *Journal of Geotechnical and Geoenvironmental Engineering,* 129, No. 4, 350-360.

Fioravante, V., Ghionna, V.N., Jamiolkowksi, M., and Sarri, H. (1999) "Shaft Friction Modelling of Non-Displacement Piles in Sand," *Analysis, Design, Construction, and Testing of Deep Foundations, ASCE GSP #88* (Not included in Proceedings), 24 pp.

Porcino, D., Fioravante, V., Ghionna, V.N., and Pedroni, S. (2003) "Interface Behaviour of Sands from Constant Normal Stiffness Direct Shear Tests," *ASTM Geotechnical Testing Journal,* 26, No. 3, 289-301.

Finnie, I.M.S. & Randolph, M.F. (1994). "Punch-Through and Liquefaction Induced Failure of Shallow Foundations on Calcareous Sediments", *Proceedings of the International Conference on Behavior of Offshore Structures, BOSS '94*, Boston, 217-230.

Fishman, K.L. and Pal, S. (1994) "Further Study of Geomembranes/Cohesive Soil Interface Shear Behavior," *Geotextiles and Geomembranes*, 13, No. 9, 571-590.

Frost, J.D., and DeJong, J.T. (2001) "A New Multi-Friction Sleeve Attachment," *Proceedings of the 15th International Conference on Soil Mechanics and Geotechnical Engineering*, Istanbul, 1, 91-94.

Frost, J.D., and DeJong, J.T. (2005) "In Situ Assessment of the Role of Surface Roughness on Interface Response," *Journal of Geotechnical and Geoenvironmental Engineering*, 131, No. 4, 498-511.

Frost, J.D., Evans, T.M., Hebeler, G.L., and Giroud, J.P., (2002) "Influence of Wear Mechanisms on Geosynthetic Interface Strengths," *Proceedings of the Seventh International Conference on Geosynthetics*, Nice, 4, 1325-1328.

Frost, J.D. and Han, J. (1999) "Behavior of Interfaces between Fiber-Reinforced Polymers and Sands," *Journal of Geotechnical and Geoenvironmental Engineering*, 125, No. 8, 633-640.

Frost, J.D., Hebeler, G.L, Evans, T.M., and DeJong, J.T. (2004) "Interface Behavior of Granular Soils," *Proceedings of Earth and Space, 9th Biennial ASCE Aerospace Division International Conference on Engineering, Construction, and Operations in Challenging Environments*, Houston, TX, 65-72.

Frost, J.D. and Jang, D.-J. (2000) "Evolution of Sand Microstructure During Shear," *Journal of Geotechnical and Geoenvironmental Engineering*, 126, No. 2, 116-130.

Frost, J.D. and Kuo, C.Y. (1996) "Automated Determination of the Distribution of Local Void Ratio from Digital Images," *ASTM Geotechnical Testing Journal*, 19, No. 2, 107-117.

Frost, J.D., and Lee, S.W., (2001) "Microscale Study of Geomembrane-Geotextile Interactions," *Geosynthetics International*, 8, No. 6, 577-597.

Frost, J.D., Lee, S., and Cargill, P.E. (1999) "The Evolution of Sand Structure Adjacent to Geomembranes," *Proceedings of Geosynthetics '99*, 1, 559-573.

Ghionna, V.N., Mortar, G., and Vita, G.P. (2003) "Sand-structure Interface Behaviour Under Cyclic Loading from Constant Normal Stiffness Direct Shear Tests," *Proceedings of the International Symposium on Deformation Characteristics in Geomaterials*, Lyon, 231-237.

Gilbert, R.B., Liu, C.N., Wright, S.G., and Trautwein, S.J. (1995) "A Double Shear Test Method for Measuring Interface Strength," *Proceedings of Geosynthetics '95*, Nashville, TN, 3, 1017-1029.

Giroud, J.P. (2004) "Quantitative Analysis of the Impact of Adhesion Between Geomembranes and Geotextiles on the Stability of Soil-Geosynthetic Systems on Slopes," JP Giroud, Inc., Ocean Ridge, FL, 14 pp.

Giroud, J.P., and Beech, J.F. (1989) "Stability of Soil Layers on Geosynthetic Lining Systems," *Proceedings of Geosynthetics '89*, San Diego, CA, 1, 35-46.

Gourvenec, S., Randolph, M.F., White, D., Senders, M., (2004) "*Offshore Foundation Systems*," Course Notes From UWA Class 610.406, University of Western Australia, Perth, pp. 557.

Graf, B., Vardoulakis, I., and Hettler, A. (1985) "Shear-band Formation in a Fine-Grained Sand," *Proceedings of the Fifth International Conference on Numerical Methods in Geomechanics*, 1, Nagoya, 517-521.

Gudehus, G. and Nübel, K. (2004) "Evolution of Shear Bands in Sand," *Géotechnique,* 54, No. 3, 187-201.

Guler, M., Edil, T.B., and Bosscher, P.J. "Measurement of Particle Movement in Granular Soils Using Image Analysis," *Journal of Computing in Civil Engineering*, 12, No. 2, 116-122.

Gupta, R.C. and Davidson, J.L. (1986) "Piezoprobe Determined Coefficient of Consolidation," *Soils and Foundations,* 26, No. 3, 12-22.

Gustafsson, L., and Gustafasson, P. (1996) "Studying Mixed Granular Flows by Image Analysis," *Proceedings of the 11th Conference of the ASCE Engineering Mechanics Division*, Reston, VA, 100-103.

Gustafsson, L., and Marklund, O. (1995) "Image Analysis of Fine Grain Granular Flow," *Proceedings of the 10th Conference of the ASCE Engineering Mechanics Division*, Reston, VA, 614-617.

Han, C. and Vardoulakis, I. (1991) "Plane-Strain Compression Experiments on Water-Saturated Fine-Grained Sand," *Géotechnique,* 41, No. 1, 49-78.

Hansbo, S. and Torstensson, B.A. (1977) “Geodrain and Other Vertical Drain Behavior,” *Proceedings of the 9th International Conference on Soil Mechanics and Foundation Engineering,* Tokyo, 2, 533-540.

Hassan, A.H. (1995) “Etude experimentale et numerique du comportement local et global d’une interface sol granulaire structure,” *PhD Dissertation*, Grenoble University.

Hebeler, G.L., Frost, J.D., Myers, A.T. (2004) "Quantifying Hook and Loop Interaction in Geomembrane-Geotextile Systems," *Geotextiles and Geomembranes*, 23, No. 1, 77-105.

Hebeler, G.L., Frost, J.D., Schneider, J.A., Lehane, B.M. (2005) "Cyclic Friction Piezocone Tests for Offshore Applications," *Proceedings of the International Symposium - Frontiers in Offshore Geotechnics, ISFOG*, Perth, (in press).

Hebeler, G.L, Frost, J.D., and Shinn, J.D. II. (2004) "Using Textured Friction Sleeves at Sites Traditionally Problematic to CPT," *Proceedings of the 2nd International Conference on Site Characterization*, Porto, 693-699.

Hefer, P.A. and Neubecker, S.R. (1999) “A Recent Development in Offshore Site Investigation Tools: The T-bar,” *Proceedings of the Conference on Australasia Oil and Gas,* Perth.

Hegazy, Y.A. and Mayne, P.W. (1998) "Delineating Geostratigraphy by Clustering of Piezocone Data", *Geotechnical Site Characterization*, 2, Balkema, Rotterdam, 1069-1074.

Hegazy, Y.A. and Mayne, P.W. (2002) "Objective Site Characterization Using Clustering of Piezocone Data". ASCE *Journal of Geotechnical & Geoenvironmental Engineering,* 128, No. 12, 986-996.

Heins, W.F. and de Leeuw, E.H. (1977) “Large Scale Cyclic Loading Tests,” *Proceedings of the 9th International Conference on Soil Mechanics and Foundation Engineering,* Tokyo, 2, 541-544.

Hird, C.C., Johnson, P., and Sills, G.C. (2003) “Performance of Miniature Piezocones in Thinly Layered Soils,” *Géotechnique*, 53, No. 10, 885-900.

Houlsby, G.T. and Teh, C.I. (1988) “Analysis of the Piezocone in Clay,” *Proceedings of the International Symposium on Penetration Testing, ISOPT-1*, Orlando, 2, 777-783.

Houlsby, G.T., Wheeler, A.A., and Norbury, J. (1985) “Analysis of Undrained Cone Penetration as a Steady Flow Problem,” *Fifth International Conference on Numerical Methods in Geomechanics,* Nagoya, 1767-1773.

House, A., Randolph, M.F., and Watson, P. (2001a) "In-Situ Assessment of Shear Strength and Consolidation Characteristics of Soft Sediments," *Internal Report*, University of Western Australia, 12 pp.

Huntsman, S.R., Mitchell, J.K., Klejbuk, L.W., and Shinde, S.B. (1986) "Lateral Stress Measurement During Cone Penetration," *Proceedings of the ASCE Specialty Conf. In Situ '86: Use of In Situ Tests in Geotechnical Engineering*, Blacksburg, 617-634.

Hryciw, R.D., and Irsyam, M. (1993) "Behavior of Sand Particles Around Rigid Ribbed Inclusions During Shear," *Soils and Foundations* 33, No. 3, 1-13.

Ikeda, K., Terada, K., and Yamakawa, Y. (2003) "Symmetry Breaking Bifurcation in Various Soils Under Shear," *Proceedings of the International Symposium on Deformation Characteristics in Geomaterials*, Lyon, 921-929.

Ingold, T.S. (1994) The Geotextiles and Geomembranes Manual, Oxford, UK, Elsevier Advanced Technology, 610 pp.

Irsyam, M. and Hryciw, R.D. (1991) "Friction and Passive Resistance in Soil Reinforced by Plane Ribbed Inclusions," *Géotechnique*, 41, No. 4, 485-498.

Ismail, M.A. (2000). *Strength and Deformation Behaviour of Calcite-Cemented Calcareous soils*, PhD Dissertation, University of Western Australia.

Issa, J.A., and Nelson R.B. (1992) "Numerical Analysis of Micromechanical Behavior of Granular Materials," *Engineering Computation 9*, 211-223.

ISSMFE (1989) "International Reference Test Procedure for Cone Penetration Test (CPT)," Report of the ISSMFE Technical Committee on Penetration Testing of Soils – TC 16, with Reference to Test Procedures, *Swedish Geotechnical Institute*, Linkoping, Information, No. 7, 6-16.

Iwashita, K. and Oda, M. (1998) "Rolling Resistance at Contacts in Simulation of Shear Band Development by DEM," *ASCE Journal of Engineering Mechanics,* 124, No. 3, 286-292.

Iwashita, K. and Oda, M. (2000) "Micro-Deformation of Shear Banding Process based on Modified Distinct Element Method," *Powder Technology* 109, 192-205.

Janbu, N., and Senneset, K. (1974) "Effective Stress Interpretation of In Situ Static Penetration Tests," *Proceedings of the European Symposium on Penetration Testing*, ESOPT, Stockholm, 2.2, 181-193.

Jang, D.-J. and Frost, J.D. (2000) "Use of Image Analysis to Study the Microstructure of a Failed Sand Specimen," *Canadian Geotechnical Journal*, 37, No. 5, 1141-1149.

Jardine, R.J., Chow, F.C. (1996) "New Design Methods for Offshore Piles," *MDT Publications 96/103, Marine Technology Directorate*, London, 48 pp.

Jardine, R.J., Chow, F.C., Matsumoto, T., and Lehane, B.M. (1998) "A New Design Procedure for Driven Piles in Its Application to Two Japanese Clays," *Soils and Foundations*, 38, No. 1, 207-219.

Jardine, R.J. and Lehane, B.M. (1993) *Research into the Behavior of Offshore Piles: Field Experiments in Sand and Clay*, Offshore Technology Report 93-401, HSE Books, 135 pp.

Jekel, J. W. A. (1988) "Wear of the Friction Sleeve and Its Effect on the Measured Local Friction," *Proceedings of the International Symposium on Penetration Testing, ISOPT-1*, Orlando, 2, 805–808.

Jewell, R.J. and Randolph, M.F. (1988) "Cyclic Rod Shear Tests in Calcareous Sediments," *Proceedings of the International Conference on Engineering for Calcareous Sediments*, 1, Perth, 215-222.

Jones, D.R.V. and Dixon, N. (1998) "Shear Strength Properties of Geomembrane/Geotextile Systems," *Geotextiles and Geomembranes*, 16, No. 1, 45-71.

Jones, G.A., Van Zyl, D., and Rust, E. (1981) "Mine Tailings Characterization by Piezometer Cone," *Proceedings of the ASCE National Convention: Cone Penetration Testing and Experience*, St. Louis, 303-324.

Kabir, M.G. and Lutenegger, A.J. (1990) "In Situ Estimation of the Coefficient of Consolidation in Clays," *Canadian Geotechnical Journal*, 35, No. 1, 58-67.

Kim, Y.S., Lee, S.R., and Kim, Y.T. (1997) "Application of an Optimum Design Technique for Determining the Coefficient of Consolidation by Using Piezocone Test Data," *Computers and Geotechnics,* 27, No. 4, 277-293.

Kishida, H. and Uesugi, M. (1987) "Test of the Interface Between Sand and Steel in the Simple Shear Apparatus," *Géotechnique,* 37, No. 1, 45-52.

Koerner, R.M. (1998) Designing with Geosynthetics, 4th Ed., New Jersey, USA, Prentice Hall, 783 pp.

Koerner, R.M., Martin, J.P. and Koerner, G.R. (1986) "Shear Strength Parameters Between Geomembranes and Cohesive Soils," *Geotextiles and Geomembranes,* 4, No. 1, 21-30.

Konrad, J.-M. (1987) "Piezo-Friction-Cone Penetrometer Testing in Soft Clays," *Canadian Geotechnical Journal*, 24, No. 4, 645-652.

Kraft, L.M., Ray, R.P., and Kagawa, T. (1981) "Theoretical t-z Curves," *Journal of the Geotechnical Divisi*on, 107, GT11, 1543-1561.

Kuo C.Y., Frost, J.D., and Chameau, J.-L.A. (1998) "Image Analysis Determination of Stereology Based Fabric Tensors," *Géotechnique*, 48, No. 4, 515-525.

Kurup, P.U., Voyiadjis, G.Z., and Tumay, M.T. (1994) "Calibration Chamber Studies of Peizocone Test in Cohesive Soils," *Journal of Geotechnical Engineering,* 120, No. 1, 81-107.

Lee, S.W. (1998) "Influence of Surface Topography on Interface Strength and Counterface Soil Structure," *PhD Dissertation*, School of Civil and Environmental Engineering, Georgia Institute of Technology, Atlanta, 336 pp.

Lee, S.W., Frost, J.D., and Righter, G.K., (1998) "The Influence of Geomembrane Surface Roughness on Geomembrane-Geotextile Interface Strength," *Proceedings of the Sixth International Conference on Geosynthetics*, Atlanta, 1, 433-438.

Lehane, B.M. (1992) "Experimental Investigations of Pile Behaviour Using Instrumented Field Piles," *PhD Dissertation*, University of London (Imperial College), London, May, 615 pp.

Lehane, B.M. (1994) "The Development of Shaft Resistance on Displacement Piles in Clay," *Proceedings of the 13th International Conference on Soil Mechanics and Foundation Engineering*, New Delhi, 2, 473-476.

Lehane, B.M. (1999) "Piling Research in Belfast Soft Clay," *Ground Engineering*, March, 31-32.

Lehane, B.M. and Jardine, R.J. (1994) "Displacement Pile Behaviour in a Glacial Clay," *Canadian Geotechnical Journal*, 31, No. 1, 79-90.

Lehane, B.M. and Jardine, R.J. (1994) "Displacement-pile Behaviour in a Soft Marine Clay," *Canadian Geotechnical Journal*, 31, No. 2, 181-191.

Lehane, B.M., Jardine, R.J., Bond, A.J., and Frank, R. (1993) "Mechanisms of Shaft Friction in Sand from Instrumented Pile Tests," *Journal of Geotechnical Engineering*, 119, No. 1, 19-35.

Lemos, L.J. and Vaughan, P.R. (2000) "Clay-interface Shear Resistance," *Géotechnique,* 50, No. 1, 55-64.

Leroueil, S. and Hight, D.W. (2003) "Behaviour and Properties of Natural Soils and Soft Rocks," *Proceedings of the International Conference on the Characterisation and Engineering Properties of Natural Soils*, Tan et al. (eds.), Swets & Zeitlinger, 29-254.

Leroueil, S., Demers, D., Martel, G., Virely, D., and La Rochelle, P. (1995) "Practical Use of the Piezocone in Eastern Canada Clays," *Proceedings of the International Symposium on Cone Penetration Testing, CPT '95*, Linköping, Sweden, 2, 515-522.

Leroueil, S., Tavenas, F., Brucy, F., La Rochelle P., and Roy, M. (1979) "Behaviour of Destructured Natural Clays," *Journal of the Geotechnical Engineering Division*, 105, No. GT6, 759-778.

Levadoux, J.N. and Baligh, M.M. (1986) "Consolidation After Undrained Piezocone Penetration. I: Prediction," *Journal of Geotechnical Engineering,* 112, No. 7, 707-726.

Levy, N.H., Chung, S.F., Yeow, K., Almeida, M.S.S., and Randolph, M.F. (2002) "Characterization of Soft Soils for Deep Water Developments - Report on Laboratory Testing on Burswood Clay," *Report GEO:02270*, Centre for Offshore Foundation Systems, The University of Western Australia, September (Revised), 107 pp.

Li, M., and Gilbert, R.B. (1999) "Shear Strength of Textured Geomembranes and Nonwoven Geotextile Interfaces," *Proceedings of Geosynthetics '99*, Boston, MA, 1, 505-516.

Liao, T. (2005) "*Post Processing of Cone Penetration Data for Assessing Seismic Ground Hazards, with Application to the New Madrid Seismic Zone*," PhD Dissertation, Georgia Institute of Technology, May, 467 pp.

Löffelmann, F. (1989) "Theoretische und experimentelle Unterschungen zur Schüttgut-Wand-Wechselwirkung und zum Mischen und Entmischen von Granulaten," PhD Dissertation, Karlsruhe University.

Lunne, T., Robertson, P.K., and Powell, J.J.M. (1997) *Cone Penetration Testing in Geotechnical Practice*, Blackie Academic & Professional, New York, 312 pp.

Lupini, J.F., Skinner, A.E., and Vaughan, P.R. (1981) "The Drained Residual Strength of Cohesive Soils," *Géotechnique,* 31, No. 2, 181-213.

Massarsch, K.R. (1976) "Soil Movements Caused by Pile Driving in Clay," PhD Thesis, Royal Institute of Technology, Stockholm.

Matlock, H., and Foo, S.H.C. (1980) "Axial Analysis of Piles Using a Hysteretic and Degrading Soil Model," Institution of Civil Engineers (ICE), *Numerical Methods for Offshore Piling,* London, 127-133.

Mayne, P.W. (2001) "Stress-strain-strength-flow Parameters from Enhanced In-situ Tests," *Proceedings of the International Conference on In-Situ Measurement of Soil Properties & Case Histories, In-Situ 2001*, Bali, 27-48.

Mayne, P.W., and Rix. G.J. (1993) "G_{max} - q_c Relationships for Clays," *ASTM Geotechnical Testing Journal,* 16, No. 1, 54-60.

Mitchell, J.K. (1988) "New Developments in Penetration Tests and Equipment," *Proceedings of the International Symposium on Penetration Testing, ISOPT-1*, Orlando, 1, 245-261.

Mooney, M.A., Finno, R.J., and Viggiani, M.G. (1998) "A Unique Critical State for Sand?" *Journal of Geotechnical and Geoenvironmental Engineering,* 124, No. 11, 1100-1108.

Morgan, J.K. (1999) "Numerical Simulation of Granular Shear Zones Using the Distinct Element Method: 2. Effects of Particle Size Distribution and Interparticle Friction on Mechanical Behavior," *Journal of Geophysical Research* 104, No. B2, 2721-2732.

Mühlhaus, B.-B., and I. Vardoulakis (1987). "The Thickness of Shear Bands in Granular Materials," *Géotechnique*, 37, No. 3, 271-283.

Muhs, H. (1978) "50 Years of Deep Sounding with Static Penetrometers," *Berlin University*, Duetsche Forschungsgesellschaft fur Boden-Mechanik (Degebo), Mitteilungen, 34, 45-50.

Muromachi, T. (1981) "Cone Penetration Testing in Japan," *Proceedings of the ASCE National Convention: Cone Penetration Testing and Experience*, St. Louis, 49-75.

Oda, M. and Iwashita, K. (2000) "Study on Couple Stress and Shear Band Development in Granular Media based on Numerical Simulation Analysis," *International Journal of Engineering Science*, 38, 1713-1740.

Oda, M. and Kazama, H. (1998) "Microstructure of Shear Bands and Its Relation to the Mechanisms of Dilatancy and Failure of Dense Granular Soils," *Géotechnique,* 48, No. 4, 465-481.

Oda, M., Konishi, J., and Nemat-Nasser, S. (1982) "Experimental Micromechanical Evaluation of Strength of Granular Materials: Effects of Particle Rolling," *Mechanics of Materials,* 1, 269-283.

Oda, M., Takemura, T., and Takahashi, M. (2004) "Microstructure in Shear Band Observed by Microfocus X-ray Computed Tomography," *Géotechnique*, 54, No. 8, 539-542.

Ogilvy, J.A. (1991) "Numerical Simulation of Friction Between Contacting Rough Surfaces," *Journal of Physics D: Applied Physics,* 24, 2098-2109.

Oie, M.; Sateo, N.; Okuyama, Y.; Yoshida, Teru; Yoshida, Tetuya; Yamada, S.; and Tatsuoka, F. (2003) "Shear Banding Characteristics in Plane Strain Compression of Granular Materials," Proceedings of the 3rd International Symposium on Deformation Characteristics of Geomaterials, IS Lyon 03 (di Benedetto et al. editors), September, 597-606.

Okuyama, Y., Yoshida, T., Tatsuoka, F., Koseki, J., Uchimura, R., Sato, N., and Oie, M. (2003) "Shear Banding Characteristics of Granular Materials and Particle Size Effects on the Seismic Stability of Earth Structures," Proceedings of the 3rd International Symposium on Deformation Characteristics of Geomaterials, IS Lyon 03 (di Benedetto et al. editors), September, 607-616.

Olsen, R.S. and Malone, P.G. (1988) "Soil Classification and Site Characterization Using the Cone Penetrometer Test," *Proceedings of the International Symposium on Penetration Testing, ISOPT-1*, Orlando, 2, 887-893.

Ooi, L.H. and Carter, J.P. (1987) "A Constant Normal Stiffness, Direct Shear Device for Static and Cyclic Loading," *ASTM Geotechnical Testing Journal,* 10, No. 1, 3-12.

O'Neill, M.W. (2001) "Side Resistance in Piles and Drilled Shafts - The Thirty-Fourth Karl Terzaghi Lecture," *ASCE Journal of Geotechnical and Geoenvironmental Engineering*, 127, No. 1, 3-16.

O'Rourke, T.D., Druschel, S.J. and Netravali, A.N. (1990) "Shear Strength Characteristics of Sand-Polymer Interfaces," *Journal of Geotechnical Engineering*, 116, No. 3, 451-469.

Paikowsky, S.G. and Hart, L.J. (2000) "Development and Field Testing of Multiple Deployment Model Pile (MDMP), *FHWA Report 99-194*, June, 238 pp.

Paikowsky, S.G., Player, C.M., and Connors, P.J. (1995) "A Dual Interface Apparatus for Testing Unrestricted Friction of Soil Along Solid Surfaces," *ASTM Geotechnical Testing Journal*, 18, No. 2, 168-193.

Paikowsky, S.G. and Xi, F. (2000) "Particle Motion Tracking Utilizing a High-Resolution Digital CCD Camera," *ASTM Geotechnical Testing Journal*, 23, No. 1, 123-134.

Parez, L.A. (1974). "Static Penetrometer: The Importance of the Skin Friction Associated with the Point Resistance," *Proceedings of the 2nd European Symposium on Penetration Testing*, ESOPT-II, Amsterdam, 2, 293-299.

Peuchen, J., Adrichem, J., and Hefer, P.A. (2005) "Practice Notes on Push-in Penetrometers for Offshore Geotechnical Investigation," *Proceedings of the International Symposium - Frontiers in Offshore Geotechnics*, *ISFOG,* Perth, (in press).

Phillips, R. (1991) "Film Measurement Machine User Manual," *Cambridge University Technical Report*, CUED/D-Soils/TR 246.

Plantema, G. (1948) "Construction and Method of Operating a New Deep Sounding Apparatus," *Proceedings of the 2nd International Conference on Soil Mechanics and Foundation Engineering*, Rotterdam, 1, 277-279.

Porcino, D., Fioravante, V., Ghionna, V.N., and Pedroni, S. (2003) "Interface Behavior of Sands from Constant Normal Stiffness Direct Shear Tests," *ASTM Geotechnical Testing Journal*, 26, No. 3, 289-301.

Potts, D.M., Dounias, G.T., and Vaughan, P.R. (1987) "Finite Element Analysis of the Direct Shear Box Test," *Géotechnique*, 37, No. 1, 11-23.

Potyondy, J.G. (1961) "Skin Friction Between Various Soils and Construction Materials," *Géotechnique*, 11, No. 4, 339-353.

Poulos, H.G. (1981) "Some Aspects of Skin Friction of Piles in Clay Under Cyclic Loading," *Geotechnical Engineering*, 12, No. 1, 1-17.

Poulos, H.G. and Chan, K.F. (1988) "Tests on Model Instrumented Piles in Calcareous Soil," *Proceedings of the International Conference on Engineering for Calcareous Sediments*, Perth, 1, 245-253.

Poulos, H.G., Randolph, M.F., and Semple, R.M. (1988) "Evaluation of Pile Friction From Conductor Tests, *Proceedings of the International Conference on Engineering for Calcareous Sediments*, Perth, 2, 599-605.

Ramiah, B.K., Dayalu, N.K., and Purushothamaraj, P. (1970) "Influence of Chemicals on Residual Strength Of Soils," *Soils and Foundations*, 10, No. 1, 25-36.

Ramsey, N., Jardine, R., Lehane, B. and Ridley, A. (1998) "A Review of Soil-Steel Interface Testing with the Ring Shear Apparatus," *Proceedings of the International Conference on Offshore Site Investigation and Foundation Behaviour – New Frontiers,* 237-256.

Randolph, M. F. (2000) "Pile-soil interaction for dynamic and static loading, *Application of Stress-Wave Theory to Piles*," Brazil, Balkema, Appendix, 3-11.

Randolph, M.F. (2003) "Science and Empiricism in Pile Foundation Design," *Géotechnique*, 53, No. 10, 847-875.

Randolph, M.F. (2004) "Characterisation of Soft Sediments for Offshore Applications," *Proceedings of the 2nd International Conference on International Site Characterisation, ISC'2*, Porto, 1, 209-232.

Randolph, M.F., and Hope, S. (2004) "Effect of Cone Velocity on Cone Resistance and Excess Pore Pressures," *Proceedings of the International Symposium on Engineering Practice and Performance in Soft Soils*, Osaka.

Randolph, M.F. and Wroth, C.P. (1979) "An Analytical Solution for the Consolidation Around a Driven Pile," *International Journal for Numerical and Analytical Methods in Geomechanics,* 3, No. 3, 217-229.

Randolph, M.F. and Wroth, C.P. (1981) "Application of the Failure State in Undrained Simple Shear to the Shaft Capacity of Driven Piles," *Géotechnique*, 31, No. 1, 143-157.

Rice, J.R. and Rudnicki, J.W. (1980) "A Note of Some Features of the Theory of Localization of Deformation," *International Journal of Soil Structures*, 16, 597-605.

Richardson, G.N., and Theil, R.S., (2001) "Interface Shear Strength: Part I - Geomembrane Considerations," *Geosynthetic Fabric Review*, June/July, 14-19.

Robertson, P.K. (1990) "Soil Classification Using the Cone Penetration Test," *Canadian Geotechnical Journal*, 27, No. 1, 151-158.

Robertson, P.K., Campanella, R.G., Gillespie, D., and Greig, J. (1986) "Use of Piezometer Cone Data," *Proceedings of the ASCE Specialty Conference In Situ '86: Use of In Situ Tests in Geotechnical Engineering*, Blacksburg, 1263-1280.

Robertson, P.K., Sully, J.P., Woeller, D.J., Lunne, T., Powell, J.J.M., and Gillespie, D.G. (1992) "Estimating the Coefficient of Consolidation from Piezocone Tests," *Canadian Geotechnical Journal,* 29, No. 4, 539-550.

Robertson, P.K., Woeller, D.J., and Gillespie, D. (1990) "Evaluation of Excess Pore Pressures and Drainage Conditions Around Driven Piles Using the Cone Penetration Test with Pore Pressure Measurements," *Canadian Geotechnical Journal*, 27, No. 2, 249-254.

Roscoe, K.H. (1970). "The Influence of Strains in Soil Mechanics," *Géotechnique*, 20, No. 2, 129-170.

Rothenburg, L. and Bathurst, R.J. (1992) "Micromechanical Features of Idealized Granular Assemblies with Planar Particles," *Géotechnique*, 42, No. 4, 79-95.

Roy, M., Blanchet, R., Tavenas, F. and La Rochelle, P. (1981) "Behavior of a Sensitive Clay during Pile Driving," *Canadian Geotechnical Journal*, 18, No. 1, 67-85.

Roy, M., Michaud, D., Tavenas, F.A., Leroueil, S., and La Rochelle, P. (1974) "The Interpretation of Static Cone Penetration Tests in Sensitive Clays," *Proceedings of the 1st European Symposium on Penetration Testing - ESOPT*, Stockholm, 2.2, 323-330.

Roy, M., Tremblay, M., Tavenas, F., and La Rochelle, P. (1980) "Induced Pore Pressures in Static Penetration Tests in Sensitive Clay," *Proceedings of the 33rd Canadian Geotechnical Conference*, Calgary, Preprint Volume, 11.3.1 to 11.3.13.

Roy, M., Tremblay, M., Tavenas, F., and La Rochelle, P. (1982) "Development of Pore Pressures in Quasi-Static Penetration Tests in Sensitive Clay," *Canadian Geotechnical Journal*, 19, No. 2, 124-138.

Rudnicki, J.W. and Rice, J.R. (1975) "Conditions for Localization of the Deformation in Pressure Sensitive Materials," *Journal of Mechanical Physics of Solids*, 23, 371-394.

Rudnicki, J.W. and Rice, J.R. (1980) "A Note of Some Features of the Theory of Localization of Deformation," *International Journal of Solids and Structures*, 16, 597-605.

Saada, A.S., Liang, L., Figueroa, J.L., and Cope, C.T. (1999) "Bifurcation and Shear Band Propagation in Sands," *Géotechnique*, 49, No. 3, 367-385.

Sagaseta, C. and Houlsby, G.T. (1988) "Elastic-plastic Incompressible Flow Around an Infinite Cone," *Proceedings of the International Symposium on Penetration Testing, ISOPT-1*, Orlando, 2, 933-938.

Sagaseta, C., Whittle, A.J., and Santagata, M. (1997) "Deformation Analysis of Shallow Penetration in Clay," *International Journal for Numerical and Analytical Methods in Geomechanics,* 21, No. 10, 687-719.

Salgado, R., Mitchell, J.K., and Jamiolkowski, M. (1997) "Cavity Expansion and Penetration Resistance in Sand." *ASCE Journal of Geotechnical and Geoenvironmental Engineering*, 123, No. 4, 344-354.

Sandbaekken, G., Berre, T., and Lacasse, S. (1986) "Oedometer Testing at the Norwegian Geotechnical Institute," *Consolidation of Soils: Testing and Evaluation, ASTM STP 892,* 329-353.

Sanglerat, G. (1972) "*The Penetrometer and Soil Exploration*," Elsevier, Amsterdam, 464 pp.

Santamarina, J.C. (2002) "Soil Behavior at the Microscale: Particle Forces," *Internal Report, Georgia Institute of Technology*, 30 pp.

Santamarina, J.C. and Cho, G.C. (2004) "Soil Behavior: The Role of Particle Shape," *Proceedings of the Skempton Conference,* London, 14 pp.

Saussus, D.R., Frost, J.D., and DeJong, J.T. (2005) "Statistical Analysis of Friction Sleeve Length Effects on Soil Classification," *International Journal for Numerical and Analytical Methods in Geomechanics*, 27, No. 12, 1257-1278.

Scarpelli, G. and Wood, D. M. (1982). "Experimental Observations of Shear Band Patterns in Direct Shear Tests," Proceedings of the IUTAM Conference on Deformation and Failure of Granular Materials, Delft, 473-484. Rotterdam: Balkema.

Schmertmann, J.H. (1974) "Penetration Pore Pressure Effects on Quasi-Static Cone Bearing, q_c ," *Proceedings of the European Symposium on Penetration Testing*, ESOPT, Stockholm, 2.2, 345-351.

Schneider, J.A., Randolph, M.F., and Chung, S.F. (2004) "Characterization of Soft Soils for Deep Water Developments - Variable Rate Penetration Tests at Burswood Site," *Report GEO:03305*, Centre for Offshore Foundation Systems, The University of Western Australia, April (Revised), 57 pp.

Seed, R.B. and Boulanger, R.W. (1991) "Smooth HDPE-Clay Liner Interface Shear Strengths: Compaction Effects," *Journal of Geotechnical Engineering,* 117, No. 4, 686-693.

Sharma, S.S. (2004) "Characterisation of Cyclic Behaviour of Calcite Cemented Calcareous Soils," *PhD Dissertation*, University of Western Australia, February, pp. 445.

Sills, G.C., May, R.E., and Henderson, T. (1988a) "Piezocone Measurements with Four Pore Pressure Positions," *Penetration Testing in the UK*, Thomas Telford, 247-250.

Sills, G.C., Almeida, M.S.S., and Danzinger, F.A.B. (1988b) "Coefficient of Consolidation from Piezocone Dissipation Tests in a Very Soft Clay," *Proceedings of the International Symposium on Penetration Testing, ISOPT-1*, Orlando, 2, 967-974.

Song, C.R., Voyiadjis, G.Z., and Tumay, M.T. (1999) "Determination of Permeability of Soils Using the Multiple Piezo-Element Penetrometer," *International Journal for Numerical and Analytical Methods in Geomechanics*, 23, No. 13, 1609-1629.

Stark, T.D. (1995) "Measurement of Drained Residual Strength of Overconsolidated Clays," *Transportation Research Record, No. 1479*, 26-34.

Stark, T.D., Williamson, T.A., Eid, H.T., 1996. "HDPE Geomembrane/Geotextile Interface Shear Strength," *Journal of Geotechnical Engineering*, 122, No. 3, 197-203.

Sully, J.P. and Campanella, R.G. (1991) "Effect of Lateral Stress on CPT Penetration Pore Pressures," *Journal of Geotechnical Engineering,* 117, No. 4, 1082-1088.

Sully, J.P., Campanella, R.G., and Robertson, P.K. (1988a) "Overconsolidation Ratio of Clays from Penetration Pore Water Pressures," *Journal of Geotechnical Engineering,* 114, No. 2, 209-215.

Sun, D.A., Matsuoka, H., Morichi, K., Tanaka, Y, and Yamamoto, H. (2003) "Frictional Behavior Between Clay and Steel by Direct Shear Type Apparatus," *Proceedings of the International Symposium on Deformation Characteristics in Geomaterials*, Lyon, 239-245.

Tabucanon, J.T., Airey, D.W., and Poulos, H.G. (1995) "Pile Skin Friction in Sands from Constant Normal Stiffness Tests," *ASTM Geotechnical Testing Journal,* 18, No. 3, 350-364.

Tanaka, H. (1995) "National Report – the Current State of CPT in Japan," *Proceedings of the International Symposium on Cone Penetration Testing, CPT '95*, Linköping, Sweden, 1, 115-124.

Tavenas, F.A., Chapeau, C., LaRochelle, P., and Roy, M. (1974) "Immediate Settlement of Three Test Embankments on Champlain Clay," Canadian Geotechnical Journal, 11, No. 1, 109-141.

Taylor R.N., Grant R.J., Robson S. and Kuwano J. (1998) "An Image Analysis System for Determining Plane and 3-D Displacements in Soil Models," *Proceedings of Centrifuge '98*, Balkema, Rotterdam, 73-78.

Teh, C. I. (1987) "An Analytical Study of the Cone Penetration Test," *PhD Dissertation*, Oxford University, London, 254 pp.

Teh, C. I., and Houlsby, G. T. (1991). ''An Analytical Study of the Cone Penetration Test in Clay,'' *Géotechnique*, 41, No. 1, 17–34.

Tejchman, J. (2000) "Behavior of Granular Bodies in Induced Shear Zones," *Granular Matter*, 2, 77-96.

Tejchman, J. and Bauer, E. (2004) "Effect of Cyclic Shearing on Shear Localisation in Granular Bodies," *Granular Matter*, 5, 201-212.

Tejchman, J. and Wu, W. (1995) "Experimental and Numerical Study of Sand-Steel Interfaces," *International Journal for Numerical and Analytical Methods in Geomechanics,* 19, No. 8, 513-536.

Tika-Vassilikos, T. (1991) "Clay-on-Steel Ring Shear Tests and Their Implications for Displacment Piles," *ASTM Geotechnical Testing Journal*, 14, No. 4, 457-463.

Tika, T.E. and Hutchinson, J.N. (1999) "Ring Shear Tests on Soil from the Vaiont Landslide Slip Surface," *Géotechnique,* 49, No. 1, 59-74.

Tika, T.E., Vaughan, P.R., and Lemos, L.J. (1996) "Fast shearing of pre-existing shear zones in soil," *Géotechnique,* 46, No. 2, 197-233.

Ting, J.N., Meachum, L.R., and Rowell, J.D. (1995) "Effect of Particle Shape on the Strength and Deformation Mechanisms of Ellipse-Shaped Granular Assemblages," *Engineering Computation*, 12, 99-108.

Torstensson, B.A. (1975) "Pore Pressure Sounding Instrument," *Proceedings of the ASCE Specialty Conference on In Situ Measurement of Soil Properties*, Raleigh, NC, 2, 48-54.

Torstensson, B.A., Jacobson, A.B., and Widmark. (1977) "The Pore Pressure Probe," *Fjellsprengningsteknikk – bergmekanikk – geoteknikk*, Oslo, 34.1-34.15.

Totani, G., Marchetti, S., Calabrese, M., and Monaco, P. (1994) "Field Studies of an Instrumented Full-Scale Pile in Clay," *Proceedings of the 13th International Conference on Soil Mechanics and Foundation Engineering*, New Delhi, 2, 695-698.

Towhata, I. and Lin, C.-E. (2003) "Microscopic Observation of Shear Behavior of Granular Material," *Proceedings of the International Symposium on Deformation Characteristics in Geomaterials*, Lyon, 1, 113-118.

Triantafyllidis, N. and Aifantis, E.C. (1986) "A Gradient Approach to Localization of Deformation, I. Hyperelastic materials," *Journal of Elasticity*, 16, 225-237.

Tsubakihara, Y. and Kishida, H. (1993) "Frictional Behaviour Between Normally Consolidated Clay and Steel by Two Direct Shear Type Apparatuses," *Soils and Foundations*, 33, No. 2, 1-13.

Tsubakihara, Y., Kishida, H., and Nishiyama, T. (1993) "Friction Between Cohesive Soils and Steel," *Soils and Foundations*, 33, No. 2, 145-146.

Tsuchiya, H., Muromachi, T., Sakai, Y., and Iwasaki, K. (1988) "A Soil Classification Method Using All Three Components of CPTU Data," *Proceedings of the International Symposium on Penetration Testing, ISOPT-1*, Orlando, 2, 1021-1026.

Tumay, M.T., Bogges, R.L., and Acar, Y. (1981) "Subsurface Investigation with Piezo-Cone Penetrometer," *Proceedings of the ASCE National Convention: Cone Penetration Testing and Experience*, St. Louis, 434-455.

Uesugi, M. & Kishida, H. (1986a) "Influential Factors of Friction Between Steel and Dry Sands," *Soils and Foundations*, 26, No. 2, 33-46.

Uesugi, M. & Kishida, H. (1986b) "Frictional Resistance at Yield Between Dry Sand and Mild Steel," *Soils and Foundations*, 26, No. 4, 139-149.

Uesugi, M., Kishida, H. and Tsubakihara, Y. (1988) "Behavior of Sand Particles in Sand-Steel Friction," *Soils and Foundations*, 28, No. 1, 107-118.

Uesugi, M., Kishida, H. and Tsubakihara, Y. (1989) "Friction Between Sand and Steel Under Repeated Loading," *Soils and Foundations,* 29, No. 3, 127-137.

Uesugi M., Kishida, H., and Uchikawa, Y. (1990) "Friction Between Dry Sand and Concrete Under Monotonic and Repeated Loading," *Soils and Foundations*, 30, No. 1, 115-128.

Vaid, Y.P. and Rinne, N. (1995) "Geomembrane Coefficients of Interface Friction," *Geosynthetics International*, 2, No. 1, 309-325.

van Deen J.K., Greeuw, G., van den Hondel, R., van Staveren, Hoefsloot, F.J.M., and Vanhout, B. (1999) "Horizontal CPTs for Reconnaissance Before the TBM Front," *Proceedings of the 12th European Conference on Geotechnical Engineering for Transportation Infrastructure,* Amsterdam, 2023-2030.

Vardoulakis, I. (1978) "Equilibrium Bifurcation on Granular Earth Bodies," *Advances in Analysis of Geotechnical Instabilities*, University of Waterloo Press, SM Study No. 13, Paper 3, 65-120.

Vardoulakis, I. (1980) "Shear Band Inclination and Shear Modulus in Biaxial Tests," *International Journal for Numerical and Analytical Methods in Geomechanics* 4, No. 2, 103-119.

Vardoulakis, I. (1989) “Shear Banding and Liquefaction in Granular Materials on the Basis of a Cosserat Continuum Theory,” *Ingenieur Archiv* 59, 106-113.

Vardoulakis, I. and Aifantis, E.C. (1991) “A Gradient Flow Theory of Plasticity for Granular Materials,” *Acta Mechanica* 87, 197-217.

Vardoulakis, I. and Graf, B. (1985) “Calibration of Constitutive Models for Granular Materials Using Data from Biaxial Experiments,” *Géotechnique*, 35, No. 3, 299-317.

Vardoulakis, I., Graf, B., and Hettler, A. (1985) “Shear Band Formation in Fine Grained Sand,” *Proceedings of the 5th International Conference on Numerical Methods in Geomechanics*, Nagoya 1, 517-521.

Vardoulakis, I., Goldscheider, M., and Gudehus, G. (1978) “Formation of Shear Bands as a Bifurcation Problem,” *International Journal for Numerical and Analytical Methods in Geomechanics,* 2, No. 2, 99-128.

Vardoulakis, I. and Sulem, J. (1995) *Bifurcation Analysis in Geomechanics*, Blackie Academic & Professional, Glasgow, Poland, 462 p.

Vardoulakis, I. and Unterreiner, P. (1995) “Interfacial Localisation in Simple Shear Tests on a Granular Medium Modeled as a Cosserat Continuum,” *Mechanics of Geomaterial Interfaces*, Selvadurai, A.P.S. and Boulon M.J. (Eds.), 487-512.

Vermeer, P.A. (1990) “The Orientation of Shear Bands in Biaxial Tests,” *Géotechnique,* 40, No. 2, 223-236.

Vermeiden, J. (1948) “Improved Sounding Apparatus as Developed in Holland Since 1936,” *Proceedings of the 2nd International Conference on Soil Mechanics and Foundation Engineering*, Rotterdam, 1, 280-287.

Vertek-Applied Research Associates (200) *DataPack 2000 User’s Manual*.

Vesic, A. S. (1972) "Expansion of Cavities in Infinite Soil Mass," *Journal of the Soil Mechanics and Foundations Division,* 98, No. 3, 265-289.

Villard, P. (1996) “Modeling of Interface Problems by the Finite Element Method with Considerable Displacements,” *Computers and Geotechnics,* 19, No. 1, 23-45.

Virely, D., La Rochelle, P., and Leroueil, S. (1995) “The Development of the Laval Piezocone,” *Proceedings of the International Symposium on Cone Penetration Testing, CPT ’95*, Linköping, Sweden, 2, 117-122.

Vlasblom, A. (1985) “The Electrical Penetrometer; a Historical Account of Its Development,” *LGM Mededelingen*, Part XXII, 92 pp.

Vucetic, M., Lanzo, G., and Doroudian, M. (1998) "Damping at Small Strains in Cyclic Simple Shear Test," *Journal of Geotechnical and Geoenvironmental Engineering,* 124, No. 7, 585-594.

Vuong, B., Donald, I.B., and Parkin, A.K. (1988) "Some Aspects of the Design of a Friction Cone Penetrometer." *Proceedings of the 5th Australia-New Zealand Conference on Geomechanics*, 198-201.

Wagner, J.D., Wagner, D.A., and Randolph, M.F. (1989) "Pipe Penetration in Cohesive Soil," *Géotechnique,* 39, No. 2, 213-229.

Ward, H.C. (1999) *Rough Surfaces*, Thomas, T.R., Ed., Longman, London, 278 pp.

Wasti, Y. and Ozduzgun, Z.B. (2001) "Geomembrane-Geotextile Interface Shear Properties as Determined by Inclined Board and Direct Shear Tests," *Geotextiles and Geomembranes,* 19, No. 1, 45-57.

Wei, L., Tumay, M.T., and Abu-Farsakh, M.Y. (2005) "Field Testing of Inclined Cone Penetration," *ASTM Geotechnical Testing Journal*, 28, No. 1, 31-41.

Wissa, A.E.Z., Martin, R.T., and Garlanger, J.E. (1975) "The Piezometer Probe," *Proceedings of the ASCE Specialty Conference on In Situ Measurement of Soil Properties*, Raleigh, NC, 1, 536-545.

White, D.J. (2002) "An Investigation into the Behavior of Pressed-in Piles," *PhD Dissertation*, Cambridge University, 384 p.

White, D.J. (2005) "A General Framework for Shaft Resistance on Displacement Piles in Sand," *Proceedings of the International Symposium - Frontiers in Offshore Geotechnics, ISFOG,* Perth, (in press).

White, D.J., Take, W.A., and Bolton, M.D. (2003) "Soil Deformation Measurement Using Particle Image Velocimetry (PIV) and Photogrammetry," *Géotechnique*, 53, No. 7, 619-631.

White, D.J., Take, W.A., Bolton, M.D., and Munachen, S.E. (2001) "A Deformation Measuring System for Geotechnical Testing based on Digital Imaging, Close Range Photogrammetry and PIV Image Analysis," *Proceedings of the 15th International Conference on Soil Mechanics and Geotechnical Engineering*, Istanbul, 539-542.

Whittle, A.J., Sutabutr, T., Germaine, J.T., and Varney, A. (2001) "Prediction and Interpretation of Pore Pressure Dissipation for a Tapered Piezoprobe," *Géotechnique,* 51, No. 7, 601-617.

Williams, N.D. and Houlihan, M. (1986) "Evaluation of Friction Coefficients Between Geomembranes, Geotextiles, and Related Products," *Proceedings of the Third International Conference on Geotextiles*, Vienna, 891-896.

Yamakawa, Y., Ikeda, K., Terada, K., and Torii, K. (2003) "Bifurication Analysis on Soil Specimens Exhibiting Diffuse Deformation Modes and Localized Slip Planes," *Proceedings of the International Symposium on Deformation Characteristics in Geomaterials*, Lyon, 1035-1042.

Yoshimi, Y. and Kishida, T. (1981a) "A Ring Torsion Apparatus for Evaluating Friction Between Soil and Metal Surfaces," *ASTM Geotechnical Testing Journal*, 4, No. 4, 145-152.

Yoshimi, Y. and Kishida, T. (1981b) "Friction Between Sand and Metal Surfaces," *Proceedings of the 10th International Conference on Soil Mechanics and Foundation Engineering*, Stockholm, 1, 831-834.

Yoshida, T. and Tatsuoka, F. (1997) "Deformation Property of Shear Band in Sand Subjected to Plane Strain Compression and its Relation to Particle Characteristics," *Proceedings of the 14th International Conference on Soil Mechanics and Foundation Engineering*, Hamburg, 1, 237-240.

Yoshida, T., Tatsuoka, F., and Siddiquee, M.S. (1994) "Shear Banding in Sands Observed in Plane Strain Compression," In: *Localisation and Bifurcation Theory for Soils and Rocks*, Chambon, R., Desrues, J., and Vardoulakis, I. (Eds.), 165-181. Rotterdam: Balkema.

Yu, H.S., Herrmann, L.R., and Boulanger, R.W. (2000) "Analysis of Steady Cone Penetration in Clay," *Journal of Geotechnical and Geoenvironmental Engineering*, 126, No. 7, 594-605.

Yu. H.S. and Houlsby, G.T. (1991) "Finite Cavity Expansion in Dilatant Soils: Loading Analysis," *Géotechnique,* 41, No. 2, 173-183.

Yu, H. S. and Mitchell, J. K. (1998) ''Analysis of Cone Resistance: Review of Methods,'' *ASCE Journal of Geotechnical and Geoenvironmental Engineering*, 124, No. 2, 140–149.

Zaman, M. and Alvappillai, A. (1995) "Soil-Structure Interfaces: Experimental Aspects," *Mechanics of Geomaterial Interfaces*, Selvadurai, A.P.S. and Boulon M.J. (Eds.), 487-512.

Zettler, T.E. (1999) "Operational Induced Changes in Geomembrane Surface Topography," M.S. Thesis, School of Civil and Environmental Engineering, Georgia Institute of Technology, Atlanta, GA, USA, 264 pp.

Zettler, T.E., Frost, J.D., and DeJong, J.T. (2000) "Shear-Induced Changes in Geomembrane Surface Topography," *Geosynthetics International*, 7, No. 3, 243-267.

Zuidberg, H.M. (1988) "Piezocone Penetration Testing – Probe Development," *Proceedings of the International Symposium on Penetration Testing, ISOPT-1*, Orlando, Specialty Session No. 13.

Zuidberg, H.M., Schaap, L.H.J., and Beringen, F.L. (1982) "A Penetrometer for Simultaneous Measurement of Cone Resistance, Sleeve Friction, and Dynamic Pore Pressure," *Proceedings of the 2nd European Symposium on Penetration Testing*, ESOPT-II, Amsterdam, 2, 963-970.

APPENDIX

PLOTS OF MFA AND MPFA SOUNDINGS COMPLETED IN THE CURRENT STUDY

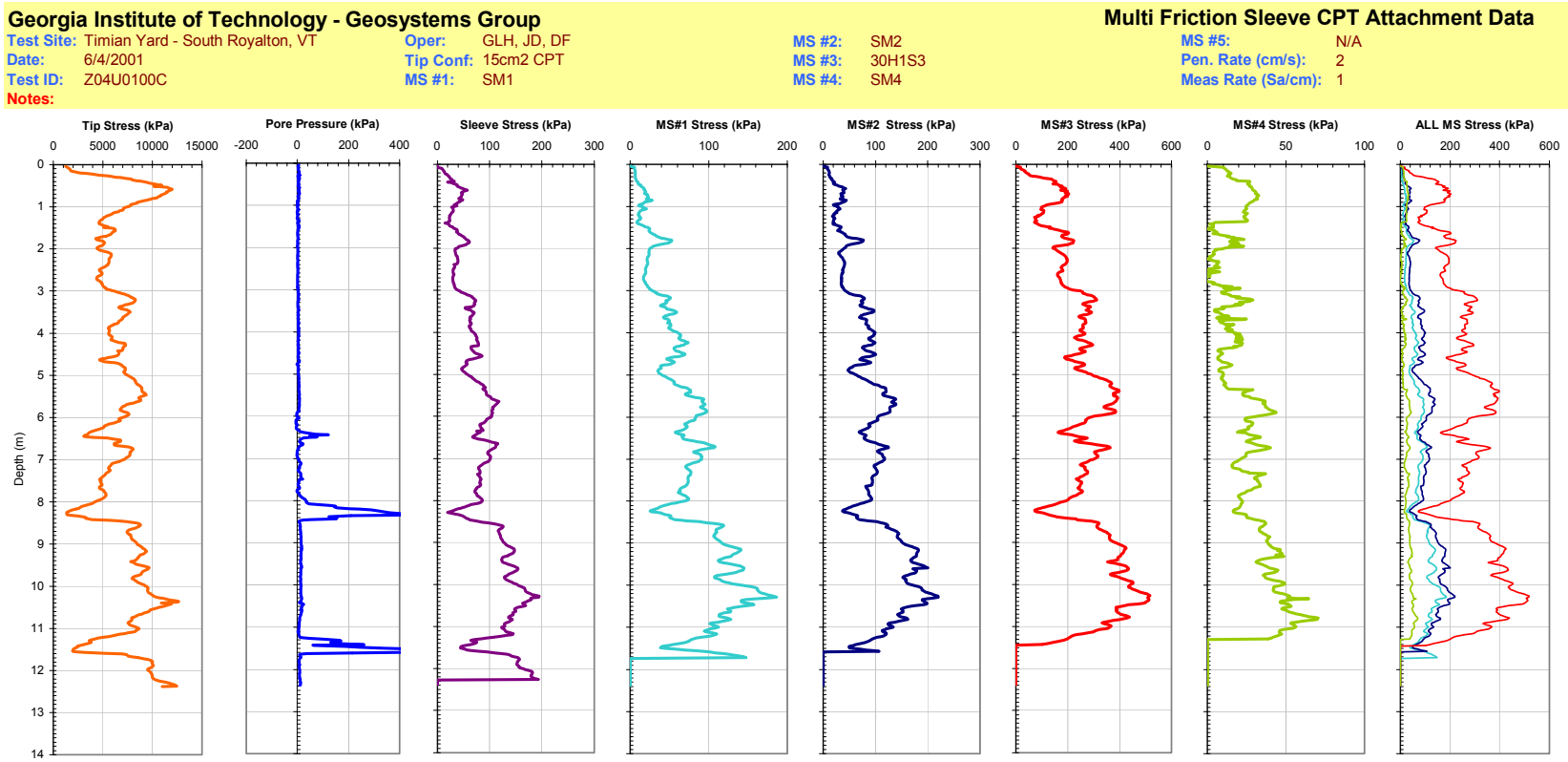

Figure A-1. Plot of CPTU-MFA Sensor Traces from Sounding MFA_40 at the SRVT Site.

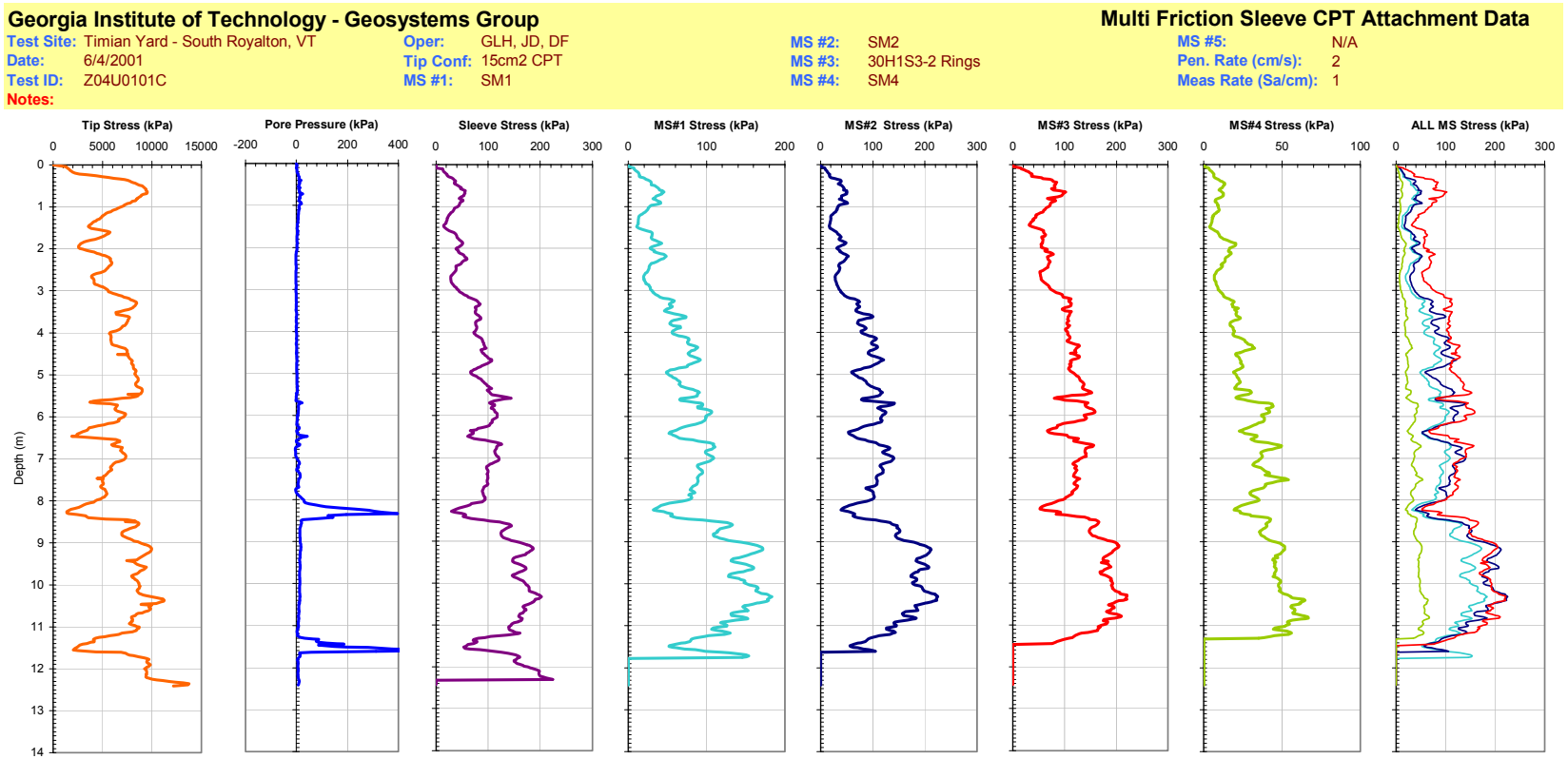

Figure A-2. Plot of CPTU-MFA Sensor Traces from Sounding MFA_41 at the SRVT Site.

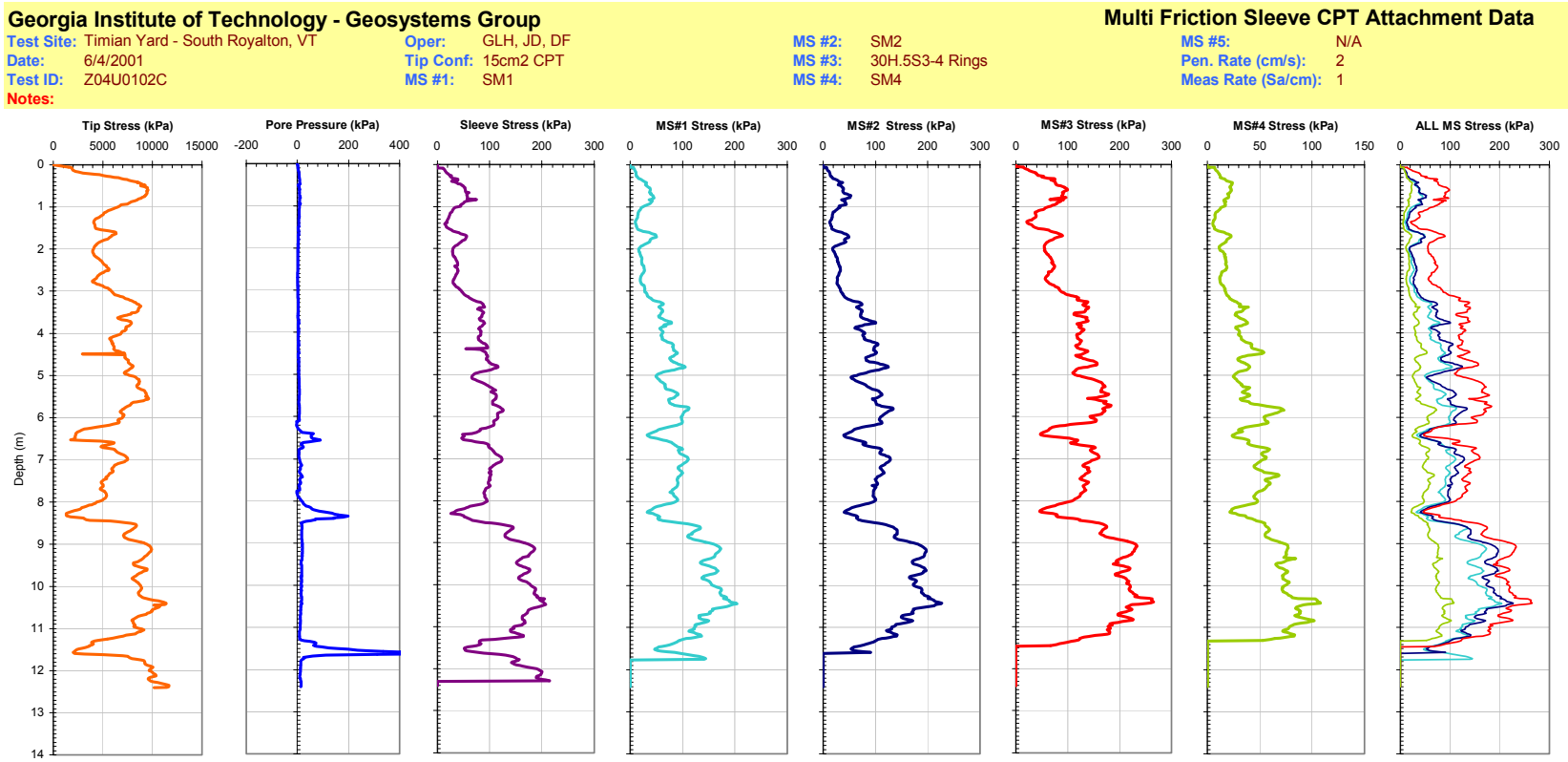

Figure A-3. Plot of CPTU-MFA Sensor Traces from Sounding MFA_42 at the SRVT Site.

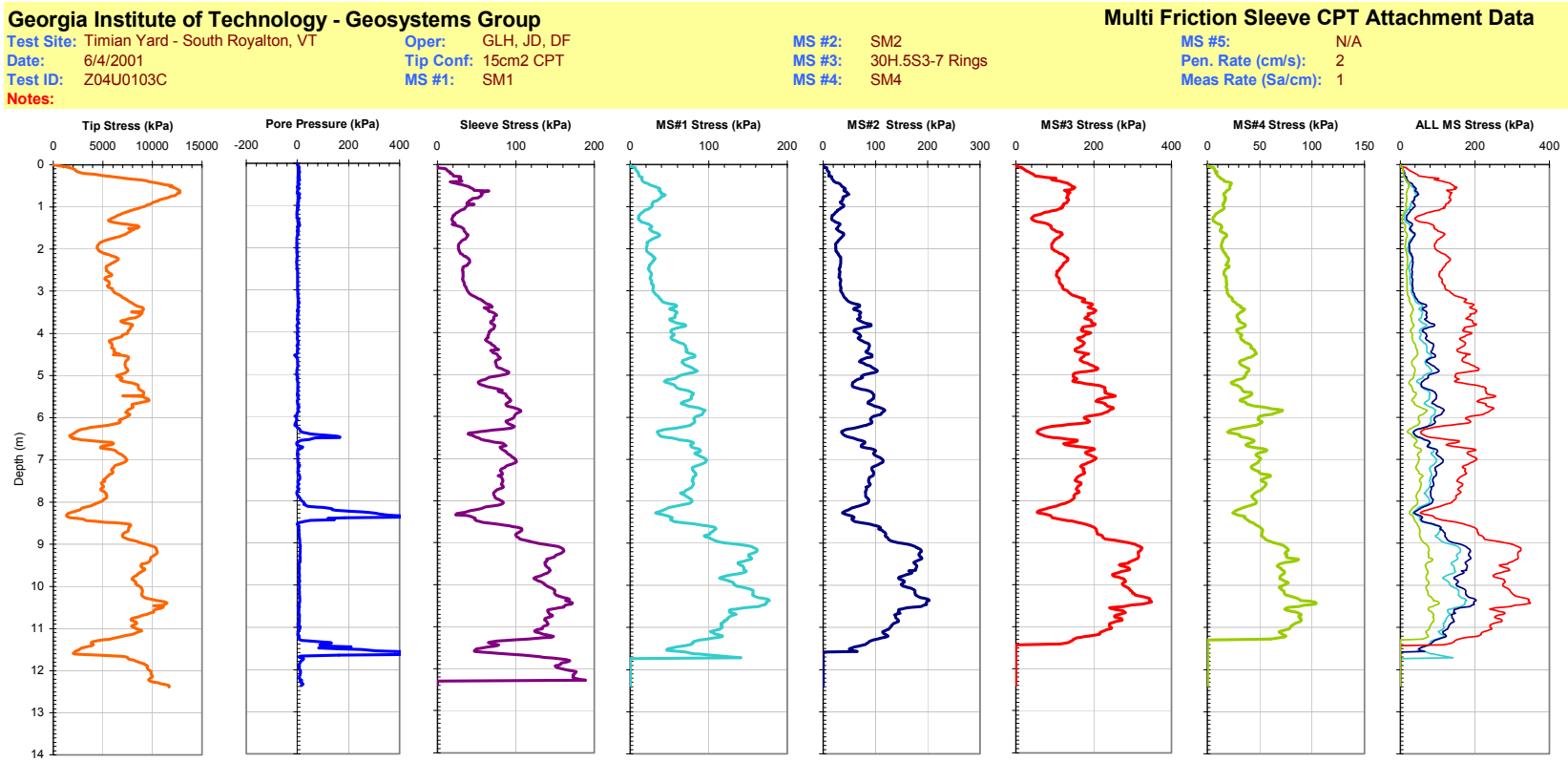

Figure A-4. Plot of CPTU-MFA Sensor Traces from Sounding MFA_43 at the SRVT Site.

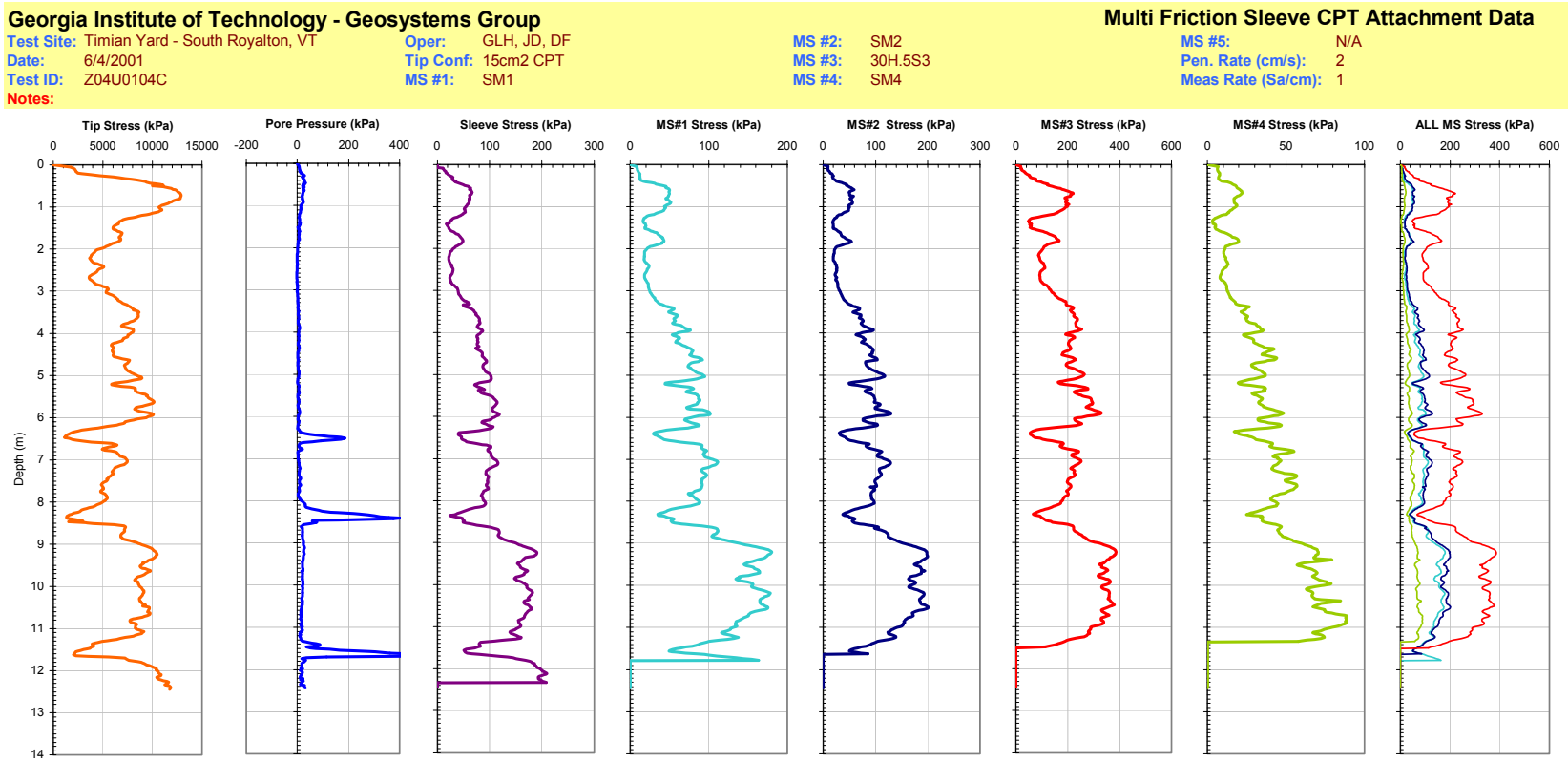

Figure A-5. Plot of CPTU-MFA Sensor Traces from Sounding MFA_44 at the SRVT Site.

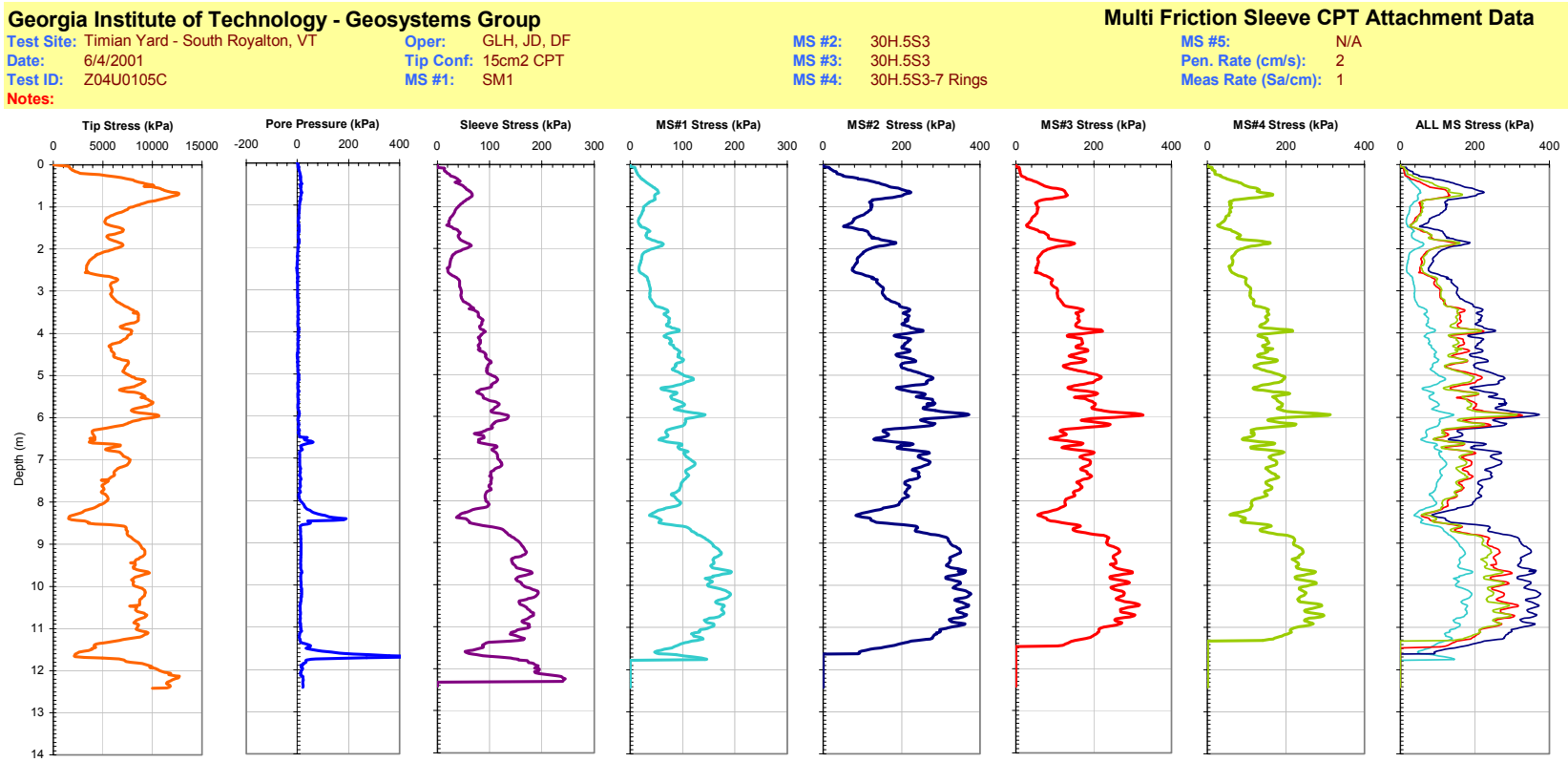

Figure A-6. Plot of CPTU-MFA Sensor Traces from Sounding MFA_45 at the SRVT Site.

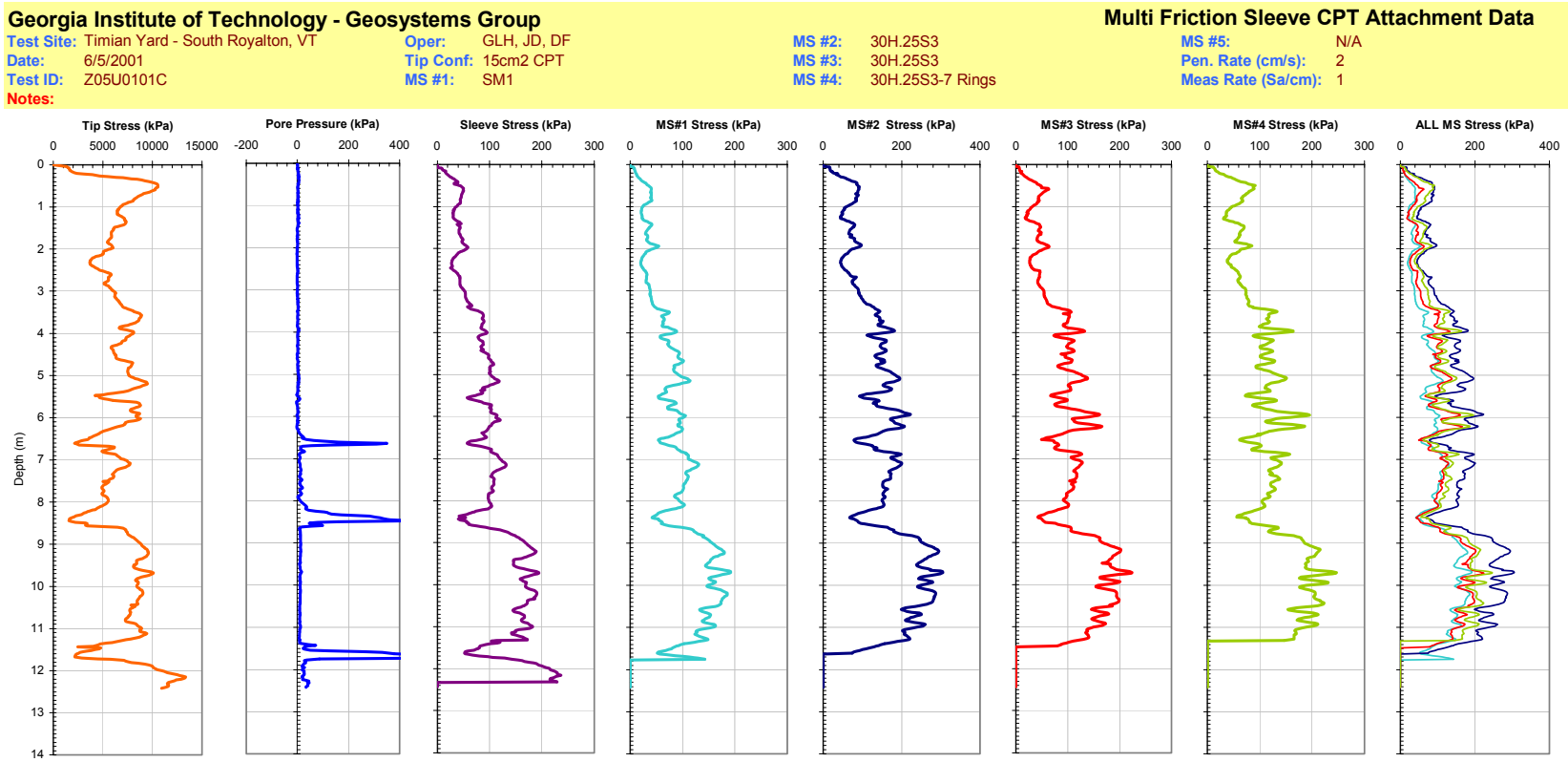

Figure A-7. Plot of CPTU-MFA Sensor Traces from Sounding MFA_46 at the SRVT Site.

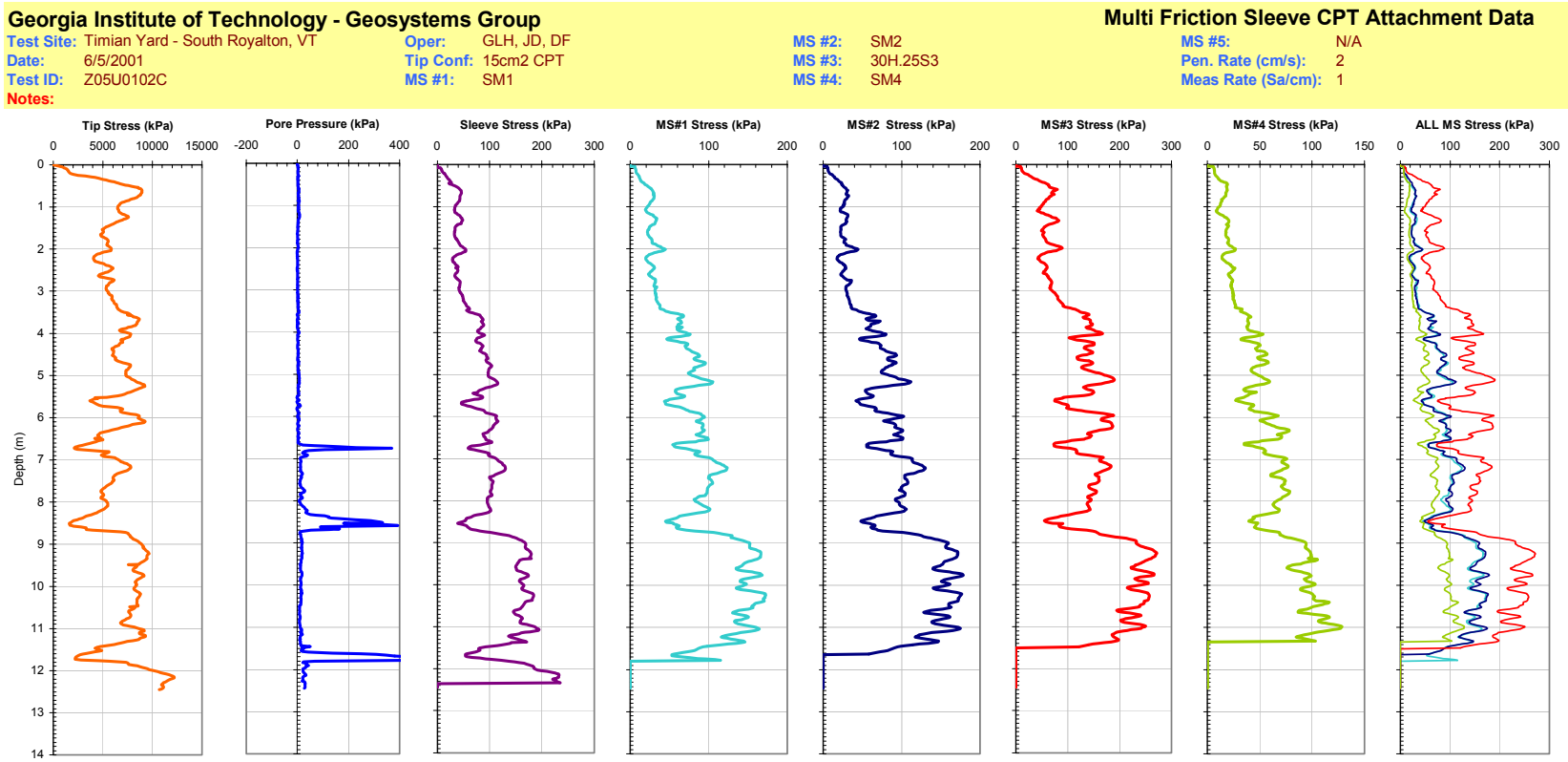

Figure A-8. Plot of CPTU-MFA Sensor Traces from Sounding MFA_47 at the SRVT Site.

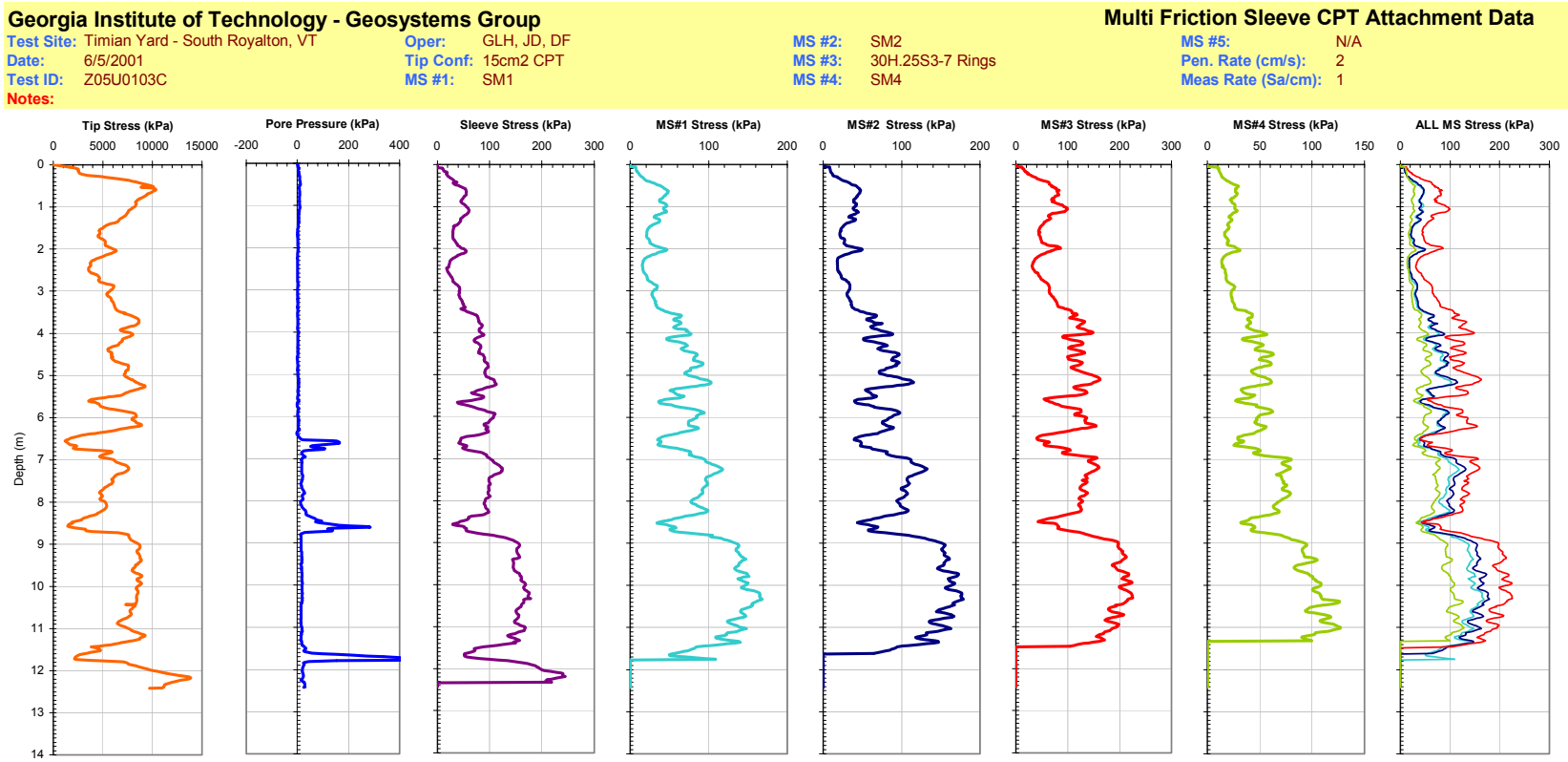

Figure A-9. Plot of CPTU-MFA Sensor Traces from Sounding MFA_48 at the SRVT Site.

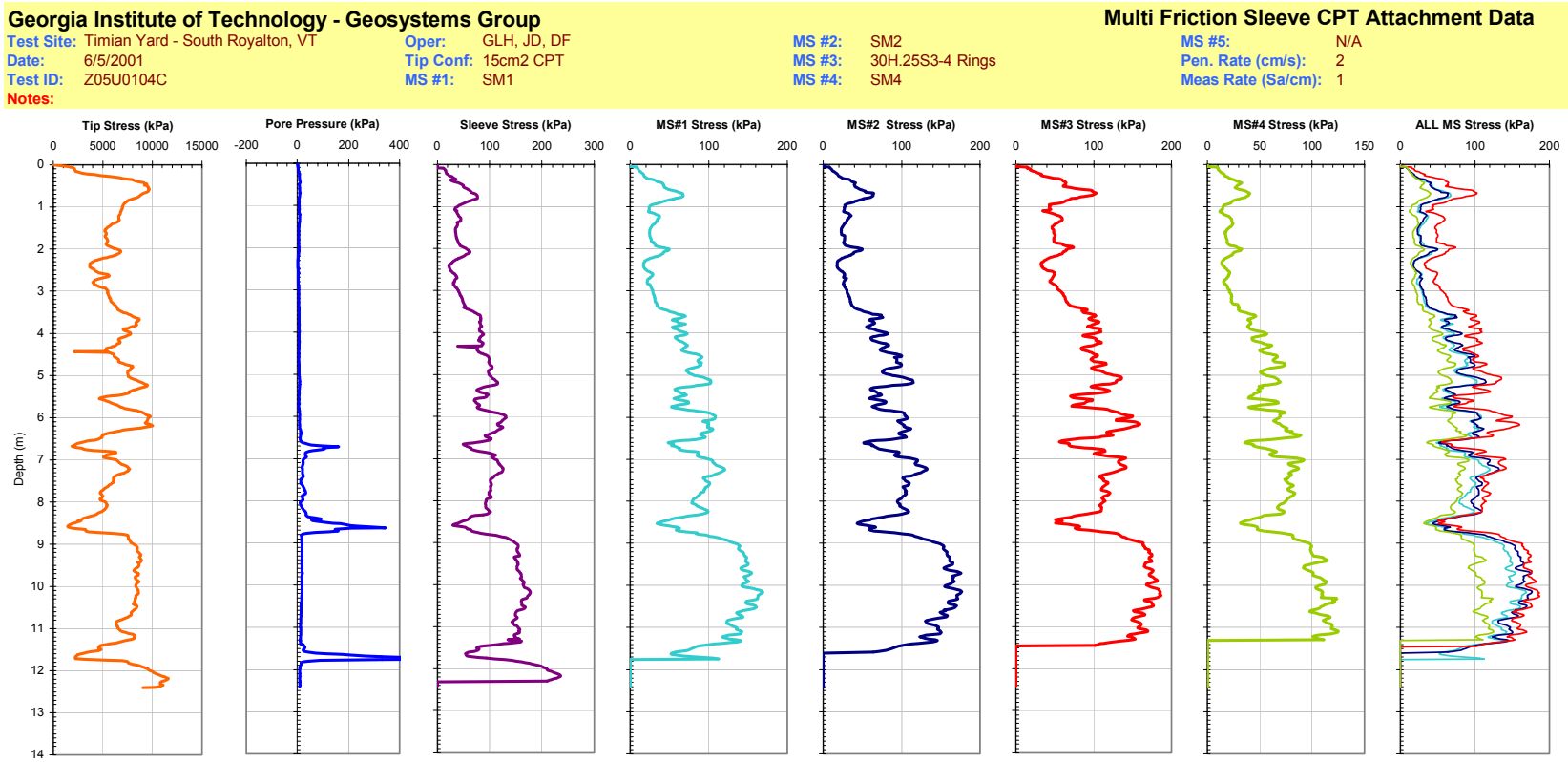

Figure A-10. Plot of CPTU-MFA Sensor Traces from Sounding MFA_49 at the SRVT Site.

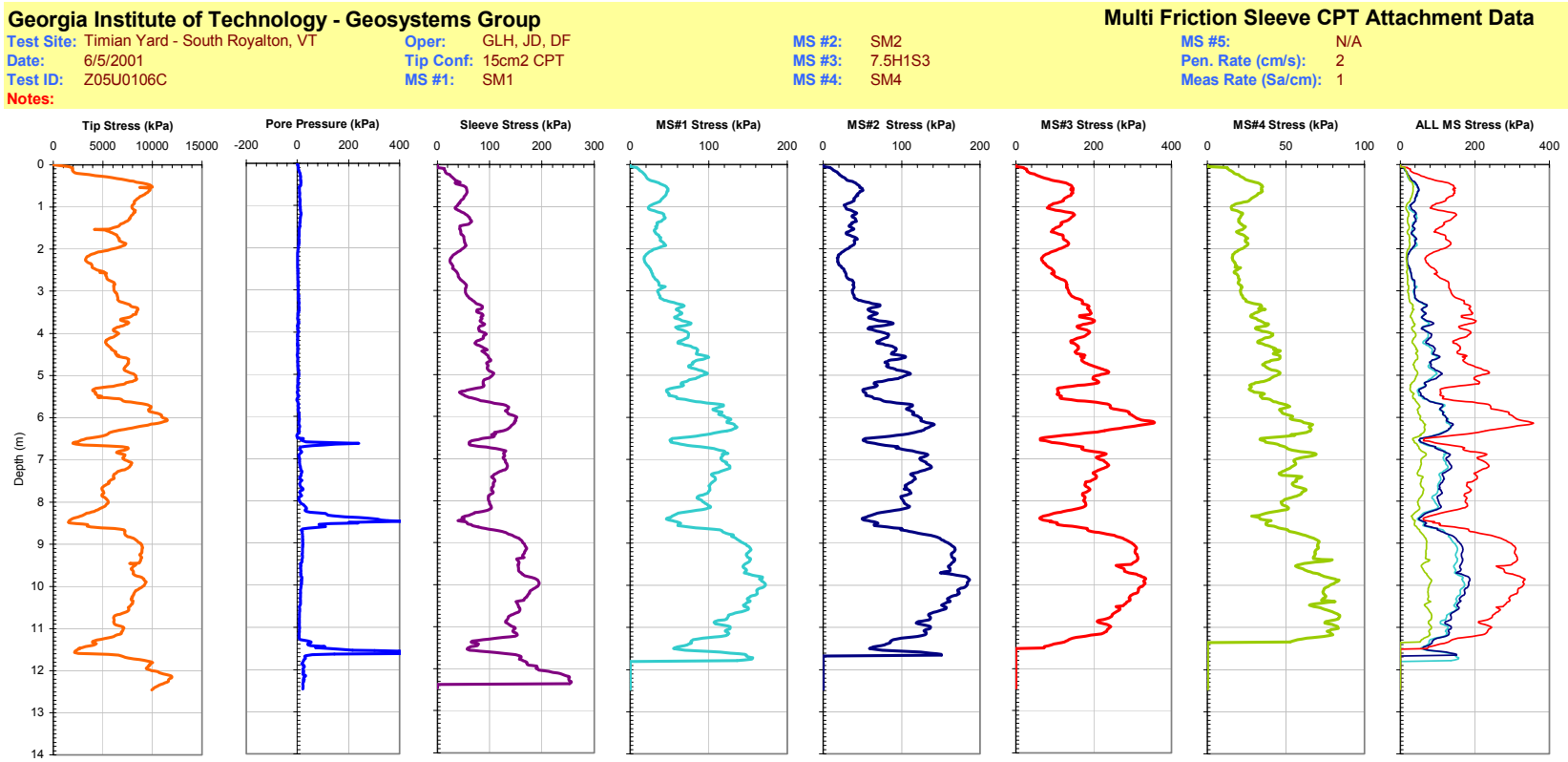

Figure A-11. Plot of CPTU-MFA Sensor Traces from Sounding MFA_50 at the SRVT Site.

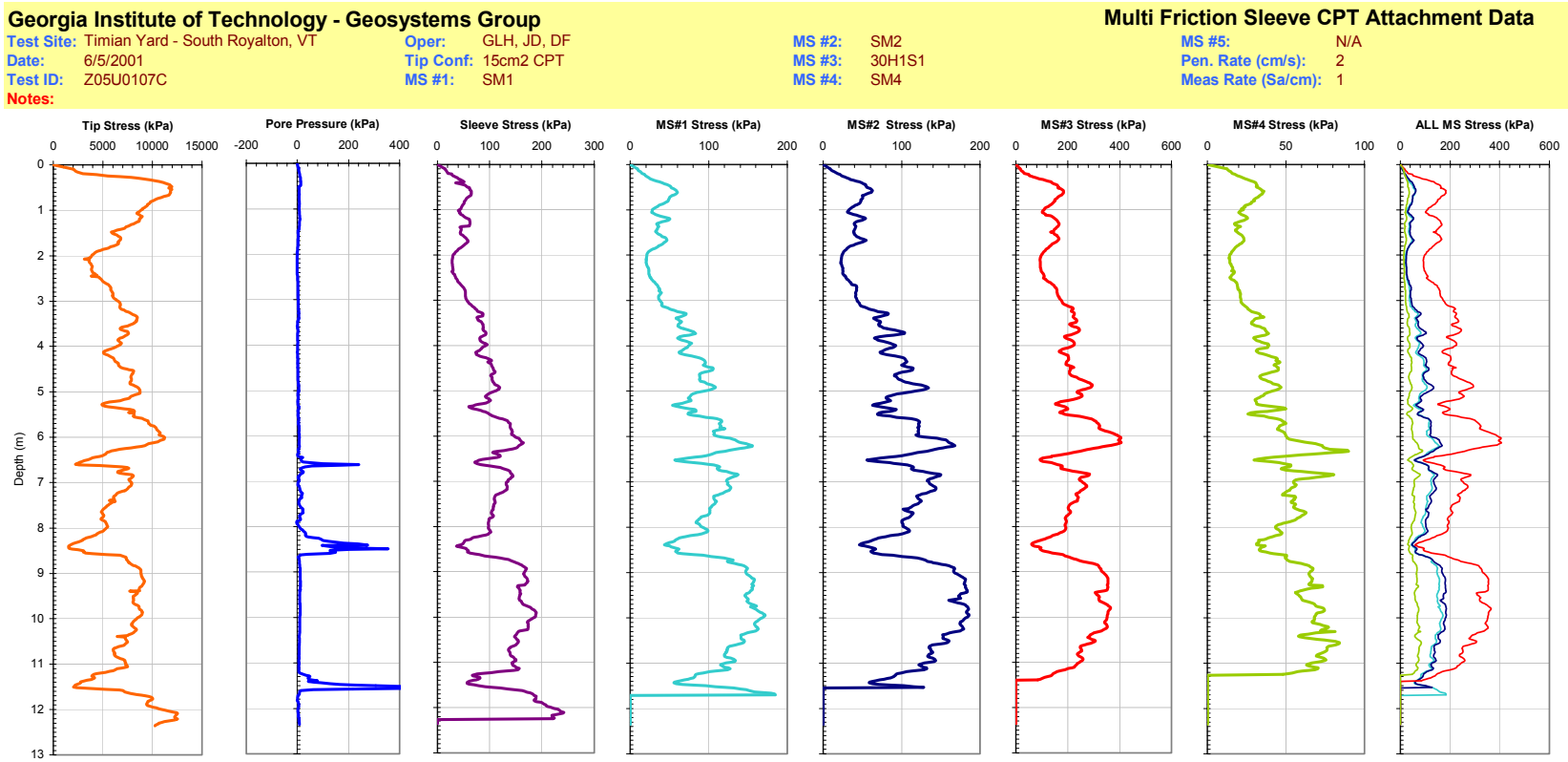

Figure A-12. Plot of CPTU-MFA Sensor Traces from Sounding MFA_51 at the SRVT Site.

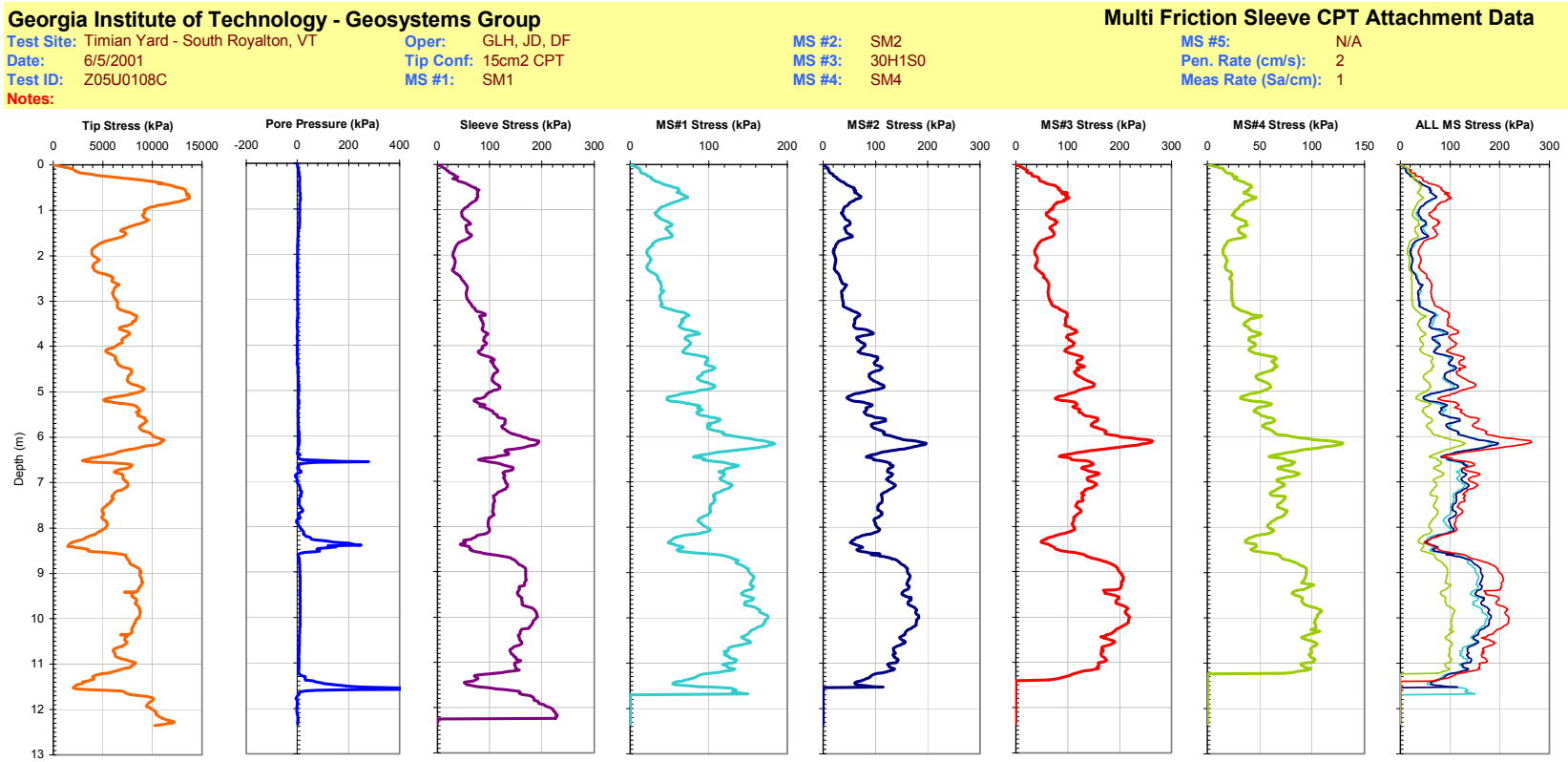

Figure A-13. Plot of CPTU-MFA Sensor Traces from Sounding MFA_52 at the SRVT Site.

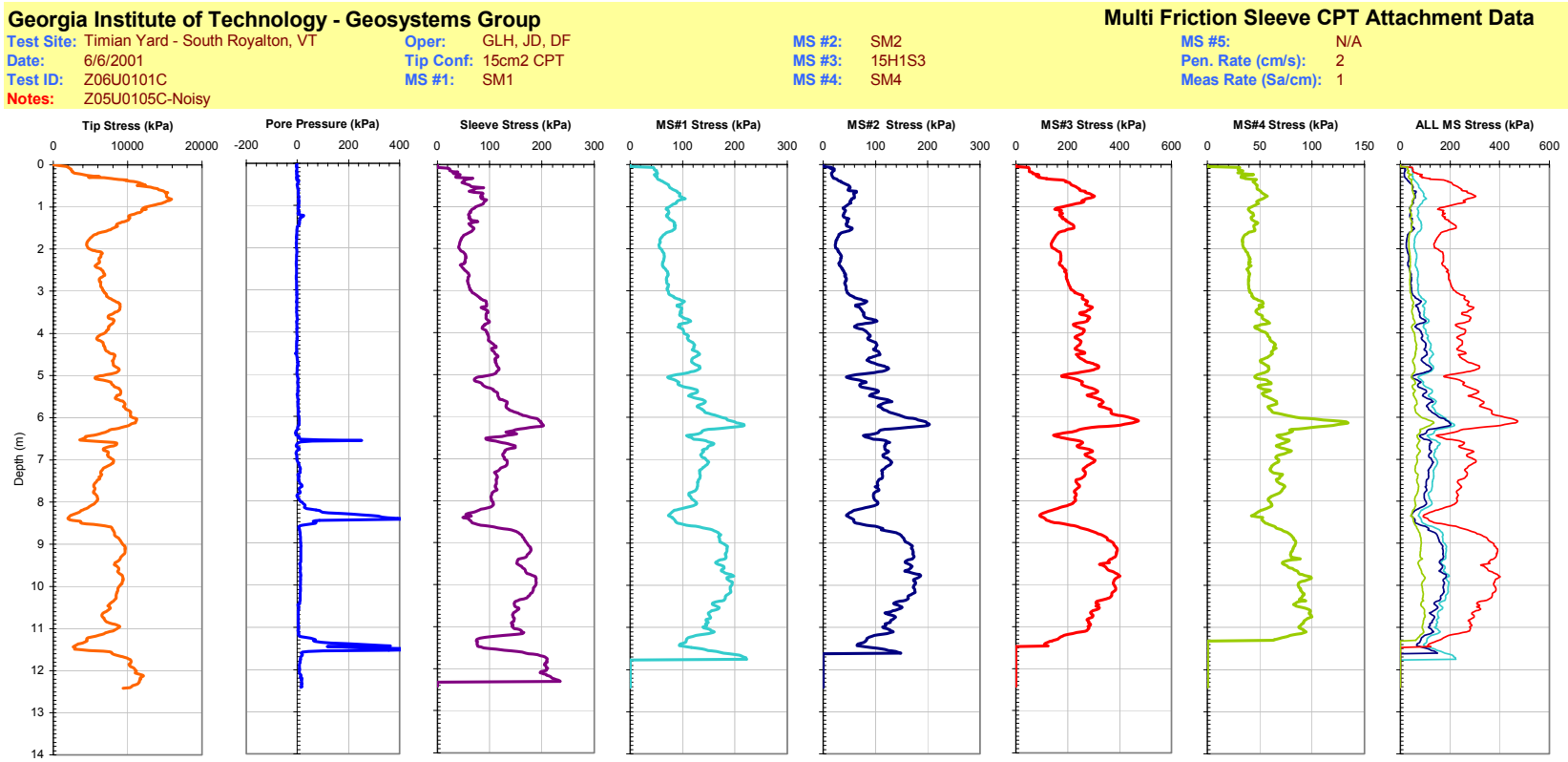

Figure A-14. Plot of CPTU-MFA Sensor Traces from Sounding MFA_53 at the SRVT Site.

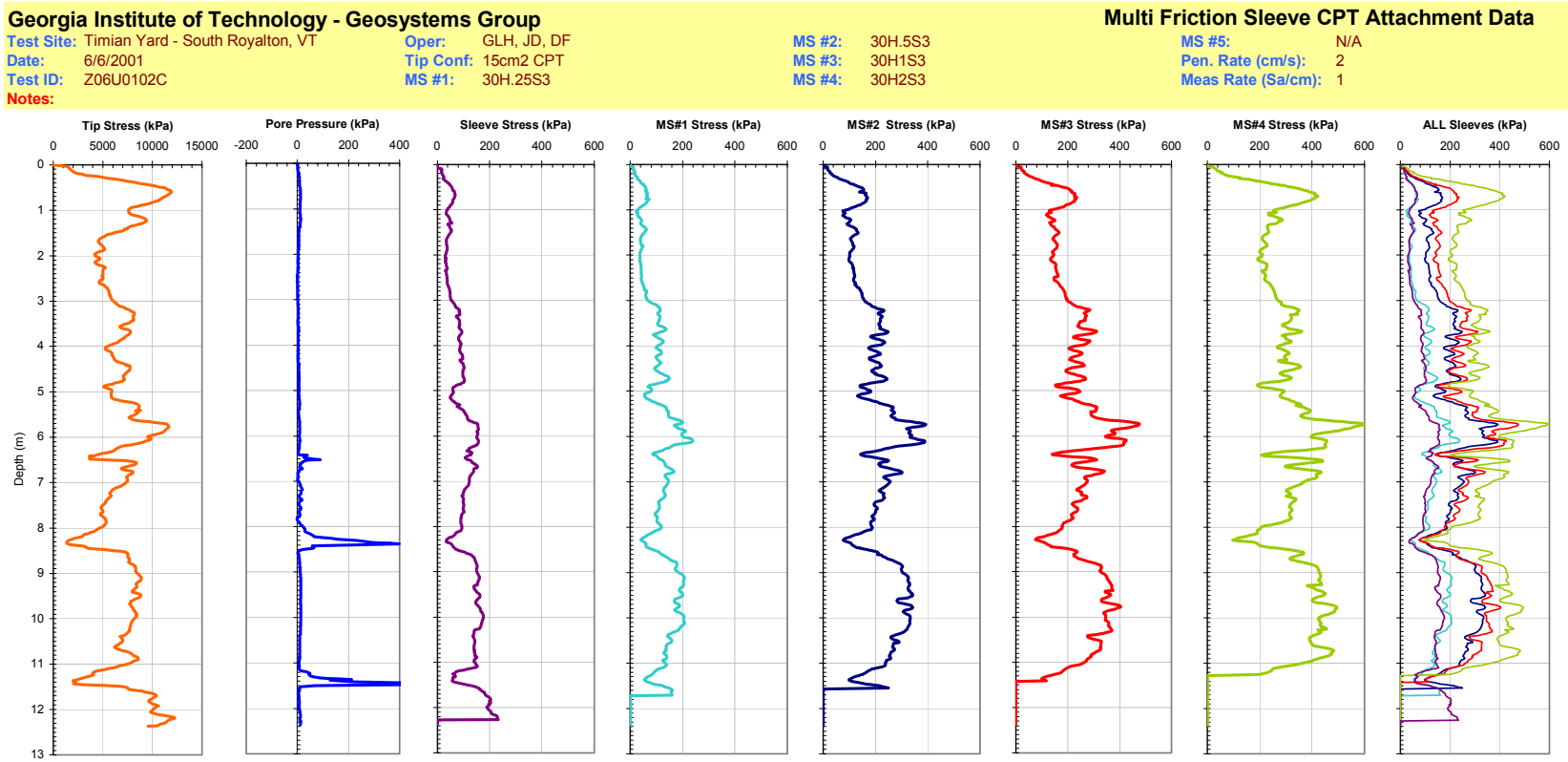

Figure A-15. Plot of CPTU-MFA Sensor Traces from Sounding MFA_54 at the SRVT Site.

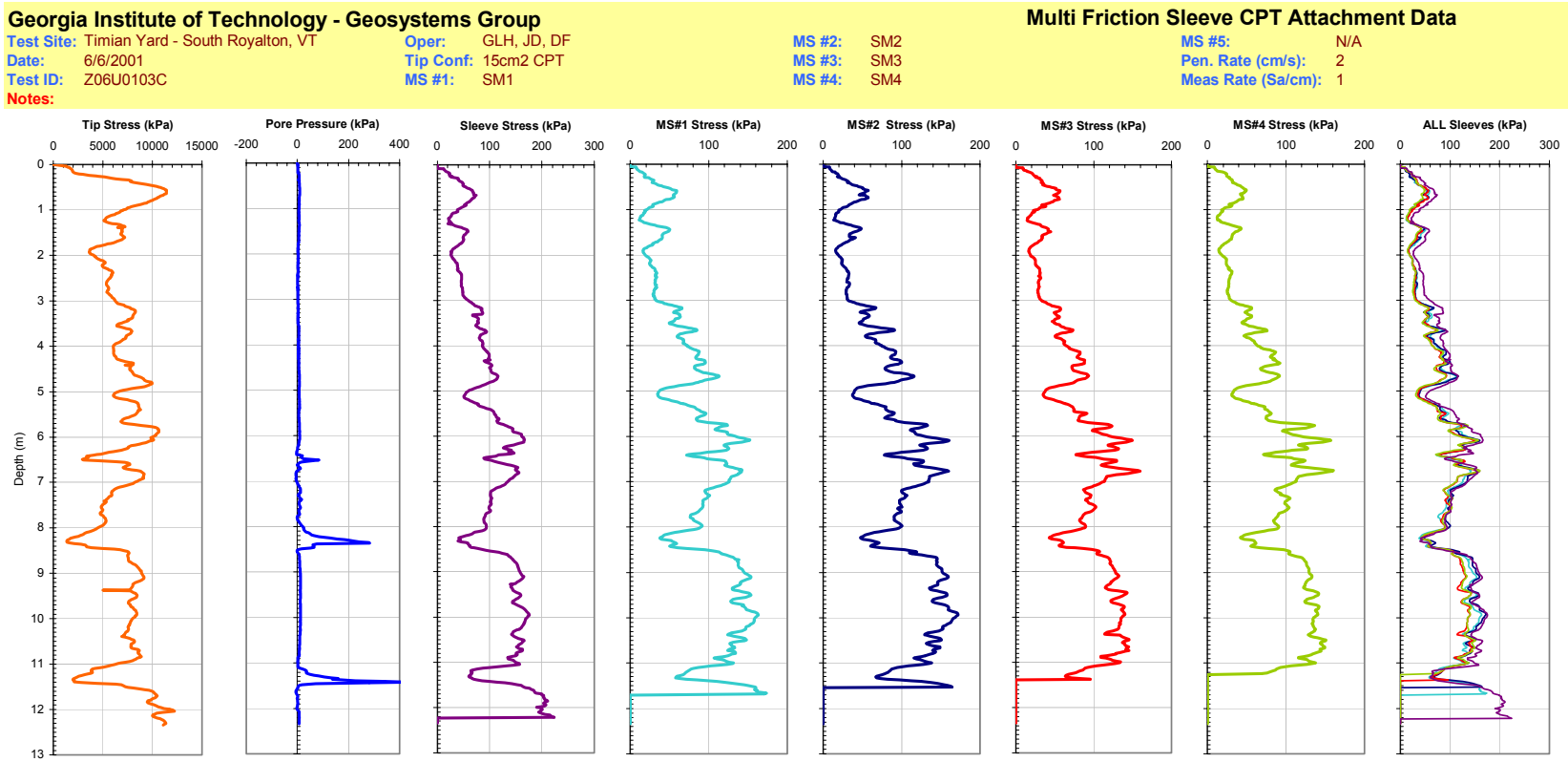

Figure A-16. Plot of CPTU-MFA Sensor Traces from Sounding MFA_55 at the SRVT Site.

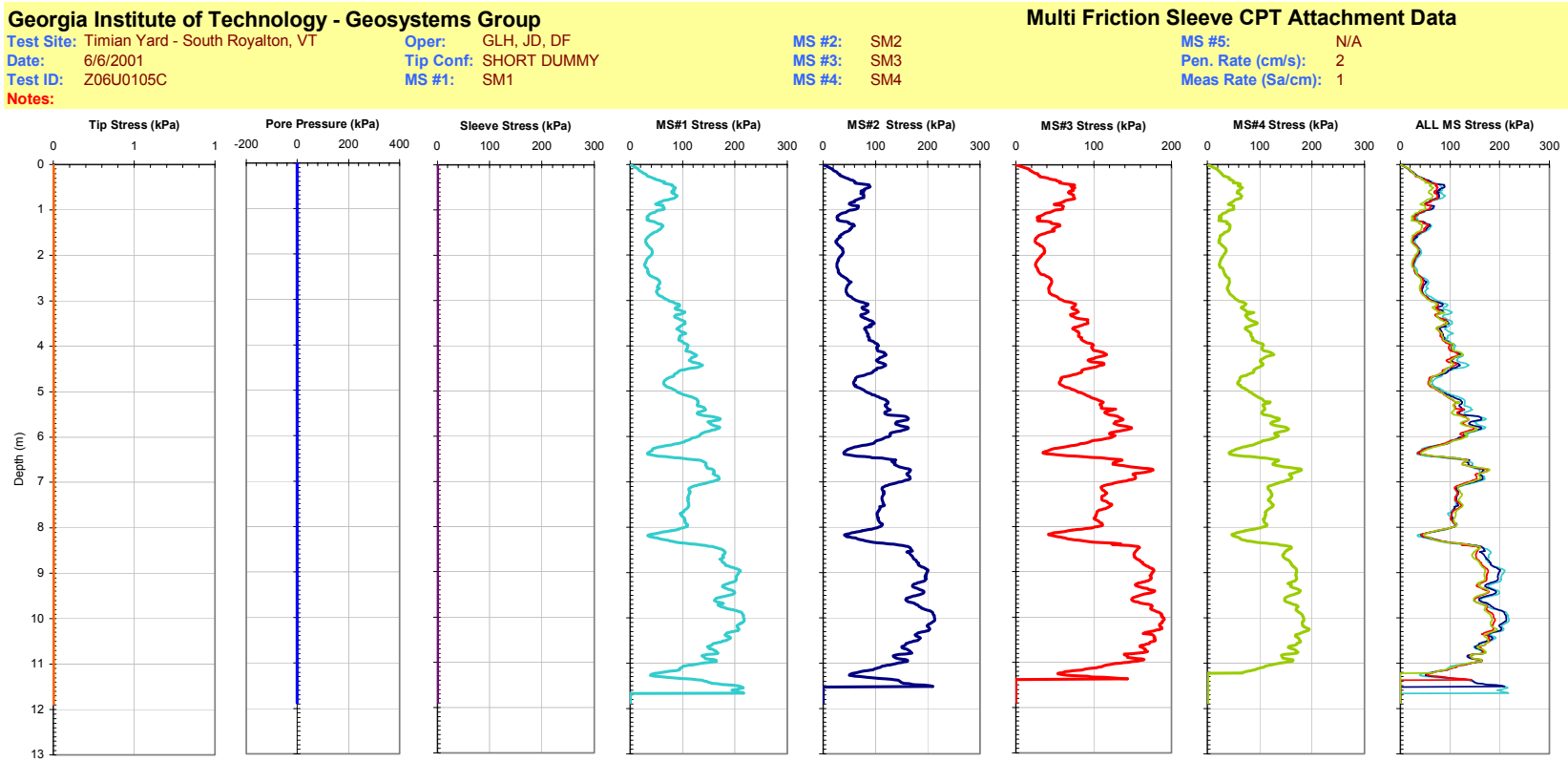

Figure A-17. Plot of CPTU-MFA Sensor Traces from Sounding MFA_56 at the SRVT Site.

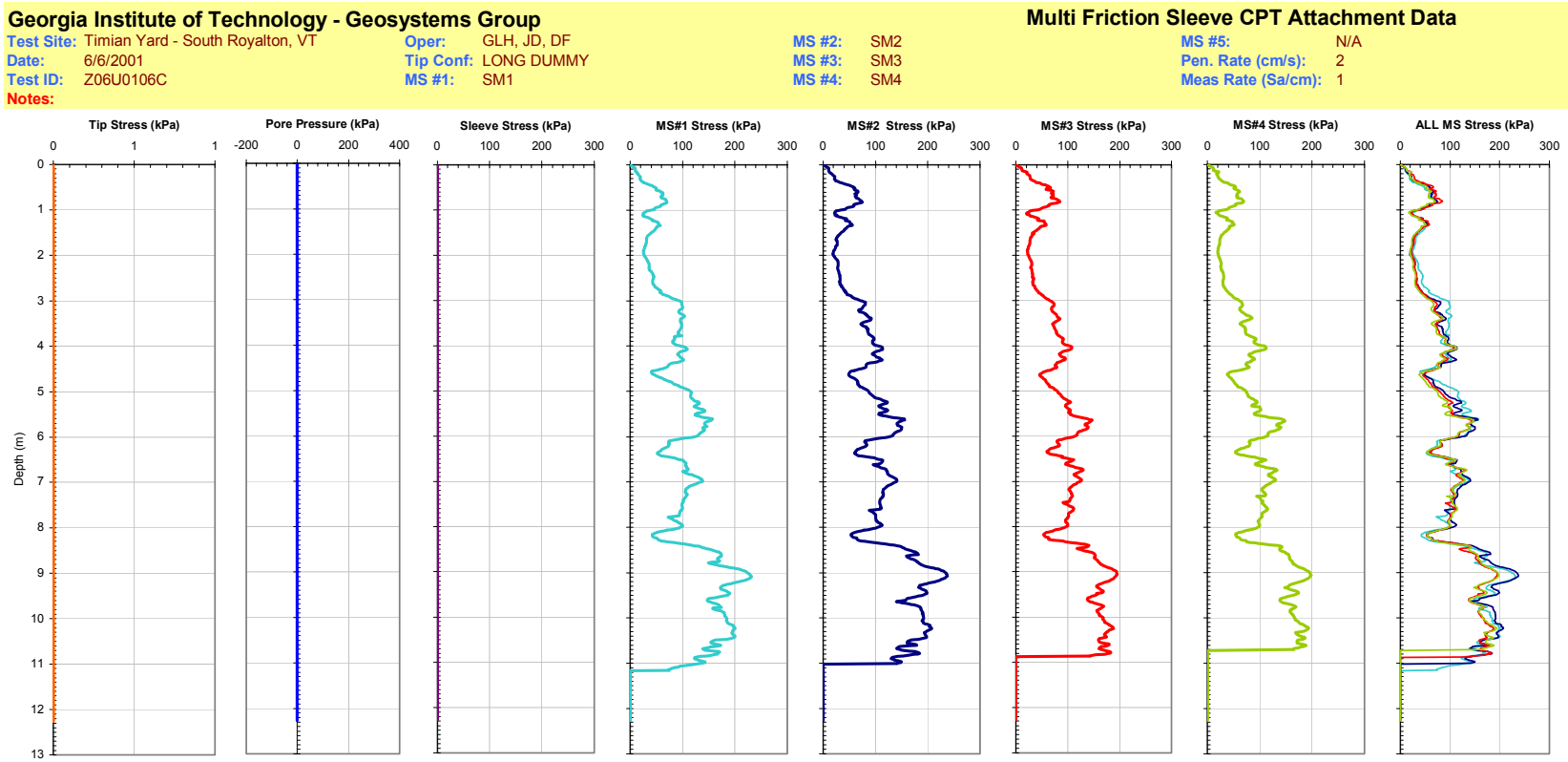

Figure A-18. Plot of CPTU-MFA Sensor Traces from Sounding MFA_57 at the SRVT Site.

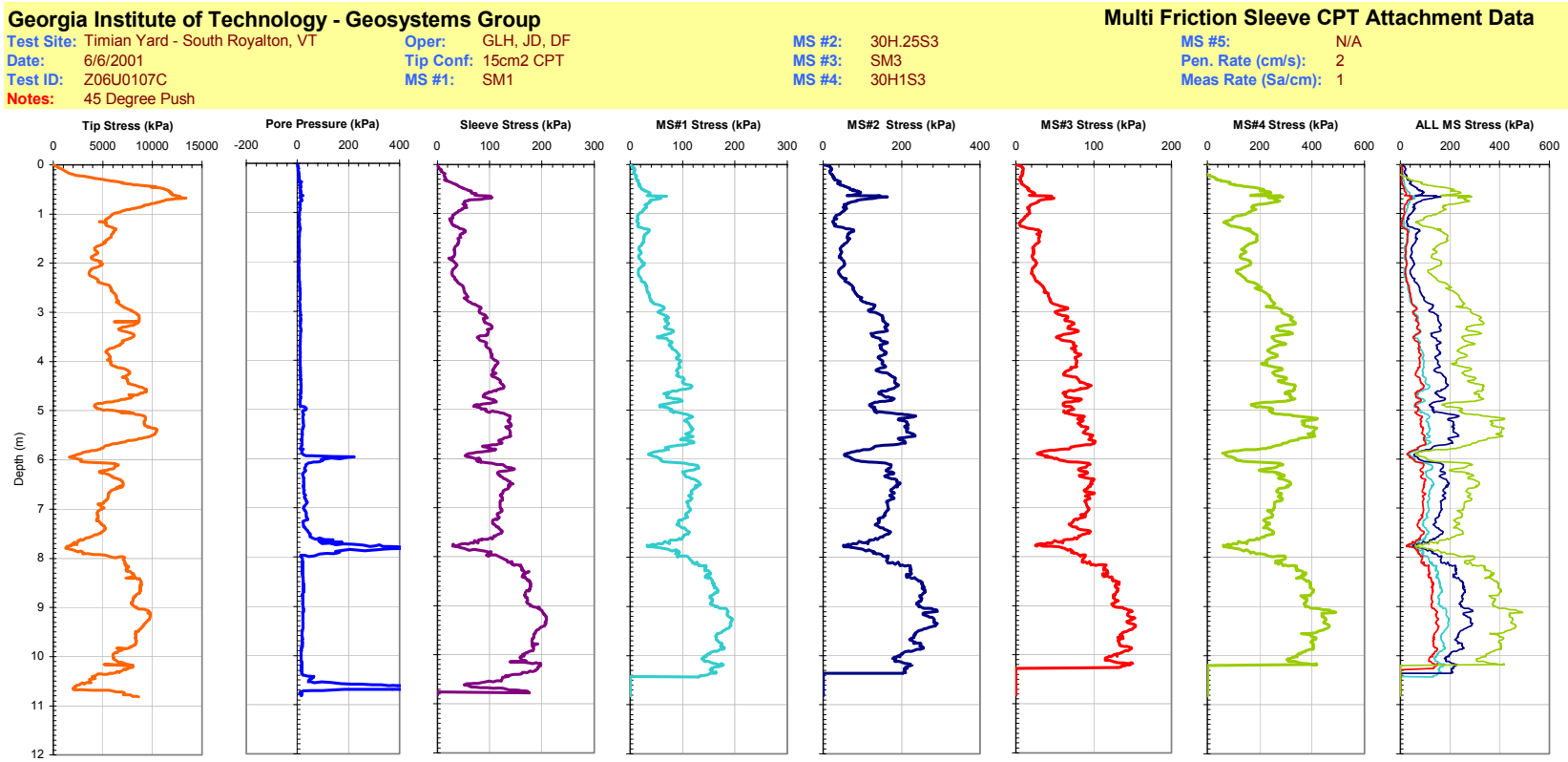

Figure A-19. Plot of CPTU-MFA Sensor Traces from Sounding MFA_58 at the SRVT Site.

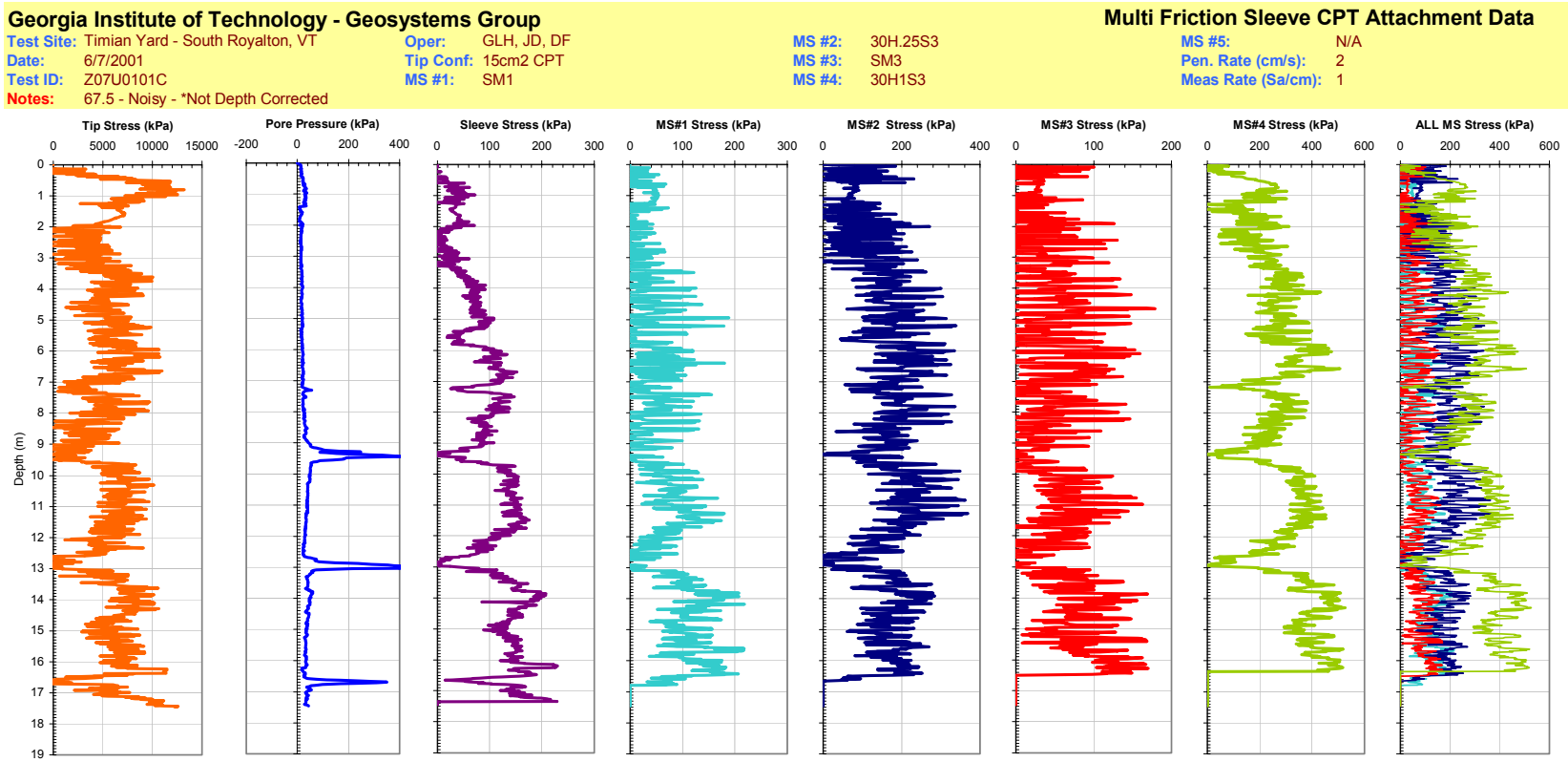

Figure A-20. Plot of CPTU-MFA Sensor Traces from Sounding MFA_59 at the SRVT Site.

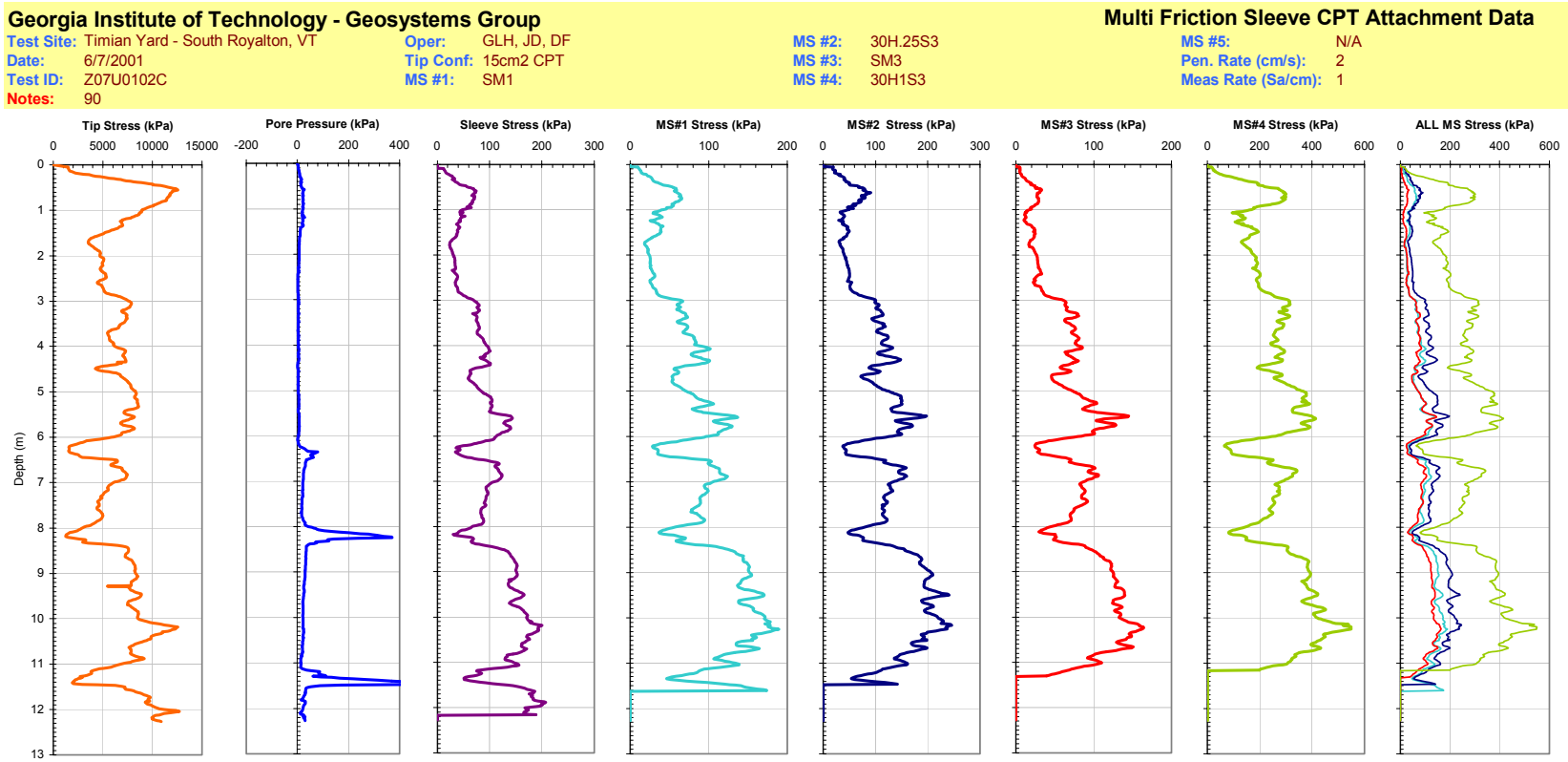

Figure A-21. Plot of CPTU-MFA Sensor Traces from Sounding MFA_60 at the SRVT Site.

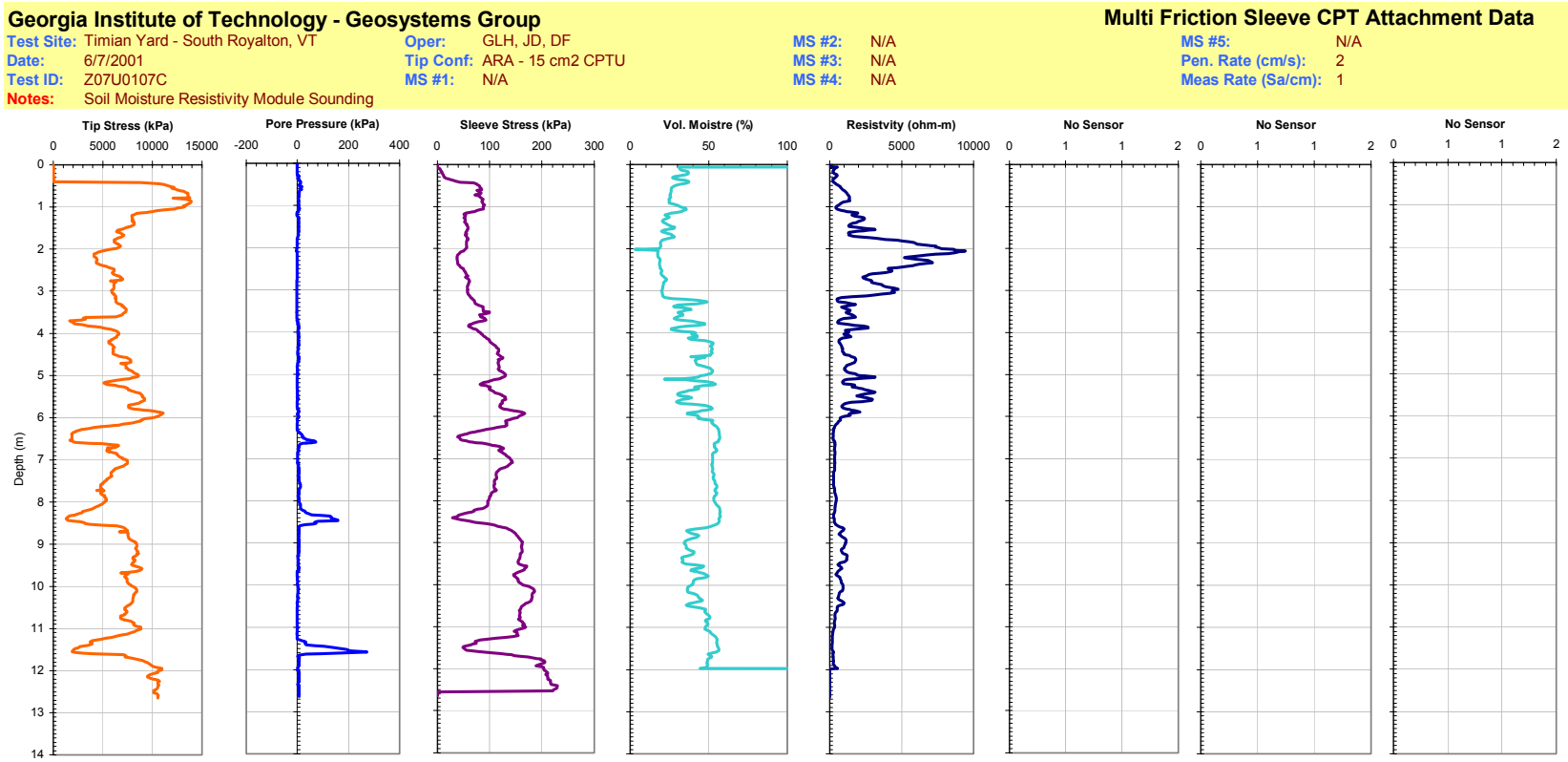

Figure A-22. Plot of CPTU-MFA Sensor Traces from Sounding MFA_61 at the SRVT Site.

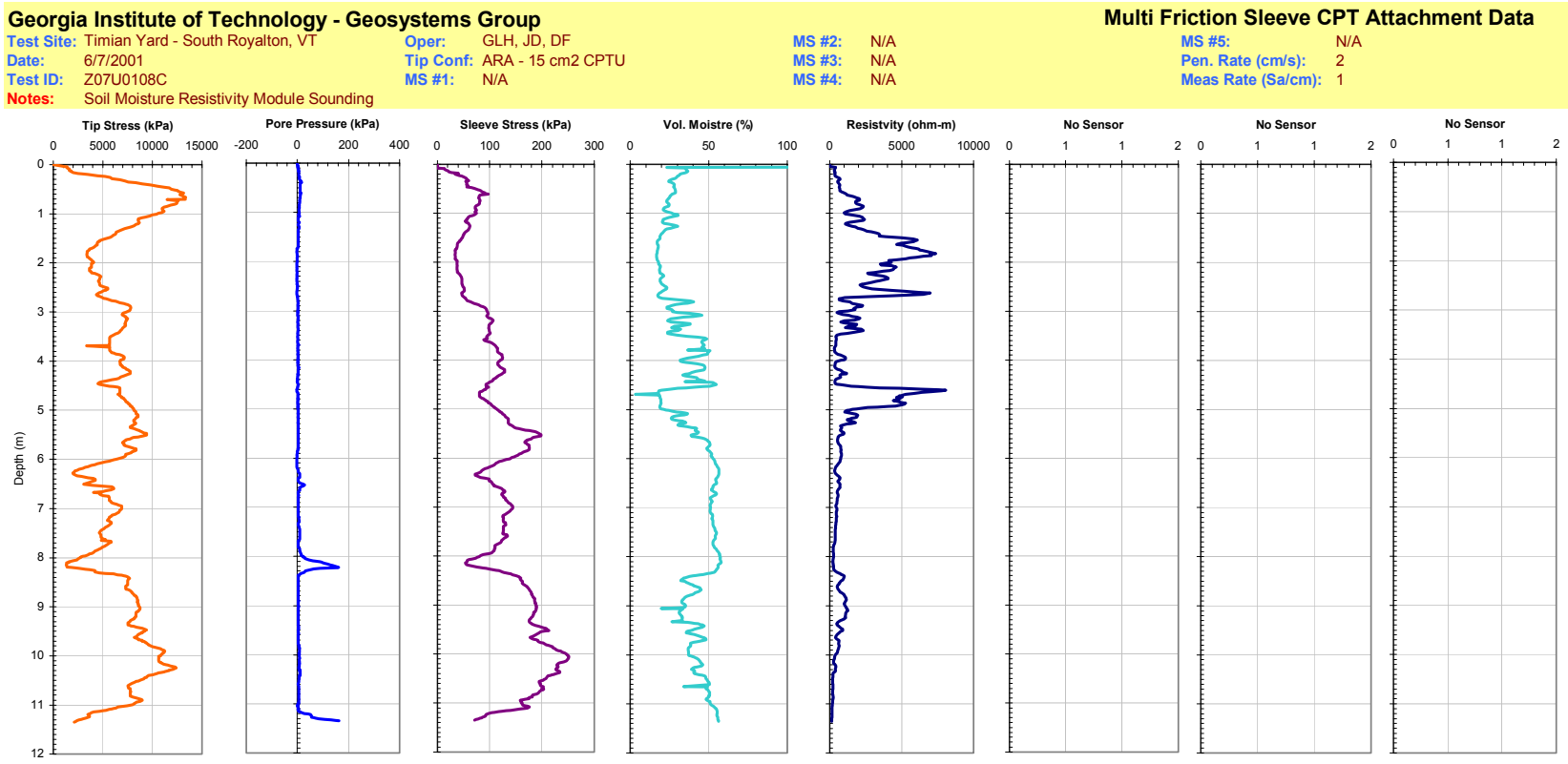

Figure A-23. Plot of CPTU-MFA Sensor Traces from Sounding MFA_62 at the SRVT Site.

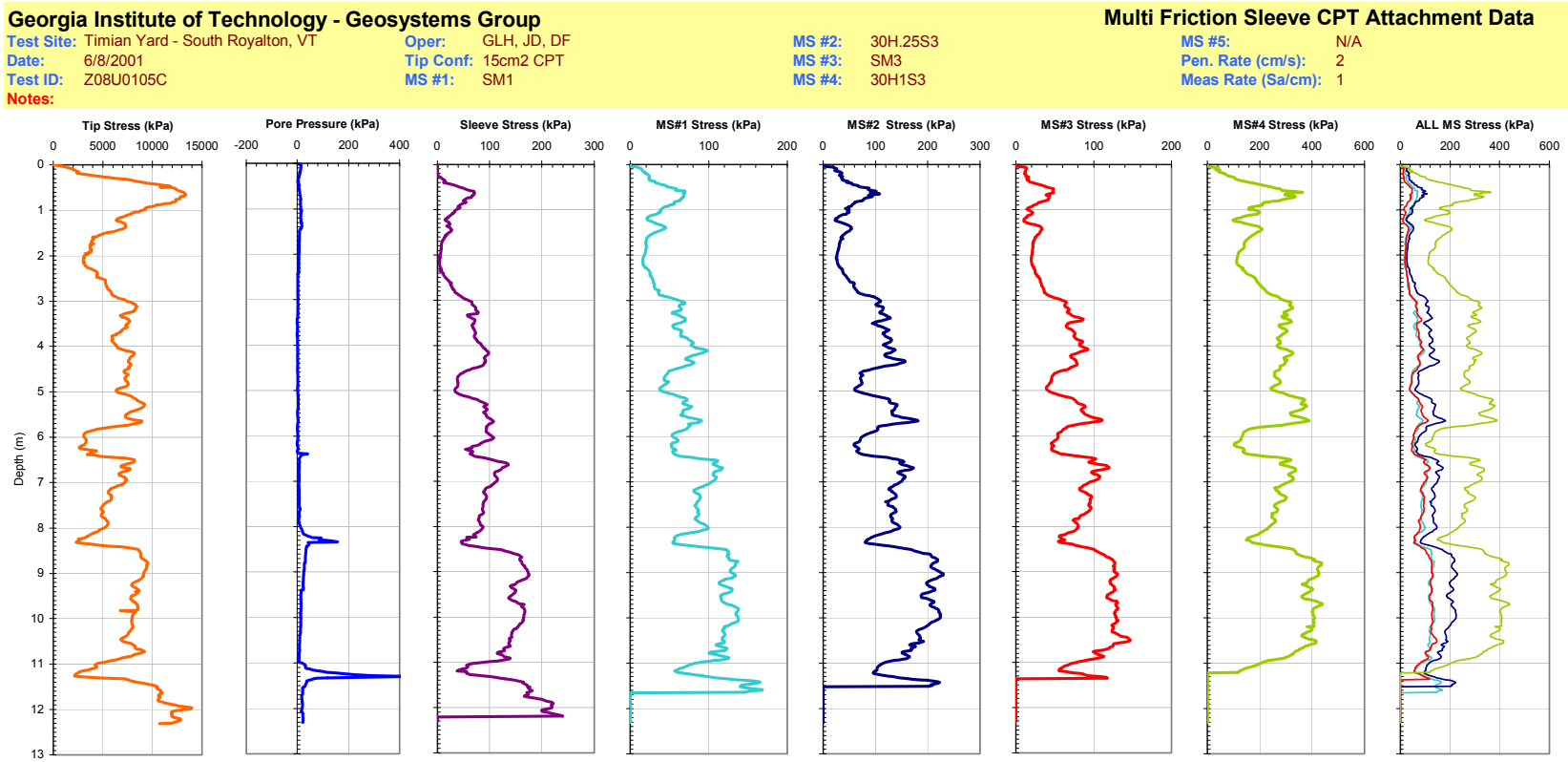

Figure A-24. Plot of CPTU-MFA Sensor Traces from Sounding MFA_64 at the SRVT Site.

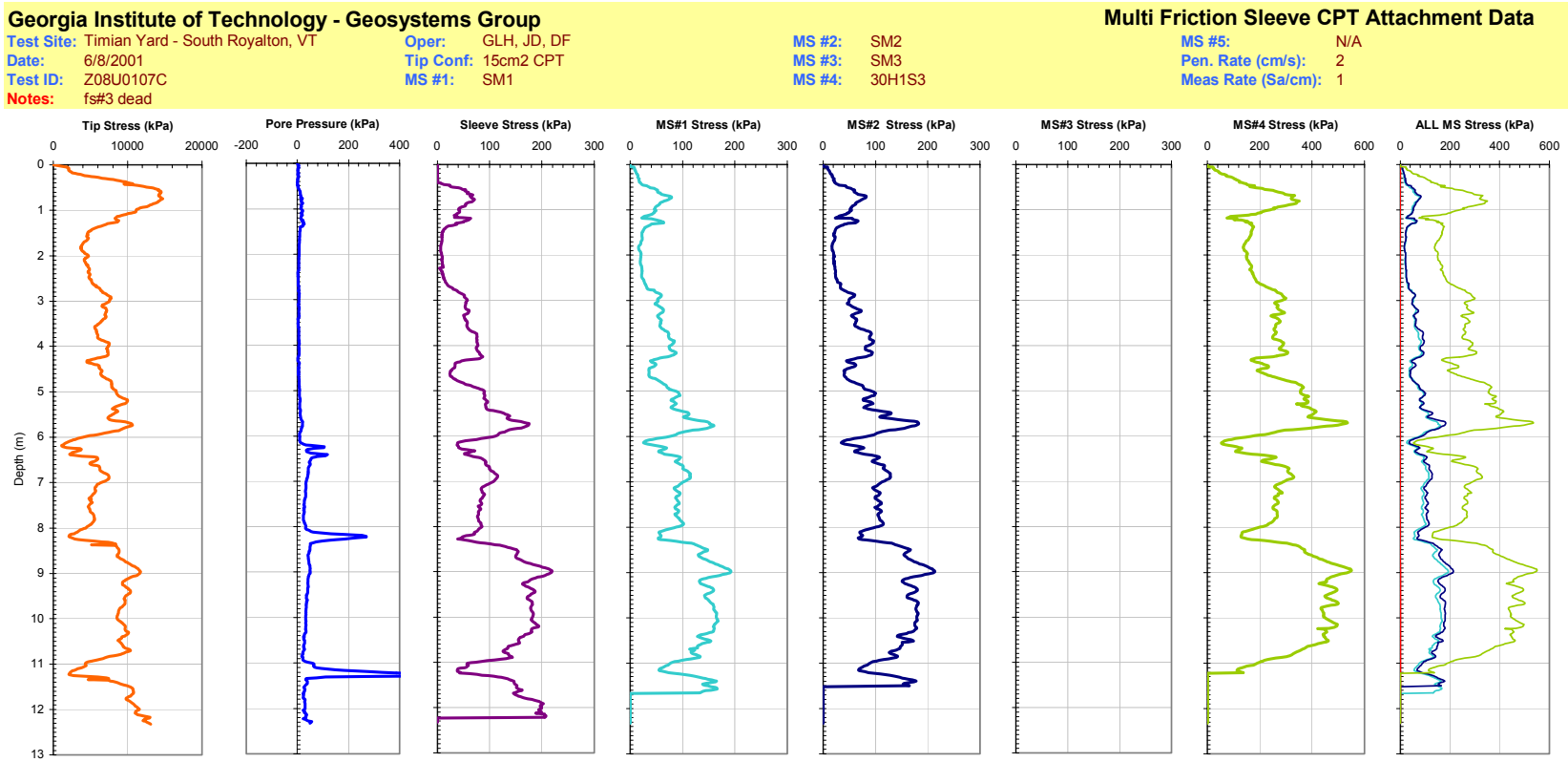

Figure A-25. Plot of CPTU-MFA Sensor Traces from Sounding MFA_65 at the SRVT Site.

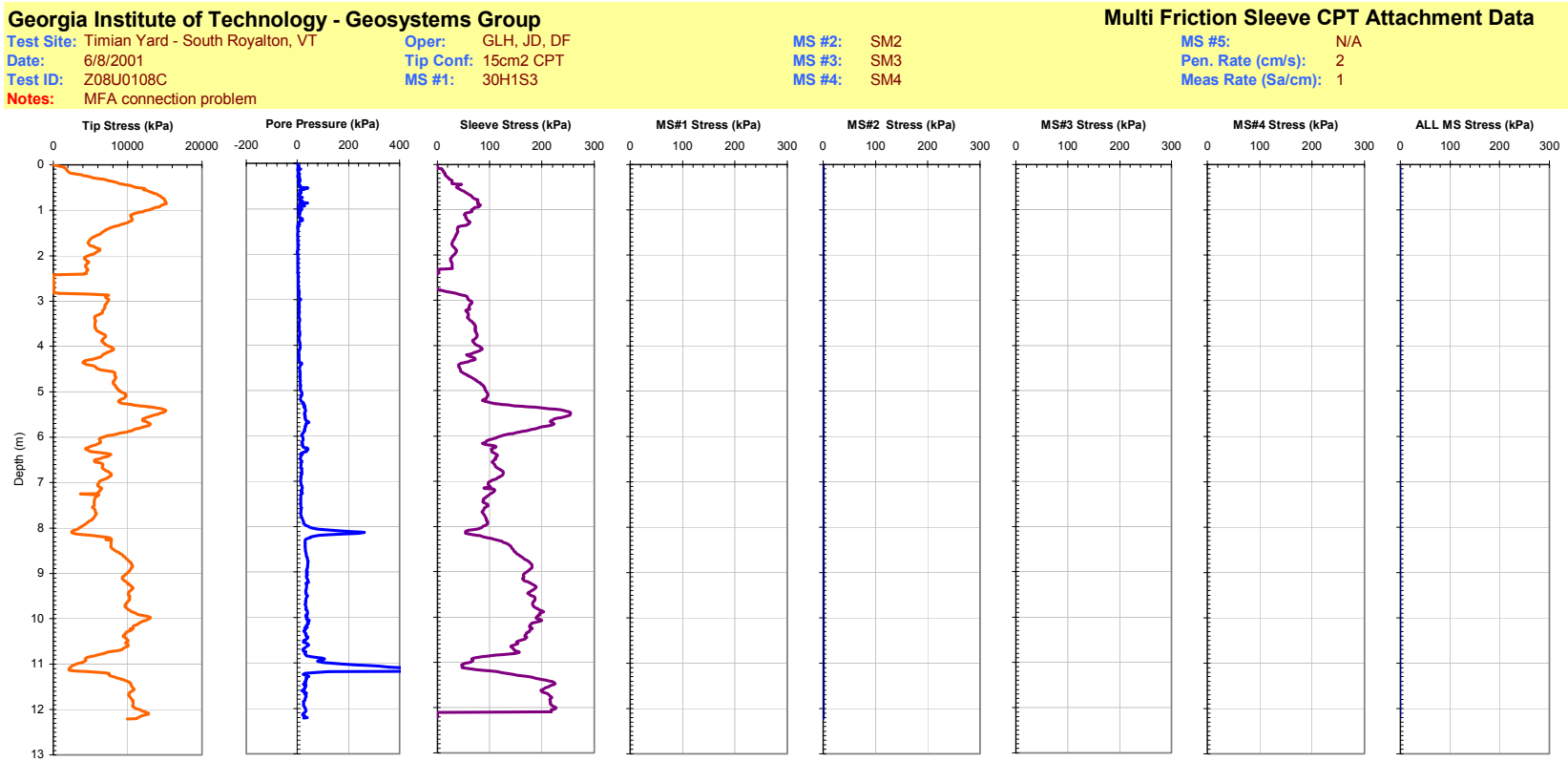

Figure A-26. Plot of CPTU-MFA Sensor Traces from Sounding MFA_66 at the SRVT Site.

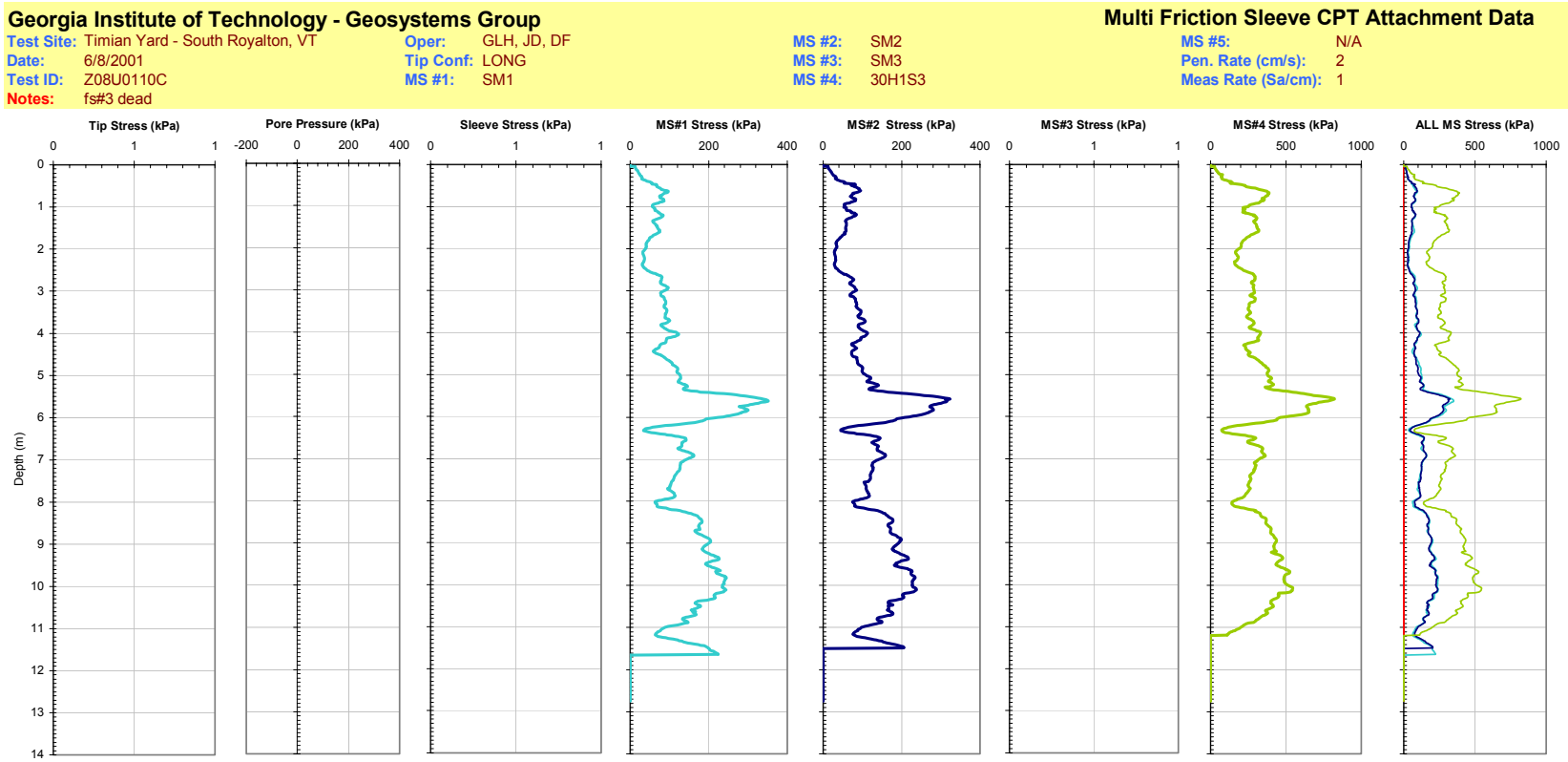

Figure A-27. Plot of CPTU-MFA Sensor Traces from Sounding MFA_67 at the SRVT Site.

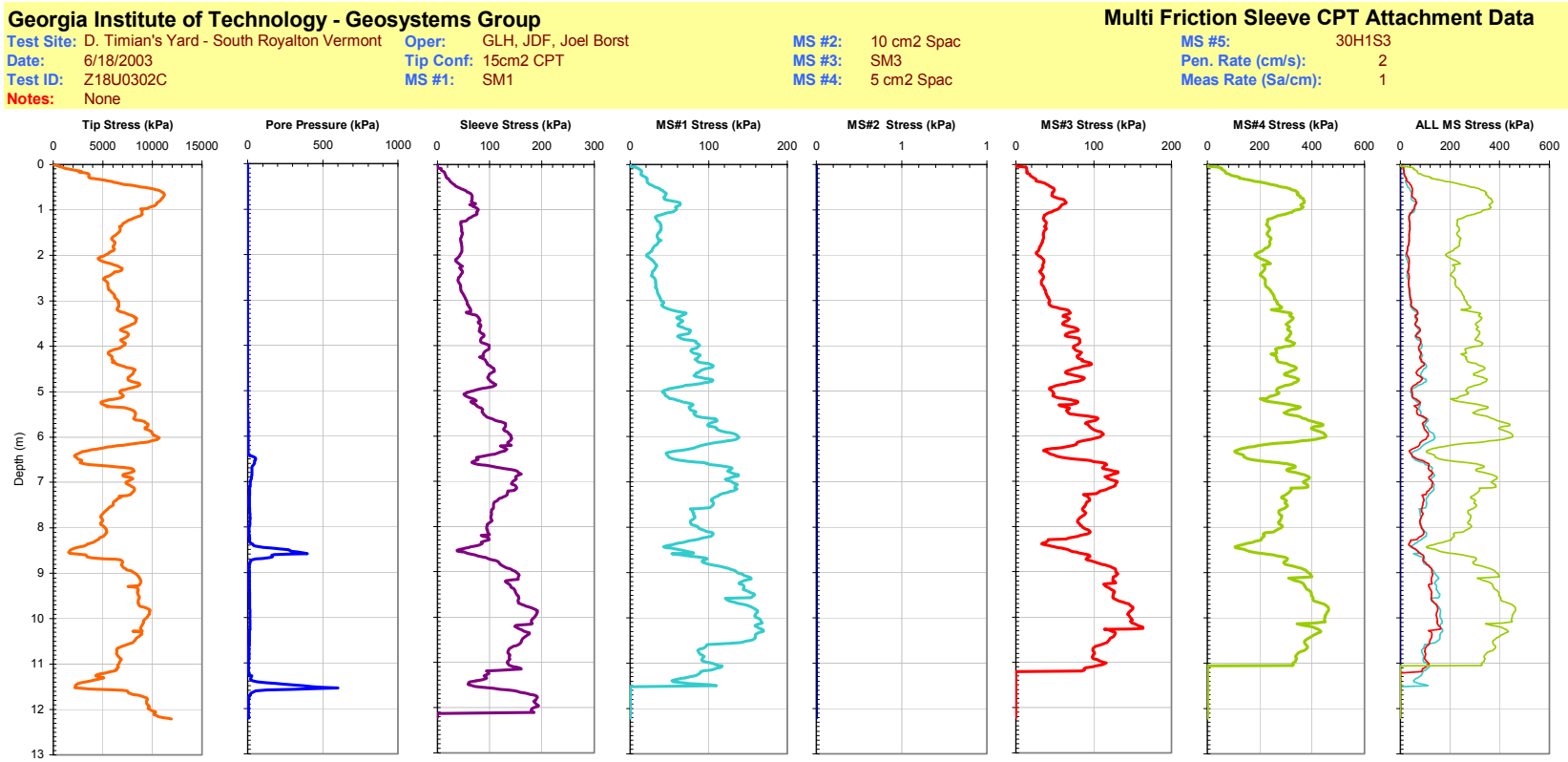

Figure A-28. Plot of CPTU-MFA Sensor Traces from Sounding MFA_68 at the SRVT Site.

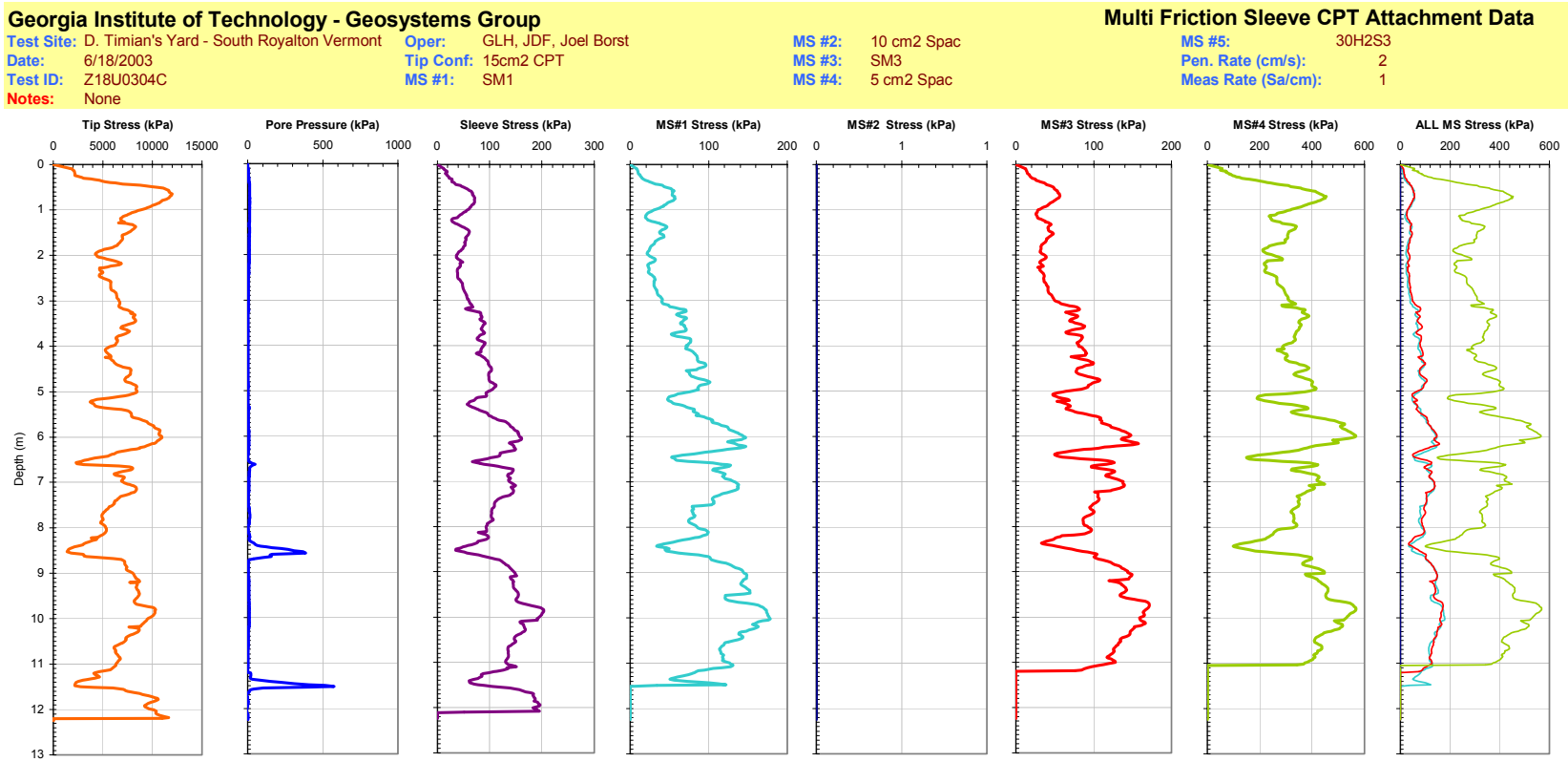

Figure A-29. Plot of CPTU-MFA Sensor Traces from Sounding MFA_69 at the SRVT Site.

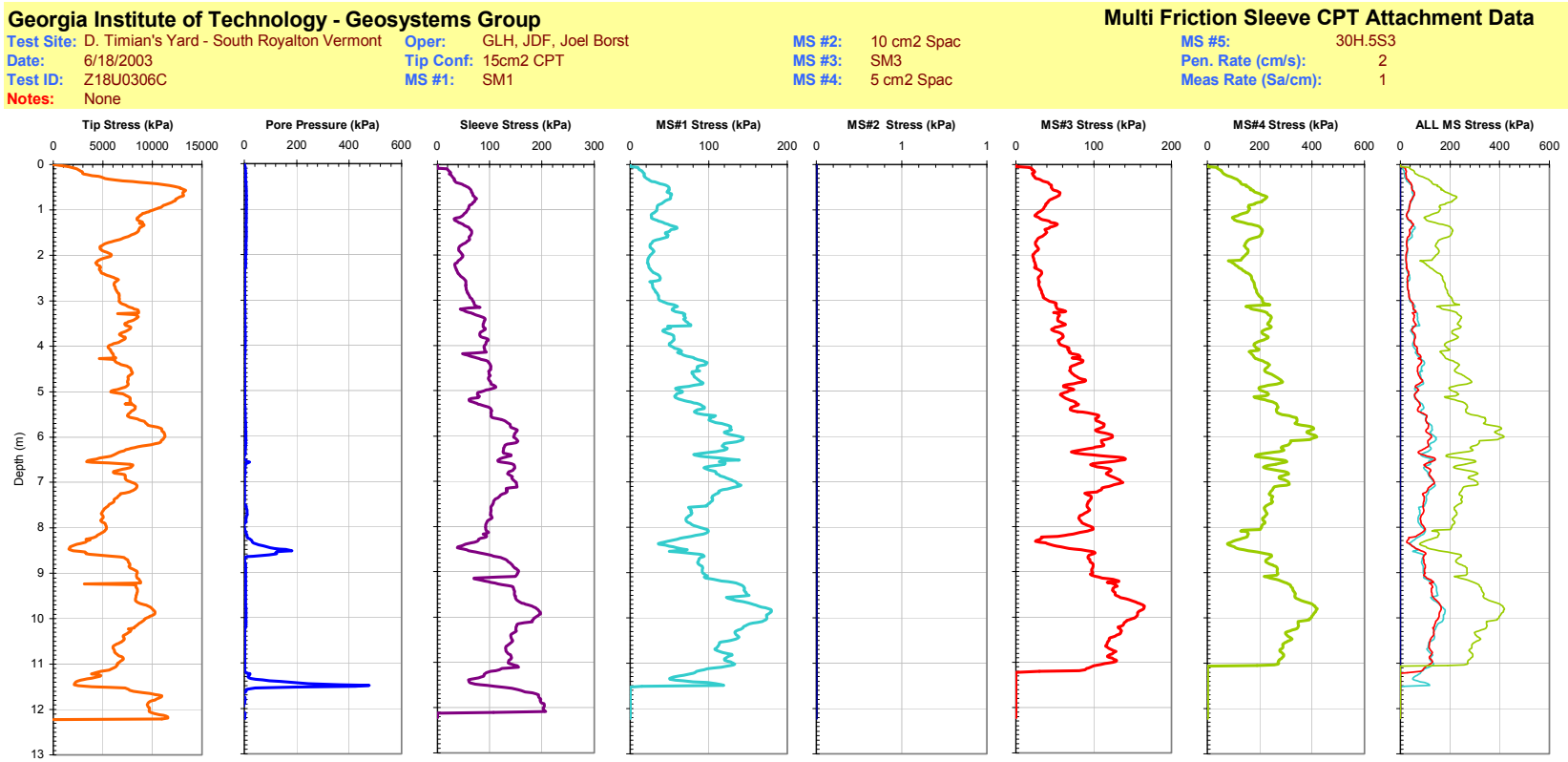

Figure A-30. Plot of CPTU-MFA Sensor Traces from Sounding MFA_70 at the SRVT Site.

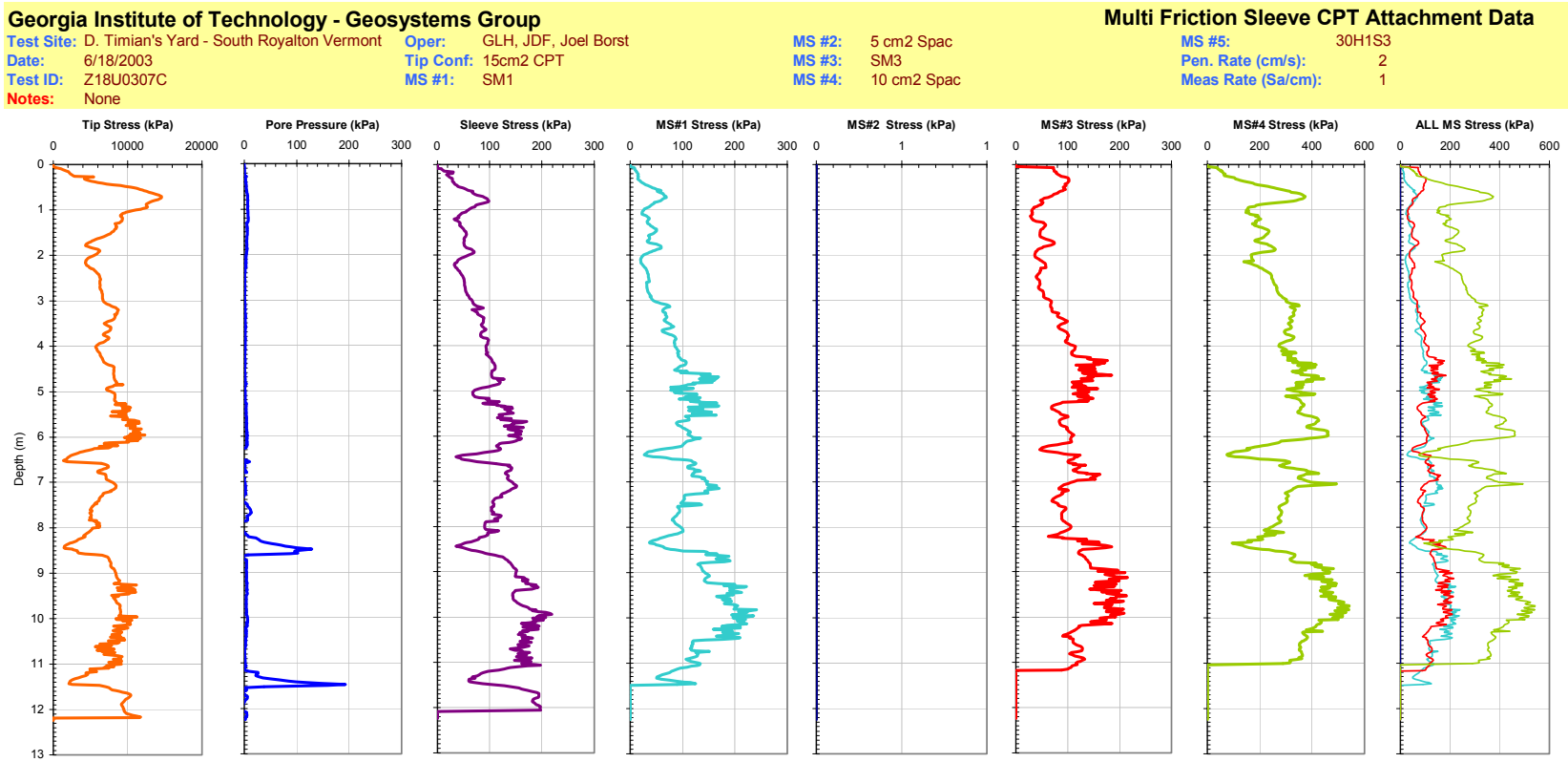

Figure A-31. Plot of CPTU-MFA Sensor Traces from Sounding MFA_71 at the SRVT Site.

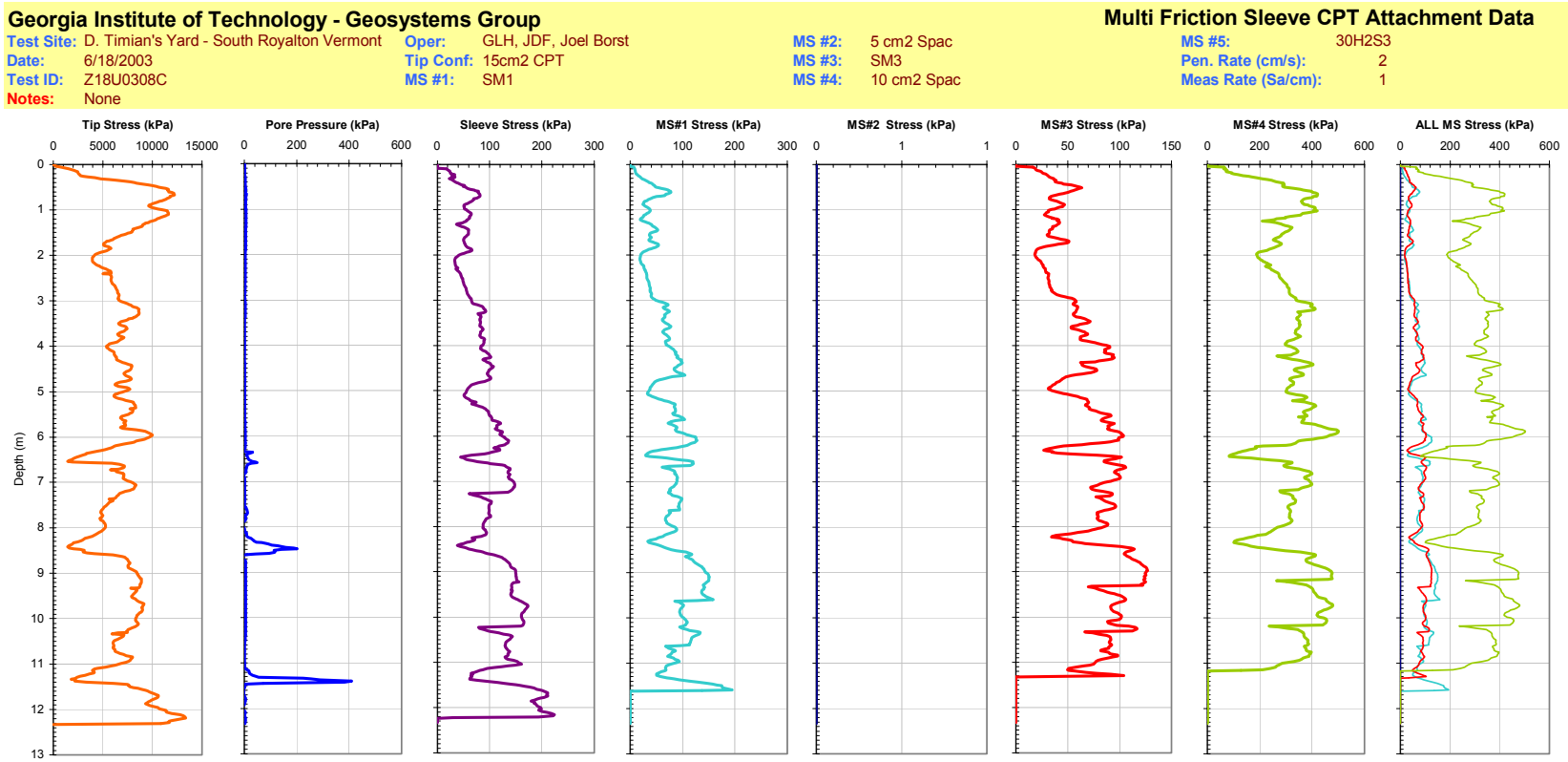

Figure A-32. Plot of CPTU-MFA Sensor Traces from Sounding MFA_72 at the SRVT Site.

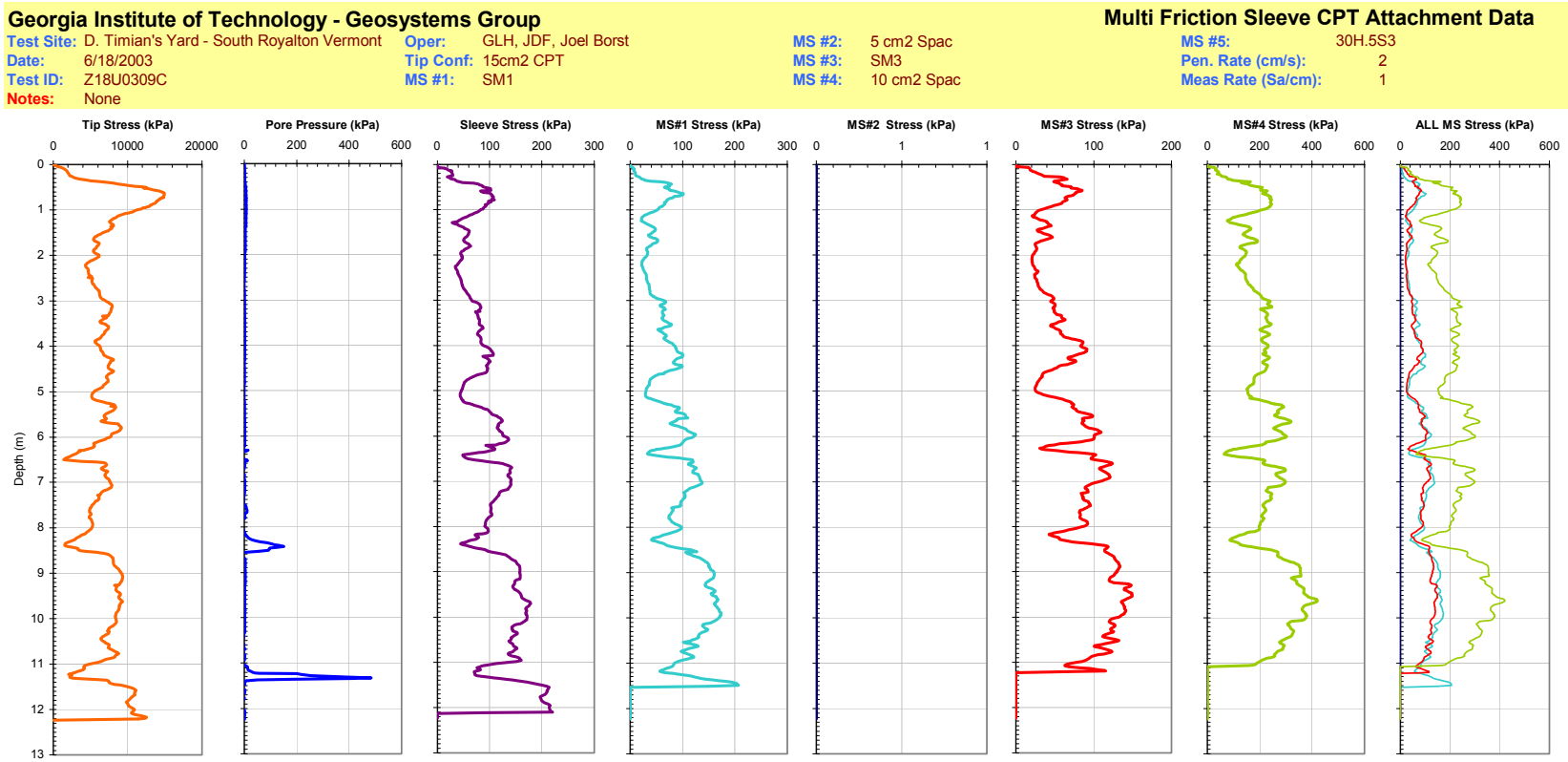

Figure A-33. Plot of CPTU-MFA Sensor Traces from Sounding MFA_73 at the SRVT Site.

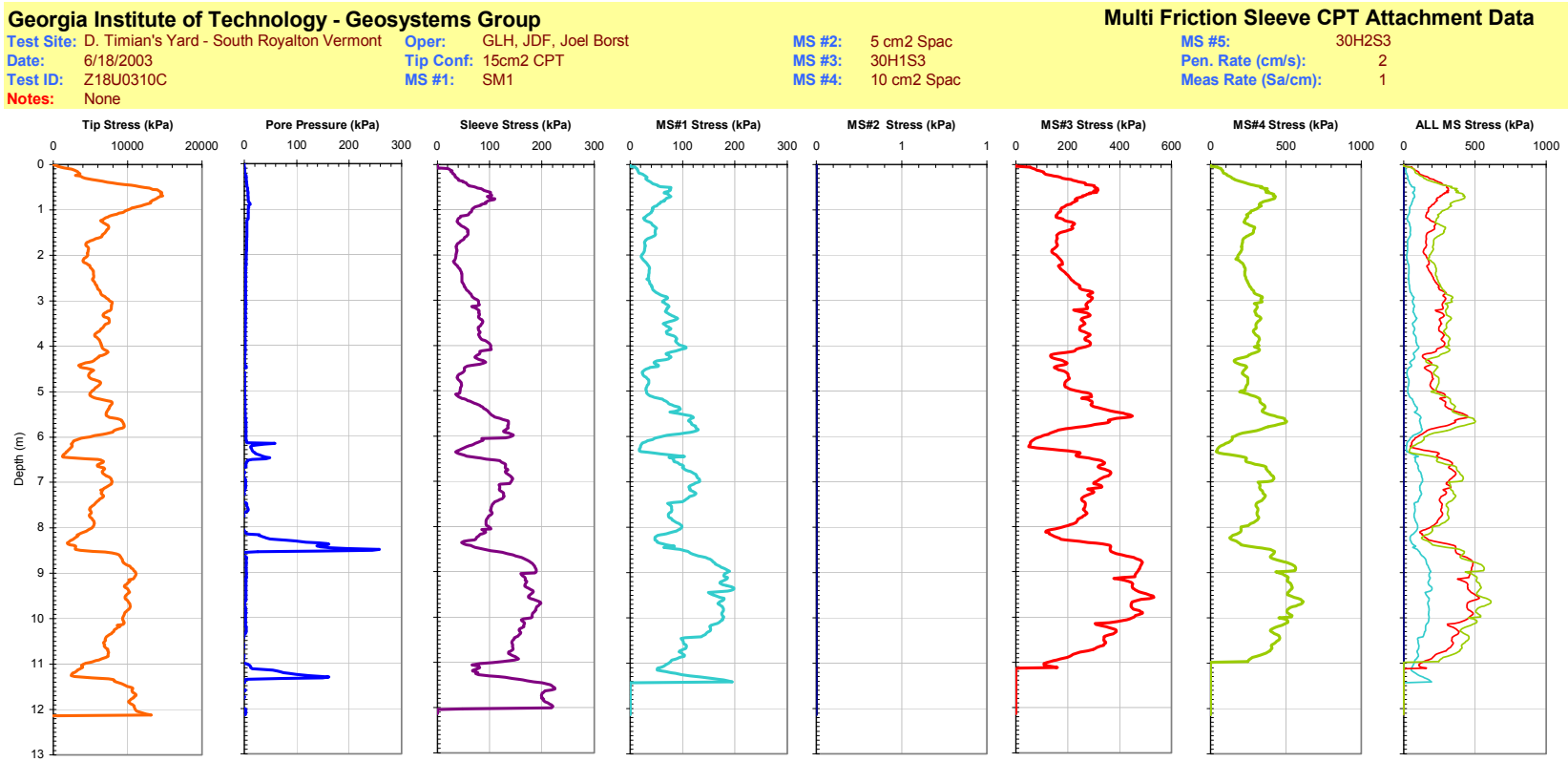

Figure A-34. Plot of CPTU-MFA Sensor Traces from Sounding MFA_74 at the SRVT Site.

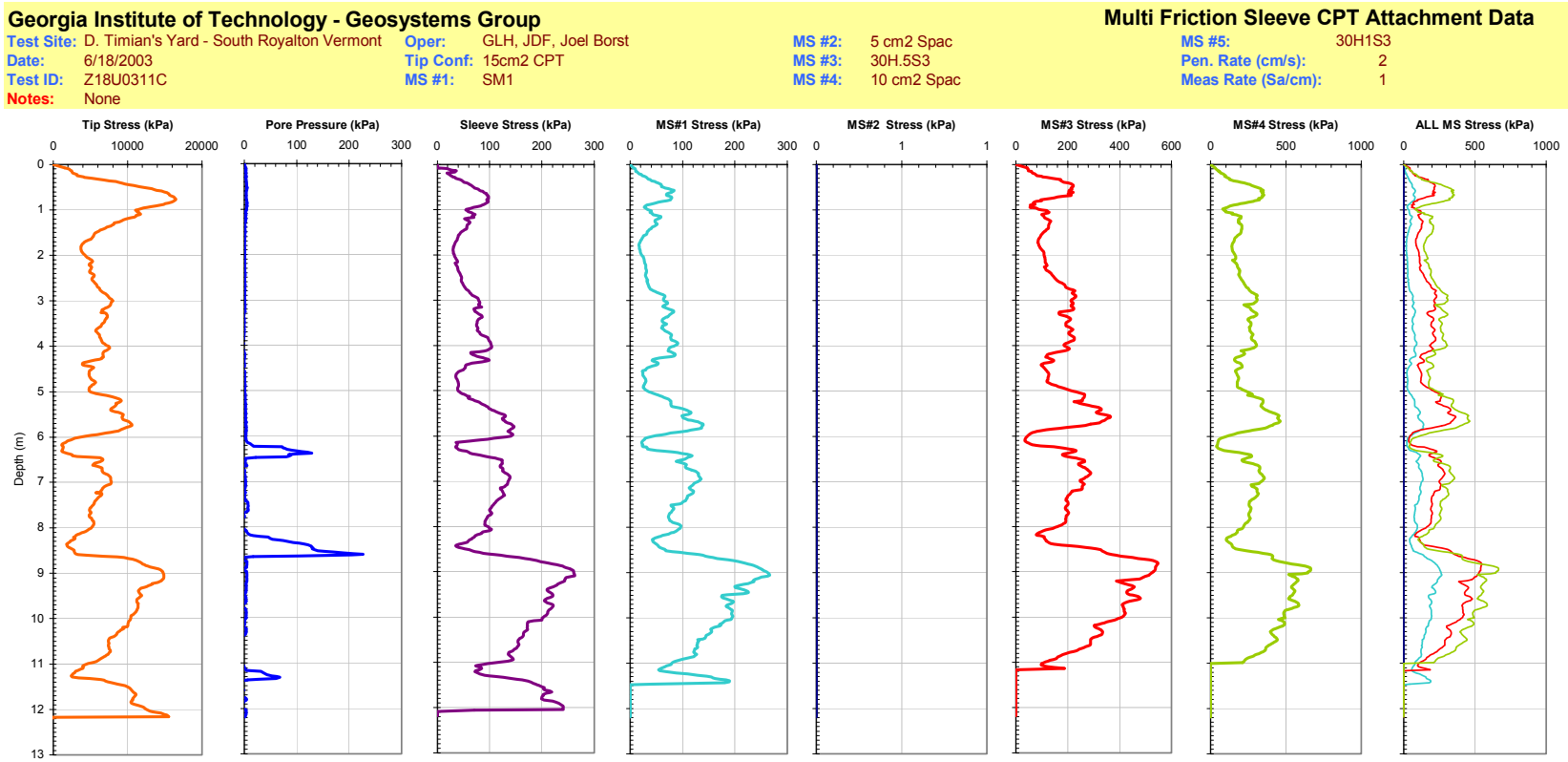

Figure A-35. Plot of CPTU-MFA Sensor Traces from Sounding MFA_75 at the SRVT Site.

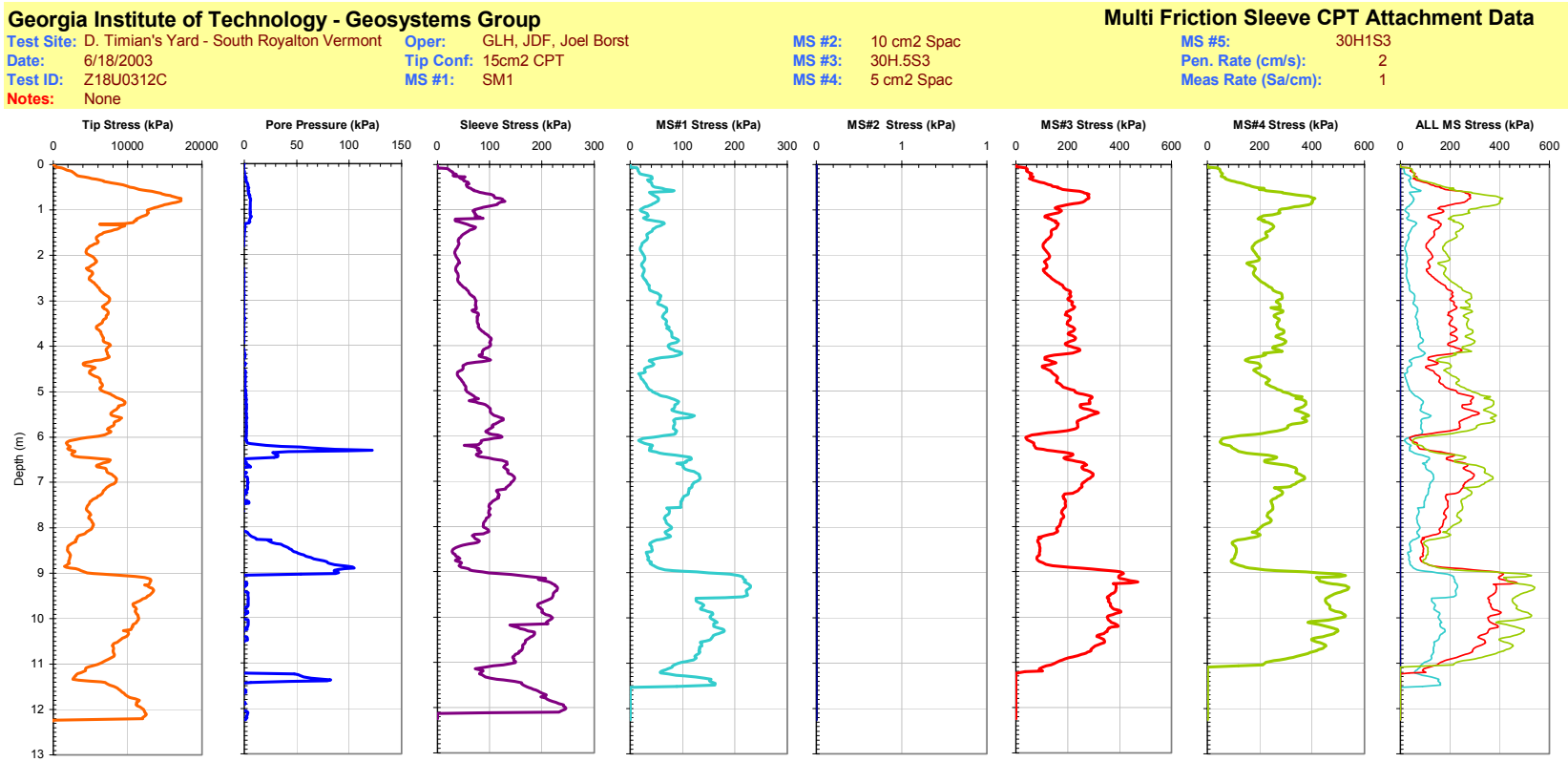

Figure A-36. Plot of CPTU-MFA Sensor Traces from Sounding MFA_76 at the SRVT Site.

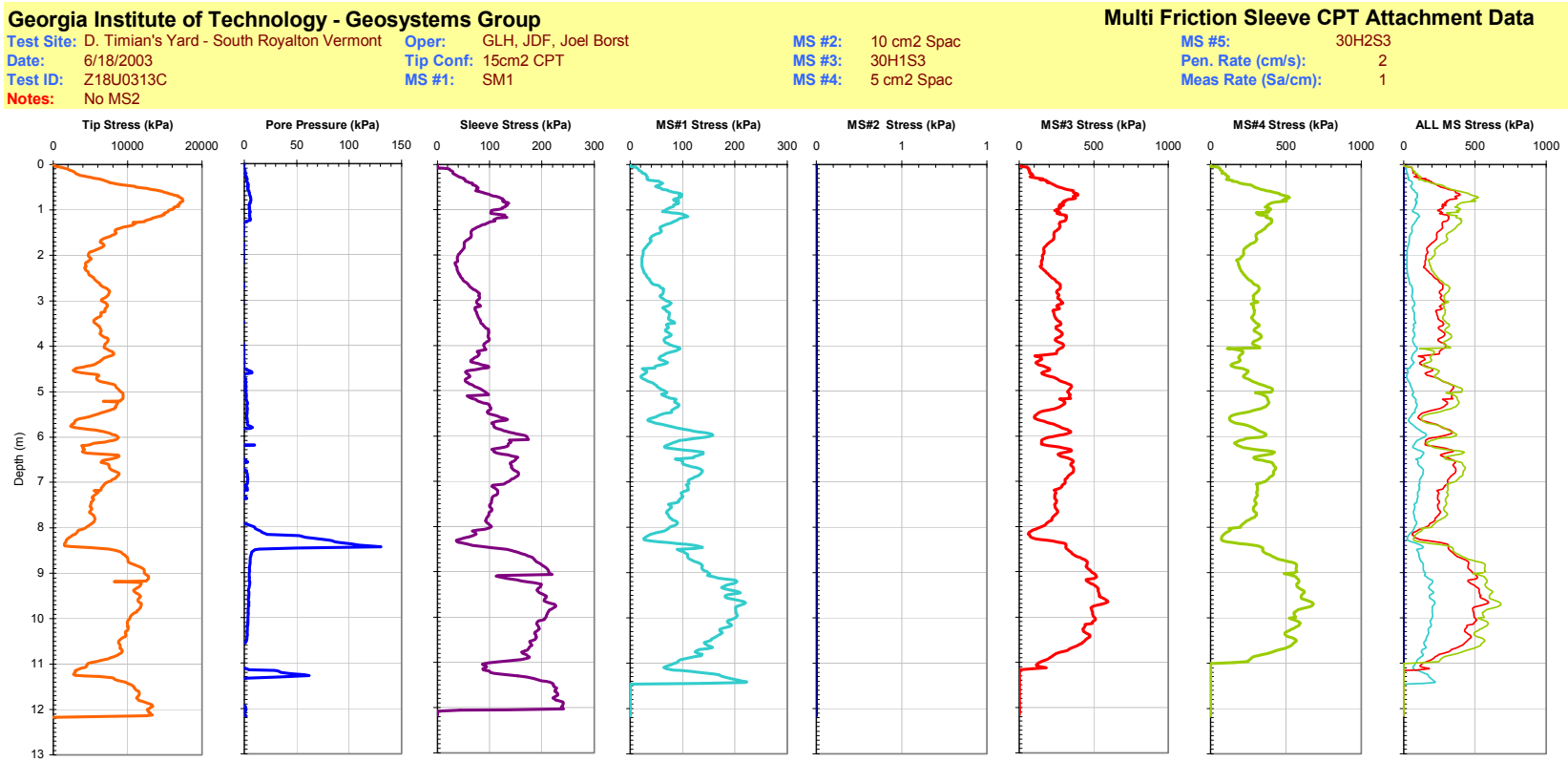

Figure A-37. Plot of CPTU-MFA Sensor Traces from Sounding MFA_77 at the SRVT Site.

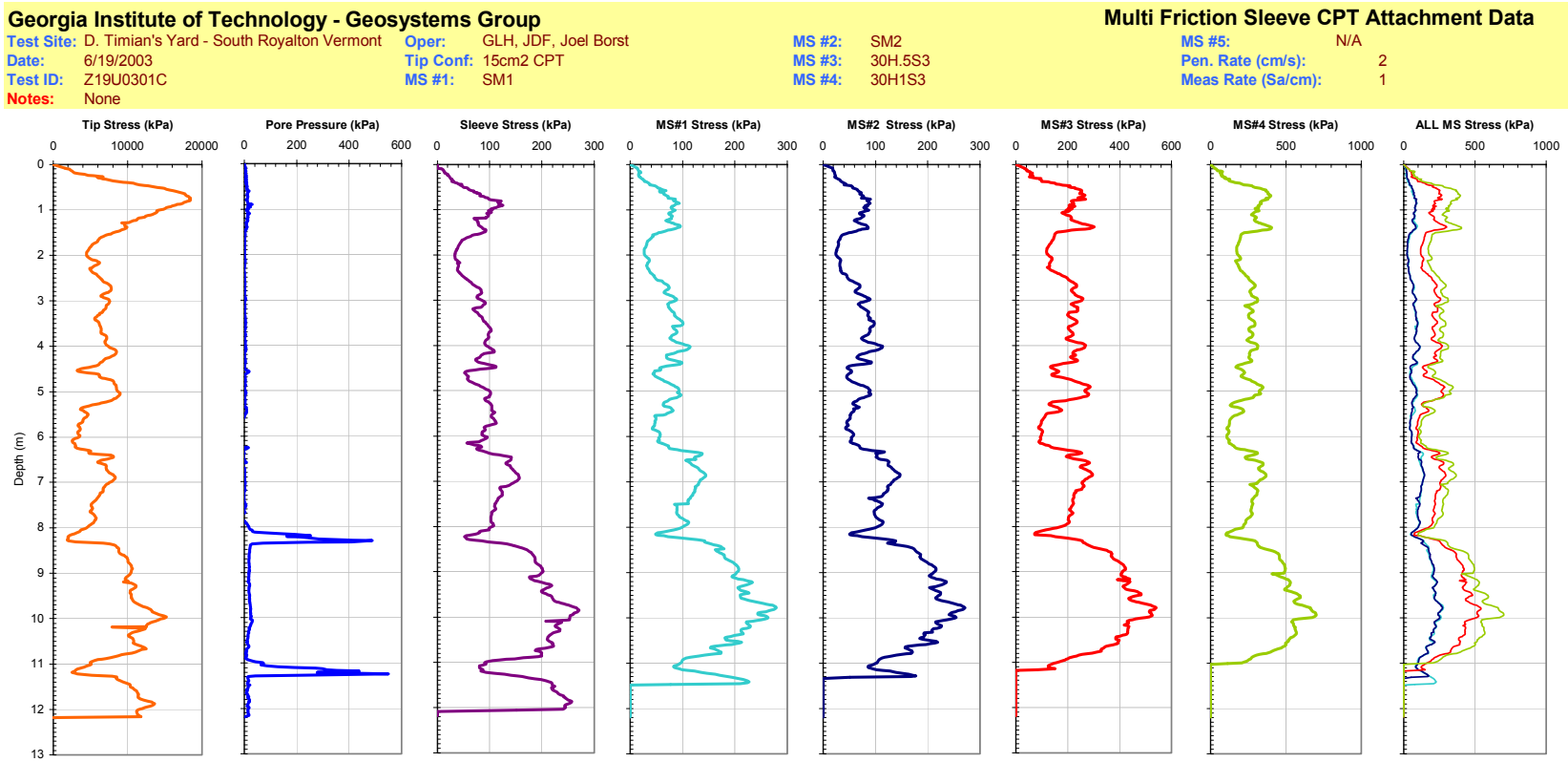

Figure A-38. Plot of CPTU-MFA Sensor Traces from Sounding MFA_78 at the SRVT Site.

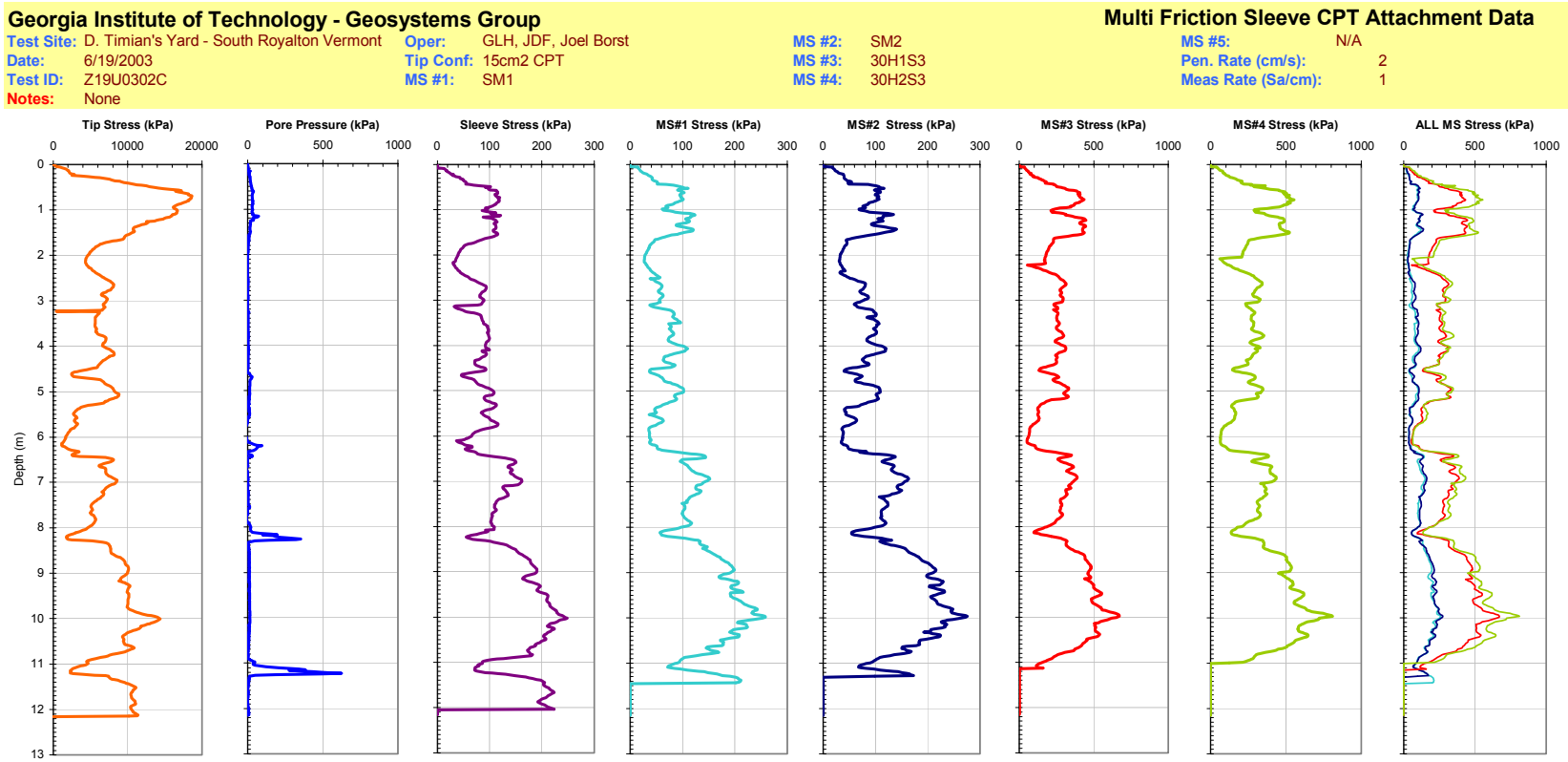

Figure A-39. Plot of CPTU-MFA Sensor Traces from Sounding MFA_79 at the SRVT Site.

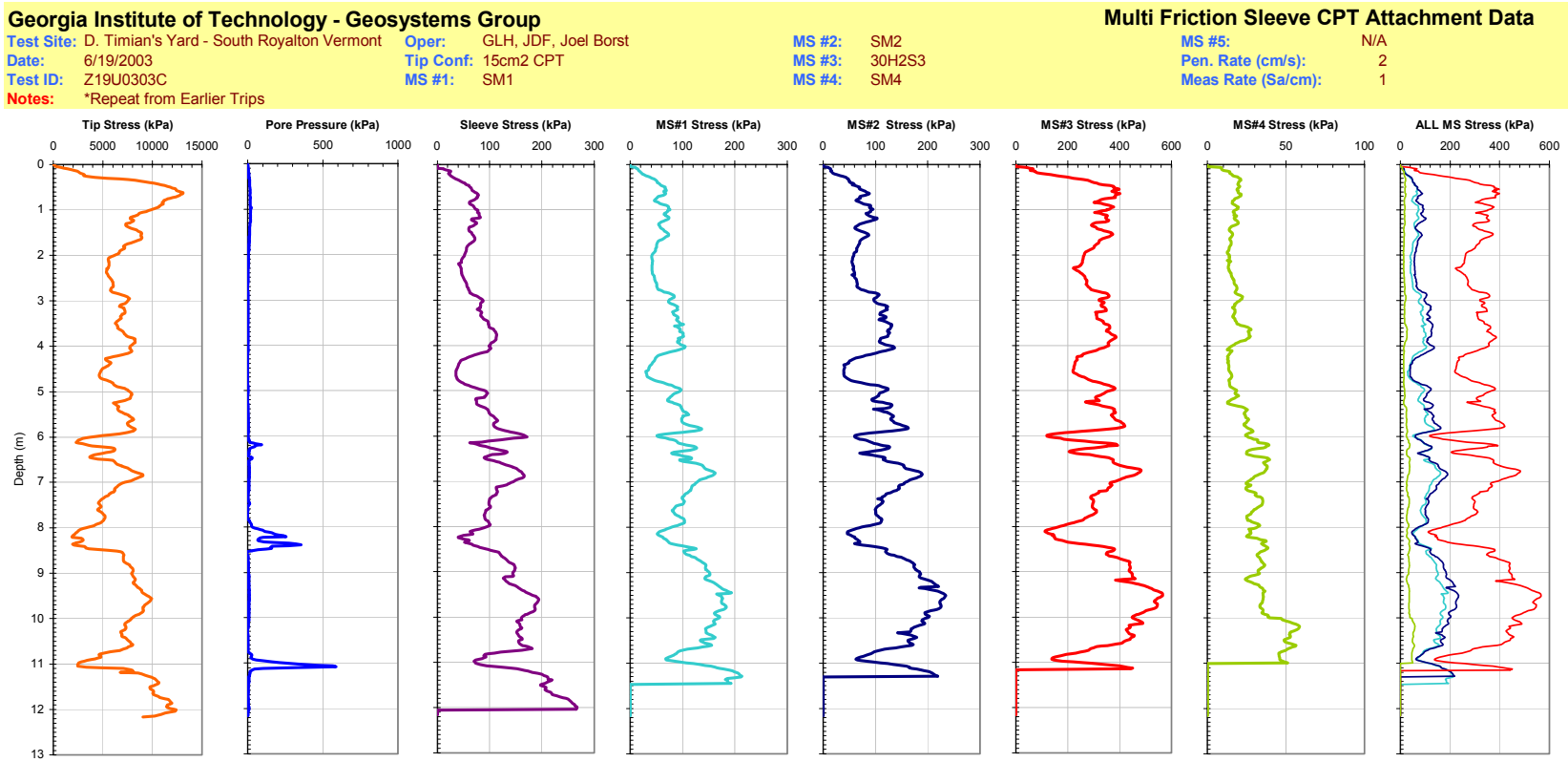

Figure A-40. Plot of CPTU-MFA Sensor Traces from Sounding MFA_80 at the SRVT Site.

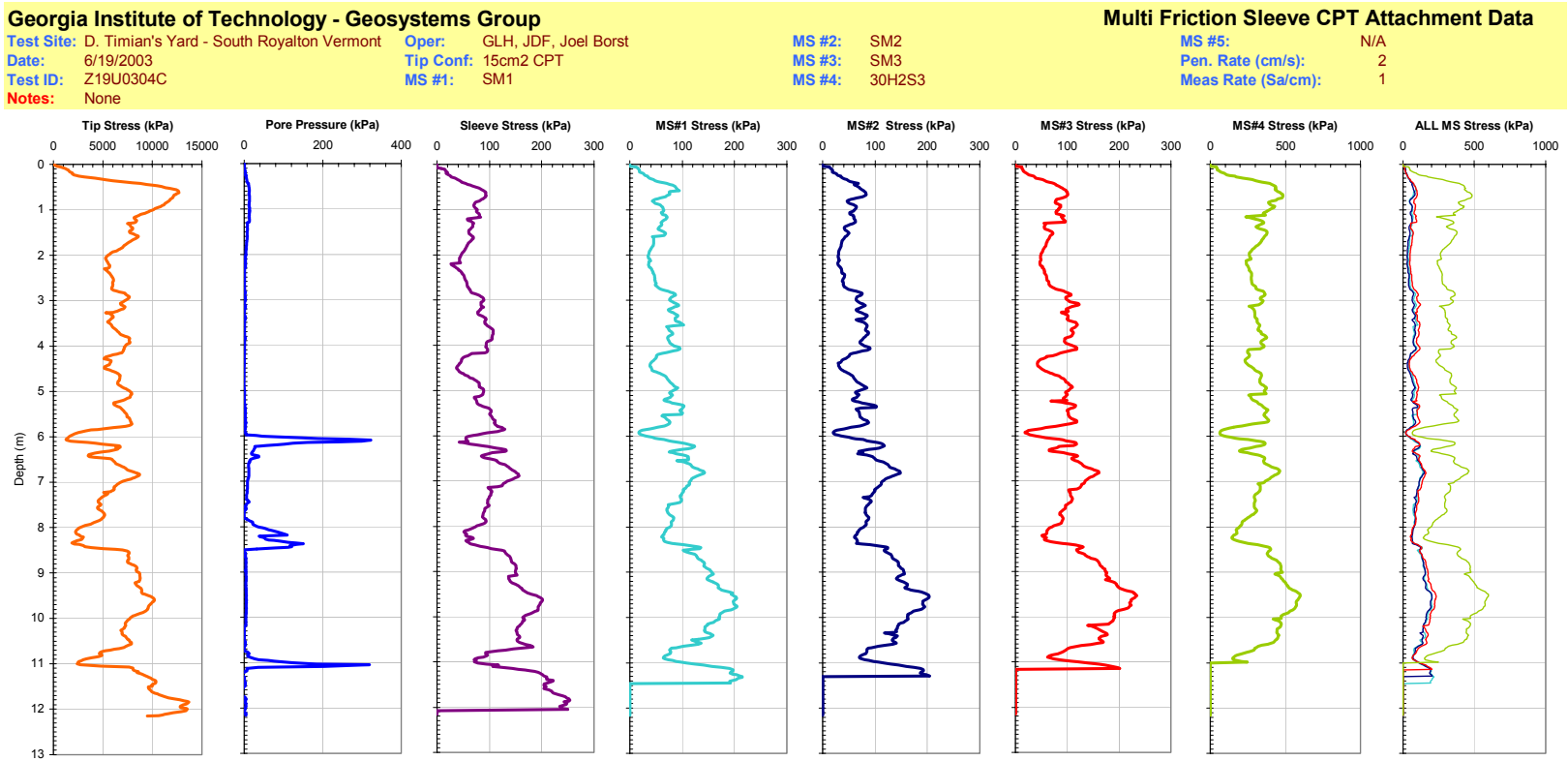

Figure A-41. Plot of CPTU-MFA Sensor Traces from Sounding MFA_81 at the SRVT Site.

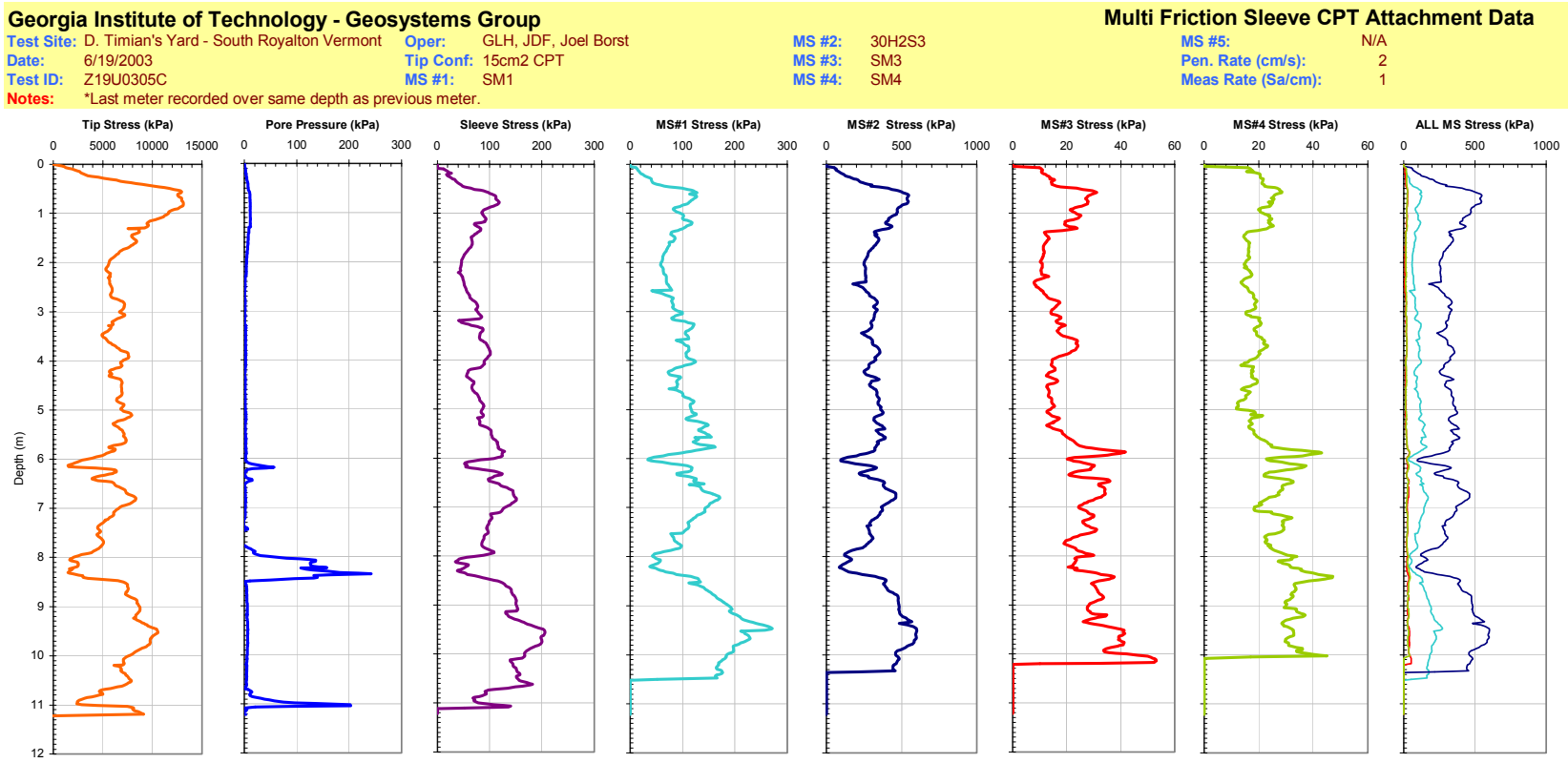

Figure A-42. Plot of CPTU-MFA Sensor Traces from Sounding MFA_82 at the SRVT Site.

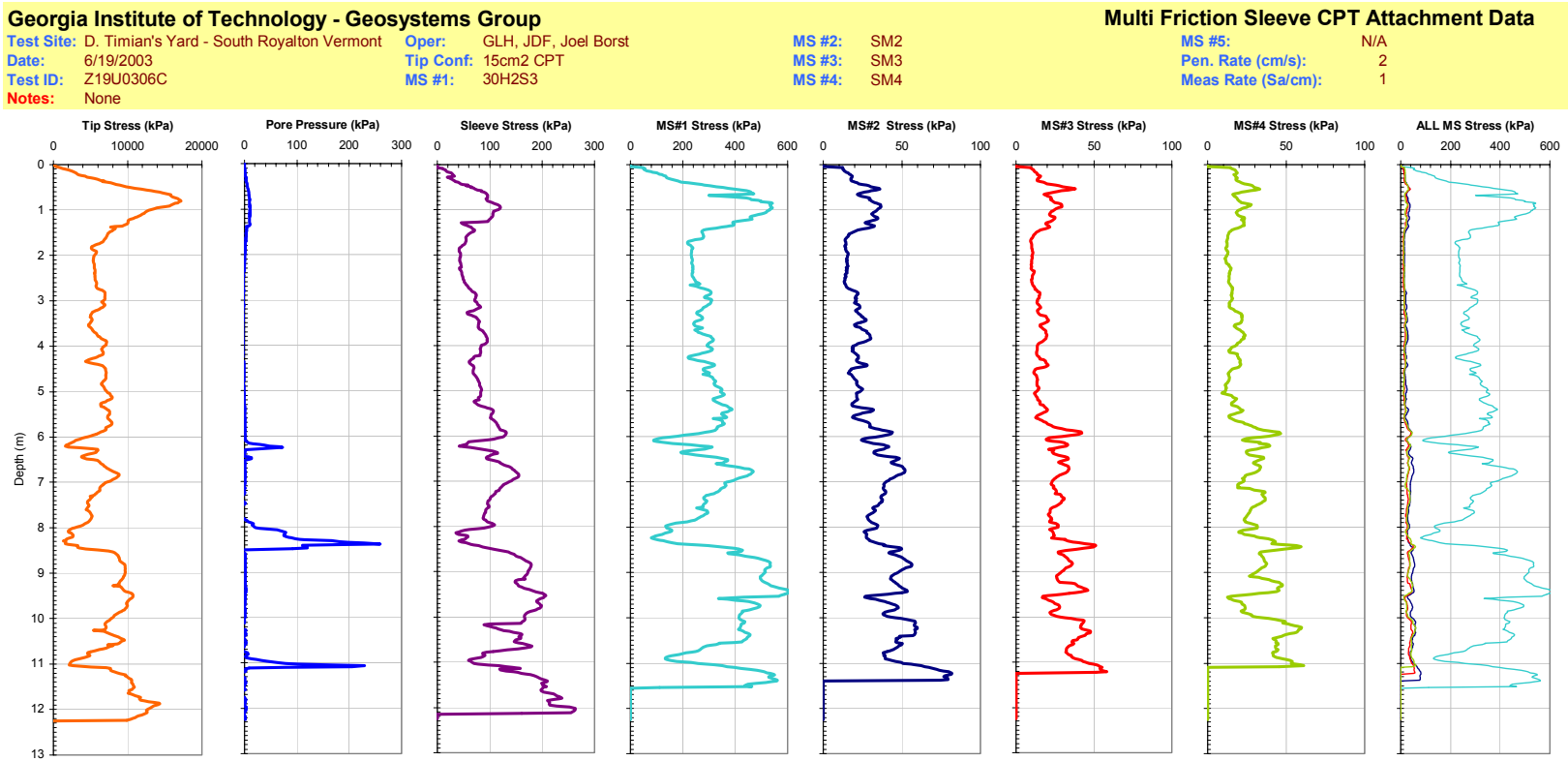

Figure A-43. Plot of CPTU-MFA Sensor Traces from Sounding MFA_83 at the SRVT Site.

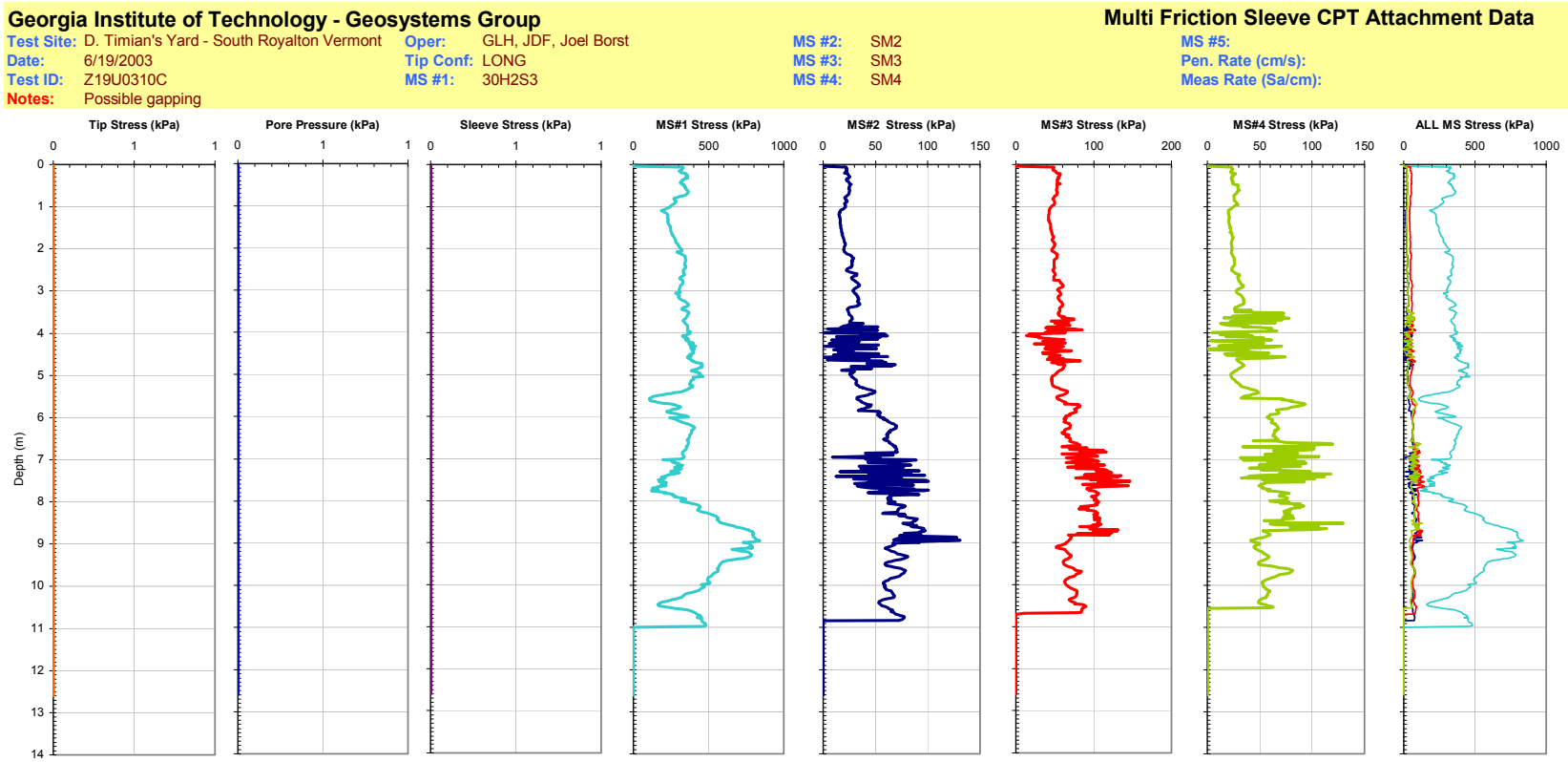

Figure A-44. Plot of CPTU-MFA Sensor Traces from Sounding MFA_84 at the SRVT Site.

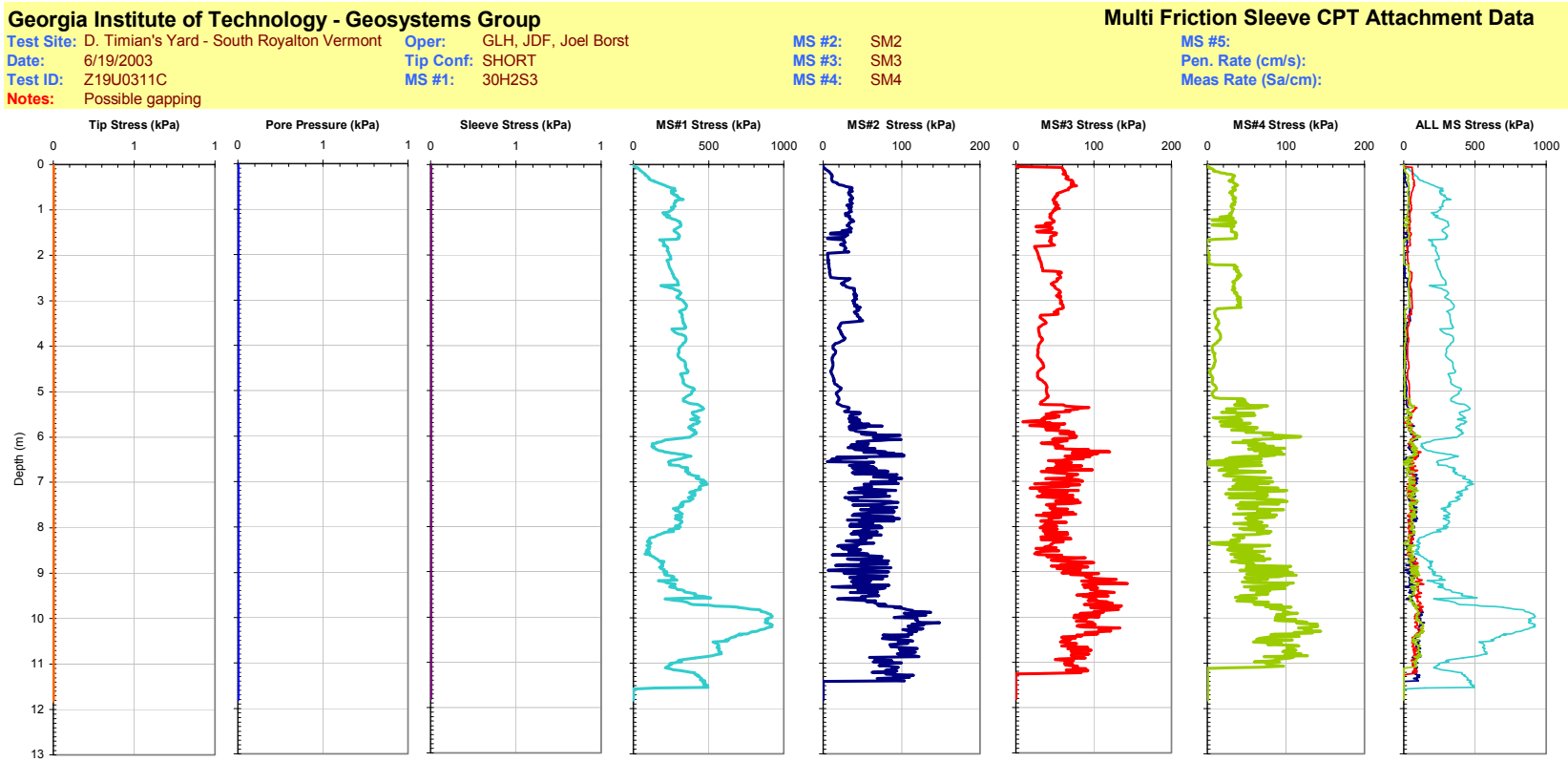

Figure A-45. Plot of CPTU-MFA Sensor Traces from Sounding MFA_85 at the SRVT Site.

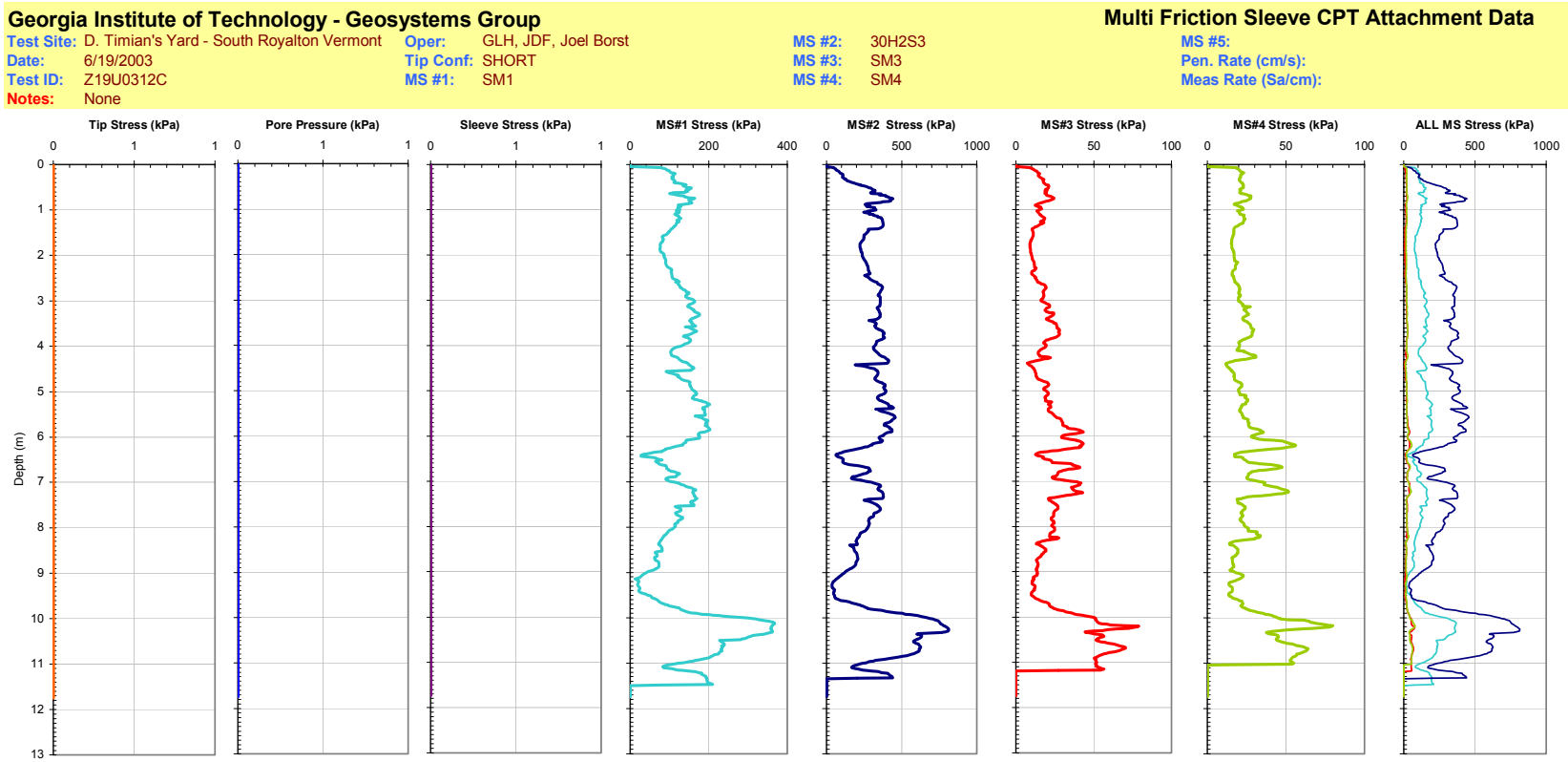

Figure A-46. Plot of CPTU-MFA Sensor Traces from Sounding MFA_86 at the SRVT Site.

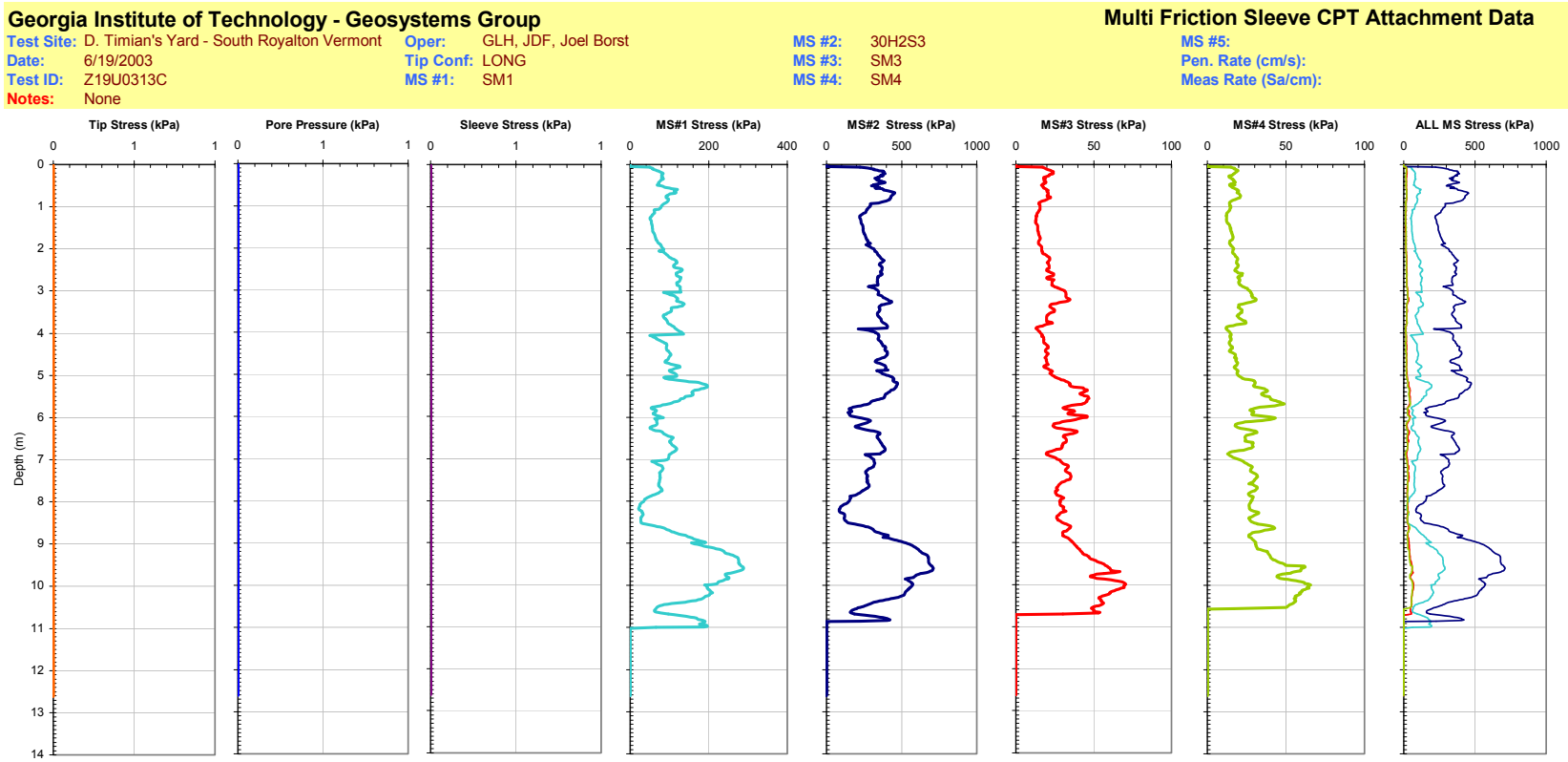

Figure A-47. Plot of CPTU-MFA Sensor Traces from Sounding MFA_87 at the SRVT Site.

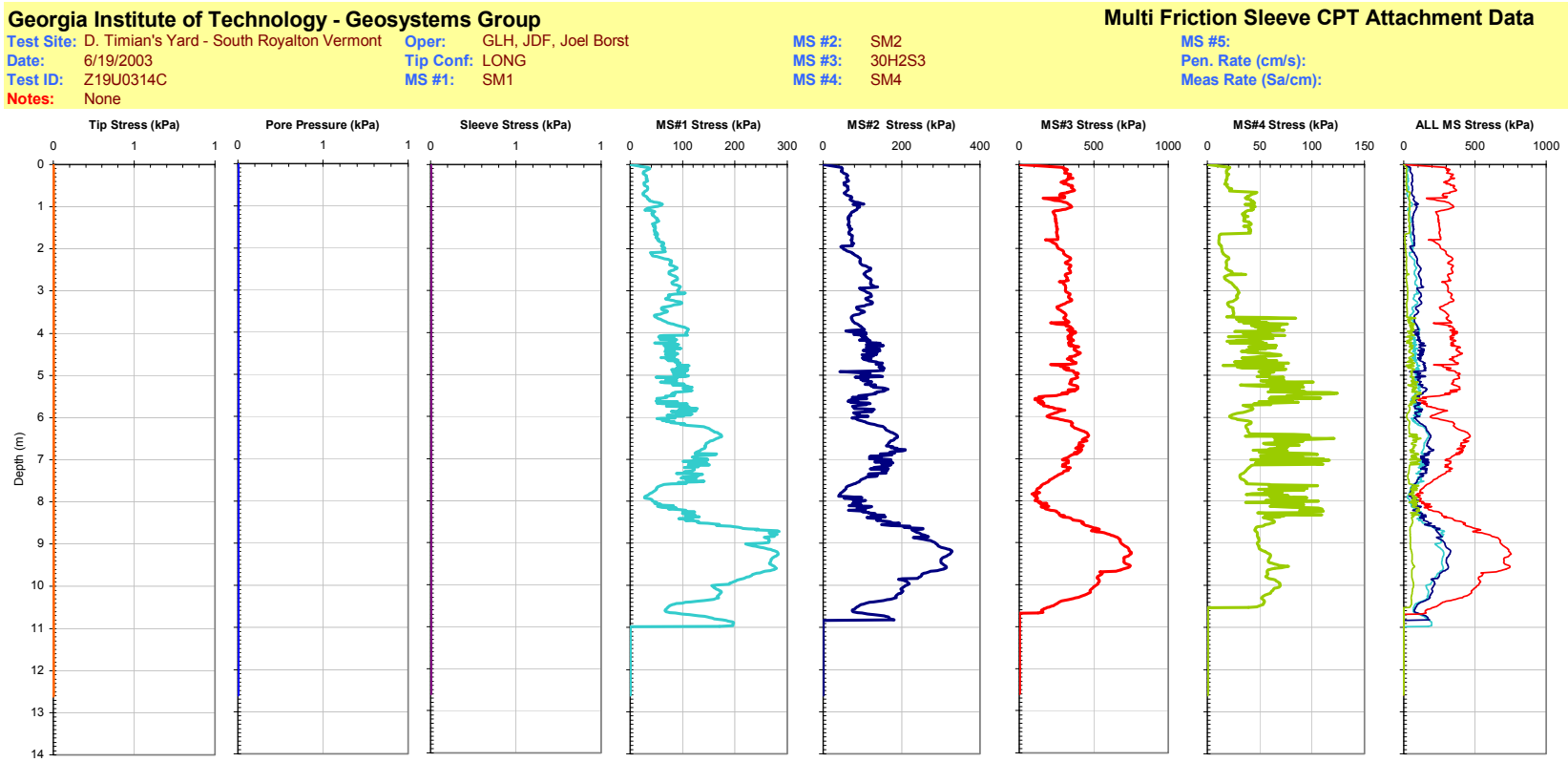

Figure A-48. Plot of CPTU-MFA Sensor Traces from Sounding MFA_88 at the SRVT Site.

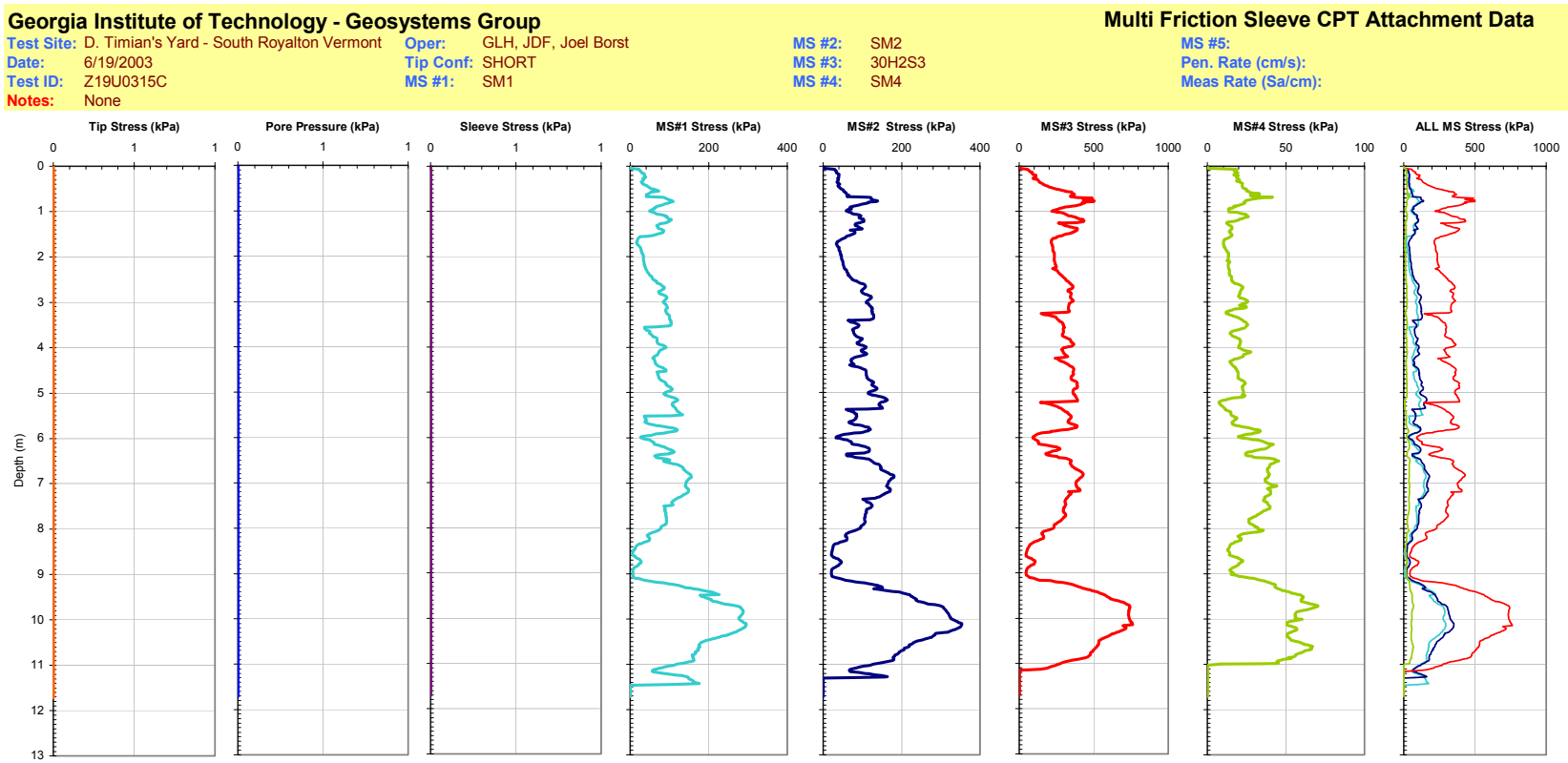

Figure A-49. Plot of CPTU-MFA Sensor Traces from Sounding MFA_89 at the SRVT Site.

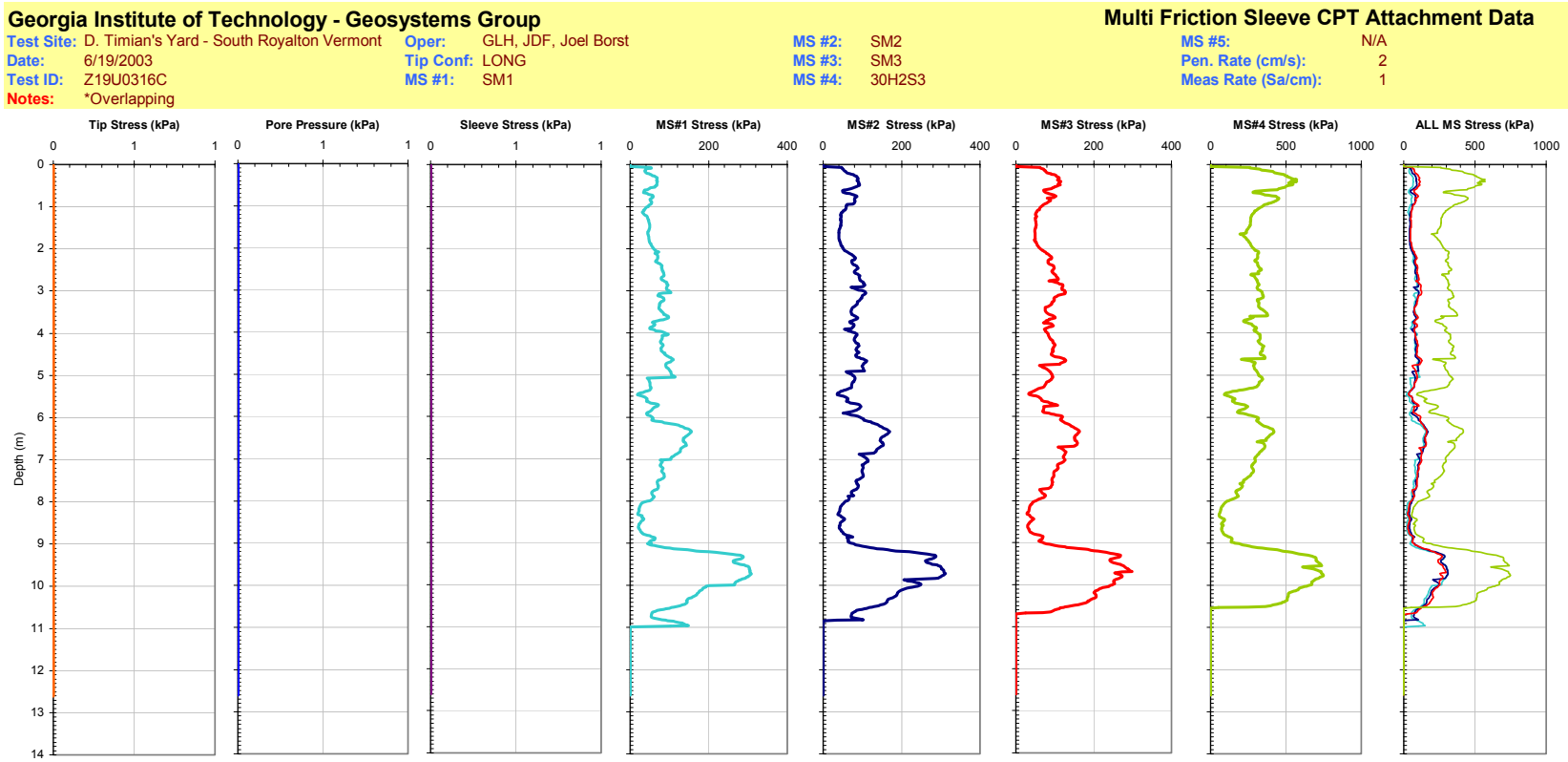

Figure A-50. Plot of CPTU-MFA Sensor Traces from Sounding MFA_90 at the SRVT Site.

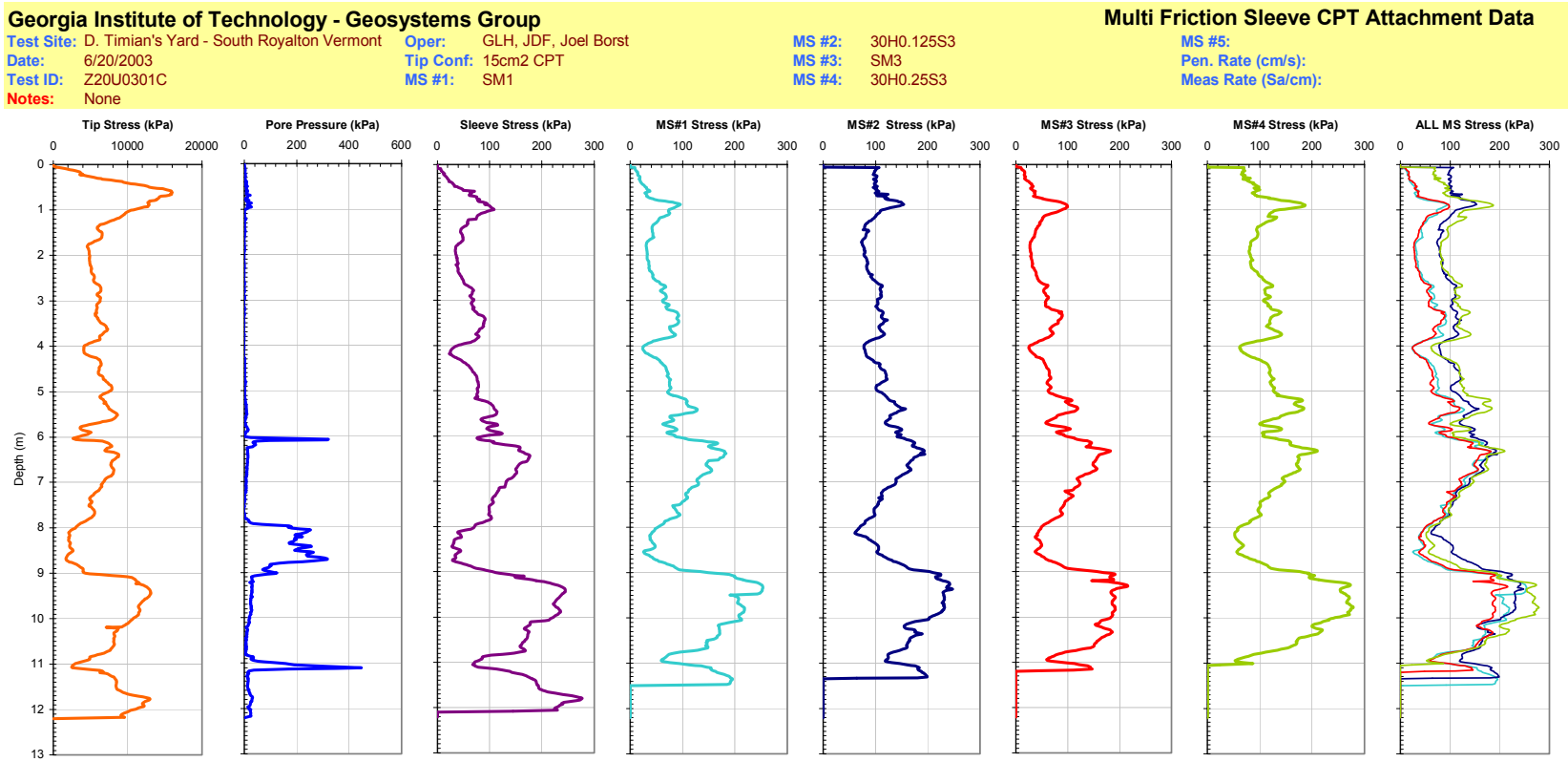

Figure A-51. Plot of CPTU-MFA Sensor Traces from Sounding MFA_91 at the SRVT Site.

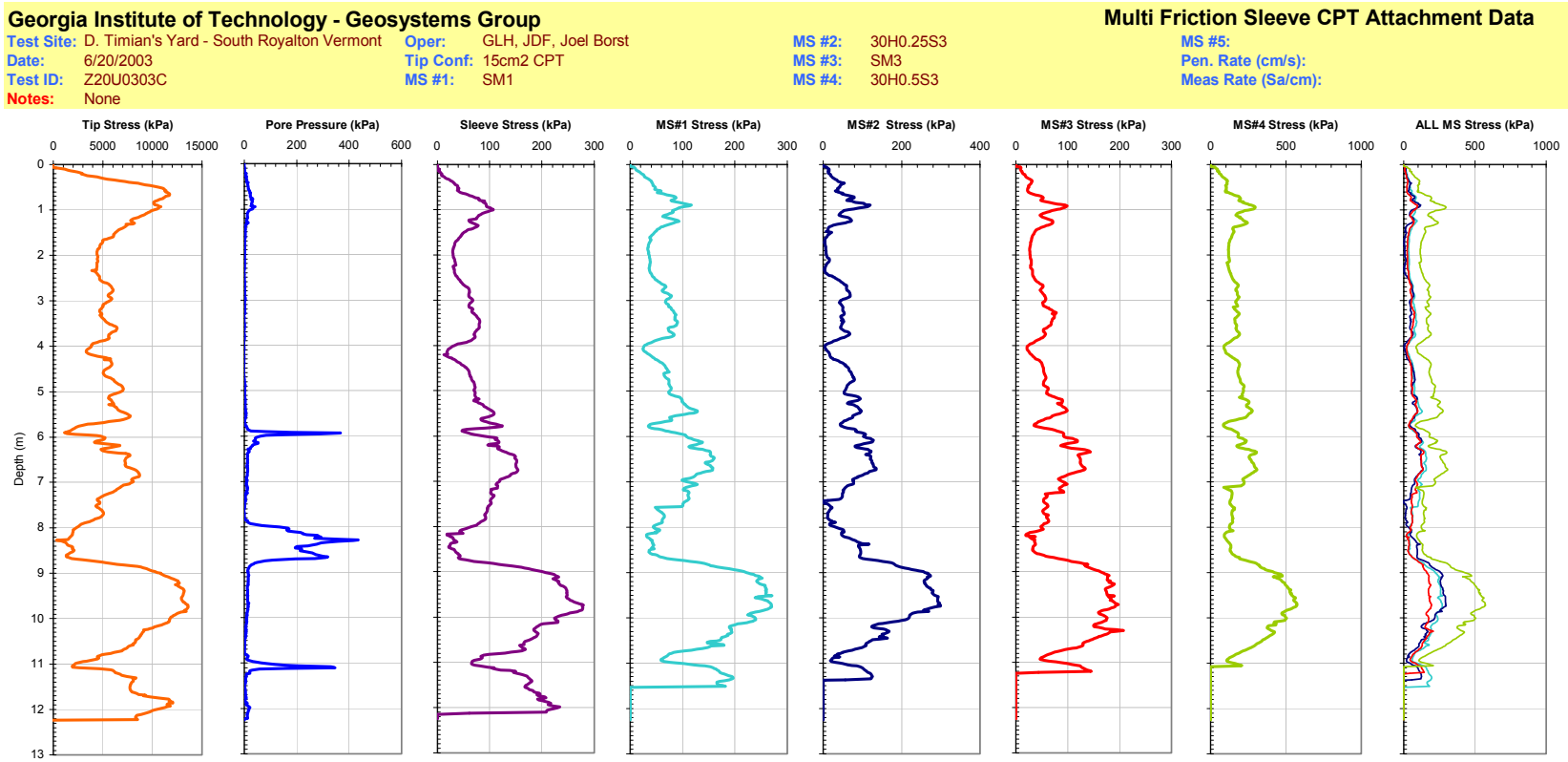

Figure A-52. Plot of CPTU-MFA Sensor Traces from Sounding MFA_92 at the SRVT Site.

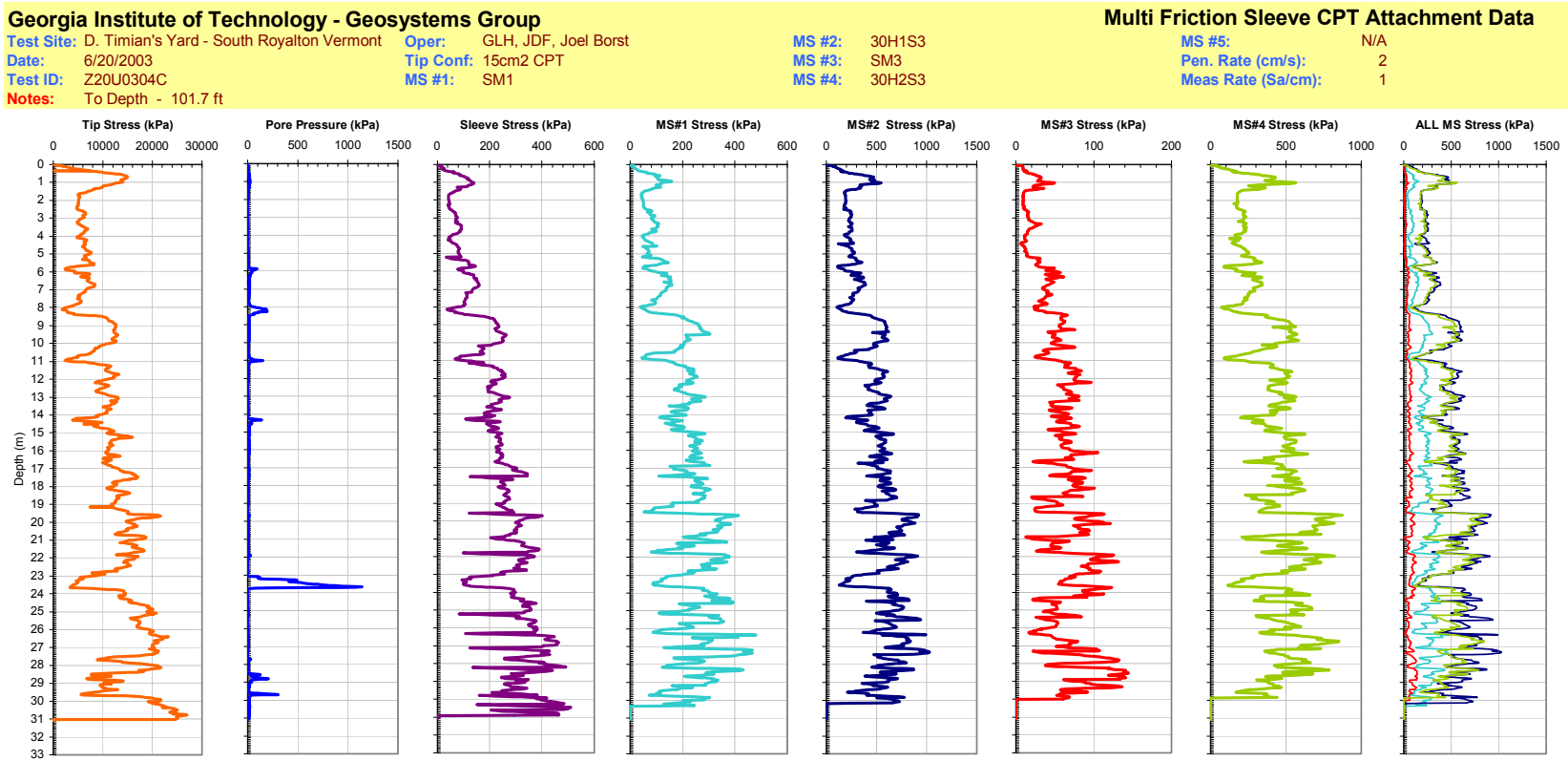

Figure A-53. Plot of CPTU-MFA Sensor Traces from Sounding MFA_93 at the SRVT Site.

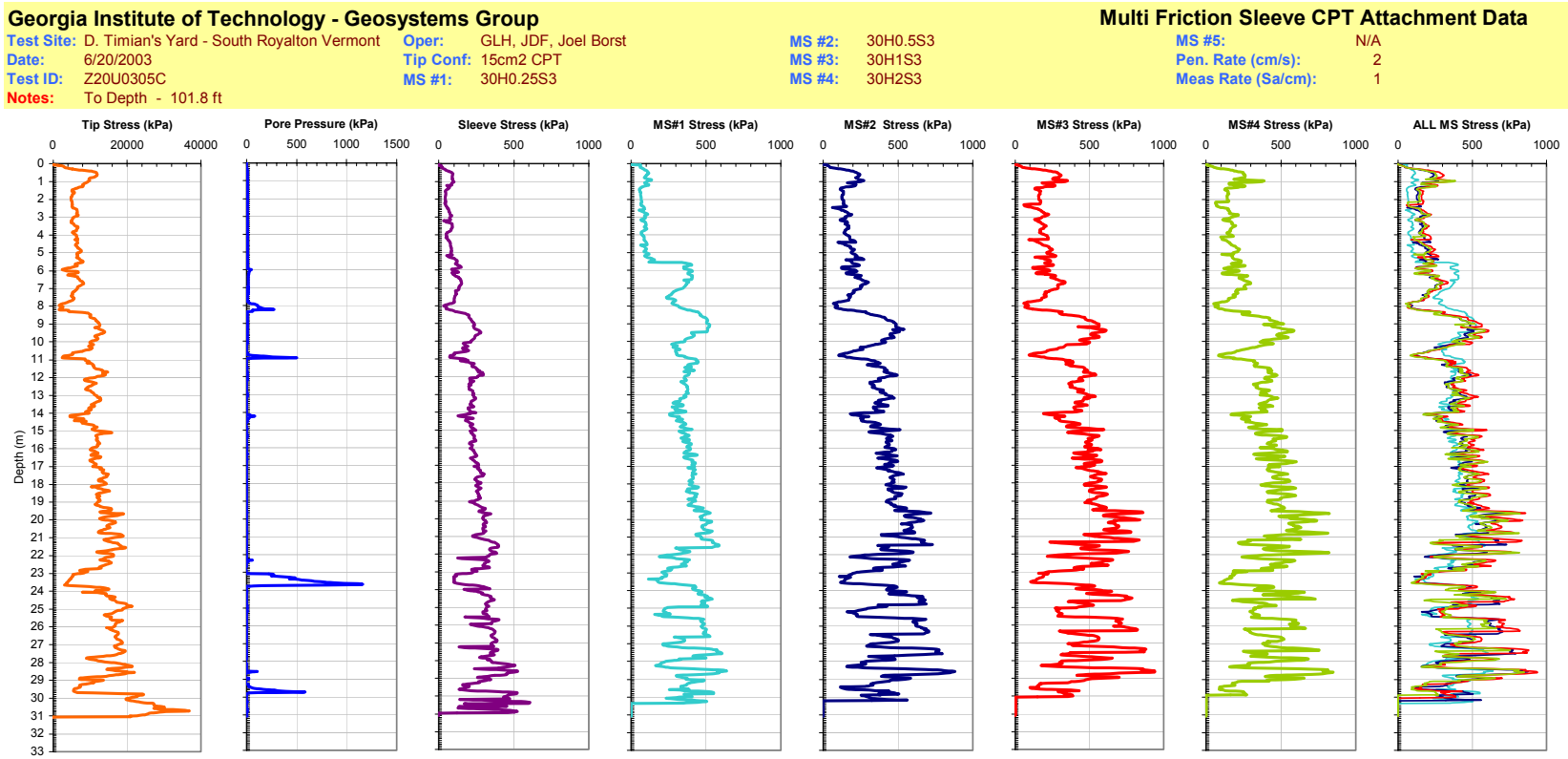

Figure A-54. Plot of CPTU-MFA Sensor Traces from Sounding MFA_94 at the SRVT Site.

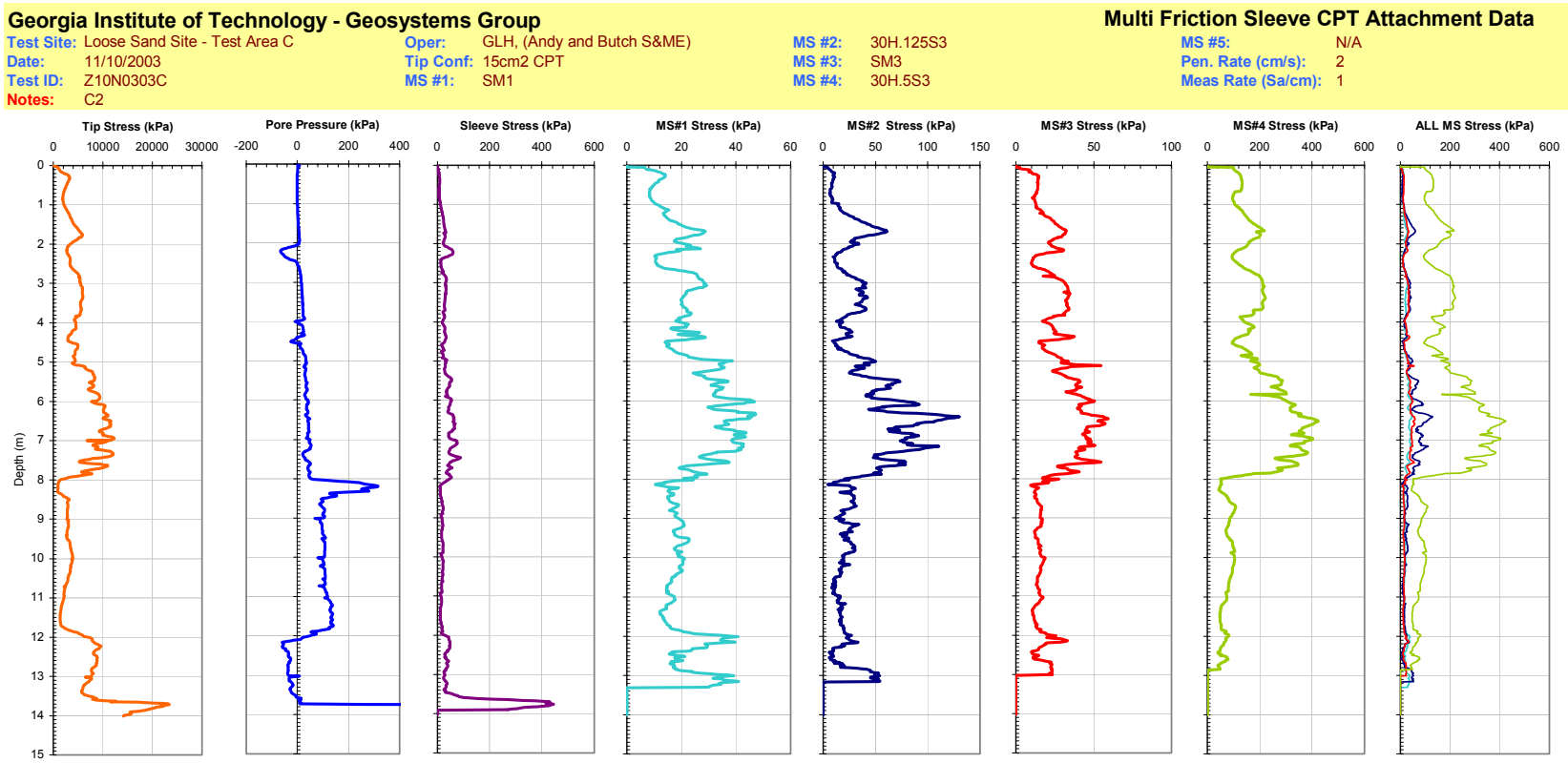

Figure A-55. Plot of CPTU-MFA Sensor Traces from Sounding MFA_95 at the LS Site.

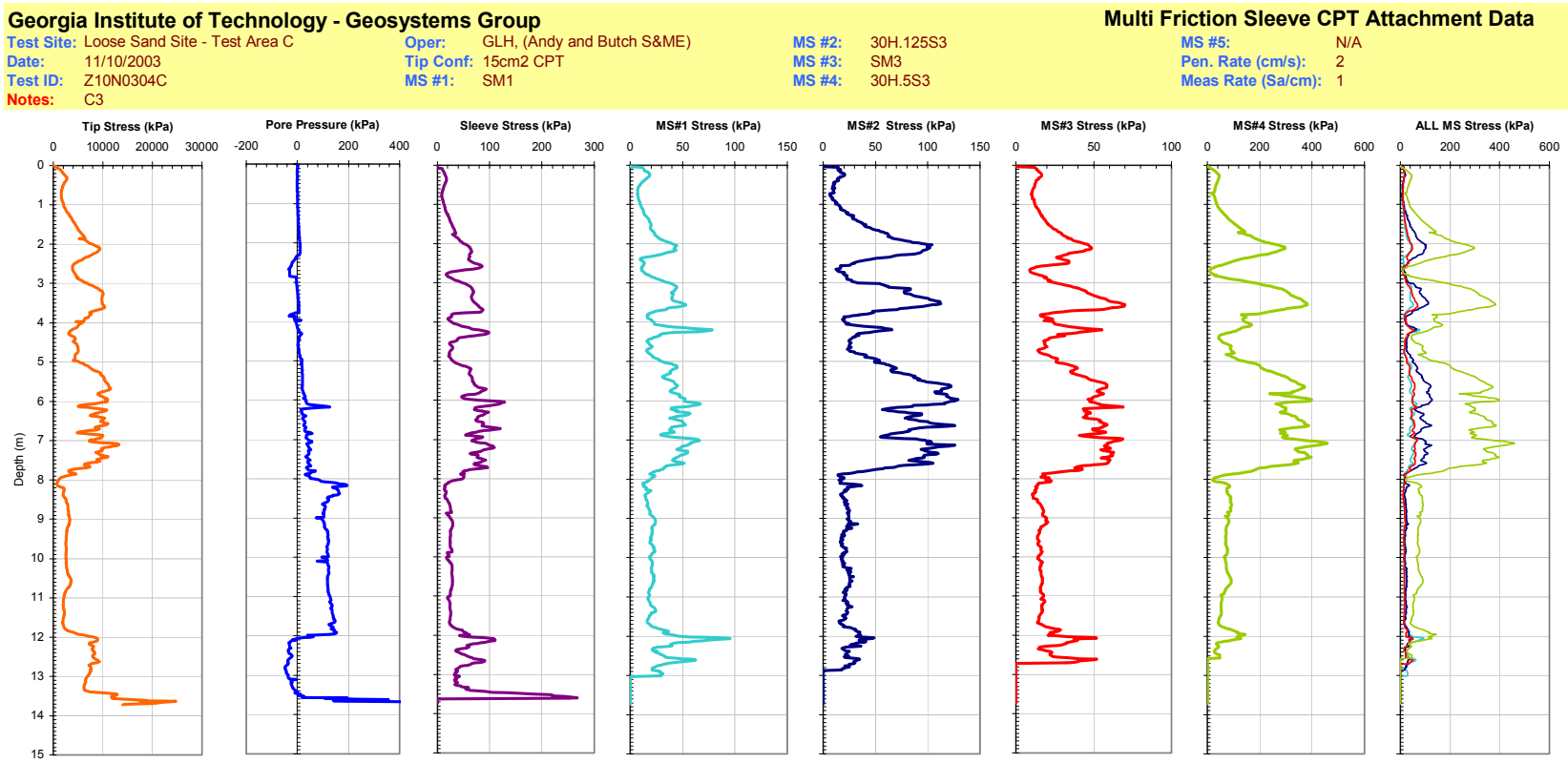

Figure A-56. Plot of CPTU-MFA Sensor Traces from Sounding MFA_96 at the LS Site.

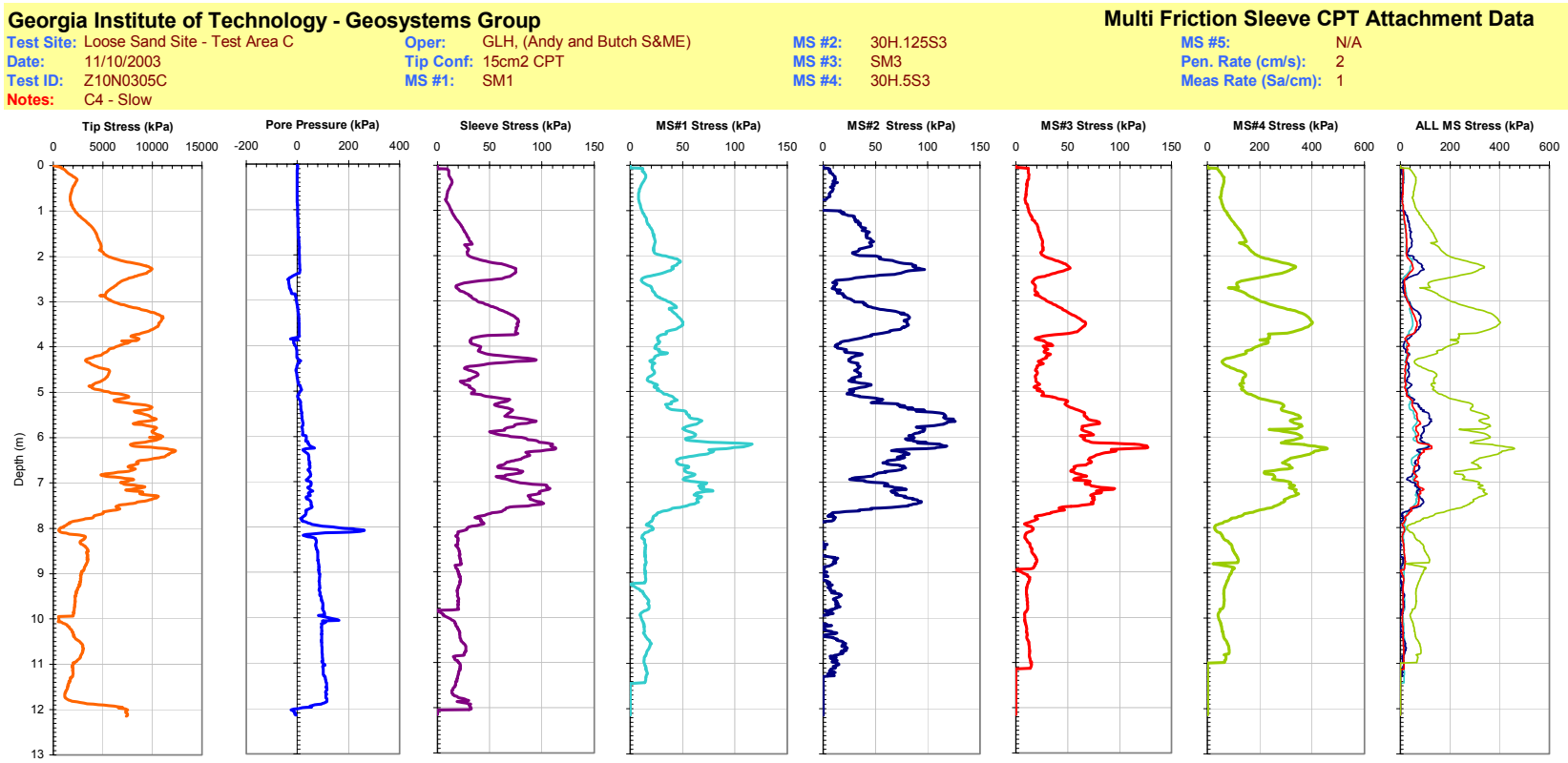

Figure A-57. Plot of CPTU-MFA Sensor Traces from Sounding MFA_97 at the LS Site.

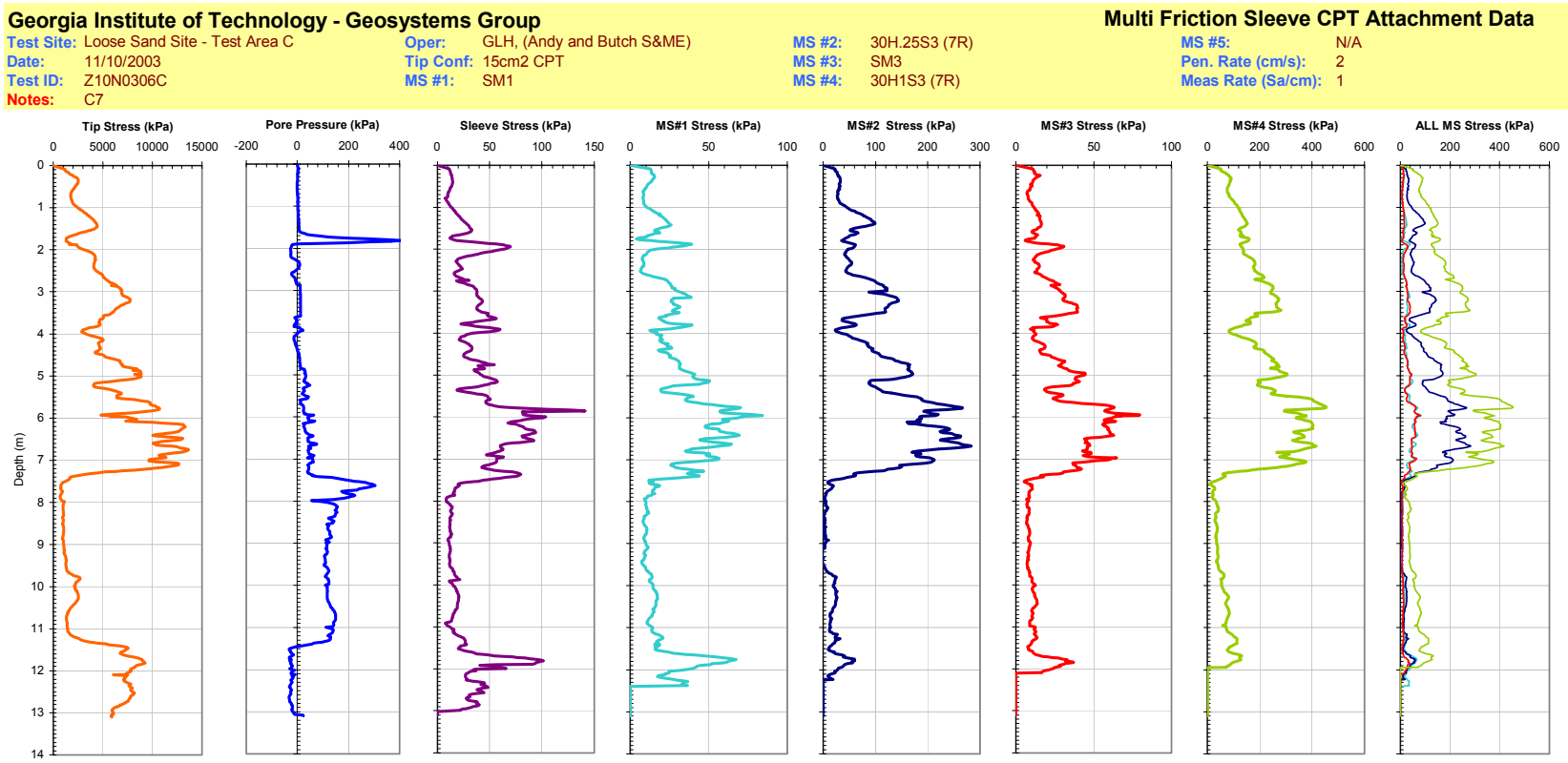

Figure A-58. Plot of CPTU-MFA Sensor Traces from Sounding MFA_98 at the LS Site.

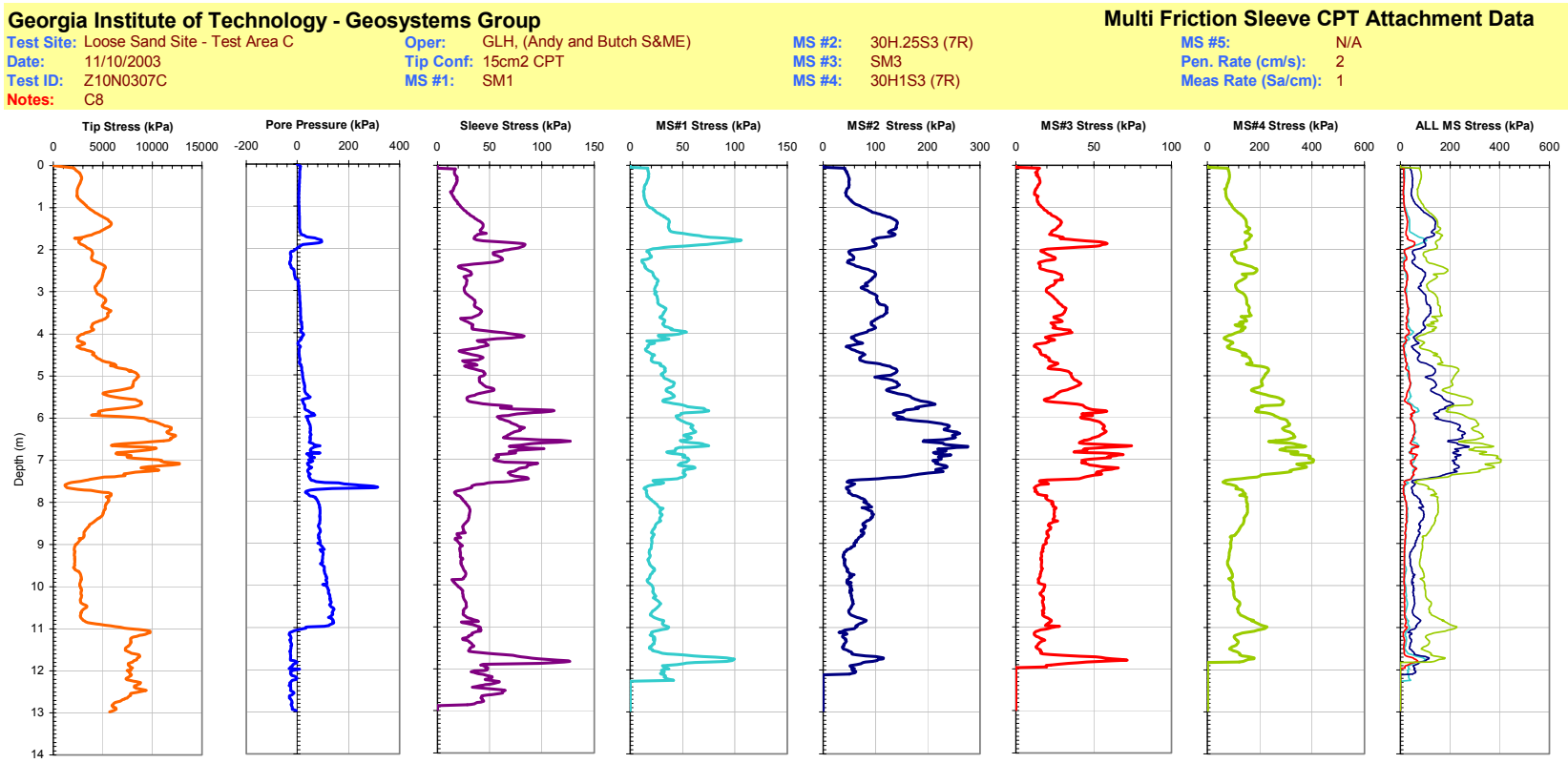

Figure A-59. Plot of CPTU-MFA Sensor Traces from Sounding MFA_99 at the LS Site.

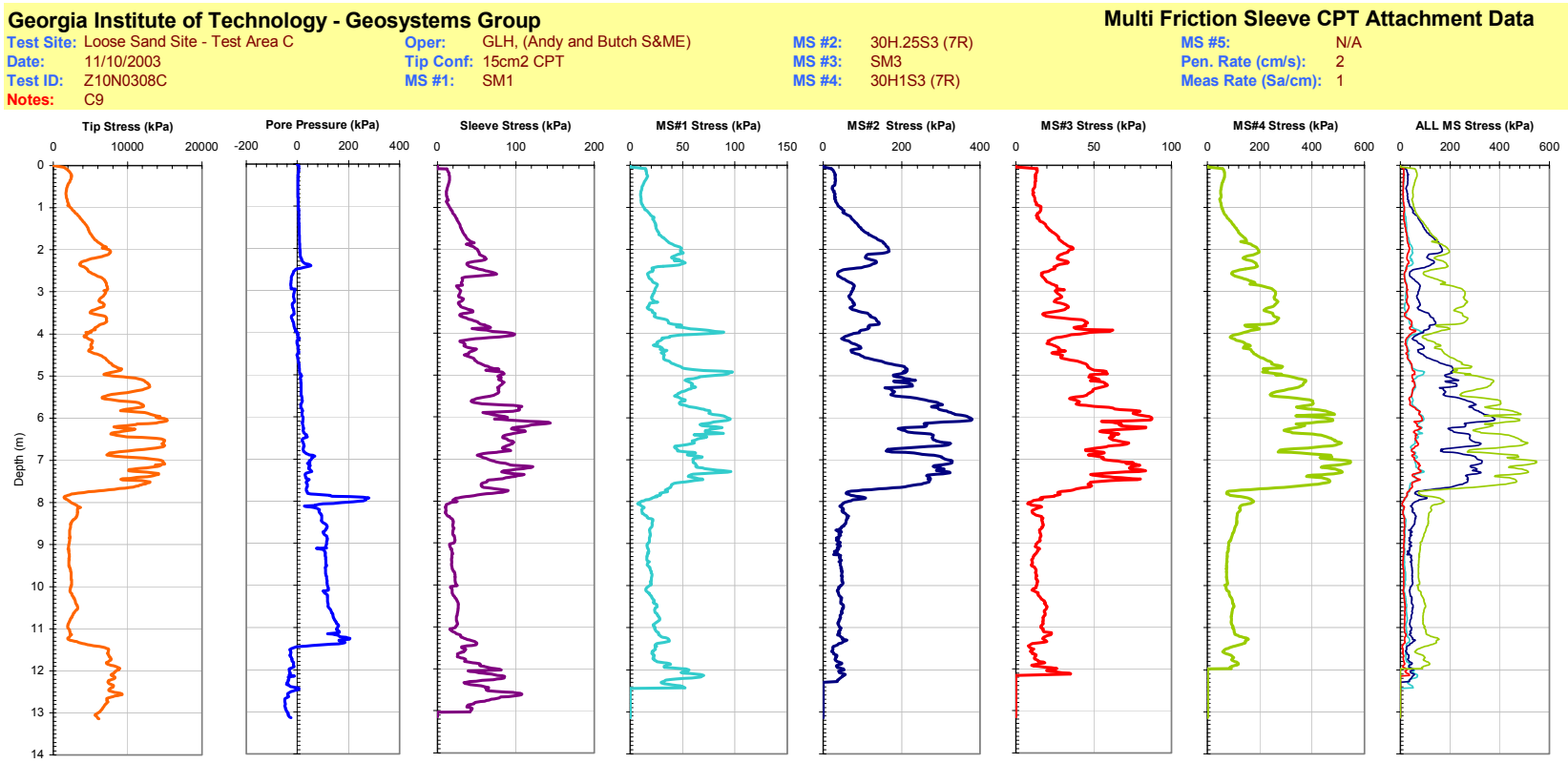

Figure A-60. Plot of CPTU-MFA Sensor Traces from Sounding MFA_100 at the LS Site.

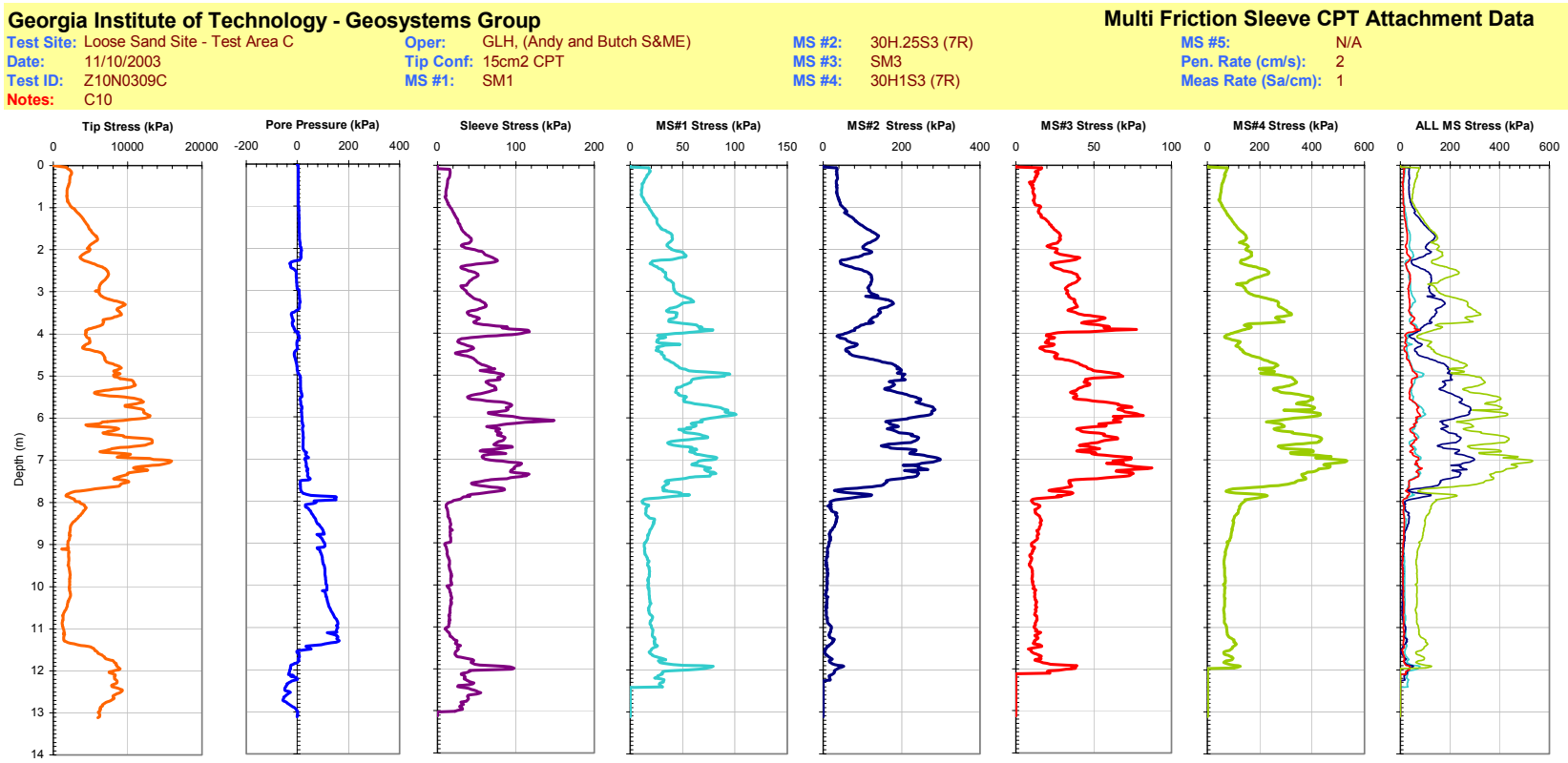

Figure A-61. Plot of CPTU-MFA Sensor Traces from Sounding MFA_101 at the LS Site.

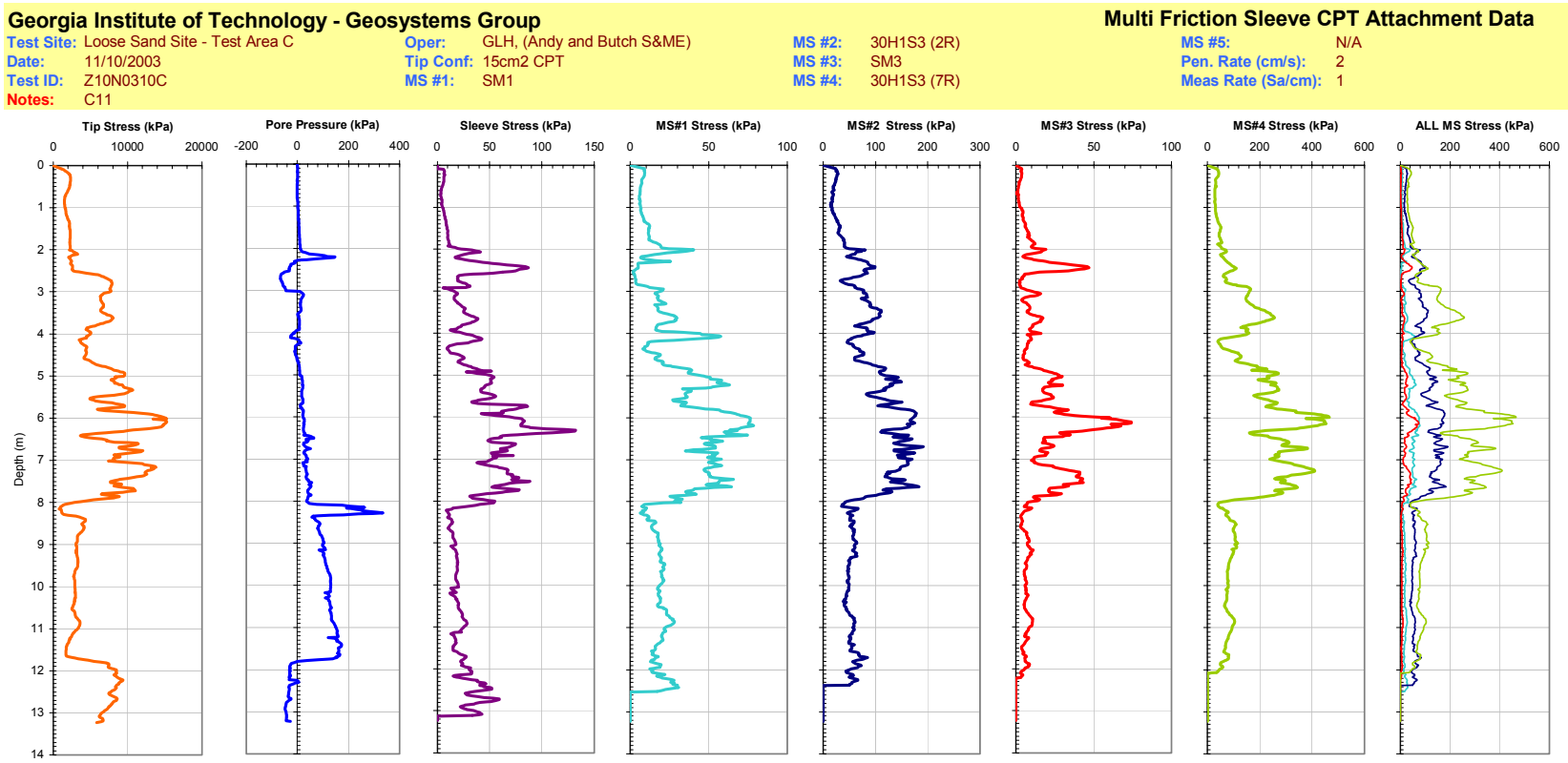

Figure A-62. Plot of CPTU-MFA Sensor Traces from Sounding MFA_102 at the LS Site.

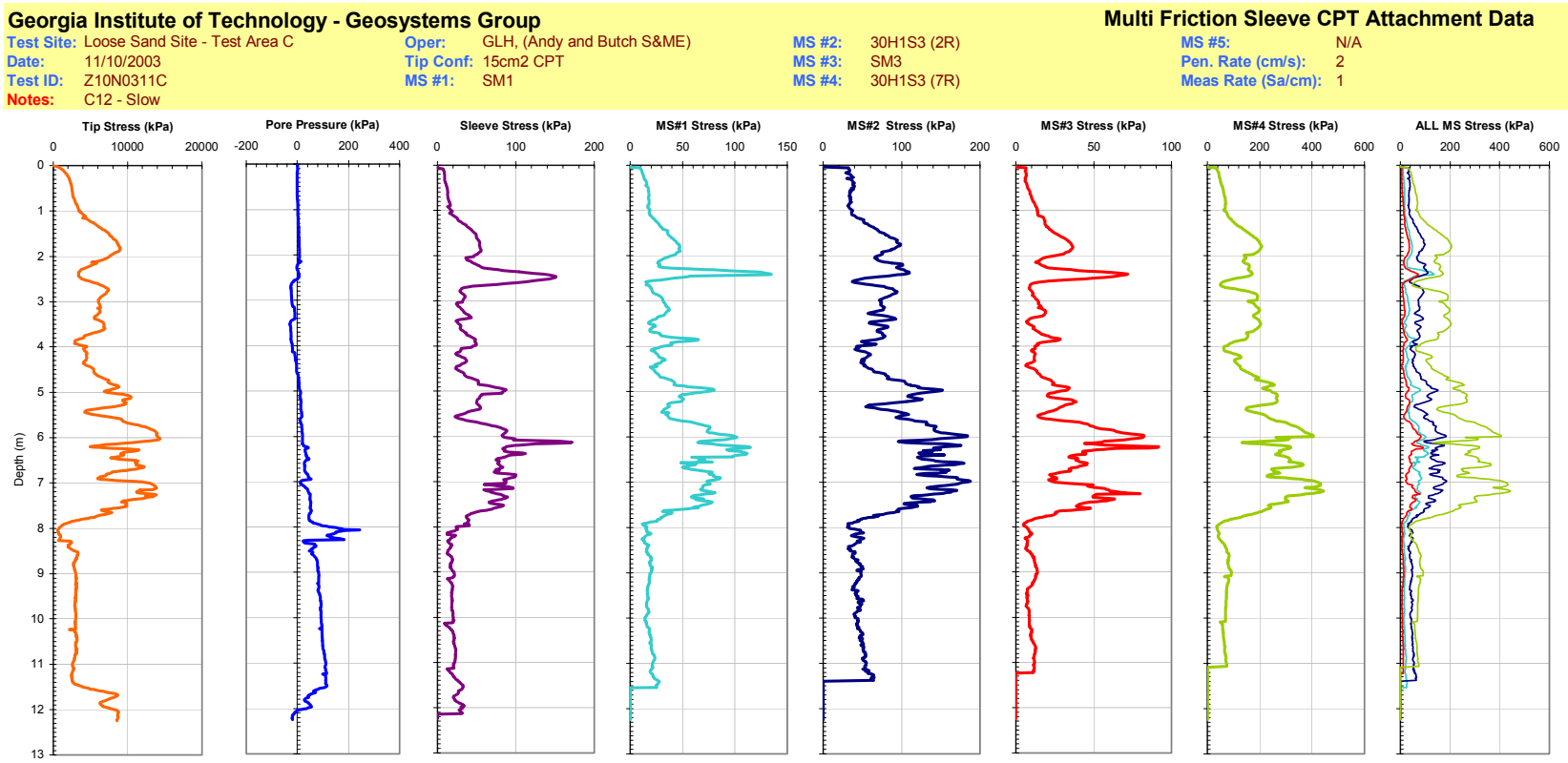

Figure A-63. Plot of CPTU-MFA Sensor Traces from Sounding MFA_103 at the LS Site.

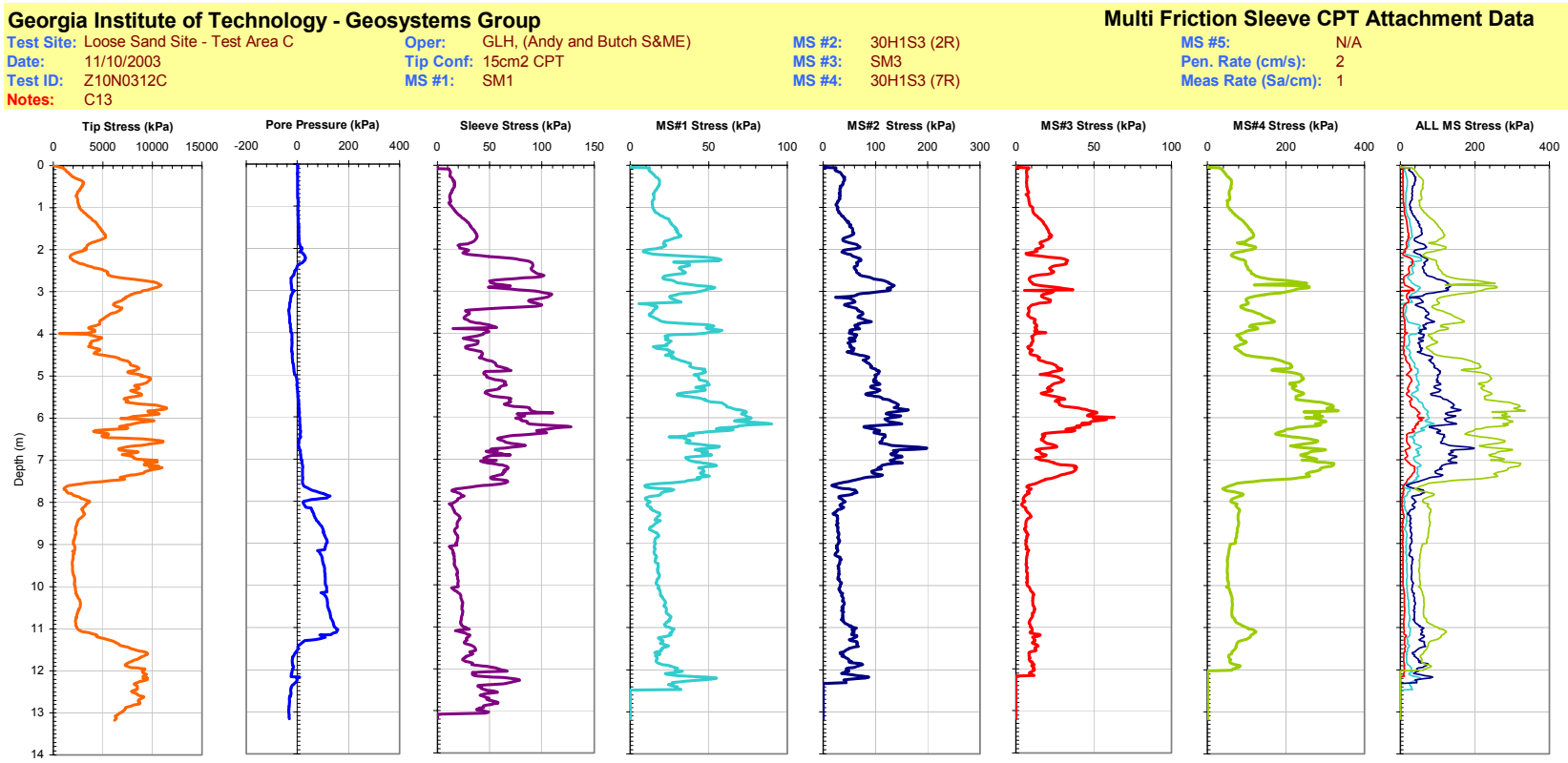

Figure A-64. Plot of CPTU-MFA Sensor Traces from Sounding MFA_104 at the LS Site.

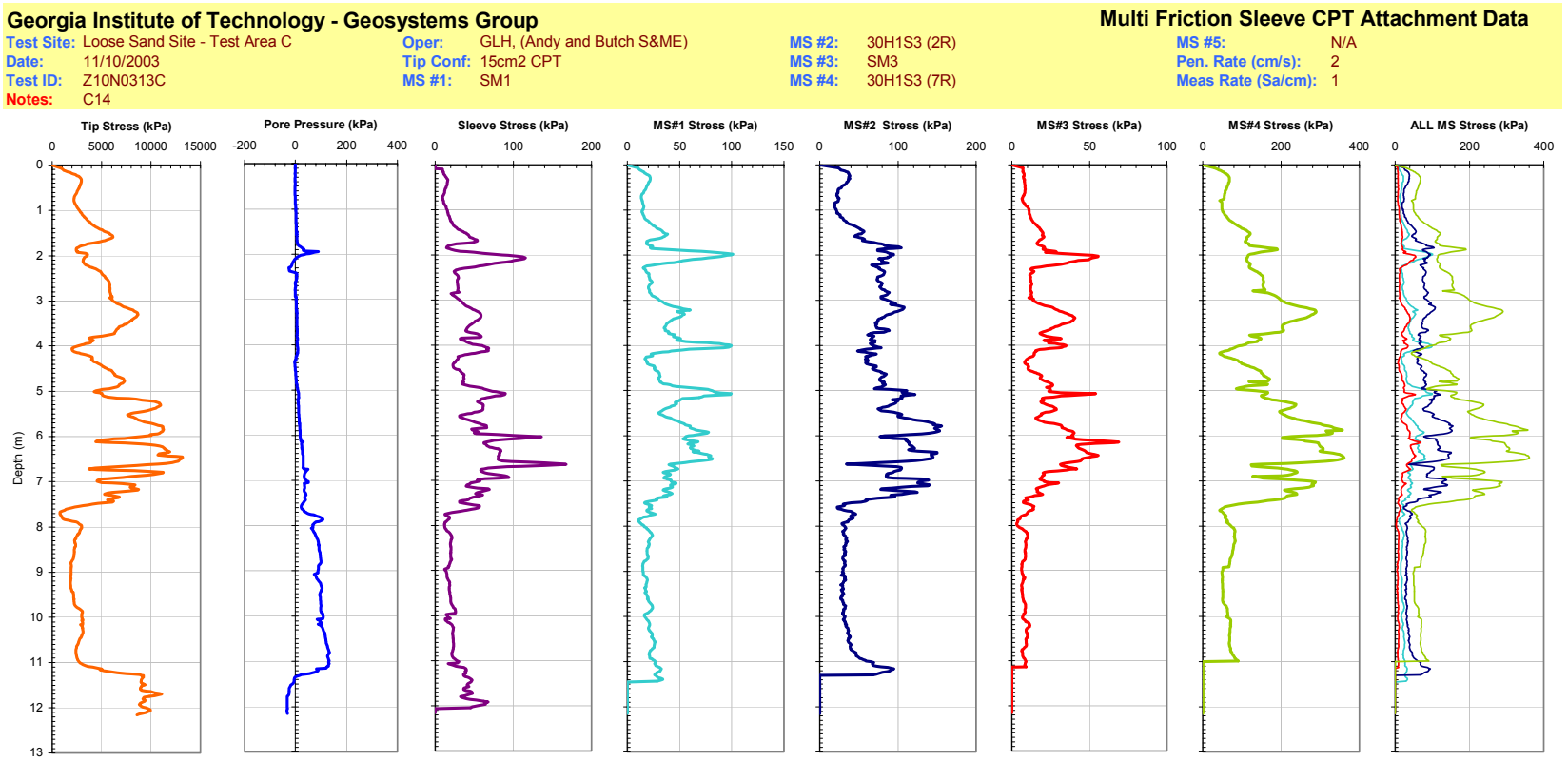

Figure A-65. Plot of CPTU-MFA Sensor Traces from Sounding MFA_105 at the LS Site.

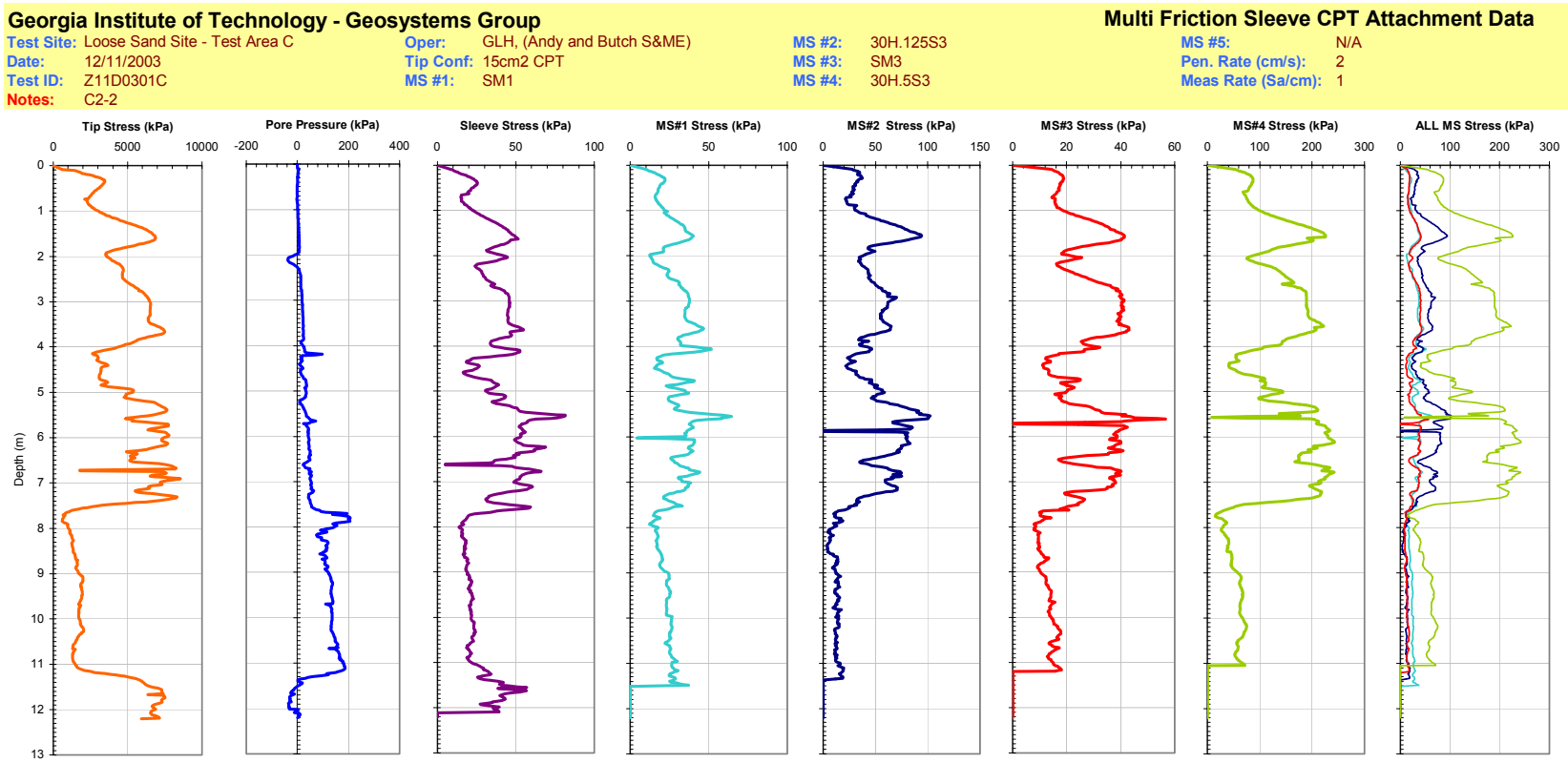

Figure A-66. Plot of CPTU-MFA Sensor Traces from Sounding MFA_106 at the LS Site.

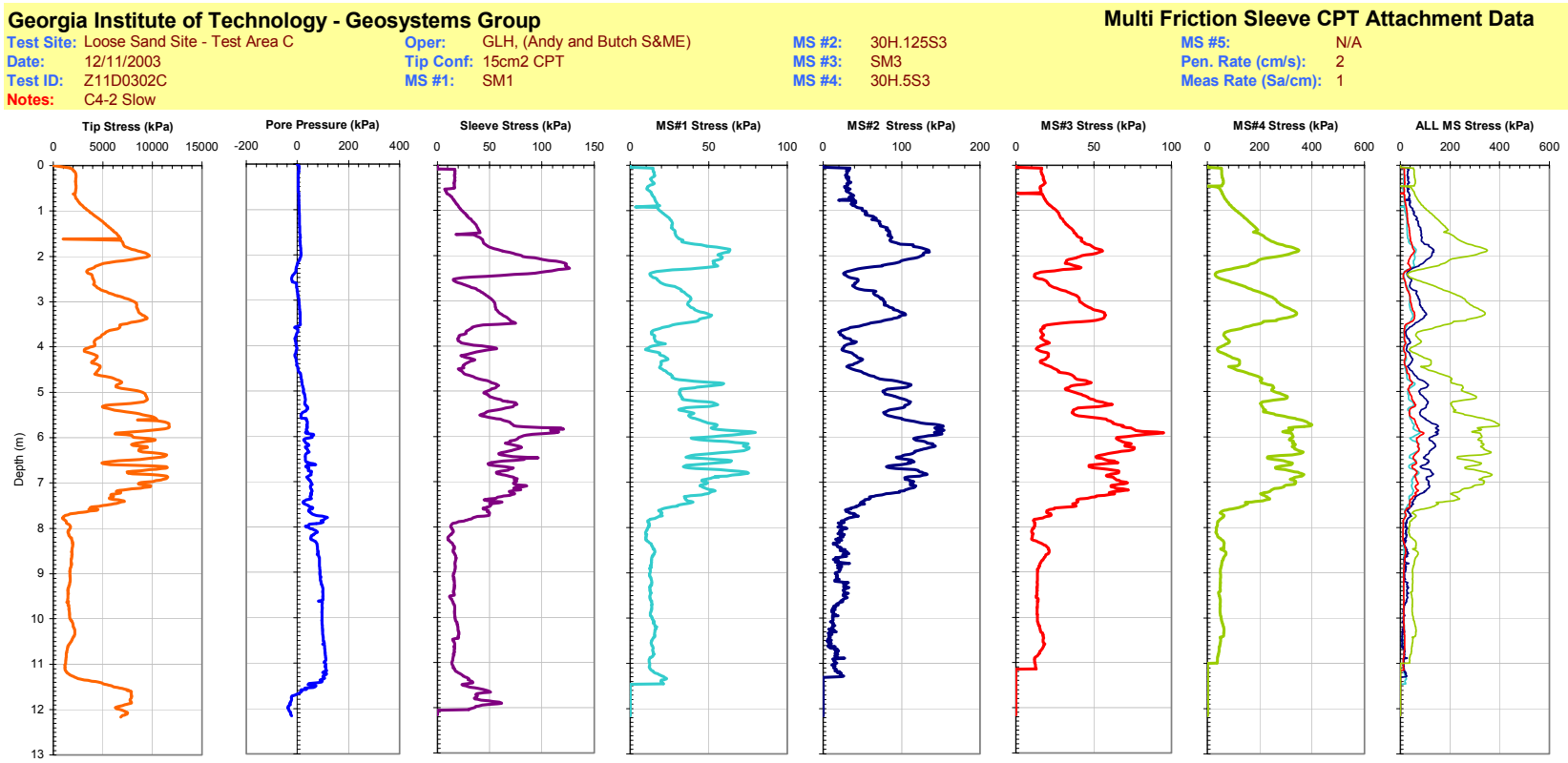

Figure A-67. Plot of CPTU-MFA Sensor Traces from Sounding MFA_107 at the LS Site.

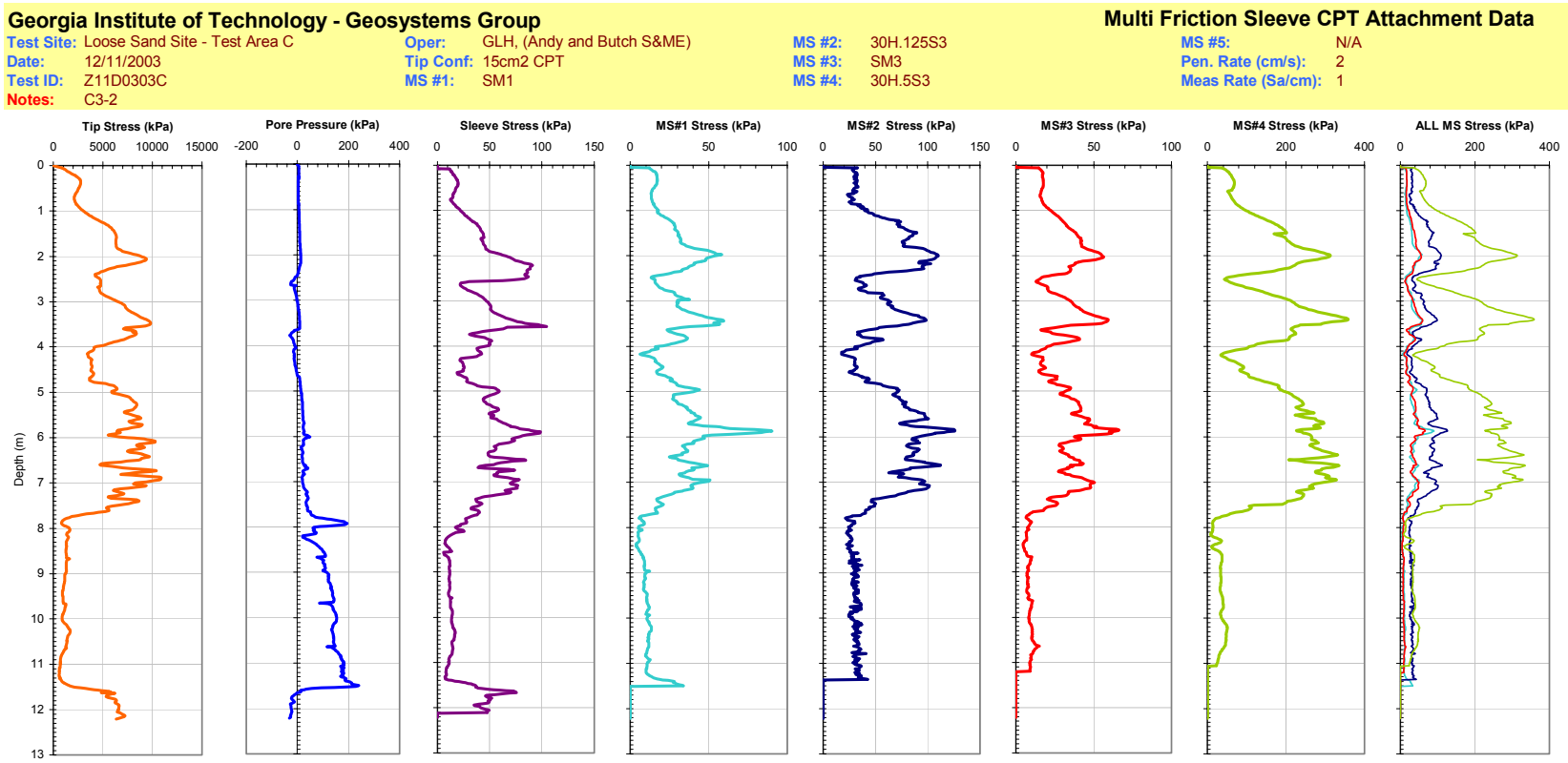

Figure A-68. Plot of CPTU-MFA Sensor Traces from Sounding MFA_108 at the LS Site.

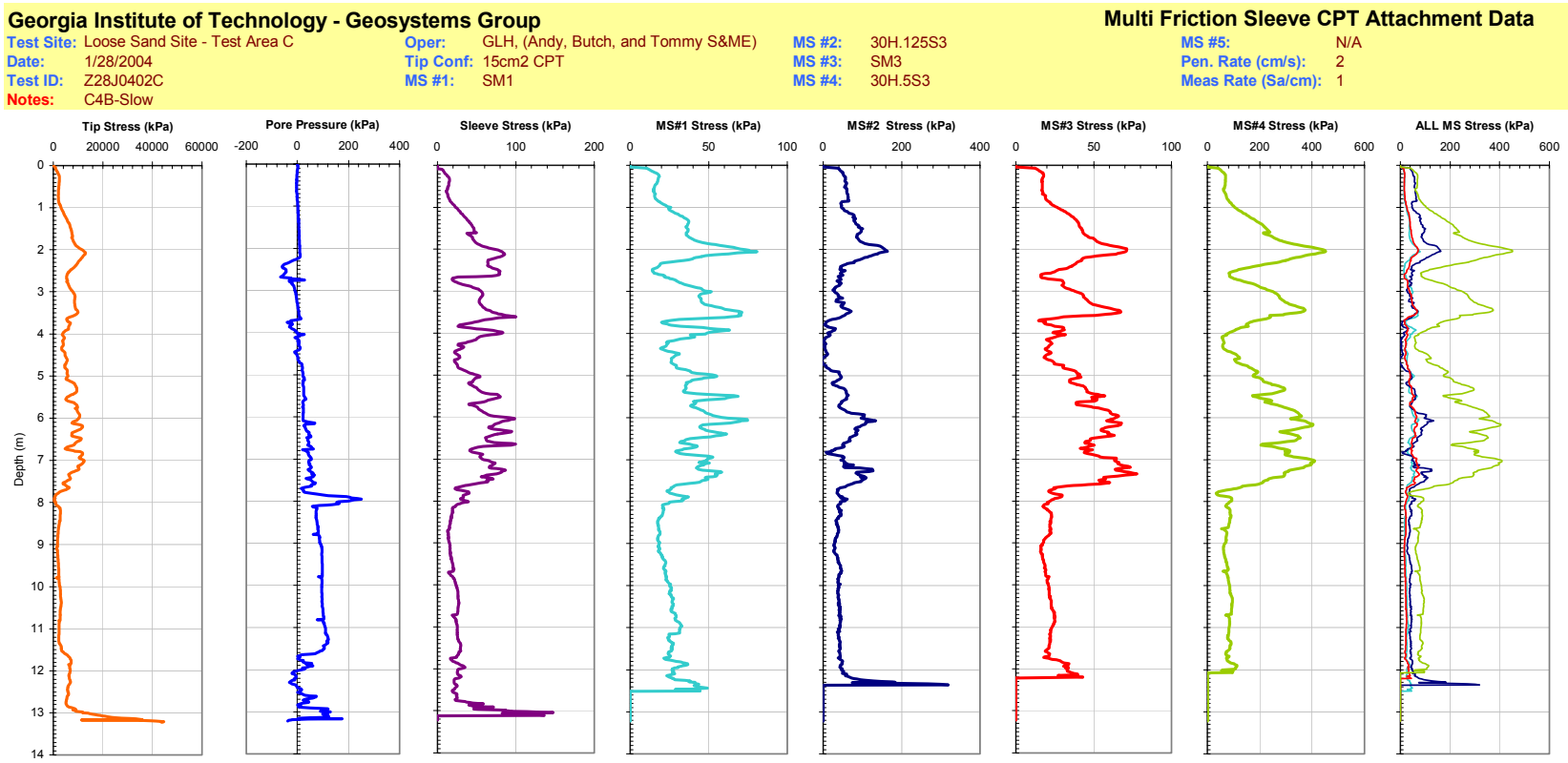

Figure A-69. Plot of CPTU-MFA Sensor Traces from Sounding MFA_109 at the LS Site.

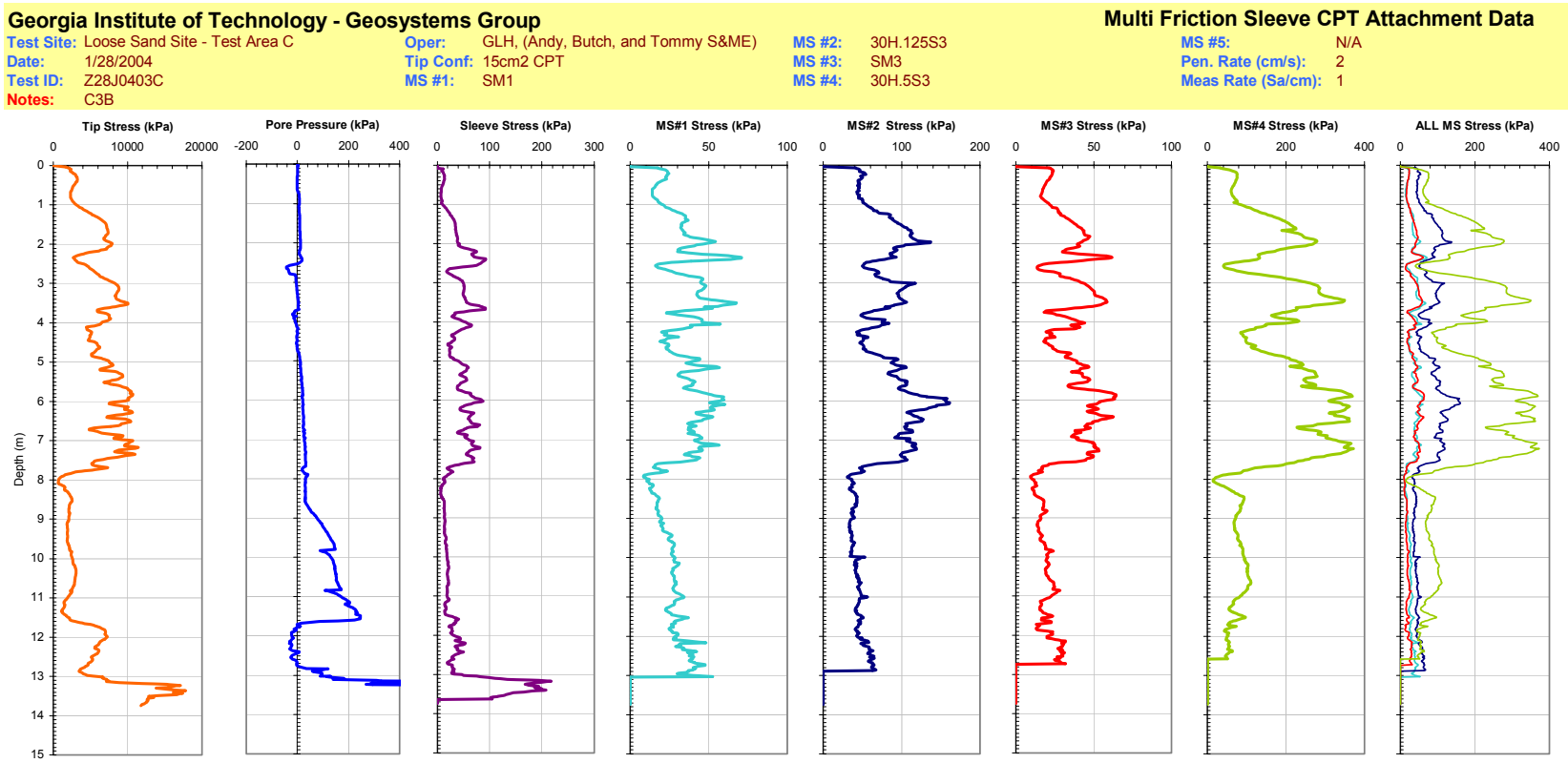

Figure A-70. Plot of CPTU-MFA Sensor Traces from Sounding MFA_110 at the LS Site.

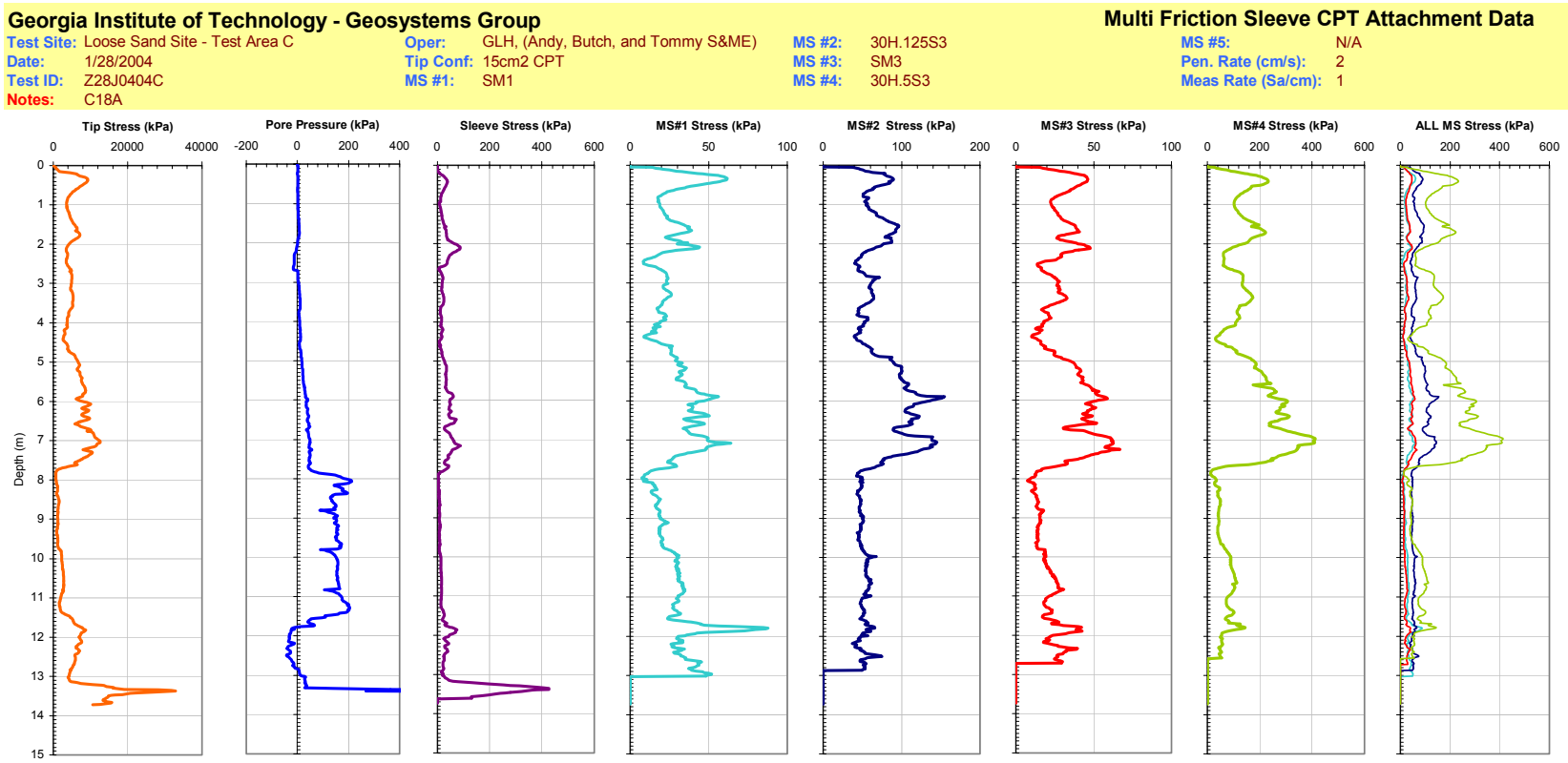

Figure A-71. Plot of CPTU-MFA Sensor Traces from Sounding MFA_111 at the LS Site.

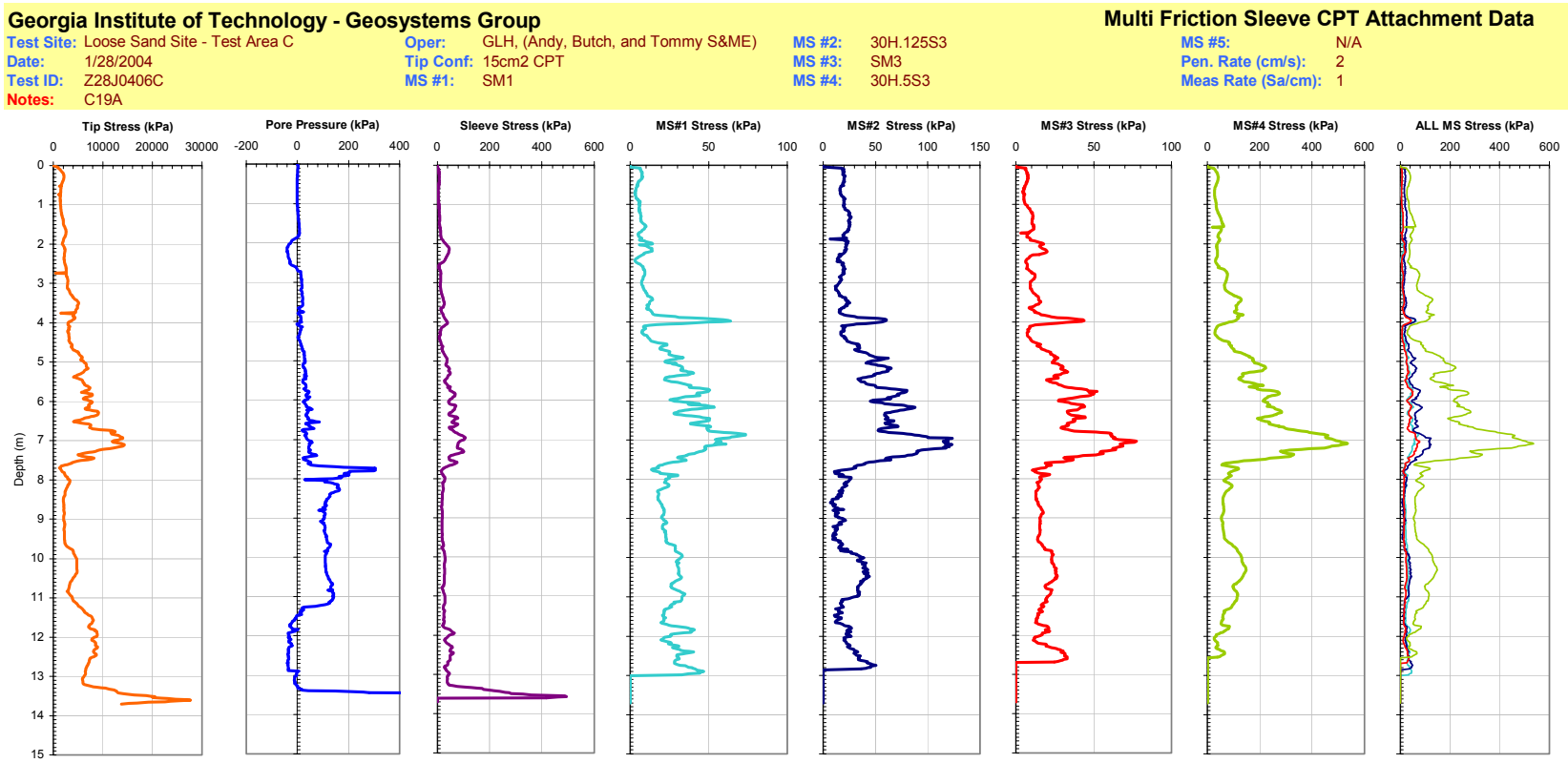

Figure A-72. Plot of CPTU-MFA Sensor Traces from Sounding MFA_112 at the LS Site.

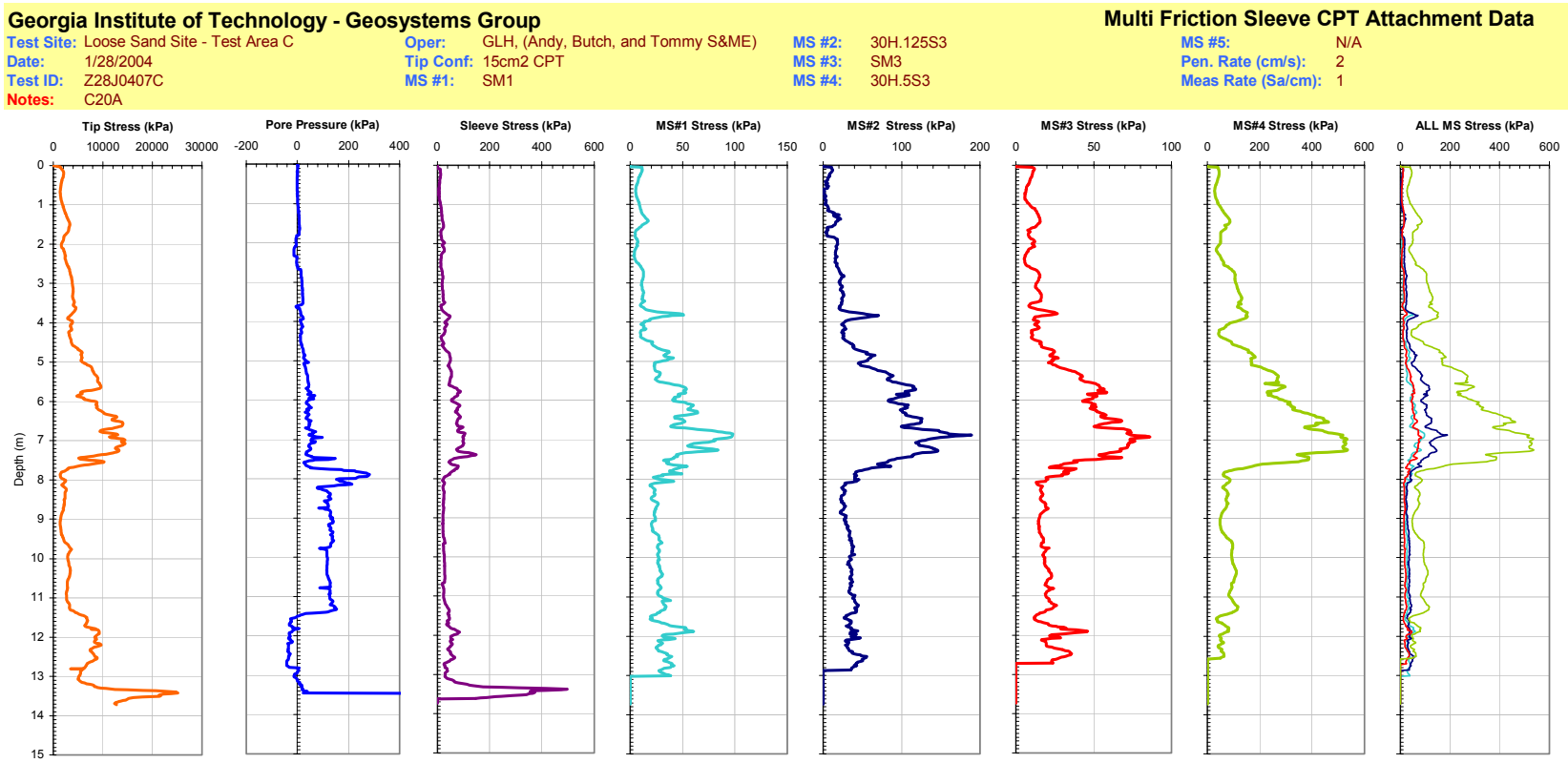

Figure A-73. Plot of CPTU-MFA Sensor Traces from Sounding MFA_113 at the LS Site.

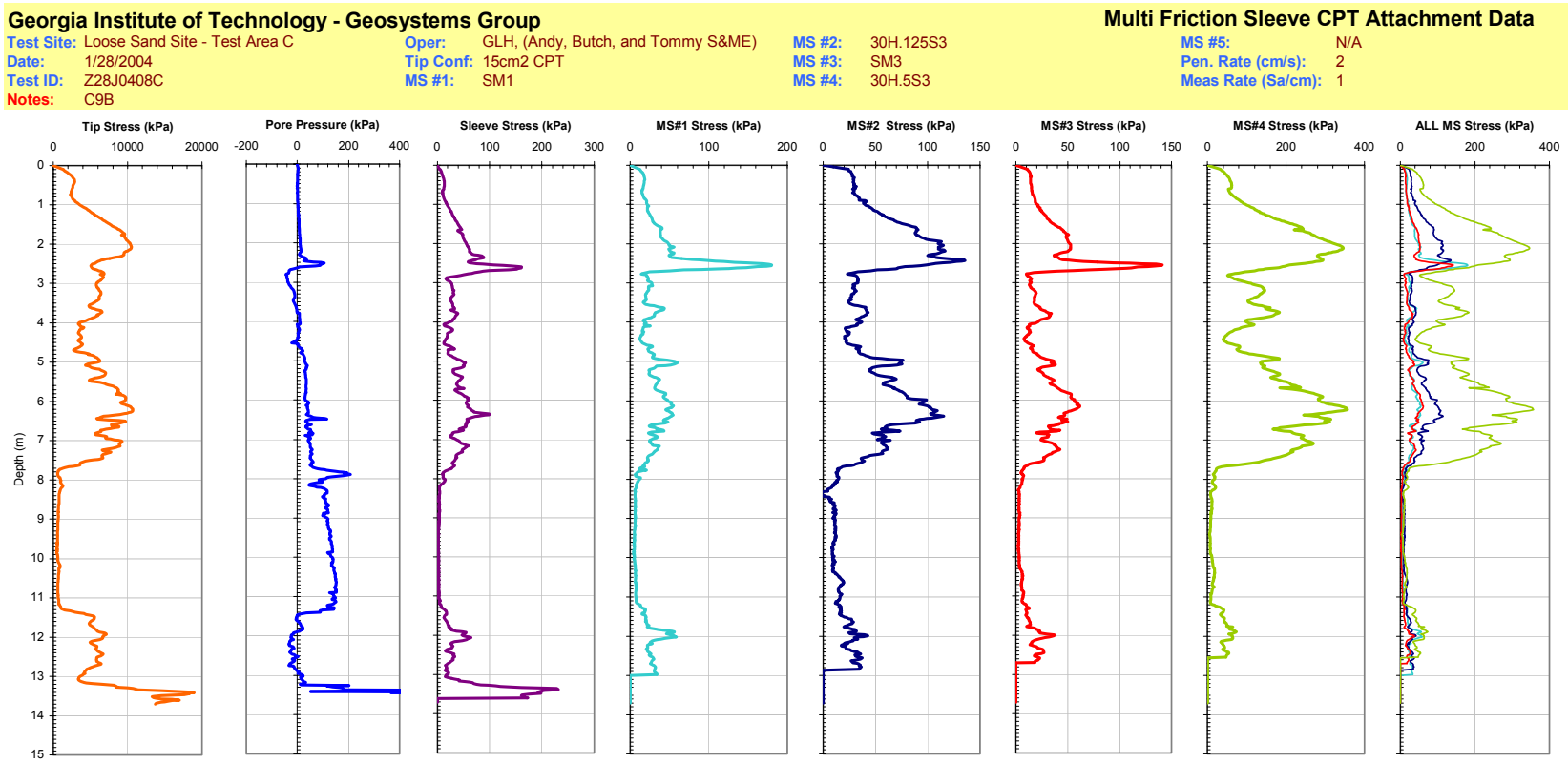

Figure A-74. Plot of CPTU-MFA Sensor Traces from Sounding MFA_114 at the LS Site.

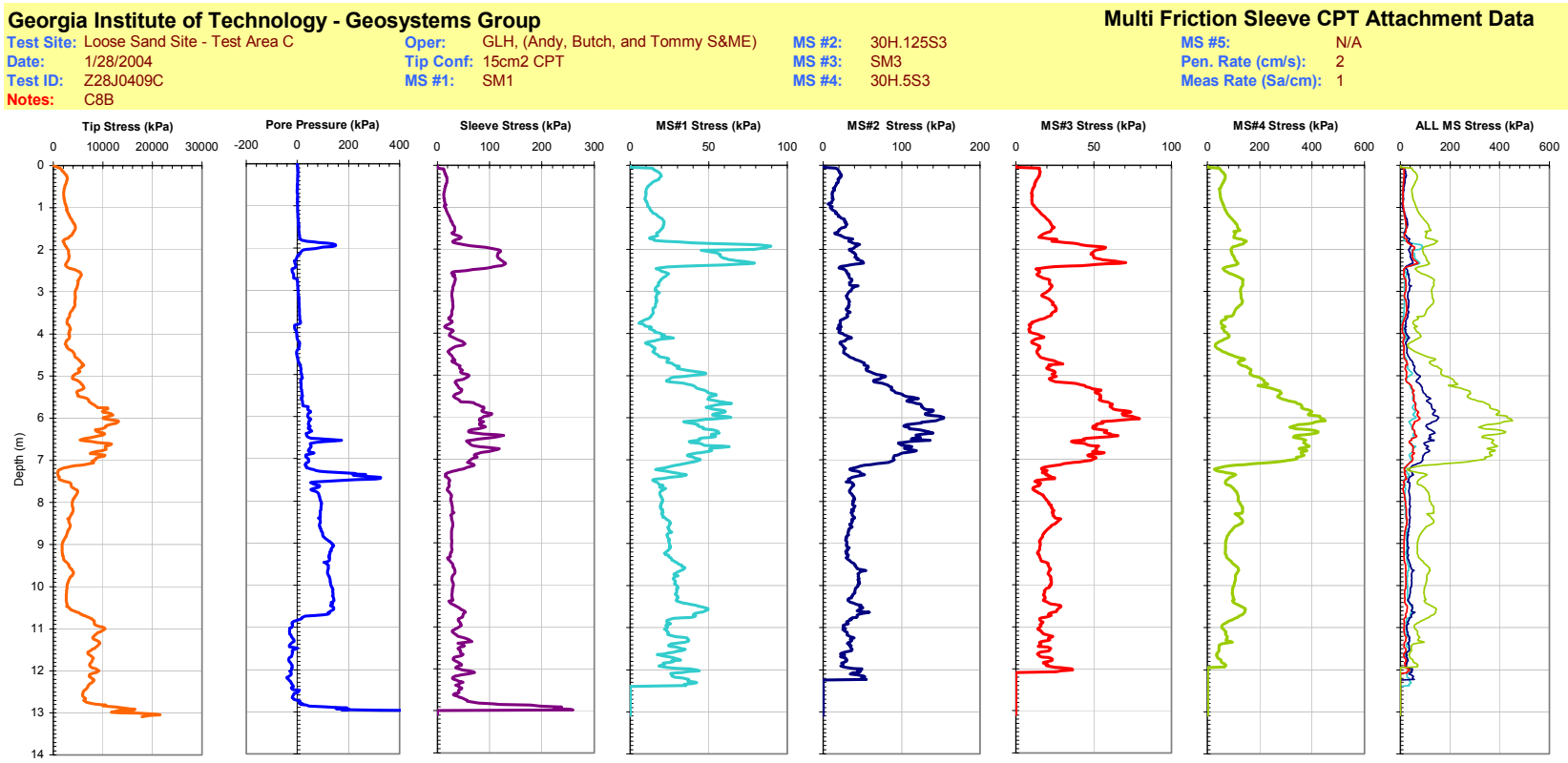

Figure A-75. Plot of CPTU-MFA Sensor Traces from Sounding MFA_115 at the LS Site.

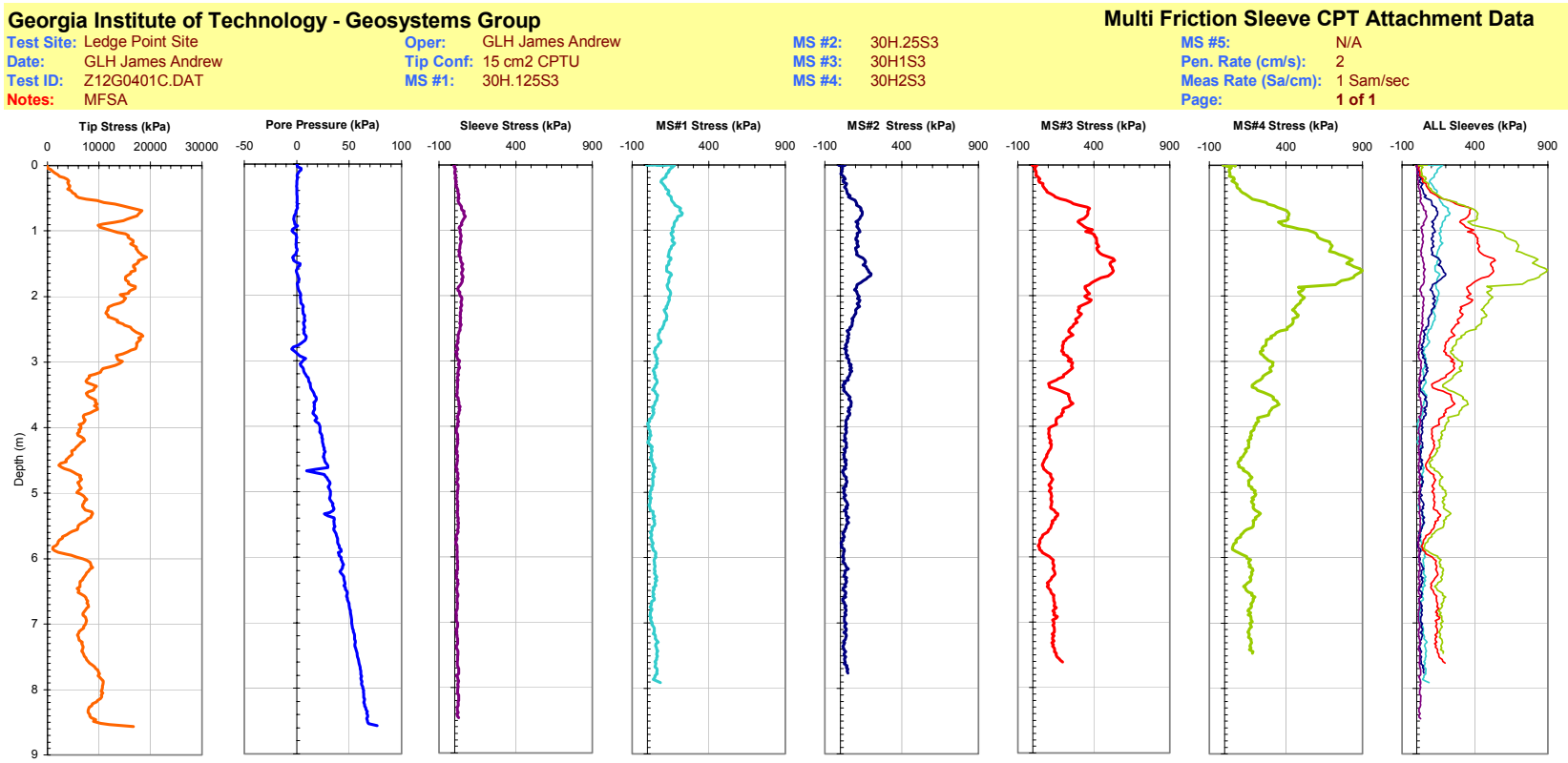

Figure A-76. Plot of CPTU-MFA Sensor Traces from Sounding MFA_126 at the LPWA Site.

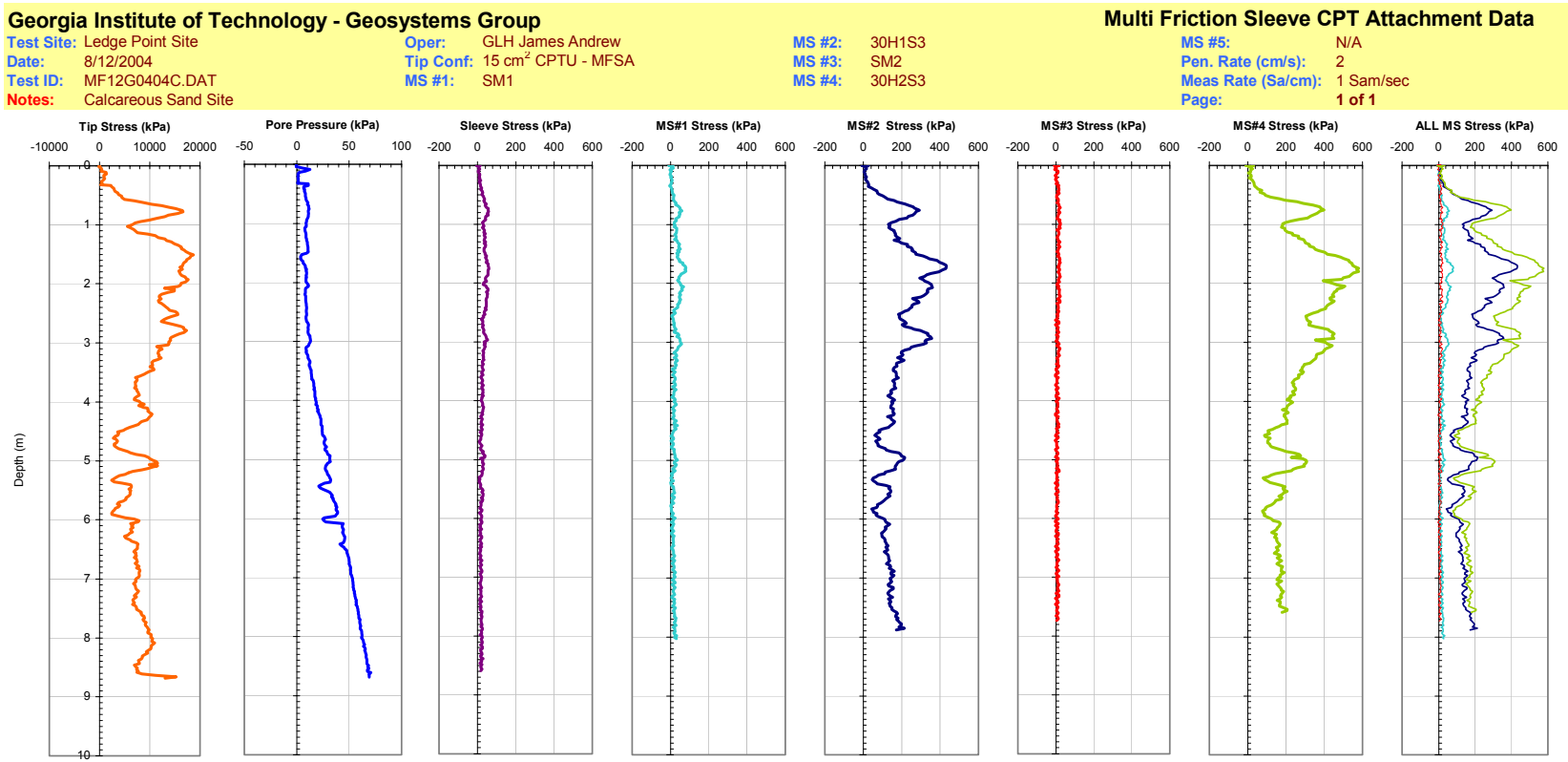

Figure A-77. Plot of CPTU-MFA Sensor Traces from Sounding MFA_127 at the LPWA Site.

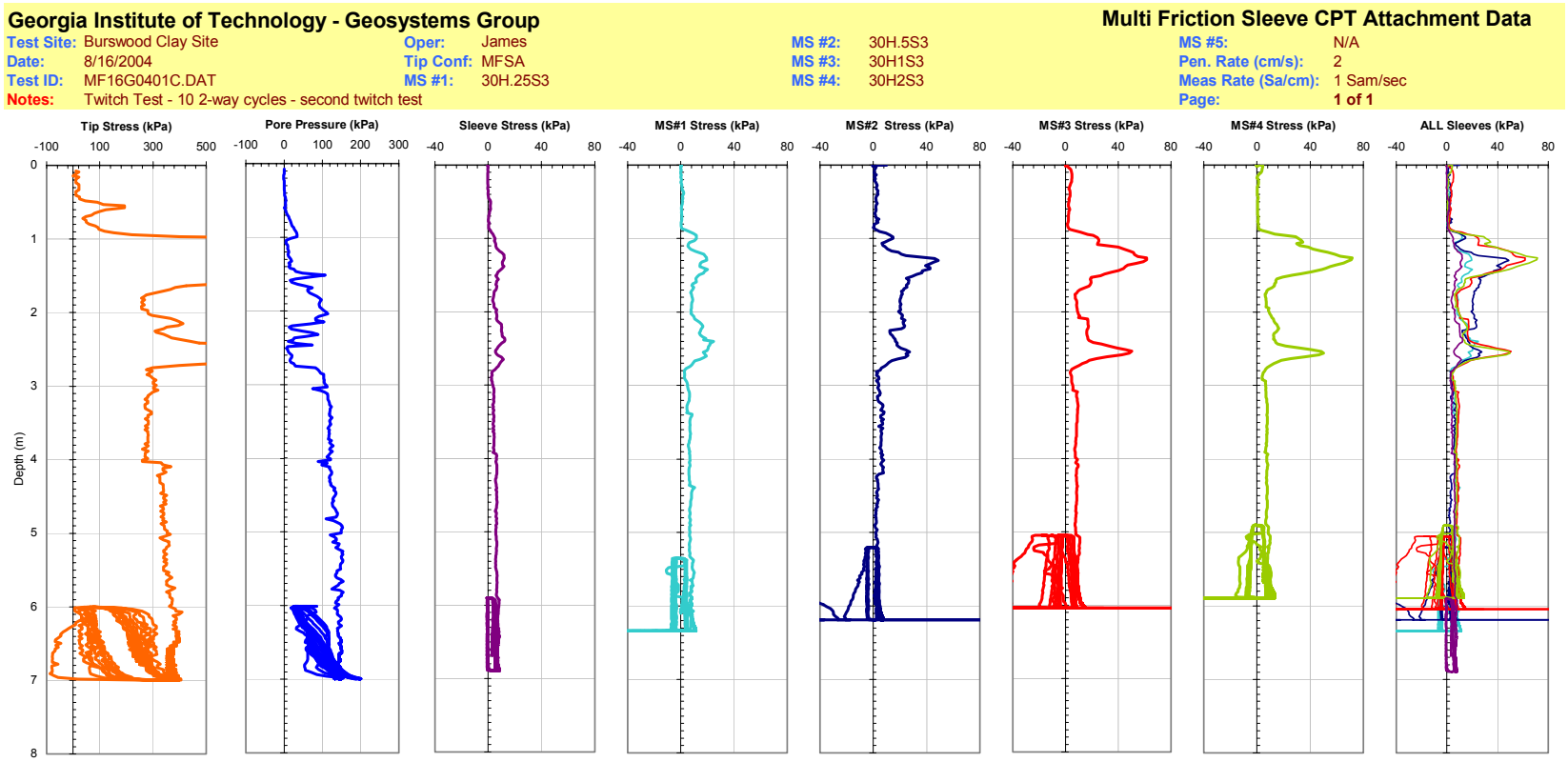

Figure A-78. Plot of CPTU-MFA Sensor Traces from Sounding MFA_131 at the BWDWA Site.

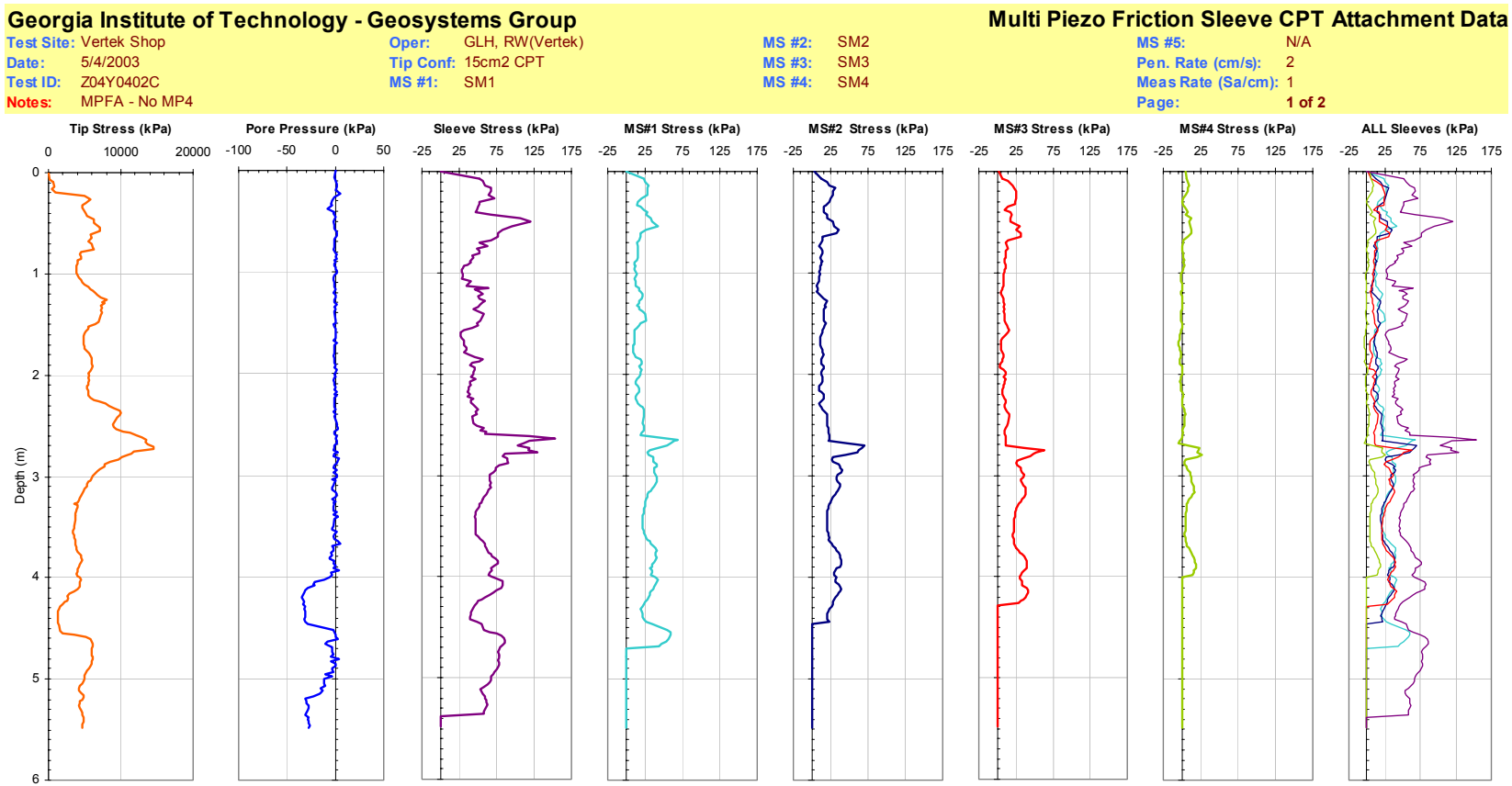

Figure A-79a. Plot of the CPTU and MPFA Friction Sensor Traces from Sounding MPFA_1 at the VTK Site.

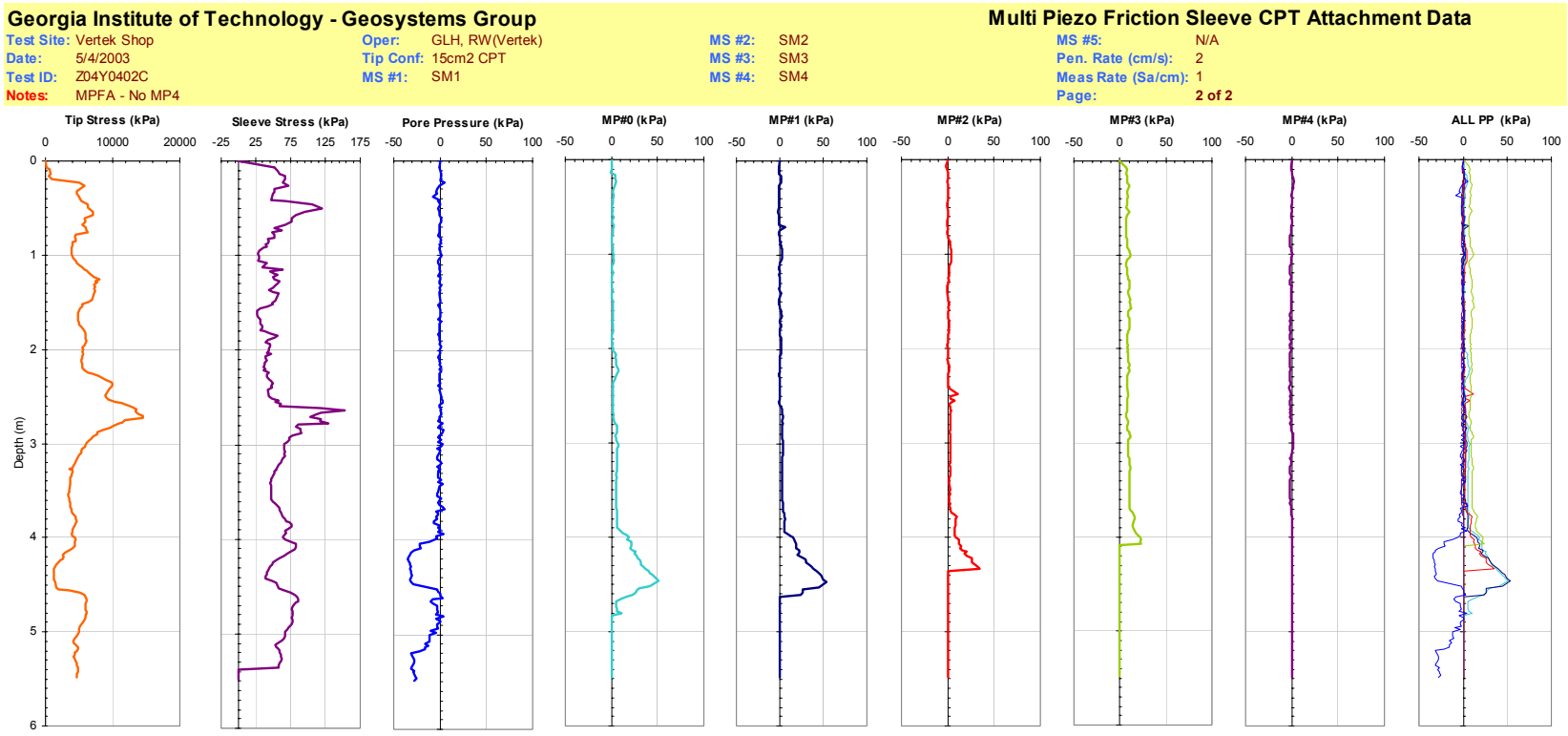

Figure A-79b. Plot of the CPTU and MPFA Piezo Sensor Traces from Sounding MPFA_1 at the VTK Site.

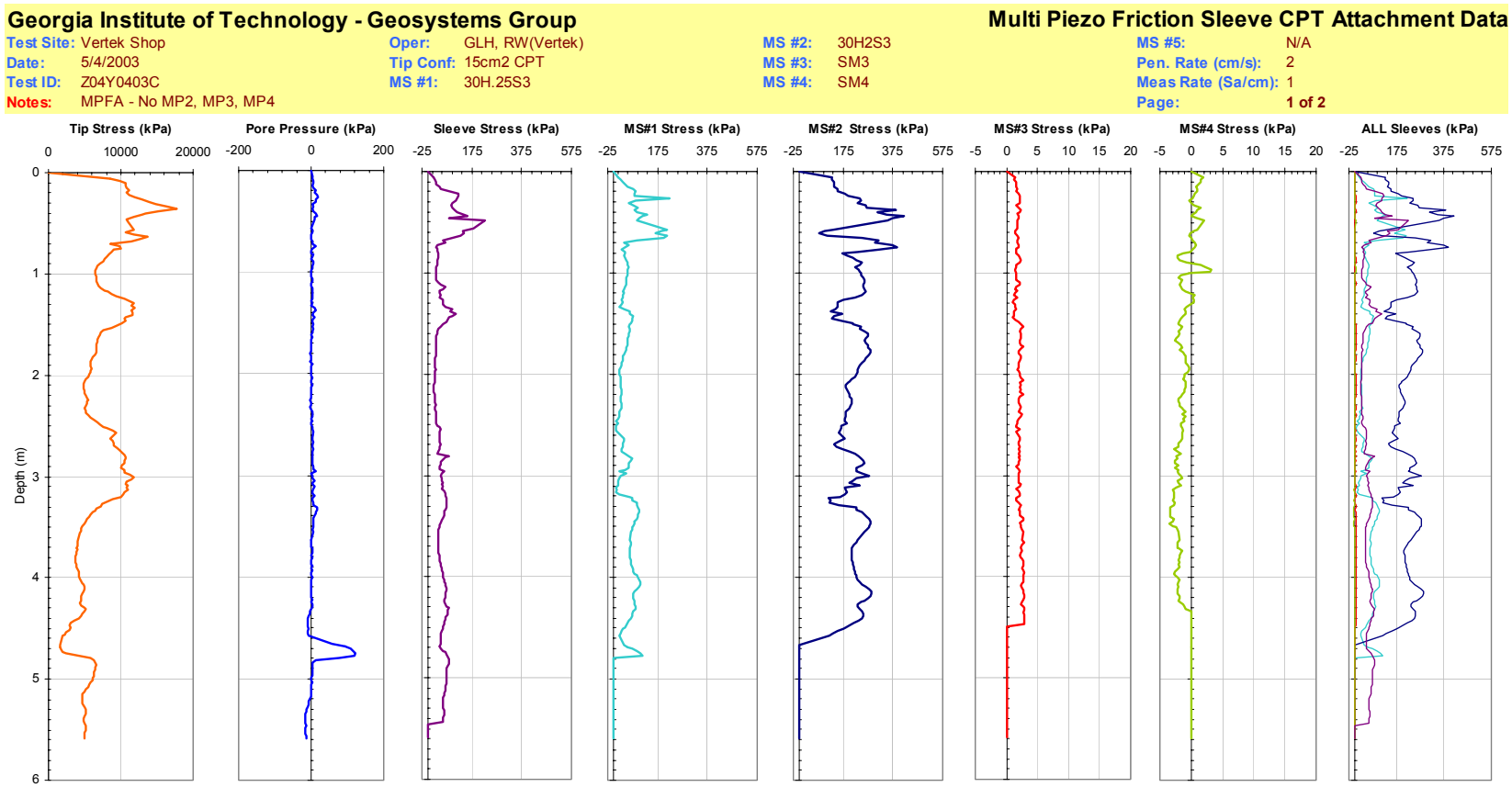

Figure A-80a. Plot of the CPTU and MPFA Friction Sensor Traces from Sounding MPFA_2 at the VTK Site.

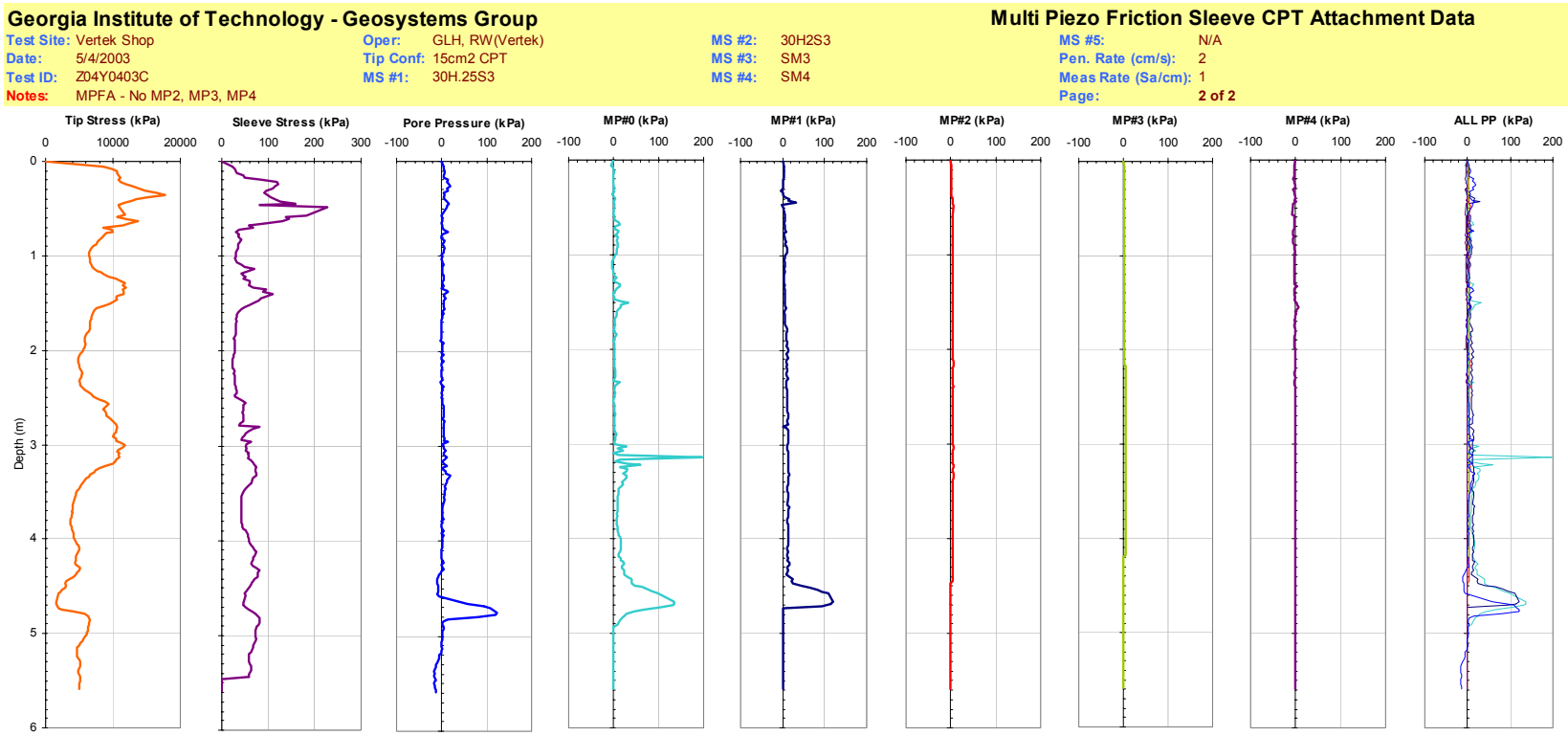

Figure A-80b. Plot of the CPTU and MPFA Piezo Sensor Traces from Sounding MPFA_2 at the VTK Site.

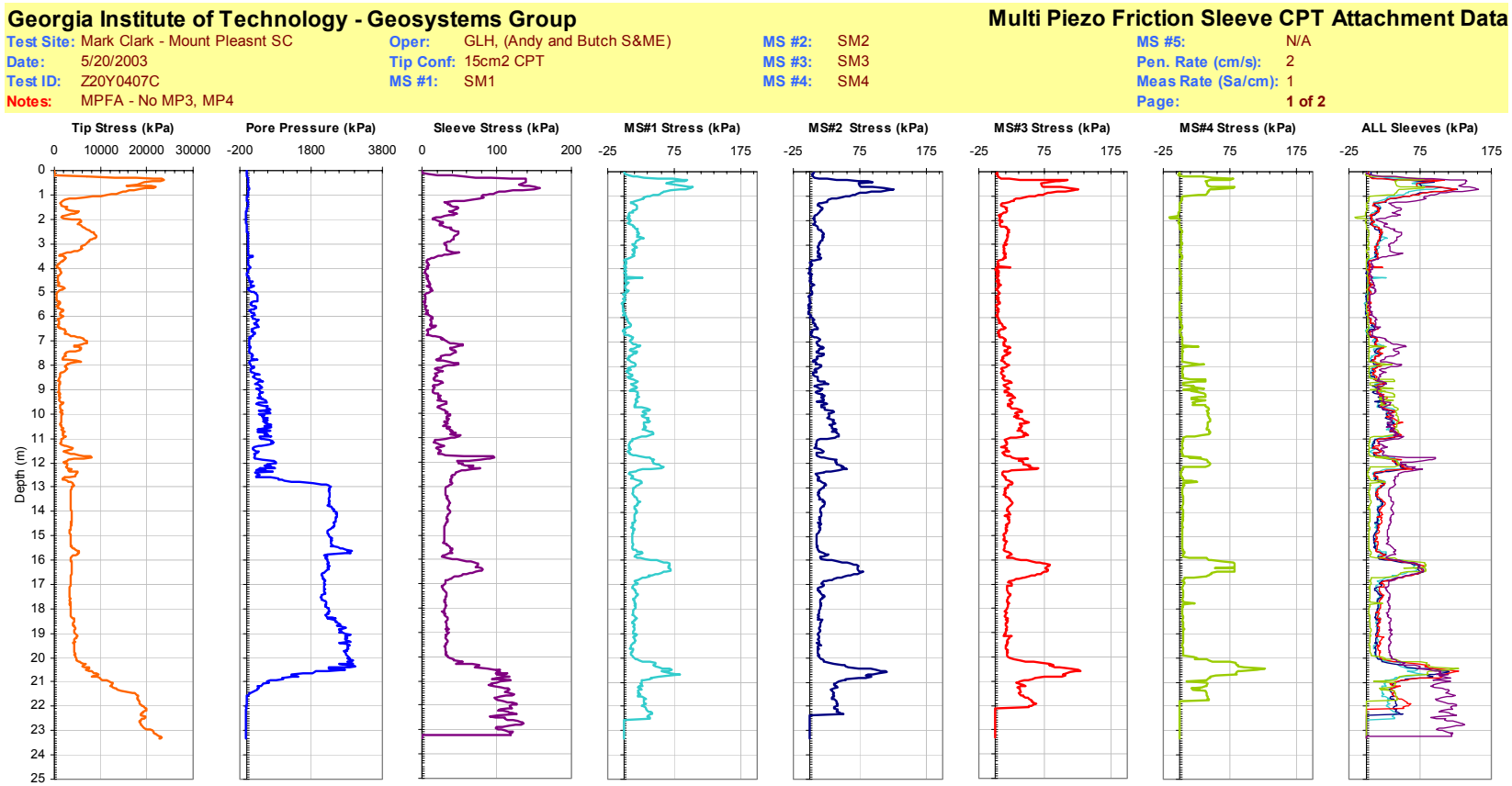

Figure A-81a. Plot of the CPTU and MPFA Friction Sensor Traces from Sounding MPFA_3 at the MPSC Site.

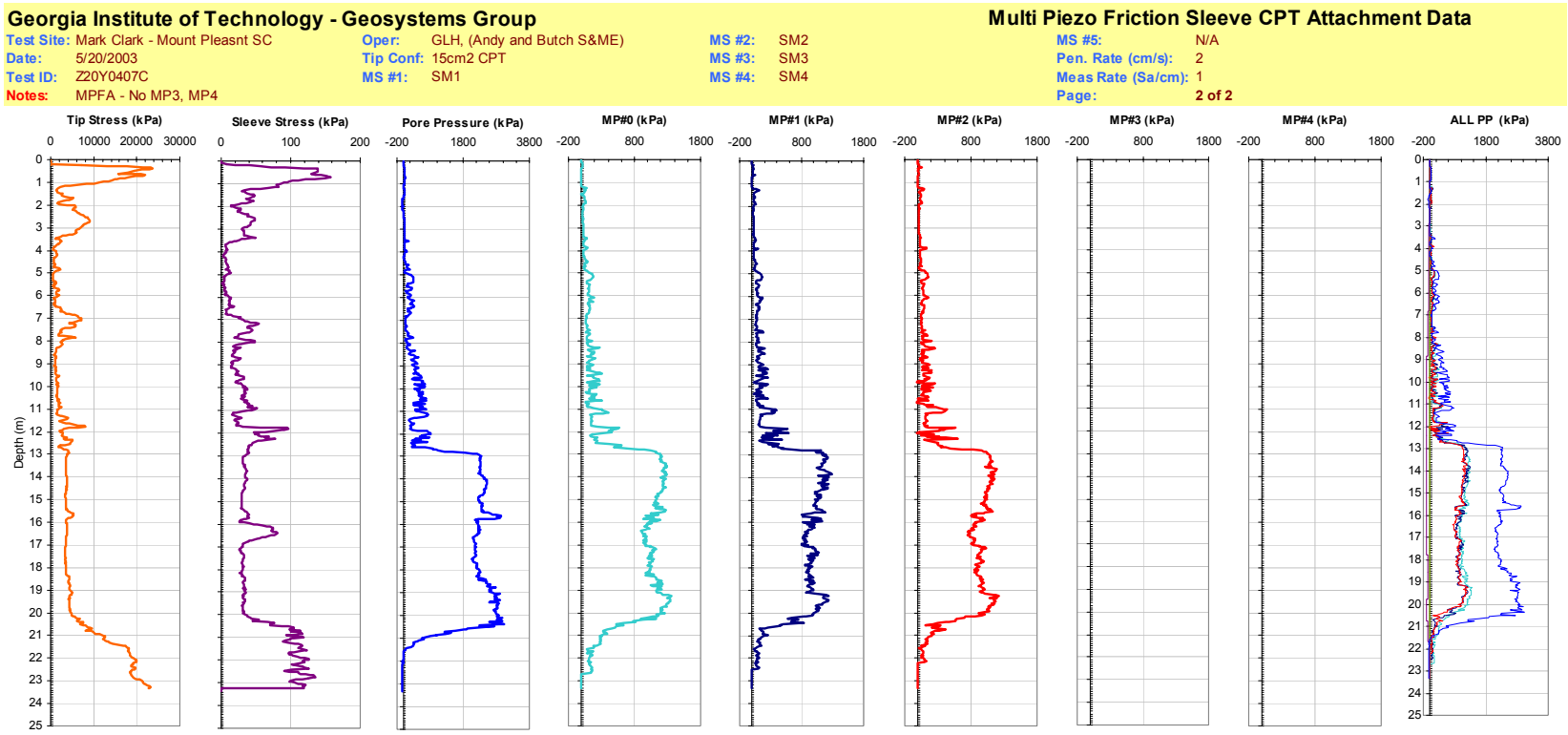

Figure A-81b. Plot of the CPTU and MPFA Piezo Sensor Traces from Sounding MPFA_3 at the MPSC Site.

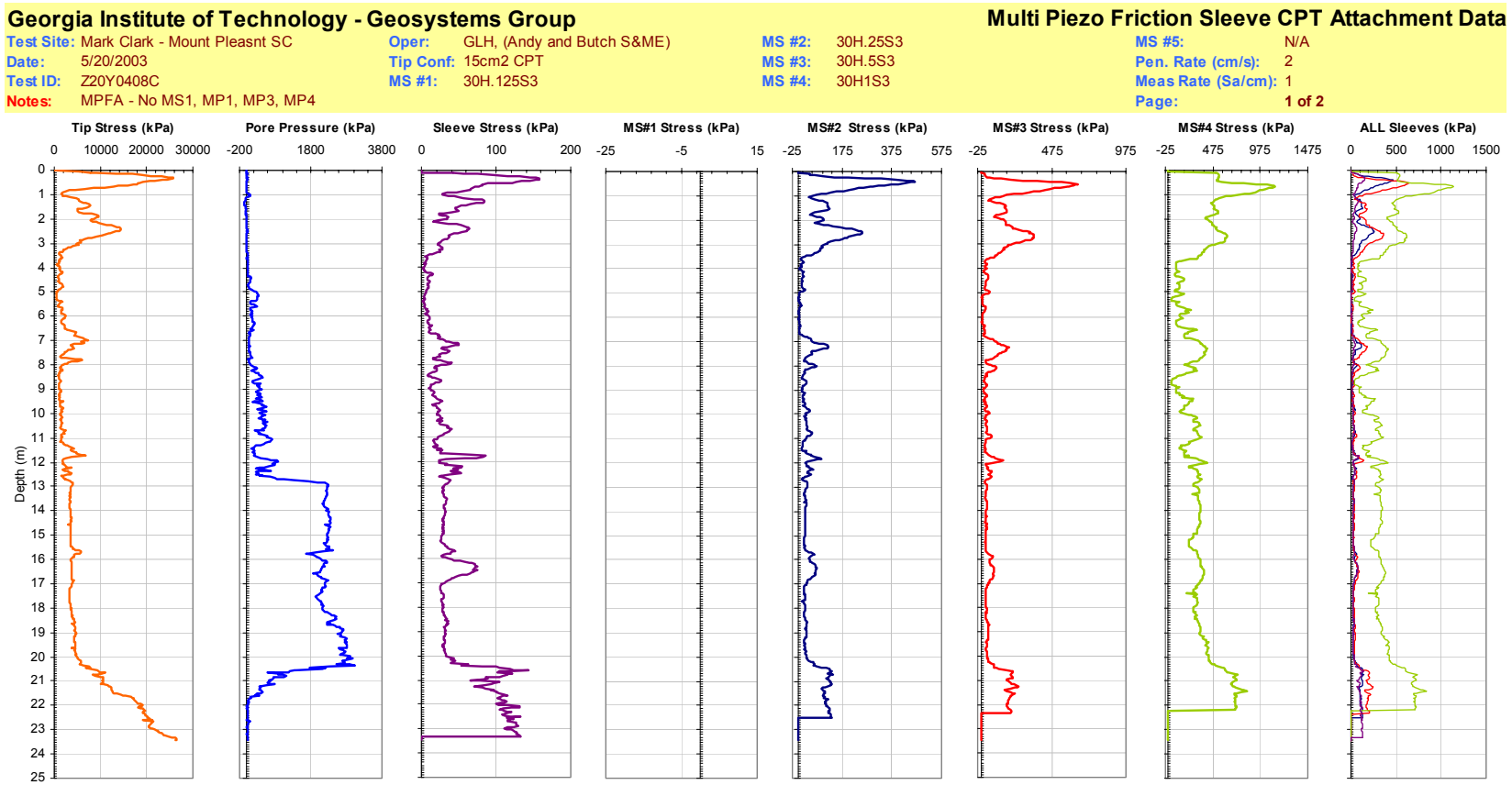

Figure A-82a. Plot of the CPTU and MPFA Friction Sensor Traces from Sounding MPFA_4 at the MPSC Site.

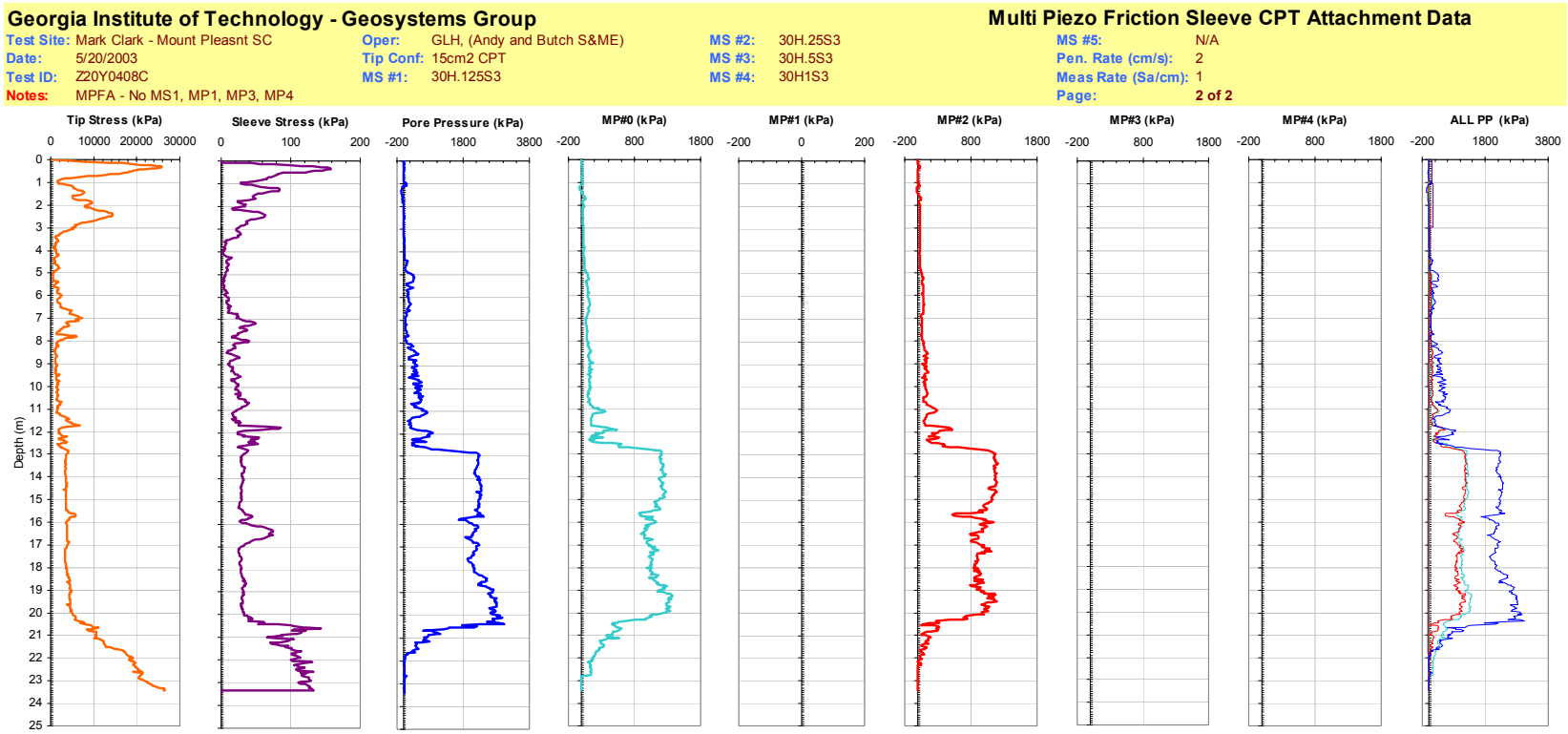

Figure A-82b. Plot of the CPTU and MPFA Piezo Sensor Traces from Sounding MPFA_4 at the MPSC Site.

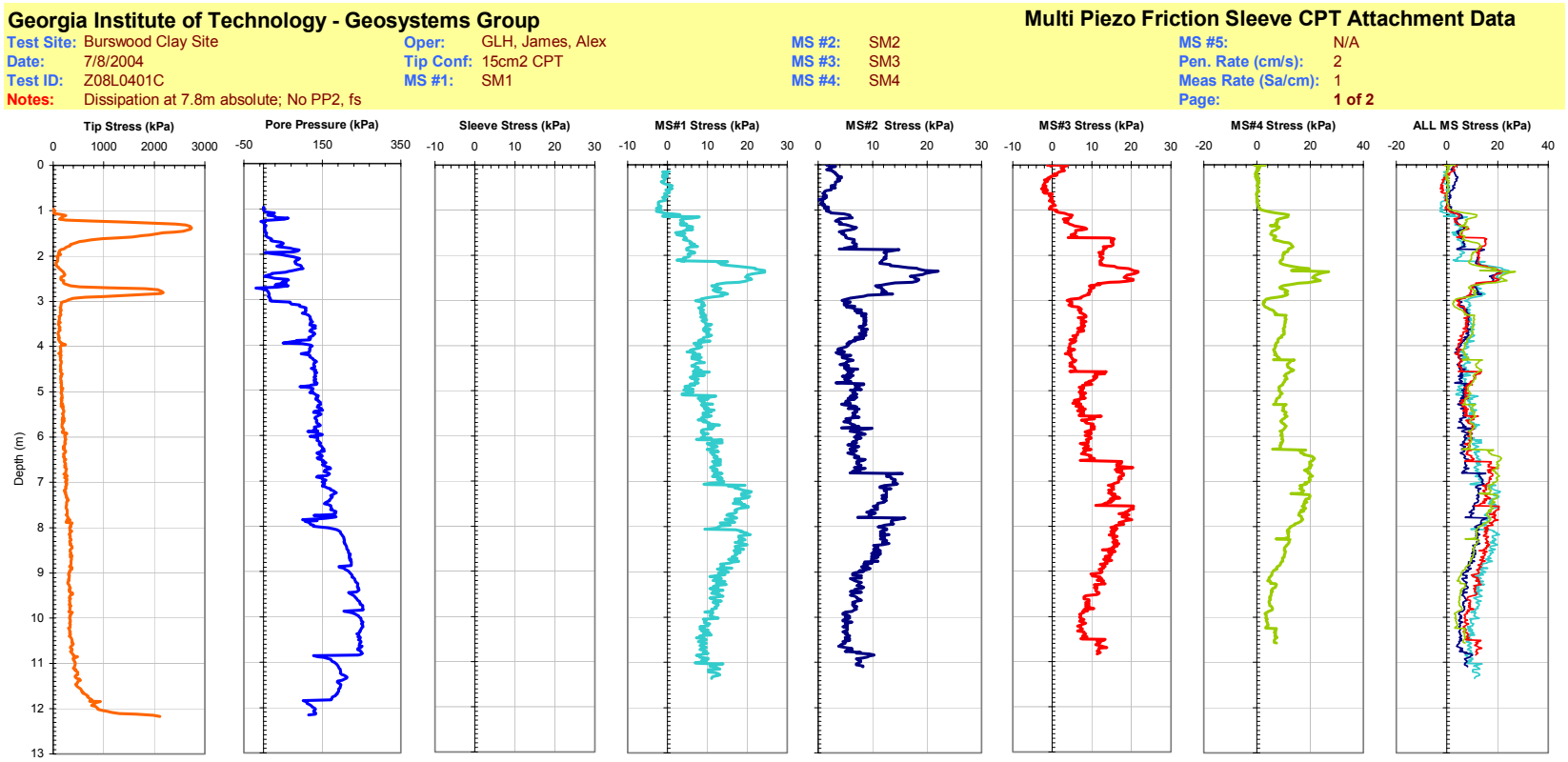

Figure A-83a. Plot of the CPTU and MPFA Friction Sensor Traces from Sounding MPFA_5 at the BWDWA Site.

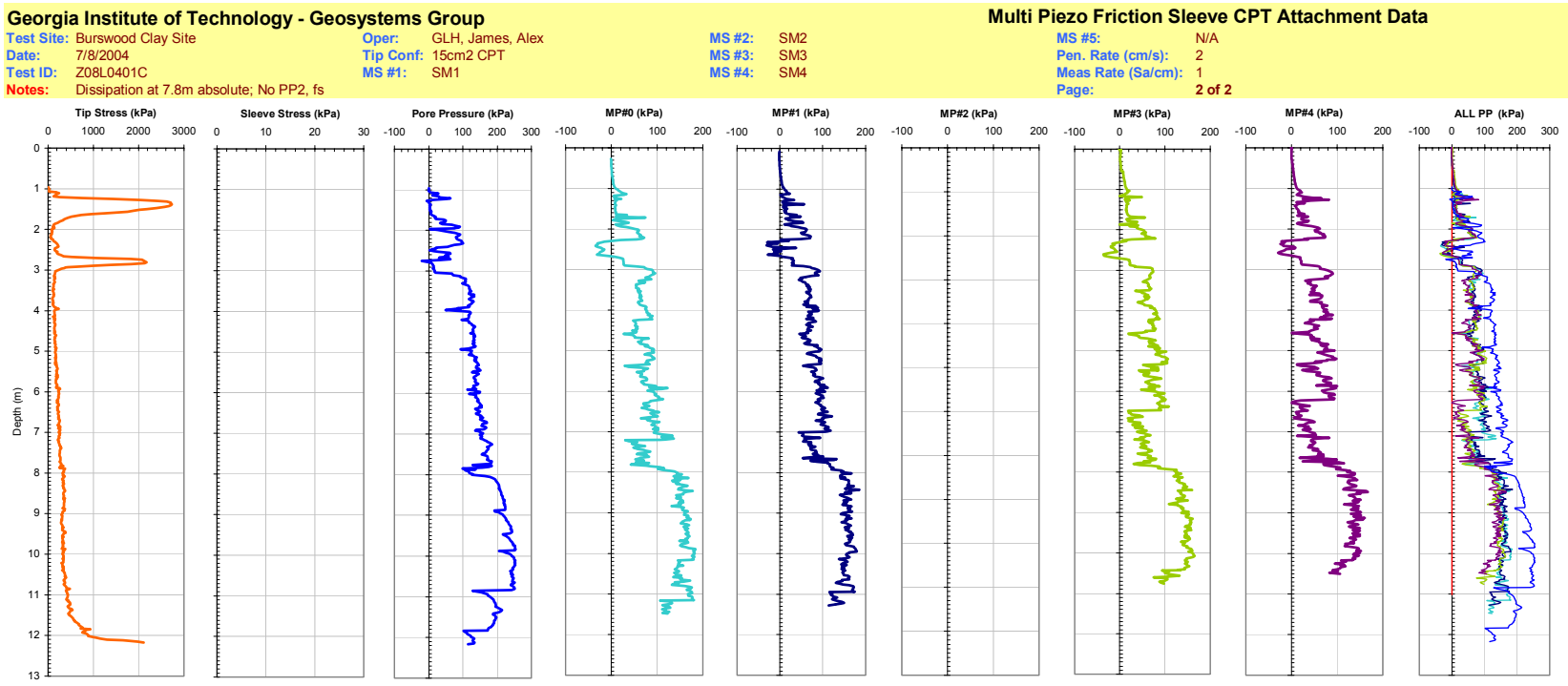

Figure A-83b. Plot of the CPTU and MPFA Piezo Sensor Traces from Sounding MPFA_5 at the BWDWA Site.

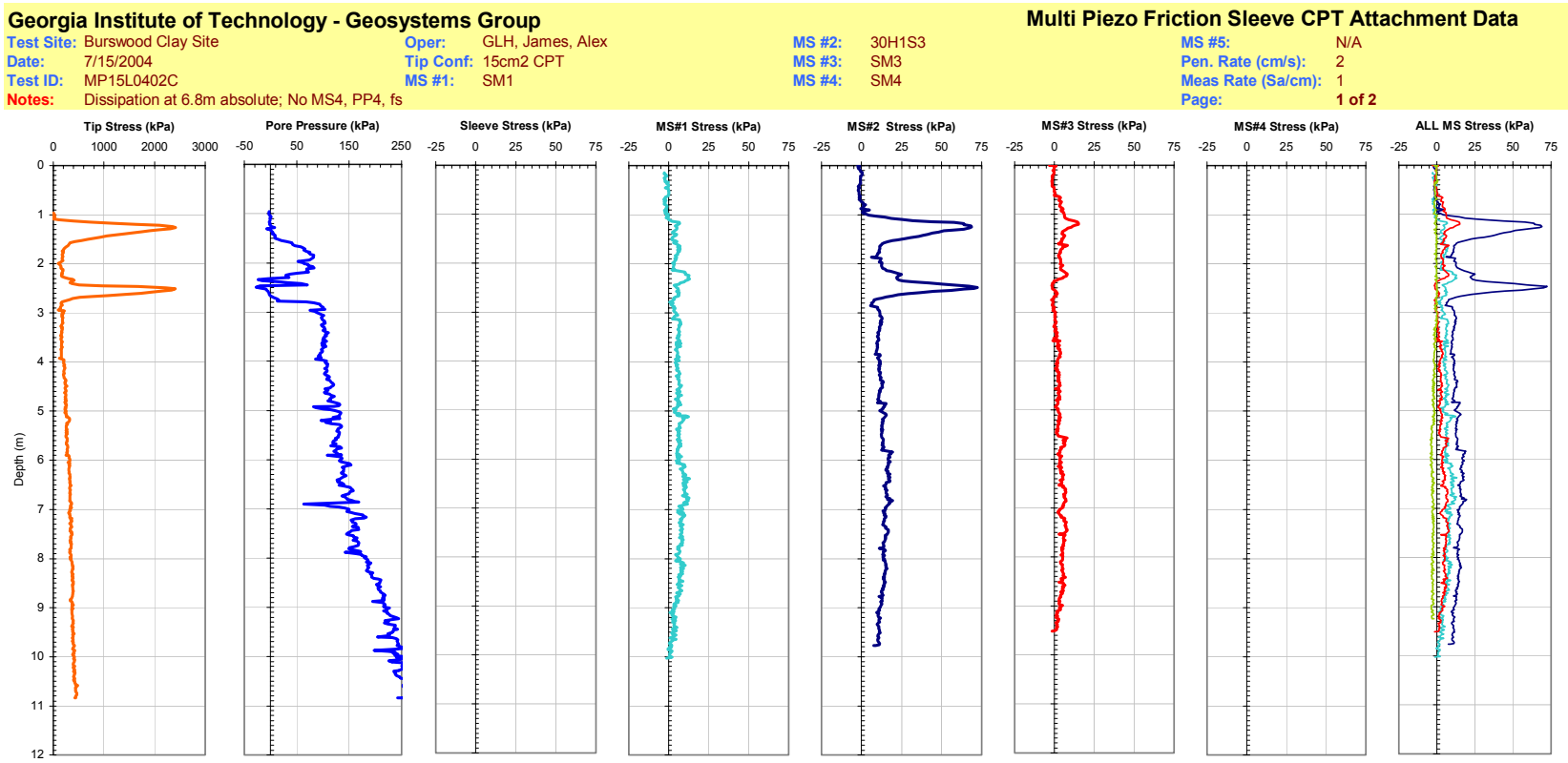

Figure A-84a. Plot of the CPTU and MPFA Friction Sensor Traces from Sounding MPFA_6 at the BWDWA Site.

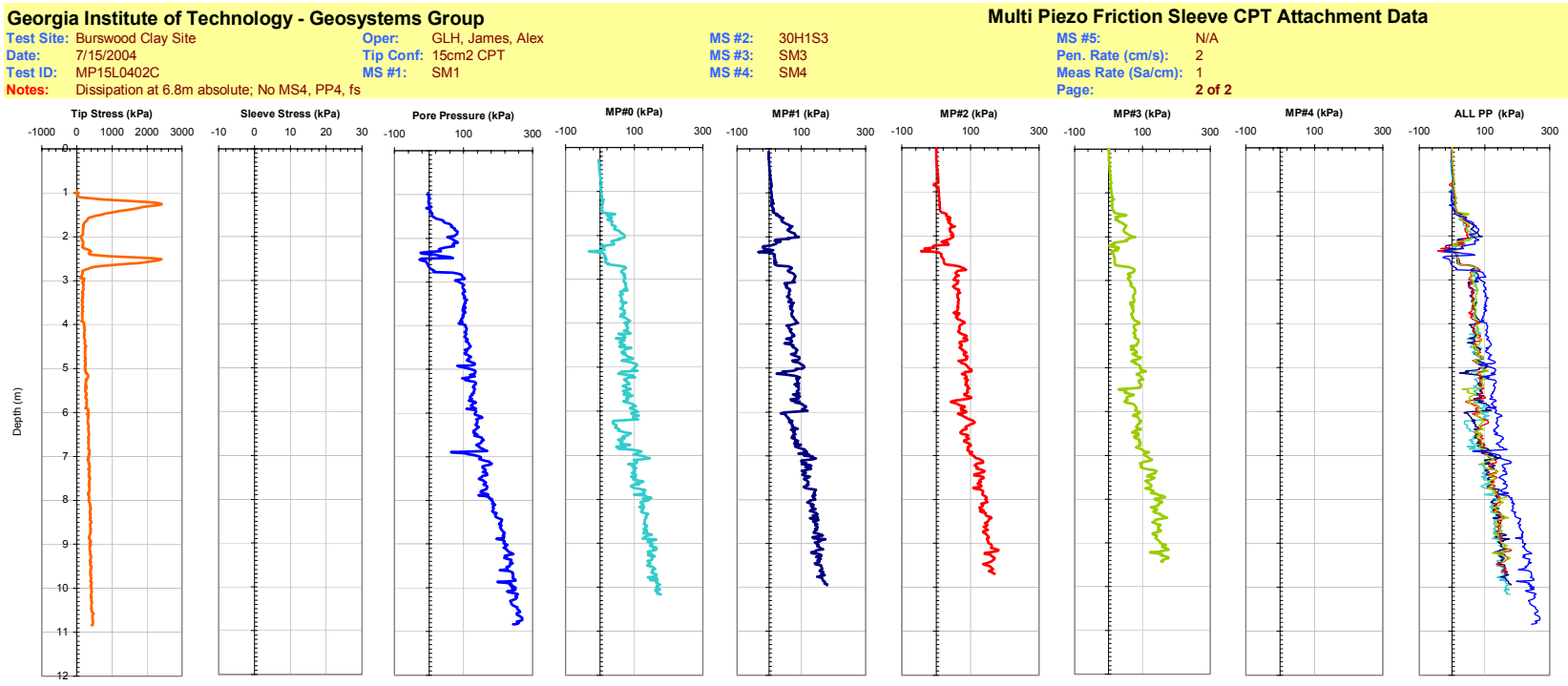

Figure A-84b. Plot of the CPTU and MPFA Piezo Sensor Traces from Sounding MPFA_6 at the BWDWA Site.

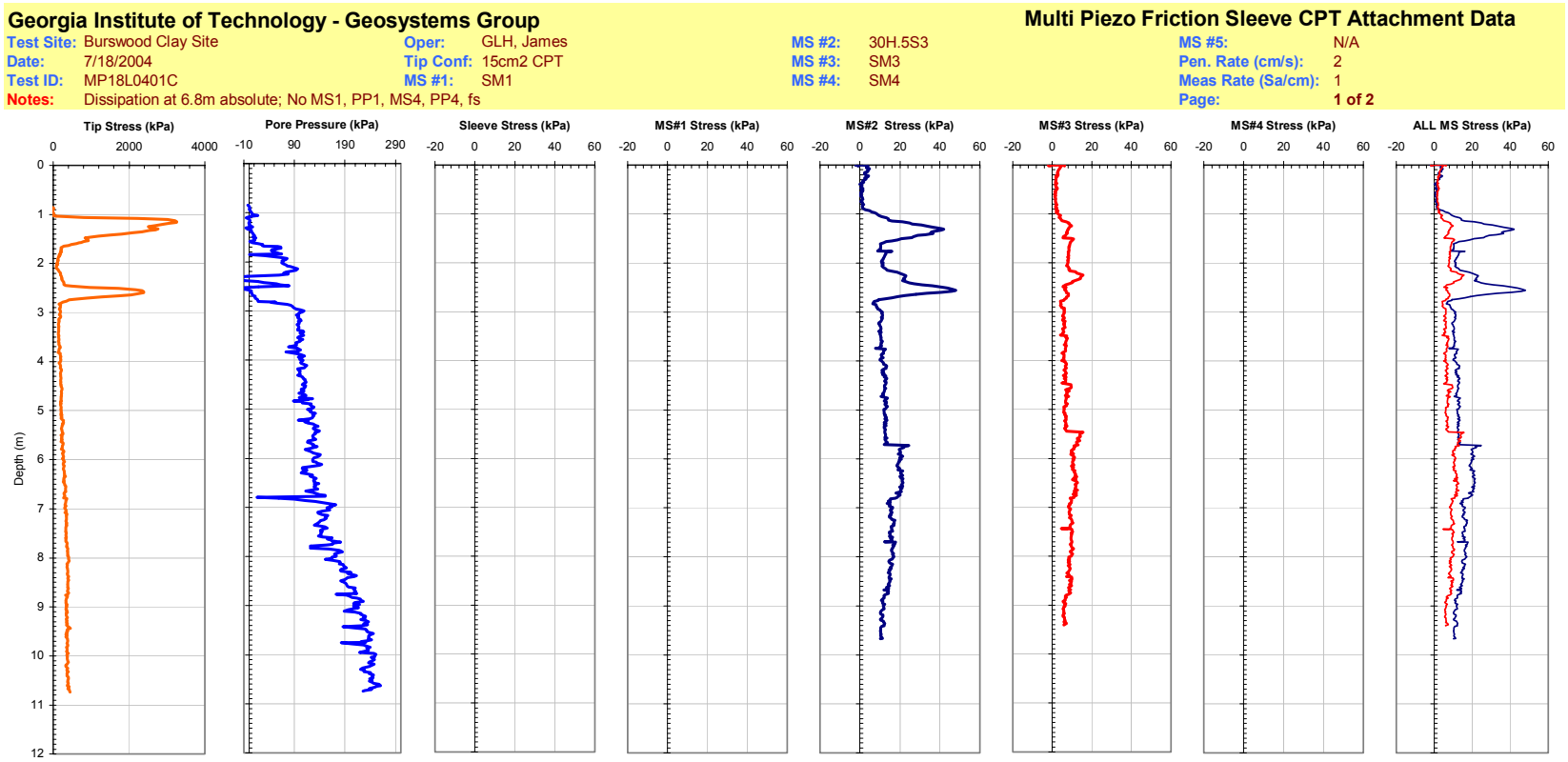

Figure A-85a. Plot of the CPTU and MPFA Friction Sensor Traces from Sounding MPFA_7 at the BWDWA Site.

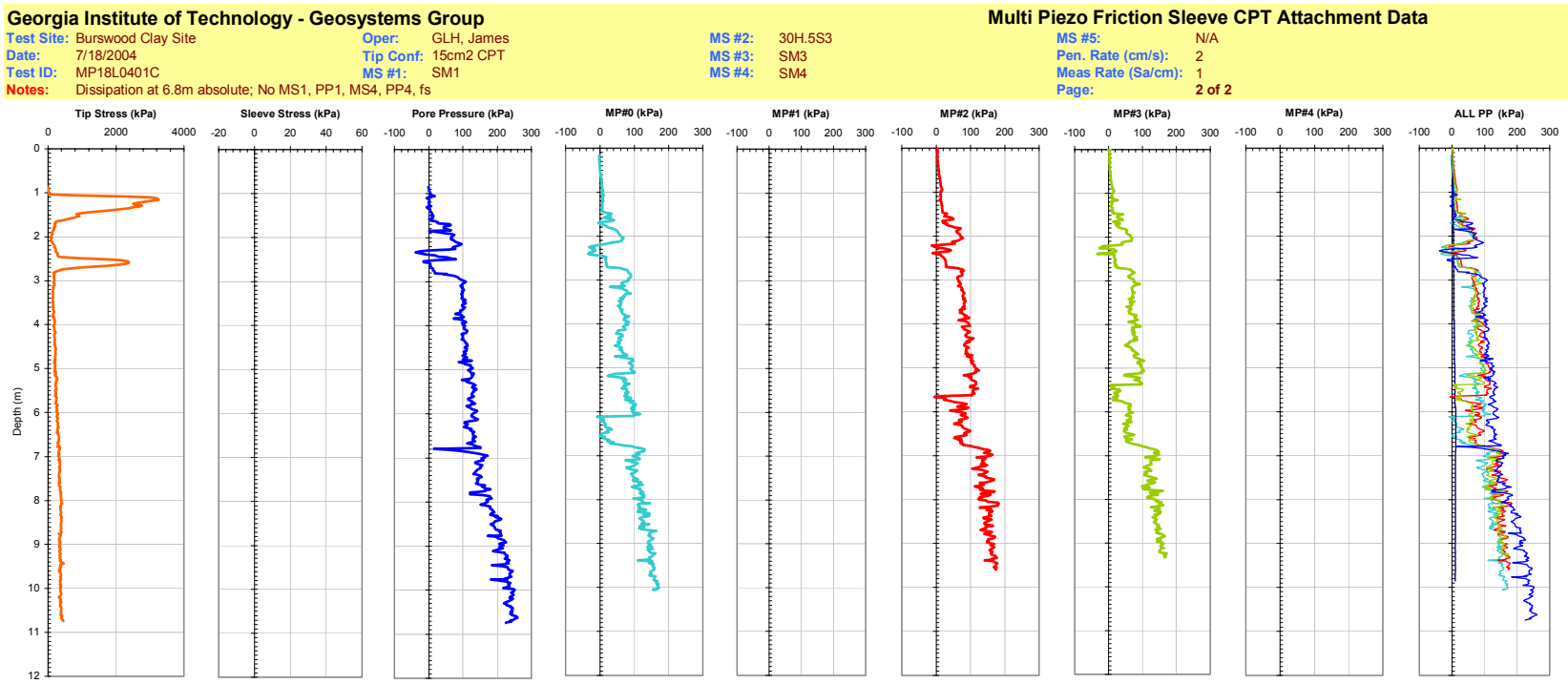

Figure A-85b. Plot of the CPTU and MPFA Piezo Sensor Traces from Sounding MPFA_7 at the BWDWA Site.

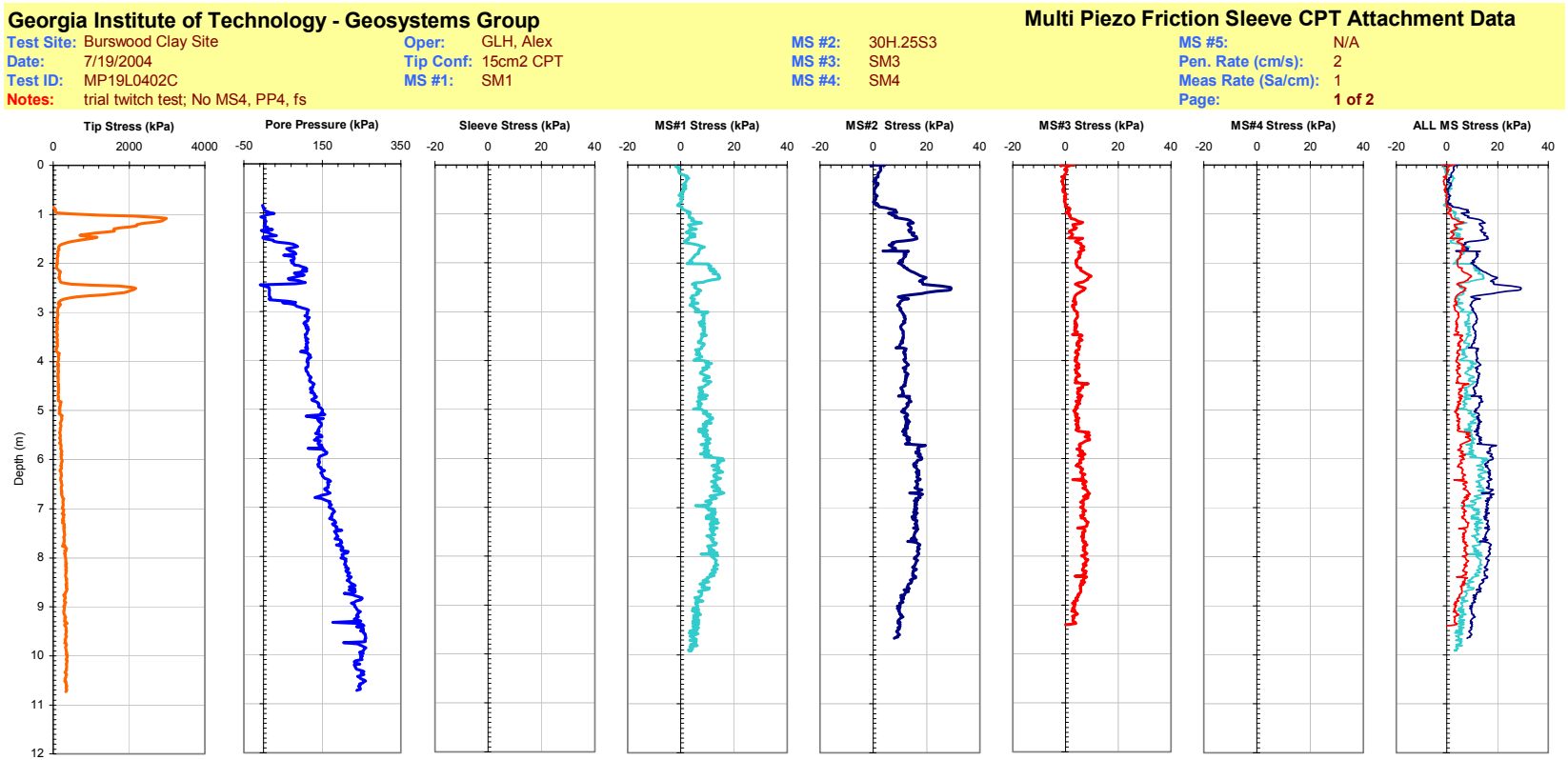

Figure A-86a. Plot of the CPTU and MPFA Friction Sensor Traces from Sounding MPFA_8 at the BWDWA Site.

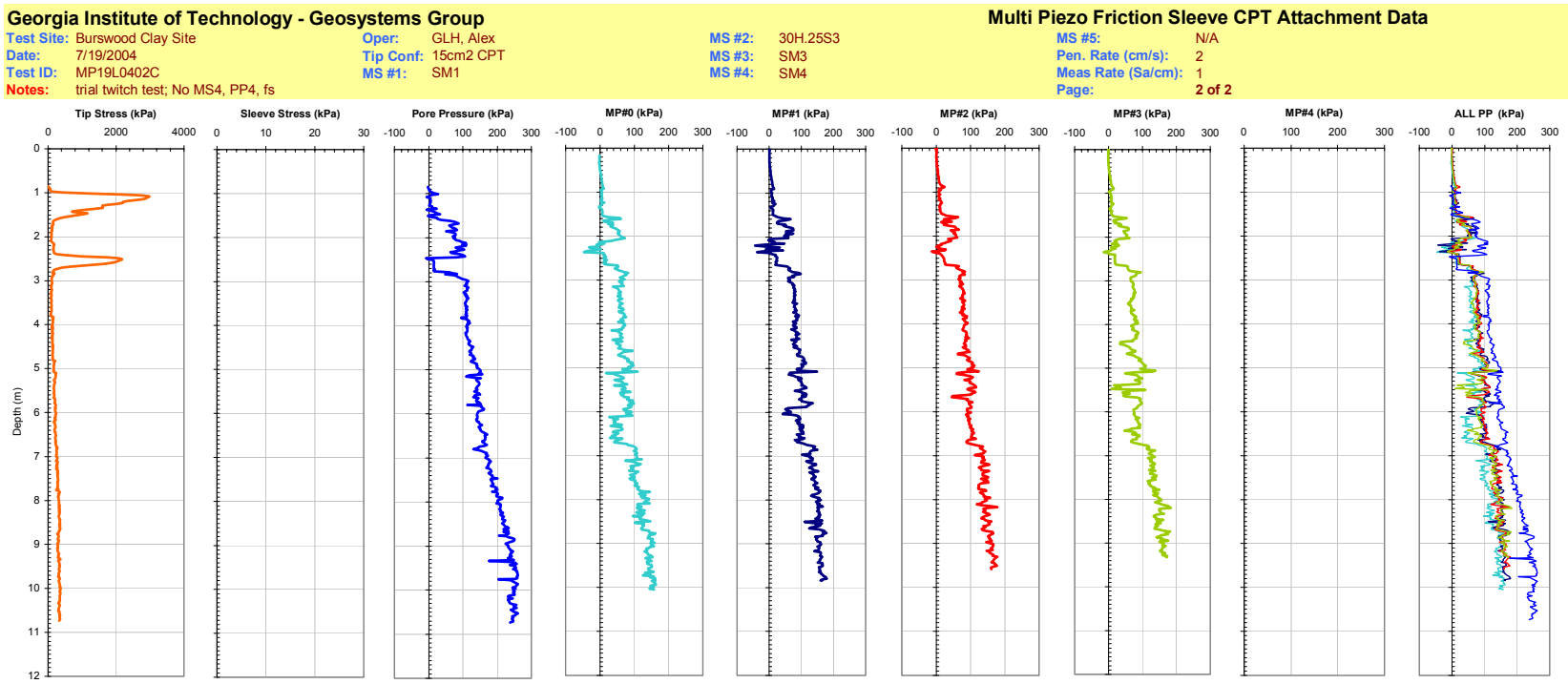

Figure A-86b. Plot of the CPTU and MPFA Piezo Sensor Traces from Sounding MPFA_8 at the BWDWA Site.

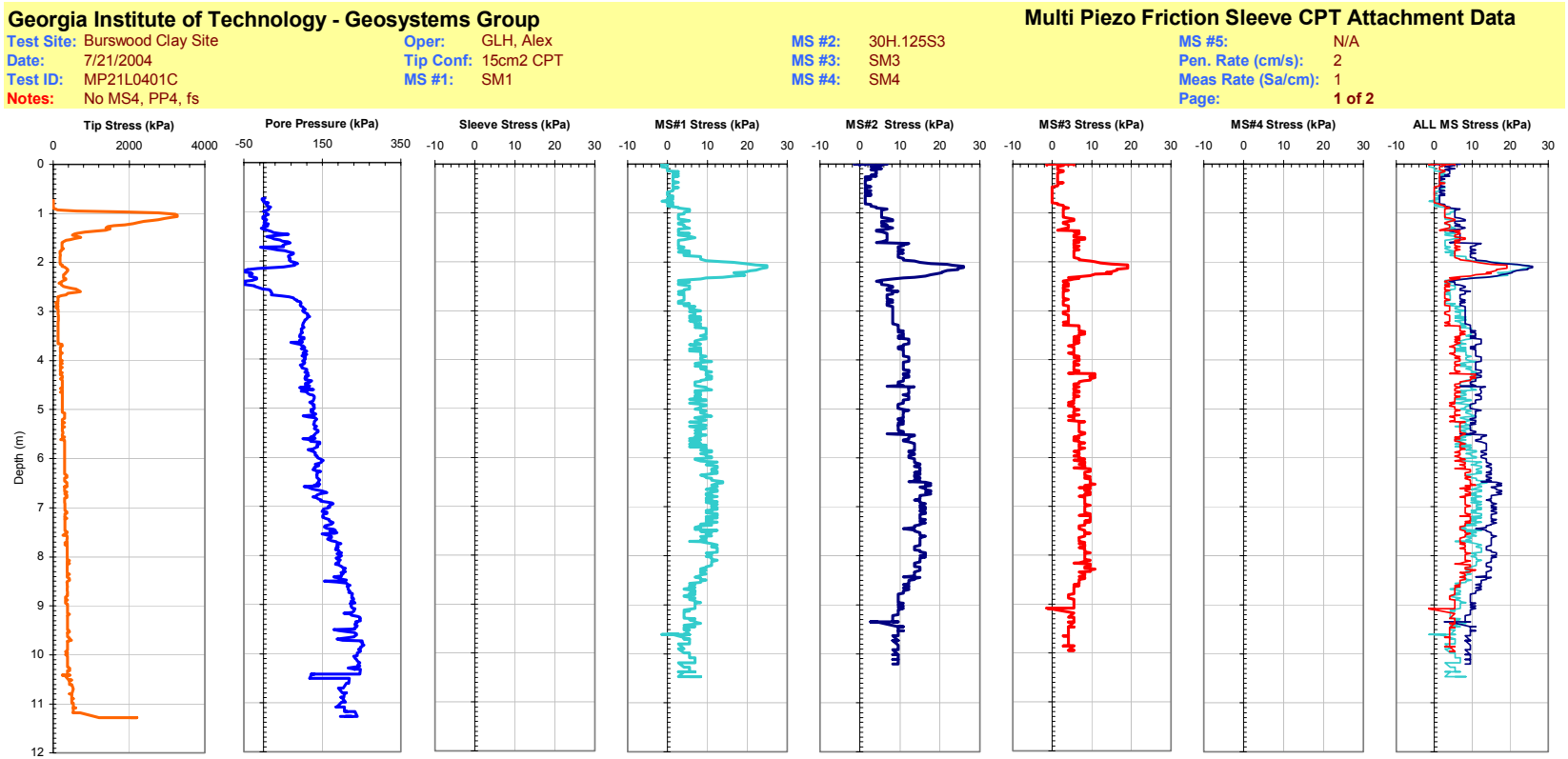

Figure A-87a. Plot of the CPTU and MPFA Friction Sensor Traces from Sounding MPFA_9 at the BWDWA Site.

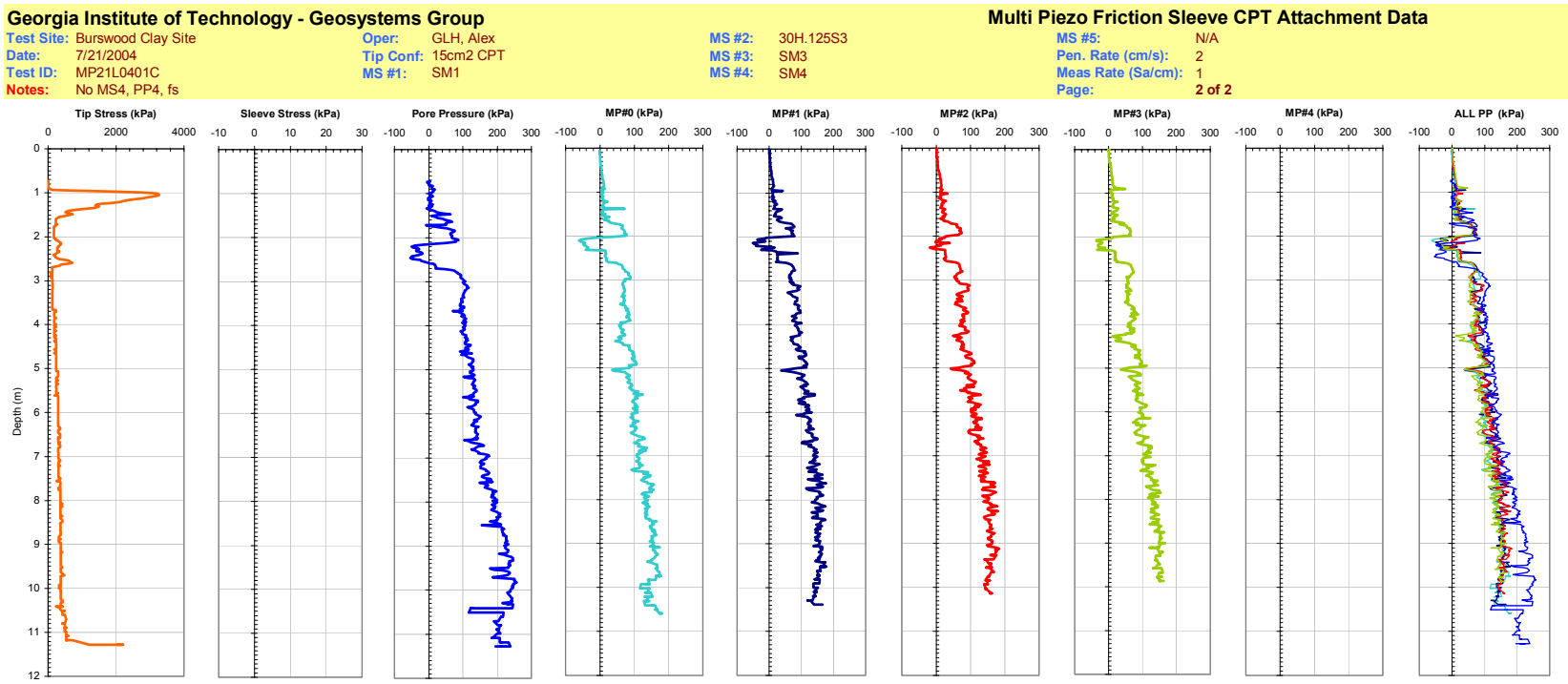

Figure A-87b. Plot of the CPTU and MPFA Piezo Sensor Traces from Sounding MPFA_9 at the BWDWA Site.

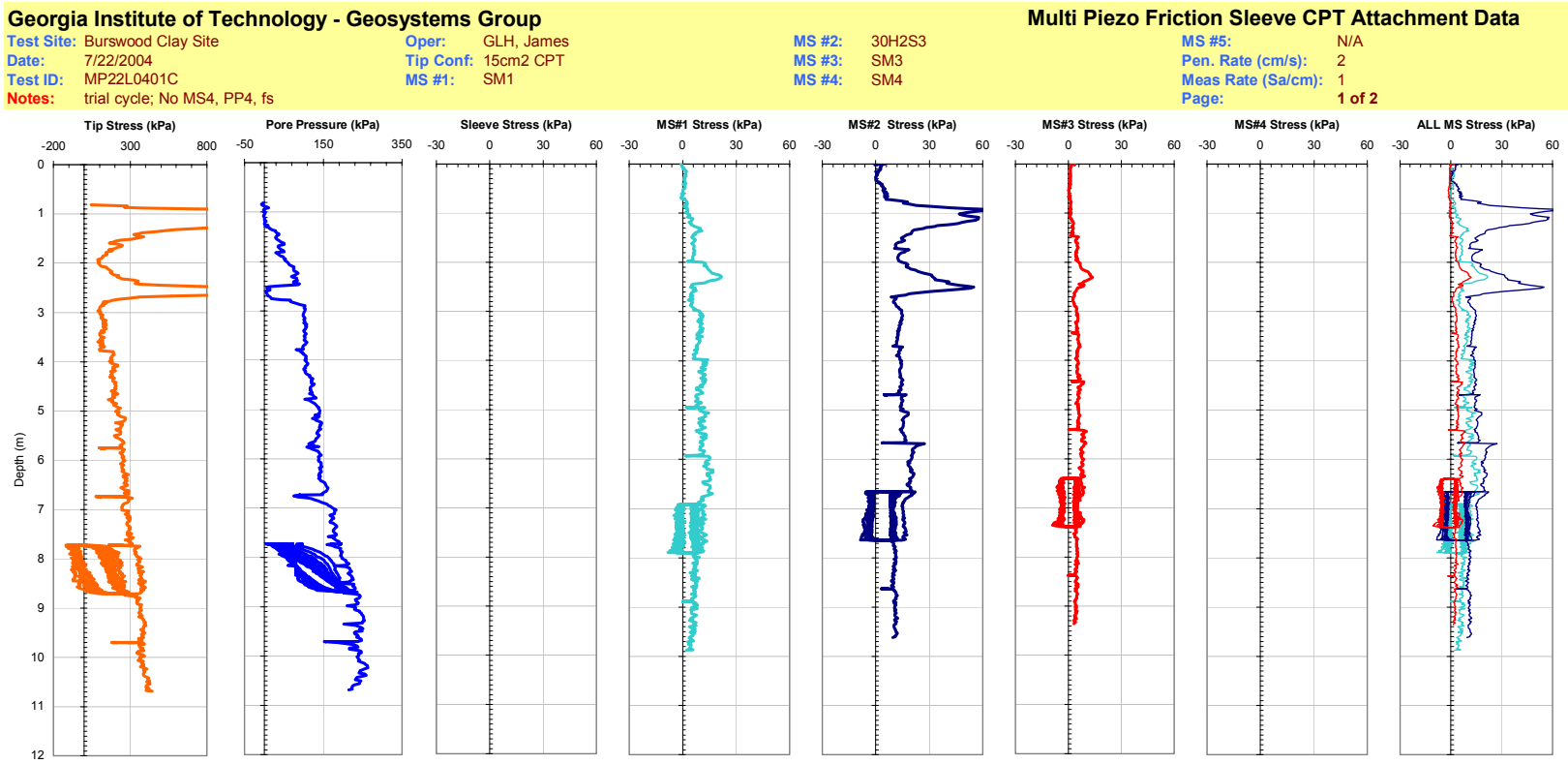

Figure A-88a. Plot of the CPTU and MPFA Friction Sensor Traces from Sounding MPFA_10 at the BWDWA Site.

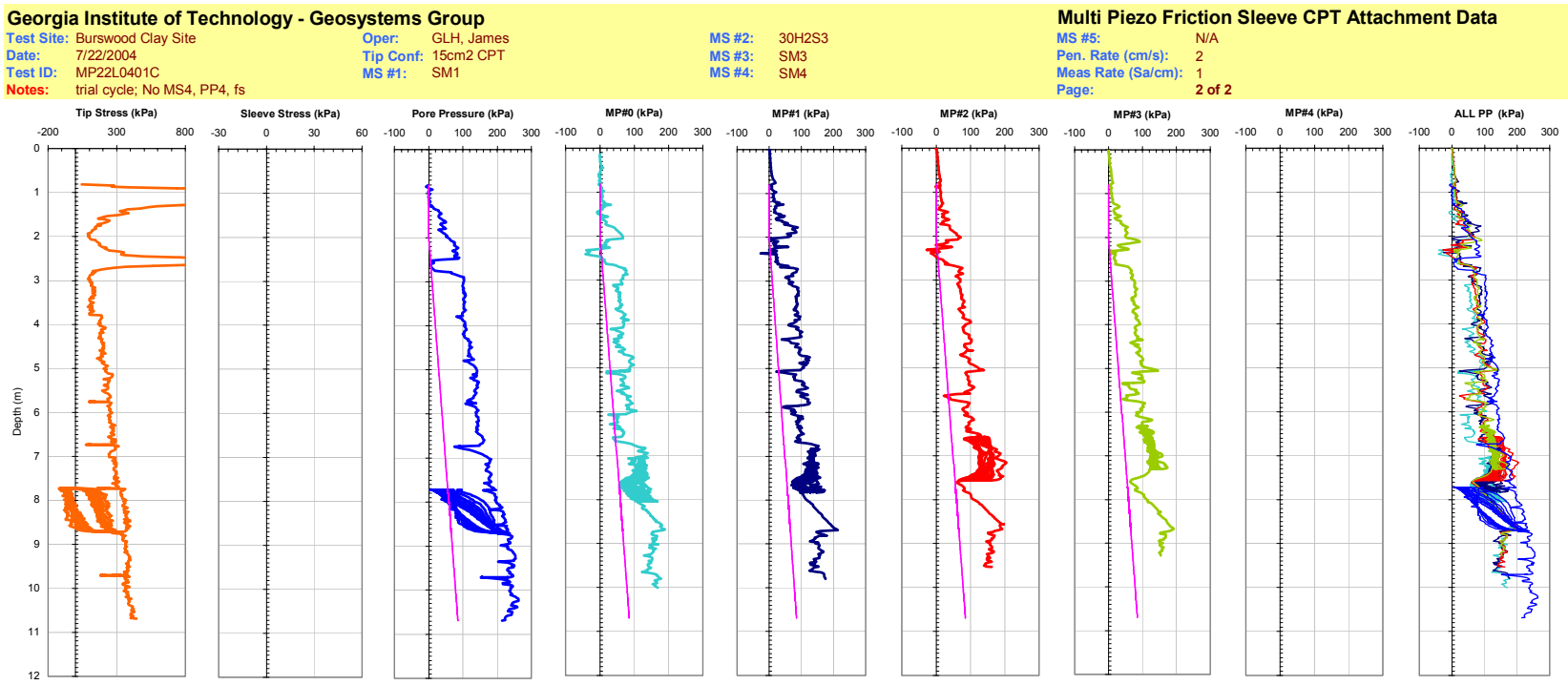

Figure A-88b. Plot of the CPTU and MPFA Piezo Sensor Traces from Sounding MPFA_10 at the BWDWA Site.

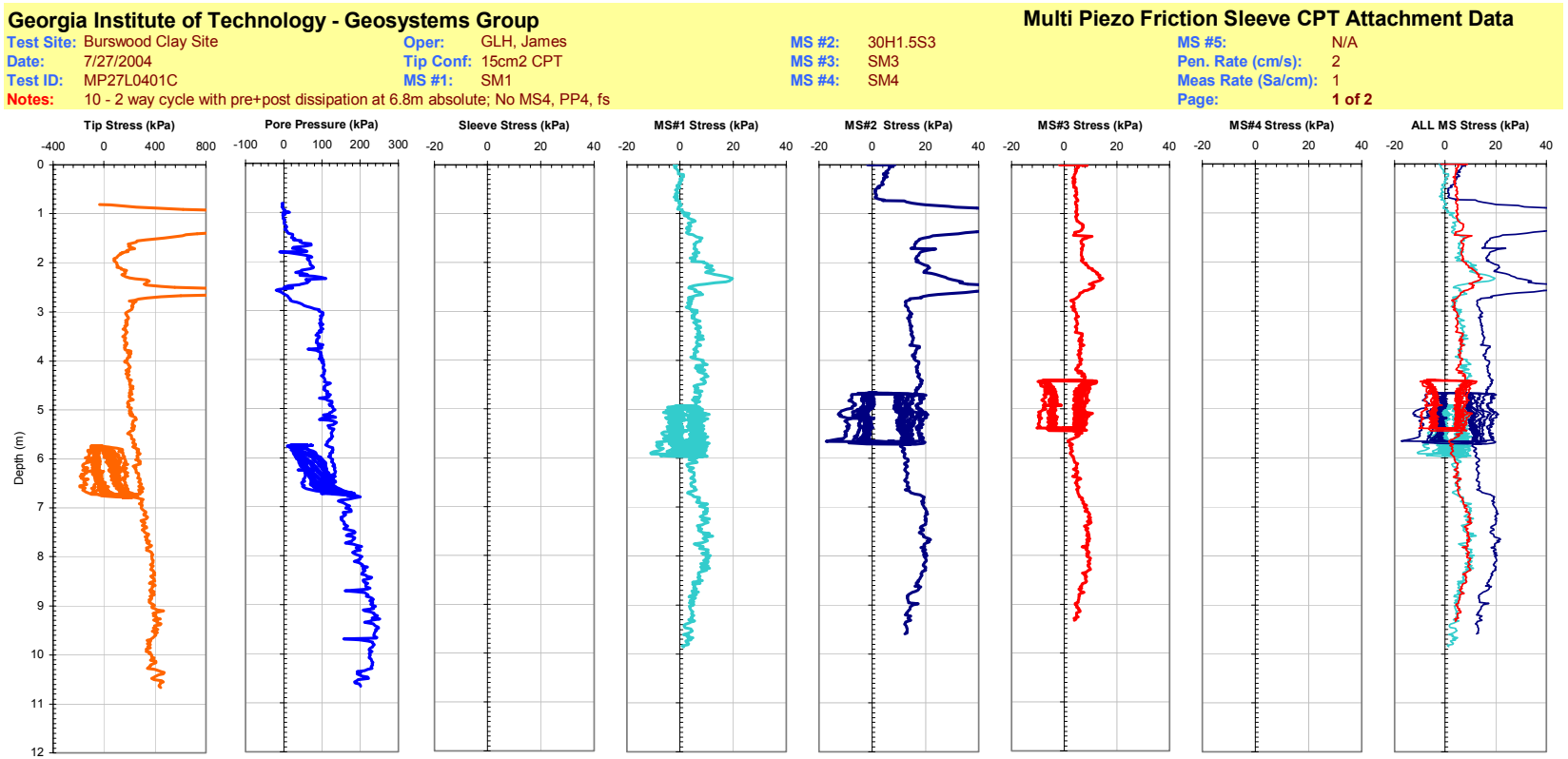

Figure A-89a. Plot of the CPTU and MPFA Friction Sensor Traces from Sounding MPFA_11 at the BWDWA Site.

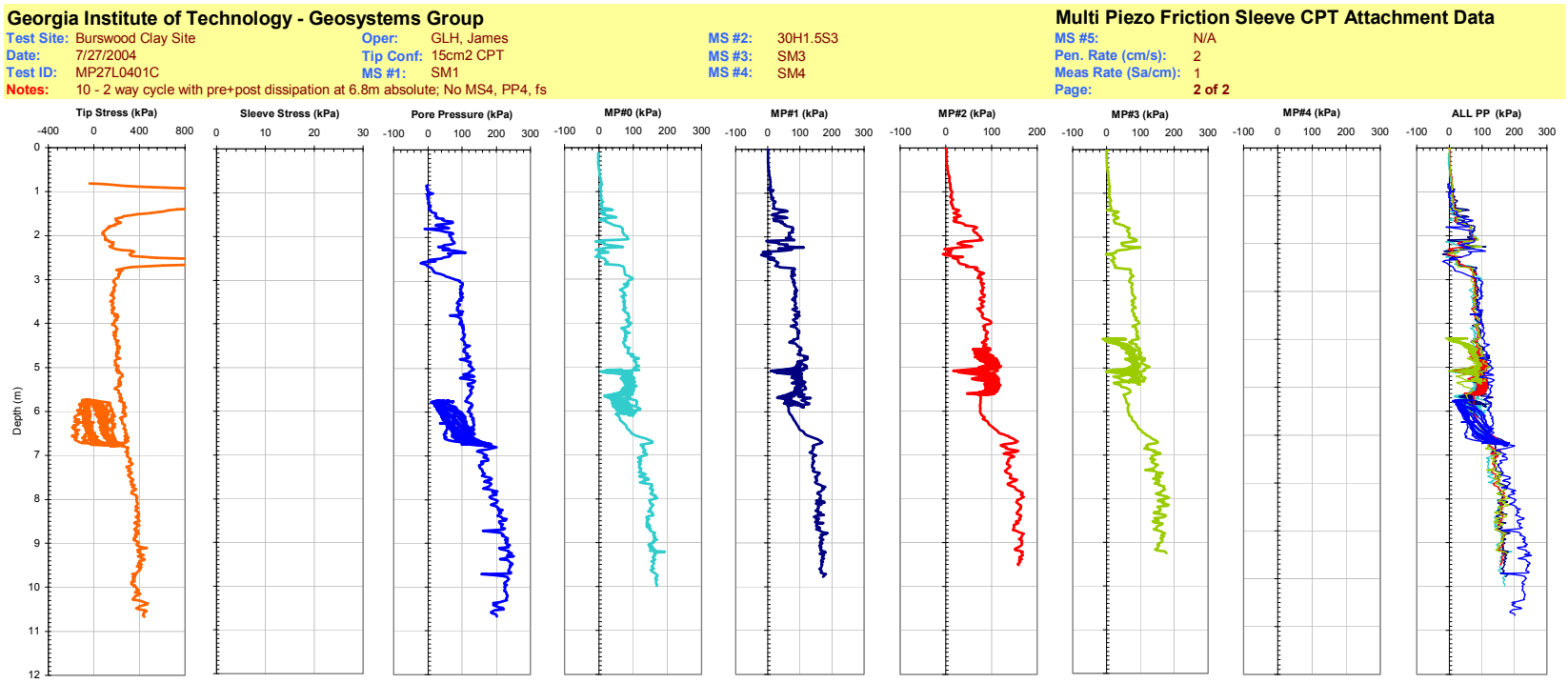

Figure A-89b. Plot of the CPTU and MPFA Piezo Sensor Traces from Sounding MPFA_11 at the BWDWA Site.

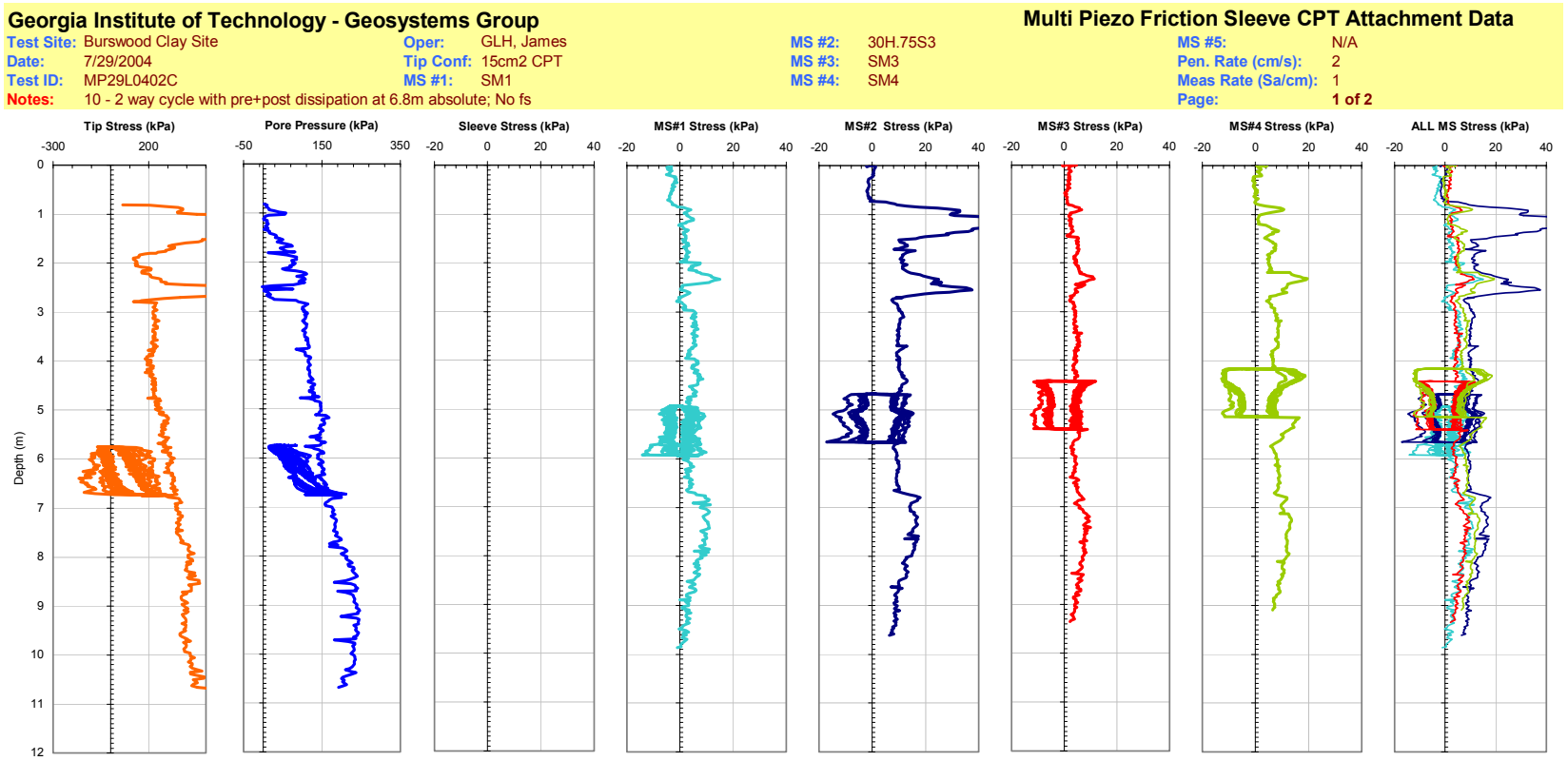

Figure A-90a. Plot of the CPTU and MPFA Friction Sensor Traces from Sounding MPFA_12 at the BWDWA Site.

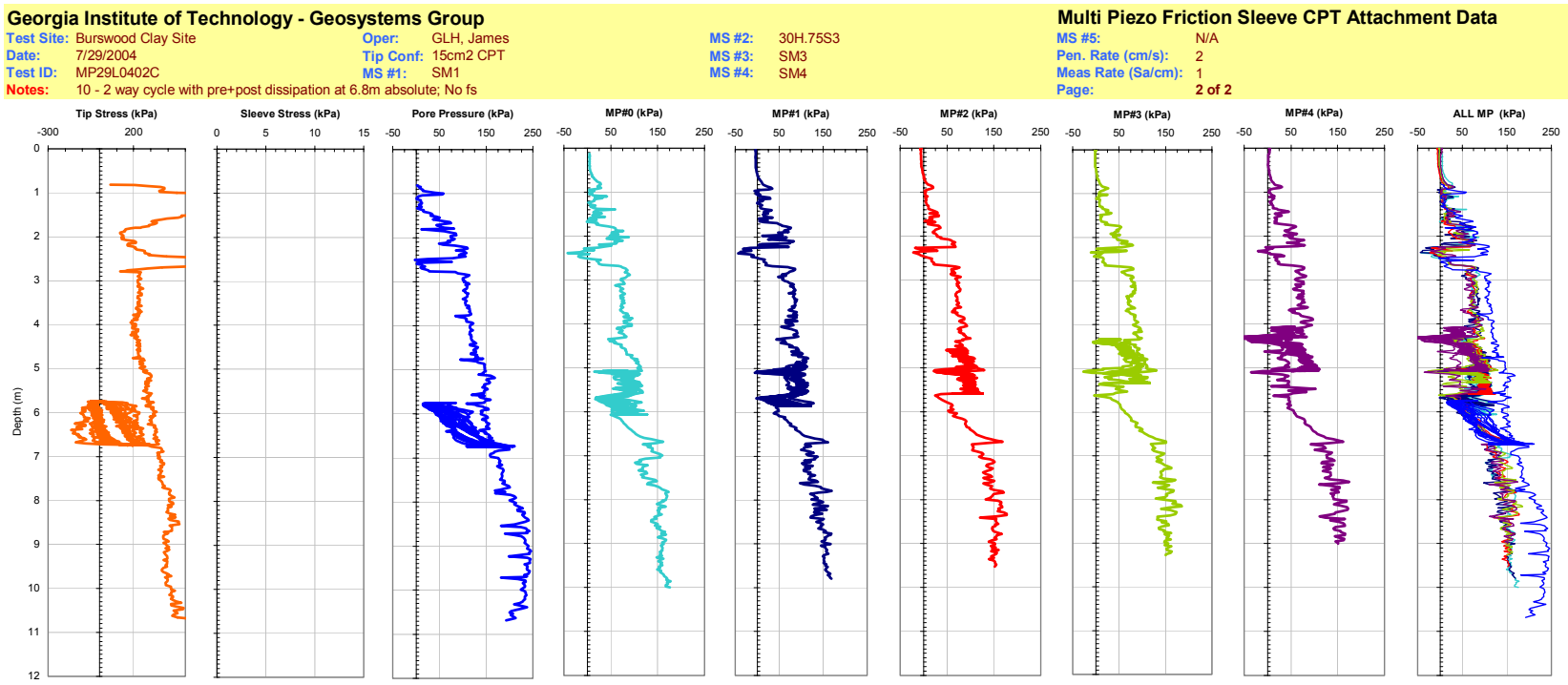

Figure A-90b. Plot of the CPTU and MPFA Piezo Sensor Traces from Sounding MPFA_12 at the BWDWA Site.

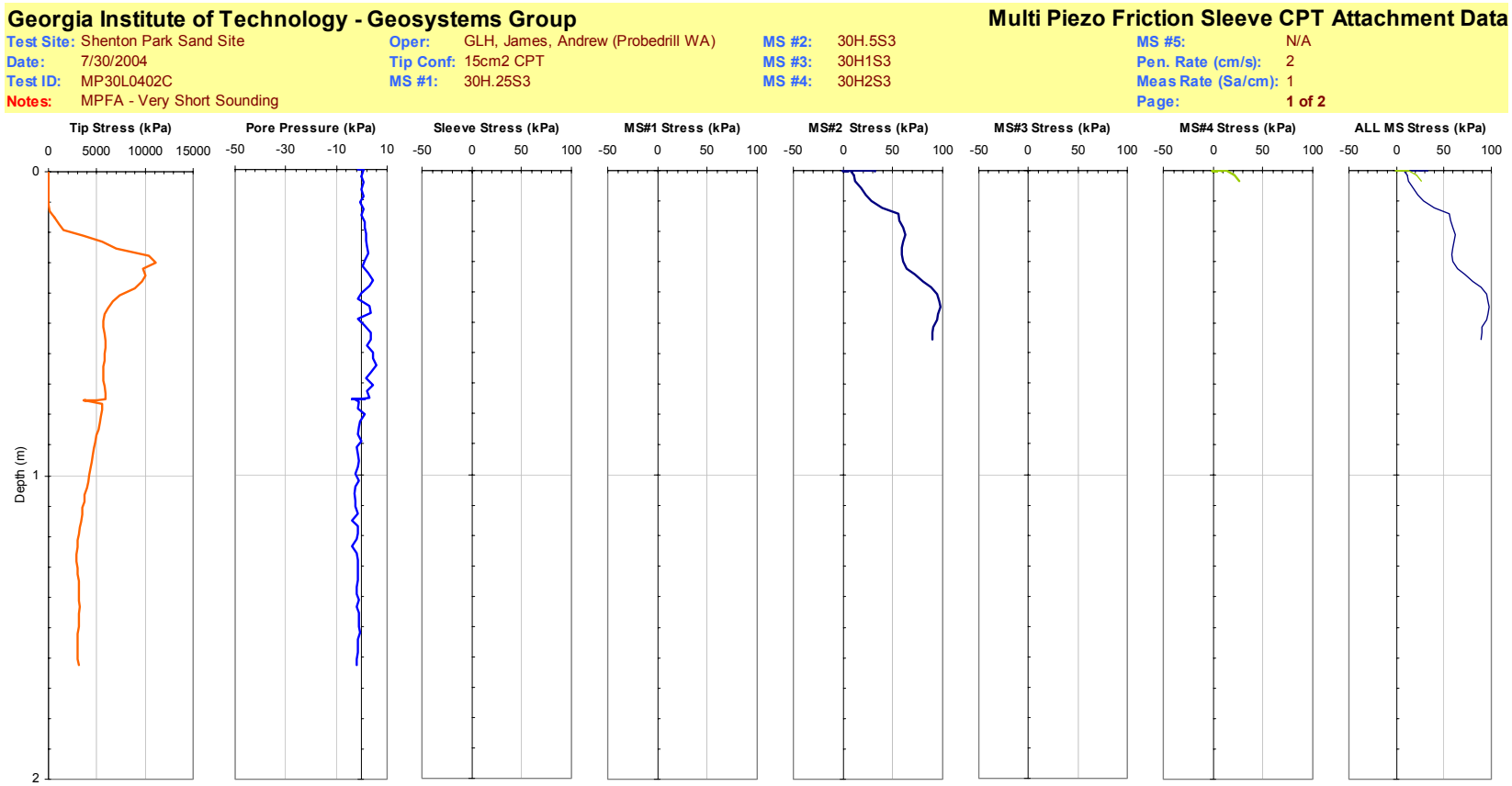

Figure A-91a. Plot of the CPTU and MPFA Friction Sensor Traces from Sounding MPFA_13 at the SPWA Site.

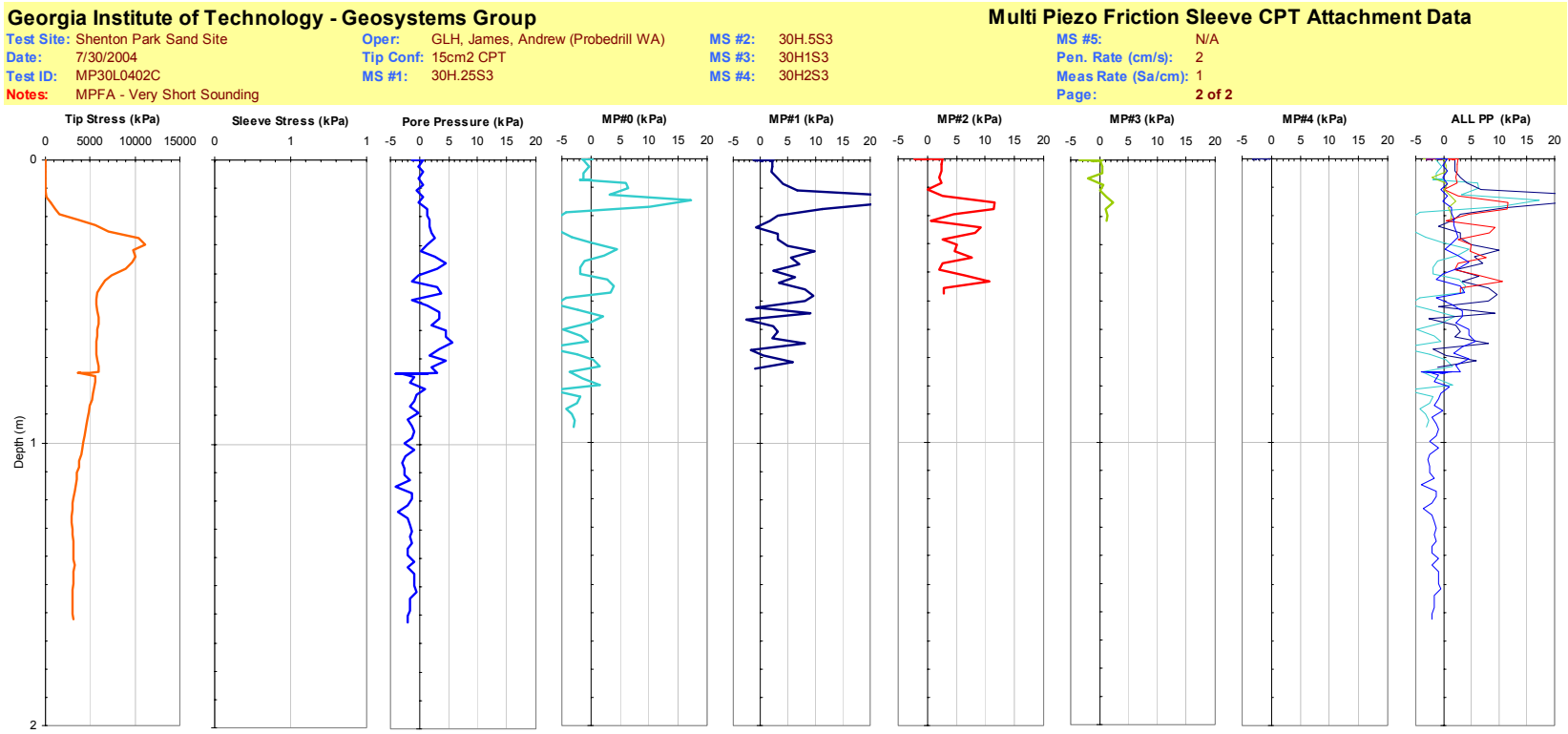

Figure A-91b. Plot of the CPTU and MPFA Piezo Sensor Traces from Sounding MPFA_13 at the SPWA Site.

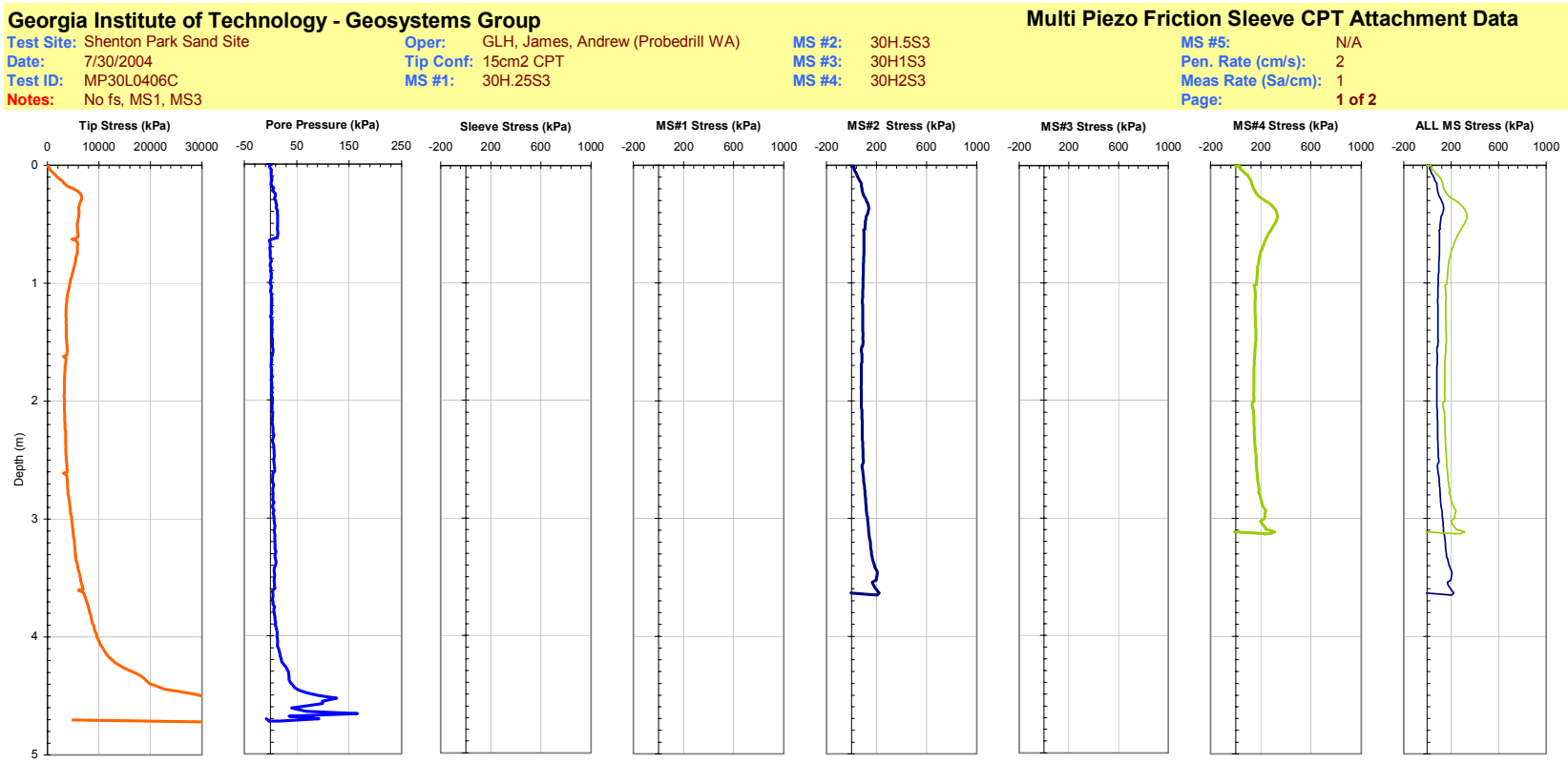

Figure A-92a. Plot of the CPTU and MPFA Friction Sensor Traces from Sounding MPFA_14 at the SPWA Site.

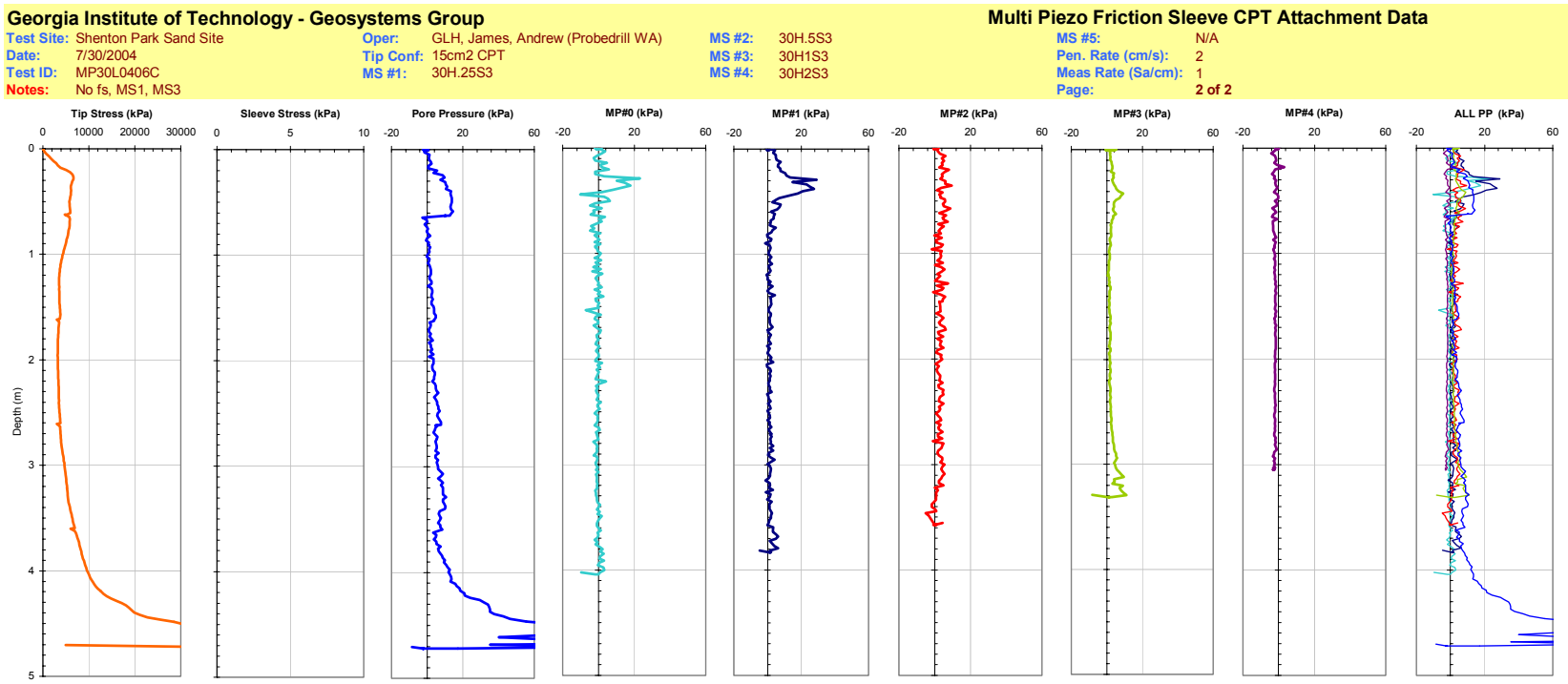

Figure A-92b. Plot of the CPTU and MPFA Piezo Sensor Traces from Sounding MPFA_14 at the SPWA Site.

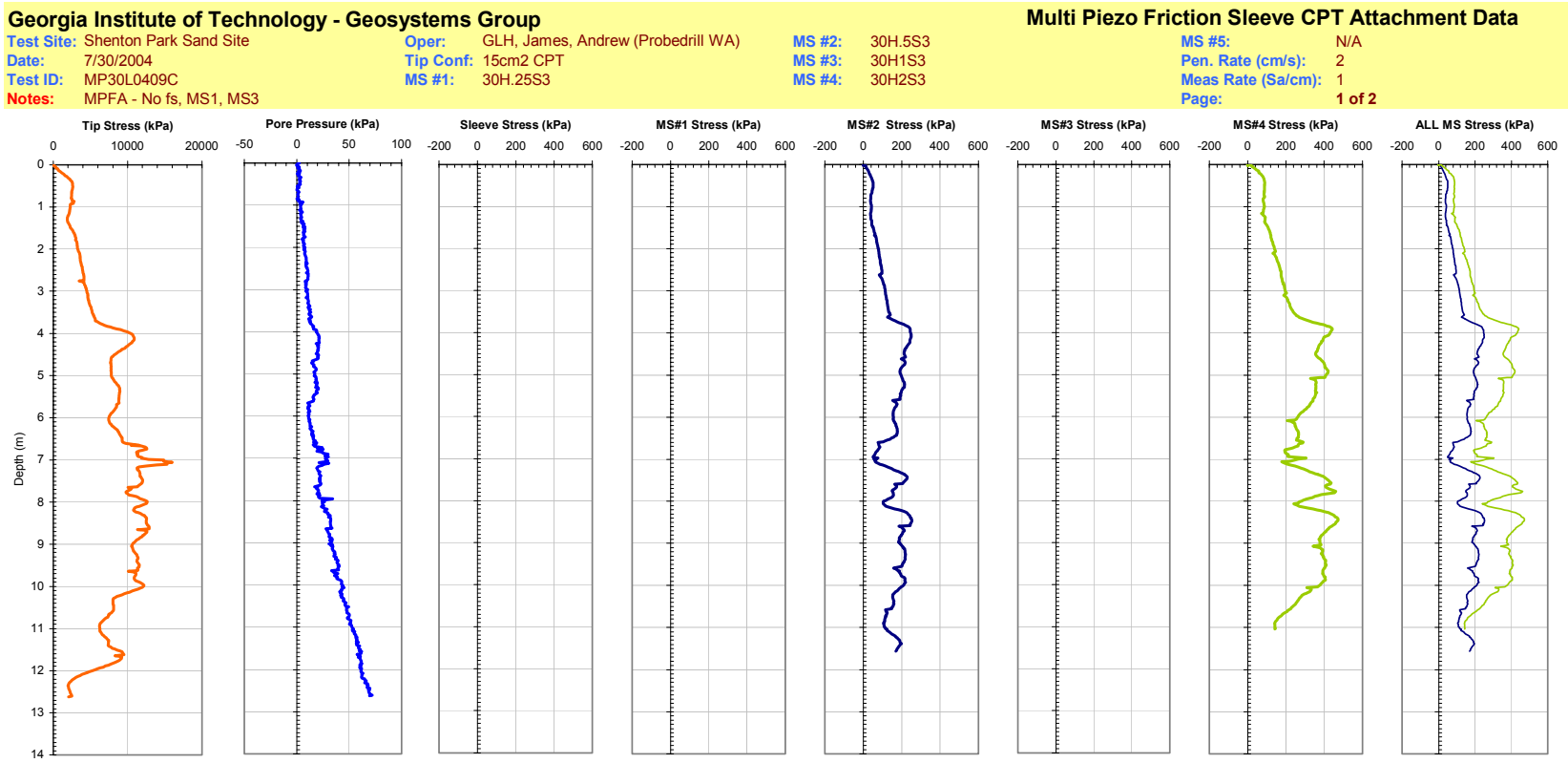

Figure A-93a. Plot of the CPTU and MPFA Friction Sensor Traces from Sounding MPFA_15 at the SPWA Site.

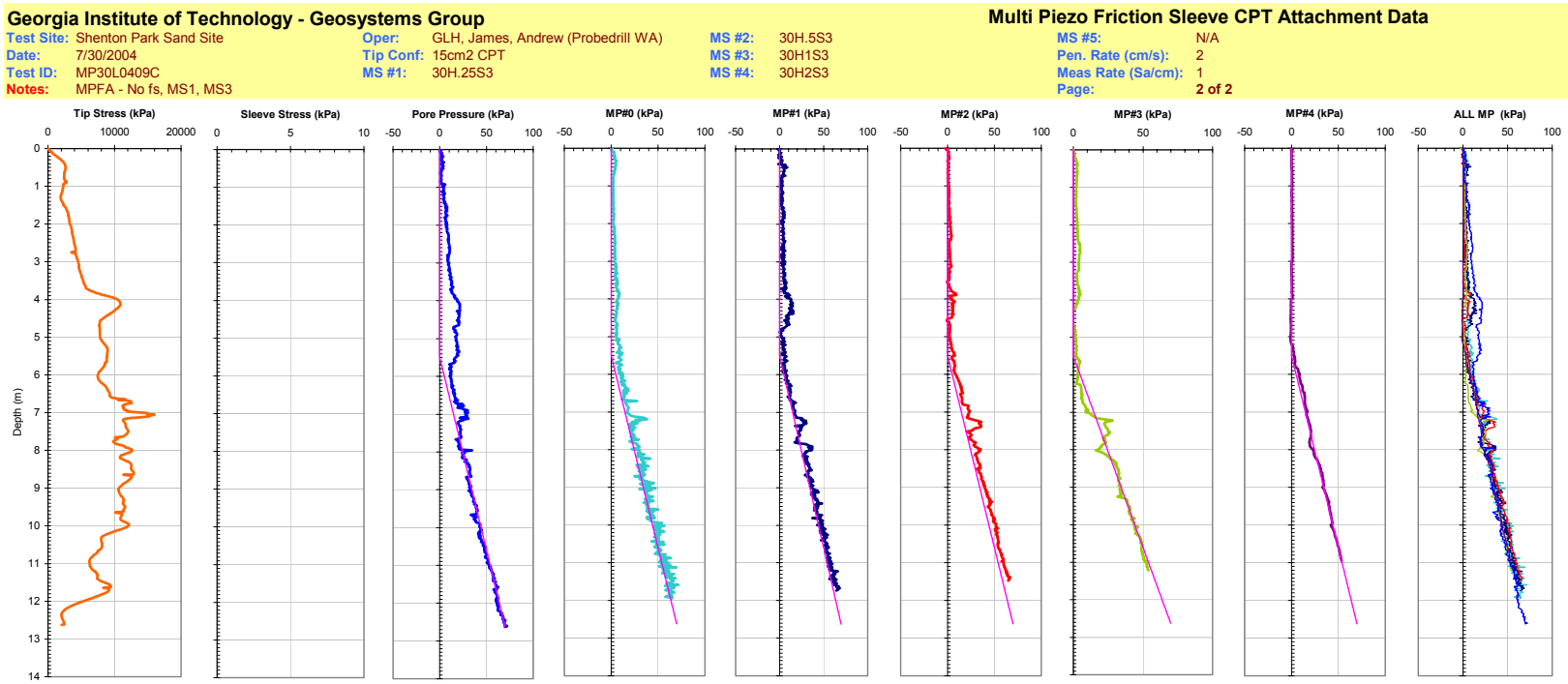

Figure A-93b. Plot of the CPTU and MPFA Piezo Sensor Traces from Sounding MPFA_15 at the SPWA Site.

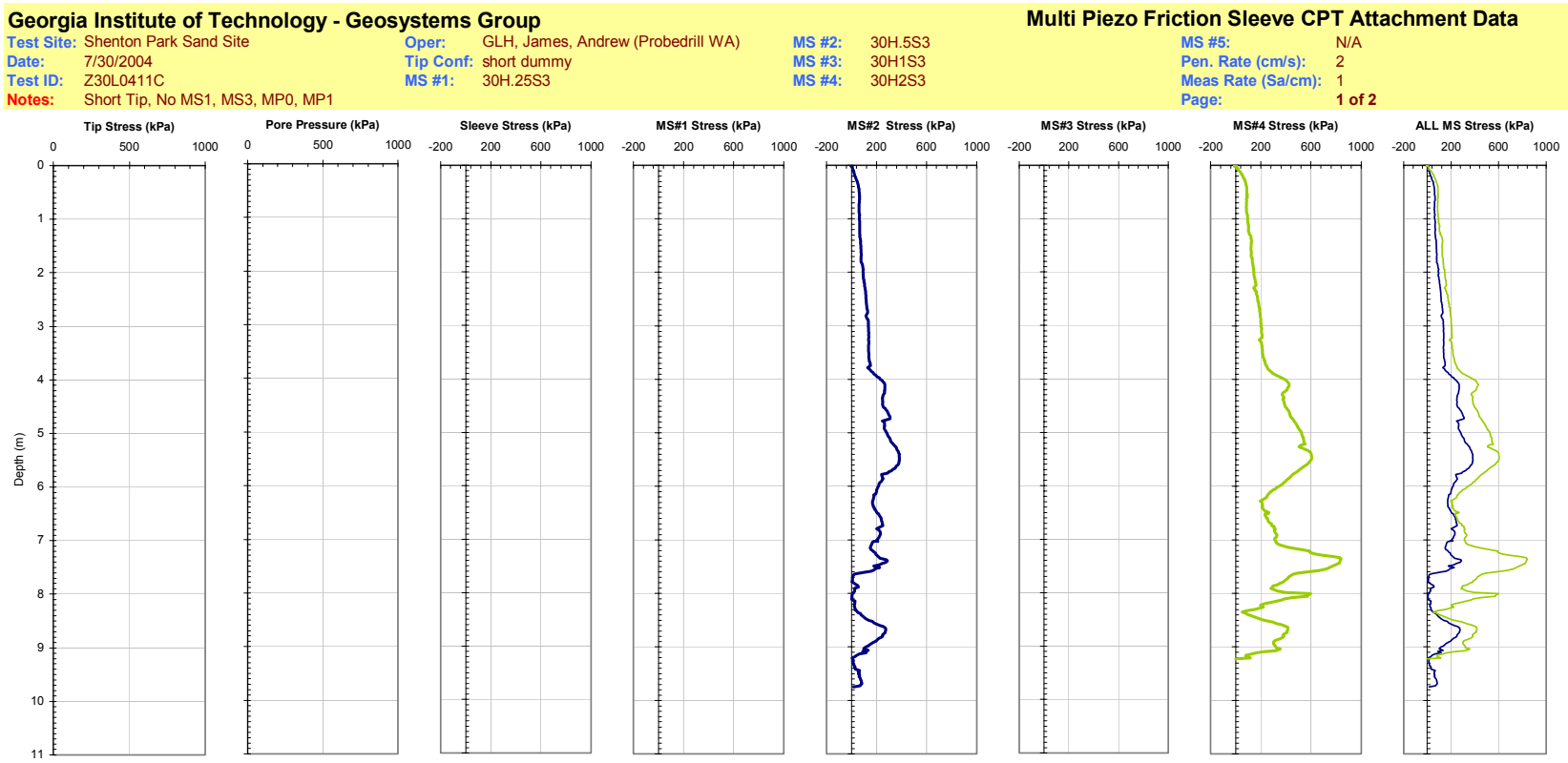

Figure A-94a. Plot of the CPTU and MPFA Friction Sensor Traces from Sounding MPFA_16 at the SPWA Site.

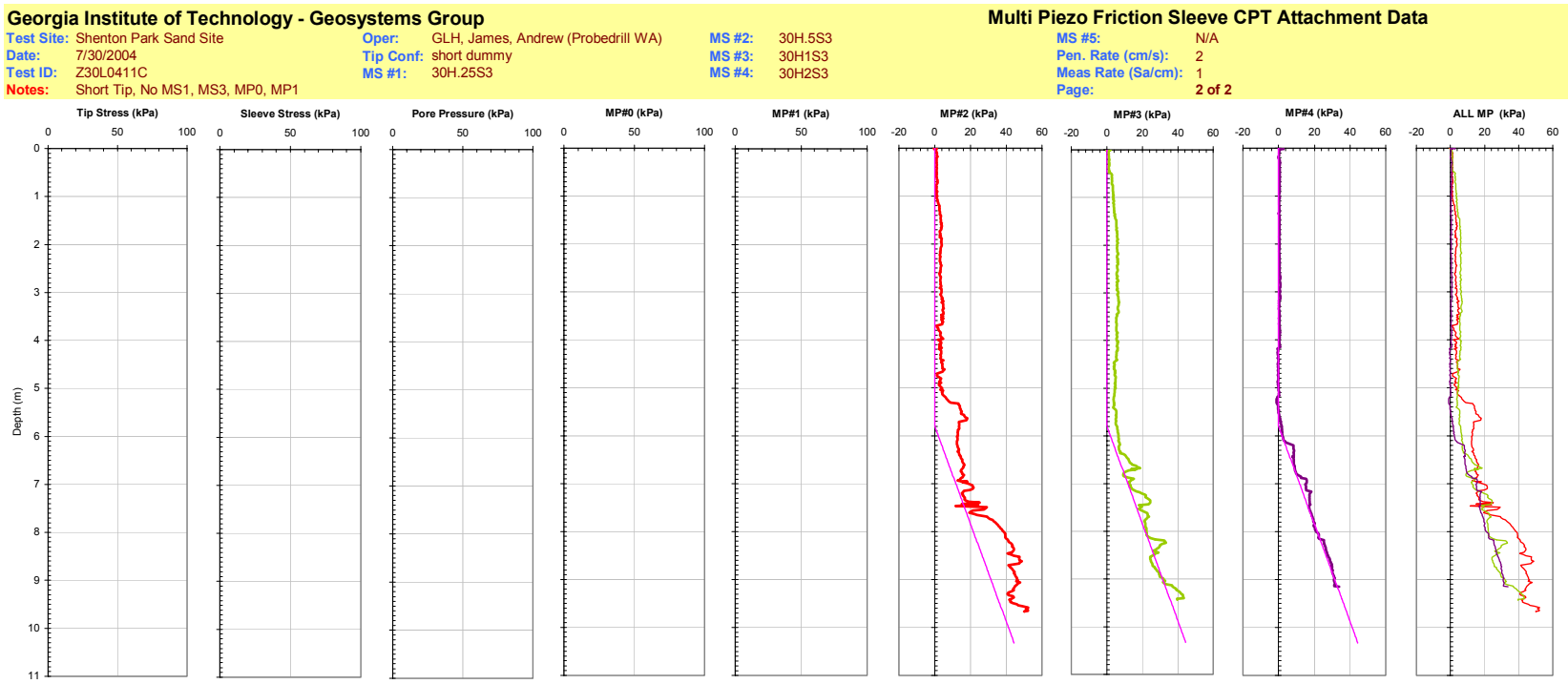

Figure A-94b. Plot of the CPTU and MPFA Piezo Sensor Traces from Sounding MPFA_16 at the SPWA Site.

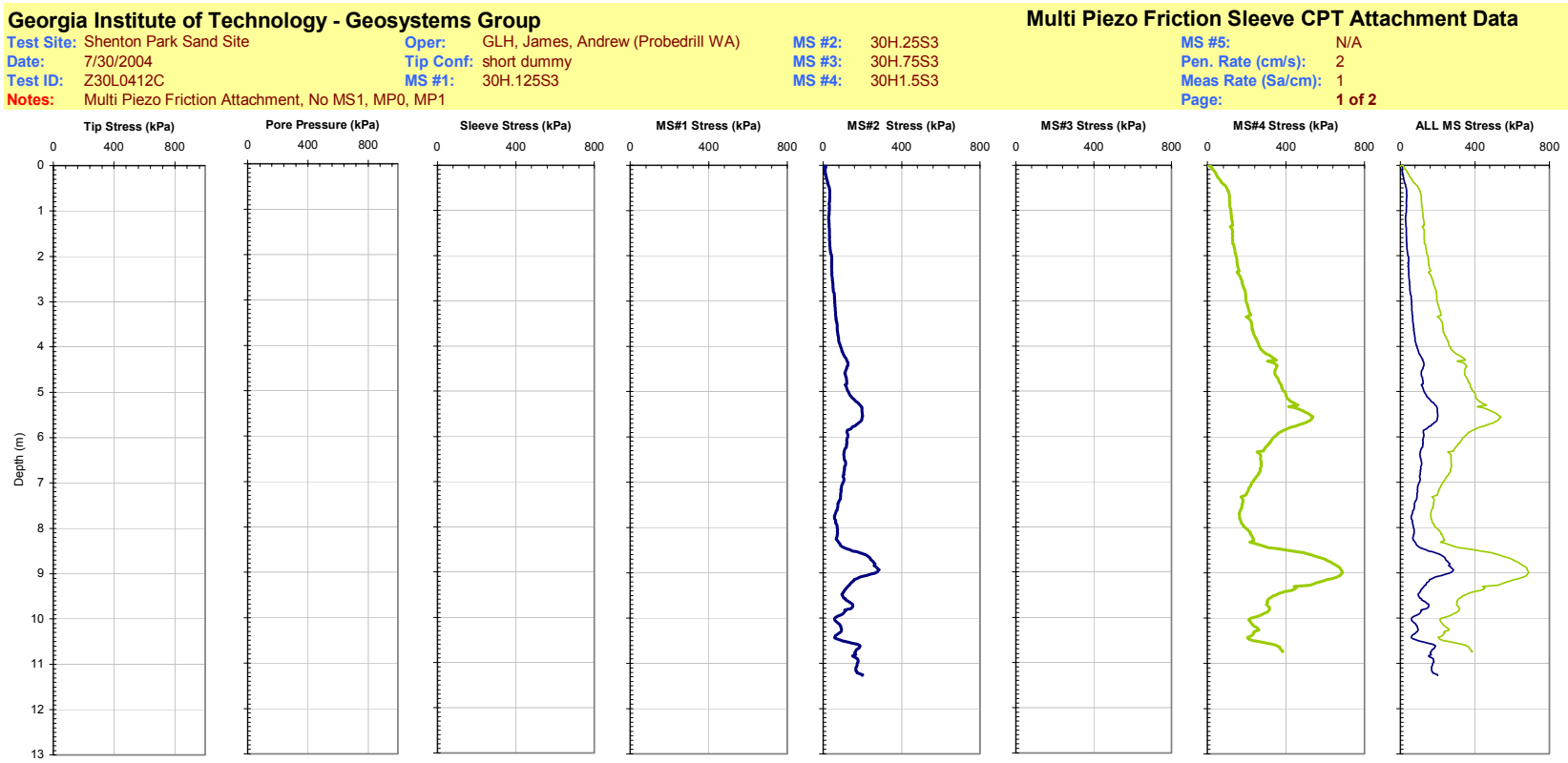

Figure A-95a. Plot of the CPTU and MPFA Friction Sensor Traces from Sounding MPFA_17 at the SPWA Site.

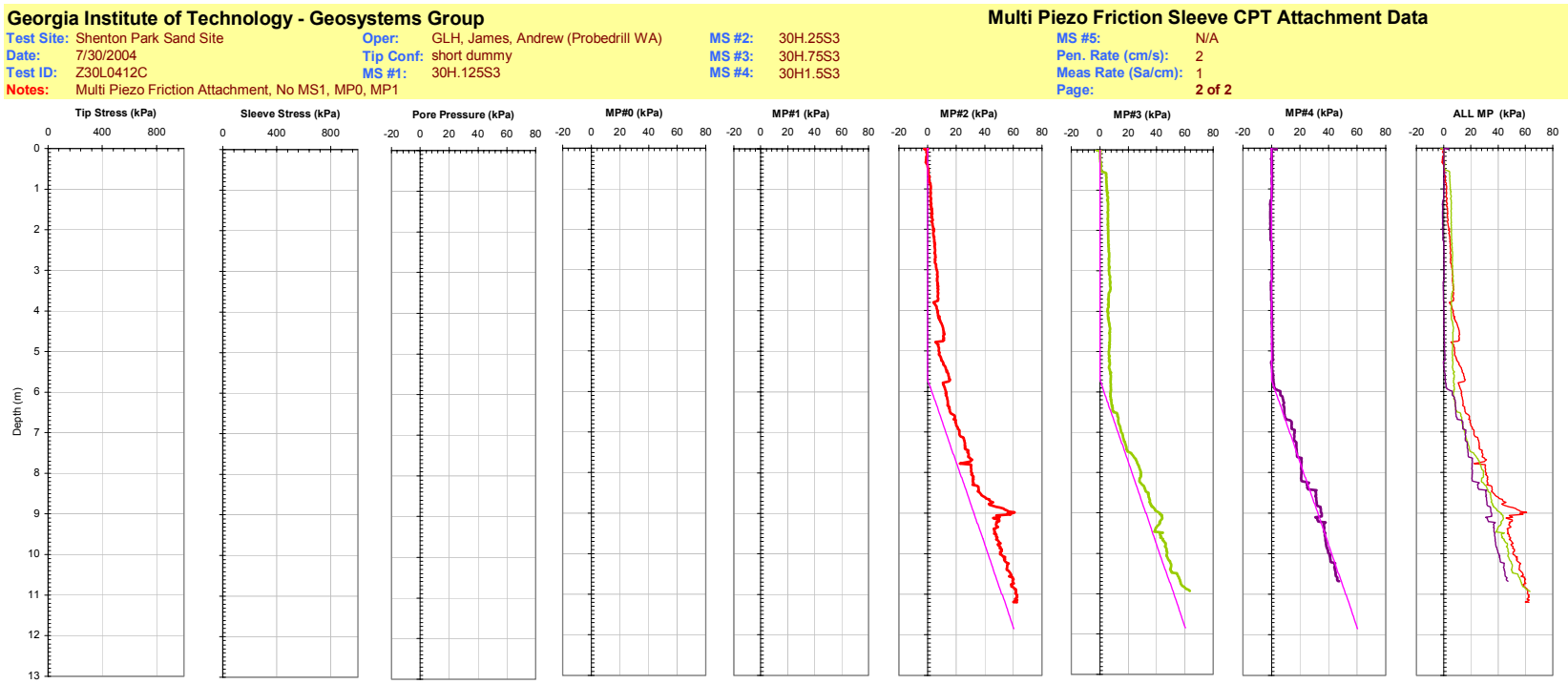

Figure A-95b. Plot of the CPTU and MPFA Piezo Sensor Traces from Sounding MPFA_17 at the SPWA Site.

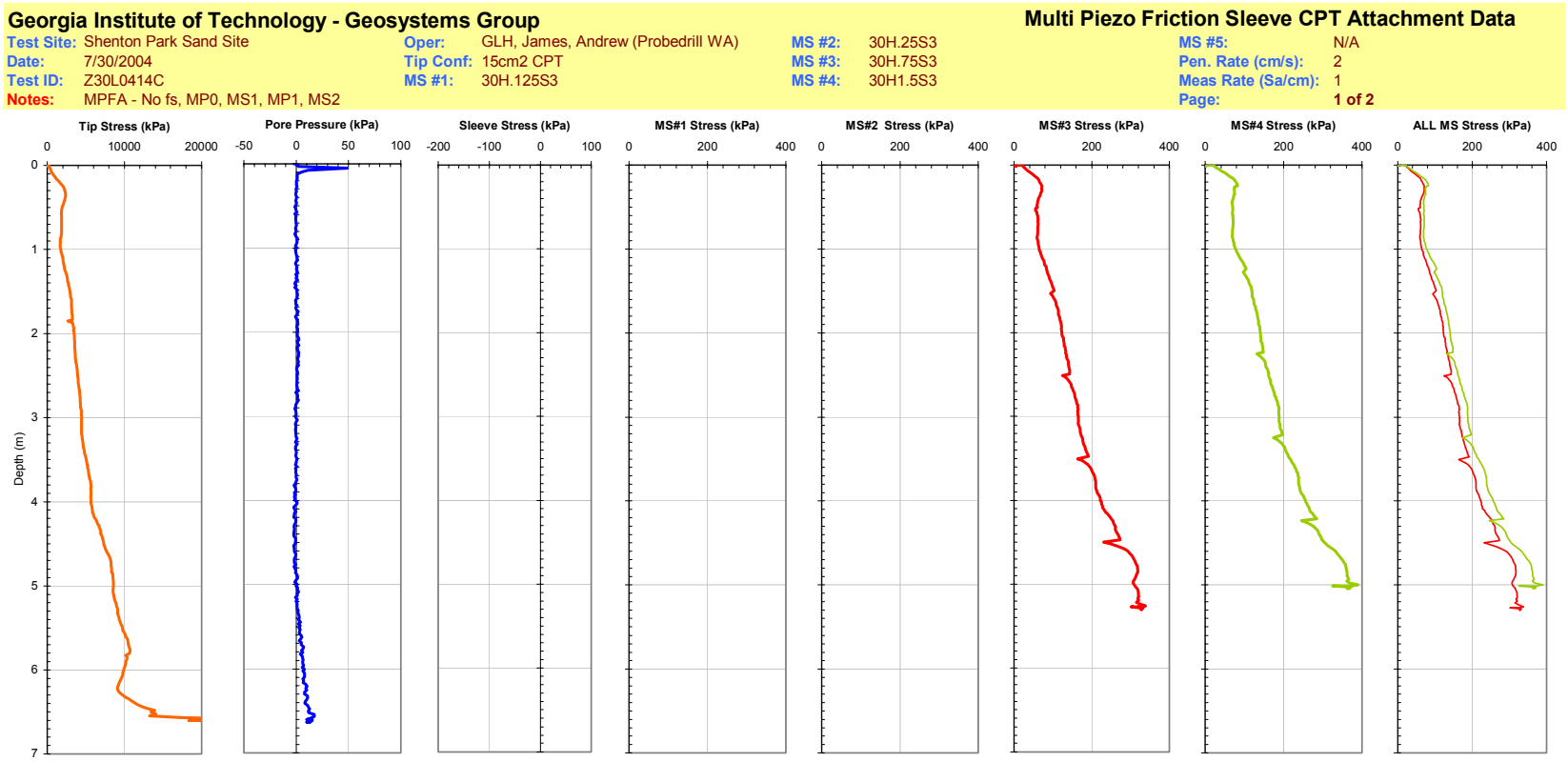

Figure A-96a. Plot of the CPTU and MPFA Friction Sensor Traces from Sounding MPFA_18 at the SPWA Site.

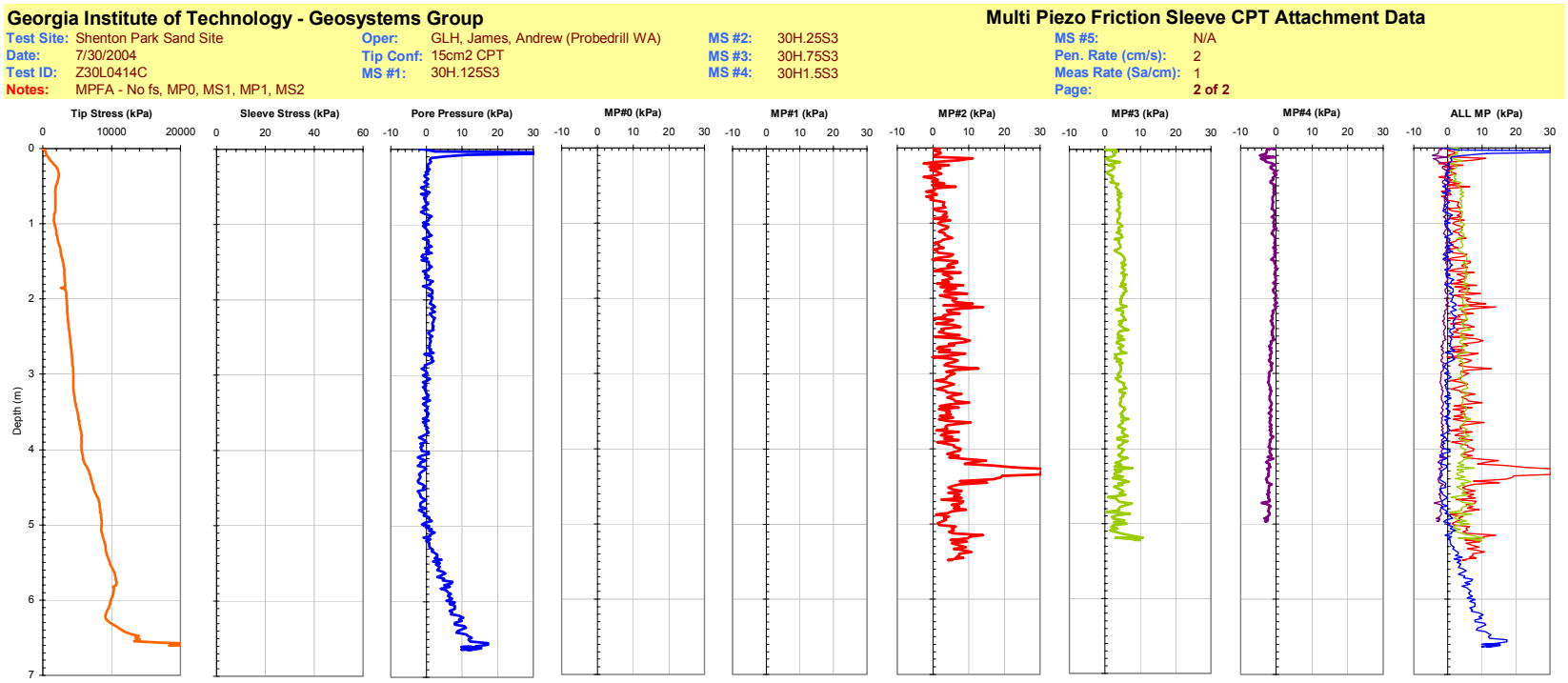

Figure A-96b. Plot of the CPTU and MPFA Piezo Sensor Traces from Sounding MPFA_18 at the SPWA Site.

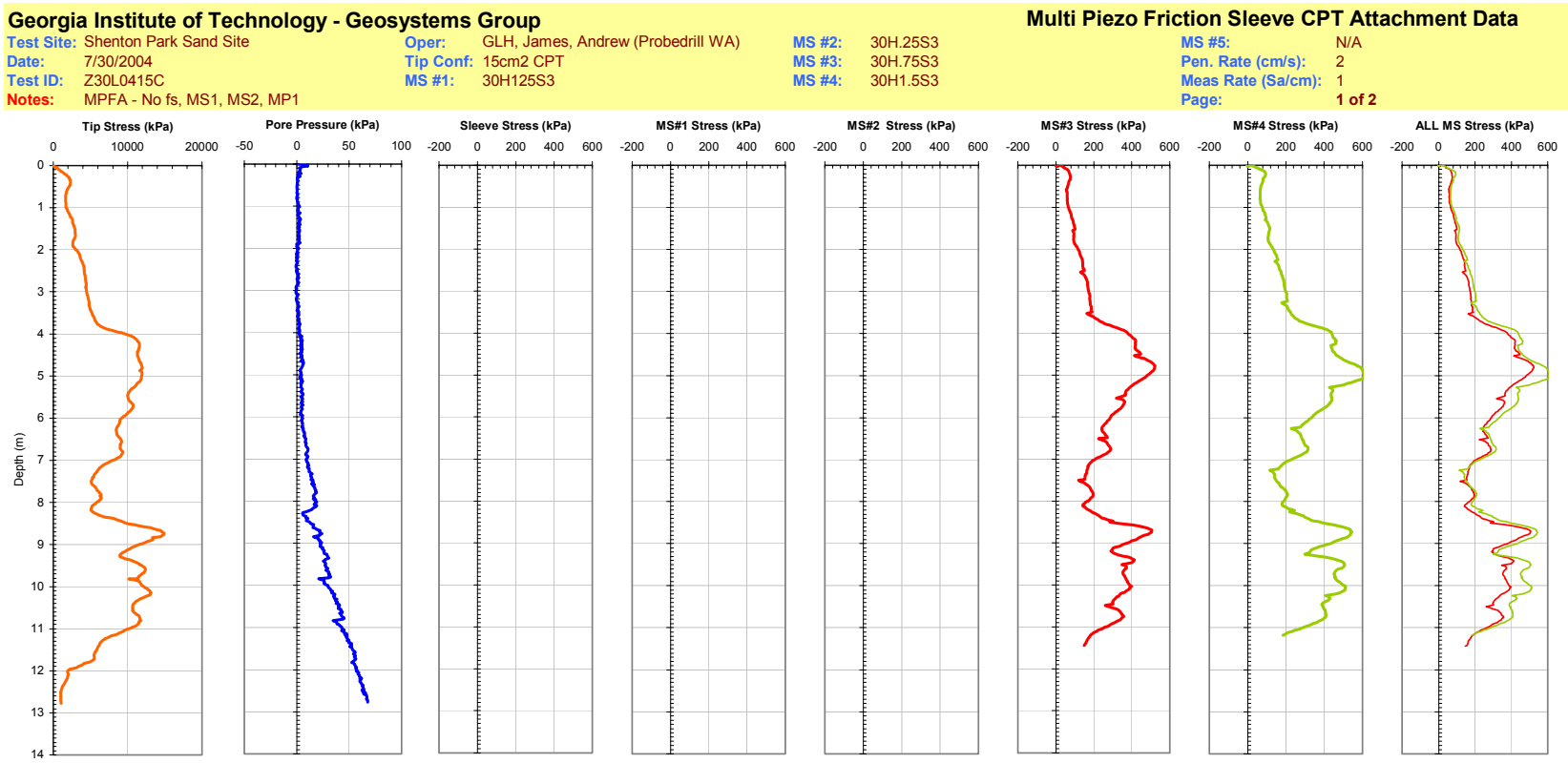

Figure A-97a. Plot of the CPTU and MPFA Friction Sensor Traces from Sounding MPFA_19 at the SPWA Site.

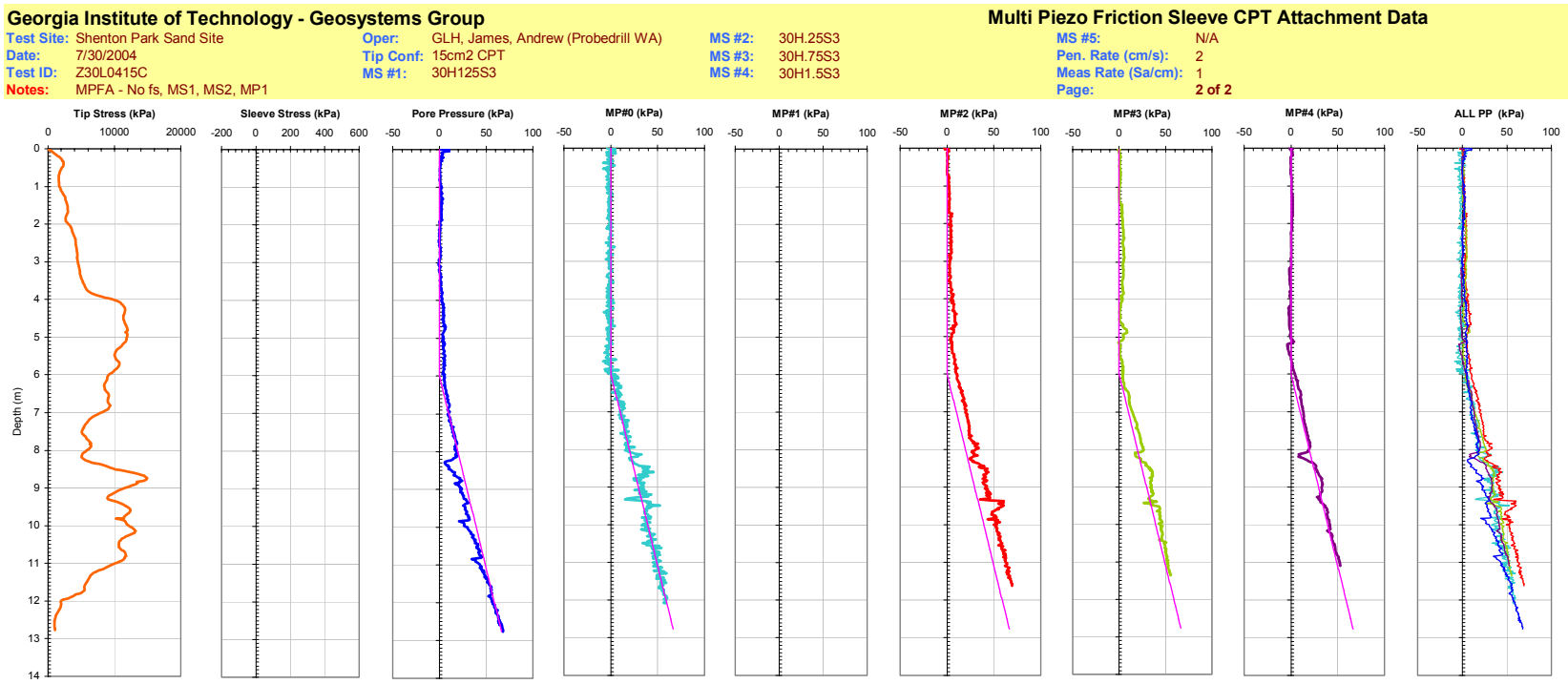

Figure A-97b. Plot of the CPTU and MPFA Piezo Sensor Traces from Sounding MPFA_19 at the SPWA Site.

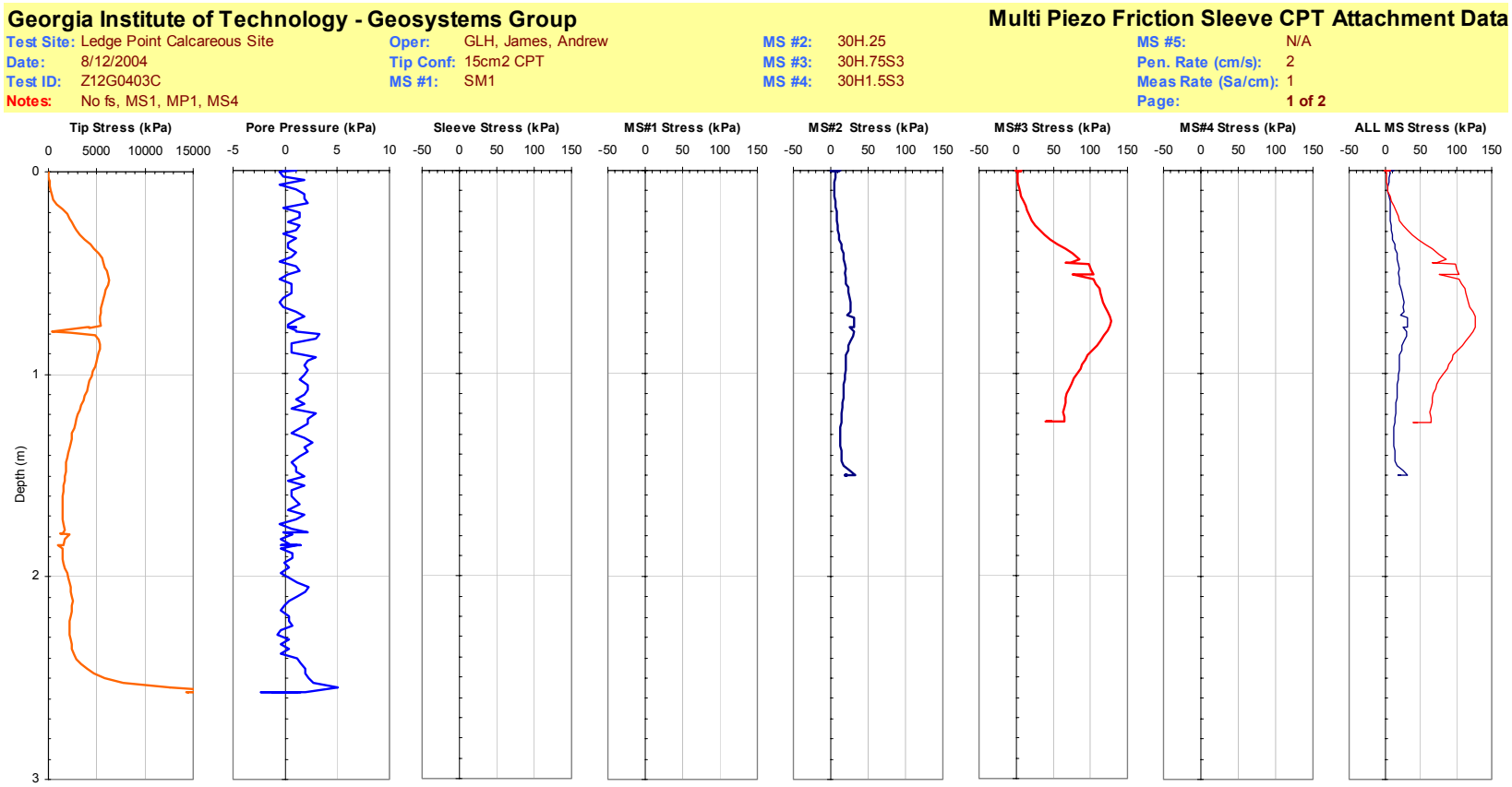

Figure A-98a. Plot of the CPTU and MPFA Friction Sensor Traces from Sounding MPFA_20 at the LPWA Site.

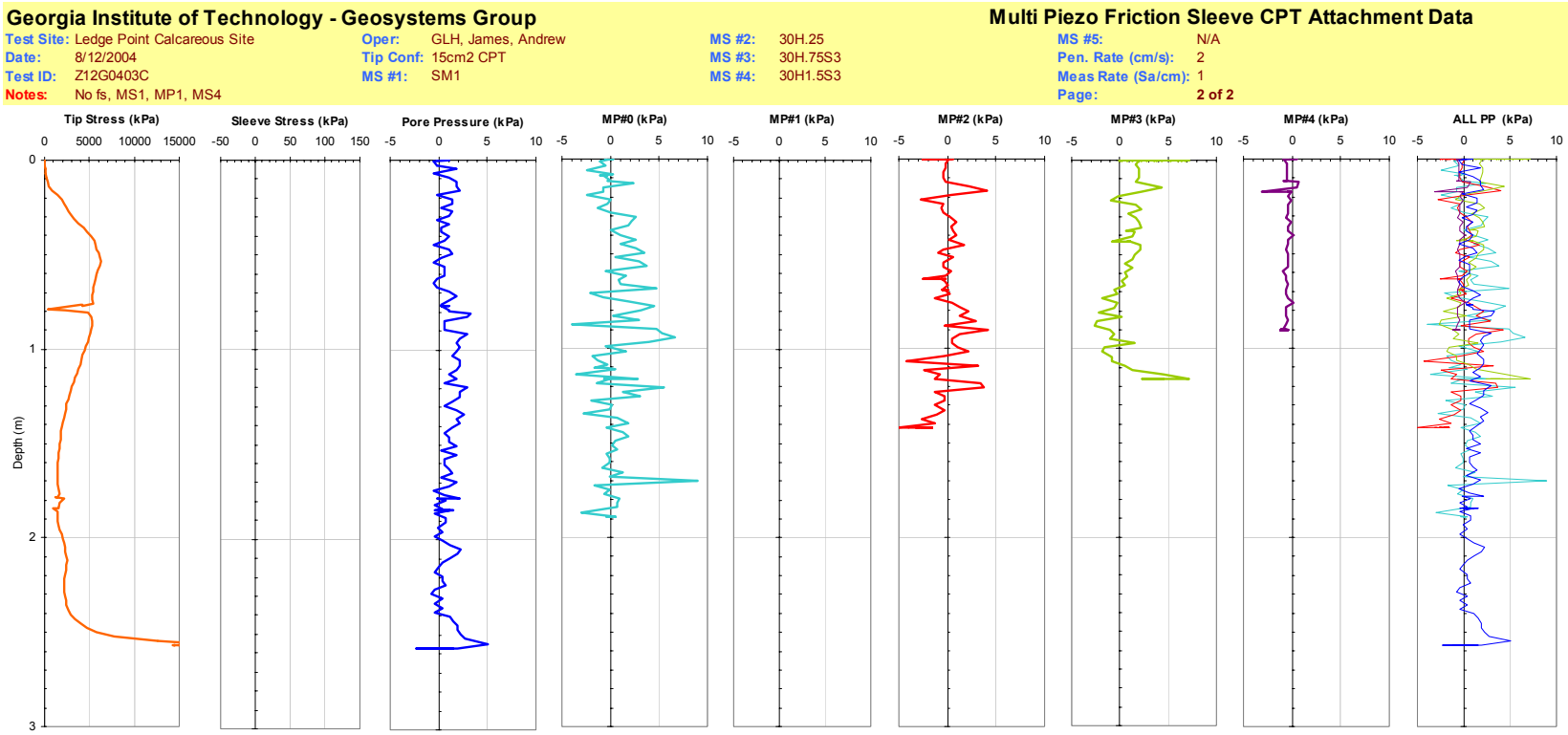

Figure A-98b. Plot of the CPTU and MPFA Piezo Sensor Traces from Sounding MPFA_20 at the LPWA Site.

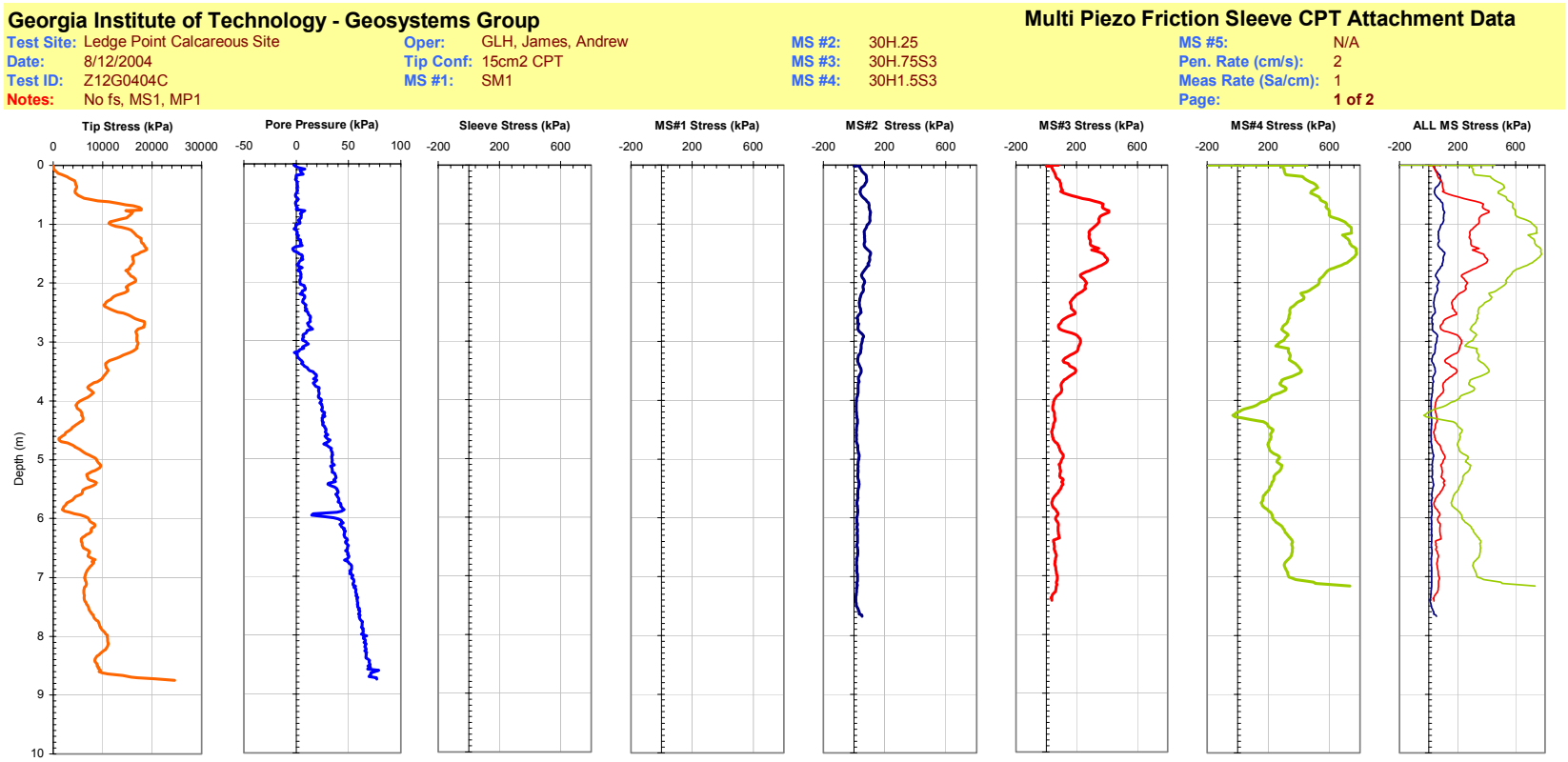

Figure A-99a. Plot of the CPTU and MPFA Friction Sensor Traces from Sounding MPFA_21 at the LPWA Site.

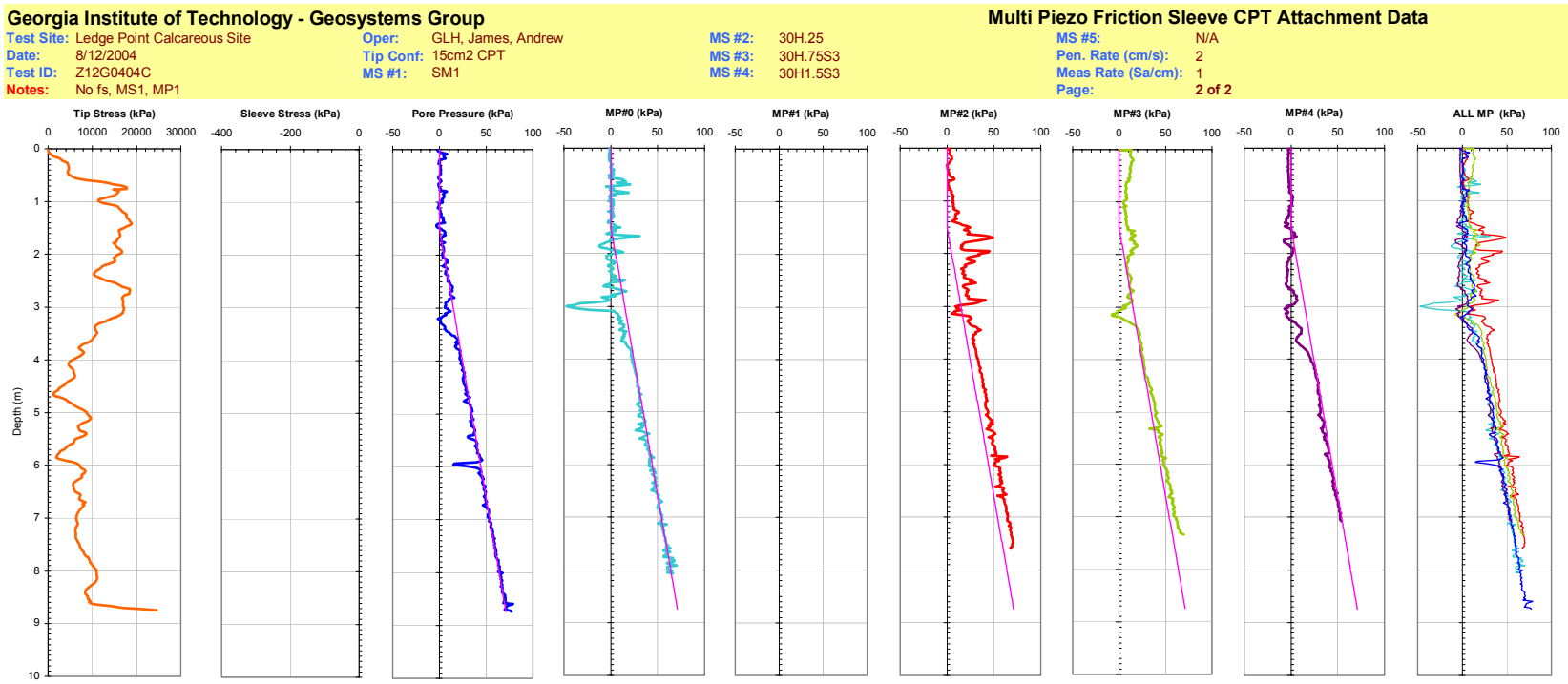

Figure A-99b. Plot of the CPTU and MPFA Piezo Sensor Traces from Sounding MPFA_21 at the LPWA Site.

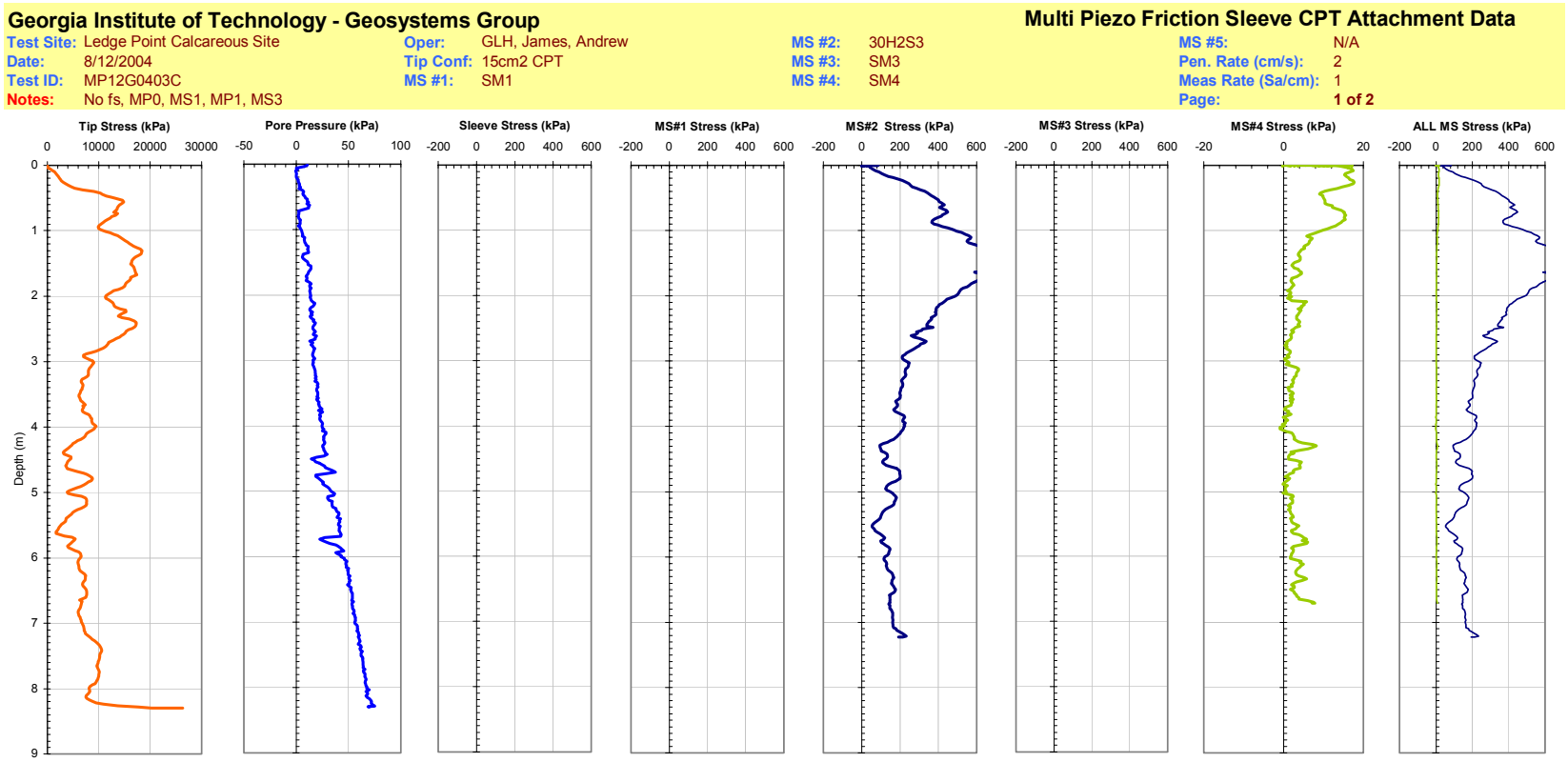

Figure A-100a. Plot of the CPTU and MPFA Friction Sensor Traces from Sounding MPFA_22 at the LPWA Site.

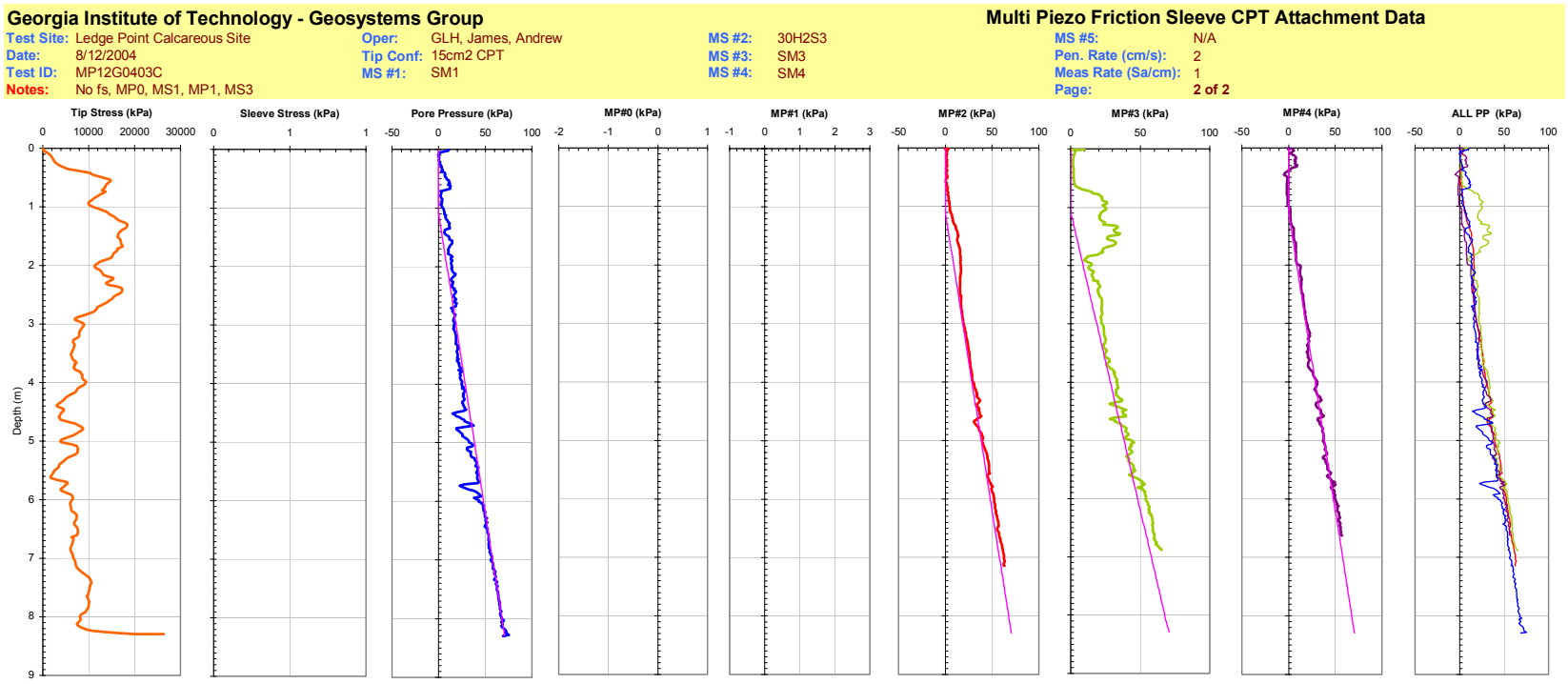

Figure A-100b. Plot of the CPTU and MPFA Piezo Sensor Traces from Sounding MPFA_22 at the LPWA Site.

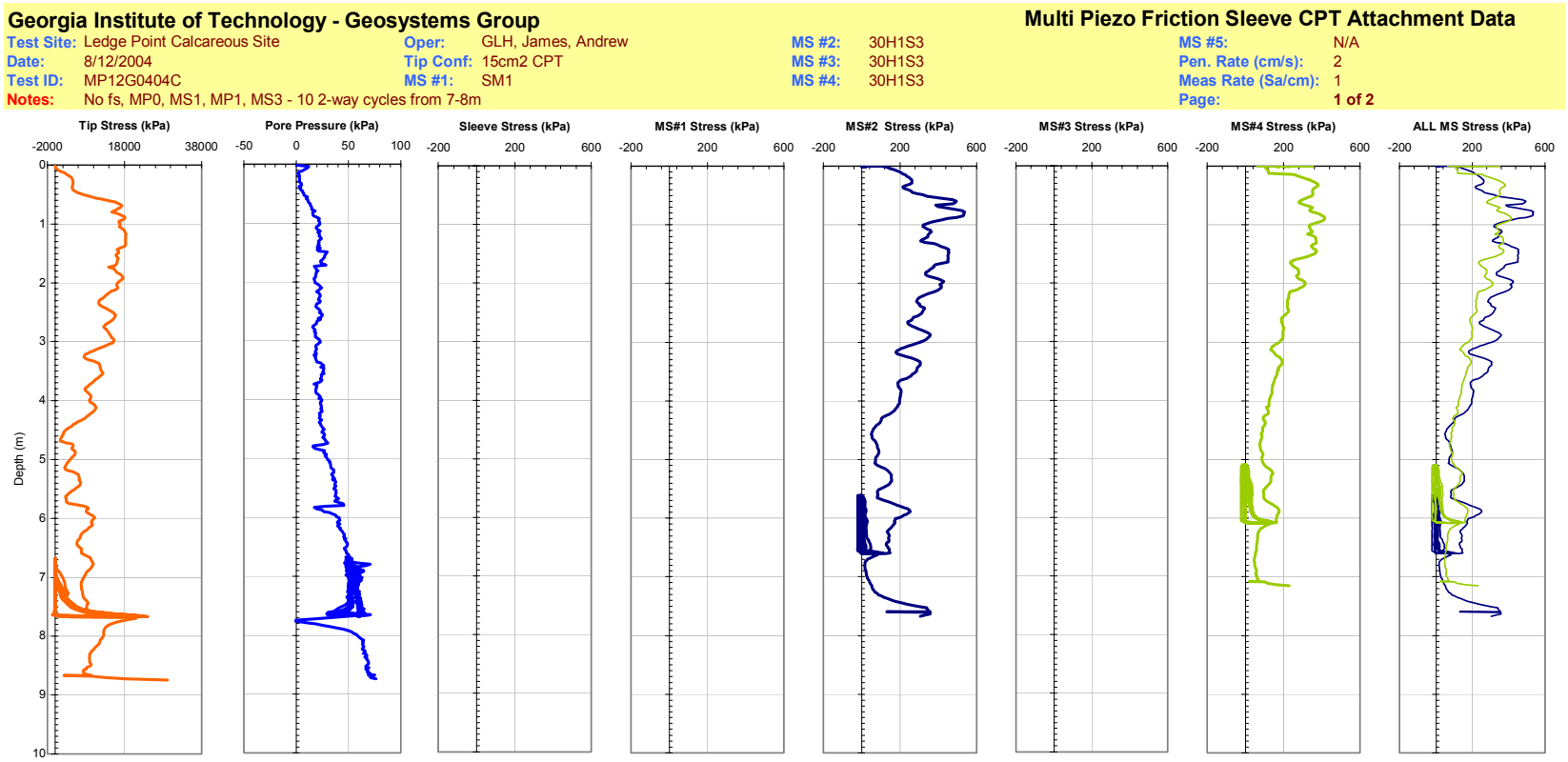

Figure A-101a. Plot of the CPTU and MPFA Friction Sensor Traces from Sounding MPFA_23 at the LPWA Site.

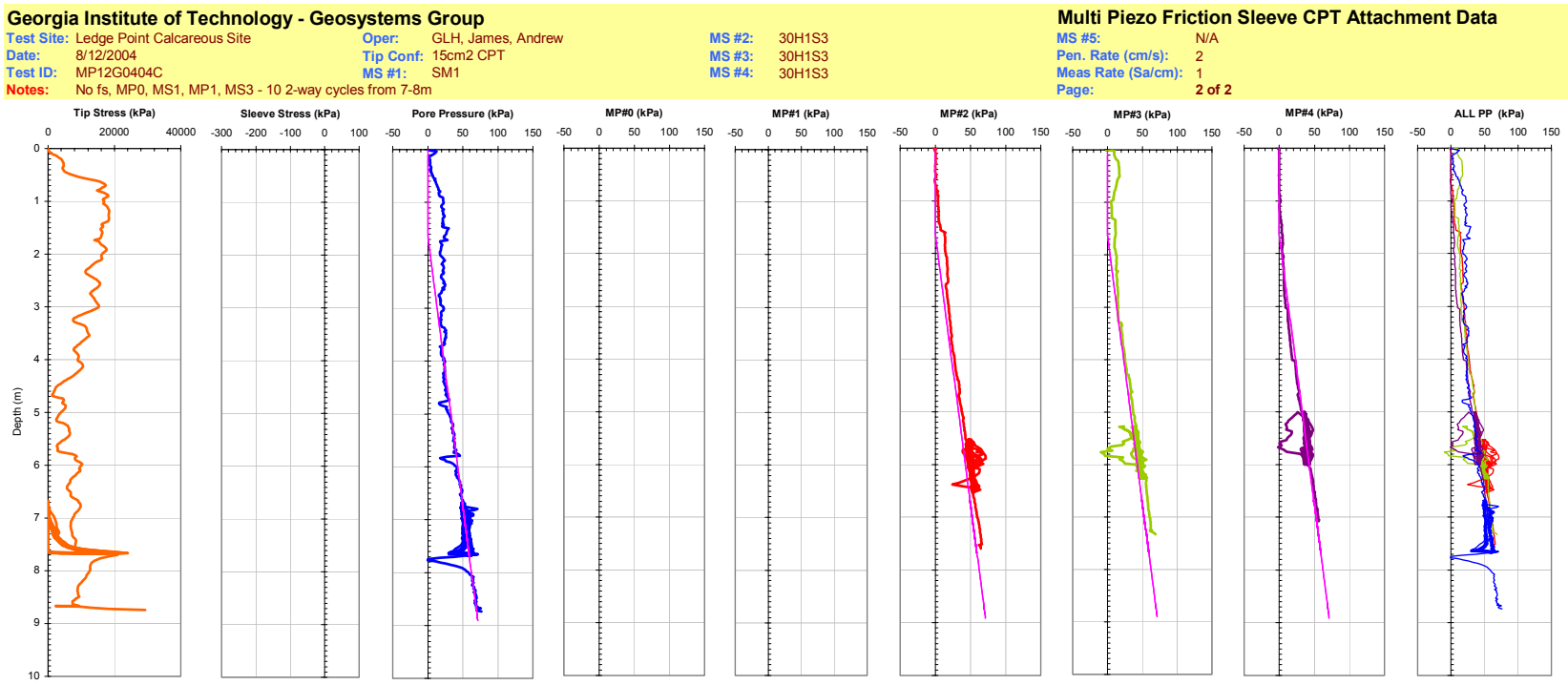

Figure A-101b. Plot of the CPTU and MPFA Piezo Sensor Traces from Sounding MPFA_23 at the LPWA Site.

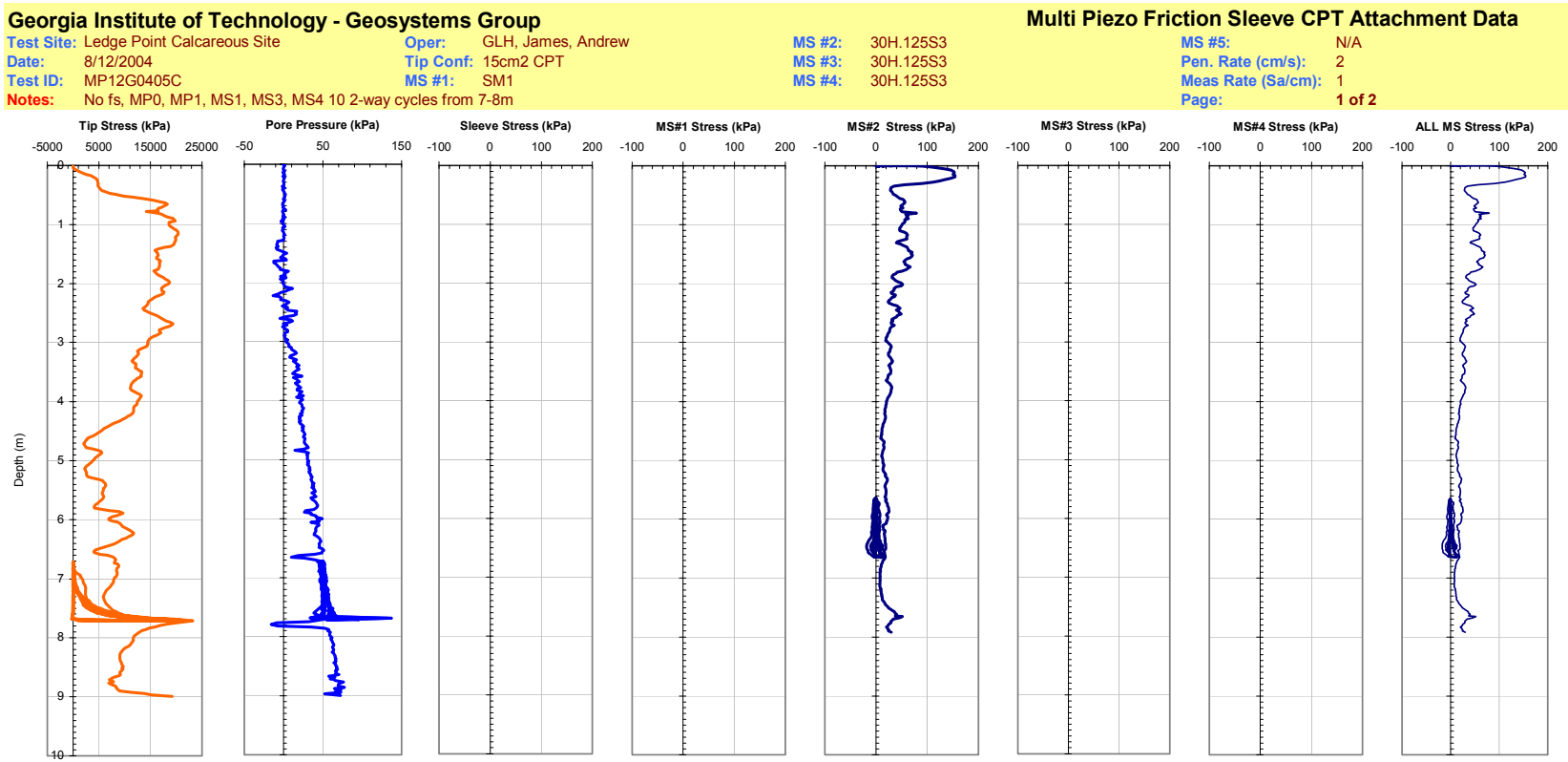

Figure A-102a. Plot of the CPTU and MPFA Friction Sensor Traces from Sounding MPFA_24 at the LPWA Site.

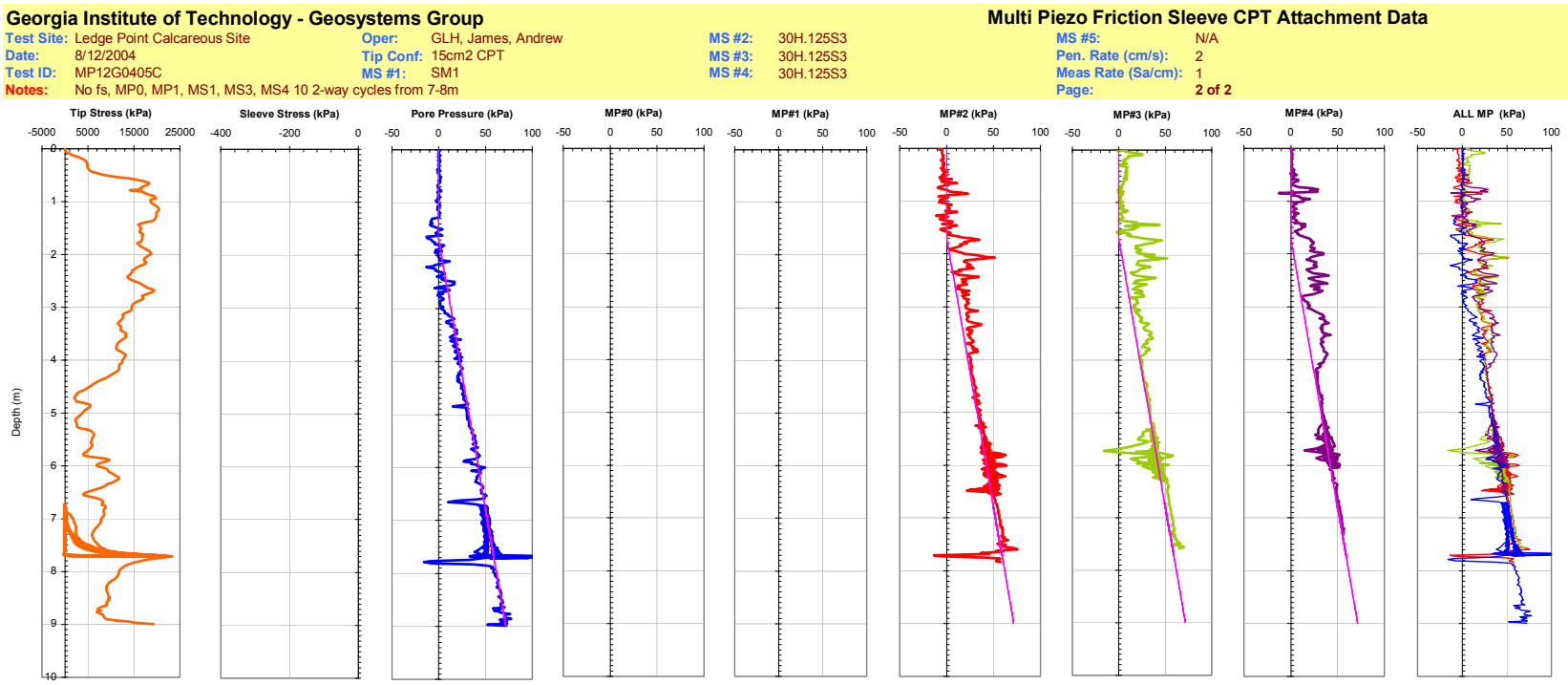

Figure A-102b. Plot of the CPTU and MPFA Piezo Sensor Traces from Sounding MPFA_24 at the LPWA Site.

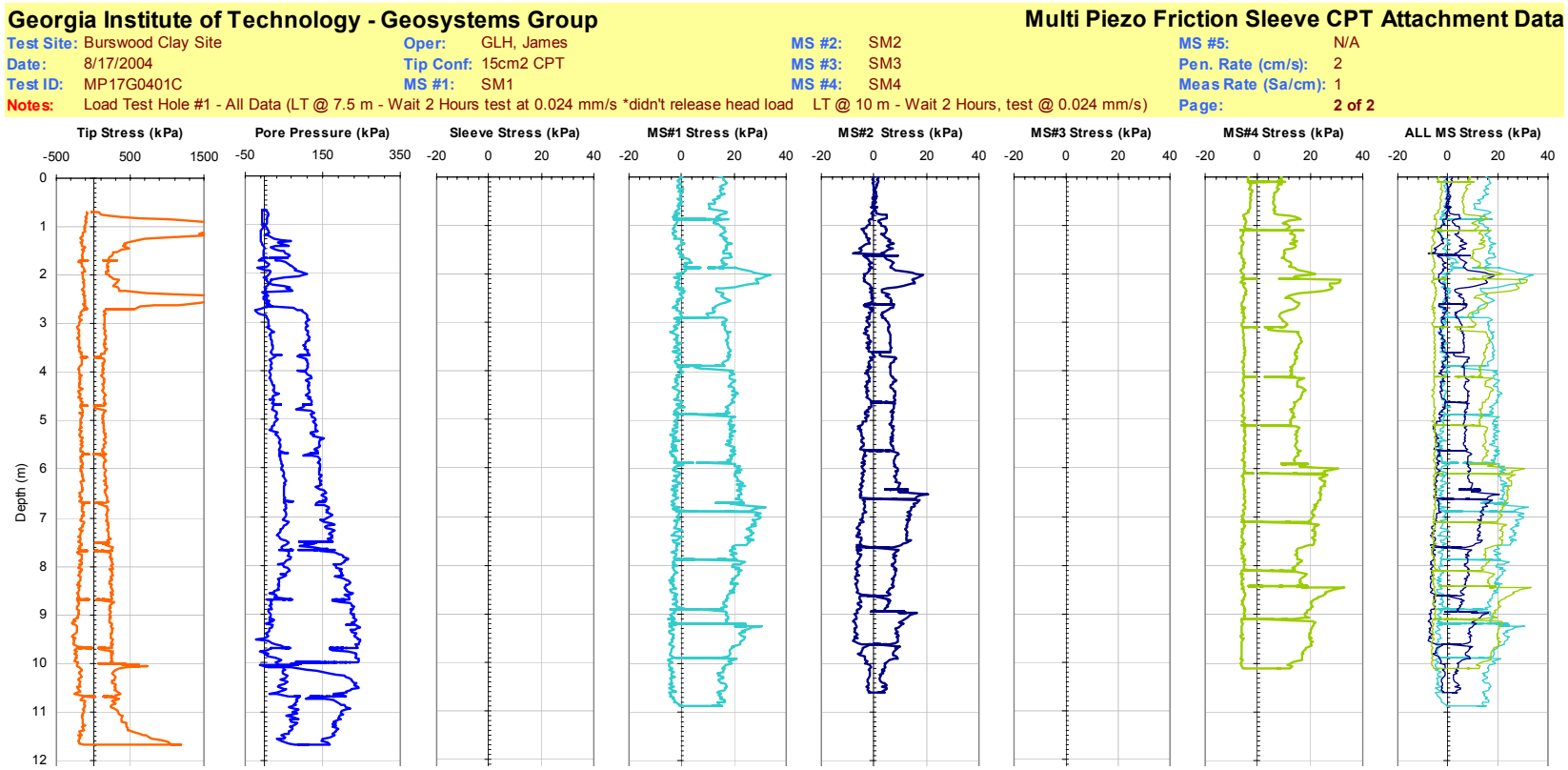

Figure A-103a. Plot of the CPTU and MPFA Friction Sensor Traces from Sounding MPFA_25 at the BWDWA Site.

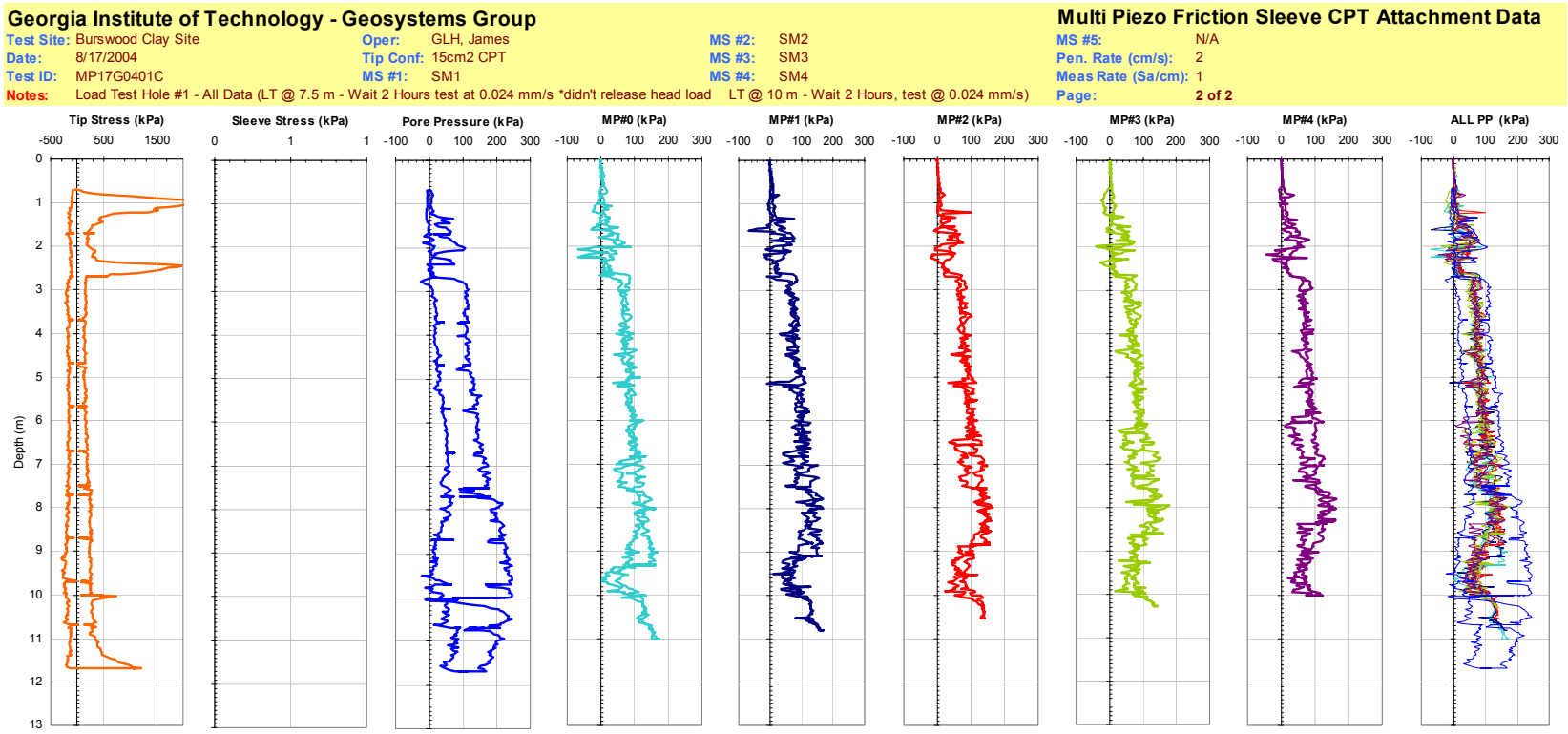

Figure A-103b. Plot of the CPTU and MPFA Piezo Sensor Traces from Sounding MPFA_25 at the BWDWA Site.

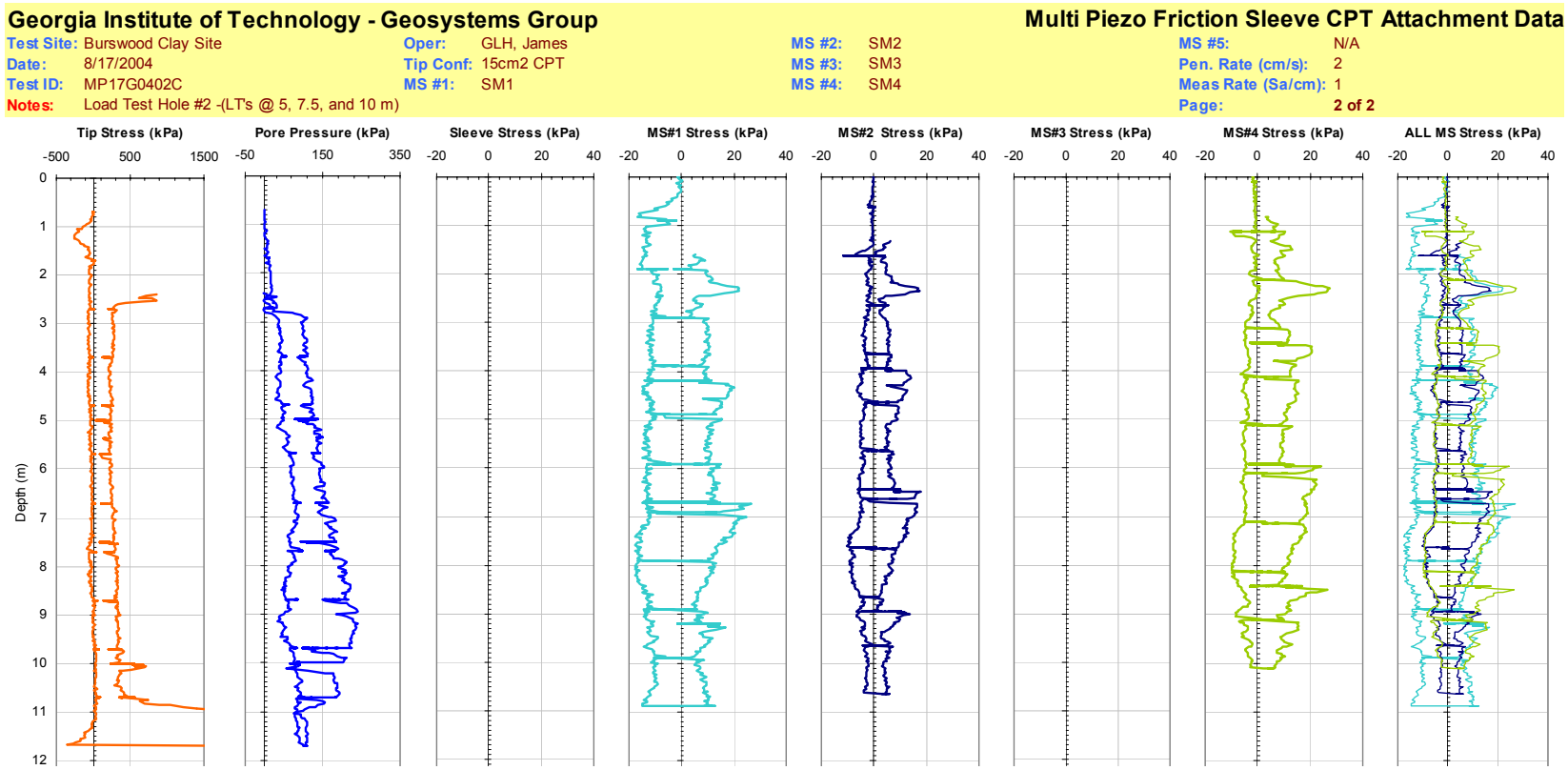

Figure A-104a. Plot of the CPTU and MPFA Friction Sensor Traces from Sounding MPFA_26 at the BWDWA Site.

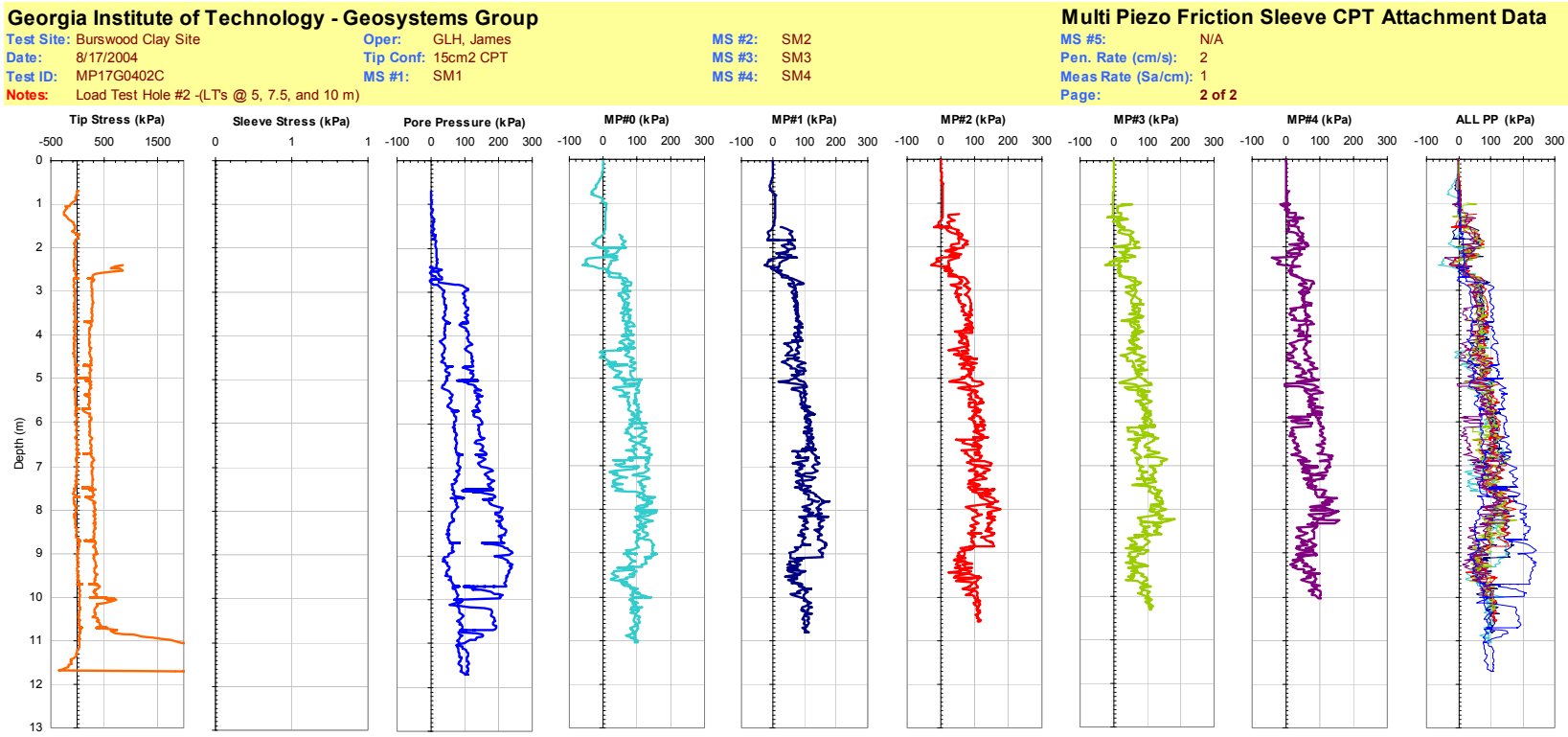

Figure A-104b. Plot of the CPTU and MPFA Piezo Sensor Traces from Sounding MPFA_26 at the BWDWA Site.

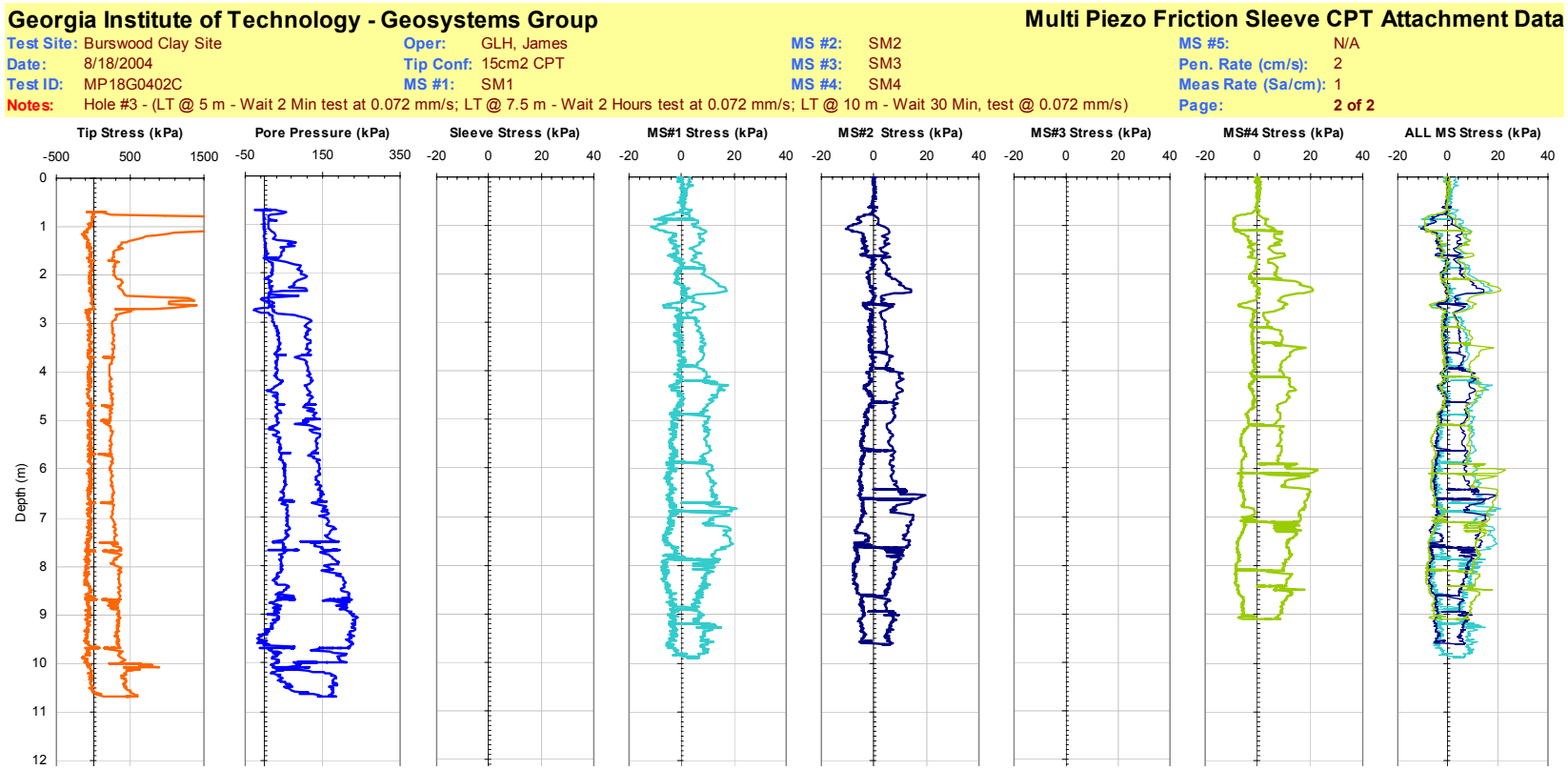

Figure A-105a. Plot of the CPTU and MPFA Friction Sensor Traces from Sounding MPFA_28 at the BWDWA Site.

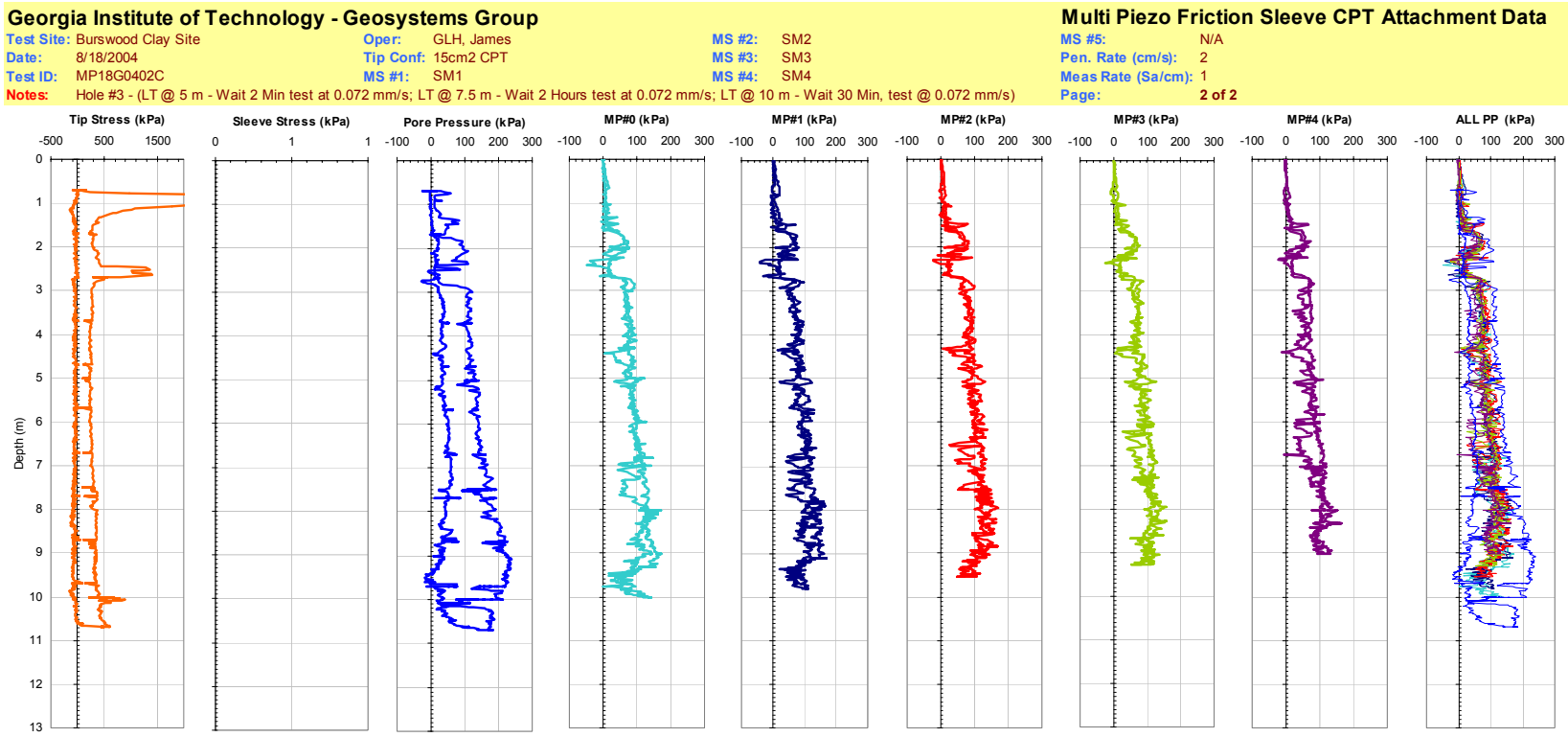

Figure A-105b. Plot of the CPTU and MPFA Piezo Sensor Traces from Sounding MPFA_28 at the BWDWA Site.

VITA

Gregory Lawrence Hebeler was born on February 22, 1978 in Falls Church, Virginia and raised by Robert and Louise Hebeler. Greg is the second of four children, with older brother Jason and younger twin sisters Kimberly and Kayleen providing for countless childhood adventures. Greg spent the majority of his childhood in Medway, Massachusetts after living in Virginia, Maryland, and Florida during his first five years.

Greg attended college at Clarkson University in Potsdam, New York where after a brief stint in chemical engineering, he found that his true calling was to follow in his father's footsteps and study civil engineering. After conducting geotechnical research under the guidance of Dr. Dayakar Penumadu at Clarkson over the summer of 1998, Greg became fascinated with the complexities and creativity afforded by using natural geomaterials in design and construction, and he decided to pursue a graduate degree in the field of geotechnical engineering. With a desire to experience a new part of the country, Greg moved to Atlanta, Georgia to attend graduate school at the Georgia Institute of Technology. Once there, he studied using seismic surface waves to characterize the dynamic soil properties of the near surface under the guidance of Dr. Glenn Rix. His Master's research was focused on improving and expanding the use of surface wave investigations and on providing local velocity measurements to the Mid-America earthquake region near Memphis, Tennessee.

After finishing his Master's degree at Georgia Tech in February of 2001, Greg decided to continue on at Georgia Tech to pursue a PhD in geotechnical engineering. In search of a breadth of geotechnical knowledge, Greg decided to leave the excellent guidance of Dr. Rix to pursue research into geotechnical interface behavior under the

guidance of Dr. J. David Frost. The research conducted with Dr. Frost resulted in a number of fundamental insights into geotechnical interface behavior and the development of a new in situ testing device, culminating in Greg completing his PhD in June of 2005.

During an introductory visit to Georgia Tech in the Spring of 1999, Greg was introduced to Tamara Elizabeth Zettler, then a masters student in geotechnical engineering. Over the course of their only overlapping semester at Georgia Tech, Tammy and Greg became good friends and eventually realized that love really can be found in the proverbial "sand box of life." Greg is to be married to Tammy in October of 2005, and looks forward to their new adventures together as partners in life and in dirt.